iib98

Intergranular and Interphase Boundaries in Materials

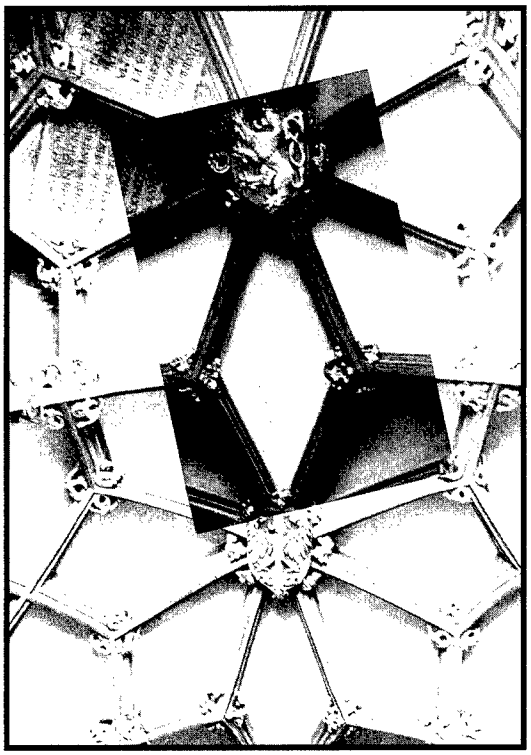

Editors:

Pavel Lejček and Václav Paidar

ttp TRANS TECH PUBLICATIONS

Materials Science Forum

ISSN 0255-5476

As of January 1992 combined with Crystal Properties and Preparation

See back inside cover for scope and subscription information

REPORT DOCUMENTATION PAGE

Form Approved
OMB No. 0704-0188

1. AGENCY USE ONLY *(Leave blank)*	2. REPORT DATE	3. REPORT TYPE AND DATES COVERED
	1999	Conference Proceedings 6 - 9 July 1998

4. TITLE AND SUBTITLE
Intergranular and Interphase Boundaries in Materials (IIB'98)
9th International Conference on Intergranular and Interphase Boundaries in Materials

5. FUNDING NUMBERS
N00014-98-1-1020

6. AUTHOR(S)
Editors: Pavel Lejcek and Vaclav Paidar

7. PERFORMING ORGANIZATION NAME(S) AND ADDRESS(ES)
Dr. Vaclav Paidar
Institute of Physics, Academy of Sciences
Na Slovance 2
180 40 Praha 8
Czech Republic

8. PERFORMING ORGANIZATION REPORT NUMBER

9. SPONSORING/MONITORING AGENCY NAME(S) AND ADDRESS(ES)
Technical Director
Office of Naval Research International Field Office (ONRIFO)
PSC 802 Box 39
FPO AE 09499-0700

10. SPONSORING/MONITORING AGENCY REPORT NUMBER

11. SUPPLEMENTARY NOTES

12a. DISTRIBUTION AVAILABILITY STATEMENT
Approved for public release, distribution is unlimited

12b. DISTRIBUTION CODE

13. ABSTRACT *(Maximum 200 words)*
Compilation of lectures and abstracts from the conference entitled "Intergranular and Interphase Boundaries in Materials (IIB'98) held in Prague, Czech Republic, on 6 - 9 July 1998.

14. SUBJECT TERMS
Key words: grain-boundary, periodic interfaces, GaN, bicrystals, alloys, thin film, HREM, interface, segregation,

15. NUMBER OF PAGES

16. PRICE CODE

17. SECURITY CLASSIFICATION OF REPORT	18. SECURITY CLASSIFICATION OF THIS PAGE	19. SECURITY CLASSIFICATION OF ABSTRACT	20. LIMITATION OF ABSTRACT

Intergranular and Interphase Boundaries in Materials

Intergranular and Interphase Boundaries in Materials

Proceedings of the 9th International Conference on Intergranular and Interphase Boundaries in Materials (iib98), held in Prague, Czech Republic, July 1998

Editors:

Pavel Lejček and Václav Paidar

TRANS TECH PUBLICATIONS LTD
Switzerland • Germany • UK • USA

Front cover illustration:

Vaulting on ceiling of the king bedroom of the Vladislav Palace of the Prague Castle (Hradčany) from 15th century with the historical Bohemian (up) and Moravian (bottom) coats-of-arms. Illustration design by Eva Lejčková, photograph by Renata Louvarová.

ISBN 0-87849-823-0

Volumes 294-296 of
Materials Science Forum
ISSN 0255-5476

***Distributed** in the Americas by*

Trans Tech Publications Inc
PO Box 699, May Street
Enfield, New Hampshire 03748
USA
Phone: (603) 632-7377
Fax: (603) 632-5611
e-mail: ttp@ttp.net
Web: http://www.ttp.net

and worldwide by

Trans Tech Publications Ltd
Brandrain 6
CH-8707 Uetikon-Zuerich
Switzerland
Fax: +41 (1) 922 10 33
e-mail: ttp@ttp.net
Web: http://www.ttp.net

Printed in the United Kingdom
by Hobbs the Printers Ltd,
Totton, Hampshire SO40 3WX

ORGANIZING COMMITTEE

Václav Paidar (Chairman)
Marcela Boháčková (Secretary)
Juliana Gemperlová
Jan Kočík
Pavel Lejček
Přemysl Málek
Petr Šittner
Mojmír Šob

INTERNATIONAL ADVISORY BOARD

G.L. Bleris (Greece)
A. Bourret (France)
D.G. Brandon (Israel)
D.R. Clarke (USA)
R.G. Faulkner (UK)
M.A. Fortes (Portugal)
W. Gust (Germany)
S. Hashimoto (Japan)
E.D. Hondros (UK)
R. Kirchheim (Germany)
R.C. Pond (UK)
V. Pontikis (France)
L. Priester (France)
S. Ranganathan (India)
M. Rühle (Germany)
D.N. Seidman (USA)
A. Serra (Spain)
L.S. Shvindlerman (Russia)
A.P. Sutton (UK)
J. Thibault (France)
V. Vitek (USA)
T. Watanabe (Japan)
M.J. Yacaman (Mexico)

LIST OF SPONSORS

Institute of Physics of the Academy of Sciences of the Czech Republic

Union of the Czech Mathematicians and Physicists

European Commission, DG XII, Science, Research and Development

Office of Naval Research International Field Office – Europe and
European Office of Aerospace Research and Development, UK

VÍTKOVICE, a.s.

AR Tour Ondráček

Magnox Electric, plc.

Nuclear Research Institute Řež, plc.

Preface

The 9th International Conference on Intergranular and Interphase Boundaries in Materials (*iib'98*) held on 6–9 July 1998 in Prague, Czech Republic, represents a successful continuation of the series of this Conference starting by the first meeting in Saint Etienne, France, in 1975. Following the scope of the preceding meetings, this Conference was focused on atomic level modeling of interfaces, structural and chemical characterization of internal interfaces, their thermodynamic, kinetic, mechanical, electric, magnetic behavior and high-T_c superconductivity, and application of present knowledge for design of polycrystalline materials with improved properties. More than 200 scientists from 27 countries of four continents actively participated in the meeting. Traditionally, a special symposium on an actual topic has been organized as a part of the Conference: During *iib'98*, the attention was paid to Non–Equilibrium Segregation in Irradiated Materials. A particular session was devoted to presentation of the results obtained during the International Cooperation in Science and Technology (COST).

The contributions presented at the *iib'98* are published in this volume. Nearly 200 papers that cover all above mentioned topics were presented as invited talks, oral contributions and – in the vast majority – posters. These papers bring new results in the study of interfaces and their properties obtained in the last years, and represent the present state of the art in this field. We are grateful to all referees for their assistance in preparation of this volume.

Successful organization of the Conference could not be possible without financial support of the sponsors. We would like to acknowledge all the sponsors for their help, we also appreciate financial support of the COST organization. Last but not least, we wish to thank for hospitality of our host, the National House of Vinohrady where the Conference took place.

The Editors

Table of Contents

Invited lectures

Contributions

Materials Science Forum Vols. 294-296 (1999) pp. 1-8

Wetting of Grain Boundaries in Metals and Ceramics

D.R. Clarke

Materials Department, University of California, Santa Barbara, CA 93106-5050, USA

Keywords: Grain Boundaries, Wetting, Intergranular Films, Segregation

Abstract. Observations of the wetting of grain boundaries in metals and ceramics are reviewed. Systematics of grain boundary wetting are introduced and the conditions for penetration of a liquid down a grain boundary presented. These concepts are sufficient to describe the macroscopic wetting behavior, such as the macroscopic contact angle, but are insufficient to describe the occurrence of thin (~ nm) intergranular films seen in some ceramics. These films require the existence of attractive and repulsive forces on the nanometer length scale. Observations by high resolution electron microscopy are necessary to establish whether intergranular films form in the metallic systems that exhibit wetting and hence whether such forces are also operative in metal systems.

1. Introduction

During the last decade or so, a series of experiments have been performed that challenge our understanding of the fundamentals of wetting of grain boundaries. As will be summarized in the following section, two types of observations of wetting have been reported. The first consists of macroscopic observations on the temperature and pressure dependence of wetting of "special" boundaries in metal bicrystals by simple liquid metals. The sceond is a series of observations, made primarily by high resolution electron microscopy, of grain boundaries in liquid-phase sintered ceramics. Although the observations are superficially similar it is likely that they represent two rather contrasting wetting behaviors, one in which surface forces play an important role and the other in which they are relatively unimportant.

2. Observations of Wetting

Although many experiments have been performed on a variety of metallic systems, amongst the most revealing are those that originated from work in the former Soviet Union seeking phase transitions in the wetting behavior of well-defined boundaries in metal bicrystals in contact with simple metals as a function of temperature and pressure [1-4]. These experiments are based on what might be termed a "penetration experiment"; the sample containing a grain boundary is placed in contact with a liquid and the conditions under which the liquid penetrates down the grain boundary are determined. Some experiments are the reverse, namely, the conditions are sought under which the liquid along a grain boundary is expelled. Whether the boundary was wet or not, was determined, after cooling, by compositional analysis using electron probe X-ray microanalysis and observations of the contact angle in cross-sections using optical microscopy. An important consideration is that these observations have a spatial resolution of no better than about one micron. From such experiments, the investigators have demonstrated that there exists a critical confining pressure to cause dewetting of Fe-Si by molten Zn [2] and a critical temperature above which a tin-rich melt will wet a tilt grain bounadry in Fe-5 a/o Si [1]. A possibly significant fact is that, at ambient pressure, the dewetting temperature appears to coincide with that of an ordering phase transformation in the solid phase, such as magnetic ordering in the Fe-Si alloys. Although the number of such careful and well-defined experiments performed to date is small, the phemonmena observed conform to expectations of wetting based on rather classical grounds.

The second class of revealing experimental observations are drawn from studies of the microstructures of ceramic systems [5-10]. The number of experiments performed is

considerably larger but, because of the lack of suitable bicrystals, have all been performed on polycrystalline materials, initially silicon nitride ceramics but more recently on zinc oxide varistors, ruthenate based thick-film resistors, debased aluminas and fiber composites. A common feature of the high resolution electron microscopy observations is that these materials commonly have a thin (~ 1nm) thick film along the grain boundaries. Although the existence of these thin films was first discovered in 1977 [5], observations with new generations of electron microscopes have confirmed the original reports [6-8] that the thickness of these films is constant from boundary to boundary and depends on the additives used in fabricating the ceramic. Similar high resolution observations of ruthenate thick-film resistors, which consist of percolating chains of ruthenate particles enveloped in a solidified amorphous matrix, also showed that the particles were separated by a ~ 1 nm film [9]. These observations also provided the earliest unequivocal evidence for the composition of the thin-film being different from that of the bulk of the liquid phase, a result since substantiated by several electron energy loss spectroscopy studies of the grain boundary films in silicon nitride ceramics [10]. The discovery that thin films separated the ruthenate grains are also of significance since they indicate that the films can exist in the absence of any capillary pressure within the liquid phase. This, again, has subsequently been reported in silicon nitride systems.

A number of penetration experiments have been performed on the ceramic systems but the results are less clear cut than those reported on the metallic bicrystals. When high purity alumina was embedded in a chemically compatible calcium aluminum silicate melt, the ceramic disintegrated with the individual grains dispersing [11]. Similar observations were made when a number of polycrystalline ceramics, including alumina, MgO and spinel, were exposed to LiF vapor [12]. In these studies, though, there remains some doubt as to whether the liquid phase was truly in chemical equilibrium with the ceramics. More recently, penetration experiments in which polycrystalline ZnO was exposed to molten Bi2O3 have shown that no penetration occurs if the Bi2O3 was saturated with ZnO but occurs if it were pure Bi2O3 [13].

As yet, no dewetting temperature has been found for any of the silicon nitride ceramics but there is clear evidence that cooling ZnO varistor ceramics below the eutectic temperature causes the liquid phase to retract from the grain boundaries to the triple grain junctions and leave behind a thin layer of segregated Bi along the grain boundaries [14,15]. The grain boundary film can also be removed by application of a confining pressure. The actual pressure at which this occurs has not been identified but pressures of 1 GPa at 700°C are reported to be sufficient in the one experiment reported [16]. In creep experiments on silicon nitride ceramics, it has been reported [17] that the thickness of the intergranular film is decreased along the compression direction and increased in the tensile direction but these studies are, understandably, not as quantified as those using a hydrostatic pressure.

Finally, although the experiments are of a different character, it has been shown that the wetting and dewetting behavior of the silicate liquid phase in zirconia can be controlled by the oxygen partial pressure in the sintering atmosphere [18]. These experiments emphasize the role played by the vapor phase in affecting the wetting behavior of grain boundaries.

This brief and incomplete summary of the observations made on metals and ceramics inevitably raise a number of questions, including whether the nanometer thick films observed along grain boundaries in the ceramics are manifestations of true wetting, whether they would be seen in the metallic systems or are peculiar to ceramics and whether their occurrence and thickness are a consequence of the very different bonding in the ceramics. In the following sections, an attempt is made to address these questions using continuum concepts of wetting incorporating, where appropriate, the effect of surface and intermolecular forces. It is, of course, important to emphasize that there are many ceramic materials in which thin intergranular films have not been observed just as there are many metallic materials which do not exhibit grain boundary wetting.

3. Systematics of Grain Boundary Wetting

To establish a consistent description of both free surface and grain boundary wetting the closed thermodynamic system shown schematically in figure 1 is considered. It consists of a solid (with flat sides), containing a single, flat grain boundary, which is in contact with the vapor from a reservoir of a liquid phase within the container. (Figure 1). For completeness, an external pressure, P, can also be applied to the system. The solid is, initially, considered to be isotropic so that issues related to crystalline anisotropy can be ignored. The behavior of the system is now considered in a Gedanken experiment as the vapor pressure is increased.

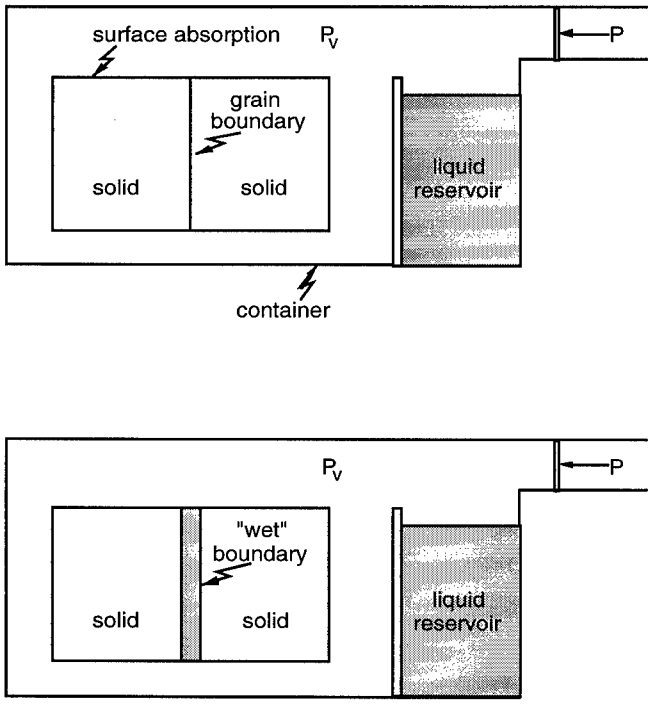

Figure 1. Thermodynamic system used to define grain boundary wetting.

The wetting behavior of the free surfaces is well known: At vapor pressures below the saturated vapor pressure, surface adsorption occurs with the thickness of the adsorbed layer being dependent on the surface contact angle. As the saturated vapor pressure is approached, the film thickness diverges and a film of macroscopic thickness forms. This, in fact, defines the saturated vapor pressure. At each vapor pressure, thermodynamic equilibrium requires that the vapor species enters into the solid as a solute with the concentration being given by the partition coefficient. As this occurs, adsorption to the grain boundary must also occur as the vapor pressure is increased. This is usually described as grain boundary segregation. The thickness of this segregated layer, which can be expressed either as a physical thickness or as a surface excess, and how it depends on the vapor pressure has not been specifically addressed until recently. A more detailed discussion will be presented later. At some vapor pressure, the thickness of the adsorbed layer along the grain boundary diverges and the grain boundary is said to be "wet". In principle, there does not seem to be any physical reason why the vapor pressure at which this occurs should be equal to the saturated vapor pressure. However, it is important to emphasize that adsorption must precede wetting.

This thought experiment allows us to now compare the energy of the wetted grain boundary with the same boundary but in its unwetted state. Specifically, the basis of the comparison is the energy with a wetted film compared with that of the same boundary but

with the adsorption on the boundary determined by the vapor pressure. If the liquid is perfectly wetting the free surface, then the thought experiment provides the insight that grain boundary wetting is energetically preferred when the following condition is satisfied:

$$2\gamma_{SL}(\varphi)<\gamma_{SS}(\varphi) \qquad (1)$$

where γ_{SS} and γ_{SL} refer to the interfacial energies of the solid-solid grain boundary and the liquid-solid interface, respectively. (The angular dependency is included to describe the more general case when the solid is crystallographically anisotropic. This suggests that if the boundary can move to alter its crystallographic orientation, for instance by facetting, then it may locally dewet or wet depending on whether it thereby can lower its energy). Whilst this inequality has the familiar form used in the majority of articles describing grain boundary wetting it is important to emphasize that the solid-solid interfacial energy γ_{SS} is that of the grain boundary with adsorption not the grain boundary energy at zero vapor pressure. The additional point to note is that the inequality is merely a *necessary* but not a *sufficient* condition for wetting.

4. Grain Boundary Penetration As A Phase Transition

As the penetration experiment is one of the key tests of grain boundary wetting, we discuss in the following the wetting behavior of a partially wetting droplet of liquid on the surface of a solid and in contact with a grain boundary intersecting the surface, such as shown in figure 2 and corresponding to a higher magnification view of the intersection in figure 1. A more complete, analytical treatment has recently been published in reference 19.

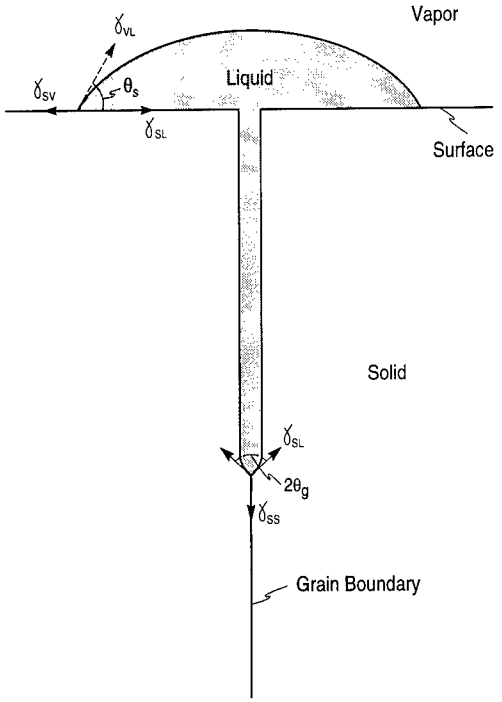

Figure 2. Droplet of liquid phase partially wetting both the free surface and the grain boundary. Changes in the contact angles at the surface and in the grain boundary will cause redistribution of the liquid phase.

There are a number of key insights revealed by such a variational calculation. First, there is a broad range of dimensional wetting parameters over which grain boundary wetting is energetically preferred. Indeed, as indicated by figure 3, wetting is preferred for most conditions. The second insight is that in the vicinity of the critical grain boundary wetting parameter, k_b, there is an abrupt transition between a grain boundary being wet and not being wet. The third important insight is that for all the equilibrium configurations, the pressure everywhere in the liquid phase is equal suggesting that distribution of the liquid between the surface and the grain boundary occurs until there is no variation in pressure within the liquid. In essence, this is a hydraulic condition. The fourth insight

is that near the critical wetting condition, small changes in the parameter, even those that might occur as a result of a phase transition in the bulk, may drive the wetting-dewetting transition.

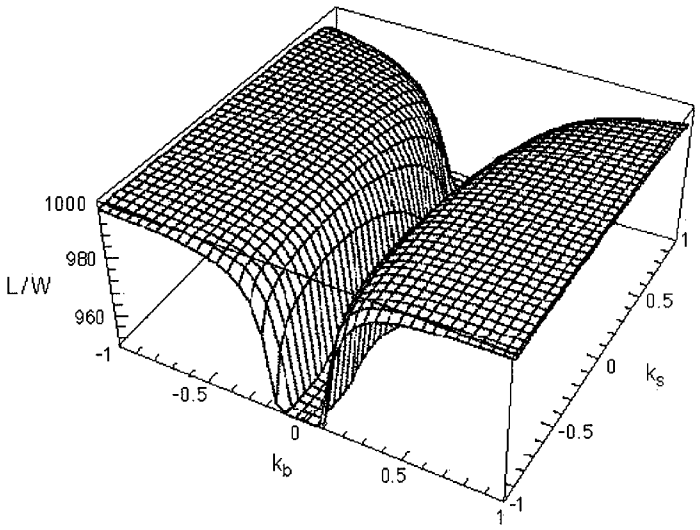

Figure 3. Grain boundary wetting, as indicated by the wetted length along the grain boundary, is preferred for all wetting parameters except near kb=0 where abrupt dewetting occurs. For dimensional reasons, the length is normalized by the film thickness.

The foregoing analysis can be extended to consider the effect of an applied pressure and relies on there being a partial molar volume difference between the liquid and solid species. As before, there are, strictly, two distinct cases to consider, the first when the free surface is perfectly wet and the second when it is only partially wet. In the former case, because of the difference in molar volume, the effect of pressure is to dewet the grain boundary if the partial molar volume of the liquid id lower than that of the solid. This has been discussed by both Lee et al. [16] and Rabkin et al.[2]. In the second case, the effect of pressure is more problematic since the effect of external pressure on the surface contact angle must also be considered.

5. Effect of Surface Forces

The preceding continuum analysis implicitly assumes that in wetting the grain boundary there is no interaction energy between the adjacent grains and so the energy gained, per unit, by wetting the boundary is simply $\gamma_{SS}(\varphi)-2\gamma_{SL}(\varphi)$ and is independent of the grain separation. (As mentioned above the effect of segregation to the grain boundaries is strictly included in this expression). In the absence of any interaction between the grains across the wetting film, the thickness of the film is indeterminate. In the limit of a large volume of liquid, the thickness diverges and the individual grains will disperse and move randomly under the effects of thermal agitation and gravitational forces. This is the

behavior seen in the penetration experiments performed by Shaw et al. [11] and is the behavior believed to occur at high temperatures during liquid phase sintering. However, it is clearly not the behavior seen in the penetration experiments on silicon nitride, those on ZnO with the Bi2O3-ZnO liquid phase and in the microstructures of the ruthenate containing glasses. These all suggest that the particles are attracted to one another to form a network structure with a ~ 1nm film in between each particle or grain. Comparison of these two contrasting behaviors brings to mind the similar behavior of colloidal particles suspended in a liquid. When the interactions between the particles is repulsive or when the temperature is sufficiently high to overcome attractive interactions, the particles disperse. However, when there is a long-range attractive force and a short-range repulsive force, the particles together form a network and they are separated by a thin film of liquid. By analogy, it has been suggested [20] that the intergranular films observed in the ceramics are also stabilized by intermolecular forces. This was placed on a formal basis in references 20 and 21, and the analysis has subsequently been elaborated upon. The essential physics is that an equilibrium film thickness is a result of a competition between attractive van der Waals interactions and a repulsive force. The nature of the repulsive force that might be acting has not yet been identified. Amongst the possible forces are some form of structural force associated with the distortion of the steric arrangement of the atoms or molecules in the film, an electrostatic repulsion and an elastic repulsion. These can typically be characterized by an exponential decay in force with distance. The competition between the power law van der Waals attraction and an exponential repulsion naturally leads to the possibility of a local energy minimum as a function of distance which would result in an equilibrium film thickness.

The appeal of this type of analysis is that since the length scales of these interactions is of the order of nanometers, it naturally leads to an equilibrium film thickness that is also of the order of a nanometer. A further feature is that the equilibrium thickness is sensitive to both the composition of the liquid phase and the solid phase through the pertinent solubilities and the dielectric properties of each phase. The detailed calculation of these interactions is complicated [20]. However, the magnitude of the attractive van der Waals force, Π_{VDW}, is given by the integral of the dielectric permittivity, ε, over all frequencies, ξ:

$$\Pi_{VDW} = \frac{h}{16\pi^3 d^3} \int_0^\infty \left[\frac{\varepsilon_{solid}(i\xi) - \varepsilon_{liquid}(i\xi)}{\varepsilon_{solid}(i\xi) + \varepsilon_{liquid}(i\xi)} \right]^2 d\xi \qquad (2)$$

where d is the grain-grain separation and h is Planck's constant. In addition to the cubed distance dependence, perhaps the most important feature of this attraction is the dependence on the *difference* in dielectric permittivity of the solid grains, assumed to be the same on either side of the boundary, and the intervening liquid. Clearly, the attractive force will be greatest for materials with low permittivity and be smallest for materials with high permittivity.

Whilst the effect of surface forces can be analyzed using continuum models, as has been described [20], the observed intergranular film thicknesses are very close to the length scale at which the models are not strictly applicable and a discrete, atomistic description may be more appropriate. Some progress is being made in this direction but the essential difficulty is that the majority of atomistic potentials are not well characterized at the pertinent length scales. Further, the potentials are commonly cut-off at such distances to make the computations tractable. The real advantage of computer simulations, however, may be to address specific questions such as the location of solute ions in an intergranular film rather than calculating the thin thickness. An excellent example of this is the recent computations of the configuration of silica molecules at a grain boundary in alumina with different concentrations of calcia additions [22]. These indicate that Ca ions preferentially segregate to the two alumina/silica interfaces rather than being randomly distributed through

the thickness of the film. Whether the same behavior occurs in the intergranular film in silicon nitride ceramics remains to be established but if it does it would provide supporting evidence for the effect of calcia additions affecting the intergranular film thickness through contributions to a double layer repulsion as proposed by Tanaka et al.[8].

6. Wetting, Segregation and Intergranular Films

The observations described and the arguments presented above naturally raise the question as to how grain boundary wetting, segregation and the existence of intergranular films are related to one another. It is relatively straightforward to argue, by analogy to the free surface wetting behavior, that grain boundary wetting corresponds to the case in which there is an indeterminate thickness of liquid phase at the boundary and that segregation corresponds to the presence of a monolayer or two of segregant. Less straightforward to classify are the one-to-two nanometer thick intergranular films seen in certain ceramics. One approach is to describe such films as multi-layer segregation as Cannon has done [23]. The other is to describe them as liquid films those thickness is determined by inter-surface forces as briefly summarized above. Whether these two apparently different descriptions are really the same remains as a challenge. Interestingly, both approaches lead to the conclusion that the composition of the intergranular film will invariably be different than that of the liquid phase in bulk equilibrium with the solid. For the liquid film approach this follows from a diffuse interface description [24]. Some of the pertinent details are given in the paper by Bobeth at this conference. The diffuse interface description also leads naturally to the existence of a critical temperature at which the intergranular film thickness diverges. The implication is that this corresponds to the wetting temperature but this has not been proven.

The discovery of thin intergranular films in a number of ceramics suggests that it would be worthwhile to also examine by high resolution microscopy the grain boundaries in the wetted metals below their wetting temperature. This is a difficult proposition for the Fe-Si alloys because of their inherent ferromagnetism but should be substantially simpler for the Al bicrystals wet by the Sn-Pb alloys [3]. However, the substantially larger dielectric permittivities of the metals, relative to those of the silicates, would suggest that the van der Waals attraction should be considerably smaller and hence there may well be insufficient stabilization for an intergranular film to form. However, if intergranular films are indeed found, it would provide further impetus for investigating the effects of multilayer adsorption at grain boundaries and re-assessing the possible origins of interparticle interactions in metals.

Acknowledgments. It is a pleasure to acknowledge the collaborations in recent years with my colleagues in Germany, principally Professors Ruhle and Pompe and Dr. Bobeth. This work is supported in part by the National Science Foundation under grant DMR9616784.

References

[1] E. I. Rabkin, V. N. Semenov, L. S. Shvindlerman and B. B. Straumal, Acta Met., **39** 627 (1991)
[2] E. I. Rabkin, W. Gust, W. Lojkowski and V. Paidar, Interface Sci., **1** 201 (1993).
[3] B. Straumal, D. Molodov and W. Gust, Mater. Sci. Forum, **207-209** 437 (1996)
[4] B. Straumal, E. Rabkin, W. Lojkowski, W. Gust and L. S. Shvindlerman, Acta Mater, **45** 1931 (1997).
[5] D. R. Clarke and G. Thomas, J. Am. Ceram. Soc, **60** 491 (1977).
[6] D. R. Clarke, in *Surfaces and Interfaces in Ceramic Materials* edited L.C. Dufour, Kluwer Academic Publishers (1989) pp 57-79.

[7] H.-J. Kleebe, M. K. Cinibulk, R. M. Cannon and M. Ruhle, J. Am. Ceram. Soc, **76** 1969 (1993).
[8] I. Tanaka, H.-J. Kleebe, J. Bruley, D. R. Clarke and M. Ruhle, J. Am. Ceram. Soc, **77** 911 (1994).
[9] Y.-M. Chiang, L. A. Silverman, R. H. French and R. M. Cannon, J. Am. Ceram. Soc, **77** 1143 (1994).
[10] H. Gu, R. M. Cannon and M. Ruhle, J. Mat. Res., **13** 376 (1998).
[11] T. M. Shaw and P. Duncombe, J. Am. Ceram. Soc, **74** 2495 (1991).
[12] Kevin Doyle, M.S. Thesis, UC Santa Barbara (1995).
[13] Y.-M. Chiang, J. R. Lee and H. Wang, in *Ceramic Microstructures*, edited A. P. Tomsia, Plenum Press, New York, (1998).
[14] D. R. Clarke, J. Appl. Phys., **49** 2407 (1978).
[15] J. P.Gambino, W. D. Kingery and G. E. Pike, J. Am. Ceram. Soc,**72** 642 (1989).
[16] J.-R. Lee, Y.-M. Chiang and G. Ceder, Acta Mater, **45** 1247 (1997).
[17] Q. Jin, X.-G. Ning, D.S. Wilkinson and G. C. Weatherly, J. Am. Ceram. Soc., **80** 685 (1997).
[18] J. Drennan, D. R. Clarke, R. H. J. Hannink and T. M. Shaw, J. Am. Ceram. Soc., **77** 2001 (1994).
[19] M. P. Brada and D. R. Clarke, Acta Mater, **45** 2501 (1997).
[20] D. R. Clarke, J. Am. Ceram. Soc, **70** 15 (1987).
[21] D. R. Clarke, T. M. Shaw, A.P. Philipse and R.G. Horn, J. Am. Ceram. Soc, **76** 1201 (1993).
[22] S. Blonski and S. H. Garofalini, J. Am. Ceram. Soc., **80** 1997 (1997).
[23] R. M. Cannon, unpublished work.
[24] M. Bobeth, D. R. Clarke and W. Pompe, J. Am. Ceram. Soc, submitted (1998).

Materials Science Forum Vols. 294-296 (1999) pp. 9-16

On the Relationship between Grain-Boundary Migration and Grain-Boundary Diffusion by Molecular-Dynamics Simulation

B. Schönfelder[1,2], P. Keblinski[1], D. Wolf[1] and S.R. Phillpot[1]

[1] Materials Science Division, Argonne National Laboratory, Argonne, Illinois 60439, USA

[2] Institut für Metallkunde und Metallphysik, RWTH Aachen, Kopernikusstrasse 14, D-52056 Aachen, Germany

Keywords: Structure-Sensitive Properties, Grain-Boundary Migration, Grain-Boundary Diffusion, Molecular-Dynamics Simulation

Abstract

A molecular-dynamics method for the simulation of the intrinsic migration behavior of individual, *flat* grain boundaries is presented. A constant driving force for grain-boundary migration is generated by imposing an anisotropic elastic strain on a bicrystal such that the elastic-energy densities in its two halves are different. For the model case of the large-planar-unit-cell, high-angle (001) twist boundary in Cu we demonstrate that the drift velocity is proportional to the applied driving force, thus enabling determination of the boundary mobility. The activation energy for grain-boundary migration is found to be distinctly lower than that for grain-boundary self-diffusion. A *decrease* in the related activation energies with increasing temperature is shown to arise from a crossover in the underlying mechanisms, from solid-like at low temperatures to liquid-like at high-temperatures that is accompanied by an underlying grain-boundary structural transition.

1. Introduction

Grain-boundary (GB) migration is the fundamental mechanism involved in the processes of recrystallization and grain growth. In spite of the importance of these processes during microstructural evolution, the atomic-level mechanism(s) by which GBs move and how the structure of a given GB affects its mobility are still largely unknown [1]. This is not only due to the poorly understood high-temperature structure of GBs but also because experimentally GB migration is very difficult to investigate since (i) the GB mobility is so sensitively affected by minute amounts of impurities, (ii) experiments are typically limited to curved GBs and (iii) quantification of an often inhomogeneous and time-dependent driving force is intrinsically very difficult. [2,3] Extrinsic factors, such as GB pinning, surface drag and thermal grooving are known to play an important role as well. [4] For example, when the displacement of a GB during migration is observed on a surface, the GB motion usually appears jerky rather than continuous [5], an effect presumably caused by thermal grooving on the surface; such a jerky movement therefore probably does not represent the intrinsic mode of GB movement [6].

Phenomenologically grain-boundary migration resembles a continuous, viscous movement of a GB through a crystal under an applied driving force. According to reaction-rate theory, irrespective of the underlying mechanism the GB drift velocity, v, and the driving force, p, should be related linearly provided that $p\Omega/kT \ll 1$ (where Ω is the atomic volume, k is the Boltzmann constant and T the absolute temperature); i.e., [3,7,8]

$$v = mp \quad , \tag{1}$$

where m is the GB mobility. The latter depends, for example, on the GB geometry and structure, temperature and the concentration and chemistry of impurities at the GB.

A continuous, viscous movement requires that the GB be subject to a sustained driving force. If a GB segment of area A moves a distance d normal to the GB and thus lowers the overall Gibbs free energy of the system by ΔG (<0), then the driving force, p (defined to be positive), acting on the GB segment is

$$p = \frac{|\Delta G|}{\Delta V} = \frac{|\Delta G|}{Ad} \quad , \tag{2}$$

where $\Delta V = Ad$ is the volume through which the GB segment has swept during such a migration step of length d [3]. (The definition in eqn. (2) demonstrates that the driving "force" is actually an energy-density difference, i.e., a force per unit area, or a pressure.)

Computer simulations are ideally suited for the study of impurity-free, individual GBs and to provide atomic-level information on the migration process that can then be compared with the related process of GB self-diffusion. Ideally one would like to simulate the migration behavior of a flat GB under the effect of a time-independent driving force, and hence with a well-characterized atomic structure and GB geometry. While simulations of the dynamical fluctuations of such a GB about its equilibrium position (i.e., in the absence of a driving force) can provide valuable insights into the atomic-level mechanism involved in GB motion [9], like the earlier simulations by Jhan and Bristowe [10] they provide no information on the *mobility* of the boundary. The key problem therefore consists in the development of a simulation method that permits application of a driving force to a *planar* GB; i.e., a boundary with no driving force due to its shape.

The basic idea of our method for the simulation of GB migration is to establish a difference between the Gibbs free-energy densities in the two halves of a given bicrystal by imposing anisotropic elastic strain on the system such that the elastic energies stored in the two grains are different. Such an energy-density difference gives rise to a net driving force for migration, resulting in the energetically favored grain to grow at the expense of the unfavored grain while lowering the overall energy of the system in the swept volume.

Our new simulation method [11] enables us to determine the activation energy for GB migration which can then be compared directly with that for self-diffusion in the same bicrystalline GB. Turnbull [8] and In der Schmitten et al. [12] have suggested that the two processes should involve essentially the same activation barriers for the movements of the atoms, although their jump distances may be somewhat different in the two processes. Following the discussion of our molecular-dynamics method for the study of GB migration, in this paper we hope to demonstrate for the case of a large-unit-cell, high-angle twist GB that the activation barriers for the diffusion jumps of GB atoms are significantly higher than those involved in the collective reshuffling of the atoms during GB migration; i.e., that GB migration and GB self-diffusion are distinct processes.

2. Elastic Driving Force for Grain-Boundary Migration

To quantify the elastic driving force to be used to induce GB migration, we define the elastic Gibbs free-energy densities, g_A and g_B, in the two grains labeled A and B (assuming that $g_A > g_B$). After the GB has moved by some distance d into grain A, the Gibbs free energy has decreased by $\Delta G = -(g_A - g_B)Ad$, and according to eqn. (2) the driving force becomes

$$p = \frac{|\Delta G|}{Ad} = |g_A - g_B| \quad . \tag{3}$$

The concept of an elastic driving force works only for elastically anisotropic materials. In a cubic system, a measure of elastic anisotropy is given by

$$c_a = 2C_{44} - [C_{11} - C_{12}] \quad , \tag{4}$$

where the elastic constants C_{11}, C_{12} and C_{44} are defined in the principal cubic axes, and Voigt's notation is implied.

As discussed in detail in our original paper [11], for (001) twist GBs the difference in the elastic energy densities stored in the lower and the upper grains is given by

$$p = \Delta E(\theta) = E^B - E^A = c_a \sin(2\theta)\, \varepsilon_{12}\, (\varepsilon_{22} - \varepsilon_{11}) \quad , \tag{5}$$

where θ is the twist angle. Notice that strains with a component in the direction of the GB normal (i.e., ε_{13}, ε_{23} and ε_{33}) do not produce an elastic energy difference between the grains.

In practice, throughout our simulation we choose

$$\varepsilon_{11} = -\varepsilon_{22} = \pm \varepsilon/2 \text{ and } \varepsilon_{12} = \varepsilon \quad ; \tag{6}$$

equation (5) then reduces to

$$p = \mathrm{Sign}(\varepsilon_{22})\, c_a \sin(2\theta)\, \varepsilon^2 \quad . \tag{7}$$

It is worth noting that, to first order in ε, deformations satisfying eqn. (6) conserve the planar unit-cell area of the simulation cell and hence its volume. Because of $\Delta E \sim \varepsilon^2$, doubling ε will quadruple the driving force; similarly, switching the signs of ε_{11} and ε_{22} should reverse the direction of GB migration.

It is interesting to estimate the magnitude of the driving force for GB migration that can thus typically be imposed on a bicrystal containing the (001) θ=43.60° (Σ29) twist GB (see Sec. 3) studied in this paper. For the interatomic potential representing Cu that will be used in our simulations (see Sec. 3), c_a=1.239x10^{12} dyne/cm^2 at T=0K and 0.572x10^{12} dyne/cm^2 at T=1000K, respectively (10^{12} dyne/cm^2 = 0.1 TPa). With $\sin(2\theta)\approx 1$, a strain of 1% (ε=0.01) gives values for ΔE of 1.239x10^8 and 0.572x10^8 dyne/cm^2 at T=0K and T=1000K, respectively; i.e., at the high end of the experimentally achievable range [3].

3. Simulation Method

The molecular-dynamics (MD) method used throughout was described in detail in Ref. [11]. Because the potential function has been used widely for GB simulations [13], we adopt the Lennard-Jones (LJ) potential, with parameters ε=0.167eV and σ=2.3151Å, obtained from a fit to the zero-temperature lattice parameter and approximate melting point of bulk copper. To avoid discontinuities in the energy and forces, the potential and its first derivative are shifted smoothly to zero at the cut-off radius, R_c=1.49a_o. For this particular parameterization and cut-off procedure, the zero-temperature lattice parameter is a_o=3.616Å and the melting temperature $T_m\approx$1200K.

The (001) θ=43.60° (Σ29) twist boundary chosen for this study, generated by a twist rotation by θ=43.60° about the [100] axis, has a square planar unit cell with an area that is Σ=29 times larger than that of the related primitive planar unit cell of perfect-crystal (001) planes; it hence contains 29 atoms per plane in the primitive planar CSL unit cell. This particular GB is well-suited for this study for a number of reasons. First, it has a relatively large planar unit cell, thus representing what we consider a "representative" *high-angle* grain boundary. Second, with an interplanar spacing of d(001)=0.5a, the (001) lattice planes are widely separated, thus permitting a clear distinction between the in-plane and out-of-plane movements of the atoms. Third, two previous simulation studies of this GB, with [10] and without application of a driving force [9], have shown it to be quite mobile at elevated temperatures; these studies also have provided insight into its migration mechanism. Finally, according to eqn. (5) a twist angle near 45° maximizes the driving force.

Throughout, 3d periodic border conditions are imposed on the simulation cell which therefore contains *two* identical GBs, however with opposite rotational sense (labeled GB_1 and GB_2 in Fig. 1). Under the influence of the driving force acting on them they will move towards each other until they annihilate, leaving behind a perfect crystal. To ensure that the GBs do not strongly interact with one another throughout most of the simulation, the number of (001) planes was chosen to differ in grains 1 and 2 (see Fig. 1). Since the simulation cell will be strained such that grain 2 grows at the expense of grain 1, 60 (001) planes are assigned to grain 1 and 24 to grain 2; the

simulation cell then contains a total of 84 planes, or 84x29=2436 atoms. With this arrangement, even after 20 migration steps of each GB, the two boundaries are still 20 (001) planes apart.

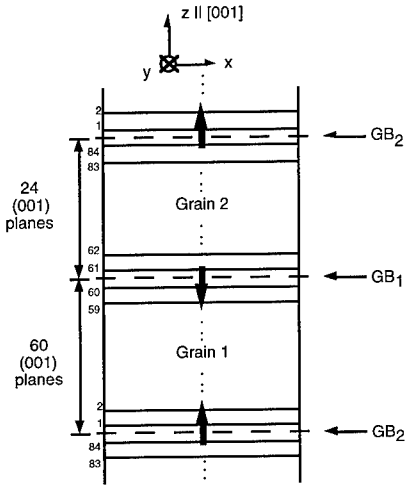

Figure 1. 3d periodic simulation cell. Under the imposed driving force, the two GBs move in the directions indicated by the arrows. Initially, 60 (001) planes form grain 1; 24 planes form grain 2.

4. Simulation Results

Our results focus on three key aspects. First we show that the GB, indeed, migrates under the effect of an elastic strain of reasonable magnitude and that a GB drift velocity can reliably be extracted. Second, we establish the existence of a linear relationship between the magnitude of the applied driving force and the observed drift velocity; according to eqn. (1) this yields the absolute value of the mobility, m, of an individual, flat GB at a given temperature. Third, the temperature dependence of the mobility is shown to exhibit Arrhenius behavior; however the related activation energy is found to be significantly lower than that for GB self-diffusion.

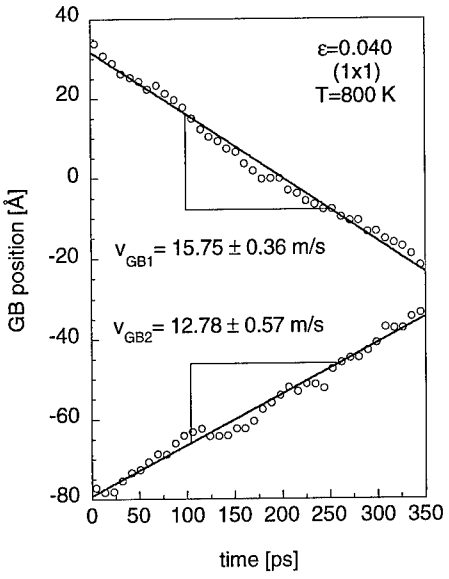

Fig. 2. Average positions of GB_1 and GB_2 versus time at T=800K and ε=0.04.

That the two GBs in the simulation cell in Fig. 1, indeed, move under the effect of an elastic driving force and that a GB drift velocity v_{GB} can be extracted is illustrated in Fig. 2 for a (relatively large [11]) strain of ε=0.04 at T=800K (~ 2/3 T_m). The figure shows the average z-positions of the two GBs versus time in the simulation cell containing 84 (001) planes (see also Fig. 1). The two boundaries move towards each other and, after 350ps, are close to annihilating one another. According to the figure, the displacement-time behavior of both GBs can clearly be described by a straight line, giving constant GB drift velocities of 12.78 ± 0.57 m/s and 15.75 ± 0.36 m/s (the average velocity being v_{GB}≈14.3 ± 2.1 m/s).

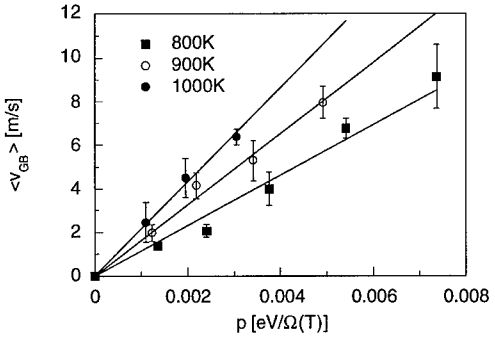

Figure 3. Average GB velocity at 800K, 900K and 1000K versus elastic driving force.

The example shown in Fig. 3 demonstrates that the GB drift velocities thus obtained are reasonable well proportional to the elastic driving force at all temperatures (solid lines) [11]. According to eqn. (1) the slopes of the straight lines yield the mobility, m, of the GB. This important result represents the foundation of our MD method for the simulation of GB migration.

For a comparison of computed mobilities, m, with experiments, it is sometimes convenient to consider the *reduced* mobility, μ=mγ, where γ is the GB energy which in the case of the Σ=29 twist GB is 0.708 J/m^2 at T=0K for the LJ potential [14]. The value of μ thus obtained, for example, at T=800K (~2/3 T_m) is m=9.269±0.309x10^{-8} m^4/Js, giving μ=6.568±0.22x10^{-8} m^2/s.

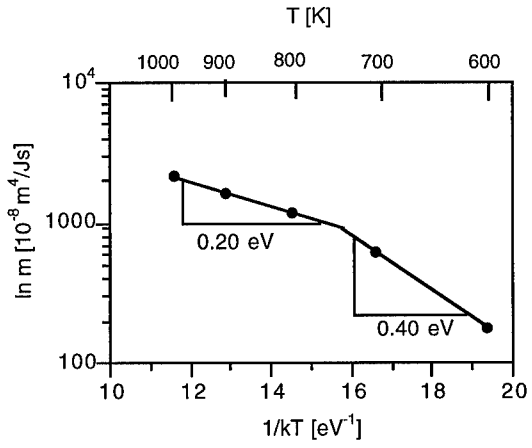

Figure 4. Arrhenius plot of the mobility, m (in units of 10^{-8} m^4/Js) for the (001) θ=43.60° (Σ29) twist GB. The error bars in the data are smaller than the symbol size.

According to Fig. 3, the mobility increases sharply with increasing temperature. If GB migration is a thermally activated process, m should obey the Arrhenius expression

$$m = m_0 \exp(-Q/kT) \quad , \tag{8}$$

where Q is the activation energy for the migration process. The related Arrhenius plot in Fig. 4 demonstrates that the mobility is, indeed, thermally activated. However, at T~750K the activation energy decreases suddenly, from a low-temperature value of ~0.40eV to a high-temperature value of only ~0.2eV.

5. Relationship between GB Diffusion and GB Migration

To investigate self-diffusion in the (001) Σ29 twist GB, simulations were performed for the unstrained system (i.e., in the absence of GB migration). Because of the relatively small mobility of atoms in the perfect-crystal regions surrounding the GB, the total measured mean-square-displacement (MSD) is dominated by the in-plane (x-y) motions of the GB atoms. In analogy to the Gibbsian excess *energy* of the GB, the MSD per unit GB area, $(\langle(\Delta x)^2\rangle+\langle(\Delta y)^2\rangle)/A$, represents the integrated, Gibbsian excess MSD of the GB, which is related to the GB self-diffusion constant, D^{GB}, via the expression

$$\langle(\Delta x)^2\rangle + \langle(\Delta y)^2\rangle / N_{GB} = 4\, t\, D^{GB} \quad . \tag{9}$$

For a GB of width δ with a planar unit-cell area, A, the number of GB atoms, N_{GB}, may be written as $N_{GB} = A\delta / \Omega$. Inserting into eqn. (9) yields

$$\delta D^{GB} = \frac{\langle(\Delta x)^2\rangle + \langle(\Delta y)^2\rangle}{A} \frac{\Omega}{4\,t} \quad , \tag{10}$$

which has the dimensions of (length)^3/time. As is well known, δ is the effective "diffusion width" probed during GB diffusion; although δ is of similar magnitude as the "structural width" of the GB, the two need not necessarily be identical. (For a detailed discussion of this distinction, see [16].)

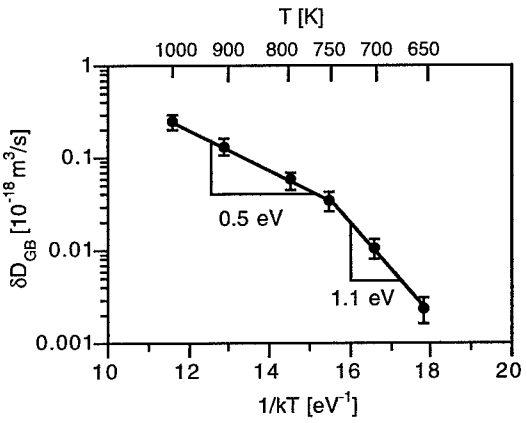

Figure 5. Arrhenius plot of δD^{GB} (see eqn. (10)).

The linear dependence of the excess GB MSDs with time observed for all simulation temperatures [11] yields the Arrhenius plot shown in Fig. 5. Interestingly, like the Arrhenius plot for GB migration, Fig. 5 reveals a crossover, at T~750K, from a low-temperature to a high-

temperature diffusion process. However, the activation energies for GB self-diffusion are more than twice as large as those for GB migration (Fig. 4), suggesting that GB migration and diffusion are distinct processes, contrary to the suggestions of Turnbull [8] and In der Schmitten et al. [12].

To gain a perspective on the magnitudes of these activation energies, we have used zero-temperature lattice-statics relaxation to determine the activation energy for self-diffusion via mono-vacancies in the perfect crystal. Although the vacancy formation and migration energies of E^f_{1V} =1.03eV and E^m_{1V} =0.88eV thus obtained differ by about 20% from the experimental values of E^f_{1V} =1.29eV and E^m_{1V} =0.72eV for Cu [15], the resulting total activation energy of E_{SD}=1.91eV is rather close to the experimental value of E_{SD}=2.01eV. [15] We have also performed constant-pressure molecular-dynamics simulations to determine the self-diffusion constant in the melt in the range of 1300 - 1000K (with the lower temperatures representing the supercooled liquid); these simulations yield an activation energy of 0.39eV [11], close to the experimental value of 0.42eV [17], but different from any of the above activation energies at temperatures close to the melting point.

6. Discussion

Intriguingly, both GB migration (Fig. 4) and GB diffusion (Fig. 5) exhibit a crossover from a low-temperature to a high-temperature process at about T~750K (or ~0.62 T_m). This type of behavior has been observed experimentally in a variety of situations during the past three decades, and not only in connection with GB *migration* and GB *diffusion* but also GB *sliding*. For example:

(a) GB migration experiments of Aust on general boundaries in Pb [18] and of Demianczuk and Aust on a <100> 37° tilt GB in Al [19] revealed a crossover at about 0.8 T_m similar to that in Fig. 4. Similar experiments of Gleiter in Pb [20] also showed a pronounced decrease in the activation energy at elevated temperatures; this behavior was attributed to a structural transformation in the GB core, and is supported by a discontinuity in the GB free energy at the same temperature [20].

(b) Similar to Fig. 5, recent self- and impurity-diffusion experiments on Cu <001> tilt GBs near the Σ5 (36.87°) misorientation [21] revealed a crossover between a strongly misorientation dependent low-temperature regime with a high activation energy and a high-temperature regime with a misorientation-*independent*, ~60% lower activation energy. This transition was interpreted as a structural transition in the GB region from an ordered low-temperature GB structure to a disordered high-temperature structure with atom jump vectors in random directions.

(c) GB sliding experiments by Watanabe et al. on various tilt bicrystals of Zn [22] revealed the existence of a transition temperature, T_c~0.7-0.9T_m, above which the activation energy for sliding was significantly lowered from its value below T_c; the value of T_c was found to depend on the GB misorientation. Similarly, sliding experiments of Lagarde and Biscondi on high-angle Cu tilt bicrystals [23] exhibited a sharp decrease (by ~75%) in the activation energy for GB sliding for T > ~0.4T_m which was again interpreted as a GB structural transition.

To investigate the origin of this crossover, we have recently performed extensive simulations of GB diffusion for a variety of high- and intermediate-energy tilt and twist boundaries in Pd. [24] Remarkably, similar to our earlier study of Si GBs [25], at high temperatures all the high-energy boundaries were found to exhibit the same, rather low self-diffusion activation energy and an isotropic, liquid-like diffusion mechanism; i.e., a diffusion behavior that is independent of the boundary misorientation. By contrast, at lower temperatures the activation energy was found to be significantly higher and strongly dependent on the GB energy, with a solid-like diffusion mechanism that involves jump vectors in discrete lattice directions. These simulations [24] not only confirm that a GB structural transition, indeed, takes place in relatively high-energy GBs, but also that (i) the transition proceeds from a solid-like low-temperature to a liquid-like high-temperature structure and (ii) the transition temperature depends strongly on the GB energy. [24]

Consistent with our observation of a liquid-like *high-temperature* structure of the GB, Mott [7] had suggested that local disordering, or "melting" of small groups of atoms at the boundary, is necessary to enable atoms belonging to one grain to reshuffle collectively while aligning themselves with the other grain (see also the description of Mott's concept in Ref. [2]). The moving GB is

therefore viewed as consisting of small islands of alternate fit and misfit between the two crystals [2,7] as small groups of atoms belonging to one crystal "melt locally" and subsequently resolidify onto the other crystal [2,7]. According to Mott's theory the activation energy for migration, $Q=nH_f$, should be given by the latent heat of fusion, H_f, and by the average number of atoms, n, involved in this local reshuffling. [2,7]

To test this idea, we have used MD simulations to determine the internal energies of the solid and liquid through the melting transition. [11] These simulations revealed approximately linear, parallel curves for the internal energies vs. 1/kT for the liquid and the crystal, giving a value of approximately 0.13eV/atom for H_f at $T_m \approx 1200K$ (remarkably close to the experimental value of 0.135eV [26]); i.e., an energy that is, indeed, *lower* than the value of Q=0.20eV in the high-temperature regime in Fig. 4. This suggests that the migration of the (001) Σ29 GB, indeed, involves the collective reshuffling of the atoms during local melting and recrystallization. Given the ratio of $n=Q/H_f \approx 1.5$, one is tempted to conclude that the reshuffling during migration involves typically only 1-2 atoms at a time; i.e., the small "islands" of alternate fit and misfit between the two crystals are extremely small. In practice, the mechanism is probably more appropriately described by a size distribution for these islands, with n representing the average, albeit very small size. [9]

Acknowledgments. We gratefully acknowledge discussions with M. Furtkamp, H. Gleiter, G. Gottstein and L. S. Shvindlerman. BS expresses his gratitude to the German Academic Exchange Service for sponsoring his extended stay at Argonne National Laboratory. PK gratefully acknowledges support from the A. v. Humboldt Foundation. DW and SRP were supported by the U.S. Department of Energy, BES Materials Science, under Contract No. W-31-109-Eng-38.

References

1. See, for example, F. S. Humphreys and N. Hatherly, *Recrystallization and Related Annealing Phenomena*, Pergamon, 1995.
2. K. T. Aust and J. W. Rutter, in *Recovery and Recrystallization of Metals* (edited by L. Himmel), AIME, Interscience Publishers, New York (1963), p. 131.
3. K. Lücke and H.-P. Stüwe, in *Recovery and Recrystallization of Metals* (edited by L. Himmel), AIME, Interscience Publishers, New York (1963), p. 171.
4. R. Viswanathan and C. L. Bauer, Acta metall. **21**, 1099 (1973).
5. S. E. Babcock and R. W. Balluffi, Acta metall. **37,** 2357 and 2367 (1989).
6. G. Gottstein and L. S. Shvindlerman, Scripta metall. mater. **27**, 1521 (1992).
7. N. F. Mott, Proc. Phys. Soc. **60**, 391 (1948).
8. D. Turnbull, Trans. AIME **191**, 661 (1951).
9. J. M. Rickman et al., J. Mater. Res. **6**, 2291 (1991).
10. R. Jhan and P. D. Bristowe, Scripta metall. mater. **24**, 1313 (1990).
11. B. Schönfelder et al., Interface Sci. **5**, 245 (1997).
12. W. In der Schmitten, P. Haasen and F. Haessner, Z. Metallk. **51**, 101 (1960).
13. D. Wolf and K. L. Merkle, Chapter 3 in *Materials Interfaces : Atomic-level structure and properties* (edited by D. Wolf and S. Yip), p. 87, Chapman & Hall, London (1992).
14. D. Wolf, Acta Metall. **37**, 1983 (1989).
15. R. W. Balluffi, J. Nucl. Mats. **69&70**, 240 (1978).
16. P. Keblinski et al., Phil. Mag. Lett. **76**, 143 (1997).
17. J. Henderson and L. Yang, Trans. Met. Soc. AIME **72**, 221 (1971).
18. K. T. Aust, Can. Met. Quart. **8**, 173 (1969).
19. D. W. Demianczuk and K. T. Aust, Acta Metall. **23**, 1149 (1975).
20. H. Gleiter, Radex Rundschau **1&2**, 51 (1980).
21. E. Budke, C. Herzig, S. Prokofjev and L. S. Shvindlerman, Mater. Sci. Forum **207-209**, 465 (1996); Def. Diff. Forum **156**, 21 (1998).
22. T. Watanabe, S. Kimura and S. Karashima, Phil. Mag. **49**, 845 (1984).
23. P. Lagarde and M. Biscondi, Mem. Scient. Revue Metall. **71**, 121 (1974).
24. P. Keblinski et al., submitted to Acta Mater. .
25. P. Keblinski et al., Phil. Mag. Letters **76**, 143 (1997).
26. CRC Materials Sci. & Eng. Handbook, ed. J. F. Shackelford, CRC Press 1994. p. S-64.

Materials Science Forum Vols. 294-296 (1999) pp. 17-26

Application of Surface Ab Initio Methods to Studies of Electronic Structure and Atomic Configuration of Interfaces in Metallic Materials

M. Šob[1], I. Turek[1] and V. Vitek[2]

[1] Institute of Physics of Materials, Academy of Sciences of the Czech Republic, Žižkova 22, CZ-616 62 Brno, Czech Republic

[2] Department of Materials Science and Engineering, University of Pennsylvania, 3231 Walnut St., Philadelphia, PA 19104-6272, USA

Keywords: Electronic Structure, Atomic Configuration, Surfaces, Interfaces, Extended Defects, Grain Boundaries, Local Density of States, Ab Initio Calculations

Abstract. Surface ab initio electronic structure methods are reviewed and their application to studies of electronic and atomic structure of interfaces in metallic materials is discussed. Examples presented here are electronic structure of the $\Sigma = 5(210)/[001]$ tilt grain boundary in tungsten, magnetic moments at the $\Sigma = 5(310)/[001]$ tilt grain boundary in iron, and magnetic behaviour of Ru and Rh overlayers at the Ag(001) substrate. Versatility and generalization of the Green's function method to include also compositionally disordered systems is emphasized. At the same time it is argued that, depending on the character of the problem, simpler methods such as central force many-body potentials may be sufficient for description and understanding of many phenomena in metallic systems but they have to be linked synergistically with first-principles methods and with experiments.

1 Introduction

Surfaces and/or internal interfaces break the crystal periodicity and introduce thus significant modifications of the electronic structure (ES) in their vicinity. Surfaces are more severe disturbances than solid–solid interfaces, since there is also an abrupt jump in the atomic density associated with them. The ES is related to the atomic configuration and vice versa so that both of them should be determined simultaneously and self-consistently.

Modern ES calculations are based on first-principles (ab initio) approaches, i.e. on the fundamental quantum theory. Here the atomic numbers of the constituent atoms and, usually, some structural information are the only input data. Such calculations are performed in the framework of the density functional theory [1, 2] in which the complicated many-body motion of all electrons is replaced by an equivalent but simpler problem of a single electron moving in an effective potential. The total energy calculations are now used routinely to evaluate equilibrium lattice parameters, elastic moduli, relative stabilities of competing crystal structures, energies associated with point and planar defects, alloy heats of formation, etc. In such studies, we also obtain information about electronic densities of states and charge densities, which enables us to gain a deeper insight and learn which aspects of the problem studied are important.

State-of-the-art electronic structure calculations have achieved considerable level of reliability in predictions of a variety of physical and chemical properties and phenomena. This is in part due to the continuing rapid development of computing power (both speed and memory) and its increasing accessibility (via networks and workstations). Even more important is advancement of new computational methods and algorithms. They yield highly accurate solutions of the one-electron Kohn-Sham equations [1, 2] and provide information at the atomic and electronic scale with an unprecedented level of detail. In many cases, we are able to design new materials and predict their properties without actually synthesizing them. Computational simulations can also provide data on the atomic scale that are inaccessible experimentally.

While a significant progress has been made in first-principles ES calculations, there is still a wide range of problems for which we have to resort to simpler schemes of total energy evaluations. Namely, the first-principles calculations become rapidly intractable if the ES and atomic configuration are to be determined in a self-consistent way for a system having more than 50–100 atoms in the repeat cell. Instead, frequently semiempirical tight-binding models are employed. They can reproduce important features of the underlying ES and yield plausible atomic configurations [3–5]. In even more complicated cases, when thousands of atoms need to be relaxed, phenomenological models are usually used. In these treatments, the total energy is taken as a chosen function of atomic positions. Examples are pair potentials [6], many-body central-force potentials (embedded atom method [7], Finnis-Sinclair potentials [8]), glue model [9], and empirical potentials for covalent solids [10]. For example, the central-force potentials for close-packed structures, where angularly dependent forces are not important, are sufficient to describe the atomic interactions. In those cases, empirical potentials are capable to discover phenomena which are not purely crystallographic in nature. However, if significant changes in the electronic structure occur with the change of atomic configuration (e.g. onset or disappearance of ferromagnetism), then only the first-principles electronic structure calculations can reveal the underlying physics. The choice of the appropriate method depends on the phenomenon studied and information sought. The following two examples demonstrate this principle.

The first is the investigation of structures and energies of $\Sigma = 3[112]$ tilt grain boundaries in Cu studied in [11]. Here grain boundary properties were calculated in dependence on the inclination of the boundary plane for a fixed misorientation of the grains. A semi-empirical N-body potential of the Finnis-Sinclair type was used as a model of the interatomic forces in Cu. Computer simulations of atomic configurations revealed that for the inclination angle of 83.65^o the grain boundary region contains predominantly bcc crystal structure. This was subsequently confirmed by HREM observations. It turns out that the bcc structure forms because it relaxes more easily the large strain at the grain boundary and not because of stabilization by electronic structure effects.

It should be noted that the atomistic simulations of this grain boundary involved about 100.000 atoms. Such calculations are impossible by the present-day first-principles methods, which can only treat about three orders of magnitude less atoms. Furthermore, if such first-principles calculations were possible, we would almost certainly obtain practically the same results but with much larger effort.

The second example concerns directional bonding and asymmetry of interfacial structure in TiAl [12]. Stoichiometric or Ti-rich TiAl alloys exhibit two-phase lamellar structure [13]. HREM observations revealed a marked asymmetry of the interfacial structure of γ/γ lamellar interfaces corresponding to an ordered twin with an antiphase-boundary (APB) shift (by an APB vector $\frac{1}{2}[\bar{1}01]$). Empirical central force potential of the Finnis-Sinclair type did not reproduced this asymmetry. In contrast, the first-principles electronic structure calculations (by full-potential LMTO method) show that in the low-energy structure the neighbouring lamellae are relatively displaced by about 0.2 Å. This introduces the asymmetry and agrees well with experimental observations. Here the underlying physics is connected with non-central covalent bonding across the interface. Symmetric configuration (found for central-force potentials) exhibits an accumulation of electrons between Ti and Al atoms at the interface, which is not energetically favourable. The asymmetric configuration (obtained by first-principles calculations) shows no such build-up of charge between Ti and Al atoms, but covalent Ti-Ti bond, similar to that found in the bulk, is formed across the interface. Here asymmetry of the interface does not arise owing to the relaxation of interfacial strains, but it facilitates formation of energetically favourable covalent Ti-Ti bonds.

These two examples demonstrate that it is important to grasp the "proper physics" in the phenomena studied and this determines which method is most appropriate ("use right horses for the courses"). Central-force potentials are successful in cases where bonding is principally metallic, as in most close-packed structures. However, they cannot reproduce the effects associated with the covalency of the bonding. Covalent bonds are intrinsically included in the

first-principles methods though semiempirical approach may also be sufficient. Similar electronic structure effects are discussed by Elsässer et al. [14].

2 Methods of ab initio electronic structure calculation of surfaces

In the last 10-15 years a large number of first-principles ES calculations of surfaces, interfaces and multilayer structures have been made. The majority of these calculations considered non-magnetic systems and a large fraction of them dealt with semiconductors.

The surface and interface first-principles ES treatments may be characterized according to (A) geometrical model and (B) calculational method (expansion of electronic wave functions into an appropriate basis and/or using multiple-scattering methods). As we discuss below, application of a particular calculational method is often closely connected with the geometrical model used.

From the geometrical point of view, a surface or an interface may be simulated using (i) a cluster, (ii) a single slab, (iii) repeated slabs, and (iv) semi-infinite bulk(s).

In the case of clusters, problems arise from artificial termination of the model. This can be taken into account by special treatments like embedding and localization techniques, which is essential when studying interfaces. In order to attain reliable results, it is imperative to study the dependence of the calculated quantities on the size of the model. A recent review may be found in [15].

Slab geometries have been used much more widely. In the single-slab geometry we consider a thin slab typically less than ten atomic layers thick. The number of layers has to be large enough so that the surface does not "feel" the presence of the surface on the other side of the slab (or at least that the studied quantity to be computed is not affected). Adequate number of layers depends on the properties calculated as well as on the surface/interface orientation. Two-dimensional periodicity is utilized in the slab. If we are interested, for example, in the behaviour of isolated adatoms or in surface/interface segregation, the repeat cell in the lateral directions must be chosen such that the interaction with the neighbouring adatoms can be neglected.

If the slab is repeated periodically in the direction perpendicular to the surface or interface, we obtain a "slab superlattice" with full three-dimensional periodicity that can be treated by standard band-structure methods. In this case, the repeat cell is usually large in the direction perpendicular to the surface or interface and a periodic array of surfaces or interfaces is studied.

A system with a planar interface may be considered as composed of two unperturbed semi-infinite bulk systems sandwiching the interfacial region; in the case of a surface, one of those semi-infinite bulk systems is vacuum. Here we study an isolated surface or interface, not a periodic array of them. When treating the ES of such system, we use the two-dimensional periodicity in the layers parallel to the interface.

To calculate the electronic structure, we may use (i) expansion of electronic wave-functions in terms of an appropriate basis, (ii) multiple-scattering (Green's function) methods, (iii) Green's function expressed in an appropriate basis.

Electronic wave-functions may be expanded via molecular orbitals (used mostly in cluster models), augmented plane waves (APW), linear muffin-tin orbitals (LMTO), plane waves, mixed basis (e.g. plane waves and localized functions) etc. The latter methods are used mostly in slab geometries.

Since the symmetry of systems with surfaces and interfaces is severely reduced relative to the bulk, it is necessary to represent the charge density and the potential very accurately. This is why full-potential all-electron versions of the above methods have usually been used in slab calculations. For single-slab calculations, a two-dimensional version of the full-potential linear augmented plane wave (FLAPW) method has been developed [16]. In repeated slab approach, the FLAPW method has also been used, together with full-potential linear muffin-tin orbital (FP-LMTO) method [17]. Plane waves combined with pseudopotentials are also very popular, especially in simple metals and semiconductors [18]. For a given element, many

different pseudopotentials can be constructed that differ in their degree of transferability, i.e. in the extent to which a pseudopotential leads to agreement with all-electron calculations for variety of different atomic configurations and environments. The problem of transferability was quite recently removed by "all-electron pseudopotentials" constructed from charge densities corresponding to the real atomic environment [19]. Recent applications of the pseudopotential approach are ab initio studies of metal-ceramic interfaces [20, 21]. A review of ES methods used in combination with the repeated slab model, including a lot of recent applications, may be found in [22, 23].

An alternative approach for evaluation of the electronic density that provides an elegant formalism for the treatment of systems characterized by reduced periodicity is based on the use of Green's functions. An important feature of this formulation is that the Green's function represents the true solution in the whole space, from which we may project out the part of the solution that corresponds to the region of interest, e.g. the vicinity of a surface or an interface. These methods are also called multiple scattering methods, as they effectively treat the scattering of propagating electrons on individual atoms.

Several first-principles approaches based on Green's functions have been developed. In the layer Korringa-Kohn-Rostoker (LKKR) method [24] the semi-infinite solid is partitioned into atomic planes parallel to the surface or interface; two-dimensional periodicity is utilized. Intra-layer scattering is described by a partial-wave basis whereas the inter-layer scattering is treated in a plane-wave basis. An alternative approach is the real-space multiple scattering method [25]. It utilizes the idea of removal invariance, i.e. the fact that removing a finite number of layers at the end of a homogeneous semi-infinite stacking of layers recovers the original semi-infinite system [25–28].

In most applications of the Green's function techniques, the one-electron potentials have been assumed to have the spherically symmetric muffin-tin form. In this case, it is not possible to calculate reliably structural energy differences associated with symmetry-lowering displacements of atoms. However, the band structures, densities of states, non-spheroidized charge densities (based on the spheroidized electronic potential) are very similar to those obtained by full-potential calculations, even for low-symmetry configurations [29]. Thus, having the corresponding atomic configuration (e.g. bcc layer in the grain boundaries in Cu [11]), the underlying electronic structure characteristics may be calculated quite reliably by these fast methods. However, we cannot relax, for example, the atomic configuration. At present, the full-potential KKR technique is being developed by several groups (see e.g. [30]). This approach has the accuracy of FLAPW and FP-LMTO slab calculations and uses a correct geometric model.

Green's functions may be constructed very efficiently within the tight-binding linear muffin-tin orbital (TB-LMTO) scheme [31, 32]. Namely, a linear combination of the standard linear muffin-tin orbitals (LMTO's) [33] can be used to construct a new set of basis functions (so-called screened LMTO's) whose range extends effectively to the second nearest neighbours [31, 32]; in this way, we obtain a first-principles tight-binding Hamiltonian (this is the reason we speak about the TB-LMTO method). This is particularly useful for surfaces or planar interfaces: the perturbation due to the surface or interface couples relatively few basis functions.

The short range of hopping integrals (structure constants) enables us to introduce the notion of principal layers [26, 28]. Each principal layer contains such a (finite) number of neighbouring layers that only the nearest principal layers interact. Thus, the whole system may be considered as a sequence of principal layers, both in the semi-infinite bulks and in the interfacial region. A detailed description of the approach using principal layers for electronic structure calculations of surfaces, interfaces and layered systems may be found in [28, 34].

Now, let us compare the repeated slab models (which employ the standard wave-functions techniques and are most frequently used at present) with the semi-infinite bulk models, usually connected with a Green's function technique.

In repeated slab geometry, the repeat cell is very long in one direction (it is tubelike). Electronic structure of many layers is calculated unnecessarily (they are bulk-like and their role is "padding" between the studied surfaces or interfaces). The "deficiency" in the geometry may

be controlled by convergence tests with respect to number of layers. In the case of semi-infinite bulk model, only electronic structure of the surface or interfacial region is calculated using Green's function approach (there is no "padding" needed). The semi-infinite bulks are matched to the interfacial region and two-dimensional periodicity in the surface or interface plane is utilized. As a result, there are no tubelike repeat cells. One of the most important facts is, however, that the methods based on the Green's functions may be easily generalized to include compositional disorder and, therefore, surfaces and interfaces in substitutionally disordered alloys may be investigated [34]. Most natural way of configurational averaging in disordered alloys is the coherent potential approximation (CPA) [27, 34].

3 Application to interfaces

All techniques discussed above are applicable to calculations of electronic structure of surfaces, epitaxial interfaces, grain, antiphase and interphase boundaries, multilayers etc. In this section, we present several illustrative examples of studies of the electronic structure of grain boundaries and disordered magnetic overlayers.

3.1 Electronic structure of the $\Sigma = 5(210)/[001]$ tilt grain boundary in tungsten

The atomic configuration of this grain boundary (GB) was determined using interatomic potentials of the Finnis–Sinclair type [8]. The electronic structure was calculated by the TB-LMTO Green's function method [34]. Two unperturbed semi-infinite bulks sandwiched the interfacial region consisting of 5 principal layers. Each principal layer contained 4 atomic layers (interactions up to the second nearest neighbours were included). More details about this calculations may be found in [35, 36].

The analysis of local densities of states (LDOS) at individual atoms shows that away from the "core" of the boundary the LDOS is very similar to that of the bulk. However, in the most perturbed GB region, a significant smoothing of the DOS and filling of the gap between bonding and antibonding d-states is observed [35, 36]. This is the consequence of lower symmetry of the local neighbourhood of atoms in the GB. Similar situation arises in amorphous materials.

3.2 Magnetism in grain boundary regions

Magnetic phenomena are very important, for example, in overlayers and multilayers. However, magnetic behaviour of atoms at grain boundaries in ferromagnetic materials may also be different when compared with the bulk.

We illustrate this situation for the $\Sigma = 5$ (310) tilt grain boundary in iron [34]. The structural model used is identical to that in Ref. [37] (symmetrical unrelaxed structure) and is shown in Fig. 1; explicit numbering of atomic layers is included. This model preserves all bcc interatomic distances between atoms belonging either to the upper or to the lower grain (atomic layers $n > 0$ and $n < 0$, respectively). The two grains are rigidly displaced along the z axis so that the resulting distance between the atomic layers $n = 1$ and $n = -1$ is the same as the nearest-neighbour spacing in the bcc lattice. This procedure increases the volume of the Wigner-Seitz cells for atoms in and near the central atomic layer ($n = 0$). In the present study, screened TB-LMTO structure constants up to the second nearest neighbours of the bcc lattice were used. This implies that principal layers consist of three neighbouring atomic layers. Self-consistency was attained in the interfacial region consisting of 7 principal layers.

It may be seen from Fig. 2a that the local magnetic moments near the grain boundary are enhanced. This is analogous to the effect observed for low-index surfaces (see e.g. [38, 39]). A detailed analysis of the dependence of the local magnetic moments on separation from the GB has not been made but it appears that most of the difference between the individual local moments and the asymptotic bulk bcc value can be attributed to the magneto-volume effect. The local magnetic moments near the $\Sigma = 5$ (310) boundary versus the atomic sphere

(Wigner-Seitz) radius are plotted in Fig. 2b and compared to those in the ideal bcc structures with varying lattice constants. This comparison obviously suggests that the local magnetic moment follows the volume dependence of the global magnetic moment in crystalline bcc iron, as reported by a number of authors (see e.g. Refs. [40, 41]).

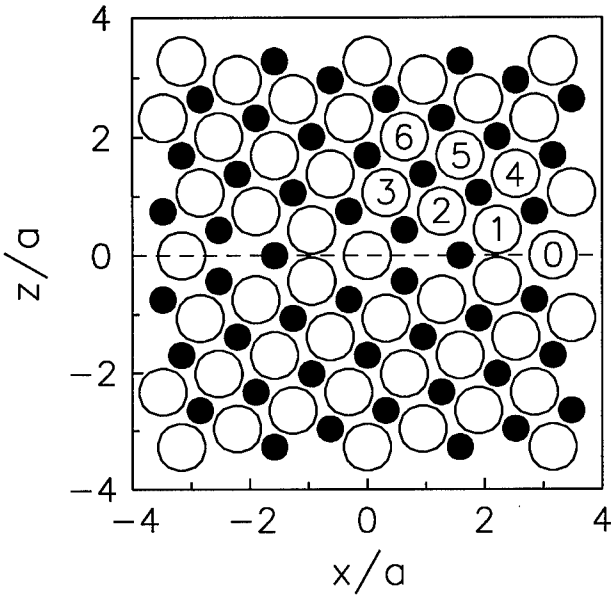

Fig. 1. Structural model of the $\Sigma = 5$ (310) tilt grain boundary in a bcc structure. All coordinates are in units of the bcc lattice constant a. The open and full circles refer to atoms with $y = 0$ and $y = a/2$, respectively. The layer numbering in the upper grain starts from the central interface layer, denoted by 0 and marked by the dashed horizontal line. For details, see text.

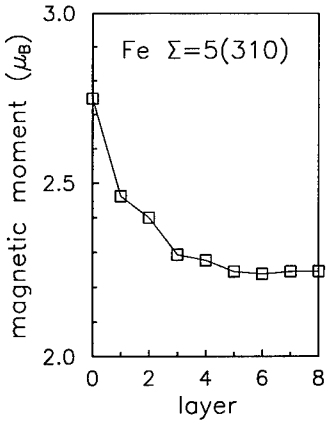

Fig. 2a. Local magnetic moments of iron atoms in atomic layers near a $\Sigma = 5$ (310) grain boundary.

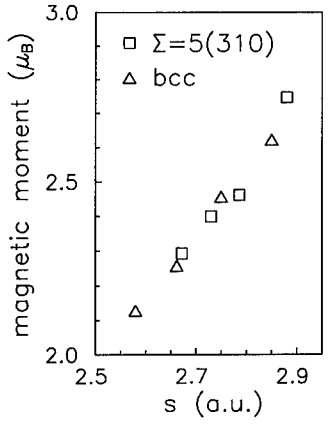

Fig. 2b. Fe magnetic moments versus atomic sphere radii near a $\Sigma = 5$ (310) grain boundary (squares) and in the unperturbed bcc Fe (triangles).

It was shown recently that in the ferromagnetic iron the enhanced magnetic polarization in the GB region dramatically reduces the GB energy and its magnitude is in much better agreement with experiments than for the models which do not include magnetic effects [42]. Thus, ferromagnetism affects significantly the inter-granular cohesion and, therefore, it should be incorporated in any realistic description of GB phenomena in ferromagnetic materials.

3.3 Magnetic overlayers on non-magnetic substrates

Epitaxial transition-metal overlayers of monolayer thickness on non-magnetic substrates such as Cu, Ag, Au, Pd, Pt can be considered as two-dimensional itinerant magnetic systems. Recent FLAPW calculations [38, 43] predicted spontaneous magnetic order for $4d$ and $5d$ transition-metal monolayers like Ru, Rh, Ir on Ag(001) and Au(001) substrates. However, experiments using the surface magneto-optic Kerr effect failed to confirm these results [44, 45]. The most probable reason for this discrepancy is the presence of structural imperfections in the samples which are not considered in the calculations. Ample experimental evidence demonstrates that islanding, surface roughness or interdiffusion cannot be neglected in these systems.

We have studied the influence of two types of structural imperfections on the ferromagnetism of Ru and Rh monolayers on a Ag(001) substrate [46], using a combination of the surface Green's function approach with the coherent potential approximation [34]. The first case investigated corresponds to a non-integer coverage of the substrate with Ru or Rh varying between 1 and 2 monolayers. This was simulated by surface layers of composition $R_xVac_{1-x}/R/Ag(001)$, $0 \leq x \leq 1$, where R stands for Ru or Rh and Vac denotes a surface vacancy. This model describes a continuous formation of the second R layer on top of the first perfect R layer on the Ag(001) face. The dependence of the local magnetic moments of R atoms on the coverage is shown in Fig. 3.

In the second case, the importance of interdiffusion of Ru (Rh) films one monolayer thick with the Ag substrate was studied by simulating a layer sequence $R_{1-x}Ag_x/R_xAg_{1-x}/Ag(001)$, $0 \leq x \leq 1$, with all atoms occupying the positions of the ideal bulk Ag lattice. This model describes a continuous transition of the R layer from the surface ($x = 0$) to the first subsurface ($x = 1$) position. The corresponding concentration dependence of the local magnetic moments is shown in Fig. 4.

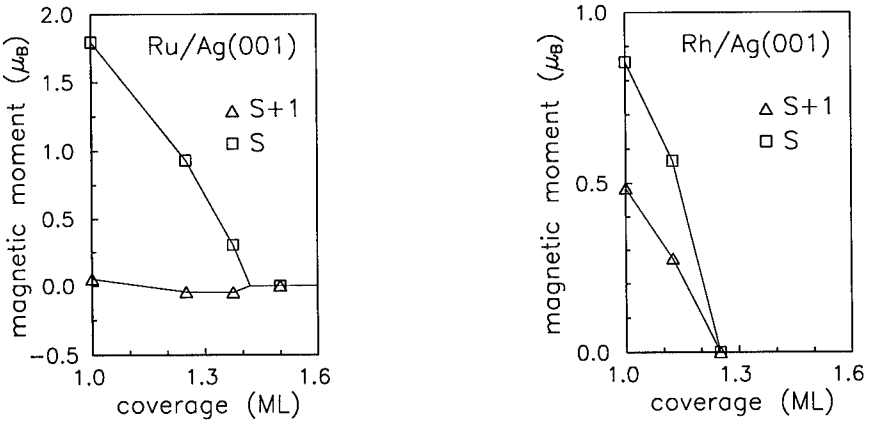

Fig. 3. Local magnetic moments in Ru (left panel) and Rh (right panel) overlayers on a Ag(001) substrate as a function of coverage. Squares and triangles refer to moments in the complete (S) and incomplete (S+1) transition-metal layers, respectively.

It is seen from both Figs. 3 and 4, that despite the relatively large local magnetic moments in the perfect monolayer ($M_{\mathrm{Ru}} = 1.8\,\mu_B$, $M_{\mathrm{Rh}} = 0.9\,\mu_B$), the local moments of Ru and Rh

atoms are very sensitive to both types of structural imperfections. In the first model, two-dimensional ferromagnetism disappears for coverages higher than 1.5 monolayer (Fig. 3). This is in a reasonably good agreement with FLAPW calculations for perfect double layers [47] yielding nearly negligible local magnetic moments for $4d$ and $5d$ transition-metal double layers on a Ag(001) substrate. An even more complicated behaviour transpires from the second model of structural imperfections. A perfect R monolayer in the surface layer ($x = 0$) as well as in the first subsurface layer ($x = 1$) carries a sizable local moment while ferromagnetic behaviour of monolayers strongly affected by interdiffusion (for intermediate values of x) is substantially reduced (Fig. 4). This leads to a magnetic gap for $0.5 \leq x \leq 0.6$ in the Ru case and to a deep minima in both local moments near $x = 0.6$ in the case of Rh.

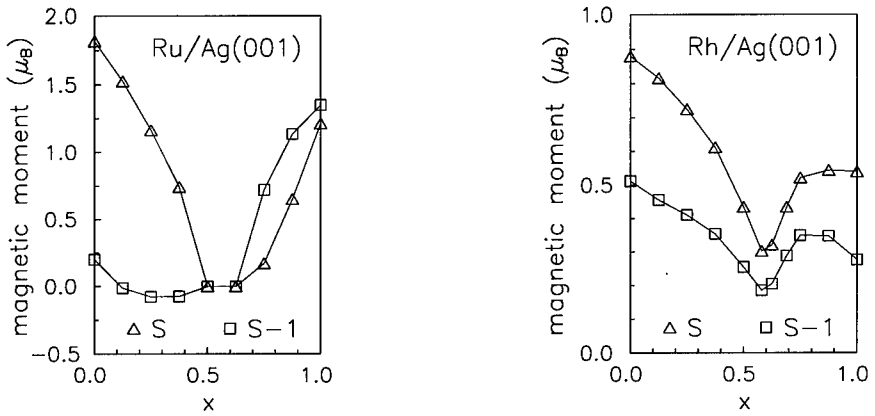

Fig. 4. Influence of interdiffusion on the local magnetic moments in Ru (left panel) and Rh (right panel) overlayers on a Ag(001) substrate. Triangles refer to the moments in the top surface (S) layer, squares refer to the first subsurface (S–1) layer. For details, see text.

The rapid decrease of the local moments with increasing coverage (Fig. 3) and interdiffusion (Fig. 4) can be understood from the shape of the local DOSs of R atoms; a more detailed discussion may be found in [34, 46].

4 Conclusions

In this paper we have demonstrated how the surface first-principles ES methods may be applied to interface problems and how such calculations contribute to a deeper understanding of the underlying physics at interfaces. In this framework, a variety of phenomena may be analyzed, including e.g. surface and interface magnetism. Among the methods listed, the Green's function method within the tight-binding LMTO formalism is particularly convenient since it is computationally very effective and provides reliable results, fully comparable with the more sophisticated approaches. An attractive feature of the Green's function methods is that they may be easily generalized for compositionally disordered systems.

The significance of first-principles calculations is in high reliability of predictions of new properties and phenomena. There are no adjustable parameters and well defined approximations are introduced on the most fundamental level. Nevertheless, similarly as in other atomistic studies, the goal of the ES calculations is not to obtain numbers, but insights. The results include electronic wavefunctions, charge densities, and magnetic moments. On the basis of these results, further material characteristics may be calculated, e.g. cohesive energy, elastic constants, some strength characteristics, magnetic susceptibility, transport coefficients etc. Specifically, in

this paper we have shown that the magnetic moment is significantly different at grain boundaries when compared with the bulk. This phenomenon was not considered in previous studies of atomic structure and properties of interfaces, although it may substantially affect the interfacial cohesion and other characteristic quantities [42]. The information available from the first-principles calculations allow us both to test and construct simpler models, which, in turn, may be used in very extensive atomic level studies while the state-of-the-art first-principles calculations can only be made for a relatively small number of atoms (less than ≈ 100).

The first-principles calculations may also be used for "measurements in the computer". Thus, computer simulations can substitute a real experiment and, more importantly, provide data on atomic scale that are not accessible experimentally. We expect that in future the first-principles methods will contribute most significantly to studies of electronic structure and atomic configuration of interfaces, especially in systems with covalent bonds, such as non-close-packed metals, non-cubic intermetallics, metal-ceramic interfaces, semiconductor systems etc.

Notwithstanding, simpler methods, such as embedded atom method and N-body central force potentials, will remain essential for studies of very large systems. However, it is imperative to combine simpler methods with the first-principles approaches on one side and experiment on the other.

Acknowledgements

This research was supported by the US-Czech Program of the National Science Foundation (INT-96-05232) and the Ministry of Education of the Czech Republic and the Grant Agency of the Academy of Sciences of the Czech Republic (Projects No. A1010817 and A1010708). A part of this study was performed in the framework of the COST Action P3 "Simulation of physical phenomena in technological applications" and of activities of the Centre for Computational Materials Science sponsored by the Academy of Sciences of the Czech Republic.

References

[1] P. Hohenberg and W. Kohn, Phys. Rev. **136** (1964) B864; W. Kohn and L.J. Sham, Phys. Rev. **140** (1964) A1133.
[2] R.G. Parr and W. Yang, *Density-Functional Theory of Atoms and Molecules*, Academic Press, London-San Diego 1992.
[3] W.A. Harrison, *Electronic Structure and Properties of Solids*, Dover Publications, New York 1989.
[4] A.T. Paxton, J. Phys. D: Appl. Phys. **29** (1996) 1689.
[5] D.R. Bowler, M. Aoki, C.M. Goringe, A.P. Horsfield, and D.G. Pettifor, Modelling Simul. Mater. Sci. Eng. **5** (1997) 199.
[6] V. Vitek, Mat. Res. Soc. Bull. **21** (1996) No.2, 17.
[7] A.F. Voter, in *Intermetallic Compounds*, vol. 1, eds. J.H. Westbrook and R.L. Fleischer, Wiley, Chichester-New York 1995, p. 77.
[8] M.W. Finnis and J.E. Sinclair, Phil. Mag. A **50** (1984) 45.
[9] F. Ercolessi, E. Tosatti, and M. Parinello, Phys. Rev. Lett. **57** (1986) 719; Surf. Sci. **177** (1986) 314.
[10] M.I. Baskes, Phys. Rev. B **46** (1992) 2727.
[11] C. Schmidt, F. Ernst, M.W. Finnis, and V. Vitek, Phys. Rev. Lett. **75** (1995) 2160; C. Schmidt, M.W. Finnis, F. Ernst, and V. Vitek, Phil. Mag. A **77** (1998) 1161.
[12] R. Siegl, V. Vitek, H. Inui, K. Kishida, and M. Yamaguchi, Phil. Mag. A **75** (1997) 1447.
[13] S.C. Huang and J.C. Chestnut, in *Intermetallic Compounds*, vol. 2, eds. J.H. Westbrook and R.L. Fleischer, Wiley, Chichester-New York 1995, p. 73; M. Yamaguchi, Met. Technol. **60** (1990) 34.
[14] C. Elsässer, O. Beck, T. Ochs, B. Meyer, M. Mrověc, V. Vitek, D. Nguyen-Manh, and D.G. Pettifor, this Proceedings.
[15] J.L. Witten and H. Yang, Surf. Sci. Rep. **24** (1996) 55.
[16] E. Wimmer, H. Krakauer, M. Weinert, and A.J. Freeman, Phys. Rev. B **24** (1981) 864; M. Weinert, E. Wimmer, and A.J. Freeman, Phys. Rev. B **26** (1982) 4571.

[17] M. Methfessel, D. Hennig, and M. Scheffler, Phys. Rev. B **46** (1992) 4816.
[18] M.C. Payne, M.P. Teter, D.C. Allan, T.A. Arias, and D.J. Joannopoulos, Rev. Mod. Phys. **64** (1992) 1045.
[19] J. Vackář, M. Hyťha, and A. Šimůnek, Phys. Rev. B **58** (1998), in press.
[20] M. Kohyama, Modelling Simul. Mater. Sci. Eng. **4** (1996) 397; M. Kohyama and J. Hoekstra, this Proceedings.
[21] S. Köstlmeier, C. Elsässer, B. Meyer, and M.W. Finnis, phys. stat. sol. (a) **166** (1998) 417; this Proceedings.
[22] E. Wimmer, J. Phys. IV (France) **7** (1997) C6-75.
[23] P. Ruggerone, C. Ratsch, and M. Scheffler, in *Growth and Properties of Ultrathin Epitaxial Layers*, eds. D.A. King and D.P. Woodruff, Elsevier, Amsterdam 1997, p. 490.
[24] J.M. MacLaren, S. Crampin, D.D. Vvedensky, and M.E. Eberhart, Phys. Rev. B **40** (1989) 12164.
[25] X.-G. Zhang, A. Gonis, and J.M. MacLaren, Phys. Rev. B **40** (1989) 3694.
[26] B. Wenzien, J. Kudrnovský, V. Drchal, and M. Šob, *J. Phys.: Condens. Matter* **1** (1989) 9893.
[27] A. Gonis, *Green Functions for Ordered and Disordered Systems*, North Holland, Amsterdam 1992.
[28] F. Garcia-Moliner and V.R. Velasco, *Progr. Surf. Sci.* **21** (1986) 93; *Theory of Single and Multiple Interfaces*, World Scientific, Singapore-New Jersey-London-Hong Kong 1992.
[29] O.K. Andersen, A. V. Postnikov, and S. Yu. Savrasov, in *Applications of Multiple Scattering Theory to Materials Science*, eds. W.H. Butler, P.H. Dederichs, A. Gonis, and R.L. Weaver, Mater. Res. Soc. Symp. Proc. vol. **253**, Pittsburgh, PA 1992, p. 37.
[30] N. Papanikolaou, R. Zeller, P.H. Dederichs, N. Stefanou, Phys. Rev. B **55** (1997) 4157.
[31] O.K. Andersen and O. Jepsen, Phys. Rev. Lett. **53** (1984) 2571.
[32] O.K. Andersen, O. Jepsen, and M. Šob, in *Electronic Band Structure and Its Applications*, ed. M. Yussouff, Springer-Verlag, Berlin 1987, p. 1.
[33] O.K. Andersen, Phys. Rev. B **12** 3060 (1975).
[34] I. Turek, V. Drchal, J. Kudrnovský, M. Šob, and P. Weinberger, *Electronic Structure of Disordered Alloys, Surfaces and Interfaces*, Kluwer Academic Publishers, Boston-London-Dordrecht 1997.
[35] M. Šob, I. Turek, and V. Vitek, Nukleonika **42** (1997) 209.
[36] M. Šob, I. Turek, and V. Vitek, in *Tight-Binding Approach to Computational Materials Science*, eds. P.E.A. Turchi, A. Gonis, and L. Colombo, Mater. Res. Soc. Symp. Proc. vol. **491**, Pittsburgh, PA 1998, p. 79.
[37] K. Hampel, D.D. Vvedensky, and S. Crampin, Phys. Rev. B **47** (1993) 4810.
[38] A.J. Freeman and R. Wu, J. Magn. Magn. Mater. **100** (1991) 497.
[39] M. Aldén, H.L. Skriver, S. Mirbt, and B. Johansson, Surf. Sci. **315** (1994) 157.
[40] O.K. Andersen, J. Madsen, U.K. Poulsen, O. Jepsen and J. Kollár, Physica B **86-88** (1977) 249.
[41] D. Bagayoko and J. Callaway, Phys. Rev. B **28** (1983) 5419.
[42] D. Yeşilleten, M. Nastar, T.A. Arias, T. Paxton, and S. Yip, to be published.
[43] M. Weinert and S. Blügel, in *Magnetic Multilayers*, eds. L.H. Bennett and R.E. Watson, World Scientific, Singapore 1994, p. 51.
[44] G.A. Mulhollan, R.L. Fink, and J.L. Erskine, Phys. Rev. B **44** (1991) 2393.
[45] C. Liu and S.D. Bader, Phys. Rev. B **44** (1991) 12062.
[46] I. Turek, J. Kudrnovský, M. Šob, V. Drchal, and P. Weinberger, Phys. Rev. Lett. **74** (1995) 2551.
[47] S. Blügel, Phys. Rev. B **51** (1995) 2025.

Materials Science Forum Vols. 294-296 (1999) pp. 27-34

High Resolution Study of a Quasiperiodic Grain Boundary in Gold

J.M. Pénisson[1], F. Lançon[1] and U. Dahmen[2]

[1] Département de Recherches Fondamentales sur la Matière Condensée CEA-Grenoble, 17 Avenue des Martyrs, F-38054 Grenoble Cedex 9, France

[2] National Center for Electron Microscopy, LBNL, University of California, Berkeley, Ca 94720, USA

Keywords: Electron Microscopy, Atomic Modeling, Quasicrystals

Abstract : A mazed bicrystal of gold has been obtained by vacuum deposition of gold onto a [001] germanium substrate. Amongst the different grain boundaries existing in this bicrystal, there exits facets which are completely assymetric and presenting a non periodic structure. It is shown that specific groups of atoms are present. Their spatial distribution along the boundary plane is analyzed. The diffractogram of the experimental high resolution images reveals the presence of intensity streaks in a non periodic distribution. The calculated structure of this boundary is in good agreement with the experimentally observed one. The complete analysis of the experimental results leads to the conclusion that this boundary represents a one dimensional quasi-crystal.

1 Introduction.

Although most of the work on the structure of grain boundaries in metals and semiconductors has been concerned with periodic tilt or twist boundaries, there are a number of results on non periodic boundaries. The possibility of quasiperiodic boundaries has been envisaged from the theoretical point of view by several authors [1,2]. These authors applied the methodology developed in the study of quasicrystals to quasiperiodic boundaries by treating them as a one dimensional quasicrystal. Most of the experimental observations of non periodic grain boundaries [3,4] refer to boundaries possessing a very long period and which can be understood within the frame of the standard description using CSL and DSC lattices. Only a brief description of a non periodic segment in aluminum [5] has been published in which the authors using a pattern recognition procedure found a non periodic distribution of pentagonal structural units. In the present paper, a true quasiperiodic boundary is observed in evaporated gold specimens. Although the boundary is not periodic and cannot be described using the standard theories, special groups of atoms can still be found along the boundary. These groups of atoms can be considered as structural units although the exact definition of the structural units [6] does not seem to be fully applicable in this particular example.

2 Experimental Procedure.

The gold films were produced by thermal evaporation onto a [100] germanium single crystal. Before evaporation, the germanium substrate was carefully cleaned in a mixture of hydrofluoric and nitric acids. During the evaporation process, the substrate was held at 280°C. In order to release internal strains in the gold films, the temperature was slowly decreased to 200°C and the specimen maintained at this temperature for 2 hours. At this temperature, the solubility of gold into germanium is negligible. The gold films were removed by chemical dissolution of the substrate followed by a careful wash in distilled water and subsequently mounted on standard 3 mm copper grids. A mean thickness in the range 8-10 nm was achieved by controlling the weight of evaporated gold. In this thickness range, the film was not completely uniform and there were many holes. In the regions close to the holes, the local thickness was smaller and the conditions for high resolution work were very good. The specimens were observed at 800 kV in the Berkeley ARM and at 300 kV in a JEOL 3010 high resolution microscope. Images were processed using special routines running either under Digital Micrograph or Semper 6 image processing systems. The image simulations were conducted using EMS [7] and NCEMSS [8] programs and the standard parameters of the two microscopes.

3 Experimental results and analysis of the images.

During the evaporation process, the gold film grows on the [100] germanium substrate in an <011> orientation. Due to the symmetry of the substrate-film system, two perpendicular orientation variants are present. This type of configuration produces a special morphology called a mazed bicrystal [9] in

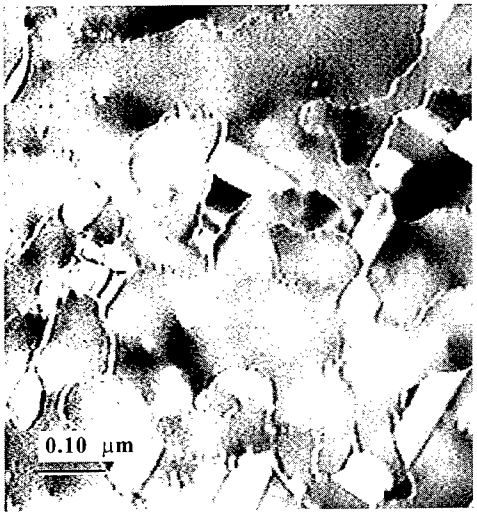

Figure 1 : General view of the gold mazed bicrystal.

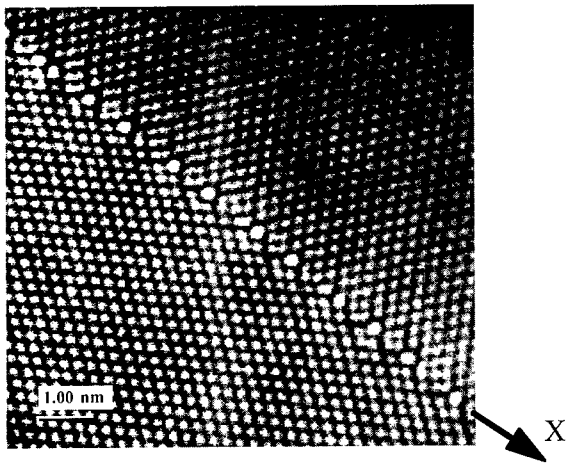

Figure 2 : -a High resolution image of the non periodic boundary. The grain boundary plane is parallel to (100) planes of one crystal and to (110) planes of the second crystal. High intensity white dots in a non periodic distribution appear at the boundary.

-b Intensity profile (in arbitrary units) along the boundary plane. The white dots correspond to the highest intensity peaks. Their distribution is non periodic.

which a large variety of grain boundaries is present. All these boundaries have a tilt character and the misorientation is either 90° or very close to this value. The same situation has already been observed

in aluminium films evaporated onto silicon substrates. In this case, a fully symmetric Σ=99 {557} θ= 89.4° coincidence boundary has been observed in detail and the experimental structure quantitatively compared to calculated models [10].
A general view of the morphology of the mazed bicrystal is shown in figure 1. Amongst all the existing boundaries, it is relatively easy to observe the non periodic ones. The misorientation angle is exactly 90° and the boundary plane is non symmetric and corresponds to (100) of crystal 1 parallel to (110) of crystal 2. The length of these facets is limited to values in the range 10 to 12 nm. Images were taken at different defocus settings corresponding to white or black atomic positions. Using a special defocus value slightly away from the exact white atomic positions, high intensity white dots appear at the boundary core as shown in figure 2a. A carefull inspection of this type of images reveals that the distribution of these white dots is not periodic along the boundary as revealed by the intensity profile along the boundary shown in figure 2b.

3.1 Atomic description of the boundary

When observed in detail, the high resolution images of the boundaries reveal special features. In white- atom images, characteristic arrangements of atoms can be found along the boundary. One of the most easily recognizable feature appears as a centered pentagon (in projection).The distribution of the pentagons along the boundary can be studied by a real space cross correlation procedure [5]. A template image of a pentagon was choosen and correlated with the image of the boundary. The local maxima of the correlation map reveal the presence of similar groups of atoms. The exact value of the different maxima is an indication of the degree of similarity between the pentagons (the value 1 indicating identical units). The position of the maxima of the correlation map shows that the center of the pentagons lie on a single crystallographic plane. Further there are two different spacings between the pentagons : they are always separated by 2a or 3a (a=gold atomic parameter=0.404 nm). This measurement (done with respect to the upper crystal in which the boundary plane is parallel to (100)) is only a rough estimate as it does not take into account the exact position of the center of the pentagons. A more accurate measurement can be done on the bright spots (which represent the center of the pentagons). In this case, the ratio between the two sets of distances is found close to $\sqrt{2}$. These two different spacings are non uniformly distributed along the boundary. However, in some cases, very short portions of the boundary are non planar and periodic. In this case the period was 2.5a and the pentagons were located alternatively on two adjacent planes. This type of structure is similar to the one observed by Paciornik et al [5] in aluminum. The correlation of a single template with all the other ones reveals the presence of all the pentagons but does not reveal the intimate structure of the distribution. In addition, the actual values of the correlation factors depend on the starting template. In order to get a more detailed information, images of each pentagon were extracted from the micrograph of the boundary. Then the pentagon images were correlated with the image of their adjacent neighbors. The correlation factors obtained using this procedure reveal two sets of values. One set of values is > 0.8 while the other one is around 0.7. It can be easily seen that two pentagons separated by a distance 2a have always a correlation factor higher than 2 pentagons separated by a distance 3a.

3.2 Diffractograms of the experimental images.

Figure 3 shows a numerically calculated diffractogram of the experimental image(figure 2a). The analysis of the diffractogram shows that :

i : the misorientation angle is exactly 90°.

ii : in most of the diffractograms, the presence of the boundary induces the presence of typical streaks perpendicular to the boundary plane. The intensity of the streaks is higher in the case of the images displaying the very bright spots. Some of these streaks intercept the diffraction spots (including the central spot). Some others do not intercept any diffraction spots. The distribution of the streaks along the direction parallel to the boundary plane is not periodic. The position of any streak obeys to a simple law : m*L1+n*L2. In this expression, m and n are integers and L1 and L2 represent the position of two particular streaks which act as a basis. The choice of the basis is arbitrary. For convenience, the most intense streaks have been chosen

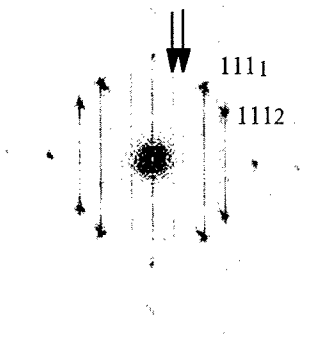

Figure 3 : Numerical diffractogram of an experimental image. The diffraction spots of both crystals are superimposed on an array of streaks coming from the grain boundary itself. The arrows indicate the position of the two streaks which form the basis used for the indexing of all the other streaks

3.3 Fourier filtering and image reconstruction using the streaks.

In order to get more information about the presence of the streaks and their contribution to the images of the boundary, the high resolution images were Fourier filtered. Two types of masks were used to isolate the contribution of the streaks from that of the gold crystals. The first type of mask had an ellipsoidal shape so that the streaks can be selected individually. The inverse Fourier transform gives the contribution of the selected streak to the image. Extreme care should be taken in the interpretation of the reconstructed images since the intensity of the streaks is very low and in this case, the Fourier transform of the mask itself becomes important and can introduce artifacts. The important results derived from this treatment are : i) the contribution of the streaks is localized in the boundary region. This result is in good agreement with previous results obtained on periodic boundaries.
ii) if only one streak is selected, the intensity profile in the reconstructed image is periodic. However if two streaks are selected (for example the streaks corresponding to those marked by the arrows in the figure 3), then the intensity profile becomes non periodic.

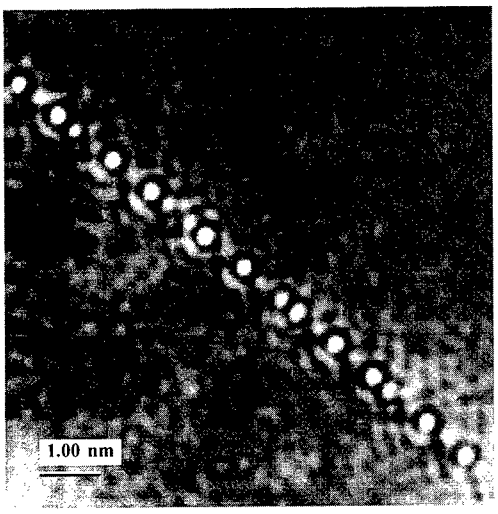

Figure 4 : Fourier filtered image of the boundary using a circular mask. The contribution of the major part of the streaks is included in the mask while the contribution of the two crystals is excluded.

The second type of mask is circular and centered on the central peak. Its diameter is calculated to exclude the 111 diffraction spots of the two crystals. The artifacts introduced by the shape of the mask are then minimized and the reconstructed image shows again a thin intensity slab located at the grain boundary plane (see figure 4). The intensity profile along the slab is non periodic.

4 Interpretation of the results

The high resolution images as well as the filtered images on the streaks of the diffractograms clearly reveal the non periodic character of this boundary. The central question will then be the relation with the standard theories of grain boundaries which have mostly been developed for the coincident or near coincident boundaries on one hand and on the other hand the possible relation with the theory of quasi-crystals.

The high resolution images show that some particular groups of atoms (centered pentagons) can be found at different places of the boundary. Their analysis show they are not exactly identical. This latter observation is in contradiction with the structural unit description [6] although it is generally admitted and it has been experimentally shown [11] that the structural units can be distorted. Another difficulty in the application of the structural unit concept is that it involves the presence of the so called favoured boundaries. Any boundary whose misorientation lies between those of two favored boundaries can be described by a more or less complex sequence of the structural units describing the favored boundaries.

However the description using the centered pentagons seems to have a physical basis. Even in a purely geometrical model, these groups of atoms can be found and the two different spacings between them (2a and 3a) also exist. Furthermore this very simple description is independent of a possible rigid body translation parallel to the boundary plane. When such a translation is applied, the detail of the distribution changes but the pentagons still remain as well as their relative spacings.

Computer simulation of the 1:$\sqrt{2}$ grain boundary

In order to determine the atomic relaxations, the grain boundary has been simulated using an interatomic potential based on the second moment tight binding approximation and fitted to the gold physical properties : atomic parameter, cohesive energy and bulk modulus[12]. Starting from two unrelaxed gold grains with the experimental orientations, the potential energy of this system has been minimized through a relaxation procedure. Let the x and z directions be respectively along the incommensurable and the commensurate direction of the grain boundary. Let the y direction be perpendicular to the grain boundary.

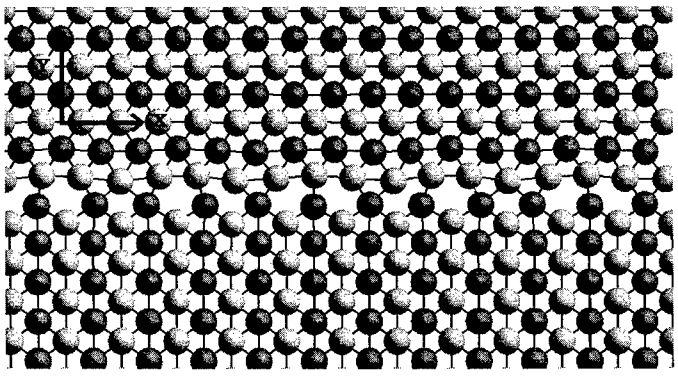

Figure 5 : model of the 1:$\sqrt{2}$ grain boundary. Inter-atomic distances shorter than 0.03 nm are drawn. The darker and lighter atoms are respectively in the two layers at altitudes 0 and a/2 along the z-direction

We have used periodic boundary conditions which are naturally incompatible with a quasicrystalline structure. Hence along the x direction, the irrational spacings a and a $\sqrt{2}$ are facing each other. Thus we have simulated periodic approximants of the structure, namely a 12:17 approximant (figure 5) and a 29:41 approximant (for the Fourier transform calculations), i.e., in this last case for instance, 29 long spacings are facing 41 short spacings leading to an error of $[2 - (41 / 29)] / \sqrt{2} \cong 3\ 10^{-4}$. On the other hand two semi-infinite crystals are neither possible to fit in a periodic box and we have

actually included two grain boundaries perpendicular to the y direction at the closest distance equal to 21a ≅4.3 nm, i.e., we have two crystal slices. We have checked that no crystal distortion occurs in the center of the grains. The size of the box along the y direction has been relaxed during the minimization to take into account the rigid body translation of the grains. The size of the box along the x direction has also been allowed to relax, while the size along the commensurate z direction have been fixed. Some random tiny displacements have been applied to the initial atomic positions to move the system from a possible saddle point of the energy. Figure 5 shows the relaxed atomic structure.
The largest individual atomic relaxations take place in the first row of grain 1 (corresponding to the interatomic distance a). This gives rise to a wavy appearance of this plane when it is observed at a glancing incidence parallel to the boundary plane, i.e. along O-x . This feature is also present in the experimental images.

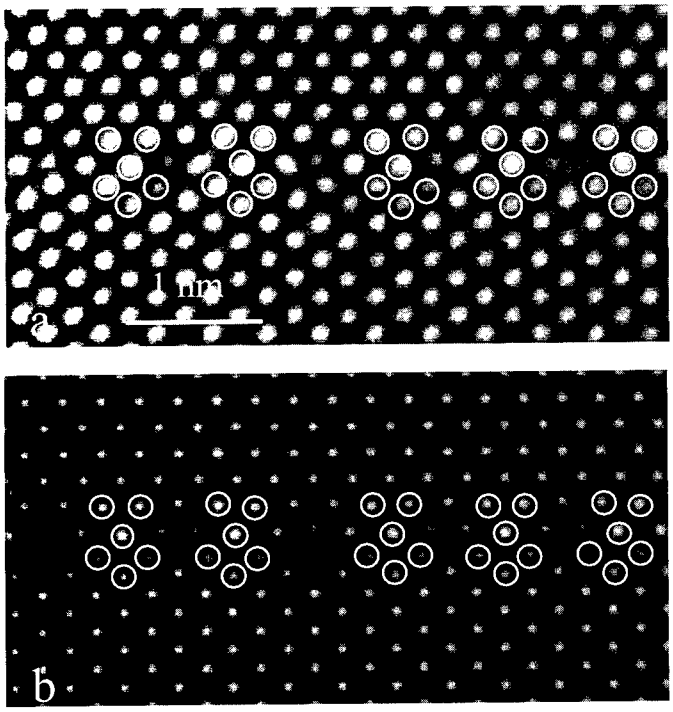

Figure 6 - a experimental image - b simulated image using the atomic positions of figure 5 as input. The parameters correspond to the microscope and to the experimental conditions: specimen thickness t =10 nm and defocus δz=-50 nm. The stacking of the centered pentagons (outlined by the small circles on the pictures) is similar in experimental and simulated images.

High resolution images were simulated using the calculated structure as an input as well as the experimental conditions: specimen thickness, defocus and microscope characteristics. All the contrast features have been found in agreement with the experimental images and in particular the high intensity white spots were reproduced using a thickness t = 10 nm and a defocus δz=-50 nm. It has been possible to find exactly the same sequence of pentagons in both the calculated and experimental images as shown in figure 6 a and b. Although some details in the intensity of the white spots are not exactly in agreement, the correlation procedure applied to the pentagonal units gives the same result: the correlation coefficient is higher for the 2a spacing than for the 3a one; the only difference between experimental and simulated images is the presence of noise which lowers the values. The correlation can be made between corresponding pentagons in experimental and simulated images : the correlation factors are all greater than 0.8 indicating a very good match between both images.
The diffractogram calculated from the simulated image has the same distribution of streaks. The diffracted intensity corresponding to the x direction of the simulated grain boundary is shown in figure 7 and is typical of modulated structures and quasicrystals. Some peak positions q_X are multiple of the fundamental basis reciprocal vector, $q_S = 2\,\pi./\,a$ of grain 1 or vector $q_L = 2\,\pi./\,(a\,\sqrt{2})$ of grain 2. However, because of the mutual modulation of one grain by the other, some other peak

positions are not multiple of q_S or q_L , but all the q_X can be written as $n_S\, q_S + n_L\, q_L$ where : $(n_S,n_L) \in N^2$

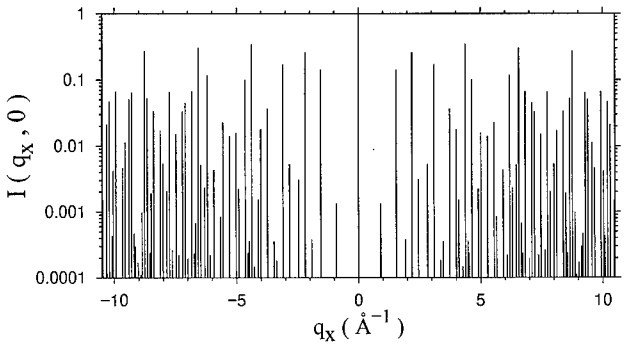

Figure 7 : Diffraction pattern $I(q_X, 0)$ calculated from a 29:41 periodic approximant of the $1/\sqrt{2}$ grain boundary. The boundary is parallel to the x direction. Only the first atomic row on each side of the boundary has been taken into account.

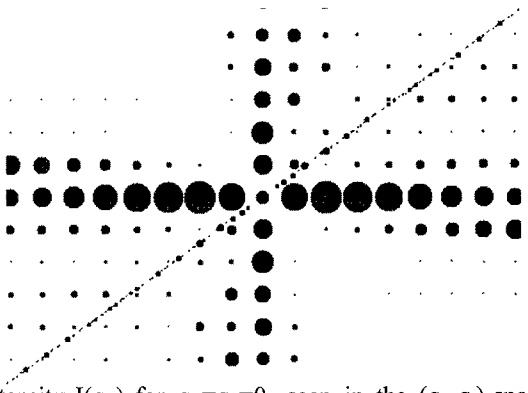

Figure 8 : Diffracted intensity $I(q_X)$ for $q_Y=q_Z=0$, seen in the (q_X,q_i)-space, i.e. indexed with 2 indices. The surface of the disks is proportional to the intensity. The usual diffraction pattern is the orthogonal projection of these spots on the q_x line (black disks on the straight line of slope $1:\sqrt{2}$, the radii are 4 times smaller than the previous spots). The diffracted intensity have been calculated from a 29:41 approximant of the boundary which is parallel to the x direction. Only the first atomic row on each side of the boundary has been taken into account.

Hyper-space description of the $1/\sqrt{2}$ grain boundary

Since the diffracted intensity $I(q_X)$ (restricted to $q_Y=0$ and $q_Z=0$) needs two integer indices n_S and n_i to be indexed, it is more convenient to plot it in a 2D-diagram using a space spanned by $O\text{-}q_X$ the physical reciprocal space and by $O\text{-}q_i$, a virtual space [13] perpendicular to $O\text{-}q_X$ (figure 8) In this plane, all the peaks of $I(q_X)$ can be set on the sites of a square lattice whose the projections onto $O\text{-}q_X$ are the actual peak positions.

If the two atomic rows on each side of the grain boundary would have been a mere juxtaposition of two unrelaxed rows, one corresponding to crystal 1 and the other to crystal 2, the intensity would have been present only on the horizontal and vertical axes of figure 8. All the other spots are the result of the mutual lattice modulation.

By doing an inverse Fourier transform of the 2D-embedded diffracted amplitude we get a periodic density with a square lattice unit cell. Alternatively, we can directly determine this two-dimensional

embedding, since its intersection with O-x is the set of the x atomic coordinates: the coordinate x_i of each particle i corresponds to a point of components $X_S = x_i \sqrt{2/3}$ and $X_L = x_i \sqrt{1/3}$. Figure 9 shows that the non periodic grain boundary is associated to a periodic structure when we adopt this two dimensional view.

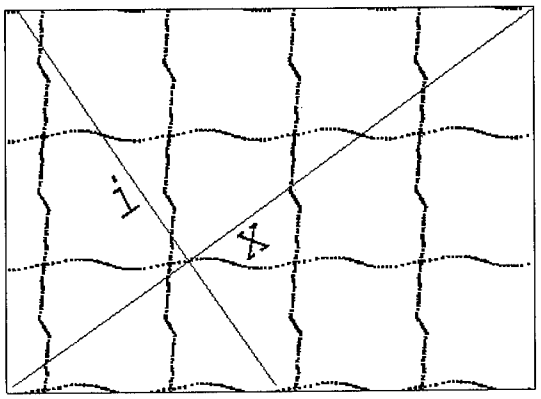

Figure 9 : Hyper-space embedding of the 1:√2 grain boundary : periodic two-dimensional structure in the virtual (x,i)-space; its intersection with a straight line of slope 1:√2 (parallel to the physical x direction) are the coordinates of the atoms. The almost horizontal lines lead to the position along the boundary of the atomic row of grain 1; the almost vertical lines correspond to the first atomic row of grain 2.

Conclusion

The experimental results obtained on the non symmetric (100)/(110) boundary show clearly that the structure of this boundary is non periodic. Some groups of atoms can be found at different locations along the boundary. However, these groups of atoms do not obey to the definition of the structural units which derived mostly from the study of periodic and symmetric boundaries. The diffraction effects induced by the boundary and their indexing establish the one dimensional quasicrystalline state of this boundary. The simulation results are in good agreement with the experimental ones and the mutual relaxations of the grains can be described with a hyper-space analysis.

Acknowledgements : this work was supported by DOE under Contract No. DE-ACO3-76SFOOO98.

References.

[1] A. P. Sutton, Acta Met.36 (1988), p 1291.
[2] D. Gratias and A. Thalal, Phil. Mag. Lett. 57 (1988) p 63.
[3] K.L. Merkle and D. Wolf, Materials Letters 17 (1993), p 217.
[4] Y.C. Wang, Q. Kang, C.B. Zhang and H.Q. Ye, Phil. Mag. Lett.75 (1997) p.91.
[5] S. Paciornik , R. Kilaas, J. Turner and U. Dahmen Ultramicroscopy 62 (1996), p 15.
[6] A.P. Sutton and V. Vitek Phil. Trans Roy. Soc. Lond. A309 (1983) p 1.
[7] P. Stadelmann Ultramicroscopy 21 (1987) p 131.
[8] M. O'Keefe and R. Kilaas, Scanning Micr. Suppl. 2 (1988), p. 225.
[9] U. Dahmen, K.H. Westmacott MRS 229 (1991), p. 167.
[10] U. Dahmen,C.J.D. Hetherington, M.A. O'Keefe, K.H. Westmacott, M.J. Mills, M.S. Daw and V.Vitek Phil. Mag. Lett. 62 (1990) p. 327.
[11] J. M.Pénisson J. de Phys 49 C5 (1988) p.87.
[12] T. Deutsch, P. Bayle, F. Lançon and J. Thibault, J. Phys.: Condens. Matter 7 (1995) p. 6407.
[13] T. Jansen , A. Janner Advances in Physics 36 (1987) p. 519.

Corresponding author : J.M. Pénisson - Email : jpenisson@cea.fr - fax 33 4 76 88 50 97

Materials Science Forum Vols. 294-296 (1999) pp. 35-42

Effect of Grain Boundary Dislocations on 9R Stacking Errors at an Incoherent Twin Boundary in Copper

D.L. Medlin[1], S.M. Foiles[1], G.H. Campbell[2] and C.B. Carter[3]

[1] Materials and Engineering Sciences Center, Sandia National Laboratories, Livermore, California 94550, USA

[2] Chemistry and Materials Science Directorate, University of California, Lawrence Livermore National Laboratory, Livermore, California 94550, USA

[3] Department of Chemical Engineering and Materials Science, University of Minnesota, Minneapolis, Minnesota 55455, USA

Keywords: Grain Boundary Dislocation, Atomistic Modeling, 9R, Incoherent Twin, Stacking Faults

Abstract

We consider the nature of faults in the dissociated 9R phase at an incoherent twin boundary in copper. Analysis of the dislocation content of a five-layer break in the normal ABC/BCA/CAB stacking sequence of the 9R shows that this defect is associated with a secondary grain boundary dislocation (SGBD) of Burgers vector $a/6[\bar{2}11]$. Atomistic simulations of SGBDs at the incoherent twin interface show that the sign of the Burgers vector is important to determining the core structure of the dislocation. The resulting atomistic structures and the five-layer width of the fault can be directly understood by analyzing the set of twinning dislocations that make up the boundary. Atomistic calculations show further, in agreement with the experimental observations, that a shear parallel to the interface causes an increase in the fault width that accompanies the growth of the 9R phase.

Introduction

Experiment and modeling shows that there is a general mode of grain boundary dissociation, common in low stacking fault energy FCC metals, that can be well understood as the emission of arrays of stacking faults from the grain boundary plane [1, 2]. Most extensively studied of such dissociated interfaces are the Σ=3 incoherent twin boundaries. Many observations now exist of grain boundary dissociation at such interfaces showing a region of interfacial dissociation that is well described as a narrow, several nanometer wide slab of 9R stacked material. The 9R stacking sequence is equivalent to a close-packed stacking of FCC {111} planes with an intrinsic stacking fault inserted every three planes (*i.e.*, a stacking sequence of ABC/BCA/CAB ...). The 9R dissociation has been observed and atomistically modeled at incoherent twin boundaries in gold [3], silver [4, 5], and copper [6, 7, 8].

Recent calculations [9] and observations [10] have demonstrated that the width of the 9R slab is not rigidly fixed, but can vary depending on external conditions. An example, from HRTEM observations of an incoherent twin boundary in copper [10,11], is shown in Figs. 1a,b. The 9R stacking at the incoherent twin interface can be identified in both micrographs by the stacking

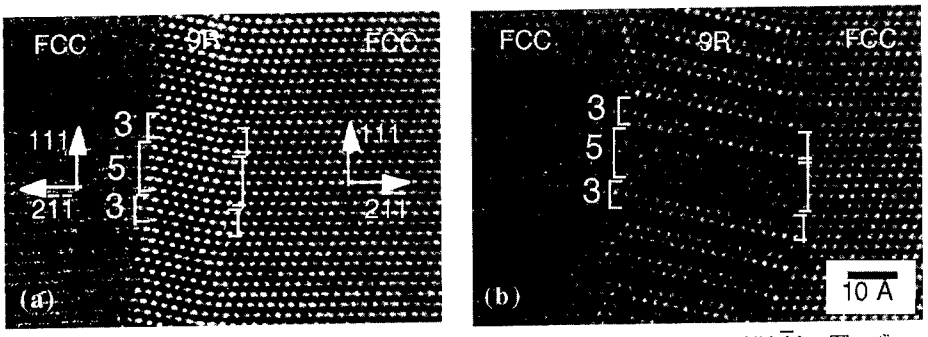

Fig. 1. (a) HRTEM image of the copper Σ=3 interface, imaged along $[01\bar{1}]$. The five-layer fault in the 9R interphase region is labeled. (b) Image from same area as (a), taken after expansion of the 9R region. Note the increase in offset of the parallel (111) planes in the two FCC halves.

sequence of the close-packed fringes. The time interval between these observations is approximately five minutes, and in this time the interfacial 9R region has thickened from a width of 14Å to about 30Å. This change in 9R width was accompanied by a local shear of the two halves of the bicrystal in a direction parallel to the boundary plane, as can be seen by the change in offset of the parallel FCC (111) fringes on the two sides of the interface. The precise driving force for this change is undetermined, though it is likely that the shearing is in response to a change in specimen stress state induced by the electron beam in the TEM (*e.g.*, through heating).

Although a majority of the material within the interface is in the 9R configuration, defects that break the 3-layer 9R stacking, are observed. An example of one such fault, a 5-layer defect, is indicated in Figs. 1(a) and (b). As is shown in the two figures, this region of stacking error expands along with the remainder of the interfacial region as the 9R region grows. One possibility is that the defects in the 9R stacking are associated with secondary grain boundary dislocations (SGBDs). Such defects could be present to accommodate small angular deviations from the ideal Σ=3 coincidence orientation.

These observations motivate the present study. Here, we analyze the defect content associated with the observed 9R fault, apply atomistic calculations to investigate the effect of defect sign on the core configuration and fault width, and relate these calculated structures to a simple model based on the intrinsic twinning dislocations that comprise the Σ=3 interface.

Experiment and Calculations

The bicrystal used for these studies was prepared by diffusion bonding high purity 99.999% copper single crystals, initially configured in a Σ=3 $\{100\}\{1\bar{2}\bar{2}\}/[01\bar{1}]$ orientation. Bonding was performed over a six hour period at a load of 2.0 MPa and a temperature 950°C. During the bonding, the interface relaxed from the original $\{100\}\{1\bar{2}\bar{2}\}$ habit to form facets on $\{111\}$ and $\{\bar{2}11\}$ type planes. HRTEM specimens were prepared by jet polishing followed with a final thinning by Ar^+ ion sputtering. Micrographs were recorded parallel to the $[01\bar{1}]$ direction using a JEOL 4000EX microscope, operated at 400 kV. Additional details regarding the bicrystal fabrication and TEM sample preparation can be found elsewhere [10,12].

Atomistic calculations of the interfacial defects were conducted using the Embedded Atom Method (EAM) [13, 14]. Because the original copper EAM potential developed in 1986 [15] gives an unphysically low value for the stacking fault energy, a new EAM potential, fit explicitly to the

stacking fault energy of copper was used for these calculations[16]. Structural results obtained with this and the older potential were essentially identical. Secondary grain boundary dislocations were introduced into the models by tilting the unrelaxed starting crystals several degrees away from the ideal Σ=3 coincidence orientation. Specifically, a boundary containing SGBDs of *positive* Burgers vector (**b**=$a/6[\bar{2}11]$) was defined with an interface normal of [-15,7,7]. This is equivalent to 1.8° rotations of the left (counterclockwise) and right (clockwise) halves of the bicrystal away from the ideal Σ=3 orientation (total misorientation from Σ=3 of 3.6°). In contrast, by rotating the two halves of the bicrystal in the directions opposite those used for the positive dislocations, an interface containing SGBDs of negative Burgers vector (**b**=$a/6[2\bar{1}\bar{1}]$) was generated. The interface normal in this case was [-13,7,7], which is equivalent to 2.0° rotations of the left (clockwise) and right (counterclockwise) halves of the bicrystal from the Σ=3 orientation. Periodic boundary conditions were applied in the directions parallel with the interface: 5.11 Å in the $[01\bar{1}]$ direction and 45.9 Å and 41.8 Å along the interface for the boundaries containing the positive and negative SGBDs, respectively. Free surface conditions, with a total slab width of 60Å, were used normal to the interface. In addition to calculating the relaxed structures, the effect of a shear strain on the defect configurations was simulated by incrementally applying fixed displacements to the atoms in 0.1Å steps parallel to the interface. At each step, atoms at > 15Å and <-15Å away from the interface were held fixed while the atoms close to the core of the interface were relaxed.

Results

The dislocation content associated with the 9R stacking defects was determined by constructing a closed Burgers circuit about the faulted region and evaluating the closure failure upon transferring this loop to the perfect Σ=3 DSC lattice (Figs. 2a,b). The DSC lattice (Displacement Shift Complete) [*e.g.*, 17] represents the combined set of all lattice points for the two coincidence related crystals: for a Σ=3 bicrystal, the DSC lattice vectors are of type a/3[111] and $a/6[\bar{2}11]$ (*e.g.*, see Fig. 4a). Since the 9R stacking sequence also falls on the Σ=3 DSC lattice, the Burgers circuit across this interphase region remains well-defined. The closure failure shows that the stacking defect is associated with a dislocation of Burgers vector $a/6[\bar{2}11]$ indicating that it is a *positive* pure edge SGBD.

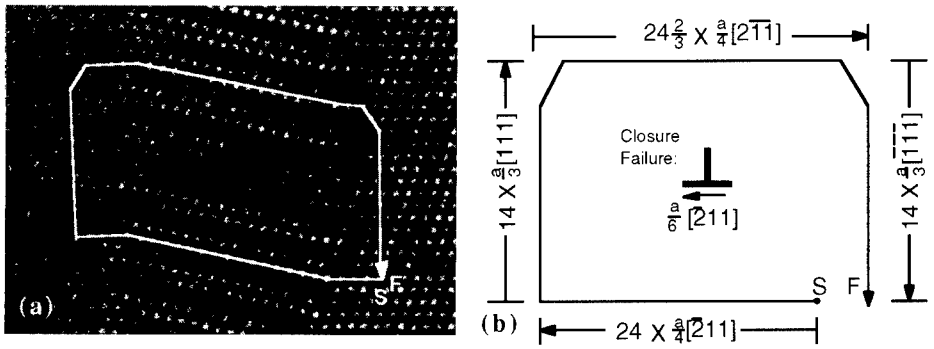

Fig. 2. (a) HRTEM image overlaid with the Burgers circuit constructed around the five-layer defect. (b) Schematic showing the dimensions of the Burgers circuit about the 5-layer defect transferred to the perfect Σ=3 DSC lattice. The closure failure indicates a 90° pure edge dislocation with positive Burgers vector of $a/6[\bar{2}11]$.

Because of the reduction in symmetry resulting from the bicrystal geometry, dislocations of opposite sense (*positive* or *negative*) produce different structures[18]. This is illustrated in Figs. 3a and b, which show the calculated atomistic structures for positive and negative SGBDs at the incoherent twin interface. In this projection, atoms at the same height in the $[01\bar{1}]$ direction are shaded the same color. The key structural units characterizing the boundary have been annotated on the figures. Kite shaped features, consisting of a triangle of atoms at the same height followed by a row of atoms of alternating height, are indicated on the left side of the interface. These structural features can be found and have been identified in many previous calculations of the incoherent twin for different FCC metals [*e.g.*, 3,4,18,19]. The kite shaped units on the right side of the interface are also found in calculations of the perfect interface, though their position varies with the degree of interfacial dissociation. As has been discussed by Wolf *et al.*[3], the vertices of these units correspond to the position of pure edge Shockley partial dislocations that in the perfect Σ=3 interface terminate the stacking faults that form the interfacial 9R phase.

For a perfectly aligned Σ=3 interface, the periodic length along the boundary is three {111} planes, and these two sets of kite shaped motifs are continuously linked. However, for the misoriented boundary shown here, the geometrically necessary SGBDs disrupt the sequence of these structural units. For the case of a positive SGBD (Fig. 3a), an additional triangular unit of atoms at the same height forms between the kites on the left side of the interface. This results in a five plane separation of the pure edge Shockley partial dislocations terminating the right side of the interface. The negative dislocation (Fig. 3b) also results in a triangular unit on the right side of the interface, but also forms a second pair of atoms at the same height. Furthermore, at the right side of the interface, an additional pure-edge negative Shockley partial dislocation is identified. The structure for the boundary containing the negative dislocation is closely related to that calculated and observed by Hofmann and Finnis in their study of 9R formation in silver [5].

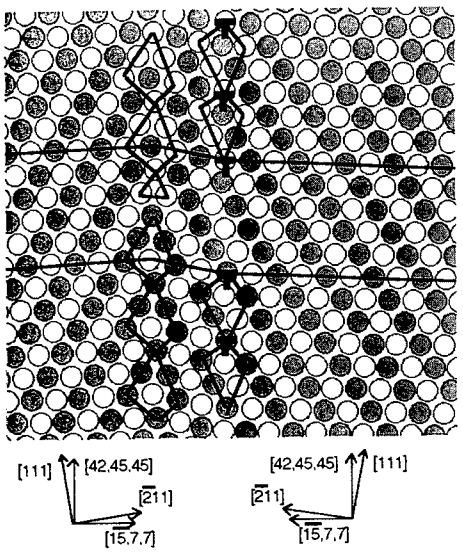

Fig. 3a. Relaxed structure for incoherent twin boundary in copper with SGBDs of positive Burgers vector (**b**=$a/6[\bar{2}11]$).

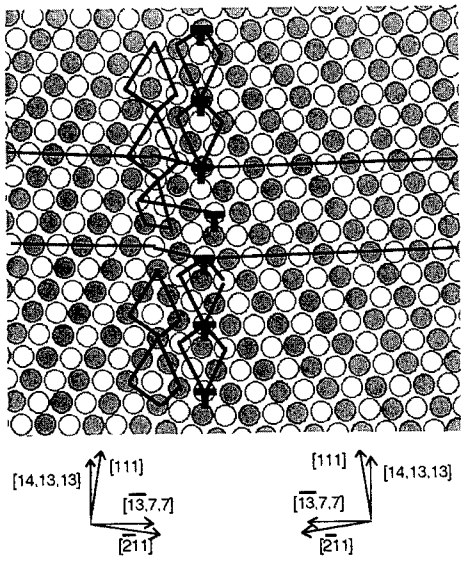

Fig. 3b. Relaxed structure for SGBDs of negative Burgers vector (**b**=$a/6[2\bar{1}\bar{1}]$).

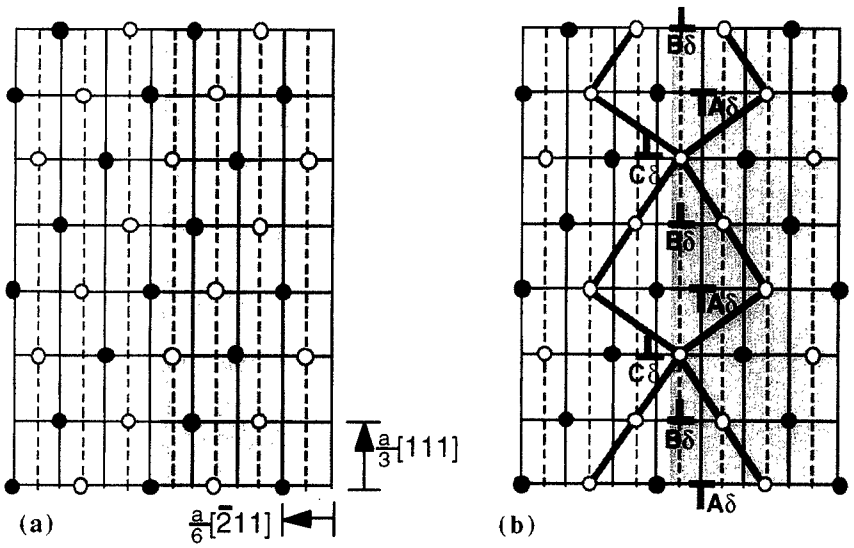

Fig. 4. (a) Σ=3 DSC lattice. Dashed lines are set into the page by $a/4[01\bar{1}]$.
(b) Topological arrangement of atoms at interface produced by a repeated sequence of negative 90° and positive 30° Shockley partial dislocations. ...**Aδ Bδ Cδ** ..... that transform the atoms on the left side of the crystal (gray) to the twinned configuration producing the Σ=3 $(\bar{2}11)$ interface.

Discussion:

The calculated atomistic structures can be understood in terms of the intrinsic dislocations that comprise the incoherent twin interface. We model the perfect Σ=3 $\{\bar{2}11\}$ interface as an array of Shockley partial dislocations on adjacent (111) planes [9] *i.e.*,

... **Aδ Bδ Cδ** | **Aδ Bδ Cδ** | **Aδ Bδ Cδ** ... Eq. 1

where, using Thompson's notation, **Aδ** represents a negative, pure edge Shockley partial dislocation, and **Bδ** and **Cδ** represent two positive, 30° dislocations. Each grouping of three dislocations sums to zero net Burgers vector. Fig. 4a shows a single FCC crystal mapped onto the Σ=3 DSC lattice. Shearing the atoms on the right side of the crystal (marked in gray) by amounts equivalent to the insertion of the sequence of Shockley partial dislocations, reverses the stacking of these atoms producing the twinned configuration shown in Fig. 4b. This sequence produces the same topological configuration of atoms as that found in atomistic relaxations: specifically, a kite shaped motif consisting of a triangle of atoms at the same height followed by a row of atoms at alternating height. Thus, in addition to accounting for the reversal of stacking across the interface, these dislocations also describe the arrangement of atoms at the interface.

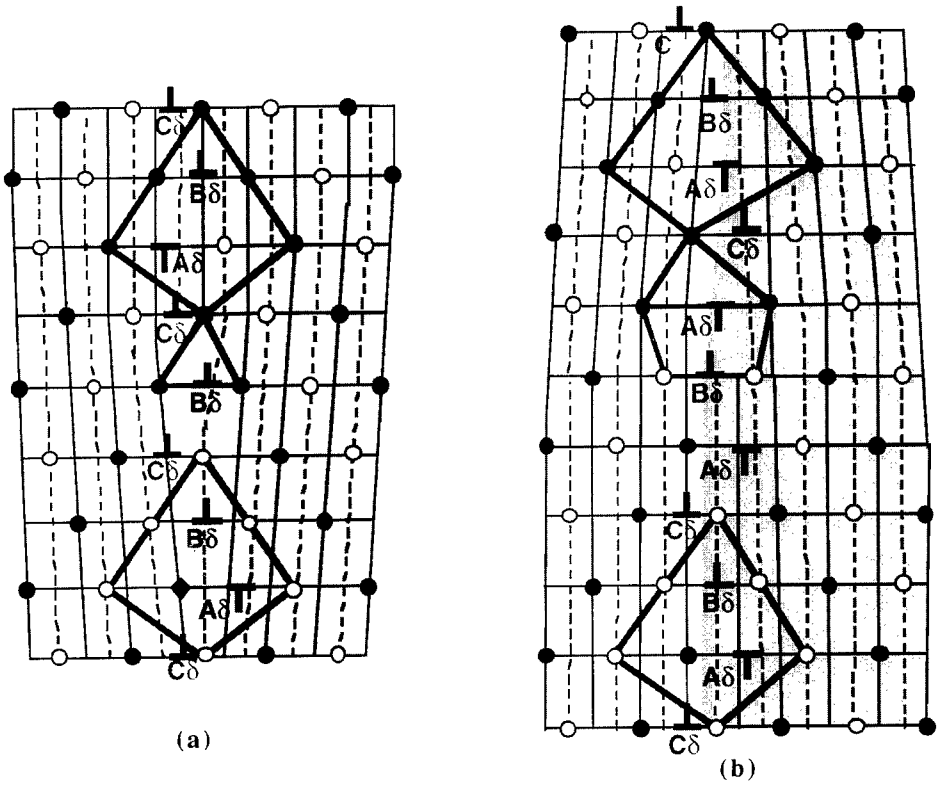

Fig. 5. DSCL models for pure edge secondary grain boundary dislocations of positive and negative Burgers vector represented as arrays of Shockley partial dislocations. (a) Dislocation of positive Burgers vector modeled as the sum of two 30° dislocations **B**δ+**C**δ=δ**A**. (b) Dislocation of negative Burgers vector produced by inserting an additional negative 90° dislocation (**A**δ) into the sequence.

This description, of course, says nothing about the local interatomic relaxations. Its strength, however, is that it can be straightforwardly extended to predict and describe the geometry of the structures and faults resulting from a misoriented boundary. In this case, rather than arranging the twinning dislocations in groups of three that sum to zero Burgers vector, we instead group the dislocations to yield a net dislocation content, in effect creating a fault in the *dislocation* stacking. For instance, a dislocation of negative Burgers vector (**b**=$a/6[2\bar{1}\bar{1}]$) is produced by inserting an additional **A**δ dislocation into the sequence of twinning dislocations:

... **A**δ **B**δ **C**δ **A**δ **B**δ **A**δ **C**δ **A**δ **B**δ **C**δ ... Eq. 2a

Alternatively, since **B**δ + **C**δ = δ**A**, arranging the twinning dislocations as:

... **A**δ **B**δ **C**δ **B**δ **C**δ **A**δ **B**δ **C**δ ... Eq. 2b

yields a defect with a net positive Burgers vector (**b**=$a/6[\bar{2}11]$).

The configurations generated by these arrays of dislocations are given in Figs. 5a and b, for the positive and negative SGBDs, respectively. These bicrystal configurations were produced from a single FCC crystal, initially all in the orientation of the left side of the interface, by displacing the atoms on the right (marked in gray) by the amounts specified by the indicated arrays of Shockley partial dislocations. In the schematics, the gaps in the lattice resulting from the net dislocation content have been removed to illustrate the DSC lattice half-planes associated with each dislocation. These dislocation arrays reproduce the topological arrangements at the core of the interface identified in the atomistic simulations. As with the perfect interface, the groupings of three dislocations that sum to zero (*i.e.*, **A**δ **B**δ **C**δ), produce the kite shaped structural units. For the positive dislocation (Fig. 5a) an additional triangle of atoms at the same height is positioned between the kites. For the negative dislocation (Fig. 5b) a triangle of atoms at the same height, plus a pair of atoms at the same height but offset by $a/4[01\bar{1}]$, is produced.

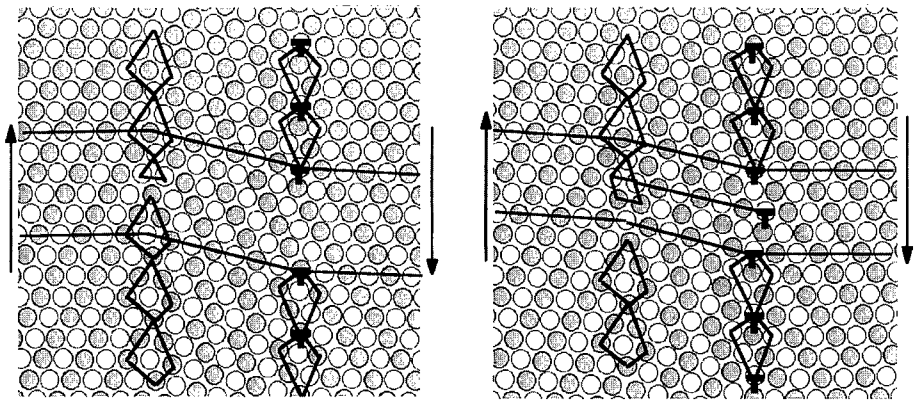

Fig. 6. Atomistic configurations after shearing structures shown in Fig. 3 by 3 Å parallel to the interface. The **A**δ dislocations on the right side of the interface are indicated. (a) Positive SGBD. (b) Negative SGBD.

Conclusion

We can now explain the origin and behavior of the five-layer fault shown in Figs. 1 and 2. The calculations and analysis show that for this geometry a positive SGBD results in a five layer separation between the pure edge **A**δ dislocations. In the ideal Σ=3 boundary these dislocations occur every three planes, terminating the periodic array of stacking faults that correspond to the 9R phase. At the positive SGBD, the five-layer separation between **A**δ dislocations then produces a corresponding five-layer separation between stacking faults. The position of the **A**δ dislocations is sensitive to shear loading [9,10]. Thus, as is illustrated in Figs. 6a and b, as the bicrystal is sheared parallel to the interface, the array of **A**δ dislocations moves to the right, increasing the width of interfacial dissociation. Under such loading, the positive SGBD then produces a wide, five layer high region of local FCC stacking, whereas the negative SGBD would produce a local region of HCP stacking.

Acknowledgments

This work is supported by the U.S. Department of Energy, Office of Basic Energy Sciences, Division of Materials Science, under contracts DE-AC04-94AL85000 (Sandia) and W-7405-Eng-48 (LLNL).

References

1. K.L. Merkle, *Ultramicroscopy* **37** (1991) p. 130.
2. J.D. Rittner, D.N. Seidman, K.L. Merkle, *Physical Review B* **53** (8) (1996) p. R4241.
3. U. Wolf, P. Gumbsch, H. Ichinose, and H.F. Fischmeister, *J. Phys., Paris,* **51**, (1990) p. C1-359.
4. F. Ernst, M.W. Finnis, D. Hofmann, T. Muschik, U. Schönberger, U. Wolf, and M. Methfessel, *Phys. Rev. Lett.* **69**(4) (1992) p. 620.
5. D. Hofmann and M.W. Finnis, *Acta metall. mater.* **42** (10) (1994) p. 3444.
6. U. Wolf, F. Ernst, T. Muschik, M.W. Finnis, and H.F. Fischmeister, *Phil. Mag.* A**66**(6) (1992) p. 991.
7. T. Muschik, W. Laub, U. Wolf, M.W. Finnis, and W. Gust, *Acta metall. mater.* **41** (7) (1993) p. 2163 .
8. D. Hofmann and F. Ernst, *Ultramicroscopy* **53** (1994) p. 205 .
9. C. B. Carter, D.L. Medlin, J.E. Angelo and M.J. Mills, *Materials Science Forum* **207-209** (1996) p. 209.
10. G.H. Campbell, D.K. Chan, D.L. Medlin, J.E. Angelo, and C.B. Carter *Scripta Materialia* **35** (7) (1996) p. 837.
11. D.L. Medlin, G.H. Campbell, C.B. Carter, *Acta Materialia.***46** (14) (1998) (to be published).
12. W. Wien, G.H. Campbell, and W.E. King, *Microstructural Science* **23** (1996) p. 213.
13. M.S. Daw and M.I. Baskes, *Phys. Rev. Lett.* **50** (1983) p. 1285 .
14. M.S. Daw, S.M. Foiles, and M.I. Baskes, *Materials Science Reports* **9** (1993) p. 251.
15. S.M. Foiles, M.I. Baskes, and M.S. Daw,*Physical Review B* **33** (12) (1986) p. 7983.
16. The copper EAM potential was fit using the functional forms described in Voter, A.F., Chen, S.P., Albers, R.C., Boring, A.M., and Hay, P.J. in *Atomistic Simulation of Materials: Beyond Pair Potentials,* edited by V. Vitek and D. J. Srolovitz (Plenum, 1989). The parameters from the fit are D_m = 0.07505 eV, R_m = 2.819 Å, α_M = 1.876 Å^{-1}, β = 1.396 Å^{-1} and r_{cut} = 4.95. Also, the r^6 in the density form is modified to r^4 and the 2^9 changed to 2^7. The resulting properties, with fit values in parenthesis, are: Elastic constants (GPa): c_{11}: 1.694 (1.700), c_{12}: 1.228 (1.225), c_{44}: 0.715 (0.758); Vacancy formation energy (unrelaxed) (eV): 1.27 (1.3); Stacking fault energy (mJ/m^2): 40.1 (45); $\nu_{100,l}$ (THz): 7.47 (7.25), $\nu_{100,t}$ (THz): 4.89 (5.13).
17. W. Bollmann, *Crystal Defects and Crystalline Interfaces* , Springer-Verlag-New York (1970).
18. A.P. Sutton and V. Vitek, *Phil. Trans. R. Soc. London* A **309** (1983) p. 1.
19. R.C. Pond and V. Vitek, *Proc. Royal Society London* B **357** (1977) p. 453-470.
20. D.L. Medlin, M.J. Mills, W.M. Stobbs, M.S. Daw, and F. Cosandey in *Atomic Scale Imaging of Surfaces and Interfaces*, eds. D.K. Biegelsen, D.J. Smith, S.Y. Tong, Materials Research Society Proceedings 295 (1993) p. 91.

Materials Science Forum Vols. 294-296 (1999) pp. 43-50

In situ High-Resolution Transmission Electron Microscopy of Interfaces in Phase Transformations

J.M. Howe[1], K.T. Moore[1], A.A. Csontos[1], W.E. Benson[1] and M.M. Tsai[2]

[1] Department of Materials Science & Engineering, University of Virginia, Charlottesville, VA 22903-2442, USA

[2] Heraeus Incorporated, Materials Technology Division, 301 North Roosevelt Avenue, Chandler, AZ 85226,USA

Keywords: Interphase Boundary Dynamics, Phase Transformations, *In situ* High-Resolution Transmission Electron Microscopy (HRTEM), Energy-Filtering TEM

Abstract

This paper discusses the use of *in situ* high-resolution transmission electron microscopy (HRTEM) techniques to determine the structure, composition and interphase boundary dynamics during phase transformations at the atomic level. Three main *in situ* HRTEM techniques are described: 1) *in situ* HRTEM dynamic studies that are performed on the same precipitate plates from different viewing directions in order to determine the three-dimensional structure and dynamics of the interfaces, 2) *in situ* compositional mapping of precipitate interfaces obtained by enery-filtering TEM (EFTEM) experiments at temperature in a HRTEM, and 3) real-time HRTEM image simulations that are being created for comparison with and interpretation of experimental *in situ* HRTEM dynamic observations. The results from these studies demonstrate that it is possible to understand the mechanisms and kinetics of interphase boundary motion at the atomic level.

1. Introduction

In order to understand the atomic mechanisms of phase transformations, or more generally, the motion of interphase boundaries, it is necessary to determine the structure and composition of moving interfaces as close to the atomic level as possible [1-4]. The way that the structural and compositional changes occur relate directly to the local interphase boundary dynamics. One major goal of this research is to use *in situ* high-resolution transmission electron microscopy (HRTEM) to follow the structure, composition and interphase boundary dynamics during phase transformations at the atomic level.

In this research, precipitate plates in Al alloys are used as model systems for studying the atomic mechanisms of phase transformations and interphase boundary motion. Reasons for this include: 1) plates are the most common precipitate morphology found in alloys and it is technologically and scientifically important to understand their behavior [2,5], 2) it is often possible to study both fully coherent and semicoherent interfaces simultaneously on the same plate [6-8], 3) plates are highly anisotropic and ideal for understanding faceting and anisotropy [9,10], and 4) plates usually grow by a terrace-ledge-kink (TLK) mechanism, and it is useful to contrast the behavior of this mechanism at solid-solid interfaces with TLK interfaces in solid-liquid and solid-vapor interfaces [4,8,11,12].

The following experimental results are divided into three main sections which illustrate experiments that are being performed to understand the atomic structural and compositional changes and mechanisms of interphase boundary motion at growing precipitate interfaces. These sections include descriptions of: 1) *in situ* HRTEM dynamic studies that are performed on the same precipitate plates from different viewing directions so that it is possible to obtain a three-dimensional description of the interfaces [8], 2) *in situ* compositional mapping of precipitate interfaces obtained by enery-filtering TEM (EFTEM) experiments at temperature in a HRTEM [13], and 3) real-time HRTEM image simulations that are being created for comparison with and interpretation of experimental *in situ* HRTEM dynamic observations [14].

2. Experimental Procedures

A high-purity Al-4.2 at.% Ag alloy was vacuum melted and cast, homogenized at 535°C for about 40 h to reduce segregation, and hot and cold rolled to 180 μm final thickness. Disks 3 mm in diameter were punched from the sheets and solution annealed for 30 min at 550°C, quenched in cold water, aged for 10 min at 350°C, and again quenched in cold water. The 10 min aging treatment was used to produce a dense distribution of γ' Ag_2Al plates in a partially supersaturated matrix, for subsequent heating in the HRTEM [6]. Samples from high-purity Al-3.9wt.%Cu-0.5wt.%Mg-0.5wt.%Ag homogenized sheet were solution heat-treated for 12 hours at 525°C and quenched into cold water. They were then aged above the Guinier-Preston II zone solvus for 24 hrs at 250°C and quenched into cold water for subsequent heating in the HRTEM [15]. The Al alloy specimens were electropolished in a twin-jet Fischione apparatus using a 25% nitric acid-75% methanol electrolyte at about -40°C, 16 V and 20 mA. After perforation, the foils were rinsed in two methanol and one ethanol bath and stored in vacuum until examination.

The Al-Cu-Mg-Ag alloy was examined at 400 kV in a JEOL 4000EX microscope equipped with a UHP40X hot-stage pole piece (spherical aberration coefficient = 1.1 mm and point resolution = 0.18 nm) and a double-tilt holder (±10°) using temperatures in the range of 180-450°C [8,10]. Experiments were performed in two different precipitate orientations (along $[001]_\theta//[1\text{-}11]_\alpha$ and along $[\text{-}110]_\theta//[111]_\alpha$) so that a three-dimensional description of the interfacial structure and dynamics could be obtained. Images were recorded on a videocassette recorder connected to a Gatan fiber-optically coupled TV camera with an image intensifier. A Canon EOS A2 35 mm camera with a 1/8 s exposure was used to obtain photographs directly from the TV monitor during playback of the videocassettes. Real-time kinetic data were obtained directly from the television monitor during playback of the videocassettes.

The *in situ* hot-stage EFTEM experiments were performed on a JEOL 2010F Schottky field-emission TEM operating at 200 kV using a Gatan Model 652 double-tilt heating holder. The 2010F was equipped with a high-tilt pole-piece (C_s = 1.0 mm and ±30° tilt) so that the point resolution is 0.23 nm at Scherzer defocus (-60.0 nm); the information limit is 0.14 nm. Thin foils were tilted into a $<110>_\alpha//<11\text{-}20>_{\gamma'}$ zone axis and slowly heated to 280-300°C. Once the temperature and drift had stabilized, energy-filtered images of growing ledges were acquired on the CCD camera in a Gatan Model 678 Imaging Filter (GIF) [16] utilizing EL/P (v. 3.0) and DigitalMicrograph (v. 2.5) software [17]. The microscope magnification was 60 kX and exposure times of 5-10 s were used to acquire the energy-filtered images. In most cases, objective and spectrometer apertures were not used, so the energy-filtered images were obtained using the maximum possible collection angle allowed by the GIF. Ag jump-ratio images were formed using the Ag $N_{2,3}$ edge at approximately 45 eV using an 8 eV slit centered 6 eV ahead of the $N_{2,3}$ edge for the pre-edge image and 8 eV behind for the post-edge image. Jump-ratio images were obtained using DigitialMicrograph software [17] to correlate and divide the image intensities, and intensity profiles were also obtained using this software. In order to obtain accurate jump-ratio images of the precipitate interfaces, it was necessary to manually correlate the pre-edge and post-edge images with high precision. Further experimental details are provided in [13].

Real-time HRTEM image simulations of a ledge migrating across the face of a h.c.p. γ'Ag_2Al precipitate plate in an f.c.c. α Al matrix were created for comparison with experimental HRTEM images. The interface was constructed using the CrystalKit software program [18], which interfaces directly to MacTempas software [19] for calculating HRTEM images. The orientation relationship between the γ' precipitate plate and α matrix is $(0001)_{\gamma'}||\{111\}_\alpha$ and $<11\text{-}20>_{\gamma'}||<110>_\alpha$, with the interface parallel to $(0001)_{\gamma'}||\{111\}_\alpha$ and the electron beam parallel to a $<110>_\alpha$ direction contained in this plane [6]. In the interface model, Sr atoms, which have the same average atomic number as a disordered Ag_2Al solid solution, were used in the precipitate phase for convenience. The ledge in the simulations was six $\{111\}_\alpha$ planes high (the equivalent of each of three different type of Shockley partial dislocations on alternate $\{111\}_\alpha$ planes), since this configuration is often found on plates because it minimizes the elastic strain energy of the ledges [20].

The x-axis of the ledge unit-cell was parallel to the interface and contained 34 atoms for a unit-cell width of 8.4 nm. In order to simulate movement of a ledge across this interface, 34 atomic models of a ledge that was six $\{111\}_\alpha$ planes high were constructed using CrystalKit, and a HRTEM image was simulated for each model, assuming a crystal thickness of 11.4 nm. Parameters used for the image simulations were typical for a JEOL 4000EX microscope operating at 400 kV at Scherzer

defocus (-48.5 nm) with C_s = 1.0 mm, objective lens aperture radius = 7.0 nm^{-1}, half-width of Gaussian spread of focus = 8.0 nm, convergence semi-angle = 0.60 mrad, slice thickness = 0.1 nm, and sampling matrix = 512x512. The 34 frames were then imported into Adobe Premiere 4.2 [21] and ordered into a movie. Each image was given a duration of one frame (1/30 s). Four seperate sequences of motion were created, each representing a different type of ledge behavior that has been observed in actual *in situ* HRTEM dynamic studies. These four sequences are referred to as fast, slow, oscillatory, and oscillatory with a jump, in the experimental results. The fast and slow movies were created with frames 1 to 34 in chronological order and varying only the number of frames of each ledge, for example 15 frames of each ledge position for a total movie of 17 s duration in the slow case and 2 frames of each ledge position for a total movie of about 4.2 s duration in the fast case. The oscillatory simulation was constructed using the following sequence of frames: 1,2,3,4,5 - 6,7,6,8 - 7,8,7,9 - 8,9,8,10 - ... - 29,30,29,32 - 31,32,33,34. The oscillatory motion with a jump utilized the same numerical sequence but included a jump from 8,9,8,10 to 15,16,15,17, with frames 11 to 14 deleted. The movie was then saved onto the hard drive in a PowerCenter 150 computer using the hardware MPEG compression provided by a miroMOTION DC20 video card. The final movie was printed to video from Adobe Premiere using the miroMOTION DC20 video card and a Panasonic Model 1960 videocssette recorder.

3. Results and Discussion

3.1. *In Situ* HRTEM Dynamic Studies

Recent *in situ* hot-stage HRTEM studies of precipitate plates in Al-Cu-Mg-Ag and Al-Ag alloys performed both parallel and perpendicular to the plate faces, and comparison of these studies with prior HRTEM and conventional *in situ* hot-stage TEM investigations, have clearly established the terrace-ledge-kink (TLK) mechanism [11] as the primary atomic mechanism involved in growth and dissolution of faceted precipitates in metal alloys [6,8,10,12,22]. This process is illustrated schematically in Fig. 1, which shows a perspective view of a precipitate plate growing by ledges which nucleate on the habit plane and propagate out to the edge, where they stack one above the other. Figure 1 shows two additional views, one perpendicular to the habit plane of the plate, i.e., face-on, and the other parallel to the habit plane, i.e., edge-on. It is clear from the two lower illustrations, that when the plate is viewed edge-on parallel to the facets, it is possible to observe the atomic structure and dynamics of individual ledge motion and also the motion of the ledges stacked at the plate edges by *in situ* HRTEM. When the edge of the plate is viewed in the face-on orientation, the electron beam is parallel to the ledges and this makes it possible to observe kinks which form on and propagate along the ledges. By combining information from these two orientations, it is possible to obtain a three-dimensional description of the atomic mechanisms of interfacial motion, as illustrated by the following data for {111} θ plates in an Al-Cu-Mg-Ag alloy.

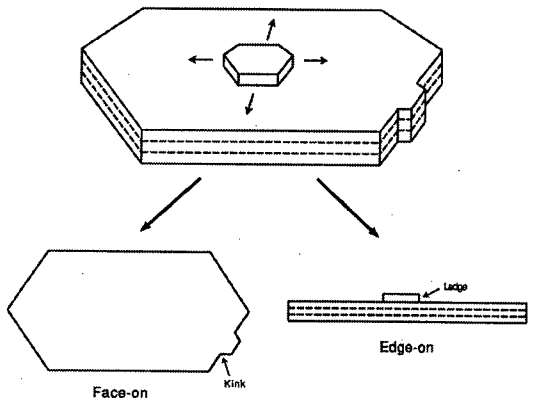

Figure 1. (Top) Perspective view, (bottom-left) face-on and (bottom-right) edge-on views of a precipitate plate growing by a TLK mechanism.

3.1.1. Structural and Kinetic Analyses in Edge-On Orientation

The orientation relationship of the {111} θ phase with the matrix is $(-110)_\theta \| (111)_\alpha$, $[110]_\theta \| [101]_\alpha$ and $[001]_\theta \| [1\text{-}11]_\alpha$, which is a low-energy orientation relationship relationship for θ phase designated as a Vaughan II orientation relationship [23]. Figure 2(a) shows a HRTEM image of a ledge on the face of a θ plate viewed edge-on along a $[001]_\theta \| [1\text{-}21]_\alpha$ direction, as in the lower-right illustration in Fig. 1. The ledge is approximately two $\{111\}_\alpha$ matrix planes high, or half of a unit cell

of the θ structure (0.424 nm). This was the smallest ledge size that was observed on the faces of the θ plates and higher ledges were often observed [7,8]. The image was photographed from the videocassette during growth at about 220°C and the ledge was observed to oscillate several times per second over a distance of about two unit-cells of the θ phase along the precipitate face while moving

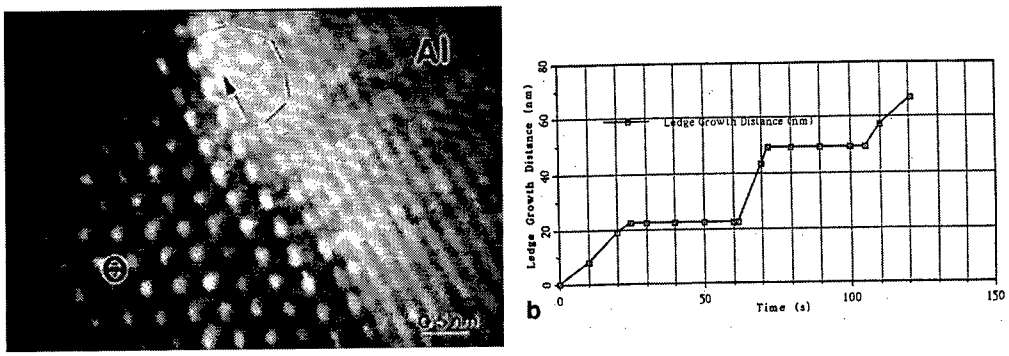

Figure 2. (a) HRTEM image of a single ledge on a θ plate during growth at about 220°C and (b) graph of growth distance versus time for the ledge in (a) (from [10]).

slowly across the face toward the precipitate edge in the direction indicated by an arrow. *In situ* experiments performed perpendicular to the plate face indicate that the oscillatory motion is due to the formation and annihilation of kinks along the ledge, as demonstrated in the next section. The videocasette recording also revealed direct experimental evidence of enhanced atomic motion in the matrix just ahead of the ledge and this leads to slight blurring in the photograph, which is visible in the enclosed area in Fig. 2(a). It is important to note that the precipitate structure only one unit cell behind the ledge appears completely transformed, indicating that the structural and compositional changes which are necessary for diffusional growth occur simultaneously within a few atomic distances of the ledge. Although the ledge appeared to move smoothly across the precipitate face over short periods of time, it displayed start-stop behavior when viewed over longer times, as shown in Fig. 2(b) [8]. Such periodic lack of mobility during the migration of ledges has been observed previously and attributed to a lack of sites for atomic attachment along the ledges as they align along low-energy matrix directions, in this case $<121>_\alpha$ [7].

3.1.2. Structural and Kinetic Analyses in Face-On Orientation

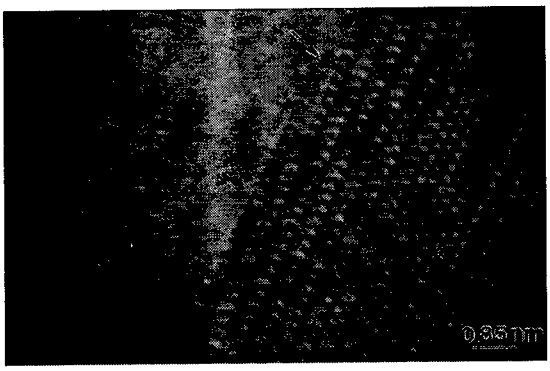

Figure 3. An isolated kink (indicated by arrow) travelling along the $[110]_\theta$ facet of a {111} θ precipitate plate during growth at about 275°C (from [8]).

Figure 3 shows a HRTEM image taken at the edge of a θ plate viewed face-on along a $[-110]_\theta \| [111]_\alpha$ direction, as in the lower-left illustration in Fig. 1, during an *in situ* hot-stage experiment at about 275°C. The prominent rectangular pattern of white spots outlined in Fig. 3 with dimensions of 0.244 nm by 0.429 nm relates directly to positions of Cu atoms in the θ structure, as determined by HRTEM image simulation [10,15]. During the *in situ* HRTEM experiments, the θ plate was observed to grow by the nucleation of half unit-cell high (0.429 nm) double kinks along the $(110)_\theta \| (101)_\alpha$ plate edge, which propagated along the edge until they reached the intersecting facet. The arrow in Fig. 3 indicates the end of one such kink. The smallest kinks were one-half of the θ unit cell in height (one rectangular pattern of white spots about 0.429 nm long) but sometimes

two or three kinks nucleated and/or dissolved in rapid succession in an oscillatory manner about an average position, similar to the behavior described for the ledge in Fig. 2. It is important to note that the kink in Fig. 3 is well defined to within two or three half unit cells of the {111} θ structure. Although the image in Fig. 3 was taken at the edge of the θ plate where several ledges may be stacked vertically parallel to the electron beam direction, when this perspective is combined with the one in Fig. 2, it is possible to conclude that the phase transformation is occurring at kinks in ledges on the θ plates and that the transformation is completed within a volume as small as about one unit cell of the θ phase along the $[-110]_\theta$ and $[110]_\theta$ directions. This volume contains about four atoms of Cu and eight atoms of Al. Thus, performing *in situ* HRTEM allows observation of the atomic mechanisms of the transformation (the TLK mechanism) as well as the dynamics of transformation. It is also possible to study the dynamics of the kinks at the edges of the plates, as described in detail elsewhere [8,10].

3.2. *In Situ* Energy-Filtering TEM

In the previous section, it was stated that the transformation was completed within a unit cell at kinks in the ledges. This conclusion was based on the HRTEM image contrast at the ledges, which appeared similar to that of the fully formed precipitate plate. Although this interpretation is likely correct, it is difficult to directly determine the compositional change at the ledge from the HRTEM images. The following experiment shows the potential of high-resolution energy-filtering TEM (EFTEM), also referred to as electron spectroscopic imaging (ESI) [24], for determining compositional changes at transformation interfaces with subnanometer spatial resolution, which allows one to follow the compositional change directly, in addition to the structural change. In this experiment, elemental edges are used to form compositional maps (jump-ratio images) [24-27] of ledges on the faces of γ' (Ag_2Al) precipitates plates in an Al-Ag alloy during growth at temperature using a heating holder and EFTEM, i.e., *in situ* EFTEM [13].

Figure 4 shows a Ag jump-ratio image of a double-ledge, 0.92 nm high, that was migrating across the face of a γ' precipitate at 280°C. Intensity profiles averaged over 10 pixels across the adjacent terrace (habit plane) and the ledge, are shown in Figs. 4(a) and (b), respectively. The Ag gradient across the terrace, which is known to be atomically flat, occurs over a distance of about 9 pixels (indicated by arrows) or 0.4 nm, demonstrating the excellent spatial resolution that can be obtained across a transformation interface at temperature by *in situ* EFTEM. The intensity profile

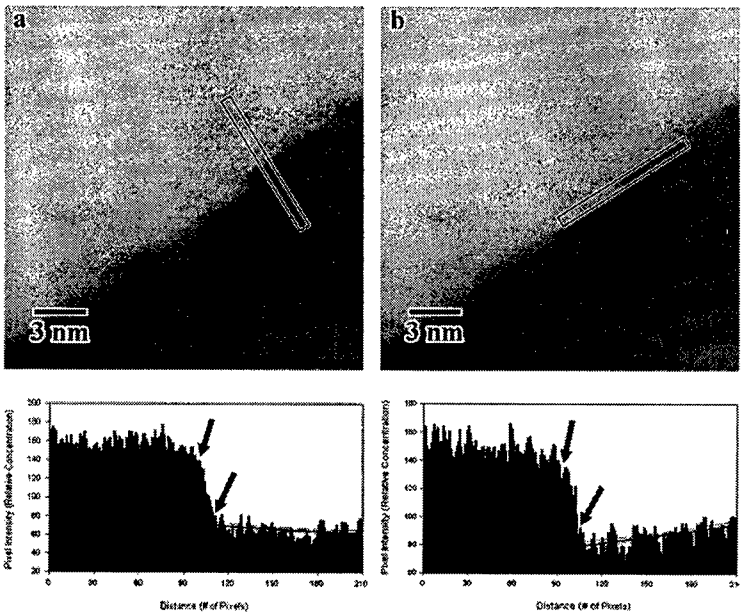

Figure 4. Ag jump-ratio image of a 0.92 nm ledge on a γ' plate with an intensity profile across the (a) terrace plane and (b) ledge, averaged over ten pixels. Arrows indicate the interface widths and gray lines indicate average linear profiles in the matrix up to the terrace and ledge (from [13]).

across the ledge in Fig. 4(b) changes abruptly on the matrix side of the interface and then slopes gradually into the precipitate. This change occurs over about 11 pixels (indicated by arrows), indicating that the transformation is complete within about 0.5 nm (or two atomic spacings) at the ledge. In addition, it is also important to note that there appears to be a slight depletion in the Ag concentration ahead of the ledge in Fig. 4(b) as compared to the terrace in Fig. 4(a). This point is illustrated by the two bold lines which are superimposed on the intensities in the matrix up to the interface. The bold lines are a first-order linear regression analysis of the intensity values and the fine lines on either side represent 99% confidence limits for the lines. There is a distinct downward slope in the intensities (Ag concentration) ahead of the growing ledge. A depleted region ahead of the ledge is expected for a diffusional transformation where solute flows down the gradient ahead of the advancing interface [4,28] and these results indicate that it may be possible to detect such gradients at ledges using EFTEM. Although the atomic structure of these ledges has been previously determined by HRTEM, this is the first direct confirmation of the compositional change at the ledges at this level of resolution. Note that the intensity change (Ag concentration) is achieved within a few atomic distances at the ledge, indicating that the compositional and structural components of the transformation occur simultaneously at the advancing ledge, as deduced from the HRTEM images of the {111} θ phase described in Secion 3.1.

A model precipitation process was chosen for the study, but this technique can be applied to many other important diffusional transformations, including reactions at semiconductor and composite interfaces for example [1]. It has recently been applied to understand the role of hydrogen in growth of g-TiH in Ti-H alloys [29,30] and because EFTEM is particularly well-suited to the study of light elements [25], e.g., C and N, this technique should prove extremely valuable for understanding diffusional phase transformations in alloys involving other interstitial elements.

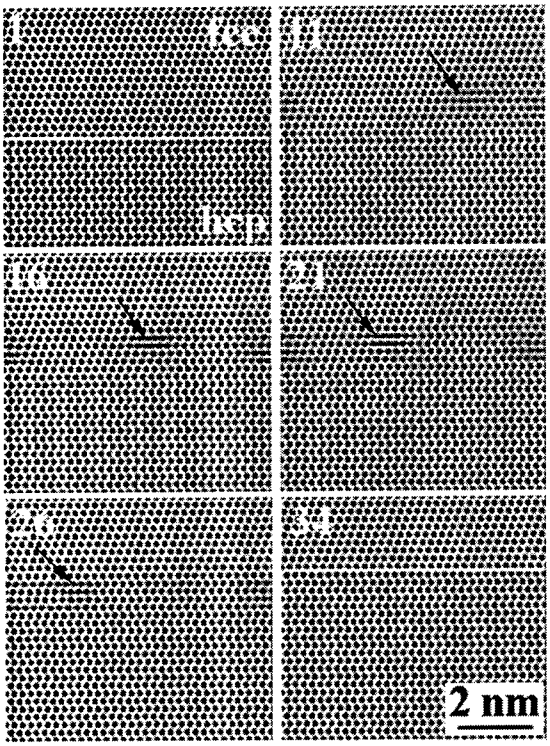

Figure 5. Six of thirty-four simulated HRTEM images used to create real-time videos of ledge motion across the face of a γ' precipitate plate in an Al-Ag alloy with the behavior shown in Fig. 6.

3.3. Real-Time HRTEM Image Simulations

Figure 5 shows six of thirty-four ledge image simulations (frames) that were used to create real-time videos of ledge motion across a planar precipitate interface, such as the one shown in Figs. 1, 2 and 4. The position of the original α/γ' interface is indicated by a horizontal line in image 1 (top left) and the position of the interface six {111} α planes higher after passage of the six-plane ledge from right to left across the interface, is indicated by the line in image 34. The position of the ledge in images 11, 16, 21 and 26 (indicated by arrows), as well as in the other twenty-eight images containing the ledge, is evidenced by the slight blurring that occurs in the images due to distortions of the atomic columns at the ledge.

Figures 6(a) and (b) show graphs of the four different video sequences that were produced from the thirty-four images, including the images in Fig. 5. Copies of the actual videos can be obtained from the authors by request (E-mail: jh9s@virginia.edu). The two sequences shown in Fig. 6(a) appear as fast and slow continuous motion of the ledges across the interface in the videos, although in the graphs the motion is stepped, due to the discrete number of frames used for each position. The average velocities of the ledges in these two videos are 2.0 and 0.49 nm/s, respectively. In these graphs the entire ledge moves forward one atom at a time through the entire thickness of the crystal. Experimentally, it has been observed that ledge motion actually occurs

by kinks which propagate along the ledge parallel to the electron-beam direction (Fig. 3 for example), so that the ledge gradually moves forward through the foil thickness. The next step in creating these videos is to model this situation using a layered multislice program [19], which will allow the ledge to overlap with varying amounts of matrix. This is similar to a kink propagating parallel to the ledge through the foil with time. This will cause the graphs in Figs. 6(a) to smooth out and is likely to make ledge motion appear smoother at slow velocities in the video recordings.

Figure 6(b) shows two additional types of ledge behavior that are commonly observed in experimental *in situ* HRTEM experiments [8,10,30]. One is labeled oscillatory and the other is

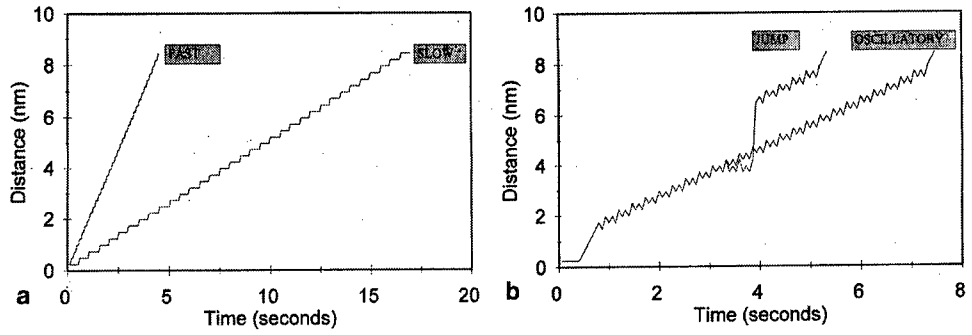

Figure 6. Graphs of ledge distance versus time for two dynamic simulations of ledges moving across a γ' plate with (a) constant step-wise velocities and (b) constant but oscillatory velocities, one including a jump.

labeled jump, which is similar to the oscillatory case except for a period of ledge stasis followed by a rapid jump, partway through the sequence. The average velocities of the ledges in these two sequences are about 1.1 and 1.8 nm/s, respectively. These two sequences of ledge motion display the type of behavior observed in *in situ* studies of migrating ledges, where the ledge front oscillates back and forth over a few atomic spacings about an average position as the ledge moves forward with an overall average velocity. This oscillation causes ledge fronts to appear blurred, as discussed with regard to the image in Fig. 2. This effect is reproduced by the oscillating ledges in the two videos. Thus, it is possible to reproduce the oscillatory behavior of migrating ledges in the real-time image simulations. In essence, this reproduces the dynamic behavior of the ledges, which is due to kinks which come and go along the ledge as it moves forward. As discussed above, the next level of complexity in these simulations is to produce similar oscillatory behavior using a layered multislice which can more closely simulate kinks which extend partway through the thickness of the foil. Also notice that the jump behavior displayed in the simulation in Fig. 6(b) is similar to the start-stop behavior of the ledge in Fig. 2(b), although the ledge in Fig. 2(b) did not advance at all in between the jumps, and the jumps were not as fast as that in Fig. 6(b). However, the sort of kinetic behavior shown in Fig. 6(b) and appearance of the simulated videos is approaching the behavior observed in actual *in situ* HRTEM experiments. It is possible to envision that in the near future, it will be possible to match the appearance and kinetic behavior of dynamic HRTEM experiments dynamic image simulations, the same way as static image matching is currently performed [6,19].

4. Conclusions

1. *In situ* HRTEM experiments performed along perpendicular crystallographic directions can be used to determine the three-dimensional atomic structure of transformation interfaces and the mechanisms and dynamics of interfacial motion. In this study, plates were shown to grow by a TLK mechanism with the tranformation completed within a volume of about one unit-cell at the kinks.
2. It is possible to obtain sub-nanometer compositional information at transformation interfaces *in situ* using a heating holder and EFTEM. The results of this study show that the Ag gradient across moving ledges is more diffuse than across stationary terraces, and that the compositional component is fully achieved at the ledges.
3. Real-time HRTEM image simulations can be created for comparison with *in situ* HRTEM dynamic experiments to determine the details of atomic motion at interfaces.

Acknowledgments

The authors gratefully acknowledge the help of Dr. A. Garg (NASA LeRC) and Dr. Y.-C. Chang (CSIST) on the Al-Cu-Mg-Ag alloy studies. This research was supported by the National Science Foundation under Grant DMR-9630092.

References

[1] Wolf D, Yip S (Eds.), *Materials Interfaces: Atomic-Level Structure and Properties*, Chapman & Hall, London (1992).
[2] Wayman CM, Aaronson HI, Hirth JP, Rath BB (Eds.), Proceedings of the Pacific Rim Conference on the Role of Shear and Diffusion in the Formation of Plate-Shaped Transformation Products, *Metall. Mater. Trans.* 25A (1994) 1781-2068.
[3] Sutton AD, Balluffi RW, *Interfaces in Crystalline Materials*, Clarendon Press, Oxford (1995).
[4] Howe JM, *Interfaces in Materials: Atomic Structure, Thermodynamics and Kinetics of Solid-Vapor, Solid-Liquid and Solid-Solid Interfaces*, John Wiley & Sons, New York (1997).
[5] Aaronson HI, *J. Microscopy* 102 (1974) 275-350.
[6] Howe JM, Dahmen U, Gronsky R, *Phil. Mag A* 56 (1987) 31-61.
[7] Garg A, Chang Y-C, Howe JM, *Acta Metall. Mater.* 41 (1993) 235-251.
[8] Benson WE, Howe JM, *Phil. Mag A* 75 (1997) 1641-1663.
[9] Garg A, Howe JM, *Acta Metall. Mater.* 39 (1991) 1939-1946.
[10] Howe JM, Benson WE, *Interface Science* 2 (1995) 347-363.
[11] Burton WK, Cabrera N, Frank FC, *Phil. Trans. Roy. Soc.* A243 (1950-52) 299-358.
[12] Howe JM, Prabhu N, *Acta Metall. Mater.* 38 (1990) 881-896.
[13] Csontos AA, Tsai MM, Howe JM, *Micron* 29 (1998) 71-79.
[14] Howe JM, Csontos AA, Tsai MM, in *Microscopy and Microanalysis,* Bailey GW, Dimlich RVW, Alexander KB, McCarthy JJ, Pretlow TP (Eds.), Springer-Verlag, New York (1997) pp 627-628.
[15] Chang Y-C, Ph.D. Thesis, Carnegie Mellon University, Pittsburgh, PA (1992).
[16] Gubbens AJ, Krivanek OL, *Ultramicroscopy* 51 (1993) 146-159.
[17] Gatan, Inc., *Gatan Imaging Filter Users Guide, Digital Micrograph 2.5 Users Guide, EL/P 3.0 Users Guide*, Pleasanton, CA (1995).
[18] Kilaas R, *CrystalKit Software*, RKCS, Berkeley, CA (1992).
[19] Kilaas R, in *Proc. 45th Ann. Meeting EMSA,* Bailey GW (Ed.), San Francisco Press, San Francisco (1987) pp 66-69.
[20] Enomoto M, Hirth JP, *Metall. Mater. Trans.* 27A (1996) 1491-1500.
[21] Adobe, *Adobe Photoshop 4.0/Premiere 4.2*, Adobe Systems Incorporated, Mountain View, CA (1995).
[22] Laird C, Aaronson HI, *Acta Metall.* 17 (1969) 505-519.
[23] Vaughan D, Silcock JM, *Phys. Stat. Sol.* 20 (1967) 725-736.
[24] Reimer L, in *Energy-Filtering Transmission Electron Microscopy*, Reimer L (Ed.), Springer-Verlag, Berlin (1995) pp 347-400.
[25] Egerton RF, *Electron Energy-Loss Spectroscopy in the Electron Microscope, 2nd Ed.* Plenum Press, New York (1996) pp 113, 302, 330, 433.
[26] Johnson DE, in *Introduction to Analytical Electron Microscopy*, Hren JJ, Goldstein JI, Joy DC (Eds.), Plenum Press, New York (1979) pp 245-258.
[27] Hofer F, Warbichler P, Grogger W, *Ultramicroscopy* 59 (1995) 15-31.
[28] Zener C, *J. Appl. Phys.* 20 (1949) 950-953.
[29] Tsai MM, Howe JM, in *Microscopy and Microanalysis 1996*, Bailey GW, Corbett JM, Dimlich RVW, Michael JR, Zaluzec NJ (Eds.), San Francisco Press, San Francisco (1996) pp 108-109.
[30] Tsai MM, Ph.D. Thesis, University of Virginia, Charlottesville, VA (1997).

Materials Science Forum Vols. 294-296 (1999) pp. 51-58

The Effects of Thermomechanical Processing on Interfacial Crystallography in Metals

V. Randle

Department of Materials Engineering, University of Wales Swansea, Swansea SA2 8PP, UK

Keywords: Grain Boundary Engineering, Coherent Twins, Coincidence Site Lattice Boundaries, Relative Boundary Specialness, Σ3 Regeneration Model

Abstract

Thermomechanical processing can be used effectively to manipulate the crystallography of grain boundaries in metals and alloys. Several examples are quoted here accompanied by an elucidation of the factors which influence the grain boundary network geometry. Twinning is the principal means of introducing improved boundaries into the microstructure, and this paper examines the reasons for this and proposes a model for the proliferation of Σ3 boundaries, as distinct from Σ3 twins, in the microstructure. It is concluded that the *relative* specialness of boundaries adjoining coherent twins, rather than the *absolute* specialness, is the critical factor.

Introduction

It is now recognised that the structure of the intergranular network in metallic materials can be manipulated by certain thermomechanical processing regimes. This premise forms the basis for 'grain boundary engineering', where a material is processed so as to approach an 'optimised' population of boundaries - without changing other parameters such as grain size - usually in terms of its resistance to intergranular degradation during service. The change in the grain boundary population is monitored in terms of the frequency of boundaries having low-Σ coincidence site lattice (CSL) geometries. Processing routes are based on combinations of deformation and annealing, devised largely empirically. The effects in terms of properties can be quite dramatic: for example intergranular attack of lead alloy electrodes in lead acid batteries, measured as weigh loss, is almost halved by increasing the proportion of Σ-boundaries from 10% to more than 50% [1].

This paper will examine the effects that processing, mainly cold work/annealing cycles, has on the grain boundary crystallography. First, grounds for use of the CSL - the main classification tool for grain boundary engineering - will be appraised followed by a summary of factors which influence the grain boundary population. Experimental evidence for successful grain boundary engineering will be reviewed and finally discussed in terms of a model for its achievement.

Categorisation of grain boundaries

As mentioned in the Introduction, the coincidence site lattice (CSL) is used as a categorisation method for grain boundary types in polycrystals. The CSL model was first propounded several decades ago [2]. Since then it has become a cornerstone of grain boundary structural research, particularly in cubic materials. Briefly, if the lattices of two grains were allowed notionally to interpenetrate, certain combinations of orientation relationship between the two lattices would result in a periodic array of coinciding sites - an abstraction which becomes physically real at a grain boundary. A boundary with

a high density of coincidence points implies 'good fit' of adjacent grains with a concomitant modification of properties such as diffusivity, energy or mobility. The reciprocal density of CSL points is denoted by Σ.

In the early 1980s the initiative of *'grain boundary engineering'* or *'grain boundary design'* was proposed [3]. It was a premise of the original concept that 'special' boundaries, i.e. those having good properties, were assumed to be low-Σ CSLs. The second proposition was that the proportion of special boundaries in a material is metastable, and can be manipulated. Since grain boundary engineering was first proposed in 1984 there have been some convincing demonstations of its application, but progress towards understanding the fundamental aspects which underpin it is proceeding at a slower rate.

Within the last few years the commercial viability of grain boundary engineering has started to be accepted and implemented. One of the most notable successes has been the processing technologies for GBE™[1] wrought austenitic steels and high performance nickel alloys. This industrial process guarantees material with the proportion of special boundaries enhanced to >60%. In turn, this provides increased protection against intergranular corrosion, cracking, stress corrosion cracking, embrittlement and sensitisation thus extending service reliability [4]. Almost all of the special boundaries are in fact twin-related ($\Sigma 3^n$ in CSL notation).

Having established that the CSL population is metastable and can be modified, the important question with respect to the application of the CSL model to grain boundary engineering is: does the experimental evidence support a link between CSLs and special properties [5]? Notable demonstrations of such a connection in polycrystals have been quite specific to particular CSLs and material conditions. In other words, the idea that *all* low-Σ CSLs are beneficial is not borne out in practice. However, there are some specific situations where much higher than random proportions of CSLs have been achieved. These are one- or two-dimensional polycrystals (e.g. wires or sheets) having a strong texture, which allow CSLs with a specific misorientation axis and a favourable boundary plane to develop; materials containing a high proportion of low angle boundaries ($\Sigma 1$); materials containing a high proportion of twins ($\Sigma 3$) [5].

The CSL is not a sufficient predictor of special properties. Knowledge of just the Σ-value does not predict the location of the boundary plane - a key element in boundary geometry and properties [6]. Furthermore, the CSL is a geometric model and does not account for the extrinsic structure of the boundary, which has an effect on properties, and also factors other than the intrinsic or extrinsic structure of the boundary may affect its behaviour, e.g. the orientation of the interfacing grains, the orientation of external features such as a tensile axis, or particularly extreme environmental conditions.

In summary, although all the discrepancies concerning the CSL model have not been resolved, the experimental convenience has turned out to be the overriding factor and justification for the ubiquitous use of the CSL.

Factors which influence the grain boundary population

The main circumstances which can be exploited to influence the grain boundary population are texture, external factors, twinning and boundary migration.

Texture A high proportion of grains having nearly the same orientation will inevitably result in a large number of low angle boundaries, which in turn improves the intergranular properties. Furthermore specific textures modify the misorientation axis between grains. For example, a 111 fibre texture results in an increased proportion of CSLs misoriented on 111. Whether or not these boundaries are beneficial in terms of properties then depends on the degree of fit at the boundary, i.e. the location of

[1] GBE™ is a registered trademark of Ontario Hydro.

the boundary plane . Fig. 1 shows the CSL distribution associated with aluminium having a strong 111 texture [7]. Note that the trend was predicted by computer simulation, indicating that texture is responsible for the distribution. Production of strong texture alone is not in general a viable route for grain boundary engineering because of other factors concurrently introduced, e.g. marked directionality of properties.

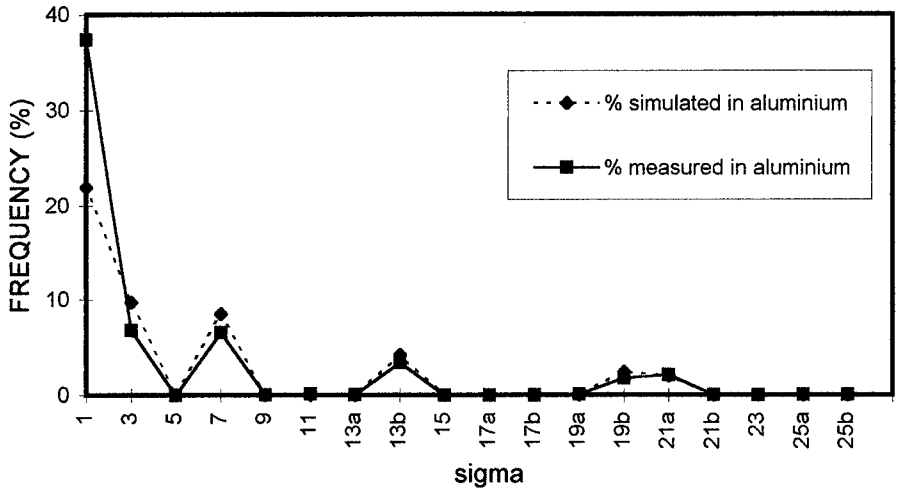

Fig. 1 Comparison between computer simulated and experimentally measured proportions of CSLs in aluminium (adapted from [7]).

External factors Certain external factors, for instance the component/specimen geometry or external forces such as the direction of a stress axis, will dominate the grain boundary parameters. For example, Fig. 2 shows 'bamboo' grains in thin sheet where the boundaries are oriented perpendicular to the sheet surface. Usually such a specimen is very strongly textured and the boundaries are constrained to be <hkl> tilts. Similarly, twist boundaries result from 'pancaked' grains and a strong texture after severe cold rolling. These are examples of grain boundary *plane* engineering [6].

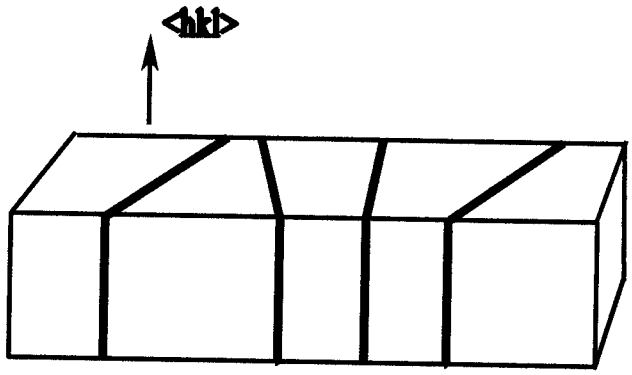

Fig. 2 Illustration of grain boundary geometry for 'bamboo' grains. A strong <hkl> fibre texture produces <hkl> tilt boundaries [6].

Twinning By far the majority of grain boundary engineering relies on multiple twinning, resulting in generation of large numbers of $\Sigma 3^n$ boundaries. Fig. 3 shows average proportions of $\Sigma 3$s in various materials, taken from over 200 investigations. In general, the lower the stacking-fault energy the higher the $\Sigma 3$ proportion. Multiple twinning is governed by the following rule concerning the joining or dissociation of CSLs:

$$\Sigma A + \Sigma B \leftrightarrows \Sigma(A \times B) \qquad \text{or} \qquad \Sigma A + \Sigma B \leftrightarrows \Sigma(A/B) \qquad (1a,b)$$

(Equation 1b applies only if A/B is an integer and A>B). Hence if two boundaries at a triple grain junction are $\Sigma 3$ and $\Sigma 9$, the third junction is either another $\Sigma 3$ or a $\Sigma 27$. Typically in a grain boundary engineered material the proportion of $\Sigma 3$s is high, the proportion of $\Sigma 9$s is about one-fifth that of the $\Sigma 3$s and the proportion of $\Sigma 27$s is only slightly higher than that for a random distribution [5]. Extensive twinning will affect the texture of the material, sometimes producing randomisation, depending on the twin variants selected. $\Sigma 3$ 'coherent twins' on 111 planes have particularly low 'excess volumes' (where 'excess volume' is the principal intrinsic feature which governs boundary behaviour) whereas other $\Sigma 3$s (sometimes known as 'incoherent twins') and some $\Sigma 9$s typically have higher volumes but these are still much lower than an average high angle boundary. Hence both these Σ-values may display 'special' behaviour in terms of an inhibited response to intergranular degradation. Twinning is discussed further below.

Grain boundary migration In general low free volume boundaries display higher migration rates than random high angle boundaries because of reduced solute drag at the former. (An exception to this is coherent twins and very low angle boundaries which are virtually immobile). Hence phenomena such as recrystallisation and grain growth will promote the preferential migration of low free volume boundaries. However, as such special boundaries migrate and encounter other boundaries, their geometry will inevitably change and initial benefits are lost.

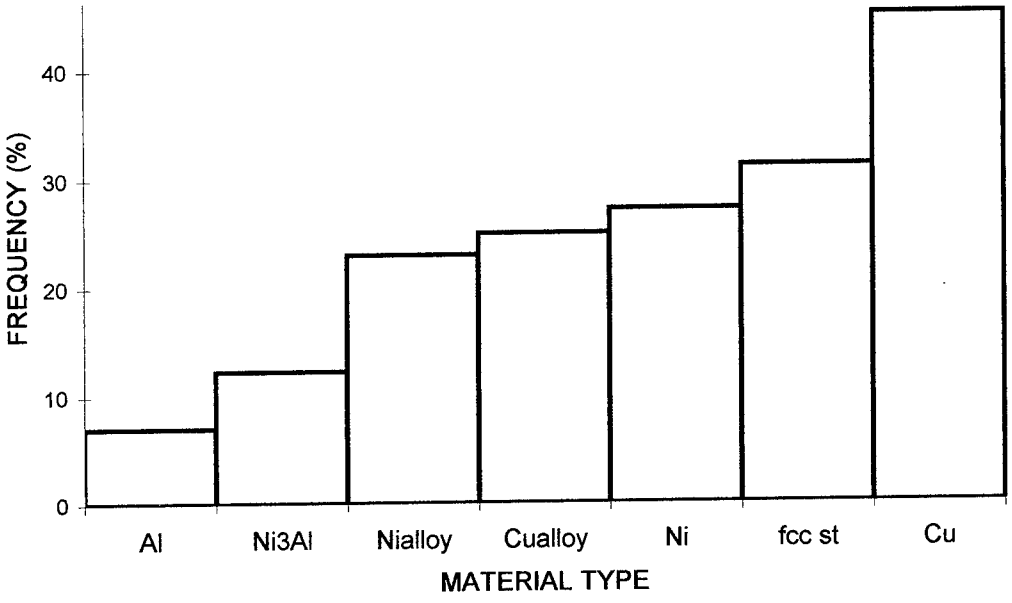

Fig. 3 Average proportions of $\Sigma 3$ boundaries in various face-centred cubic materials. The statistics were collated from over 200 investigations [5].

Grain boundary population modification

There are few publications which actually report the deliberate exploitation of treatments to change the grain boundary population. We will focus on those that use twinning rather than strong textures and/or thin film type specimen geometry. In general in a low stacking fault material a medium/high level of cold work followed by a very short high temperature anneal will result in much twinning and a small grain size during recrystallisation. For example, a treatment consisting of 70% cold rolling followed by an anneal at 1000°C for 1 minute has been used to generate deliberately a high proportion of twins in 304 stainless steel for the purpose of investigating twin-associated carbide growth [8].

The processes used for the primary purpose of increasing the proportion of $\Sigma 3^n$ boundaries fall into four categories:

- Multiple-step recrystallisation
- One-step recrystallisation
- Multiple-step strain annealing
- One-step strain annealing.

Multiple-step recrystallisation Some work emphasises the importance of recrystallisation iterations [9]. For example in a nickel-based alloy (Ni-16Cr-9Fe) five sequential steps of 20% cold work followed by 3 minutes at 1000°C resulted in a grain boundary population containing 47% Σ3 and 10% Σ9, almost double that obtained by conventional processing. Similarly, strain-recrystallisation treatments in copper of three iterations comprising 30% compression plus 10 minutes at temperatures around 375°C increased the proportion of Σ3s to 58% [10]. Several variants on the multi-stage heat treatments in copper have recently been found to increase greatly the proportion of $\Sigma 3^n$s, for instance five iterations of 20% deformation plus 5 minutes at 750°C gave 45% Σ3s and 7% Σ9s [11]. In all these cases the grain size remained small.

One-step recrystallisation As in [8], a short anneal at a high temperature after medium levels of deformation can also produce a high twin density accompanied by the required small grain size. For example in copper 50% deformation plus 1000°C for 1 minute produced higher proportions of twins than the multi-step treatments [11]. It remains, however, to test which gives the better properties.

Mutiple-step strain annealing If only a low level of deformation is applied, i.e. up to 6%, an increase in $\Sigma 3^n$ has been found to occur during subsequent annealing without recrystallisation. Two or three stages were more successful than a single stage. In alloy 600 (Ni-16Cr-9Fe) deformations of 2-5% followed by anneals at 890°C-940°C for 1-20h have been found to increase the proportion of Σ3s and Σ9s from 6% to 12% and 5% to 12% respectively accompanied by a marked improvement in properties [12]. Note that in these investigations coherent twin boundaries were omitted from the data set, therefore the proportions appear low compared with other statistics. For copper, the most successful low strain treatment was found to be 6% compression followed by 14h at 275°C then 7h at 375°C, giving 67% Σ3s and 9% Σ9 [13]. Although the twin fraction decreased slightly during the first anneal, it was found to be a necessary step in the evolution of the final fraction of CSLs.

One-step strain annealing A single anneal, either following a small applied strain or utilising the residual strains present after recrystallisation, has been observed to modify the crystallography of the grain boundary population both by altering the crystallographic alignment of the grain boundary planes [14] and by producing a grain boundary population in which the $\Sigma 3^n$ boundaries are nearer to the exact CSL configuration [15]. Fig. 4 illustrates the latter effect after 6% strain plus annealing. It is striking that only $\Sigma 3^n$ boundaries showed a consistent trend to have both fairly low deviations from exact matching and for the deviation to decrease with increasing annealing time. This was construed as a gradual decrease in free volume for the Σ3 boundaries, accompanied by a 'geometrically necessary' decrease for the Σ9 and Σ27s since they usually conjoin Σ3s.

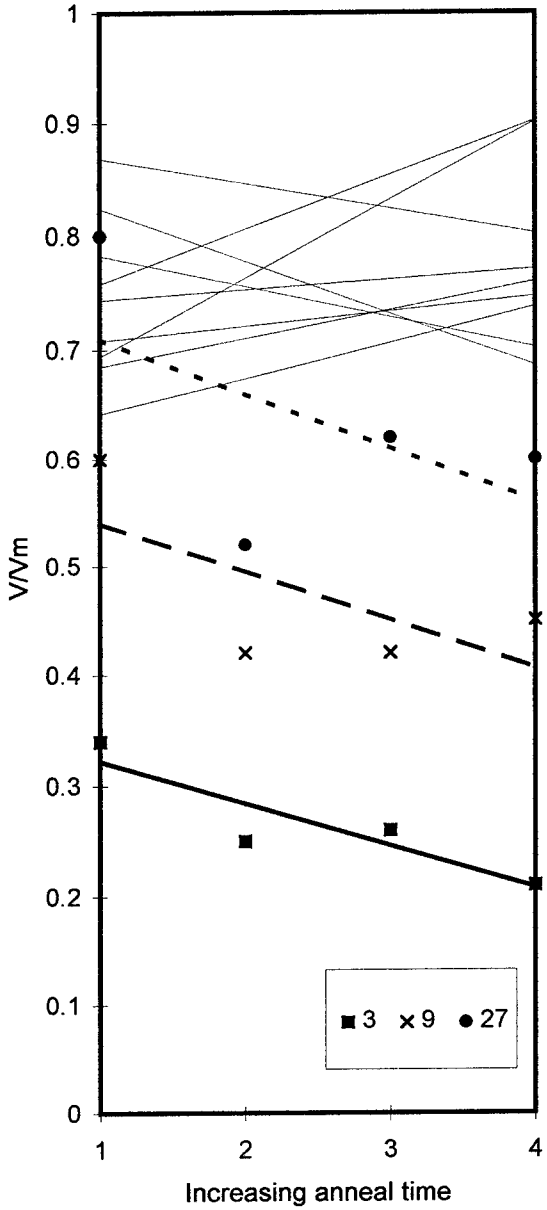

Fig. 4 The normalised deviation from exact CSL matching, v/v_m, for boundary populations (over 3000 boundaries) in nickel annealed for various times. The Σ-values with the lowest average v/v_m are $\Sigma 3^n$, and these v/v_ms also decrease with annealing time. All other Σ-values (up to Σ25 and shown as light lines) have higher v/v_ms which tend conversely to increase with annealing time [15].

Discussion

Although in the various investigations quoted above it is recognised that twinning is central to the development of superior intergranular properties, the mechanisms by which this is effected are as yet unclear. The critical feature cannot be the presence of the transgranular coherent annealing twins on 111 planes, because interfaces of this type are not, from a properties rather than a crystallographic point of view, part of the grain boundary network - for example they are virtually both immobile and take no part in intergranular transport. By contrast other types of Σ3 are indeed part of the grain boundary network. They are present from relationships at triple junctions (Eqn. 1), as incoherent portions of twins or from encounters between grains having a Σ3 orientation relationship. It is unfortunate that most investigations which report Σ3 fractions do not distinguish between the statistics and distribution of the different categories of Σ3.

Annealing twinning occurs for two reasons: to decrease the overall interfacial energy when the energy of the boundaries between a grain's neighbours and its twin would be less than that of the boundaries between the neighbours and the grain itself [16], or to reorient grain boundaries so as to facilitate dislocation absorption and mobility during recrystallisation [17]. The former was proposed to acount for the presence of twins during grain growth, when reduction in total grain boundary energy is the driving force. However, as seen in the previous section most treatments to increase the proportion of Σ3s involve recrystallisation or strain-induced boundary migration rather than grain growth and so the energy reduction mechanism of [16], which is sometimes quoted in this context, is not strictly applicable. Rather, the mobility and dislocation absorption mechanism applies [17].

A new model is proposed here for Σ3 grain boundary enhancement during and immediately following recrystallisation, which relies on an encounter between a mobile grain boundary and a twin as illustrated on Fig. 5. The model involves impingement of two newly recrystallised grains, both of which have

twinned in order to produce more mobile boundary portions [17]. For the purposes of the model it is considered that the twinned portion of the left-hand grain in Fig. 5a is the most mobile boundary and hence migrates preferentially to impinge onto the right-hand grain (Fig. 5b) and subsequently onto the first coherent twin in this grain (Fig. 5c). The mobile boundary continues to migrate until the twin in the left-hand grain reaches the twin in the right-hand grain, thus forming a Σ3-Σ3-Σ9 junction, where the Σ3s are the coherent type (Fig. 5d). Of these three boundaries, the Σ9 is the most mobile and therefore continues to migrate (Fig. 5e) until it encounters the second coherent twin in the right-hand grain (Fig. 5f). Now a new Σ3-Σ3-Σ9 junction is formed *but one Σ3 is not coherent.* This new Σ3 grain boundary is the most mobile in the junction and continues to migrate for as long as a driving force is available or until it encounters other boundaries. Hence the presence of coherent Σ3s allows, through these interactions, mobile Σ3 boundaries to develop. The model is consistent with the results in [12] where both Σ3 grain boundaries - excluding coherent twins - and Σ9s doubled during strain annealing. It is also consistent with work which shows that Σ3s may deviate both from the exact misorientation and also from the {111} planes configuration [14].

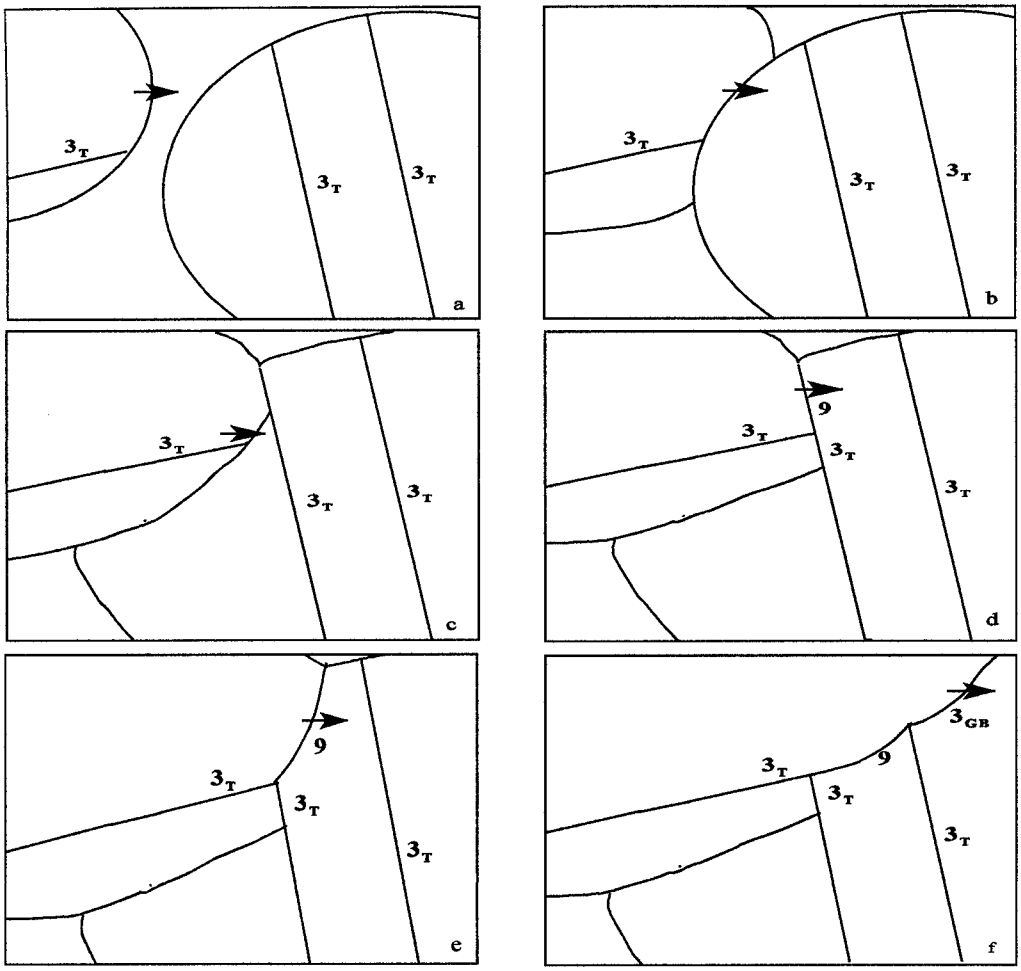

Fig. 5 Model for the generation of Σ3 grain boundaries from twins during and just after recrystallisation, beginning with the impingement of two grains containing twins. The most mobile boundary is indicated by an arrow. Unlabelled boundaries are random and others are labelled by their Σ-value with the subscript T for twin and GB for grain boundary. See text for details.

The model relies on the condition that an encounter between a Σ9 and a Σ3 gives a Σ3 boundary rather than a Σ27. This is supported by experimental evidence since few Σ27 boundaries are reported in investigations. Furthermore, the generation of an incoherent Σ3 is preferred both on the basis of lower energy and greater mobility than a Σ27. By the same argument if a Σ9 does encounter a Σ27, a Σ3 would again be generated rather than a Σ243. In general, then, it can be stated

$$\Sigma 3^n + \Sigma 3^{n+1} \rightarrow \Sigma 3 \qquad (2)$$

which is a method by which mobile Σ3s - which still have markedly better properties than random boundaries even though they are incoherent - enter the microstructure. Once additional Σ3s have been generated by this means, it has been shown that further annealing can allow grain boundary planes to more closely approach low volume configurations if grain growth is minimised [14].

Although this model is successful in rationalising the proliferation of Σ3s in the grain boundary network, it still does not provide the entire reason for the marked improvement in intergranular-related properties observed in a material after enhanced twinning. It has been suggested that when a twinning event occurs, one additional 'special' boundary, which is assumed to mean a lower-Σ CSL (although *all* Σ boundaries are not necessarily special) is added to the microstructure [1]. However, if the boundary was a very high Σ in the first place, the twinning reaction makes little difference. It is suggested here that there must be other reasons why the new boundary is 'more special' than the old boundary it replaced as a consequence of the twinning event. From a geometrical point of view, it could relate to the fact that a common rotation axis exists at the three conjoined interfaces, and/or that the 111 planes of the twin influence the choice of boundary planes in the adjoining boundaries. Both these suggestions are reasonable since there is previous evidence that triple junction-related $\Sigma 3^n$ boundaries are geometrically constrained in terms of deviations from exact CSL (Fig. 4), [15]. The 'specialness' requirement might be only for one of the non-twin boundaries to be *slightly* better than the other one to suppress effectively intergranular transport. In other words the critical factor is *relative specialness* rather than *absolute specialness* of conjoined boundaries.

References

[1] E.M. Lehockey, G. Palumbo, P. Lin and A. Brennenstuhl, Met. Mat. Trans. 29A (1998), p. 387.
[2] M.L. Kronberg and F.H. Wilson, Met. Trans. 185 (1949), p. 501.
[3] T. Watanabe, Res. Mech. 11 (1984), p. 47.
[4] P. Lin, G. Palumbo, U. Erb and K.T. Aust, Scripta Met. 33 (1995), p. 1387.
[5] V. Randle, *The role of the coincidence site lattice in grain boundary engineering,* Inst. Materials, London (1996).
[6] V. Randle, Acta Mat. 46 (1997), p. 1459.
[7] Y. Pan and B.L. Adams, Scripta Met. Mat. 30 (1994), p. 1055.
[8] R.J. Romero and L.E. Murr, Acta Met. Mat. 43 (1995), p. 461.
[9] G. Palumbo, International Patent Application no. PCT\CA93\00556
[10] A.J. Schwartz and W.E. King, JOM February (1998), p. 50.
[11] P. Davies and V. Randle, work in progress.
[12] G.S. Was, V. Thaveeprungsriporn and D.C. Crawford, JOM February (1998), p. 44.
[13] W.E. King and A.J. Schwartz, Scripta Mat. 38 (1998) p. 449.
[14] V. Randle, P. Davies and B. Hulm, Phil. Mag., in press.
[15] C.B. Thomson and V. Randle, Acta Mat. 45 (1997) p. 4909.
[16] R.L. Fullman and J.C. Fisher, J. Appl. Phys. 22 (1951), p. 1350.
[17] G. Gindraux and W. Form, J. Inst. Met. 101 (1973), p. 85.

Email: v.randle@swansea.ac.uk Fax: +44-1792-295244.

Materials Science Forum Vols. 294-296 (1999) pp. 59-66

Grain Boundaries in Superplastic Ceramics

T. Sakuma

Department of Materials Science, The University of Tokyo,
Bunkyo-ku Hongo 7-3-1, Tokyo 113-8656, Japan

Keywords: Ceramics, Superplasticity, Grain Boundary, Electron Microscopy, Segregation

ABSTRACT

Superplastic flow in fine-grained materials takes place mainly by grain boundary sliding. Micrograin superplasticity has been discussed mainly from the analysis of flow stress against strain rate relationship to find an accommodation process for grain boundary sliding. The phenomenological analysis has commonly been used to make clear the general features on micrograin superplasticity and will also be a major approach for superplasticity research in the future. However, some experimental facts reported in recent years, particularly in ceramic materials, cannot be understood from this type of analysis. This paper aims to show that microscopic analysis on grain boundary structure, chemistry and local atomic bonding state is very effective to break through the limitation of phenomenological approach.

GENERAL FEATURES ON MICROGRAIN SUPERPLASTICITY

Fine-grained materials often exhibit a large tensile elongation in excess of several hundreds percent at conventional strain rates in a temperature range above about $0.5T_m$, where T_m is the absolute melting temperature [1]. The plastic flow in such fine-grained materials takes place mainly by grain boundary sliding, and is termed structural or micrograin superplasticity. Major results on micrograin superplasticity in metals, ceramics and intermetallics are compiled in Table 1 [2].

In a material deformed by grain boundary sliding, stress concentration arises at grain boundary corners due to compatibility requirement between adjacent grains. It has generally been accepted that an accommodation process to relieve the stress concentration controls the overall superplastic flow in fine-grained materials. The accommodation process is expected to involve lattice diffusion, grain boundary diffusion and dislocation activity. To identify the accommodation process, the steady-state flow stress (σ) against strain rate ($\dot{\varepsilon}$) relationship is usually analysed to estimate the deformation parameters, the activation energy (Q), the stress exponent (n, inverse strain rate sensitivity) and the grain size exponent (p). The typical values in metallic alloys are n=2, p=2 and Q=Q_{gb}, where Q_{gb} is the activation energy for grain boundary diffusion as shown in Table 1 [3].

Table 1 Characteristic features of micrograin superplasticity [2]

Feature	Metals	Ceramics	Intermetallics
Maximum elongation	5500% (Al-bronze, 1985)	1038% (TZP*-5wt%SiO_2, 1993)	810% (Ti_3Al, 1992)
Critical grain size	10μm	1μm	10μm
σ-$\dot{\varepsilon}$ relationship†‡	Three regions	Single region (?)	Three regions
Activation energy	Grain boundary diffusion	Grain boundary diffusion (?)	Grain boundary diffusion (?)
Strain rate sensitivity	~0.5	~0.5	~0.5
Grain size exponent	2	2 or 3	(?)
Necking	Yes	No	Yes
Factor determining the elongation to failure	m§	$\dot{\varepsilon}\exp(Q/RT)$#	m§(?)

*TZP, tetragonal zirconia polycrystal; †σ, $\sigma=k\dot{\varepsilon}^m$(where k is a constant); ‡$\dot{\varepsilon}$, strain rate; §m, strain rate sensitivity exponent; # Zener-Hollomon parameter (where Q is the activation energy). (?) Refers to unknown data.

The elongation to failure in fine-grained metallic alloys is correlated with strain rate sensitivity exponent m, and a large tensile elongation is obtained for a high m value of about 0.5. In contrast, the elongation to failure in superplastic ceramics is not related to m but is described as a function of Zener-Hollomon (ZH) parameter $\dot{\varepsilon}\exp(Q/RT)$, where and RT is the gas constant times absolute temperature [4].

General features on micrograin superplasticity have been clarified mainly from phenomenological analysis so far. However, there are limitations of this type of approach as described in the previous paper [2]. For instance, it is not so easy to estimate the steady-state flow stress during superplastic flow because of the change of strain rate during plastic flow in conventional tensile or compression testing and of microstructure change such as concurrent grain growth and cavitation during deformation [5]. Even if the flow stress is accurately determined, a rate-controlling accommodation process may not be decided unambiguously because a similar form of the σ-$\dot{\varepsilon}$ relationship is predicted from several different models [6]. It may also be hard to explain the tensile elongation precisely in terms of steady-state flow stress because high-temperature failure is a consequence of damage accumulation during plastic flow, and is often affected by local stress concentration to induce cavity nucleation and growth. Actually, several experimental data recently found in superplastic ceramics are not consistent with the conclusions obtained from the analysis of σ-$\dot{\varepsilon}$ relationship. To make clear the superplastic flow in ceramic materials, more microscopic approach such as grain boundary analysis seems to be very important.

SUPERPLASTICITY IN GLASS-DOPED TZP

The superplastic flow in glass-doped TZP must be a good example to demonstrate

the importance of grain boundary analysis. Superplastic flow in TZP is significantly affected by the presence of grain boundary glass phase [5-16]. In general, the glass addition in TZP results in the reduction of high-temperature flow stress and in improved deformability [7].

Fig. 1 shows the microstructures of TZP (a) and TZP-5wt%SiO_2 (b) in as-sintered state [13]. The grains are mostly facetted in TZP as in Fig. 1 (a) and their grain size is as small as about 0.3μm. Fine grain size of TZP is extremely stable even at high temperatures in comparison with other ceramic materials, and hence TZP is a typical superplastic ceramic [17]. In SiO_2-added TZP, amorphous phase is located at multiple grain junctions as indicated by the arrows in Fig. 1 (b), and the grain boundary corners become spherical. This is a typical microstructure change in TZP with glass addition [5, 6, 7, 9, 11]. It was originally insisted that amorphous glass phase with a thickness of about 1nm exists in two grains junctions, i. e., grain boundary faces are wetted by glass phase [6, 7, 9] in accordance with a model of intergranular glass thickness in ceramic materials [18]. On the basis of the microstructural features on glass-added TZP, their plastic flow behavior was discussed from the models of solution-precipitation creep [19-22], which were proposed to explain the enhanced creep in polycrystalline materials containing grain boundary liquid phase.

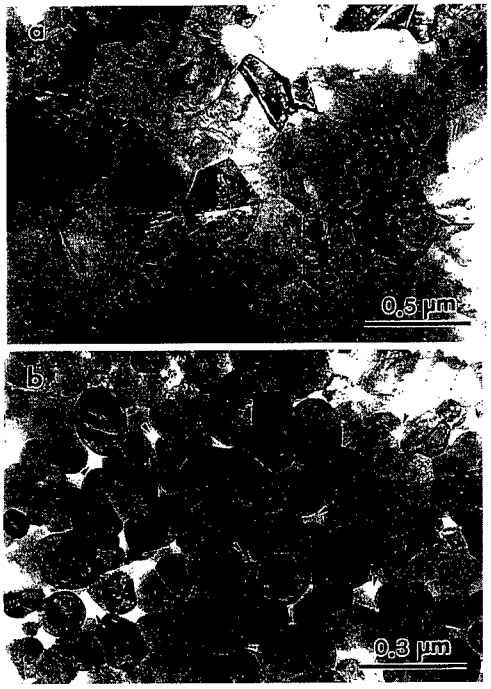

(a) TZP (b) TZP–5wt%SiO_2

Fig.1 Conventional TEM micrographs of TZP(a) and TZP-5wt%SiO_2(b) [13].

However, more careful high-resolution electron microscopy studies revealed that amorphous phase is present in multiple grain junctions but not in grain boundary faces of glass-doped TZP [14, 15, 23, 24]. Fig. 2 is an example of such electron micrographs of pure SiO_2-doped TZP [23]. The grain boundary is clean without any second phase. This is not a special case in pure SiO_2-doped TZP but is common in various glass-doped TZP. The result means that the superplastic flow in glass-doped TZP cannot be explained simply in terms of solution-precipitation models.

The grain boundary sliding must be more easily accommodated by the presence

of amorphous glass phase at multiple grain junctions in glass-doped TZP because the high-temperature flow stress is often drastically reduced by the glass-doping. Judging from the fact that the high-temperature flow stress in glass-doped TZP is correlated with the glass viscosity [9], either diffusion or viscous flow in glass phase at multiple grain junctions must be responsible for the accommodation process for superplastic flow.

It is interesting to note that the elongation to failure in glass-doped TZP is not described by their flow stress. Fig. 3 is a comparison of tensile elongation in TZP and two glass-doped TZP deformed at 1400℃ [12]. The flow stress in undoped TZP is 250MPa in this testing condition, and the elongation to failure of 123% is obtained. The flow stress is drastically reduced to be 1.6MPa by aluminosilicate glass doping into TZP but the elongation is only 48%. In contrast, the elongation to failure is highly enhanced by pure SiO_2 doping into TZP, although the reduction in flow stress is not so large as in aluminosilicate glass-doped TZP. The result demonstrates that the elongation to failure in glass-doped TZP is not given by ZH parameter as reported previously [4], because this parameter is a function of flow stress.

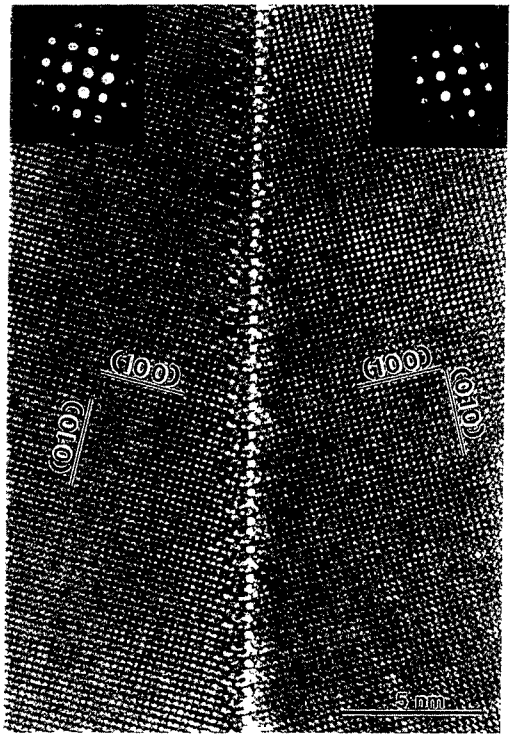

Fig.2 A High-resolution electron micrograph of a [001] Σ17 grain boundary in as-sintered TZP-5wt%SiO_2 [23].

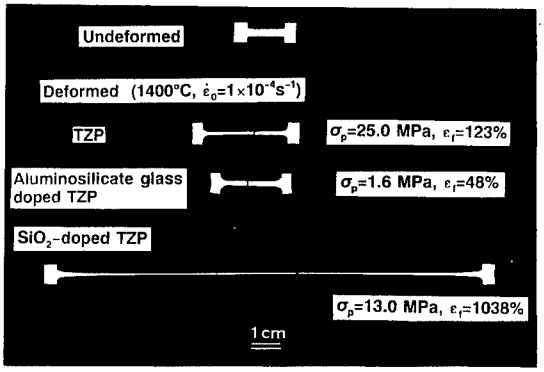

Fig.3 Comparison of tensile elongation in TZP, 5wt%aluminosilicate glass-doped TZP and 5wt%SiO_2-doped TZP at 1400℃ and a strain rate of 1×10^{-4}s^{-1} [12].

The tensile elongation in SiO_2-doped TZP is extremely large but is usually deteriorated by a small dopant cation in SiO_2 phase added. For instance, the elongation at 1400℃ and an initial strain rate of $1.2\times10^{-4}s^{-1}$ is about 1000% in TZP-5wt%SiO_2, but is only about 200% in TZP-5wt%(SiO_2-2wt%Al_2O_3) [24]. The reduction in tensile ductility with Al_2O_3 doping in SiO_2 phase is likely to be caused by the segregation of Al^{3+} ions grain boundary faces as shown in Fig. 4, which is a plot of the relative intensity ratio of Y^{3+}, Si^{4+} and Al^{3+} ions with respect to Zr^{4+} ions against the distance from a grain boundary in TZP-5wt%SiO_2(a) and TZP-5wt%(SiO_2-2wt%Al_2O_3)(b) [24]. Al^{3+} ions segregate in grain boundaries as well as Y^{3+} and Si^{4+} ions in the latter material. Essentially, the tensile ductility in TZP-5wt%SiO_2 is very sensitive to a small dopant cation in SiO_2 glass, and such dopant effect is likely to be a consequence of grain boundary segregation as typically seen in Al^{3+} ions.

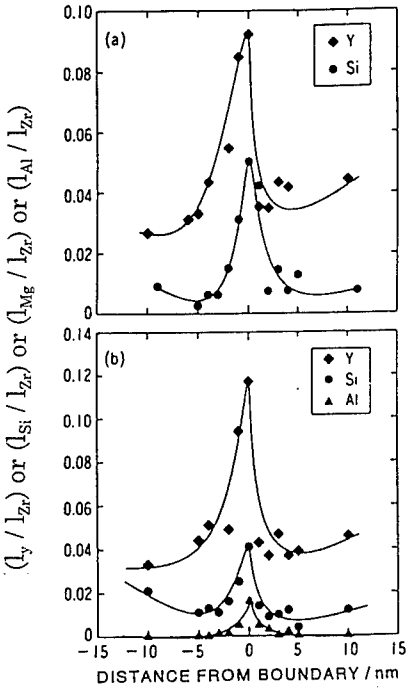

Fig. 4 Element distribution profiles across grain boundaries in (a) SiO_2-doped TZP and (b) (SiO_2-2wt%Al_2O_3)-doped TZP [24].

Since the flow stress is related to the glass viscosity in glass-doped TZP [9], the grain boundary sliding must be accommodated by amorphous glass phase located at grain boundary corners or multiple junctions. However, the elongation to failure is not determined by flow stress, i. e., the elongation is not dependent on glass viscosity. The nature of grain boundary faces must be responsible for the ductility limitation because the failure occurs along zirconia grain boundaries and zirconia grain/glass phase interfaces in glass-doped TZP, and the majority of interfaces at multiple junctions consists of grain boundaries. A next step is to make clear the change of atomic bonding in grain boundaries with dopant segregation and to find its role of tensile ductility.

HIGH-TEMPERATURE PLASTICITY IN POLYCRYSTALLINE Al_2O_3

High-temperature plastic flow in high-purity, polycrystalline Al_2O_3 is very sensitive to an addition of small dopant cation and to its grain boundary segregation. Fig. 5 is the stress-strain curves in polycrystalline Al_2O_3 with a nominal purity of 99.99%

and three doped Al_2O_3 at 1400℃ and an initial strain rate of $1.2\times10^{-4}s^{-1}$. The high-purity Al_2O_3 exhibits a large strain hardening after initial yielding and its tensile elongation is about 20% in this testing condition. The strain hardening and the limited ductility are explained from rapid concurrent grain growth during plastic flow [17]. The MgO-doping into high-purity Al_2O_3 results in a reduced strain hardening and improved tensile ductility as shown in Fig. 5. The elongation to failure of over 100% is obtained in 0.1wt%MgO-doped Al_2O_3 at suitable testing conditions [17], i. e., polycrystalline Al_2O_3 becomes superplastic due to MgO-doping. HRTEM-EDS analysis revealed that Mg^{2+} ions are not in solution but segregate in Al_2O_3 grain boundaries [23].

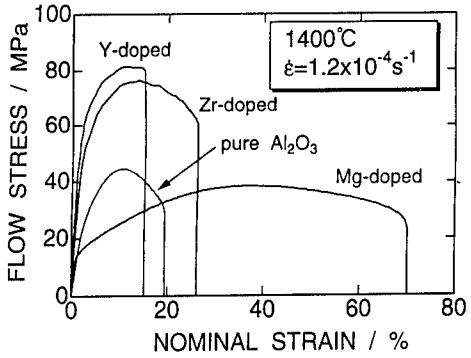

Fig. 5 Stress-strain curves of high-purity polycrystalline Al_2O_3 and Y- or Zr- or Mg-doped Al_2O_3 at 1400℃ and an initial strain rate of $1.2\times10^{-4}s^{-1}$. The dopant content is 0.1wt%.

On the contrary, the doping of Y_2O_3 or ZrO_2 into high-purity Al_2O_3 results in the increment of high-temperature flow stress and does not improve its tensile ductility. This is also caused by the grain boundary segregation of Y^{3+} or Zr^{4+} ions. Fig. 6 is an

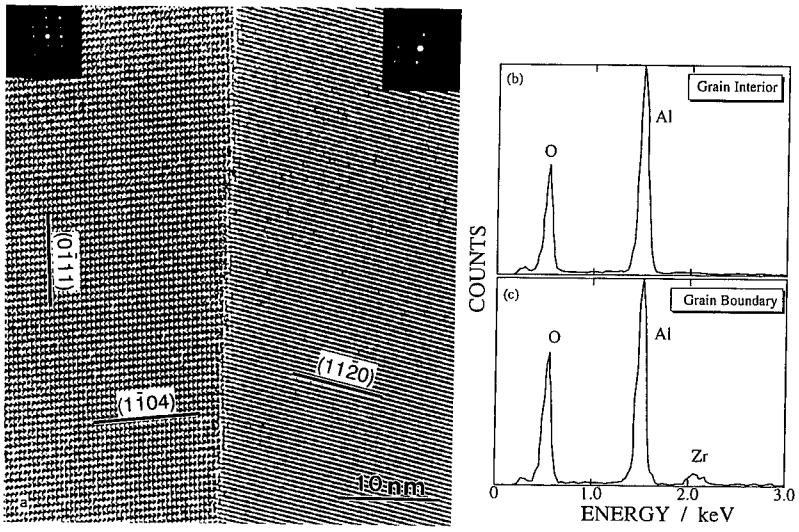

Fig. 6 A high-resolution electron micrograph of a grain boundary in 0.1wt%ZrO_2 doped-Al_2O_3 together with EDS sectra taken from a grain interior (a) and the grain boundary (b) with a probe size of about 1nm [23].

example of the HRTEM images and EDS spectra from a grain interior and from a grain boundary in 0.1wt%ZrO_2-doped Al_2O_3 [23]. The grain boundary is clean without any second phase, and the segregation of Zr^{4+} ions in the Al_2O_3 grain boundary is clearly detected in the EDS spectrum.

It has been reported that high-temperature strength or creep resistance in polycrystalline Al_2O_3 in highly improved by ZrO_2 dispersion [24-26]. However, we have demonstrated recently that the major effect of the excellent high-temperature strength or creep resistance comes from the segregation of Zr^{4+} ions in Al_2O_3 grain boundaries rather than dispersion effect [27].

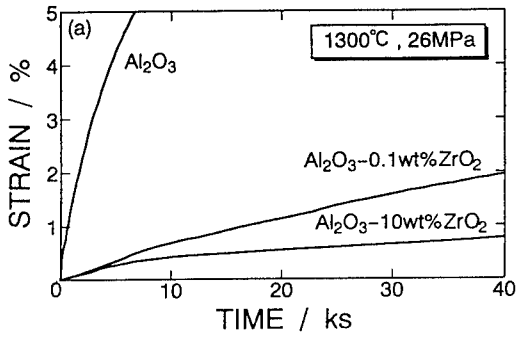

Fig. 7 The creep curves in high-purity Al_2O_3, 0.1wt%ZrO_2-doped Al_2O_3 and Al_2O_3-10wt%ZrO_2(2.5mol%Y_2O_3) under an applied stress of 26MPa at 1300℃ [27].

Fig. 7 shows the creep curves in high-purity Al_2O_3, 0.1wt%ZrO_2-doped single-phase Al_2O_3, and Al_2O_3-10wt%ZrO_2, which contains ZrO_2 dispersion in polycrystalline Al_2O_3 [27]. The creep rate is very much reduced by ZrO_2-doping, and is further lowered by ZrO_2 dispersion. The activation energy for plastic flow is 430kJ/mol in high-purity, polycrystalline Al_2O_3, 650kJ/mol in 0.1wt%ZrO_2-doped Al_2O_3 and 700kJ/mol in two-phase Al_2O_3-10wt%ZrO_2 in a temperature range of 1150-1400℃. The activation energy values correspond well with the creep resistance in these materials. It is noted that a doping of ZrO_2 in the level of 0.1wt% causes a drastic increase of activation energy. Since the plastic flow in this temperature range is likely to be controlled by grain boundary diffusion, the segregation of Zr^{4+} ions must retard very effectively the grain boundary diffusivity of Al_2O_3. Similar effect has been found is various rate earth doped-Al_2O_3 [28].

CONCLUDING REMARKS

High-temperature plastic flow in polycrystalline ceramics, in particular, superplastic flow in fine-grained ceramics are highly dependent on small dopant cation segregated in grain boundaries. The chemical bonding state of constituent ions in grain boundaries must change with dopant segregation and affect high-temperature flow behavior. Detailed analysis on the grain boundary structure and chemistry to make clear the ionic bonding state in grain boundaries will break through the present understanding on some topics on superplastic or high-temperature plastic flow in polycrystalline

ceramics, e. g., tensile ductility in glass-doped superplastic ceramics and the plastic flow in high-purity, polycrystalline Al_2O_3 are such topics because these results cannot be explained only from phenomenological approach based on the analysis of flow stress against strain rate relationship.

Acknowledgement

The author wishes to express his thanks to the financial support of the Grant-in Aid for Development Scientific Research 06555202 from the Ministry of Education, Science and Culture, Japan.

REFERENCES

1. A. K. Mukherjee, Mater. Sci. Tech., Vol. 6, Plastic Deformation and Fracture of Materials, Ed. by H. Mughrabi, Weinheim, VCH, p. 407 (1993).
2. T. Sakuma, Current Opinion in Solid State and Mater. Sci., **2**, 296 (1997).
3. T. G. Langdon, Acta Metall. Mater., **42**, 2437 (1994).
4. W-J. Kim, J. Wolfenstine and O. D. Sherby, Acta Metall. Mater., **39**, 199 (1991).
5. K. Kajihara, Y. Yoshizawa and T. Sakuma, Scripta Metall. Mater., **28**, 509 (1993).
6. T. G. Nieh, J. Wadsworth and O. D. Sherby, Superplasticity in Metals and Ceramics, Cambridge Univ. Press, (1997).
7. J. G. Wang and R. Raj, J. Am. Ceram. Soc., **67**, 399 (1984).
8. C. M. J. Huang and I. W. Chen, J. Am. Ceram. Soc., **73**, 1626 (1990).
9. Y. Yoshizawa and T. Sakuma, J. Am. Ceram. Soc., **73**, 3069 (1990).
10. Z. C. Wang, T. J. Davies and N. Ridley, Scripta Metall. Mater., **28**, 301 (1993).
11. M. Gust, G. Goo, J. Wolfenstine and M. L. Mecartney, J. Am. Ceram. Soc., **76**, 1681(1993).
12. T. Sakuma and Y. Yoshizawa, Mater. Sci. Forum, **170-172**, 369 (1994).
13. K. Kajihara, Y. Yoshizawa and T. Sakuma, Acta Metall. Mater., **43**, 1235 (1985).
14. P. Thavorniti and T. Sakuma, Mater. Sci. Eng., **202A**, 249 (1995).
15. T. G. Nieh and J. Wadsworth, Mater. Sci. Forum, **233-234**, 383 (1997).
16. T. Sakuma, Y. Ikuhara, Y. Takigawa and P. Thavorniti, Mater. Sci. Eng., **236**, 226 (1997).
17. Y. Yoshizawa and T. Sakuma, Acta Metall. Mater., **40**, 2943 (1992).
18. D. R. Clarke, J. Am. Ceram. Soc., **70**, 15 (1987).
19. R. L. Coble, J. Appl. Phys., **34**, 1679 (1963).
20. R. A. Stocker and M. F. Ashby, Rev. Geophys. Space Phys., **11**, 391 (1973).
21. R. Raj and C. K. Chyung, Acta Metall., **29**, 159 (1981).
22. F. Wakai, Acta Metall. Mater., **42**, 1163 (1994).
23. Y. Takigawa, Y. Ikuhara and T. Sakuma, Mater. Sci. Forum., **243-245**, 425 (1997).
24. F. Wakai, I. Iga and T. Nagano, J. Ceram. Soc. Jpn., **96**, 1206 (1988).
25. J. Wang and R. Raj, Acta Metall. Mater., **39**, 2909 (1991).
26. K. Okada, Y. Yoshizawa and T. Sakuma, Superplasticity in Advanced Materials, Ed. by S. Hori, M. Tokizane and N. Furushiro, The Jpn. Soc. Research on Superplasticity, p. 227 (1991).
27. H. Yoshida, K. Okada, Y. Ikuhara and T. Sakuma, Phil. Mag. Lett., **76**, 9 (1997).
28. H. Yoshida, Y. Ikuhara and T. Sakuma, J. Mater. Res., in press.

Materials Science Forum Vols. 294-296 (1999) pp. 67-74

Radiation-Induced Grain Boundary Segregation

R.G. Faulkner, S. Song, D. Meade and C.C. Goodwin

Institute of Polymer Technology and Materials Engineering, Loughborough University, Loughborough, Leics, LE11 3TU, UK

Keywords: Neutron Irradiation, Modelling, Steels, Electron Microscopy, Segregation, Binding Energy, Site Competition, Self-Interstitial, Vacancy

Abstract

Experimental evidence for phosphorus segregation and chromium depletion at grain boundaries in steels is presented. Theories for irradiation-induced inter-granular segregation are described. Non-equilibrium (NES) and rate theory approaches have similar success in predicting phosphorus behaviour in the practically important temperature range although site competition and micro-structural effects are better accounted for by the NES theory. NES theory predicts chromium behaviour reasonably well but there is a need to consider site competition more closely in relation to large atom effects from elements like Zr and Hf. The need for better data on diffusion constants and point defect-impurity binding energy is emphasised.

Introduction

This paper will be divided into two main sections: experimental and theoretical. Because of the difficulty in carrying out long term test irradiations, and the increasing lack of availability of neutron sources for this purpose, the experimental part of the subject is less advanced than the theory part. Apart from the early fundamental studies by Johnson and Lam [1] on Ag-Zn, most of the practical studies have centred on the behaviour of phosphorus in ferritic steels and on chromium in austenitic steels. Theory has been based on two main approaches: non-equilibrium or solute drag mechanisms and rate theory or inverse Kirkendall effect mechanisms. Much of the success of the various models depends upon the availability of suitable data on binding energies, site competition parameters, and diffusion data, much of which is likely to be supplied in future by molecular dynamics calculations.

Experimental Observation of Radiation-induced Grain Boundary Segregation

The techniques used for the analytical determinations are a mixture of field emission gun transmission electron microscope (FEGTEM) and Auger electron spectroscopy (AES) results. The AES results are likely to be in error because they only locate the weakest boundaries and thus heavily emphasise the element responsible for initiating inter-granular failure. The FEGTEM results are likely to be underestimates because the beam spreading causes the grain boundary concentration signal to be analysed to emanate from a slightly wider region than one monolayer. There are many conversions of fractional monolayer coverage to atomic percent measured on the grain boundary. The method used here is to assume that 100% monolayer coverage is 25 at.%

concentration. Enrichment factors are then determined using a knowledge of the impurity content in the alloy.

Zn in Ag

The earliest indications of radiation-induced segregation are found in the work of Johnson and Lam, [1]. They studied the effect of charged particle irradiation on the surface segregation of zinc in silver over a range of temperature, showing the characteristic peak in a regime 0.3 to 0.4Tm, where Tm is the absolute melting point of the matrix material. Thermal equilibrium segregation is assumed to be negligible in the temperature range examined.

Ferritic Steels

Since that time, workers have concentrated on more practical systems, primarily phosphorus grain boundary segregation in ferritic steel. A combined survey picture of the experimental results obtained for P grain boundary segregation as a function of temperature dependence for a variety of steels and iron-based binary alloys is shown in Fig. 1. It should be emphasised that these results come from experiments with widely-differing conditions of dose, dose rate, composition and microstructure and should therefore only be reviewed in a qualitative sense.

Fig. 1 Phosphorus Intergranular Segregation in PSV Steels

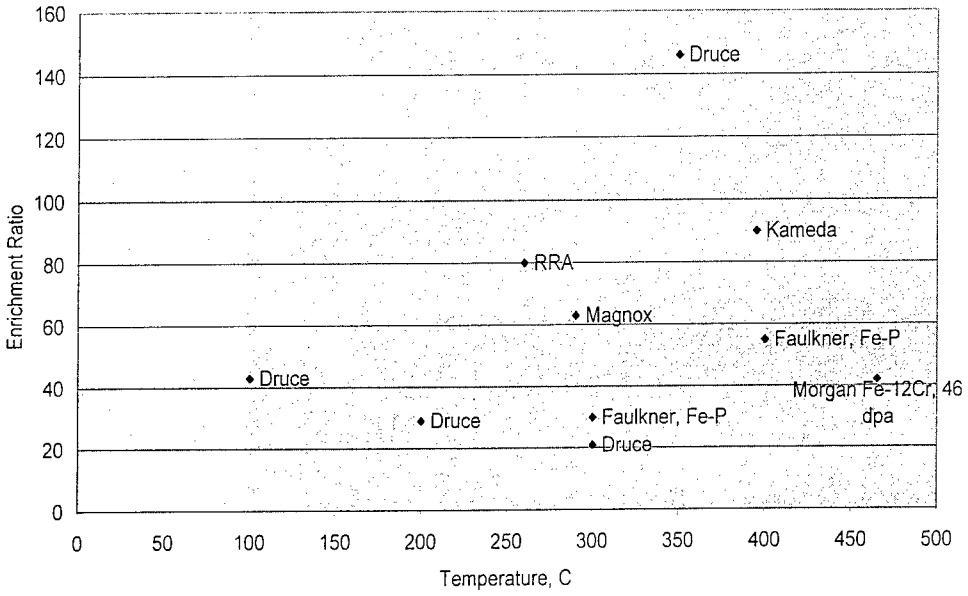

Reference Key
Druce [2]; Kameda [3]; RRA[4]; Magnox [5]; Faulkner Fe-P [6]; Morgan [7].

Several interesting features emerge. The first is that the temperature dependence is seen to have two peaks; the first is due to non-equilibrium segregation, caused by streams of point defect-impurity complexes being drawn to the boundary by the irradiation. The second, high temperature peak is due to thermal equilibrium segregation. Secondly, there is evidence for site competition

effects, particularly from carbon. The effect of increasing carbon causing reduced phosphorus segregation is seen in the work of Beere [8], shown in Fig.2. In this Figure the solid line represents the trend line derived from regression analysis of the experimental data points.

Fig. 2 Phosphorus and Carbon Intergranular Segregation in PSV Steels

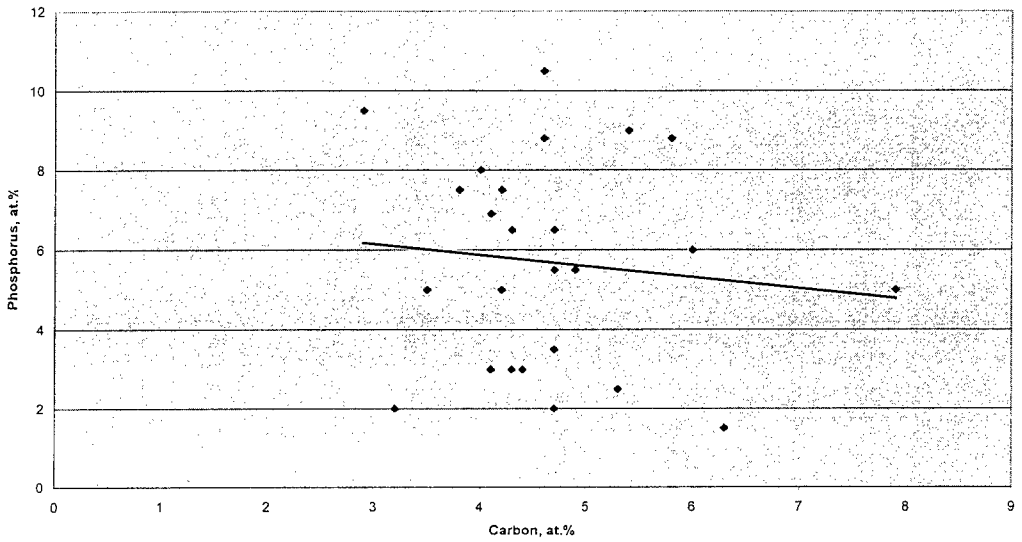

Kameda and Bevolo [3] have observed similar trends. Thirdly, increasing dose increases the amount of phosphorus segregation, but there does seem to be a saturation limit.

There are strong correlations of these effects with mechanical properties: higher phosphorus coverage leads to larger amounts of inter-granular fracture. It should be realised that the yield properties also increase with dose due to matrix hardening, and, in the case of some older pressure vessel steels, copper precipitation due to irradiation.

There have been even higher resolution studies of segregation than those from FEGTEM or AES. Atom probe field ion microscopy (AFIM) has confirmed the presence of P and Mo on grain boundaries in VVER pressure vessel steels (Miller and Burke [9]).

Austenitic Steels

The behaviour of Cr in austenitic steels during irradiation is the reverse of the phosphorus situation. Substantial Cr depletion occurs, and this is important because it appears to be the explanation for irradiation-assisted inter-granular stress corrosion cracking (IASCC)(Nishimura [10] and Bruemmer [11]). This observation is the conclusion drawn from several experimental studies completed in the USA, Japan and the UK (Jennsen [12]). The interesting point to note is that there is a reversal of the effect on moving from the heat treated condition prior to irradiation, when the Cr is segregating, to depletion when the irradiation is turned on (Fig. 3).

No studies have so far been undertaken to separate the segregation and precipitation components of the observations because this must be an urgent and necessary component of future work. The

results described above insist on the fact that no chromium carbide precipitation was present on the boundaries from which the depletion measurements were taken. Mo and Ni grain boundary segregation are also seen in austenitic steels [13]. Probably some of the most commercially-significant work is that of Kato et al [14]. They show that the addition of Zr and Hf reduce the Cr depletion effect to almost zero. They also have explored a range of strong carbide forming additions and they show that the effect is not simply due to size factor effects. Nb and V have very large positive misfits but they do not have any effect on irradiation-induced Cr depletion.

Fine scale FEGTEM studies of irradiated austenitic steels have further revealed segregation of Ni to cavity clusters, Shepherd [15] and faulted dislocation loops, Kenik [16].

Modelling of Radiation-induced Inter-granular Segregation

Two modelling approaches have been adopted.

The first is to model non-equilibrium segregation (NES) (Faulkner [17]) and represents a simplified method, which has the advantage that fewer data are required, site competition effects can be included, and micro-structural effects are easier to incorporate. It assumes that point defect-impurity complexes are formed during non-equilibrium processes such as quenching and neutron irradiation and that these become absorbed at a sink like a grain boundary. This sets up a point defect concentration gradient around the sink, which can be quantified in terms of the non-equilibrium process producing it. If impurity atoms in the material have a positive binding energy with the point defects then some of these impurities will be dragged towards the boundary down the point defect concentration gradient. If the diffusion constants of these complexes can be estimated, then the kinetics and magnitude of the impurity enrichment can be predicted. During irradiation it is assumed that the interstitials are the dominant point defect, because they have the highest binding energies with typical impurities and because they have very low activation energies for diffusion.

The key equations used to predict the magnitude and kinetics of the segregation are as follows. Site competition effects are included.

$$C^{m}_{br(Sj)} = C^{Sj}_{g}\,\frac{E^{ip}_{b(Sj)}}{E^{p}_{f}}\left[\frac{C^{Sj}_{g}\exp\left(\frac{E^{ip}_{b(Sj)}}{kT}\right)}{\sum_{j} C^{Sj}_{g}\exp\left(\frac{E^{ip}_{b(Sj)}}{kT}\right)}\right]\left[1+\frac{BGF(\eta)}{A_{p}D_{p}k^{2}_{dp}}\exp\left(\frac{E^{p}_{f}}{kT}\right)\right](j=1,2) \qquad (1)$$

and

$$\frac{C^{Sj}_{br}(t)-C^{Sj}_{g}}{C^{m}_{br(Sj)}-C^{Sj}_{g}} = 1-\exp\left(\frac{4D^{ip}_{c(Sj)}t}{\alpha^{2}_{n(Sj)}d^{2}}\right)erfc\left(\frac{2\sqrt{D^{ip}_{c(Sj)}t}}{\alpha_{n(Sj)}d}\right)(j=1,2) \qquad (2)$$

where $C^{m}_{br(Sj)}$ is the maximum time-independent concentration of the Sjth element on the boundary, C^{Sj}_{g} is the grain concentration of the Sjth element, $E^{ip}_{b(Sj)}$ is the interstitial-impurity (Sj) binding energy, E^{p}_{f} is the interstitial formation energy, k is Boltzmann's constant, T is the absolute temperature, B is the proportion of freely migrating defects (assumed to be 1%), G is the point

defect generation rate, $F(\eta)$ is the recombination rate, discussed more fully in ref [6], A_p is the pre-exponential term in the equation describing the interstitial concentration, D_p is the interstitial diffusion coefficient, k^2_{dp} is the sink efficiency of the matrix for the interstitial point defect, taking into account the dislocation density and grain size, $C^{Sj}_{br}(t)$ is the boundary concentration of the Sjth element after time t, $D^{ip}_{c(Sj)}$ is the complex diffusion coefficient for the Sjth element, $\alpha_{n(Sj)}$ is the maximum enrichment ratio for the Sjth element, i.e., $C^{m}_{br(Sj)}/C^{Sj}_{g}$, and d is the grain boundary width (assumed to be 1 nm).

Site competition is totally accounted for by assuming that $C^{Sj}_{br}(t)$ is modified to $C^{Sj}_{br}(t)^*$, according to the relative binding energies which the segregating species have to the grain boundary itself, Q_{Sj}.

$$C_{br}^{S1}(t)^* = C_{br}^{S1}(t)\left(\frac{C_g^{S1}\exp\left(\frac{Q_{S1}}{kT}\right)}{C_g^{S1}\exp\left(\frac{Q_{S1}}{kT}\right)+C_g^{S2}\exp\left(\frac{Q_{S2}}{kT}\right)}\right) \qquad (3)$$

The NES model further indicates that after a critical time saturation will take place and a permanent segregation situation will continue until the radiation is turned off.

The second modelling approach is the more rigorous rate theory, or inverse Kirkendall model ([1], [18], [19], [20], [21]). This sets up a series of partial second order differential equations to describe the time dependence of the concentrations of point defects and all elements present as a function of irradiation conditions and time. These equations are all solved simultaneously to forecast the behaviour, particularly of the impurity species, in the neighbourhood of grain boundaries. Many of the data required are unobtainable, and so curve fitting to the available experimental data is employed. The Druce [2] work fits to phosphorus in ferritic steel data by varying the interstitial-phosphorus binding energy. Simonen [20] fits the Cr depletion data from austenitic steels by varying the ratio of the Ni to Cr complex diffusion coefficients.

Data

The most inscrutable data required for modelling are those connected with the diffusion characteristics of the interstitial-impurity complexes and the impurity-interstitial binding energy.

The complex diffusion can take place in bcc lattices by a variety of mechanisms. Barbu and Lidiard [22] has treated these and it seems that the most likely mechanism is the interstitial migration plus 60° rotation (RT_1). Under these circumstances we have assumed that the total energy required to move the complex involves binding a self-interstitial/impurity atom complex (energy required, E^{ip}_b), followed by migration of the interstitial (energy required, E^{p}_m). The activation energy for diffusion of the complex ($D^{ip}_{c(Sj)}$) is given by the sum of the two above energies.

The interstitial binding energy is derived from a continuum elasticity analysis of the lattice surrounding the impurity atom in the interstitial-impurity split (110) dumbbell configuration. Although Hardy and Bullough [23] have shown that lattice statics based on the discrete nature of the lattice is a better approach to use, we feel justified in using continuum elasticity because the continuum approach only breaks down in the long range component of the energies involved. For nearest neighbour distances it seems a good approximation, unless, of course, strong electronic effects are important, as is the case if non-metallic bonding applies, as with ceramics or polymers. It may be that in future molecular dynamics calculations will provide answers to these binding

energy questions (e.g., Calder and Bacon [24]). For the time being, the best information available comes from the continuum elasticity results and these are shown for austenitic steel matrices in Fig. 4 [25].

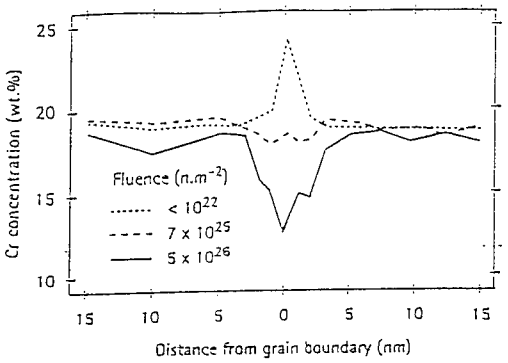

Fig. 3 Averaged FEGTEM Cr Concentration Profiles After Various Neutron Irradiations [12]

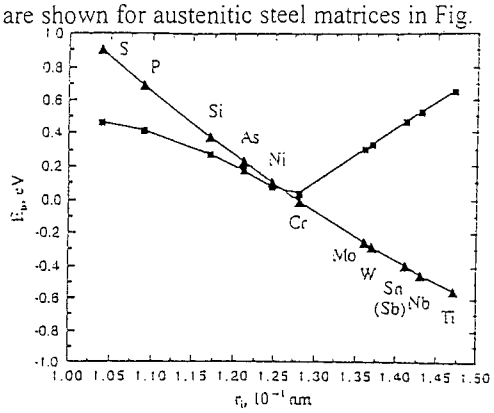

Fig. 4 Impurity-Point Defect Binding Energies in an Austenitic Steel Matrix

It is seen that for vacancy-impurity interactions the binding energy is always positive (attractive). But for interstitial-impurity complexes the binding energy goes negative for positive misfit situations. This implies that the impurities lock the dumbbells in stable positions, and no further impurity drag towards the boundary occurs.

Discussion

Figure 5 provides the appropriate modelling predictions of the temperature dependence of phosphorus grain boundary segregation in ferritic steel, and the experimental data are given for comparison/validation purposes.

The important issue is that the NES model is very sensitive to the site competition effect when carbon is considered. Carbon competes for sites on the grain boundary and within the complexes that are transporting the phosphorus to the grain boundary. The rate theory predictions of Druce [2] give quite good fits with observed data, but they do not include

Fig. 5 Experimental and model Phosphorus Segregations in PSV Steels

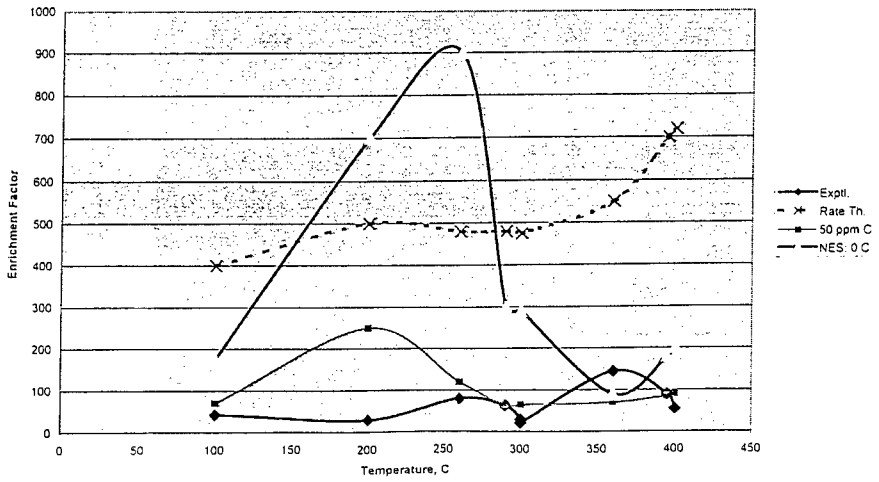

site competition, and, in any case, have been evaluated by curve-fitting to the data in the first place. The NES model results suggest that the magnitude of the segregation is reduced by two orders of magnitude to levels close to those observed in the 300°C temperature range on increasing the carbon content from 0 to 0.005 at.% C. This is not unreasonable if one remembers that this figure of 0.005 at % represents the free carbon, i.e., that not tied up in carbides. The steels from which the experimental results are taken contain around 0.5 at. % C. Fig. 2 shows the experimental evidence for a carbon effect on P grain boundary segregation in ferritic steels

The parabolic dose-dependence is supported by both rate theory and NES models. The NES model predictions are not shown on this graph but they predict similar asymptotic behaviour once the critical time for saturation is exceeded.

In austenitic steels the behaviour of chromium is of high importance in view of IASCC. Fig. 3 shows that thermal, pre-irradiation heat treatment produces Cr segregation. This can be explained by NES theory on the basis that thermal effects cause solute drag mechanisms to operate based on the vacancy-impurity complex. The binding energy of Cr to vacancies in austenitic matrices is positive (Fig. 4). For irradiation, we have indicated that interstitials play a more important role than vacancies. In this case, Fig. 4 shows that the slight positive misfit of Cr leads to a negative binding energy with the interstitial (repulsion, implying zero drag). Under these circumstances it is assumed that all the segregation calculations will be reversed so that enrichment predictions now become equal but opposite depletions. Therefore it is expected that Cr depletion will occur during irradiation and that the depletion will increase with dose. This is supported by the experimental observation in Fig.3. We must remember that NES theory has been developed for dilute impurity scenarios. Clearly Cr in austenitic steels is a concentrated alloy situation and therefore the predictions do not have so much validity as those for the P in ferritic steel.

Rate theory predictions concerning the Cr depletion effect have recently been made by, for example, Martin [26].

It is possible that the Kato [14] results on inhibition of Cr depletion by large atoms like Zr and Hf can be explained using NES theory using the site competition arguments discussed for C-P interactions in ferritic steels.

Conclusions

A summary of existing experimental results for phosphorus grain boundary segregation in ferritic steels has been presented. These show that phosphorus segregation is present before irradiation and that irradiation enhances this segregation. The temperature dependence of the irradiation induced segregation is complex but is now reasonably well understood. At temperatures above 400°C in ferritic steels thermal equilibrium segregation dominates. Site competition arguments and available experimental data suggest that elements like carbon play a major role in controlling phosphorus segregation. Model predictions of the temperature dependence based on a) non-equilibrium segregation and b) rate theory support the data well, although site competition and microstructural effects are current more completely described by the NES theory.

The behaviour of chromium at grain boundaries in irradiated austenitic steels has been reviewed. The irradiation-induced depletion of chromium at the grain boundaries can be explained by the NES theory. The depletion occurs because interstitial-chromium pairs are prevented from forming

because of the negative binding energy between the two components. This leads to the reverse of segregation, i.e., depletion.

Methods for obtaining data on complex diffusion coefficients and impurity-point defect binding energy have been discussed.

References

1. R.A. Johnson and N.Q. Lam, Phys. Rev., 1976, 13 , 4364.
2. S.G. Druce, C.A. English, A. J. E. Foreman, R.J. McElroy, I.A. Vatter, C.J. Bolton, J.T. Buswell and R.B. Jones, Proc 17th Symposium on Radiation Effects in Materials, ASTM STP 12XX, Eds., D.S. Gelles, R. K. Nanstead, A.S. Kumar and E.A. Little, Philadelphia, 1996, in press.
3. J. Kameda and A.J. Bevolo, Acta. Metall., 1989, 37, 3283.
4. D.Meade, R.G. Faulkner and D. Ellis, 19th International Symp. on 'Effects of Irradiation on Materials', ASTM STP1366, Eds., M.L. Hamilton, A.S. Kumar, S.T. Rosinski, and M.L. Grossbeck, ASTM, Philadelphia, 1999.
5. R.B. Jones, J.R. Cowan, R.C. Corcoran, aand J.C. Walmsley, BNFL-Magnox Generation. Private communication, 1998.
6. R.G. Faulkner, S.Song, P.E.J. Flewitt, M. Victoria, and P. Marmy, J. Nuclear Materials, 1998, In press.
7. E.A. Little, T.S. Morgan, and R.G. Faulkner, Materials Science Forum, 1992, 97-99, 323.
8. W.B. Beere, BNFL Magnox Generation, Private Communication, 1998.
9. M.K. Miller and M.G. Burke, 1992, 195, 68.
10. S. Nishimura and M. Kodama, Proc Symp on 'Diffusion in Materials', CARET, Hokkaido University, 1997.
11. E.P. Simonen, R.H. Jones and S.M. Bruemmer, 1992, J. Nuc. Mat., 191-194, 1002.
12. A. Jenssen, L.G. Ljungberg, J. Walmsley, and S.B. Fisher, 'Corrosion 96, NACE Int. Ann. Conf., 1996, paper 101, to be published.
13. C.C. Goodwin, PhD. Thesis, Loughborough University, UK, 1997.
14. T. Kato, H. Takahashi, and M Izumia, J. Nuc. Mat., 1992, 189, 167.
15. C.M. Shepherd, J. Nuc. Mat., 1990, 175, 170.
16. E.A. Kenik, J.Nuc. Mat., 1993, 205, 317.
17. R.G. Faulkner, S. Song and P.E.J. Flewitt, Metall. Mater. Trans., 1996, 27A, 3381.
18. P.R. Okamoto and H. Wiedersich, J. Nucl. Mater., 1974, 53, 336.
19. Y. Grandjean, P. Bellon and G. Martin, Phys. Rev., 1994, B50, 4228.
20. E.P. Simonen, E.R. Bradley and R.H. Jones, in 'Effects or irradiation on Materials', (Ed., N.H. Packan et al), ASTM STP 1046, p. 411, 1989.
21. T. Hashimoto, Proc Symp on 'Diffusion in Materials', CARET, Hokkaido University, 1997.
22. A. Barbu and A.B. Lidiard, Phil. Mag., 1996, A74, 709.
23. J.R. Hardy and R. Bullough, Phil. Mag.,1967, 15, 237.
24. A.F. Calder and D.J. Bacon, J.Nuc. Mat., 1993, 207, 25.
25. R.G. Faulkner, S.Song, and P.E.J. Flewitt, Mater.Sci. and Tech., 1996, 12, 904.
26. G.Martin and M. Nastar, paper I12 of this conference, 1998.

r.g.faulkner@lboro.ac.uk
http://www.lboro.ac.uk/departments/iptme/staff/rgthp.html
+44 (0)1509 223949

Materials Science Forum Vols. 294-296 (1999) pp. 75-82

Grain Boundary Composition and Effects on Environmental Degradation

S.M. Bruemmer

Pacific Northwest National Laboratory, P.O. Box 999 Richland, Washington 99352, USA

Keywords: Grain Boundary, Segregation, IGSCC, Corrosion, RIS, IASCC

Abstract

Environmental degradation of metallic alloys is shown to depend on its local microstructure and microchemistry in many instances. Equilibrium and non-equilibrium processes can produce significant changes to the grain boundary composition and promote intergranular stress corrosion cracking (IGSCC). Austenitic stainless steels are used as an example to illustrate equilibrium effects of Gibbsian segregation and second-phase precipitation as well as non-equilibrium effects of quench-induced and radiation-induced segregation. Interfacial Cr concentration is shown to be the dominant material variable promoting IGSCC of austenitic stainless steels in oxidizing environments. Cracking susceptibility is a direct function of the boundary Cr content regardless of depletion width. However, grain boundary Cr depletion does not adequately explain IGSCC in stainless steels strengthened by cold work or neutron irradiation. Significant interfacial enrichment of Cr, Mo and B are often present in annealed stainless steels which may play a role in the IGSCC of cold-worked materials and delay IASCC to higher radiation doses. Impurity segregants (e.g., P) can promote IG hydrogen-induced cracking but do not have a strong detrimental effect on cracking in high-temperature water environments.

Introduction

Grain boundary composition has been inferred to control intergranular (IG) fracture in a wide range of materials systems. Although many authors have attempted to link grain boundary composition and environmental cracking susceptibility, few have made direct measurements. In most cases, bulk composition and/or heat treatment is varied and it is assumed that interfacial segregation is systematically changed. Indirect measurements are often made (e.g., IG corrosion tests) indicating grain boundary composition of an isolated element. Within selected well-understood cases, such approaches can give reproducible results. However, quantitative measurements of grain boundary composition are essential to enable any reasonable assessment of variables controlling cracking susceptibility. With the commonplace use of high-resolution techniques such as analytical transmission electron microscopy (ATEM) and scanning Auger microscopy (SAM), quantitative relationships have been established between interfacial composition and cracking susceptibility for many metallic alloy systems. [1] Perhaps the alloy system that has been most closely examined has been austenitic stainless steel due to its widespread use as a corrosion-resistant structural alloy in nuclear power systems. The vast majority of failures have been in high-carbon, 300-series stainless steels thermally sensitized during fabrication. Extensive basic and applied research activities were initiated about 25 years ago to develop a mechanistic understanding of the IGSCC process and, more importantly, identify remedial actions and corrective measures to cracking problems in boiling-water

reactor (BWR) power plants. For the most part, those research activities were highly successful. IGSCC of sensitized stainless steel is probably the best-understood and effectively modeled environmental cracking process. [2] However, recent observations of IG cracking in cold-worked, or in irradiated stainless steels, have been difficult to explain.

This paper examines austenitic stainless steels as an example alloy system to demonstrate the influence of grain boundary composition on IGSCC. Emphasis is placed on identifying equilibrium and non-equilibrium segregants that may promote susceptibility, or improve resistance, to cracking. In each case, current understanding of grain boundary composition development in stainless steels is reviewed and assessed relative to IG fracture in corrosive environments.

Grain Boundary Composition and IGSCC

The general conditions necessary to promote IGSCC are a susceptible material microstructure-microchemistry, a sufficiently corrosive environment, and the presence of tensile stresses. Many of the important aspects controlling environmental crack advance are illustrated in Fig. 1. In nearly all cases of IG cracking, grain boundary composition plays a dominant role. Interfacial composition can be significantly changed from the matrix by equilibrium and/or nonequilibrium processes resulting in segregation/depletion of alloying/impurity elements and precipitation of second phases. These compositional changes in the grain boundary region can influence IG crack advance through effects on electrochemical behavior (e.g., dissolution, repassivation and hydrogen recombination) as well as effects on interfacial mechanical behavior (e.g., deformation and cohesive strength).

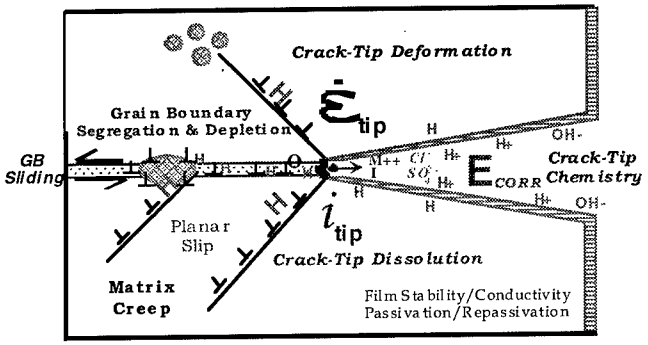

Figure 1. Schematic Illustrating Critical Crack-Tip Processes Controlling IGSCC.

Precipitation & Grain Boundary Composition Changes

The dominant material variable controlling IGSCC susceptibility in austenitic stainless steels results from the precipitation of Cr-rich $M_{23}C_6$ carbides at high-energy interfaces. This promotes the development of a Cr depleted region adjacent to carbide precipitates. This depletion is controlled by the thermodynamics of carbide formation and differences between the diffusivities of Cr and C. ATEM-EDS has enabled Cr depletion profiles to be routinely measured demonstrating that interfacial Cr concentrations decrease (from ~18% to <10%) as the heat treatment temperature is decreased due to changes in C and Cr activities. The width of depleted zone increases with time after IG carbides are nucleated.

The extent of grain boundary Cr depletion has been directly linked to the IG corrosion and SCC susceptibility of austenitic stainless steels. [3-6] The threshold concentration to promote IG degradation can be quite different for corrosion and SCC as illustrated in Fig. 2. Classical IG

corrosion is detected in a standard sensitization test when the grain boundary Cr concentration drops below ~13.5 wt%. On the other hand, IGSCC in high-temperature aerated water environments can be initiated during slow-strain-rate (SSR) tests when local Cr levels drop below ~17 wt%. Additional tests varying the width of the Cr depletion zone (and keeping boundary Cr concentration approximately constant) reveal that only a very narrow (<4 nm) width is necessary to promote cracking (Fig. 3). IGSCC susceptibility is not sensitive to increases in depletion width beyond that necessary to establish a continuous path for crack advance. On the other hand, standard sensitization tests will show much more aggressive IG corrosion with increasing depletion widths. [5] The correlations presented in Fig. 2 point out the critical importance of Cr depletion, and Cr minimums in particular, on IG degradation of austenitic stainless steels. Specific relationships between IGSCC and grain boundary composition will always depend on many other critical factors including mechanical loading characteristics and environmental conditions as well as secondary material variables. For example, the threshold grain boundary Cr concentration has been shown to depend on the strain rate during SSR tests. [4,5]

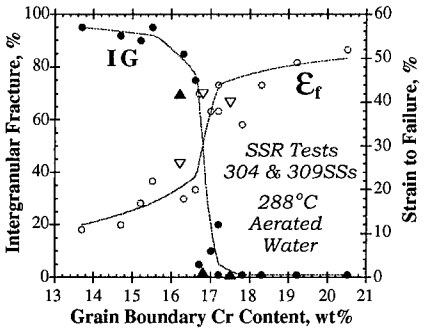

Figure 2. Grain Boundary Cr Concentration on IGSCC in BWR Water Environment.

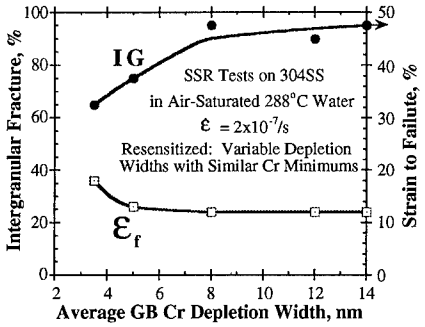

Figure 3. Grain Boundary Cr Depletion Width on IGSCC in BWR Water Environment.

Equilibrium Impurity Segregation

Impurity elements present at low levels in austenitic stainless steels can reach high levels at grain boundaries due to equilibrium segregation. The most prevalent segregant is P that can reach grain boundary P contents >10 at% in commercial stainless steels after intermediate temperature heat treatments (500 to 750°C). Thus, materials in the "sensitized" condition will most likely have considerable P segregation along with $M_{23}C_6$ carbides and Cr depletion defining the local microchemistry. Segregation of other impurity elements to stainless steel grain boundaries has been observed, but often requires high bulk contents or special thermal treatments. Sulfur segregates rapidly to boundaries if preexisting sulfides are dissolved by a high-temperature (>1200°C) exposure. Without such treatment, grain boundary S segregation is very slight even in doped alloys. Another element that has been shown to strongly segregate to austenitic stainless steel grain boundaries is N. Grain boundary segregation of N in commercial 304 and 316 grades is likely since bulk N levels are typically greater than 0.02 wt% (higher in L grades).

Grain boundary impurity segregation has been shown to promote hydrogen-induced cracking (HIC) in many iron- and nickel-base alloys. [7] Phosphorus segregation induces HIC during low-temperature SSR tests at cathodic potentials as illustrated in Fig. 4, but appears to have no effect on IGSCC in high-temperature water as indicated by the triangular points in Figure 2. The influence of grain boundary Cr content on IG cracking is not affected by P segregation (~10 at%). These results

are consistent with the crack growth rate tests of Andresen and Briant [8] who found that grain boundary P (and N) enrichment did not promote IG cracking of 304L SS in high-temperature water, while S had a small detrimental effect. However, there remains a need for additional crack growth experiments to evaluate segregation effects on SCC in stainless steels strengthened by cold work where cracking has been identified in laboratory tests and in service without Cr depletion. [9, 10]

Nonequilibrium Thermal Segregation

Recent ATEM characterizations [11-15] in annealed stainless steels have clearly demonstrated that significant grain boundary segregation occurs as a result of high-temperature heat treatment and subsequent rapid cooling. Alloying elements that are enriched are Cr and Mo compensated by Ni and Fe depletion as illustrated in Figure 5 for 316SS. Normal rapid air cooling from the solution anneal temperature (~1100°C) can increase boundary Cr and Mo levels by ~10 wt% over that in the matrix. Isolated measurements on stabilized stainless steels indicate that Nb and Ti may also be enriched by a few percent in the solution-annealed condition. This "presegregation" is commonly thought to result from a nonequilibrium, vacancy drag process with the degree of boundary enrichment dependent on the annealing temperature and the cooling rate. Although data are limited, maximum segregation appears to occur at higher annealing temperatures and at intermediate cooling rates. The mechanism of this presegregation is not well understood as indicated by Simonen and Bruemmer [16] who demonstrated that Cr enrichments cannot be explained by simple solute-vacancy interactions. Large Cr-vacancy binding energies are required to achieve the observed segregation during quenching which are completely inconsistent with available data and with nonequilibrium segregation during irradiation. The strongest nonequilibrium segregant in stainless alloys is probably B that cannot be easily detected by ATEM techniques. Quench-induced B segregation has been observed in stainless steels by atom-probe and radiography techniques and in conjunction with Cr and Mo. [14, 15] It appears to be likely that B cosegregates with Cr and Mo to grain boundaries during cooling and promotes the presegregation commonly detected due to strong binding between B and vacancies, and between B and transition metals. Other elements such as C and N may also reach grain boundaries during cooling and influence presegregation through interactions with Cr and Mo.

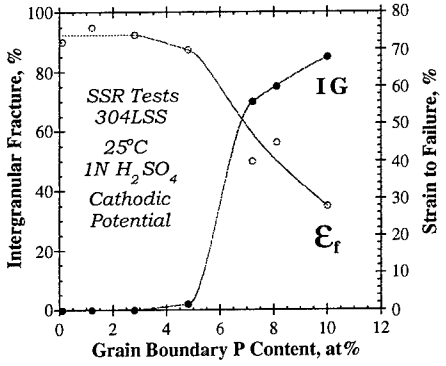

Figure 4. Grain Boundary P Concentration on HIC in Low-Temperature Acidic Environment at Cathodic Electrochemical Potential.

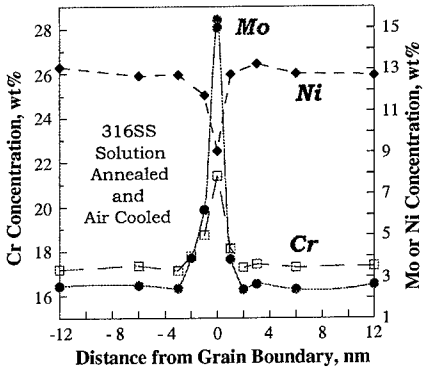

Figure 5. Example of Nonequilibrium Grain Boundary Segregation of Mo and Cr During Air Cooling from Annealing Temperatures.

Interfacial enrichment of Cr (and Mo) should impact the local grain boundary repassivation behavior and may be critical in the IGSCC resistance of stainless steels. Large heat-to-heat and processing variability can produce boundary Cr concentrations ranging from 18 to 30%. While enhanced

IGSCC resistance might be expected by these large increases in Cr due to improved passivation behavior, much depends on the mechanism of cracking. Austenite stability at the boundary will certainly be altered as well as the oxidation characteristics. In addition, B cosegregation with Cr and Mo to interfaces may influence the chemical and mechanical properties of the grain boundary. Research is needed to assess what role (if any) presegregation plays on the IGSCC of cold-worked stainless steels. Interfacial enrichment of Cr (or other elements that strongly oxidize in preference to the base metal) may be detrimental under specific electrochemical conditions where internal oxidation can occur. Recent results have indicated that this mechanism may control IGSCC of Ni-Cr stainless alloys in high-temperature water at low electrochemical potentials. [17, 18]

Radiation-Induced Segregation (RIS)

The RIS process is driven by the flux of radiation-produced defects to various sinks including grain boundaries. During irradiation, vacancies and interstitials can reach concentrations orders of magnitude greater that the thermal equilibrium concentration. Major alloying elements in stainless steels (Fe, Cr and Ni) are directly influenced by the flow of radiation-induced vacancies to sinks. The slowest diffusing element (Ni) becomes enriched, while faster diffusers (Cr and Fe) are depleted. Undersized minor elements and impurities such as Si can bind with interstitials and migrate preferentially to sinks.

RIS promotes a sharp change in interfacial composition at low-to-moderate fluences (0.1 to 5 displacements per atom or dpa) with a much smaller rate of change seen at higher dose. ATEM measurements of neutron fluence effects on grain boundary Cr profiles are illustrated in Fig. 6. General Cr RIS in 300-series stainless steels is summarized in Fig. 7 showing considerable scatter for low-dose conditions due primarily to differences in the initial grain boundary composition. Taking into account the wide range of materials and starting conditions (typically not characterized), most data show a consistent exponential decrease in Cr content to ~12 wt% with increasing fluence. Presegregation of Cr promotes the formation of W-shaped profiles (narrow depleted regions adjacent to an enriched boundary) at low dose and delays the development of a steady-state depletion profile. [12-14] The formation of a W-shaped profile also supports some type of binding for Cr and Mo within the boundary plane and interactions with a cosegregated element such as B.

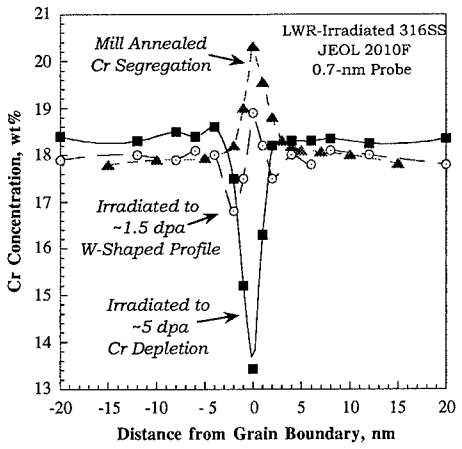

Figure 6. Irradiation Effects of Cr Composition Profiles Across High-Energy Grain Boundary in a Commercial Type 316SS.

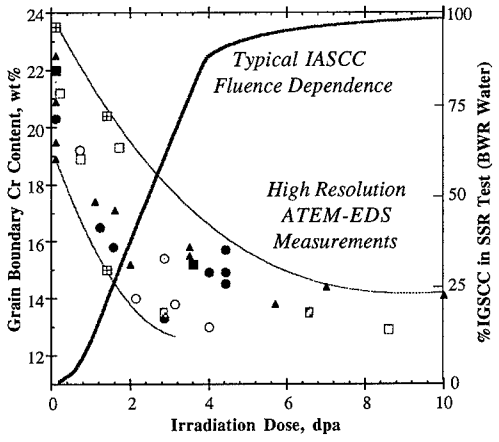

Figure 7. RIS of Cr as a Function of Neutron Irradiation Dose in Comparison to Typical IASCC Susceptibility Exhibitted in SSR Tests.

Although Cr RIS is most often reported, other alloying elements Fe, Ni, Si, Mn and Mo also segregate in response to the defect flux. Fe depletes in a fashion similar to Cr, while Ni enriches as a function of dose to compositions >20 wt% at grain boundaries. Strong segregation of Si occurs in most commercial SSs and can reach levels >25 at% at high doses [12], however silicide precipitation has not been detected at grain interfaces in LWR-irradiated SSs. Mn and Mo both deplete with increasing dose with the rate of Mo depletion influenced by its initial enrichment and steady-state depletion profiles only established at higher doses.

Although impurities (i.e., P and S) have long been suggested to play a role in IASCC, no consistent measurements of RIS have been reported. Phosphorus is often seen enriched at grain boundaries by ATEM and SAM techniques, but appears to primarily result from thermal segregation before irradiation. [3] Interfacial compositions range from not detectable to several percent regardless of dose. As noted earlier in this paper, P strongly segregates to grain boundaries in both Fe- and Ni base stainless alloys during thermal treatments. Unfortunately, unirradiated archive materials are rarely characterized and compared to results on neutron-irradiated samples.

Irradiation-Assisted Stress Corrosion Cracking (IASCC)

Radiation exposure has a strong influence on IGSCC as illustrated by service experience and ex-situ SCC tests. [19, 20] A distinct threshold fluence at which IASCC is observed under LWR conditions typically is seen near 1 dpa for high electrochemical potential BWR conditions (Fig. 7) and closer to 3 dpa for low-potential, hydrogen-water chemistry (HWC) or PWR conditions. The existence of a threshold fluence indicates that radiation-induced changes in material microstructure and/or microchemistry are responsible for IASCC susceptibility. While it is likely that radiation microstructure development and hardening play critical roles, the following discussion will focus on comparisons between RIS and IGSCC.

Radiation-induced Cr depletion has been the focus of many IASCC studies because of its well-documented effects in promoting IGSCC in sensitized stainless steels. Data where radiation-induced Cr depletion and IGSCC in post-irradiation SSR tests have been measured indicate that some level of depletion exists in all stainless steels which fail by IGSCC in BWR-type (moderate-to-high electrochemical potentials) water environments. As the grain boundary Cr concentration drops by 1 to 2 wt% (below ~17 wt% for 304SS), irradiated stainless steels become susceptible to cracking under the specific conditions of the SSR test as illustrated in Fig. 7. The data points for 316SS suggest a slightly lower minimum, corresponding to an interfacial Cr depletion of ~2 wt% below the matrix, consistent with the 304SS results. [6, 21]

All irradiated specimens that show IG cracking have sufficient grain boundary Cr depletion for IGSCC susceptibility in the SSR tests. Thus, Cr depletion can explain the observations of IGSCC in oxidizing water without considering other radiation effects on microstructure and microchemistry. However, questions still remain as to why many LWR-irradiated stainless steels show resistance to IGSCC even with significant radiation-induced Cr depletion (down to ~12%). Proton-irradiated high-purity 304-type stainless steels have also shown similar IGSCC resistance in SSR tests with severe Cr depletion. [22] These results suggest that other microstructural (e.g., radiation hardening) and/or microchemical (grain boundary or adjacent matrix) aspects influence cracking susceptibility. Nevertheless, it is critical to recognize the statistical aspects of the SCC process particularly for poorly controlled SSR and in-core tests where crack initiation and propagation play a role in the results. Nearly all SCC data of this type will show considerable scatter in comparison to crack-growth-rate experiments. Existing data are remarkable limited and contain many testing

inconsistencies among various laboratories. Therefore, it is not possible to make quantitative assessments concerning RIS effects on IGSCC.

Although this discussion has only considered radiation-induced Cr depletion, comparisons between grain boundary compositions and IASCC susceptibility can also be made for other segregants such as Ni, Fe, Si and P. Since the measured enrichment of Ni and depletion of Fe is nearly always consistent with the depletion of Cr, similar relationships to IGSCC result. However, it is difficult to envision a strong mechanistic influence of slight changes in Ni and Fe at interfaces. There is no evidence that minor elements or impurities impact IASCC susceptibility, since high-purity stainless steels (RIS limited to Fe, Cr and Ni) show cracking similar to commercial alloys with significant boundary enrichment of minor elements and impurities. As a result, radiation-induced Cr depletion appears to be responsible for IGSCC in oxidizing water environments consistent with behavior for sensitized stainless steels. This depletion does not explain IASCC susceptibility in non-oxidizing water environments and further research is needed to elucidate radiation-induced materials changes that promote IG cracking.

Summary

Grain boundary composition development and its effect on environmental degradation of austenitic stainless steels has been assessed. Cr depletion is shown to be the dominant material variable promoting IGSCC of austenitic stainless steels in most service environments. Cracking susceptibility is a direct function of the interfacial Cr concentration regardless of depletion width. For specific alloys and specific mechanical loading and environmental conditions, threshold grain boundary chemistries for IGSCC can be identified. Very small levels of depletion, 1 to 2 wt% below bulk Cr concentrations, are sufficient to promote IGSCC in oxygenated high-temperature water. As a result, most observations of IASCC in BWR environments are consistent with radiation-induced Cr depletion that occurs with fluence in 300-series stainless steels.

Grain boundary Cr depletion does not explain IGSCC in (unsensitized) cold-worked stainless steels at high electrochemical potentials (BWR) or IASCC of stainless steels at low potentials (BWR-HWC and PWR). Assessment of stainless steel segregation behavior indicates that many alloys are expected to have significant interfacial enrichment of Cr, Mo and perhaps B in the solution-annealed condition. The influence of this microchemistry on IGSCC has not been examined, but may play a role in cold-worked materials. Other elements such as P, C and N thermally segregate and Si segregates during irradiation, however existing data do not indicate a direct effect on IGSCC or IASCC susceptibility. Sulfur will promote IG cracking, but rarely segregates to sufficient levels at grain boundaries in commercial stainless steels after conventional processing. Therefore, no clear linkage has been established between grain boundary composition and IGSCC in these high-strength stainless steels. Critical research isolating grain boundary composition effects on IG crack growth is needed for both cold-worked and irradiated stainless steels.

Acknowledgments

Critical discussions and assistance from co-workers E. P. Simonen, D. J. Edwards, B. W. Arey and L. A. Charlot at Pacific Northwest National Laboratory are recognized. Support from the Materials Sciences Branch of the Office of Basic Energy Sciences, U.S. Department of Energy under contract DE-AC06-76RLO 1830 and from the Electric Power Research Institute is gratefully acknowledged.

References

1. Grain Boundary Chemistry and Intergranular Fracture, ed. G. S. Was and S. M. Bruemmer, Materials Science Forum 46 (1989).
2. P. L. Andresen and F. P. Ford, Mat. Sci. Eng. A103 (1988) p. 167.
3. S. M. Bruemmer, Corrosion 98 (1998) Paper 138.
4. S. M. Bruemmer, B. W. Arey and L. A. Charlot, Corrosion, 48-1 (1992) p. 42.
5. S. M. Bruemmer, B. W. Arey and L. A. Charlot, 6th Int. Symp. Environmental Degradation of Materials in Nuclear Power Systems - Water Reactors, ed. R. E. Gold and E. P. Simonen, The Minerals, Metals & Materials Society (1993) p. 277.
6. S. M. Bruemmer, L. A. Charlot and E. P. Simonen, 5th Int. Symp. Environmental Degradation of Materials in Nuclear Power Systems - Water Reactors, ed. E. P. Simonen, R. E. Gold and D. E. Cubicciotti, American Nuclear Society (1992) p. 821.
7. R. H. Jones and S. M. Bruemmer, Proc. Environment-Induced Cracking of Metals, NACE-10, ed. R. P. Gangloff and M. B. Ives, National Association of Corrosion Engineers (1990) p. 287.
8. P. L. Andresen and C. L. Briant, Proc. 3rd Int. Sym. Environmental Degradation of Materials in Nuclear Power Systems - Water Reactors, eds. G. J. Theus and J. R. Weeks, The Metallurgical Society (1988) p. 371.
9. S. Tahtinen, H. Hanninen and M. Trolle, ibid 5, p. 265.
10. T. M. Angeliu, et al., 8th Int. Symp. on Environmental Degradation of Materials in Nuclear Power Systems - Water Reactors, ed. S. M. Bruemmer and A. R. McIlree, American Nuclear Society (1997) p. .
11. P. Doig and P.E.J. Flewitt, Metallurgical Transactions A, 18A (1987) p. 399.
12. J. Walmsley, P. Spellward, S. Fisher and A. Jenssen, 7th Int. Symp. on Environmental Degradation of Materials in Nuclear Power Systems - Water Reactors, ed. S. M. Bruemmer, A. R.McIlree and R. E. Gold, National Association of Corrosion Engineers (1996) p. 985.
13. A. W. James and C.M. Shepherd, Mater. Sci. Technol., 5 (1989) p. 33.
14. L. Karlsson, et al., Acta Metall., 36-1 (1988) p. 1.
15. S. Dumbill, R. M. Boothby and T. M. Williams, Mater. Sci. Technol., 7 (1991) 385.
16. E. P. Simonen and S. M. Bruemmer, ibid 10, p. 985.
17. P. M. Scott and M. Le Calvar, Corrosion-Deformation Interactions, EUROCORR96, The Institute of Materials (1997) p. 384.
18. S. M. Bruemmer, L. E. Thomas, J. Daret and P. M. Scott, submitted to Corrosion, 1998.
19. P. M. Scott, J. Nucl. Mat., 211 (1994) 101.
20. P. L. Andresen, F. P. Ford, S. M. Murphy, and J. M. Perks, 4th Int. Symp. Environmental Degradation of Materials in Nuclear Power Systems - Water Reactors, ed. D. Cubicciotti and G. J. Theus, 1989, National Association of Corrosion Engineers (1990) p. 1-83.
21. S. M. Bruemmer and E. P. Simonen, Corrosion, 50-12 (1994) P. 940.
22. J. Cookson, R. D. Carter, D. L. Damcott, G. S. Was and P. L. Andresen, ibid 5, p. 573.

Materials Science Forum Vols. 294-296 (1999) pp. 83-90

Modelling Nonequilibrium Grain Boundary Segregations

M. Nastar and G. Martin

CEA-Saclay, CEREM, Section de Recherches de Métallurgie Physique,
F-91191 Gif sur Yvette Cedex, France

Keywords: Diffusion, Inverse Kirkendall Effect, Irradiation, Point-Defect Sinks

Abstract : Non-equilibrium interfacial segregations have often their origin in the non conservation of point defects at interfaces; under appropriate circumstances, point defect fluxes to or from interfaces can be triggered which, because of inverse Kirkendall effect, induce an alteration of the composition field in the vicinity of the interface. While this effect has long been modelled in a reliable manner in the special case of dilute ideal solid solutions, describing concentrated alloys raises interesting problems, the solution of which is not fully established. We discuss the available models and present advances, based on kinetic mean field approximations (vacancy and interstitial drag).

Introduction

Equilibrium interfacial segregations are indeed very rare and difficult to observe; most materials are either "*clamped*" or "*driven*" far from equilibrium. Materials *clamped* in a non equilibrium state are those materials which have been prepared by some high temperature process and then quenched or slowly cooled to their operating temperature, a temperature too low for solid state diffusion to bring the material to equilibrium. Materials *driven* far from equilibrium are exposed to some external forcing (irradiation, sustained shearing, steady evaporation or condensation, corrosion...) which drives them into a dynamical state (which may be a stationary state) distinct from the equilibrium state. Both clamped and driven materials exhibit interfacial segregations of strong practical relevance, which do not obey the rules of thermodynamics, i.e. cannot simply be understood in terms of the cohesive energy of the solid solution and of the atomic structure of the interface. Describing such segregations requires modelling, for *clamped* materials, the kinetic pathway toward equilibrium and, for *driven* materials, the dynamical balance between the damaging and the restoring processes which they experience. This has been achieved with some sophistication, up to now, in the particular but very relevant case where all such above mentioned processes can be described in terms of the formation, the diffusion and the elimination of point defects in a solid solution : the coupling between point defects- and solute- fluxes leads to solute segregations, at places where defects eliminate. Other types of non-equilibrium segregations include those resulting from solidification (solute drag by the moving solid-liquid interface), from recrystallisation (solute drag by moving grain boundaries), etc. The latter are not discussed in this review which focuses on those non-equilibrium segregations which result from the migration of point defects.

A key experiment : interfacial segregation in quenched and annealed Al base dilute solutions

In 1970, Anthony [1] reported the following very simple and enlightening experiment : anneal a dilute AlX (X= Zn, Cu, Ge) solid solution ≈10 Kelvin below the melting point for 10 minutes; then cool the specimen down to room temperature at a rate ≈ 7 Kelvin per minute. The excess vacancies close to the surface (which is covered by a thin layer of alumina) reach the Al - Al_2O_3 interface, where they cluster into pyramidal shaped cavities (visible by standard metallography) the volume of which gives the number of vacancies which have clustered. Electron microprobe analysis of the vicinity of the vacancy cluster reveals an enrichment (Zn), a depletion (Ge) or no change (Cu) of the solute content : enrichment implies a positive coupling between solute and vacancy fluxes and depletion, a negative one. As discussed by Anthony, the solute excess or depletion δC_s at the

vacancy sink is proportional to ratio of the solute flux to the vacancy flux J_s/J_v and to the total number of vacancies reaching the sink during the experiment, i.e. the vacancy flux integrated over the duration of the clustering process :

$$\delta C_s / C_s = (J_s / J_v)\frac{\int J_v dt}{C_s} \qquad (1)$$

In dilute solutions, J_s/J_v can be expressed in terms of a small number of jump frequencies of the vacancy in the vicinity of the solute atom [2]; e.g. in the face centred cubic lattice, five such frequencies (far away from the solute -W_0-, associating -W_4- and dissociating -W_3- the solute-vacancy complex, along the first neighbour shell of the solute atom -W_1- and finally exchanging with the solute atom -W_2) allow to estimate the solute to vacancy flux ratio. Anthony deduced W_3/W_1 ratios which complemented the few existing data. Moreover, Anthony predicted from his experiments that major non equilibrium grain-boundary segregations could be anticipated under irradiation, because irradiation induced vacancies (and dumbbell interstitials) would steadily eliminate at grain boundaries; the point defect flux so induced would trigger a solute flux leading to solute accumulation or depletion at the grain boundary. Such a phenomenon has indeed been observed few years later (1974), not at grain boundaries, but at interstitial dislocation loops forming in dilute NiSi solid solutions under ion irradiation as shown in fig. 1 [3].

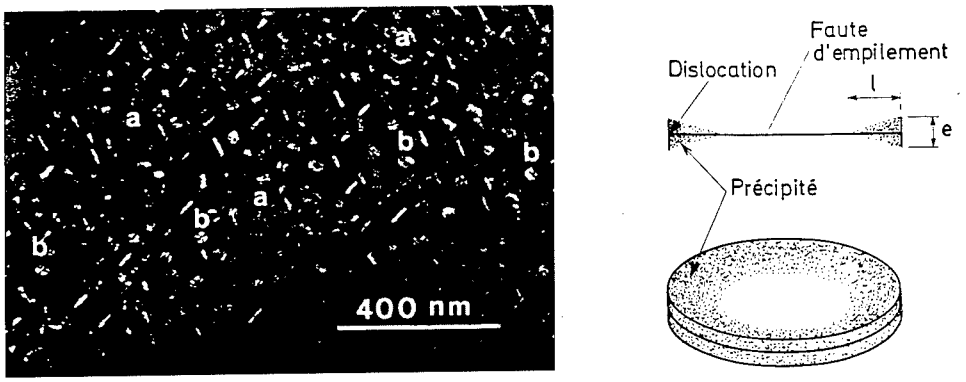

Figure 1 : Interstitial Frank loops decorated by a disk of Ni_3Si precipitate formed in a Ni 4 at% Si undersaturated solid solution under 2 MeV electron irradiation at 10^{-8} dpa/s at 623 K, 10^{-2} dpa [4, 5]. Left : dark field TEM image of Ni3Si; right : drawing from Barbu's Thesis [5].

Modelling irradiation induced interfacial segregations in dilute solutions

The first attempt to model irradiation induced segregation goes back to the pioneering work by Johnson and Lam in 1976 [6]. The model identifies *six* relevant species : the vacancy, the dumbbell, the mixed dumbbell, the dumbbell trapped in the vicinity of the solute, the vacancy-solute complex, and the isolated solute atom. A local concentration of each species $C_\alpha(\mathbf{r}, t)$ (α=1 to 6) is defined at any position $\mathbf{r}$ and any time t, and is governed by a partial differential equation which describes the balance between the formation (e.g. of vacancies or interstitials by irradiation, of complexes by bimolecular association reactions, of free defects by dissociation reactions etc.), the destruction (e.g. dissociation of complexes, or by vacancy-interstitial recombination...), and the accumulation by diffusion (minus the divergence of the diffusion flux). A system of *six* coupled differential equations (of the diffusion-reaction type) results which is solved numerically with appropriate boundary

conditions. The problem has been solved in planar geometry (segregation at a free surface) or in spherical symmetry (segregation at the surface of a cavity); the free vacancy concentration at the surface is fixed to its thermal equilibrium value, that of free interstitials is set to zero, and the solute quits and enters the solid with two distinct jump frequencies (W_{out} and W_{in} respectively), which allows to take into account thermal equilibrium segregation effects since at thermal equilibrium, $C_{surf.}/C_{bulk} = W_{out}/W_{in}$. Faulkner's model [7], is an extension of the above model. Many relevant questions have been addressed with this type of model [8].

The drawback of the above formalism is to introduce some degree of arbitrariness in the choice of the reactions to be described by the balance equations (e.g. the annihilation reaction between a mixed dumbbell and a solute vacancy pair was not retained in the original Johnson Lam model) and in the definition of the appropriate diffusion coefficients. Since many solute-defect association and dissociation reactions should occur in the course of the diffusion of each defect to the sink, it is reasonable to assume a *local equilibrium* between the defect and solute populations, as is done in the atomistic theory of diffusion in dilute solid solutions [2]. The Johnson Lam model was reformulated along this idea, few years later [9]. As a result, we are left with three independent species (dumbbells -i-, vacancies -v- and solute -s-), the splitting of the defects concentrations into that of free- and associated defects being unambiguously defined by the condition of local equilibrium. The three independent concentration fields are governed by three coupled differential equations :

$$\begin{aligned} \partial C_i / \partial t &= G_i - RC_iC_v - \mathrm{div}\, J_i & J_i &= -D_{ii}\nabla C_i - D_{iv}\nabla C_v - D_{is}\nabla C_s \\ \partial C_v / \partial t &= G_v - RC_iC_v - \mathrm{div}\, J_v & J_v &= -D_{vi}\nabla C_i - D_{vv}\nabla C_v - D_{vs}\nabla C_s \\ \partial C_s / \partial t &= - \mathrm{div}\, J_s & J_s &= -D_{si}\nabla C_i - D_{sv}\nabla C_v - D_{ss}\nabla C_s \end{aligned} \qquad (2)$$

In the above equations, G_i (resp. v) is the production rate of interstitials (resp. vacancies) by irradiation, R is the rate constant for interstitial-vacancy recombination (R is proportional to $D_{ii}+D_{vv}$) and all the diffusion coefficients D_{pq} can be expressed in terms of defect jump frequencies in the solvent and in the vicinity of the solute. The expressions for the vacancy diffusion mechanism are well established, those for the dumbbell diffusion in the FCC lattice have been derived by Barbu et al. [10]. The above model has been reformulated some years later by [11]. It has been used not only for irradiation induced surface segregations, but also to derive a theory of self organisation of solid solutions under irradiation (see below) [12].

The common feature to all such models is to describe *ideal* solid solutions, i.e. solutions where the solute atoms do not interact. When needed, a solubility limit can be introduced as a threshold concentration beyond which a precipitate forms, but the latter is inconsistent with the thermodynamics of the model which implies unrestricted solubility. The next section describes the recent attempts to overcome this limitation.

Modelling irradiation induced interfacial segregations in concentrated alloys.

Beyond a few atomic per cent of solute in the solution, the above models loose their efficiency, since they only consider isolated solute atoms and simple complexes (e.g. one vacancy attached to one solute). Some attempts have been done to use eqs. 2, with adequate expressions for the diffusion coefficients in concentrated alloys [13, 14]. The latter are based on an extension of Manning's alloy model, where the defect jump frequency only depends on the chemical species it exchanges with : as a result, the local alloy concentration enters in a linear way in the partial diffusion coefficients, while experimental data on e.g. FeNiCr ternary alloys point to a concentration dependence of the formation and migration *energies* of vacancies [15]. This implies a much stronger local concentration dependence of the parameters (exponential of a polynomial) which has been taken into account in the model described below, developed in Saclay in the last few years [16, 17].

The aim of the model is to handle both the thermodynamics *and* the kinetics of the alloy with the same degree of sophistication. For this, we assume that the configurational energy of the alloy is a sum of pair interactions (three-body or higher order interactions can be included if required) and write the jump frequency of an atom of species α on site i' to a nearest neighbour vacancy site i :

$$\Gamma^{v,\alpha}_{i,i'}(\mathbf{n}) = \nu^{\alpha} \exp -\beta \Delta E^{v,\alpha}_{i,i'}(\mathbf{n}) \tag{3}$$

where **n** describes the atomistic configuration of the alloy at time t, i.e. the type of atom on each site, ν^{α} is the attempt frequency, $\Delta E^{v,\alpha}_{i,i'}(\mathbf{n})$ the configuration dependant activation barrier for exchanging the α atom on site i' with the vacancy on site i, and β is 1/kT. The activation barrier is the difference between the energy of the system with atom α at the saddle point between sites i and i' (E_{saddle}), and the energy $E(\mathbf{n})$ of the configuration **n**. Because of the finite range of atomic interactions, only few bounds are modified when going from the stable to the activated state, so that :

$$\begin{aligned} \Delta E^{v,\alpha}_{i,i'}(\mathbf{n}) &= E_{saddle} - E(\mathbf{n}) \\ &= \sum V_{s.p.} - \sum V_{b.b.} = E_{s.p.} - \sum V_{b.b.} \end{aligned} \tag{4}$$

The sum $\sum V_{b.b.}$ (b.b. stands for "broken bounds") represents the binding energy of the complex V-α to sites i, i' in configuration **n**, and $E_{s.p.}$ is the binding energy of the jumping atom to the saddle point; for the sake of simplicity, we often assume the following : $E_{s.p.}$ neither depends on α nor on **n**, $\nu^{\alpha} = \nu$, and that the atomic interactions reduce to pair interactions only. Such assumptions are by no means essential and can be relaxed if needed. Similar expressions can be written for the dumbbell diffusion mechanism. Eqs. 3-4 give the jump frequency of each defect in each direction as a function of the actual occupation of the sites close to the defect. We are, however, interested in a less detailed description, namely a time dependent concentration profile : the concentration at a site is the mean occupation of the site. It is shown by adequate averaging of equations 3 and 4, that the concentration $C^{\alpha}_{i}(t)$ of species α on site i follows eq. 5 :

$$\begin{aligned} &\partial_t C^{\alpha}_{i}(t) = -\sum_{i'} J^{\alpha}_{i,i'} \\ &J^{\alpha}_{i,i'} = -\sum_{i'} 2M^{\alpha}_{i,i'} \sinh\left[\beta(\mu'^{\alpha}_{i} - \mu'^{\alpha}_{i'})/2\right]; M^{\alpha}_{i,i'} = \sqrt{\Gamma^{v,\alpha}_{i,i'}\Gamma^{\alpha,v}_{i,i'}}\ ; \mu'^{\alpha}_{i} = \mu^{\alpha}_{i} - \mu^{v}_{i} \end{aligned} \tag{5}$$

where $J^{\alpha}_{i,i'}$ is the flux of species α from site i to i', the μ's are the chemical potentials which are easily evaluated in the Bragg Williams approximation for the alloy model under consideration*; the vacancy jump frequencies Γ are computed by replacing, in the activation barrier of eq. 3, the actual occupation of the sites by the concentrations. Notice that the mobilities M are composition dependent [18, 19]. As can be seen, the above model neglects the correlation effects in diffusion since the flux $J^{\alpha}_{i,i'}$ depends on the gradient of the chemical potential of species α only, and not of other species. Such a limitation has recently been overcome close to uniform equilibrium [20]. This induces a small error in the cross-diffusion coefficients $D_{\alpha\beta}$. Work is in progress to include this effect in the model.

Eqs. 5 can be solved for a slab of finite thickness (typically few 10^2 to 10^4 lattice planes),

* The free energy par atom in the point approximation used for deriving eq. 5 is :
$\beta F\left\{C^{\alpha}_{i}\right\} = \sum_{i,\alpha}\left(C^{\alpha}_{i} \ln C^{\alpha}_{i}\right) + 1/2\,\beta \sum_{i,j;\alpha,\beta} V^{\alpha\beta}_{i,j} C^{\alpha}_{i} C^{\beta}_{j}$

where each surface plane is treated as a buffer which acts as defects sink and source : in particular, whenever an atom jumps from the bulk into the buffer, with a frequency as defined above, a vacancy is thermally injected into the bulk; the composition dependence of the vacancy formation energy is thus built into the model, an important feature in some cases. The same is true for the equilibrium segregation isotherm, including for ternary alloys [21]. Under irradiation, the defect production and recombination in each plane is added to the balance equation eq. 5. Ballistic mixing can be incorporated, as well as the shift in depth of the interstitial and vacancy generation rates, which is relevant when modelling ion implantation.

The above model has been used both in binary [16] and ternary [17] concentrated alloys. The classical qualitative features of irradiation induced segregation (RIS) are recovered : existence of a temperature and flux window for RIS to occur, typical shape of the segregation profile and of its time evolution (the solute which segregates is carried to the grain boundary from a distance which increases with time...). Moreover, with a careful parametrization procedure, a good quantitative agreement can be obtained with published data.

For binary alloys, Grandjean et al. [16] well reproduce Wagner's data [22] on irradiation induced segregation at free surfaces in Cu_xNi_{1-x} solid solutions with x= 0.1 and 0.6. It is found that inverse Kirkendall effect due to vacancies only suffices to account for the time dependence of the amount of surface segregation at three distinct temperatures, and for the two compositions, with a unique set of parameters. More details are published elsewhere [16].

Ternary FeNiCr alloys, have been modelled by Nastar et al. [17]. In such alloys, it is found that the contribution of dumbbells must be taken into account as shown in the three figures below : the dashed curves are those computed with vacancies only (parameter set 1), the solid ones are obtained taking into account the dumbbells (parameter set 2). Again all such curves are obtained with a unique set of parameters. Notice that the intriguing behaviour of the Cr depletion, which goes through an extremum at intermediate doses [23, 24], is reproduced by our model : in our model, this results from a competition between inverse Kirkendall effect which depletes the fast moving Cr (low activation energy for the Cr-Vacancy exchanges) on the one hand, and the thermodynamics of the alloy, where a strong Ni-Cr ordering energy attracts Cr in Ni rich regions, on the other hand [17].

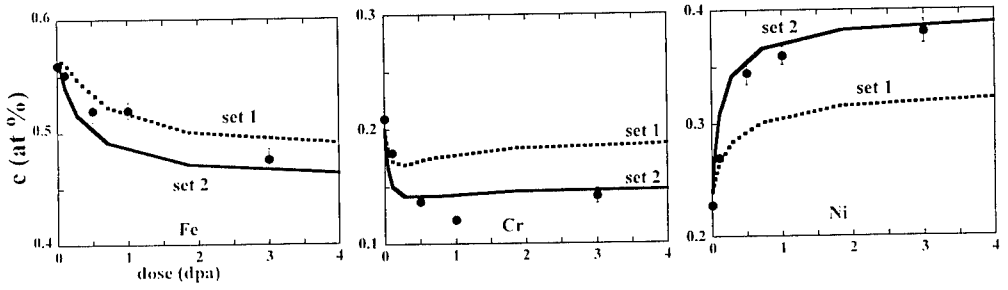

Figure 2 : Grain boundary Fe, Cr and Ni concentrations plotted as a function of irradiation dose in Fe-20Cr-24Ni, as measured by Auger Electron Spectroscopy (AES) [23] (dots) and as predicted from the model using vacancies only (parameter set 1, dashed line) or both vacancies and dumbbells (parameter set 2 , solid line).

The details of the parametrization procedure are given elsewhere [16, 17]; briefly, the choice of the pair interaction energies must yield the cohesive energy of the pure compounds, the heat of mixing of the alloy and the vacancy formation energy; the kinetic parameters (ν in eq. 3 and $V_{s.p.}$ in eq. 4) must yield the known diffusion properties. For dumbbell interstitials, such data are not

available; we use Bocquet's simple model which implies a minimum number of parameters : the migration energies for pure and mixed dumbbells, the binding energies of the various dumbbells [25]. The total number of parameters is large, but a systematic procedure described in [17] consists in using a small number of experiments and then to assess the set of parameters on a large set of systematic data which are now available in few cases, e.g. [23, 26]. In all cases discussed above, the whole set of experiments (for a given system, all compositions, temperatures and doses) was reproduced with a unique set of parameters. As discussed in [27] this points to an improved efficiency of the model compared to others [28]. Moreover, the beneficial effect of large oversized impurities as segregation inhibitors, observed experimentally [29], could be reproduced with our model [17].

Self organisation in alloys under irradiation

Large scale concentration fluctuations in concentrated solid solution [30], as well as, very regular arrays of precipitates in undersaturated solid solutions (as shown fig. 3 [5]) have been reported under irradiation. The models described above (eqs. 2 and 5) yield a possible explanation for such self organisations [12, 31-34].

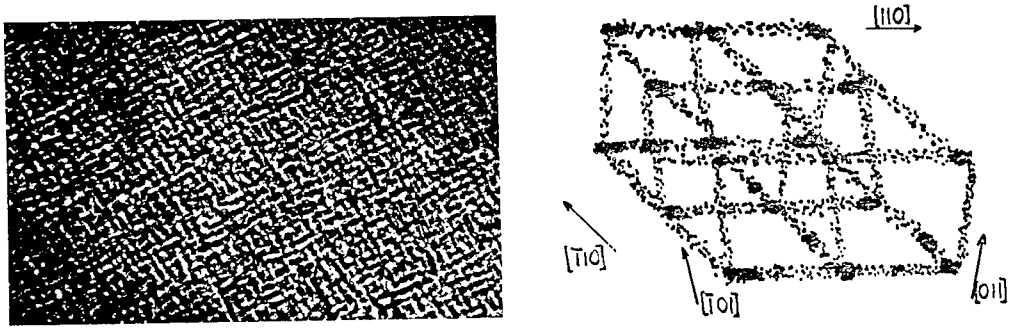

Figure 3 : Modulated structure triggered by 500 keV Ni^+ irradiation in Ni 6at% Si, at 4 10^{-3} dpa s^{-1}, 733 K 20 dpa.(500 x 120 nm^2) [5].

Indeed, all the parameters in eqs. 2 are a priori composition dependent, so that a solute rich region might e.g. favour vacancy-interstitial recombination; assuming that the defects are produced homogeneously throughout the solution, a defect flux toward the solute rich region will be sustained by irradiation and might reinforce the solute accumulation by inverse Kirkendall effect. This yields an intrinsic instability mechanism for solid solutions under irradiation. Since the amplitude of the driven segregation is larger the longer the diffusion distance of point defects, a natural length scale appears in the problem : the mean free path of point defects. If the vacancy-interstitial recombination is the dominant elimination mechanism for Frenkel pairs, the modulated structure is expected to develop with a finer scale the higher fluxes and the lower the temperatures. This is indeed observed in NiSi dilute solutions [5].

Conclusion

In view of the growing sophistication of experimental observations, it is important, when modelling irradiation induced segregation, to take into account the alloy chemistry in a consistent manner (including the equilibrium interfacial segregation, the composition dependent defect formation energy, etc.). The techniques we introduced describe the alloy thermodynamics and kinetics at the same level of sophistication, that of classical mean field theory (Bragg Williams approximation). Although this is still a rather naive picture for complex real alloys, it warrants internal consistency of the model and contains important feedbacks which are omitted by other models.

Acknowledgements : We gratefully acknowledge the contribution of Pr. P. Bellon (U. of I at Urbana) to many parts of this work, and of Dr. C. Abromeit to the discussions on self organisation. Part of this work has been done with the financial support of EDF.

References

[1] T. R. Anthony, J. Appl. Phys. **41** (1970) 3969; Phys. Rev. **B2** (1970) 264; Acta Met. **17** (1970) 307.
[2] A.R. Allnatt and A.B. Lidiard, *Atomic Transport in Solids* (Cambridge University Press).
[3] A. Barbu and A.J. Ardell, Scripta Met. **9** (1977) 771.
[4] A. Barbu, A. Chamberod and G. Martin, J. Appl. Phys. **51** (1980) 6192.
[5] A. Barbu, Thesis (1976), unpublished.
[6] R.A. Johnson and N.Q. Lam, Phys. Rev. **B13** (1976) 4364 & Phys. Rev. **B15** (1977) 1794.
[7] R.G. Faulkner, Shenhua Song, P.E.J. Flewitt, M. Victoria and P. Marmy, J. Nucl. Mater. **255** (1998) 189.
[8] R.S. Averback, L.E. Rhen, W. Wagner, H. Wiedersich and P.R. Okamoto, Phys. Rev. **B28** (1983) 3100.
Cambridge 1993.
[9] R. Cauvin and G. Martin : Proc. Yamada Conf. V, Point Defects and Defects Interactions in Metals, Takamura et al. Eds., U. of Tokyo Press (1982) 931.
[10] A. Barbu, Acta. Metall. **28** (19980) 499; A.R. Allnatt, A. Barbu, A.D. Franklin and A.B. Lidiard, Acta. Metall. **31** (1983) 1307.
[11] S.M. Murphy, Phil. Mag. **59** (1989) 953; Phil. Mag. **59** (1989) 1163.
[12] G. Martin and P. Bellon, Solid State Physics, **50** (1996) 189.
[13] H.Wiedersich, P.R. Okamoto and N.Q. Lam, J. Nucl. Mater. **83** (1979) 98.
[14] W.G. Wolfer, J. Nucl. Mater. **114** (1983) 292.
[15] A. Benkaddour, C. Dimitrov and O. Dimitrov, J. Nucl. Mater. **217** (1994) 118.
[16] Y. Grandjean, P. Bellon and G. Martin, Phys. Rev. **B50** (1994-II) 4228; & Y. Grandjean, Report CEA-R-5731 (1994).
[17] M. Nastar, P. Bellon, G. Martin and J. Ruste, Mater. Res. Soc. Proc. **481** (1998) 383.
[18] G. Martin, Phys. Rev. **B41** (1990) 2279.
[19] V.G. Vaks, S.V. Beiden and V.Yu Dobretsov, Pis. Zh. Eksp. Teor. Fiz. **61** (1995) 65, Engl. Transl. JETP Lett. **61** (1995) 68.
[20] V. Yu Dobretsov, G. Martin and M. Nastar, submitted.
[21] C. Gallis, Report CEA-R-5731 (1997).
[22] W. Wagner, L.E. Rhen, H. Wiedersich and V. Naundorf, Phys. Rev. **B28** (1983) 6780.
[23] D. L. Damcott, T. R. Allen, and G. S. Was, J. Nucl. Mater. **225**, 97 (1995); & G. S. Was and T. Allen, J. Nucl. Mater. **205**, 332 (1993).
[24] W. Kesternich and A. Gracia-Borquez, Scripta Materialia, **36** (1997) 1127.
[25] J.L. Bocquet, Phil. Mag. **47** (1983) 547.
[26] H. Takahashi, T. Kato, S. Watanabe and N. Sakaguchi, Annales de Physique, Col. C3, suppl n° 3, **20** (1995) C3-109.
[27] T.R. Allen and G.S. Was, *Effects of Radiation on Materials :* 18th International Symposium, R.K. Nanstad Ed., ASTM STP 1325 (1997) in print.
[28]. J.M. Perks, A.D. Marwick and C.A. English, Report AERE R 12121 (1986).
[29] T. Kato, H. Takahashi and M. Izumiya, J. Nucl. Mater, **189** (1992) 167.
[30] F.A. Garner, H.R. Brager, R.A. Dodd and T. Lauritzen, Nucl. Instr. Meth. **B16** (1986) 244.
[31] G. Martin, Phys. Rev. **B21** (1980) 2122; Phys. Rev. Letters **50** (1983) 250.
[32].C. Abromeit and G. Martin, *Rad. Induced Changes in Microstructure*, 13th Int. Symp., F.A. Garner, N.H. Packan, A.S. Kunar Eds., ASTM-STP 955 Part I (1987) 822.
[33] C. Abromeit and G. Martin, J. Nucl. Mater, in Print.
[34] S. Murphy, Phil. Mag. **A58** (1988) 417.

Materials Science Forum Vols. 294-296 (1999) pp. 91-94

Triple Junction Structure and Properties

A.H. King

Department of Materials Science & Engineering, State University of New York at Stony Brook, Stony Brook, NY 11794-2275, USA

Keywords: Triple Junctions, Taxonomy, Dimensionality, Structure, Energy, Segregation

Abstract

We provide a brief overview of the nature and behavior of triple junctions, including a description of their impact upon materials properties. It is shown that triple junctions may have distinct structures and thermodynamically definable energies. They may comprise strain fields in the form of dislocations or disclinations, and sustain chemical segregation.

Introduction

Grain boundary research proceeds from an understanding that the properties of polycrystals cannot be predicted simply on the basis of ensembles of the properties of the single crystals of which they consist. Although it is certainly necessary to understand the properties of the single crystals, this is not sufficient because the grain boundaries themselves contribute to the properties of the material. By a similar logic, it may not be sufficient to understand the properties of isolated grain boundaries, either. Just as it is necessary to understand the connectivity between the grains in a polycrystal, and how the connectivity affects the properties of the grains themselves, it is also potentially important to understand the connectivity between the grain boundaries.

Taxonomy

Triple junctions may be described in a hierarchical taxonomy based upon dimensionality. While grain boundaries are two-dimensional structures (often referred to as "defects") that join three-dimensional grains, triple junctions are one-dimensional structures that join two-dimensional grain boundaries. Two-dimensional grain boundaries join two grains, while one-dimensional triple junctions (typically) join three grain boundaries. Viewed from the perspective of the perfect crystal, a grain boundary is a defect, and viewed from the perspective of a grain boundary, a triple junction is also a defect. This taxonomy is readily extended to junctions between triple junctions, as shown in Table 1. The same taxonomy can also be adapted to two- or one-dimensional spaces. The defect dimensionality, D_d, is always one fewer than the dimensionality of the joined objects, D_j, and for a three-dimensional space ($D_s = 3$)the sum of the dimensionality of the joined objects and the number of joined objects is always 5. In a two-dimensional space, the corresponding sum is reduced to 4, and in a one-dimensional space it is 3[†].

We view triple junctions as interfaces between grain boundaries, and quadruple points as the interfaces between triple lines, and all of them in general, as "junctions." Many of the properties of these generalized "junctions" can be inferred from the well-known properties of grain boundaries.

[†] We infer that in a four-dimensional space, the junction between two hypergeometric objects that we might dub "hypergrains" would be a three-dimensional grain-like object; and that there could be two-dimensional junctions between triplets of these three-dimensional grains, *etc.*

Table 1: Dimensionality-based taxonomy of interfacial defects, for a three-dimensional space.

Type of Defect	*Object Joined by the defect*	*Defect Dimensionality,* D_d	*Dimensionality of Joined Objects* D_j $(= D_d + 1)$	*(Minimum) Number of Joined Objects* N_j $(= 1 + D_s - D_d)$
Grain Boundary	Grains	2	3	2
Triple Line	Grain Boundaries	1	2	3
Quadruple Point	Triple Lines	0	1	4

Furthermore, facet junctions can also be included in the taxonomy, if we consider that they include one "virtual" grain boundary so they can be treated as triple junctions.

Geometry and Periodicity

The geometry of triple junctions has been studied quite widely, if only sporadically. It is widely recognized that junctions between CSL-forming grain boundaries obey the relationship

$$\Sigma_1 = \Sigma_2 \cdot \Sigma_3 \qquad (1)$$

where Σ_i are the coincidence parameters of the three grain boundaries. Less well recognized about this simple formula are two other important facts:
First; where the formula holds, the DSC lattices of grain boundaries 2 and 3 are sublattices of the DSC lattice of grain boundary 1. This allows for continuity of secondary dislocation structure through the triple junction, as demonstrated in detail by Clarebrough and Forwood [1].
Second; the formula only holds true for boundaries with misorientations at or very close to the exact coincidence orientation, and even then it may depend upon the method of assignment of CSL correspondence. A survey of all possible triple junctions with a common [111] axis reveals that the product rule is only obeyed in 18% of all cases, if we follow the Brandon criterion and use Σ-values up to 31, despite the fact that 99% of the grain boundaries can be characterized as "coincidence-related" [3]. Adopting different criteria will alter the exact figure but not the conclusion that most triple junctions do not satisfy the Σ-product rule. Where the Σ-product rule fails, there is generally no commensurability among the DSC lattices of the three grain boundaries and therefore no simple basis for the continuity of secondary dislocations. As shown by Dimitrakopoulos, Karakostas and Pond, however, continuity is still assured for the primary grain boundary dislocations defined by Frank's formula [4]. Since the secondary dislocations are defined by groupings of the primary dislocations, the overall dislocation content of the grain boundaries is conserved at all triple junctions, whether they satisfy the Σ-product rule or not.

A more general statement about the periodicity of the junction can be made, which applies to all types of junction, in spaces of any dimensionality: The structural periodicity of the junction, measured in any given direction, is the least common multiple (LCM) of the periodicities of all of the joined objects, in the same direction. Applying this statement to grain boundaries allows us to predict periodicities matching the dimensions of the CSL either in two or three dimensions, as required. Applying it to triple lines we find that for cases that satisfy Eq. 1, the triple line has a structural period equal to the CSL of Grain Boundary 1 (*i.e.* the boundary with the largest CSL). This periodicity applies along the length of the triple junction, and also laterally, as the junction migrates. In most cases, however, the triple junction's structural period is infinite and the structure may be seen as being randomly variable. A triple junction may be described in terms of its strain field and its core structure, much as any line defect is treated.

Strain Field. We have demonstrated elsewhere that, aside from the primary and secondary dislocations that cross a triple junction, the junctions may embody disclinations with real strain fields, that accommodate rotational incompatibilities [5]; and dislocations [6] which derive from translational incompatibilities among the grains comprising the polycrystal. As shown in [5], the disclination content of a triple junction is a damped periodic function of the length of the boundary, having stronger oscillations for smaller boundaries. In [6] we show that the dislocation content of a triple junction can also be a function of the dimensions of the grains abutting the junction, since their translational incompatibilities depend upon their size. Thus, if all other components of a microstructure are held fixed, motion of a single triple junction (accompanied by migration of the attached grain boundaries) causes a change in the defect content of the junction, consistently with the comments on periodicity, above.

Core Structure. In a study of $\Sigma3$-$\Sigma3$-$\Sigma9$ triple junctions in diamond, we have shown that although the three grain boundaries may by formed without dangling bonds by forming 5- 6- or 7-sided rings of atoms (in a [110] projection) [7], it is not possible to join these together without some form of bonding error at the triple junction [5]. The nature of the bonding error is a function of position, and it varies with a period identical to the largest CSL involved in the junction. In general, we find that grain boundaries with ideal, energy-minimized structures cannot be joined together without forming rather obvious atomic misfits at the triple junction. Hollow-cored triple junctions may be favorable in cases where the core energy is large, much as hollow-cores are allowed for certain dislocations, depending upon the balance of core energy and surface energy [8].

Energy

Since a triple junction embodies a core structure with atomic-level strain or bonding defects, and also may have a long-range strain field with both disclination and dislocation nature, it embodies a line energy in the same sense that any other line defect does.

For any defect, it is required that the energy (per atom) must be greater than the energy of the thermodynamic ground state - perfect crystalline material. It is not necessary, however, that any junction must have greater energy than the objects that it joins, with the sole exception of the joint of highest dimensionality for the space in question. In three dimensions, for example, grain boundaries join material in the ground state, so their energy must be positive. Triple lines, however, are only required to have energies greater than, or equal to the energy of the perfect crystal and there is no restriction on the sign of their energy with respect to the grain boundaries that they join. It is readily conceivable that a triple junction may have positive or negative strain energy since the misfit strains at the triple junction may enhance or cancel those of the constituent grain boundaries. The core structure can also be more like the perfect crystal than are the structures of the adjoined grain boundaries. Thus, the triple junction can have lower energy (per unit volume) than the grain boundaries, and may correctly be described as having negative energy, with respect to the "perfect" grain boundary structures in which it exists. Although such a junction, with negative energy, might be expected to expand spontaneously and without limit, it must also be recognized that any such expansion in length also necessarily increases the grain boundary area, so the total system energy can still increase, depending upon the geometrical details of the configuration. If the expansion is generated by forming the triple junction into a wave-like form, changing its line direction, then it is likely that its energy will change, too, since it is likely to be highly anisotropic. Thus, unlimited expansion is not expected, although a balance of triple junction energy and grain boundary energy may lead to configurations that are stable against grain growth.

If the energy of the triple junction depends upon the chemical composition of the material, then segregation effects may occur, and these have been observed in the case of bismuth in copper [9] wherein some triple junctions have been found to have bismuth enrichment well beyond that of the adjoining grain boundaries, which are, respectively, enriched far beyond the bismuth concentration

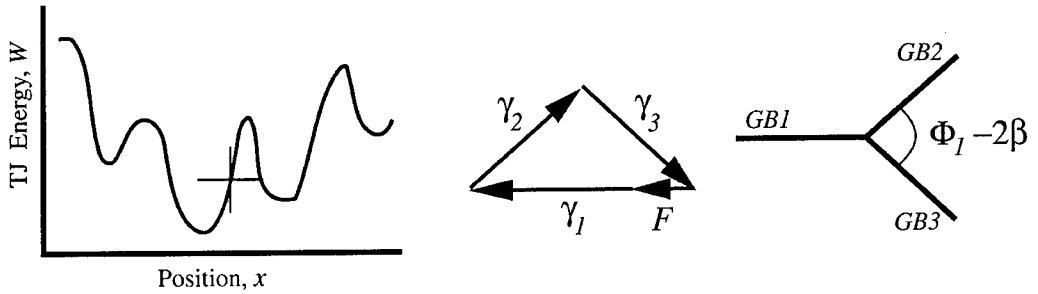

Figure 1. Schematic illustration of the variation of energy of a triple junction with position. At any position (*e.g.* as marked) the energy gradient constitutes a force which increases from zero as the junction moves out of its energy minimum. This resists motion, and affects the junction equilibrium as shown in the vector diagram, reducing the dihedral angle in the shrinking grain.

in the grain interiors. The observation of segregation is direct evidence that triple junctions have energy distinct from that of the interfaces in which they exist.

Forces Acting on Triple Junctions

Because the core structure and the defect content of a triple junction are both functions of the junction position, the junction energy may vary quite markedly with its position. Any gradient in the energy produces a force upon the triple junction, in the same sense that interactions with the crystal lattice produce the force on a dislocation, generally known as the Peierls force. The force per unit length acting on a triple junction is simply

$$F = -\nabla W \qquad (2)$$

where W is the energy per unit length. This force is responsible for moving the triple junction into local energy-minimizing positions and also provides a "pinning" or "friction" force on the junction as it starts to move. The effect of this on grain boundary migration and grain growth are discussed elsewhere [10].

Acknowledgment: This work is supported by the US National Science Foundation, grant number DMR9530314.

References

[1] L.M. Clarebrough and C.T. Forwood, *Phil. Mag. A* **55** (1987), p. 217.
[2] D.G. Brandon, *Acta Met.* **14** (1966), p. 1479.
[3] K. Owusu-Boahen, unpublished work.
[4] G.P. Dimitrakopoulos, Th. Karakostas and R.C. Pond, in *Interface Science and Materials Interconnection, Proceedings of JIMIS-8* (1996), Jap. Inst. Met. p. 347.
[5] A.H. King and Y. Zhu, *Phil. Mag. A*, **67** (1993), p. 1037.
[6] A.H. King, F.R. Chen, L. Chang and J.J. Kai, *Interface Sci.* **5** (1997), p. 287.
[7] J. Hornstra, *Physica* **26** (1959), p. 198.
[8] F.C. Frank, *Acta Crystall.* **4** (1951), p. 497.
[9] K.M. Yin, A.H. King, T.E. Hsieh, F.R. Chen, J.J. Kai and L. Chang, *Microsc. & Microanalysis* **3** (1997), p. 417.
[10] G. Gottstein and L.S. Shvindlerman, *Scripta Met.* **38** (1998), p. 1541.

Materials Science Forum Vols. 294-296 (1999) pp. 95-98

Ab Initio Calculations of SiC/Metal Interfaces

M. Kohyama[1] and J. Hoekstra[1,2]

[1] Department of Material Physics, Osaka National Research Institute, AIST, 1-8-31, Midorigaoka, Ikeda, Osaka 563-8577, Japan

[2] Present Address: Department of Materials, Oxford University, OX1 3PH, UK

Keywords: Ceramic/Metal Interface, Density-Functional Theory, First-Principles Molecular Dynamics Method, Adhesive Energy, Schottky-Barrier Height, SiC, Al, Ti, TiC

Abstract

The SiC(001)/Al and SiC(001)/Ti interfaces have been studied using the *ab initio* pseudopotential method. For each system, the C-terminated and Si-terminated interfaces have quite different features from each other, such as atomic configurations, bonding nature, bond adhesion and electronic properties. For the C-terminated interface of the SiC/Al system, the C-Al bond with covalent and ionic characters generates large adhesive energy as well as large interfacial dipole, which greatly affects the Schottky-barrier height. For the C-terminated interface of the SiC/Ti system, the interfacial C and Ti layers have features rather similar to TiC compounds because of the strong covalent interactions between C $2p$ and Ti $3d$ orbitals.

1. Introduction

It is of great importance to study ceramic/metal interfaces for structural and electronic applications. It is essential to understand the bonding nature and the origin of adhesion of direct interfaces [1,2]. In this paper, we report our recent *ab initio* calculations of SiC/Al [3] and SiC/Ti interfaces. It is possible to apply *ab initio* calculations based on the density-functional theory to such complex systems using the first-principles molecular dynamics (FPMD) method [4–6]. The SiC/Al and SiC/Ti interfaces are of great importance for the practical applications. These interfaces are also typical examples of *reactive* interfaces between covalent solids and metals in contrast to *non-reactive* ones between ionic solids and metals. For *non-reactive* interfaces such as MgO/Ag or MgO/Al interfaces, recent *ab initio* calculations [7] have indicated that the origin of adhesion is mainly explained by the electrostatic effects [8]. For *reactive* interfaces, there should exist rather strong interactions such as charge transfer and orbital hybridization. In this paper, we examine both the C-terminated and Si-terminated interfaces of the SiC(001)/metal systems so as to clarify the C–metal and Si–metal interactions.

2. Theoretical Method

Total energy and stable configurations of large systems can be obtained in the framework of the *ab initio* pseudopotential method by using the FPMD method, where the electronic ground state is efficiently obtained by novel iterative techniques. Various iterative schemes for obtaining the electronic ground state have been developed since the original Car–Parrinello algorithm [4–6]. We have determined the most efficient scheme for the relevant systems [9]. The conjugate-gradient method by Bylander, Kleinman and Lee [6] is the most efficient, although the other methods [4,5] frequently fail to obtain the ground state because of the charge sloshing.

Each supercell contains a slab of 9 SiC(001) atomic layers, where both surfaces are terminated by the same species. Two sets of five 5 Al or Ti(001) layers are stacked on these surfaces. Fcc Ti is dealt with similarly to Al, although hcp Ti is the most stable. Two free metal surfaces are separated by a vacuum region of about 15 a.u. in the supercell, which ensures stable interlayer distances without any constraint. Coherent interfaces with ideal (1×1) periodicity are dealt with, where metal layers are expanded along the interface by about 8% for Al and about 6% for Ti. About the rigid-body translation parallel to the interface, we examine four special translations corresponding to the energy extrema.

We use the TM-type optimized pseudopotentials [10] to reduce the number of the plane-wave basis functions. Ten special **k** points per irreducible part are used. A plane-wave cuttoff energy of 45 Ry is used for the SiC/Al system, and that of 50 Ry is used for the SiC/Ti system.

3. SiC/Al Interfaces

Figure 1 shows the most stable configurations. In the C-terminated interface, the interfacial C atoms are three-fold coordinated. The C–Al bond length is similar to the back C–Si bond length (3.51 a.u.). The charge density is pulled from the Al atom toward the C atom. This charge transfer is clear in Fig. 2(a), where a charge depletion region exists near the interfacial Al atom. In the Si-terminated interface, the interfacial Si atoms are four-fold coordinated. The Si–Al bond length is much larger than the C–Al bond length (4.72 a.u.). The charge density is rather broadly distributed. In Fig. 2(b), only a shallow depletion region is present.

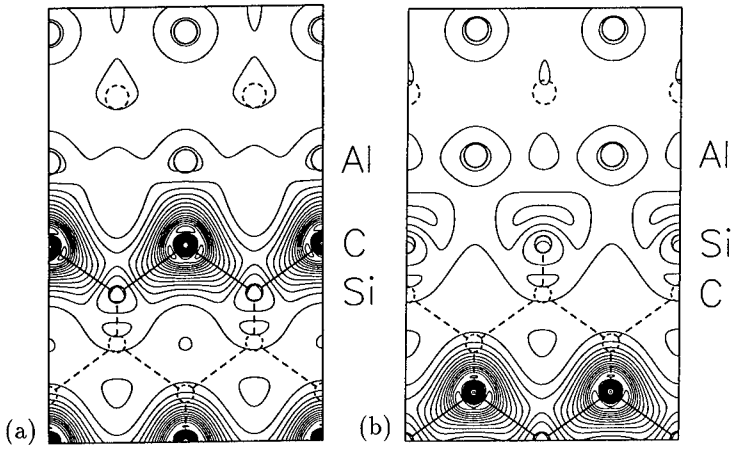

Figure 1. Stable configurations of the SiC(001)/Al interface. (a) $(1\bar{1}0)$ cross section of the C-terminated interface, and (b) (110) cross section of the Si-terminated interface. Contours of the valence electron density are plotted from 0.01 a.u.$^{-3}$ to 0.29 a.u.$^{-3}$ in spacing of 0.02 a.u.$^{-3}$.

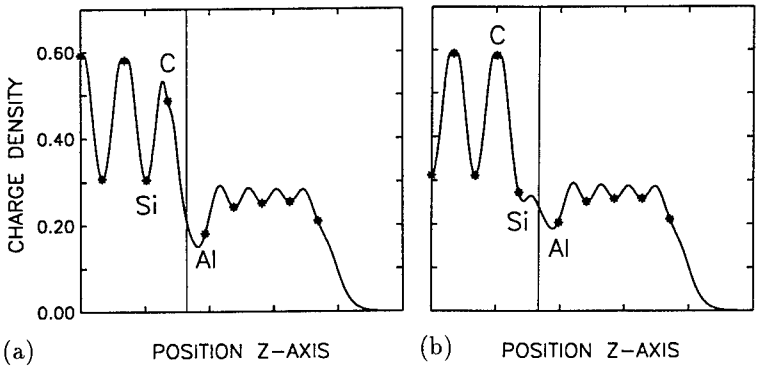

Figure 2. Charge density averaged on each (001) plane in the supercell plotted along the ⟨001⟩ axis. Asterisks indicate atomic positions. (a) The C-terminated interface and (b) the Si-terminated interface.

We have examined the local densities of states (LDOS). For the C-terminated interface, the LDOS curves at the interface and at the back Si–C bonds are substantially different from the bulk regions. This indicates that the back Si–C bonds and the interface have peculiar electronic structure caused by the three-fold coordination. For the Si-terminated interface, the LDOS at the interface region has an appearance similar to that of the metallic Al region. This suggests a more metallic nature of the Si–Al bond, as well as the broad charge distribution.

The adhesive energy is 6.42 J/m^2 for the C-terminated interface, and 3.74 J/m^2 for the Si-terminated one. The C–Al bond with covalent and ionic characters is twice as strong as the Si–Al bond with more metallic characters. However, both values are much larger than the values for *non-reactive* ceramic/metal interfaces, for example, 1.10 J/m^2 for the MgO(001)/Al interface [7]. This confirms the hypothesis that *reactive* interfaces should have much larger adhesive energies than *non-reactive* ones. The present values are also larger than the adhesive energy of two Al(001) surfaces, 2.04 J/m^2 [7].

The Schottky-barrier height (SBH) can be calculated as the difference between the Fermi level of the supercell and the valence-band top in the bulk SiC region in the supercell, which corresponds to the SBH for p-type samples. For the C-terminated interface, the SBH is 0.08 eV, and for the Si-terminated one, 0.85 eV. The latter is in good agreement with the experimental value, 0.9 eV, for the Si-terminated interface [11]. The dramatically smaller SBH of the C-terminated interface can be explained by the interfacial dipole caused by the interfacial charge transfer from the Al layer to the C layer as shown in Fig. 2(a). The present dependence of the SBH on the interfacial structure is contrary to previous models for the SBH [12] which deny such dependence. However, this is consistent with recent experiments and *ab initio* calculations of other semiconductor/metal interfaces [12].

4. SiC/Ti Interfaces

Figures 3 and 4 show the results. In both configurations, the interfacial C or Si atoms are four-fold coordinated. The adhesive energy is 8.74 J/m^2 for the C-terminated interface, and 2.52 J/m^2 for the Si-terminated one. For the C-terminated interface, the configuration of which the interfacial C atoms are three-fold coordinated seems to have similar energy. Calculations of that configuration as well as those of the LDOS and SBH for all the interfaces are now in progress, and will be presented in future.

The Si-terminated interface has features rather similar to that of the SiC/Al interface. The Si–Ti bond length is similar to the Si–Al bond length (4.79 a.u.), and the interfacial charge density is rather broadely distributed as that in the SiC/Al interface.

The C-terminated interface has peculiar features quite different from that of the SiC/Al interface. The C–Ti interlayer distance is very small (2.15 a.u.). The interfacial charge in Fig. 3(a) clearly reveals the p–d σ covalent bonds between C $2p$ and Ti $3d$ orbitals, which is similar to the bulk TiC [13]. The local configuration on the (110) plane at the interface is common to the bulk TiC, although the C–Ti bond length (3.83 a.u.) is less than that in the bulk TiC (4.09 a.u.). On the other hand, the distance between the interfacial Ti layer and the 2nd Ti layer is larger by about 21% than the averaged interlayer distance in the bulk Ti region, which greatly reduces the charge density as shown in Fig. 4(a). The d electrons of the interfacial Ti atoms facing the 2nd Ti layer also have features different from those of the bulk Ti atoms. These features are in contrast to all the other interfaces, where the charge density and interlayer distance between the 1st and 2nd metal layers already recover the bulk metallic features.

All these points of the present C-terminated interface as well as the very large adhesive energy mean that the interfacial C–Ti layers should be regarded as some kind of TiC compound layers quite different from the bulk SiC and bulk Ti. The plane between the 1st and

2nd Ti layers should be the interface between the compound and Ti. It can be said that the solid reaction has occurred only at the interface layers, which should proceed if the diffusion is permitted. The present results are consistent with the observed strong reactivity of Ti for the surface C layers of SiC, forming TiC and free Si [14].

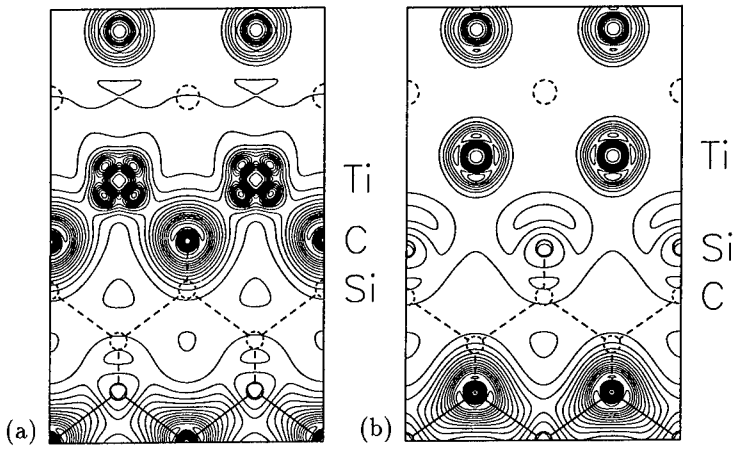

Figure 3. Relaxed configurations of the SiC(001)/Ti interface. (a) (110) cross section of the C-terminated interface, and (b) (110) cross section of the Si-terminated interface. Contours of the valence electron density are plotted from 0.01 a.u.$^{-3}$ to 0.27 a.u.$^{-3}$ in spacing of 0.02 a.u.$^{-3}$.

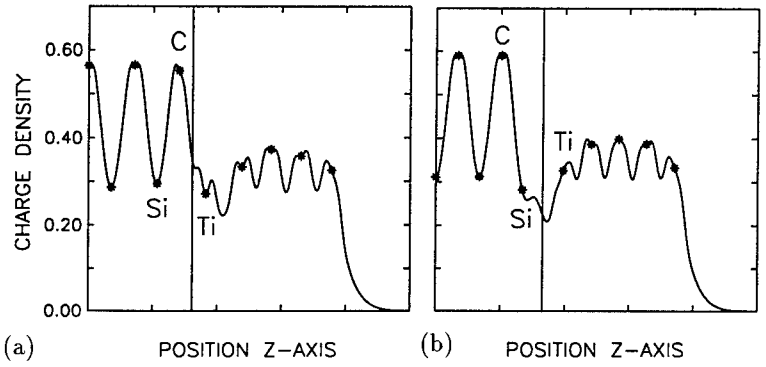

Figure 4. Charge density averaged on each (001) plane in the supercell plotted along the ⟨001⟩ axis. Asterisks indicate atomic positions. (a) The C-terminated interface and (b) the Si-terminated interface.

References

[1] F.S. Ohuchi and M. Kohyama, J. Am. Ceram. Soc. **74**, 1163 (1991).
[2] M.W. Finnis, J. Phys. Condens. Matter **8**, 5811 (1996).
[3] J. Hoekstra and M. Kohyama, Phys. Rev. B. **57**, 2334 (1998).
[4] R. Car and M. Parrinello, Phys. Rev. Lett. **55**, 2471 (1985).
[5] M.C. Payne *et al.*, Rev. Mod. Phys. **64**, 1045 (1992).
[6] D.M. Bylander, L. Kleinman, and S. Lee, Phys. Rev. B **42**, 1394 (1990).
[7] J.R. Smith, T. Hong and D.J. Srolovitz, Phys. Rev. Lett. **72**, 4021 (1994).
[8] P.W. Tasker and A.M. Stoneham, J. Chimie Phys. **84**, 149 (1987).
[9] M. Kohyama, Modelling Simul. Mater. Sci. Eng. **4**, 397 (1996).
[10] N. Troullier and J.L. Martins, Phys. Rev. B **43**, 1993 (1991).
[11] V.M. Bermudez, J. Appl. Phys. **63**, 4951 (1988).
[12] A.P. Sutton and R.W. Balluffi, *Interfaces in Crystalline Materials* (Oxford, 1995).
[13] P. Blaha *et al.*, Phys. Rev. B **31**, 2316 (1985).
[14] J.J. Bellina, Jr. and M.V. Zeller, MRS Symp. Proc. **97**, 265 (1987).

Materials Science Forum Vols. 294-296 (1999) pp. 99-102

Atomic-Scale Studies of the Electronic Structure of Ceramic/Metal Interfaces: {222}MgO/Cu

D.A. Muller[1,2], D.A. Shashkov[3], R. Benedek[3], L.H. Yang[4], J. Silcox[1] and D.N. Seidman[3]

[1] School of Applied and Engineering Physics, Cornell University, Ithaca, NY 14853, USA

[2] Bell Laboratories, Lucent Technologies, Murray Hill, NJ 07974, USA

[3] Department of Materials Science and Engineering, Northwestern University, Evanston, IL 60208, USA

[4] Condensed Matter Physics Division, Lawrence Livermore National Laboratory, Livermore, CA 95551, USA

Keywords: Ceramic/Metal Heterophase Interfaces, Electron Energy Loss Spectroscopy, Local Density Functional Theory, {111}MgO/Cu Heterophase Interfaces, Electronic Structure of Interfaces

ABSTRACT

{222} MgO/Cu interfaces produced by internal oxidation are studied by electron energy loss spectroscopy (EELS) using an atomic sized electron beam. We determine interfacial chemistry of this interface with subnanometer spatial resolution and use EELS to measure directly the electronic states pertaining to the buried interface. The O-*K* edge gives evidence of metal-induced gap states (MIGS) within the bandgap of MgO, at the interface, which we find to be O terminated. Both experiment and *ab initio* calculations show the MIGS to be strongly localized at the interface.

INTRODUCTION

We are investigating ceramic/metal (C/M) heterophase interfaces with transmission electron, high-resolution electron, Z-contrast, and atom-probe field-ion (APFIM) microscopies, and EELS in conjunction with *ab initio* atomistic modeling and molecular dynamics (MD) simulations. APFIM identifies the terminating polar plane and segregation to the C/M interface, while EELS is used to study the electronic structure of the C/M interface. Detailed experimental results exist for the {222}MgO/Cu [1], {222}CdO/Ag [2], {222}MgO/Cu(Ag) [3], and {222}CdO/Ag(Au) heterophase interfaces. All the C/M interfaces are created employing internal oxidation of high-purity binary or ternary metallic alloys, thereby producing atomically clean heterophase interfaces. Solute-atom segregation is induced at the {222} C/M interfaces by annealing specimens containing a ternary addition at 500°C and the Gibbsian interfacial excess of solute directly determined by APFIM, without data deconvolution. *Ab initio* atomistic calculations for the {222}MgO/Cu interface (zero misfit approximation), based on local density functional theory (LDFT) within the plane-wave pseudopotential representation, have been performed for two polar (111) and two nonpolar (100) MgO/Cu interfaces [4]. MD simulations of the dislocation structure of the {222}MgO/Cu interface are compared with scanning transmission electron microscope (STEM) observations [5]. EELS is used to measure directly the electronic states of the interface. The O-*K* edge exhibits a prepeak that we identify with MIGS within the bandgap of MgO at the interface [6]. In this paper we compare the EELS results with recent LDFT calculations of the {222}MgO/Cu interface electronic structure, which show localized interface states (MIGS) that lie within the insulating gap of MgO. The MIGS, particularly in the occupied region, are significant for interface bonding.

EXPERIMENTAL APPROACH

Atomically clean {222}MgO/Cu interfaces for this study were produced by internally oxidizing a Cu 2.5 at.% Mg alloy for 2 h at 1223 K in a classical Rhines pack, which yields MgO precipitates, 10 to 30 nm in diameter. For the EELS studies, a VG-HB501 100 kV STEM equipped with a cold-field-emission gun and a McMullan-style parallel EELS spectrometer was used. The spectrometer resolution was set at 1 eV to increase the signal/background ratio. This microscope has been modified to achieve high energy-drift stability (<0.2 eV min^{-1}) and spatial drift stability (<0.05 nm min^{-1}). The minimum attainable probe size is ≈0.22 nm. The EELS spectra were recorded simultaneously with the annular dark field (ADF) signal, under conditions optimized for atomic resolution imaging: the objective and collector apertures are 10 and 16 mrad, respectively.

The O-*K*, Mg-*K*, and Cu-$L_{2,3}$ EELS edges provide information on the unoccupied O-p, Mg-p, and Cu-d electronic densities of states (DOS), respectively [7]. The effect of the 2p core hole on the Cu L edge is minimal. Furthermore, recent LDFT calculations (S. Koestlmeier and C. Elsaesser, private communication) of the local densities of states at the oxygen sites in several oxides agree closely with EELS O-K edge measurements, even without correction for core-hole effects. This allows a single particle interpretation of the EELS spectra, which are proportional to the local DOS partitioned by site (as the incident probe is localized), chemical species (as each element has unique core level binding energies), and angular momentum (from the dipole selection rules) [8, 9]. In the STEM, the EELS measurements are made at internal interfaces, not free surfaces, which is achieved by passing the 100 keV electron beam (0.2 - 0.5 nm diameter) through a thin film. The interface is oriented parallel to the beam, so that a column of atoms in the interface plane can be measured separately from any atoms in adjacent columns.

To determine the chemistry of the {222} MgO/Cu interface, EELS spectra were recorded at and in the vicinity of an interface by scanning the beam over narrow strips of dimensions 0.3 nm x 7 nm that run parallel to the interface. This technique minimizes the electron dose on the specimen, while maintaining the highest spatial resolution normal to the interface. All spectra were acquired for 4 s or less, a dose 120 times less than the threshold for observable changes, thus avoiding any question of radiation damage at the interface. The specimen was tilted to a <110> orientation to place the {222} MgO/Cu interface parallel to the electron beam.

RESULTS AND DISCUSSION

The effect of the interface on the oxygen bonding is striking: we find a finite density of states throughout the unoccupied portion of the MgO bandgap at the interface. Figure 1 shows the O-*K* edge recorded across a {222} MgO/Cu interface. The large signal-to-noise ratios enabled deconvolution of the intrinsic spectra from the spectrometer point-spread function. This does not greatly alter any of the features, but makes the background subtraction much simpler. The edges collected at the interface appear much broader, with a well pronounced prepeak on the bulk edge onset. The prepeak extends approximately 6 eV on the low-energy side (consistent with the unoccupied portion of the MgO band gap). The prepeak intensity decays rapidly with distance from the interface: 0.4 nm from the interface, it is almost gone. Fitting the prepeak intensity to an exponential yields a decay length of less than 0.3 nm. This should be viewed as an upper limit, as the probe FWHM is 0.22 nm and probe tails decay inelastically with a 0.25 nm decay length. Deconvolving the inelastic point spread function give a decay length of (averaged over the prepeak energies) of $\lambda_{avg} = 0.13 \pm 0.05$ nm. The physical origin of this prepeak and its decay are discussed below in terms of MIGS. Finally, the Mg-*K* edge was recorded in different locations across the

interface. Within experimental error, the edge always retained the shape characteristic of bulk MgO. This is consistent with an O-terminated interface.

EELS has identified three key features at the {222} MgO/Cu interface: (1) that the interface is O terminated; (2) that the number of d holes/Cu site is not significantly different from the bulk Cu, implying that the interfacial Cu atoms remain almost neutral; and (3) that there is a prepeak on the O-*K* edge, which is sufficiently broad in energy to remove the gap between the filled and empty oxygen states near the interface.

All three features are found in self-consistent, first principles, electronic structure calculations. We have examined the layer-projected DOS of a coherent, oxygen-terminated {222} MgO/Cu interface calculated with the planewave pseudopotential method. In spite of the large misfit (≈15 %) at the {222} MgO/Cu interface, coherent patches cover more than 50% of the interface and therefore calculations based on the coherent interface approximation are expected to yield useful insight into the true interface. The local DOS is integrated over slabs centered on each of the layers. While LDFT underestimates the width of the gap by 2 -3 eV, the calculation of the offset of the MgO valence band with respect to the Cu involves only occupied states and is described accurately. Figure 2 exhibits the calculated layer-projected electronic DOS near {222}MgO/Cu interface and {222}MgO free surface. The second panel from the bottom curve corresponds to MgO two layers below the interface, which is already similar to the bulk. Panels 3-6 (from the bottom) show a peak a few tenths of an eV below the Fermi energy, associated with a localized interface state. This state corresponds to a Cu(3*d*)-O(2*p*) antibonding hybrid, and appears either for the bulk interface or a monolayer of Cu. Note that this feature does not appear either in bulk Cu (top panel) or the oxygen termination layer of an unreconstructed {222} MgO free surface, and can therefore identified as a *metal-induced gap state*. On the Cu side of the interface, this feature shifts some *d*-electron states to energies higher than the *d*-band edge in bulk Cu, but still within the occupied region, so that no *d*-electron holes are introduced. These states would therefore not produce a Cu-*L* white line and the EELS spectra for Cu [6] at the interface in fact is little different from that in the bulk. The unoccupied states just above the Fermi energy, which include the tail of the MIGS, are the ones probed experimentally using EELS in Fig. 1. A comparison of this measurement (for the O-*K* edge) with theory is shown in Fig. 3. Plotted are the O-*K* edge measured by EELS (Fig. 1) at the terminating oxygen layer of a {222} MgO/Cu interface and the calculated electronic DOS at the interface oxygen layer. The theory curve represents a magnification of the results shown in fourth panel of Fig. 2 in the region above the Fermi energy. The agreement between theory and experiment is strong evidence for MIGS, which have not previously been directly observed either for any ceramic/metal or semiconductor/metal interfaces.

In summary, we find the {222} MgO/Cu interface to be oxygen terminated. Localized metal induced gap states at the interface are predicted by theory. The gap states in the unoccupied region are manifested in a prepeak to the EELS O-*K* edge. The possible relation between gap states and interface bonding was mentioned a few years ago by Noguera and Bordier[10]. Their precise role in regard to the adhesion of specific interface remains to be elucidated.

This research was supported by the U. S. Department of Energy (Grants No. DE-96ER45597 (Northwestern), No. DE-FG02-87ER45322 (Cornell), and Contract No. W-7405-ENG-48 at LLNL). The Cornell Materials Science Center STEM was operated and acquired with NSF grants No. DMR-8314255 and No. DMR-9121654 and upgraded through AFOSR F49620-95-1-0427. Most of the simulations were performed at the National Energy Research Supercomputer Center. Helpful discussions with P. Rez (Cu-O states by EEELS), J. J. Rehr, and D. R. Hamann are acknowledged.

REFERENCES

[1] H. Jang, D. N. Seidman, and K. L. Merkle, Interface Science **1**, 61 (1993).

[2] D. K. Chan, D. N. Seidman, and K. L. Merkle, Phys. Rev. Lett. **75**, 1118 (1995).

[3] D. A. Shashkov and D. N. Seidman, Phys. Rev. Lett. **75**, 268 (1995).

[4] R. Benedek, M. Minkoff, and L. H. Yang, Phys. Rev. B **54**, 7697 (1996).

[5] R. Benedek, D. N. Seidman, and L. H. Yang, Microsc. Microanal. **3**, 333 (1997); D. A. Shashkov, Ph.D. thesis, Northwestern University (1997).

[6] D. A. Muller, D. A. Shashkov, R. Benedek, L. H. Yang, J. Silcox, and D. N. Seidman, Phys. Rev. Lett. **80**, 4741 (1998).

[7] R. F. Egerton, *Electron Energy Loss Spectroscopy in the Electron Microscope*, 2nd ed. (Plenum Press, New York, 1996).

[8] C. Colliex and B. Jouffrey, Philos. Mag. **25**, 491 (1972).

[9] J. E. Müller and J. Wilkins, Phys. Rev. B **29**, 4331 (1984).

[10] C. Noguera and G. Bordier, J. Phys. III France **4**, 1851 (1994).

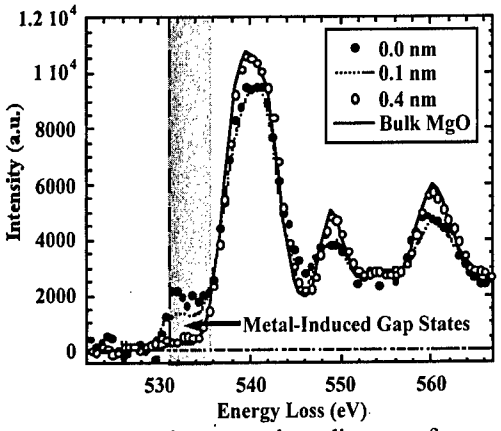

Figure 1. O-*K* edges at various distances from a {222} MgO/Cu heterointerface.

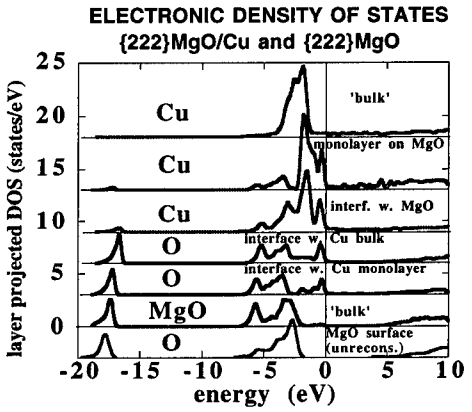

Figure 2. Calculated layer-projected DOS near {222}MgO/Cu heterointerface and near a free surface.

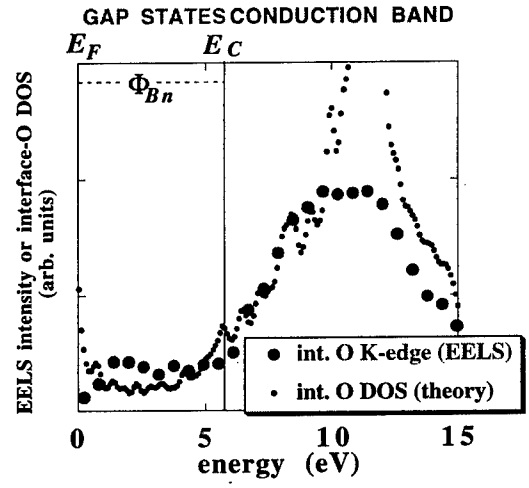

Figure 3. Plotted are the O-*K* edge measured by EELS at the terminating oxygen layer of a {222}MgO/Cu heterointerface and the calculated electronic DOS at the interface oxygen layer. The theory curve represents a magnification of the results shown in the fourth panel of Fig. 2 in the region above the Fermi energy. The agreement between theory and experiment is strong evidence for metal-induced gap states (MIGS).

Materials Science Forum Vols. 294-296 (1999) pp. 103-106

Special [100] Tilt Grain Boundaries in Iron: A Segregation Study

P. Lejček[1], V. Paidar[1] and S. Hofmann[2,3]

[1] Institute of Physics, Academy of Sciences of the Czech Republic, Na Slovance 2, CZ-180 40 Praha 8, Czech Republic

[2] Max-Planck-Institut für Metallforschung, Seestraβe 92, D-70174 Stuttgart, Germany

[3] Present address: National Research Institute for Metals, Sengen 1-2-1, Tsukuba 305, Japan

Keywords: Bicrystals, Grain Boundaries, Solute Segregation, Structure/Property Relationship

Abstract. A systematic study of solute segregation in numerous bicrystals of an Fe–3.5at.%Si alloy enabled us to find all special [100] tilt grain boundaries. Various plots of segregation enthalpy vs. grain boundary orientation were compared to the grain boundary plane classification. From the correlation obtained we conclude that the {012}, {013} and {015} symmetrical, and (001)/(013) and all (011)/(0*kl*) asymmetrical grain boundaries are special. All other (001)/(0*kl*) asymmetrical boundaries exhibit low tendencies to solute segregation and can be considered as vicinal interfaces.

Introduction

The atomic structure of grain boundaries forming a structural unit is primarily controlled by five degrees of freedom given by the grain misorientation and boundary plane inclination. Structural units of individual grain boundaries either are simple and have low energy (*singular* or *special* interfaces), or are complex and have high energy (*general* boundaries). The transition between these two groups is represented by *vicinal* interfaces [1]. It is known that, e.g., the {111} symmetrical tilt grain boundary in f.c.c. metals, and the {112} one in b.c.c. structures are special, however, the family of all special interfaces has not been completely determined yet. This holds particularly for asymmetrical grain boundaries where two different crystallographic planes are joined together.

A correlation of the properties of symmetrical tilt grain boundaries with the hierarchy of formation of their structures resulted in a geometrical classification of grain boundary planes [2]. The boundaries on the low classification levels (special) are composed of simple structural units while the structure of the boundaries on higher classification levels (general) is increasingly more complex. Nevertheless, this classification cannot predict a border level between special and general interfaces. Recently, the classification was extended to asymmetrical tilt grain boundaries with a general conclusion that special asymmetrical tilt grain boundaries can be composed exclusively of combinations of the planes creating special symmetrical tilt interfaces [3,4].

Our measurements of solute segregation of Si, P and C at [100] symmetrical tilt grain boundaries of an Fe–Si alloy corresponding to different classification levels showed unambiguously that only the {013}, {012} and {015} grain boundaries are special, i.e., only those created by the planes of the 1st and 2nd classification levels [5,6]. Further studies, focused on the segregation behaviour of the [100] asymmetrical tilt grain boundaries revealed that also the (001)/(034) and (011)/(017) exhibit lower tendency to solute segregation as compared to other Σ=5, 36.9°[100] asymmetrical interfaces [7]. A similar behaviour was found for the (001)/(011) incommensurate non-coincidence interface [8]. On the other hand, segregation behaviour of the Σ=5, 36.9°[100], (018)/(047) boundary is typically general but not vicinal as would be expected if the very close (015)/(012) boundary is special [9]. These results lead to the conclusion that *special asymmetrical tilt grain boundaries should be created by combinations of those planes which themselves create special symmetrical tilt grain*

boundaries supposing one of them is (001) or (011). In the present contribution we will identify all special [100] tilt grain boundaries in α-iron on the basis of a comparison of grain boundary segregation with grain boundary plane classification.

Experimental

Cylindrical bicrystals of an Fe–Si alloy (3.55at.%Si, 0.0089at.%P and 0.014at.%C) were grown by the floating zone technique using a [100] bicrystalline seed with desired asymmetrical tilt grain boundary parallel to the rod axis. Details concerning the growth procedure are given in [10]. The orientations of grain boundaries in the prepared bicrystals were (001)/(015), (001)/(013), (001)/(012), (011)/(012), (011)/(013) and (011)/(015). Their positions in the orientation map are displayed in Fig. 1 as *e, f, g, k, j* and *i*, respectively.

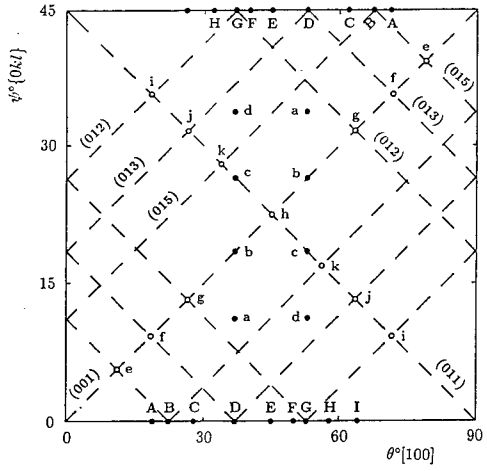

Fig. 1. Orientation map of [100] tilt grain boundaries. θ is the misorientation angle, ψ is the inclination angle of the boundary plane from the symmetrical boundary. The dashed lines parallel to diagonals depict the boundaries created by given (0*kl*) crystallographic plane. Empty symbols represent the grain boundaries measured in this work (*e,f,g,i,j,k*). The segregation behaviour of the asymmetrical boundaries *a–d* and *h*, as well as of the symmetrical boundaries *A–I* was studied previously (c.f., [5,7–9]).

Individual samples for Auger electron spectroscopy (AES) were annealed at different temperatures (1173 K/24 h, 1073 K/24 h, 973 K/48 h, 873 K/96 h and 773 K/168 h) and quenched in water to preserve equilibrium segregation at the particular temperature. Annealed samples were fractured in-situ in an ultra–high–vacuum chamber ($<10^{-7}$ Pa) of a SAM PHI 600 Scanning Auger Microprobe (Perkin–Elmer). The chemical composition of the fracture surfaces was immediately studied by AES (primary beam voltage of 10 kV, current of 350 nA and diameter of 1 μm). To check the attainment of equilibrium segregation in the monolayer regime, depth profiles were measured during Ar^+ ion sputtering (voltage of 3 kV, sputtered area of about 3×3 mm^2, analyzed area of about 7×7 μm^2, sputter rate of about 1 nm/min).

Results and Discussion

The AES study of fracture surfaces disclosed the presence of iron as the matrix element, and silicon, phosphorus and carbon as the segregants. The presence of oxygen, detected at the fracture surfaces is due to contamination from the residual gas atmosphere and was not considered for the evaluation [11]. The Auger peak–to–peak heights in the derivative AES spectra of the fracture surfaces were transformed into chemical composition of monatomic layers at grain boundaries using the standard method [11] applied previously for this evaluation in our work. From the temperature dependence of the chemical composition of each selected interface, the enthalpy and entropy of grain boundary segregation were determined according to the Guttmann quasichemical model of segregation in multicomponent systems [12]. Details concerning this evaluation are described elsewhere [11]. Values of the segregation enthalpies for the studied grain boundaries are given in Table 1. The

orientation dependence of segregation enthalpy is shown in Fig. 2, where the data measured previously for other (001)/(0*kl*) and (011)/(0*kl*) boundaries [7,8] are also shown for comparison.

Table 1. Enthalpy, ΔH^0_I (in kJ/mol), of solute segregation at measured grain boundaries.

	(001)/(015)	(001)/(013)	(001)/(012)	(011)/(015)	(011)/(013)	(011)/(012)
ΔH^0_{Si}	– 8	– 7	–10	– 7	– 6	– 6
ΔH^0_P	–22	–19	–26	–18	–17	–17
ΔH^0_C	–41	–38	–47	–40	–36	–34

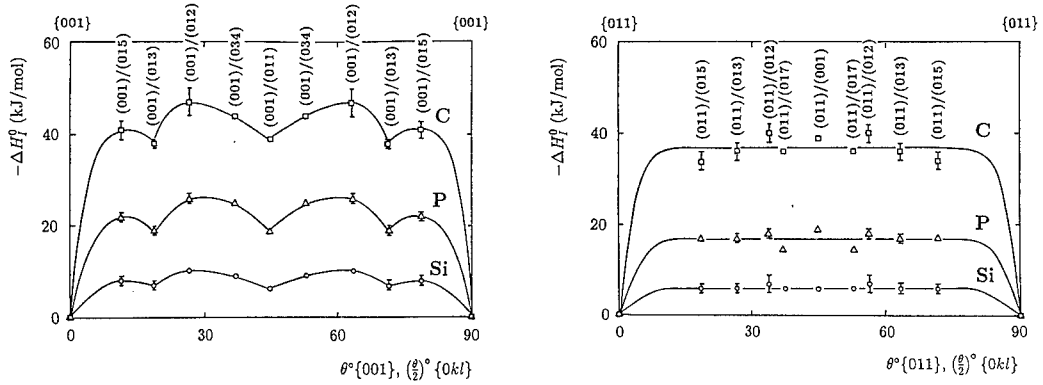

(a) (b)

Fig. 2. Dependences of segregation enthalpies ΔH^0_I (I = Si, P, C) for individual (a) (001)/(0*kl*) and (b) (011)/(0*kl*) asymmetrical tilt grain boundaries in α-iron.

It is seen in Fig. 2(a) that two non-equivalent minima of $|\Delta H^0_I|$ appear on the orientation dependence for (001)/(0*kl*) asymmetrical tilt grain boundaries, corresponding to (001)/(013) and (001)/(011). The values of ΔH^0_I for these grain boundaries are comparable to those of special {012}, {013} and {015} symmetrical tilt grain boundaries [6]. Both these findings lead to the conclusion that the (001)/(013) and (001)/(011) asymmetrical tilt grain boundaries are special. The absolute values of ΔH^0_I of other (001)/(0*kl*) grain boundaries are lower than those of typical general boundaries [6] and thus, they represent local minima on various orientation dependences (e.g., (001)/(034) on the dependence of ΔH^0_I on the inclination angle ψ from the {013}symmetrical tilt grain boundary [6]). These boundaries can be considered as vicinal.

In the case of the (011)/(0*kl*) grain boundaries (Fig. 2b), no apparent difference is observable among corresponding values of ΔH^0_I for all interfaces studied. All the values of ΔH^0_I are comparable to those of other special grain boundaries [6]. Therefore, we can conclude that all (011)/(0*kl*) asymmetrical tilt grain boundaries are special from the segregation point of view.

The fact that the (001)/(011) asymmetrical tilt grain boundary (*h* in Fig. 1) was found to be special conveys well with the classification scheme [8] since it represents the combination of two basic crystal planes (001) and (011) on the 0^{th} classification level. Similarly, the (001)/(013) grain boundary represents the combination of the basic (001) plane with the (013) plane belonging to the 1^{st} classification level and forming the special {013} symmetrical tilt grain boundary. Combinations of (001) plane with planes of higher classification levels do not result in special asymmetrical tilt grain boundaries (cf. the behaviour of the (001)/(012) and (001)/(015) interfaces). The behaviour of

the (011)/(0*kl*) grain boundaries is more complex and cannot be explained on the basis of the above classification. Probably, the presence of the most dense (011) plane in the bcc structure controls the behaviour of corresponding asymmetrical interfaces disregarding the other adjoining boundary plane.

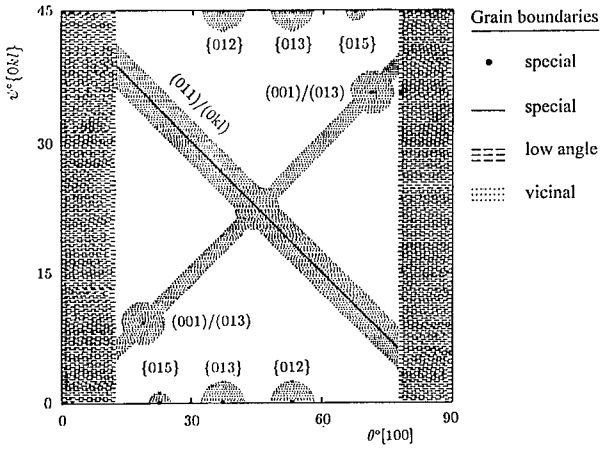

Fig. 3. Map of the character of [100] tilt grain boundaries in α-iron, as indicated by the different symbols. All boundaries in the white area are general interfaces.

Conclusions

Based on the above discussion and previous findings [5,6,11], we can construct a map of the character of [100] tilt grain boundaries in α-iron (Fig. 3). We can identify (a) the {015}, {013} and {012} symmetrical tilt grain boundaries, and (b) (001)/(013) and all (011)/(0*kl*) asymmetrical tilt grain boundaries as special. The boundaries in the vicinity of the special interfaces as well as the other (001)/(0*kl*) boundaries exhibit vicinal behaviour. All other boundaries except low angle grain boundaries ($\theta°[100] < 15°$ and $\theta°[100] > 75°$) are general.

Acknowledgment

This work was supported by the Commission of European Communities (CIPA CT93 0112), by the Grant Agency of the Academy of Sciences of the Czech Republic (A1010708) and by the International Collaboration COST Action 517 (OC 517.40).

References

[1] A. Sutton and R.W. Balluffi, Interfaces in Crystalline Materials, Clarendon, Oxford 1995.
[2] V. Paidar, Acta Metall. 35 (1987) 2035.
[3] V. Paidar, Philos. Mag. A66 (1992) 41.
[4] V. Paidar and J. Erhart, Interface Sci. 1 (1993) 115.
[5] S. Hofmann, P. Lejček and J. Adámek, Surf. Interface Anal. 19 (1992) 601.
[6] P. Lejček and S. Hofmann, Crit. Rev. Sol. State Mater. Sci. 20 (1995) 1.
[7] P. Lejček, J. Adámek and S. Hofmann, Surface Sci. 246 (1992) 449.
[8] P. Lejček, V. Paidar, J. Adámek and S. Hofmann, Acta Mater. 45 (1997) 3915.
[9] P. Lejček and S. Hofmann, Mater. Sci. Forum 207–209 (1996) 745.
[10] S. Kadečková, P. Toula and J. Adámek, J. Crystal Growth 83 (1987) 410.
[11] P. Lejček, Anal. Chim. Acta 297 (1994) 165.
[12] M. Guttmann and D. McLean, in: Interfacial Segregation, J. Blakely and W.C. Johnson, Eds, ASM, Metals Park OH, 1979, p. 261.

Materials Science Forum Vols. 294-296 (1999) pp. 107-110

High Resolution Electron Microscopy of Misfit Dislocations at Metal-Oxide Interfaces

H.B. Groen, B.J. Kooi, W.P. Vellinga and J.T.M. De Hosson

Department of Applied Physics, Materials Science Center, University of Groningen, Nijenborgh 4, NL-9747 AG Groningen, The Netherlands

Keywords: Metal-Oxide, HRTEM, Dislocations, Simulations, Bonding

Abstract

Misfit dislocations at metal-oxide interfaces are studied using HRTEM. By observing misfit dislocations the bonding across the metal-oxide interface can be studied. This is done for two cases, a parallel Cu-MgO {111} interface and tilted interfaces in Pd-ZnO and Ag-ZnO. From the Cu-MgO micrographs the strain fields introduced by the misfit dislocation network could be observed. From the tilted ZnO interfaces it can be seen how different materials (Ag, Pd) adapt to this situation.

Introduction

The macroscopic properties of metal-ceramic materials depend on the microstructure and chemistry of the interfaces which in turn are affected by the processing conditions. An important aspect is the bonding behavior between these dissimilar materials and the basic idea put forward in this paper is that atomic structure determination of the core structure of misfit dislocations at metal-oxide interfaces, coordinated with atomistic calculations may lead to a better physical understanding of the bonding at the interface.

At present basic understanding of the interplay between structure and properties of intraphase interfaces like grain boundaries in metals and oxides is still unsatisfactory but somewhat more advanced as far as general features are concerned. However, the situation is much less advanced for metal-oxide interfaces, where the nature of the bonding across the interface still needs further physical clarification. Studies of misfit dislocations which fully incorporate atomic structure and bonding in both the ceramic substrate and the metal cannot be made at this stage. Therefore a simplified model is explored [1] in which the atomic interactions in the metal are described by Finnis-Sinclair type many-body central force potentials. The ceramic crystal in our approach is regarded as a rigid, undeformable substrate so that no description of interatomic forces in this material is needed. The atomic interactions across the interface are described by adjustable interaction functions which lead to different strengths of bonding.

This picture of the metal-oxide interface, although simple, does allow to investigate the core structure of the misfit dislocations as a function of the strength of bonding across the interface. Furthermore, from the experimental side we may study the effect of bonding behavior by observing crystallographic relaxations near tilted interfaces. Here, metal-oxide interfaces obtained by internal oxidation are studied by HRTEM. Observation of these interfaces at an atomic level might reveal the structure of the misfit dislocations as they could act as a detector of the nature and strength of the metal-oxide interaction. An indicator of the interaction strength is the localization of the misfit dislocations, as for incoherent interfaces no localization takes place. As the misfit dislocation networks are observed in projection it is not always possible to interpret an image directly. In that case, comparison with simulated images from the calculated structures should give clarification. In this paper Cu-MgO, Ag-ZnO and Pd-ZnO interfaces are described. The Cu-MgO system is interesting

because of the strain fields at the interfaces resulting from the misfit dislocation network, whereas the hcp ZnO inside an fcc metal matrix produces slightly tilted interfaces which can provide other indications of interaction across the interface.

Experimental

The metal-oxide interfaces are obtained by internal oxidation and sample preparation was done using the straightforward grinding, dimpling and ion-milling tools. Microscopy was performed using a Jeol 4000 EX/II electron microscope with 0.165 nm point resolution and at one instance the Jeol ARM1250 at the MPI Stuttgart (0.12 nm point resolutionMgO precipitates of about 50 nm inside the Cu matrix have an octahedral shape with the {111} planes parallel to the corresponding planes in Cu.). The MgO precipitates are oxygen terminated at the used oxidation parameters [2]. The ZnO precipitates in Ag and Pd are around 1 μm wide with a thickness of about 100 nm. The majority have a truncated trigonal shape, with large {0001} basal plane facets parallel to {111} planes in Pd and the [1120] direction in ZnO parallel to the [110] direction in Pd.

Results and Discussion

Cu-MgO interfaces

Cu and MgO have a misfit of 16.7%. When the {111} planes of Cu an MgO meet this misfit must be relieved if there is an interaction present, resulting in a (semi-)coherent interface. In the case of an incoherent interface, with no interaction present, it is also possible to define dislocations, but only in a formal sense since they can always be defined due to the misfit. Localization of the misfit dislocations can be observed by local straining of one of the lattices resulting in delocalised atomic columns or a shift of entire columns. This affects the local brightness and contrast of the image. Since the strain fields cannot be directly interpreted a cross-check with a simulated image is necessary.

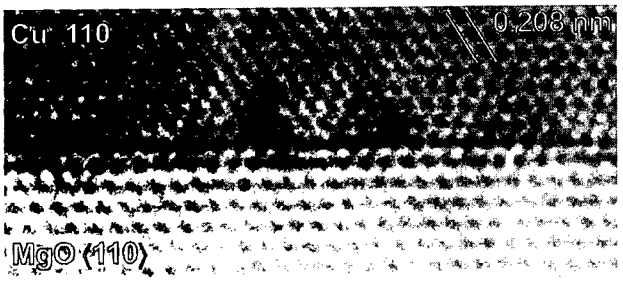

Fig. 1: Cu-MgO interface observed along ⟨110⟩. The strain fields are observable as the periodic dark 'triangular' regions above the interface.

According to the calculations [3] the structure of the Cu at the interface can be interpreted as a trigonal network of 1/6 ⟨112⟩ misfit dislocations [4]. This structure can be used as input for image simulation that predicted periodic trigonal shaped strain fields at the interface. Looking at the interface edge-on along the ⟨110⟩ direction (fig1)[1], the strain fields predicted from the simulated image could be observed with similarity in shape and period. However, for a full check also an observation along the ⟨112⟩, orthogonal to the ⟨110⟩ direction, is necessary. This was done with the Jeol ARM1250 electron microscope at the Max Planck Institut für Metallforschung in Stuttgart with a point resolution of 0.12 nm, enough to resolve Cu lattice along ⟨112⟩. At first sight, no strain fields from misfit dislocations could be observed at the interfaces. The strain fields could be extracted from the micrographs by averaging the intensities between two layers parallel to the interface, as shown in fig 2. The averaging has to be done some distance away from the interface to prevent the introduction of Moiré effects which have the same periodicity as the strain fields. The simulated image also show small effects from the strain fields and the results of the simulation are also shown in fig 2. The intensity and the contrast show the same periodic behavior that was pre-

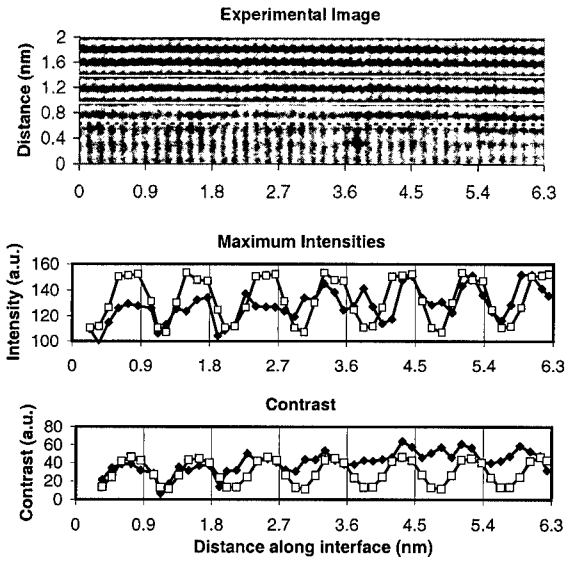

Fig. 2: Brightness and contrast of the bright spots, averaged from on top of the second to on top of the fourth Cu{111} layer (white lines) with respect to the interface (dashed line), as a function of distance along the interface, based on the experimental HRTEM image (filled markers) and the simulated image (open markers).

dicted from the simulations. A full-quantitative analysis is however not (yet) possible since absolute brightness and contrast values are not properly implied in simulation of HRTEM images. This analysis shows that misfit dislocation networks might easily be overlooked, which could lead to the wrong conclusion that an interface is incoherent.

Ag,Pd-ZnO interfaces

At the basal plane interface of Pd-ZnO no strain fields in Pd can be seen. This does not necessarily indicate that the interface is incoherent, as observation of the misfit dislocation network is not trivial. Because of the hexagonal structure of ZnO inside an fcc matrix interfaces with a small tilt are formed. In Ag-ZnO this small tilt is relieved by emission of Shockley partial dislocations which leave behind a stacking-faulted area in the Ag (fig 3). This is schematically depicted in fig. 4. The extension of the stacking-faulted areas are an indication of the interaction over the interface, depending also on the angle and the elastic properties of Ag. In Pd-ZnO the tilted interfaces the tilt is relieved by steps in the ZnO instead of the metal (opposite to Ag-ZnO interfaces) An example of a tilted interface in Pd-ZnO is shown in fig. 5. Here, the first pyramidal plane of ZnO is in contact with a {200} plane in Pd. The two planes are at an angle of 6.84 degrees. This angle is compensated by steps in the oxide, this in contrast to the Ag-ZnO case where the angle is compensated by steps in the metal (fig. 3). Furthermore, no relaxations can be observed in the Pd.

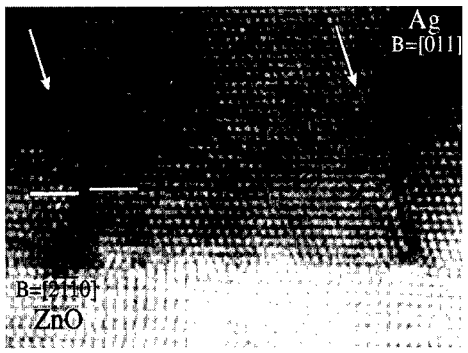

Fig. 3: Slightly tilted Ag-ZnO interface. The arrows indicate the emitted stacking-faults.

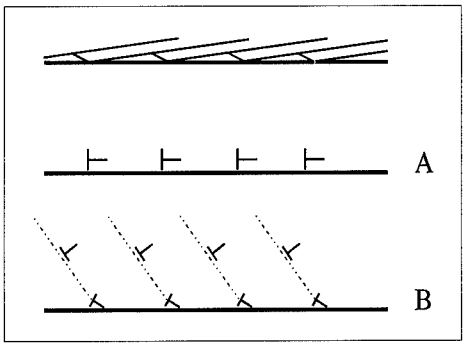

Fig. 4: Schematic representation of the steps at the interface in fig 3 as Frank partial dislocations (A) and dissociation in to 'stair-rod' partial dislocations and Shockley partials at the interface (B).

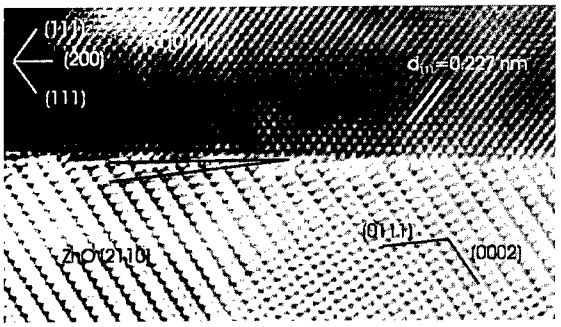

Fig. 5: Pd in contact with the first pyramidal plane of ZnO. Note the steps in the oxide.

In the Ag-ZnO very small angles are compensated by emission of Shockley partial dislocations [5], resulting in a stacking faulted area. This does not occur in the Pd-ZnO system. The stepped oxide interfaces could be due to differences in stiffness. The shear moduli of Pd and ZnO are 53 GPa and 46 GPa respectively. This is a rather even distribution compared to the majority of metal-oxide systems where the oxide can be regarded rigid compared to the metal. When we compare Pd-ZnO with the Ag-ZnO system no stand-off dislocations are formed to relieve the small tilt of the interface [6]. This could be explained by the high stacking fault energy of palladium (180 mJ/m^2) compared to that of silver (17 mJ/m^2) [7].

Conclusions

Using HRTEM to study metal-oxide interfaces can give valuable insight into the interaction across the interface. Strain fields caused by the (localized) misfit dislocations at Cu-MgO interfaces could be observed along two directions, although not always at first sight. Tilted interfaces in Pd-ZnO are compensated by the ZnO crystal, in contrast to the Ag-ZnO case where the Ag adapts to the tilted interfaces. Small tilts in Ag-ZnO are relieved by emission of Shockley partials which could act as a measure of the interaction at the interface. No relaxations of Pd in Pd-ZnO could be seen, but this does not a necessarily mean that the interfaces are incoherent since observation of the strains caused by the misfit and interaction are sometimes hard to observe.

Acknowledgements

The authors gratefully acknowledge the Max Planck Institute Stuttgart for the provided opportunity to use the ARM 1250 microscope and particularly thank F. Phillipp and R. Höschen for their assistance during the experiments. The work described in this paper is part of the research program of the Foundation for Fundamental Research of Matter (FOM-Utrecht).

References

[1] W.P. Vellinga, J.Th.M. De Hosson, V. Vitek, Acta Mater., 45, (1997), p. 1525
[2] H.Jang, D.N. Seidman, K.L. Merkle, Interface Science, 1, (1993), p. 61
[3] H.B. Groen, B.J. Kooi, W.P. Vellinga, J.T.M. De Hosson, Phil. Mag. A, (*submitted,*1998)
[4] F. Ernst, Phil. Mag. A, 68, (1993) p. 1251
[5] W.P. Vellinga, J.Th.M. De Hosson, Acta Mater. 45, (1997), p.933
[6] H.B. Groen, J.T.M. De Hosson, Scripta Met, 38, (1997), p.769
[7] Hirth, J.P., Lothe, J., *Theory of dislocations*, 764, McGraw-Hill (1973)

Materials Science Forum Vols. 294-296 (1999) pp. 111-114

Analysis of the Interfacial Relationship in GaN/(0001) Al_2O_3 Layers

B. Barbaray, V. Potin, P. Ruterana and G. Nouet

Laboratoire d'Etudes et de Recherches sur les Matériaux, UPRESA CNRS 6004, Institut des Sciences de la Matière du Rayonnement, 6 Boulevard du Maréchal Juin, F-14050 CAEN Cedex, France

Keywords: Step, Stacking Fault, Inversion Domain Boundary, High Resolution Electron Microscopy, Sapphire, Gallium Nitride

Abstract : A geometric approach has been used to determine the planar defects induced in the bulk by the interfacial structure. By considering a continuous stacking between the oxygen and nitrogen frameworks of Al_2O_3 and GaN respectively, the residual translation between islands is determined and then compared to the translation of planar defects of the wurtzite structure. In these conditions, a correlation is established between the steps on the Al_2O_3 surface and the planar defects (stacking faults and inversion domain boundaries) observed by high resolution electron microscopy.

Introduction

Gallium nitride thin films present a high density of defects such as threading dislocations, stacking faults, inversion domain boundaries, pinholes and nanopipes. A non-exhaustive review of these defects has been recently published [1]. Although these defects have been identified and characterized, the role of the interface structure on their formation is still under discussion for some of them. For instance, it has been shown that the very high density of threading dislocations ($10^{10}cm^{-2}$) is due to the island growth mode [2]. In the same way, prismatic stacking faults in AlN or GaN grown over silicon carbide (SiC) have been analyzed and it was shown that their formation is linked to interface steps [3]. All these defects have been identified in GaN or AlN layers whatever the nature of the substrate : silicon carbide (SiC) or sapphire (Al_2O_3).

In the other hand, inversion domain boundaries are only found when the growth of the GaN layer is carried out on sapphire. So, in this paper, we have aimed at determining the origin of the formation of these extended defects from the interface GaN/Al_2O_3 by using a geometric approach. Experimental results obtained by high resolution electron microscopy are in agreement with the predicted defects.

Experimental procedure

The analysed samples were 1 to 2 μm thick GaN grown at 800°C by molecular beam epitaxy on (0001) sapphire substrate. The specimens for electron microscopy were prepared in the conventional way by mechanical polishing followed by ion milling down to electron transparency. The experimental micrographs were recorded in the 002B Topcon microscope operated at 200 kV, its point to point resolution is 0.18 nm. A Fourier filtering is used to reconstruct the image into chosen directions. This process consists in calculating the Fourier transform of the numerised image. Before this, a Gaussian filter may be applied in order to reduce the noise (low pass filter). On the Fourier amplitude image, that is equivalent to a diffraction pattern, the intensity of the spots that correspond to the $\{10\bar{1}0\}$ lattice planes in GaN and to $\{11\bar{2}0\}$ lattice planes in Al_2O_3 are multiply by 20. Thus, after an inverse Fourier transform, this planes can be easily seen as well as defects in those directions. Furthermore, the mismatch dislocation cores appear and can be used to locate the interface position.

Crystallographic data

The substrate, Al_2O_3, belongs to the rhombohedral $R\bar{3}c$ space group. The anion framework forms a hexagonal closed packed (hcp) structure with the approximation (x, y, z) = (0.33, 0, 0.25). The lattice parameters are a = 0.476 nm and c = 1,2991 nm. The layer, GaN, has the wurtzite structure, $P6_3mc$, with the lattice parameters a = 0.319 m and c = 0.518 nm. The anions, N^{3-}, also form a hcp structure in which the Ga^{3+} cations occupy only one of the two families of tetrahedral sites.

Epitaxial relationship

GaN layers grow epitaxially on Al_2O_3 substrate according to the well-known relationship :

$$(0001)_{GaN} // (0001)_{Al_2O_3},\ [0\bar{1}10]_{GaN} // [11\bar{2}0]_{Al_2O_3}$$

This relationship leads to the continuation of the anion compact stacking : O^{2-} in the substrate and N^{3-} in the layer. The apparent 30° rotation between the two crystals is due to the choice of the unit cells for Al_2O_3 and GaN. The difference between the parameters leads to a mismatch along the $<11\bar{2}0>$ and <0001> directions : 13,9 % and 16,5 % respectively.

Geometric approach

In the interface plane, the mismatch is accommodated by a hexagonal network of 60° dislocations with their Burgers vector b = 1/3 $\langle 11\bar{2}0 \rangle$ but steps on the substrate surface induce a translation between the GaN crystallites growing on adjacent terraces of the step. According to the height of the step, different translations are expected. Moreover, the continuation of the two hcp structures may be described by three types of polyhedra at the interface. They are built with oxygen (O) and nitrogen (N) at their vertices, the metal (M) at the centre: one tetrahedron (3O, M, N) that leads to upward polarity, one tetrahedron (O, M, 3N) and one octahedron (3O, M, 3N) that both lead to downward polarity. All these factors are taken into account in this approach to analyze how the resulting translation can be accommodated in the GaN layers by the intrinsic planar defects of the wurtzite structure : stacking faults (SF) and inversion domains boundaries (IDB). Since this structure belongs to the hcp system, the stacking faults are those of the hcp one : two intrinsic faults I_1, R_{I1} = 1/6 $\langle 20\bar{2}3 \rangle$, I_2 , R_{I2} = 1/3 $\langle 10\bar{1}0 \rangle$ and one extrinsic fault E, R_E = 1/2 <0001>. The wurtzite structure is non-centrosymmetric and inversion domains are possible : the two atoms A and B of the hcp stacking being different, the (0001) mirror is forbidden. In the wurtzite structure, three types of IDB are known :

- Austerman model [4] : m_{0001}
- Holt model [5] : m_{0001}+ 3/8c
- IDB* model [6] : m_{0001}+ 1/8c.

The mirror m_{0001} is localized on an anion plane and the translations correspond to the shift of the anionic planes.

In a first stage, we analyze the various stackings of GaN over Al_2O_3 on the same terrace and after that, we determine the modifications brought by the step according to their heights and finally we compare the resulting translations with the intrinsic translations of the planar defects which are likely to compensate them.

Growth on a single terrace

On an O-terminated surface, there are four ways to build a hcp stacking of nitrogen atoms, they are related by one of the three stacking fault vectors, R_{SF}, of the wurtzite structure (R_{I1}, R_{I2} and R_E). Since two families of tetrahedral sites are available for the Ga^{3+} cation, this leads to eight GaN stackings linked by the operator $W_{CE} = R_{SF}$ or $W_{CE} = R_{SF} + m$ with opposite polarities. In the case of Al-terminated surface, the number of stackings is reduced to three polyhedra, in order to respect the aluminium position in the Al_2O_3 structure. The systematic analysis of the polyhedra combinations allows to denombrate the relative proportions of the planar defects induced by the operator W_{CE}. For instance, if the interface polyhedra are exclusively downward tetrahedra, the R_{SF} will be only R_{I1}, and combinations of downward tetrahedra and octahedra will lead to the formation of R_{I1} and R_{I2} faults in equal proportions. If the R_{SF} contains a component 1/2<0001>, it is expected to find a prismatic stacking fault corresponding to the Drum model (R = 1/2<10 $\bar{1}$ 1>) [3].

Growth on adjacent terraces

A step between two terraces on which two GaN islands have grown introduces a translation T_S. Its component along c axis can be reduced in R_E=1/2 <0001> and a residual translation T_R. The number of R_E is calculated to minimize the absolute value of this residual translation. For instance, the step between two A terraces with a height equal to c/3 in Al_2O_3 (0.433 nm) is equivalent in GaN to 0.835 c_{GaN}, either : $T_S = 2R_E + T_R = T_R$ with T_R = - 0.165 $c_{GaN} \approx c_{GaN}/6$. By considering all the steps between A or B terraces (A or B layers of the hcp stacking), the T_S translation can be written as : $T_S = aR_E + T_R$ with a = 0 or 1 and T_R may take four special values with the approximation $2c_{Al_2O_3} \sim 5c_{GaN}$(tab. 1) :

Table 1 : Residual translation in GaN as a function of the step height in Al_2O_3

Steps	$h_{c_{Al_2O_3}\ unit}$	T_R c_{GaN} unit	T_R nm
A-A or B-B	nc (n: integer)	0	0
A-B	1/6, 5/6, 7/6 ,11/6	~ 1/12	~ 0.0432
A-A or B-B	1/3, 2/3	~ 1/6	~0.0863
A-B	1/2, 3/2	~ 1/4	~ 0.1295

So, the operator linking the adjacent terraces must involve this additional parameter, T_R :

$$W_{CE} = R + m + T_R \text{ where } R = R_{SF} + aR_E.$$

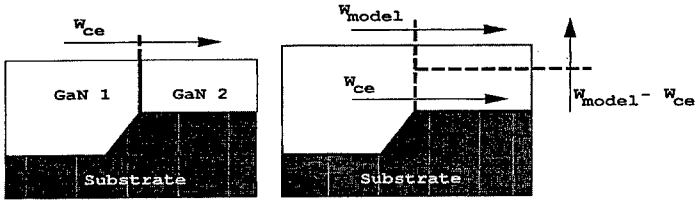

Figure 1: During the coalescence, the two islands may form an interface characterized by W_{CE}. A model characterized by W_{model} can be adopted with creation of a defect which operator is $W_{model} - W_{CE}$.

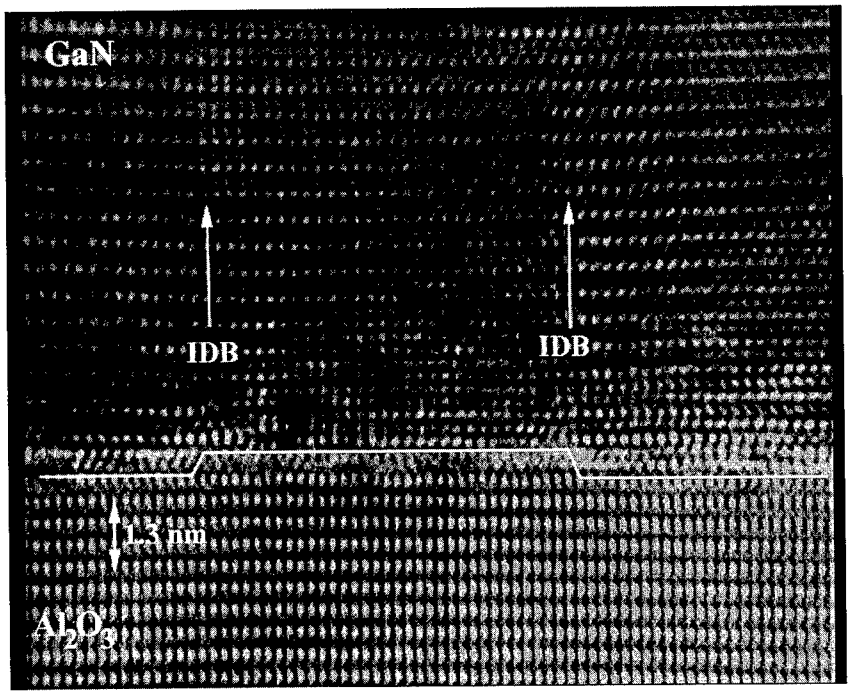

Figure 2a : HREM image of the GaN/Al_2O_3 interface, showing an inversion which boundaries are on both c/3 steps.

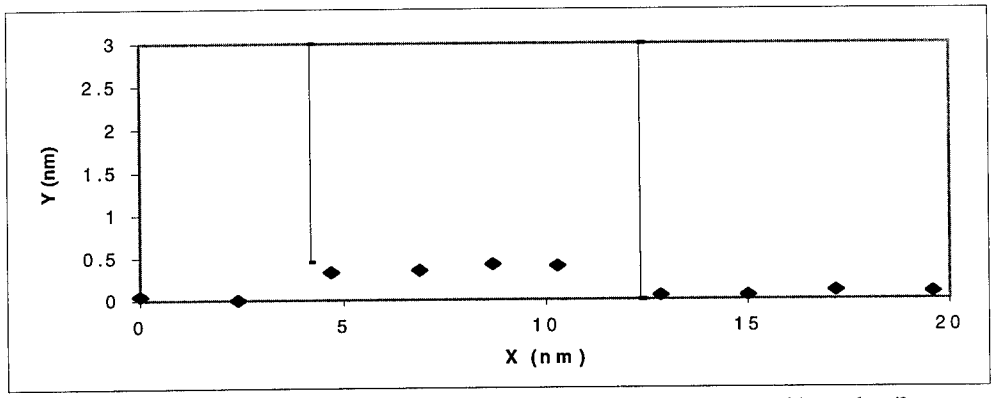

Figure 2b : Misfit dislocation cores of the same HREM image, that indicate the interface position and a c/3 terrace, with the inversion domain boundaries.

Coalescence of the crystallites

During the growth of the layers, the islands are brought to coalesce with the formation of an interface characterized by the operator W_{CE} (Fig. 1). When $T_R = 0$, the situation is equivalent to the stepless surface ($W_{CE} = R + m$) and the accommodation along c axis can be carried out by introduction of SF and IDB to compensate R and m, respectively. In the second and third cases ($T_R \sim c/12$ and c/6), some models of IDB involving a translation of c/8 can reduce the residual translation to c/24. So, such steps may favour the formation of IDB* (m + c/8) or Holt IDB (m + c/2 - c/8). For the last case (c/4), the two above models give a final translation of c/8. However, we can propose a hypothetic inversion domain boundary model defined by the operator (m + c/4) and characterized by the cation sublattice undeviated.

According to the chosen model, except for the first and the last case with the hypothetic IDB, a final translation (c/24 for the second and third cases, and c/8 for the last one) is kept but its amplitude is always small and should be accommodated elastically.

Results and discussion

Analysis of the GaN/Al_2O_3 interfaces by HREM has pointed out the occurrence of a lot of steps of various heights, the majority is of c/3. Most of the defects predicted by this geometric approach have been identified. Close to the GaN/ Al_2O_3 interface, they are many basal SFs, some of them were found to fold from basal to prismatic planes (Drum model). When inversion domains formed, they were always seen to originate from steps. As shown on Fig. 2a and b, the inversion domain [7] is on an upward terrace of the A-A type limited by two c/3 steps. Thus, it seems clear that the residual shift T_R along c introduced by the steps on Al_2O_3 surface can be accommodated by the introduction of IDBs. Although no IDB has been observed on a stepless surface, it is obvious that the coalescence of two opposite tetrahedra, for instance, induces the formation of an inversion domain.

Acknowledgements

The samples were kindly provided by Prof. Morkoç and his group Dr A. Salvador and Dr A. Botchkarev of the Department of Electrical Engineering of the Virginia Commonwealth University of Richmond (USA).

References

1. V. Potin, P. Ruterana, G. Nouet, J. Elect. Mat., **27** (1998) 266.
2. X.J. Ning, F.R. Chien, P. Pirouz, J.W. Wang, M.A. Khan, J. Mater. Res., **3** (1996) 580.
3. P. Vermaut, P. Ruterana, G. Nouet, H. Morkoç, Phil. Mag. A, **75** (1997) 239.
4. S.B. Austerman, W.G.. Gehman, J. Mater. Sci., **1** (1966) 249.
5. D.B. Holt, J. Phys. Chem. Solids, **30** (1969) 1297.
6. J.E. Northrup, J. Neugebauer, L.T. Romano, Phys. Rev. Lett., **77** (1996) 103.
7. V. Potin, P. Ruterana, G. Nouet, J. Appl. Phys., **82** (1997) 2176.

nouet@lermat.ismra.fr
fax : 33 2 31 45 26 60

Materials Science Forum Vols. 294-296 (1999) pp. 115-118

Nanosized Lead Inclusions in Aluminum-Magic Sizes and Aspect Ratios

E. Johnson[1], A. Johansen[1], U. Dahmen[2], S.-J. Chen[2] and T. Fujii[2]

[1] Ørsted Laboratory, Niels Bohr Institute, University of Copenhagen, Universitetsparken 5, DK-2100 Copenhagen Ø, Denmark

[2] National Center for Electron Microscopy, E.O. Lawrence Berkeley National Laboratory, Berkeley, CA 94720, USA

Keywords: Edge Energy, Magic Sizes, Nanosized Precipitates, Wulff Construction

ABSTRACT

Aluminum-lead alloys containing dense distributions of nanosized lead precipitates have been made by rapid solidification and ion implantation. Embedded precipitates grow in parallel-cube alignment with the aluminum matrix; they have a cuboctahedral shape resulting from a minimization of the total interface energy, and atomically smooth {111} and {100} facets. The smallest precipitates, less than about 20 nm in size, adopt a series of magic sizes determined by periodic minima in the residual strain energy. In this size range the energy of the cuboctahedral edges becomes significant. This leads to changes in the aspect ratio of the precipitates so that the smaller precipitates are less truncated. Fitting the experimental data to an analytical expression gives a value of 1.15 for the ratio between the {100} and {111} interface energies and a value of $2.06 \cdot a_{Pb}$ for the ratio of energies between the <110> edges and {111} interfaces.

INTRODUCTION

The equilibrium shape of a free crystal is obtained from the Wulff construction which mathematically is equivalent to a minimization of the surface energy under the condition of constant volume, and with the added constraint that no external forces are acting on the crystal. For faceted crystals the distances between pairs of opposite facets scale with the surface energies of these facets[1]. By comparison, for a crystal embedded in a matrix the surface energy is replaced by an interface energy and in most cases an elastic strain energy term will have to be added to the total energy that must be minimized to obtain the equilibrium shape[2]. This strain energy term scales with the third power of the size and it usually dominates for larger precipitate sizes, while the interface energy which scales with the second power of the size dominates at small sizes. The occurrence of edges on faceted crystals contributes extra energy terms which increase linearly with the size of the crystals[3-5]. These terms are only significant for nanoscale crystals where the fraction of atoms on the edges is no longer negligible, thus invalidating the classical Wulff construction. If the embedding medium is crystalline, the matrix may act as an alignment field for the solid inclusions or precipitates, often forcing all precipitates to adopt the same orientation in space.

In the present work, we use transmission electron microscopy to investigate the equilibrium shape of small Pb precipitates in Al as a function of their size. The Al-Pb alloy system is ideal for studies of nanoscale precipitates. The equilibrium phase diagram is monotectic with virtually no mutual solibility in the solid phase and very limited solubility of Al in liquid Pb[6]. The equilibrium shape of Pb precipitates in Al is cuboctahedral with large atomically smooth {111} facets and smaller {100} facets. Despite a lattice mismatch of 22% (a_{Al} = 0.404 nm and a_{Pb} = 0.495 nm) the Pb precipitates grow in a perfect parallel cube orientation relationship with the Al matrix[7-10]. The relatively high thermal vacancy concentration and mobility in Al just above 200°C provides efficient accommodation of volume stress around the precipitates, which therefore form near-ideal closed systems extremely suitable for studies of both equilibrium shapes and thermal behavior.

EXPERIMENTAL PROCEDURE

Pb precipitates were produced either by rapid solidification of Al-0.5wt.%Pb alloys using Pb and Al of 99.999% purity or by ion implantation of Pb into Al foils. Transmission electron micrographs were always recorded in <110> zone axis orientations of the Al lattice where six of the fourteen facets of the cuboctahedral shape are seen edge-on. Figures 1a and 1b illustrate distributions of precipitates ranging in size from about 3 to 50nm. To ensure that precipitate shapes were at equilibrium, the alloys were annealed for at least 1h at 300°C or higher to let precipitates equilibrate in the solid state.

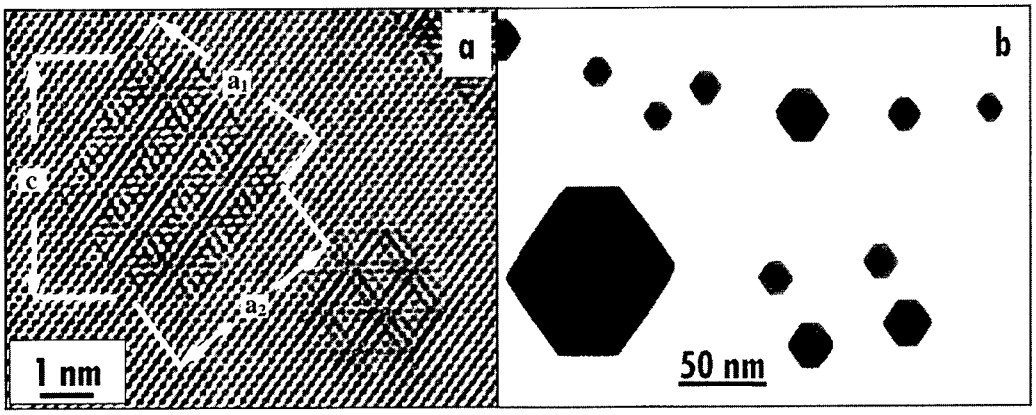

Figure 1. Nanosized Pb precpitates in Al seen along the <110> direction. Samples made by ion implantation (a) and by rapid solidification (b). Schematics of the facet pair distances measured is shown in (a)

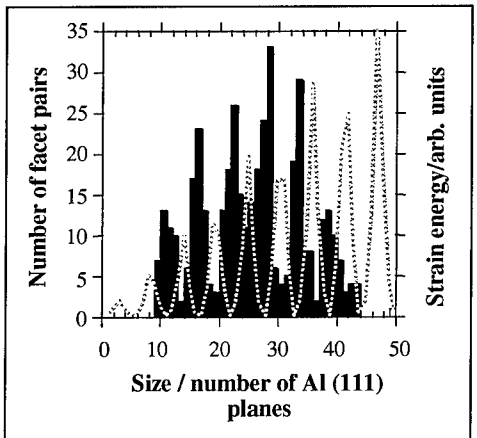

Figure 2. "Magic" size effects in the size distribution measured as the {111} facet pair distance for Pb precipitates in Al. The dotted line shows the calculated residual misfit strain energy. Note that the minima in the residual misfit strain energy coincide with the frequently occurring sizes.

Determination of the precipitate shapes was obtained from measurements of opposite facet pair distances for both {111} facet pairs (a_1 and a_2) and the {100} facet pair (c) as shown in figure 1a.

MAGIC SIZE EFFECTS

To characterize the Pb precipitate size accurately, the {111} facet pair distances of the precipitates were measured separately from high resolution micrographs, using the Al matrix lattice for calibration. A histogram of these data (figure 2) showed the unexpected result that the precipitate sizes were distributed such that some sizes were preferred while others were avoided. This so-called "magic" size effect can be understood as a consequence of the confinement of the Pb precipitates in the solid Al matrix when volume strain is accommodated by matrix vacancies as much as possible. The residual misfit strain, calculated from the atomic plane positions in an undistorted interface, contributes with an oscillating energy term whose periodicity matches the moiré function between the two lattices[11,12]. The dashed line in figure 2 shows the perfect match between the calulated oscillating energy function representing the residual misfit strain energy and the experimental size histogram.

A more precise description of the residual strain that takes into account the polyhedral shape can be obtained from an analogy between a stacking fault tetrahedron and the cuboctahedral precipitate shape. A stacking fault tetrahedron may be considered as a self-inclusion bounded by four planar triangular stacking fault facets and a set of six stair rod dislocations with Burgers vector $b=a_o/6<110>$ along the edges[13]. Similarly, a perfect octahedral precipitate may be approximated by a "stacking fault octahedron" with the eight {111} Pb/Al interfaces as the {111} stacking faults and the twelve edges as the stair rod dislocations, though with variable Burgers vectors representing the oscillating residual strain. Using analytical expressions for the interaction of straight dislocation segments given by deWit[14], the residual elastic energy for an octahedral Pb precipitate in Al is again found to oscillate with a period given by the moiré function but now with an amplitude proportional to $a \cdot \ln(a)$.

ASPECT RATIOS

In the classical Wulff construction in the absense of volume strain the anisotropy of the interface energy can be obtained directly from the shape of a precipitate by measuring the distances between opposite pairs of facets. From the aspect ratio c/a (figure 1a) the interface energy anisotropy $\rho = \gamma_{100}/\gamma_{111}$ has been found to be 1.14, close to the value of $2/\sqrt{3}$ expected from a simple geometrical nearest neighbor broken bond model[15]. However, a considerable increase to a value of 1.28 has been observed for precipitates small enough also to display "magic" size behavior. In the present work, we present measurements of the equilibrium shape of nanoscale Pb precipitates in Al as a function of size ranging from 2nm - 60nm. Emphasis is given to the shape as a function of size averaging over the sequence of "magic" sizes which gives a direct measure of the effect of the edge energy on the degree of truncation of the cuboctahedral shape.

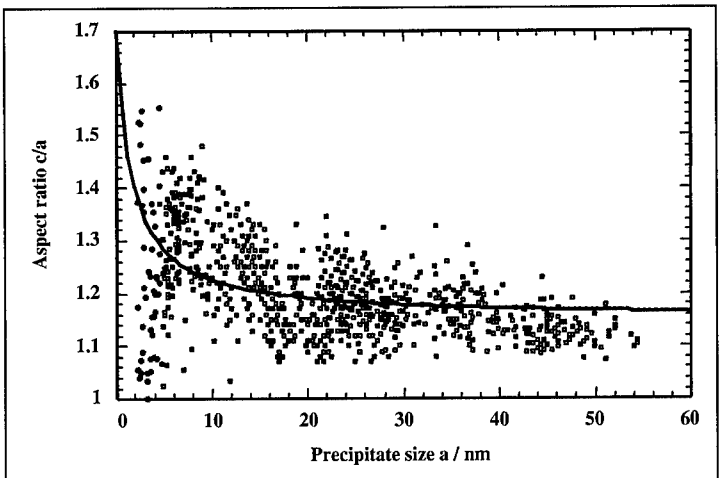

Figure 3. The aspect ratio c/a measured for Pb precipitates in Al as a function of the precipitate size a. The curve shows the two-parameter least squares fit to equ. 1.

Figure 3 shows a plot of measured values of the aspect ratio c/a for Pb precipitates as a function of their size a. The data show a very large scatter that increases with decreasing precipitate size. This is not due to measurement errors which for the small size precipitates is of the order of ± one lattice spacing. It is a scatter that originates from the tendency of the smaller precipitates to retain "magic" size inter-facet distances when the precipitates do not contain a perfect "magic" size number of Pb atoms. These precipitates will adopt asymmetric shapes giving large deviations from the ideal aspect ratio[12]. A detailed statistical analysis of the data in figure 3, based on datasets binned for different precipitate sizes, shows that the aspect ratio increases significantly for small sizes. This increase is a direct consequence of the contribution of edge energy to the total energy[3-5]. For a relative edge energy $\tau = \varepsilon_{110}/\gamma_{111}$ where ε_{110} is the energy of a <110> edge of unit length, the equilibrium aspect ratio can be calculated to be

$$\frac{c}{a}=\left(\rho+\sqrt{6}\frac{\tau}{a}\right)\Big/\left(1+\sqrt{2}\frac{\tau}{a}\right) \qquad (1)$$

which shows that large precipitates should have an aspect ratio of c/a = $\rho = \gamma_{100}/\gamma_{111}$ while small precipitates should have gradually less truncation with a limiting aspect ratio of $\sqrt{3}$, the value for the untruncated octahedron. This result, which was predicted earlier from numerical calculations, agrees well with the present set of data as seen from the two-parameter least squares fit in figure 3 (solid line) to the expression for the aspect ratio using ρ and τ as independent fitting parameters. The value for the "energy" parameters from the fit in figure 3 are $\rho = 1.151 \pm 0.005$ and $\tau = (2.06 \pm 0.16)a_{Pb}$, where a_{Pb} is the lattice parameter for Pb. The value for ρ agrees surprisingly well with the value of $2/\sqrt{3} = 1.16$ obtained from a geometrical nearest neighbor broken bond model, while this model predicts a value for τ ($a_{Pb}/\sqrt{6} = 0.41a_{Pb}$) which is about 5 times smaller than the measured value.

CONCLUSION

Interfacet distances describing the equilibrium shape of nanoscale Pb precipitates has been measured by transmission electron microscopy. A strong preference for "magic" sizes has been interpreted in terms of an oscillating residual misfit strain, and an increase in aspect ratio with decreasing precipitate size is due to an increasing influence of edge energy on the total energy of the precipitates.

ACKNOWLEDGEMENTS

This work is supported by the Director, Office of Energy Research, Office of Basic Energy Sciences, Materials Sciences Division of the U.S. Department of Energy under Contract No. DE-ACO3-76SFOOO98 and by the Danish Natural Sciences Research Council.

REFERENCES

1. C. Herring, Phys. Rev. 82 (1951), p. 87.
2. A.G. Kachaturian, Theory of Structural Transformations in Solids, (Wiley Interscience, New York), 1983, p. 445.
3. M.J. Kelley, Scr. Met. Mat. 33 (1995), p. 1493.
4. L.D. Marks, Surf. Sci. 150 (1985), p. 358.
5. E. Schroer, S. Hopfe, P. Werner, U. Gösele, G. Duscher, M. Rühle and T.Y. Tan, Appl. Phys. Lett. 70 (1997), p. 327.
6. T.B. Massalski (ed.), Binary Alloy Phase Diagrams, (American Society for Metals, Metals Park, OH), 1986, Vol. 1, p. 148.
7. H.H. Andersen and E. Johnson, Nucl. Instrum. Meth. B106 (1995), p. 480.
8. S.Q. Xiao, E. Johnson, S. Hinderberger, A. Johansen, K.K. Bourdelle and U. Dahmen, J. Microscopy, 180 (1995), p. 61.
9. U. Dahmen, E. Johnson, S.Q. Xiao and A. Johansen, J. Surf. Anal. 3 (1997), p. 185.
10. K.L. Moore, D.L. Zhang and B. Cantor, Acta Met. Mat. 38 (1990), p. 1327.
11. U. Dahmen, S.Q. Xiao, S. Paciornik, E. Johnson and A. Johansen, Phys. Rev. Lett. 78 (1997), p. 471.
12. U. Dahmen, E. Johnson, S.Q. Xiao and A. Johansen, MRS Bulletin, 22 (1997), p. 49.
13. G. Kalonji and J.W. Cahn, J. de Physique, Coll. 43 (1982), C6-25
14. R. de Wit, Phys. Stat. Sol. 20 (1967), p. 575.
15. D.A. Porter and K.E. Easterling, Phase Transformations in Metals and Alloys, (Chapman & Hall, London), 2nd ed. 1992, p. 112.

Corresponding author: johnson@fys.ku.dk

Materials Science Forum Vols. 294-296 (1999) pp. 119-122

Growth Induced Grain Boundary Plane Oscillations in $YBa_2Cu_3O_7$ Thin Film Bicrystals

J. Ayache[1], A. Thorel[2], S. Jong Kim[1], J. Lesueur[1],
K.H. Westmacott[3] and U. Dahmen[3]

[1] CSNSM-CNRS, Université Paris XI-Orsay, F-91405 Orsay, France

[2] Centre des Matériaux de l'Ecole des Mines de Paris,
BP87, F-91003 Evry Cedex, France

[3] National Center for Electron Microscopy, Lawrence Berkeley National Laboratory,
University of California, Berkeley, CA-94720, USA

Keywords: YBCO Thin Film Superconductors, Grain Boundary, Bicrystal, Structure

Abstract : We have combined TEM (Transmission Electron Microscopy), HREM (High Resolution Electron Microscopy) and AFM (Atomic Force Microscope) techniques to study growth induced defects in YBCO thin film bicrystals. AFM images clearly evidence "in-plane waviness" of the grain boundary (GB) and a quantitative analysis of HREM images shows unambiguously the oscillation of the grain boundary plane. This GB structure and morphology results from the island growth mechanism of the film.

1- Introduction

$YBa_2Cu_3O_7$ (YBCO) grain boundaries formed during thin film deposition on $SrTiO_3$ (STO) bicrystals are used as Josephson junctions in SQUIDS for electronic applications. One of the most promising processes to synthesize such devices is laser ablation. On the basis of TEM analyses, previous reports showed that the grain boundary in the YBCO film did not always follow the substrate grain boundary faithfully, but rather undulated about the average boundary plane. In this paper we give clear evidence that this undulation takes its origin in the growth mechanism of the YBCO film on top of the STO bicrystal.

2- Experimental

The YBCO thin film bicrystals grown epitaxially by laser ablation were deposited on melt-grown STO bicrystals with a misorientation of 24° around the <100> tilt axis. The growth procedure has been previously described in detail [1,2].
The morphology and crystallography of YBCO thin film bicrystals have been studied from macroscopic to atomic scale by means of analytical electron transmission microscopies SEM/TEM /HREM techniques coupled with quantitative measurements on HREM images and atomic force microscopy. Mechanical tripod thinning has been used to prepare TEM samples in order to avoid spurious effects (such as defect diffusion, amorphization...) due to ion milling bombardment.

3- Characterization

AFM observations

Growth islands with well-defined terraces were observed by AFM (fig.1) on both sides of the grain boundary as well as in its immediate vicinity. The size of the islands ranged from 300 to 1200nm in diameter, and their roughness were 10nm in height in the matrix and 3 to 6nm close to the grain boundary. A schematic of the growth islands of YBCO deposited film, derived from AFM observations, is displayed in figure 2. It consists of an array of terraced domes associated with a corresponding hole array at triple junctions of the islands. Some of them are located at the grain

boundary. Figure 1 shows clearly the meandering of the YBCO grain boundary in agreement with previously observed YBCO GB structures [1-5]

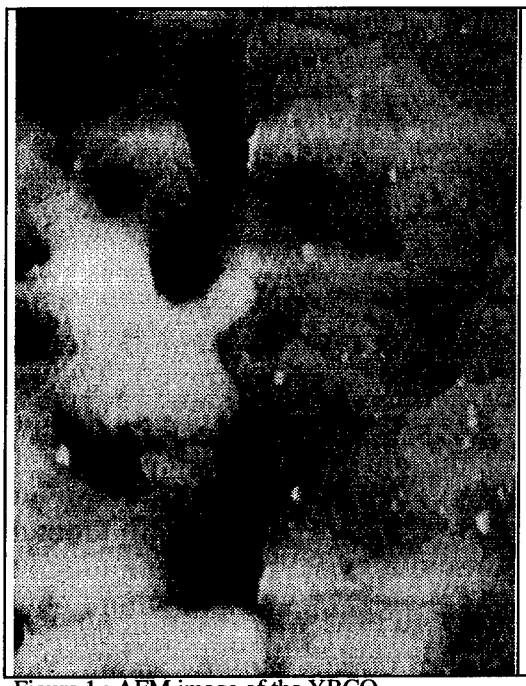

Figure 1 : AFM image of the YBCO grain boundary

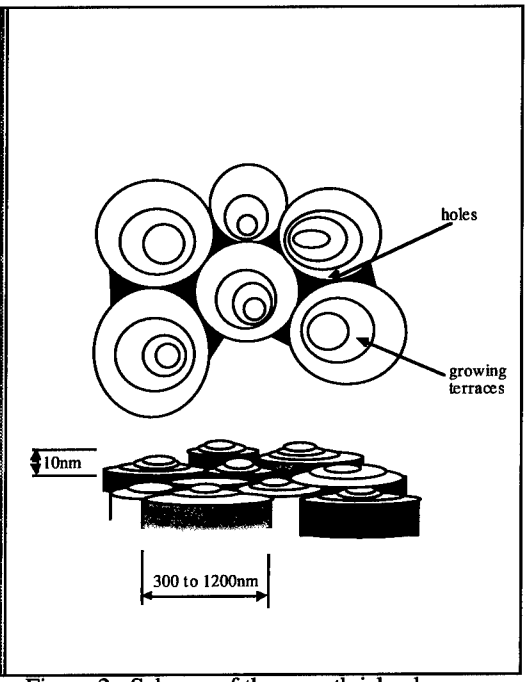

Figure 2 : Scheme of the growth islands

TEM observations

An average misorientation of 24° around the <100> tilt axis was found for both the STO and YBCO bicrystals. TEM images show that the grain boundary in the film did not always follow the substrate grain boundary faithfully, but undulated about the average boundary plane. Figures 3b-d exhibit the Fourier diffractograms obtained respectively from the left hand side of the HREM image of Figure 3a (grain1), the central moiré zone and the right hand side (grain 2). HREM observations of the apparently complex undulating boundary structures can be explained as a result of an overlap of YBCO grains from the two sides of the bicrystal. The wavelength of the undulations was similar to the characteristic lateral film roughness detected by complementary SEM and AFM imaging.

Quantitative analysis

Analysis of HREM images demonstrated that the complex undulating boundary structures are related to regions with different moiré contrast.To get a more quantitative description of the local GB structure, we have carried out a Fourier analysis of the HREM images and analyzed the observed moiré patterns arising from the underlying crystalline structure in the vicinity of the GB. Experimental moirés are gathered on the schematic of the reciprocal lattice bicrystal network of figure 4. The diffraction diagrams explain all the experimentally observed moirés by an overlap between YBCO crystals only when the lattice parameters were allowed to vary over the range 0.380nm< a(YBCO)<0.385nm and 0.384nm<b(YBCO)<0.392nm. A detailed analysis of the local lattice orientation indicated a ±2° angular variation. Thus the YBCO bicrystal angle was found to vary locally from 22° to 26°. It may also occur that locally the YBCO crystal prefers to align its (110) planes to the (110) planes of the cubic STO substrate rather than the (100)/(100) alignment, leading to a ± 1.8° angular deviation between the (100) planes. Comparison between the experimental moiré interfringe distances and orientations, and what could be expected from a perfect <100> epitaxy showed that each undulation is the result of an overlap between the two parts of the YBCO bicrystal.

Nevertheless, local distortions of the moiré fringe spacing and orientation can only be fully interpreted if one takes into account the orthorhombicity variations observed by Fourier analysis close to the grain boundary as well as different crystallographic YBCO variants resulting from the growth of YBCO [001] on top of STO [001].

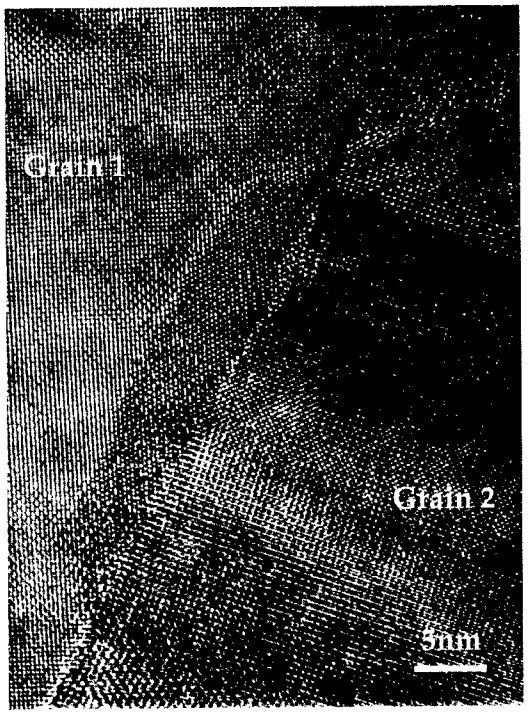

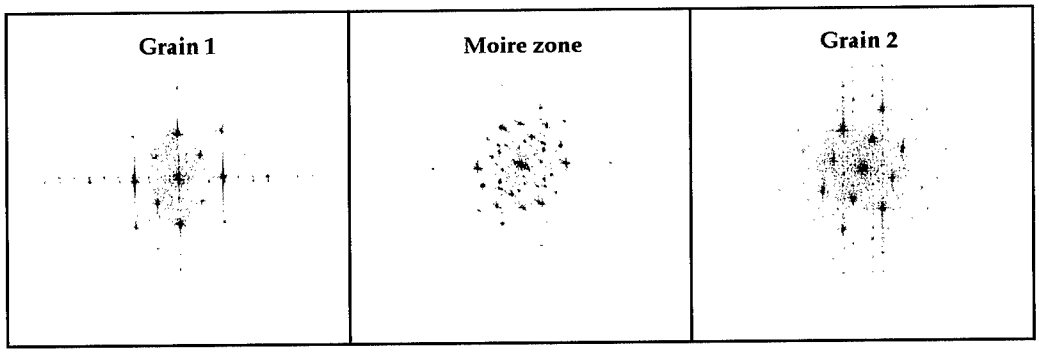

Figure 3 : (a) HREM image of the YBCO GB; (b): FFT in the grain1 of the image; (c) FFT in the central moire zone; (d): FFT in the grain 2.

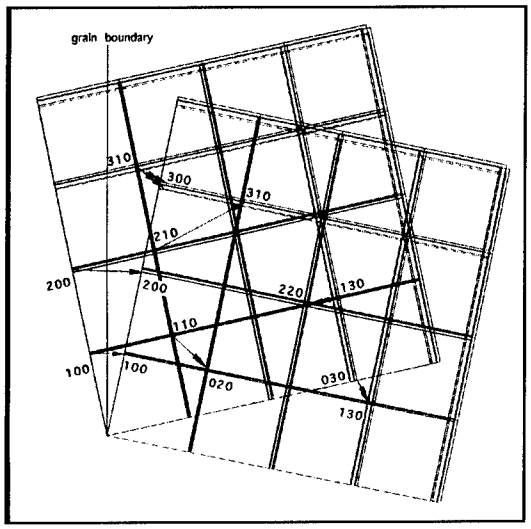

Figure 4 : Schematic of the bicrystal network showing experimental moiré vectors obtained from Fourier analysis of HREM images. The network corresponds to YBCO [100] epitaxial growth on cubic STO, including orthorhombicity variations and lattice parameter changes.

4-Conclusion

From AFM/SEM/HREM analysis it can be inferred that the YBCO grain boundary plane follows the straight STO interface during the initial growth of the YBCO layer. After that initial stage growth terraces start to alternatively cross over to either side of the bicrystal. As a consequence, the interface follows a sinuous path about the original GB. A wide range of inclinations for the interface plane resulting from the growth mechanism has been observed, showing that the grain boundary in the YBCO layer displays a complex 3-d curvature. This is thought to have a strong effect on the superconducting properties such as the phase shift of the order parameter or the critical current density.

5-References

[1]. J.Ayache, A.Thorel, J. Le Duigou, J.Bonevich, U.Dahmen, (1997) Journal of Alloys and Compounds **251** 78-82.
[2]. J.Ayache, A.Thorel, J. Lesueur and U.Dahmen, (1998). To be published in Journal of Applied Physics.
[3]. Traeholt, J.G.Wen, H.W.Zandbergen, Y.Shen, J.W.M. Hilgenkamp, Physica C230 (1994) 425-434
[4]. D.J.Miller, T.A.Roberts, J.H.Kang, J.Talvacchio, D.B.Bucholz, and R.P.H.Chang, Appl.Phys.Lett. 66 (1995) 2561.
[5]. J.A.Alarco, E.Olsson, Z.G.Ivanov, P.A.Nilsson, D.Winkler, E.A.Stepantsov, and A.Ya Tzalenchuk, Ultramicroscopy 51, (1993) 239

Address for correspondence ;
Dr Jeanne Ayache:
CSNSM-CNRS, Université Paris XI-Orsay, 91405 Orsay (FRANCE)
Tel : 33 1 69 15 52 19
Fax : 33 1 69 15 52 68
E-mail : ayache@csnsm.in2P3.fr

Materials Science Forum Vols. 294-296 (1999) pp. 123-126

Material Fluxes in Interfacial Processes

T. Nixon and R.C. Pond

Materials Science and Engineering, Department of Engineering,
University of Liverpool, Liverpool L69 3BX, UK

Keywords: Interfacial Defects, Motion, Intersection, Diffusional Fluxes

Abstract.
The boundary conditions for calculating diffusional fluxes in processes occurring by the movement of interfacial defects are established. These are expressed in terms of the topological parameters (Burgers vectors and step heights) of the defects involved and the chemical compositions and densities of the adjacent crystals. The equations derived enable the constraints imposed on diffusionless processes, such as twinning and martensitic transformation, to be identified.

Introduction.
A substantial amount of evidence has been accumulated showing that many interfacial processes proceed through mechanisms involving the motion of line-defects [1]. Our objective in the present paper is to identify the boundary conditions for calculating the overall fluxes in such processes. This will enable the special conditions that must pertain for diffusionless processes such as twinning and martensitic transformations to be established. The discussion of diffusive fluxes is based on the work of Hirth and Pond [2] which enables fluxes to be calculated in terms of the topological parameters (Burgers vectors and step heights) of interfacial defects and the chemical compositions and densities of the adjacent crystals.

Diffusive Flux Arising Due to Defect Motion
Consider first the flux of material associated with the climb of a crystal dislocation. Let the line direction of the defect, ξ, be parallel to the x-axis of a reference co-ordinate frame, and imagine motion of the defect to be in the x-y plane. If the Burgers vector of the dislocation, **b**, has a component parallel to z, designated b_z, motion will require a flux of material to flow to or from the defect. When a length L of defect moves a distance δy, the incremental number, δN_A, of atoms of species A required is given by

$$\delta N_A = X_A L b_z \delta y, \qquad (1)$$

where X_A is the number of atoms of species A per unit volume in the crystal. Similar expressions can be written for incremental fluxes of the other species present, δN_B, δN_C etc. Equation (1) clearly relates the well-known result that zero flux arises when $b_z = 0$, i.e. when **b** is parallel to the plane of motion.
For line-defects in interfaces the description of the flux associated with their motion is more complex than the case in equation (1) because interfacial defects may exhibit step character as well as dislocation character. The dislocation character of interfacial defects is prescribed by the symmetry of the adjacent crystals and their relative orientation [3]. Formation of admissible defects can be visualised by a Volterra procedure in which surfaces of the two crystals, each exhibiting parallel but incompatible features, are bonded together. If the operation required to bring these misfitting surfaces together is a displacement, **b**, the resulting defect has dislocation character with Burgers vector, **b**. When the parallel surface features are steps having the same sense, but not

necessarily the same magnitude, the defect formed after bonding of the surfaces will exhibit step character in addition to dislocation character. Hirth and Pond [2] have defined the 'overlap' step height, h, for such defects to be the smaller of the two free-surface step heights. Defects having both step and dislocation character are referred to as disconnections [2]. If the parallel surface features before bonding are steps with opposite senses, or either one or both of the crystal surfaces is unstepped, the 'overlap' step height, h, is zero, and the resulting defect exhibits only dislocation character. Important examples of this latter category of interfacial defects include crystal dislocations and twinning dislocations; such defects when residing at an interface do not possess step character, i.e. h = 0, in the sense defined here. It is also possible for interfacial defects to exhibit pure step character, i.e. when the abutting surface features are complementary surface steps.

Let the line direction, ξ, be parallel to x, and the plane of motion (interface plane) be the x-y plane, Fig.1. Hirth and Pond [2] have shown that the step and dislocation parts of interfacial defects can be treated independently for the purpose of calculating fluxes, although these two aspects of a disconnection do not have separate physical meaning. The incremental number of atoms required due to movement through δy is given by [2]

$$\delta N_A = [h\Delta X_A + b_z X_A^{\lambda/\mu}]L\delta y, \qquad (2)$$

where ΔX_A is the difference in the concentration of species A between the upper (λ) and lower (μ) crystals, and $X_A^{\lambda/\mu}$ is the concentration in either λ or μ (depending on the relative signs of b_z and h for the defect in question). The second term in equation (2) represents the flux due to motion of the dislocation part, and is similar to equation (1). The concentration term X_A^{λ} or X_A^{μ} arises because motion of the dislocation part causes material to be added to or removed from the λ or μ crystals, but not to be transferred from λ to μ or vice versa. On the other hand, motion of the step portion involves the transfer of atoms between the adjacent crystals, and hence a flux will arise if a concentration difference, ΔX_A, is present. Similar expressions for incremental numbers of atoms of other species, δN_B, δN_C etc. can be written.

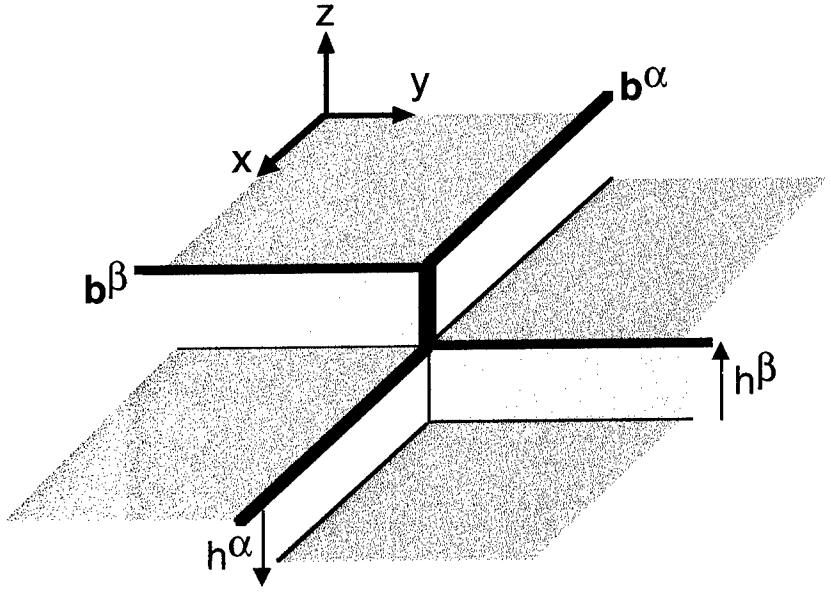

Figure.1 Schematic illustration of two intersecting interfacial disconnections.

Diffusionless Motion of Interfacial Defects

In the case of grain boundary defects the situation is straightforward because ΔX is zero for all species present, and hence the first term in equation (2) is zero irrespective of the magnitude of h. In other words, when material is transferred across the step portion, no diffusive flux arises because there is no concentration difference. Thus, material flux is only associated with motion of the dislocation portion, and is directly analogous to the single crystal case; i.e. motion is diffusionless for defects with **b** parallel to the interface plane. We note that this condition is not restricted to rational interfaces, and hence includes, for example, the important case of Type II twinning [4].

The situation regarding defects in interphase boundaries is more complex since both terms in equation (2) will contribute to a resultant flux in general. There are only two circumstances where diffusionless motion arises, namely (i) when h and b_z are both zero, and (ii) when the notional fluxes to the dislocation and step portions are equal and opposite, i.e. $h\Delta X_A = -b_z X_A^{\lambda/\mu}$. The former situation can arise for example in epitaxial interfaces when misfit dislocations move during misfit accommodation [5]. The latter situation is very restrictive, and is unlikely to arise for disconnections in any interface between crystals with different chemical compositions. However, diffusionless motion of disconnections can arise if the chemical compositions of the crystals are the same but where their structures are different, as is the case in martensitic interfaces. In such cases, ΔX_A, ΔX_B etc. are finite in general because of the structural differences between the crystals. Hirth and Pond [2] have demonstrated that the only circumstance in which the condition $h\Delta X_A = -b_z X_A^{\lambda/\mu}$ is satisfied occurs where the area per atom of species A projected onto the interface, designated g_A, is identical for atoms in both crystals. Thus, in order that the diffusive flux be zero overall, the interface must be such that $g_A^{\lambda} = g_A^{\mu}$, and similarly for all other species present. This condition is very restrictive and is only consistent with planes that are invariant-plane-strains of the transformation. An invariant-plane-strain deformation can be expressed as the combination of a simple shear and a pure extension, and it is clear that neither of these deformations modify the values g_A, g_B etc. when the λ crystal is transformed into the μ crystal or vice versa. We also note that fulfilment of this condition does not necessarily imply that the interface plane be rational.

Diffusive Fluxes Arising Due to Motion of Defect Intersections

When a dislocation moving in the bulk of a single crystal intersects another dislocation it becomes jogged, and continued motion of the defect may require an additional flux of material due to the presence of the jog [6]. An analogous situation arises when two interfacial disconnections, designated α: $[b_x^{\alpha}, b_y^{\alpha}, b_z^{\alpha}]$, h^{α} and β: $[b_x^{\beta}, b_y^{\beta}, b_z^{\beta}]$, h^{β}, intersect, with the difference that both defects are constrained to lie in the interface plane. Following Hirth and Pond [2], it is helpful to consider the step and dislocation portions of disconnections separately for flux calculation. Let defect α lie along x and β lie along y, as indicated schematically in Fig.1. The two disconnections are mutually stepped by each other, and the dislocation portions interact where they coincide at the intersection (in Fig.1. the dislocation portions are depicted as bold lines). Imagine that defect α is moving in the direction y and β in the direction x; the diffusive fluxes associated with these motions can be calculated by applying equation (2) to the α and β defects in turn. However, an additional flux contribution will arise due to the motion of the extra length of α and β dislocation created at the intersection; defect α has increased in length by h^{β} and, similarly, β has increased by h^{α}. Thus, the incremental contribution to the flux δN_A^{i}, due to motion of the intersection through $\delta x + \delta y$ is given by

$$\delta N_A^{i} = X_A^{\alpha} h^{\beta} [b_y^{\alpha} \delta x + b_x^{\alpha} \delta y] + X_A^{\beta} h^{\alpha} [b_y^{\beta} \delta x + b_x^{\beta} \delta y], \qquad (3)$$

where $X^{\alpha} = X^{\lambda/\mu}$ for defect α, and $X^{\beta} = X^{\lambda/\mu}$ for defect β. For the case where the two defects both lie parallel to x, motion of α through β would involve an incremental flux contribution, δN_A^P, due to the climb of the two dislocation components up/down each others steps, given by

$$\delta N_A^P = L[\, X_A^{\beta} h^{\alpha} b_y^{\beta} - X_A^{\alpha} h^{\beta} b_y^{\alpha} \,], \tag{4}$$

where the minus sign arises because the motion of α is left-to-right with respect to β, but that for β with respect to α is opposite to this [7]. Expressions similar to (3) and (4) can be written for all other species present, B, C etc.

Summary and Discussion.

It has been found that the formalism of Hirth and Pond [2] is valuable for calculations of material fluxes in processes occurring through the motion of interfacial defects. Using this approach, both the dislocation and step character of defects are taken into account quantitatively. Furthermore, for the purpose of calculating material fluxes, these two aspects of defect topology can be treated separately, even though they do not have separate physical meaning. A further advantage arising from this notional separation of dislocation and step character is that the topological nature of interactions between intersecting and passing parallel defects can be established. In this framework, the boundary conditions for calculating material fluxes have been expressed through three equations, (2), (3) and (4), which enumerate the contributions due to the motion of (i) individual defects in an interface, (ii) nodal intersections, and (iii) the passing of parallel defects respectively.

The equations derived demonstrate clearly that processes in interphase interfaces which are diffusionless overall are subject to severe topological constraints; in mathematical terms the integral of $\delta N + \delta N^i + \delta N^p$ must be zero for each species present when summed over all the contributory defect motions. Thus, for example, a mechanistic model of martensite formation in terms of interface defects must not only be consistent with the Frank-Bilby equation [4] for the total defect content of an interface, but also with the topological constraints for diffusionless mechanisms set out here. Preliminary modelling along these lines has been described elsewhere [8], and it is anticipated that further work will elucidate the mechanism of martensite formation consistently with the phenomenological approaches of Wechsler et al. [9] and Bowles and Mackenzie [10].

Acknowledgements.

One of the authors (T. Nixon) thanks the EPSRC for financial support.

References.

[1] A. P. Sutton and R. W. Balluffi, Interfaces in Crystalline Materials (Oxford Science Publications: Oxford, 1995).

[2] J. P. Hirth and R. C. Pond, Acta Mater., **44** (1996), p. 4749.

[3] R. C. Pond, Dislocations in Solids, **8**, ed. F.R.N. Nabarro (Amsterdam: North Holland, 1989), 1.

[4] J. W. Christian, Theory of Transformations in Metals and Alloys, 2nd edition (Oxford: Permagon, 1975).

[5] Handbook on Semi-Conductors, **3**, ed. S. Mahajan (Amsterdam: North Holland, 1994).

[6] J. P. Hirth and J. Lothe, Theory of Dislocations in Solids, 2nd edition (Krieger: Melbourne, FL, 1992).

[7] R. C. Pond and F. Sarrazit, Interface Science, **4** (1996), p. 99.

[8] J. P. Hirth, T. Nixon and R. C. Pond in Boundaries & Interfaces in Materials: The David A. Smith Synposium, ed. R.C.Pond, W.A.T. Clark, A.H. King, and D.B. Williams (TMS, 1998), p. 63.

[9] D. S. Lieberman, M. S. Wechsler and T. A. Read, J. Appl. Phys., **26** (1955), p. 473.

[10] J. S. Bowles and J. K. Mackenzie, Acta Met., **2** (1954), p. 224.

Materials Science Forum Vols. 294-296 (1999) pp. 127-130

Magnetically Forced Motion of Specific Planar Boundaries in Bi-Bicrystals

D.A. Molodov[1], G. Gottstein[1], F. Heringhaus[2] and L.S. Shvindlerman[3]

[1] Institut für Metallkunde und Metallphysik, RWTH Aachen, Kopernikusstr. 14, D-52074 Aachen, Germany

[2] National High Magnetic Laboratory, Tallahassee, Florida 32310, USA

[3] Institute of Solid State Physics, Russian Academy of Sciences, Chernogolovka, Moscow Distr., RU-142432, Russia

Keywords: Grain Boundary Migration, Bicrystals, Mobility, Magnetic Field, Driving Force, Activation Enthalpy

Abstract. For the first time a crystallographically defined planar grain boundary in a specially grown bicrystals was moved under the action of a magnetic driving force. The mobility of 90°<112> tilt grain boundaries with identical misorientation but different boundary inclination in Bi-bicrystals was investigated. The driving force for grain boundary motion was created by the action of a magnetic field on bicrystals of bismuth, which is magnetically anisotropic with different susceptibilities parallel and perpendicular to the trigonal axis. The driving force dependency of boundary velocity was measured and the absolute value of grain boundary mobility was determined. The grain boundary mobility was found to strongly depend on grain boundary inclination. The mobility of the asymmetrical grain boundary was found to depend on the direction of motion.

1. Introduction

The motion of grain boundaries constitutes the fundamental process of recrystallization and grain growth. There is a large body of evidence that grain boundaries are not alike in their structure and, therefore, different boundaries exhibit different properties. The clearest evidence for an orientation dependence of grain boundary structure follows from migration data. Since experiments on polycrystals can only provide information on average grain boundary behaviour, the structural dependence of boundary mobility must be retrieved from investigations of the motion of boundaries with known crystallography under the action of a defined driving force.

A driving force for grain boundary migration occurs, if the boundary displacement leads to decrease of the total free energy of the system, i.e. the driving force is the free energy difference of the adjacent grains per unit volume. The most frequently used method for the study of grain boundary motion in bicrystals is the displacement of a curved grain boundary [1,2]. The driving force in this case is provided by the capillary pressure, and the decrease of the free energy of the system during the grain boundary motion manifests itself in the reduction of grain boundary area. However, a curved grain boundary implies that its structure changes along the boundary, since it is composed of different grain boundary planes. The obtained mobilities can therefore not be related to a specific grain boundary structure. However, a plane boundary can be forced to move in a bicrystal with grains that have such orientation dependent property like magnetic susceptibility. A driving force for grain boundary migration in the current experiments was generated by the action of a magnetic field on a bicrystal of Bi, which is magnetically anisotropic with different susceptibilities parallel and perpendicular to the trigonal axis. Under the impact of a respective directed magnetic field, a free energy difference between adjacent grains is created that exerts a driving force for boundary displacement. Since this driving force is induced by an external field and does not depend on boun-

dary properties, the method provides an opportunity to investigate the motion of a planar grain boundary with defined structure.
Therefore, in contrast to experiments with curved grain boundaries, the measurement of boundary motion under a constant magnetic driving force allows to determine the absolute value of grain boundary mobility. Furthermore, by a variation of the magnetic field the boundary velocity can be measured as a function of the driving force.
In the current study grain boundary motion was measured by applying a strong magnetic field to specially prepared Bi-bicrystals, and the dependence of the mobility of symmetrical and asymmetrical tilt boundaries on temperature and driving force was investigated.

2. Experimental

The experiments were carried out on bicrystals of high purity (99.999%) bismuth. Symmetrical and asymmetrical pure tilt boundaries with 90°<112> misorientation were examined. The misorientation angle between the trigonal <111> axes in both grains of the bicrystals was chosen to be 90° in order to gain the maximum possible magnetic driving force, which is given by [3]

$$p = \mu_0 \frac{\Delta\chi}{2} H^2 (\cos^2\theta_1 - \cos^2\theta_2), \qquad (1)$$

where H is the magnetic field strength, $\Delta\chi$ is the difference of the susceptibilities parallel and perpendicular to the trigonal axis and θ_1 and θ_2 are the angles between the direction of the magnetic field and the trigonal axes in both grains of the Bi-bicrystal.
Bismuth is a suitable material for an investigation of grain boundary migration by the magnetic method, since it is magnetically uniaxial with different susceptibilities parallel and perpendicular to the trigonal axis [4]. The susceptibility of Bi does not depend on H up to $2 \cdot 10^7$A/m, and the energies associated with magnetostriction at $0.8 \cdot 10^7$A/m are less than 1% of the magnetic free energies and thus, can be neglected [3].
The bicrystals were grown by directional crystallization in a horizontal mold under a protective atmosphere of high purity argon. The orientation of the crystallographic axes of the crystals was measured by the Laue back-reflection method. The grown bicrystals were sectioned into slices of 17 mm length, 4 mm width and 3 mm thickness by electrical discharge machining. The deformed surface layer after this operation was removed by etching in a mixture of 20 ml HCl and 20 ml HNO_3. Before annealing the samples were electrolytically polished to improve the surface quality.
The experiments were carried out using the high magnetic field facilities of the National High Magnetic Field Laboratory in Tallahassee, Florida, USA. A resistive, steady-state 20 T Bitter magnet with 50 mm bore diameter was used, and a field strength between $0.80 \cdot 10^7$ and $1.59 \cdot 10^7$ A/m was applied. The magnetic field was imposed on the samples at different temperatures ranging from 210 to 260°C. High temperature annealings were conducted under an atmosphere of high purity argon using specially designed and fabricated cartridge heaters. The temperature of annealing was kept constant within ±1°. The position of the boundary before and after the annealing was determined by optical means from grain boundary grooves. Prior to each annealing in the high magnetic field the specimen was polished to remove the grooves.

3. Results

In numerous experiments it was confirmed that grain boundaries in Bi-bicrystals actually move under the action of a magnetic driving force (Fig. 1). To prove that boundary motion was caused exlusively by the magnetic driving force, the experiment was carried out in two different ways. Firstly, a specimen was mounted in a holder such that the *c* axis (<111>) of crystal 1 was directed parallel to

the field (Fig. 2a). The <111> axis in crystal 2 in this case was perpendicular to the field, and the grain boundary moved in the direction of the latter crystal due to its higher magnetic free energy. Secondly, a specimen was mounted in a position where the axis <111> in crystal 2 was close to the field direction and the corresponding axis in crystal 1 was perpendicular to the field. The direction of boundary motion in this case was opposite, from crystal 2 toward crystal 1 (Fig. 2b). This result provides unambiguous evidence that the grain boundaries in our bicrystals were forced to move by the magnetic driving force only. In addition, some bicrystals were annealed in a magnetic field in both positions, and boundary motion in opposite directions was observed in the same specimen dependent on its position with regards to the magnetic field.

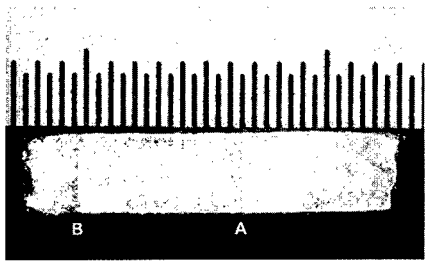

Fig. 1: Grain boundary displacement (from A to B) in a Bi-bicrystal under a magnetic driving force of $H=1.63\cdot10^7$ A/m after annealing during 180 s at 252°C.

The possibility to change the magnitude of the driving force for boundary migration by exposing the samples to magnetic fields of different strength yields the unique opportunity to obtain the driving force dependence of grain boundary velocity (Fig. 3). The driving force in our experiment was extremely low, varying from 7.4 to 29.6 J/m^3. For comparison, the driving force acting on a curved boundary with a radius of curvature of about 0.5 mm in bicrystals of high purity aluminium is of the order of 10^3 J/m^3 [1,2]. The motion of boundaries driven by such a small force was expected to be very sensitive to the influence of perturbations like boundary grooves, surface roughness or small angle grain boundaries. However, the current measurements of boundary migration in different magnetic fields revealed that even in the region of very small driving forces the boundary velocity v changed linearly with the driving force $v = mp$ (Fig.3). Therefore, from the current results the absolute value of the grain boundary mobility $m = v / p$ can be immediately extracted, and the dependence of grain boundary mobility on temperature and on the specific grain boundary character can be determined.

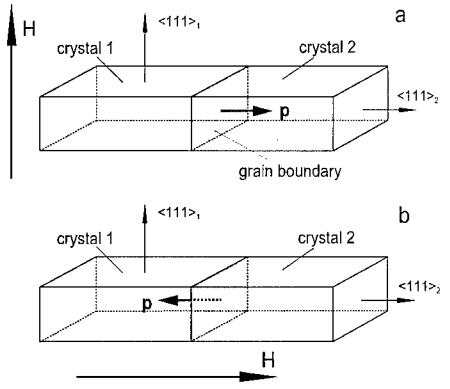

Fig. 2: Movement of the same grain boundary in opposite directions in a bicrystal differently positioned with regard to the magnetic field.

The temperature dependence of the mobility $m = m_0 \exp(-Q / kT)$ of two differently inclined 90° <112> tilt grain boundaries revealed that the migration parameters (activation enthalpy Q and mobility preexponential factor m_0) for the symmetrical boundary (Q=0.51 eV, m_0=0.67 m^4/J·s) drastically differed from the migration parameters for the asymmetrical boundary ($Q_{\|}$=3.38 eV, $m_{0\|}=2.51\cdot10^{26}$ m^4/J·s and $Q_{\perp}$=3.79 eV, $m_{0\perp}=1.26\cdot10^{30}$ m^4/J·s, where the symbols $\|$ and $\perp$ refer to the orientation of the *c*-axis with regard to the boundary plane normal, as referred to below). As a consequence, the symmetrical boundary has a higher mobility than the asymmetrical boundary in the entire investigated temperature range up to the melting point of Bi (Fig. 4). The obtained result shows that the inclination of the tilt boundary in Bi has a very strong influence on boundary mobility.

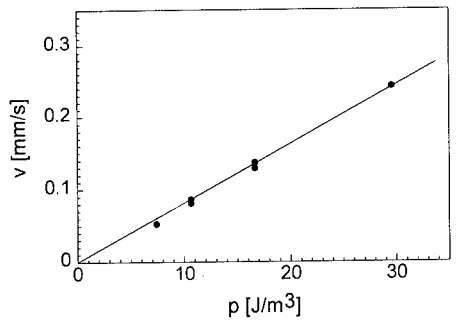

Figure 3: Dependence of the velocity of a 90°<112> symmetrical tilt boundary on the magnetic driving force at 250°C.

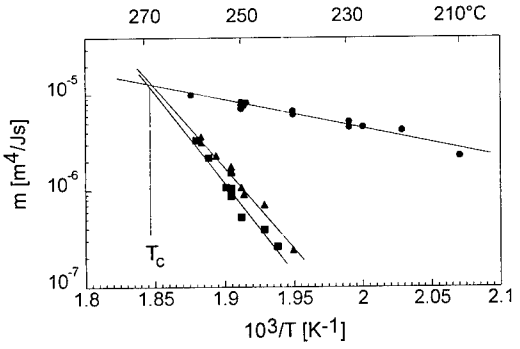

Fig. 4: Temperature dependence of mobility of 90°<112> symmetrical (●) and asymmetrical (▲, ■) boundaries in Bi-bicrystals. Trigonal axis in the growing grain parallel (▲) or perpendicular (■) to the growth direction.

The measurement of the temperature dependence of migration of an asymmetrical 90°<112> tilt grain boundary revealed that the mobility of this boundary is different for the motion in opposite directions. In the entire investigated temperature range, the measured mobility was found to be distinctly higher, i.e. the mobility parameters (activation enthalpy and preexponential factor) were lower, when the trigonal (*c*) axis in the growing grain was parallel to the direction of motion. Conversely, the boundary moved more slowly, i.e. with a higher activation enthalpy and preexponential factor, when the *c* axis in the growing grain was perpendicular to the direction of motion. This result provides clear evidence for an anisotropy of grain boundary mobility perpendicular and parallel to the trigonal *c*-axis in Bi.

The change of Arrhenius parameters of boundary migration obtained in our experiment comply with the compensation effect, which manifest itself in a linear relationship between activation enthalpy and the logarithm of the preexponential mobility factor. Such linear dependence means that there is a temperature (compensation temperature T_c), at which the Arrhenius plots of all boundaries mobility intersect, i. e. at T_c the mobilities of all grain boundaries are equal. Such behaviour is indeed observed in the current experiment. Interestingly, the compensation temperature derived from the experiments (T_c=269°C) is very close to the melting point of Bi (271°C).

Acknowledgments

The authors express their gratitude to the Deutsche Forschungsgemeinschaft for financial support of the project. This work was partly supported by the Visiting Scientist Program of the National High Magnetic Field Laboratory (NHMFL) and a portion of this work was performed at the NHMFL, which is supported by NSF Cooperative Agreement No. DMR-9527035 and by the State of Florida.

References

[1] D. A. Molodov, U. Czubayko, G. Gottstein and L. S. Shvindlerman, Acta mater., 46 (1998), p. 553.
[2] G. Gottstein, D. A. Molodov and L. S. Shvindlerman, Interface Science, 6 (1998), p. 7.
[3] W. W. Mullins, Acta metall., 4 (1956), p. 421.
[4] A. Goetz and A. Focke, Phys. Rev., 45 (1934), p. 170.

Materials Science Forum Vols. 294-296 (1999) pp. 131-134

The Influence of Grain Boundary Structure on Diffusional Creep

P.A. Thorsen and J.B. Bilde-Sørensen

Materials Research Department, Risø National Laboratory,
DK-4000 Roskilde, Denmark

Keywords: Nabarro-Herring Creep, Coincident Site Lattice, Grain Boundary Dislocations, Grain Boundary Sliding, Cu-Ni Alloy

Abstract

A Cu-2wt%Ni-alloy was deformed in tension in the diffusional creep regime (Nabarro-Herring creep). A periodic grid consisting of alumina was deposited on the surface of the creep specimen prior to creep. This makes it possible to separate the deformation caused by grain boundary sliding from the deformation caused by deposition of material at (or removal of material from) grain boundaries. The misorientation across the grain boundaries, and hence the character of the boundaries, was measured with the use of electron back-scattering patterns. The deformation behavior of the individual boundaries was correlated with the boundary character.

Introduction

The diffusional creep mechanism was suggested by Nabarro in 1947 [1]. The essential idea of this mechanism is that boundaries in tension emit vacancies that diffuse through the lattice to boundaries in compression where they are absorbed. This corresponds to a flow of material in the opposite direction. The structure of grain boundaries was not very well understood in 1947, and the most natural assumption to make at that time therefore was that all boundaries are perfect sinks and sources for vacancies. In the following we shall discuss the diffusional creep process in the light of contemporary grain boundary theory and demonstrate experimentally how the grain boundary structure influences the creep properties.

Theory

The discussion is necessarily based on the coincident site lattice (CSL) model, since the structure of general boundaries is not as yet sufficiently well understood. The CSL misorientations are misorientations that lead to a high degree of coincidence between lattice sites on either side of the boundary. Small deviations from CSL misorientations are accommodated by structural grain boundary dislocations (GBDs) with Burgers vectors that are translation vectors of the DSC lattice. The GBDs are associated with a step in the boundary [2].

It is commonly assumed, and has been experimentally corroborated [3], that absorption and emission of vacancies can occur only at GBDs. This has several implications for the diffusional creep process. First, boundaries close to an exact CSL misorientation will contain very few GBDs. It is therefore obvious that these boundaries cannot participate efficiently in the creep process. Secondly, it is possible that threshold stress effects [4] may occur in boundaries containing many dislocations: When a GBD is displaced from its equilibrium position in a regular array, the other dislocations in the array will exert a force on it tending to move it back to its original position.

In the boundaries that do act as efficient sinks and sources, the GBDs must in the general case move by a combination of glide and climb, since they are confined to the boundary plane. This implies that the absorption (or emission) of vacancies is coupled to grain boundary sliding. A GBD must move as an entity and will of course move so that it contributes positively to the strain. Some of the

GBDs may have their Burgers vector oriented relative to the stress axis in such a way that the forces on the glide and the climb component have opposite signs. A grain boundary may therefore be forced to slide in the negative direction in order that the climb of the GBDs can make a larger, positive contribution to the deformation. Theoretically, this is expected to occur predominantly at boundaries that are almost perpendicular to the stress axis [5,7]. Likewise negative climb may occur in order that grain boundary sliding can make a larger, positive contribution to the deformation. This is expected to occur predominantly at boundaries that are almost parallel to the stress direction [6,7]. The step that is associated with a GBD must move with the dislocation. The movement of a GBD by glide and climb therefore leads to concurrent grain boundary migration.

Experiments

The experiments were performed on samples of Cu-2 wt% Ni. The samples were machined, ground and polished. They were then annealed for 10 h at 1073 K and given a polishing etch. The dimensions of the reduced section were approximately 37.5 x 5 x 1 mm^3. A grid of aluminium was deposited on one of the major surfaces prior to creep. The grid was left to oxidize in air to form alumina before the creep experiments. The specimen considered below was crept for 46.3 days under a stress of 1.14 MPa in a vacuum better than 10^{-5} torr. For most of the time the temperature was 1073 K, but for 6.2 days the temperature was raised to 1103 K in order to obtain an estimate of the activation energy. The total strain was 2.4 %.

After creep the deformation at the individual boundaries was measured in a scanning electron microscope with use of the grid. Consider a boundary that contains i sets of dislocations. When n_i dislocations with Burgers vector $\mathbf{b}_i$ pass along the boundary, the adjoining grains will be displaced by $\Sigma\, n_i\mathbf{b}_i$ with respect to each other. If the orientation of the grain boundary plane is known, this displacement can be resolved into a glide component lying in the boundary and a climb component perpendicular to the boundary. The crystallographic orientation of the grains adjoining a boundary was measured by electron back-scattering diffraction.

Results and discussion

A boundary seen from the edge is shown in fig. 1. It is obvious from the appearance of the boundary region that the boundary has migrated in a continuous way during deformation. Measurements made on the images in fig. 2 show that the boundary has slid 1.8 μm in the negative direction, while 4.8 μm was being deposited on the boundary. From electron back-scattering

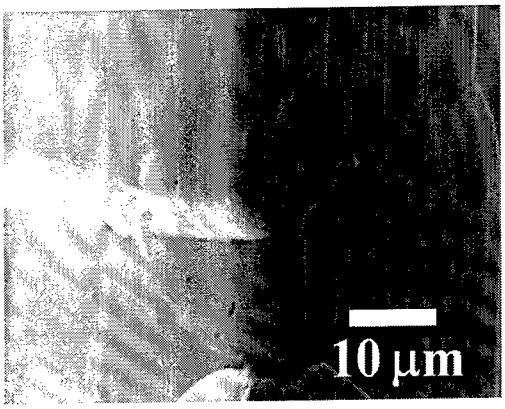

Fig. 1. Grain boundary seen from an edge. The tensile stress axis is vertical.

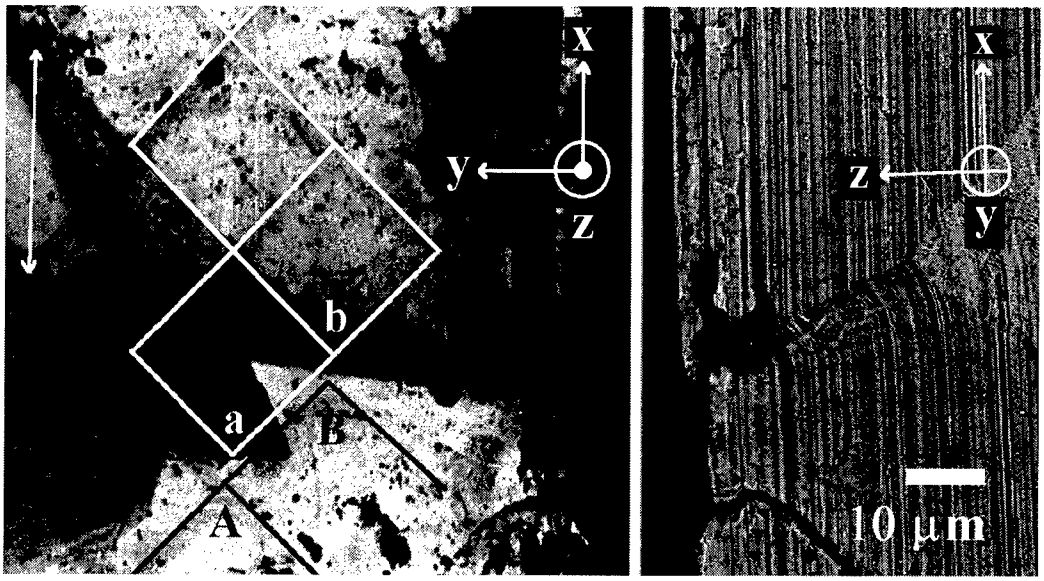

Fig. 2. *(Left)* The boundary in fig. 1 seen from the grid-covered surface. Lines have been drawn as a help to define the grid positions. The tensile axis is indicated with the double arrow. *(Right)* The same boundary seen from the machined side.

diffraction the misorientation across the boundary was found to be $(\theta,\mathbf{u}) = (45.5°, 0.78, 0.58, 0.22)$, $\mathbf{N}_1$ 6.5° from [-2, -2, 1], $\mathbf{N}_2$ 3.0° from [-2, 2, 1]. Based on the Brandon criterion [8]. the boundary is a $\Sigma = 85e$ boundary with a deviation of $v/v_m = 0.66$, but based on the Palumbo-Aust criterion [9], it must be described as a general boundary. It is therefore interesting to note that the boundary structure seems to impose restrictions for emission of vacancies that lead to negative sliding for this boundary. Negative climb was observed at some of the longitudinal boundaries. The ratio between sliding and deposition or removal of material was observed to vary from boundary to boundary.

Fig. 3 illustrates that the deformation behavior of the individual boundary depends heavily on the boundary character. The two coherent twin boundaries marked "t" are close to the exact $\Sigma = 3$ misorientation (deviation on the Brandon criterion $v/v_m = 0.05$). These two boundaries do not

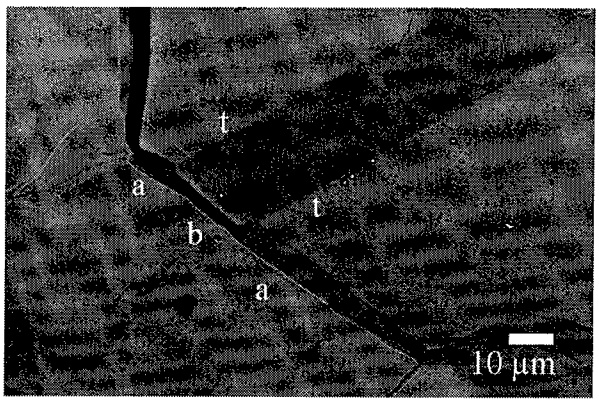

Fig. 3. The deformation behavior of the segment "b" is different from the deformation behavior of the segments "a" because the misorientation across the boundary "a-b-a" is changed where it is met by the twin boundaries "t".

participate in the deformation process. Where the twin meets the boundary "a-b-a", it changes the misorientation of the boundary from $(\theta,\mathbf{u})$ = (54.6°, 0.675, 0.587, 0.446) in the segments marked "a" to $(\theta,\mathbf{u})$ = (40.7°, 0.747, 0.614, 0.255) in the segment marked "b". The content of GBDs is therefore also changed. Consequently, the segment "b" deforms markedly different from the segments "a".

The misorientation has been measured for 39 $\Sigma = 3$ boundaries, out of which 28 were found to be inactive. The value of v/v_m, based on the Brandon criterion, was in the range 0.02 to 0.15 for the inactive boundaries and in the range 0.10 to 0.99 for the active boundaries. Likewise 3 $\Sigma = 9$ boundaries with v/v_m below 0.15 were found to be inactive, while 2 $\Sigma = 9$ boundaries with higher values of v/v_m were active.

Conclusions

A number of the phenomena expected on the basis of grain boundary theory have been observed experimentally: (i) deposition (or removal) of material at a boundary is coupled to grain boundary sliding and migration, (ii) the climb/glide ratio varies from boundary to boundary confirming that it depends on the boundary structure, (iii) negative sliding occurs at some transverse boundaries, (iv) deposition of material occurs at some longitudinal boundaries, and (v) boundaries close to an exact CSL misorientation are inactive during deformation. It is concluded that the model for diffusional creep should be modified to account for the effects of the grain boundary structure.

Acknowledgment

This work was carried out within the Engineering Science Center for Structural Characterization and Modelling of Materials.

References

[1]. F. R. N. Nabarro, Report on a conference on the strength of solids, Bristol 7-9 July 1947 (The Physical Society, London, 1948), 75.
[2]. A. H. King and D. A. Smith, Acta Cryst. **A36** (1980), 335.
[3]. A. H. King and D. A. Smith, Philos. Mag. **A42** (1980), 495.
[4]. A. H. King and D. A. Smith, Metal Sci. **7** (1980), 57.
[5]. J. B. Bilde-Sørensen and D. A. Smith, Proc. 8th Internat. Conf. on the Strength of Metals and Alloys, (Pergamon Press, Oxford, 1988), 869.
[6]. J. B. Bilde-Sørensen and D. A. Smith, Scripta metall. mater. **30** (1994), 383.
[7]. J. B. Bilde-Sørensen and P. A. Thorsen, Boundaries and Interfaces in Materials: The David A. Smith Symposium, (The Minerals, Metals & Materials Society, Pennsylvania, 1998), 179.
[8]. D. G. Brandon, Acta metall. **14** (1966), 1479.
[9]. G. Palumbo and K. T. Aust, Acta metall. **38**(1990), 2342.

e-mail address: j.bilde@risoe.dk
fax number: +45 4677 5758

Materials Science Forum Vols. 294-296 (1999) pp. 135-138

The Role of the Interface Oxide/Metal in the High Temperature Corrosion Resistance of Alloys

H.J. Grabke

Max-Planck-Institut für Eisenforschung GmbH,
Postfach 140 444, D-40074 Düsseldorf, Germany

Keywords: Oxidation, Protective Scales, Interface Oxide/Metal, Oxide Adherence, Reactive Element Effects, Nonmetal Element Effects

Abstract

Essential for the protection of high temperature alloys against corrosion is a dense, well adherent oxide layer. Interfacial phenomena in the nucleation, growth and adherence of such protective oxide scales are described and their mechanisms are discussed. Various positive effects are exerted by alloying with reactive elements, i.e. Ce, Y, La, Ti, Zr ... in small concentrations, rather negative effects are caused by sulfur in the alloys, nitrogen and carbon may act favorably.

Introduction

High temperature alloys must form slow growing protective oxide layers,which prevent the attack by components of hostile environments such as SO_2, HCl, CO, CO_2, hydrocarbons etc. Up to about 900 °C chromia forming alloys are used, at higher temperatures alumina forming alloys. The oxide layers should be adherent also upon thermal cycling, in spite of the different thermal expansion coefficients of metal and oxide. In contrast to ceramic coatings, small cracks in the scale caused by growth stresses or thermal stresses and by creep or fatigue of the substrate can heal by oxide growth [1-3]. The formation, growth and adherence of the protective scale may strongly be improved by the presence of relatively low concentrations of reactive elements, such as Ce, Y, Ti, Zr ... in the high temperature alloys [4-10], the "reactive element effects" and their possible explanations will be shortly described. Rather negative effects are exerted by sulfur, even small concentrations in alloys degrade the scale adherence [11-22], this "sulfur effect" and its explanation [19-22] are shortly discussed. Also the nucleation and first stages of oxide growth are affected by nonmetal elements - as will be shown, positively by nitrogen and negatively by sulfur [23,24].

Reactive Element Effects in the Formation of Protective Adherent Oxide Layers

The effects of rare earth elements on the adherence of protective layers on high temperature alloys are known since long [25]. Later on, it was detected that also other reactive elements such as Ti and Zr exhibit effects which are generally positive: (i) improved adherence oxide/metal, (ii) the selective oxidation of Cr or Al is favored, (iii) the oxide growth rate is retarded (not in all cases), (iv) a more fine grained oxide layer with good plasticity is formed. The research and discussion on these effects goes on since about 60 years and various explanations have been put forward by many authors all of which are more or less true [5-10]. A list of 12 possible explanations is given here followed by examples which prove one or the other of these explanations.

1. A compound is formed between oxide and metal, which can act as a *'graded seal'*, i.e. provide a graded transition of lattice constants, thermal expansion coefficient etc. An example is the formation of a Ti(C,O) layer between Al_2O_3 and alloy on ferritic steels. Its formation was observed by AES for Fe-Al-Ti alloys [26,27].

2. The *nucleation* of the protective oxide is favored, thus many nuclei lead to rapid growth of a fine grained oxide layer. For Fe-Cr alloys this effect is established by small concentrations of Ce [28,29] which is oxidized at first. Nucleation sites are created for protective Cr_2O_3, instead of less protective spinels or iron oxides. The nucleation of protective α-Al_2O_3 is favored by small concentrations of Y in the widely used Fe-Cr-Al (Kanthal) alloys [10,30] or by dispersed Y_2O_3 in ODS alloys.
3. The favored nucleation leads to a fine grained oxide layer with a *better ductility*. The high ductility is improving adherence especially upon creep of the components in high temperature applications.
4. Somehow the reactive elements can affect a *change in the growth mechanism* of Cr_2O_3 and Al_2O_3. These oxides generally grow by outward diffusion of cations and inward diffusion of oxygen in the grain boundaries, which causes lateral growth and stresses leading to buckling of oxide layer. As has been shown by oxidation studies using the isotopes ^{16}O and ^{18}O, the growth mechanism is changed to prevailing inward oxygen diffusion, which causes less stress [31-33]. No buckling was observed for Fe-Cr-Al alloys doped with Y [34].
5. The combined effect of Y on nucleation and growth mechanism of Al_2O_3 causes columnar growth of the Al_2O_3-crystallites and a *textured microstructure*. In such a structure the growth and thermal stresses are mainly lateral, i.e. parallel to the alloy surface and less apt to cause decohesion. The stresses measured in such Al_2O_3 layers are higher for Y doped materials than for undoped Fe-Cr-Al alloys [34,35], in spite of that there is less spalling, since the stress is parallel to the surface.
6. The suppression of cation outward diffusion also causes a *retarded growth rate* of the oxide layer - thus the growth stresses will generally increase slower. Accordingly, scale failure by cracking and spalling is retarded.
7. The reactive elements if present in an alloy even in small concentrations can effectively *tie up sulfur*, since they form very stable sulfides and/or oxy-sulfides. This effect reduces the formation of voids and cavities at the interface oxide/metal which would be favored by sulfur surface segregation (see next chapter of this paper) [19-22].
8. The formation of a protective, slow growing, stable α-Al_2O_3 on alloys needs high temperatures >1000 °C and/or the *initiation* by reactive elements, such as Y, otherwise fast growing metastable δ, γ or θ alumina are formed. This was demonstrated by in-situ X-ray diffraction studies on NiAl doped with Y, Ce or Hf [36].
9. Mechanical anchoring of scales by oxide intrusions into the metal substrate, *i.e. pegging or keying* was observed in some cases, but not in all cases of enhanced adherence.
10. Since many scales grow by outward diffusion of cations, vacancies may accumulate at the oxide/metal interface and cause cavity formation or separation at this interface. The oxides or other compounds of the reactive element may form *sinks for vacancies* and prevent oxide/metal separation [5,6].
11. A most dubious explanation of the reactive element effect has been proposed [37,38], namely the *enhanced chemical oxide-metal bonding* caused by reactive elements in the interface, however, these elements are certainly present in the oxidized state, therefore they cannot exert an enhanced bonding strength.
12. The newest hypothesis on the reactive element effect [39,40] assumes that the transfer of metal atoms from the metal phase to the oxide phase is hindered by *blocking of the interface* by segregated reactive elements. Thus, oxidation and development of growth stresses would be retarded. Experimental evidence is still sparse.

Sulfur Effect on the Adherence of Scales

Several years ago the deteriorating effect of even small sulfur concentrations in alloys on scale adherence was demonstrated by several authors [11-18]. Decreasing the content of sulfur by

desulfurization or by tying up instable sulfides by reactive elements (see chapter 1) was shown to be advantageous for the oxidation resistance of Ni-base superalloys. The authors claimed that sulfur would deteriorate the oxide adherence by segregating to the oxide/metal interface, like in grain boundary embrittlement. Certainly there is a strong driving force for segregation of sulfur to free metal surfaces and grain boundaries in metals [41-47], but not for segregation of sulfur to the oxide/metal interface, since there are no free bonds and there is no free space for the relatively large sulfur atoms resp. $S^{\delta-}$ions (formed upon surface segregation). Thus, it was concluded and proved by experiments [19-22] that the sulfur segregates to voids and separations at the oxide/metal interface, decreasing the surface energy in these defects and favoring the growth of cavities or cracks. This view of the sulfur effect was proved by AES studies on Fe-Cr alloys and on the intermetallic NiAl [19-22]. After short-term oxidation (some hours) no sulfur was detected beneath the oxide scales in the coherent oxide/metal interface - but after prolonged oxidation cavities were observed beneath the oxide scales and the cavity surface was saturated with adsorbed sulfur. Thus, the sulfur acts by surface segregation, segregating to the free metal surface of any voids or cracks forming at the oxide/metal interface and in this way enhancing and accelerating the decohesion of oxide and metal.

Nonmetal Element Effects in the Formation of Protective Oxide Layers

Coming from the gas phase or from the solid solution in the alloy, i.e. by adsorption or by segregation, the nonmetal elements S, N and C can affect the oxide formation. For Fe-Cr and Ni-Cr alloys the presence of S, N and C, either from the gas phase or from the alloy can enhance the Cr-concentration in the alloy surface. Gases containing these elements, such as H_2S, N_2 or CH_4 establish a certain activity of S, N or C in the surface, but which also may stem from their presence dissolved in the alloy. In both ways, by chemisorption induced segregation or by cosegregation of dissolved nonmetal elements X and Cr, two-dimensional compounds CrX are formed on the alloys at elevated temperatures. Such two-dimensional compounds have been studied in detail [48-50], they distinctly affect the oxide growth and morphology on Fe-Cr-, Ni-Cr- and related alloys [23,24].

In the case of nitrogen adsorption or segregation a surface nitride is formed which comprises one outer layer of N and two inner layers of Cr [50]. Upon oxidation, the nitrogen is rapidly removed and the presence of the high surface concentration of Cr leads to a high density of Cr_2O_3 nuclei and a fine grain oxide layer. Similar oxidation behavior is induced by the presence of carbon. In contrast, sulfur is not easily removed, only a few nuclei of Cr_2O_3 are formed which grow to islets slowly displacing the sulfur. Thus, a coarse grained slow growing oxide layer is attained.

The enhancement of chromia nucleation and acceleration of the initial growth of a dense chromia layer by the presence of nitrogen is of advantage for applications with carburizing, sulfidizing and/or chloridizing components at low pO_2. In such environments it is of great importance for high temperature alloys to form the protective scale rapidly before ingress of C, S or Cl. Therefore, preoxidation in N_2-H_2-H_2O in the start of a new plant appears to be favorable.

References

[1] H.W. Grünling, B. Ilschner, S. Leistikow, A. Rahmel, M. Schmidt: Werkst.Korr. 29 (1978) 691
[2] M. Schütze: Oxid. Met. 24 (1985) 25, (1986) 409
[3] J. Barbehön, A. Rahmel, M. Schütze: Oxid. Met. 30 (1988) p 85
[4] E. Lang (Ed.), 'The Role of Active Elements in the Oxidation Behaviour of High Temperature Metals and Alloys', Elsevier Appl. Science, London 1989
[5] D.P. Whittle, J. Stringer: Phil. Trans. R. Soc. London A 295 (1980) 309
[6] J. Stringer: Mat. Sci. Engg. A 120 (1989) 129
[7] D.P. Moon: Mater. Sci. Techn. 5 (1989) 754

[8] D.P. Moon, M.J. Bennett: Mat. Sci. Forum 43 (1989) 269
[9] J. Jedlinski: Solid State Phenomena 21/22 (1992) 335
[10] H.J. Grabke, M. Siegers, V.K. Tolpygo: Z. Naturforschung 50a (1995) 217
[11] Funkenbusch, A.W., Smeggil, J.G., Bornstein, N.S.: Met. Trans. 16A, 1985, p. 1164
[12] J.G. Smeggil, A.W. Funkenbusch, N.S. Bornstein: Met. Trans. 17A (1986) 923
[13] K.L. Luthra, C.L. Briant: Oxid. Met. 30 (1988) 257
[14] J.G. Smeggil, N.S. Bornstein, M.A. DeCrescente: Oxid. Met. 30 (1988) 259
[15] J.L. Smialek: Met. Trans. 18A (Jahr) 163
[16] P. Fox, D.G. Lees, G.W. Lorimer: Oxid. Met. 36 (1991) 491
[17] D.R. Sigler: Oxid. Metals 29 (1988) 23
[18] P.Y. Hou, J. Stringer: in 'Microscopy of Oxidation' (Eds. M.J. Bennett and G.W. Lorimer), Inst. of Metals, London 1991, p 1345
[19] H.J. Grabke, D. Wiemer, H. Viefhaus: Appl. Surf. Sci. 47 (1991) 243
[20] D. Wiemer, H.J. Grabke, H. Viefhaus: Fresenius Z. Analyt. Chemie 341 (1991), 402
[21] H.J. Schmutzler, H. Viefhaus, H.J. Grabke: Surf. and Interf. Analysis 10 (1992) 581
[22] H.J. Grabke, G. Kurbatov, H.J. Schmutzler: Oxid. Metals 43 (1995) 97
[23] H.J. Grabke, R. Dennert, B. Wagemann: Oxid. Metals 47 (1997) 495
[24] H.J. Grabke, R. Dennert, B. Wagemann: Proc. ECASIA '91, Eds. I. Olefjord, L. Nyborg, D. Briggs 1997, John Wiley & Sons, p. 297
[25] W. Hessenbruch: Metalle und Legierungen für hohe Temperaturen, Springer 1940 p. 105
[26] J. Peters, H.J. Grabke: Werkstoffe u. Korr. 35 (1984) 385
[27] J. Peters, H.J. Grabke, H. Viefhaus: Proc. 10th Symp. Reactivity of Solids, Dijon, Eds. P. Barret, L.C. Dufour, Elsevier 1985, p. 151
[28] T.N. Rhys-Jones, H.J. Grabke, H. Kudielka: Corros. Sci. 27 (1987) 49
[29] T.N. Rhys-Jones, H.J. Grabke: Mat. Sci. & Technol. 4 (1988) 446
[30] M. Siegers, H.J. Grabke, H. Viefhaus: in 'Microscopy of Oxidation 2', Ed. S.B. Newcomb, M.J. Bennett. The Inst. of Materials, London 1993, p. 269
[31] W.J. Quadakkers, H. Holzbrecher, K.G. Briefs, H. Beske: Oxid. Met. 32 (1989) 67
[32] J. Jedlinski, S. Mrowec: Mater. Sci. Engg. 87 (1987) 281
[33] S. Mrowec, J. Jedlinski: Trans. TMS AIME 247 (1988) 1099
[34] V.K. Tolpygo, H.J. Grabke: Oxid. Met. 41 (1994) 343
[35] A.G. Evans, G.B. Crumley, R.F. Demaray: Oxid. Metals 20 (1983) 193
[36] I. Rommerskirchen, V. Kolarik: Materials & Corr. 47 (1996) 625
[37] A.B. Anderson, S.P. Mehandru, J. Smialek: J. Electrochem. Soc. 132 (1985) 1695
[38] S.Y. Hong, A.B. Anderson, J.L. Smialek: Surf. Sci. 230 (1990) 175
[39] B. Pieraggi, R.A. Rapp: J. de Physique IV, Colloque C9, Vol 3 (1993) 275
[40] R.A. Rapp: 'Adhesion of Oxide Scales' in Mat. Sci. Forum Vol. 154 'Surface Layers', Eds. M.A. J. Somers, E.J. Mittemeijer, J. Schoonman, Trans. Tech. Publ. 1994, p. 119
[41] H.J. Grabke, W. Paulitschke, G. Tauber, H. Viefhaus: Surf. Sci. 63, (1977) 377
[42] H.J. Grabke, E.M. Petersen, S.R. Srinivasan: Surface Sci. 67 (1977) 501
[43] G. Tauber, H.J. Grabke: Ber. Bunsenges. physikal. Chemie 82 (1978) 298
[44] H.J. Grabke: Mater. Sci. Engg. 42 (1980) 91
[45] H.J. Grabke: ISIJ Int. 29 (1989) 529
[46] H.J. Grabke, H. Viefhaus: Surface Segregation of Nonmetal Atoms on Metal Surfaces in 'Surface Segregation Phenomena', Ed. P.A. Dowben, A. Miller, CRC Press Inc. 1990, p. 207
[47] G. Panzner, B. Egert: Surface Sci. 144 (1984) 651
[48] C. Uebing, H. Viefhaus, H.J. Grabke: Appl. Surface Sci. 72 (1988) 363
[49] C. Uebing: Surface Sci. 225 (1990) 97
[50] C. Uebing, V. Scheuch, M. Kiskinova, H.P. Bonzel: Surf. Sci. 321 (1994) 89

Materials Science Forum Vols. 294-296 (1999) pp. 139-144

Interface Diffusion Controlled Reactions in Multilayers

L.M. Klinger[1], Y.J.M. Bréchet[2] and G.R. Purdy[3]

[1] Department of Materials Engineering, Technion, Haïfa, IL-32000, Israël

[2] L.T.P.C.M., Groupe "physique du métal", Domaine Universitaire de Grenoble, BP 75, F-38402 Saint Martin d'Heres, France

[3] Department of Materials Science and Engineering, McMaster University, 1280 Main Street West, Hamilton, Ontario, L8S4L7, Canada

Keywords: Interface Diffusion, Multilayers

Abstract We consider the reaction $\alpha + \beta \rightarrow \omega$ where ω is either a solid solution or a stoichiometric compound. We consider this reaction inside multilayers to occur at a single interface, and at a temperature low enough that volume diffusion is frozen and surface diffusion is controlling. We compute both the reaction front velocity and its morphology. It is shown that depending on the conditions of the experiment, two classes of solutions are possible: a single propagating front sweeping the multilayer, or a fingering solution propagating along the original α/β interfaces.

1.Introduction

Interface diffusion provides, an efficient at low temperature short circuit for mass transfer in the absence of bulk diffusion [1]. This efficiency may even be greater if interface migration is coupled to interface diffusion [2]. Examples of such situations are frequent in physical metallurgy: they can lead to alloying or de-alloying (DIGM)[3], they can be associated with a phase transformation such as the Pearlite transformation [4] or discontinuous precipitation [5]. In the present paper we investigate equivalent situations in multilayers. In these artificially grown structures, both the composition of each layer and the periodicity of the layering are well under control [6] so that they can be seen as ideal model systems to check theoretical models. Ideas developed in this framework might prove useful for the more usual transformations involving interface migration and interface diffusion.

This paper aims at giving an overview of different interface diffusion controlled mechanisms which may be active in the destabilisation of a multilayer, depending on the thermodynamics of the system under consideration.We will consider two idealized situations, namely the case of full mutual solubility of the two parent phase α and β in order that the reaction product ω is a solid solution (§2), and the case of three phases with fixed stoechiometries (§3). The key difference between these two classes is related to the driving force for mass transport along an interface. In both cases, the driving force is the gradient in chemical potential. However, when the phase is stoichiometric, only gradients in curvature can provide the driving force for mass transport. In contrast, mass transport along a grain boundary can be a response to a gradient in concentration. The two situations have generated two streams of literature in physical metallurgy: Mullins's [7] and Cahn's[8] classical papers on interface diffusion and mass transport. We have recently shown that the combination of the two types of kinetics allowed to remove the degeneracy in pattern selection in discontinuous precipitation [9].

In both cases under consideration in the destabilising of a multilayer, namely the homogeneisation and the intermetallic reaction, we will investigate the possible steady states, and two topologically different situations will be considered: either a single front periodically distorted propagating at a constant velocity (§2a and §3a), or a solution formed of "fingers" developping along the interfaces present initially in the multilayer structure (§2b and §3b). In both case we

compute the propagation velocity V and the interface shape. In Conclusion (§4) , we will suggest some possible experiments to be developped along these lines and further theoretical developements to be investigated.

2.Discontinuous homogeneisation of multilayers

We consider here a multilayer of pure miscible elements A and B, threaded by a grain boundary as schematised in fig. 1. The layer thickness is d. The equilibrium state of the system is an homogeneous solid solution. Two regimes of homogeneisation by a moving grain boundary may be considered [10]: at low driving force, the grain boundary moves as a whole, whereas at high driving force, fingers develop along the existing interfaces between A and B. Each of these situations requires a separate treatment

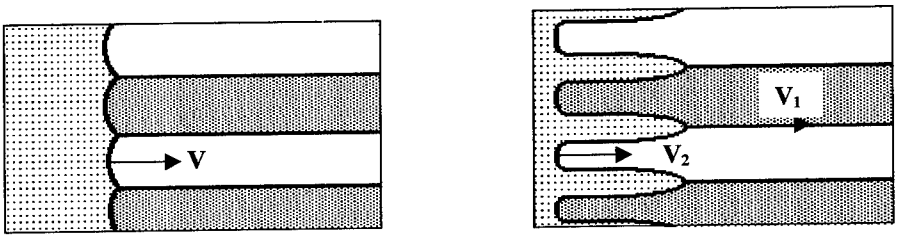

Fig. 1: Two possible mechanisms for multilayer homogeneisation: single propagating front and interlayer fingering (V_1 and V_2 are velocities of the leading and trailing interface)

2a Single propagating front [10]

The concentration in the multilayer is c_0 (step function), and c in the daughter phase. Assuming a quadratic dependance of the thermodynamic driving force , the local description of motion of the grain boundary is written:

$$V.\cos\theta = M[g(c-c_0)^2 - \gamma\frac{\partial\theta}{\partial s}] \qquad (1)$$

M is here a mobility of the grain boundary and γ is the interfacial free energy assumed to be constant irrespectively of the local composition. The concentration profile is governed by the generalized Cahn equation [8]:

$$D\delta\frac{\partial^2 c}{\partial s^2} = (c-c_0).V.\cos\theta \qquad (2)$$

D and δ are here the diffusion coefficient and the width of the grain boundary respectively. These equations with the appropriate boundary conditions (for more details see ref [9]) are solved numerically in order to compute the velocity of the front, its shape and the concentration profile in its the wake. The convenient parameters to describe the system happen to be:

$$\alpha = \frac{gd}{\gamma}, \qquad \beta = \frac{M\gamma^2}{D\delta g} \qquad (3)$$

Fig. 2 shows the shape of the moving interface (2a), the concentration profile corresponding to a partial homogeneisation (2b), and the velocity of the interface (2c) as a fuction of α for different values of β.

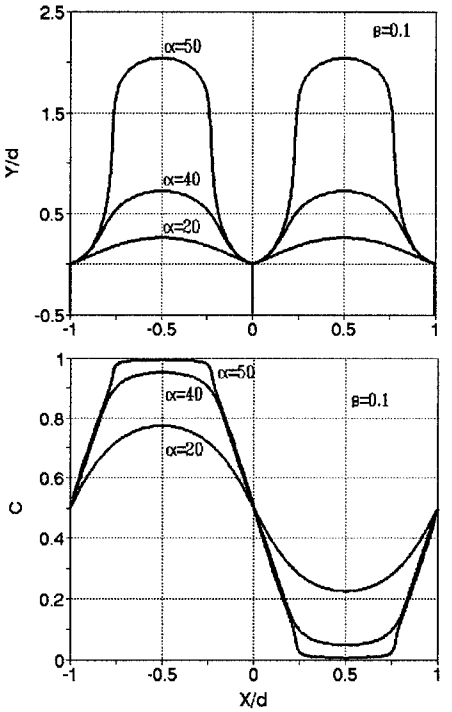

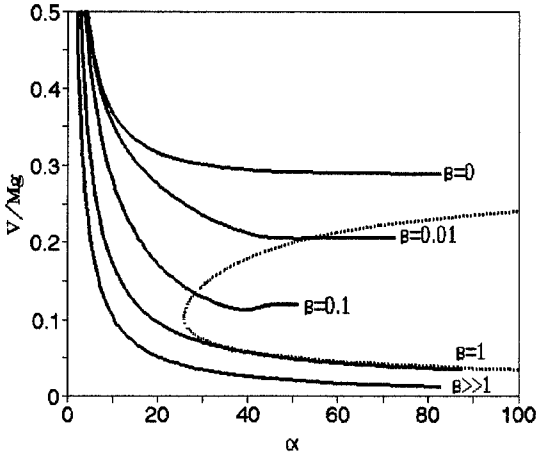

Fig. 2: Discontinuous homogeneisation by a propagating front; **a)** shape of the interface; **b)** concentration profile, **c)** velocity of the front for different values of α and β. Dotted line restricts the domains of existence of the fingering solution

For larger values of α, it has been shown that steady state solution is no longer possible, but instead the moving grain boudary breaks down into a fingering solution propagating along the AB interface.

2b. Interlayer fingering [10]

Both the width Δ of the finger, its shape and its velocity are of interest. This fingering phenomena can occur only for large values of α, i.e. when the driving force is sufficiant for the system to afford an increase in surface energy associated with the lengthening of the fingers. The equations to be solved are identical to (1) and (2) but with different boundary conditions. Fig.3 shows the results of the numerical solution for the fingering geometry, with the assumption that all surface tensions are equal.

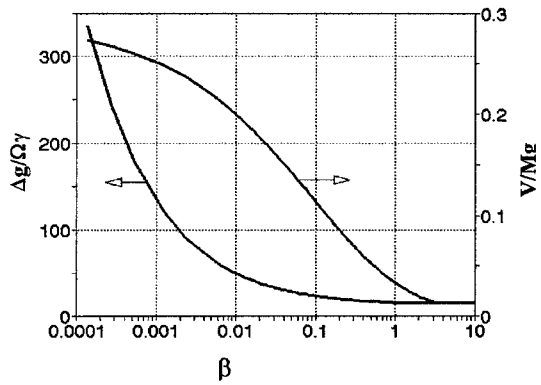

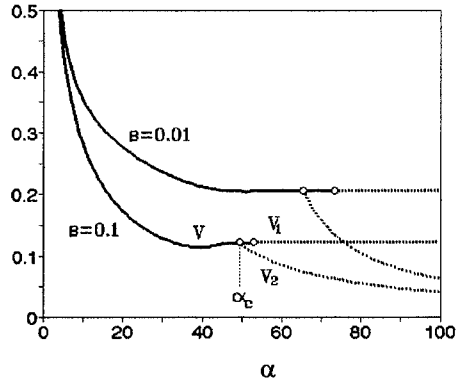

Fig.3:Discontinuous homogeneisation by finger propagation a) width and velocity of the finger as a function of β b) 'bifurcation' map: velocity of the leading (V_1) and trailing interface (V_2) as a function of α. For a given β, the fingering solution can occur only for values of α larger that a critical value α_c.

3. Intermetallic reaction in multilayers

After the investigation of the case of full miscibility, the other natural case is the reaction of two stoichiometric phases α and β to give a third stoichiometric phase ω. If the composition of the ω phase is equal to the average composition of the two parent phases, a front propagation solution may be possible. If in contrast, stoichiometry cannot be maintained, a fingering solution at the $\alpha\beta$ interface will be observed. At the triple point we will assume both a thermodynamic equilibrium and a mechanical equilibrium, respectively given by:

$$\frac{\Delta G_0 . H}{\Omega} = H_\alpha K_{\alpha\omega}\gamma_{\alpha\omega} + H_\beta K_{\beta\omega}\gamma_{\beta\omega} \tag{4}$$

$$\begin{aligned} \gamma_{\alpha\beta} &= \gamma_{\alpha\omega}.\sin\theta_\alpha + \gamma_{\beta\omega}.\sin\theta_\beta \\ \gamma_{\alpha\omega}.\cos\theta_\alpha &= \gamma_{\beta\omega}.\cos\theta_\beta \end{aligned} \tag{5}$$

ΔG_0 is the available free energy for the reaction as it can be read using the classical tangent construction on the free enthalpy curves for the three phases. γ denotes surface energies, H dimension, and K curvatures. The single subscript refers to a phase, the double subscript to an interphase. The same equations will be solved numerically with different geometrical boundary conditions to describe both the propagating front and the fingering solution.
The relevant equations for the mass transport in the present problem are Mullins' equations [8]. The driving force for mass transport is the gradient of curvature. This leads to the following expression for the flux J and a mass conservation equation:

$$J = \frac{L.\Omega.\gamma}{(c - c_\omega)} . \frac{\partial^2\theta}{\partial s^2}, \qquad (c - c_\omega).V\cos\theta = \frac{\partial J}{\partial s} \tag{6}$$

Ω is the atomic volume, L a mobility coefficient, γ a surface energy, c are concentrations of the diffusing element, and s is the curvilinear coordinate. This flux equation has to be written both for the α and the β phase.

3a. Single propagating front.

In the small slope approximation, a full analytical solution can be obtained. It leads to an explicit expression for V:

$$V = A.\frac{1}{H^3}.(\gamma_{\alpha\beta} + \frac{\Delta G_0 . H}{\Omega}) \tag{7}$$

where the numerical constant A depends on the concentrations of the three phases and on the mobilities L.

The general solution, obtained numerically, has new and interesting features. For each phase α and β, one can derive a relation:

$$\frac{VH^3}{B} = F(\theta, KH) \tag{8}$$

B is related to the mobility L. The mechanical equilibrium prescribes the angles, the thermodynamic equilibrium relates the curvatures K to the driving force. For the sake of simplicity we focus on the case where all surface tensions are equal to γ. One can then derive a relation between the velocity and the driving force:

$$\frac{VH^3}{B} = \Phi(\frac{H\,\Delta G_0}{\gamma\Omega}) \tag{9}$$

Fig. 5 shows the function Φ. It can be observed that a steady state front propagating solution exist only in a limited range of driving forces, and that for a given driving force multiple solutions are possible

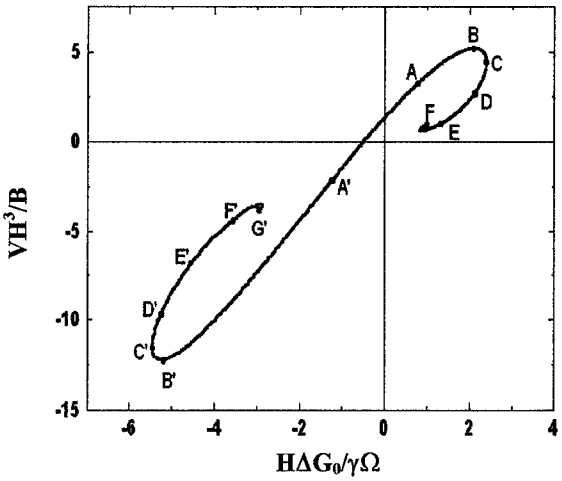

Fig. 5: Intermetallic reaction: Velocity as a function of the driving force in the non linear regime.

The possible shapes of the propagating front are shown on Fig.6 corresponding to the points marked in Fig.5. Both non re-entrant and re-entrant patterns are possible. Self crossing shapes are also possible which would correspond to droplets of parent phase included in the daugther phase after the reaction has taken place.

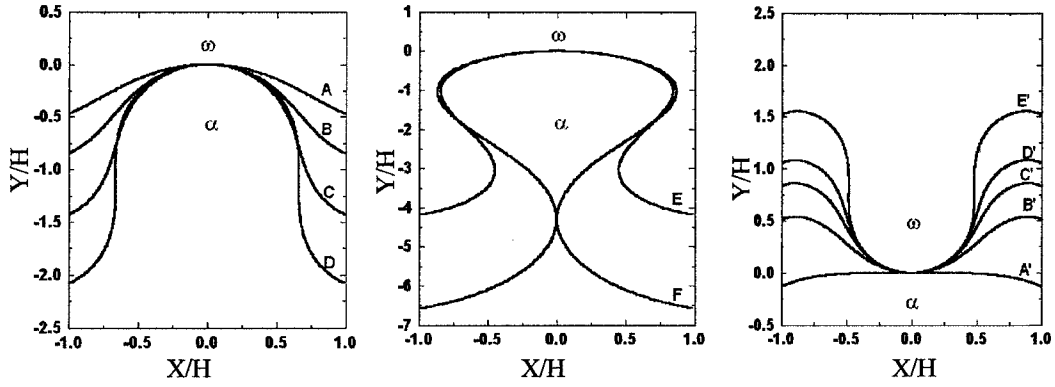

Fig. 6: Intermetallic reaction: Possible shapes for the propagating front corresponding to the points marked in Fig.5. Both non re-entrant and re-entrant patterns are possible.

3b.Interlayer fingering [11]

A fingering solution propagating at the αβ interface is also possible.
It obeys to the same equation as before. Using a solution given by Rice [12] for the growth of intergranular cavities, one can derive an approximate analytical solution to the problem which provides an expression for the thickness H and the velocity V of the finger:in the case of totally equivalent interfaces, and for a composition of α,β and ω equal to A, B and AB, it reduces to:

$$H = (4 - 2\sqrt{3}).\frac{\Omega\gamma}{\Delta G_0} \quad , \qquad V = 143.L.\frac{\Delta G_0^3}{(\Omega\gamma)^2} \tag{10}$$

(the formulae in the most general case can be found in reference [11]). The simple scaling laws predicted as function of the driving force should be amenable to experimental investigation.

4.Conclusions

In this paper we have investigated two classes of destabilising mechanisms in multilayers, associated with interface diffusion and migration. One possibility is the migration of a single preexisting front, the other possibility is the formation of "reaction fingers " along the initial interfaces in the multilayer. These two classes of solutions are theoretically possible both when the initial multilayers are fully miscible and tend to form a solid solution, or when they consist in two stoichiometric phases reacting to form a third one. In both cases, it was shown that steady states with propagating fronts exist only for a limited range of driving forces.

From the theoretical viewpoint, the question of the morphological stability of the front, when such a solution exists, is still an open one. The intermediate case of a non stoichiometric phase needs also to be investigated.

From the experimental viewpoint, the situations investigated in the present paper can be realised in artificial multilayers containing grain boundaries (ideally a multilayer grown by MBE on a bicrystal substrate, more realistically, a polycrystalline textured multilayer). However it must be noticed that the ideas developed here find application in a much more wider range of materials problems. For instance the model for discontinuous homogeneisation by fingering has been adapted sucessfully to the modeling of surface alloying by grain boundary migration [13]. The intermetallic reaction model will likely find application, either to the reversion of pearlites, or to the intermetallic reactions attending mechanical alloying.

Acknowledgements

Two of the authors (YB and LK) acknowledge funding from a Franco Israelian collaborative program. GRP is grateful for the support of the Natural Science and Engineering council of Canada.

References

[1] I.Kaur, W.Gust. *Fundamental of Grain and Interphase Boundary Diffusion.* Ziegler press, Stuttgart ,1989.
[2} G.Purdy Material., v.5, R.W.Cahn, P. Haasen, E. Kramer ed., VCH, Weinheim, 1993, 305.
[3] M. Hillert, G. Purdy *Acta Metallurgica,* **26**, 233 (1978)
[4] B. Sundquist *Acta Metallurgica,* **16**, 1413 (1968)
[5] G. Solorzano, G.Purdy, G.Weatherly, *Acta Metallurgica,* **32**, 1709 (1984)
[6] *Scripta Materialia,* **27**, 649 (1992)
[7] W.W. Mullins, *J.Appl. Phys.*, **28**, 333 (1957)
[8] J.W. Cahn, *Acta Metallurgica.*, 7, 8 (1959)
[9] L.M.Klinger, Y.J.M.Brechet, G.R.Purdy *Acta Materialia,* **45**, 5005 (1997)
[10] L.M.Klinger, Y.J.M.Brechet, G.R.Purdy *Acta Materialia,* . **45**, 4667 (1997)
[11] L.M.Klinger, Y.J.M.Brechet, G.R.Purdy *Acta Materialia* , **46** ,2617 (1998)
[12] T.J. Chuang, J.R.Rice *Acta.Metallurgica,* **21**, 1625, (1973)
[13] L.M.Klinger, Y.J.M.Brechet, G.R.Purdy *Scripta Materialia,* **33**, 639 (1997)

Materials Science Forum Vols. 294-296 (1999) pp. 145-148

Diffusion Along the Moving Reaction Front of Discontinuous Precipitates in Ni-4 at.% Sn Alloy

P. Zięba[1,2] and W. Gust[2]

[1] Polish Academy of Sciences, Institute of Metallurgy and Materials Sciences, Reymonta St. 25, PL-30059 Cracow, Poland

[2] Institut für Metallkunde der Universität Stuttgart, Seestr. 75, D-70174 Stuttgart, Germany

Keywords: Discontinuous Precipitation, Grain Boundary Diffusion, EDX Microanalysis

Abstract. The technique of analytical electron microscopy has been used to determine the solute concentration profiles left behind the moving reaction front of the discontinuous precipitation reaction in a Ni-4 at.% Sn alloy. These profiles have been converted into grain boundary diffusivity values, using Cahn's diffusion equation and the data of the growth rate of the discontinuous precipitates obtained from independent measurements, but relevant for the same individual cell for which the solute distribution had already been obtained. Such a procedure was applied for the first time in the Ni-Sn system ant it provides diffusivity data, which are very similar to the values given in the literature for stationary grain boundaries.

1. Introduction

The diffusion process at a moving interface is the rate-controlling factor in many solid state phase transformations like discontinuous precipitation (DP). Quantitative studies of this reaction are mainly focused on providing a chemical solute diffusivity ($s\delta D_b$) value which is the triple product of the grain boundary chemical diffusion coefficient D_b, the grain boundary thickness δ and the segregation factor s. The technique of analytical electron microscopy (AEM) has been shown [1-5] to have a great potential in determining the redistribution of the solute atoms, resulting in the formation of a new phase during the DP reaction.

In the present paper the technique of AEM was used to determine the solute concentration profile left behind the moving reaction front of the DP reaction in a Ni-4 at.% Sn alloy after ageing at various temperatures. This allowed, for the first time, to treat the DP reaction as a local phenomenon occurring in a single cell.

2. Experimental

A series of samples of the Ni-4 at.% Sn alloy was prepared as previously [6] and aged in evacuated silica capsules in the temperature range from 725 to 875 K. Thin foils for the transmission electron microscopy (TEM) study were prepared by dimpling and ion beam thinning using a GATAN Duo-Mill 600 instrument. The observation of the microstructure was carried out, using a transmission electron microscope Philips CM 20 Twin operating at 200 kV and equipped with an energy dispersive X-ray spectrometer (EDX) Link exL, enabling a high spatial resolution analysis of the local changes in the solute content. The details of the EDX analysis are described elsewhere [6].

The reaction front velocities for the DP reaction were assessed directly on thin foils during the TEM observation. In order to accomplish this, a two step ageing was applied described in details in Ref. [5]. The first stage was to develop the DP reaction at most of the grain boundaries. During the second stage, always at a temperature 50 K higher than the previous one, a new layer of discontinuous precipitates grew. As the interlamellar spacing obtained in the second stage was larger than that formed at the lower temperature, it was easy to distinguish the growth distance of the second stage from that of the first one. The thickness of the α lamellae was determined directly from the TEM micrographs for the lamellae oriented perpendicularly to the field of view by appropriate tilting of the thin foil holder.

3. Results and Discussion

In agreement with previous studies of the ageing behaviour of Ni-Sn alloys [6-8], the supersaturated solid solution α_o decomposes into a lamellar mixture of α solid solution of a lower tin content and the intermetallic compound Ni_3Sn. The typical overall morphology of the DP reaction is illustrated in Fig. 1a, which is a colony of several alternating α and Ni_3Sn lamellae, moving into the supersaturated solid solution at the so-called steady state growth of the reaction.

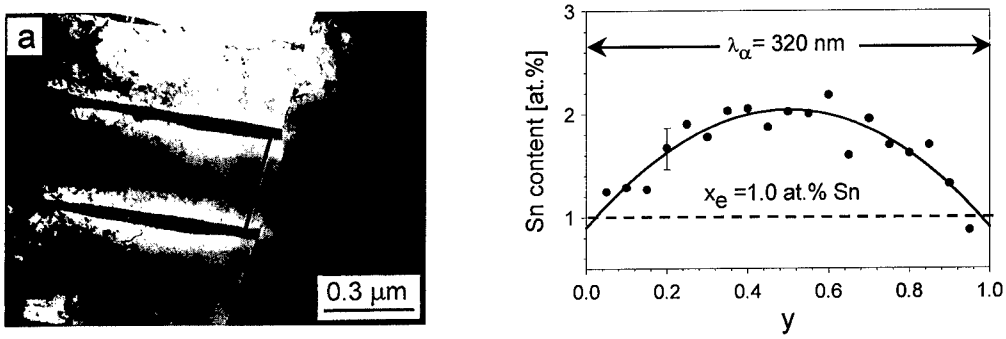

Fig. 1. Ni-4 at.% Sn alloy aged for 250 h at 725 K followed by 60 h at 775K. (a) TEM micrograph, and (b) example of a tin concentration profile measured across the α lamella. The location of the EDX line-scan is shown in Fig. 1a.

The measurements of the solute profiles across the α lamellae were performed only in those lamellae, which exhibited parallel growth for a distance of at least 1 μm, not disturbed by branching or re-nucleation of the new Ni_3Sn lamellae. Only those colonies were considered where the arrays of cells were perpendicular to the reaction front. In order to avoid the influence of the stop- and -go fashion of the reaction front (RF) movement on the solute concentration profiles [5, 9, 10], the EDX analysis across the α lamellae was preceded by the measurements of the solute content within the α lamellae in the direction perpendicular to the RF, starting from the RF till a distance of approximately 200 nm with steps of 25 nm. Cells, for which remarkable variations in the tin content were detected, were not taken into account. A typical tin concentration profile is shown in Fig. 1b. As one can see, the profile clearly reflects the excess in the tin content compared to the equilibrium concentration x_e due to an incompleteness of the DP reaction. It is symmetrical in regard to the middle of the α lamellae, which suggests that the growth of the cell was not disturbed by any crystallographic or concentration instabilities. The solid line represents the best fit of the experimental points to Cahn's equation [11]:

$$x(y) = (x_e - x_o)\frac{\cosh\left[(y-0.5)\sqrt{C}\right]}{\cosh(\sqrt{C}/2)} + x_o \qquad \text{with} \qquad C = \frac{v^2\lambda_\alpha^2}{s\delta D_b} \tag{1, 2}$$

Here, x_o is the solute content in the alloy, v is the growth velocity of the DP reaction and y is the normalized co-ordinate measured from the edge of the β lamella in the direction perpendicular to the α lamella.

The fitting procedure provides the optimum value of the parameter C as well as the solute concentration x_e at the α/β interface by extrapolation of the solid line to the positions $y = 0$ and $y = 1$. Table 1 contains all the details of the EDX analysis made across 10 lamellae randomly chosen from 10 different colonies for which the growth rates were previously determined after ageing at 775 K. As one can see, every lamella is characterized by different values of the C parameter. Also, the growth rate can differ even by a factor of ten. The values of the Sn concentration at the α/Ni_3Sn interface are in a rather good agreement with the equilibrium value (x_e = 1.0 at.%) [12] which is consistent with previous results obtained for the same alloy [6] and also by Porter and Edington [1] for Mg-Al alloys and by Zięba [5] for the Co-13 at.% Al alloy. The same holds true for the ageing at 825 and 875 K.

Table 1. Details of the discontinuous precipitation after ageing at 775 K.

Lamella No.	λ_α [nm]	v [m/s]	C	x_e [at.% Sn]	$s\delta D_b$ [m^3/s]
1	250	$1.1\cdot10^{-9}$	3.51	1.10	$1.8\cdot10^{-23}$
2	170	$4.3\cdot10^{-9}$	2.74	0.95	$4.5\cdot10^{-23}$
3	200	$7.2\cdot10^{-9}$	2.35	1.02	$1.2\cdot10^{-22}$
4	280	$9.3\cdot10^{-10}$	4.24	0.98	$1.7\cdot10^{-23}$
5	300	$3.2\cdot10^{-9}$	4.67	1.01	$6.2\cdot10^{-23}$
6	270	$1.3\cdot10^{-9}$	4.52	0.91	$2.1\cdot10^{-23}$
7	350	$4.3\cdot10^{-9}$	5.75	1.07	$9.1\cdot10^{-24}$
8	320	$2.8\cdot10^{-9}$	4.31	0.90	$6.6\cdot10^{-23}$
9	400	$2.3\cdot10^{-10}$	6.33	0.97	$5.8\cdot10^{-23}$
10	320	$5.1\cdot10^{-10}$	4.79	1.06	$1.1\cdot10^{-23}$

The diffusivity at the migrating reaction front of the DP reaction is the final information, which can be drawn from the EDX measurements of the solute content profiles. The triple products $s\delta D_b$ extracted directly from the values of the C parameters are presented in Fig. 2 in the form of the Arrhenius dependence along with the values obtained by Frebel, Predel and Klisa [7] for the DP reaction in the Ni-4 at.% Sn alloy, and the values of tracer diffusion of tin along stationary grain boundaries in polycrystalline nickel [13]. One should note that Frebel et al. [7] applied the so-called global concept of the DP reaction and the Petermann-Hornbogen equation [14]. Here it is assumed that the reaction proceeds with an average velocity for an average lamellae thickness and an average released saturation expressed by an average solute content within the lamellae. This resulted in average values of the diffusivity at the reaction front. This information was derived by quantitative metallography and X-ray diffraction performed for the whole population of cells representative for the whole sample. The solid line for the $s\delta D_b$ obtained applying the local concept of the DP reaction is an arithmetic mean from 10 independent measurements (crosses) for each ageing temperature.

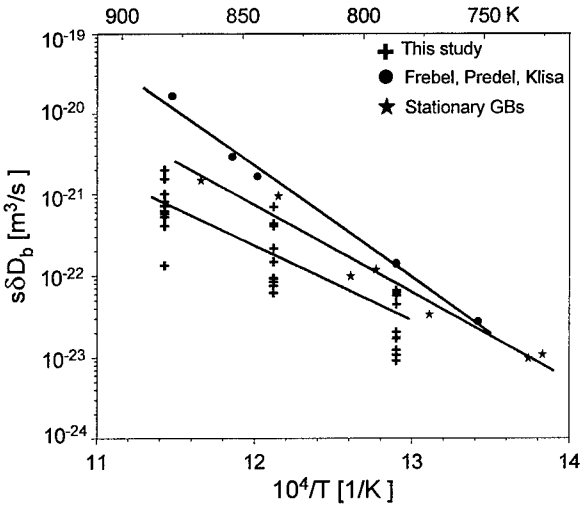

Fig. 2. Arrhenius diagram for the chemical diffusion along the moving reaction front of the discontinuous precipitation in Ni-4 at.% Sn. The data of Frebel, Predel, Klisa [7] for the same alloy as well as the $s\delta D_b$ values for the tracer diffusion of tin in nickel along stationary grain boundaries (GBs) [13] are also given for comparison.

One can see that the application of the local concept for the DP reaction gives $s\delta D_b$ values extracted from Cahn's equation, which are one order of magnitude smaller than the data of Frebel et al. [7] calculated from the Petermann-Hornbogen equation. This difference diminishes significantly with the decrease of the ageing temperature.

Considering the above discussion and the fact that the volume diffusion is much to slow to affect the occurrence of the DP reaction in the investigated temperature range, it can be concluded that this phase transformation is governed by the diffusion of tin atoms along the reaction front. Moreover, the data of the tracer diffusivity for stationary grain boundaries (see Fig. 2) are slightly greater but rather on the same order of magnitude as those obtained applying the local concept as well as the Petermann-Hornbogen equation for the DP reaction. This leads to the conclusion that the diffusion along migrating and stationary grain boundaries occurs about equally fast.

Acknowledgement-One of the authors (P.Z.) would like to expresses his gratitude to the Humboldt Foundation for financial support during this work.

References

[1] D.A. Porter, J.W. Edington, Proc. Royal Soc. A 358 (1977), p. 335.
[2] D. Duly, M.C. Cheynet, Y. Brechet, Acta Metall. Mater. 42 (1994), p. 3843.
[3] I.G. Solorzano, G.R. Purdy, G.C. Weatherly, Acta Metall. 32 (1984), p. 1709.
[4] P. Zięba, Acta Mikrochimica, Suppl. 15 (1998), in press.
[5] P. Zięba, Acta Mater. 46 (1998), p. 369.
[6] P. Zięba, W. Gust, Z. Metallk. 88 (1997), p. 270.
[7] M. Frebel, B. Predel, U. Klisa, Z. Metallk. 65 (1974), p. 311.
[8] M. Frebel, B. Predel, U. Klisa, Z. Metallk. 65 (1974), p. 469.
[9] A. Bögel, W. Gust, Z. Metallk. 79 (1988), p. 296.
[10] S. Abdou, I.G. Solorzano, M. El-Boragy, W. Gust, B. Predel, Scripta Mater.34 (1996), p. 1431.
[11] J.W. Cahn, Acta Metall. 7 (1959), p.18.
[12] P. Nash, A. Nash, Bull. Alloy Phase Diagrams 6 (1985), p. 350
[13] P. Neuhaus, C. Herzig, Acta Metall. 35 (1987), p. 881.
[14] J. Petermann, E. Hornbogen, Z. Metallk. 59 (1968), p. 814.

Materials Science Forum Vols. 294-296 (1999) pp. 149-152

Reversal from Depletion to Enrichment of Solute Elements in Radiation-Induced Segregation at Grain Boundaries

W. Kesternich[1], A. Garcia-Borquez[2] and G. Crecelius[3]

[1] Institut für Festkörperforschung, Forschungszentrum Jülich, D-52425 Jülich, Germany

[2] Instituto Politecnico Nacional, MX-07738 Mexico D.F., Mexico

[3] Institut für Schicht- und Ionentechnik, Forschungszentrum Jülich, D-52425 Jülich, Germany

Keywords: Irradiation, Segregation, Precipitates, Defects, Grain Boundaries, Steel, Intergranular Corrosion

Abstract

Ni^{++} ion irradiations of a Nb-stabilized steel of type 1.4981 were performed at 400, 500, and 600°. Dislocation loop evolution with increasing dose and radiation-induced segregation at grain boundaries were observed by transmission electron microscopy. At low doses the typical radiation-induced segregation behaviour at grain boundaries, as commonly observed in steels and Fe-Ni-Cr alloys, is confirmed. At high doses the segregation behaviour at grain boundaries was found to be completely inverted, i.e. elements which were radiation-enriched at the grain boundaries at low doses were now depleted and vice versa. This is attributed to the formation and growth of radiation-induced precipitates with increasing dose. The precipitates were only found after irradiation at 500 and 600°C and to doses higher than 5 dpa. They are rich in Ni, Si, and Nb. The effect of inverse radiation-induced segregation at grain boundaries could possibly be useful for solving the problems arising from radiation-assisted sensitization and stress corrosion cracking.

1. Introduction

Thermal segregation of solute atoms at grain boundaries causes changes of their structural and physical properties. As a result, the integrity of materials may be lost. Intergranular stress corrosion cracking (IGSCC) in austenitic steels and Ni-base alloys is the most prominent example and is due to Cr depletion at grain boundaries which is caused by the formation of Cr-rich grain boundary precipitates. Even stronger are changes in the grain boundary composition under irradiation originating from radiation-induced segregation (RIS) [1]. RIS results from fluxes of excess vacancies and interstitials to their respective sinks and the discriminative coupling of certain species of solute atoms to these point defect fluxes. Many investigations of RIS have been performed on binary alloys and also on more complex alloys [1,2]. While original work has been predominantly carried out on RIS at specimen surfaces and its effect on phase stability, recently the study of RIS at grain boundaries has experienced a revival due to the severe problems which irradiation-assisted stress

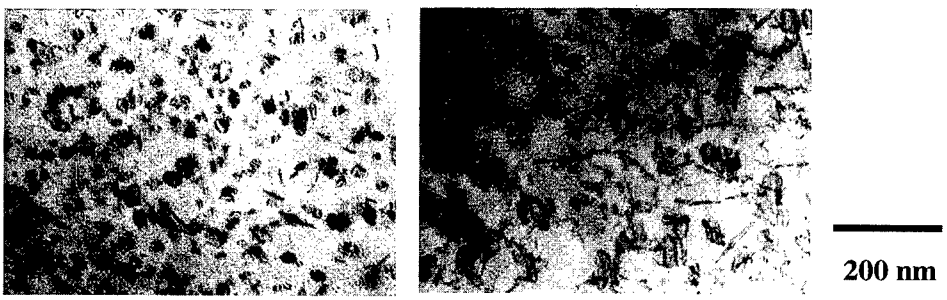

Fig. 1: Dislocation loops after irradiation at 600°C to 9.6 (left) and 51 (right) dpa

corrosion cracking (IASCC) creates for water-cooled core components in fission reactors [3] and possibly for the ITER fusion reactor concept [4]. It is implicated that the dominant contribution to IASCC in austenitic stainless steels and high-temperature Ni-base alloys is due to RIS by Cr depletion and possibly Si enrichment at the grain boundaries [4]. Ti- and Nb-stabilizations that have been used to prevent IGSCC are ineffective, however, in reducing IASCC, due to the different mechanisms responsible for the Cr depletion. A Nb-stabilized steel has been used in the present investigation to study the effect of irradiation temperature and dose on RIS and precipitation (RIP).

2. Experiment

The Nb-stabilized steel is of type 1.4981 (German DIN specification). Its composition in weight percent is 64.3 Fe, 15.9 Ni, 15.5 Cr, 1.8 Mo, 1.2 Mn, 0.59 Nb, 0.50 Si, and 0.03 C. The specimens were cold rolled to 0.1 mm thickness and solution annealed at 1100°C for 1 hour. 3.66 MeV Ni^{++} ion irradiation was performed to various doses at 400, 500, and 600°C. Specimens for transmission electron microscopy (TEM) were prepared at special depths of interest below the irradiated surface applying controlled depth and cross-section electropolishing techniques [5]. Energy dispersive X-ray (EDX) spectroscopy for microchemical analysis of precipates and across grain boundaries was carried out in a TEM with LaB_6 source and in a dedicated scanning TEM with field emission gun (FEG). The electron beam diameters, experimentally determined at TiC/precipitate interfaces in a Ti-containing steel, were 20 to 30 and 2 to 3 nm for LaB_6- and FEG-TEM, respectively. Specimen thicknesses for the estimation of beam broadening and for absorption and fluorescence corrections were determined from X-ray yield [6]. For obtaining quantitative segregation results, the EDX spectra were in-hole, absorption, and fluorescence corrected.

3. Results and Discussion

At all three temperatures, irradiation led to the formation of dislocation loops visible at relatively low doses in the form of black dots. Dislocation loops, revealing stacking fault contrast are shown in Fig. 1 after irradiation at 600°C to 9.6 and 51 dpa. At increasing doses, the interaction of dislocation loops leads to formation of dislocation networks (see 51 dpa). Radiation-induced precipitates (RIP), probably nucleated at dislocation loops as a consequence of RIS, were only found at 500 and 600°C and not at the lower temperature of 400°C. Precipitates at 600°C and 250 dpa are shown in Fig. 2. Some have bulky, others platelet shape. The latter are revealed in the figure via two families of platelet precipitates which are viewed edge-on. After 600°C irradiation, RIP in the matrix was observed at 9.6 dpa and higher, RIP at grain boundaries at 17 dpa and higher.

For all three irradiation temperatures, RIS at grain boundaries was observed. The effect increased

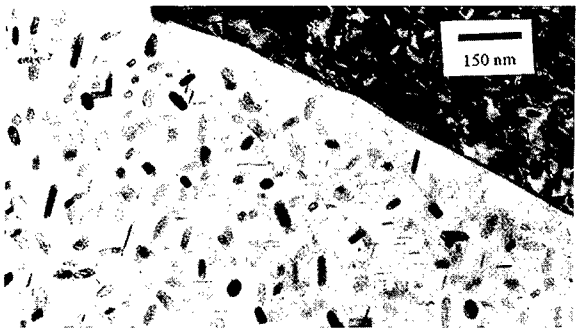

Fig. 2: Radiation-induced precipitates after irradiation at 600°C to 250 dpa

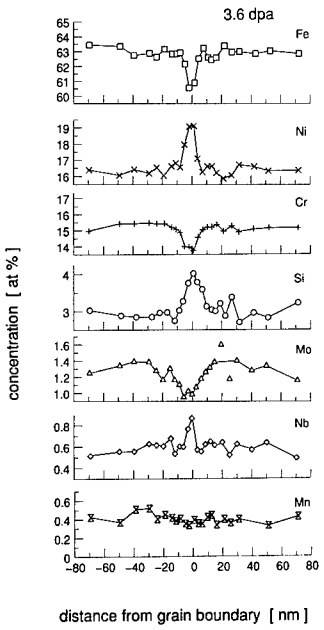

Fig. 3: RIS at a grain boundary, 600°C, 3.6 dpa

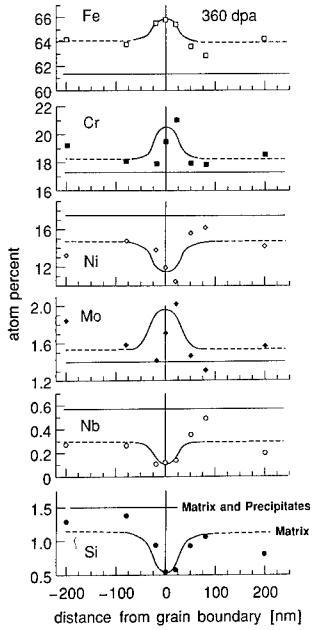

Fig. 4: Inverted RIS at a grain boundary, 600°C , 360 dpa

with temperature from 400 to 600°C and was investigated in detail at 600°C. As is shown in Fig. 3, Ni and Si are enriched, and Cr and Mo depleted at the grain boundaries, while a local change of Mn concentration cannot be detected within the present measuring accuracy. These RIS effects are in agreement with previous RIS observations at grain boundaries in Fe-Ni-Cr alloys and steels. In addition we observed a Nb enrichment at grain boundaries. At high doses of 360 dpa, the investigation of segregation at grain boundaries was repeated in the same way. Results are shown in Fig. 4. All elements which were depleted at grain boundaries at low doses (Fe, Cr, Mo) were now enriched and vice versa (Ni, Nb, Si). Hence, at high dose irradiation, segregation at grain boundaries in the Nb-stabilized steel was completely inverted (i.e. for all elements) as compared to the low dose and compared to all previously reported RIS observations in steels.

In addition to the data points for the concentration profiles across the grain boundary, Fig. 4 contains a dashed line for each element, indicating the average concentration measured in the matrix far away from grain boundaries, and a solid horizontal line each, indicating the total concentration of the respective element. The latter values were measured by using a wide, defocussed electron beam, thus including an average of matrix and precipitates, but no grain boundaries. The differences for each of the two lines shows that the precipitates are rich in those elements, which are depleted at the grain boundaries and vice versa. This preferential incorporation of certain elements into radiation-induced precipitates can also directly been measured by EDXS on individual preicipitates. Fig. 5 shows an EDX spectrum of a precipitate extending into the hole of the electropolished specimen. As is seen in the inset of the figure the indicated precipitate is covered with only a thin layer of matrix. For a quantitative evaluation of the precipitate composition, knowledge of the thickess of the matrix layers above and below the precipitate would be required. Qualitatively, however, the high affinity of the radiation-induced precipitates to Si, Ni, and Nb is obvious from this spectrum when compared with the matrix composition given in Sec. 2.

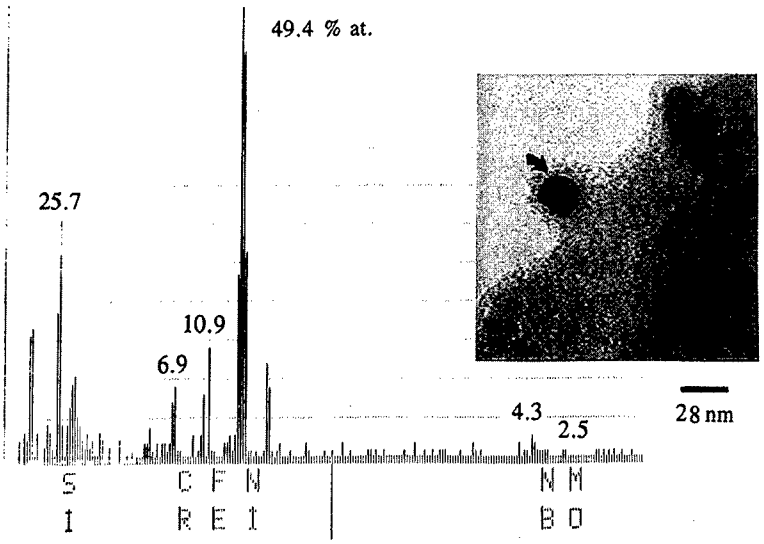

Fig. 5: EDX spectrum and image of a radiation-induced precipitate (arrow), 600°C, 250 dpa

In the sequence of irradiation doses, at first dislocation loops and segregation at grain boundaries were observed, at higher doses RIP in the matrix, and at still higher doses RIP at grain boundaries and finally inverted RIS at grain boundaries. It is suggested that inverted RIS is a consequence of RIP formation at the grain boundaries. Analogously to the reduction of Cr content at grain boundaries, which occurs as a consequence of Cr carbide precipitate formation at the grain boundaries under thermal aging, it is concluded that the formation of radiation-induced grain boundary precipitates, being rich in Ni, Si, and Nb, lead to a depletion of Ni, Si, and Nb in the grain boundaries. It is further assumed that radiation-enhanced diffusion of these elements is faster along grain boundaries to the precipitates than from the matrix into the grain boundaries thus leading eventually to the observed inversion of the segregation. This is again analogous to the thermal diffusion of Cr which is obviously faster along grain boundaries including incorporation into the growing Cr carbide precipitate than is diffusion of Cr from the matrix towards the grain boundary for restoration of the Cr deficiency. These are two analogous mechanisms leading, however, to opposite results regarding intergranular corrosion. In the case of thermal precipitate formation, Cr is depleted leading to sensitization, while in the case of RIP formation Cr is enriched leading to radiation stabilization against intergranular corrosion. Two processes have alternatively been made responsible for IASCC: Cr depletion in the one case and Si enrichment in the other. The present radiation-stabilization is effective in both cases, since Cr is enriched as well as Si depleted at the grain boundaries.

References

[1] P.R. Okamoto, L.E. Rehn, J. Nucl. Mater. 83 (1979) p. 2.
[2] L.E. Rehn, P.R. Okamoto, in: Phase Transformations during Irradiation, F. Nolfi, ed. (1983) p. 247.
[3] G.S. Was, S.M. Bruemmer, J. Nucl. Mater. 216 (1994) 326.
[4] E.P. Simonen, R.H. Jones, S.M. Bruemmer, J. Nucl. Mater. 1002 (1992) p. 191.
[5] A. Garcia-Borquez, W. Kesternich, Microscopy Research and Techn. 25 (1993) p. 255.
[6] W. Kesternich, in: Proc. 8th Europ. Congr. on Electron Micr., Budapest, vol 2 (1984) p. 837.

Materials Science Forum Vols. 294-296 (1999) pp. 153-156

Local Segregation at the Grain Junction: Elastic Singularity and its Effect on Radiation Embrittlement

A.A. Zisman and V.V. Rybin

Central Research Institute of Structural Materials-«Prometey»
49 Shpalernaja, St. Petersburg RU-193015, Russia

Keywords: Grain Junction, Junction Disclination, Mesoscopic Stress, Point Defect Re-Distribution, Phosphorus Impurity, Local Decohesion

Abstract Under consideration are the long-range stress field generated in deformed polycrystals by grain boundaries and junction lines and corresponding re-distribution of impurity atoms due to their elastic interaction with this stress field. Evaluation of the effect is made for deformed bcc polycrystals at 270°C containing the phosphorus impurity. It is assumed that under neutron irradiation the impurity atoms are in interstitial positions and form mixed P-Fe dumb-bells having a relaxation volume of about an atomic volume of host crystal. Corresponding re-distribution results in the impurity conglomeration around grain junction lines; in the areas as wide as 10% of the grain size the local P concentration is more than 50% higher then its mean concentration. Respective local segregations are considered to facilitate the brittle fracture origination, and the impurity-dependent component of radiation embrittlement is discussed within this framework.

1. INTRODUCTION

In studying the segregation phenomenon grain boundaries are usually considered as passive two-dimensional traps that do no direct influence on far spaced point defects. Under such an assumption the segregated impurity distribution over interfaces is to be nearly uniform, and corresponding embrittlement is treated in terms of the average impurity concentrations, both the vilumetric and interfacial.

At the same time the phosphorus-dependent radiation embrittlement of ferritic-martensitic RPV steels can hardly be explained within the framework mentioned above. Numerous data [1-3] display the embritllement with no significant fraction of the intergranular fracture, nor clear signs of extensive grain boundary segregations. A most plausible explanation of the fact is that the segregation is sharply non-uniform and, consequently, manifests itself only **locally**, when facilitating the microcrack nucleation at most contaminated microareas [3].

In the present paper under consideration is the impurity re-distribution in interaction with the mesoscopic stress field generated by interfacial and junction defects. The latter are inherent in deformed polycrystals since misoriented grains display different plastic compliance in relation to the deforming stress and are subjected to different plastic strains. In accordance with [4,5] corresponding mismatches, accumulated at interfaces, represent a totality of planar stress sources stretched on the junction disclination skeleton. The junction disclinations [4] situated along triple lines are of special value in this consideration as the related elastic singularities attract point defects, in particular impurity atoms [6]. In what follows the mesoscopic stress field in deformed bcc polycrystals is evaluated in accordance with the analytical technique presented in detail in Ref .[6].

Molecular dynamics simulation of the phosphorus impurity interaction with primary radiation defects shows that under irradiation the impurity atoms take interstitial positions and form mixed P-Fe dumb-bells [7]. Taking in mind the relaxation volume of the host Fe-Fe dumb-bell being about 1.5 V_{at}, [8], where V_{at} is an atomic volume in iron crystal, and the phosphorus being undersized impurity, we will estimate its relaxation volume in irreadiated iron as $V_{at} = 1.162 \cdot 10^{-29}$ m^3.

2. STRESS FIELD AND IMPURITY DISTRIBUTION AT TRIPLE LINE

Under consideration is three grains of hexagonal cross section embedded altogether into homogeneous equivalent medium representing the average polycrystal properties. The internal stress due to the grain interaction is related only with the non-uniform component ξ of the the plastic strain [6], which is assumed to be of 0.2% magnitude and to differ among neighboring grains in direction of main axes, Fig .1 :

$$\xi_i = 0.002(\mathbf{e}_1\mathbf{e}_1 - \mathbf{e}_2\mathbf{e}_2)^{(i)} . \qquad (1)$$

The hydrostatic component σ_o of the respective stress field, calculated following Ref.[6], is represented at lower part of Fig.2 and displays an essential singularity around the triple line. The equilibrium distribution of the impurity is expressed as

$$\mathbf{c} = \langle \mathbf{c} \rangle \exp\{- W^{int} / kT \} , \qquad (2)$$

where **c** and $\langle \mathbf{c} \rangle$ are respectively local and mean impurity concentration, W^{int} is its interaction energy with the stress field considered, k is Boltzman's coefficient and T is the absolute temperature in K. For the first approximation the interaction energy can be estimated as

$$W^{int} = - \sigma_o V_{at} . \qquad (3)$$

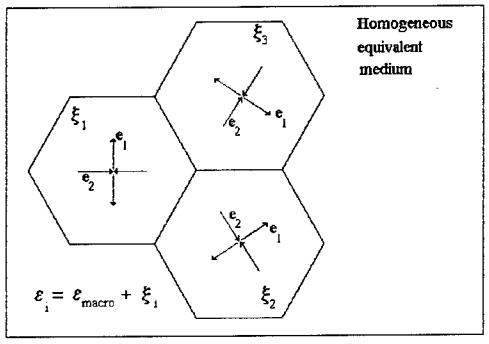

Figure 1. Incompatible parts of grain plastic strains at triple junction.

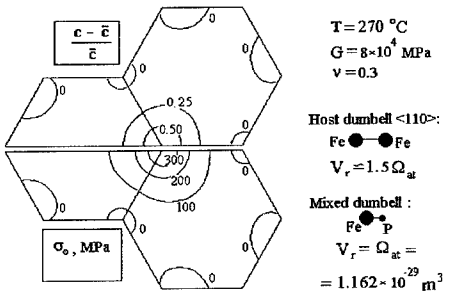

Figure 2. Hydrostatic stress field (lower) and corresponding equilibrium distribution of P impurity (upper) at the triple grain junction.

The equilibrium impurity distribution calculated with equations (2) and (3) at 300°C is represented on the upper half of Fig.2.

3. RADIATION EMBRITTLEMENT

The segregation effect on the radiation embrittlement is most easy to interpret with the Ioffe scheme [9], Fig. 3(a), for definition of the ductile to brittle transition tempereture (DBTT). In this scheme the segregation-related interfacial decohesion, reflected by a reduction of the resistance R to brittle fracture, is distinguished from the hardening effect represented by shifting the temerature dependence of the yield stress σ_y, Fig.3(b).

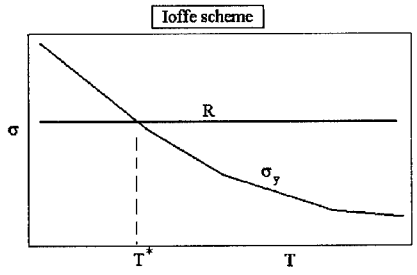

Figure 3 (a) . Ioffe scheme for DBTT.

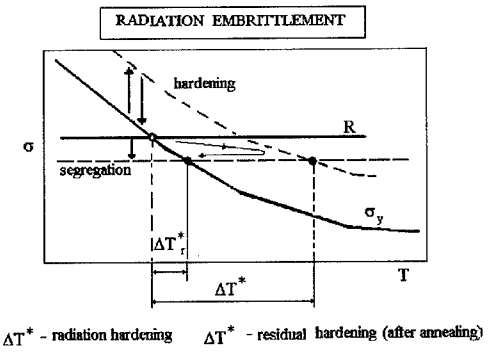

Figure 3(b). Radiation hardening and segregation effects. DT* is the residual embrittlement after annealing.

The resistance to brittle fracture R is expressed through the origin microcrack length L*, Ref.[10], as

$$R=(4\gamma_o E /\pi L^*)^{1/2} , \quad (4)$$

where γ_o is the free surface specific energy and E is Young`s modulus. It is supposed that the origin microcrack arises at the local boundary area and then propagates by the transcrystalline manner. Under such an assumption, let us consider the residual embrittlement after the radiation hardening was eliminated by annealing, yet more stable local segregations are still kept together with respective R reduction, Fig.3(b). In this case

$$\Delta T^* = (R-R^*) /(\Delta\sigma_y / \Delta T) . \quad (5)$$

The slope $\Delta\sigma_y /\Delta T$ for RPV steels in the region of interest is about –2Mpa /°C, while ΔT^* is about 40°C, [1-3]. Taking a typical value R=1000 MPa, one obtains from equation (5) the residual value R*=920 MPa. According to equation (4), that corresponds to the critical microcrack length of 0.5 to 1 mkm. In view of the results, represented on Fig.2 above, it does no seem unlikely that a local conglomeration of phosphorus within the area of more than 2 mkm diameter around the triple line results in respective local segregation and decohesion.

4. CONCLUSION

Real RPV steels, subjected to phase transformation and plastic deformation on the technological stage, contain the mesoscopic (grain scaled) stress fields due to the grain difference in plastic or

phase deformations. This stress, when interacting under irradiation with impurity atoms results in the latter`s local conglomeration around grain junction lines and, consequently, local segregation on grain boundaries. Corresponding decohesion in those areas facilitate nucleation of brittle microcracks, which then can develop within the grain volume. Proposed model gives some explanation of impurity-related radiation embrittlement in case when extensive segregation and high fraction of intergranular fracture are not observed.

REFERENCES

[1] N.N Alekseenko, A.D.Amaev, I.V.Gorynin and V.A.Nikolaev, Izv.Akad. Nauk SSSR. Metally **2** (1981), p.2 (in Russian).
[2] V.A.Nikolaev and V.I.Badanin, Atomnaja Energija **47** (1979), p.21 (in Russian).
[3] V.A.Nikolaev, V.V. Rybin and V.I.Badanin, Atomnaja Energija **47** (1979), p.21 (in Russian).
[4] V.V.Rybin, A.A.Zisman and N.Yu.Zolotorevsky, Acta Metall.Mater. **41** (1993),p.2211.
[5] A.A.Zisman and V.V.Rybin, Acta Metall.Mater. **44** (1996),p.403.
[6] A.A.Zisman and V.V.Rybin, Acta Metall.Mater. **46** (1998),p.457.
[7] A.A.Vasiliev, V.V.Rybin and A.A.Zisman, Journ.Nucl.Mater. **231** (1996), p.249.
[8] R.A.Jonhson, Phys.Rev. **A134** (1964), p. 1329.
[9] A.F.Ioffe, Uspekhi Fizich.Nauk **8** (1928), p.489 (in Russian).
[10] A.N.Stroh, Adv.Phys. **6** (1957), p.3.

Materials Science Forum Vols. 294-296 (1999) pp. 157-160

Effects of Interaction between Point Defects and Solutes on Grain Boundary Segregation and Migration

H. Kanda, H. Takahashi, N. Hashimoto and N. Sakaguchi

Center for Advenced Research of Energy Technology, Hokkaido University,
Kita-ku, kita-13, nishi-8, Sapporo 060-8628, Japan

Keywords: Grain Boundary Migration, Segregation, Point Defects, Size Effect, Electron Irradiation, Ni-Si Alloy

Abstract: In order to investigate the mechanisms of radiation-induced grain boundary migration,a 316 model steel and Ni-(2-10)at%Si model alloys were electron-irradiated. Boundary migration was often observed in stainless steels and the model alloys during irradiation. An initial incubation and three migration stages were observed.The incubation period depended on irradiation temperature and solute concentration. From the temperature dependence of boundary migration velocity during the first stage and the incubation response, activation energies were estimated. The activation energies obtained for each alloy were lower than that for boundary migration under thermal annealing. It is suggested from these results that the grain boundary migration under irradiation is caused by enhanced boundary diffusion and preferential rearrangement of under sized interstitial solute atoms diffusing via a mixed dumbbell mechanism towards the grain boundary.

1. Introduction:

Under irradiation, solute redistribution in concentrated alloys occurs because of the preferential interaction between solute atoms and super-saturated point defects moving toward point defect sinks, such as surfaces or grain boundaries. The grain boundary migration phenomenon is a well-known process controlling recrystallization and grain growth during annealing. It is caused by the diffusion and absorption of vacancies. Diffusion-induced grain boundary migration has been recognized in various binary alloy systems[1,2].On the other hand, under irradiation environments such as in light water reactors and fast breeder reactors, grain boundary migration often occurs even at low temperatures where no grain boundary migration occurs by thermal annealing. Furthermore it has been found that solute redistribution simultaneously occurs in the grain boundary regions[3,4]. Therefore, radiation-induced grain boundary migration and solute segregation can result in significant degradation in physical,chemical and/or mechanical properties because of changes in grain boundary characteristics. It is therefore of great importance to investigate the mechanism for retardation of radiation-induced solute redistribution and the behavior of concurrent grain boundary migration under irradiation.

In this paper, the grain boundary migration phenomenon with concurrent segregation of solute atoms was studied using in-situ observation under electron irradiation for 316 stainless steel and Ni-Si model alloys.

2.Experimental procedures:

The specimens used in the present study were Fe-15wt%Cr-20wt%Ni and Ni-2,6 and 10 at%Si model alloys. The alloys were heat-treated at 1173K for 30 min and then water quenched. Thin foils were prepared from the specimens by jet-electron-polishing and then were electron-irradiated with 1000kV electrons using a high voltage electron microscope to 6 dpa in the temperature range of 573K to 773K at a damage rate of 2 x 10^{-3}dpa/sec.

3. Results

3.1. Grain boundary migration

When the region including grain boundaries was irradiated, grain boundary(G.B.) migration was often observed for each specimen and the migration behavior depended on the orientation relationship between the two grains and on the irradiation dose(time).

Fig.1 shows an example of observed G.B. migration. It was found that grain boundaries migrate under irradiation in each alloy. It has been reported that the occurrence of G.B. migration under irradiation was closely related to the orientation relation of the interfacial boundary planes facing each other[5]. Fig.2(a) shows the distance of grain boundary motion as a function of irradiation dose for Fe-15wt%Cr-20wt%Ni steel. It can be seen that the migration distance for a G.B. at a given dose became larger with increasing irradiation temperature and that the velocity of G.B. migration changed during irradiation. Furthermore, at lower temperature, the G.B. migration started after a given irradiation time and the time to initiate migration was shorter at higher irradiation temperatures. Similar behavior for G.B. migration was observed for Ni-Si model alloys as shown in Fig.2(b). From these results, the G.B. migration stages during irradiation can be divided into three stages. The first stage corresponds to G.B. migration at a high velocity during early stages of irradiation, but with further irradiation the migration slowed down (corresponding to the second stage), and then the boundary again moved at high velocity (corresponding to third stage). At lower irradiation temperature,an incubation period before the start of G.B. migration appeared prior to the first stage.

Fig.3 shows the incubation period as a function of irradiation temperature for Ni-Si and Fe-15wt%Cr-20wt%Ni alloys. It is obvious that the incubation

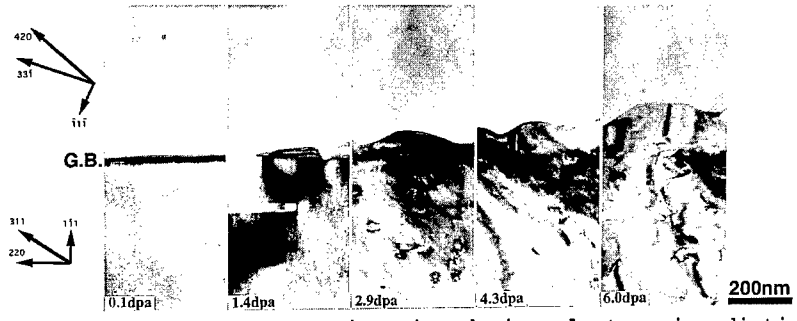

Fig.1 Microstructures showing G.B. migration during electron irradiation of Fe-15wt%Cr-20wt%Ni alloy at 723K.

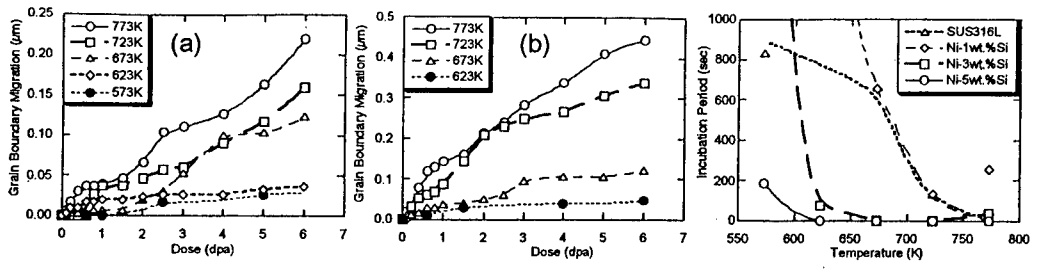

Fig.2 Relation between G.B. migration distance and dose in (a) Fe-Cr-Ni,and (b) Ni-Si alloys.

Fig.3 Incubation periods as a function of temperature.

period for each alloy was shorter at higher irradiation temperatures and with increasing Si concentration in Ni-Si alloys. Furthermore, the effect of irradiation temperature on the incubation period in Fe-15wt%Cr-20wt%Ni alloy was similar to that in the Ni-2 at% Si alloy.

3.2 Segregation after irradiation

Fig.4 shows the amount of segregation on grain boundaries after electron - irradiation at 723K to a dose of 6 dpa in Fe-15wt%Cr-20wt%Ni.

The segregation enriches Ni and depletes Cr. When the relative amount of segregation between Ni and Cr at grain boundaries is compared, it is clear that Ni solute segregation is significantly higher than Cr depletion. This means that accumulation of interstitials via a mixed-dumb-bell mechanism [6] is higher than that of vacancies which causes deple - tion of over-sized Cr solute atoms. Similar segregation behavior was observed in Ni-Si and Ni-Al binary alloys, in which Si and Cr in Ni based alloys are under-sized and over-sized solutes, respectively[7,8].

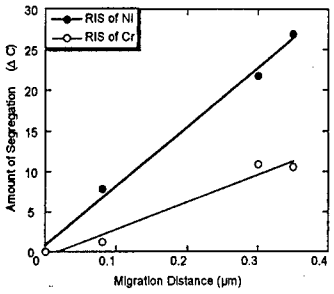

Fig.4 Segregation of Ni and depletion of Cr after G.B migration in Fe-15wt% -20wt%Ni during irradiation at 773K.

4. Discussion

As shown above, the G.B. migration velocities change depending on irradiation temperature and solute concentration. The boundary migration behavior will be closely related to G.B. diffusion and rearrangement of atoms on the migrating boundary interface. The relation between boundary migration velocity and temperature has been given by C.L.Bauer[9].Namely, G.B. migration velocity V is given by following relation:

$$V = FD/nkT \qquad (1)$$

where F,D,n,k and T denote,respectively,driving force,diffusion coefficient for the mobile atoms, number of atoms per unit boundary plane, Boltzmann constant and absolute temperature. The logarithm of G.B. velocity, V, as a function of reciprocal absolute temperature 1/T for the first stage of G.B. migration for each alloy are shown in Fig.5. The activation energies were estimated from the slopes and the activation energies obtained for migration of Ni-2,6 and 10at%Si alloys were 0.46eV,0.29eV,0.17eV, respectively. During electron-irradiation, segregation of solutes occurred and under-sized solute enriches and over-sized one depletes at defect sinks such as G.B, and this segregation is closely associated with the behavior of interstitials and vacancies. In present and previous studies it has been clarified that under-sized solutes, Si in Ni-Si alloy and Ni in a Fe-15wt%Ni-20wt%Cr alloy are segregated at G.B. This segregation and G.B. migration often occurred simultaneously. Thus, we should consider the effect of the flux of excess point defects that flow into the G.B. We assume that the incubation period before the start of G.B. migration corresponds to the time for rearrangement of atoms on coarse boundary planes into denser configurations. This rearrangement depends on the difference ($\Delta\rho$) of atomic density between two atomic planes constituting the G.B. and time (t_o) required for the rearrangement. By combining this relation with Fick's 1st Law

(assuming the concentration gradient($\Delta c/\Delta x$) is constant(A) at steady state under irradiation)

$$\Delta\rho/t_o = AD \qquad (2),$$

where A is constant,D diffusion coefficient of interstitial defect combined with under-sized solute. Fig.8 shows the relation between the logarithm of the incubation time,t_o, and reciprocal absolute irradiation temperature. An activation energies obtained from this relation were 0.21eV and 0.42eV,for Ni-6at%Si and Ni-2at%Si, respectively. The activation energy of 0.40eV was obtained for Fe-15wt%Cr-20wt%Ni. These values are consistent with those obtained from equation (1), and are very low comparing to the values for G.B.migration during thermal annealing [10], i.e for vacancies. Therefore, the activation energies obtained under electron irradiation should be for interstitial atoms in conbination with the solutes with preferential segregation of under-sized solutes. The diffusion to allow G.B. migration may be controlled by G.B. diffusion which is enhanced by irradiation. Furthermore,the diffusivity will be affected by solute concentrations combining with interstitial defects.

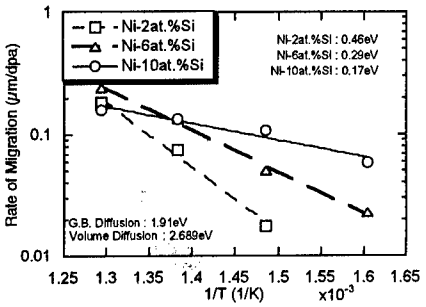

Fig.5 G.B.migration velocities as a function of 1/T in Si-Ni alloys.

5. Summary

Grain boundary migration phenomena under electron-irradiation was investigated in Fe-15wt%Cr-20wt%Ni and Ni-2,6,10at%Si alloys using a high voltage electron microscope. Grain boundary migrations were found in each alloy and during irradation three migration stages and an incubation period were observed. The velocities of the migration became faster with increasing irradiation temperature and with Si concentration in Ni based alloys. From the activation energies evaluated from G.B. migration, it is suggested that the irradiation-enhanced grain boundary diffusion of Si solute takes place and that the boundary migration is attributed to preferential rearrangement of Si solute diffused across grain boundaries on coarser atomic planes.

References

[1] F.A.Den Broeder,Acta Met.,20 (1972),P.319.
[2] Z.S.Yu and P.G.Shewmon,Met.Trans.,14A (1983),P.1579.
[3] H.Takahashi,N.Sakaguchi,N.Hashimoto and S.Watanabe,Materials Science Forum 79(1996),P.561.
[4] H.Takahashi,N.Hashimoto and H.Kanda,INTERFACE SCIENCE 4 (1997),P.221.
[5] N.Hashimoto,Y.Eda and H.Takahashi,J.Nucl.Mater.,239(1996),P.180.
[6] P.H.Dederichs,G.Lehmann,H.R.Scholz,and R.Zeller,J.Nucl.Mater., 69 (1978),P.176
[7] P.R.Okamoto and H.Wiedersich,J.Nucl.Mater.,53,336 (1974),P.176.
[8] H.Takahashi,S.Ohnuki,and T.Takeyama,J.Nucl.Mater.,103 &104 (1981),P.1415.
[9] C.L.Bauer,Defect and Diffusion Forum 66-69 (1989),P.749.
[10] W.Assassa and P.Guiraldenq,C.R.Acad.Sci.,Ser.C,279 (1974),P.59.

Materials Science Forum Vols. 294-296 (1999) pp. 161-164

Vacancy Formation and Vacancy-Induced Structural Transformation in Si Grain Boundaries

M.F. Chisholm[1], A. Maiti[1,2], S.J. Pennycook[1] and S.T. Pantelides[1,2]

[1] Solid State Division, Oak Ridge National Laboratory, Oak Ridge, TN 37831, USA

[2] Department of Physics and Astronomy, Vanderbilt University, Nashville, TN 37235, USA

Keywords: Electron Microscopy, Grain Boundary Structure, Vacancy Formation, Z-Contrast

Abstract

Atomic resolution Z-contrast scanning transmission electron microscopy reveals preferential nucleation of electron-beam-induced damage in select atomic columns of a Si tilt grain boundary. Atomic scale simulations find that the region of initial damage nucleation corresponds to columns where the formation energies of vacancies and vacancy complexes are very low. The calculations further predict that vacancy accumulation in certain pairs of columns can induce structural transformations of the grain boundary core region.

Introduction

Herein we report experimental data showing that the energetic electron beam of a scanning transmission electron microscope (STEM) induces nucleation of damage at specific locations within a Si grain boundary. This region of initial damage is found to correspond to atomic positions that are calculated to have low vacancy formation energies. We also report atomistic simulations that provide an explanation for this effect and further predict a structural transformation that may occur under suitable experimental conditions.

The experimental study was performed on a silicon bicrystal wafer containing an isolated 16° symmetric tilt boundary with the tilt axis parallel to the <001> direction ($\Sigma = 25$ {710} <001>). Plan view samples with a <001> surface normal were prepared by mechanical polishing and ion milling with 1-3 keV Ar ions, followed by characterization with high resolution Z-contrast imaging using a HB603U STEM operating at 300 kV. The compositional sensitivity of the images, which is a function of the inner detector angle, can approach the atomic number (Z) squared dependence of the Rutherford scattering. With the resulting image, no preconceived model structures are required for image interpretation, and the projected atomic arrangements are apparent immediately [3].

Results and Discussion

A symmetric $\Sigma = 25$ boundary with its common {710} plane has a period of one conventional lattice parameter (a = 5.43 Å) parallel to the tilt axis, and a period of 38.4 Å ($a\sqrt{50}$) in a direction normal to the tilt axis. In each repeat period normal to the tilt axis the grain boundary consists of two extended cores, one being a mirror image of the other, separated by a perfect crystalline region. Figures 1(a, b) display, in the projection normal to the tilt axis, Z-contrast images of one of these extended cores at two stages of exposure to electron irradiation: (a) a nearly unaffected core with nearly uniform intensity from all the columns; and (b) a partially affected core with a few of the columns having reduced brightness. Figure 2(a) displays, in the same projection, the three dimensional computer model of the boundary structure.

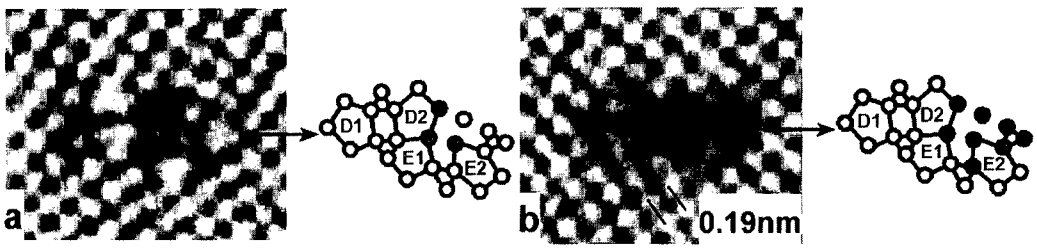

Fig. 1. Z-contrast images and derived structures of the Σ=25 {710} < 001> symmetric tilt boundary at two stages of exposure to electron irradiation: (a) a nearly unaffected core with all columns visible but those shaded showing reduced intensity; (b) a partially affected core with several columns appearing darker.

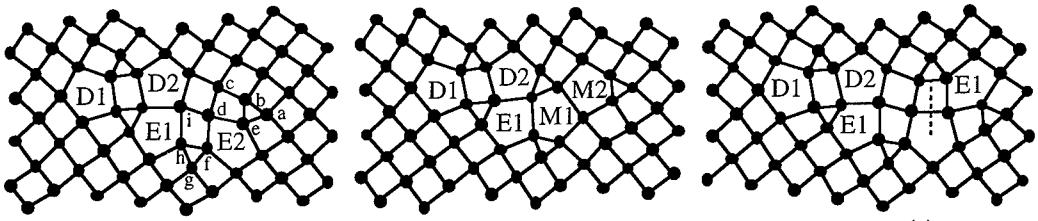

Fig. 2. (a) Three-dimensional atomic model of the boundary structure identifying the individual dislocation cores and labeling various sites, (b) the atomic structure of the transformed grain boundary resulting from the segregation of the [b, c] divacancy chain. The edge dislocation core E2 of the original grain boundary dissociates into two mixed dislocation cores M1 and M2, and (c) the transformed structure resulting from the segregation of the [a, b] divacancy chain creating an extended edge dislocation core.

A closer look at the structure of Fig. 2(a) reveals that in the undamaged grain boundary core there are four dislocation cores;[4] each dislocation core appearing as a "pentagon-triangle" combination in the projection normal to the tilt axis. All these cores have Burgers vectors in a plane normal to the tilt axis and are, therefore, perfect edge dislocations. Two of the cores, D1 and D2 are adjacent to each other and have opposite Burgers vectors, thereby constituting a dislocation dipole. The other two edge dislocation cores E1 and E2 have Burgers vectors $\frac{a}{2}<110>$ and $\frac{a}{2}<1\bar{1}0>$ respectively, where the x-direction is taken normal to the boundary plane and the y-direction taken in the grain boundary plane normal to the tilt axis. The Burgers vectors of E1 and E2 add up to a, which is the total dislocation content of the boundary core. It is interesting to note that all the columns with reduced brightness in the damaged core are located on and around the edge dislocations E1 and E2.

In the following, we discuss results of a computational analysis to understand: (1) why a small region localized around E1 and E2 is preferentially affected by electron irradiation, (2) the atomic scale processes that underlie the observed phenomenon, and (3) any possible low-energy defect configuration that might lead to a structural transformation of the boundary. To address the above points it is necessary to examine the nature of structural defects in Si produced by electron irradiation. In a relativistic elastic collision between an electron and an atomic nucleus initially at rest, the conservation of linear momentum and kinetic energy lead to the following expression for the energy transferred to the nucleus [5]:

$$E_n = T_m \sin^2(\theta / 2) \qquad (1a),$$

where,

$$T_m = \frac{E(E+2mc^2)}{Mc^2} \qquad (1b).$$

In the above, E is the kinetic energy of the electron (~ 300 keV in our case), m (M) is the rest mass of the electron (nucleus), θ is the angle through which the electron is scattered, and T_m is the maximum energy that could be transferred to the nucleus. In order to knock an atom out of its position and create structural damage, T_m must be greater than the "displacement energy" E_d. The displacement energy is somewhat larger than the formation energy of a Frenkel pair because of kinetic barriers, and has been determined experimentally to be 15 ± 5 eV for a bulk Si crystal [6]. It is expected to be smaller at a grain boundary where the formation energy of a Frenkel pair is generally smaller (by 2-4 eV; see below). Substituting for E ~ 300 keV in eq. (1b) we obtain T_m ~ 30 eV for Si, i.e., large enough to cause damage by primary knock-ons in the bulk crystal as well as in the grain boundary. The fraction of atoms in a column initially knocked out by the electron beam (i.e., the fraction of Frenkel pair defects) can be estimated from the formula:

$$f_F = n_{el}\, \sigma_d \qquad (2).$$

In eq. (2), n_{el} is the number of electrons passing through per unit area, estimated to be ~ 10^5 /Å^2 from the scan time and the electron current in the microscope probe; σ_d is the total Mott scattering cross-section of the electron [7], which decreases rapidly with increasing E_d. Since Si is a light element, the Mott cross-section can be accurately computed using the McKinley-Feshbach formula [8]. Using appropriate values of E_d, we find that the electron beam creates 2-5% vacancies in bulk atomic columns and as many as 20% in grain boundary columns. Point defects in Si are, however, known to be very mobile under electron irradiation conditions [9]. Therefore, these initial defects would either recombine, escape to the surface, or segregate at low-energy sites in the grain boundary. This analysis suggests that the low-intensity columns in Fig. 1(b) correspond to sites with large segregation energies of point defects.

To address the nature of these defects, we have computed the formation energies of both vacancies and interstitials in the bulk crystal and at various sites within the grain boundary core. The segregation energy is the difference between formation energies in the grain boundary and the bulk crystal. To describe the interatomic interaction for Si we used the many-body potential due to Tersoff [10], which reproduces well the local density approximation (LDA) results for vacancy and interstitial formation energies in the bulk crystal (see Table III of Ref. [10] for more details). To test the accuracy of the Tersoff potential at grain boundaries we computed, using both LDA and this potential, the vacancy formation energies at various sites in the Σ=5 {310} <001> tilt boundary, which has a smaller repeat cell than the Σ=25 grain boundary. The vacancy formation energies, as well as the relaxed atomic structures obtained by the Tersoff potential, were in good agreement with the LDA results for all sites within the Σ=5 boundary (formation energy agreement to within ~ 0.3 eV).

For the Σ=25 boundary, we computed the formation energy of isolated vacancies, isolated divacancies, chains of monovacancies (i.e.., removal of an entire column of atoms) and pairs, triplets, etc. of such chains. In each case, the relevant atom(s) were removed and the surrounding lattice fully relaxed using a combined scheme of simulated annealing and conjugate gradient relaxation. Similar calculations were done for self-interstitials.

Table 1 lists the formation energies (normalized per vacancy) of the most stable vacancy structures in various configurations. The site and chain designations are displayed in Fig. 2(a). The vacancy formation energies at all other sites are at least 2.5 eV or higher. It is clear from the table that all the low-energy structures occur in a localized region of the core in and around the dark region in the micrograph of Fig. 1(b).

Vacancy configurations	Formation Energy (eV/vacancy)
bulk	3.7
[b]	1.7
[d]	1.7
[i]	1.8
[a, b]	1.0
[b, c]	1.6
[b]-chain	0.8
[d]-chain	1.4
[d, i]-chain	1.3
[a, b]-chain	0.3*
[b, c]-chain	0.2*
[a, b, e]-chain	1.2
[f, g, h]-chain	1.4
[b, c, d, e]-chain	1.3
[d, f, h, i]-chain	1.3

*structural transformation

Table 1. The formation energies of the most stable vacancies in various configurations. Configurations are isolated unless indicated explicitly as a chain configuration. The letters indicate sites at which the vacancies are initially placed, as designated in Fig. 2(a).

From the computational study of interstitials, we find that the lowest formation energies are around 2.5 eV, and the low-energy sites are scattered all over the dislocation core, showing no particular affinity to the low-intensity region of Fig. 1(b). These results lead to the conclusion that interstitials are not trapped in specific regions and either recombine with vacancies or move to the surface. We

conclude that vacancies segregated in various low-energy configurations are primarily responsible for the low-intensity columns observed in Fig. 1(b). The localized image degradation is most likely the result of amorphization of regions centered at specific atom column positions.

A closer look at Table I shows that the chain configurations have lower formation energy than the isolated vacancies, which indicates a significant attraction between neighboring vacancies. However, of the many different chain configurations explored, two divacancy chain structures, i.e. the [a, b]-chain and the [b, c]-chain, have extremely low formation energies, an order of magnitude smaller than the vacancy formation energy in the bulk [11]. Figure 2(b) and (c) display the structures following the relaxation of the [b, c] and the [a, b] divacancy chains, respectively. Both these structures have a noteworthy feature: all atoms are fourfold-coordinated, i.e. the segregation of a chain of divacancies has led to new structures without any dangling bonds!

A comparison of the dislocation cores of Fig. 2(a) and (b) indicates that the pure edge dislocation core E2 with Burgers vector $\mathbf{b} = \frac{a}{2}<1\bar{1}0>$ has dissociated into two mixed dislocations, M1 ($\mathbf{b_1} = \frac{a}{2}<10\bar{1}>$) and M2 ($\mathbf{b_2} = \frac{a}{2}<0\bar{1}1>$), while all the other cores remain unchanged. The atomic arrangement shown in Fig. 2(c) is more complicated – here E2 splits up into an edge dislocation with Burgers vector $\mathbf{b} = \frac{a}{2}<110>$ and an "extended" edge dislocation with $\mathbf{b} = a<0\bar{1}0>$ indicated by the dotted line. These reconstructed dislocation cores have lower atomic density. In addition, we found that the formation energy of interstitials in these cores is reduced by almost an electron-volt compared to that in the non-transformed grain boundary, making them effective diffusion pipes. Another interesting feature is the presence of a chain of "long" bonds ~ 2.6 Å, which provide ideal sites for the cooperative segregation of certain dopants in the form of substitutional dimers [12].

As is evident from the micrographs of Fig. 1, electron irradiation can induce vacancy segregation in the select regions of the grain boundary core, but does not lead to the predicted reconstruction. The key difference is that the simulations involved annealing at high temperatures, whereas the experiment was done at room temperature. Alternative ways to generate nonequilibrium concentration of vacancies might be used to test our theoretical prediction. For example, nitridation of Si is known to inject vacancies [13]. Finally, external stress might be used to induce a spontaneous transformation.

We would like to thank Mark Robinson for useful discussions. This research was supported in part by Lockheed Martin Energy Research Corp. under DOE contract No. DE-AC05-96OR22464, and ONR grant No. N00014-96-1-1286, and by an appointment to the ORNL Postdoctoral Research Associates Program administered jointly by ORNL and ORISE.

References

* present address: MSI, 8 North East Executive Park, Burlington, Massachusetts 01803-5297.

1. See e.g. "Ion Implantation and Beam Processing", edited by J. S. Williams and J. M. Poate, (Academic Press, New York, 1984).
2. G. J. Clark, et. al., Nucl. Inst. and Meth., B**32**, 405 (1988).
3. D. E. Jesson and S. J. Pennycook, Proc. R. Soc. Lond. A **449**, 273 (1995).
4. We refer to these "structural units" as dislocations because they retain the characteristic "edge," "screw," or "mixed" character that isolated dislocations in bulk crystals exhibit. They are also characterized by Burger's vectors. This practice goes back to the classic paper by Hornstra [J. Hornstra, Physica **26**, 198 (1959)].
5. L. Reimer, *Transmission Electron Microscopy*, Springer-Verlag, New York (1993), Chapter 5.
6. J. W. Corbett and J. C. Bourgoin, in *Point Defects in Solids*, Vol. 2, Chapter 1, Section 7, edited by J. H. Crawford and L. M. Slifkin, Plenum, New York (1975).
7. N. F. Mott, Proc. R. Soc. A **135**, 429 (1932).
8. W. A. McKinley and H. Feshbach, Phys. Rev. **74**, 1759 (1948).
9. G. D. Watkins, in "*Radiation Damage in Semiconductors*," DUNOD, Paris (1964), P. 97.
10. J. Tersoff, Phys. Rev. B **38**, 9902 (1988).
11. Chains of interstitials were also found to be more stable than isolated interstitials. However, the formation energy of the most stable chain was found to be around 0.9 eV per interstitial, significantly higher than the formation energy of the most stable divacancy chains.
12. A. Maiti, M. F. Chisholm, S. J. Pennycook, and S. T. Pantelides, Phys. Rev. Lett. **77**, 1306 (1996).
13. P. Fahey, P.B. Griffin and J.D. Plummer, Rev. Mod. Phys. **61**, 289 (1989).

Materials Science Forum Vols. 294-296 (1999) pp. 165-168

Electromagnetic Connectivity and Microstructure in $YBa_2Cu_3O_{7-\delta}$ Films on Rolling-Assisted Biaxially-Textured Substrates

S.E. Babcock[1], Ch.-Yu. Yang[1], J.L. Reeves[1], Yu. Wu[1], A.E. Pashitski[1], A. Polyanskii[1], D.C. Larbalestier[1], A. Goyal[2], M. Paranthaman[2], F.A. List[2], D.P. Norton[2], D.M. Kroeger[2] and A. Ichinose[3]

[1] Materials Science and Engineering & Applied Superconductivity Center, University of Wisconsin, 1500 Engineering Drive, Madison, WI 53706, USA

[2] Oak Ridge National Laboratory, P.O. Box 2008, Oak Ridge, TN 37831, USA

[3] Visiting Scientist at the University of Wisconsin Applied Superconductivity Center, Permanent affiliation: Central Research Institute of Electric Power Industry, Tokyo, Japan

Keywords: Coated Conductors, RABiTS™, Buffer Layers, YSZ, $YBa_2Cu_3O_{7-\delta}$, Electron Microscopy, Magneto Optic Imaging, Critical Current Density, Granularity

ABSTRACT

Biaxially-textured $YBa_2Cu_3O_{7-\delta}$ (YBCO) coated conductors are a central thrust of current efforts to fabricate high-critical-current-density (J_c) wire for large-scale applications of high-T_c superconductivity. Encouragingly high J_c values are obtained in laboratory-length samples. However, magneto-optic imaging indicates that the supercurrent path is percolative even in the best materials. Thus, it seems clear that the full potential current carrying capability of these composites has not been reached. This paper describes coupled magneto-optic imaging and microstructural studies of RABiTS™ type coated conductors that indicate (1) the important roles of other microstructural features in addition to grain boundaries and (2) the need to explore the roles of the oxide buffer layer microstructure in optimizing the composite.

INTRODUCTION

The "weak-link" electromagnetic properties of most grain boundaries with misorientation angles of greater than about 10° drives the need to biaxially texture the high-T_c superconductors for wire and tape (i.e., high current) applications. $YBa_2Cu_3O_{7-\delta}$ (YBCO) coated conductors are a central thrust area of current efforts to fabricate such materials. In the RABiTS™ approach, one of two major competing methodologies to produce a biaxially-textured composite coated conductor, the strong crystallographic texture is established in a Ni or alloy substrate tape in a rolling and recrystallization process. Epitaxial buffer and YBCO layers are then deposited on the metal tape to transfer the texture to the YBCO [1], which has a large lattice mismatch with Ni (and most of its alloys) and can be poisoned by cation interdiffusion. To date, from a J_c viewpoint, the most effective layer configuration for RABiTS™ has been $Ni/CeO_2/Y_2O_3$-stabilized ZrO_2 (YSZ)/YBCO [2,3]. However, yet to be determined are the optimum YBCO and buffer layer microstructures for high J_c tapes and the optimum deposition methods and conditions for a process that can be scaled up to the kilometer-long lengths of material that are needed for large scale applications. High J_c values of over 1 MA/cm^2 have been achieved by post-annealing of YBCO precursors deposited by electron beam evaporation on a RABiT substrate [4,5]. Transport J_c values as high as 3 MA/cm^2 at 77K, 0T have been obtained on a RABiT substrate where the oxide buffer layers were deposited using a combination of e-beam and magnetron sputtering [6]. J_c values of 0.8 MA/cm^2 have been obtained on a RABiT substrate in which the buffer layers both were deposited by e-beam evaporation [7]. In both cases mentioned immediately above, the YBCO was deposited by pulsed laser deposition. This paper describes combined magneto-optic imaging and scanning and transmission electron microscopy investigations of the YBCO and buffer layer microstructure of YBCO-coated conductor on Ni/CeO_2/YSZ RABiTs-type substrates. The YSZ surface topography also was studied.

EXPERIMENTAL

The layer structure of the samples studied and the critical current density measured for each YBCO film (in transport and at 77K and 0T) are described in Fig. 1. The thin films were deposited as described in references [6-9]. Magneto-optic imaging [10] was used to investigate the electromagnetic connectivity of the tapes on which superconductor was deposited. Cross-sectional specimens for TEM and high resolution SEM were prepared by the tripod polishing method [11]. Plan-view SEM samples were mounted directly for imaging, without further sample preparation. Tapes C and D were used to investigate the microstructure and surface topography of the YSZ buffer layer on which the YBCO is deposited.

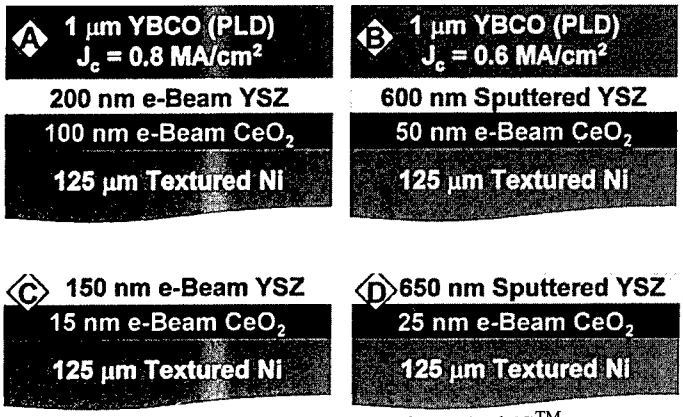

Figure 1: Layer structure of composite RABiTS^{TM}-type tapes investigated in this study.

RESULTS

Fig. 2 shows magneto-optic images of Samples A and B. Both samples were cooled in an applied magnetic field to 77K. The applied field was reduced to zero after cooling, thus the contrast in the image indicates the pattern of flux flow out of the sample. The mottled contrast in the image of Sample B indicates that the current pattern is granular and is considerably percolative. The rib shaped contrast in the image of Sample A indicates that the remaining magnetic flux profile is more Bean-Model-like, and, therefore, the current pattern is more uniform. However comparison of these images with simulated images for uniform current flow and with magneto-optic images of high quality YBCO single crystals indicates that there still is a significant perolative component to the current even in Sample A. The SEM cross-sectional images shown in Fig. 3 indicate that the origin of the increased granularity in the pattern of current flow in Sample B may be due more to other features of the microstructure, like cracks, physical connectivity, and second phase particle incorporation, than to the grain boundary network alone. The microstructure of Sample A is rather featureless on this length scale. Diffraction contrast TEM images of these films show a grain size of about 1 μm for the low angle boundaries that exist in the YBCO film in Sample A, a measurable density of threading dislocations within the grains, "a-axis grains", a great deal of mottled contrast in diffraction contrast images that suggests a high density of defects within the grains, and stacking faults on the basal plane of the YBCO.

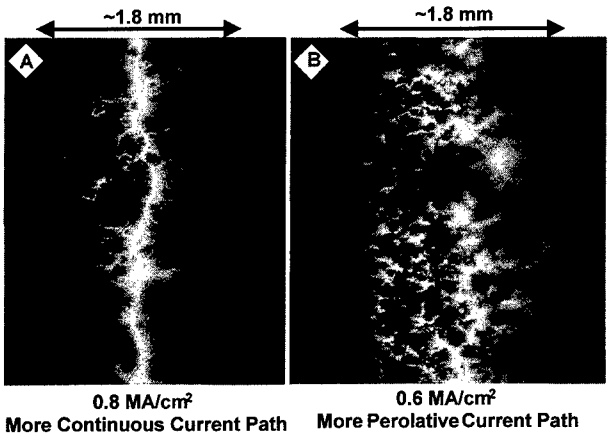

Figure 2: Magneto-optic images of the Samples A and B. Current densities are for 77K and zero applied field.

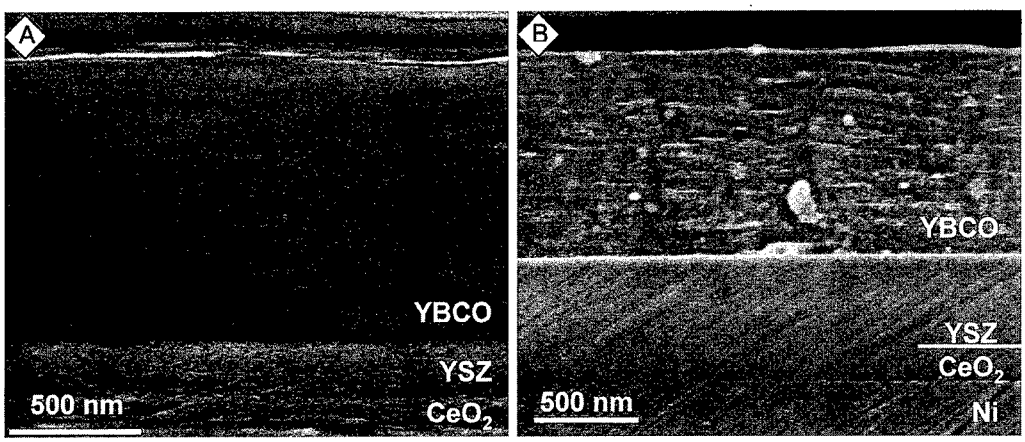

Figure 3: Secondary electron SEM images of the polished cross-sections of Samples A and B. Notice the more heterogeneous microstructure of the YBCO in Sample B and the relatively featureless microstructure in Sample A. Conversely, the YSZ layer is featureless in Sample B and porous and columnar in sample A. The current flows more homogeneously in Sample A.

A striking difference in the composite microstructure of these two samples is observed in the YSZ layer. Further investigation of the as-deposited microstructure of the YSZ buffer layer that supported the electromagnetically more homogenous YBCO revealed that it is highly columnar, comprised of slab-shaped grains with dimensions of ~ 10 nm x 50 nm by the film thickness, and not very dense (See Fig. 4). Furthermore, the column caps are roof-top shaped, resulting in a very regular nanoscale roughness with a peak-to-valley height and peak-to-peak spacing of about 10 nm. The magnetron-sputtered YSZ in Sample D showed neither columnar grains nor surface roughness when examined on the same length scale. In fact, the surface of the magnetron-sputtered YSZ appeared to be flatter than that of the underlying CeO_2, which showed gentle undulations on a length scale of 10 nm in high-resolution SEM images.

DISCUSSION AND CONCLUSIONS

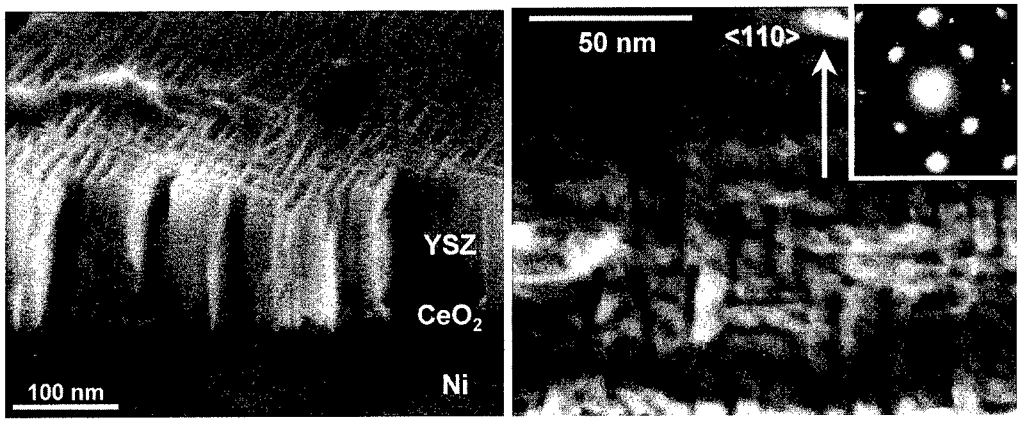

Figure 4: (a) Secondary electron high-resolution SEM image of a fracture surface of Sample C that shows both the surface and cross-sectional column topography of the e-beam deposited YSZ film. (b) plan-view diffraction contrast TEM image of this same microstructure.

This study revealed the porous, columnar nature of the YSZ of RABiTS^{TM} when it is e-beam deposited, and indicates that high quality YBCO can be deposited on top of it. One might have predicted that the rough YSZ surface and the columnar nature of the grains would lead to a porous, columnar, and consequently low J_c microstructure in the YBCO, but this appears not to be the case. Perhaps of equal significance is the actual or incipient porosity in the e-beam YSZ layers. It seems possible that this porous, columnar microstructure might accommodate lattice and thermal expansion coefficient mismatch and/or externally applied mechanical stresses in the buffer layers of the structure, thereby reducing cracking in the YBCO over layer. Clearly the growth mechanism of YBCO on such a porous, nano-scale rough YSZ surface is not understood, nor is it clear what microstructure is most desirable in the buffer layers. However, the growth of high quality YBCO on what, on first impression, appears to be a less than ideal YSZ microstructure suggests that it may be possible to optimize the YSZ buffer layer microstructure to address other design criteria, for example mechanical properties, in addition to the J_c of the superconductor.

ACKNOWLEDGEMENTS

The work performed at the University Of Wisconsin (UW) is supported by the ORNL and the NSF MRSEC Program. The electron microscopy facilities used for this research are maintained by the UW Materials Science Center with partial support from the NSF MRSEC. The research performed at the ORNL was sponsored by the Division of Materials Sciences, the Office of Basic Energy Sciences, the Office of Energy Efficiency and Renewable Energy, and the Office of Utility Technologies-Superconductivity Program. The ORNL is managed by Lockheed Martin Energy Research corporation for the U.S. Department of Energy under contract # DE-AC05-960R22464.

REFERENCES

1. D. P. Norton, A. Goyal, J. D. Budai, D. K. Christen, D. M. Kroeger, E. D. Specht, Q. He, B. Saffian, M. Paranthaman, C. E. Klabunde, D. F. Lee, B. C. Sales and F. A. List, Science 274 (1996) p.755.
2. A. Goyal, D. P. Norton, J. D. Budai, M. Paranthaman, E. D. Specht, D. M. Kroeger, D. K. Christen, Q. He, B. Saffian, F. A. List, D. F. Lee, P. M. Martin, C. E. Klabunde, E. Hartfield, and V. K. Sikka, Appl. Phys. Lett. 69 (1996) p.1795.
3. A. Goyal, D. P. Norton, D. K. Christen, E. D. Specht, M. Paranthaman,D. M. Kroeger, J. D. Budai, Q. He, F. A. List, R. Feenstra, H. R. Kerchner, D. F. Lee, E. Hatfield, P. M. Martin, J. Mathis and C. Park, Applied Superconductivity 4 (1996) p.403.
4. R. Feenstra et al., Oak Ridge National Laboratory, unpublished results.
5. M. Paranthaman, et al, Proceedings of the 9th CIMTEC-World Ceramics Congress and Forum on New Materials, Editor: P. Vincenzini (Florence, Italy, June 14-19 1998).
6. J.E. Mathis, A. Goyal, F.A. List, M Paranthaman, D.K. Christen, E.D. Specht, D.M. Kroeger, D.F. Lee, and P.M. Martin, Submitted to Appl. Phys. Lett.
7. F.A. List, A. Goyal, M. Paranthaman, D.P. Norton, E.D. Specht, D.F. Lee, and D.M. Kroeger, Physica C 302 (1998) p.87.
8. M. Paranthaman, A. Goyal, F. A. List, E. D. Specht, D. F. Lee, P. M. Martin, Q. He, D. K. Christen, D. P. Norton, J. D. Budai, D. M. Kroeger, Physica C 275 (1997) p.266.
9. Chau-Yun Yang, S.E. Babcock, A. Goyal, M. Paranthaman, F. A. List, D. P. Norton, D.M. Kroeger, and A. Ichinose, submitted to Physica C.
10. A. Pashitski, A. Polyanskii, A. Gurevich, J. Parell, D. Larbalestier, Physica C 246 (1995) p.133.
11. J. Benedict, R. Anderson, and S.J. Klepeis, Specimen Preparation for Transmission Electron Microscopy of Materials III, Materials Research Society Symposium Proc. 254 (1992) p. 121.

For correspondence (S.E. Babcock): babcock@engr.wisc.edu or Fax USA-608-263-1087

Materials Science Forum Vols. 294-296 (1999) pp. 169-172

Propagation Behaviour of Intergranular Stress-Corrosion Cracking of Cu-9at.%Al Bicrystals Shaped to the Tapered Double Cantilever Beam Specimen

T. Mimaki[1], H. Ando[1], H. Miyamoto[1], Y. Kaneko[2,3] and S. Hashimoto[2]

[1] Department of Mechanical Engineering, Faculty of Engineering, Doshisha University, Kyo-Tanabe 610-0321, Kyoto, Japan

[2] Department of Engineering Physics and Mechanics, Graduate School of Engineering, Kyoto University, Kyoto 606-8501, Japan

[3] Now at Department of Mechanical Systems Engineering, Faculty of Engineering, Kanazawa University , Kanazawa 920-8667, Japan

Keywords: Bicrystal, Intergranular Crack Growth, Stress-Corrosion Cracking, αCu-Al Alloy

Abstract

Intergranular stress-corrosion cracking (SCC) in a αCu-Al alloy has been investigated on bicrystals shaped to a tapered double cantilever beam (TDCB) specimen. The SCC property was estimated by the relationship between crack growth rate *da/dt* and energy release rate *g*. The bicrystal specimens of two kinds (Σ5 and random boundaries) were prepared. During the SCC tests, the applied load continued to decrease and was saturated subsequently. Surface observation after the SCC tests revealed that the crack propagated along the Grain Boundary. In both specimens, the *da/dt–g* curves calculated from the load relaxation could be divided into Regimes I and II at low and high *g*-values, respectively. The crack growth rates increased with the increasing *g*-value in Regime I and was independent of the *g*-value in Regime II. Both of the threshold *g*-value in Regime I and the crack growth rate in Regime II, which can characterize the SCC properties, were certainly different between the specimens. It is likely that such differences are attributed to the GB structure and the geometry of operative slip systems.

1. INTRODUCTION

The materials subjected to corrosive environment are often fractured by intergranular SCC. It has been suggested that intergranular SCC behaviour is sensitive to a character of GB [1,2]. Some special boundaries of low Σ-values showed substantial resistance, which was evaluated by an inverse of the time to failure tested under a constant load. However, such a fracure life, which we employed to estimate the intergranular SCC property, consists of the time to both initiation and propagation of crack: this conventional evaluation method takes no account of the details of fracture processes. The specimens should experience several SCC stages before fatal fracture. It is feasible that the role of the GB structure on the SCC is different between the individual stages.

The crack growth behaviour is frequently estimated by applying fracture mechanics. However, the measurement of crack length —— which is required to obtain the parameters such as crack growth rate ——— is difficult in the corrosive solution. In order to solve this problem, the TDCB specimen having a characteristic shape has been employed [3,4]. The TDCB specimen enables us to measure both of crack growth rate and energy release rate from a load relaxation curve without direct observation of a crack length.

In the present study, the intergranular SCC tests have been performed in αCu-Al alloy bicrystals shaped to the TDCB specimen as schematically illustrated in Fig.1. Change in the role of the GB structure at different SCC stages was investigated by measuring the crack growth rate and the energy release rate.

2. EXPERIMENTAL

Two bicrystals were produced by Bridgman method from Cu-9at.%Al material alloyed with 99.9999% Cu and 99.9998% Al. These bicrystals had [001] symmetrical tilt boundaries. The rotation angle around the tilt axis is 39.5° (Σ5) in Specimen A and 30.0° (random) in Specimen B

respectively.

In order to estimate a resistance of the GB against SCC, the energy release rate g is adopted in the present study. The energy release rate is calculated from the compliance method defined in the fracture mechanics (Eq.1).

$$g = \frac{P^2}{2b}\frac{d\lambda}{da} \tag{1}$$

where P is the applied load, b is the specimen thickness, a is the crack length and λ is the compliance. The compliance λ is given by δ / P (δ is the displacement at loading point).

According to the theory of cantilever beam, the deflection of the stressed beam is given by Eq.2.

$$\delta = \frac{P}{b}\left(\frac{8a^3}{Eh^3} + \frac{3a}{Gh}\right) \tag{2}$$

where E is the Young's modulus, G is the shearing modulus, h is the height of beam and a is the beam length corresponding to the crack length in a cantilever beam specimen. Since $\lambda = \delta / P$, we can obtain the following equation by differentiating λ with respect to a.

$$\frac{d\lambda}{da} = \frac{3}{b}\left(\frac{8a^2}{Eh^3} + \frac{1}{Gh}\right) \tag{3}$$

Hence, when we employ the specimen shape in which $d\lambda / da$ is independent of the crack length, the energy release rate can be calculated from Eq.1 only by measuring the applied load. If the loading point is fixed at constant δ-value during the SCC test, the crack growth rate da / dt is also calculated from the load relaxation curve giving P and dP / dt values (Eq.4).

$$\frac{da}{dt} = -\frac{\delta}{d\lambda/da}\left(\frac{1}{P^2}\right)\frac{dP}{dt} \tag{4}$$

Figure 1 shows a schematic illustration of the TDCB specimen where $d\lambda / da$ is constant. Prior to the SCC tests, we measured anodic polarization curves and the λ–a relations in the TDCB specimens in which the artificial pre-crack was introduced stepwise. The SCC tests were carried out in an ammoniacal solution (NH_4OH; 1l + NaOH; 500g + H_2O; 4l) at 303K. The displacement at loading point was set at about 0.03mm. The potential differences between the specimen and the solution was controlled at -207.5 and -227.5 mV (vs. NHE) for Specimens A and B, respectively. During the SCC tests, the decrease in applied load due to crack growth was recorded continuously.

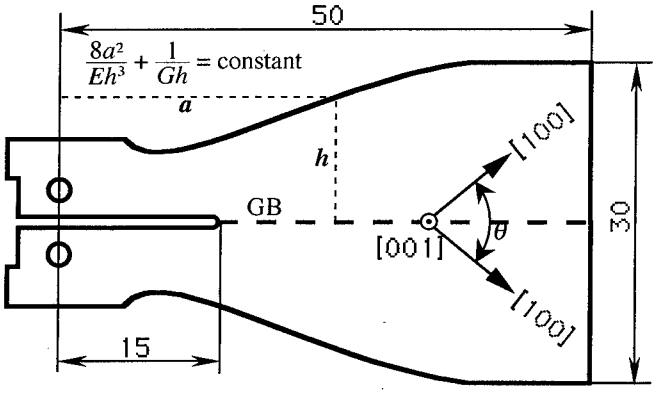

Fig.1 Schematic illustration of the TDCB bicrystal specimen.

3. RESULTS

After an immersion into the solution and an application of the electrode potential, the specimens were covered with dark passive film. The loads decreased continuously during the SCC tests under the experimental condition of the constant δ-value. The load relaxation curves are shown in Fig.2. After the gradual decrease, the load was saturated in both specimens. Figure 3 shows the crack observed after the SCC test. The stress-corrosion cracks were initiated and propagated along the GBs. It is concluded that the GB is a preferred path in the corrosive environment of the present study. The crack propagation was terminated at the GB. This halt of the crack growth corresponds

to the saturation of the load. Figure 4 shows the relationship between the crack growth rate *da/dt* and the energy release rate *g*, which are calculated from the above load relaxation curves. In both specimens, the *da/dt–g* curves could be divided at least into Regime I and II at low and high *g*-values, respectively. The crack growth rates increased rapidly with increasing *g*-value in Regime I and was independent of the *g*-value in Regime II: the crack growth was decelerated rapidly and terminated, after the propagation at the constant velocity. The threshold *g*-values of the SCC are estimated to be 6.6 and 4.4 J/m^2 for Specimens A and B, respectively. The crack growth rate at Regime II is also different between specimens. The *da/dN* of Specimen A was two times higher than that of Specimen B in Regime II.

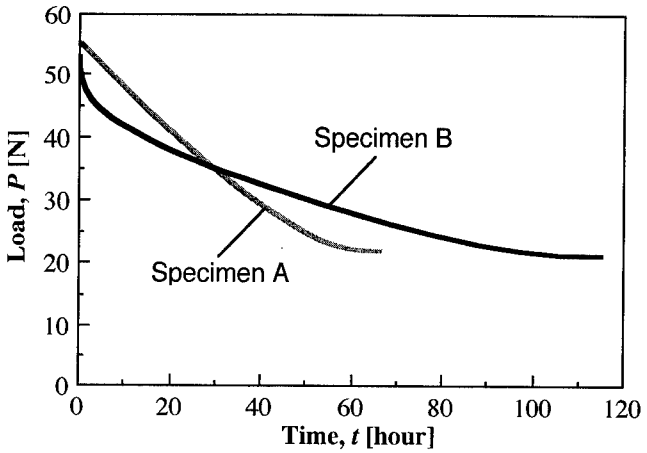

Fig.2 Load relaxation curves of Specimens A and B.

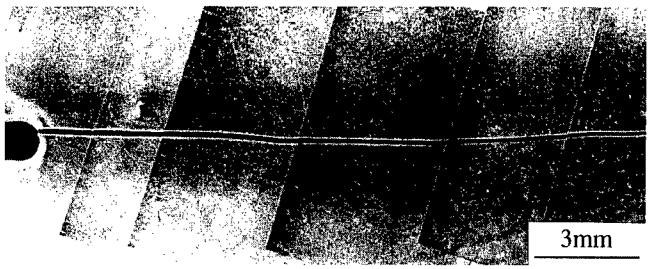

Fig.3 A SEM photograph showing the intergranular SCC in Specimen B.

4. DISCUSSION

For the intergranular SCC, the slip step dissolution (SSD) model has been proposed [5]. The SSD model involves following processes. Localized slip and film rupture would occur at crack tip because of high stress concentration. The GB at the new surface created at slip step is dissolved preferentially. Subsequently, the crack tip is covered with the passive film, again. The crack is assumed to propagate by repeating the above processes in the SSD model. In Regime II where *da/dN* is constant, one of these processes controls the crack growth rate. It is probable that the chemical kinetics of the passivation and/or the dissolution control the crack velocity in Regime II.

The rapid decrease in *da/dN* at Regime I implies that the rate-determining mechanism is no longer operated. One of the SSD processes should be decelerated due to the reduction in the applied load. For example, the increase in time to the film rupture and the reduction in the dissolved amount can be considered. Likewise, the halt of the crack growth should be attributed to the inactivation of one of the SSD processes. It is likely that the film rupture is prevented owing to the substantial load relaxation. It can be said that Specimen A has higher resistance against the SCC nucleation than Specimen B since the threshold *g*-value was larger at Specimen A. Although detail of physical mechanism is still unclear, one can interpret such a different threshold value in the following manner. Even at the crack that is almost stopped, the passive film is partly broken and thus some GB grooves produced by the dissolution could be formed. According to the studies on the intergranular corrosion in the Al [6] and Cu-9at.%Al [7] bicrystals having [001] tilt boundaries, the corrosion grooves of random boundary is deeper than that of Σ5(013) one. It is expected that the stress distributed at the remaining passive film increases with increasing depth of the GB groove. This stress can induce a new film rupture. In summary, the susceptibility to the GB corrosion (i.e., the GB structure) can be associated with the observed difference in the threshold *g*-value.

In Regime II, the crack growth rate of Specimen A was faster than that of Specimen B. This seems inconsistent with the low susceptibility to the GB corrosion referred in above. The SSD model assumes that the local slip activity around crack tip plays an important role for the SCC: the

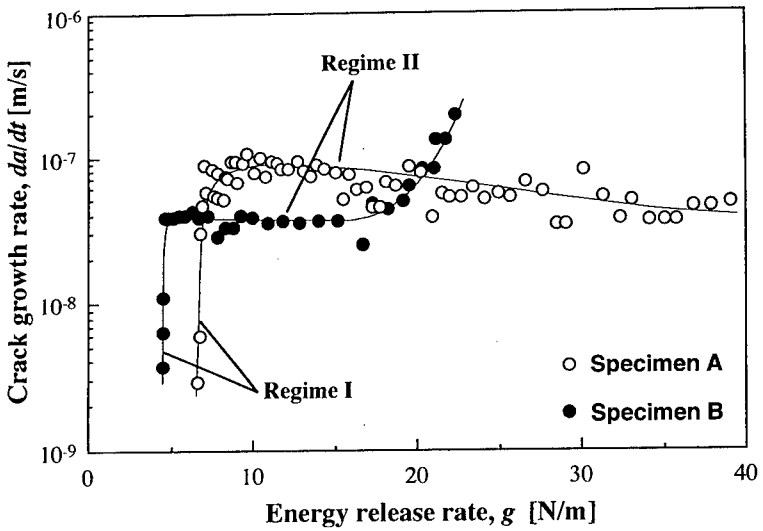

Fig.4 Relationship between crack growth rate and energy release rate.

crack growth increment of the SCC contains the ductile crack growth increment due to slip deformation in addition to the GB dissolution. The slip geometry is different between the two specimens. The stress calculation based on the stress intensity factor revealed that shear stress acting on a responsible slip system in Specimen A is larger than that of Specimen B under the equivalent load. Thus, the faster crack growth rate in Specimen A can be understood in terms of such a difference in the geometry of slip system.

5. SUMMARY

1. It was recognized that the GB in Cu-9at.%Al is a preferred path for the stress-corrosion cracking in the ammoniacal solution. The relationship between crack growth rate and energy release rate was divided into Regime I and II at low and high g-values, respectively.

2. The threshold energy release rate of the specimen having $\Sigma5(013)$ boundary was higher than that of the random boundary. This can be attributed to the difference in the GB structure.

3. The crack growth rate of the specimen with $\Sigma5(013)$ boundary was higher than that of the random boundary. It can be explained qualitatively by the slip step dissolution model and shear stress analysis in the vicinity of the crack tip, suggesting that the crack growth rate at Regime II is sensitive to the geometry of slip system rather than the GB structure.

References

1. M. Yamashita, M. Yoshioka, T. Mimaki, S. Hashimoto and S. Miura, *Acta Metar.Mater.*, **38** (1990), 1619.

2. M. Yamashita, T. Mimaki, S. Hashimoto and S. Miura, *Phil.Mag.A*, **63** (1991), 707.

3. J.A. Kargol and D.L. Albright, *J.Test.Eval.*, **3** (1975), 173.

4. J.A. Kargol and D.L. Albright, *Metall.Trans.*, **8A** (1976), 27.

5. H. Vehoff, H. Stenzel and P. Neumann, Z. Metallkd., 78 (1987), 550.

6. G. Hasson, J.-Y. Boos, I. Herbeuval, M. Biscondi and C. Goux, *Surf.Sci.*, **31** (1972), 115.

7. M. Yamashita, T. Mimaki, S. Hashimoto and S. Miura, *Phil.Mag.A*, **63** (1991), 667.

Materials Science Forum Vols. 294-296 (1999) pp. 173-176

Anisotropy and Oxygen Activity Dependency of the Liquid or Solid Metal-Oxide Interfacial Free Energy: Case Study on MgO-Cu

M. Backhaus-Ricoult and S. Laurent

Centre d'Etudes de Chimie Métallurgique, CNRS, 15 Rue G. Urbain,
F-94407 Vitry sur Seine, France

Keywords: Metal/Oxide Interfaces, Interfacial Free Energy, Wetting, Precipitate Morphology

Abstract

The present study of the equilibrium shape of liquid or solid metal inclusions in oxides or oxide inclusions in solid metals presents a novel approach for the study of anisotropy and oxygen partial pressure dependency of metal-oxide free specific interfacial energies. In the case of solid-liquid or incoherent or nearly incoherent solid-solid interfaces the precipitate equilibrium shape is determined by the anisotropy of the interfacial free energy. Precipitate shapes obtained at different experimental conditions can then be explored with help of the Wulff's construction in terms of relative interfacial free energies. In the present work relative values have been obtained in the MgO-Cu system for solid and liquid precipitates under different oxygen activities.

Introduction

The various parameters influencing the wetting behaviour are often studied by sessile drop experiments, however, even for non-reactive wetting interfaces, wetting angle and specific interfacial free energy depend not only on the type of substrate and metal, but also on temperature, oxygen chemical potential and crystallographic orientation of the substrate (surface plane). Even though sessile drop experiments have been conducted for many different oxide-metal systems, see [1,2], the data scatter due to surface pollution, missing control of the gas atmosphere (specially of the oxygen activity), insufficient definition of the oxide surface plane and many more factors. Therefore it is rather difficult to deduce fine details such as the influence of the crystal anisotropy or the oxygen chemical potential dependency from simple sessile drop experiments. In the present work a complementary approach is proposed with the study of the equilibrium shape of small liquid metal inclusions within an oxide matrix. From the liquid metal inclusions shape which reflects the anisotropy of the interfacial free energy, part of the γ-plot can be obtained by the inverse Wulff construction [3]. Equilibration of the metal inclusions at different oxygen activities allows to obtain the oxygen partial pressure dependency of the relative interfacial free energies.
The approach can also be applied to solid equilibrium inclusions in a solid matrix: In the case of incoherent or almost incoherent interfaces relative interfacial free energies can be obtained by the same procedure.

In the present work, equilibrium shapes of liquid copper metal inclusions within magnesia and solid MgO conclusions in copper are studied.

Experimental Part

Copper-doped magnesia single- and polycrystals containing 3at% CuO are partially reduced at 1400°C, at fixed oxygen activity ranging between 10^{-20} and 10^{-6} . A (Cu,Mg) alloy with 3% magnesium is partially oxidised at 900°C, at oxygen activities fixed between 10^{-34} and 10^{-8}.

Oxygen activities are experimentally set with gas or solid-state buffers: continuous flow of various CO/CO_2 gas mixtures, C/CO, CuO/Cu_2O or Mg/MgO buffer inside a sealed ampoule. Annealing times of 100 hours at 1400°C and up to 1000 hours at 900°C are chosen in order to achieve the precipitate equilibrium shape. Details on the internal reactions are reported in [4-6].
For transmission electron microscopy (TEM) investigations, reacted samples are sectioned, mechanically polished and further thinned by argon bombardment in a cold stage to electron transparency. Thin foils are investigated in a JEOL 2000FX transmission electron microscope. Projected views of the precipitate shape are studied along different directions in order to reconstitute the detailed precipitate shape.

Experimental results

Liquid copper inclusions in MgO

At 1400°C for all oxygen activities liquid copper inclusions within magnesia (obtained by internal reduction of the mixed (Mg,Cu)O oxides and subsequent long time annealing) adopt cubo-octahedral shape. Only {001} and {111} facets form. The relative importance of the two types of facets depends on the oxygen chemical potential. At low oxygen activities truncated cube shape is adopted with $\{001\}_{MgO}$ main and small $\{111\}_{MgO}$ facets, at high oxygen activities $\{111\}_{MgO}$ facets increase in size. The detailed ratios are given in Table 1 and illustrated in Fig.1 by [011] projected views of typical copper inclusions.

a_{O2}	10^{-20}	10^{-12}	10^{-5}
{001}/{111} facet size ratio	1.40 ± 0.08	1.10 ± 0.08	0.90 ± 0.08

Table 1: Size ratios of {001} and {111} cubo-octahedrael facets of liquid copper inclusions at 1400°C for different oxygen activities

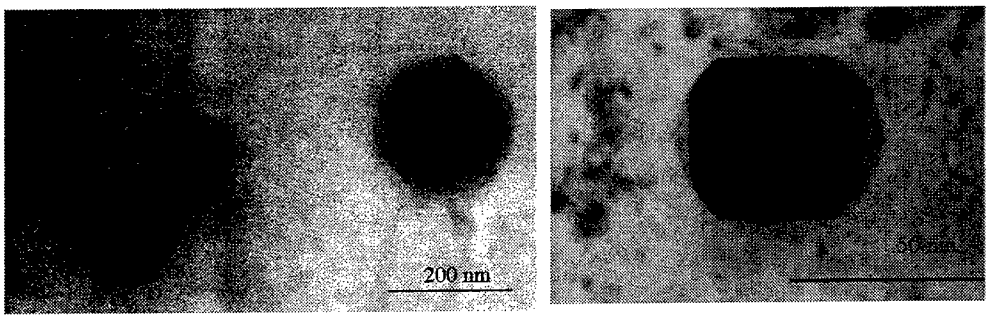

Fig. 1 TEM bright field images of copper inclusions obtained at 1400°C at different oxygen activities with <011> being parallel to the electron beam and all interfaces being end on
a) $a_{O2} = 10^{-5}$ and b) $a_{O2} = 10^{-20}$

MgO precipitates in solid copper

Solid MgO precipitates in Cu obtained by internal oxidation of (Cu,Mg) alloys and subsequent equ ilibration are found in a wide range of oxygen activities in cube on cube orientation relationship

with the solid copper matrix. Their equilibrium shape changes with the oxygen activity. At high oxygen activities, they adopt an almost perfect octahedron with main {111} facets. With decreasing oxygen activity the octahedron becomes more and more truncated by {001} facets. At $a_{O2} = 10^{-20}$ a truncated cube shape is adopted where the {111} facets have become very small. Results obtained at 900°C for different oxygen activities are presented in Table 2 and illustrated in Fig.2.

a_{O2}	10^{-20}	10^{-12}	10^{-8}
{111}/{001} facet size ratio	0.8 ± 0.1	1.1 ± 0.1	1.35 ± 0.10

Table 2: Size ratios of {001} and {111} cubo-octahedrael facets of topotactical MgO precipitates in copper at 900°C for different oxygen activities

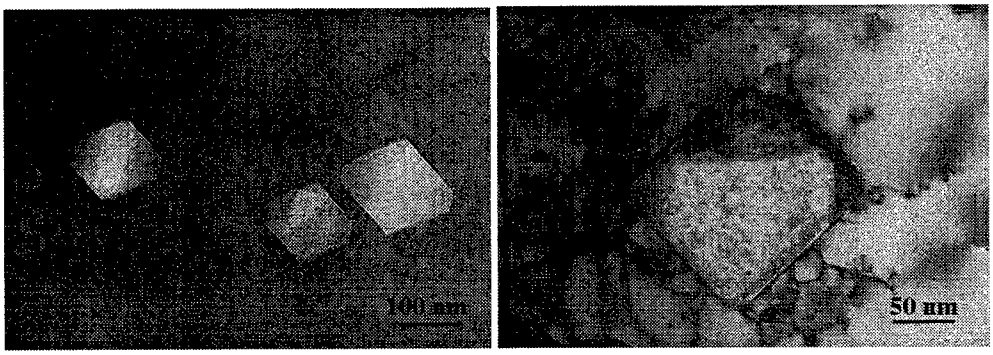

Fig. 2: TEM bright field images of the topotactical MgO precipitates obtained at 900°C at different oxygen activities with <011> being parallel to the electron beam
a) $a_{O2} = 10^{-8}$, c) $a_{O2} = 10^{-20}$

Discussion

The variation of liquid copper inclusion equilibrium shape can be interpreted in terms of a variation of the interfacial free energy with the oxygen chemical potential. From our experiments we can conclude that $\{111\}_{MgO}$//liquid Cu and $\{001\}_{MgO}$//liquid Cu constitute the low energy interfaces. Since no other facets appear we conclude that all other facets must have a considerable (by a factor two or more) larger energy. For high oxygen activities {111} facets are energetically favoured compared to {001} facets, for lower oxygen activities their energies become similar. The exact ratio of the free interfacial energies is obtained from the Wulff construction in the [011] shape projection as the ratio of the distances of the facet surfaces from the precipitate centre and corresponds then exactly to the ratio of the facet sizes given in Table 1.

The exact equilibrium shape of a solid precipitate is determined by the minimisation of the total energy of the precipitate-matrix system and is then controlled not only by the anisotropy of the free interfacial energy, but also by the anisotropy of the strain energy. In the present system of solid magnesia precipitates in a copper host matrix, however, strain due to the precipitation reaction has been relaxed during long time annealing at high temperature by diffusion and dislocation motion. The residual equilibrium strain energy is vanishing in the case of incoherent interfaces where no

lattice deformation occurs at the interface and is very important in the case of coherent interfaces. In the present case of the magnesia-copper interfaces, high resolution electron microscopy studies have shown that the magnesia crystal lattice remains undisturbed at the interface while in copper phase lattice perturbations extend only a few atomic planes into the copper lattice [7]. From this we conclude that the contribution of the elastic deformation energy remains very small and that the shape anisotropy of the topotactic precipitates in a first approximation can be interpreted in terms of the anisotropy of the free interfacial energy. Then the ratios of the facet sizes in Table 2 can be taken as the ratio of the interfacial free energy. Similarly to the magnesia-liquid copper system we conclude from the cubo-octhedral shape of the precipitates that the two types of interfaces $\{111\}_{MgO}//\{111\}_{Cu}$ and $\{001\}_{MgO}//\{001\}_{Cu}$ constitute the low energy interfaces. The rare appearance of very small $\{011\}_{MgO}//\{011\}_{Cu}$ facets suggests that these facets are also low energy facets, but have relatively higher energy. From the values in Table 2 can be seen that at high oxygen activities the $\{111\}_{MgO}//\{111\}_{Cu}$ interfaces constitute the energy minimum and that with decreasing oxygen activity $\{001\}_{MgO}//\{001\}_{Cu}$ interfaces become energetically more and more favourable.

Thermodynamic models as the Gibbs' adsorption isotherm or atomistic models on electronic structure of the interface and the type of interfacial bonding are used to explain the observed evolution.

At high oxygen activities, when the copper(I)oxide activity becomes almost one, copper has a high tendency to form metal-oxygen bonds across the interface. It is shown by a combination of HREM study and EELS spectroscopy by the same author [8] that interfacial copper in this condition is preferentially found in contact with polar $\{111\}_{MgO}$ planes terminated by oxygen. It was further demonstrated that this oxygen plane is completely occupied and that copper suffers important charge transfer at the interface while adopting a formal valence state of Cu^{1+} in a Cu_2O-like structure. The interface in this configuration possesses an excess in oxygen compared to stoechiometric MgO (half-filled oxygen end plane) which, in the Gibbs' language, can be considered as the excess of adsorbed oxygen in the interface.

At intermediate oxygen activities, charge transfer between copper and oxygen is very weak or non-existing [8], promoting then mixed, neutral $\{001\}_{MgO}$ planes in contact with copper planes as low energy configuration.

At very low oxygen activities, when the magnesium activity becomes close to one, a strong tendency to form metal bonds exists. As a consequence, low energy configurations are expected to show interfaces between polar $\{111\}_{MgO}$ planes terminated by a magnesium layer and copper.

From the above described changes in the interfacial bonding with oxygen activity it is understandable that the interfacial free energy changes in the same manner and that as a consequence the relative interfacial free energy of polar and mixed facets evolves with the oxygen activity.

[1] J.Naidich,Progress in surface and Membrane Science, p 353, ed D.A.Cadenhead, J.F.Danielli, Acad. Press, London (1981)
[2] D.Chatain, F.Chabert, V.Ghetta, J.Fouletier, J. Am. Ceram. Soc. 77, 197 (1994)
[3] G.Wulff, Z. Kristallogr. 34, 449 (1901)
[4] M.Backhaus-Ricoult, S.Laurent, J.Devaud,M.Hÿtch, D.Imhoff, S.Hagège, Proc of Colloque de métallurgie: ségrégation dans les interfaces solides, Saclay (1998)
[5] M.Backhaus-Ricoult, Z. Phys. Chem. 206, 1 (1998)
[6] M.Backhaus-Ricoult, S.Laurent, NATO Conf Proc. Joining, Bled (1997)
[7] S.Laurent, D.Imhoff, C.Colliex, M.Hÿtch, J.Devaud, S.Hagège, M.Backhaus-Ricoult, in iib 1998
[8] M.Backhaus-Ricoult et al, iib proceedings 1998

Materials Science Forum Vols. 294-296 (1999) pp. 177-180

Low-Energy Configurations of the Σ=5 (210)[001] Tilt Grain Boundary in FCC Crystals

P. Grigoriadis[1], Th. Karakostas[1], Ph. Komninou[1] and V. Pontikis[2,1]

[1] Physics Department, Solid State Section, Aristotle University of Thessaloniki, GR-54006 Thessaloniki, Greece

[2] Laboratoire des Solides Irradiés, CEA-CNRS UMR 7642-Ecole Polytechnique, F-91128 Palaiseau Cédex, France

Keywords: Grain-Boundaries, Structure, Phase Transitions, Atomistic Simulations

Abstract By using molecular statics we investigate atomic configurations of the Σ=5 (210)[001] tilt grain boundary in face centered cubic (fcc) crystals that correspond to local minima of the internal energy of the bicrystal. Two cohesion models have been used the first of which is a n-body potential adapted to copper whereas the second is the Lennard-Jones potential, well adapted to the case of solids in which dispersion forces are dominant. Whatever cohesion model is used, energy minimization shows that one stable and symmetrical and two metastable asymmetrical configurations of this boundary exist at T=0 K.

Introduction

In a bicrystal, when the misorientation relationship between grains and the orientation of the grain boundary plane are fixed, several minimum energy configurations can exist that correspond to specific values of rigid-body translations with respect to the symmetrical configuration, a commonly used reference state. Computer modelling by means of molecular statics has permitted the first determinations of rigid-body translations to be made [1] whereas experimental values were obtained by using the 'alpha fringes' method [2] and, more recently, from High Resolution Electron Microscopy (HREM) observations of grain boundaries [3]. The comparison between computed and experimental values of rigid-body translations is a crucial test of the transferability to the case of interfaces of cohesion models that satisfactorily fit bulk properties [4]. Moreover, there is a hope that such a comparison could indicate if the semi-empirical models often used in computer modelling of interfaces are adequate or if the need exists for more sophisticated cohesion schemes to be developed. In present work we study the atomic structure of configurations of the Σ=5 (210)[001] tilt grain boundary in face centred cubic (fcc) crystals that correspond to local minima of the internal energy of the bicrystal. In agreement with previous work that has shown that for a given grain boundary several low-energy structures can exist [5,6], we found that this boundary can adopt three different configurations at T=0 K among which that of lowest excess energy is symmetrical. Simulations of the HREM images that would be produced if these configurations were present in an experimental sample show that they could be unambiguoysly identified.

Computations

Starting from a configuration consisting of two adequately oriented single-crystalline grains in a mirror-symmetrical relation, located at a (210) interplanar spacing distance one from another, several initial configurations have been produced by applying rigid-body translations parallel to the interface plane. These uniformly sample the two-dimensional grain boundary cell spanned by the crystallographic directions, [$\bar{1}$20] and [001]. The bicrystals are made of 6[210]x3[$\bar{1}$20]x4[001] cells thus containing N=1440 point particles. Interatomic forces derive from a n-body potential adapted to copper the parameters of which have been fitted to the cohesion energy, the lattice parameter (a=3.6015 Å) and the elastic constants extrapolated at T=0 K, the stacking fault energy and the vacancy formation energy (Table 1, [7]). For the purpose of comparison with previous work [8], the stability of the equilibrium configurations found by using this model, has also been checked when cohesion is instead described by the standard Lennard-Jones, (12-6) potential (Table 1). Periodic

LJ (12-6)	ε/k_B=119.8 K	σ=3.405 Å	-	-	rc=2.75 σ
n-body	A=0.07157 eV	ξ=1.1485 eV	p=11.652	q=2.0214	rc=1.65 a

Table 1 Potential parameters (refer to [7] for details)

boundary conditions are applied along the [$\bar{1}$20] and [001] directions whereas the bicrystal terminates with free surfaces normal to the [210] direction. Therefore, the condition of a zero stress component normal to the interface is automatically satisfied when the total energy has reached a minimum. The energy of the initial geometrical configurations has been minimized by using a newtonian algorithm including damping forces and a timestep, $\delta t=10^{-15}$s [9]. We considered that the system energy has reached a minimum when its value remained constant within $\delta E/E\approx10^{-6}$. The stability of the minima has been tested by assigning to the atoms of the corresponding configurations initial velocities, sampled from a Maxwelian distribution at T=1000 K and by verifying, after a new minimization run has converged, that initial and final configurations are identical. Similarly, the stability of each minimum has been further checked for invariance of the associated atomic positions when small rigid-body translations are applied to them and the energy of these perturbed configurations is again minimized.
It is worth examining on whether or not the stable configurations of the studied interface can be experimentally observed by HREM. To this end the atomic positions obtained from molecular statics have served simulating the contrast HREM images would display if such grain boundary configurations were present in a real sample, by using the EMS software package [10]. Input data to this package have been fixed at values characteristic of the JEOL 4000 microscope and a series of through and through thickness images have been simulated.

Results
In Fig. 1 atomic positions of the stable configurations of the boundary are shown together with profiles of the relaxations of interplanar distances normal to the interface and simulated HREM images. The difference in the values of the excess energy of the symmetrical (996 mJ/m^2) and the asymmetrical (1013 mJ/m^2) configurations is weak in agreement with previous work [5]. In complement to the projections along the tilt axis of the atomic positions, relaxation profiles help in identifying unambiguously the symmetric (resp. asymmetric) character of the minimum energy configurations. This is also apparent when examining the simulated HREM images. The rigid-body translation vectors corresponding to these stable interfacial configurations are found respectively equal to, $\mathbf{t}_s$=(0,3,0)a and $\mathbf{t}_\alpha$=(0,3.934,0)a, where a, represents the lattice parameter and the subscripts s and α refer respectively to the symmetrical and asymmetrical structures. Symmetry reasons impose that an additional, metastable boundary configuration exists in mirror-symmetrical relationship with the asymmetrical configuration and of same energy. The associated rigid-body translation vector is, $\mathbf{t}_{\alpha'}$=(0,4.066,0)a.
Provided the cohesion model we used realistically describes the studied grain boundary in copper, these configurations could be experimentally identified by determining the associated rigid-body translations. This possibility is further supported by few additional calculations in which the n-body potential for Cu has been replaced by the standard Lennard-Jones (LJ) (12-6) pair potential. The same boundary configurations are found to be stable thus suggesting that our results are not much sensitive to the change in the character of atomic interactions from pair to n-body nor to a substantial change in bonding strength.
The multiplicity of interfacial structures and its possible impact on various grain boundary phenomena has been discussed in details by Wang, Sutton and Vitek [5] who have also explored the low-energy configurations of the Σ=5 (210)[001] tilt grain boundary in copper by means of molecular statics and of an empirical cohesion model. One of the two low-energy symmetrical configurations found by these authors is identical to that shown in Fig. 1. The other is unstable for both potentials used in this work, as is revealed from energy minimizations that used as an input atomic positions reproducing the second symmetrical configuration found by Wang et al. [5]. Upon convergence, these calculations led to one of the mirror-related asymmetrical grain boundary configurations identified in present work (Fig. 1).

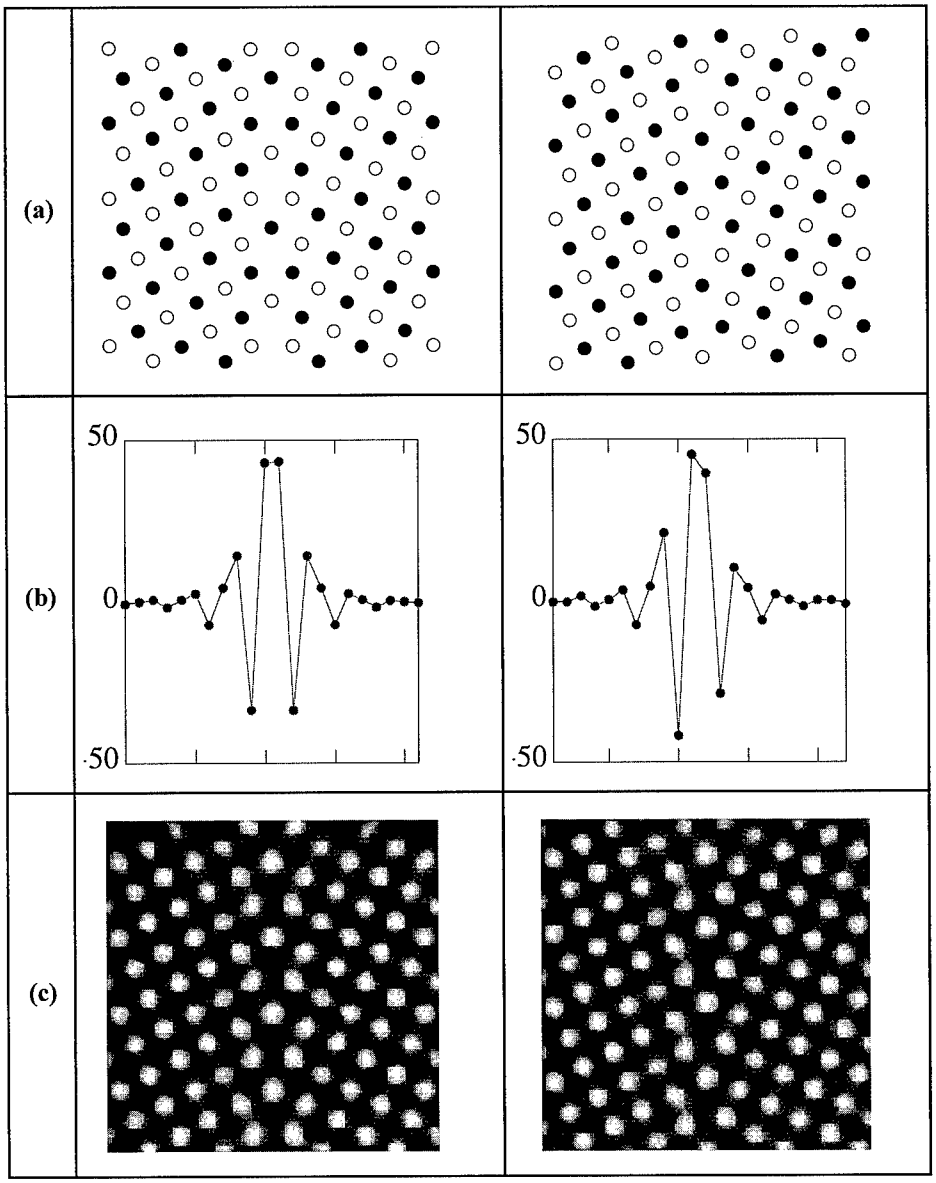

Figure 1 Symmetric and asymmetric configurations of theΣ=5 (210)[001] tilt grain boundary in Cu corresponding to local minima of the potential energy. (a): projections of the relaxed atomic configurations parallel to the [001] tilt axis. Full and open dots stand respectively for atoms at heights z=0 and z=1/2 (b): relaxations of the atomic planes, $\delta d / d_{bulk}(\%)$, as a function of the position along the [210] direction, normal to the interface (c): HREM image contrast simulations as expected for a JEOL 4000 microscope operating at 400 kV. For the imaging conditions used, defocus Δz=-59 nm and a specimen thickness e=8.7 nm, the white dots correspond to the projection of the atomic columns.

Discussion and conclusions

This is the first time, at least in our knowledge, that an asymmetrical configuration has been identified for the studied boundary, which stability is in some limited extent potential independent. Because the excess energy difference with the symmetrical configuration is weak, it is likely that all these boundary structures can exist or coexist at high temperatures and be frozen in if the bicrystal is rapidly cooled. Structural phase transitions may thus occur for this boundary consisting in to its transformation from one structure to another. To which extent such transitions occur and resemble to that previously discovered for this boundary [8] is the subject of work currently in progress [11]. It is worth asking the question on whether or not these findings can be experimentally confirmed. Rigid-body translation measurements would help clarifying this point. Moreover, if all these boundary configurations coexisted at high temperatures, quenching the bicrystal would possibly stabilize boundary steps of known height since separating regions of different structure. Electron microscopy observations of boundary steps might therefore help in deconvoluting the signature of the coexistence at high temperatures of multiple boundary structures and to assess the validity of the results reported in this work.

Acknowledgments

This work has been supported from the Greek Secretariat of Research and Technology in the frame of PENED' 94 n°A1504. VP thanks the Aristotle University of Thessaloniki for hospitality.

References

[1] R. J. Harrison, G. A. Bruggeman and G. H. Bishop, in *Grain Boundary Structure and Properties*, Eds. G. A. Chadwick and D. A. Smith (London: Academic Press) (1976), p. 45.
[2] R. C. Pond, in *Grain Boundary Structure and Kinetics*, ASM (1980), p. 13.
[3] L. Priester, J. Thibault and V. Pontikis, Solid State Phenomena 59-60 (1998), p. 1.
[4] M. Bacia, J.M. Pénisson, J. Morillo and V. Pontikis, Phil. Mag., 76 (1997), p. 945.
[5] G. J. Wang, A. P. Sutton and V. Vitek, Acta Met. 32 (1984), p. 1093.
[6] G. Hasson, J. Y. Boos, I. Herbeuval, M. Biscondi and G. Goux, Surf. Sci. 31 (1972) p. 115.
[7] A. Aslanides and V. Pontikis, Comp. Mat. Sci., 10 (1998), p. 401.
[8] M. Guillopé, J. Phys. 47 (1986), p. 1347.
[9] J. R. Beeler and G. L. KulcInski, in *Interatomic potentials and simulation of lattice defects*, Eds. P. C. Gehlen, J. R. Beeler and R. I. Jaffee (New York: Plenum press) (1972), p. 735.
[10] P. A. Stadelmann, Ultramicroscopy 21 (1987), p. 131.
[11] P. Grigoriadis, Th. Karakostas, Ph. Komninou and V. Pontikis, in preparation.

Materials Science Forum Vols. 294-296 (1999) pp. 181-186

On the Applicability of the CSL Model to Grain Boundaries in Non-Cubic Materials

V.Y. Gertsman and J.A. Szpunar

Department of Metallurgical Engineering, McGill University,
3610 University Street, Montreal, PQ, H3A 2B2, Canada

Keywords: Crystallography, Grain Boundary, Coincidence Site Lattice (CSL)

Abstract Crystallography of grain boundaries in crystal structures of lower symmetry is considered. It is suggested that only twin boundaries are singular in nature. Difficulties in the application of the CSL model to analyzing interfaces in non-cubic materials are discussed. It is shown that the reciprocal volume density of coincident sites, Σ, is not the primary parameter determining the grain boundary structure and properties.

Introduction

The underlying idea in all the models of the grain boundary (GB) structure, which are trying to link physics and crystallography, is that the GB adopts a low-energy structure dictated by some geometrical lattice. First, it is necessary to distinguish a physical model from a geometrical approach. While the coincidence cite lattice (CSL) model is a purely geometrical theory, the widespread misconception is that there is a firm correlation between the reciprocal density of coincident sites, Σ, and physical properties of grain boundaries. There is certainly nothing new in posing the problem that the CSL theory may not be all-encompassing. More than a decade ago, Sutton and Balluffi [1] overviewed the geometrical criteria for GB 'specialness' and concluded that no such a general and useful criterion existed. Nothing has changed since then, which would indicate that the conclusion should be reversed. However, Σ is still being widely used as the main (and, sometimes, the only) parameter describing the GB structure. The present paper is an attempt to demonstrate that while the CSL model may be a useful geometrical approach, any physical conclusions drawn on the basis of some 'magic' numbers, such as Σ, should be treated with caution. Some examples are given to support this conclusion.

Singularity of Twin Boundaries

Let us first restate the fact, already known for a long time, that there is no specific demarcation between 'special' and 'general' boundaries and there is no definite rationale by which a GB may be designated as special or otherwise. The term 'special' implies that the GB has singular properties, i.e. it displays exceptional behavior. The only firmly established boundaries with singular properties in real materials are twin boundaries, the most well-known example being Σ3 coherent twin boundary in f.c.c. materials. Why coherent {111} Σ3 boundaries are so outstanding among all other GBs in the f.c.c. structure? Is it just because of the smallest Σ-value? However, for example, (*i*) Σ5 is not much higher, but there is no reliable evidence that such a GB is really special; (*ii*) Σ3 in the b.c.c. structure does not seem to be so special. What seems to be really unique for Σ3 (111) in f.c.c. is that it lies on the most densely packed crystal plane, and all lattice sites in the GB plane are coincident.

It has been recognized before (see e.g. [1]) that a symmetrical tilt boundary is an extreme example of anisotropy of structure leading to anisotropy of properties, and usually such a boundary corresponds to an extremum in the GB energy. In all known cases, coherent twins have symmetrical tilt boundaries along low-index crystal planes and their structure is two-dimensionally periodic with a small repeat cell. General consideration of such boundaries in lattices of low symmetry shows that, depending on the lattice constants, they can have very large Σ values (see e.g. [2, 3]). That the special (singular) boundary in the f.c.c. structure is described by the lowest possible Σ value ($\Sigma 3$) seems to be rather an exception than a general rule. In a general case, a twinning operation produces only a two-dimensional CSL. For an exact twin boundary, there is a high reticular coincident site density in the twin plane and no constraint is required to create the two-dimensional coincidence. In particular examples, especially when using lattice constraints, three-dimensional CSLs may be formed. It is unclear, however, why this should have any physical significance.

It would be wonderful to have such a simple law as "the lower the Σ value, the more special is the grain boundary", and such a relationship would be extremely useful for such concepts as GB engineering etc. Unfortunately, the laws of nature are not always as simple as we wish them to be. The widely spread belief that 'special' GBs are almost always 'low-Σ' boundaries has actually originated from considerations of the cubic lattices. As mentioned above, symmetrical boundaries along the planes with low Miller indices are expected to have special structure and properties. Misorientation of such a boundary can be described by a 180° rotation around the axis perpendicular to the boundary plane. In a cubic lattice, direction [*hkl*] is perpendicular to the (*hkl*) plane. Then, as can be easily seen e.g. from the quaternion description of misorientations [4-6], for such boundaries $\Sigma=h^2+k^2+l^2$ or $(h^2+k^2+l^2)/2$. Therefore, in the cubic crystal structures, all symmetrical boundaries with a relatively high reticular density of lattice sites (i.e. with low values of $h^2+k^2+l^2$) will have low values of Σ. This is, however, not always the case for other crystal systems. Generally, Σ is a function not only of *h, k, l*, but also of lattice periods and angles, (see e.g. [4-6]). As such, the value of Σ can be high for the symmetrical grain boundaries along low-index planes in non-cubic structures.

Examples of Twin Boundaries in Systems of Lower Symmetry

In the most general case of a triclinic lattice, at least the following twin boundaries are possible: (*i*) on the (100) plane, misorientation 180° about the normal to (100); (*ii*) (010), 180°[⊥(010)]*; (*iii*) (001), 180°[⊥(001)]. We will not analyze them because of two reasons. First, we are not aware of any observations of triclinic lattice twins. Second, the analysis would be similar to the analysis of the (100) and (001) twin boundaries in the monoclinic lattice given below.

An example of material having a monoclinic crystal structure with frequently observed twins is zirconia. A schematic of the unit cell is shown in Fig.1. Several non-equivalent twin variants are possible in monoclinic ZrO_2. Detailed formal analysis of them in the framework of the constrained CSL model can be found in [3, 7]. Here we give a more illustrative consideration of the boundary crystallogeometry. Concerning experimental observations of the twin boundary structure in ZrO_2, because of the limited space provided for the current paper, we have no other choice as to refer to the original publication even though it still

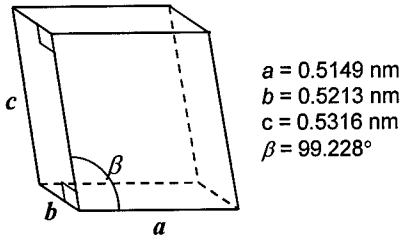

Fig.1. Schematic of the monoclinic unit cell

* [⊥(*hkl*)] denotes normal to the (*hkl*) plane

in press [8].

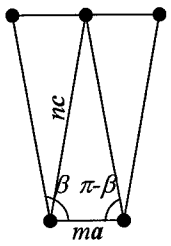

Fig.2. CSL for (001) twin

Let us start e.g. from the (001) twin boundary, which is described by the misorientation 180°[100]⇔180°[⊥(001)]. In a general case, for a CSL to exist at this misorientation in any monoclinic lattice, the following relationship must be satisfied (see Fig.2):

$\frac{1}{2}ma = nc\cos(\pi-\beta) = -nc\cos\beta$, or

$$\frac{c\cos\beta}{a} = -\frac{m}{2n}, \qquad (1)$$

where m and n are integers.

Crystal lattice unit cell volume, $V_\Omega = a\times b\times c\times\sin\beta$.

CSL unit cell volume, $V_{CSL} = ma\times b\times nc\times\sin\beta$.

Then, the reciprocal density of coincident sites:

$$\Sigma = V_{CSL}/V_\Omega = mn \qquad (2)$$

Consideration of the (100) twin boundary is similar. Instead of Eq.1 we have:

$$\frac{a\cos\beta}{c} = -\frac{m}{2n} \qquad (3)$$

and again $\Sigma = mn$.

Thus, for some arbitrary lattice we can obtain very big m and n, and as a consequence, huge Σ values. Moreover, approximation of a given crystal lattice by integers m and n may not be unique. This would lead to non-uniqueness (ambiguity) of Σ for a given misorientation.

Let us consider a concrete example of the monoclinic lattice of zirconia. With the lattice parameters given above (see Fig.1), we have:

$c\cos\beta/a = -0.16557$ and $a\cos\beta/c = -0.15532$.

With m=1 and n=3, which correspond to the approximation used in [3, 7]: $a = c$ and $\cos\beta = 1/6$, we obtain Σ=3. Thus, the two misorientations considered above have been designated $\Sigma 3a$ and $\Sigma 3b$, respectively [3]. However, it should be mentioned that while this approximation is good enough for the first misorientation (Eq.1 fulfills with an accuracy of 0.7%), it is rather rough for the second misorientation, i.e. the lattice constraints for constructing the CSL are relatively high, leading to the 6.8% difference between $a\cos\beta/c$ and 1/6. Alternatively, one can choose other approximations of the lattice parameters and, of course, there exist an infinite number of variants. For example, the variant m=4, n=12 produces 0.9% mismatch in Eq.3 and gives Σ=52 for the "$\Sigma 3b$" boundary, whereas at m=9, n=29 the mismatch in Eq.3 is only 0.1% and Σ=261. This is an illustration of the above statement about multiplicity and ambiguity of Σ for a given misorientation (as suggested also in [2]). Two points are to be mentioned, however, in this particular example. First, different constraints of the lattice parameters may seem appropriate for different grain boundaries in the same crystal structure. Second, high-resolution TEM images of $\Sigma 3a$ and $\Sigma 3b$ boundaries in zirconia are actually very similar [8], thus suggesting similar atomic structures. The latter boundary can be assigned some other, large value of Σ, but in the given case the magnitude of Σ tells nothing about the special structure of the boundary.

What about the other twin variants experimentally observed in monoclinic zirconia? Two of them are twin boundaries on the {011} and {110} planes. With the lattice parameters indicated on Fig.1, the former boundary has misorientation 89.6°[100]⇔180°[⊥{011}] and the misorientation of the latter boundary is 91.5°[001]⇔180°[⊥{110}]. When the approximation a=b=c and $\cos\beta$ =1/6 is employed, the 'near-right' misorientation angle becomes 90.8° in both

cases, and both misorientations are characterized by Σ71 (in [3, 8] they are denoted Σ71*a* and Σ71*b*, respectively). No reasonable constraints of the lattice parameters enable obtaining a smaller Σ value. (In other monoclinic lattices, such twin boundaries may be described by even larger Σ values.) HRTEM study [8] has shown that Σ71 twins possess perfect structure and, by the way, Σ71*b* are twice as frequent as Σ3*b* in that particular microstructure. This example clearly demonstrates that the magnitude of Σ tells nothing about the boundary singularity and, in general, the value of Σ can be high for the symmetrical boundaries along low-index planes in non-cubic structures. It should be noted that in such cases as described above, the plane matching concept of GB structure [9] is not of much help because low-index planes in two adjacent grains must not only be parallel, but also have the same orientation to provide for a complete coincidence in the boundary plane. What is happening in such a case is not just "plane matching", but complete "plane coincidence".

The two other twin systems in monoclinic zirconia are those on the (101) and $(10\bar{1})$ crystal planes. The misorientation of the (101) symmetrical twin boundary can be described as $180°[10\bar{1}]\Leftrightarrow 180°[\perp(101)]$. Similarly, the misorientation of the $(10\bar{1})$ twin is $180°[101]\Leftrightarrow 180°[\perp(10\bar{1})]$. If the constrained CSL is constructed with the $a=c$ approximation, then both these boundaries can be formally described by Σ=1 [7]. Moreover, with the above approximation, the two misorientations (not to be confused with the twin planes) become equivalent: $180°[101]\Leftrightarrow 180°[10\bar{1}]$. The term Σ1 is used somewhat loosely in the literature as a synonym to the "low-angle boundary". Therefore, we have denoted such twins as Σ1′ [3]. Because in the non-constrained lattice the misorientations of the (101) and $(10\bar{1})$ twins are physically distinct (although they may not always be distinguishable experimentally [8]), they may be symbolized as Σ1′a and Σ1′b, respectively. Any other approximation of the lattice parameters leads to a huge Σ.

{110)** twin in $YBa_2Cu_3O_{7-\delta}$ is somewhat similar to the previous example. The orthorhombic crystal lattice unit cell of this ceramic has the following parameters: a=0.382, b=0.389 and c=1.167 nm (for the nominal composition, i.e. δ=0). Misorientations of these boundaries can be described as 89.0°[001]⇔91.0°[001]. More precisely, the first rotation angle is equal to 2arctan(a/b), the second — 2arctan(b/a). The other equivalent descriptions of this misorientation are 180-degree rotations about ⟨110] and the normal to {110), that is, $180°\langle\lambda\nu 0]$ ($\lambda{:}\nu=b^2{:}\,a^2$).

Zhu and Suenaga [10] have analyzed the constrained CSL for this misorientation and found the value of Σ to be 64. It should be noted, however, that the lattice superposition corresponding to these boundaries is actually incommensurate, that is, no lattice sites are in exact coincident positions except for the sites in the twin boundary plane (where there is a complete coincidence of all crystal lattice sites). Therefore, using different approximations for the a and b periods, one can, as in earlier examples, obtain different values of Σ. It could be shown that Σ=64 corresponds to $a^2{:}b^2$=63:65, which is no better approximation than $a^2{:}b^2$=29:30 (which contains an inaccuracy less than 0.2% for the nominal axial ratio). With the latter approximation, Gertsman [6] obtained Σ=59 for the misorientation under consideration.

As already mentioned, assigning a Σ value to a misorientation between non-cubic crystals depends, in general, on the choice of the lattice constraints. Moreover, the lattice parameters of YBCO depend on chemical composition. As such, an approximation of $a^2{:}b^2$ by a large number ratio, as used above, may be too fine. Most researchers seem to agree that $a=b$ is a fairly good approximation. It can be shown that in this case instead of 90°–Δ or 90°+Δ rotations about [001], the misorientation is described simply as 90°[001], and the corresponding Σ is equal to 1. This

** Different opening and closing brackets are used here (and below for direction indices) to indicate that changing the signs of the first two indices gives crystallographically equivalent variants.

misorientation in YBCO can be denoted as $\Sigma 1'$, as has been done in a similar situation in zirconia (see above).

Different approximations and, as a consequence, different CSL reference systems create some problems. It is implied in the CSL model that Burgers vectors of full grain boundary dislocations are determined by the DSC lattice which is derived from CSL. In the $\Sigma 1'$ reference system, interfacial Burgers vectors would be limited to lattice vectors, which is apparently not true (see e.g. [10]). Ambiguity in choosing a high-Σ approximation, however, does not allow defining the Burgers vectors precisely, either. Also, use of a large-but-finite-Σ reference system leads to another difficulty. The (110) and $(1\bar{1}0)$ planes are equivalent in any orthorhombic lattice and, as such, the (110) and $(1\bar{1}0)$ twins in YBCO are crystallographically equivalent (contrary to what was implied in [11]). As such, the same boundary can have both the (110) and $(1\bar{1}0)$ facets. If one were to draw a high-Σ CSL (e.g. 59 or 64) for the (110) and $(1\bar{1}0)$ facets with respect to the same matrix crystal, the two identical CSLs would be obtained, but they would not coincide with each other being instead mutually rotated. By definition, however, a CSL should depend only on the misorientation and not on the position of the boundary surface and all facets of the same boundary should belong to the same reference CSL system.

Discussion and Conclusions

The reciprocal density of coincidence sites, Σ, is a convenient parameter describing the boundary geometry, in the sense that it allows (although not always unambiguously) replacement of three parameters describing a misorientation by a scalar number. That is, multiple crystallographic variables are replaced by a single parameter. However, historically the significance of this parameter has been overvalued and it has often been assumed that there might be a correlation between the magnitude of Σ and some physical properties. Analyses of non-cubic crystal lattices clearly demonstrate that the Σ value depends on the approximation of the lattice parameters (constraints) used in the model and the same boundary structure may be interpreted in different ways according to the choice of reference. As mentioned above, this causes some serious problems. For cubic lattices there has been a weak consolation that although not all misorientations with small Σ values correspond to 'special' GBs, but at least all singular GBs have small Σ. For non-cubic structures even this rule of thumb does not work.

Summarizing, the Σ parameter is fundamentally incapable of predicting the GB properties and it is probably not a primary parameter describing the GB structure. Therefore, for example, a GB character distribution with respect to Σ might be a classification according to a secondary parameter. Discussions of the upper limit of Σ and allowable deviations from 'specialness' based on this parameter also have little physical sense. Thus, criterions for deviation from exact coincidence, such as Brandon's [12] actually presume that the boundary structure varies systematically with the Σ value. Strictly speaking, however, neither the original Brandon criterion nor its modifications [13-15] attempting to improve it have ever been rigorously proven from 'first principles' applicable to the whole range of possible misorientations. There are doubts concerning the applicability of such a criterion even for the cubic structures, see e.g. [16], and certainly there is no guarantee that it should work well for other lattices, as mentioned e.g. by King and Singh [2]. As shown above, the possible twin variants in zirconia have very different Σ values. It is totally unclear why one should expect that a deviation e.g. from the (100) twin would lead to less dramatic changes in the interfacial structure and energy than a similar deviation from the (110) twin.

Probably, the utility of the CSL model, particularly of a constrained CSL, is that it provides a rather convenient nomenclature for designating GBs. Also, in many cases, CSL theory has proven its usefulness e.g. for determination of Burgers vectors of GB dislocations (through the DSC lattice approach), at least, in cubic structures. However, it is a purely geometrical approach, and attempts to assign some oversimplified physical meanings to geometrical parameters (for example, establishing some straightforward correlations between Σ and GB properties, such as energy) are doubtful. Apparently, some other approaches are needed for a GB model, which would have a predictive power for the interfacial structure and properties. For example, a rather old idea that a two-dimensional periodicity in the boundary may be more important than a three-dimensional periodicity of the bicrystal is worth consideration. Such ideas resurface from time to time (see e.g. [18-20] among recent examples) Actually, what seems to be important for special GBs is not that Σ is low, but that the CSL has some planes with a high reticular density of coincident sites. Since GBs are essentially two-dimensional, it seems likely that the periodicity in the boundary plane is more significant for the GB energy than any periodicity in the direction normal to the plane. Alternative (or, maybe, complimentary) consideration is the requirement of a bicrystal symmetry for really singular GBs. Pond's approach [17] may be relevant in this regard. There might be, however, a small drawback in the latter approaches because there exist some experimental indications that not only symmetrical twin boundaries are singular, but also some asymmetrical planes of twin boundaries may be special. For example, HRTEM study [8] has revealed that (010) facets are present along with the symmetrical (100) planes of Σ3b twin boundaries. These asymmetrical GBs are also planar, extended and seem to have an ordered structure.

References

[1] A.P.Sutton and R.W.Balluffi, Acta Metall. **35** (1987) 2177.
[2] A.H.King and A.Singh, J. Phys. Chem. Solids **55** (1994) 1023.
[3] V.Y.Gertsman, A.P.Zhilyaev and J.A.Szpunar, Modelling Simul. Mater. Sci. Eng. **5** (1997) 35.
[4] H.Grimmer, Acta Cryst. **A45** (1989) 320; 505; Scripta Metall. **23** (1989) 1407.
[5] V.Y.Gertsman, Sov. Phys. Crystallography **30** (1989) 349; J. Physique. **51** (1990) C1-145.
[6] V.Y.Gertsman, Scripta Metall. Mater. **27** (1992) 291.
[7] V.Y.Gertsman, A.P.Zhilyaev and J.A.Szpunar, Sripta Mater. **35** (1996) 1247.
[8] V.Y.Gertsman, Y.P.Lin, A.P.Zhilyaev and J.A.Szpunar, Phil Mag. A (1998) in press.
[9] P.H.Pumphrey, Scripta Metall. **6** (1972) 107.
[10] Y.Zhu and M.Suenaga, Phil. Mag. **A66** (1992) 457.
[11] A.H.King and Y.Zhu, Phil. Mag. **A67** (1993) 1037.
[12] D.G.Brandon, Acta Metall. **14** (1966) 1479.
[13] P.H. Pumphrey, in Grain Boundary Structure and Properties, Eds. G.A.Chadwick and D.A.Smith, Academic Press, NY (1976), p.139.
[14] M.Dechamps, F.Baribier and A.Marrouche, Acta Metall. **35** (1987) 101.
[15] G.Palumbo and K.T.Aust, Acta Metall. Mater. **38** (1990) 2343.
[16] V.Gertsman and K.Tangri, Scripta Metall. Mater. **32** (1995) 1659.
[17] R.C.Pond, in Dislocation in Solids, Vol.8, Ed. F.N.R.Nabarro, North-Holland, Amsterdam (1989).
[18] I.MacLaren and M.Aindow, Phil. Mag. Lett. **76** (1997) 25.
[19] P.Lejček, V.Paidar, J.Adamek and S.Hofmann, Acta Mater. **45** (1997) 3915.
[20] V.Randle, Acta Mater. **46** (1998) 1459.

Materials Science Forum Vols. 294-296 (1999) pp. 187-190

The Variety of Structures of the Σ=3 Incoherent Twin Boundary in β-SiC

K. Tanaka, M. Kohyama and M. Iwasa

Department of Material Physics, Osaka National Research Institute, AIST, 1-8-31 Midorigaoka, Ikeda, Osaka 563-8577, Japan

Keywords: Grain Boundary, Atomic Structure, Incoherent, β-SiC, HREM, Structural Unit Model

Abstract: The variety of structures of Σ=3 incoherent twin boundary in β-SiC was studied by high resolution electron microscopy (HREM). The structure of Σ=3 incoherent twin boundary consists of an array of structural units and the array changes its features depending on its length. The array is comprised of aligned symmetrical structural units which are composed of 5, 7, and 6 membered rings in this order at short boundary, both symmetrical and asymmetrical structural units at middle boundary, and zigzag or obliquely distributed symmetrical structural units at long boundary. It is known from tight-binding calculation that the energy difference between the symmetrical 5-7-6 membered rings structural unit and the asymmetric one is not so large if Si atoms are reconstructed, and then both structures can occur. The results of HREM were in good agreement with the theoretical calculation.

Introduction: The study of grain boundary (GB) by high resolution electron microscopy (HREM) is now one of the main tools for understanding materials. Especially, the structure of Σ=3 incoherent twin boundary has long been discussed in many materials (Au [1], Si [2], Ge [3], Diamond [4], SiC [5]) experimentally and theoretically. A rigid body translation of one grain relative to the other is an important part of the atomic relaxation of a grain boundary. The presence of a rigid body translation along the common <111> direction was found in some materials [1-3], whereas no rigid body translation was found under different conditions [2] or in the other materials [4]. It was also pointed out that the translation state was sensitive to the environment of the boundary. Finally, the inclination of the boundary plane can also be a possible factor in the decrease of the energy. In fact, a minimum of the energy has been found theoretically [6] for a deviation angle of 8 degrees away from the symmetric position in Cu.

In the present study, several types of Σ=3 incoherent twin boundaries of different length in β-SiC, and its junction with {111} Σ=3 coherent twin boundaries have been investigated by HREM and compared with a theoretical study [7].

Experiment: The transmission electron microscope (TEM) specimen of chemical vapor deposition (CVD) β-SiC was prepared by mechanical thinning and ion milling. CVD techniques can easily provide dense materials of high purity, and interfaces that are well defined even in covalent materials. Moreover, CVD specimens often exhibit preferential orientation during growth, and this enhances the probability of coincident site lattice (CSL) grain boundary formation. HREM analysis was performed on CVD β-SiC with a preferential orientation of {220} and grain size of approximately

Fig. 1 HREM image of several types of Σ=3 and Σ=9 boundaries. A small letter c and i indicate coherent and incoherent, respectively.

10μm using field emission TEM (JEOL, JEM-3000F).

Atomic models were given on the basis of structural unit model. Lattice relaxation has been performed by using the self-consistent tight-binding (SCTB) method following our previous studies[8]. The SCTB method can deal with energies and atomic and electronic structures of complex systems of semiconductors as well as the usual tight-binding method. In the SCTB method, the charge transfer effects are included self-consistently into the on-site terms of the Hamiltonian. Thus, self-consistent charge distributions and electrostatic interactions can be dealt with more correctly than the usual method, which is essential in SiC. The results of HREM and SCTB calculation are compared.

HREM: Most of the grains contained many stacking faults and twin boundaries due mainly to the low stacking fault energy and CVD technique. The majority of grain boundaries were Σ=3 coherent twins lying on a {111} plane, showing a sharp and well defined contrast. Twins were often very thin, usually only a few atomic layers thick. Figure 1 shows several types of Σ=3 and Σ=9 in β-SiC. It is seen that there are short, middle and long Σ=3 incoherent boundaries, and the long boundary is curved. In the present study, these Σ=3 incoherent twin boundaries of different length, and its junction with a {111} Σ=3 coherent twin boundary in β-SiC have been investigated by HREM and atomic models were given.

Theoretical Calculation: Polar and non-polar interfaces in grain boundaries in cubic binary compounds can be defined by the interface stoichiometry. About symmetrical tilt boundaries, non-polar interfaces can be constructed with both non-polar surfaces or by cation-terminated and anion-terminated polar surfaces. Polar interfaces can be constructed with two cation-terminated polar surfaces or with two anion-terminated polar surfaces. On the other hand, a paratwin and orthotwin can be defined by the relation between the polarity of the two grains for symmetrical tilt boundaries in binary compounds. In a paratwin, the polarity of the two grains displays mirror symmetry to each other with respect to the interface. One additional paratwin can be constructed by inverting the polarity of the two grains. An orthotwin is constructed by inverting the polarity of one of the two grains of the paratwins. Thus, for symmetrical tilt boundaries of which the interface consists of polar surfaces such as {111} and {211}, two polar and one non-polar interfaces can be constructed, which correspond to two paratwins and one orthotwin. And symmetrical tilt boundaries of which the interface consists of non-polar such as {211} should have only non-polar interfaces.

In configurations without any coordination defects similar to those of the symmetrical tilt boundaries in Si or Ge [8-10], the interface stoichiometry should dominate the relation between the numbers of the two kinds of wrong bonds, cation-cation bonds and anion-anion bonds. The polar interfaces should contain only one kind of wrong bonds or one kind of excess wrong bonds, although non-polar interfaces should contain no wrong bonds or the same number of the two kinds of wrong bonds.

The {211} Σ=3 incoherent boundary is connected perpendicularly with the {111} Σ=3 coherent boundary in β-SiC [5]. Thus, the observed Σ=3 incoherent boundary should be a paratwin because the {111} Σ=3 coherent boundary must be a orthotwin with normal Si-C bonds. In this paper, we deal with only the paratwins.

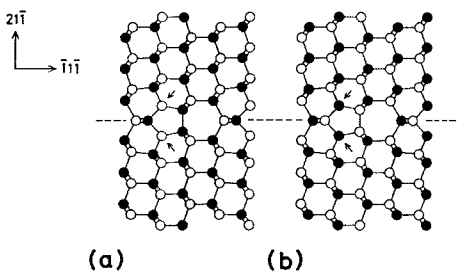

Fig. 2 Atomic models of the {211} Σ=3 incoherent boundary in β-SiC. (a) Type A and (b) Type B of the p2'mm' (1x2) model. Arrows indicate the <011> bonds. The open and closed circles are Si and C atoms, respectively.

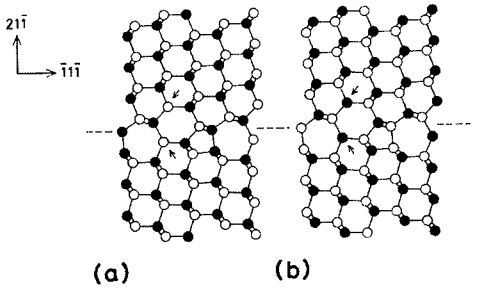

Fig. 3 Atomic models of the {211} Σ=3 incoherent boundary in β-SiC. (a) Type A and (b) Type B of the pm (1x2) model. Arrows indicate the <011> bonds. The open and closed circles are Si and C atoms, respectively.

Figure 2 and 3 show the atomic models of the non-polar interfaces of the {211} Σ=3 incoherent twin boundary in β-SiC. These are the p2'mm' (1x2) and pm (1x2) models. Two paratwins, Type A and B, are constructed for the respective models.

The present models contain the same number of the two kinds of wrong bonds because of the non-polar interfaces. The wrong bonds exist at the two types of positions. These are the intergranular bonds and the <011> bonds. The intergranular bonds exist on the {022} plane and cross the interface. The <011> bonds which are reconstructed connect the two atoms on the neighboring {022} planes, and double the periodicity along the <011> direction as indicated by (1x2). The kinds and positions of the wrong bonds in Type A are inverted in Type B.

In Si or Ge, there exist experimental and theoretical studies [9-11] showing the presence and stability of the <011> bonds in Σ=3 incoherent boundary. And it is considered that the cm (2x2) model is the most stable in Si or Ge, where only the succession of the <011> bond along the <111> direction is different from the pm (1x2) model and the periodicity along the <111> direction is double in addition to the <011> direction. However, the energy difference between the pm (1x2) and cm (2x2) models seems to be very small in Si [10, 11]. Thus, we deal with only (1x2) models for simplicity.

Table 1 Calculated interfacial energy E_{gb} values of the models of the {211} Σ=3 boundary in β-SiC.

	p2'mm' (1x2)		pm (1x2)	
	Type A	Type B	Type A	Type B
E_{gb}	1.71J/m^2	2.37J/m^2	1.39J/m^2	2.42J/m^2

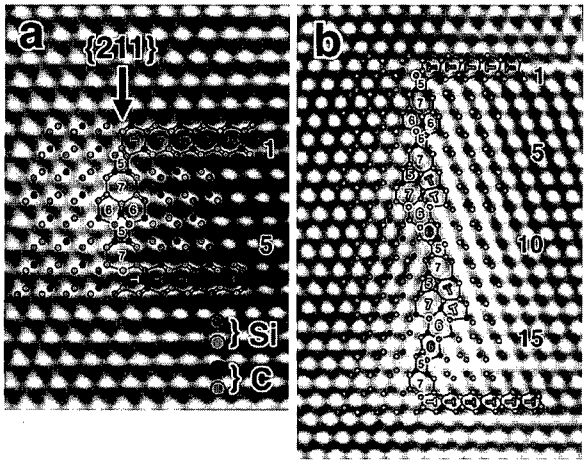

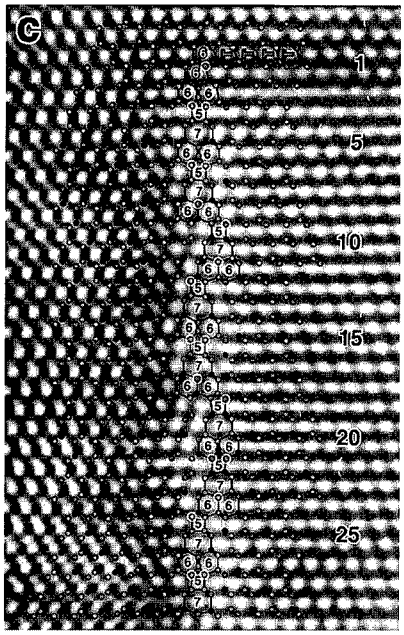

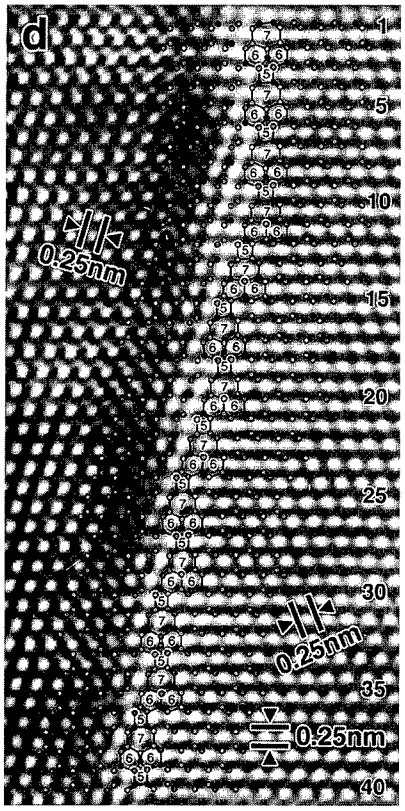

Fig. 4 Structural unit models superimposed on HREM images. The length of Σ=3 incoherent boundary is (a) 6 {111} layers, (b) 18 {111} layers, and(c) and (d) long, respectively.

The details of tight-binding calculation are written in ref. [7]. Table 1 shows the energies of the relaxed configurations. Type A of the pm (1x2) model is the most stable and Type B of the pm (1x2) has the largest energy. The energy difference between Type A of the p2'mm' (1x2) and Type A of pm (1x2) is not so large, which indicates both structures can occur. The rigid body translation in Type A of p2'mm' model is a dilation of 0.001nm, and that Type B is a dilation of 0.024nm. The rigid body translation in Type A of the pm (1x2) model is a shift of 0.072nm along the <111> direction with a dilation of 0.016nm. That in Type B is a shift of 0.068nm along the <111> direction with a dilation of 0.032nm. In both the models, the interfaces where the Si-Si bonds are the intergranular bonds contain larger dilations. The translations in the pm (1x2) models are qualitatively similar to those in the pm (1x2) or cm (2x2) models in Si or Ge [9-11].

Discussion & Conclusion: Figure 4(a)~(d) are structural unit models superimposed in HREM images. The length of twins is (a) 6 {111} layers, (b) 18 {111}layers, and (c) and (d) long. White circles represent the reconstruction along <011> direction. It is obviously seen that structural unit which consists of symmetrical 5-7-6 membered rings align along the boundary in Fig. 4(a), symmetrical structural units are filled in near the corner between coherent and incoherent boundaries and asymmetrical 5-7-6 membered rings structural units are filled in at the middle of the incoherent boundary in (b), symmetrical 5-7-6 membered rings structural units zigzag in (c) and incline in (d). All structural unit models fit with the HREM images very well. It should be noted that the position of all white circles corresponds the Si site, which agrees with the theoretical prediction.

It should be noted that the structure of {111} Σ=3 coherent boundary is very stable and rigid, which means it plays like an anchor, and in real materials a {211} Σ=3 incoherent boundary always stay with a {111} coherent boundary, which is essentially different from the ideal bicrystal in the simulation. It also should be remembered that an asymmetrical structural unit (pm (1x2)) makes the rigid body translation along the common <111> direction. At the short boundary, it is difficult to translate along the common <111> direction because the top and bottom of the incoherent boundary are anchored by the {111} coherent boundaries. However, the <111> translation can occur at the relatively long boundary because the restriction from the coherent boundary is not so severe near the center of the boundary. And probably the zigzag and inclined distribution of symmetrical structural units might be the possible factor to decrease the boundary energy. It is also important to note that an inclined distribution of symmetrical structural units can make a different boundary deviated away from {211} plane.

As discussed above, the structures of Σ=3 incoherent twin boundaries in β-SiC were explained very well by the prediction of SCTB calculation.

References:

[1]H. Ichinose, Y. Ishida, N. Baba and K. Kanaya, Phil. Mag. A52(1985), p. 51
[2]H. Ichinose, Y. Tajima and Y. Ishida, Grain Boundary Structure and Related Phenomena, (The Japan Institute of Metals), (1986), p. 253
[3]A. Bourret and J.J. Bacmann, ibid., p.125
[4]Y. Zhang, H. Ichinose, Y. Ishida, K. Ito and M. Nakanose, Mat. Res. Soc. Symp. Proc. Vol. 426 (1996), p.355
[5]P. Pirouz and J. Yang, Mat. Res. Soc. Symp. Proc. Vol. 183 (1990), p.173
[6]U. Wolf, P. Gumbsch, H. Ichinose and H.F. Fischmeister, Intergranular and Interphase Boundaries in Materials (Les editions de Physique) C1, 51(1990), p.275
[7]M. Kohyama and R. Yamamoto, Mat. Res. Soc. Symp. Proc. Vol. 339 (1994), p. 9
[8]M. Kohyama, S. Kose, M. Kinoshita and R. Yamamoto, J. Phys. Condens. Matter 2(1990), p. 7791
[9]A. Bourret and J.J. Bacmann, Surf. Sci. 162(1985), p. 495
[10]A.T. Paxton and A.P. Sutton, J. Phys. C21(1988), L481
[11]M. Kohyama, R. Yamamoto, Y. Watanabe, Y. Ebata and M. Kinoshita, J. Phys. C21(1988), L695

Correspondence to: Dr. Koji Tanaka
Department of Material Physics
Osaka National Research Institute, AIST
1-8-31 Midorigaoka, Ikeda, Osaka, 563-8577, Japan
e-mail: koji@onri.go.jp, Fax: +81-727-51-9627

Materials Science Forum Vols. 294-296 (1999) pp. 191-194

On the Existence of Periodic Interfaces in the Layered Compound $TlBiS_2$

E.K. Polychroniadis[1], N. Frangis[1] and M. Ozer[1,2]

[1] Department of Physics, Aristotle University of Thessaloniki;
GR-54006 Thessaloniki, Greece

[2] Permanent address: Physics Department, Yildiz Technical University, Istanbul, Turkey

Keywords: Electron Microscopy, Periodic Interfaces, Superstructures

Abstract

Single $TlBiS_2$ crystals are studied by transmission electron microscopy. It is found that the compound has a very long period superstructure –in addition to an already known one due to ordering of Tl and Bi atoms on separate $(111)_R$ planes- which rises by periodic ordering of $(114)_R$ interfaces in the basic superstructure matrix. Models for this superstructure, which is probably related to composition modulation are proposed.

Introduction

$TlBiS_2$ is a layered narrow-gap semiconductor belonging to the Tl_2S-Bi_2S_3 system, structurally and electronically analogous to $TlBiTe_2$ and $TlBiSe_2$. Members of this family of compounds, under the general formula $TlBiX_2$ (X: Te, Se, S), have been proposed for different interesting applications (acousto – optic modulators, thermoelectric generators, IR-detectors etc [1,2]). $TlBiS_2$ is referred also as preudo-PbS, because Tl and Bi lie on both sides of Pb in the periodic table. Similarly to PbS, it has a NaCl-type structure, although a slight elongation along $[111]_R$ creates its rhombohedral (pseudocubic) structure (space group: $R\bar{3}m - D_{3d}^5$). In this structure Tl and Bi are randomly distributed on one of the two f.c.c. sublattices. Apart of this basic structure, a superstructure has been reported –also found for $TlBiSe_2$ and $TlBiTe_2$ [3,4]- which occurs by ordering of Tl and Bi on separate $(111)_R$ planes creating a sequence of ...Tl S Bi S Tl S Bi... layers. In this way the lattice parameter along $[111]_R$ is doubled. This basic superstructure can be described by a nearly cubic multiple cell of lattice parameters a_R=12.434 Å and α_R=88.64° [5]. $TlBiS_2$ is a layered material with an easy cleavage perpendicular to $[111]_R$.

Electron microscopy observations

The electron diffraction study of $TlBiS_2$ crystals confirms the already known superstructure as the period along $[111]^*_R$ is halfed, i.e. is doubled in the real space. Apart from this type of superstructure spots, another family of satellite spots is present in the electron diffraction patterns (Fig. 1). They lie along the $[114]^*$ direction and they have a very small separating distance between them, corresponding to a period of about 80 Å in the real space. It is obvious that a long period superstructure occurs. Since the satellite spots accompany both the basic and the superstructure reflections the parent structure of this has to be considered the basic superstructure described above.

Bright field images (Fig. 1) show the presence of linear periodic contrast; its period is consistent with the one found from electron diffraction. As also expected the satellite spots sequences are perpendicular to these lines. Tilting around $[111]_R$ both the satellite spots in the diffraction pattern and the

black lines in the image remain present. It is remarkable that a similar effect is also observed in the mixed crystals of the compounds family $(TlBiS_2)_x - (TlBiSe_2)_{1-x}$ [6].

Another remarkable point is that this long period modulation presents a lot of faults. An example is shown in Fig. 2. In area A and B the dark lines have a "twin" configuration. In areas C and D the "twin" crystals are superimposed (i.e. the twin interface is parallel to the plane of observation). In area B a sequence of "antiphase boundaries" is observed. The dark lines of modulation are shifted as they intersect these interfaces. This observation clearly demonstrates that this long period modulation is a structural property of the compound and it cannot be attributed to any artifact due to several reasons, as for example specimen preparation techniques.

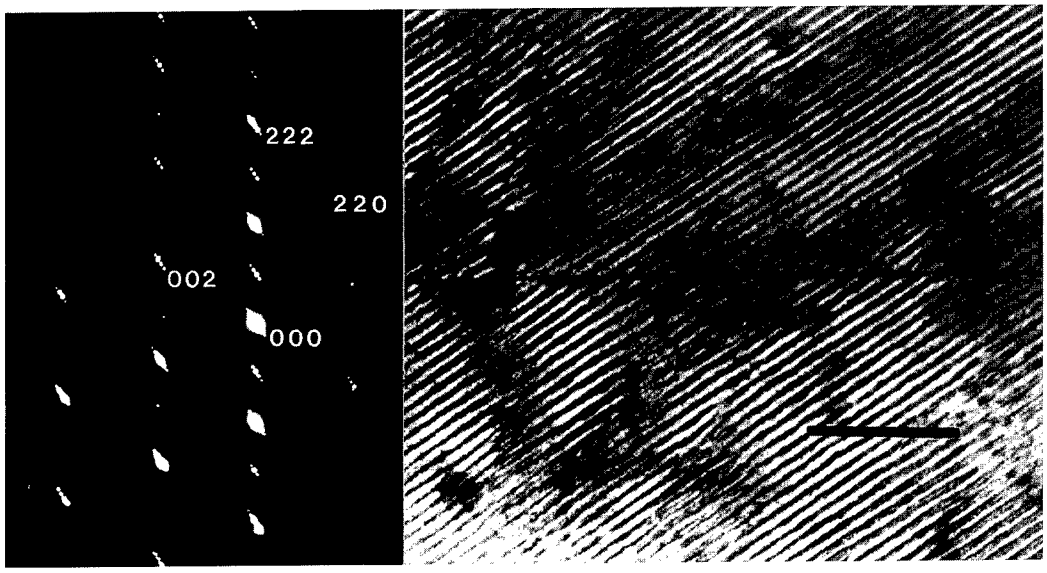

Figure 1: Bright field image showing the periodic modulation planes in $TlBiS_2$. An isolated fault parallel to $(111)_R$ planes is present. The corresponding $(1\bar{1}0)^*$ electron diffraction pattern is also presented. The indices refer to the pseudocubic basic structure (bar =100 nm).

Discussion and conclusion

Due to the small separating distance between them, the satellite spots are always present in the diffraction pattern, because they are very close to the Ewald sphere. For this reason the accurate determination of the plane of the reciprocal space where they lie is not so straightforward. A criterion to decide about this, it might be the sharpness of the dark lines in the corresponding bright field image. Under these circumstances we have determined that the satellite spots lie along $[114]^*$ direction.

Also the basic diffraction spots remain at their initial positions in the electron diffraction patterns. Hence the lattice of the basic NaCl structure remains undisturbed. Therefore all the possible models have to conform to this assumption.

This type of modulation is related to compositional modulation as suggested in [7-9]. In our case it is the cations' or/and the anions' composition which fluctuates in the bulk material almost periodically and gives rise to the appearance of this contrast.

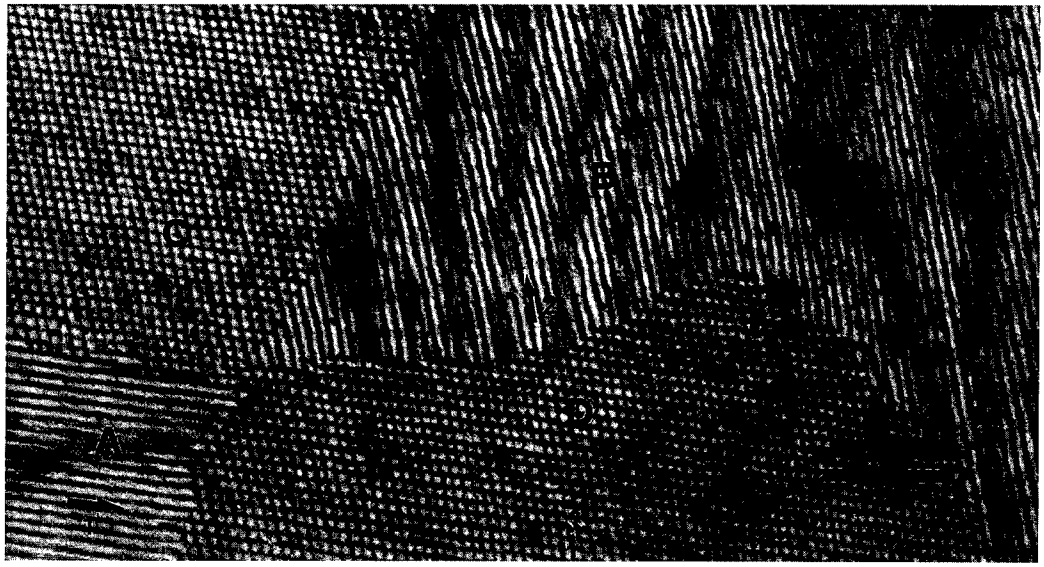

Figure 2: Image from an area with "faults" of the modulated structure. The traces of the modulation planes are indicated by arrows 1 and 2 in the "twinned" areas A and B, respectively. Both gratings are visible at areas C and D because of the presence of "twin" crystals with their interface parallel to the plane of the photograph. Note the presence of "antiphase boundaries" in area B. The relative shift is shown by looking along the direction 2 (bar =100nm).

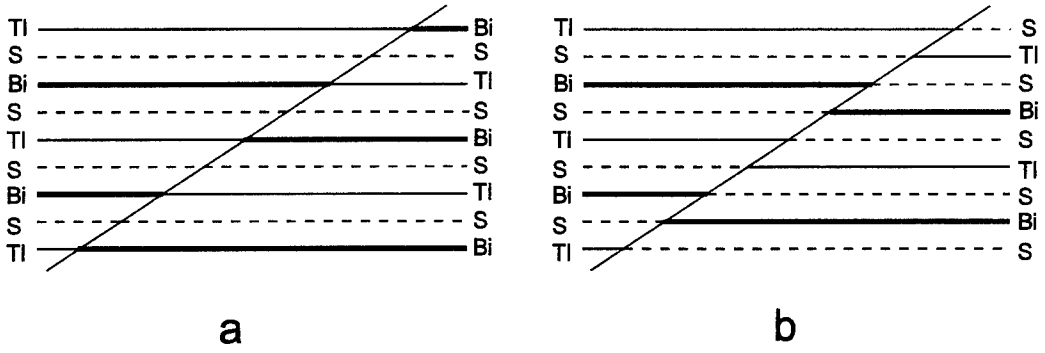

Figure 3: Two possible models for the periodic interfaces observed in $TlBiS_2$ crystals. a) The S layers remain undisturbed and Tl and Bi layers interchange their positions on both sides of the $(114)_R$ interface. b) Cations and anions layers interchange their positions.

An alternative interpretation can be given considering, according to the fractional shift method [10], that the origin of these spots can be a periodic sequence of shear planes with a displacement vector **R**. Two possible models explaining the present modulation are shown in Fig. 3. In both cases **R** is not parallel to $(114)_R$. In the first case the planar interfaces can be characterised as antiphase boundaries in the basic structure and in the second case as antiphase boundaries in the basic superstructure. It is worthy to note that depending on the exact position of the interfaces and at the exact value of **R** these boundaries can be non-conservative for the stoichiometry. So in this way the overall composition can be modified to $TlBiS_{2-x}$. Such a composition is not surprising, because S is the most volatile element of the three constituents of the compound and therefore some small quantity has been possibly evaporated during the preparation procedure.

Having all these experimental data, the coexistence of both modes for modifying the composition cannot be excluded.

References

[1] L.G.Voinova, V.A.Bazakutsa, S.A. Dembovskii, L.G.Lisovskii, E.P.Sokol and Ch.T.Kantser, Izv.VUZ. Fizika **5**, (1971), p.154.
[2] R.Feigelson, Jap.J.Appl.Phys. **19** Supplement **19-3**, (1980), p.371.
[3] E.K.Polychroniadis, J.Stoemenos, J.Mater.Sci. **17** (1982), p.2077.
[4] S.N.Toubektsis, E.K.Polychroniadis, J.Cryst.Growth, **84** (1987), p.316.
[5] M. Ozer, K. M. Paraskevopoulos, A. N. Anagnostopoulos, S. Kokkou and E. K. Polychroniadis, Semicond. Sci. Technol. . **11** (1996), p. 1405.
[6] M. Ozer, K. M. Paraskevopoulos, A. N. Anagnostopoulos, S. Kokkou and E. K. Polychroniadis, Semicond. Sci. Technol. **13** (1998), p. 86.
[7] N. Nakayama, K. Kosuge and S. Kachi, J. Sol. State Chem. **36** (1981), p. 9.
[8] A. C. Holladay and L. Eyring, J. Sol. State Chem. **64** (1986), p. 113.
[9] N. Frangis, C. Manolikas and S. Amelinckx, Phys. Stat. Sol. (a) **125** (1991), p.97.
[10] J. Van Landuyt, R. De Ridder, R. Gevers and S. Amelinckx, Mat. Res. Bul. **5** (1970), p. 353.

Materials Science Forum Vols. 294-296 (1999) pp. 195-198

Defect Structure and Processes in a 1-D Periodic Interface

A. Serra[1], D.J. Bacon[2] and R.C. Pond[2]

[1] Universitat Politècnica de Catalunya, Departament de Matemàtica Aplicada III, E-08034 Barcelona, Spain

[2] The University of Liverpool, Materials Science and Engineering, Department of Engineering, L69 3BX Liverpool, U.K.

Keywords: Incommensurate, Atomistic Simulation, Interfacial Defects

Abstract

The majority of experimental observations and atomistic simulations of interfaces are concerned with two dimensionally periodic structures. However, most interfaces in engineering materials have a more general character, and it is important to study these. The present work describes computer simulation of a one-dimensionally periodic interface and represents the first step towards study of more general interfaces.

The particular interface investigated is a [1-210]/90^0 tilt boundary in α-Ti (h.c.p.), where the boundary plane is (10-10) in one crystal and (0001) in the other. This configuration exhibits periodicity along the tilt axis but is incommensurate perpendicular to this. A many-body potential of the Finnis-Sinclair type has been used in the simulation. The minimum energy structure has been determined and the nature of defects investigated. In contrast to periodic interfaces, the defects are not localised in some cases.

Introduction

The interface considered here is the 90^0 tilt boundary formed when the (0001) basal plane of one crystal is joined to a {10-10} first-order prism plane of another with <11-20> axis in common. It is periodic along this axis but incommensurate in the orthogonal direction. This is the first time that defect processes in such an interface have been studied at the atomic level and it represents a preliminary step towards the study of defects in non-periodic boundaries.

Method of Atomic Simulation

The model was created by simply orientating the basal plane of the lower crystal (μ) parallel to the first-order prism plane of the upper crystal (λ), with the close packed direction [1-210] common to each. Since the period along the direction Y (perpendicular to the [1-210] axis) is different on each side of the interface, unless c/a is $\sqrt{3}$, exact periodicity was not achieved. However, the lattice parameter ratio c/a in α-titanium is such that the magnitude of 12 [10-10] is similar to 13 [0001], i.e., $12\sqrt{3}a$ (= 20.785a) is close to 13c (= 20.693a), with a misfit of 0.4%, and it was found helpful to describe the boundary structure in terms of this pseudo-periodicity.

Periodic boundary conditions were employed along the common [1-210] axis with the block thickness equal to the lattice repeat distance a. Fixed boundary conditions were imposed on the surrounding outer regions in the other two directions. The length of the relaxable crystal in the Y direction was $36\sqrt{3}\ a \approx 39c$. The inner relaxable region contained up to 6000 atoms and was relaxed by minimising the potential energy by the method of conjugate gradients. For the simulation of the interaction of a crystal dislocation with the interface, the core of a dislocation with

line direction [1-210] was created near the boundary by imposing the displacement field of isotropic elasticity on all the atoms prior to relaxation. Simulations of interfacial defects not formed directly by decomposition of crystal dislocations were initiated by introducing them at the relaxed interface. The potential used for α-Ti is of the Finnis-Sinclair type derived by Ackland [1] and has been used for the simulation of interfaces and crystal defects [5] in good agreement with HREM observations.

Structure of the defect-free interface

After an initial relaxation the interface was almost unchanged and is plotted in fig.1(a). The arrows superimposed on the plot show the sign and magnitude of the pressure at each atomic site. The pseudo-periodicity corresponding to $12\sqrt{3}$ a in the lower crystal and 13c in the upper is apparent. The regions where the pressure has the largest magnitude are apparent (compression on (0001) and tension on (10-10)). However, the mismatch is not concentrated exclusively in these zones but is distributed rather evenly along the boundary. This implies that the γ-surface [2] for this interface is relatively flat along the direction orthogonal to the common [1-210] axis, and that the easy accommodation of relative shifts of the two half-crystals along this direction may influence the product of dislocation decomposition in this boundary. On simulating an interaction of a screw dislocation (**b** = **a**) with this interface, we found that it was totally absorbed by splitting into two **a**/2 dislocations which where accommodated in the two adjacent, highly-stressed zones (HSZ) of fig.1(a). This absorption *lowered* the boundary energy, showing that the interface in fig.1(a) is metastable. The state of stable equilibrium can be obtained by relaxation from the structure of fig.1(a) following the introduction in the HSZ of a pair of closely spaced screw dislocations of opposite sign and Burgers vectors ± **a**/2 = ±1/6[1-210]. The relaxed boundary therefore exhibits a series of screw dipoles. Since the dipole spacing is small compared with the separation of HSZ, there is little interaction between the dipoles and the interface between them is similar to that in fig.1(a). The energy of this interface is 390 mJm^{-2} and its structure is plotted in fig.1(b).

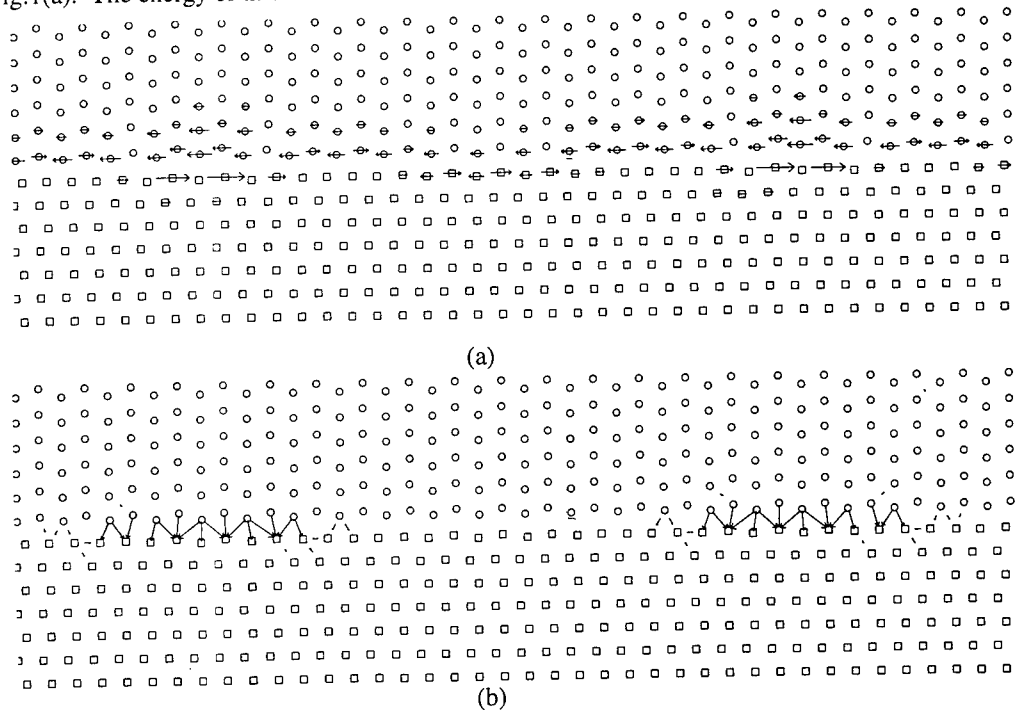

Figure 1. (a) Interface in [1-210] projection after an initial relaxation where no displacements along the tilt axis occur. The arrows show the pressure at each atomic site. (b) Stable interface. The arrows showing relative displacements locate the position of the screw dipoles.

Topological description of interfacial defects

The topological properties of interfacial defects were set out in recent papers using an integrated and comprehensive treatment based on the fundamental consequence of symmetry-breaking in crystalline materials [3,4]. For interface line defects, the theory shows that admisible defects are characterized by operations $Q_{ij} = (\mathbf{Q}_{ij}, \mathbf{q}_{ij})$ that are given by the product of two symmetry operations, one from each of the two crystals (see ref. 3 for details). Interface dislocations arise when the crystal surfaces to be joined in the creation of the interface exhibit surface features which are not complementary or when the relative position of the crystals breaks otherwise coincident point symmetry elements. If $\mathbf{t}(\lambda)$ and $\mathbf{t}(\mu)$ are translation vectors present on the two crystal surfaces, the Burgers vectors of interface dislocations are given by :

$$\mathbf{b}_{ij} = \mathbf{t}(\lambda)_j - \mathbf{P}\,\mathbf{t}(\mu)_i\,, \qquad (1)$$

where **P** expresses the relationship between the coordinate frames of the two crystals. The parallel alignment of basal mirror planes in the upper (λ) crystal with {10-10} mirror-glide planes in the lower (μ) yields a dislocation with :

$$\mathbf{b} = \mathbf{P}\,\mathbf{c}(\mu)/2 \qquad (2)$$

Structure of interfacial defects

We found that crystal dislocations do not decompose into interfacial defects in this incommensurate interface. However, it was possible to create interfacial defects which exhibit finite step height and have **b** inclined to the interface. Fig. 2 shows an unstressed defect forming a boundary step 10 planes high in both crystals. The interplanar spacing of the prism and basal planes in the upper and lower crystals, respectively, is unequal and the normal component of the Burgers vector is $5(\sqrt{3}a - c)$. This defect exhibits a distinct riser structure whereby the (10-12) planes of the adjacent crystals are slightly strained into parallel abutment. In other words, the riser relaxes into a configuration closely resembling that of the (10-12) twin structure.

Dislocations with Burgers vector parallel to the interface were simulated but did not remain localized after their initial formation. The interface is not able to sustain shear stresses parallel to Y and defects of this type were observed to spread out along the entire interface in the inner region of the computational cell during the simulation. An interfacial dislocation with Burgers vector equal to **c/2**, as defined by eq.(2), is depicted in fig.3. This defect is localized and the core structure depends on the nature of the atom terminating the 'extra half' (0002) plane.

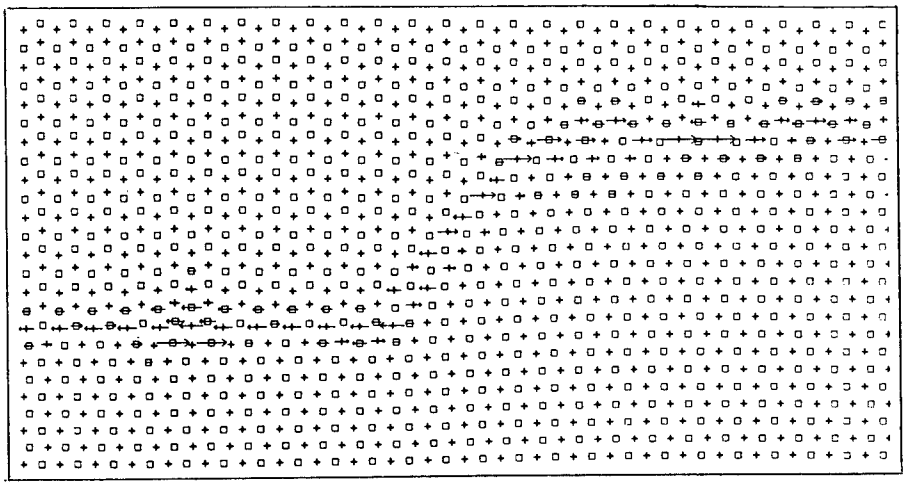

Figure 2. Interfacial defect forming a boundary step 10 planes high in both crystals. The normal component of its Burgers vector is $5(\sqrt{3}a - c)$. The configuration of the riser closely resembles that of the (10-12) twin structure.

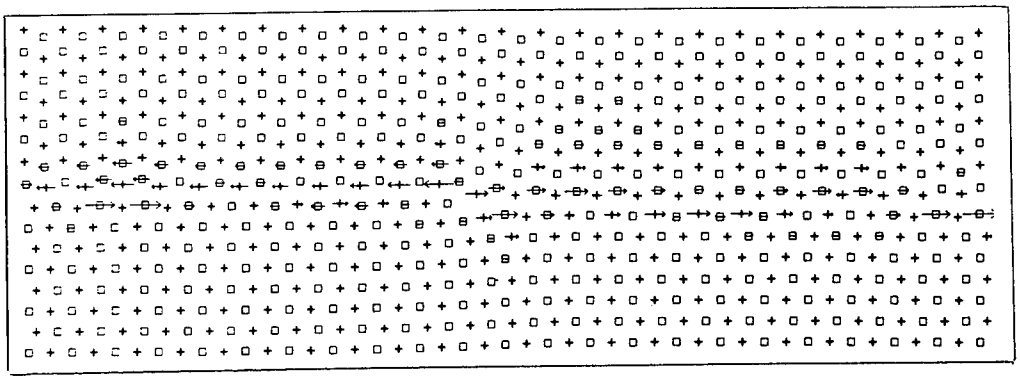

Figure 3. An interfacial dislocation with Burgers vector equal to **c/2**, as defined by eq.(2)

Interaction with crystal dislocation

The interaction with the boundary of perfect dislocations with **b=a** in both the upper and lower crystals has been simulated. It was found that the dislocation was not fully absorbed in either situation and a residual distortion remains in the crystal. An important interaction of the screw part of the dislocation with the screw dipoles in the boundary was observed. A full description of the different interactions will be published elsewhere.

Summary and conclusions

The structure of a 90^0 tilt boundary, which is incommensurate in one direction, and its interaction with crystal dislocations, have been studied by atomic-scale computer simulation.

The structure of the boundary does not resemble a misfitting heterointerface with an array of localized dislocations, but exhibites ribbons of screw dipoles arranged parallel to the tilt axis with the pseudo-periodicity of the interface perpendicular to the tilt axis.

The boundary cannot sustain moderate shear stresses perpendicular to the tilt axis, with the result that components of crystal dislocations absorbed into the boundary become delocalized.

The core structures of the localized interfacial defects exhibit preferred riser configurations, resembling (10-12) twins. This fact has important consequences for the movement of the interfacial defects under applied stress.

Acknowledgments

This work was supported by the project PB96-170-CO3-03 of the Spanish Ministerio de Educacion y Cultura and NATO Science grant CRG910900

References.

[1] G.J. Ackland, Phil.Mag.A, **7**, (1992), p. 917
[2] V. Vitek, Phil. Mag., **18**, (1968), p. 773
[3] R.C. Pond and J.P. Hirth, Solid State Phys., **47**, (1994), p. 287
[4] J.P. Hirth and R.C. Pond, Acta Metall. Mater., **44**, (1996), p. 4749
[5] A. Serra and D.J. Bacon, Phil.Mag.A, **73**, (1996), p. 333

Materials Science Forum Vols. 294-296 (1999) pp. 199-202

Atomic Level Studies of Dislocation Networks in Niobium-Sapphire Interfaces

A. Lévay[1,2,3], G. Möbus[1], V. Vitek[2], M. Rühle[1] and G. Tichy[3]

[1] Max-Planck-Institut für Metallforschung, Seestrasse 92, D-70174 Stuttgart, Germany

[2] Department of Materials Science and Engineering, University of Pennsylvania, Philadelphia, PA 19104, USA

[3] Department of Solid State Physics, Eötvös University, Múzeum körút 6-8, H-1088 Budapest, Hungary

Keywords: Atomic Structure, Metal-Ceramic Interface, Misfit Dislocation, HREM Image Simulation

ABSTRACT In this paper we present atomistic modelling of the $(0001)_{Al_2O_3} \parallel (111)_{Nb}$ interface using a simple description of atomic interactions. The goal is to reveal the influence of the strength of bonding between the two materials upon the misfit dislocations formed in Nb at or near the interface. The calculations show that two types of networks of misfit dislocations may be formed depending on the strength of bonding but only the triangular network with 1/2<111> dislocations occurs if the transport of material, for example by diffusion, can take place. This is, indeed, the network found by electron microscopic studies [1]. The core structure of the misfit dislocations also depends on the strength of bonding. Comparison of simulated high resolution electron microscope (HREM) images, based on the atomistic model, with observations leads to an excellent agreement for a reasonable strength of bonding and provides means for assessment of this physical quantity.

Introduction

Metal-ceramic interfaces play an important role in composites, devices employing thin films and in protective coatings since they often control their physical and mechanical properties [2-4]. A significant characteristic of such interfaces is the mode of accommodation of the lattice mismatch between a metallic film and ceramic substrate. If the thickness of the film exceeds a critical thickness this is provided by a network of misfit dislocations [5-9] and when the accommodation is complete this dislocation network satisfies the Frank-Bilby formula [1, 10]. This is a geometrical rule which must be fulfilled when the misfit is completely compensated but it does not determine uniquely the dislocation network appropriate for a given interface. Which dislocations participate in such network, as well as its form, depend on both crystallography of adjoining materials and bonding at the interface. In the present paper we investigate by atomistic modelling formation of networks of misfit dislocations at an interface between Nb and Al_2O_3. This is a very suitable model system in which the interfaces have been studied by electron microscopy [1, 11, 12]. Specifically, we have modeled the $(0001)_{Al_2O_3} \parallel (111)_{Nb}$ interface. At this interface the misfit is 2% and a triangular network of 1/2<111> dislocations was found to compensate the misfit [1]. The calculations reveal how the bonding strength between the two materials affects the form of the network of misfit dislocations as well as the atomic structure of the cores of these dislocations. The latter has been studied by high resolution electron microscopy (HREM) [13, 14] and a direct comparison of experimental observations with images simulated on the basis of the atomistic model is presented.

Method of calculation

In the present study we have adopted the same simple approach that was used successfully in earlier modelling of misfit dislocations [14, 15]. The substrate has been taken as an undeformable, uniformly strained b.c.c. lattice the orientation of which is defined by the symmetry observed experimentally. Hence, corresponding crystallographic planes parallel to the boundary are the same on each side of the interface and the uniform strain represents the misfit δ between the substrate and the metal (Nb). A justification for this model is provided by HREM observations [11, 13, 14] that at the coherent parts of interfaces the relative position of Nb and Al_2O_3 lattices is characterised by a

continuous transition of a number of lattice planes belonging to the aluminium sublattice in sapphire into the principal planes of the niobium lattice and vice versa.

Since the substrate is considered undeformable, the atomic positions in the strained b.c.c. lattice representing the substrate are fixed and no description of interatomic forces in the substrate is needed. The atomic interactions in Nb were described by Finnis-Sinclair type many-body central force potential [16] and the interaction between the substrate and Nb by a pair potential, V_{MS}, constructed such as to reproduce different strengths of bonding across the interface. (For more details see [14]). The interfacial cohesive energy is evaluated as

$$E_I = \sum_i \left(E_i - E_i^S\right) + \sum_{i,k} V_{MS}(R_{i,k})$$

where the summation over i extends over all the atoms representing the metal and the summation over k over all the atoms representing the substrate; E_i is the energy of a Nb atom i and E_i^S the energy of the same atom when a free surface has been formed by removing the substrate. The strength of bonding is then characterised by the parameter $R = E_I / E_{(111)}$, where $E_{(111)}$ is the cohesive energy across {111} planes in niobium, identified with twice the energy of the relaxed {111} surface.

The block employed in the study of this interface is a rectangular cell with the edges parallel to the $[10\bar{1}]$, $[1\bar{2}1]$ and [111] axes of niobium. Periodic boundary conditions were applied in both the $[10\bar{1}]$ and $[1\bar{2}1]$ directions but not in the [111] direction; the block has to extend in this direction at least to the distance comparable with the size of the planar repeat cell.. The unit cell in the interface is $N[10\bar{1}]$ x $N[1\bar{2}1]$ in the substrate and $(N+1)[10\bar{1}]$ x $(N+1)[1\bar{2}1]$ in niobium. The misfit is then $\delta = 1/N$. For misfit of 2% at least $2x10^6$ atoms are needed in the block. Hence, to be able to use a smaller block we investigated larger misfits, 6.66% (N = 15) and 4% (N = 25). The results are principally the same for both misfits, only separations of the corresponding misfit dislocations are different. Therefore, it can be expected that the same configurations of misfit dislocations would be found for $\delta = 2\%$. The relaxation calculations were performed by minimizing the energy of the part of the block representing niobium using a molecular statics method.

Structure of Misfit Dislocations

The results of calculations for $\delta = 6.66\%$ are shown in Figs 1a and b for two different strengths of bonding corresponding to $R = 0.87$ and 0.27, respectively. In these figures the strain field in the Nb layer adjacent to the interface is plotted as arrows representing relative displacements of atoms that occur as the result of relaxations; the atoms are not shown. The dislocation lines can be identified with the regions of largest strains. In both cases the strain pattern possesses the three fold symmetry but is obviously different in the two cases. The dislocation network emerging in Fig. 1a is hexagonal with dislocation lines parallel to $[1\bar{2}1]$, $[11\bar{2}]$ and $[\bar{2}11]$ directions, respectively. The Burgers vectors of these dislocations must be $[\bar{1}01]$, $[1\,\bar{1}0]$ and $[01\,\bar{1}]$, respectively, since these are the only lattice dislocations with short Burgers vectors that satisfy the Frank-Bilby formula. On the other hand, the network in Fig. 1b is triangular with two types of non-equivalent triangles. The dislocation are parallel to $[10\bar{1}]$, $[\bar{1}\,10]$ and $[0\,\bar{1}\,1]$, respectively, and for these line orientations the Frank-Bilby formula is satisfied when their Burgers vectors are $1/2[1\,\bar{1}\,1]$, $1/2[11\,\bar{1}]$ and $1/2[\bar{1}\,11]$, respectively [14].

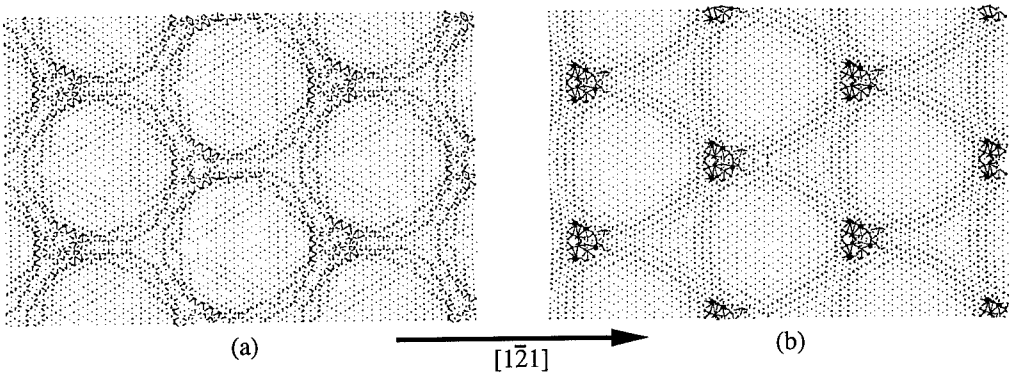

Fig. 1. Strain field maps for the relaxed interface with the misfit 6.66% . (a) $R = 0.87$, (b) $R = 0.27$.

Atomic structures of the dislocations constituting the two types of networks are shown in Figs. 2a and b. In these, and following figures, the dark circles depict Nb atoms and the light circles atoms representing the substrate. Six consecutive $(1\bar{2}1)$ planes are shown for the hexagonal network and two consecutive $(\bar{1}01)$ planes for the triangular network; the cross sections are from the regions between the dislocation intersections. The dislocations are clearly visible. However, while the $1/2[1\bar{1}1]$ dislocation in Fig. 2b is positioned directly at the interface, the $[\bar{1}01]$ dislocation in Fig. 2a is split according to the reaction $[\bar{1}01]=1/2[\bar{1}\,\bar{1}\,1]+1/2[\bar{1}11]$. Each 1/2<111> dislocation stands away from the interface which was attained by glide on the (123) and (321) planes, respectively.

An important feature of the interface shown in Fig. 2b is that while on the right from the dislocation the atomic planes $((1\bar{1}1))$ match well, a gap appears to the left. This is reflected in Fig. 1b in that the two adjacent triangular regions are always different. The reason is that the $1/2[1\bar{1}1]$ dislocation has the Burgers vector component perpendicular to the interface, equal to the (111) interplanar spacing, and when it is formed at the interface it produces the step of this height on one side of the dislocation line. No such step is produced by $[\bar{1}01]$ dislocation (Fig. 2a) since its Burgers vector lies in the (111) plane. This is the reason why different dislocation networks are found for different strengths of bonding. The energy associated with the formation of the gap obviously increases with the strength of bonding and, therefore, if this is high, it is energetically favourable to form network which does not lead to the gap although the Burgers vectors of the dislocations are larger (<101> type). At a lower strength of bonding the dislocations with shorter Burgers vectors (1/2<111>) become favourable even when their formation is associated with gaps at the interface.

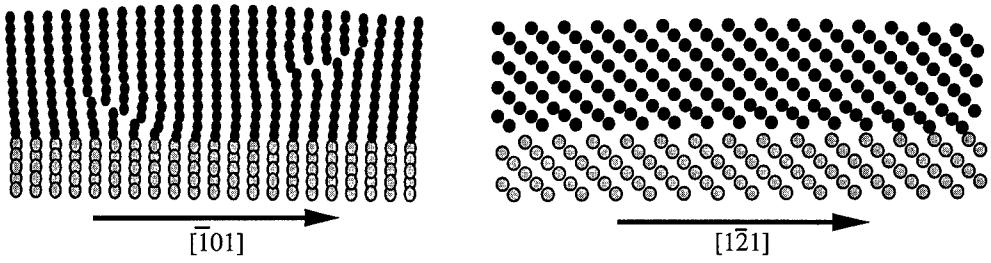

(a) (b)

Fig. 2. Section of the block perpendicular to the dislocation lines forming the hexagonal (a) and triangular (b) networks shown in Fig. 1.

However, this situation arises in the computer simulation where no transport of matter is possible. When such transport can occur the gaps can be filled and the triangular network will always be favoured since the corresponding Burgers vectors are shorter. This is, of course, what can be expected in reality since diffusion of Nb atoms can usually take place during the preparation of interfaces. In order to investigate this phenomenon we have filled those triangular regions in which the gap occurs by Nb atoms. This was done by a Monte Carlo type procedure when the energy of the system is minimised as a function of the number of inserted atoms. Indeed, when the gap is filled the triangular dislocation network occurs for any reasonable strength of bonding.

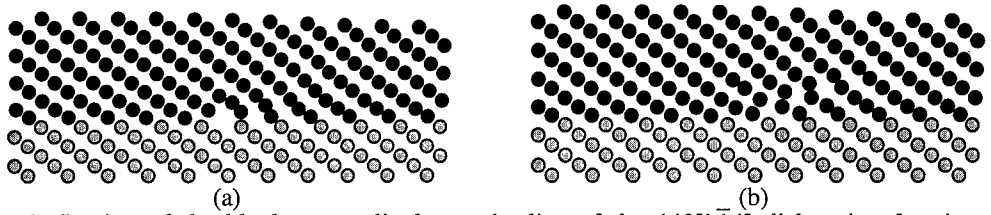

(a) (b)

Fig. 3. Section of the block perpendicular to the line of the $1/2[1\bar{1}1]$ dislocation forming the triangular network with filled gaps for $\delta = 4\%$ (a) $R \leq 0.35$ (b) $R > 0.35$.

Atomic structures of the $1/2[1\bar{1}1]$ dislocations in the triangular networks, after filling the gaps, are shown in Figs 3a and b in the same way as in Fig. 2b. In both cases the misfit $\delta = 4\%$ but the strength of bonding is lower in Fig. 3a ($R \leq 0.35$) than in Fig. 3b ($R > 0.35$). In the former case the dislocation is attached to the interface while in the latter case it is at a stand-off attained by glide along the (121) plane. The structure shown in Fig. 2a is in a very good agreement with HREM observations

[14]. This is seen in Fig. 4 where the observed HREM image is compared with that simulated on the basis of the structure shown in Fig. 3a.

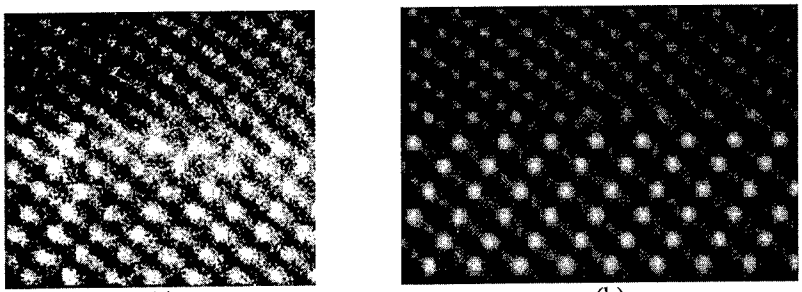

(a) (b)

Fig. 4. HREM images of the $1/2[1\bar{1}1]$ misfit dislocation. (a) Observation [11, 14]; (b) Simulation based on the structure shown in Fig. 3a. In the simulation the artificial b.c.c. substrate was replaced by the sapphire structure following the same procedure as in [14] and the sample thickness and defocus close to those in the experimental study were used.

Conclusions

The modelling of the $(0001)_{Al_2O_3} \parallel (111)_{Nb}$ interface suggests that the network of misfit dislocations will be usually triangular, composed of 1/2<111> edge dislocations with {112} slip planes, in agreement with observations [1]. However, formation of this network requires mass transport near the interface and if this were not available hexagonal network of <110> dislocations might form, depending on the strength of bonding across the interface. The core structure of the 1/2<111> dislocations found by modelling is in an excellent agreement with HREM observations for an intermediate level of strength of bonding. However, it may change if the strength of interfacial bonding is altered. In particular if it reaches a critical level the misfit dislocations will not be attached to the interface but will be positioned at a stand-off distance.

Acknowledgments

This research was supported by the US Department of Energy, Grant No. DE-FG02-87ER45295 (AL, VV), Volkswagen Foundation grant I/71 104 (GM, MR), Hungarian National Science Foundation OTKA T017609 (AL, GT) and Max-Planck Institut Stuttgart. Grant from the DAAD that enabled one of the authors (AL) to perform part of the research at the MPI, Stuttgart, is gratefully acknowledged.

References

1. G. Gutekunst, J. Mayer, V. Vitek and M. Rühle, *Philos. Mag. A* **75**, 1357 (1997).
2. M. Rühle, A. G. Evans, M. F. Ashby and J. P. Hirth, *Metal-Ceramic Interfaces*, Pergamon Press: Oxford (1990).
3. M. Rühle, A. H. Heuer, A. G. Evans, M. F. Ashby, *International Symposium on Metal/Ceramic Interfaces, Acta Metall. Mater.* **40** (1992).
4. M. Rühle, *J Eur Ceram Soc* **16**, 353 (1996).
5. F. C. Frank and J. H. Van der Merwe, *Proc. Roy. Soc. London A* **198**, 205 (1949).
6. J. W. Matthews, *Dislocations in Solids* (edited by F. R. N. Nabarro), North-Holland: Amsterdam, p. 461 (1979).
7. J. R. Willis, S. C. Jain and R. Bullough, *Philos. Mag. A* **62**, 115 (1990).
8. J. H. Van Der Merwe, *Crit Rev Solid State Mat Sci* **17**, 187 (1991).
9. R. Hull and J. C. Bean, *Crit Rev Solid State Mat Sci* **17**, 507 (1992).
10. J. P. Hirth and J. Lothe, *Theory of Dislocations*, Wiley-Interscience: New York (1982).
11. G. Gutekunst, J. Mayer and M. Rühle, *Defect-Interface Interactions* (edited by E. P. Kvam, A. H. King, M. J. Mills, T. D. Sands and V. Vitek), Materials Research Society, Pittsburgh, Vol. 319, p. 3 (1994).
12. G. Gutekunst, J. Mayer and M. Rühle, *Philos. Mag. A* **75**, 1329 (1997).
13. G. Gutekunst, J. Mayer and M. Rühle, *Scripta. Metall. Mater.* **31**, 1097 (1994).
14. V. Vitek, G. Gutekunst, J. Mayer and M. Rühle, *Philos. Mag. A* **71**, 1219 (1995).
15. W. P. Vellinga, J. T. M. DeHosson and V. Vitek, *Acta Mater.* **45**, 1525 (1997).
16. G. J. Ackland and R. Thetford, *Philos. Mag. A* **56**, 15 (1987).

Materials Science Forum Vols. 294-296 (1999) pp. 203-206

Computer Simulation and High Resolution Electron Microscopy Study of the Σ=5 (210) [001] Symmetric Tilt Grain Boundary in Molybdenum

M. Bacia[1], J. Morillo[2], J.M. Pénisson[1] and V. Pontikis[2]

[1] Département de Recherche Fondamentale sur la Matière Condensée, CEA/Grenoble, 17, rue des Martyrs, F-38054 Grenoble Cedex 9, France

[2] Laboratoire des Solides Irradiés, Commissariat à l'Énergie Atomique-DSM/DRECAM/LSI, CNRS UMR 7642, École Polytechnique, F-91128 Palaiseau Cedex, France

Keywords: Transition Metals, Molybdenum, Semi-Empirical Potential, Atomic-Scale Simulation, Grain Boundary, High Resolution Electron Microscopy

ABSTRACT We present the results of a parallel study of the atomic structure of the Σ = 5 (210) [001] symmetric tilt grain boundary in bcc Mo, by computer simulation and High Resolution Electron Microscopy (HREM). Excess energy values of different boundary configurations are obtained via a quasi-dynamic minimisation scheme while cohesion is described by a new n-body, central-force, phenomenological potential which satisfactorily reproduces static and dynamic properties of the bulk material. HREM observations and numerical modelling both show the symmetric configuration of the Σ = 5 (210) [001] symmetric tilt grain boundary (GB) to be of lowest energy.

INTRODUCTION

Mechanical properties of body centred materials have motivated extensive theoretical and experimental investigations a large number of which is devoted to their well known room temperature intergranular brittleness. This brittleness stems from segregated and/or precipitated residual impurities at grain boundaries, due to inefficient purification treatments of refractory metals which therefore contain usually significant amounts of light elements (H, C, N, O...). Impurity segregation and/or precipitation and the resulting macroscopic mechanical behaviour of polycrystals, are strongly dependent on the interfacial atomic structure [1,2], which can be studied by HREM only in the case of tilt grain boundaries. However it has been scarcely done up to now [2-5]. Atomic scale numerical simulations can palliate this lack of experimental results. Moreover, the comparison of the predictions of the simulations with the experimental results is a test of the validity of the cohesion model used in the simulations. This is why we decided to study the atomic structure of the Σ = 5 (210) [001] tilt grain boundary in Mo by HREM and numerical simulation using a new phenomenological, central-force, many-body potential.

In Sec. I, we present the simulation procedure and the model potential. In Sec. II, the HREM experimental details are given and Sect. III is devoted to the experimental and simulation results which are then discussed in Sec. IV with reference to previous works.

I. SIMULATIONS

In this paper, we adopt the following convention for the description of a tilt GB: in the GB plane (GBP), the two directions are labelled *Ox* ([$\bar{1}$20]) and *Oz* ([001] tilt axis), and the direction normal to the GBP ([210]) is *Oy*. The simulation box of volume V ($V = d_x \times d_y \times d_z \equiv 3 \times 6 \times 4$ cells) contains N = 720 atoms. In the simulation course, periodic boundary conditions are applied, introducing two identical interfaces (through a 180° rotation around *Oy*) in the simulation cell and allowing free rigid-body translations parallel to *Ox* and *Oz*. The Molecular Dynamics (MD) simulations have been carried out in the canonical (N, V, T) ensemble. The fully relaxed configurations at T = 0 K for a given set of parameters have been obtained for different simulation cell dimensions, d_y, via a quasi-dynamic procedure (damping forces [6]) with an initial 200 K temperature. The final (d_{ymin}) minimum energy configuration, E_{min} (N, $V(d_{ymin})$, $T = 0$ K) gives us the excess energy of the GB. Starting from initial geometric configurations, relying on the coincidence

site lattice theory (CSL), different sets of atomic positions are generated by applying rigid body translations. These, in sufficient number to uniformly sample the two-dimensional cell ([$\bar{1}$20],[001]) serve as an input to the energy minimisation procedure.
All MD simulations have been performed with a newly designed n-body potential based on the second moment approximation of the tight binding scheme whose expression is given in ref. [7]. It contains ten parameters which were fitted on static 0 K bulk properties with interactions up to the fourth neighbours shell: lattice constant at atmospheric pressure and 800 kbar, cohesive energy and elastic constants. It was verified that the bcc structure was actually the most stable one compared to the fcc and hcp ones. This potential reveals to be particularly adapted to the description of bulk static and dynamic properties (0 K equation of state, thermal expansion, Gruneisen constant and phonon spectra, vacancy formation energy) whereas its predictions concerning surface properties are poor (energy and mainly relaxation of the (100) surface) [7].

II. EXPERIMENTAL PROCEDURE

Small pieces of bicrystal (details concerning the preparation of these bicrystals can be found in [2,7]) have been cut perpendicular or parallel (for transversal observations) to the tilt axis using a wire saw. The specimens have been mechanically thinned down to a 40 μm thickness and finally thinned in an ion beam miller until the grain boundary was located in a suitable area.
Images have been taken in a JEOL 4000 EX high resolution electron microscope at a magnification value 500,000. The negatives were digitised by means of a CCD video camera and further processed with the Semper software package [8]. Using conditions comparable to those adopted in ref. [9] digitised images have been sampled at 0.008 nm per pixel. For the purpose of comparison between calculated lowest-energy boundary configurations and HREM observations, we used the atomic positions obtained from the simulations as an input to the E.M.S. software package [10]. Among the remaining input data, some are fixed at the values characteristic of the 4000 EX microscope [11] whereas others at values of the parameters either measured (defocus) or estimated (thickness) and thus specific to each given image.

III. RESULTS

III.1 *simulation results*

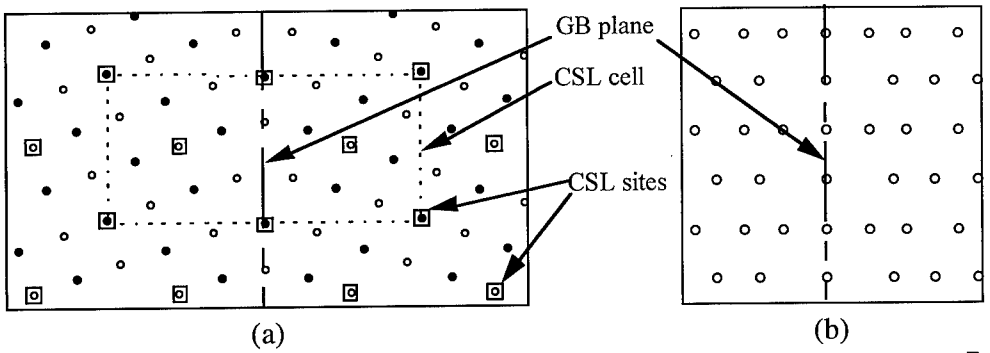

Figure 1: *Minimum symmetric energy configuration views: (a) along the tilt axis, (b) along the [$\bar{1}$20] direction (full and open circles: atoms in two successive (002) planes).*

Regardless of the rigid-body translation introduced in the initial atomic configuration, the minimisation procedure leads systematically upon convergence to a single perfectly symmetric structure (Fig. 1 a and b) with an 1525 mJ/m^2 excess energy and a 0,053 Å expansion normal to the boundary plane. Accordingly, the profile of interplanar spacing between (210) planes as a function of the distance from the interface is perfectly symmetric.

We also tested the sensitivity of the lowest-energy structure to the border conditions by suppressing the system periodicity along the normal to the interface plane. No changes were found to occur so that the results obtained using computational boxes with 3D periodic border conditions can be safely trusted.

III.2 *HREM observations*

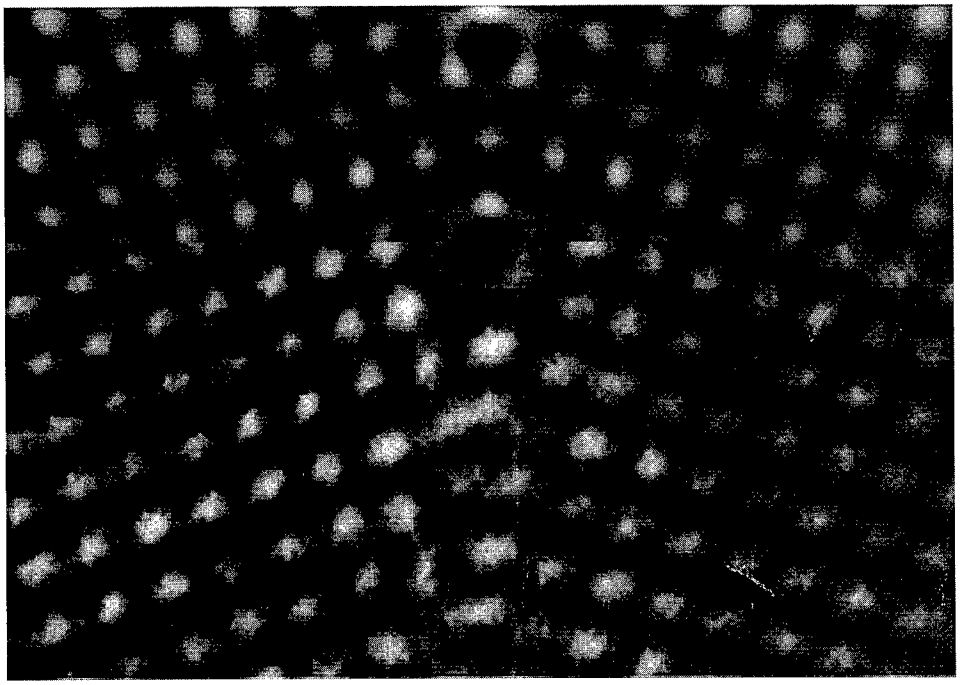

Figure 2: *View along the tilt axis of the structure of the Σ = 5 (210) [001] symmetric tilt grain boundary. Upper part: computer-simulated image(thickness t = 8 nm and defocus δz = -4 nm); lower part: HREM image at 400 keV.*

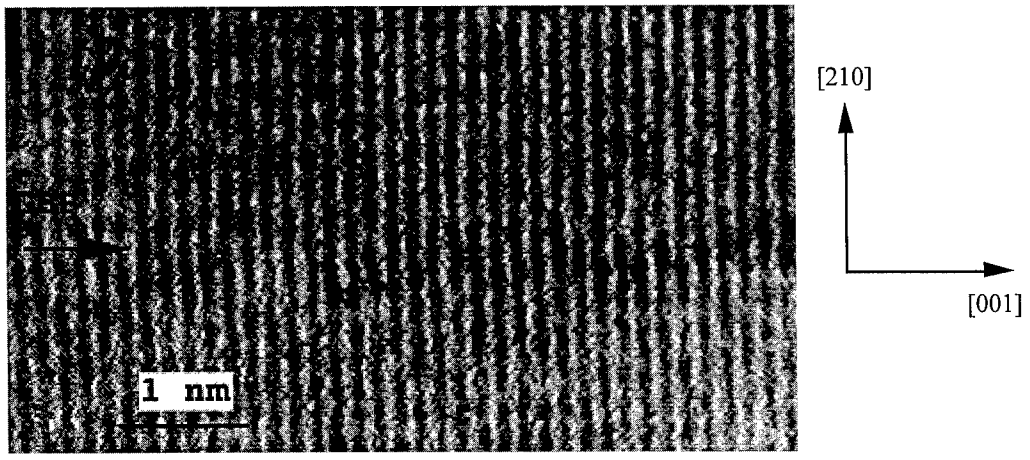

Figure 3: *HREM image at 400 keV along the [$\bar{1}$20] direction of the structure of the Σ = 5 (210) [001] symmetric tilt grain boundary (GBP stands for grain boundary plane).*

Different specimens containing the (210) boundary have been observed along the [001] tilt axis and the [$\bar{1}$20] direction. Figure 2 gives a combined representation of computer simulated (upper part) and experimental (lower part) images of the (210) boundary of one of the specimens, viewed along the tilt axis. One cannot measure any rigid-body translation on the HREM image. A similar result is obtained in the view along the [$\bar{1}$20] direction (Figure 3): the favoured configuration is symmetric. The combined representation of Fig. 2 allows a direct comparison between the experimental boundary and the lowest-energy computer-simulated one. The agreement is excellent except within the boundary plane where the contrast in the experimental image is less marked than in the simulated image. One can see on both images that the perturbation introduced by the interfaces does not extend beyond the first CSL cells adjacent to the grain boundary.

IV. DISCUSSION AND CONCLUSION

In this study a comparison is made between HREM observations and computer simulations of the structures of the $\Sigma = 5$ (210) [001] symmetric tilt grain boundary in bcc Mo. Both studies have shown that the most stable configuration is a symmetric one. A central, n-body, phenomenological cohesion model was developed for Mo. It predicted not only bulk static and dynamic properties in overall good agreement with experiments but also leads to the experimentally observed lowest energy structure for the studied GB. A previously published simulation study [12] predicted non symmetric configurations for the same GB whatever the cohesion model they used (central or angular-forces), in contradiction with our experimental observations. Reasons for which our implementation of a central-force potential adapted to Mo consistently reproduces the experimental observations whereas others do not are not clear. However it is worth pointing out that (i) it differs from others models of interaction found in the literature in that it satisfactorily reproduces a large number of bulk thermodynamic properties, (ii) it works well with GB whereas its predictions concerning surfaces are poor. This might be an indication that the cohesive model must primarily behave well with regard to bulk properties and not surfaces properties in order to describe properly grain boundaries in a bcc metal like Mo.

ACKNOWLEDGEMENTS

Professor Michel Biscondi at École des Mines de Saint Étienne is warmly acknowledged for fruitful discussions and advises as well as for the experimental facilities he provided. JMP and VP thank René Franck for having facilitated their collaboration. One of us (MB) acknowledges financial support from CEA/DTA/CEREM during her stay in Grenoble.

REFERENCES

[1] M. Bacia, J. M. Pénisson and M. Biscondi, Materials Science Forum 207-209 (1996), p. 193.
[2] M. Bacia, PhD Thesis, Ecole des Mines de Saint-Etienne, France (1994).
[3] J.-M. Pénisson, T. Nowicki and M. Biscondi, Phil. Mag. A 58 (1988), p. 947.
[4] J.-M. Pénisson, M. Bacia and M. Biscondi, Phil. Mag. A 73 (1996),p. 859.
[5] G.H. Campbell, S.M. Foiles, P. Gumbsch, M. Rühle and W.E., King, Phys. Rev. Lett. 70 (1993), p. 449.
[6] J. R. Beeler and G. L. Kulcinski, in "*Interatomic potentials and simulation of lattice defects*", ed. P. C. Gehlen, J. R. Beeler and R. I. Jaffee, Plenum Press, New York (1972), p. 735.
[7] M. Bacia, J. Morillo, J. M. Pénisson and V. Pontikis, Phil. Mag. A 76 (1997), p. 945.
[8] W.O. Saxton, T. J. Pitt and M. Horner, Ultramicroscopy 4 (1979), p. 343.
[9] M. I. Buckett and K.L. Merkle, Ultramicroscopy 56 (1994), p. 71.
[10] P. A. Stadelmann, Ultramicroscopy 21 (1987), p. 131.
[11] A. Bourret and J. M. Pénisson, Jeol News Electron Opt. Instrum. 25E (1987), p. 2.
[12] A. G. Marinopoulos, V. Vitek and A. E. Carlsson, Phil. Mag. A 72 (1995), p.1311.

Materials Science Forum Vols. 294-296 (1999) pp. 207-210

Investigation of Assemblies of Grain Boundary Dislocations in Nanostructured Copper by Computer Simulation

I.V. Alexandrov, N.A. Enikeev and R.Z. Valiev

Institute of Physics of Advanced Materials, Ufa State Aviation Technical University,
K. Marksa 12, RU-450000 Ufa, Russia

Keywords: X-Ray Analysis, Grain Boundary Dislocations, Nanostructured Materials, Computer Simulation

Abstract. Computer simulation of X-ray diffraction patterns of nanostructured copper has been carried out on the basis of the kinematic theory of X-rays scattering, taking into account various configurations of extrinsic grain boundary dislocation assemblies. The conclusion based on comparison with experimental data about possible configurations of extrinsic grain boundary dislocation assemblies in nanostructured materials processed by severe plastic deformation has been done. The ways of further development of the suggested approach are shown.

Introduction

Nanostructured materials are world-wide acknowledged as having unique physical and mechanical properties. Among the most perspective methods of their processing there is the method of severe plastic deformation (SPD), i.e. large deformation under high imposed pressure [1]. X-ray analysis proved to be a powerful tool of structural characterization of materials which allows to get statistically averaged information on various parameters of polycrystals. In fact, numerous experimental studies carried out have shown that X-ray diffraction patterns (XRDPs) of nanostructured materials processed by SPD demonstrate a whole number of peculiarities in comparison to those of corresponding coarse-grained materials [2-4]. Among them are: changed integral intensity, sufficient broadening, long-range tails, shifted positions of centroids of X-ray diffraction peaks, and elevated diffuse background intensity. Interpretation of XRDPs of nanostructured materials meets considerable troubles by virtue of simultaneous contribution to the peaks shape of small grain size and specific defect structure [2-4].

The data obtained by using direct HREM method observations [5] allow suggesting that the peculiarity of this defect structure is the presence of extrinsic grain boundary dislocations (EGBDs) of extremely high density (about 10^8-10^9 m^{-1}) which appear due to SPD. These EGBDs provide long-range internal stress fields which cause considerable atomic displacements. Low temperature annealing leads to a significant decrease in density of EGBDs and to a concurrent radical change in properties of nanostructured materials even if a fine grain size still remains unchanged [6]. It testifies a leading role of EGBDs in this process. However, it is not clear yet which configurations of EGBDs assemblies are possible, how they change during annealing and what assemblies are responsible for unusual properties of nanostructured materials processed by SPD.

Computer simulation seems to be useful in solving this problem. Previous works [7] have shown that unusual view of these XRDPs may be caused by presence of EGBDs of high density. However, the chosen approach did not take into consideration the configuration of EGBDs assemblies and could not describe significant broadening due to displacement fields caused by these assemblies. The present work suggests a new approach in computer simulation of nanostructured materials processed by SPD which allows to take into account a contribution of various configurations of any dislocations.

Computational method

As earlier [7], the computer simulation was performed in terms of kinematic theory of X-ray scattering. The hypothetical Cu polycrystal, consisted of rectangular crystallites which were oriented in some definite way, was considered. For each crystallite atomic displacements were calculated according to assigned edge EGBDs configuration. For *i*-th atom its displacements were calculated using Eqn.1.1-2. in terms of dislocation theory for continuous isotropic matter [8]:

$$U_x = \frac{b}{2\pi}\left\{arctg\frac{y}{x} + \frac{1}{2(1-\sigma)}\frac{xy}{x^2+y^2}\right\} \tag{1.1}$$

$$U_y = -\frac{b}{4\pi(1-\sigma)}\left\{(1-2\sigma)\ln\sqrt{x^2+y^2} + \frac{x^2}{x^2+y^2}\right\} \tag{1.2}$$

The intensity of X-rays scattered by a separate crystallite was calculated by determining the result of X-ray scattering by all atoms of the crystallite:

$$I = |\Phi_0|^2 / R^2 \times \sum_j \sum_k f_i f_j exp(2\pi i / \lambda \times (\boldsymbol{s}, (\boldsymbol{r}_k - \boldsymbol{r}_j))) \tag{2}$$

where Φ_0/R is the amplitude of scattered wave at the observation point, $\boldsymbol{s}$ is defined from $\boldsymbol{s}=\boldsymbol{s}_1-\boldsymbol{s}_0$, where $\boldsymbol{s}_1$ and $\boldsymbol{s}_0$ are unit vectors in direction of diffracted and primary beams respectively, $\boldsymbol{r}_i$ and $\boldsymbol{r}_j$ are position vectors of *i*-th and *j*-th atoms, λ stands for wavelength of primary beam and *f* is atomic scattering factor.

This value was multiplied by thermal and polarization factors taking into account a release of diffraction peak intensity due to thermal vibrations of atoms and partial polarization of X-rays during scattering. Calculations of intensity scattered by the whole polycrystal were carried out by summation of intensities scattered by each crystallite taking into account crystallographic texture. Such an approach gave us full control over all the structural changes induced by any dislocations configuration.

Results and discussion

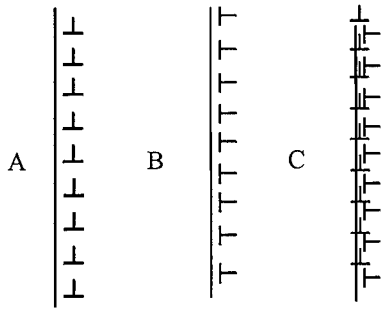

Fig.1. A boundary containing sessile dislocations (A), gliding dislocations (B), mixture of sessile and gliding dislocations (C).

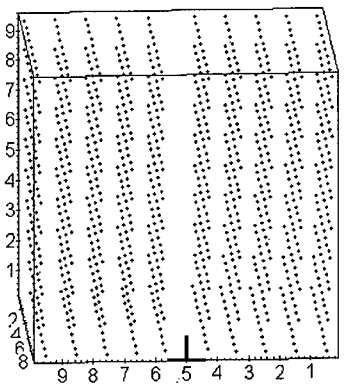

Fig.2. Atomic displacements due to a single dislocation.

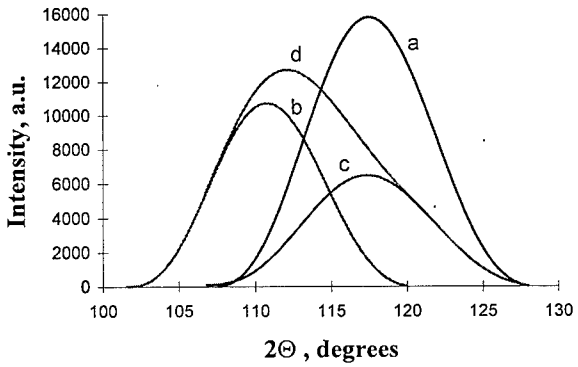

Fig.3. Dependence of the peak (400) profile change on EGBDs configuration : a) no dislocations, b) configuration A, c) configuration B, d) configuration C.

Several configurations of basic edge EGBDs assemblies (Fig.1.) have been considered in comparison to dislocation-free state. This choice is based on the assumption that a single lattice dislocation trapped by a boundary is decomposed into a number of EGBDs with small Burgers vectors. After annihilation of the dislocations with opposite signs dislocations of one sign remain. All further calculations have been made for the grain size equal 5 lattice parameters because of considerable increasing of computing time with grain size growing. Results of simulation for the dislocation density equal 10^8 m^{-1} are presented on Fig.3 where curve d is derived as a superposition of curves b and c. Values of centroid positions and peak broadening are listed in Table 1.

Table 1. Peak parameters for various dislocation configurations.

	Centroid position, degrees	Broadening, degrees
No dislocations	117.68	9.42
Configuration A	110.8	8.34
Configuration B	117.52	9.71
Configuration C	113.59	12.09

One can see that configurations A and B do not lead to significant broadening formation, though they entail change in intensity and shift of centroid positions. Meanwhile, their superposition quite well could describe the experimental results [9,11].

Summary

A new approach to computer simulation of XRDPs taking into consideration various configurations of assemblies of EGBDs allows to get valuable information on structure of nanostructured materials. It is shown that typical view of XRDP of nanostructured Cu processed by SPD could be described by equidistant distribution of gliding and sessile EGBDs which cause sufficient broadening and shift of centroid positions of X-ray peaks but that requires further investigations. Preliminary results allow to consider this approach to be fruitful in structural studies of nanostructured materials. The further investigations will involve into consideration assemblies of screw EGBDs allowing to estimate contribution of polarized tilt walls and polarized dipolar walls [11], chaotic distribution of dislocations, disclinations in triple lines, low-angle dislocation walls forming cell structure, and transformation of defect structure during plastic deformation and annealing. The presented approach is also supposed to be applied to larger grain sizes.

References

[1] Ultrafine-grained materials produced by severe plastic deformation, Special issue, ed. by R.Z. Valiev, Annales de Chimie - Science des Materiaux, 21 (1996) 369-556.
[2] K. Zhang, I.V. Alexandrov, A.R. Kilmametov, R.Z. Valiev, K. Lu, J.Phys.D: Appl.Phys., 30 (1997), 3008-3015.
[3] K. Zhang, I.V. Alexandrov, R.Z. Valiev, K. Lu, J.Appl.Phys. 80(10), (1996) 5617-5624.
[4] I.V. Alexandrov, N.A. Enikeev, A.R. Kilmametov, R.Z. Valiev, Proceedings of Int. Conf. on the Quantitative Description of Materials Microstructure Q-MAT'97, Warsaw, April 1997, 173-184.
[5] Z. Horita, D.J. Smith, M. Furukawa, M. Nemoto, R.Z. Valiev, T.G. Langdon, J.Mater. Res.(1996) 11, 1880-1890.
[6] R.Z. Valiev, Mat. Sci. And Engng A, 243-236 (1997), 59-66.
[7] I.V. Alexandrov and R.Z. Valiev, Philos. Mag. B, vol. 73 (1996) pp 861-872.
[8] L.D. Landau, E.M. Lifshitz Theory of elasticity, 1987,"Nauka", Moscow (In Russian).
[9] K. Zhang, I.V. Alexandrov, A.R. Kilmametov, R.Z. Valiev, K. Lu, J.Phys.D: Appl.Phys., 30, (1997) 3008-3015..4, 1993, 1033-1040.
[10] M. Zehetbauer, Acta Met. Mater., 41, N2 (1993) pp. 589-599.
[11] M. Mueller, M. Zehetbauer, A. Borbely, T. Ungar, Z.Metalkd., 86 (1995) 12, pp.827-831.

Materials Science Forum Vols. 294-296 (1999) pp. 211-214

Atomic Scale Simulation of the (310) [001] Symmetric Tilt Grain Boundary in the B2 Stoichiometric FeAl Ordered Alloy

R. Besson[1,2], M. Biscondi[1] and J. Morillo[2]

[1] Centre de Sciences des Matériaux et des Structures, CNRS URA 1884, École Nationale Supérieure des Mines, F-42023 Saint-Étienne Cedex 2, France

[2] Laboratoire des Solides Irradiés, Commissariat à l'Énergie Atomique-DSM/DRECAM/LSI, CNRS UMR 7642, École Polytechnique, F-91128 Palaiseau Cedex, France

Keywords: Iron Aluminides, Semi-Empirical Potential, Atomic-Scale Simulation, Grain Boundaries, Segregation, Point Defects

ABSTRACT The T = 0 K atomic structure of the (310) [001] symmetric tilt grain boundary in the B2 ordered FeAl stoichiometric alloy was studied by means of numerical simulations using a semi-empirical potential. The approach based on the relaxation of geometric models is insufficient (because the variants cannot be discriminated) and intergranular composition changes cannot be properly accounted for in a simple independent-defect framework. Interactions between defects are thus essential to classify unambiguously the structures according to their stability. A pseudo-symmetric variant is found to be the most stable one at T = 0 K. It is very close to the pseudo-symmetric model of the coincidence site lattice theory and its central plane is made up of Fe atoms only. This is the indication of a possible tendency to Fe segregation in this B2 ordered FeAl alloy.

INTRODUCTION

An increasing number of studies demonstrate the potential ability of aluminides to replace traditional superalloys for applications in very demanding conditions (for a review, see [1]). Among them, iron aluminides, possessing a high specific stiffness as well as an excellent high-temperature corrosion resistance, are especially relevant. However, their intergranular brittleness has impaired their industrial use up to now. A better understanding of this complex phenomenon of embrittlement is doubtless necessary, starting with a better knowledge of the intrinsic Grain Boundary (GB) properties. In this context, numerical simulations are extremely valuable, in so far as they can provide useful hints about trends in the properties of materials.
The paper is organised as follows: in section I, we briefly describe the methods and procedures used throughout our study; section II presents the results of the simulations of the GB and finally we draw some conclusions and perspectives for future work.

I METHODS AND COMPUTATIONAL PROCEDURES

Our simulations were performed with a recently developed semi-empirical potential [2-5], mixing EAM and angular interactions to mimic the bond directionality (due to the partially covalent bonds responsible for the negative Cauchy pressure in FeAl).
In this paper, we adopt the following convention for the description of a tilt GB: in the GB plane (GBP), the two directions are labelled *Ox* ([1$\bar{3}$0]) and *Oz* ([001] tilt axis), and the direction normal to the GBP ([310]) is *Oy*. The simulation box used contains 2160 atoms (d_x x d_y x $d_z \equiv 3$ x 6 x 6 cells). In the simulation course, periodic boundary conditions are applied, introducing two identical interfaces (through a 180° rotation around *Oy*) in the simulation cell and allowing free rigid-body translations parallel to *Ox* and *Oz*. All molecular dynamics simulations have been carried out in the (N_i, V, T) ensemble. The fully relaxed configurations for a given (N_i, V, $T = 0$ K) set of parameters have been obtained for different simulation cell dimensions, d_y, via a quasi-dynamic procedure (damping forces [6]) with an initial 200 K temperature. From the final (d_{ymin}) minimum energy con-

figuration, E_{min} (N_i, $V(d_{ymin})$, $T = 0\,K$), its excess energy at 0 K was calculated through $E_{xc} = E_{\min} - \sum_i \mu_i N_i$, where μ_i is the chemical potential of species i.

The minimisation scheme thus consists in: i/ starting from the Coincidence Site Lattice (CSL) models, search for the lowest energy configurations relative to (Ox, Oz) rigid-body translations at fixed stoichiometric composition; ii/ evaluation of the formation energies of the elementary point defects in the vicinity of the boundary plane for the previously found lowest energy configurations and iii/ subsequent composition changes for these configurations to get the actual lowest energy configuration. A detailed description of the computational procedures can be found in ref. [4].

II GRAIN BOUNDARY CONFIGURATIONS

II.1 Stoichiometric relaxed models

CSL models are often considered as a useful approach to build plausible GBs, with well-defined rigid-body translations in the GBP. In the case of an alloy with the B2 structure, there are two CSL variants for the (310) [001] symmetric tilt GB [7], called the S (symmetric) and PS (pseudo-symmetric) models thereafter. These models, locally preserving the stoichiometric composition, can be deduced from each other by a 1/2 CSL cell period rigid-body translation in both directions in the GBP. However, in principle, no physical argument prevents other structures, with unexpected values of these translations, from being more stable. Thus a more general analysis of the energetics of the grain boundary as a function of rigid-body translations has been carried out, leading to the results of Fig. 1. Two stable structures emerge with close energies much lower than those of the other metastable structures. In these structures, atomic positions are very close to those in the geometric S and PS models. Table 1 gives their geometric and energetic properties.

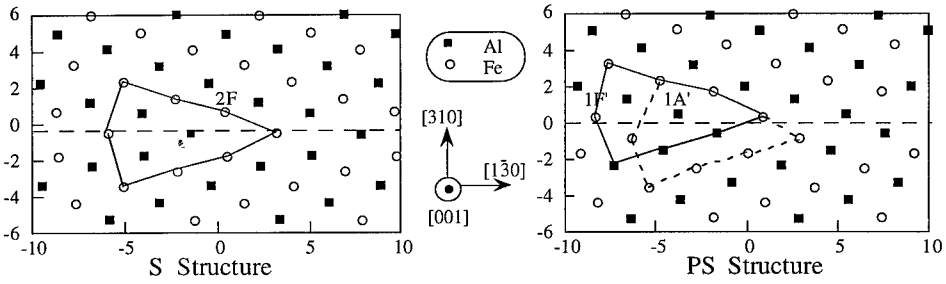

Figure 1: *Relaxed S and PS grain boundary structures (axes units in Å).*

Table 1: *Characteristics of the relaxed S and PS structures.*

	Excess energy (mJ/m²)	Expansion along Oy, [310] (Å)
S structure	958	0.22
PS structure	943	0.17

In an ordered alloy, the search for the equilibrium structure of the GB must also take into account possible changes in the chemical ordering, and the precedent results thus cannot be regarded as physically meaningful, as long as this additional degree of freedom has not been properly treated. In the most simple approach, this can be achieved through the examination of the stability of elementary point defects in the vicinity of the GBP. Defects, whose formation is accompanied by a decrease in the excess energy, are favoured in real structures and induce chemical compositional changes at the GB.

II.2 Elementary point defect formation energies in the vicinity of the GBP

The various sites (Fig. 1) are quoted nA (nF) where A and F stand for Al and Fe and n denotes the distance to the GBP. A single or double prime is added when the two grains are not equivalent (PS structure). It appears that only one defect has a negative weak formation energy (-0.075 eV/atom): the Fe antisite atoms on 1A' sites in the PS structure (in the pseudo-symmetry GB plane). This is the hint of a possible tendency to Fe segregation in the GBP at T = 0 K.
Assuming that these defects remain independent even when their densities are equal to 1 per GB period, enrichment of the central plane up to 100 % Fe results in a negligible energy gain equal to 18 mJ/m^2 for the PS structure. This value is so low that the segregated structure should be very unstable as soon as T rises above 0 K. An exact calculation of the energy of the corresponding structure, taking into account the interactions between the so introduced point defects, is then necessary to conclude about this possible Fe segregation.

II.3 Intergranular changes in composition

The new GB structure, derived from the PS structure through a full (100 %) Fe enrichment with Fe 1A' antisites, will be labelled PS-1A'. In fact, it turns out that the interactions between defects do not rule out the Fe segregation trend, but on the contrary clearly confirm it: after total minimisation, we are led to a GB excess energy equal to 767 mJ/m^2, much lower than the energy of the relaxed PS stoichiometric model (943 mJ/m^2). *Thus, the (310) tilt GB displays a very strong trend to Fe segregation at T = 0 K.* Fig. 2 shows this relaxed PS-1A' structure (expansion equal to -0.1 Å along Oy). It is therefore clear that the interactions between point defects cannot be considered as minor corrections to the results deduced from an independent-defect approach, since they can increase the excess energy variation by an order of magnitude.

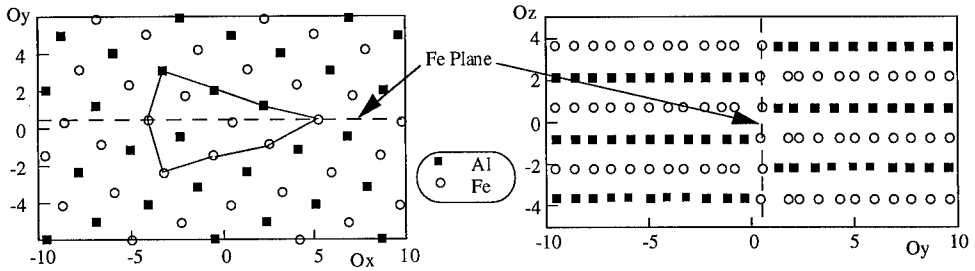

Figure 2: *Relaxed PS-1A' grain boundary structure (axes units in Å).*

To investigate the influence of interactions between other kinds of defects in both S and PS structures, we restrict to the structures obtained through a full enrichment with those defects having the lowest T = 0 K formation energies. Some of them (S-2F, PS-1F') have slightly lower excess energies than their initial structure (S or PS) despite the positive formation energy value of the corresponding isolated point defect. Nevertheless, the PS-1A' structure remains unambiguously the most stable one, the excess energy of the next metastable structure being 109 mJ/m^2 (13 %) higher .
Taking into account the interactions between defects, thus removes the uncertainty bearing on the nature of the stable GB structure at T = 0 K: one single 100 % Fe enriched structure clearly emerges.
The last step is to evaluate the influence of the creation of isolated defects in this PS-1A' structure (Table 2). Fe antistructure atoms are always energetically unfavourable, irrespective of the site studied, whereas sites 1F and 3F are significantly preferred to bulk sites by antistructure Al. GB Aluminium vacancies, if less energetic than in the bulk, remain very improbable, while Fe vacancies

are strongly favoured in sites 2F. All values being significantly positive, the procedure can reasonably be considered to have reached the energy minimum.
Of course, in spite of the care taken in carrying out our procedure, nothing prevents us from having missed a more complex structure, involving several types of defects. One must recall that no rigorous criterion exists that ensures that the absolute energy minimum is actually reached.

Table 2: *Energies of antisite defects and vacancies in the PS-1A' grain boundary (eV).*

	Plane 1	Plane 2	Plane 3	Bulk [2-5]
Al on a F site	0.428	1.220	0.502	0.899
Vacancy on a F site	1.437	0.333	0.876	0.896
Fe on a A site		1.105	1.653	0.767
Vacancy on a A site		2.383	2.582	2.854

III CONCLUSIONS

The present work is the first atomic-scale simulation of grain boundaries in B2 Fe - Al alloys. It emphasises several important features of GBs in B2 FeAl. Firstly, and provided we admit that our results can be generalised to a vast variety of GBs, there is probably a strong enrichment in iron at these interfaces, at least at low temperatures and for the stoichiometric composition. It is also a striking feature that, in the stoichiometric S and PS variants, among the numerous types of intergranular point defects, only one type (an antisite Fe atom in a precise site of the PS structure) has a negative formation energy at T = 0 K. Interactions between intergranular defects are also shown to have a strong influence on the stability of the GB structures.
To go beyond this elementary approach, Monte-Carlo Simulations in the reduced grand canonical ensemble are in progress, as well as high-temperature studies of this PS-1A' GB structure (thermodynamics of elementary point defects and molecular dynamics simulations).

ACKNOWLEDGEMENTS

It is a great pleasure for us to thank O. Hardouin Duparc, Anna Fraczkiewicz and V. Pontikis for scientific discussions. One of us (R. B.) also wishes to thank the Centre S.M.S. (École Nationale Supérieure des Mines de Saint-Étienne) and the L.S.I. (Commissariat à l'Énergie Atomique) for material support during this work.

BIBLIOGRAPHY

[1] *Intermetallic Compounds: Principles and Practice*, ed. J. H. Westbrook and R. L. Fleischer, Wiley & Sons, New York (1994).
[2] R. Besson, A. Fraczkiewicz et M. Biscondi, J. Phys. IV, colloque 2, supplément à J. Phys. III **6** (1996), p. 47.
[3] R. Besson and J. Morillo, Phys. Rev. B **55** (1997), p. 193.
[4] R. Besson, Thèse de doctorat, École Nationale Supérieure des Mines, Saint-Étienne (1997), CEA-R-5775 (1997).
[5] R. Besson and J. Morillo, Comput. Mater. Sci. **10** (1998), p. 416.
[6] J. R. Beeler and G. L. Kulcinski, in "*Interatomic potentials and simulation of lattice defects*", ed. P. C. Gehlen, J. R. Beeler and R. I. Jaffee, Plenum Press, New York (1972), p. 735.
[7] T. Takasugi and O. Izumi, Acta Metall. **31** (1983), p. 1187.

Materials Science Forum Vols. 294-296 (1999) pp. 215-218

Computer Simulation of Tilt Grain Boundaries in Alloys with $L1_2$ and B2 Superlattices

M.D. Starostenkov, B.F. Demyanov, E.L. Sverdlova, S.L. Kustov and E.L. Grakhov

General Physics Dept., Altai State Technical University, Lenin st. 46, RU-656099 Barnaul, Russia

Keywords: Coincidence Site Lattice, Excess Volume, Grain Boundary Sliding

Abstract

Computer simulation of grain boundaries (GB) was carried out in alloys Ni_3Al with $L1_2$ superlattice and NiAl with B2 superlattice. This work studies simmetrical tilt grain boundaries Σ=5 [100](012) and Σ=5 [100](013) (special boundaries) with an axis of turn [001] and with angles of misorientation θ = 53.1° and 36.9°. The atomic interaction has been described by Morse empirical central-force potentials. The atomic structure and energy of GB were investigated by means of construction of γ-surface using three relaxation techniques: rigid two-dimensional relaxation in which the atoms at shift of one grain relatively another remain in sites of corresponding lattices, rigid three-dimensional relaxation and full atomic relaxation. It is shown that Σ=5 tilt GBs in Ni_3Al and NiAl have several steady states. Value of the GB excess volume was calculated. Comparison of our results with geometrical model of coincidence site lattice (CSL) was carried out. GBs in model CSL are unstable, the stabilization is achieved by additional displacement on some vector along the plane of defect.

Introduction

Properties of grain boundaries (GB) depend considerably on their atomic structure. GB atomic structure analysis allows to understand a number of processes that take place in polycrystals: creep, recrystallization, plasticity, diffusion. Many experimental and theoretical studies of GB have been conducted in Ni_3Al and NiAl. Important results on atomic structure of GB in this alloys have been made in [1-3]. Coincidence site lattice (CSL) model is an efficient one, allowing to study GB atomic structure [4]. Usage of translation degrees of freedom within the CSL model (the so called displacement shift complete (DSC) lattice [5]) makes it possible to describe GB defects and rearrangement. The disadvantage of the CSL model is that it does not take into account the atomic relaxation in the GB area. Computer simulations of GB using atomic relaxation discover more complicated characteristics of GB structure, not predicted by the CSL model: excess volume, additional displacements, metastable states [1-3,6,7] and other effects confirmed by the results of direct observations by high resolution transmission electron microscopy [8,9].

Method of Calculation

The work deals with a computer simulation of tilt GB atomic structure in ordered alloys Ni_3Al with $L1_2$ superlattice and NiAl with B2 superlattice. Special GBs Σ=5 (012) and Σ=5 (013) with misorientation angles 53.1^0 and 36.9^0 respectively were investigated. The atomic interaction is described by Morse empirical central-force potentials, taking into account interaction in three coordination spheres. Constants of the potentials were found from equilibrium properties of Ni and

Al (lattice constants, cohesive energy, bulk elastic modulus) and properties of completely ordered alloys Ni_3Al and NiAl (lattice constants and ordering energy) [10].

GB energy was defined as the difference between defected crystal energy and ideal crystal energy. The investigation of GB energy states was carried out by constructing a γ-surface [11]. The energy relief of γ-surface allows to define all steady states of GB, both stable and metastable as well as different variants of GB rearrangement from one state into another. The initial GB structure for γ-surface construction was chosen within the CSL model. Fig.1 shows the GB(012) structure in Ni_3Al alloy. The coordinate axes were chosen in the following way: x-axis is parallel to grain misorientation axis [100], y-axis is parallel to GB plane, z-axis is normal to GB plane. A any GB of a special type consists of identical periodically repeated elements - structural units, so it is enough to construct γ-surface within one structural unit.

Calculations of energy and atomic structure of GBs was carried out using several relaxation techniques: (1) rigid shift relaxation where one grain is shifted relatively the other along the defect plane, (2) rigid three-dimensional relaxation where grains are shifted both parallel and normal to GB plane, (3) full atomic relaxation by method of molecular statics.

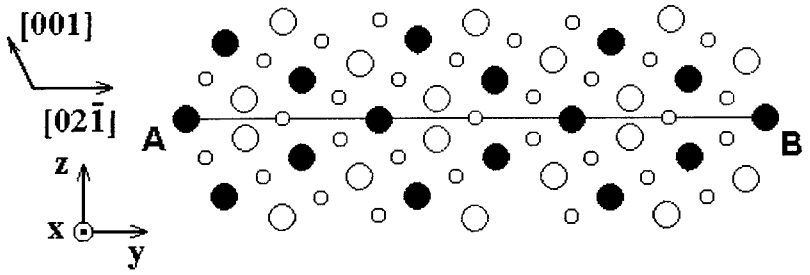

Fig.1. The structure of GB [100](012) in Ni_3Al. AB – plane of GB; x - axis is directed along axis of turn [100], y - axis – along plane of defect, z -axis is normal to the plane of defect. Two planes (100) normal to GB plane are shown. ● - atoms Al, ○ - atoms Ni in top plane; o - atoms Ni in bottom plane.

Results and Discussion

In [7] we had carried out an investigation of GBs Σ=5 in a rigid model in Ni_3Al ordered alloy. It was shown that the geometrical criterium, used in the CSL model, did not allow to define steady states of GBs. GBs with a CSL structure correspond to maxima on γ-surface, i.e. are non-stable and convert into a steady state as a result of an additional displacement. There are several steady states in the investigated GBs. The state with the lowest energy is stable, other states are metastable. The additional displacement vector **f** generally is not the DSC lattice vector. It depends both on geometrical parameters (alloy lattice, GB type) and on atomic interaction forces. Calculations made in this work for NiAl alloy prove the laws formulated in [7]. Table 1 contains GB energy value E_{CSL} and the stable state energy E_R, received by the usage of rigid model. High energy values in the CSL model E_{CSL} are connected with the atomic convergence at tilt GB forming. Usage of translation degrees of freedom allows to spread the converged atoms and to decrease GB energy substantionally.

At the second stage we used a rigid three-dimensional relaxation which allowed to conduct grains relative shift not only parallel (along x- and y- axes) but normal to GB plane (along z-axis) as well. The γ-surfaces, constructed within this model, are shown in Fig.2,3. The energy pattern of γ-surface is rather complicated. The highest maxima correspond to atom positions in GB plane, the

minima define steady states, the saddle points allow to find the directions of grains relative displacement at the rearrangement of GBs from one state to another.

Table 1. Energy of GB (mJ/m^2) in Ni_3Al and NiAl alloys. E_{CSL} – energy of GB in the CSL model . E_R, E_{3D}, E_A – energy of stable states of GB, calculated with the usage of rigid, rigid three-dimensional and atomic relaxation techniques, respectively.

Alloy	Type of GB	E_{CSL}	E_R	E_{3R}	E_A
NiAl	(012)	10.54	2.26	1.65	1.53
	(013)	3.64	2.29	1.73	1.36
Ni_3Al	(012)	7.02	4.18	2.87	2.06
	(013)	23.41	4.66	3.22	2.67

In Ni_3Al alloy GBs (012) and (013) have two steady states each. In NiAl GB (012) has one state, GB (013) - three states. Stable states (i.e. having the minimal energy value) energy E_{3R}, received within a rigid three-dimensional model, are shown in Table 1 Position of minima on γ-surface can be characterized by the displacement vector $\mathbf{f}=(f_x,f_y,f_z)$ from the position given by the CSL model. GB structure in the CSL model on γ-surface has the coordinates x=y=z=0. Displacement value f_z can be used to measure excess volume ΔV per GB if we make f_z equal Δd ($\Delta d=d-d_0$ where d is interplanar distance in GB core, d_0 - in an ideal lattice). Relative change of free volume, defined by the formula $\Delta V/V_0=\Delta d/d_0$, is shown in Table 2.

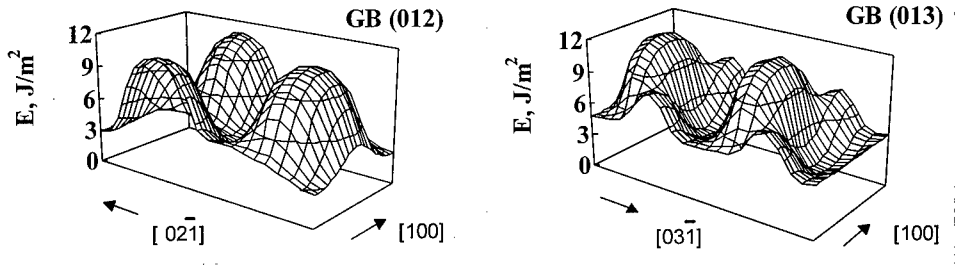

Fig.2. The γ-surfaces of GBs in Ni_3Al.

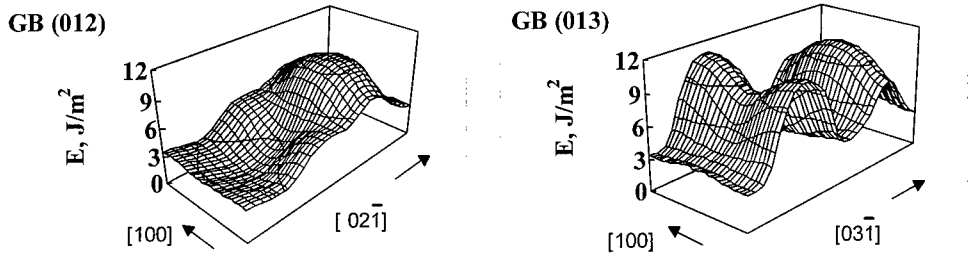

Fig.3. The γ-surfaces of GBs in NiAl.

Full atomic relaxation decreases GB energy E_A additionally (Table 1). Positions of minima remain the same as in a rigid three-dimensional model. Components of additional displacement vector f_x, f_y, f_z corresponding to the stable state are given in Table 2. Only GB (012) in Ni_3Al has a stable state close to the CSL model ($f_x=f_y=0$) which differs only by the presence of excess volume $\Delta V/V_0=0.34$. All the rest investigated GBs are characterized by the additional displacement.

Table 2. Components of vector **f** characterizing displacement of one grain relatively the other with conversion from the CSL structure to completely relaxed structure of GB and relative value of excess volume $\Delta V/V_0$ of a stable GB; a – lattice constant, in Ni_3Al a=0.3544 nm, in NiAl a=0.288 nm.

Alloy	Type of GB	f_x	f_y	f_z	$\Delta V/V_0$
NiAl	(012)	0.5a	0.54a	0.06a	0.25
	(013)	0.5a	-1.52a	0.07a	0.22
Ni_3Al	(012)	0	0	0.08a	0.34
	(013)	0.5a	-0.32a	0.06a	0.40

The γ-surface analysis allows to define GB sliding variants. GB sliding is conversion of a GB from one stable state into another. In the process of GB sliding rearrangement of GB structure can take place through an intermediate metastable state. The shift follows the optimal trajectory with the lowest energy and passes the saddle point. Using the calculated γ-surfaces we defined the directions of the easiest shift. In Ni_3Al the following GB sliding directions are possible: [100] and $[12\bar{1}]$ for GB (012); [100] and $[13\bar{1}]$ for GB (013). In NiAl the GB sliding follows the directions [100] for GB (012); [100] and $[13\bar{1}]$ for GB (013). The saddle point energy defines the value of GB sliding potential barrier. The lowest energy value is observed for all boundary types in the direction [100].

References

[1]. V.Vitek, S.P.Chen, Scr. Met. 25 (1991), p.1237.
[2]. D.E.Luzzi, M.Yan, M.Sob, V.Vitek, Phys. Rev. Lett. 67 (1991), p.1894.
[3]. M.Yan, V.Vitek, Interface Sci. 3, (1995), p.17.
[4]. H.Grimmer, W.Bollmann, D.H.Worrington, Acta. Cryst. A30 (1974), p.194.
[5]. A.N. Orlov, B.N. Perevezentsev, V.V. Rybin, Granitzi zeren v metallach (Metallurgia, Moskva) 1980, p.26.
[6]. R.Najafabadi, D.J.Srolovitz, R.LeSar, J. Mater. Res. 6 (1991), p.999.
[7]. M.D.Starostenkov, B.F.Demyanov, S.L.Kustov, E.G.Sverdlova, E.L.Grakhov, Computational Mat. Sci. 10 (1998), p.436.
[8]. W.Krakov, Acta Met. 38 (1990), p.1031.
[9]. M.Shamsuzzoha, I.Vazquez, P.A.Deymier, D.J.Smith, Interface Sci. 3 (1996), p.227.
[10]. M.D.Starostenkov, B.F.Demyanov, Metallofizika 7 (1985), p.105.
[11]. M.Yamaguchi, V.Paidar, D.P.Pope, V.Vitek, Phil. Mag. A45 (1982), p.876.

Corresponding author B.F.Demyanov : e-mail : pva@agtu.altai.su

Materials Science Forum Vols. 294-296 (1999) pp. 219-222

Calculation of the Energy of Extend Defects in Zinc by the Semi-Empirical Tight-Binding Method

A. Béré, A. Hairie, G. Nouet and E. Paumier

Laboratoire d'Etudes et de Recherches sur les Matériaux, UPRESA CNRS 6004, Institut des Sciences de la Matière et du Rayonnement, 6 Boulevard du Maréchal Juin, F-14050 Caen Cedex, France

Keywords: Zinc, Defect, Tight-Binding, Energy, Recursion, Linear Scaling

Abstract. An improved interatomic potential for zinc is proposed, based on the semi-empirical tight-binding method, including s, p and d atomic orbitals. The fitting procedure considers elastic constants, lattice parameters, with special care to the c/a ratio, and the vacancy energy. Tests are performed on the stability of various structures, compared to the h.c.p. structure. The potential is applied to calculate structures and energies of the basal stacking fault and the $(11\bar{2}2)$ and $(10\bar{1}2)$ twin boundaries, with coherent results.

Introduction

Accurate total energy calculations are needed for atomic scale simulations. Ab initio methods, based on the density functional theory are accurate but not tractable for extended defects. At the opposite, empirical potentials have very low computing costs, but are also less accurate. To study defects in zinc pair potentials have first been used [1].

Two teams [2,3] have proposed empirical potentials giving an unacceptable negative energy for the $(11\bar{2}2)$ twin boundary. We have previously presented [4] results based on tight-binding calculations limited to s and p orbitals, producing correct positive energies for all the studied defects. We have found useful to test the effect of adding d orbitals in the treatment. We introduce here the results obtained in that case.

We first briefly recall the previous results and the method used, based on tight-binding and recursion methods. We then develop the parametrization procedures and the results of the validation tests. The results concerning complex extended defects are then presented and discussed.

Empirical potentials

Igarashi et al. [2] have proposed parameters of the Finnis-Sinclair [5] potential for hexagonal metals. For zinc, the predicted energy for the stacking fault in the basal plane is extremely low ($0.4 mJ/m^2$). This value is quasi equal to zero and not acceptable when compared to observation and also to the published evaluations [6], ranging from 15 to $300 mJ/m^2$. Using pseudo-potential calculations, well suited to the problem, Legrand [7] has found the value of $35 mJ/m^2$.

Mikhin and de Diego [3] have tried to build an improved empirical potential by including a repulsive term deduced from pseudo-potential calculations. The value obtained for the stacking fault energy is $10 mJ/m^2$, still rather low.

When applied to the $(11\bar{2}2)$ twin boundary, the two empirical potentials give negative values of the energy, a pathological behavior corresponding to a defect which would be more stable than the perfect crystal! Considering this, we found that it was necessary to perform quantum calculations to include some realistic electronic properties in the total energy calculations in zinc. We have presented our preliminary results, limited to sp orbitals, in a recent paper [4].

The semi-empirical tight-binding method (SETB)

The SETB method is the most tractable quantum method for total energy computations of extended defects. An alternative way could be the pseudo-potential method, but probably at higher computing cost. Anyway, considering the development of atomistic simulations in materials, it is useful to

explore any reasonable way, and to compare the achievements. Up to now, we are working on the SETB way.

In this scheme, the total energy of the system is the sum of the electronic energy, mainly attractive, and the ion-ion energy, which is repulsive [8].

$$E_{tot} = E_e + E_{rep}$$

The repulsive term is crudely approximated by an empirical pair potential, with a negligible computing cost.

The electronic energy is deduced from an approximated hamiltonian (H), according to the Harrison scheme with the standard values for the hopping integrals [9]. The matrix elements are multiplied by a cutoff term:

$$f_1(r) = \frac{1}{2}\left(1 - \tanh\frac{r - r_1}{\Delta r_1}\right)$$

The electronic energy is

$$E_e = Tr\,(\rho . H)$$

where ρ is the density matrix

$$\rho = 2\left(1 + \exp\frac{H - E_f}{kT}\right)^{-1}$$

where E_f is the Fermi energy. This expression seems simple but it is a matrix expression, very heavy to compute because H is quite large. Old diagonalization methods have been replaced by modern linear scaling methods [10, 11, 12], taking into account the finite spatial range of ρ.

In the present calculation, we make a crude extra assumption, computing ρ in a region limited to the first neighbours. We have no a priori evaluation of the consequences of this approximation, and we can only judge the method according to the final accuracy versus cost ratio compared to other calculations. We can however notice that we have a theoretical improvement with respect to usual empirical potentials: a quantum treatment within the "cage" defined by the first neighbours, instead of an empirical analytical expression in the same surrounding.

The density matrix is computed using the recursion method [13] and the Fermi level is adjusted to obtain charge neutrality per atom. The process is repeated for each atom to obtain the total electronic energy of the system.

Relaxation process

According to our short range calculation of the density matrix, the hypotheses of the Helmann-Feynman theorem are not fulfilled, and we cannot apply it to compute the electronic forces. To minimize the energy, we have found efficient to apply a fixed step method. Each atom is moved in six directions to test the existence of a new position of lower energy. If it is the case, the atom is placed there.

Fitting procedure

The Hamiltonian is calculated according to Harrison tables, and then the electronic energy is well defined. At the opposite, the repulsive pair potential must be parametrized to fit the bulk properties: interatomic distance, c/a ratio, elastic constants, Grüneisen constants and vacancy formation energy.

We define the repulsive term as the product of two functions:

$$E_{rep} = F(r)\ f_2(r)$$

where F(r) is a polynomial expression

$$F(r) = A_0 + A_1\,(r/r_a\text{-}1) + A_2\,(r/r_a\text{-}1)^2 + A_3\,(r/r_a\text{-}1)^3 + A_4\,(r/r_a\text{-}1)^4$$

and $f_2(r)$ is a cutoff function of the same type as $f_1(r)$

$$f_2(r)= \frac{1}{2}\left(1-\tanh\frac{r-r_2}{\Delta r_2}\right)$$

The values of the parameters have been fixed to the values given in table.

Table 1 : Parameters for the cutoff function in r_0 units, where $r_0 = 2.665$ Å .

	Electronic		Repulsive	
	r_1	Δr_1	r_2	Δr_2
SETB (s, p)	1.20	0.02	1.28	0.02
SETB (s, p, d)	1.28	0.02	1.27	0.012

Table 2 : Parameters for the polynomial repulsive term.

	A_0(eV)	A_1(eV)	A_2(eV)	A_3(eV)	A_4(eV)	r_a(Å)
SETB (s, p)	2.35	- 8.47	22.25	- 53.04	0	2.78864
SETB (s, p, d)	2.40	- 8.82	23.51	- 52.0	30.0	2.78864

These parameters lead to a vacancy formation energy of 1.04 eV with s,p orbitals and with s,p,d orbitals as well. The known experimental value is 0.52 eV [14].

Tests and results

We have tested our method by calculating the energy of the 4H and 6H polytypes and of the f.c.c. structure, compared to the energy of the h.c.p. structure, reported in table 3.

Table 3 : Energy (in meV/atom) of different polytypes

Polytype	h.c.p.	4H	6H	f.c.c.
SETB (s, p)	0	20.8	25.8	33.9
SETB (s, p, d)	0	23	28	37

The c/a ratios are given in table 4.

Table 4 : c/a ratios of different polytypes. The experimental value of the h.c.p structure is equal to 1.856.

Polytype	h.c.p.	4H	6H	f.c.c.
SETB (s, p)	1.801	1.708	1.676	1.633
SETB (s, p, d)	1.856	1.719	1.687	1.632

Another set of results is obtained for the relaxed structure of three planar extended defects : the basal stacking fault, the $(11\bar{2}2)$ and the $(10\bar{1}2)$ twins.

For the stacking fault an experimental estimation has been obtained by Harris and Masters [6]. The two twins have been studied by Simon [15] with a pseudopotential and by Serra and Bacon [16] for all h.c.p. metals with six Lennard-Jones potentials. Moreover, the $(10\bar{1}2)$ has been studied theoretically by Hagège, Mori and Ishida [17] with a Lennard-Jones potential and by Braisaz, Ruterana, Lebouvier and Nouet [18] with Igarashi et al. potential, and experimentally by Lay and Nouet [19] and by Braisaz, Ruteranan, Nouet and Pond [20]. Table 5 gives the energy found in each case, either directly in the quoted papers or calculated from them. As usual it is impossible to

compare the energy of the twin with experimental values, but our values are acceptable when compared to the other available ones.

Table 5 : Energy of extended defects in mJm^{-2}, with respect to the perfect crystal (* calculated with Igarashi potential [2]).

Defect	Basal Stacking fault	$(11\bar{2}2)$ twin	$(10\bar{1}2)$ twin
Pseudopot [15]		290	1270
Pseudopot [7]	35		
Lennard-Jones [17]			372.4
Many-body [2]	0.4 [2]	- 1.8*	125 [18]
Many-body [3]	10		
SETB (s, p)	119.1	45.5	110
SETB (s, p, d)	133	68	266

Conclusion

We have calculated improved values for several extended defects in zinc, using the SETB method with s, p, d orbitals. We avoid the pathological behaviour of previous empirical potentials, obtaining coherent results.

Reference

1. A. Serra, R. Pond and D.J. Bacon, Acta Metall. Mater. **39**, 1469 (1991) and literature quoted therein.
2. M. Igarashi, M. Khantha and V. Vitek, Phil. Mag. **B63**, 603 (1991).
3. A.G. Mikhin and N. de Diego, Phil. Mag. **A73**, 1211 (1996).
4. A. Béré, A. Hairie, G. Nouet and E. Paumier, Mat. Res. Soc. Symp. Proc., **491** (1998) 333.
5. M.W. Finnis and J.E. Sinclair, Phil. Mag. **A50**, 45 (1984).
6. J.E. Harris and B.C. Masters, Proc. Roy. Soc. **A292**, 240 (1966).
7. B. Legrand, Phi. Mag. **B49**, 171 (1984).
8. A.P. Sutton, M.W. Finnis, D.G. Pettifor and Y. Ohta, J. Phys. **C21**, 35 (1988).
9. W.A. Harrison, Electronic Structure and the Properties of solids (W.H. Freeman and Company, 1980).
10. X.P. Li, R.W. Nunes and D. Vanderbilt, Phys. Rev. **B47**, 10891 (1993).
11. A. Hairie, F. Hairie, B. Lebouvier and E. Paumier, Mat. Sci. Forum **207-209**, 105 (1995).
12. J. Chen, A. Béré, A. Hairie, G. Nouet and E. Paumier, Comput. Mat. Sci. **10**, 392 (1998).
13. R. Haydock, Solid State Physics (ed. F. Seitz and D. Turnbull, 1980) **35**, 215.
14. A. Seeger, Phil. Mag. **A64**, 735 (1991).
15. J.P. Simon, J. Phys. F : Metal Phys. **10**, 337 (1980).
16. A. Serra and D.J. Bacon, Phil. Mag. **A54**, 793 (1986).
17. S. Hagège, M. Mori and Y. Ishiba, J. Phys. C1 **51**, 161 (1990).
18. T. Braisaz, P. Ruterana, B. Lebouvier and G. Nouet, Phys. Stat. Sol. **B191**, 267 (1995).
19. S. Lay and G. Nouet, Phil. Mag. **A70**, 261 (1994).
20. T. Braisaz, P. Ruterana, G. Nouet and R.C. Pond, Phil. Mag. **A75**, 1075 (1997).

Materials Science Forum Vols. 294-296 (1999) pp. 223-226

Modified Stillinger-Weber Potential for Planar Defects Modeling in GaN

A. Béré, P. Vermaut, A. Hairie, E. Paumier, P. Ruterana and G. Nouet

Laboratoire d'Etudes et de Recherches sur les Matériaux, UPRESA CNRS 6004, Institut des Sciences de la Matière et du Rayonnement, 6 Bd Maréchal Juin, F-14050 Caen Cedex, France

Keywords: Nitride, AlN, GaN, InN, Stillinger-Weber, Defects

Abstract: The Stillinger-Weber potential is modified to study properties of GaN. A gaussian term was added to the Stillinger-Weber potential to be able to include the third nearest neighbours interactions. The results reproduce all the equilibrium lattice constants and the bulk modulus for the wurtzite and zincblende structures. Using the modified Stillinger-Weber potential, we investigate the atomic structure of the $\{11\bar{2}0\}$ planar defects, and its stability. It is found that the Drum model is energetically more favorable than the Amelinckx model.

Introduction

III-V nitride semiconductors AlN, GaN and InN have attracted considerable interest as materials for the possibilities that they offer for fabricating optical devices such as detectors, solid-state lasers and light-emitting diodes. Accurate experimental and theoretical studies of their electronic and structural properties in equilibrum and under external perturbations are therefore timely.

In spite of the rapid development in the application of quantum mechanical techniques for the electronic studies, leading to many studies for bulk properties [1-4], few theoretical works [5-7] to our knowledge, have been proposed to study the defects of these materials. Thus, the use of empirical potentials for modeling materials at atomistic level is still necessary.

Wurtzite (hexagonal system) and zincblende (cubic system) are the most common crystal structures of compound semiconducting materials. Their structure can be described by stacking sequence of tetrahedra as proposed by Pirouz et al [8]. Concerning the cubic semiconductors, many types of empirical interatomic potentials have been proposed [9-13]. Among them, the Stillinger-Weber potential [11] is quite general, and can be used to deal with any arbitrary number of neighbour atoms. Having tried to use it in order to investigate the properties of hexagonal materials, we have noticed that, in its standard form, it could not correctly reproduce the c/a ratio which is characteristic of the hexagonal materials. The range of standard SW potential is short and it is necessary to take into account the neighbour atoms interactions beyond the second neighbours. This was done by adding to the SW potential, a gaussian pair term which allows it to reach the third neighbour atoms.

In the present work, we determine parameters for the modified Stillinger-Weber (MSW) potential to study the bulk properties of gallium nitride in the wurtzite and the zincblende phases. Using the potential, we calculate the energy and determine the atomic structure of the $\{11\bar{2}0\}$ planar defects of gallium nitride.

Modified Stillinger-Weber potential

In the standard Stillinger-Weber [11] potential, there are two-body and three body terms which respectively correspond to a pair and pseudo-many body interaction potential. The parameters of the potential have a direct influence on a special property of the perfect crystal. This model is unable to predict the values of the non ideal c/a and the vector u which characterizes the displacement along the c axis between the two hcp

sublattices of the wurtzite structure. We add a simple gaussian term allowing the interaction potential to reach the neighbour atoms beyond the second neighbours. Among the third neighbours in the wurtzite structure, the nearest one is mainly responsible for the non ideal c/a ratio. The gaussian term is given by

$$v = \varepsilon C \exp\{-(\frac{d_{ij} - r_1}{\Delta r_1})^2\}$$

where d_{ij} is the bond length between atoms i and j, r_1 the center of the gaussian is situated between the second and third neighbours distances and Δr_1 is the width of the gaussian.

According to the sign of C and the value of r_1, we can increase or decrease the value of the c/a ratio with respect to the ideal value.

Lattice relaxation and fitting procedure

The relaxation procedure is performed using the so-called quenched molecular dynamics method [14]. The parameters of the MSW potential are fitted to the perfect crystal properties. Then, the energy of the crystal may be considered as a function of c/a ratio and u, and by trial and error method, the experimental values of the c/a ratio and the internal parameter u giving the minimum energy are determined. Finally, with the values of the equilibrium bond length d and of the cohesive energy ε, the best values of the constants are shown in table 1.

Table 1 The equilibrium bond length d, the cohesive energy ε, and the obtained MSW potential parameters σ, λ, A, B, C, r_1 and Δr_1.

	d	ε	σ	λ	A	B	C	r_1	Δr_1
GaN	1.948	2.24	1.695	3.8365	5.9661028	0.70140157	-0.001668	1.64	0.08

d, and σ are in Å , r_1 and Δr_1 are in d units, ε in eV/bond and A, B, C dimensionless parameters. The cutoff parameter is taken to be 1.8 and γ to be 1.2, as originally proposed by Stillinger-Weber.

Structural properties

The calculated ground state properties of the perfect wurtzite and zincblende are presented in table 2. The obtained equilibrium lattice constants, the c/a ratio, the internal vector and the bulk modulus agree very well with experiment. The positive structural energy difference (ΔE) indicates that the wurtzite phase is more stable than the zincblende phase.

Table 2: Calculated structural properties of zincblende and wurtzite gallium nitride. ΔE is the relaxed energy difference. Experimental values are in parentheses.

	Wurtzite	Zincblende
a_0 (Å)	3.185[a], (3.189)[c]	4.50[a], (4.49, 4.50)[d]
c/a	1.626[a], (1.625)[c]	
u	0.376 (0.377 0.380)	
B_0 (GPa)	190[a], (188-245)[c]	191[a],173-200[d],201[c], 170[b],(190)[e], (237, 245)[d]
ΔE (meV/at)	0.0	1.7

(a) → Present work, (b) → [3], (c) → [1] , (d) → [15], (e) → [16]

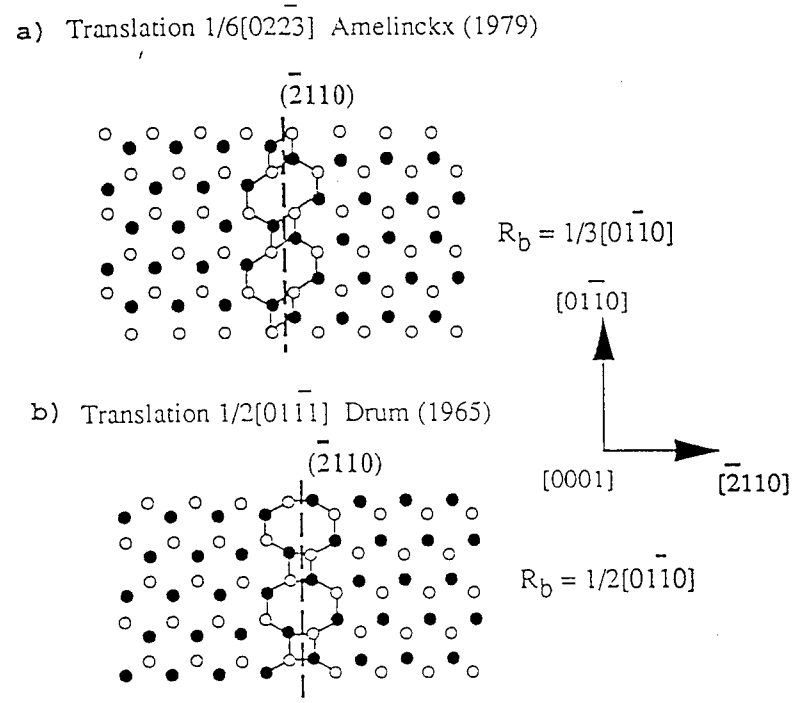

Figure 1: Projection along [0001] of the atomic structure of the stacking faults R_b=1/6<2$\bar{2}$03> (a) and R_b=1/2<1$\bar{1}$01> (b).

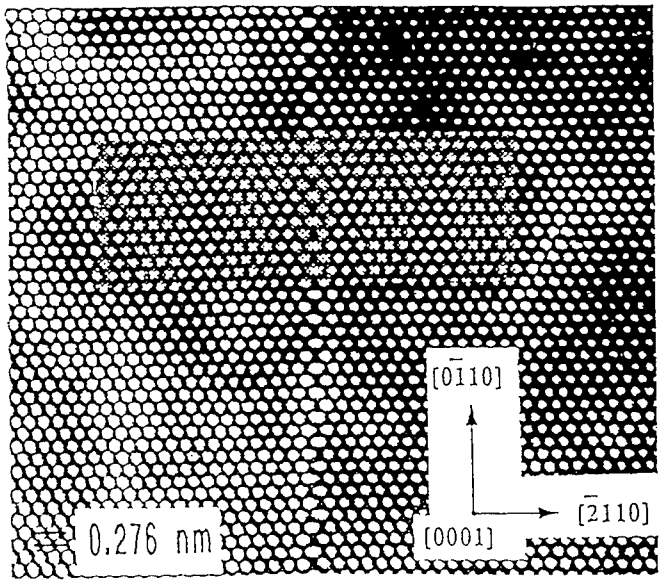

Figure 2: HREM experimental image. The inserts show simulated image for the stacking fault R_b=1/2<1$\bar{1}$01>.

Atomic structure of the $\{11\bar{2}0\}$ GaN planar defects

The potential produced in the previous section is applied to investigate the atomic structure of the $\{11\bar{2}0\}$ stacking fault. Two atomic models [17-18] were taken into account for comparison with the experimental observations.The first one corresponds to the intrinsic stacking fault I_1 of the h.c.p system $1/6<2\bar{2}03>$ which folds from the basal to the prismatic plane keeping its fault vector as observed for the first time by Amelinckx et al [19]. The second one was proposed by Drum [20] and its fault vector is $1/2<1\bar{1}01>$. It needs the formation of a $1/6[10\bar{1}0]$ stair-rod each time it passes from the prismatic to the basal plane. Their atomic projection along the [0001] axis are shown in figure1. They both exhibit 4 and 8 atom cycles in the interface plane.

Recently, Northrup[4] has studied the atomic and electronic structure of a $\{11\bar{2}0\}$ prismatic stacking fault in GaN from first principles calculations. The fault vector determined is consistent with the Drum model.

We applied the method of lattice relaxation to a set of 1984 atoms containing the defect for the two atomic models. The optimal structure of the Drum (respectively Amelinckx) model has a formation energy equal to 22 (respectively 78) meV/$\dot{A}^2$ compared to the calculations of Northrup which gives 72 (respectively 123) meV/$\dot{A}^2$. The calculations determine that the Drum model is energetically favorable, in agreement with Northrup calculations and experimental observations which mainly exhibit the $1/2<1\bar{1}01>$ sacking fault.

CONCLUSION

In the paper, we have presented a theoretical study of the bulk properties for gallium nitride using a modified Stillinger-Weber potential. The lattice constants and the bulk modulus were obtained for both zinc-blende and wurtzite fully relaxed structures and are in good agreement with other calculations and experimental data. The calculations concerning the atomic structure of the $\{11\bar{2}0\}$ GaN planar defects determine that the Drum model is energetically favorable. The method is very simple to apply and the computing cost is reasonable compared to ab initio calculations. We project to extend the method to other nitride semiconductors as AlN and InN.

[1] K. Kim, W. R. L. Lamrecht, and B. Segall, Phys. Rev. B **53**, 16310 (1996).
[2] J. Xie, Jian Zi, and K. Zhang, Phys. Stat. Sol. (b) **192**, 95 (1995).
[3] M. B. Nardelli, K. Rapcewicz, and J. Bernholc, Phys. Rev. B **55**, 55 (1997) .
[4] J. E. Northrup, Appl. Phys. Lett. **72**, 2316 (1997).
[5] J. E. Northrup, J. Neugebauer and L. T. Romano, Phys. Rev. Let. **77**, 103 (1996).
[6] J. E. Northrup and J. Neugebauer, Phys. Rev. B **53**, 10477 (1996).
[7] J. E. Jaffe, R. Pandey and P. Zapol, Phys. Rev. B **53**, R209 (1996).
[8] P.Pirouz and J. W. Yang, Ultramicroscopy, **51**, 189 (1993)
[9] P. N. Keating, Phys. Rev. **145**, 637 (1966).
[10] G. A. Baraff, E. D. Kane and M. Schlüter, Phys. Rev. B **21,** 5662 (1980).
[11] F. H. Stillinger and T. A. Weber, Phys. Rev. B **31**, 5262 (1985).
[12] J. Tersoff, Phys. Rev. B **39**, 5566 (1989).
[13] M. Ichimura, Phys. Stat. Sol. (a) **153**, 431 (1996) .
[14] C. H. Bennet, Diffusion in solids, Recent developments, Ed. Nowicki A. S. et Ed. de Physique, **91** (1975) .
[15] E. Ruiz, S. Alvarez, and P. Alemany, Phys. Rev. B **49**, 7115 (1994) .
[16] M. E. Sherwin, and T. J. Drummond, J. Appl. Phys. **69**, 8423 (1991).
[17] P. Vermaut, Thesis, University of Caen (1997).
[18] P. Vermaut, P. Ruterana, G. Nouet and H. Morkoç, Phil. Mag. A **75,** 239 (1997)
[19] H. Blank, P. Delavignette, R. Gevers and S. Amelinckx, Phys. Stat. Sol. **7**, 747 (1964).
[20] C. M. Drum, Phil. Mag., A **11**, 313 (1965).

Materials Science Forum Vols. 294-296 (1999) pp. 227-230

Relative Stability of Two Structures of the Σ=11<011> Tilt Grain Boundary in Silicon and Germanium by the Tight-Binding Method

J. Chen, A. Hairie, G. Nouet and E. Paumier

Laboratoire d'Etudes et de Recherches sur les Matériaux, UPRESA CNRS 6004,
Institut des Sciences de la Matière et du Rayonnement,
6 Boulevard du Maréchal Juin, F-14050 CAEN Cedex, France

Keywords: Tilt Grain Boundary, Silicon, Germanium, Atomic Structure, Stability, O(N) Method, Semi-Empirical Tight-Binding

Abstract. The Σ = 11 <011> tilt grain boundary is known to exhibit two atomic structures A and B. Moreover, at low temperature, the A structure has been observed is silicon and the B structure in germanium. The classical empirical potentials are unable to describe this unexpected difference between two elements which are very close in many other respects. Wilder and Teichler used an empirical bond charge model to account for these phenomena. In the present paper, the semi-empirical tight-binding method is used with a relaxation method that also leads to results in agreement with observations.

Introduction

The problem of the stability of grain boundaries in semiconductors as silicon and germanium received a great attention these last years [1-9]. The Σ = 11 tilt grain boundary was found in Si and Ge with two different structures at low temperature : the A type was observed in Si [2] and the B one in Ge [3,4]. A series of theoretical studies was performed by using different numerical simulations [4-9]. We have shown that the classical potentials such as those of Keating [10], of Barraff et al. [11] and of Stillinger and Weber [12] are not able to describe so small structural difference in such sensitive environment. Wilder and Teichler [13] have successfully reproduced the phenomenon with their anharmonic bond charge model. The anharmonic correction seems to have the decisive role in the grain boundary formation.

We have reported the first semi-empirical tight-binding total energy calculation for the same problem with an atomic box relaxed by the classical potentials mentioned above [14]. The result showed a tendency in agreement with the experimental observations. In the present communication, we give the result of a complete total energy calculation for the A and B type structures in Si and Ge relaxed by a linear scaling semi-empirical tight-binding scheme.

The O(N) Tight-Binding Relaxation Scheme

The atomic configuration under study contains more than 1000 atoms. One of the reasons to choose a tight-binding method is that the ab-initio one could not suit to a dynamic study with more than 200 atoms. The classical accurate diagonalisation tight-binding method would be very hard to perform for the same reason : it is too much computer time consuming. We apply our relaxation procedure with a linear scaling density matrix computation scheme [14]. In this method, the density matrix is calculated in a spherical region of radius R. A local tridiagonal hamiltonian is obtained by the Lanczos-Haydock recursion method and is directly diagonalized. This O(N) method allows us to relax a relatively large system such as a grain boundary although some accuracy is lost. The loss

of accuracy is partially compensated in our problem because we are interested only in the energy difference between two structures of the same grain boundary.

Due to the short range calculation of the density matrix, the forces derived from the electronic term cannot be calculated by using the Hellmann-Feynman theorem. Thus we used a direct relaxation method : at each step of the procedure each atom is moved along six directions and placed in the position giving the lowest energy.

The more difficult point in the tight-binding simulation is to find a good transferable parametrisation. Numerous models were proposed but only for silicon ! The transferable models which work for both Si and Ge are rare. We have chosen the Mercer and Chou's one [15] for two reasons. The first reason is that it is based on the data obtained from ab-initio band structure calculations with a different exchange-correlation function for silicon and germanium : the Wigner exchange function gives germanium a more metallic character compared with the Ceperley-Alder correlation function used in silicon. The second reason is the repulsive term which also comes from ab-initio calculations and has a very rich angular dependence. This last point is important in grain boundaries because the difference between two variants is small.

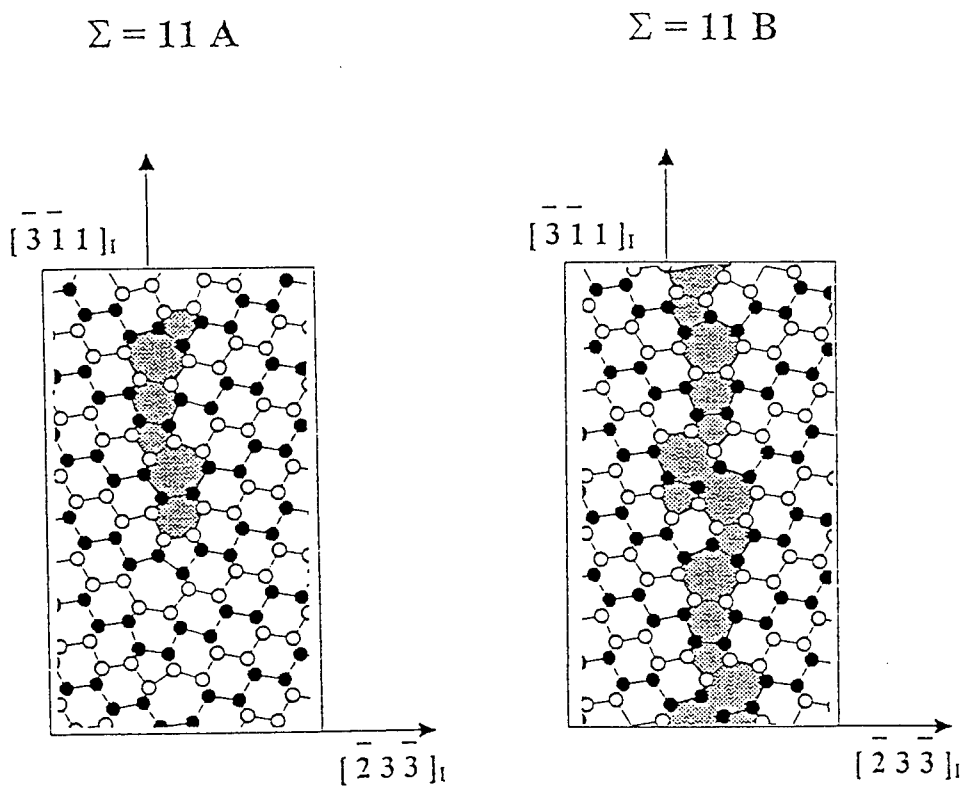

Fig. 1 : Two possible atomic structures of the $\Sigma = 11\ (\bar{2}3\bar{3})[011]$ grain boundary in silicon and germanium. Open and full circles denote different positions along the [011] axis perpendicular to the figure plane.

The Σ = 11 Grain Boundary in Si and Ge

The Σ = 11 $(\bar{2}3\bar{3})$ [001] grain boundary has been observed in silicon and germanium under different experimental conditions. In silicon, it was observed after deformation of a Σ = 9 [001] bicrystal [2] with the A structure or the B one according whether the deformation is performed at 450°C or at 1200°C. In germanium, the B structure was observed in an as-grown bicrystal [3] and, more recently [4], it has been shown that the B structure is stable at low temperature (20°C) and the A one at high temperature (850°C). The transition is reversible.

The Σ = 11 corresponds to a rotation θ = 50.48° around a <110> rotation axis and its two variants Σ = 11A and B can be described by some structural units. The A structure is composed by two structural units M and T and the B one by three units M, T and P. The M and T units exist in the Σ = 9 and Σ = 3 grain boundaries respectively. The P unit is formed by five and seven atom rings. The B structure has a period twice that of Σ = 11A and the sequences of the two variants shown in Fig. 1 are :

$$\Sigma = 11A : M^{-}TM^{+}T$$

$$\Sigma = 11B : M^{+}TM^{-}P^{+}M^{-}TM^{+}P^{-}$$

where superscripts + and – correspond to structural units which are connected by a mirror symmetry with respect to the grain boundary plane.

We note here that the B structure has the P units which do not exist in the A one, resulting in more significant angular distortions in B.

Results and discussion

The relaxation was performed in the box with 1328 atoms in both Σ = 11A and Σ = 11B structures with improvements with respect to preceding results [16]. The cutoff radius R was taken as 4 times the equilibrium atomic distance in the perfect crystal. The calculated energy of the grain boundary is shown in table I.

Table I: Energy E_p of Σ = 11A and Σ = 11B in Si and Ge. D is the difference of E_p between Σ = 11B and Σ = 11A in units of mJ/m^2:

	Σ = 11A	Σ = 11B	D
Si	431	520	89
Ge	343	283	- 60

The clear difference between silicon and germanium is shown in the table above. These results confirm the experimental observations : they mean that at zero temperature, the Σ = 11A tilt grain boundary is more stable in silicon and the Σ = 11B in germanium. Wilder and Teichler [13] have recently obtained the same tendency using an anharmonic bond charge model with a less important energy difference. They contribute this improvement over the classical potentials to the anharmonic effect. It is clear that the classical models are not precise enough to describe such sensitive grain boundary energy as discussed in [9]. The more pronounced energy difference between silicon and germanium with our semi-empirical tight-binding model could be understood by an environmental dependence more complex in Mercer and Chou's potential than in bond charge

model . The natural difference between silicon and germanium, such as the d behaviour of the germanium was involved in the parameters along with the effect of anharmonic terms.

Conclusion

The total energy of the two types of the $\Sigma = 11$ tilt grain boundary in silicon and germanium is calculated by using our O(N) semi-empirical tight-binding scheme with the Mercer and Chou's parametrisation for fully relaxed atomic structures. The results reproduce the experimental observation : the $\Sigma = 11$A structure is found in silicon at low temperature and the $\Sigma = 11$B one in germanium.

References

[1] J. Thibault, J.L. Rouvière and A. Bourret, Materials Science and Technology edit. by Schröter, **4** (1991) 321.
[2] J. Thibault, J.L. Putaux, A. Jacques, A. George, H.M. Michaud and X. Baillin, Mater. Sci. Eng. **A164**, (1993) 93.
[3] A. Bourret and J.J. Bacmann, Rev. Phys. Appl. **22**, (1987) 563.
[4] M. Elkajbaji, J. Thibault, and H.O.K. Kirchner, Phil. Mag. Lett. **73** (1996) 5.
[5] A. Hairie, F. Hairie, B. Lebouvier, G. Nouet, E. Paumier, N. Ralantoson and A.P. Sutton, Interface Science **2** (1994) 17.
[6] O. Hardouin Duparc and M. Torrent, Interface Science **2** (1994) 7.
[7] B. Lebouvier, A. Hairie, F. Hairie, G. Nouet and E. Paumier, Mat. Sci.For. **207/209** (1996) 277.
[8] B. Lebouvier, A. Hairie, F. Hairie, G. Nouet and E. Paumier, Interface Science and Materials Interconnection, Proceeding of JIMIS 8 ed. by the Japan Institute of Metals (1996) 299.
[9] J. Chen, B. Lebouvier, A. Hairie, G. Nouet and E. Paumier, Comput. Mat. Sci. **10** (1998) 334.
[10] P.N. Keating, Phys. Rev. **145** (1966) 637.
[11] G.A. Baraff, E.O. Kane and M. Schlüter, Phys. Rev. **B21** (1985) 5262.
[12] F.H. Stillinger and T.A. Weber, Phys. Rev. **B31** (1985) 5262.
[13] J. Wilder and H. Teichler, Phil. Mag. Lett. **76** (1997) 83.
[14] J. Chen, A. Béré, A. Hairie, G. Nouet and E. Paumier, Comput. Mat. Sci. **10** (1998) 392.
[15] J.L. Mercer Jr. and M.Y. Chou, Phys. Rev. **B47** (1993) 9366.
[16] J. Chen, A. Hairie, B. Lebouvier, G. Nouet and E. Paumier, Mat. Res. Soc. Symp. Proc., **492** (1998) 133.

Materials Science Forum Vols. 294-296 (1999) pp. 231-234

Ab Initio Study of Grain Boundaries in SiC and Si

M. Kohyama and K. Tanaka

Department of Material Physics, Osaka National Institute, AIST,
1-8-31, Midorigaoka, Ikeda, Osaka 563-8577, Japan

Keywords: Density-Functional Theory, First-Principles Molecular-Dynamics Method, Tight-Binding Method, High-Resolution Electron Microscopy, Coincidence Boundary, Electronic Structure, Si, SiC

Abstract

We have obtained the atomic and electronic structure of the $\{122\}\Sigma$=9 grain boundaries in Si and SiC using the first-principles molecular-dynamics method based on the density-functional theory. The results are compared with our previous tight-binding calculations. The agreement between the present and tight-binding results is rather good about the energy and configurations, although serious disagreement exists about the electronic structure of the SiC boundary. The results are also compared with our recent high-resolution electron microscopy observation in SiC, which shows the real existence of the calculated configuration.

1. Introduction

It is of great importance to study the atomic and electronic structure of grain boundaries in Si and SiC. Grain boundaries in Si dominate the properties of polycrystalline Si used for solar cells or thin film transistors, and grain boundaries in SiC dominate the properties of SiC ceramics. Currently, it is possible to perform *ab initio* calculations of such complex systems using the first-principles molecular dynamics method (FPMD) based on the density-functional theory [1,2]. Experimentally, it is also possible to obtain a lot of information on the atomic and electronic structure of grain boundaries using recent techniques of high-resolution transmission electron microscopy (HRTEM). In this paper, we report our recent *ab initio* calculations of coincidence tilt boundaries in Si and SiC. Results are compared with our previous tight-binding (TB) calculations [3,4], and with our recent HRTEM observation in SiC [5].

2. Theoretical Method

Large systems can be dealt with in the framework of the *ab initio* pseudopotential method by using the FPMD method, where the electronic minimization is performed efficiently through iterative techniques [1,2]. For the minimization of the total-energy functional E_{tot} with the orthonormalization constraint of wave functions $\{\psi_i\}$, we consider the functional $\Omega = E_{tot} - \sum \lambda_{ij}(\langle\psi_i|\psi_j\rangle - \delta_{ij})$ where λ_{ij} is the Lagrange multipliers. Its gradient with respect to ψ_i can be expressed as $\delta\Omega/\delta\psi_i^* = (H-\lambda_i)\psi_i$ where $\lambda_i = \langle\psi_i|H|\psi_i\rangle$, if the orthonormalization process is performed separately. The negative of this gradient can be regarded as a force acting on ψ_i. Thus the wave functions can be iteratively updated according to this force and can reach the true eigen functions minimizing E_{tot}. In addition, we use the optimized pseudopotentials [6] to reduce the number of plane-wave basis functions. The structural properties of bulk Si, SiC and diamond are reproduced accurately within the local density approximation [7] using the plane-wave cutoff energy of 35 Ry for Si and of 60 Ry for SiC and diamond.

3. Si Grain Boundary

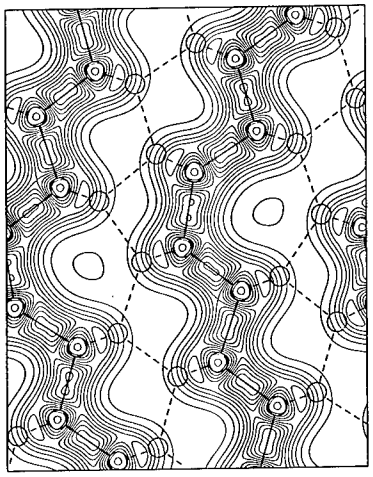

We deal with the {122}Σ=9 boundary in Si. We examine the glide-plane model [3] observed experimentally. A 64-atom cell and two special **k** points per irreducible eighth of the Brillouine zone are used. The ridid-body translation optimized by the TB calculatons [3] is used for the initial configuration. After the relaxation, the energy increase against the bulk crystal is calculated, where four special **k** points are used so as to deal with a small energy difference more accurately.

Figure 1. Relaxed configuration of the {122}Σ=9 boundary in Si. Contours of the valence electron density are plotted from 0.003 a.u.$^{-3}$ to 0.091 a.u.$^{-3}$ in spacing of 0.008 a.u.$^{-3}$. Circles indicate the atomic positions.

Table 1. Calculated results of the {122}Σ=9 boundary in Si. E_{gb} is the boundary energy, which is the energy increase per unit area of one interface against the bulk crystal. Δr and $\Delta\theta$ are the bond-length and bond-angle distortions. Our previous TB results [3] are also listed.

	$E_{gb}(J/m^2)$	$\Delta r(\%)$	$\Delta\theta(degree)$
ab initio (64-atom cell)	0.18	−1.8 to +1.4	−16.3 to +22.2
TB (144-atom cell)	0.32	−1.9 to +1.5	−16.0 to +19.9

Figure 1 and Table 1 show the results. The present configuration is stable with small bond distortions. All the interfacial bonds are well reconstructed, although stretched bonds have reduced bond charges. The agreement between the present and TB results is rather good. About the electronic structure, there exist no electronic states inside the band gap, although there exist states with relatively large probabilities at the interface region near the band edges. In the local density of states (LDOS), there exist small changes in the valence band DOS. The *s*-*p* mixing peak is decreased and the states are increased at the valleys among the three peaks. The *p*-*p* bonding peak tends to be flattened. All these features are similar to the TB results [3]. The changes in the LDOS should be caused by the odd-membered rings.

4. SiC Grain Boundary

We deal with the {122}Σ=9 boundary in cubic SiC. For the same bonding network as the boundary in Si, three kinds of models can be constructed by inverting the polarity of grains. These are two kinds of polar (non-stoichiometric) interfaces and a non-polar (stoichiometric) interface [4]. Odd-membered rings at the interface induce C–C or Si–Si wrong bonds. The N-type (C-rich) polar interface contains C–C bonds, and the P-type (Si-rich) polar interface contains Si–Si bonds. The non-polar interface contains both types of wrong bonds. We use a 64-atom cell and two special **k** points. The supercell of the polar interface must contain two inequivalent polar interfaces by the crystallographic constraint. Initial configurations contain the rigid-body translations optimized by the TB calculations [4].

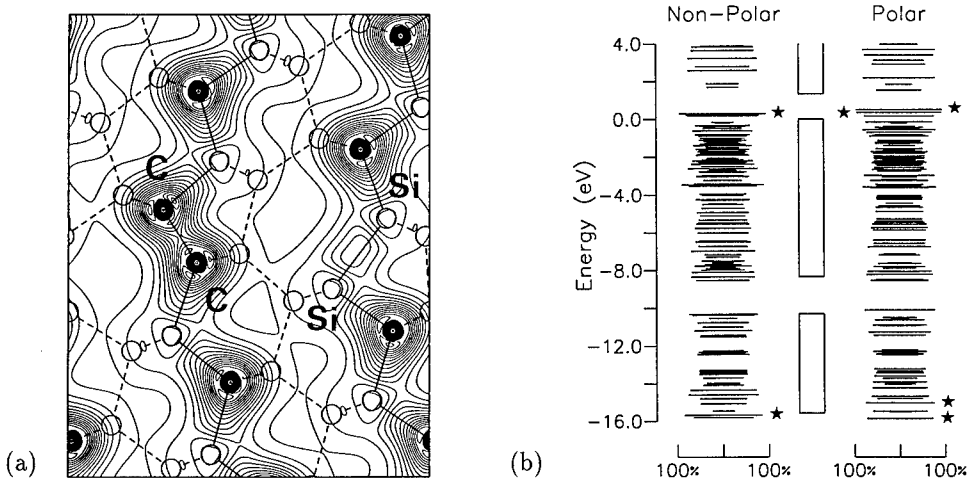

Figure 2. (a) Relaxed configuration of the non-polar interface of the $\{122\}\Sigma$=9 boundary in SiC. Contours of the valence electron density are plotted from 0.015 a.u.$^{-3}$ to 0.295 a.u.$^{-3}$ in spacing of 0.020 a.u.$^{-3}$. (b) Eigen energy levels at the Γ point for the polar and non-polar interfaces. Length of each horizontal line represents the probability of each state in the interface regions, which correspond to one half of the cell volume. Boxes are the bulk band projection. Stars indicate the C–C bond localized states.

Table 2. Calculated results of the polar and non-polar interfaces of the $\{122\}\Sigma$=9 boundary in SiC. ΔE_{tot} is the energy increase per cell against bulk SiC. E_{gb} is the boundary energy, which is obtained only for the non-polar interface. Δr and $\Delta\theta$ are the bond-length and bond-angle distortions. Ranges of Δr include only distortions of Si–C bonds. Values of Δr for C–C and Si–Si bonds mean the deviations against the bond lengths in bulk diamond and Si, respectively. Our previous TB results [4] are also listed.

	$\Delta E_{tot}(eV/cell)$	$E_{gb}(J/m^2)$	$\Delta r(\%)$	$\Delta\theta(degree)$
Non-Polar				
ab initio	4.44	1.27	−2.9 to +2.9	−22.4 to +27.9
(64-atom cell)			C–C:+3.6, Si–Si:−4.4	
TB	5.07	1.43	−2.5 to +2.2	−23.1 to +24.1
(144-atom cell)			C–C:+3.8, Si–Si:−4.3	
Polar				
ab initio	4.31			
N-type			−2.7 to +2.0, C–C:+4.5	−20.1 to +22.5
P-type			−2.7 to +2.5, Si–Si:−1.1	−13.0 to +24.0
TB	4.52			
N-type			−2.5 to +2.1, C–C:+2.5	−21.8 to +19.7
P-type			−2.1 to +1.4, Si–Si:−1.9	−13.1 to +21.1

Figure 2 and Table 2 show the results. The detailed results and analysis will be presented elsewhere [8]. All the interfacial bonds are well reconstructed in each interface. The bond lengths and bond charges of the C–C and Si–Si bonds in each interface have features similar to those in bulk diamond and Si. The C–C bonds has a two-peak structure in the valence charge

density, typical of bulk diamond. The agreement between the present and TB results is rather good, especially about the atomic configurations.

As shown in Fig. 2(b), the present interfaces have a clear band gap. However, electronic states strongly localized at the C–C bonds are observed at the top and bottom of the valence band. The C–C bond states at the valence-band top exist at about 0.3 eV and 0.5 eV above the upper bulk valence-band edge for the non-polar and N-type polar interfaces, respectively. The origin of the C–C bond states can be explained by electronic structure of a small diamond region embedded in SiC. The width of the valence band of diamond is much larger than that of SiC. Thus a diamond region may produce states outside the bulk valence-band edges of SiC. This idea is consistent with the features that the C–C bond states at the top and bottom of the valence band consist of C *p*-like orbitals and C *s*-like orbitals, respectively, similarly to the bulk band-edge states of diamond. In the TB results [4], the C–C bonds generate localized states only at the bottom of the valence band, and the Si–Si bonds generate localized states at the top of the valence band. This seems to be a serious fault of the TB method for SiC [9].

Recently, we have performed the HRTEM observation of grain boundaries in chemical vapour-deposited (CVD) SiC [5]. A specimen was prepared by mechanical thinning and ion milling, and observed using the field emission TEM (JOEL JEM-3000F). Each grain has a preferential {022} orientation, and a lot of ⟨011⟩ coincidence tilt boundaries are contained. Figure 3 shows the image of the {122}Σ=9 boundary. Each ⟨011⟩ atomic column can be identified clearly as compared with the previous observation [10]. The estimated atomic positions are superimposed. The interface clearly consists of a zigzag arrangement of five-membered and seven-membered rings similarly to our theoretical results. From the relation to the {111} Σ=3 twins associated with this interface, this is considered as the non-polar interface. The detailed results of the observation and the detailed comparison between the calculations and the observation will be presented elsewhere [5].

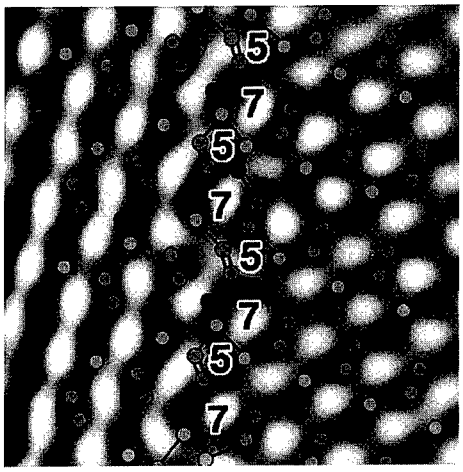

Figure 3. HRTEM image of the {122}Σ=9 boundary in CVD-SiC. "5" and "7" indicate the five- and seven-membered rings.

References

[1] R. Car and M. Parrinello, Phys. Rev. Lett. **55**, 2471 (1985).
[2] M.C. Payne *et al.*, Rev. Mod. Phys. **64**, 1045 (1992).
[3] M. Kohyama and R. Yamamoto, Phys. Rev. B **49**, 17102 (1994); *ibid.* **50**, 8502 (1994).
[4] M. Kohyama *et al.*, J. Phys. Condens. Matter **2**, 7809 (1990); **3**, 7555 (1991).
[5] K. Tanaka, M. Kohyama and M. Iwasa, to be submitted.
[6] N. Troullier and J.L. Martins, Phys. Rev. B **43**, 1993 (1991).
[7] J.P. Perdew and A. Zunger, Phys. Rev. B **23**, 5048 (1981).
[8] M. Kohyama, to be published.
[9] M. Kohyama *et al.*, J. Phys. Condens. Matter **2**, 7791 (1990).
[10] K. Hiraga, Sci. Rep. Res. Inst. Tohoku Univ. A **32**, 1 (1984); S. Hagège *et al.*, J. Physique **51**, C1-167 (1990).

Materials Science Forum Vols. 294-296 (1999) pp. 235-238

TEM Investigation of Metal-Oxide Interfaces in the Ni-20Cr System

G. Calvarin[1], A.-M. Huntz[1] and R. Molins[2]

[1] LEMHE, Université Paris XI, F-91405 Orsay, France

[2] ENSMP, Centre des Matériaux, F-91003 Evry, France

Keywords: Oxidation, NiCr Foils, TEM

ABSTRACT

The oxidation behaviour of Ni-20Cr strips was studied between 500 and 900°C in order to get a better understanding of the oxidation process and of its influence on adhesion and mechanical behaviour of nickel based alloys. SEM and TEM examinations allow us to describe the morphology of the oxide scales according to the oxidation conditions and in relation with oxidation kinetics.
The structure of the resulting metal-oxide interfaces is characterized as well as outer and inner oxidation zones. From two hours up to two days oxidation in air environment, an external scale of NiO columnar grains and internal precipitates of Cr_2O_3 are formed at 600°C whereas at higher temperatures, a continuous layer of Cr_2O_3 is observed adjacent to the alloy, below a two-zoned layer composed of NiO and $NiCr_2O_4$.

1- INTRODUCTION

This study deals with the oxidation behaviour of Ni-Cr foils. The aim is to improve the understanding of the influence of an oxide layer on the mechanical behaviour. Thin strips were chosen in order to enhance the oxide scale effect on the deformation mechanism.
Ni-20Cr alloy was considered as a model for studying oxidation embrittlement of more complex nickel superalloys. In a first time, the microstructural aspects of the oxidation were considered and further on, applied to explain the oxidation influence during creep testing.

2- EXPERIMENTAL

The Ni-20Cr alloy was provided as thin strips of 200 μm thickness. The alloy grain size is about 40 μm. The alloy is relatively pure and no precipitate was detected in the as-received alloy.
Oxidized samples were observed by SEM and TEM equipped with X-ray spectrometers. TEM observations were performed on cross-sectional specimens oxidised at various times and temperatures in order to specify the nature and morphology of the oxide layers, the metal-oxide interface structure, and the structural and chemical evolutions in the alloy beneath the oxidised surface.

3- RESULTS AND DISCUSSION

SEM observations of the outer surface of the oxidized samples indicate a different oxidation along the grain boundaries of the underlying substrate compared to the grain surfaces. EDX analyses clearly indicate a chromium rich oxide along grain boundaries.
SEM cross-section observations of samples oxidized 96 hours, at various temperatures, indicate that the scale appears as festoons with curved inner and outer interfaces, as shown in figure 1. The edges of the festoons correspond to grain boundaries of the underlying substrate.
TEM observations were performed on cross-sectional thin foils for two temperatures (600 and 900°C) after three oxidation durations (10 minutes, 2 and 48 hours) and at 500°C after 96 hours of oxidation. The oxide scale nature was identified by electron diffraction and X ray analysis.
After 96 hours of oxidation at 500°C, the scale consists of an external layer, 250 nm thick, composed of columnar grains of NiO, and an intermediate layer of 150 nm composed of small equiaxed grains of NiO and Cr_2O_3.
After 10 minutes at 600°C, a thin intermediate layer (about 10 nm) made of NiO and Cr_2O_3 particles is present between the outer NiO layer (60 nm) and the substrate. After 2 hours of oxidation, the outer NiO layer is about 200 nm thick and the intermediate layer now contains $NiCr_2O_4$ particles in addition to NiO and Cr_2O_3. Moreover, an internal oxidation zone made of small Cr_2O_3 sticks is observed in the substrate extending approximately on 100 nm from the oxide-substrate interface. After 48 hours of oxidation (figure 2), the same layers are observed with increased thicknesses.
An epitaxial relationship is observed between the chromia particles and the NiCr substrate:

$$[111]_{NiCr} // [0001]_{Cr_2O_3}$$

$$(\bar{2}02)_{NiCr} // (\bar{3}030)_{Cr_2O_3}$$

At 900°C, after 10 minutes of oxidation, the scale consists of a 500 nm NiO scale and an intermediate continuous layer (1.5 μm) made up of $NiCr_2O_4$. Internal precipitation of Cr_2O_3 is also observed in the substrate. After 2 hours, the NiO layer reaches 3 μm and is composed of columnar grains of approximately 2 μm in the outer part and of small equiaxed grains in the inner part (figure 3). Near the metal-oxide interface a thin but continuous Cr_2O_3 layer (about 900 nm) is now observed made of small equiaxed grains. There is always an intermediate layer of $NiCr_2O_4$. After 48 hours of oxidation, the same layers are observed.
The interface between the outer NiO layer and the inner $NiCr_2O_4$ appears very straight, which seems to indicate the initial substrate surface. Moreover, cube to cube orientation relationships are found between the alloy and $NiCr_2O_4$.
Analytical SEM and TEM studies allowed to analyse composition changes in the underlying alloy behind the oxidized zone. At temperatures equal to or above 700°C, the underlying alloy is depleted in chromium due to the formation of a continuous chromia layer. The greater the temperature and the longer the oxidation time, the more important the depletion. At 900°C, behind the chromia continuous layer, a significant chromium depletion, down to about 11wt%, clearly appears behind the oxide/alloy interface. At temperatures lower than 700°C, no chromium depletion is observed behind the internal oxidation zone, since a Cr_2O_3 layer cannot form continuously. However, an important nickel enrichment is noticed in the alloy matrix from one side to another of Cr_2O_3 internal particles.

Our observations are in good agreement with the kinetic study described elsewhere [1]. Depending on the oxidation conditions, time and temperature, TEM examinations revealed distinct oxide layers.

At low temperatures, whatever the allowed duration and during the first stage at 900°C, only a continuous scale of NiO forms at the outer grain surface. This layer grows over a mixture of oxides (NiO, Cr_2O_3, $NiCr_2O_4$) formed on the grain surface. A continuous layer of Cr_2O_3 does not form until 2 hours at 900°C. Nevertheless, Cr_2O_3 islands form at grain boundaries whatever the oxidizing temperature, due to a higher diffusion rate of chromium in grain boundaries and preferential nucleation sites. Chromium can diffuse laterally from grain boundaries to bulk areas to form a continuous layer. The lateral diffusion increases with the temperature. A continuous layer forms first near the grain boundaries and extends all along the grains by coalescence of chromia islands. NiO continues to grow as long as a continuous Cr_2O_3 layer is not formed at the alloy surface. Therefore, areas of the alloy are oxidized at different rates, which explains the observed " festoon " shape, whose edges correspond to the grain boundary emergence [2, 3, 4].
The structure of NiO scale examined on TEM cross-sections looks like NiO scale in pure nickel at high temperatures [5, 6, 7]. A duplex layer is observed, consisting of a fine grain inner layer and a larger, columnar outer layer. The columnar grain size increases with temperature and oxidation time. A mixed anionic and cationic diffusion is responsible for the morphology of the scale with the festoons developed outward as well as inward and justifies that the middle of the festoons is confused with the initial surface of the samples.
This counter current diffusion also agrees with the fact that internal oxidation of chromium and epitaxial relationships are observed. Whereas the NiO scale grows outward, internal precipitates of Cr_2O_3 or an intermediate layer of $NiCr_2O_4$ develop in the alloy. The internal oxidation zone consists of Cr_2O_3 within a nickel matrix. The precipitates look like fingers and are similar to that observed in more dilute alloys at higher temperatures [5]. A special orientation relationship is observed and directions of the hcp Cr_2O_3 structure are parallel to close-packed directions in the fcc Ni structure.
The cube to cube orientation between $NiCr_2O_4$ and Ni-Cr, as verified by electron diffraction, suggests that $NiCr_2O_4$ is formed according to the following reaction :

$$Cr_2O_3 + Ni_{NiCr} + 1/2\ O_2 \rightarrow NiCr_2O_4.$$

These structural observations and the corresponding oxidation mechanism will allow us to justify the oxidation effect on the creep behaviour of Ni-20Cr strips at different temperatures. Creep rates obtained under vacuum at 500°C are lower than in air environment. At higher temperatures, creep rates are nearly the sames in air and under vacuum. The weakening or strengthening oxide effect depends on the testing temperature and is linked to the nature of the oxide which acts as a diffusion barrier.

REFERENCES

1- G. Calvarin, R. Molins, A. M. Huntz, « Oxidation mechanism of Ni-20Cr foils and relation with the oxide layer microstructure », submitted at Oxidation of Metals

2 - C.S. Giggins et F.S. Pettit, Trans Met. AIME **245**, (1969), p.2495

3 - G.C. Wood, F.H. Stott, D.P. Whittle, Y. Shida and B.D. Bastow, Corr. Sci. **23**, n°1, (1983), p.9.

4 - Y. Saïto, T. Inoue, T. Maruyama and T. Amano, Proceedings JIMIS-3 in High Temperature Corrosion of Metals and Alloys,The Japan Institute of Metals, Ed., Supplement, (1983), p.191.

5 - C.K. Kim, L.W. Hobbs, Oxid. Met. **45**, n°3/4, (1996), p. 247

6 - H.V. Atkinson, Oxid. Met., **28**, n°5/6, (1987), p. 353

7 - H.T. Sawhill and L.W. Hobbs, Journal de Physique, colloque C4, supplément au n°4 **46**, C4-117 (1985).

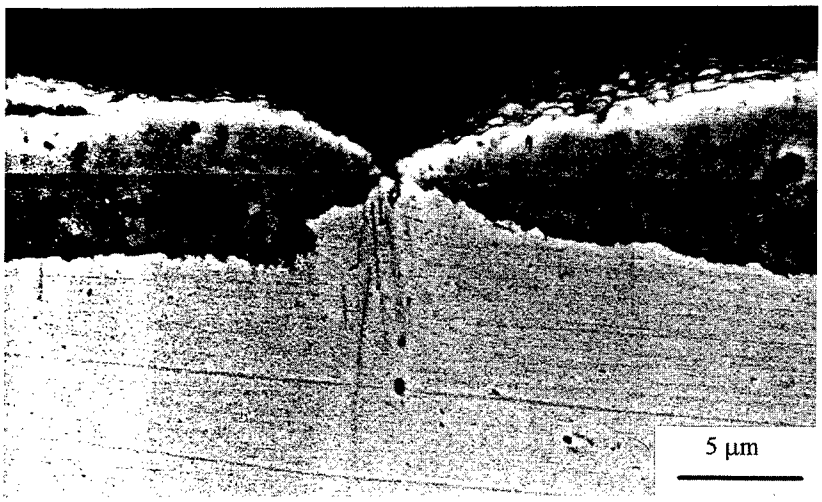

Fig. 1: SEM cross-section, view of festoons

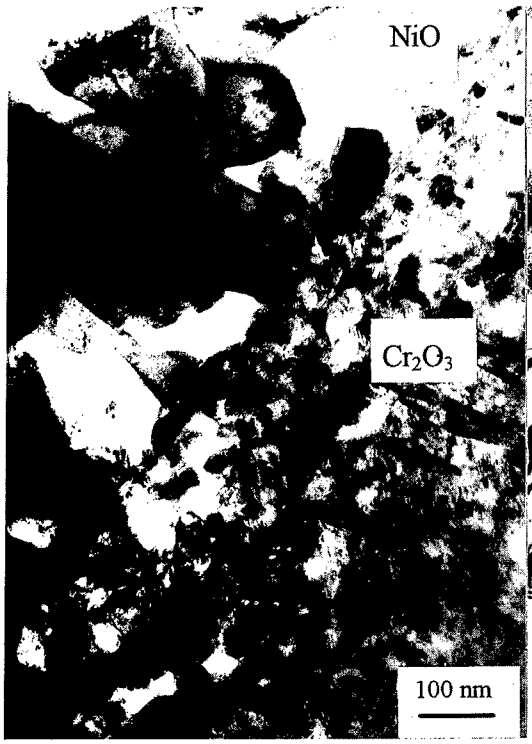

Fig: 2: TEM cross-section.
Oxidation 48h at 600°C

Fig. 3: TEM cross-section.
Oxidation 2h at 900°C

Materials Science Forum Vols. 294-296 (1999) pp. 239-242

The Character of Steps on Gamma/Alpha-2 Interfaces in Lamellar TiAl-Based Alloys

P. Shang, T.T. Cheng and M. Aindow

School of Metallurgy and Materials & IRC in Materials for High Performance Applications, The University of Birmingham, Elms Road, Edgbaston, Birmingham, B15 2TT, England

Keywords: TiAl-Based Alloys, Lamellar Microstructure, Interfacial Dislocations, Steps, HREM

ABSTRACT: HREM images obtained with **B**//[10$\bar{1}$] from lamellar γ-α_2 interfaces in a TiAl-based alloy have been used to show that the interfacial steps have a more diverse range of heights and Burgers vectors than has been reported previously. These observations are not consistent with a Shockley partial dislocation description for the interfacial steps but instead correspond to the defects expected on the basis of the topological theory of interfacial defects. The discrepancy between our observations and those reported elsewhere is explained on the basis of projection effects in HREM.

1. INTRODUCTION

Alloys based on the intermetallic compound γ-TiAl have considerable potential for use in aerospace applications because of their low density, high strength and good oxidation resistance; however the major problem with single phase alloys is their lack of ductility [1]. Recent research has shown that alloys with the two-phase (γ plus α_2) fully lamellar microstructure exhibit higher strengths and ductilities than those with other microstructures [2]. Moreover, many of the other mechanical properties of these alloys such as fracture toughness, fatigue and creep resistance are affected strongly by the lamellar spacing. It is thought that the structure of the γ-α_2 interfaces plays a significant role in determining these mechanical properties. There have been several transmission electron microscopy (TEM) studies on the character of the γ-α_2 interfaces and it is usually accepted that there are two types of defects present; arrays of perfect dislocations with Burgers vectors 1/2<110>γ which exist to accommodate the lattice mismatch between the two phases [4] and dislocations with Burgers vectors 1/6<112>γ which are associated with interfacial steps two atomic layers high [5,6]. These latter Burgers vectors are the same as those of Shockley partial dislocations in the bulk of the γ phase, and this has led to misleading comparisons being drawn between the motion of the steps in the $\alpha \leftrightarrow \alpha_2+\gamma$ phase transformation and that of Shockley partials during deformation twinning in the γ phase.

In our work we have performed HREM studies on lamellar interfaces in a TiAl-based alloy for which there is minimal mismatch between the two phases in the γ-α_2 interfaces. The interfacial ledges were observed along [10$\bar{1}$] and [$\bar{1}$10] and the projected Burgers vectors measured were compared with those expected on the basis of Pond's topological theory of interfacial defects to recover the out of plane components [7,8]. It was found that the range of step heights and Burgers vectors is more diverse than has been reported previously and that these are not consistent with a partial dislocation description for the ledges. In this paper we present a overview of these observations highlighting probable reasons for the discrepancies between our findings and those of previous studies.

2. CRYSTALLOGRAPHY OF γ/α_2 INTERFACES

The γ -TiAl and α_2-Ti_3Al phases exhibit the $L1_0$ and $D0_{19}$ crystal structures which are ordered forms of FCC and HCP packing, respectively. In the lamellar structure these phases exhibit an orientation relationship whereby close-packed planes and directions in the two structures lie parallel to one another in the interface plane (e.g. [3]) thus:

$$\{111\}\gamma//(0001)\alpha_2 \text{ and } <1\bar{1}0>\gamma//<1\bar{2}10>\alpha_2$$

The atomic arrangements in the planes $(111)\gamma$ and $(0001)\alpha_2$ which meet across the γ-α_2 interfaces are shown schematically in Fig. 1.

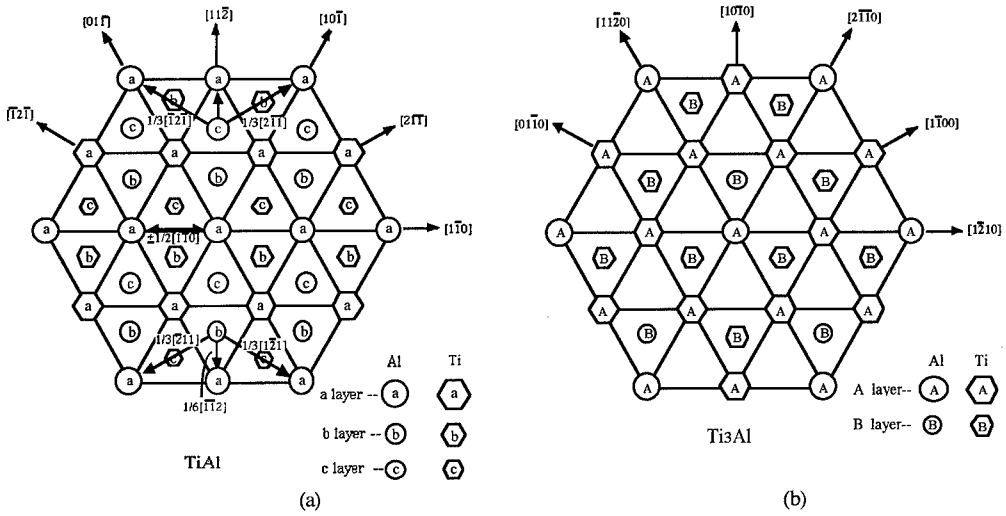

Fig. 1 Atomic arrangements on; (a) the (111)γ plane, (b) the (0002)α_2 plane.

3. EXPERIMENTAL PROCEDURE

For simplicity the investigations were performed on samples of an alloy with a nominal composition Ti-44Al-4Zr-4Ta-0.2Si in which the misfit between the γ and α_2 phases is <0.1%, i.e. much smaller than for binary alloys. The alloy was annealed at 1350°C and furnace-cooled to give the lamellar microstructure. TEM specimens were prepared by electropolishing to perforation in a solution of 6% perchloric acid, 34% butan-1-ol, and 60% methanol followed by Ar^+ ion milling to remove any oxidised / contaminated surfaces. HREM was performed in a JEOL 200CX operating at 200 kV.

4. RESULTS AND ANALYSIS

Several γ / α_2 interfaces were observed by HREM in this alloy. No isolated misfit dislocations with Burgers vectors 1/2<110> were observed in any of these interfaces but a wide variety of different steps were found. These were mainly two, four and six atomic layers in height. In the following sections we consider firstly the Burgers vectors which would be expected for such steps on the basis of the topological theory and then compare these with the experimental observations.

4.1 Admissible interfacial defects

If the steps on the interfaces separate crystallographically equivalent interfaces then the Burgers vectors associated with them are given by Pond's topological theory of interfacial defects [7]. For the simplest case of Class 1 interfacial dislocations in an interface between two grains related by the transformation **P**, the Burgers vectors, **b**, are given by combinations of translation vectors $\mathbf{t}_\lambda$ and $\mathbf{t}_\mu$, one from each of the adjacent crystals thus:

$$\mathbf{b} = \mathbf{t}_\lambda - \mathbf{P}\,\mathbf{t}_\mu$$

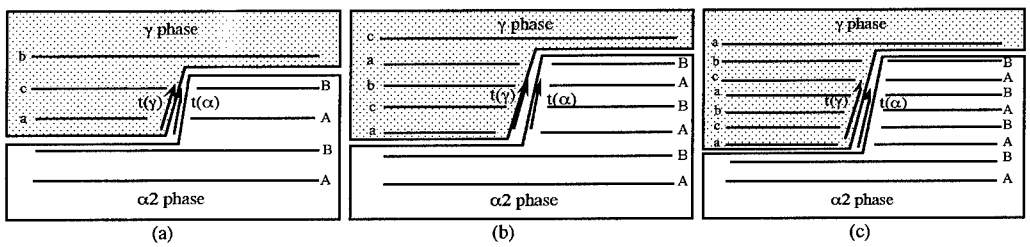

Fig. 2 Rigid body diagrams showing the character of two-, four- and six-layer up steps

Schematic diagrams of two-, four- and six-layer high steps are shown in Fig. 2. The convention adopted here is that the upper crystal is γ, the stacking of (111)γ is ...*abcabc*..., that of (0002)α_2 is ...*ABABAB*... and the sense of the step is taken from left to right (i.e. all three steps in Fig. 2 are "up" steps). If we further take the origin as being on the left of the diagram where the interface is formed by the overlay of *a* and *B* planes then for a two-layer up step (Fig. 2(a)), we would expect the overlay of *b* and *B* planes on the right of the step. Thus for an equivalent interface to be formed the Burgers vector for the step must give a shift of the *b* layer to *a* positions. If (111)γ//(0001)α_2 in the interface then from Fig. 1(a) it is clear that there are only three possibilities which have modest magnitudes; 1/6[$\bar{1}\bar{1}$2], 1/3[1$\bar{2}$1] and 1/3[$\bar{2}$11]. Similarly the Burgers vectors for two-layer down steps must give a shift from *c* to *a* positions and thus they can only take the values 1/6[11$\bar{2}$], 1/3[$\bar{1}$2$\bar{1}$], and 1/3[2$\bar{1}\bar{1}$], i.e. the opposite of those for the up steps. Applying the same approach to four-layer steps, from Fig. 2(b) we can see that the Burgers vectors of up steps should give a shift of the *c* layer to *a* positions, i.e. they can adopt the same values as for two-layer down steps. Similarly, we would expect that four-layer down steps can adopt the same values as for two-layer up steps. For six-layer high steps, however, *a* and *B* layers would be matched on either side of the step (Fig. 2(c)) and the Burgers vector can be either zero or a translation vector ±1/2[1$\bar{1}$0].

4.2 Analysis of [10$\bar{1}$] HREM images from steps

To identify the Burgers vectors of the interfacial steps, HREM images were obtained with the beam direction, **B**, parallel to [10$\bar{1}$] in the γ phase because the different possible Burgers vectors for the interfacial steps which were identified from the topological theory would each have different projected components along this axis. Analysis of several such HREM images from two-layer steps in the γ-α_2 interfaces revealed that they exhibited preferred Burgers vectors: representative examples are shown in Fig. 3. All of the up steps (e.g. Fig. 3(a)) had an in-plane Burgers vector component **b'** = 1/6[$\bar{1}$2$\bar{1}$], and by performing the circuit mapping to recover the out of plane components [8] it was found that **b** = 1/3[$\bar{2}$11]. For the down steps, however, (e.g. Fig. 3(b)) **b'** = 1/12[$\bar{1}$2$\bar{1}$] and **b** = 1/6[11$\bar{2}$]. The [10$\bar{1}$] HREM images from four-layer steps (e.g. Fig. 4) also revealed preferred Burgers vectors. For up steps, such as in Fig. 4(a), **b'** = 1/12[$\bar{1}$2$\bar{1}$] and **b** = 1/6[11$\bar{2}$], which is the same Burgers vector as that observed for two-layer down steps. Similarly, for four-layer down steps (e.g. Fig. 4(b)), **b'** = 1/6[$\bar{1}$2$\bar{1}$] and **b** = 1/3[$\bar{2}$11] as for two-layer up steps. Very few six-layer steps were observed so it is difficult to draw any conclusions about the distribution of Burgers vectors. One example is shown in Fig. 5 for which **b'** = 1/4[$\bar{1}$2$\bar{1}$] and **b** = 1/2[$\bar{1}$10].

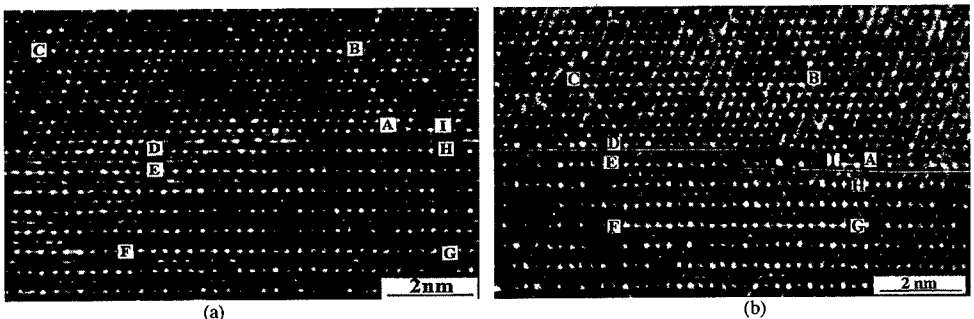

(a) (b)

Fig. 3 [10$\bar{1}$] HREM images of two-layer steps.

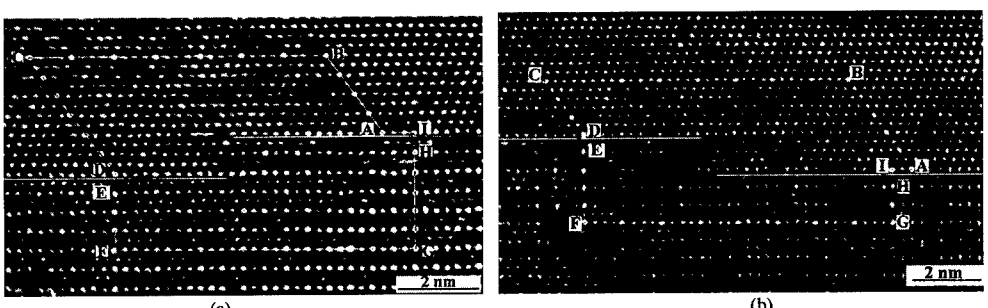

(a) (b)

Fig. 4 [10$\bar{1}$] HREM images of four-layer steps.

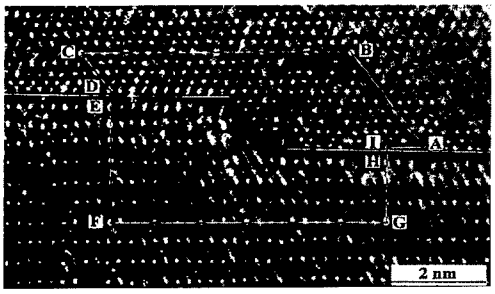

Fig. 5 [10$\bar{1}$] HREM image of a six-layer step.

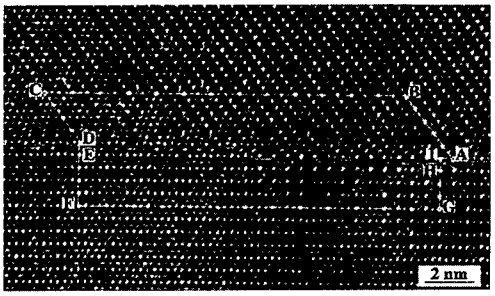

Fig. 6 [$\bar{1}$10] HREM image of a two-layer step.

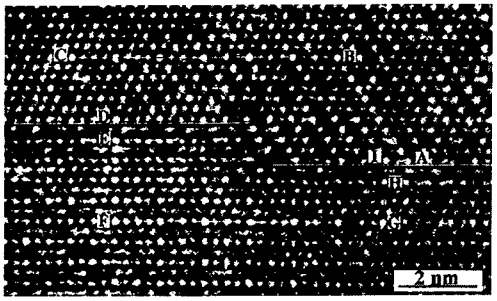

Fig. 7 [$\bar{1}$10] HREM image of a four-layer step.

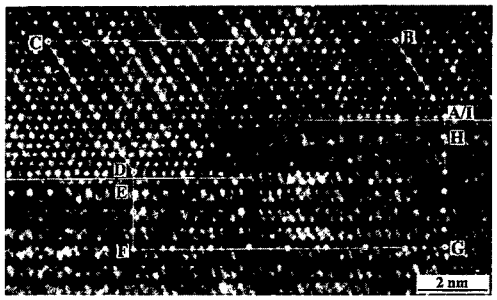

Fig. 8 [$\bar{1}$10] HREM image of a six-layer step.

4.3 Comparison with [$\bar{1}$10] HREM images from steps

There is clearly a discrepancy between the Burgers vectors observed here and those which have been reported previously. The most likely reason for this is that most investigators have obtained HREM images with **B**//[$\bar{1}$10] because the ordering in the γ phase is revealed along this axis. Unfortunately, the different Burgers vectors for a particular step type all have the same projected component along this axis. Thus the Burgers vectors values 1/6[11$\bar{2}$], 1/3[$\bar{1}$2$\bar{1}$], and 1/3[2$\bar{1}\bar{1}$], which can be adopted by two-layer down steps (e.g. Fig. 6) and four-layer up steps all have **b'** = 1/6[11$\bar{2}$]. Similarly, the Burgers vectors which can be adopted by two-layer up steps and four-layer down steps (e.g. Fig. 7) all have **b'** = 1/6[$\bar{1}\bar{1}$2], and for six-layer steps all modest Burgers vectors have **b'** = 0 (e.g. Fig. 8).

5. SUMMARY

HREM images have been obtained with **B**//[10$\bar{1}$] from steps on lamellar γ-α_2 interfaces in a TiAl-based alloy where the misfit between the phases is very low. The range of step heights and Burgers vectors is much more diverse than has been suggested previously and the observations are not consistent with the Shockley partial dislocation description which is often used for the interfacial steps. The Burgers vectors are, instead, consistent with values from the topological theory of interfacial defects for perfect Class 1 interfacial dislocations and certain values seem to be preferred for particular step types, presumably because of the core structures. These differences would not be apparent from HREM images obtained with **B**//[$\bar{1}$10] because of projection effects.

Acknowledgements We are grateful to Prof. R.C. Pond for helpful discussions, Profs. I.R. Harris and M.H. Loretto for provision of the laboratory facilities, and EPSRC for financial support.

REFERENCES

[1] H.A. Lipsitt, D. Shechtman and R.E. Schafrik, Met. Trans. A, **6** (1975), p.1991.
[2] S.A. Court, J.P.A. Lîfvander, M.H. Loretto and H.L. Fraser, Phil. Mag. A, **61** (1990), p.109.
[3] M.J. Blackburn, The Science, Technology and Applications of Titanium, edited by R. Jaffee and N.E. Promisel, 1970, Oxford, Pergamon Press.
[4] L. Zhao and K. Tangri, Phil. Mag. A, **64** (1991), p.361.
[5] G.J. Mahon and J.M. Howe, Met. Trans. A, **21** (1990), p.1655.
[6] S.R. Singh and J.M. Howe, Phil. Mag. A, **66** (1992), p.739.
[7] R.C. Pond, Dislocations In Solids, 1989, Ed. F.R.N. Nabarro, (North Holland), **8**, Ch. 38
[8] R.C. Pond, Interface Science, **2** (1995), p.299.

Materials Science Forum Vols. 294-296 (1999) pp. 243-246

The Atomic Structure of Tilt Grain Boundaries in AlN/GaN Layers Grown on (0001) Sapphire: A Case Study, the Σ31 ($11\bar{4}\bar{7}0$) Symmetric Grain Boundary

V. Potin, A. Béré, P. Ruterana and G. Nouet

Laboratoire d'Etudes et de Recherches sur les Matériaux, UPRESA CNRS 6004,
Institut des Sciences de la Matière et du Rayonnement, 6 Boulevard du Maréchal Juin,
F-14050 CAEN Cedex, France

Keywords: Tilt Grain Boundary, GaN, AlN, Sapphire, High Resolution Electron Microscopy, Dislocation Core

Abstract

In this work, an analysis of the coincidence rotation around the [0001] axis has been carried out for several Σs (Σ=91, Σ=73, Σ=43, Σ=31, Σ=67 and Σ=13). The atomic structures of the symmetric grain boundary planes have been constructed for GaN and AlN. The structural units are based on three atomic configurations of the **a** dislocation. A detailed experimental analysis was carried out on the Σ=31 boundary found in an AlN buffer layer and it is showed that two structural units are sufficent for the atomic configuration of the boundary.

Introduction

Due to their large band gap, the III-V nitrides have been under important research effort for the last few years as the most promising wide band gap semiconductors for optoelectronic devices applications. This was confirmed by the fabrication and marketing of high brightness blue/green light emitting diodes [1] and the rapid development of high efficiency blue laser diodes [2]. One of the most surprising feature of these devices is the very high density of defects in the active layers (10^{10} cm^{-2}); that is in contrast with other semiconductors like gallium arsenide for which the worst used material contains 10^4 cm^{-2} defects [3]. A non-exhaustive review of these defects (threading dislocations, stacking faults, inversion domains boundaries and nanopipes) has been recently published [4]. The majority of the threading dislocations were reported to have pure edge character, with Burgers vectors of 1/3 $\langle 11\bar{2}0 \rangle$ even if **c** pure screw and **a** + **c** ones are present as well [5]. The origin of the **a** dislocations was shown to be the mosaic growth mode which leads to epitaxial layers made of individual islands slightly rotated around the c-axis, whereas the **c** and **a** + **c** dislocations may be due to small tilts of the c-axis [5,6]. The rotation angles between islands have been measured to be less than 1° [5] in optimised layers, but also 3° [7] or 8° [8], and even as high as 20° by other workers [9, 10]. According to the values of the rotation angle, these boundaries can be classified as low-angle and high-angle grain boundaries. Some of these high angle grain boundaries correspond to special misorientations which can be described in terms of coincidence site lattice [11]. In this work, a systematic analysis of the coincidence rotation around the c-axis has been carried out for rotation angles less than 30°. The geometrical models of the corresponding boundaries have been constructed, on the base of the structural units of the dislocation cores. A detailed investigation was made for a Σ31 boundary, using high resolution electron microscopy and image simulation.

Experiment

The GaN layers were grown on the (0001) sapphire substrate by electron cyclotron RF source assisted molecular beam epitaxy at a rate of 40 nm h^{-1} at 800°C. Depositions started by an AlN buffer layer at the same temperature with 30 nm thickness.

The TEM specimens were mechanically polished down to 100 μm and next dimpled down to 10 μm. Electron transparency was obtained by ion milling with a LN2 cold stage at 5 KeV. HREM observations were carried out along the [0001] zone axis on a Topcon 002B microscope operating at 200 KeV with a point to point resolution of 0.18 nm. Models of the 1/3 $\langle 11\bar{2}0 \rangle$ dislocations were generated by applying the displacement field using anisotropic elasticity [12] on supercells which exhibit periodicity along the c-axis. Simulations of the experimental images used the EMS software [13].

Dislocation core models

The geometrical models for the grain boundaries are based on the structural units observed for the core dislocations of the pure edge ones. In order to construct the possible atomic configurations of these isolated dislocations, we have used 1/3 <11-20> Burgers vectors in anisotropic elasticity calculations. As the calculations present a singular point in the core of a dislocation, each generated configuration was reconstructed at hand, the distances between nearest neighbour atoms inside the core were chosen close to the usual ones in AlN/GaN. Thus, three possible configurations were obtained for the core : 4, 8 and 5/7 atom rings as shown on Fig. 1a , 1b and 1c. The 4 atom rings is characterized by four bonds practically in the same plane, the 5/7 atom rings exhibit N-N and Ga-Ga bonds inside its core. The 8 atom rings present one dangling bond inside its core, whereas the two other configurations do not.

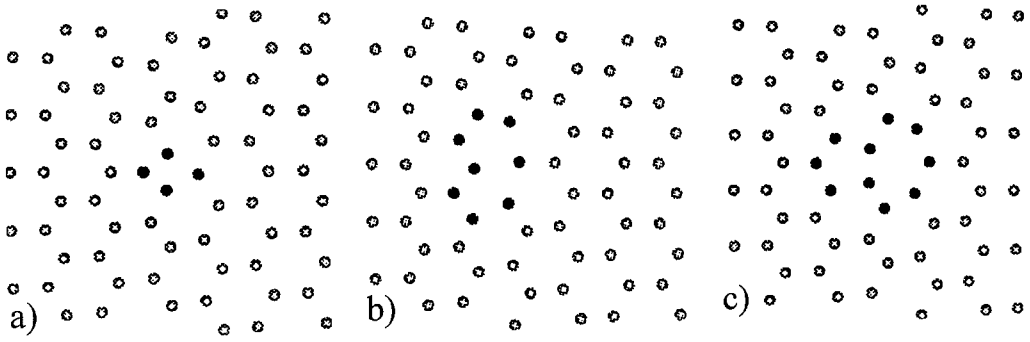

Fig.1 Three atomic configurations of the **a** dislocation, a) 4/6, b) 8/6, c) 5/7, as generated by anisotropic calculations.

The 8 and 5/7 core configurations are similar to the geometrical models already discussed by Hornstra for the Lomer dislocation in the diamond lattice [14]. Their observations have been carried out in diamond materials like Si, Ge [15] as well as at the GaAs/Si interface [16] or ZnO [17] leading in all the cases to the 5/7 atomic configuration. In gallium nitride, the first observations have recently been done. The atomic structure of the **a** threading dislocations was found to correspond to 5/7 and 8 atom rings core in rather equal frequency [18] whereas other workers have only observed the 8 one [19]. Until now, the 4 atom rings core observations has not yet been reported.

Grain boundaries atomic structure

Most of the time, high resolution electron microscopy and electron diffraction experiments confirm that the usual epitaxial orientation relationship is observed between the AlN, GaN grown layers and the sapphire substrate : $(0001)_{sap}$ // $(0001)_{AlN,GaN}$ and $[11\text{-}20]_{sap}$ // $[10\text{-}10]_{AlN,GaN}$. However, small rotated grains around the c-axis can be present [10]. It appears that the values of the rotation angle are very close to those of Σ boundaries in the coincidence site lattice (CSL) notation. For the

hexagonal lattice, the values of Σ and those corresponding to the rotation angle around [0001] have been calculated by Warrington [20]. In this work, we have studied the configurations of rotation angle less than 30°, leading to symmetrical boundaries along the diagonal of the CSL unit cell. Thus, six different boundaries were generated as deduced from dichromatic complexes by superimposing two rotated GaN crystals in the {0001} projection plane. A CSL unit cell was then defined and the grain boundary was chosen as the diagonal. The atomic model of the grain boundary was constructed by eliminating the atoms of one crystal on one side and the atoms of the other crystal on the other side. Afterwards, we managed to keep the tetracoordination of the atoms and the distances between nearest neighbours close to those of GaN. The results are shown in table 1 for the six different Σs and an example for Σ = 13 is presented in Fig. 2. The first four geometrical configurations with the smallest rotation angles contain two 5/7 atom rings and one 4 one, the other atom rings are more or less deformed but are the six atom rings of the bulk. The indices 1 and 2 characterizing the 6 atom rings in table 1 indicate the localization of the units at the boundary : a 6_1 unit is crossed by the boundary plane whereas it passes symmetrically between two 6_2 units. The Σ = 67 boundary is characterized by the presence of four 5/7 atom rings and two 4 ones whereas the Σ = 13 boundary plane contains one example of each core configuration (4, 8 and 5/7).

Σ	rotation angle	period along the boundary plane
91	10.42	6_2 5 7 6_2 6_1 6_2 6_1 6_2 5 7 6_2 6_1 6_2 6_1 6_2 4 6_1 6_2 6_1
73	11.64	6_2 5 7 6_2 6_1 6_2 5 7 6_2 6_1 6_2 6_1 6_2 4 6_1 6_2 6_1
43	15.18	5 7 6_2 6_1 6_2 5 7 6_2 6_1 6_2 4 6_1 6_2
31	17.90	5 7 6_2 5 7 6_2 6_1 6_2 4 6_1 6_2
67	24.43	6_2 4 5 7 6_2 5 7 6_2 5 7 6_2 5 7 6_2 4 6_1
13	27.80	4 6_1 8 6_2 5 7 6_2

Table1 : geometrical models of one period along the symmetrical boundary plane according to the rotation angle and the corresponding Σ values.

The Σ = 31 boundary

The AlN buffer layer often contains grains rotated around the c-axis. In this case, the rotation between the grain and the surrounding matrix was equal to 19°, close to the coincidence orientation Σ = 31 (θ = 17.9°). This grain was facetted and one facet was investigated in detail [11]. A comparison between image simulations and experimental ones was carried out for different atomic configurations of the grain boundary. A reasonable agreement was obtained for a period along the symmetric interface plane made of structural units : 5 7 6_2 5 7 6_2 6_1 8 6_2 6_1 6_2 (Fig. 3). This is different from the geometrical one by the replacement of one 6_2 4 atom rings by an 8 6_2 one.

Therefore, the main criterion for the generation of the geometrical models which was the lenght of the GaN/ AlN bonds seems to be inadequate. In fact, even if the three atomic configurations for the **a** dislocations are rather different, we can easily generate one from the others. In this case, the 6_2 4 core can give rise to the 8 6_2 core by deleting one atom and replacing the two neighbours by only one atom, the boundary remaining symmetric in this transformation. The transition of one configuration to the other one is determined by the distances between the atoms of the boundary plane. In some cases, the choice between the two configurations can be difficult. Moreover, for isolated dislocations, only the 5/7 and the 8 cores have been observed whereas the observation of the 4 core has not yet been reported. Other experimental grain boundaries have been observed in GaN layers and are now under investigation.

Conclusion

The AlN and GaN layers layers contain grain boundaries which are rotated around [0001]. The values of the rotation angle can be close to those of Σ boundaries in the CSL formalism. The atomic structures of these boundaries have been generated, based on the models proposed for the **a**

dislocation cores. The analysis of a Σ=31 boundary indicates that the 5/7 and 8 atom rings seem to be favoured over the 4 one as it was previously reported for isolated dislocations.

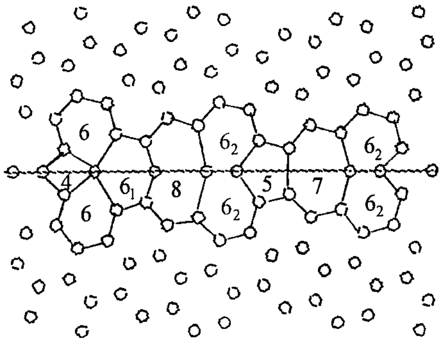

Fig. 2 : Geometrical atomic structure of the diagonal plane for the Σ=13 boundary

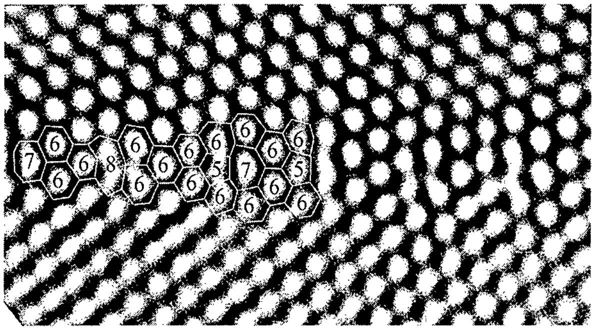

Fig. 3 : High resolution micrograph of the Σ=31 grain boundary in AlN taken along [0001]

References

[1] S. Nakamura, T. Mukai and M. Senoh, Appl. Phys. Lett. **64** (1994) 1687.
[2] S. Nakamura, M. Senoh, S. Nagahama, N. Iwasa, T. Yamaha, T. Matsushita, K. Kiyoku and Y. Sugimoto, Jpn. J. Appl. Phys. **66** (1996) L74.
[3] J. Herzog, J. Appl. Phys. **43** (1972) 600.
[4] V. Potin, P. Vermaut, P. Ruterana and G. Nouet, J. Elec. Mat. **27** (1998) 266.
[5] X.J. Ning, F.R. Chien, P. Pirouz, J.W. Yang and M.A. Khan, J. Mater. Res. **3** (1996) 580.
[6] F.A. Ponce, MRS Bulletin **22** (1997) 51.
[7] W. Qian, M. Skowronski, M. De Graef, K. Doverspike, L.B. Rowland and D.K. Gaskill, Appl. Phys. Lett. **66** (1995) 1252.
[8] P. Vennegues, B. Beaumont and P. Gibart, J. Mater. Sci. Eng. B **43** (1997) 473.
[9] H. Selke, S. Einfeldt, U. Birkle, D. Hommel and P.L. Ryder, Proceeding of the X^{th} Microscopy of Semiconducting Materials, Oxford (1997)
[10] V. Potin, P. Ruterana, A. Hairie and G. Nouet, Mat. Res. Sym. Proc. **482** (1998) 435.
[11] V. Potin, P. Ruterana and G. Nouet,. Mater. Sci. Eng. B **50** (1997) 29.
[12] R. Bonnet, Acta. Met. **29** (1981) 437.
[13] P. Stadelmann, Ultramicroscopy **21** (1987) 131.
[14] J. Hornstra, J. Phys. Chem. Solids **5** (1957) 129.
[15] J. Thibault, J.L. Rouviere and A. Bourret, Mat. Sci. and Tech. **4** (1991) 321.
[16] A. Vila, A. Cornet, J.R. Morante, P. Ruterana, M. Loubradou, R. Bonnet, Y. Gonzalez and L. Gonzalez, Phil Mag A **71** (1995) 85.
[17] A.N. Kiselev, F. Sarrazit, E. A Stepantsov, E. Olsson, T. Claeson, V.I. Bondarenko, R.C. Pond and N.A. Kiselev, Phil. Mag A **76** (1997) 633.
[18] P. Ruterana, V. Potin and G. Nouet, Mat. Res. Symp. Proc. **482** (1998) 459.
[19] Y. Xin, S.J. Pennycook, N. D. Browning, P. D. Nellist, S. Sivananthan, F. Omnes, B. Beaumont, J.P. Faurie and P. Gibart, Appl. Phys. Lett. **21** (1998) 2680
[20] D. H. Warrington, J. de Phys. **36** (suppl. to No 10) (1975) C4-87.

Corresponding author : V. Potin (email : potin@lermat.ismra.fr)

Materials Science Forum Vols. 294-296 (1999) pp. 247-250

Grain Boundary Structure in $BaTiO_3$ with a Small Excess of Ti-site Dopant

T. Yamamoto, Y. Ikuhara, K. Hayashi and T. Sakuma

Department of Materials Science, School of Engineering, The University of Tokyo,
7-3-1 Hongo Bunkyo-ku, Tokyo 113-8656, Japan

Keywords: Chemical Bonding State, EELS, HREM, Nonstoichiometry

ABSTRACT Grain boundary structure was examined with HRTEM and EELS for $BaTiO_3$ doped with a small amount of cations with a special interest in chemical bonding state. It was found that the grain boundary structure was sensitive to a small excess of Ti-site dopant. The grain boundaries are facetted with {210} habits and an ordered structure is formed. HRETM and EELS examination combined with molecular orbital calculation clearly revealed that TiO_6 octahedral linkage changes from corner-sharing in the grain interior to edge-sharing at the grain boundary.

INTRODUCTION

Electroceramic components based on $BaTiO_3$ often use grain boundary phenomena, for example, thermistors, boundary layer capacitors and so on [1, 2]. The electrical properties at grain boundaries largely depend on the type and the amount of dopant cations. Meanwhile, not only electrical properties but also microstructure in $BaTiO_3$ is sensitive to such dopant effects. Yamamoto and Sakuma revealed that the grain growth behavior of $BaTiO_3$ is closely related to small cation nonstoichiometry at a level of 0.001 [3]. Hayashi et al. succeeded to fabricate a coarse-grained sinter with a grain size of more than 1mm by annealing $BaTiO_3$, the cation nonstoichiometry of which was carefully controlled to be slightly Ti-excess by 0.05mol% [4]. To understand the grain boundary-related phenomena, the grain boundary analysis from the viewpoint of small dopant effect must be very effective. In this study, grain boundaries in $BaTiO_3$ doped with several types of cations were examined by high resolution transmission electron microscopy (HRTEM) and electron energy-loss spectroscopy (EELS).

EXPERIMENTAL PROCEDURE

Commercial high purity $BaTiO_3$ powders (Sakaikagaku Co. Ltd., BT01, Lot. No. 000001) were used for the raw material. The nominal purity, grain size and Ba/Ti ratio of the powders are 99.98%, 0.1μm and 1.000, respectively. Ba^{2+}, Ca^{2+} or Y^{3+} ions, and Ti^{4+}, Zr^{4+} or Nb^{5+} ions were used for the A-site or B-site dopant cations in a perovskite structure ABO_3, respectively. The amount of each dopant was fixed to be 0.1mol%. Details of sample preparation are described in Ref. [3]. Hereafter, each compound will be named after the respective cation, for example, Ba-doped compound, Ti-doped one, and so on. Specimens for HRTEM and EELS analysis were prepared with conventional methods using ion-thinning technique. HRTEM observation was made with 200kV type HRTEM (TOPCON, EM-002B) and EELS analysis was carried out with PEELS detector (GATAN model 666) equipped to a HRTEM (TOPCON, EM-002BF) with a field-emission type

gun operated at 200kV. A probe size of about 1nm was used for the EELS analysis.

RESULTS AND DISCUSSION

Microstructures in $BaTiO_3$ compounds were found out to be separated into two groups from the view point of the A/B ratio. The A-site excess compounds exhibit a uniform grain structure with a grain size of about 10μm, and the B-site excess show a bimodal grain structure consisting of abnormally coarse grains of about 100μm and fine grains of about 2μm, respectively.

Fig. 1 shows a bright field TEM image of a Ti-doped compound, which is one of the B-site excess compounds, in the as-sintered state. As seen in the figure, the grain boundary is clearly facetted. From TEM-trace analysis, the habit planes can be indexed as (210) and (120) with respect to the grain B, and (13, 4, 2) and (12, 13, 10) with respect to the grain A. Most of the facets examined in this study are found to have {210} type habit planes from one side of grain and high index planes from the other.

Fig. 2 is a HRTEM image of a facetted grain boundary. In the figure, the grain with (210) habit plane is oriented in the [001] beam direction, while the adjacent grain is slightly inclined from the [110] direction. The habit is parallel to (210) on an atomic scale. The important feature to note is that white dots appear periodically along the grain boundary as shown by the arrows. This suggests the existence of an ordered structure along the grain boundary.

A comparison of the oxygen K-edge ELNES taken from the grain interior and the facetted grain boundary in the Ti-doped compound is shown in Fig. 3. In the figure, the theoretical spectra for $BaTiO_3$ and rutile TiO_2 are also shown. The theoretical spectra are calculated with the molecular orbital method (DV-Xα method) using a $(Ba_8Ti_7O_{36})^{28-}$ cluster for $BaTiO_3$ and a $(TiO_6)^{8-}$ one for TiO_2 with rutile structure, respectively [5]. The partial density of states (PDOS) of O-2p is shown as the oxygen K-edge ELNES. In the experimental ELNES, the spectrum from the grain interior clearly shows separated peaks as shown in (a) while that from the facetted grain boundary shows a plateau as indicated by the arrow in (b) in the energy-loss range from 520 to 540eV. The plateau-like spectrum in (b) may be caused by an increase of the intensity between the two peaks in (a) as indicated by the arrow. This is a common feature of the spectrum obtained from facetted grain boundaries. This fact indicates that the chemical bonding state differs between

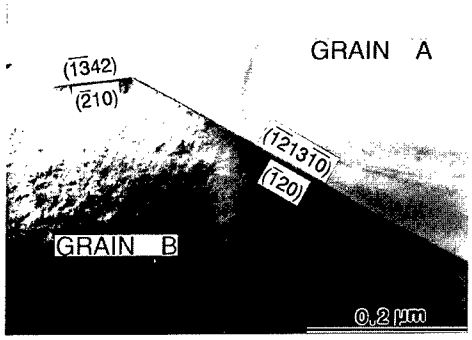

Fig. 1 TEM bright field image of a facetted grain boundary in a Ti-doped compound. Indices are obtained from TEM-trace analysis.

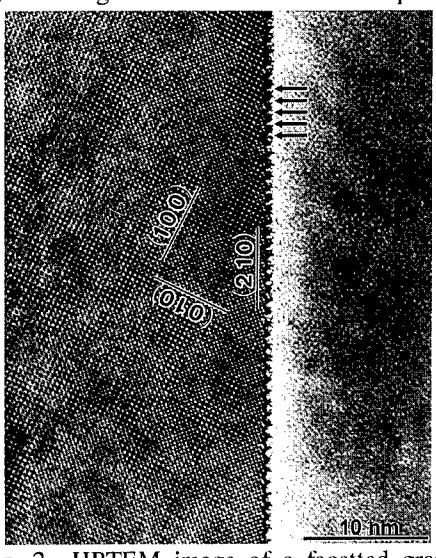

Fig. 2 HRTEM image of a facetted grain boundary in a Ti-doped compounds. Note that an array of white dots exists along the grain boundary as indicated by the arrows.

grain interiors and grain boundaries in the Ti-doped compound.

In the theoretical ELNES, three peaks (1, 2, and 3) appear in $BaTiO_3$, and two peaks (4 and 5) exist in TiO_2 in this energy-loss range. The peak 2 in $BaTiO_3$ has a shoulder in the low energy-loss range. Tanaka et al. insisted that the height ratio of the peaks 1 and 2 or 4 and 5 strongly depends on the bonding angle of Ti-O-Ti [6]. The bonding angle is different between perovskite and rutile structures because the perovskite structure has corner-shared TiO_6 octahedra while rutile has edge-shared TiO_6 octahedra. Therefore, the bonding angle of Ti-O-Ti is 180° in the perovskite structure and about 100° in rutile. As a result, the intensity of the peak 1 is higher than that of the peak 2 in the perovskite structure (Fig. 3(c)) while the peak 4 is lower than the peak 5 in rutile (Fig. 3(d)). The Ti-doped compound exhibits the plateau-like peak at the grain boundary. This can be interpreted in terms of the overlapping of the two profiles of $BaTiO_3$ (Fig. 3(c)) and TiO_2 (Fig. 3(d)), which is caused by the existence of a chemical bonding state similar to that of the rutile structure. Namely, the TiO_6 octahedral linkage changes from corner-sharing in the grain interior to edge-sharing at the grain boundary in the Ti-doped compound.

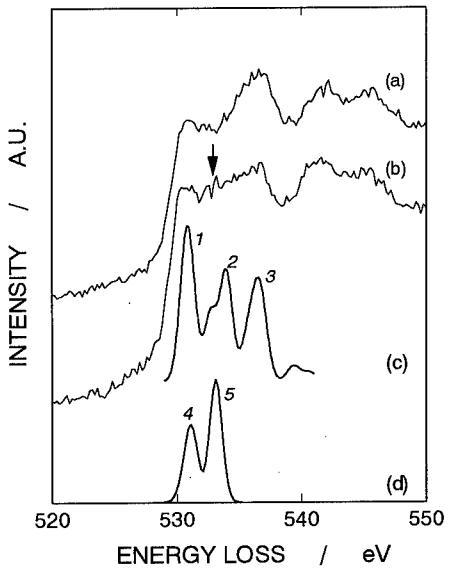

Fig. 3 Experimental oxygen K-edge ELNES of (a) grain interior and (b) grain boundary in the Ti-doped compound, and theoretical ELNES derived from molecular orbital calculation for (c) $BaTiO_3$ and (d) rutile TiO_2. Note that the spectrum of the grain boundary has a plateau-like shape as indicated by the arrow in (a).

Fig. 4 shows the structure model for the facetted grain boundary and the HRTEM image of the facetted grain boundary with an inserted simulated image calculated from the structure model. In the perovskite structure, two kinds of {210} planes exist, i.e., the plane consisting of Ba and O

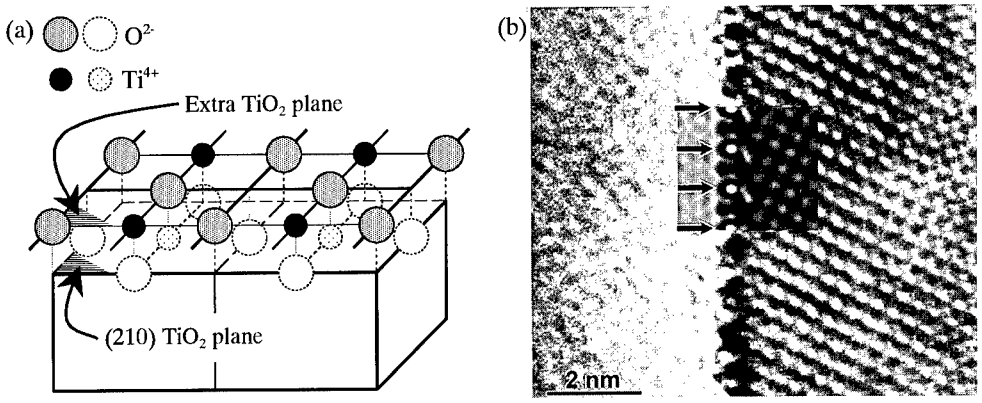

Fig. 4 A structure model for the facetted grain boundary (a) and HRTEM image of the Ti-doped compound with a simulated image inserted (b). Note that the array of white dots is well simulated by the structure model.

ions (BaO plane) and that consisting of Ti and O ions (TiO_2 plane). The structure model shown in the figure can be obtained by adding an extra TiO_2 plane to the {210} TiO_2 plane. In this model, the linkage of TiO_6 octahedra is edge-sharing type like that of the rutile TiO_2 structure, which is consistent with the result of the EELS analysis. As can be seen in the simulated image, the structure model well-expresses the observed HRTEM image.

Fig. 5 is the oxygen K-edge ELNES obtained from grain boundaries of the other A-site and B-site excess compounds. The spectra of the B-site excess compounds are plateau-like as indicated by the arrow, while the A-site excess ones are clearly splitted into two peaks. The plateau-like peaks in the B-site-excess compounds are similar to that in the Ti-doped compound as in Fig. 3(b). Thus, the grain boundary structure in $BaTiO_3$ compounds can be well interpreted in terms of the A/B-site ratio.

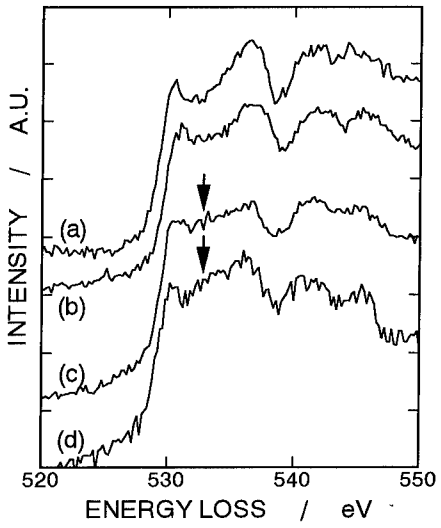

Fig. 5 Oxygen K-edge ELNES of grain boundaries in (a) Zr-doped, (b) Nb-doped, (c) Ca-doped and (d) Y-doped compounds.

It is well known that the B-site excess $BaTiO_3$ exhibits abnormal grain growth. Rios et al. reported that the abnormal grain growth is caused by the initial suppression of normal grain growth from a kinetic point of view [7]. The initial suppression of the grain growth in the B-site excess compounds may be explained in terms of the presence of edge-shared TiO_6 octahedra in grain boundaries.

CONCLUSIONS

Grain boundaries in the B-site excess $BaTiO_3$ are found to be facetted with {210} habit plane. B-site excess $BaTiO_3$ exhibits different oxygen K-edge ELNES spectra at grain boundaries and in grain interiors. The spectra from grain boundaries in the B-site excess compounds are characterized by a plateau-like form, while that from grain interiors are splitted into two peaks. On comparing between the experimental ELNES and molecular orbital calculations, it is revealed that the plateau-like spectra of the B-site excess compounds is caused by the formation of edge-shared TiO_6 octahedra at grain boundaries. The structure model for the facetted grain boundary constructed from this assumption is consistent with the HRTEM image of grain boundaries with a {210} habit plane.

REFFERENCES

[1] B. Huybrechts, K. Ishizaki and M. Tanaka, J. Mater. Sci. 30 (1995), p.2463.
[2] M. Kuwabara, K. Morimo and T. Matsunaga, J. Am. Ceram. Soc. 79 (1996), p.997.
[3] T. Yamamoto and T. Sakuma, Eur. J. Solid State Inorg. Chem. 32 (1995), p.731.
[4] K. Hayashi, T. Yamamoto and T. Sakuma, J. Am. Ceram. Soc. 79 (1996), p.1669.
[5] H. Adachi and K. Taniguchi, J. Phys. Soc. Jpn. 49 (1980), p.1944.
[6] I. Tanaka, T. Nakajima, J. Kawai, H. Adachi, H. Gu and M. Ruhle, Phil. Mag. Lett. 75 (1997), p.21.
[7] P. R. Rios, T. Yamamoto, T. Kondo and T. Sakuma, Acta Mater. 46 (1998), p.1617.

Materials Science Forum Vols. 294-296 (1999) pp. 251-254

Microstructural Investigations of Interfaces in PVD TiN Coated Tool Steels

N.J.M. Carvalho[1], A.J. Huis in't Veld[2] and J.Th.M. De Hosson[1]

[1] Department of Applied Physics, Materials Science Centre, University of Groningen, Nijenborgh 4, NL-9747 AG Groningen, The Netherlands

[2] Department of Surface Engineering, TNO Institute of Industrial Technology, De Wielen 6, P. O. Box 6235, NL-5600 HE Eindhoven, The Netherlands

Keywords: Physical Vapour Deposition, TiN Coatings, Monolayers, Interfacial Fatigue Stress

Abstract

The microstructure of PVD TiN coated tools steels composites has been investigated by scanning electron microscopy (SEM) and transmission electron microscopy (TEM). It was found that the microstructure of the coatings consists of a dense fibrous structure typical of a zone T structure. When the composite material is subjected to a rolling contact test the failure is mainly initiated at the interface with crack grow in the coating parallel to the surface. The interfacial failure stress is closely associated with the coating-substrate bonding conditions.

Introduction

Major developments have been made over the last decade in extending the service life of cutting and forming tools and mechanical components, by successfully applying thin hard films, such as titanium nitride (TiN) and titanium carbide (TiC), to improve the tribological or corrosion behaviour [1-5]. TiN produced either by physical vapour deposition (PVD) [6] or chemical vapour deposition (CVD) [7], has a high hardness and a gold–like appearance being widely used in the industrial applications ranging from machining tools, mechanical parts to decorative applications. If the advantages of such thin hard films are to be fully employed in improving the surface properties of engineering components, it is necessary to understand more thoroughly the detailed mechanisms by which surface properties are changed and enhanced. This understanding can be supplied either through modelling the response of coated systems or, experimentally, by determining the changes conferred on the system by the coating.

Since the performance of a coated material is dependent on good coating adhesion, the measurement of this interface property is of considerable practical importance. The coated substrates were submitted to a rolling contact test technique to obtain some clarification on the mechanism of interfacial failure [8]. This mechanism can be characterised by understanding the interrelation between surface roughness, surface hardness, contact stress and fatigue durability.

In this paper we present results of an investigation of TiN coating on tool steel substrate using X–ray diffraction (XRD), Auger electron spectroscopy (AES), scanning electron microscopy (SEM) and transmission electron microscopy (TEM).

Experimental details

PVD TiN coatings were deposited on hardened and tempered alloy steels (tool steel) with a hardness of 60 HRc by a Bai 640R unit, which has a specially developed deposition process based on the standard Balzers TiN process, using a triode ion plating (e-gun) with high plasma density. The detailed deposition process is described elsewhere [8]. Since it is evident that the state of the substrate surface before coating has a strong influence on the bonding strength of hard coatings [9], the substrate surface was polished or ground to investigate the influence of these two pre-treatments.

Tribological tests, namely rolling contact fatigue tests were performed with a modified pin-on-ring tester, to characterise the adhesion strength and the mechanism of failure of the coated system under

conditions of dynamic loading. The experimental procedures and the main results are described elsewhere [8].

The coatings were structurally characterised by X–ray diffraction (XRD), scanning electron microscopy (SEM) and transmission electron microscopy (TEM). For the XRD analyses, a Philips PW710 Based diffractometer with Cu Kα radiation was used. Coating morphology and microstructure were studied on plan-view and fractured cross-sections in SEM as well as, on plan-view and cross-sections in TEM. Sample preparation for plan-view TEM consisted of cutting out a disc with 3 mm diameter using the Nb-YaG laser followed by grinding and polishing from the substrate side to a thickness of 50 μm. The disc was further thinned to electron transparency by dual gun Ar^+ -ion milling. The specimen was kept on rotation while the Ar^+ beam at 5kV and with an ion current of 0.5 mA was directed towards the substrate side with an incident angle of 15° from the specimen surface. The final etching was performed from both sides of the sample with the tilt angle reduced to 10° in order to clean the coating surface, to reduce ion induces artefacts and to remove any amorphous redeposited surface layer. Specimens for cross-sectional TEM were prepared by gluing two samples film to film in a Ti grid. After mechanical grinding and polishing on both sides to a thickness of 50 μm, ion beam milling was performed by using the two guns in mirror-image positions on both sides of the specimen. In this case the angle of incidence is less than 6° (ion energy 5 kV and ion current 40 μA) and the sample is rotated. Finally, to obtain a sample with a large electron transparency area, the sample was rocked ($-30° < \omega < +30°$) with the incoming ion beam at 4° and perpendicular to the film/substrate interface until perforation took place and the hole reaches the region of interest. The TEM observations were carried out using a JEOL 4000 EX/II, operating at 400 kV.

Results and Discussion

From the XRD analysis it was found that the TiN films investigated have a predominantly cubic NaCl structure of the δ-TiN phase with a (111) preferred orientation. No differences due the two different substrates were observed.

Scanning electron micrographs of surface and fracture morphology of the TiN films on tool steel substrates are shown in Figure 1 and Figure 2. The TiN films deposited on polished pre-treated surface substrates have a much finer substructure (see Fig. 1 (*a*)) than films deposited on ground surfaces (see Fig. 1 (*b*)), which consists of large substructures with a very slight waviness. A relative smooth surface is obtained on both films giving it a shiny yellow appearance. The fractograph shows (see Fig. 2) a dense fibrous structure typical of a zone T structure according to the zone classification proposed by *Thornton* [10]. The coatings obtained were approximately 5 μm thick.

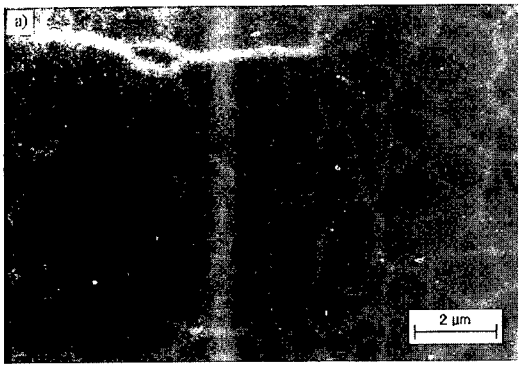

The microstructure of the coatings was investigated using transmission electron microscopy. Plan-view TEM micrographs from the top region of the coatings revealed a structures with dense grain boundaries (see Fig. 3), which are difficult to discern, and a high defect densities typically observed in ion-plating deposited TiN films [11]. The grain sizes were within the range of 50-70 and 100-150 nm for polished and ground surfaces, respectively. It should be pointed out that one fibre or column can consist of several grains or subgrains, therefore the grain size is smaller than the column width. Several observations may be made from the selected area electron diffraction

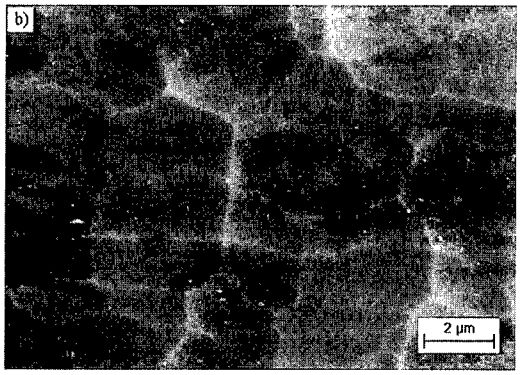

Figure 1. Surface morphology of TiN coatings prepared on (a) polished surface substrate, and on (b) ground surface substrate.

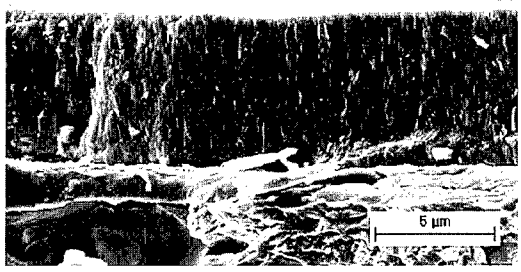

Figure 2. Fracture surface morphology of TiN coatings on tool steel substrates.

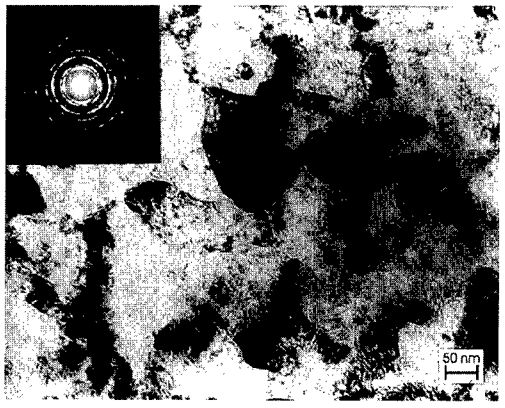

Figure 3. Plan view TEM bright field image and selected area diffraction pattern of TiN coatings.

(SAED) pattern insets in Figure 3. Firstly, the concentric rings are related to single-phase coatings with NaCl structure. Secondly, the diffuse and continuous rings indicate both a relatively finer grain size and poorer crystalline perfection, i.e. lattice distortion is retained. These features have been reported by *Quinto* [12] as a consequence of the PVD deposition process.

When the TiN coated systems were subjected to rolling contact tests the major failure mode was interfacial debonding. From the experimental results it is clear that under the present testing conditions, fatigue failure of the coating-substrate composites is initiated at the interface region, and the interfacial failure stress, σ_c, is closely associated with the coating-substrate bonding conditions.

Factors such as, smooth substrate surface and polishing before coating, which are known to substantially improve the coating-substrate bonding strength [13], also improve the interfacial failure stress. The σ_c of the polished surface is higher than that of the ground one. This implies that the shear strength in the interface region is increased when the mechanical bonding is improved, and the value of interfacial failure stress increases. These results are in agreement with the analysis by contact mechanics, which show that the shear stress range $\Delta\tau_{zx}$ at the interface is the appropriate parameter that should be used to characterise the interfacial failure stress and cyclic bonding strength of hard coatings [14].

In the SEM micrograph of Figure 4, can be visualised the proposed trend for crack initiation and propagation in the coating. The cracks are generally initiated at the interface and grow in the coating parallel to the surface. When subcracks are formed they grow, along the grain boundary between two grains, perpendicular to the interface until they reach the free surface. When adjacent cracks grow together a small piece of material is released, resulting in the so-called spalling failure. The TEM micrograph of Figure 5 shows the interface between the TiN coating and the tool steel substrate, and grain boundaries in the coating. The arrows indicate the location of cracks present in the system, being at the interface, in the coating close to the interface and in the grain boundary of two

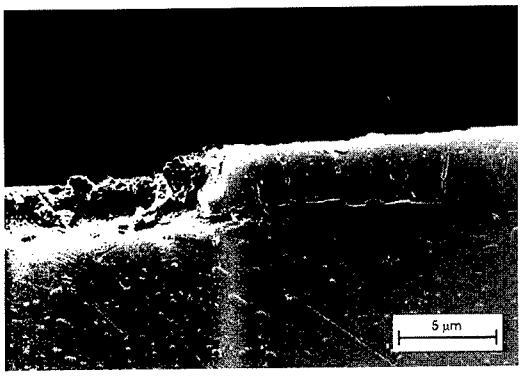

Figure 4. Cross sectional polished SEM micrograph of TiN coating-substrate composite, fractured due to rolling contact fatigue tests.

Figure 5. Cross sectional TEM micrograph of a TiN coating-substrate composite. The arrows show fractured zones due to rolling contact fatigue tests.

columns. In the coating, close to the interface there is a region concentrated with cracks and dislocations, which is believed to be the first stage of damage, created by the cyclic shear stress component of the contact stress. From HRTEM images of the interface and Auger measurements, it seems that there is some diffusion of titanium to the substrate when nucleation occurs in the deposition process and steady growth is quickly achieved, resulting in growth of well-defined columns from the substrate.

Conclusions

The present work shows that the morphology of PVD TiN coatings is dependent on surface finishing. The microstructure of the coatings consists of a dense fibrous structure typical of a zone T structure. The failure of the composite system is mainly initiated at the interface with crack grow in the coating parallel to the surface. When subcracks are formed they grow, along the grain boundary between two grains, perpendicular to the interface until they reach the free surface.

Acknowledgements

The work described in this paper has been founded by TNO Institute of Industrial Technology. The authors acknowledge Balzers Group for the deposition of PVD TiN coatings on tool steel rings.

References

[1] R. Buhl, H. K. Pulker, and E. Moll, Thin Solid Films 80 (1981), p. 265.
[2] R. L. Hatschek, Am. Mach. Special Report 752 (1983), p. 129.
[3] M. Wittmer, B. Studer, and H. Melchiar, Journal Applied Physics 52 (1981), p. 5722.
[4] B. Zega, M. Kornmann, and J. Amiguet, Thin Solid Films 54 (1977), p. 577.
[5] E. Valkonen, T.Karlsson, B. Karlsson, and B. O. Johansson, Proceedings of SPIE International Technical conference 401, (1983), p. 41.
[6] M. Bromark, M. Larsson, P. Hedenqvist, and S. Hogmark, Surface and Coatings Technology 90, (1997), p. 217.
[7] K. –H. Habig, Journal Vacuum Science Technology A4 (6), (1986), p. 2832.
[8] N. J. M. Carvalho, A. J. Huis in 't Veld, and J. Th. M. De Hosson, Surface and Coatings Technology 105 (1998), p. 109.
[9] H. Chen, M. –Z.Yi, K. –W. Xu, and J. –W. He, Surface and Coatings Technology 74-75 (1995), p. 253.
[10] J. A. Thornton, Annual Review Materials Science 7 (1977) p. 239.
[11] D. T. Quinto, J. Vac. Sci. Technol. A 6(3) (1988) p. 2149.
[12] D.T. Quinto, A. T. Santhanam, and P. C. Jindal, Materials Science and Engineering A105/106 (1988) p. 443.
[13] R. S. Gao. C. D. Bai, K. –W. Xu, and J. –W. He, The Royal Society of Chemistry 2 (1993) p. 285.
[14] J. –W. He, B. C. Hendrix, N. –S. Hu, Surface Engineering 12(1) (1996) p. 46.

Materials Science Forum Vols. 294-296 (1999) pp. 255-258

Modification of Metal/Oxide Interfaces by Dissolution of Sb in Oxide Precipitates Containing Metal Matrices

B.J. Kooi, A.R. Westers, J.A. Vreeling, D.T.L. van Agterveld and J.Th.M. De Hosson

Dept. of Applied Physics, Materials Science Centre, University of Groningen, Nijenborgh 4, NL-9747 AG Groningen, The Netherlands

Keywords: Metal/Oxide Interfaces, Segregation, Interface Modification, HRTEM

Abstract

The influence of dissolution of a segregating element (Sb) in a metal matrix in which oxide precipitates are present on the precipitate morphology and the interface structure is studied using HRTEM. The influence on Mn_3O_4 precipitates in Ag is distinct: (i) the initial precipitates, sharply facetted by solely {111}, are changed into a globular shape with sometimes also short {220} and (002) facets, (ii) a partly reduction of Mn_3O_4 into MnO occurs for a part of the precipitates. Further Sb appeared to prevent Oswald ripening of the precipitates. The influence on MnO and MgO precipitates in Cu is more subtle: only a small but significant increase of the facet lengths of the {200} (and {220}) relative to the {111} occurs. The influence of Sb can be explained by a large decrease of the energy of steps at Ag/Mn_3O_4 interfaces and by a stronger tendency for segregation of Sb to {200} and {220} than to {111} facets of the Ag/Mn_3O_4, Cu/MnO and Cu/MgO interfaces.

Introduction

Metal/ceramic interfaces play an important role in many advanced engineering materials. The structure and chemistry of the hetero-phase interfaces then often govern the performance of these composites. Solute segregation to the hetero-interfaces is known to affect the adhesive strength at interfaces [1]. However, in contrast to segregation at grain boundaries only very few studies have addressed segregation at metal/ceramic interfaces [2].
In the present study a segregating element, Sb, is dissolved in a metal matrix containing a highly dispersed ceramic phase in the form of oxide precipitates. The influence of this dissolution on the precipitate morphology and interface structure is studied using HRTEM. The following systems are addressed: Ag/Mn_3O_4, Cu/MgO and Cu/MnO. To analyze the effect of the Sb dissolution, first the oxide precipitates were grown in the pure metal matrix using internal oxidation. Subsequently the Sb was dissolved in the metal matrix by annealing the composite in an evacuated quartz tube, also separately containing a small amount of Sb, at a temperature just above the melting point of Sb. The Sb vapor pressure allows transport of the Sb to the composite. Then, the Sb can be distributed relative homogeneously over the metal matrix via solid state diffusion provided the relative amount of Sb present corresponds to a concentration lower than the solubility limit of Sb in the metal. Since this process of introducing Sb in the alloy generally takes 1 week at a temperature of 650 or 700 ^{0}C, the influence of Sb on the precipitates can only be determined if a comparison is made with the effect of annealing the sample under identical conditions but without the presence of Sb. So, three types of samples are compared: as-grown, Sb-dissoluted and vacuum annealed.

Ag/Mn_3O_4

The Mn_3O_4 precipitates in pure Ag were obtained by internal oxidation of Ag-3at.%Mn in air at 900

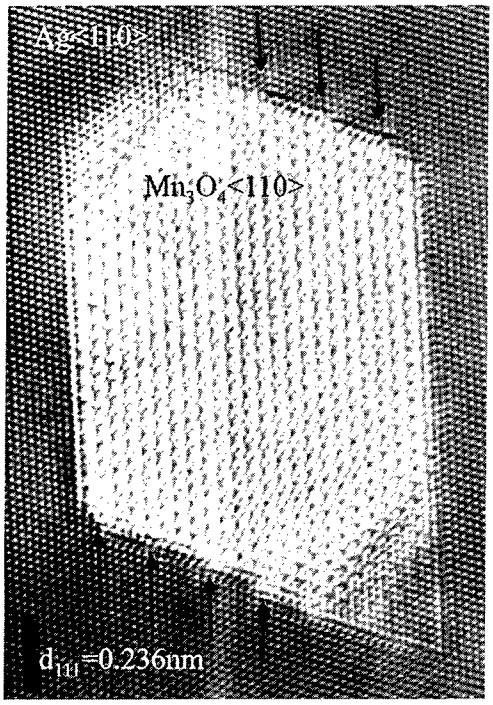

Fig.1 Mn_3O_4 precipitate in Ag as obtained by internal oxidation.

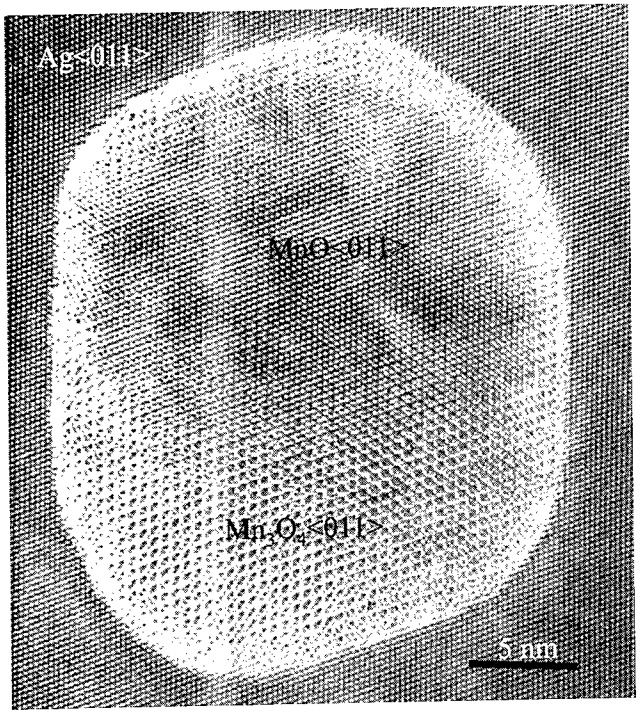

Fig.2 partly Mn_3O_4 and partly MnO precipitate in Ag as produced by internal oxidation followed by dissolution of 4 at.% Sb in the Ag matrix.

^{0}C. This system is well characterized [3] and the precipitates with a size of 10-20 nm have octahedral shape since they are bounded by 8 {111} planes (close packed oxygen planes) of the tetragonal spinel lattice of Mn_3O_4. These {111} planes all tend to be parallel to the {111}'s of Ag. However, owing to the tetragonality of the Mn_3O_4 this parallelism can only be achieved for one pair of {111} facets. Then, at another pair of facets a tilt of 7.6 ^{0} occurs between the (111)'s of Mn_3O_4 and Ag, which is accounted for by ledges in the Ag. This case is depicted in Fig.1; the viewing direction of the HRTEM image is along the common <110> of Ag and Mn_3O_4 (from the six possible <110>'s only this one is common for Ag and Mn_3O_4). A detailed analysis of misfit dislocations at parallel and tilted Ag/Mn_3O_4 {111} interfaces is given in Refs 3 and 4.

The dissolution of 4 at.% of Sb in the Ag matrix showed according to HRTEM observations 2 major effects on the precipitates: (i) a change from a precipitate sharply facetted by solely {111} to a globular shape with sometimes also short {220} and (002) facets and (ii) a partly reduction of Mn_3O_4 in MnO for a part of the precipitates. An HRTEM image showing both effects is presented in Fig.2. The lower interfacial strain energy for Mn_3O_4/Ag with respect to MnO/Ag [3] is probably responsible for the tendency to keep the outer core of the precipitate Mn_3O_4. The reduction of Mn_3O_4 into MnO can be understood since annealing in Sb vapor will result in equilibrating the sample with respect to the dissociation pressure of Sb-oxide and this pressure is significantly lower than the original oxygen partial pressure used for internal oxidation. To test this explanation, a pure Ag/Mn_3O_4 sample was annealed in Zn instead of Sb vapor. The dissociation pressure of ZnO is in-between these pressures for MnO and Mn_3O_4 and therefore full reduction of Mn_3O_4 in MnO is expected. This expectation was indeed confirmed: only MnO

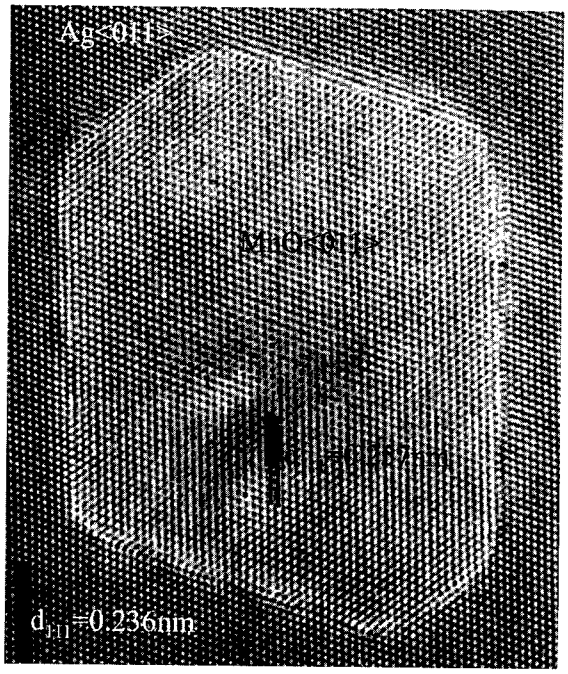

Fig.3 MnO precipitate in Ag as produced by internal oxidation followed by dissolution of 3 at.% Zn in the Ag matrix which reduces the Mn_3O_4 precipitates .

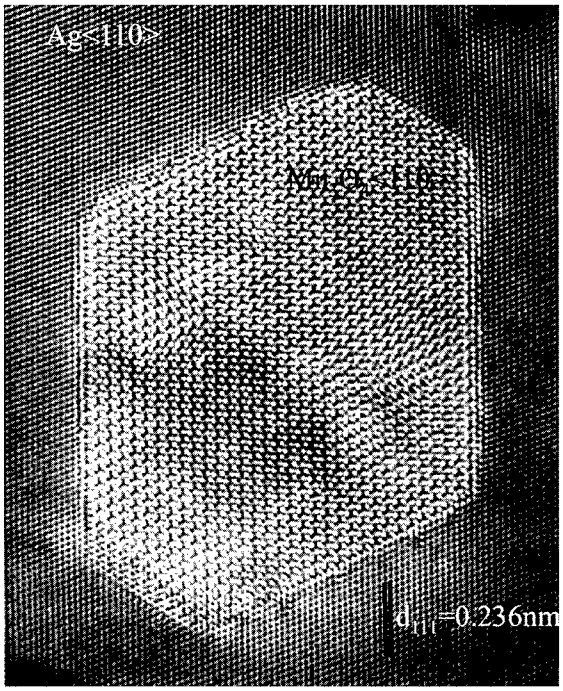

Fig.4 Mn_3O_4 precipitate in Ag as obtained by internal oxidation followed by 1 week anneal in vacuum at 650 ^{0}C.

precipitates with {200} truncated octahedral shapes were observed in the Zn treated sample; see Fig.3. Vacuum anneal of the Ag/Mn_3O_4 under identical conditions as used for the introduction of Sb also resulted in some differences with the as-grown case, however, completely different from the changes due to the Sb dissolution: (i) next to the {111} facets of the Mn_3O_4 which remained predominant also {200} and (002) facets developed during the anneal for precipitates which did not exhibit growth (see Fig.4), (ii) regions where these precipitates without growth were observed adjacent to regions where large (several 100 nm) non-facetted, sometimes poly-crystalline Mn_3O_4 clusters had 'consumed' by Oswald ripening all original small precipitates. In the Sb dissoluted samples such growth of the Mn_3O_4 precipitates was never observed and thus Sb prevents this process. These results make also clear that Sb is responsible for the spheroidizing effect on the precipitates.

Cu/MnO and Cu/MgO

The MnO and MgO precipitates in pure Cu were obtained by internal oxidation of Cu-1at.%Mn, Cu-3at.%Mn and Cu-2.5at.%Mg with the so-called Rhines pack method, i.e. foil of the alloy together with Cu/Cu_2O/Al_2O_3 powder is wrapped in Cu-foil and put in an evacuated quartz tube and annealed in a furnace. Details about the MnO precipitates in Cu in which also a minor fraction of Mn_3O_4 precipitates is present as studied with HRTEM are given in Refs 4 and 5. Both MnO and MgO precipitates currently of interest show parallel topotaxy with Cu and have {200} truncated octahedral shape and have average sizes of 200 nm and 40 nm after 1 week vacuum anneal at 700 ^{0}C, respectively. Assuming that this anneal results in precipitates with equilibrium shapes the ratio of the {200} and {111} interfacial energy γ_r can be obtained from the relative {200} and {111} facet lengths using the Wulff theorem. For Cu/MnO

γ_r=1.64±0.04 is obtained from the average of 10 precipitates and for Cu/MgO γ_r=1.27±0.1 [6]. During the one week anneal at 700 ^{0}C about 2.5 at.% Sb is dissolved in the Cu matrix and the ratio γ_r appears to be significantly affected, namely γ_r=1.50±0.06 for Cu(Sb)/MnO (average of 16 precipitate shapes) and γ_r=1.07±0.14 for Cu(Sb)/MgO (average of 14 precipitates). For instance, for Cu/MnO this corresponds to an increase of the relative length of the {200} facet with a factor of 3. It is interesting to note that previous experiment with 2.5 at.% Au dissolution in Cu/MgO showed a decrease of the relative length of the {200} facet, i.e. an effect opposite to that of the Sb dissolution.

General influence of Sb metal matrix dissolution on metal/oxide interfaces

The general picture that arises from the Sb dissolution in the systems Ag/Mn_3O_4, Cu/MnO, Cu/MgO (and also Ag/ZnO and Pd/ZnO) is that the original dominant facets of the precipitates as formed by parallel close-packed oxide and metal planes are destabilized by the Sb dissolution. Since we expect the precipitates to have equilibrium shapes after 1 week anneal at 650 or 700 ^{0}C the change in shape thus directly reflects the change in relative interfacial energies of different interface configurations. Apparently, the interfacial energy corresponding to parallel close-packed oxide and metal planes decreases relatively to the ones of the other types of interfaces.
The following possible explanation can be proposed for the change in precipitate shape. Sb, which is known to be a strongly segregating element in general and at Ag surfaces in particular [7], is largely reducing the energy of steps/ledges at the Ag/Mn_3O_4 interface in accordance with the observations in Ref.7 for a Ag{111} surface. This explains the spheroidizing effect of Sb on Mn_3O_4 precipitates in Ag. Further, Sb is segregating anisotropically to interfaces formed by different crystal planes. The stronger the segregation to a certain interface the larger the decrease in interfacial energy. The destabilizing effect of Sb on the parallel close-packed oxide and metal interface can be understood if Sb segregation to this interface is much less compared to (an)other interface(s). Since the atomic radius of (metallic) Sb is larger than the ones of Ag and Cu, Sb will exhibit the tendency to segregate to interfaces with a relative open structure. In general the interface formed by parallel close-packed planes have least open structure and so is not preferable for segregation. Moreover, segregation to the parallel close-packed plane interfaces is even less preferable for the present metal/oxide interfaces as for fcc metal/metal interfaces. This difference originates from the 2 fcc sublattices, one for the anions and one for the cations present in the oxide compared to one fcc lattice in the metals. The ratio of the number of atoms in the terminating layer of the oxide and in the adjacent first metal layer is, for the parallel close-packed plane interface, equal to the ratio of the lattice constants of the metal and the oxide. For parallel non-polar metal/ oxide interfaces, such as parallel {200}, {220} in NaCl structure-type oxides, this ratio is a factor 2 higher. This factor 2 comes from the fact that only one of the two sublattices in the oxide tends to continue in the metal at the non-polar interface and this results in relative more free volume experienced by the metal layer at the non-polar interface compared to at the polar close-packed interface. Hence, segregation is expected to occur much more strongly to these non-polar than to the parallel close-packed plane interface. This expectation will be verified using high spatial resolution elemental analysis (< 0.5 nm probe EDX) in a JEOL 2010F.

References

[1] J.R. Smith, T. Hong, D.J. Srolovitz, Phys. Rev. Lett. 72 (1994), p.4021.
[2] D.A. Shashkov, D.N. Seidman, Appl. Surf. Sci. 94/95 (1996), p.416.
[3] B.J. Kooi, H.B. Groen, J.Th.M. De Hosson, Acta Mater. 45 (1997), p.3587.
[4] B.J. Kooi, H.B. Groen, J.Th.M. De Hosson, Acta Mater. 46 (1998), p.111.
[5] B.J. Kooi, J.Th.M. De Hosson, Acta Mater. 46 (1998), p.1909.
[6] W.P. Vellinga, PhD thesis, University of Groningen, 1996.
[7] J.Vrijmoeth, H.A.v.d.Vegt, J.A.Meyer, E.Vlieg, R.J.Behm, Phys. Rev. Lett. 72 (1994), p.3843.
correspondence: E-mail: B.J.Kooi@phys.rug.nl, fax: +31 503634881.

Materials Science Forum Vols. 294-296 (1999) pp. 259-262

Structure of a [101] Tilt Grain Boundary in a Molybdenum Bicrystal

T. Vystavěl[1,2], J.M. Pénisson[1] and A. Gemperle[2]

[1] Département de Recherche Fondamentale sur la Matière Condensée CEA-Grenoble, 17, Avenue des Martyrs, F-38054 Grenoble Cedex 9, France

[2] Institute of Physics AS CR, Na Slovance 2, CZ-182 21 Praha 8, Czech Republic

Keywords: Grain Boundary, Dislocation Structure, TEM, HREM

Introduction

The presence of secondary grain boundary dislocations compensating small angular deviation from delimiting boundaries was demonstrated many times by conventional transmission electron microscopy [1, 2]. Their Burgers vectors and directions of dislocation lines were determined. The high resolution electron microscopy confirmed this description at the atomic level as demonstrated for example in [3, 4]. The possible Σ characterisation of the bicrystal is not necessarily unique in some cases. It depends not only on the misorientation angle-axis pair but also on the exact position of the grain boundary plane. In this paper the two different descriptions of the same grain boundary structure are shown. A molybdenum bicrystal containing a [101] tilt boundary has been observed by weak beam dark field and high resolution electron microscopy. Several weak beam diffraction conditions confirm the presence of a dense set of parallel dislocation lines spaced 19Å. The same spacing has been found in the HREM images. The possibility of interpretation of both electron microscopic observations based on the geometrical analysis is discussed.

Experimental technique

A molybdenum bicrystal was prepared by electron beam floating zone melting technique [5]. Oriented $[101]_{A,B}$ slices were cut by spark erosion technique and mechanically thinned to the thickness of 0.5mm. Then 3mm discs were prepared by ultrasonic cutting. Discs were mechanically thinned to the thickness of 0.1mm. Thin foils were electrochemically prepared in a double jet polishing unit in the electrolyte of sulphuric acid in methanol (1:7) at the temperature -20°C. The samples were examined in a transmission electron microscope operating at 400kV.

Results

Geometrical analysis

The grain boundary plane was determined directly from the high resolution image as $(11\ 8\ \overline{11})_A = (11\ \overline{8}\ \overline{11})_B$. The total misorientation of two grains was determined by Kikuchi line technique [6] with a precision of 0.1°. The total misorientation axis $\mathbf{R}_R$ and the angle Θ_R were found as:

$$\mathbf{R}_R=[0.6990, 0.0006, 0.7151],\ \Theta_R=54.33°.$$

Using Brandon criterion [7], for allowed deviation from coincidence, the Σ=11 description of misorientation can be used. By inspection of possible coincidences and using measured grain boundary plane the Σ=153 description was found also suitable and was used for following analysis:

Σ	Θ_c	GB plane	Basic DSC vectors		
11	50.48°	$(3\,2\,\bar{3})$	$\frac{a}{11}[3\,2\,\bar{3}]$	$\frac{a}{11}[714]$	$\frac{a}{11}[\bar{1}31]$
153	54.43°	$(11\,8\,\bar{11})$	$\frac{a}{306}[11\,8\,\bar{11}]$	$\frac{a}{2}[101]$	$\frac{a}{306}[\bar{4}\,11\,4]$

Table 1 Misorientation angle, grain boundary plane and basic displacement shift complete (DSC) vectors considered for Σ=11 and Σ=153 descriptions of bicrystal.

For the detailed analysis of the relationship between two crystals, the exact coincidence misorientation R_C, Θ_C was subtracted from the total misorientation R_R, Θ_R. Resulting small rotations R_S, Θ_S describe the deviation from the exact singular coincidence:

R_{S11}= [0.5985, -0.0574, 0.7991] = [21, -2, 28] Θ_{S11}=3.89°
R_{S153}= [-0.7561, -0.4008, 0.5174] = [-240, -128, 165] Θ_{S153}=0.59°

This supplementary rotation can be decomposed according to method used in [8] into two components: twist R_W, Θ_W, and tilt R_T, Θ_T then:

R_{W11}= [0.6288, 0.4573, -0.6288]=[11, 8, -11] Θ_{W11}=-0.59°
R_{T11}= [0.7025, 0.0125, 0.7116]=[840, 19, 855] Θ_{T11}=3.85°

R_{W153}= [0.6288, 0.4573, -0.6288]=[11, 8, -11] Θ_{W153}=-0.58°
R_{T153}= [-0.7727, 0.2773, -0.5710]=[-209, 76, -154] Θ_{T153}=0.11°

This decomposition is important for the prediction of the grain boundary structure [9].

Conventional TEM observation

Using weak beam dark field technique the presence of two regular sets of grain boundary dislocations was confirmed in several diffraction conditions. Set marked 1 in Fig.1 with line spacing 19Å and direction near the [101] common tilt axis, and set 2 with dislocation spacing 220Å and direction nearly parallel to set 1. A third set predicted according to [9] was not verified on TEM images due to the specimen geometry and the tilting stage limitations. The dislocation lines parallel to the intersection of grain boundary with the foil surface and spacing in the range of tens of angstroms are expected.

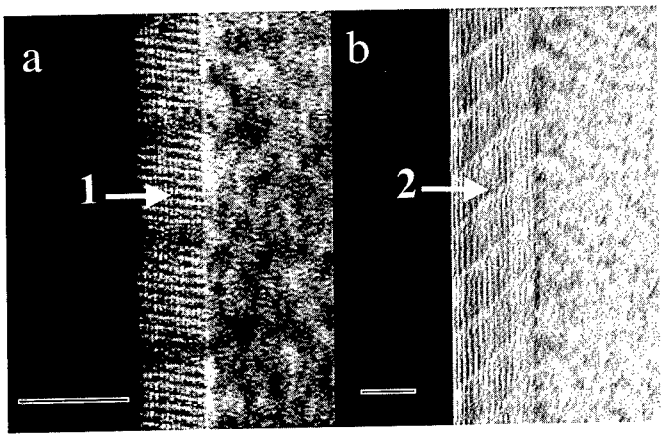

Figure 1 Weak beam dark field images a) $\vec{g}_B = 12\bar{1}$, b) $\vec{g}_B = \bar{2}\bar{1}1$. The scale marker represents 200Å

High resolution observation

High resolution electron microscopy observation allows the detailed study of the arrangement of atomic positions. The analysis of the HREM images reveals a 19.42Å structural periodicity along the grain boundary. This periodicity corresponds to the half period of the Σ=153 grain boundary, but as the difference between the two half periods is only a difference of the atomic coordinates along the axis parallel to the incident beam, HREM images are not sensitive to it.

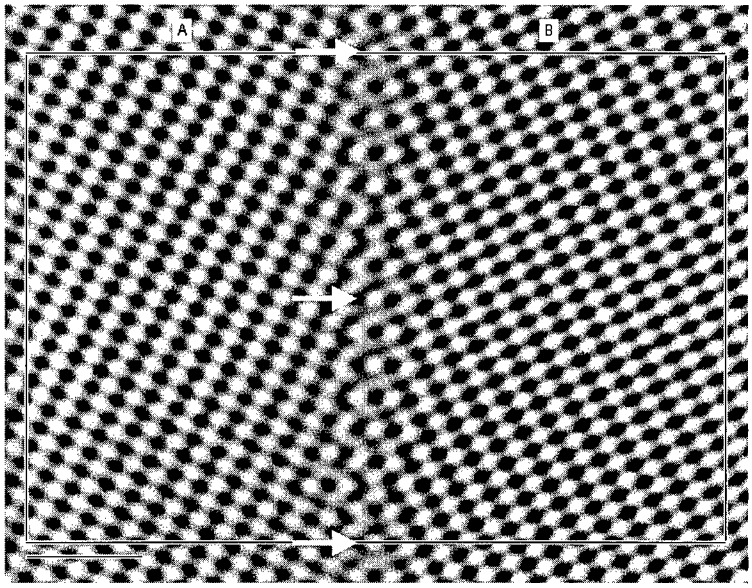

Figure 2 Filtered high resolution image, the scale marker represents 9Å. The arrows show the half period (19.42Å), the frame the coincidence site lattice of Σ=153.

Discussion and interpretation of the observed structure

The set 1 observed on WBT images corresponds to the periodicity of 19Å. Using the Σ=11 description, this set of line defects can be explained as edge secondary grain boundary dislocations with Burgers vector $\frac{a}{11}[32\bar{3}]_A$. This dislocation system compensates the tilt component of the supplementary misorientation R_{T11}= [0.7025, 0.0125, 0.7116]$_A$, Θ_{T11}=3.85°. The Frank-Read formula $\frac{1}{2}\Delta\Theta = \sin\frac{b}{2d}$, d is dislocation spacing; b is Burgers vector, gives reasonable result: $\Delta\Theta_{11} = 4.04°$. However, this set cannot represent the secondary grain boundary dislocations for the Σ=153 description, since The Frank-Read formula gives an additional rotation 0.55°, which is inconsistent with the geometrical analysis. The possibility to explain set 1 using Σ=153 description is given by the detailed analysis of the high resolution images. The periodicity 19.42Å has been found many times along different segments of the grain boundary. This observation is in good agreement with weak beam observations, provided the line contrast is caused by primary grain boundary periodicity. Due to the resolution limit of the weak beam technique this contrast can be observed only in particular cases i.e. when the periodicity is higher then 10-15Å [10].

In the next part of the discussion we will try to explain the influence of the small additional twist deviation from coincidence on the grain boundary structure. For both considered coincidence descriptions, the same additional twist component of the supplementary rotation was found to result from the geometrical analysis. The set 2 (Fig 1b) can be explained as secondary grain boundary dislocations with Burgers vector $\frac{a}{11}[714]$ for Σ=11 or $\frac{a}{2}[101]$ for Σ=153 description. In both cases the

twist approximately 0.6° is obtained. For the complete explanation of the supplementary twist component a third system of grain boundary dislocations with line direction approximately perpendicular to the dislocation set 2 must be present. The presence of this set with spacings 50Å for Σ=11 or 14Å for Σ=153 descriptions respectively was not confirmed because of the geometry of the TEM sample. If the dislocation lines are parallel with the intersection of the grain boundary and the foil plane, the interaction with thickness fringes obscures their contrast and due to limitation of the tilting of the microscopy stage (max. 20deg), the projected spacing is at the best only 17Å for Σ=11 and 4Å for Σ=153 descriptions.

Conclusion

Two different descriptions of one grain boundary structure are presented. Each description of grain boundary satisfies better the results of only one analysing method i.e. either conventional or high resolution microscopy. Due to the density of the grain boundary defects the deviation from exact coincidence is approaching to the limit of the validity of the Brandon criterion. The resolution limit of the weak beam electron technique is nearly attained. On the atomic scale observation the two dimensional feature is obtained and the defects having direction not lying in the projected plane are not detected. Therefore for complete analysis the conventional electron microscopy and observation in different projections i.e. other TEM samples would be needed.

Acknowledgement

This work was partially supported by French-Czech cooperation program Barrande.

References:

[1] C.T. Forwood and L.M. Clarebrough, *Electron microscopy of Interfaces in Metals and Alloys,* Adam Hilger, Bristol (1991)

[2] E.P. Kvam and R.W. Balluffi, *Phil.Mag.* A, **56**, 137-148, (1987)

[3] L. Priester, J. Thibault, V. Pontikis, in *Solid State Phenomena*, **59-60**, 1-50, (1998).

[4] D. Bouchet and J. Thibault, *Microsc. Microanal. Microstruct.*, **3**, 1-13, (1992)

[5] V.G. Glebovsky and V. Semenov, *Int. J. of Refractory Metals and Hard Materials*, **12**, 295-301, (1993-1994)

[6] A. Gemperle, J. Gemperlova, *Ultramicroscopy,* **60**, 207-218, (1995)

[7] D.G. Brandon , *Acta Met* , **14**, 1479-1484, (1966)

[8] T. Vystavel, V. Paidar, A. Gemperle and J. Gemperlova, *Interface Science,* **5**, 215-222, (1997)

[9] A. Gemperle, T. Vystavel and J. Gemperlova, *this proceedings*

[10] W.M. Stobbs, in *Electron Microscopy in Material Science*, part II (edited by U.Valdrè and E.Ruedl), 593, (1975).

Address for correspondence with readers: vystav@fzu.cz

Materials Science Forum Vols. 294-296 (1999) pp. 263-268

Twist Angle Dependence of Josephson Junction Effect Measured in the [001] Twist Boundary of $Bi_2Sr_2CaCu_2O_x$ Superconductor Bicrystals

B.S. Xu[1], H. Ichinose[2] and S. Tanaka[1]

[1] Tanaka Solid Junction Project, ERATO, Japan Science and Technology Corporation, 1-1-1 Fukuura, Kanazawa-ku, Yokohama 236-0004, Japan

[2] Department of Materials Science, University of Tokyo, 7-3-1 Hongo, Bunkyo-ku, Tokyo 113-8656, Japan

Keywords: Bi-Sr-Ca-Cu-O Superconductor, Josephson Junction, Interface, S/N/S, Proximity Effect, Weak Link

ABSTRACT- We present a study of the twist angle dependence of the Josephson junction effect measured in the [001] twist boundary of $Bi_2Sr_2CaCu_2O_x$ (S) superconductor bicrystals. Josephson junctions that have both direct (S/S) and indirect, thin silver layer (S/Ag/S) structures were fabricated by diffusion bonding of the (001) surfaces of two flaky S single crystals. A small junction area measuring 100-200 μm in diameter, was fabricated by Ar ion selective etching of one of the two thin single crystal superconductor S flakes. A 2-100-nm-thick silver layer was deposited on the (001) planes by sputtering prior to the joining of the surfaces to produce an S/Ag/S junction. It was clarified that the critical current, I_c, of the S/Ag/S junction is a function of temperature with $I_c=I_{OH}(1-T/T_c)^2$ for $T\geq 0.6T_c$, and $I_c=I_{OL}(-GT^{1/2})$ for $T\leq 0.5\ T_c$. In these junctions, a high I_c value was obtained when the [001] twist angle θ was 23°, 28° or 37°. Our results indicated that the Josephson effect is strongly influenced by both the temperature T and the [001] twist angle θ in the S/S and S/Ag/S junctions.

1. INTRODUCTION

Since the discovery of high-temperature oxide superconductors of Y-Ba-Cu-O [1] and Bi-Sr-Ca-Cu-O [2], investigations on the applications and properties of Josephson junctions have attracted the attention of many researchers, since these junctions are very important for application to various electronic devices. For the development of Josephson junctions, such as superconductor/normal conductor/superconductor (S/N/S) [3-6], superconductor/insulator/superconductor (S/I/S) [7], superconductor/semiconductor/superconductor (S/Se/S) [8], and superconductor/superconductor (S/S) [5,6], the relationship between electronic characteristics and interface structures of S/N, S/Se, S/I and S/S must be examined in detail because the junction properties are strongly influenced by the interface structure. Since the present high-temperature superconducting oxide has pronounced electronic anisotropy, an investigation of the effects of interface orientation is indispensable. In the present work, in order to verify the hypothesis by Tomita et al. [9] that a bicrystal boundary can serve as a Josephson junction, and to study the relationship between interface structure and electronic characteristics, two types of S/Ag/S and S/S junctions were fabricated by diffusion bonding of the (001) surfaces of two flaky S single crystals with [001] twist angle ranging from 0° to 45° [6].

2. EXPERIMENTAL

2.1. Single-crystal specimens

Single-crystal S flakes were obtained by melting. A mixture of Bi_2O_3, $SrCO_3$, $CaCO_3$ and CuO (Bi:Sr:Ca:Cu=2.2:2:1:2) was calcined at 1073 K for 20 h in air. The black powder obtained was heated at 1273 K for 10 h, and then cooled at the rate of 2 K/h. Single-crystal specimens were obtained from the ingot; their dimensions ranged from 1 to 4 mm in diameter by approximately 0.1 mm thick. A clean surface parallel to the (001) plane was obtained by cleavage. The critical temperature T_c of S was 80 K.

2.2. S/S and S/Ag/S junctions

S/S and S/Ag/S junctions were fabricated using the cleavage (001) plane of S [6]. A plateau was formed on the (001) plane by Ar ion milling to allow a limited region of single-crystal S to be in contact at various twist angles [6]. Hot pressing was performed at a temperature range between 1073 K and 1113 K for 5 h, and at a pressure of 0.33 MPa. Silver barriers with thicknesses of 2 nm and 100 nm, respectively, on the (001) planes were prepared by sputtering for S/S and S/Ag/S junctions, respectively. Current-voltage (I-V) characteristics at 4.2 K and 30 K without microwave irradiation were measured using the four-probe technique. The high-resolution transmission electron microscope (HRTEM) used was a specially improved version of JEM-200CX operated at 200 kV.

3. RESULTS

3.1. I-V characteristics

3.1.1. S/S junction

The I-V characteristics of the S/S junction at 30 K, whose [001] twist angle θ is 28°, are shown in Fig. 1. It is known that the critical current (I_c) is evaluated as 0.9 mA. The normal state resistance

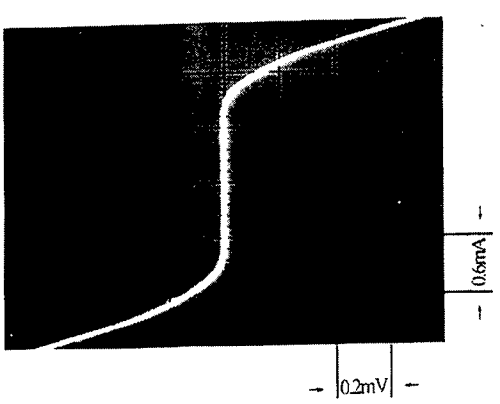

Fig. 1 I-V characteristicsofthe S/S junction at 30 K, whose [001] twist angle θ is 28°. It is known that the critical current I_c is evaluated as 0.9 mA. The normal state resistance R_n is estimated as 2 Ω fromthe slope ofI-Vcurve. The I_cR_n product ofthe junction is 1.8 mV, which is approximately equal to the gap voltage ofS.

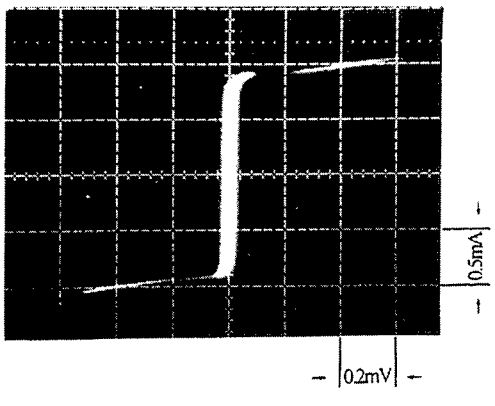

Fig. 2 I-V characteristicsofthe S/Ag/S junction with a 73-nm-thick silver interlayer at 30 K. The [001]twist angle θ is 37°, the critical current I_c is 0.85 mA, The normal state resistance R_n is 1Ω, and I_cR_n is 0.85 mV.

(R_n) is estimated as 2 Ω from the slope of I-V curve. The I_cR_n product of the junction is 1.8 mV, which is approximately equal to the gap voltage of S.

3.1.2. S/Ag/S junction

Figure 2 shows the I-V characteristics of the S/Ag/S junction with a 73-nm-thick silver interlayer at 30 K. The [001] twist angle θ is 37°, I_c is 0.85 mA, R_n is 1Ω, and I_cR_n is 0.85 mV.

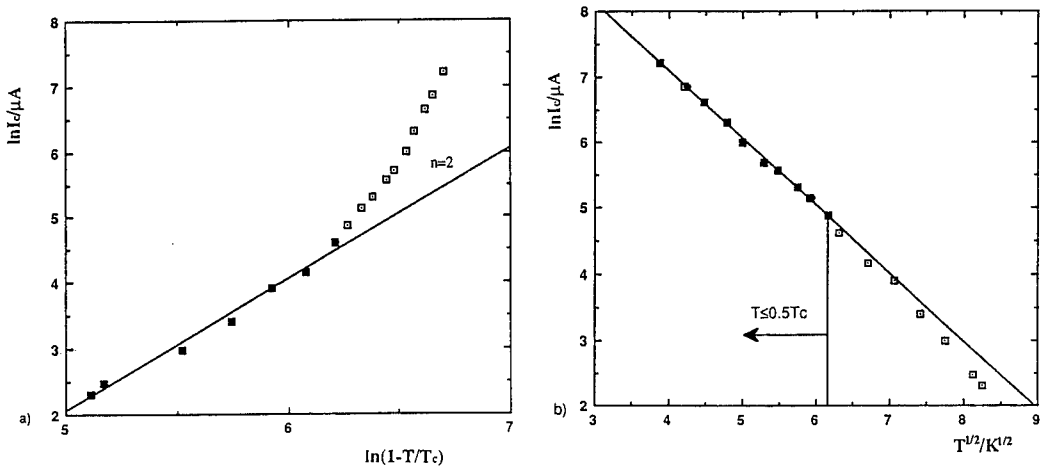

Fig. 3 Critical current I_c as a function of temperature T. The I_c vs. temperature curve consists of two regions that are represented by two different functions. a) $T \geq 0.6T_c$, $I_c=I_{OH}(1-T/T_c)^2$, and b) $T \leq 0.5T_c$, $I_c=I_{OL}(-GT^{1/2})$.

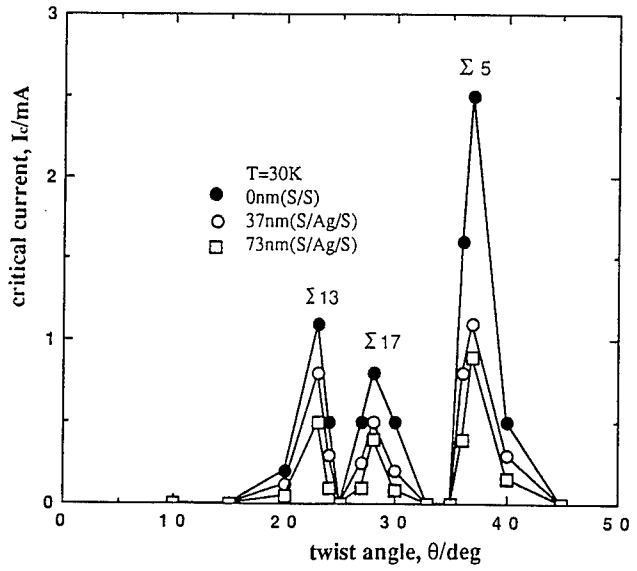

Fig. 4 Twist angle θ dependence of critical current I_c of S/S (●) and S/Ag/S (○,◇) junctions, measured at 30 K. The peak values of I_c were obtained from the S/S and the S/Ag/S junctions at [001] twist angles of 23°, 28° and 37°. These interfaces form with low energy which leads to a high I_c value.

The typical Josephson effect of the S/S and S/N/S junctions is shown in Figs. 1 and 2. The results agree with those of Clarke [10] and Akoh et al. [11]. Similar I-V characteristics were also obtained for the S thin-film junction by Takami et al. [12]. The results indicate that the S/S and S/Ag/S junctions are of good quality.

3.2. I_c-T

I_c is shown as a function of temperature in Fig. 3. The I_c vs. temperature curve consists of two regions represented by two different functions. In the temperature region of $T \geq 0.6T_c$, the curve is well represented by $I_c=I_{OH}(1-T/T_c)^2$, as shown in the logarithmic plot of I_c and $1-T/T_c$, where I_{OH} is a constant (Fig. 3a). In the region $T \leq 0.5T_c$ (below about 38 K), it is represented by $I_c=I_{OL}(-GT^{1/2})$, where I_{OL} and G are constants (Fig. 3b).

3.3. I_c -θ

In the S/S and S/Ag/S junctions, the I_c values were obtained for a bicrystal with [001] twist angles (θ) 0° and 45° at 30 K, as shown in Fig. 4. From the relationship between I_c and θ, it is clear that three I_c peak values appear for both S/S and S/Ag/S junctions. The peak value occurs at θ at 23°, 28° and 37°, respectively. The results indicate that the Josephson effect is strongly influenced by the [001] twist angle in these junctions.

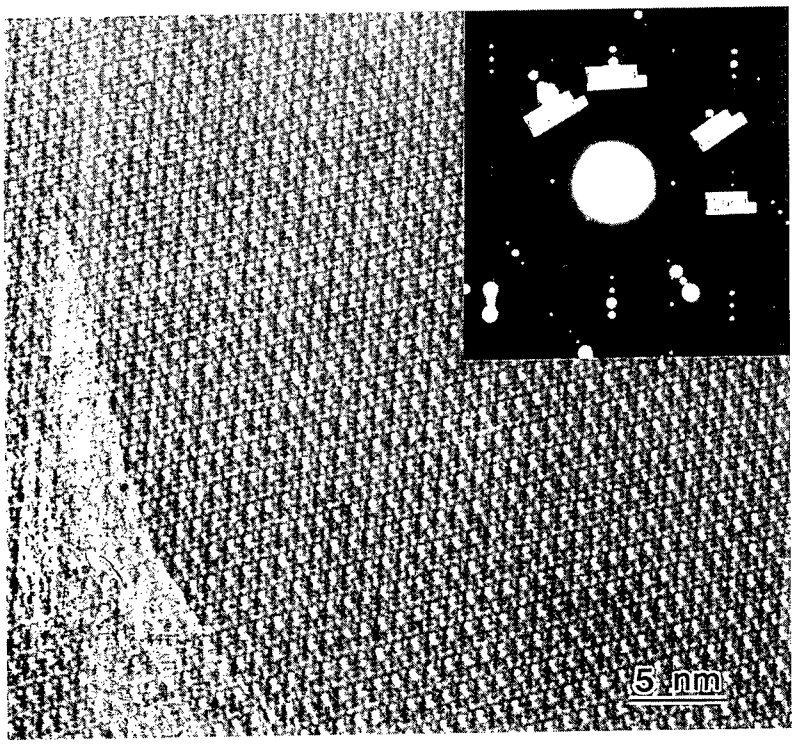

Fig. 5 HRTEM image of the (001) plane view and the electron pattern of the S/S junction with a twist angle of 37°.

4. DISCUSSION

4.1. Mechanisms of Josephson effect in S/S and S/Ag/S junctions

In these junctions, an artificial bicrystal boundary (S/S) and an interface (S/Ag) have been fabricated by controlling the [001] twist angle. The S/S junction is formed by bonding two (001) planes of two flaky S single crystals. The boundary is formed by directly bonding a (Bi-O) plane to another S single-crystal (Bi-O) plane, although, their twist angles are different. Figure 5 shows an HRTEM image and the electron diffraction pattern of the S/S junction with a twist angle of 37°. The S/S twist bicrystal boundary structure reveals that, if the boundary is not directly bonded by of the (Bi-O) planes, the I-V characteristics exhibit hysteresis [6], which indicates that the I-V characteristics are influenced by junction capacitance [3]. The S/S junction exhibits the Josephson effect due to the weak link of the bicrystal boundary that behaves as a barrier [9]. Such behavior has also been reported at [001] a tilt of 5° in the Y-Ba-Cu-O bicrystal film [13]. In the S/Ag/S junctions, electron pairs are transported through the S/Ag interface [14,15] when $L_{Ag} < \xi_{Ag}$, where L_{Ag} is Ag film thickness, ξ_{Ag} is Ag coherence length. The results also show that I_c decreases with increasing L_{Ag} [6].

4.2. I_c-T

The I_c-T curve in Fig. 3a is concave. In the S/Ag/S junctions, the critical current depends on the temperature, especially at low temperatures. The de Gennes-Werthamer theory (dGW) of the proximity-effect model [14,15] is useful for explaining the present results, especially in the temperature region below 38 K. In Fig. 3b, at temperature regions $T \geq 0.6T_c$, I_c is proportional to $(1-T/T_c)^2$, which suggests that the electric transport is also affected by the S/Ag/S proximity effect. The experimental results show that the relationship I_c-T agrees with those obtained using $I_c=I_o(1-T/T_c)^2\exp(-2L_{Ag}K_{Ag})$ [14,15], where K^{-1}_{Ag} is a characteristic length describing the penetration depth or Ag coherence length (ξ_{Ag}). The temperature dependence of I_c shows that these values are controlled by a factor of $(1-T/T_c)^2$, when $T \geq 0.6\ T_c$. When $T \leq 0.5\ T_c$, the I_c values are controlled by the major factor of $\exp(-2L_{Ag}K_{Ag})$, which agrees with the factor of $(-GT^{1/2})$ [6].

4.3. I_c-θ

The peak values of I_c were obtained from the S/S and the S/Ag/S junctions at [001] twist angles of 23°, 28° and 37°. In the S/S junction, it is known that boundary with the twist angles of 23°, 28° and 37° correspond to the values of Σ13, Σ17 and Σ5, respectively, according to the coincidence site lattice (CSL) theory, [6,9]. The presence of boundary energy cusps for coincidence orientation in [001] twist bicrystals was reported by Smith et al. [16]. It was indicated that the Σ13, Σ17 and Σ5 coincidence boundaries with low energy led to a high critical current I_c or a high current density (J_c) [9]. In other words, it may be considered that the coherence ξ and the order parameter Ψ ($|\Psi|^2$ are directly proportional to the pair transport through the barrier density) of Σ13,Σ17 and Σ5 coincidence boundaries are larger than those of other twist angle junctions. The S/Ag/S junctions may also have a large I_c due to a large Ψ [6]. The results were indicated that the order parameter Ψ related the proximity effect because a lot of the electron pair transport through S/Ag interface and Ag layer.

5. CONCLUSIONS

We obtained S/S and S/Ag/S junctions by diffusion bonding of the (001) surfaces of two flaky S single crystals with various [001] twist angles. We are the first to report the twist angle dependence of Josephson junction effect measured in the [001] twist boundary of $Bi_2Sr_2CaCu_2O_x$ superconductor bicrystals. It was clarified that the critical current I_c of the S/Ag/S junction is a function of temperature with $I_c=I_{OH}(1-T/T_c)^2$ for $T\geq 0.6T_c$, and $I_c=I_{OL}(-GT^{1/2})$ for $T\leq 0.5\ T_c$. In the S/S and S/Ag/S junctions, a high I_c value was obtained when the [001] twist angle θ was 23°, 28° or 37°. We suggested that I_c observed in the Josephson junctions is a result of pair transport through the barrier of S/S and S/Ag interfaces, and that the I_c peak due to coherence ξ and order parameter Ψ is large. The results indicated that the Josephson effect is strongly influenced by both temperature T and the [001] twist angle θ in the S/S and S/Ag/S junctions.

Acknowledgment

We gratefully acknowledge the late Y. Ishida, Emeritus Professor of University of Tokyo, Dr. J. Chen and Professor T. Yamashita both of Tohoku University, for useful suggestions and encouragement.

REFERENCES

[1] J. G. Bednorz and K. A. Muller, Z. Physik, B64 (1996), 189.
[2] H. Maeda, T. Tanaka, M. Fukutomi and T. Asano, Jpn. J. Phys., 27 (1998), L209.
[3] G. F. Virshup, M. E. Klausmeier-Brown, I. Bozovic and J. N. Eckstein, Appl. Phys. Lett., 60 (1992), 2288.
[4] M. E. Klausmeier-Brown, G. F. Virshup, I. Bozovic, J. N. Eckstein and K. S. Ralls, Appl. Phys. Lett., 60 (1992), 2806.
[5] B. S. Xu and H. Ichinose, S.-I. Tanaka and Y. Ishida, Proc. Int. Conf. ICEM-13., V2A (Paris, 1994), p. 229.
[6] B. S. Xu and H. Ichinose, S.-I. Tanaka and Y. Ishida, J. Jpn. Institute of Materials (Japanese) 60 (1996), 121.
[7] R. P. Robertazzi, R. H. Hoch, R. B. Laibowitz and W. J. Gallagher,Appl. Phys. Lett., 61 (1992), 711.
[8] H. Tsuge, T. Satoh, N. Matsukura, J. Fujita and T. Yoshitake, Proc. 11th Symp. Future Electron Device, (Chiba, 1992), p.147.
[9] N. Tomita, Y. Takahasi, M. Mori and Y. Ishida, Jpn. J. Appl. Phys., 31 (1992), L942.
[10] J. Clarke, Proc. R. Soc. London, Ser. A308 (1969), 447.
[11] H. Akoh, C. Camerlingo and S. Takato, Appl. Phys. Lett. 56 (1990), 1487.
[12] T. Takami, K. Kuroda, K. Kojima, O. Wada, J. Tanimura, M. Kataoka, T. Ogama and K. Hamanaka, Jpn. J. Appl. Phys., 31 (1992), L249.
[13] J. Mannhart, P. Chaudhari, D. Dimos, C. C. Tsuei and T. R. McGuire, Phys. Rev. Lett., 61 (1988), 2476.
[14] N. R. Werthamer, Phys. Rev., 132 (1963), 2440.
[15] P. G. de Gennes, Rev. Mod. Phys., 51 (1964), 225.
[16] D. A. Smith, M. F. Chisholm and J. Clabes, Appl. Phys. Lett., 53 (1988), 2344.

Materials Science Forum Vols. 294-296 (1999) pp. 269-272

Characterization of Grain Boundaries of Al-doped Sintered β-SiC by Both HRTEM and STEM

K. Kaneko[1], T. Saitoh[2] and S. Tsurekawa[3]

[1] Ceramics Superplasticity, ICORP, JST, c/o JFCC, Nagoya, 456-8587, Japan

[2] JFCC, Nagoya, 456-8587, Japan

[3] Lab. of Materials Design and Interface Engineering, Dept. of Machine Intelligence and System Eng., Faculty of Engineering, Tohoku University, Sendai, 980-8579, Japan

Keywords: Deformation, Grain Boundary, SiC, HRTEM, STEM, EDS, EELS, Sintering Additives

Abstract Both high-resolution transmission electron microscope (HRTEM) and scanning transmission electron microscope (STEM) were carried out to observe the structure and chemistry of grain boundaries of Al-doped sintered β-SiC. Two specimens, an as-sintered and an compressed Al-doped sintered β-SiC specimens, were provided. Although, it was shown by energy dispersive X-ray spectroscopy (EDS) that Al and O segregated at grain boundaries of both specimens, it was discovered by electron energy loss spectroscopy (EELS) that the chemistry of grain boundaries of both specimens were different.

I. Introduction

In general, the non-oxide ceramics, such as SiC and Si_3N_4, are difficult to densify by normal sintering method without additives due to their extremely low self-diffusiveness, so that B, C and/or Al composites are usually chosen as sintering additives to lower the grain boundary energy for promoting sintering process [1]. In the case of Al composites, they are in the form of metal Al, Al_2O_3 or AlN. Although Al_2O_3-doped specimen shows stronger toughness than the B- or C- doped specimen, Al_2O_3 usually participates in liquid phase formation so that SiC becomes fragile at elevated temperatures at around 2200 K, and the liquid phase acts as the mass transport media during the densification via a solution-reprecipitation mechanism. The transport properties of the liquid phase will be dependent on its volume fraction and chemical environments. These are determined by the characteristics of additives, the relevant eutectic temperatures, and the densification parameters such as the temperature and the atmosphere [2, 3].

Additives alter the chemical stability of the final material and degrade its mechanical properties at high temperatures, due to their segregation at the grain boundaries and the formation of glass phase. The glass phase softens at elevated temperatures then becomes as negative effects on the mechanical and the chemical properties. The relationship between the mechanical properties and additives has been studied carefully by many researchers, with respect to the micro- and nano-structures for both α- and β-SiC [4-6].

In this paper, addition to the structural observation of grain boundaries by HRTEM, both compositions and chemical environments are examined for two types of β-SiC[Al] specimens. Addition to the EDS analysis showing that there were traces of both O and Al at the grain boundaries of the as-sintered and the compressed specimens, it was shown by EELS that the chemical environments of the grain boundaries were different from as-sintered to compressed β-SiC[Al] specimen.

II. Experimental Procedure

1. Specimens

β-SiC[Al] was produced by using the precursor-derived ceramic method from polycarbosilane at Hitachi Research Laboratory [4, 7]. Before pyrolyzing this powder, it was heated at 463 K for 1.8 ks in the air to promote cross-linking of the polymer structure. Pyrolization of the oxidized polycarbosilane was performed at 1573 K for 3.6 ks under vacuum, then fine β-SiC powders were prepared by grinding polycarbosilane powder. The grain size of the specimen at 2023 K was estimated from the sharpness of the XRD lines, as around 0.1 μm [7].

The impurity content of the specimen was measured by inductively coupled plasma spectrometry, showed 1.67 wt. % of Al, and by fourier transform infrared spectroscopy, showed 2.35 wt. % of O. Although Al and O may have been dissolved into SiC during the sintering process, the segregations of Al and/or Al_2O_3 at grain boundaries were expected for this case. Since, the solubility limit of Al in SiC was measured by powder X-ray diffraction method (Debye-Scherrer method) as almost 0.4 wt. % Al_2O_3, thus about 0.2 wt. % of Al, at around 2200 K [5, 8].

Those two specimens available for this investigations were; as-sintered specimen, compressed specimen at 2173 K with strain rate $5 \cdot 10^{-5}$ s^{-1} for 4.2 ks with final strain 0.1 in Ar.

2. Electron microscopy

HRTEM imaging was carried out on a Topcon 002B equipped with a LaB_6 gun having a point resolution of 0.18 nm operated at 200 kV. AEM was performed with a dedicated STEM (Thermo, Vacuum-Generators HB 601 UX) operated at 100 kV, equipped with a high-resolution pole piece and a cold field emission gun. An energy resolution of better than 0.4 eV was obtained from the full-width half-maximum (FWHM) of zero-loss peak with the spectrometer entrance aperture limited to about 12 mrad. The STEM is equipped with an Oxford Instruments EDS system with a Super ATW [Si(Li)] window and with a Parallel-EELS spectrometer, Gatan 766 with photodiode array.

III. Results and Discussion

1. HRTEM imaging

HRTEM imaging of grain boundaries showed that the presence of amorphous secondary phase from the as-sintered specimen, Fig. 1(a), and clean grain boundaries from the compressed specimen, Fig. 1(b). The secondary phases may be completely removed from the grain boundaries by evaporation/liquidation of glass phase at elevated temperature.

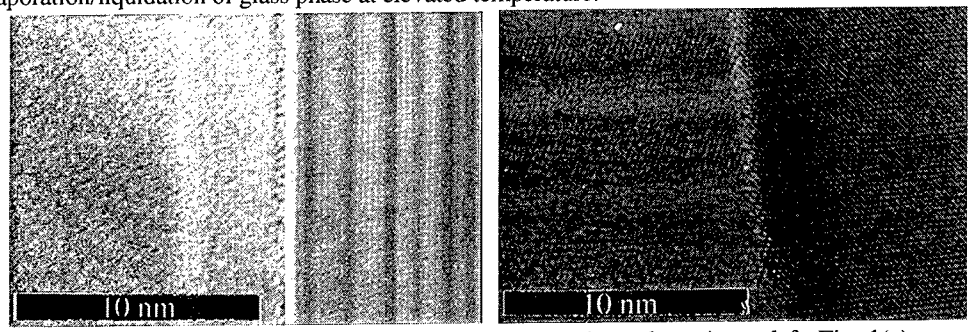

Fig. 1. HRTEM images of grain boundary from the as-sintered specimen, left, Fig. 1(a) and the compressed specimen, right, Fig. 1(b). The scale indicates 10 nm.

2. Energy Dispersive X-ray Spectroscopy

Line profile method near grain boundaries of specimens were achieved along a direction vertical to the grain boundaries, then the elemental compositions of grain boundaries were analyzed. The impurity contents were detected in terms of the intensity of X-ray radiation from the Al-K edge and O-K edge relative to the intensity of the Si-K edge signal. The results obtained from the as-sintered, Fig. 2(a), and the compressed specimen, Fig. 2(b), present apparent segregations of Al and O at grain boundaries. In all cases, EDS spectra were acquired for 50 seconds from each spots.

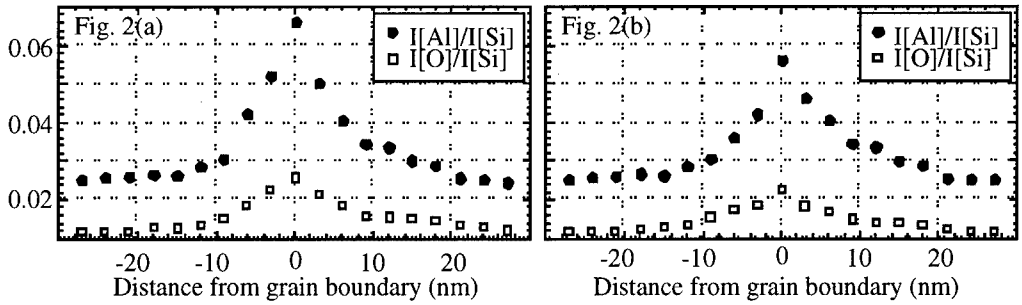

Fig. 2. EDS line profile method over grain boundaries, from the as-sintered specimen, Fig. 2(a), and compressed specimen, Fig. 2(b).

It was assumed from these results that the composition of grain boundaries were either $Al_xSi_yO_z$ glass or aluminum-oxides.

3. EELS/ELNES

The results of EDS only indicate the chemical composition of grain boundaries but not their chemistries. Therefore, addition to the EDS results, EELS measurement had to be carried out to extract information about the chemical composition of light elements, the bonding, the valence states, the atomic coordination, the symmetry, and other useful information of the specimen [9].

The spectra were taken with the beam scanning a 2.0×2.0 nm^2 [10] and also with the stationary spot beam method with probe size about 3 Å. In comparison to a stationary spot-mode beam, the scanning method not only reduces the beam damage on the specimen but also allows a manual correction of the specimen drift by minor adjustments to the beam deflection coils, since the grain boundary can simultaneously be imaged on the dark field detectors.

(1) As-sintered specimen

It was clearly shown by EDS results that there were segregation of Al and O atoms at grain boundaries. Oxygen is believed to be located on the exterior of SiC grains originally as a contaminant during the material processing. ELNES of energy range between 50 and 150 eV showed that there are edges starting from almost 75 eV. The pre-edge of Si-$L_{2,3}$ edges, an indicative of Al-$L_{2,3}$ edges, see Fig. 3(a), were still too weak to justify the chemical composition at grain boundaries, and only verified the presence of Al atoms. The O-K edge was also analyzed to determine the oxygen environment, and compared with O-K ELNES obtained from other form of alumino-oxides.

The production of alumino-silicate-glass at grain boundaries are favored, due to the occurrence of oxygen molecule vaporization due to the irradiation effect (known as electron-hole drilling, see Fig. 4(a), marked X). The HRTEM image obtained, see Fig. 1(a), showed the presence of glass phase at the grain boundaries and the O-K edge, Fig. 4(a), strongly indicated the fabrication of alumino-silicate-glass at the grain boundaries.

(2) Compressed specimen

The same procedure was carried out for the compressed specimen as the as-sintered specimen. As can be seen from Al-L ELNES spectrum obtained from the grain boundaries, Fig. 3(b), the presence of Al atoms at the grain boundaries are very evident. The O-K ELNES spectra, Fig. 4(b), was then compared with various types of Al_2O_3 spectra as in the case of as-sintered specimen, to confirm that it was very similar to the spectrum obtained from the four-fold coordinated alumino-oxides, such as γ–Al_2O_3.

According to the annealing experiment, the vaporization process takes place above 1400 K;

$$SiC\ (s) + Al_2O_3\ (s) \rightarrow Al_2O\ (g) + SiO\ (g) + CO\ (g)$$

so that the Al-Si-O glass becomes vaporized [11]. This process may be assisted by the cavitation damage, promoted by the evaporation of the amorphous phase. However, in the case of compressed specimen, the compressive stress seems to suppress the vaporization process. Meantime, the Al and O atoms remaining at the grain boundaries may alter its forms from the Al-Si-O glass to four-fold coordinated material.

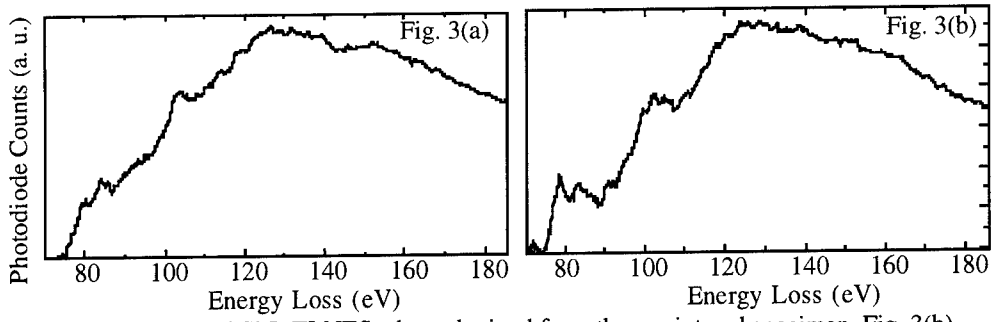

Fig. 3(a) Al-L and Si-L ELNES edges obtained from the as-sintered specimen, Fig. 3(b) from the compressed specimen.

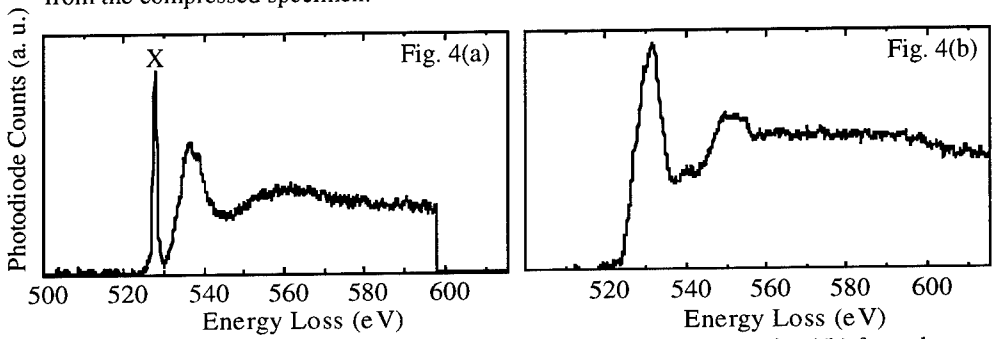

Fig. 4(a) O-K ELNES edge obtained from the as-sintered specimen, Fig. 4(b) from the compressed specimen.

V. Conclusions

Effect of deformation process on grain boundaries, particulary on sintering additives were investigated by using both HRTEM and STEM. HRTEM images presented that the presence of amorphous secondary phase at the grain boundaries of as-sintered specimen, disappearance of amorphous phase at the grain boundaries of the compressed specimen. Although EDS results clearly showed the presence of Al and O at grain boundaries from both as-sintered and compressed specimens, EELS analysis confirmed that the chemical environments of them are different. The disappearance of the glass phases may be caused by the evaporation by the application of high temperature in the compressed, though Al and O atoms still remained.

Although it is still too early to conclude that the effects of sintering additives at the grain boundaries are directly related to the deformation mechanisms or not, specimens with other sintering additives suitable for SiC must be studied to compare with the results obtained from both macroscopic and microscopic investigations in the future.

References

[1] R. A. Alliegro, L. B. Coffin and J. R. Tinklepaugh, J. Am. Ceram. Soc. 39 (1956), p. 386.
[2] F. F. Lange, J. Mater. Sci. 10 (1975), p. 314.
[3] M. H. Lewis and R. J. Lumby, Powder Metallurgy 26 (1983), p. 73.
[4] H. Kodama and T. Miyoshi, J. Am. Ceram. Soc. 73 (1990), p. 3081.
[5] T. Kinoshita, S. Munekawa and S.-I. Tanaka, Acta. Metall. Mater. 45 (1997), p. 801.
[6] L. K. L. Falk, J. Euro. Ceram. Soc. 17 (1997), p. 983.
[7] H. Kodama and T. Miyoshi, Adv. Ceram. Mater. 3 (1988), p. 177.
[8] Y. Tajima and W. D. Kingery, J. Am. Ceram. Soc. 65 (1982), p. C-27.
[9] P. R. Kenway, J. Am. Ceram. Soc. 77 (1994), p. 349.
[10] K. Kaneko, T. Gemming, I. Tanaka and H. Müllejans, Phil. Mag. A. 77 (1988), p. 1255.
[11] T. Grande, H. Sommerset, E. Hagen, K. Wiik, and M-A. Einarstrud, J. Am. Ceram. Soc. 80 (1997), p. 1047.

Corresponding author: Kenji KANEKO, E-mail: kaneko@ngo.jst.go.jp, FAX: +81-52-883-6201

Materials Science Forum Vols. 294-296 (1999) pp. 273-276

Atomic Structure and Chemical Bonding State of Sapphire Bicrystal

Y. Ikuhara, T. Watanabe, T. Saito[1], H. Yoshida and T. Sakuma

Department of Materials Science, Faculty of Engineering, The University of Tokyo, 7-3-1, Hongo, Bunkyo-ku, Tokyo 113-8656, Japan

[1] Japan Fine Ceramics Center, 2-4-1, Mutsuno, Atsuta-ku, Nagoya 456-8587, Japan

Keywords: Alumina, Bicrystal, Grain Boundary, Atomic Structure, Bond Overlap Population, Net Charge, Molecular Orbital Method, DV-Xα Method, High Resolution Electron Microscopy

Abstract

Sapphire bicrystal with symmetrical $\Sigma7[0\bar{1}11]/180°$ grain boundary was fabricated by a hot joining technique at 1500°C. The stability of grain boundary structure was evaluated by DV-Xα molecular orbital method, calculating the bond overlap population (BOP) and net charge (NC) as a function of the interplanar distance between two adjacent grains across the grain boundary. As a result, the grain boundary structure was determined so that two oxygen-terminated $(01\bar{1}2)$ planes are joined each other at the interplanar distance of about 0.13nm. This result agrees well with the atomic grain boundary structure experimentally obtained from high resolution electron microscopy (HREM) analysis.

Introduction

Alumina ceramics are the most common structural ceramics, and their properties closely related to the atomic structure and chemical bonding state at grain boundaries. Therefore, an investigation of the grain boundary structure and bonding state is needed to understand and develop its properties further. For characterizing atomic structure, high resolution electron microscopy (HREM) has been successfully applied to elucidate the grain boundary atomic structure in many kinds of ceramics (1,2). For evaluating bonding state, several theoretical methods including band calculation(3), molecular dynamics(4) and molecular orbital method(5) have been applied, reflecting the recent technological improvement of computer sciences. In this study, we fabricated the bicrystal with $\Sigma7[0\bar{1}11]/180°$ grain boundary and characterize its atomic structure by HREM. In addition, a first principles molecular orbital (MO) calculation was made using discrete-variational (DV)-Xα method (5) for a model cluster to understand the grain boundary bonding state.

Experimental

The bicrystal with $\Sigma7[0\bar{1}11]/180°$ grain boundary was obtained by joining two sapphire crystals to overlap their respective $(01\bar{1}2)$ planes[2,7]. The crystals were set so that one crystal is rotated by 180° around the $[0\bar{1}11]$ axis with respect to the other. Figure 1 shows the atomic projection observed along the $[2\bar{1}\bar{1}0]$ in which large circles and small circles represent oxygen and aluminium ions, respectively. S-plane corresponds to the $(01\bar{1}2)$ plane which is reported to have the lowest surface energy(6). The grain boundary of $\Sigma7[0\bar{1}11]/180°$ can be represented , thus, as the boundary joined with two S-planes in which one crystal is rotated by 180° with respect to the other(7).

TEM specimens were prepared using a standard technique involving mechanical grinding to a thickness of 0.1 mm, dimpling to a thickness of 20μm and ion beam milling to electron transparency at about 4kV. HREM observations were performed using a Topcon 002B microscope with a point to point resolution of 0.18 nm. Image simulations were performed using a standard multi-slice program, and molecular orbital (MO) calculation was made by the discrete-variational (DV)-Xα method developed by Adachi (6). By using a $(Al_2O_{10})^{14-}$ cluster model, surrounded by Mardellung potential, bond overlap population (BOP) and net charge (NC) at the grain boundary were calculated as a function of the interplanar spacing between two adjacent grains across the grain boundary.

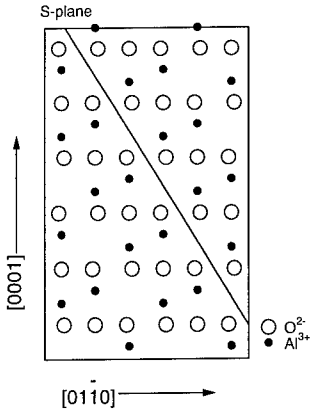

Fig.1. Atomic arrangement of α-Al_2O_3 observed from [$2\bar{1}\bar{1}0$] direction, in which large white circles and small black circles represent O ions and Al ions, respectively. S-plane corresponds to the ($01\bar{1}2$) plane which is reported to have the lowest surface energy.

Results and discussion

In order to construct the atomic model of $\Sigma7[0\bar{1}1\bar{1}]/180^\circ$ grain boundary (GB), the relative displacement between two crystals is needed to be determined. The displacement parallel to the GB can be fixed by considering a simple geometry between two crystals, but the displacement vertical to the GB must be determined by evaluating the bonding state as a function of the displacement. That is, BOP and NC are required to be obtained as a function of the displacement perpendicular to the GB. In this procedure, as a first approximation, lattice relaxation was not taken into account(7).

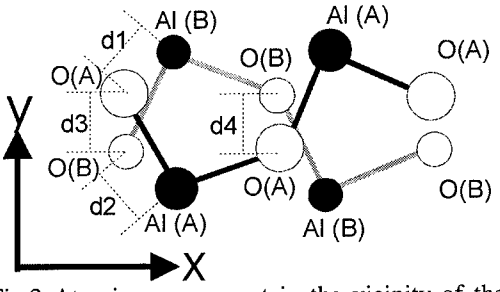

Fig.2 Atomic arrangement in the vicinity of the Σ7 grain boundary, which is project along the normal to the boundary plane. A and B represent the different two crystals across the grain boundary.

For setting up the optimum displacement parallel to the GB, we assume that crystal A and crystal B are connected by the Al-O bonding across the GB. Fig.2 is an atomic projection observed perpendicular to the GB, and the following procedure is required to construct the atomic model.

1. The distance between Al in crystal A and O in crystal B (d_1 in Fig.2) is set so as to be equal to that between O in crystal A and Al in crystal B (d_2 in Fig.2). This procedure is needed to keep force balance along the x-axis and minimize the Al-O bond length across the GB to form the strongest bonding at the boundary.
2. The distance between O in two crystals is set so as to have the same interatomic distance (d_3 and d_4 in Fig.2). This procedure is needed to keep force balance along the y-axis and maximize the O-O bond length across the GB to minimize the repulsive force between the atoms.

Thus, the relative displacement parallel to the GB along x-axis can be determined by taking into account the condition 1, and the relative displacement along the y-axis can be determined by the condition 2.

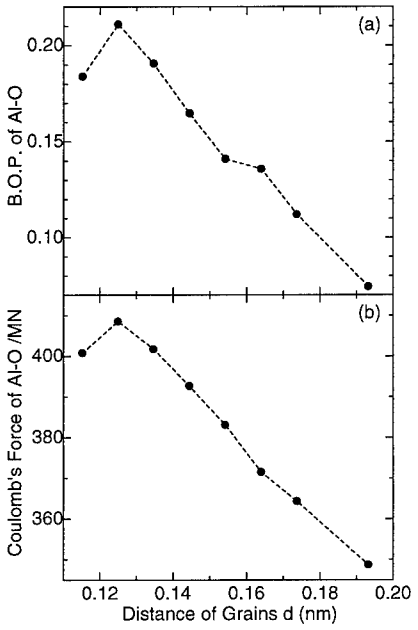

Fig.3. (a) Bond overlap population of Al-O bonding and (b) Al-O Coulomb's force perpendicular to the grain boundary as a function of distance of two adjacent grains.

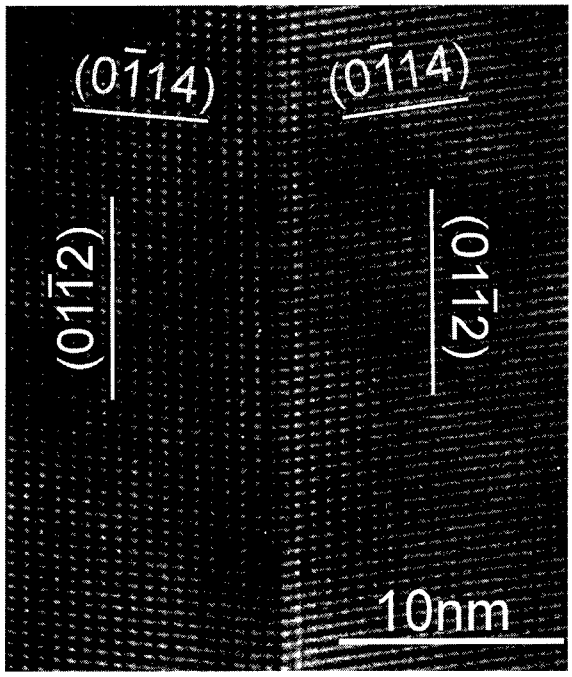

Fig.4. HREM image of symmetrical $\Sigma 7[0\bar{1}11]/180°$ grain boundary in sapphire bicrystal.

As a next step, the relative displacement perpendicular to the GB should be determined, keeping the relative displacement parallel to the GB obtained in the above. Here, d represents the interplanar distance between the oxygen-terminated surface in crystal A and B. The displacement perpendicular to the GB was determined by calculating BOP and NC at every 0.01nm as a function of d. BOP used in the present study was an average BOP between Al in crystal A and O in crystal B, and between Al in crystal B and O in crystal A.

Fig.3(a) shows the Al-O BOP as a function of d, indicating that the BOP is maximized at around d=0.13nm. Since BOP corresponds to the degree of covalency, the degree of covalency is considered to be maximum at around d=0.13nm.

Fig.3(b) shows the Coulomb's force of Al-O bonding perpendicular to the GB as a function of d, which was obtained by calculating the values of NC. In this calculation, the charges of Al and O were assumed to be the respective NC. This result indicates that the ionicity also maximizes at around d=0.13nm. Consequently, the most stable atomic structure in $\Sigma 7[0\bar{1}11]/180°$ grain boundary will be such that the two oxygen-terminated $(01\bar{1}2)$ plane are joined each other with the distance of about 0.13nm, keeping the geometric relationship mentioned above .

Fig.4 is a high resolution electron micrograph of the $\Sigma 7[0\bar{1}11]/180°$ grain boundary. The observed direction is parallel to the $[2\bar{1}\bar{1}0]$ for both adjacent grains. The set of (0001) and $(0\bar{1}11)$ planes can be seen in each grain, and the grain boundary plane is identified to be the $(01\bar{1}2)$ plane. As seen in the micrograph, two crystals are joined together with an atomic scale.

The atomic model obtained by the DV-Xα method is shown in Figure 5(a) where the oxygen atoms correspond to small circles and the aluminium atoms large ones. The parameters of the super-

cell in the calculations were 3.683× 3.589× 0.475nm with 742 atoms. The calculations were actually performed over a range of thickness from 2 to 20nm, and a range of defocus from 20 to -60nm. The best matching was obtained at a thickness of 11nm and defocus of -12nm as shown in Fig.5(b). This simulated image agrees well with the experimental image in Fig.5(c), which suggests that the actual structure of the grain boundary is similar to that in Fig.5(a). In conclusion, the DV-Xα calculation is considered to be effective to understand the actual atomic structure in grain boundaries in ceramics.

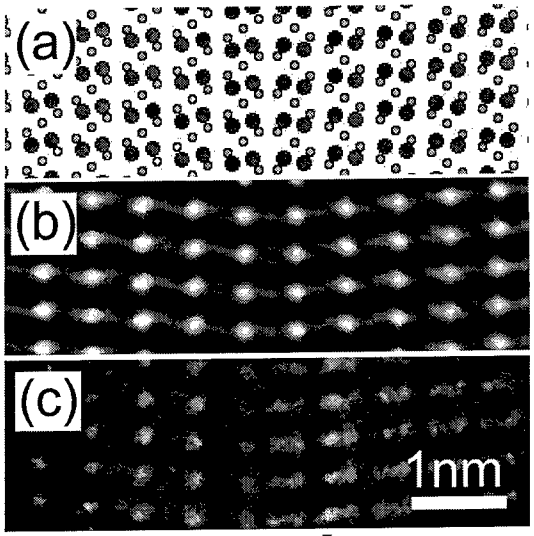

Fig.5. (a) A model oh the $\Sigma7[0\bar{1}1]/180°$ symmetrical grain boundary which is constructed from the present study and (b) computer-simulated and (c) experimental HREM image obtained at the sample thickness of 11nm and defocus of -12nm.

Conclusion

The bicrystal with $\Sigma7[0\bar{1}1]/180°$ grain boundary was fabricated by hot-joining method, and the atomic structure was calculated by DV-Xα molecular orbital method. The atomic structure was compared with the experimental high resolution electron image, and the following results were obtained.

1. The displacement parallel to the GB between two crystals can be determined by a simple geometry.
2. The displacement perpendicular to the GB can be determined by calculating the BOP and NC between Al-O bonding across the GB.
3. The atomic structure of $\Sigma7[0\bar{1}1]/180°$ grain boundary is formed so that the two oxygen-terminated $(0\bar{1}\bar{1}2)$ planes are joined each other at a distance of about d=0.13nm. This result agrees well with the experimental high resolution image of the grain boundary.

Acknowledgement

This work was supported by the Grant-in-Aid for Developmental Scientific Research (09450256) from the Ministry of Education, Science and Culture, Japan, and Iketani Science and Technology Foundation.

Reference

[1]B.Jouffrey and C.Colliex Ed., Proc.13th ICEM, Paris (1994)
[2]F.R.Chen, C.C.Chu, J.Y.Wang and L.Chang, *Phil.mag.A* **72**(1995),p.529
[3]M.Kohyama and R.Yamamoto, *Phys.Rev.B,* **50**(1994),p.8502
[4]P.Keblinski, S.R.Phillpot, D.Wolf and H.Gleiter, *Acta.mater.* **45**, (1997),p.987
[5]H.Adachi, M.Tsukada and C.Satoko, *J.Phy.Soc.Jpn.*, **45**(1978),p875
[6]J.Guo, D.E.Ellis and D.J.Lam, *Phys.Rev.B,* **45**(1992),p13647
[7]T.Watanabe, Y.Ikuhara and T.Sakuma, *J.Ceram.Soc.Jpn.*, In Press (1998)

Materials Science Forum Vols. 294-296 (1999) pp. 277-280

Grain-Boundaries in β-SiC: A Joined HRTEM and Numerical Atomic Study

C. Godon[1], C. Ragaru[1], O. Hardouin Duparc[2] and M. Lancin[1]

[1] CMC, Laboratoire de Physique Cristalline, Institut des Matériaux de Nantes, Rue de la Houssinière, B. P. 32229, F-44322 Nantes, France

[2] Laboratoire des Solides Irradiés, CEA-CEREM, CNRS UMR 7642, École Polytechnique, F-91128 Palaiseau Cedex, France

Keywords: Grain Boundary, β-SiC, HRTEM, Atomistic Simulation

Abstract

The β-grains which develop during recrystallisation contain many small {112}Σ=3 boundaries. Their structure is characterised by HRTEM performed at 300 kV and image contrast is simulated in order to determine the atomic reconstruction. We perform atomistic calculations (molecular dynamics) with the angular N-body Tersoff potential adapted to SiC in order to compare these reconstructions with our HRTEM observations.

Introduction

During sintering of β-SiC with B and C additives, grain growth results in the formation of faulted β-SiC and α-SiC. The structures of the observed grain boundaries depend on the growth mechanism which is related to the polytype. Pirouz and Yang [1] made a previous study of a {112}Σ=3 twin in SiC-CVD, but the atomic structure was not clearly established. In this paper, we focus our attention to {112}Σ=3 boundaries both from an experimental and a calculational point of view.

Boundary structures

The twins are imaged by HRTEM with a 300 keV microscope with a point to point resolution equal to 0.17 nm (H9000NAR Hitachi). The images are filtered and Si and C atoms localised as described in ref. [2, 3]. In figure 1, we show the image of a $(11\bar{2})\Sigma=3$ boundary obtained in white atoms. From this image, we can deduce that the boundary is a paratwin and that there is no significant rigid body translation along the [111] direction. Four atomic models with no rigid translation along this direction have been investigated by the way of the simulation of image contrasts [2, 3] using the multislice method (Stadelmann EMS software). Two of these models are derived from Möller's one and from Pond et al's one proposed in Si [4, 5]. The two others are alternative models, one with one structural unit (S.U.), the other with two S.U.'s which are symmetrical with respect to the $(11\bar{2})$ plane. The calculated positions of the atoms which form these S.U.'s can be seen in figure 4.
Pond et al.'s model gives rise to a contrast which is not similar to the one of the HRTEM image (fig. 2). The three other models are in closest agreement with experiment and a difference between them is difficult to detect. However, the alternative model with one S.U. seems to better describe the asymmetry of the experimental image (fig. 3).

Atomistic calculations

We perform molecular dynamics simulated annealing calculations using the angular N-body potential of Tersoff adapted to SiC. One can find in the literature several sets of parameters for this empirical potential. We choose to test the original one, published by Tersoff [6] and a second one, which is described in a paper from Huang et al. [7], and which introduces a different set of parameters for the

carbon. The Tersoff potential uses parameters for Si-Si and C-C interactions which are fitted for these pure elements and parameters for Si-C interactions which are obtained by arithmetic or geometric averages of the parameters determined for simple elements.
In the Tersoff potential, the assumption is made that only the nearest neighbours interact with each atom, so that one atom has four nearest neighbours. But, as previously shown by Tang and Yip [8], under large compression of the cubic cell, second nearest neighbours between Si-Si begin to interact with each other, and the cohesive energy increases too much with respect to theoretical equations like the Birch equation. This effect occurs when the bond length r_{ij} is lower than $0.984*r_0$, r_0 being the bond length at equilibrium. To avoid this problem, we choose to carry out the calculations taking only into account the neighbours which are located at less than 2.55 Å from one atom. Let us recall that with this potential, r_0 is equal to 1.87 Å, and that Si-Si bond length is equal to 2.34 Å in Si diamond cubic crystal and C-C bond length to 1.54 Å in diamond.

We carry out the calculations for the three models which are in closest agreement with the experimental data, as previously mentioned. We also check the model derived from Pond et al.'s reconstruction proposed for Si [4] together with a fifth model, derived from Papon and Petit's one [9]. Although these last two models have been found to disagree with the experiment, the first one because of the contrast of the simulated image which is not similar to the experimental one, and the second one because of the body rigid translation of 0.65 Å it involves, it is interesting to compare their interfacial energies found with our calculations with those published by Kohyama and Yamamoto [10].
All models have two dimensional periodicity parallel to the interface. Because SiC is not centro-symmetric, one can neither use the anti periodic (Möbius) nor the periodic (Born von Karman) boundary conditions normal to the interface. We have to either use rigid borders or free surfaces. We prefer this latter solution since it lets the rigid body displacements, if any, occur freely. Thanks to the short range character of the Tersoff potential, the supercells have only two slices in the $[1\bar{1}0]$ direction. The periodicity unit in the [111] direction is either one or two when we have to take into account one or two different structural units (S.U.) respectively.
For the model derived from Pond et al's and for the two alternative models, we choose to bond together the trivalent carbon atoms in the $[1\bar{1}0]$ direction. For all these three models , the C-C bond length is included in the range 1,64 - 1,67 Å. The bond length distortions at the interface are generally smaller than 10%.
In table 1 we give the interfacial energies obtained with the two sets of parameters for the cells which do not involve a large rigid body translation along the [111] direction. In the case of the model with a large rigid translation (model derived from Papon and Petit's), the interfacial energy is 1.238 J/m^2 (original set of parameters) or 1.283 J/m^2 (second set). Let us notice that since our models all have the same stoichiometry, we have not taken into account chemical potentials in our calculations. The corresponding calculated atomic positions are shown in figure 4.
If we except the model derived from Möller's one, the calculations carried out with the two sets give similar results. The low energy obtained with the original set described by Tersoff [6] for the Möller's model seems odd, because this model involves pentavalent silicon and trivalent carbons and should have a high energy. We conclude that the second set of parameters is more valid.
Let us notice that the alternative model with one structural unit actually involves two rigid body translations, a first one of 0.6 Å in the $[1\bar{1}0]$ direction, which cannot be seen in HRTEM images, and a second one of 0.25 Å in the [111] direction, which is small enough to be undetectable on images.

Discussion

The model derived from Papon and Petit's one, which implies a large rigid translation, has a larger energy than the Pond et al.'s model, in agreement with Kohyama and Yamamoto calculations [10]. The lowest energy is obtained for the reconstruction derived from the Pond et al.'s model. But it disagrees with the simulation made with the multislice method. The comparison between the HRTEM image, the simulations and the calculations seems to indicate that a model with a higher interfacial energy is in better agreement with experiment. Some explanations can be proposed. We first have indeed to be careful with the empirical potential used, because of the spurious effect induced by the Si-Si second neighbours interaction which can sometimes appear. For this reason, we had to limit the neighbourhood we take into account. As a result we have probably neglected the influence of some interactions between Si-Si atoms which are just a little more further apart than the chosen cut-off

radius. Moreover the calculations are carried out with supercells which simulate one twin, infinite in size, whereas the twins actually observed and reported here have only a limited size. They consist of a stacking of six planes which is limited by two (111)Σ=3 twins. These two twins may influence the atomic structure of the sample. It could be interesting to observe a larger boundary to verify the effect of the {112}Σ=3 twin size on the image contrast and then on the atomic reconstruction. Improving Tersoff's potential or using quantum semi-empirical tight binding modelisations could also be useful although this latter modelisation is much more computer demanding. *Ab initio* calculations still seem to be out of reach to simulate several boxes with several hundreds of atoms each.

Table 1 : Calculated interfacial energies

Model	Original set	Second set
A-model : derived from Möller's one	1.057 J/m^2	1.424 J/m^2
B-model : derived from Pond et al's one	1.171 J/m^2	1.186 J/m^2
C-model : alternative model with one S.U.	1.522 J/m^2	1.508 J/m^2
D-model : alternative model with two S.U.'s	1.676 J/m^2	1.654 J/m^2

References :

[1] P. Pirouz and J. Yang, Mat. Res. Soc. Symp. Proc., 183 (1990), p. 173.
[2] C. Ragaru, PhD. Thesis, Université de Nantes (1997).
[3] C. Ragaru, M. Lancin and C. Godon, submitted to MMM (1998).
[4] R. C. Pond, D. J. Bacon and A. Bastaweesy, Inst. Phys. Conf. Ser., 67 (1983), p. 253.
[5] H. J. Möller, Phil. Mag., A43 (1981), p.1045.
[6] J. Tersoff, Phys. Rev. B, 39, (1989), p. 5566.
[7] H. Huang, N. M. Ghoniem, J. K. Wong and M. I. Baskes, Modelling Simul. Mater. Sci. Eng., 3 (1995), p. 615.
[8] M. Tang and S. Yip, Phys. Rev. B, 52 (1995), p. 15150.
[9] A. M. Papon and M. Petit, Scripta Metallurgica 19 (1985) p. 391.
[10] M. Kohyama, R. Yamamoto, Solid State Phenomena, 37-38 (1994), p. 55.

Fig.1 : Fourier filtered image of the $(11\bar{2})\Sigma$=3 viewed along the $[1\bar{1}0]$ direction .

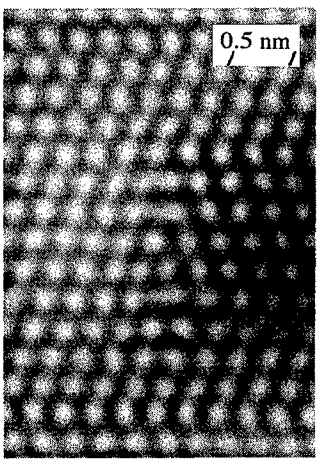

Fig. 2: Simulation of the model derived from Pond et al.' one
Δz = 8 nm, thickness = 2.1 nm

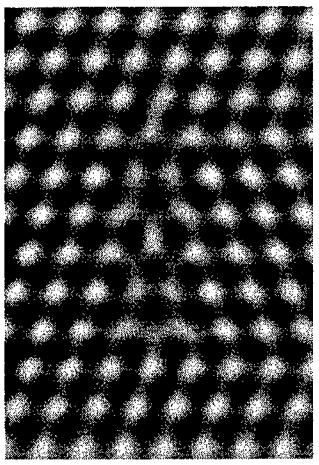

Fig. 3: Simulation of the alternative model with one S.U.
Δz = 8 nm, thickness = 2.1 nm

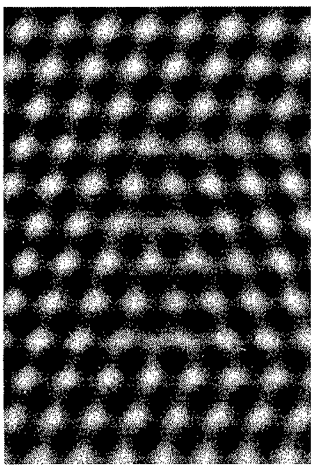

Fig 4 : Calculated supercells
Large circles correspond to silicon atoms, small circles to carbon atoms

a) A-model : derived from Möller's one

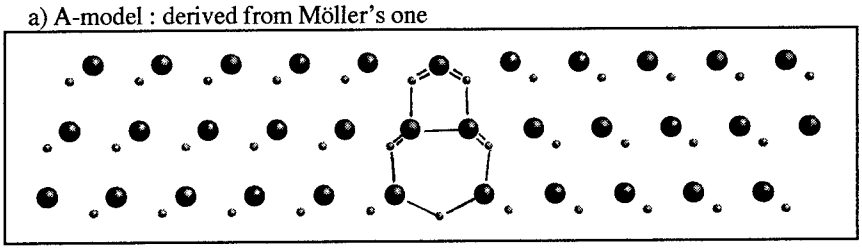

b) B-model : derived from Pond, Bacon and Bastaweesy's one

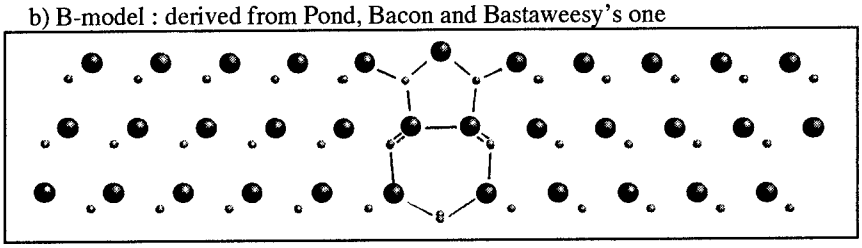

c) C-model : alternative model with one S.U.

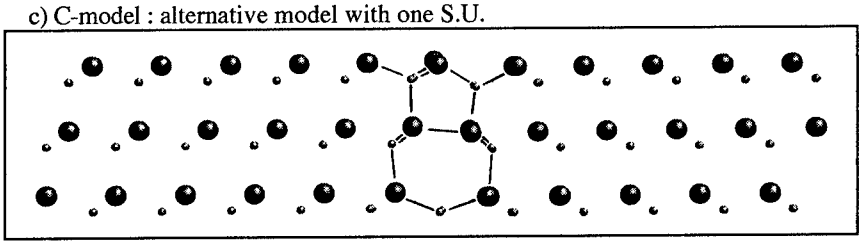

d) D-model : alternative model with two symmetrical S.U.'s / $(11\bar{2})$ plane

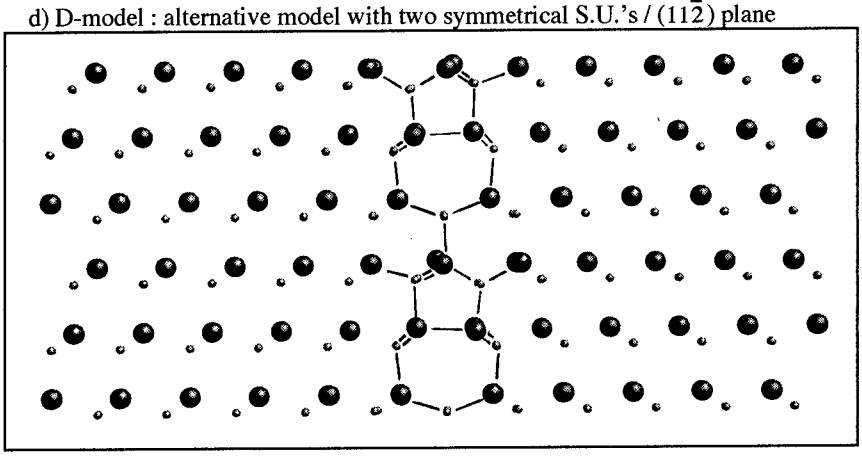

Materials Science Forum Vols. 294-296 (1999) pp. 281-284

Near Coincidence Grain Boundary in Alumina

S. Lartigue-Korinek[1] and S. Hagège[2]

[1] Laboratoire d'Etude des Matériaux Hors d'Equilibre, Université Paris XI, F-91405 Orsay, France

[2] Centre d'Etudes de Chimie Métallurgique, UPR CNRS 2801, F-94407 Vitry-sur-Seine, France

Keywords: Alumina, Twin Boundary, Near Coincidence Orientation, Intrinsic Dislocations, TEM, HREM

Abstract : The rhombohedral twin orientation in alumina has been obtained by diffusion bonding and studied by transmission electron microscopy. It corresponds to a Σ7 near coincidence orientation with a grain boundary plane parallel to $(01\bar{1}2)$. The grain boundary contains two arrays of dislocations with the same line direction and alternately distributed Burgers vectors which are translation vectors of the DSC lattice. The associated step vectors are large, up to 1.75nm. Starting from symmetry considerations on the various dichromatic complexes, all possible unrelaxed atomic configurations are constructed. Oxygen terminated grain boundary structures as well as those passing through non occupied aluminium sites are selected on the basis of optimal compacity at the interface. Correlations between simulated and experimental high resolution images favor the structures based on empty octahedral sites at the interface. The most probable structure has a two fold screw axis at the interface and leaves Al-O bonds with very little distorsions from the perfect coordination in alumina.

I- INTRODUCTION

Most of TEM studies on grain boundary structure and related properties in alumina have been performed on polycrystalline materials. Our previous works have established the descriptions of near coincidence grain boundaries in rhombohedral symmetry [1] and emphasised the role of segregation of different species on the superplastic behaviour of fine grained alumina [2]. A relationship between the grain boundary characteristics and the nature and level of segregation was revealed by STEM [3]. In particular, a preferential segregation of yttrium has been detected in $(01\bar{1}2)$ planes and also on grain boundary dislocations. It is thus interesting to better analyse the structure and chemistry of grain boundaries in well defined bicrystals. This communication presents preliminary results on a symmetrical tilt bicrystal close to the Σ7 orientation with a common $(01\bar{1}2)$ plane.

II- EXPERIMENTAL

E. Stepantsov an R. Vassiliev, from the Institute of Crystallography in Moscow, obtained the bicrystals by a diffusion bonding procedure. Thin foils are cut with the grain boundary edge-on and the directions $[2\bar{1}\bar{1}0]$ of crystal 1 and $[11\bar{2}0]$ of crystal 2 set parallel to the electron beam. They are prepared using the tripode technique and a short low angle ion thinning. They are analysed by conventional TEM and HREM at 200 kv (Cs = 0.4 mm).

III- CRYSTALLOGRAPHY

A common $(01\bar{1}2)$ grain boundary plane corresponds to the rhombohedral twin orientation. As c/a is irrational, coincidence only exists in the grain boundary plane. However a 3-dim. coincidence with Σ = 7 occurs for $(c/a)^2 = 15/2$ (Fig. 1). In this case, the deformation value required to bring the two multiple into coincidence cells is equal to 0.3% [1].

The coincidence lattice is defined by $CSL_1 = 1/3\ [2\bar{1}\bar{1}0]$, $CSL_2 = 1/3\ [0\bar{1}11]$ and $CSL_3 = 1/3\ [1\bar{8}\bar{7}\bar{3}]$; the DSCL by $\mathbf{b}_1 = 1/21\ [01\bar{1}\bar{1}]$ (0.073 nm); $\mathbf{b}_2 = 1/21\ [7\underline{1}\underline{1}\bar{4}3]$ (0.421 nm) and $\mathbf{b}_3 = 1/21\ [74\bar{1}\bar{1}3]$. Only **b**1 belongs to the projection of figure 1. It corresponds to the shear vector of the rhombohedral twin.

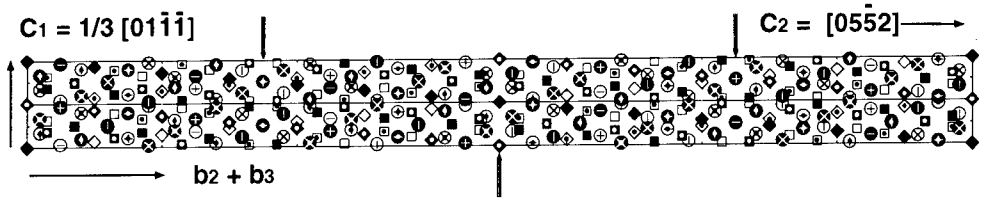

Figure 1. Dichromatic complex of the coincidence unit cell. The origin is chosen on a common non occupied octahedral site (diamond symbols at level 0, 1/2). Crystal 1 is white, crystal 2 is black. Oxygen is denoted by large circles and is located at 8 different levels along the projection axis (| = 0.153, — = 0.194, ┼ = 0.306, X = 0.347, smaller circles add 0.5 to the projection depth). Aluminium atoms are square and at level 0 and 1/2. Shaded arrows point to the second coincident octahedral site plane (x=1/2) and at the two common oxygen planes (x=1/4, 3/4) for which the atoms of the two crystals are not at the same level.

The grain boundary presents a deviation from the coincidence that is accommodated by an array of dislocations which are spaced at 26 nm (Fig. 2).The deviation axis ρ is determined from the measure of displacement vectors joining the Kikuchi map centres for several rotation axes set parallel to the electron beam. ρ is close to the dislocation line **t** situated at 10° from $[2\bar{1}\bar{1}0]_1$. Thus the deviation has mainly a tilt character with $\Delta\theta = 0.8°$.

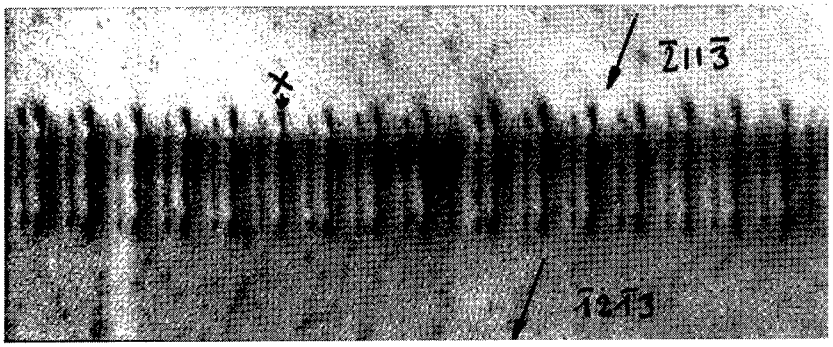

Figure 2. CTEM micrograph of an array of intrinsic dislocations imaged in a common Bragg condition and revealing two types of contrasts alternating along the boundary.

IV - INTERGRANULAR DISLOCATIONS

The grain boundary contains mainly two types of dislocations with the same line direction and Burgers vectors alternately distributed (Fig. 2). The Burgers vector can be measured on the HREM micrograph in figure 3 where $\mathbf{b} = \mathbf{S_1}\text{-}\mathbf{S_2}$. $\mathbf{S_1}$ and $\mathbf{S_2}$ relate two equivalent points in the grain boundary on each side of the defect in the two crystals. The step heights are defined as $h_1=\mathbf{S_1}.\mathbf{n_1}$, $h_2= \mathbf{S_2}.\mathbf{n_2}$.

The projected Burgers vectors of the two dislocations in figure 3 are : $\mathbf{b}_{xp}$ = 1/14 [05$\bar{5}$2] + 1/21 [01$\bar{1}\bar{1}$] and $\mathbf{b}_{yp}$ = 1/14 [05$\bar{5}$2]; $\mathbf{b}_x$ and $\mathbf{b}_y$ have a component along the $[2\bar{1}\bar{1}0]_1$. The measured step heights are consistent with the following solution :

$\mathbf{b}_x=\mathbf{b}_2+\mathbf{b}_1$ hx=1.39nm (crystal 1) and 1.75nm (crystal 2)
$\mathbf{b}_y=\mathbf{b}_3$ hy=1.05nm (crystal 1) and 1.39nm (crystal 2).

These vectors account for the measured distance between the dislocations : d= 26 nm, close to the theoretical value $d_{theo} \cong b/\theta$ = 28 nm. They are also confirmed by the contrasts of the dislocations analysed by CTEM. Our results are not in agreement with those proposed in a recent paper [4] on a similar type of bicrystal, also obtained by diffusion bonding. In that work the dislocations have the $\mathbf{b}_{xp}$ Burgers vector, misinterpreted as a DSC unit vector.

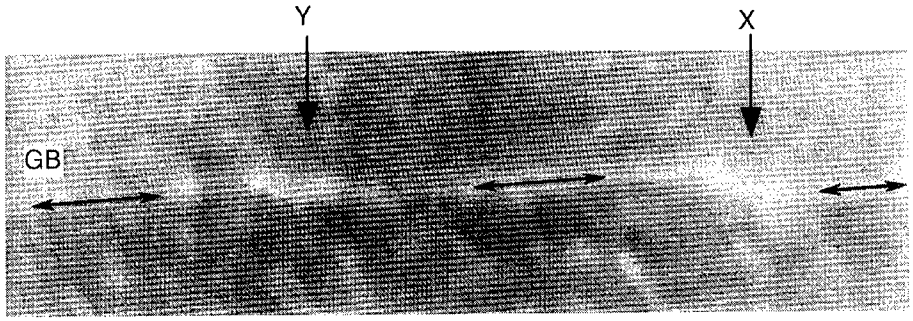

Figure 3. HREM of two intrinsic dislocations (X, Y). The interface is outlined by double sided arrows enhancing the step character of the dislocations. The scale is given by the interplanar distance parallel to the boundary (0.348 nm).

V - GRAIN BOUNDARY STRUCTURE

As seen on figure 1 the stacking of the rhombohedral planes is composed of pure oxygen, pure aluminium and empty octahedral sites. Therefore the interface can be composed by overlapping one of these plane types for each crystal. For steric reasons only interfaces containing the same type of atoms or sites from both crystals will have to be considered. The compacity of alumina is based on the packing of oxygen ions and it is therefore reasonable to have an interface based on oxygen. On the other side, empty octahedral sites are a centre of symmetry in alumina. It has been shown in hexagonal symmetry that interfaces based on a centre of symmetry have a dichromatic complex of a higher order and lead to lower energy configuration [5]. By taking into account these restrictions, only six dichromatic complexes with five different symmetry groups occur. They all have at least one symmetry element (mirror, two fold axis) parallel to $(01\bar{1}2)$. Two complexes are based on coincident empty octahedral sites at the interface, three have oxygen atoms at the interface. For each of these complexes the interface, parallel to $(01\bar{1}2)$, can be placed at two different positions for which the common atoms or sites can be at the same level or at different levels along the projection axis (fig. 1).

Figure 4f shows the experimental high resolution image of the $\Sigma 7$ interface with a symmetrical white contrast at the interface. The comparison of sets of simulated images (EMS software and multislice calculation), taken at different defocalisations and thicknesses, asserts, without ambiguity, that this image corresponds to a defocalisation of -55nm and a thickness foil of 15 nm. For these conditions white dots correspond to the non occupied octahedral sites of the structure. Four models, based on these empty sites at the interface, are represented in a, b, c and d. They differ in the symmetry element present at the interface. The first one has a 2-fold symmetry at the interface as the second one has a mirror plane. The last two are obtained by adding a glide component to these symmetry elements. These four models have a different interface structure but provide identical simulated images (Fig. 4e) which fit perfectly to the experimental image (see overlap in fig. 4f). Only the configuration in figure 4c must be retained as it involves the least distorted Al-O bonds. The models 4a and 4b have a pure symmetry element at the interface and provide distances too short to be compatible with the structure of alumina. Model 4d (glide plane) is less distorted but the model 4c (2 fold scew axis) is very close to perfect alumina. These results are in perfect agreement with the approach proposed by Geipel et al [6], based on the geometrical principles of mechanical twinning. They also indicated the "screw twin" configuration as the most probable.

REFERENCES

[1] H. GRIMMER, R. BONNET, S. LARTIGUE, L. PRIESTER, Philos. Mag. A, **61** (1990) 493.

[2] S. LARTIGUE-KORINEK and F. DUPAU, Acta Metal. Mater., **42** (1994) 293.

[3] D. BOUCHET, F. DUPAU and S. LARTIGUE-KORINEK, Microsc., Microan., Microstr. **4** (1993) 561.

[4] F.R. CHEN, C.C. CHU, J.Y. WANG and L. CHANG, Philos. Mag. **72** (1995) 529.

[5] S. HAGEGE, M. MORI and Y. ISHIDA, J. Phys. **C1-51** (1990) 161.

[6] T. GEIPEL, K.P.D. LAGERLOF, P.PIROUZ and A.H. HEUER, Acta Metall. Mater. 42 (1994) 1367.

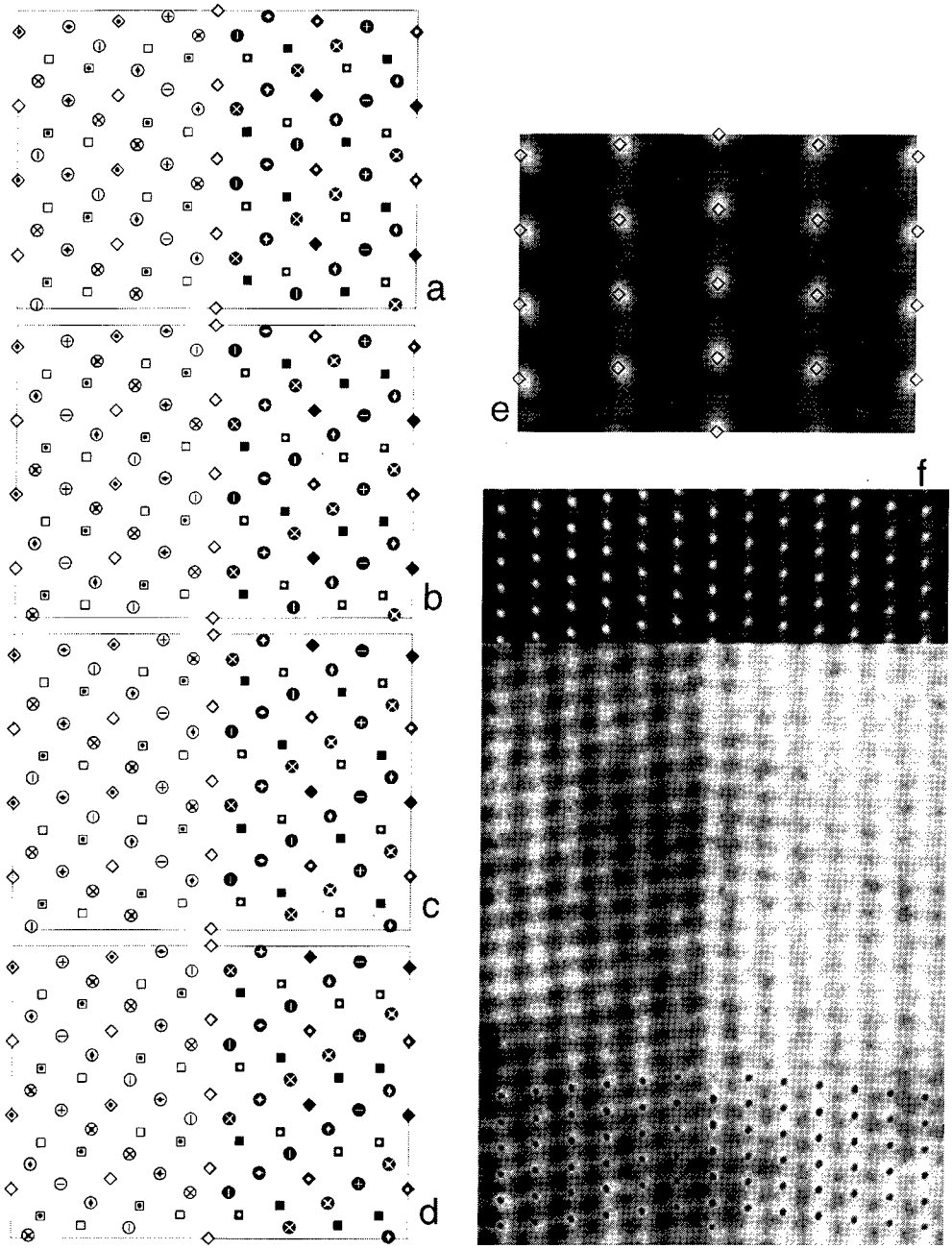

Figure 4 . Σ7 twin boundary in alumina. The simulated image (e) is calculated from either model a, b, c, or d. Same notations as for figure 1. The simulated image is overlapped on the top of the experimental image (f). Black dots at the bottom of the image are the negative of the simulated image and enhance the perfect fit between experiment and simulation. The scale is given by the interplanar distance parallel to the boundary (0.348 nm).

Materials Science Forum Vols. 294-296 (1999) pp. 285-288

Atomic Structure of the Grain Boundary in α-SiC

C. Ragaru[1], M. Lancin[1] and J. Thibault[2]

[1] CMC, Physique Cristalline, Institut des Matériaux de Nantes,
2 Rue de la Houssinière, F-44232 Nantes, France

[2] SP2M/S, CENG, 17 Rue des Martyrs, F-38054 Grenoble, France

Keywords: Grain Boundary, α-SiC, HRTEM

Abstract

The atomic structure of twin boundaries formed by β ⇒ α phase transformation in sintered SiC is derived from HRTEM images. The zones of bad match consists of 30° Shockley partials partly combined. A nucleation mechanism of the twins is discussed.

1. Introduction

Polytypic transformation was widely studied in SiC and several mechanisms were proposed [1,4]. However, the β (cubic) ⇒ α (hexagonal + rhomboedral) phase transformation which occurs during the sintering of β-SiC at temperature greater than 1900°C is still to be clarified. This phase transformation results either in α plates or α feathers [4,12] . The first exhibit no orientation relationships whereas the second are transformation twins [9,11]. The twins consist of two grains sharing a $[11\bar{2}0]$ axis. According to the dihedral angle between the (0001) planes of their twin grains, feathers are categorised into small and large angle twins. The formation of transformation twins involves a nucleation and a growth mechanism [13]. The transformation mechanisms proposed in SiC may explain the plates but not the feathers nucleation. A first HRTEM study of a feather boundary showed that it can be described as an array of dislocations [15]. However, it did not clarify the chemical type and the origin of these dislocations, the driving force and thus the feather formation. It has to be found how feathers are formed and why either feathers or plates are observed in fully transformed materials. A new study of the microstructure of sintered SiC has thus been performed [16]. This work deals with the characterisation of the boundaries of large angle twins.

2. Materials and techniques

β-SiC powder was conventionally sintered or hot pressed (12.6 MPa) with B and C additives [9, 11]. Both materials contain about 80% of α-phase which consists of feathers, a few hundred microns in size (Fig.1). HRTEM was performed at 400 keV (Jeol 4000 EX, Cs =1mm) or at 300 keV (Hitachi H9000NAR, Cs = 0.7mm)). Images were processed using Semper. C and Si atoms were localised using the asymmetry of the dumbbells after an image filtering derived from Spence method [14, 15].

3. Atomic structure of the grainboundary

Typical high angle boundaries are imaged along the common $[11\bar{2}0]$ axis (Fig. 2 and 3). Despite the large amount of stacking faults which is visible on the micrographs, both twin grains generally exhibit the same structure at the scale of electron diffraction. Large angle feathers have a 15R structure and a dihedral angle $2\alpha = 65°5$ with a few exceptions ($2\alpha = 64°5$ or 64°) related to the twin grain polytype.

3.1. Atomic structure of 15R feather, $2\alpha = 65°5$

In the 15R feathers ($2\alpha = 65°5$), the grains generally contain 4H stacking faults (Fig. 2a). Each twin grain consists of a stacking of C and T structural units describing perfect crystal β-SiC and $\{111\}\Sigma=3$ twin respectively. The α phase can thus be described as a stacking of cubic layers delimited by

{111}Σ=3 twins. In such a description, images show the projection of the Si-C dumbbells in the ($\bar{1}$01) plane. At the boundary, zones of good and bad match are clearly visible on the micrograph. The zones of good match are formed of C and T units, possibly distorted, but the stacking crosses the boundary with little distortion. Slightly distorted T are also observed next to the zones of bad match. Each zone of bad match consists of two S_2 units located on either side of the boundary. S_2 contains two trivalent silicon atoms and five faulted units called C_{tri}, T_{tri} and C^*_{tri} (tri = trivalent atom, C* = C unit with one dumbbell). Simulated and experimental images are in agreement (Fig. 2c). A Burgers circuit drawn around each S_2 results in $a_\beta/6$ <112> Burgers vector (Fig. 2d).

3.2. Atomic structure of 4H feather, 2α = 64°

Four of the seventy large angle feathers which have been identified exhibit a dihedral angle equal to 64°. Both twin grains have a 4H structure but they contain 15R stacking faults (Fig. 3a). As above, the boundary successively consists of zones of good and bad match. The zones of good match contain distorted C and T units (Fig. 3b). A single structural unit S_2', located in both twin grains, describes each zone of bad match. S_2' consists of nine faulted units, $3C_{tri}$, $2T_{tri}$ and $3C^*_{tri}$ and the trivalent atoms have the same chemical type as above (Si). It is possible to draw a Burgers circuit around the bad match located in each twin grain. We obtain one $a_\beta/6$ <112> Burger's vector in each twin grain with the same orientation as in 15R twin grains.

4. Discusion

A $a_\beta/6$<112> resultant Burgers vector corresponds to the projection of two 30° Shockley partials with either a same or a different orientation. In β-SiC [15], such as in Si [17,18], the core of one 30° Shockley partial dislocation consists of three faulted units, C_{tri}, T_{tri} and C^*_{tri}. Therefore, the S_2 unit corresponds to some reconstruction of two partials dislocations located in two successive {111} planes. These dislocations are Si(g) partials because their core contains one column of Si trivalent atoms. The S_2' unit clearly derives from two S_2 unit partly combined. This means that the partial dislocations located in both branches of a 4H feather are partly combined whereas those located in a 15R feather are contiguous but distinct.

The study of 15R feather boundaries using Burger's circuits confirms the previous result [14]. However, Burger's circuits result in the same dislocations in 15R and 4H feathers whereas the structural units are different. The analysis of the boundaries using Burger's circuit is thus not accurate enough to reveal the differences of the boundary structure as a function of the feather polytype.

The zone of bad match consists of nine and ten faulted units in 4H and 15R feathers respectively. The energy of the grain boundary must be smaller in 4H than in 15R feathers but 4H feathers are extremely rare. Therefore, the grain boundary energy likely has no influence on the feather nucleation.

The atomic structure of large angle feathers suggests that the nucleation is due to an interaction between two sets of Si(g) gliding in two sets of {111} planes. These Si(g) are located in two adjacent planes every four or five planes {111} depending on the structure. Among the models proposed for the $\beta \Rightarrow \alpha$ phase transformation, only Pirouz's one could fulfil this requirement and we thus discuss its application to the feather nucleation.

In the case of a Frank Read source, the Si(g) partials glide in one set of {111} planes and have the same Burgers vector, b_i. In the two sets of {111} planes, it is possible to find Si(g) partials, with b_1 and b_2 vector respectively, the interaction of which results in the tilt boundary observed (eg: $b_1 = a_\beta/6$ [$\bar{1}$12] and $b_2 = a_\beta/6$ [$\bar{2}$11] with a tilt axis [$\bar{1}$01]). All other possible combinations of Si(g) result in twist or mixed boundaries.

Pirouz's model is based on the different mobility of Si(g) and C(g) partials. Such a requirement seems to be fulfil in SiC, even at high temperature [19]. It also assumes i) an applied stress (σ_a) high enough to overcome the line tension force (F), and the stress σ_{SF} induced by the stacking fault energy and ii) a back stress force (σ_{bs}) applied by the gliding Si(g) partial on the source to promote for a $\beta \Rightarrow \alpha$ phase transformation. In SiC, σ_{SF} is equal or greater than 10MPa [19]. In pressureless sintered material, σ_a

$= \sigma_i$, where σ_i derives from concentration gradients of impurities in SiC [1]. The probability of a feather nucleation being similar in pressureless and hot-pressed materials, σ_i should be equal to about 10 MPa. The resultant stress $\sigma_r = \sigma_a - \sigma_{SF}$, which balances F, ranges between 0 and 20 MPa. That implies a critical source length $Dc \equiv \mu b / \sigma_r \geq 2$ μm. With such a Dc, a back stress force seems unlikely and Pirouz's model seems to be unsuitable to describe the feather nucleation. However, the activation of two Frank Read sources may explain the nucleation if we keep in mind that α phase is the most stable phase at high temperature, with B and C impurities. In such an hypothesis, the role of the back stress force is played by σ_{SF} which forces or prevents the partials to glide in successive {111} planes resulting in the α phase formation. The small difference in free energy of the polytypes and the local variation of internal stresses explain the microsyntaxy of the twin grains. The study of the boundaries of small angle feather confirms this model [15, 20].

With such a model, the α plate nucleation is more likely than the feather one. Both plates and feathers are observed at the beginning of the phase transformation but plates have nearly disappeared in materials containing more than 80% of α phase [9, 11]. The isotropy of the feather nucleus explains that feathers recrystallise at the expense of α plates during the sintering or subsequent anneals.

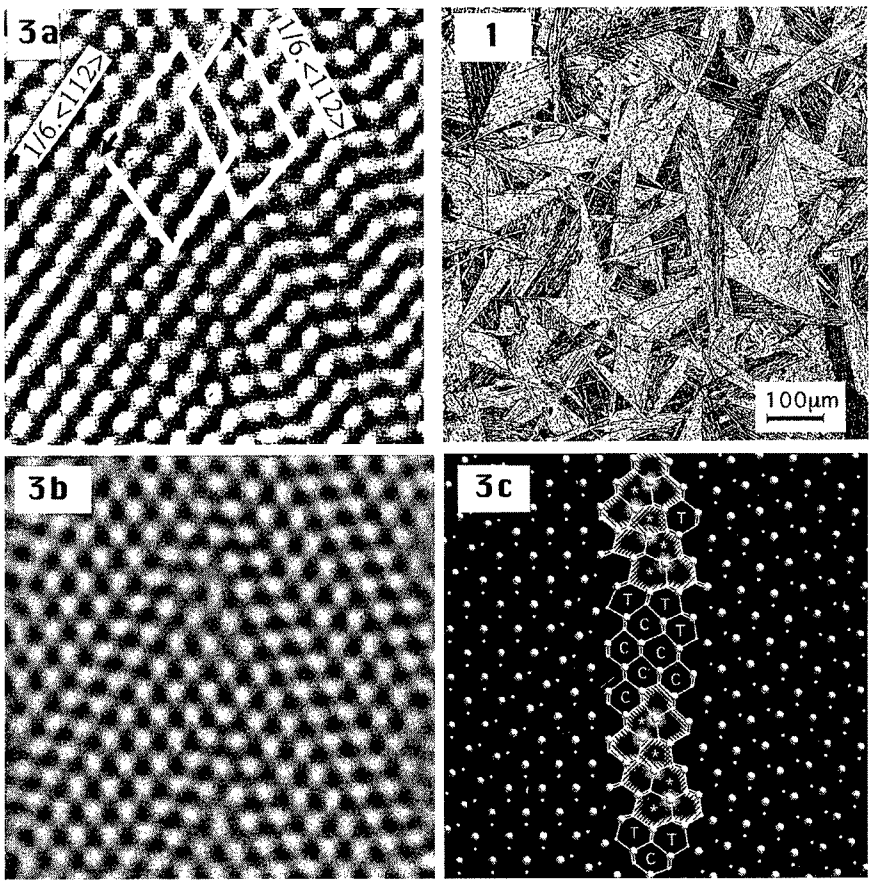

Figure1: Feathers revealed on an optical image of a sintered material (about 80% of α phase).

Figure 3: 4H feather ($2\alpha = 64°$) 3a) experimental image (white atoms) **3b)** simulated image ($\Delta z = 13$ nm, $e = 3$ nm) **3c)** Atomic reconstruction of the boundary which underlignes the S_2' SU.

Figure 2: 15R feather ($2\alpha = 65°5$) 2a) experimental image (white atoms) **3b)** simulated image (Δz = 13 nm, e = 3 nm) **3c)** Atomic reconstruction of the boundary showing S_2 in each twin grain **3d)** Burgers circuit drawn around each zone of bad match

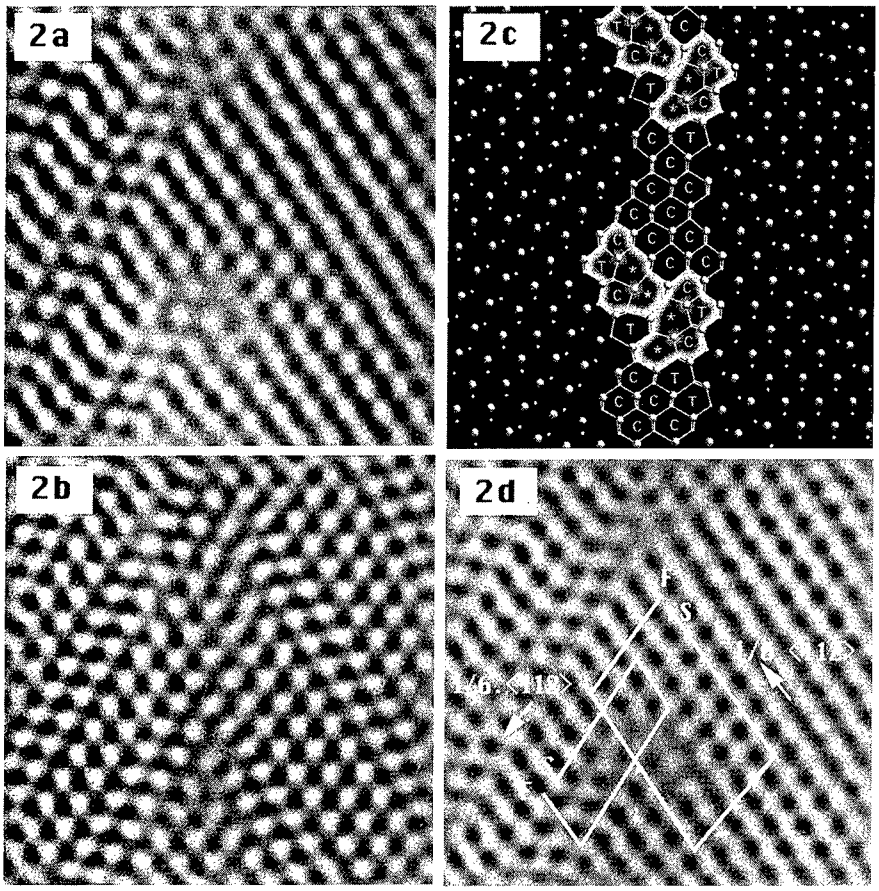

References

[1] D. Pandey, P. Krishna, Current Topics in Mat. Sciences (9) Ed. E. Kaldis, North holland (1982)
[2] P. Pirouz, J.W. Yang, Ultramicroscopy **51** (1993) p.189
[3] S.J. Lee, J. Vicens, phil. Mag. A **65** (3) (1992) p. 551
[4] T.E Mitchell, L.U. Ogbuji, A.H. Heuer, J. Am. Ceram. Soc. **61** (9-10) (1978) p. 412; L.U. Ogbuji, T.E. Mitchell, A.H. Heuer, J. Am. Ceram. Soc. **64** (2) (1981) p. 91.
[5]. C.A. Johnson, S. Prochazka, Ceramic Microstructures, Ed. R. Fulreth & J.A. Pask, Westview Press (1977) p. 366
[6] F. F. Lange T. K. Gupta, J. Am. Ceram. Soc. **59** (11-12) 537 (1976)
[7] K. R. Kinsman, S. Shinozaki, Scripta Metallurgica, **12**, 517 (1978)
[8] R. M. Williams et al. Com. Am. Ceram. Soc.C-62-64 (1984)
[9] M. Lancin, J. Mat sci., **19**, 4077 (1984)
[10] D. Stutz, S. Prochazka, J. Lorenz, J. Am. Ceram. Soc. **68** (9) 479 (1985)
[11] M. Lancin, F. Anxionnaz, J. Thibault, D. Stutz, P. Greil, J. Mat sci., **22**, 1150 (1987)
[12] T. Sakai, T. Aikawa, Com. Am. Ceram. Soc. **C-7** (1988)
[13] G. Friedel, Leçons de cristallographie, Berger-Levrault, Paris (1926)
[14] M. Lancin, J. Thibault, J. Phys. **C-5** (10) 305(1988)
[15] C. Ragaru, PhD. thesis, Université Nantes (1997)
[16] C. Godon, C. Ragaru, O. Hardouin Duparc, M. Lancin IIB 98 submitted
[17] S. Markund, Phys. Stat. Sol. B, **92** (1983) p.83
[18] A. Bourret, J. Thibault-Desseaux, F. Lancon, J. Phys. **C4**(9) (1983) p. 17
[19] M. L. Duval-Rivière, J. Vicens, Phil. Mag. A **69** (3) (1994) p. 451
[20] C. Ragaru, M. Lancin, J. Thibault, J. P. Rivière, Proceedings ICEM 14 (1998)

Materials Science Forum Vols. 294-296 (1999) pp. 289-292

Yttrium-Segregated Grain Boundaries in α-Al_2O_3: An EELS Study

M.A. Gülgün[1], W.Y. Ching[2] and M. Rühle[1]

[1] Max-Planck-Institut für Metallforschung Stuttgart, Seestr. 92, D-70174, Germany

[2] Department of Physics, University of Missouri-Kansas City, Kansas City, MO 64110, USA

Keywords: α-Al_2O_3, Segregation, EELS, ELNES, Ab-Initio Calculations, Yttrium Aluminate

ABSTRACT:

Segregated grain boundaries have a different chemistry and structure than the bulk of the grains. Yttrium segregated general grain boundaries (GB) in polycrystalline α- Al_2O_3 were investigated by electron energy loss spectrometry (EELS). Energy loss near edge structure (ELNES) spectra of Al-L and O-K edges from the segregated GBs and from the adjacent bulk alumina were experimentally obtained. Spatial difference method was applied to enhance the grain boundary features.

Reference spectra from different Y-Al-O compounds, i.e. $Y_3Al_5O_{12}$, $YAlO_3$, and $Y_4Al_2O_9$, as well as Y_2O_3 and α-Al_2O_3 were experimentally measured and theoretically calculated by the ab-initio self-consistent orthogonolized linear combinations of atomic orbitals (OLCAO) method. A comparison between the reference spectra and spatial difference spectra from the grain boundaries was used to study the local chemical and structural environment of the atoms at the segregated GBs.

INTRODUCTION:

Yttrium-doped α- Al_2O_3 (Y-AO) exhibits a creep resistance that is 1 to 2 orders of magnitude larger than the one of the undoped ceramic [1,2]. This improved creep behavior is attributed to a suppression of grain boundary diffusion in Y-AO [3]. Yttrium (Y) has a very limited solubility in α-Al_2O_3 (10 ppm) [4]. It tends to segregate to grain boundaries and free surfaces in the ceramic and precipitate out as $Y_3Al_5O_{12}$ (YAG) phase.

There are several studies on the mechanical behavior and microstructure of Y-AO as well as Y/MgO codoped α- Al_2O_3. General arguments in the literature claim that the enhanced creep resistance of the ceramic is a result of Y influence in the segregated grain boundaries (GB). The isovalent segregant, Y, is suggested to directly decrease the diffusion rate of the species (mainly oxygen) along the GBs, or to reduce GB dislocation motion, or to interfere with the dislocation accommodation process at the GBs [1,5]. All these phenomena are related to the atomic, chemical and electronic structure of these segregated boundaries. Therefore it is imperative to study the structure of the segregated GBs in order to gain insight into the enhanced properties of the material.

In recent years, electron energy loss spectroscopy (EELS), and in particular electron loss near-edge structure (ELNES) spectroscopy has gained considerable interest to investigate the local atomic and electronic structure in materials [6-8]. The ELNES of a scattering center contains information on its nearest neighbors coordination, i.e local chemical and structural symmetry around the atom under study. A carefully conducted ELNES measurement and a qualitative comparison with the reference spectra from compounds with known structures may lead to an understanding of the local symmetry around the atom undergoing electron excitation. The interpretation of the experimental spectra is also greatly facilitated through a comparison with the calculated electronic structure of the same material. EELS is especially suitable to study interphases because of the unmatched spatial resolution of dedicated electron microscopes presently available.

EELS studies of GBs in Y-AO were conducted. In order to help the interpretation of the GB spectra, O-K and Al-L edges of the compounds in the Y_2O_3 - Al_2O_3 binary phase field were also acquired. The results of a comparative study on the O-K and Al-L edge structures of Y-segregated GBs and reference compounds are presented.

EXPERIMENTAL PROCEDURES:

Yttrium doped (1000 ppm, Y/Al) α- Al_2O_3 ceramics were hot pressed at 1475°C under 50 MPa for 1/2 hour [1]. The microstructure and microchemistry of the samples were previously fully characterized by various electron microscopy techniques [9].
ELNES spectra were collected with a parallel electron energy loss spectrometer (PEELS) (GATAN 666) attached to a dedicated scanning transmission electron microscope (STEM, VG HB501 UX, Vacuum Generators) operated at 100 kV. The measurements were performed with a dispersion of 0.3 eV/ch with a 0.9 eV FWHM of the zero loss peak (energy resolution in this energy range). The convergence and collection semi-angles were 10 and 13 mrad, respectively. Spectra were acquired with the beam scanning a window of 3 nm by 4 nm. They were corrected for dark current and channel-to-channel gain variation in photodiode array. The spectra were deconvoled for multiple scattering effects.
The electronic structures of the Y-Al-O compounds were calculated using an ab-initio OLCAO method[10] within the local density approximation (LDA) of the density functional theory. Details can be found elsewhere [11]. The use of atomic orbitals in the basis set facilitates the decomposition of total density of states (DOS) into atomic and orbital components, or the local density of states (LDOS), using the Mulliken scheme. The symmetry projected unoccupied LDOS can be directly compared with the ELNES spectra.

RESULTS:

A background in the form of Ae^{-E} (E= energy loss in eV, A=const.) was subtracted from all the spectra presented in this section. Fig. 1 shows the grain boundary spatial difference spectrum and the bulk α- Al_2O_3 (AO) spectrum of the AL-$L_{2,3}$ edge together. The spatial difference spectrum was obtained by the following operation : $I_{SD} = I_{GB} - r*I_{bulk}$, where r is a constant. The two spectra are aligned in the energy axis with respect to their zero-loss peak (not shown). In the GB spatial difference spectrum, several features are different from the bulk alumina spectrum indicating a different local environment of the aluminum atoms in these Y-segregated GBs. The vertical guide lines are drawn in the graph to emphasize the difference and similarities. There is an additional low energy shoulder **A** (78.3 eV) at the edge onset of the Al-L edge in the spatial difference spectrum. The intensity of the peak labeled **C** (87.2 eV) is also enhanced with respect to the main peak **B** (79.6 eV) in the GB spectrum.

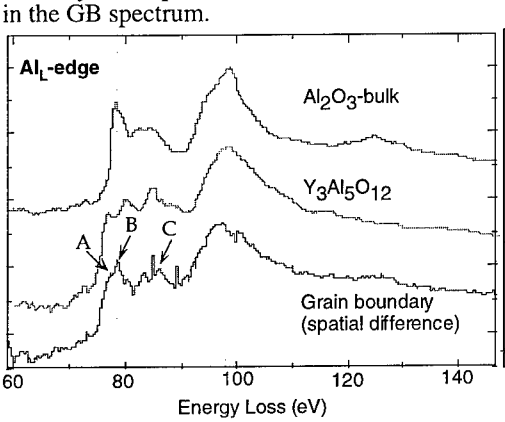

Fig. 1 . Al-L spatial difference spectrum from Y-segregated GB and spectra from bulk AO and YAG.

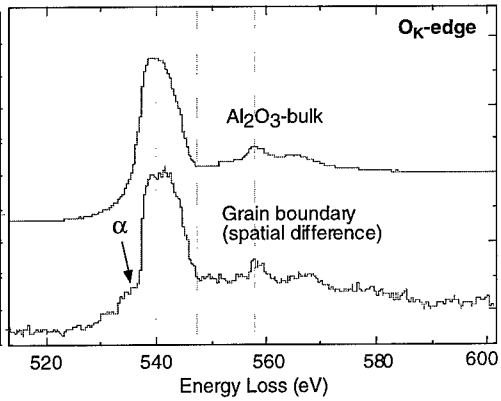

Fig. 2 . O-K spatial difference spectrum from Y-segregated GB and spectrum from bulk AO.

Fig. 2 contains the oxygen K-edge spectra for the bulk AO and the GB spatial difference. The differences between the bulk and the GB spectra are again distinguishable. There is a lower energy pre-peak α at the edge onset at approximately 535 eV. The main peak centered around 539.5 eV in the

bulk AO spectrum and the broad band in the spatial difference spectrum of the GB have the same FWHM (8 eV). However, this broad band of the GB spectrum appeared to have split into two peaks. The reference spectra for different chemical and symmetry fingerprints are acquired from the three Y-Al-O compounds and the α- Al_2O_3 and Y_2O_3.

The Al-L edges of the four aluminum (Al) containing members of the binary phase field are illustrated in Fig. 3. The oxygen (O) coordination around Al sites in these compounds are indicated on the left of each spectrum. Each Al-L edge is distinct from the others. Again the vertical guide lines are drawn to indicate the position of the peaks on the energy scale.

Fig. 4 shows the O-K edge spectra of these five compounds. Each spectrum appears to be a unique signature of the specific compound they originate from. Within the first 15 eV from the edge onset, AO has one broad peak whereas all the other compounds show a band with at least three distinguishable peaks.

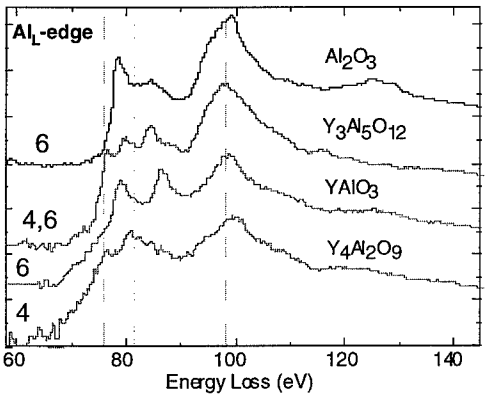

Fig. 3 . Al-L ELNES of Y-Al-O compounds along with spectrum from AO.

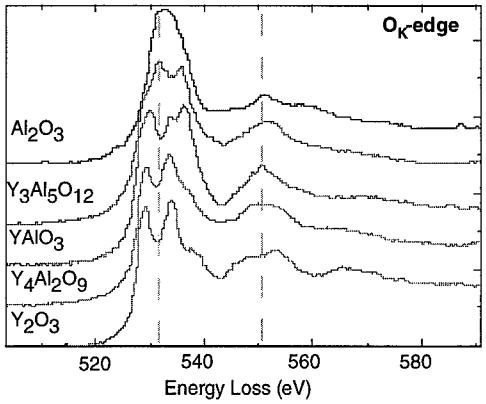

Fig. 4 . O-K ELNES of Y-Al-O compounds along with spectra from AO and yttria.

The site decomposed LDOS calculations performed for the YAG structure indicated that the first peak at the edge onset has a strong contribution originating from a tetrahedrally coordinated aluminum. Fig. 5 shows the experimental Al-L edge from a YAG crystal and the site-decomposed Al (s+d) spectra obtained by the LDOS calculations.

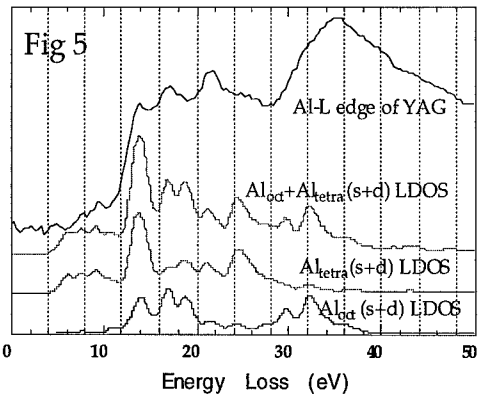

Fig. 5 . Experimental YAG Al-L ELNES and site-decomposed LDOS for Al_{tetra} and Al_{oct}.

DISCUSSION:

In a previous microstructural study on the same material [9] it was determined that most GBs in these samples were of general character. Only few GBs with a 'special' crystallographic orientation relationships were found. These boundaries did not contain detectable amount of Y. On the other hand, the general boundaries investigated revealed a varying, non-equilibrium distribution of Y in the range 1.75 ±0.5 Y atoms/nm^2. The highest amount of excess Y detected at a GB was 3.2 Y

atoms/nm^2. This corresponded only to a 1/4 monolayer coverage assuming Y would replace Al in AO structure [9]. It is not feasible to investigate the structure of these Y-segregated GBs with the help of high-resolution electron microscopy, firstly, because of the general character of the majority of GBs, and secondly, because of the submonolayer coverage of the internal interfaces. In this work, an analytical electron microscopy route was taken to study the chemical and atomic structure of the Y-segregated GBs in AO. The idea is based on symmetry fingerprinting [12-13]. The ELNES spectra of compounds with a known structure that has the same chemical species as constituents were collected to form a reference structure basis. Then the spatial difference spectra from the GBs are compared to these reference spectra to deduce the possible structural units of the segregated GBs. These compounds are especially suited to be a reference structure since the Al in these has different O-coordination. The following interpretation of the GB spectra is based on this comparison. It represents a first attempt to understand the structure of a segregated general boundary.

Al-L edge spectrum of the GB showed that there is a lower energy shoulder **A** at the edge onset. This shoulder appeared at the energy position where the signal for a 4-fold coordinated Al (Al_{tetra}) in an O-polyhedra was expected to occur [13-14]. Site-decomposed LDOS calculations also predicted a strong contribution from a Al_{tetra} at this energy position. Such observations suggest that some of the Al in these Y segregated GBs may be tetrahedrally coordinated with O-atoms. The stronger intensity of the peak **C** in figure 1 also supports this statement. A comparison of the GB spectra with the spectrum of the other Y-A-O compounds indicated that the GB structure is different from the structure of any of the compounds. However there are also similarities especially to YAG and YAM spectra. This again suggests existence of a Al_{tetra} in these boundaries.

The O-K edge of the GB is harder to interpret. It has many similarities to the bulk α-Al_2O_3 O-K edge. The discrepancy is a lower energy shoulder at the edge onset which could again be indicative of a different O-polyhedra around the cations. It is also possible that this peak is an artifact due to the sample damage during data acquisition. α- Al_2O_3 has been observed to suffer structural and chemical damage during electron irradiation [9, 15]. However, during these experiments no visual evidence of damage was observed. A comparison to the spectra from the Y-Al-O compounds did not reveal any similarities between the GB spectrum and reference compound spectra. The splitting of the main broad peak may be indicative of an environment similar to that of the YAG crystal. However, there is a need to acquire additional data with a better energy resolution before a valid statement can be made. At this stage it could only be said that there are indications that the yttrium segregated grain boundaries may contain Al atoms in a four fold oxygen coordination.

REFERENCES:

[1] J. Cho, MP. Harmer, H.M. Cahn, J.M Rickman, and A.M. Thompson, J. Am. Ceram. Soc., **80**, 1013 (1997).
[2] L. Priester, F. Dupau, S. Lartigue-Korinek, and C. Carry, Interface Science and Materials Interconnection Proceedings of JIMIS-**8**, pp. 134-142, The Japan Institute of Metals (1996).
[3] J. Fang, A. M. Thompson, M. P. Harmer, and H. M. Chan, J. Am. Ceram. Soc., **80**, 2005 (1997).
[4] J. D. Cawley and J. W. Halloran,J. Amer. Ceram. Soc., **69**, C-195 (1986).
[5] S. Lartigue, L. Priester, F. Dupau, P. Gruffel, and C. Carry, Mater. Sci. Eng., **A164**, 211 (1993).
[6] R. Brydson, H. Sauer, and W. Engel In *Transmission Electron Energy Loss Spectrometry in Materials Science*; C. C. A. M. M. Disko, and B. Fultz, Ed.; TMS: 1992; pp 131-154.
[7] C. Colliex, T. Manoubi, M. Gasgnier, and L.M. Brown, *Scanning Electr. Microsc.*, **2**, 489 (1985).
[8] J. C. H. Spence, *Ultramicroscopy* , **18**, 165 (1985).
[9] M. A. Gülgün, V. Putlayev, and M. Rühle, *submitted to J. Am. Ceram. Soc.* , (April 1998).
[10] W.-Y. Ching, *J. Am. Ceram. Soc.* , **71**, 3135 (1990).
[11] Y-N. Xu and W. Y. Ching, *To be published* , (1998).
[12] R. Brydson, H. Sauer, W. Engel, and E. Zeitler, *Microsc. Microanal. Microstruct.* , **2**, 159 (1991).
[13] M. A. Gülgün, W. Y. Ching, Y-N. Xu, and M. Rühle, submitted to Phil. Mag. (1998).
[14] P.L. Hansen, R. Brydson, D.W. McComb, and I.G. Richardson, *Microsc. Microanal. Microstruct.* , **5**, 173 (1994).
[15] G. Duscher, unpublished work
[16] Work at UMKC was supported by the US. DOE under grant number DE-FG02-84ER45170.

Materials Science Forum Vols. 294-296 (1999) pp. 293-296

Determination of Grain Boundary Atomic Structure Using Quantitative High Resolution Electron Microscopy

G.H. Campbell[1], W.E. King[1], S.M. Foiles[2] and D. Cohen[1]

[1] University of California, Lawrence Livermore National Laboratory, Chemistry and Materials Science Directorate, Livermore, CA 94550, USA

[2] Sandia National Laboratories, Livermore, CA 94550, USA

Keywords: Quantitative High Resolution Electron Microscopy, Least-Squares Optimization, Grain Boundaries, Atomic Structure Determination

Abstract

Quantitative high resolution electron microscopy has been used to study the atomic structure of grain boundaries in metals. An example of the $\Sigma 11$ (113)/[1$\bar{1}$0] symmetric tilt grain boundary in Al is given. Results for atomic column locations were compared quantitatively with atomistic simulations of the structure of the grain boundary using Embedded Atom Method (EAM) potentials and Local Density Approximation (LDA) methods. There is a statistically significant difference between the experimental image and the simulated image based on the EAM. The experimentally determined grain boundary structure is in better agreement with the LDA calculation.

Introduction

Understanding the behavior of grain boundaries (GBs) and their influence on material performance will require a knowledge of their atomic structure. For example, slip transmission across a GB will depend on the misorientation of the crystals on either side of the GB, the GBplane, and any rigid body displacements that are present due to their effects on the DSC lattice and the reaction of Burgers vectors [1]. Another example is segregation of minor impurities which will be sensitive to the arrangements of atoms at a GB due to the size effect [2].

Experiment

We have fabricated model GBs for study by diffusion bonding [3] precisely oriented single crystals [4]. The materials studied include FCC metals (Al [5], Cu [6]), BCC metals (Nb [7], Mo, Ta) and ceramics (YAG [8]). High resolution electron microscopy has been used to characterize the atomic structure of the GBs. Comparisons to atomic models of GB structure have been made through high resolution image simulation. The comparisons have been performed on a quantitative basis. The quantification has required careful preparation of the experimental data [9, 10] that includes averaging. The imaging parameters of the microscope have either been determined experimentally or determined through an optimization procedure matching the measured contrast in perfect crystal regions of the specimen with simulated images [11]. GB structure is then matched by using an optimization routine which holds the imaging parameters fixed and varies the positions of the atoms in the atomic model used to produce the simulated image [12]. Errors in the positions of the atoms in the atomic model have been assessed through a statistical analysis [5].

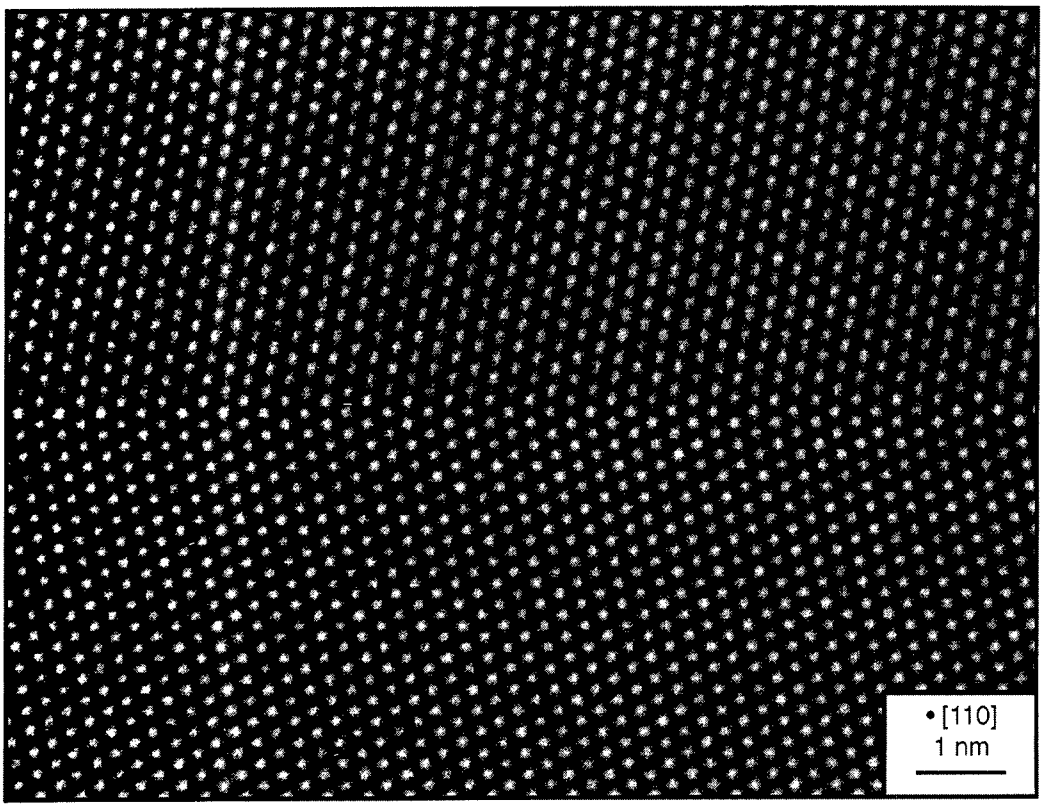

Figure 1. The experimental HREM image of $\Sigma 11(113)/[\bar{1}\,10]$ *grain boundary in Al considered as an example.*

Results and Discussion

The high resolution micrograph of a $\Sigma 11$ (113)/[1$\underline{1}$0] symmetric tilt grain boundary (STGB) considered here as an example of the analysis technique is shown in Fig. 1. In the first steps, only the perfect crystal regions of this image are considered and compared to simulations. Fig.2 shows the average image and the optimized best fit simulated image for the perfect crystal. Also shown are the normalized residuals which are the difference between the experimental and simulated values divided by the estimation of the experimental error [13]. The optimized fit determines the microscope imaging parameters while this image was collected. They are quantities such as defocus, specimen thickness, specimen tilt, beam tilt, background, and blurring. Other quantities, such as spherical aberration, beam convergence, focus spread, and angle and magnitude of 3-fold astigmatism have been measured and held constant in the optimization.

With the imaging conditions thus completely determined, they are held fixed and the match between the experimental and simulated images of the GB is considered. The GB structure used in the starting simulation was that predicted by an EAM simulation and is shown in Fig. 3b. In the plane of the GB Fig. 3c shows regions of disagreement between the experiment and simulation that are over 12 times the experimental error. The optimization is then allowed to proceed and move the atomic columns in the GB in order to minimize the normalized residuals. The resultant simulation with residuals

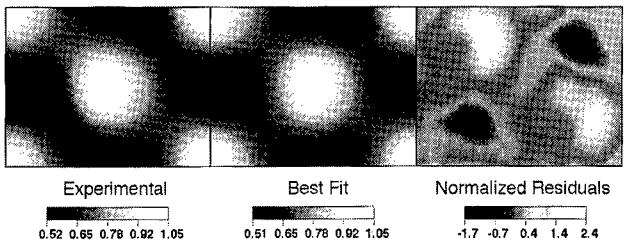

Figure 2. (left) Average experimental image, best fit image, and normalized residuals image from the images of perfect crystal regions on either side of the GB in Fig.1. Experimental image was formed by averaging over 156 unit cells of contrast.

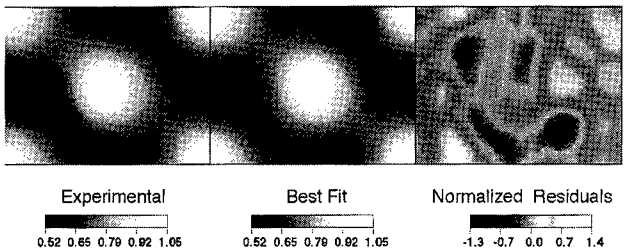

Figure 3. (below) (a) Experimental image averaged over 6 repeat units of the GB, (b) Simulation based on structure predicted by EAM (shown as overlaid squares), (c) normalized residuals corresponding to (b). (d) Best fit image after optimization based on optimized structure (shown as overlaid squares), (e) normalized residuals corresponding to (d).

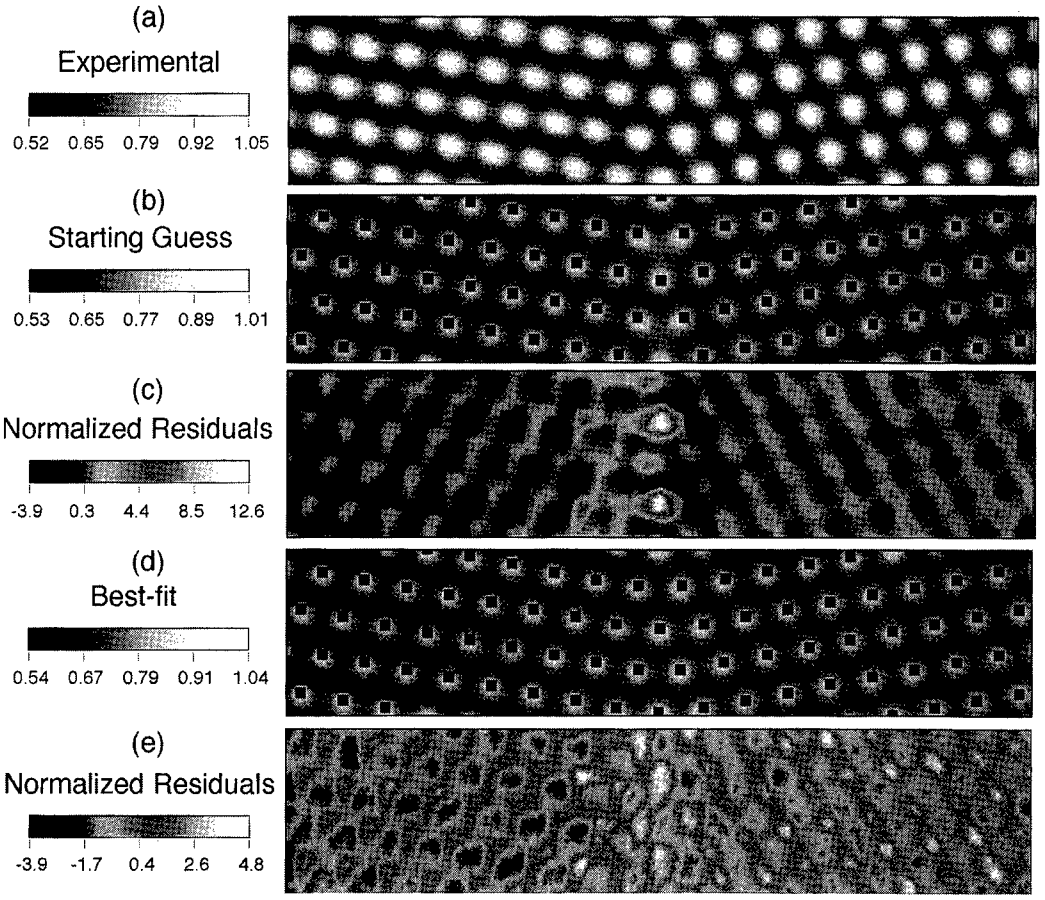

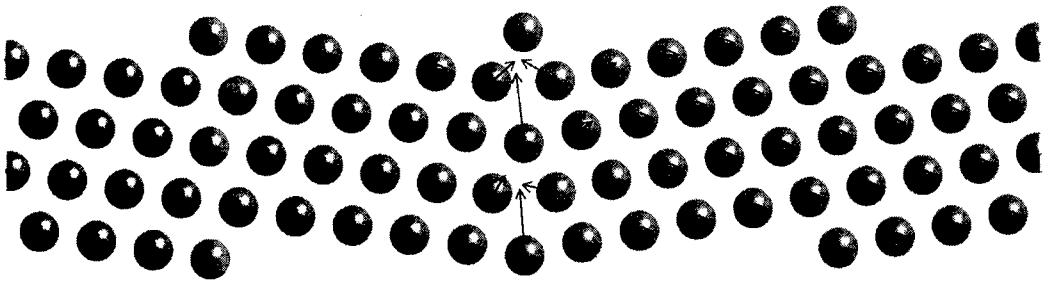

Figure 4. Vectors (10X magnification) indicating atom shifts from EAM positions due to optimization.

is shown in Figs. 3d and 3e. It is now seen that the level of residuals in the GB plane are approximately the same as in the perfect crystal regions. The resultant structure from the optimization is shown in Fig. 4. which has overdrawn vectors showing the magnitudes and directions of the shifts of the atomic columns relative to the results of the EAM calculations. The largest shift, approximately 0.03 nm, is seen to occur for the atoms in the central plane of the GB. The directions of the observed shifts are consistent with more accurate results from electronic structure calculations based on the LDA [5], however the magnitudes are about twice those predicted.

Conclusions

The positions of atoms residing in the GB (with error bars) can be used to evaluate differing schemes of atomistic simulations. For example, in the case of Al, calculations based on the EAM and the LDA give slightly different predictions of grain boundary structure. Qualitatively the boundaries appear the same, but the atoms reside at slightly different positions, with differences that can exceed 0.1 Å. These differences can be resolved by the techniques of quantitative matching and simulation optimizations.

Acknowledgement

This work performed under the auspices of the Division of Materials Science of the Office of Basic Energy Sciences, U. S. Department of Energy, and the Lawrence Livermore National Laboratory under contract No. W-7405-Eng-48.

References

[1] T.C. Lee, I.M. Robertson, and H.K. Birnbaum, Acta Metall. Mater. 40 (1992) p. 2569.
[2] S.M. Foiles, Surface Segregation Phenomenon (CRC Press, Boca Raton, 1990) p. 79.
[3] W.E. King, et al, Mat. Res. Soc. Symp. Proc. 314 (1993) p. 61.
[4] W.L. Wien, G. H. Campbell and W. E. King, Microstructural Science 23 (1996) p. 213.
[5] W.E. King, et al, J. of Microscopy, 190 (1998) p. 131.
[6] D.L. Medlin, G.H. Campbell, and C.B. Carter, Acta Mater., in press.
[7] G.H. Campbell, et al, Phys. Rev. Lett. 70 (1993) p. 449.
[8] G.H. Campbell, J. Am. Ceram. Soc. 79 (1996) 2883.
[9] G.H. Campbell, W.E. King, and D. Cohen, Microscopy and Microanalysis 3 (1997) p. 299.
[10] G.H. Campbell, W.E. King, and D. Cohen, Microscopy and Microanalysis 3 (1997) p. 451.
[11] W.E. King and G.H. Campbell, Ultramicroscopy 51 (1993) p. 128.
[12] W. E. King and G. H. Campbell, Phys. Stat. Sol. A, 166 (1998) p. 343.
[13] W.E. King and G.H. Campbell, Ultramicroscopy, 56 (1994) p. 46.

Materials Science Forum Vols. 294-296 (1999) pp. 297-300

The Distribution of Segregated Elements to Grain Boundaries Measured by Auger Electron Spectroscopy

P.E.J. Flewitt[1] and R.K. Wild[2]

[1] BNFL- Magnox Generation Technology and Central Engineering, Berkeley Centre, Berkeley, Glos. GL13 9PB, UK

[2] Interface Analysis Centre, The University of Bristol, 121 St. Michael's Hill, Bristol, BS2 8BS, UK

Keywords: Grain Boundaries, Segregation, Intergranular Fracture, Auger Spectroscopy, Phosphorus

Abstract

Auger electron spectroscopy (AES) is used extensively to determine the levels of segregation of impurity and solute atoms to grain boundaries in metals and alloys. The present work has examined the nanochemistry of grain boundaries in an iron 3% nickel alloy, containing an impurity phosphorus, following an embrittling step cooling heat treatment. Following fracture at a temperature of 77K, the two corresponding surfaces have been examined in detail. In particular consideration is given to the distribution of the segregated species over individual intergranular fracture surfaces for one grain and between two matched corresponding surfaces on each half of the fractured specimen. The results are discussed with respect to the observed fracture paths, the statistics of the AES composition measurements and the overall composition.

Introduction

When a ferritic steel is fractured in a brittle mode the crack may follow either an inter or transgranular path. Many factors influence which mode of failure will predominate but angle of incidence to the fracture path and grain boundary energy are two of the most important. Elements present in the bulk in trace quantities may segregate to the grain boundary where they reduce the grain boundary energy [1]. Elements with an atomic size greater than the matrix atoms tend to weaken the boundary while atoms with a smaller size will strengthen the boundary. P, S, Sn and Sb are all elements that embrittle ferritic steels. When fracture is intergranular it is commonly

Figure 1. Secondary electron image of two corresponding fracture surfaces showing intergranular fracture and positions for AES measurement (x100).

assumed that the grains separate along the region of discontinuity between the two grains and that any segregant is left distributed equally on each. To undertake the analysis using AES specimens are fractured at low temperature to reveal intergranular fracture surfaces. Measurements are then made at a number of locations on these surfaces to establish a measure of the segregation. The composition is then measured on the surfaces of one half of the fractured specimen. The value for composition obtained is then doubled on the assumption that equal proportions of the segregated species are retained on each half of the overall fracture surface. However, these assumptions may not be valid and more of the segregating species may be left on one side. To investigate this we have fractured an iron-3%nickel alloy that had been heat treated to cause P to be segregated to the grain boundaries and measured the composition on each fracture surface using the same grain boundaries[2,3]. The total grain boundary segregation is then determined by summing the amounts of segregant on each surface and this is compared with conventional methods for evaluating composition.

Table 1. P/Fe Ratios for Points on Grain Boundaries

GB	P/Fe(47) Side 1	P/Fe(47) Side 2	P/Fe(47) (1+2)/2	P/Fe(703) Side 1	P/Fe(703) Side 2	P/Fe(703) (1+ 2)/2
1	0.21	0.27	0.24	0.061	0.065	0.063
2	0.41	0.34	0.37	0.108	0.105	0.107
3	0.37	0.37	0.37	0.118	0.107	0.113
4	0.58	0.42	0.50	0.154	0.102	0.128
5	0.43	0.27	0.35	0.113	0.106	0.110
6	0.36	0.26	0.31	0.091	0.067	0.079
7	0.32	0.16	0.24	0.057	0.046	0.052
8	0.27	0.39	0.33	0.051	0.075	0.063
9	0.54	0.36	0.45	0.087	0.079	0.083
10	0.32	0.27	0.29	0.041	0.052	0.046
11	0.00	0.55	0.27	0.000	0.101	0.051
12	0.47	0.38	0.42	0.073	0.067	0.070
13	0.20	0.16	0.18	0.044	0.021	0.033
14	0.26	0.22	0.24	0.052	0.066	0.059
15	0.50	0.57	0.54	0.135	0.139	0.137
16	0.28	0.33	0.30	0.034	0.049	0.042
Mean	0.34	0.33	0.33	0.076	0.078	0.077
St.Dev.	0.15	0.12	0.10	0.042	0.030	0.032
Error	0.037	0.030	0.025	0.010	0.007	0.008

Experimental

Following a complex heat treatment of 1h at 1373K, 1h at 1183K, 20h at 873K and step cooling for 15h at 811K, 24h at 797K, 48h at 769K and 72h at 741K [2,3], samples of iron-3%nickel ferritic steel approximately 1mm x 1mm x 10mm with a notch at the mid point were cooled to liquid nitrogen temperature in the fracture stage of the PHI 595 scanning Auger microprobe (SAM). They were then fractured by impact in a vacuum of $1x10^{-7}$Pa and both fracture faces presented to the Auger analyser. AES spectra were recorded from sixteen grain boundaries on each fracture surface in both spot and area mode. In point analysis an area approximately 0.2μm in diameter was analysed but in area mode approximately 80% of the boundary was rastered.

Results

Figure 1 shows the two fracture surfaces with the 16 grain boundaries analysed indicated. Spectra were recorded from both points and areas on each grain. It is customary to compare the ratio of the peak height of P to the peak height of the low or high Fe peaks in order to determine the amount of phosphorus segregation. We have determined the ratio of P, Fe for both the low (47 eV) and one of the high energy (703 eV) Fe peaks and to do this have used the maximum counts in each peak above a linear background. The individual and mean values for each side are given in tables 1 and 2 for point and area analysis respectively.

Table 2 P/Fe Ratios for Areas on Grain Boundaries

GB	P/Fe(47) Side 1	P/Fe(47) Side 2	P/Fe(47) (1+2)/2	P/Fe(703) Side 1	P/Fe(703) Side 2	P/Fe(703) (1+2)/2
1	0.24	0.31	0.28	0.060	0.094	0.077
2	0.31	0.35	0.33	0.079	0.113	0.096
3	0.39	0.36	0.38	0.099	0.117	0.108
4	0.48	0.39	0.43	0.126	0.058	0.092
5	0.35	0.32	0.34	0.077	0.063	0.070
6	0.38	0.28	0.33	0.077	0.082	0.080
7	0.35	0.31	0.33	0.059	0.092	0.075
8	0.36	0.33	0.34	0.061	0.072	0.066
9	0.40	0.30	0.35	0.055	0.081	0.068
10	0.36	0.29	0.32	0.045	0.054	0.049
11	0.27	0.42	0.34	0.035	0.075	0.055
12	0.34	0.36	0.35	0.055	0.070	0.062
13	0.19	0.23	0.21	0.038	0.045	0.041
14	0.28	0.27	0.27	0.056	0.059	0.057
15	0.41	0.50	0.46	0.110	0.126	0.118
16	0.30	0.24	0.27	0.044	0.039	0.041
Mean	0.34	0.33	0.33	0.067	0.077	0.072
St.Dev.	0.07	0.07	0.05	0.026	0.025	0.019
Error	0.02	0.02	0.01	0.007	0.006	0.005

Discussion

Table 1 gives the P: Fe ratios for point analyses while Table2 gives the ratios for the areas. Clearly these results show that the distribution of P between the two fracture surfaces is not equally divided. This is a refection of the particular bonding conditions and the distribution of P at the particular grain boundary. If the two sides of a grain boundary are considered the composition of each surface may differ considerably however the mean composition averaged over the 16 grain boundary surfaces is similar for each side of the fracture surface. For example grain boundary 7, Table 1, shows 0.32 on side one and 0.16 on side 2 for the point analysis whereas the area analysis is more equally distributed. Thus the distribution with position on this surface is non uniform but the variation between sides is less marked when area measurements are taken.

If the values for each side are averaged and these used to determine the mean composition the standard deviation reduces indicating a more accurate measurement of the true grain boundary composition. This improvement is greatest for the area measurements where one is sampling

equivalent regions on both sides of the grain boundary. These results are demonstrated graphically in Figure 2 which shows the mean, standard deviation and errors for all the point measurements and in Figure 3 for the area measurements. These results are in agreement with Briant [4] who carried out a similar study on steel containing antimony. He concluded that either side of a boundary could have between 45 and 55% of the segregant but that this distribution did not account for all the scatter between grains.

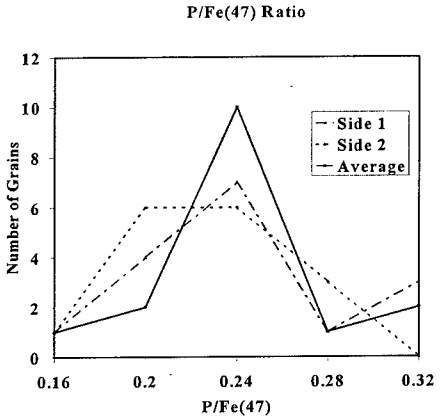

Figure 2. P/Fe (47 eV) Ratio for grain boundary areas

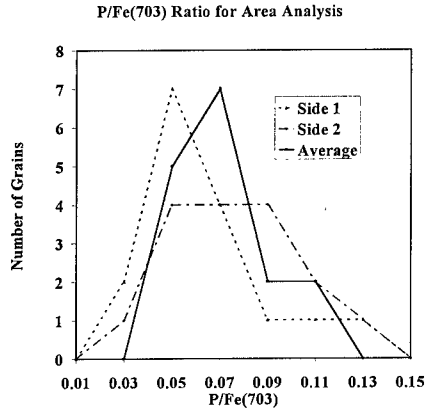

Figure 3. P/Fe (703 eV) ratio for grain boundary areas.

CONCLUSIONS

1) When grain boundaries fracture equal amounts of segregant are not left on each grain surface and this indicates the fracture path is to one side of the grain boundary interface.

2) AES area measurements from equivalent grain surfaces on each fracture face when combined result in a segregation measurement that has greater statistical significance.

ACKNOWLEDGEMENT

This paper is published with the permission of the Director of Technology and Central Engineering, BNFL - Magnox Generation.

REFERENCES

[1] M P Seah and E D Hondros, Proc. Roy Soc., **A335**, 191, (1973)

[2] A E Powers, J Iron Steel Inst., **186**, (1957) 323.

[3] C P Hunt and M P Seah, NPL Report DMM(D)110, September 1991.

[4] C L Briant, Acta Metall., **31**, (1983), 257.

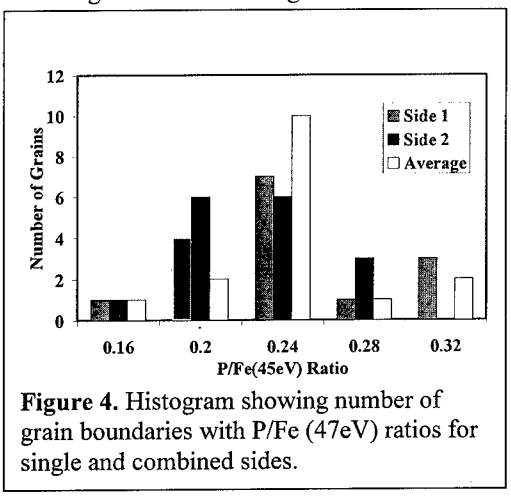

Figure 4. Histogram showing number of grain boundaries with P/Fe (47eV) ratios for single and combined sides.

Materials Science Forum Vols. 294-296 (1999) pp. 301-304

Grain Boundary Structure and Chemical Bonding in Boron Doped Silicon Carbide

H. Gu

Japan Science & Technology Corporation, "Ceramics Superplasticity" Project, Nagoya 456, Japan

Keywords: Grain Boundary (GB), Chemical Bonding, Segregation, EELS, Silicon Carbide

Abstract

EELS analysis detects boron segregation to grain boundary (GB) in SiC, the first after twenty years attempts. No glass phase was found at triple points as well as GB, the later was revealed by HREM observations. On the other hand, the local structure as GB exhibits certain degree of disorder. The amount of boron at GB can fill a monolayer of B_4C while one monolayer of silicon depleted concurrently from the same boundaries, suggesting that boron atoms form bonds with carbon and among themselves. EELS near-edge structures reveal that the segregation does not significantly change the type of bonding at GB. A chemical width of more than 1 nm was also obtained, indicating the scale of the segregation and of the partially-disordered structure of GB. Thus the boron segregation promote densification without disrupting seriously the covalent bonding as in the case of a distinct amorphous film.

1. Introduction

SiC has excellent high temperature properties but is very difficult to sinter without additives. In 1970's boron addition was found to promote densification and since then it was widely believed that there exists a GB phase with boron additives [1-2]; however, boron was not detected by AES, EDS and EELS [3-4]. On the other hand, amorphous film was observed at GB in Al-doped SiC [5-6], but not in B-doped samples [7]. Therefore the problem of GB structure and phase caused by the segregation was far from settled. Inspired by the recent progresses in EELS analysis of GB structure, chemistry and bonding in Si_3N_4 materials [8-9], here I present a similar type of analysis to unveil the effect of boron segregation to the local structure and bonding in SiC.

2. Experimental

The fully dense SiC material was sintered by hot press 2000°C for 1h. 0.3 wt% of pure boron was doped into this material, which contains also 1.3 wt% of free carbon. The phase is basically α-SiC

* The author is grateful to Y. Shinoda for providing this problem in relation to his study, as well as preparing TEM specimen; to G. D. Zhan and M. Mitomo for fabricating the ceramic sample; to F. Wakai, S. Tsurewaka and Y. Ikuhara for beneficial discussions.

with average grain size of 2 μm. More details of this material can be found in [10].

TEM specimen was prepared by ion milling without cooling. HR-TEM observation was performed on Topcon 002B microscope with a point resolution of 1.9 Å. The AEM part was carried out on a dedicated STEM, VG HB601UX/R2 with a field-emission gun and equipped with a Gatan DigiPEELS 766. The energy resolution of STEM is 0.5 eV, sufficient to reveal EELS near-edge fine structures (ELNES) for bonding and other analyses.

To achieve fully analysis of GB, EELS spectra were collected from the rastered areas (5x5 nm^2, probe and beam broadening included) *on* and *off* the intended GB. This enables not only the quantification of segregated and the matrix elements [9-10], but also the ELNES exclusive to GB region, which was obtained by separating ELNES features sensitive to the bonding nature of silicon with its ligand elements in a tetrahedral coordination [11-12]. The corresponding composition and chemical width can be subsequently obtained [8].

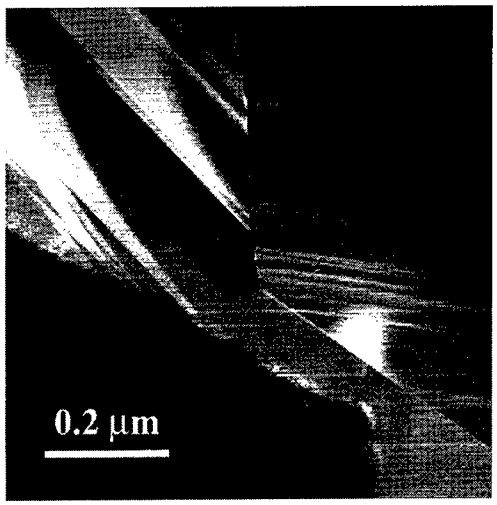

Fig. 1 STEM dark-field image of three SiC grains forming GB and a triple point without glassy phase.

3. Results and discussions

3.1 Morphology and structure

The equal-axis grains do not form pocket at triple grain junctions, as revealed by STEM dark-field image in Fig. 1. This is consistent with the fact that little or no oxygen staying after sintering. Stacking faults can be seen on these grains, their angles to GB planes can be used to justify that the later are no special boundary. It can be also seen that there is no micro-facetting at GB.

HR-TEM image in Fig. 2 reveals no amorphous 2nd phase at GB in B-doped SiC, in consistent with the absence of glass pocket. However it is perceived that GB plane is not atomic sharp, and there is visibly a certain degree of disorder near the core of GB. Fresnel fringes were used to judge whether GB plane was parallel to the electron beam. This observation echoes the previous HR-TEM works of similar materials with a "extended boundary" structure [7].

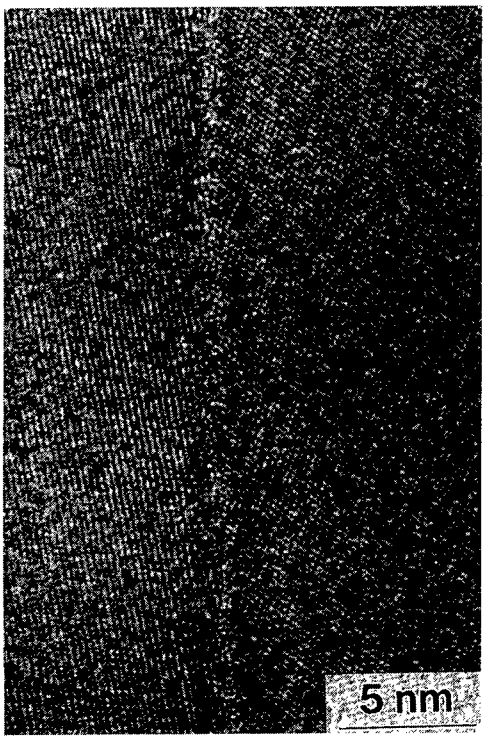

Fig. 2 HR-TEM image of a general GB in SiC which is viewed parallel to the beam. No amorphous film is found.

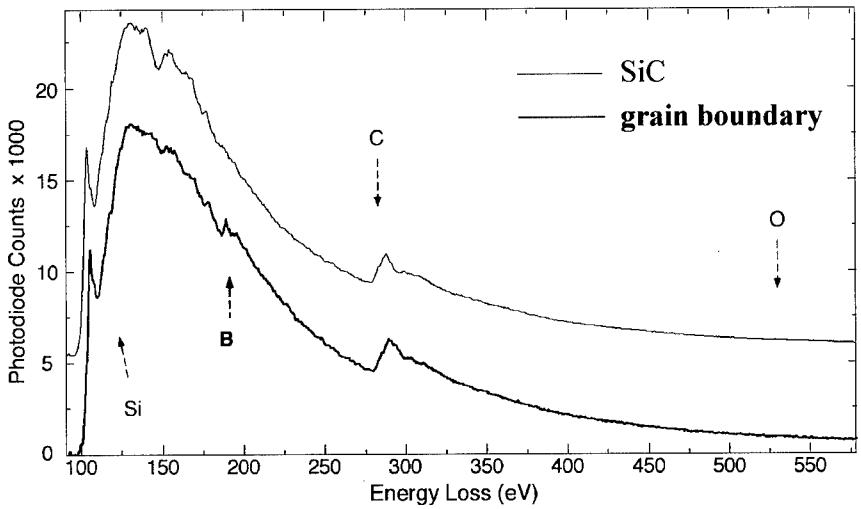

Fig. 3 EELS spectrum of B-doped GB (thick line). SiC spectrum is also shown (thin line). Boron was detecetd while oxygen was not.

3.2 B segregation and Si depletion at GB

Boron segregation was found in all of the analyzed GB. The initial detection was carried out in 1st difference spectral mode [10]. In the normal mode, boron signal is not directly visible due to the strong systematic gain variation across the PEELS detector array. After removing the matrix contribution (more than 60%) in the as-acquired spectrum covering GB, the resulted spectrum reveals boron edge as well as the remaining Si and C in GB (Fig. 3).

The chemistry of GB is first analyzed in term of interfacial excess by direct quantification of the initial spectra, with the exception of B signal integrated from processed spectra (see more details in [10]). The measurements gave the average boron excess as 21.6±5.7 at/nm^2. This large deviation signifies the variation of composition from GB to GB.

Si was concurrently found depleted from GB as revealed by negative excess in respect to carbon. Averaged over the measurements of the same GB Si depletion amounts to 13.5±4.9 at/nm^2, or a full monolayer missing in SiC structure (ML coverage taken as 2/3 power of the bulk concentration). B segregants fill 1.6 ML if they all replace Si in SiC structure; they can cover just 1 ML in B_4C structure (which has higher B concentration). Boron has to form bonds with C as Si depleted, chemically it should not prefer B-C bond in the same coordination as for Si-C bonds in SiC; rather it forms B-C and B-B bonds as in B_4C structure since B excess outnumbering Si depletion. However, it is not necessary that those bonds form a distinct B_4C layer at GB. It is likely to distribute over a distance across GB.

3.3 ELNES and covalent bonding

ELNES for silicon L and carbon K edges from GB in B-doped SiC, obtained by removing all the matrix contribution using their ELNES differences [13], were shown in Fig. 4a and 4b respectively. Most of the fine features from SiC ELNES were smeared out in GB spectrum, echoing the fact that local structure at GB is disordered to a significant degree. On the other hand, except the losing of details, there is no significant difference in the overall shape between ELNES of GB and SiC. This fact signifies that the bonding nature does not change at GB in any substantial way, i.e. GB remains

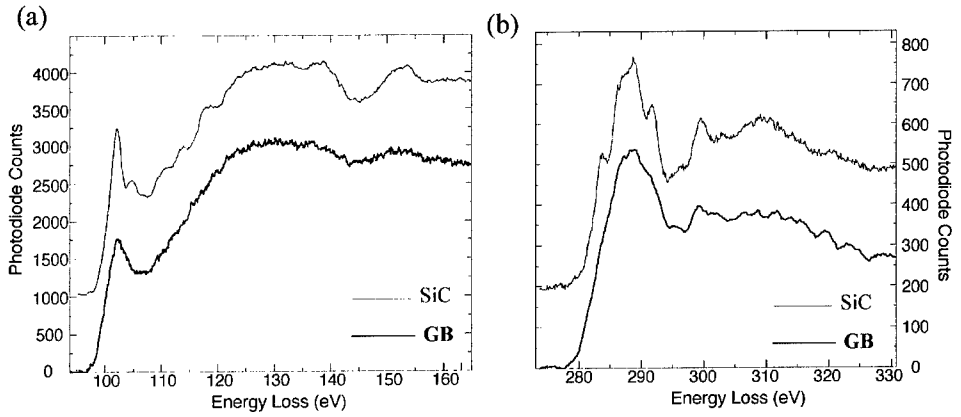

Fig. 4 Si-L (a) and C-K (b) ELNES of GB after removing SiC contribution.

basically as covalent as in SiC. Indeed, in SiC ELNES the sharp leading peak at 104 eV which gives straight indication of convalency/ionicity for Si tetrahedron [11-12] does not shift in GB ELNES. The associated chemical width [8] is estimated as 1.7 nm from GB ELNES in Fig. 4. There is definitely large number of Si and C atoms in this region, as revealed directly in Fig. 3 obtained in a similar way. This width reflects primarily the lateral scale of the distorted bonding configuration with respect to the matrix. It is also an estimation of the scale of disorder at GB, as well as the scale of B distribution.

4. Conclusions

Although there is no amorphous phase formed at B segregated GB in SiC, there is a certain layer (>1 nm) within which the local structure and chemical bonding distorted from perfect SiC structure. The covalent nature is largely unaffected, and B segregants form B-C and B-B bonds.

These finding explain that while boron segregation improves the densification through GB diffusion, no oxide phase formed at GB and the bonding remains covalent. Therefore the high temperature strength and the creep resistance in B-doped SiC are affected in a substantially less degree than in Al-doped SiC which has amorphous phases [14-15].

References

[1] T. Hase and H. Suzuki, Yogyo-Kyokai-Shi 88 (1980) p. 258.
[2] J. E. Lane, C. H. Carter and R. F. Davis, J. Am. Ceram. Soc., 71 (1988) p. 281.
[3] R. Hamminger, G. Grathwhol and F. Thümmler, J. Mater. Sci., 18 (1983) p. 3154.
[4] R. H. J. Hannink, Y. Bando, H. Tanaka and Y. Inomata, J. Mater. Sci., 23 (1988) p. 2093.
[5] L. S. Sigl, H.-J. Kleebe, J. Am. Ceram. Soc. 76 (1993) p. 773.
[6] W. J. MoberlyChan, J. J. Cao and L. C. de Jonghe, Acta Mater. (1998) in press.
[7] S. Tsurekawa, S. Nitta, H. Nakashima and H. Yoshinaga, Interface Science, 3 (1995) p. 75.
[8] H. Gu, R. M. Cannon and M Rühle, J. Mater. Res., 13 (1998) p. 376.
[9] H. Gu, X. Pan, R. M. Cannon and M. Rühle, J. Am. Ceram. Soc. (1998) in press.
[10] H. Gu, Y. Shinoda and F. Wakai, submitted to J. Am. Ceram. Soc. (1998).
[11] H. Gu, M. Ceh, S. Stemmer, H. Müllejans and M. Rühle, Ultramicroscopy 59 (1995) p. 215.
[12] H. Gu, in Frontiers of Materials Sceince and Engineering, Eds. Somiya et al Elsvier (1998) in press.
[13] H. Gu, Ultramicroscopy (1998) submitted.
[14] A. G. Evans and F. F. Lange, J. Mater. Sci. 10 (1975) p. 1659.
[15] G. Grathwohl. T. Reets and F. Thummler, Sci. Ceram. 11 (1981) p. 425.

Materials Science Forum Vols. 294-296 (1999) pp. 305-308

The Complexes of Planar Defects in Ordered Alloys

M.A. Baranov, M.D. Starostenkov and A.G. Nikiforov

RU-656099, General Phys. Dept., Altai State Techn. Univ., Lenin St., 46, Barnaul, Russia

Keywords: Superstructure, b.c.c-Lattice, Stacking Fault, Antiphase Boundary, γ-Surface, Relaxation, Atomic Configuration

Abstract

The existence of metastable planar defects which arise as a result of shifts of half-crystals at vectors multiplie of 1/6<-111>(211) in ordered alloys with superstructures B2, B32, C11b, $D0_3$ on the base of b.c.c. lattice has been revealed by method of γ-surface construction. It has been shown that lattice relaxation near defects which are created as a result of shift in opposite directions proceeds in different ways.

Introduction

The planar defects in ordered alloys on the base of b.c.c. lattice form mainly in planes (211) type in processes of dislocation sliding. Such defects can be presented as complexes of stacking faults (SF) and antiphase boundaries (APB). Detailed experimental observation of defect complexes is rather difficult, and sometimes impossible because of the small size of such objects, although the estimations of their formation energies have been done for series of pure metals and some alloys [1-3]. In this connection the method of computer simulation of lattice defects may bring useful information.

The purpose of this work is revealing of crystal-geometrical and energy regularities of formation of stable complexes of planar defects (211) orientation arising in alloys with different superstructures on the base of b.c.c. knot lattice.

Calculations.

The most complete information about planar defects can be received by means of construction of γ-surface profile [4], which is presented as dependence of planar defect formation energy on the vector of half-crystals relative shift. The block of crystals represented as the totality of parallel infinite planes (211) type was constructed for simulation of planar defect.

The profile of γ - surface was constructed by means of creating consecutive relative shifts of half-crystal at vector pa_0<-111>, where a_0 is the parameter of b.c.c. lattice, p - real and execution corresponding calculation of start and equilibrium formation energy of defect. For calculation of defect equilibrium configuration the borders of the block were fastened. The atoms of inner region of the block could move in the directions of forces acting at them until achieving the minimum of inner energy the block. The calculations were carried out by using of sets of Morse type potentials. The parameters of potentials were determined on the basis of experimental data about alloys and crystals of pure metals. Radius of action of potentials was limited by the third coordination sphere.

Results and discussions

The calculations of γ-surfaces profiles was carried out for alloys FeAl with B2 superstructure, NaTa (B32), Cr_2Al (C11b) and Fe_3Al ($D0_3$). The knot lattice of these superstructures is b.c.c., and primary sliding direction - <-111>. The least vector of complete translation along <-111> in these

superstructures doesn't exceed $2a_0$<-111>. In particular, it is equal to a_0<-111> for B2 superstructure, $1.5a_0$<-111> for C11b and $2a_0$<-111> for B32 and $D0_3$. The calculated profiles of γ-surfaces for these alloys in (211) plane of sliding at interval from $-a_0$<-111> to a_0<-111> are shown in fig. 1. The point «0» corresponds to the state of ideal crystal. The greatest maxima of γ-profiles correspond to relative shifts of half-crystals at $\pm a_0/4$<-111>, $\pm 3a_0/4$<-111> and so on. The shift at vectors multiple of $a_0/2$<-111> doesn't break the original knot lattice, however leads to formation of APB. The theoretically possible number of essentially different APB in superstructures with translation period $2a_0$<-111> is 3. However, because of the symmetry of superstructures (B2, B32, $D0_3$) or smaller vector of complete translation (B2, C11b) this number doesn't exceed 2. Superstructural intrinsic stacking faults (SISF) [5] typical also for metals and disordered alloys form as a result of relative shifts of half-crystals at vectors $\pm a_0/6$<-111>. However, if the same shifts take place at APB plane, then superstructural extrinsic SF (SESF) form. Both the distortion of original knot lattice and violation of ordered state take place near SESF. Both these factors lead to increase of formation energy of SESF in comparison with corresponding values for APB and SISF in all considered superstructures (fig.1). That is, SESF is represented as a complex of APB and SISF. The greatest number of different SESF - 4 is achieved in low-symmetrical superstructure C11b. In B32 and $D0_3$, because of mirror symmetry of γ-profiles, the number of different SESF amounts to 3, in B2- 1.

The stable complexes of plane defects in high-symmetrical superstructure can be easily determined even by using starting γ-profile. At reduction of symmetry (B32, $D0_3$) some defects (SESF2 and SESF3) can be perceived as unstable not taking into account lattice relaxation. In superstructure C11b it is quite impossible to predict the existence of stable SF by using starting γ-profile. However, taking into account the lattice relaxation all SF are presented as stable. The symmetry of γ-profile is determined by symmetry of superstructure. The correlation of values of maxima and minima at γ-profiles depends on composition of the alloy. Finally, the manners of plastic deformation and dislocation reactions are determined by this correlation.

The γ-profiles, corresponding to starting states of planar defects in superstructures B2, B32, $D0_3$ are absolutely mirror symmetrical. The equilibrium profiles are almost symmetrical. However, the lattice relaxation near the defects created by shifts at $-pa_0$<-111> and pa_0<-111> proceeds in a different way. As an example the configurations of SISF created as a result of shifts at $-a_0/6$<-111> and $a_0/6$<-111> in Fe_3Al alloy are shown in fig 2-3. Atoms of iron and aluminium are projected at plane orthogonal to SISF as circles of different color. The sizes of the circles are determined by the sizes of atoms and their distances from the observer. In the first case (fig.2) the tendency of the crystal to restoration of ideal lattice can be seen. Therefore the experimental observation of such defects is, evidently, extremely difficult. In the second case (fig.3) the structure slightly different from ideal forms near the defect. It can be seen that the rectangles formed by centers of atoms in (0 -11) plane transform in trapezes, which, in turn, form the cavities at plane of SF preferable for disposition of admixtures atoms. That is, SF can be interpreted as place of segregation. The similar effects are also observed in other superstructures, alloys and for other SFs, although quantitative differences of atomic configurations, of course, took place.

Conclusion

Thus, by method of construction of γ-profile and only taking into account of lattice relaxation it is possible to reveal the existence of stable complexes of plane defects created as a result of

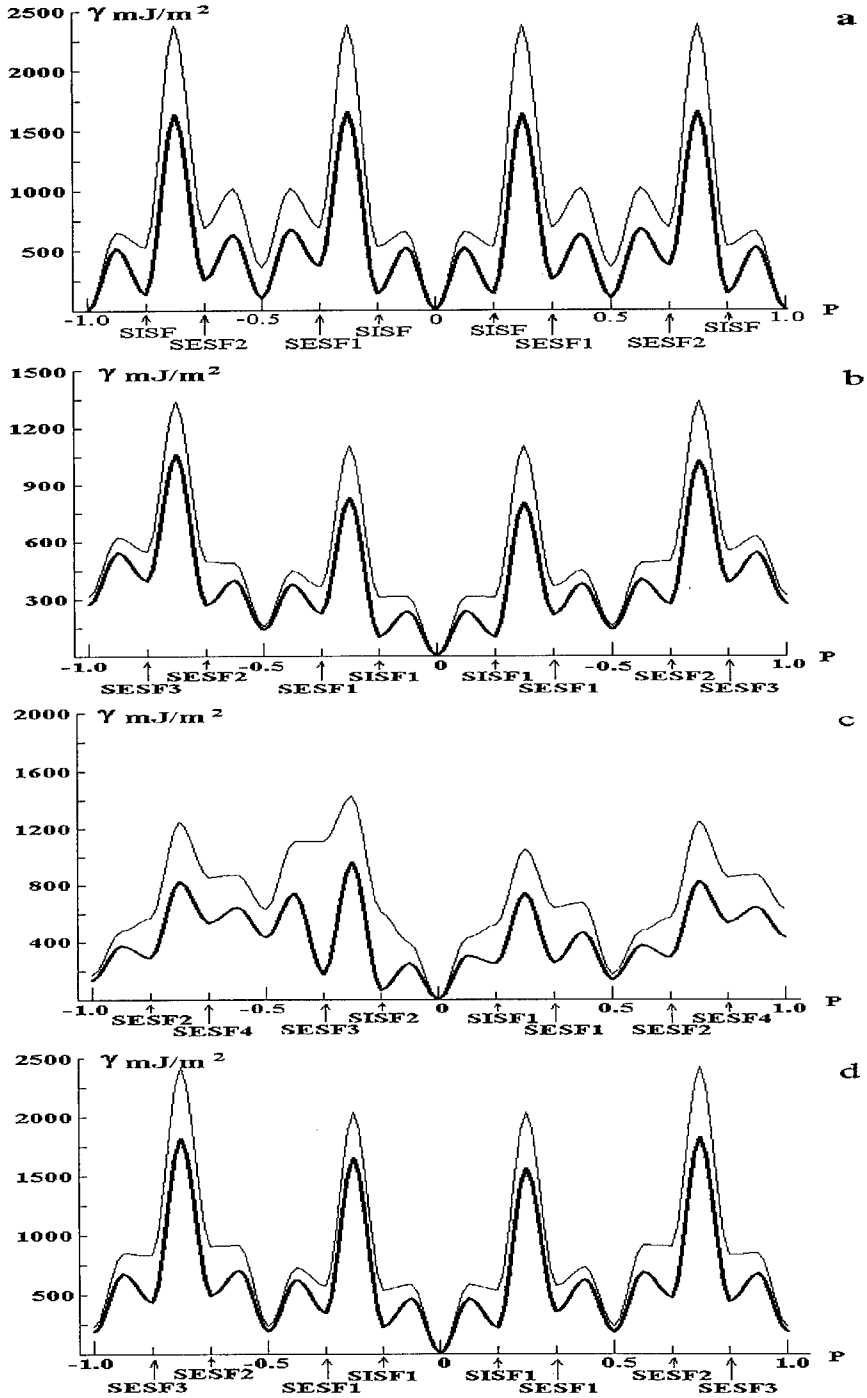

Fig.1. The dependence of formation energy (γ) of planar defects (211) orientation on value of relative shift vector p a_0<-111>of half crystal in starting (thin line) and in equilibrium (solid line) configurations in FeAl with B2 superstructure (**a**), NaTl with superstructure B32 (**b**), Cr_2Al with superstructure C11b (**c**), Fe_3Al with superstructure $D0_3$ (**d**) alloys.

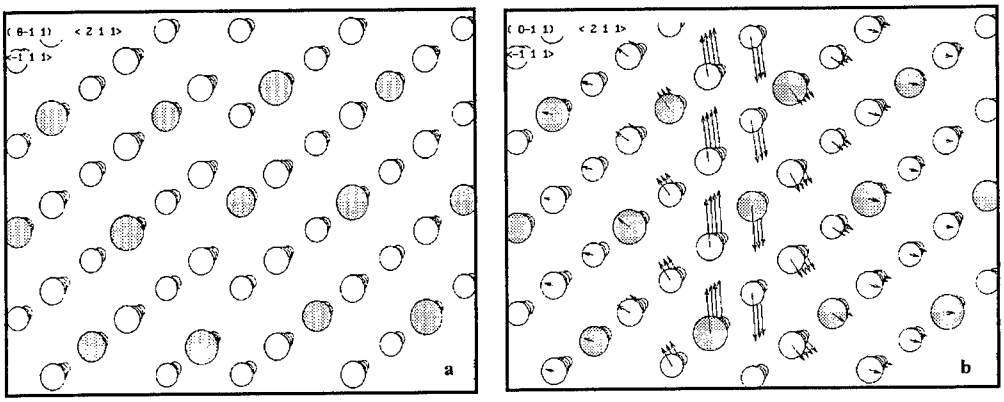

Fig. 2. Starting (**a**), and equilibrium (**b**) configurations of SISF -a_0/6<-111>(211) in Fe_3Al alloy. ○ -Fe, ◎ - Al. Arrows in scale of 4:1 show projections of displacements of atoms from their start positions at the plane of (0-11). Orientation: <211> - right, <-111> - down.

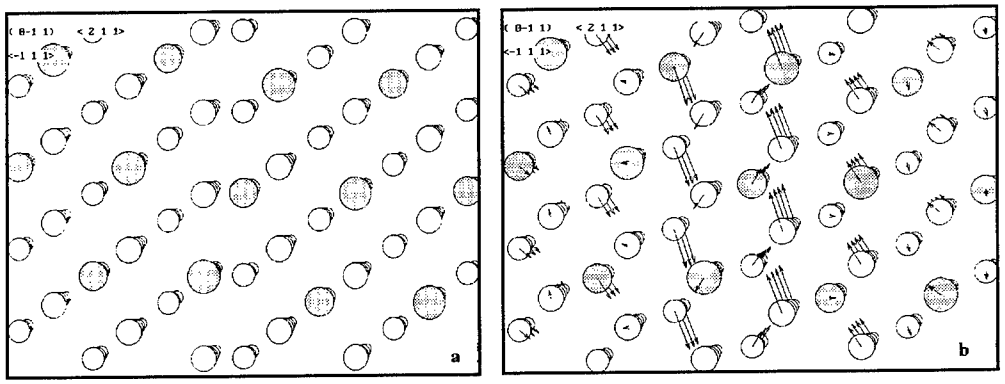

Fig. 3. Starting (**a**), and equilibrium (**b**) configurations of SISF a_0/6<-111>(211) in Fe_3Al alloy. ○-Fe, ◎ - Al. Arrows in scale of 4:1 show projections of displacements of atoms from their start positions at the plane of (0-11). Orientation: <211> - right, <-111> - down.

relative shifts of half-crystal at vectors multiple of a_0/6<-111>. The symmetry of calculated energy profiles is determined by symmetry of considering superstructure. The composition of the alloy influences on the values of maxima and minima of γ-profile. The arising atomic configurations depend essentially on direction of the original shift.

References

[1]. A.H. Ngan, J.P.Jones and R.E. Smallman, Phil. Mag. 66, N 1 (1992) p.55.
[2]. D. Shindo, M.N.Yoo, S.Hanada, K.Higara, Phil. Mag. A. 64 N 6 (1991) p 1281.
{3] D.G. Morris, M. Lebout, Phil. Mag. Lett, 70 N 1 (1994) p 29-39.
[4].The structure and properties of crystal defects / Ed. by V.Paidar, L.Lejcek.-Elsevier (1984).
[5].V Paidar, D.P. Pope, V. Vitek, Acta Met., N 3 (1984) p 435.

Materials Science Forum Vols. 294-296 (1999) pp. 309-312

Analysis of a 69.3° Near-Twist Boundary in Titanium; a Comparison of Two- and Three- Dimensional Models for the Reference Structure

S. Wang and M. Aindow

School of Metallurgy and Materials & IRC in Materials for High Performance Applications, The University of Birmingham, Elms Road, Edgbaston, Birmingham, B15 2TT, England

Keywords: Reference Structure, Grain Boundary Dislocations, O-Lattice, CSL

ABSTRACT: The structure of a high angle grain boundary in pure Ti with an axis/angle pair close to [0001]/69.43° has been studied using TEM and the observed dislocation arrangement has been modelled using the O-lattice algorithm for both two- and three-dimensional CSL reference structures. A good fit to the data was obtained for both reference structures showing that the two approaches are nearly equivalent for such special cases.

1. INTRODUCTION

For high angle grain boundaries (HAGBs) in cubic materials, interfacial dislocation arrangements are usually modelled using the O-lattice algorithm [1] with coincident site lattices (CSLs) as the reference structures and Burgers vectors given by vectors of the related DSC lattices. For hexagonal materials, however, 3D CSLs are only possible for rational values of $(c/a)^2$, except for rotations about the c axis [2]. It has been suggested that the reference structures for HAGBs in non-cubic materials could be related to constrained CSLs (CCSLs) where the small strain necessary to give a CSL is balanced by additional dislocation content in the boundary. There is, however, very little experimental evidence to support the CCSL model [e.g. 3] and it has also been shown recently that there are fundamental weaknesses in this approach [4]. There is some evidence to suggest that reference structures may instead be related to periodicity in, or near to, the boundary plane [e.g. 5,6]. In a recent study of a vicinal HAGB in α-Ti [7], it was shown that there was no feasible CSL or CCSL which could be adopted as the reference structure and an alternative two-dimensional reference structure was proposed. The expected dislocation arrangement for this reference structure was obtained using the O-lattice algorithm with Burgers vectors from Pond's topological theory of interfacial defects [8] and this arrangement matched well with that observed experimentally using TEM. In our work we have studied the reference structures adopted by boundaries between adjacent Widmanstätten α-Ti laths within prior beta grains. In this paper we describe an analysis of one such boundary where the axis/angle pair is close to [0001]/69.43° which is the relative orientation at which plausible 2D and 3D reference structures are formed. It is shown that the dislocation arrangements which would be expected for both of these models match that observed experimentally suggesting that the 2D and 3D approaches are equivalent at such special orientations.

2. EXPERIMENTAL OBSERVATIONS AND ANALYSIS

2.1 Experimental Procedure

Pieces of titanium sheet of commercial purity (≈1000-1200ppm O_2) were solution treated at 1000°C (i.e. within the β phase field) for half an hour, then quenched into water to produce the Widmanstätten microstructures. The specimens were then annealed for 20 min. at 700°C to obtain near equilibrium boundary structures. TEM specimens were prepared by twin-jet electropolishing using the acid-free solution described by Kestel [9] to prevent hydride formation. TEM observations were carried out using a Philips CM20 operating at 200 kV.

2.2 TEM Observations

The microstructure of the annealed samples consisted of many coarse (≈1μm across) α laths within each prior beta grain. One example of a HAGB separating two laths is shown in Fig. 1. This

boundary was flat over several microns and exhibited a well-defined structure with two distinct sets of periodic linear features. The first set (U_1) which is parallel to the intersection of the boundary plane and the surface of the foil had a spacing of ≈ 5.51 nm and was only observed for $\mathbf{g} = 01\bar{1}1_\lambda$ (Fig. 1a). The second set (U_2) had a spacing of ≈ 30.26 nm and was observed in both of the images (Figs. 1a, b). The contrast and orientation of these features confirm that both sets are interfacial dislocations rather than Moiré or other interference fringes.

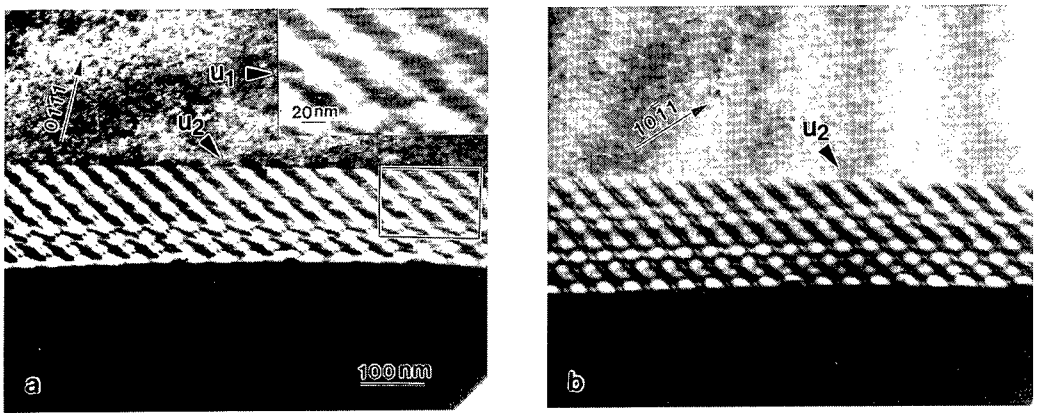

Fig.1 Weak beam dark field images of the HAGB recorded with $\mathbf{g} = 01\bar{1}1$ and $10\bar{1}1$, respectively.

Trace analysis was used to determine the line directions of sets U_1 and U_2 and these were $\mathbf{u}_1$ = [-0.6495 0.1953 0.4542 0.0128]$_\lambda$ and $\mathbf{u}_2$ = [-0.4121 0.6265 -0.2084 -0.2017]$_\lambda$, respectively. The boundary plane normal, **n**, was then calculated from the vector product of $\mathbf{u}_1$ and $\mathbf{u}_2$ giving **n** = [-0.0424 0.2292 -0.1869 0.5863]$_\lambda$. The axis/angle pair ($\mathbf{r}$,θ) relating the two grains was determined as ([0.0081 -0.0084 0.0003 0.6299]$_\lambda$ / 69.301°) from diffraction data.

2.3 Analysis Using the 2D Model

Several different candidate 2D reference structures were considered for the boundary but the most plausible is the (0001) Γ37 2D CSL which corresponds to a rotation of 69.43° about the normal to (0001). Fig. 2 is a schematic diagrams of this reference structure, showing the overlay of atomic positions in the (0001) layer for the two grains, represented by black and white circles, one rotated by 69.43° with respect to the other about their common normal. The deviation from this reference orientation was calculated as ($\mathbf{r}_{dev}$,θ_{dev}) = ([-0.2629 0.6556 -0.3927 0.0900]$_\lambda$ / 0.941°).

Following MacLaren and Aindow [7] the dislocation configuration in the boundary was modelled using the O-lattice algorithm with Burgers vectors obtained using Pond's topological theory of admissible interfacial defects [8]. For the simplest case of Class 1 interfacial dislocations in an interface between two grains related by the transformation **P**, the Burgers vectors, **b**, are given by combinations of translation vectors $\mathbf{t}_\lambda$ and $\mathbf{t}_\mu$, one from each of the adjacent crystals thus:

$$\mathbf{b} = \mathbf{t}_\lambda - \mathbf{P}\,\mathbf{t}_\mu$$

Feasible values for **b** were identified from the infinite number of possible values for **b** by considering only those where **b** is smaller than that of a crystal dislocation (and would thus not be expected to decompose), where $\mathbf{t}_\lambda$ and $\mathbf{t}_\mu$ are relatively short (and would thus perturb the reference structure over a shorter distance), and where the angle, ω, between **b** and $\mathbf{r}_{dev}$ is close to 90° (since these would accommodate the deviation most efficiently). From these feasible values, appropriate Burgers vectors for sets U_1 and U_2 were identified by comparing the observed line directions with those expected on the basis of the O2 lattice algorithm.

The appropriate Burgers vectors for sets U_1 and U_2 were: $\mathbf{b}_1^{2D}$ = -0.0897 0.0065 0.0832 0.0084]$_\lambda$ given by $\mathbf{t}_\lambda$ = 1/3 [1$\bar{2}$13], $\mathbf{t}_\mu$ = 1/3 [$\bar{1}\bar{1}$23], and $\mathbf{b}_2^{2D}$ = [0.0596 -0.1486 0.089 0.9796]$_\lambda$ given by $\mathbf{t}_\lambda$ = [0001], $\mathbf{t}_\mu$ = 0. A **b**-net was constructed using these Burgers vectors: a schematic diagram of this net projected onto the plane perpendicular to $\mathbf{r}_{dev}$ is shown in Fig. 3a. The L-net obtained directly from the **b**-net by connecting the centres of neighbouring polygons and rotating this pattern by ($\mathbf{r}_{dev}$/2 - 90) is shown in Fig. 3b, and the expected dislocation arrangement is shown in Fig. 3c. It was found that the line direction for a dislocation with a Burgers vector $\mathbf{b}_1^{2D}$ would be $\mathbf{u}_1^{2D}$ = [-0.644 0.1741 0.4699 0.0209]$_\lambda$; this makes an angle of 2.03° with $\mathbf{u}_1$ and has a spacing of 5.53 nm which compares well with the observed spacing of 5.51 nm for set U_1. Similarly, the direction for dislocations with a Burgers vector $\mathbf{b}_2^{2D}$ would be $\mathbf{u}_2^{2D}$ = [-0.2797 0.6228 -0.343 -0.2221]$_\lambda$; this makes an angle of 13.37° with $\mathbf{u}_2$ and has a spacing of 28.52 nm which compares well with the observed spacing of 30.26 nm for set U_2. Clearly, there is a good match between the line directions in Fig. 3c and those observed experimentally, and the spacings of both sets also agree well with the modelled structure.

2.4 Analysis Using the 3D CSL/DSC Method

The relative orientation of the grains separated by this grain boundary is close to the 3D CSL system Σ37 which is also associated with a rotation about [0001] by 69.43° as shown in Figure 2. Following the tables of Chen and King [10], the primitive DSC vectors for this CSL are 1/111 [$\bar{1}\bar{1}$,1,10,0]$_\lambda$, 1/111 [10,$\bar{1}\bar{1}$,1,0]$_\lambda$ and [0001]$_\lambda$ and these correspond to the Burgers vectors of possible interfacial dislocations. The line direction which dislocations with each of these Burgers vectors would adopt in the boundary was calculated using the equation given by Shin and King [11]:

$$\mathbf{U} = \mathbf{n} \times \mathbf{X}(02)$$

where **X**(02) is a vector of the O2-lattice [1]. The values of **u** obtained for each of the three Burgers vectors were compared with those observed experimentally. The line direction for a dislocation with Burgers vector $\mathbf{b}_1^{3D}$ = 1/111 [$\bar{1}\bar{1}$,1,10,0]$_\lambda$ would be $\mathbf{u}_1^{3D}$ = [-0.6437 0.1728 0.4709 0.0214]$_\lambda$; This makes an angle of 2.16° with $\mathbf{u}_1$. The spacing of $\mathbf{u}_1^{3D}$ was calculated as 5.56 nm which was close to the observed spacing of 5.51 nm for set U_1. Similarly the line direction for a dislocation with a Burgers vector $\mathbf{b}_2^{3D}$ =[0001]$_\lambda$ would be $\mathbf{u}_2^{3D}$ = [0.2506 -0.6191 0.3685 0.2248]$_\lambda$; This makes an angle of 16.11° with $\mathbf{u}_2$. The spacing of $\mathbf{u}_2^{3D}$ was calculated as 28.5 nm which compares well with the observed spacing of 30.26 nm for set U_2.

3. SUMMARY

The structure of a HAGB in Widmanstätten α-Ti with an axis/angle pair close to [0001/69.43° has been investigated by comparing diffraction contrast images of the dislocation configuration with geometric models of the defect content required to accommodate the deviation from various reference structures using both the 2D and 3D CSL models. For both models a good match was obtained between the dislocation line directions and spacings observed experimentally and those obtained using the O-lattice algorithm. For both sets, however, the network obtained using the 2D model gave a slightly better fit to the data than that obtained using the 3D CSL. This could indicate that the 2D CSL is a more appropriate description for the reference structure than the 3D CSL but the differences are not large enough to prove this conclusively.

ACKNOWLEDGEMENTS

We are grateful to Dr I MacLaren and Prof. R.C. Pond for helpful discussions, Professors I R Harris and J F Knott for the provision of the laboratory facilities, and CVCP and the School of Metallurgy and Materials at The University of Birmingham for financial support under the ORS Scheme.

REFERENCES

[1] W. Bollmann, Crystal defects and crystalline interfaces, 1970, Berlin, Springer-Verlag.
[2] G.A. Bruggemann, G.H. Bishop, and W.H. Hartt, in H. Hu (ed.), The nature and behavior of grain boundaries, 1972, Plenum, New York, p.83.
[3] F.R. Chen and A.H. King, Phil. Mag. A, 57 (1988), p.431.
[4] I. MacLaren and M. Aindow, Phil. Mag. Lett. 76 (1997), p.25.
[5] H. Grimmer, R. Bonnet, S. Lartigue and L. Priester, Phil. Mag. A, 61 (1990), p.493.
[6] S. Lay, P. Ayed and G. Nouet, Acta Met., 40 (1992), p.2351.
[7] I. MacLaren and M. Aindow, Phil. Mag. A, 76 (1997), p.871.
[8] R.C. Pond, Dislocations In Solids, 1989, Ed. F.R.N. Nabarro, (North Holland), **8**, Ch. 38.
[9] B.J. Kestel, Ultramicroscopy, 19 (1986), p.205.
[10] F.R. Chen and A.H. King, Acta Cryst., B43 (1987), p.416.
[11] K. Shin and A.H. King, Phil. Mag. A, 63 (1991), p.1023.

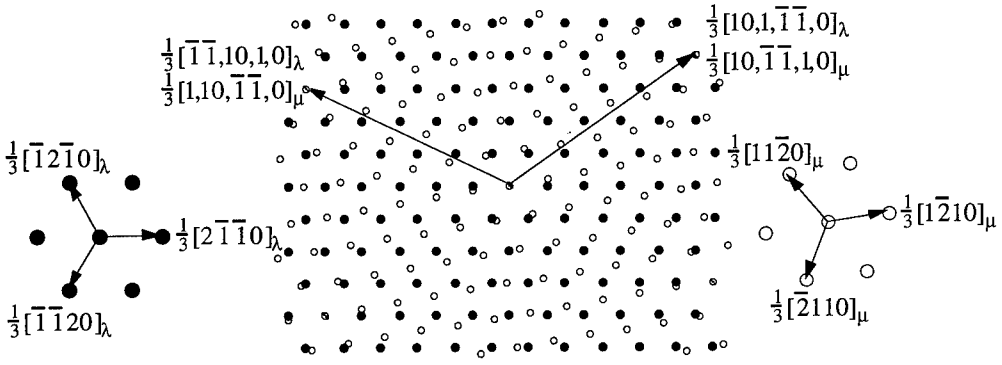

Fig. 2 A schematic diagram of the overlay of the (0001) planes of two grains, one rotated by 69.43° with respect to the other about the normal to these planes. The reference structure corresponds to a 2D exact CSL with $\Gamma = 37$, or equivalently to a 3D exact CSL with $\Sigma = 37$

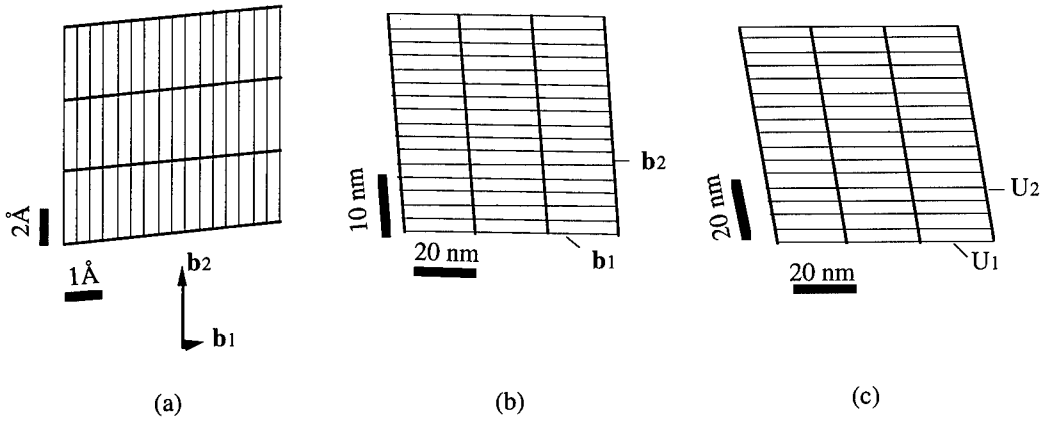

Fig. 3 Schematic diagrams showing the modelling of the dislocation configuration for the boundary in Fig. 1; (a) projection of **b**-net perpendicular to $\mathbf{r}_{dev}$; (b) corresponding L-net; (c) predicted dislocation network

Materials Science Forum Vols. 294-296 (1999) pp. 313-316

Wetting and Non-Wetting Behaviour of Silicon Carbide Grain Boundaries

S. Turan[1] and K.M. Knowles[2]

[1] Anadolu University, Department of Ceramic Engineering, Yunusemre Campus, TR-26470 Eskisehir, Turkey

[2] University of Cambridge, Department of Materials Science and Metallurgy, Pembroke Street, Cambridge CB2 3QZ, UK

Keywords: Silicon Carbide, Twinning, Interfaces, Special Grain Boundaries, Amorphous Intergranular Films, High Resolution Electron Microscopy

Abstract

Silicon carbide (SiC) grain boundaries have been observed to be free from intergranular films. On the basis of equilibrium film thickness calculations, it has been proposed elsewhere that because SiC has very high refractive index, the attractive forces are very large and thin amorphous films cannot exist at SiC grain boundaries. However, in our studies, we have observed film-free grain boundaries together with grain boundaries containing intergranular films. Possible reasons for the wetting and non-wetting behaviour of SiC grain boundaries are briefly discussed.

Introduction

Amorphous intergranular films exist at interfaces in ceramic materials and affect the mechanical properties of these materials. Clarke [1] showed theoretically that these films have an equilibrium thickness due to a competition between attractive forces and repulsive forces at interfaces, which depends on the dielectric properties of adjacent grains. The thickness is argued to be independent of crystal misorientation unless the interfaces are either low angle grain boundaries or special interfaces [2-5]. Recently, Turan and Knowles [6] demonstrated theoretically and experimentally that the film thickness is dependent on the misorientation across the interface if one or more of the crystals is highly anisotropic, such as hegzagonal boron nitride. In addition, it has also been argued [1] that SiC grain boundaries should not have intergranular films because the refractive index of SiC is very high, resulting in high attractive forces across the grain boundaries. However, it has been shown experimentally that SiC-SiC grain boundaries do indeed contain intergranular films [7,8].

Here, we report some further interesting observations on SiC-SiC grain boundaries and compare them with the observations in the literature.

Experimental procedure

The range of SiC-Si_3N_4 composites was prepared by mixing commercially available powders of pure SiC powder and Si_3N_4 powder without the addition of any sintering aids. The compacts were encapsulated in tantalum cans and then hot isostatically pressed at 2100°C for 1 hr under a pressure of 200 MPa [8]. Specimens for transmission electron microscopy (TEM) examination were prepared using standard ion beam thinning methods and examined uncoated by TEM using a JEOL 4000EX-II at 400 kV.

Experimental results and discussion

High resolution electron microscope (HREM) observations showed that the SiC-SiC interfaces in composites made from deoxidised powders do not contain intergranular films, but in contrast the interfaces in the composites made from as-received powders mostly contained thin films [6]. In the latter type of composites, in contrast to the general trend (Fig. 1(a)), some interfaces did not contain amorphous intergranular films (Fig. 1(b) and (c)).

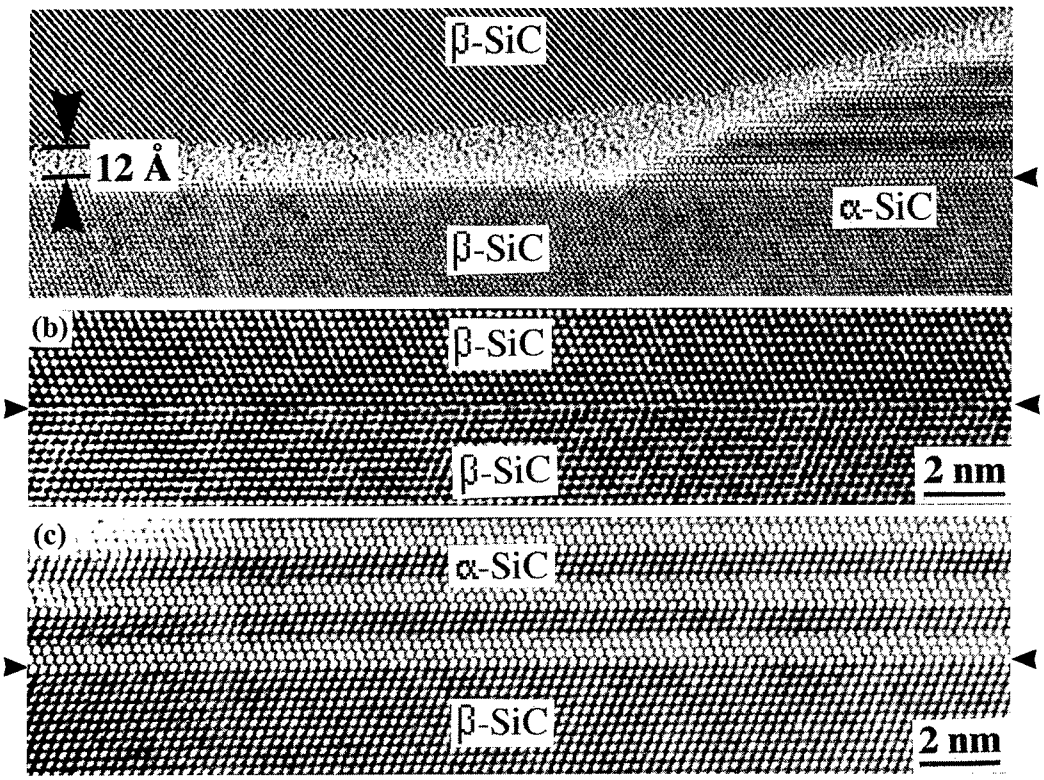

Figure 1 Different type of interfaces between SiC grains in the composites made from as-received powders: (a) a high angle grain boundary between two β-SiC grains containing an intergranular film, (b) a twin boundary and (c) a coherent interphase boundary between α-SiC and β-SiC.

The interface in Fig. 1(a) is wetted by intergranular film but on the right hand side of the micrograph where it is arrowed the intergranular film do not wet the interphase boundary. The interfaces in Fig 1(b) and (c) are special interfaces that one of them is a twin boundary (Fig 1(b)) whereas the other one is a coherent interphase boundary between β-SiC grain and α-SiC grain (Fig 1(c)) when the orientation relationship is:

$$[110]_{\beta\text{-SiC}} \parallel [\bar{2}110]_{\alpha\text{-SiC}} \text{ and } (1\bar{1}\bar{1})_{\beta\text{-SiC}} \parallel (0001)_{\alpha\text{-SiC}} \qquad \textbf{(OR-1)}$$

For an interface to be non-wetting with an intergranular film given that the material contains liquid phases at the fabrication temperature, it should satisfy that the interfacial energy for the non-wetted interface is smaller than the wetted interface [3]. This condition is satisfied for these special interfaces in Fig. 1(b) and (c)).

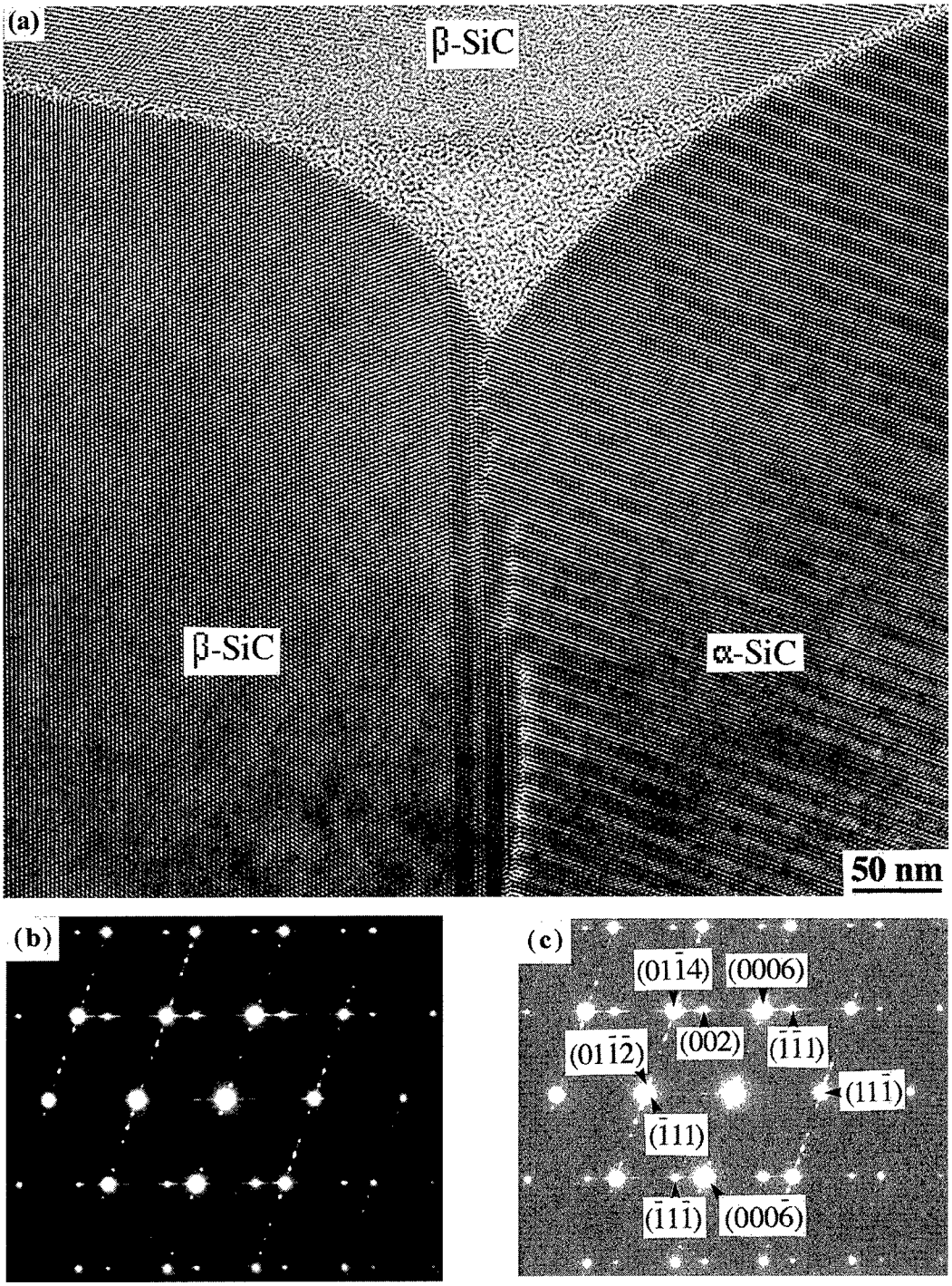

Figure 2 (a) An amorphous triple junction phase between SiC grains showing that amorphous phase is wetting the arrowed interfaces whereas it does not wet the interphase boundary between α-SiC and β-SiC, (b) diffraction pattern obtained from the latter interphase boundary and (c) its indexed diffraction pattern.

A second interface is shown in Fig. 2 where the amorphous triple junction phase does not appear to extend into the interphase boundary where α-SiC and β-SiC grains meet. Amorphous intergranular films do exist at the arrowed interfaces at the top of the figure. In this case, the orientation relationship can be deduced from the diffraction pattern shown in Fig. 2(b) to be:

$$[110]_{\beta\text{-SiC}} \parallel [\bar{2}110]_{\alpha\text{-SiC}} \text{ and } (1\bar{1}1)_{\beta\text{-SiC}} \parallel (0001)_{\alpha\text{-SiC}} \qquad \textbf{(OR-2)}$$

It should be noted that the grain on the left hand side is actually a twinned β-SiC grain, but here only the minor twinned part is present and the strong diffraction spots arising from the bulk of the SiC grain is not shown here. The interface plane in Fig. 2 is different from that seen in orientation relationship (OR-1). Here, the interface plane is parallel to $(\bar{1}11)$ plane of β-SiC and $(10\bar{1}\bar{2})$ plane of α-SiC, with (0001) planes of α-SiC making an angle of 70.6° with the interface plane. From the diffraction pattern the interface can be identified as a twin boundary. Twinning occurs on $(\bar{1}11)$ plane of β-SiC and $(10\bar{1}\bar{2})$ plane of α-SiC. Therefore, the interface is "special" and according to qualitative energy considerations [3,4] it should not be wetted by intergranular films, as we have observed.

When the interface boundary is examined closely, a distinct microtwin can be observed near the interface. Starting from the tip of the triple junction dislocations with irregular spacings at the interphase boundary exist and away from the start of the interface the thickness of the microtwins increases.

The α-SiC grain is mostly 6H SiC, but at the tip of the triple junction there is a ≈ 2 nm thick band of β-SiC (arrowed). In the composites made from as-received powders, it was found that α-SiC transformed into β-SiC through a nitrogen containing liquid phase by a solution re-precipitation route [9]. Therefore, it is likely that the β-SiC grain is growing at the expense of α-SiC and the interphase boundary is moving towards the α-SiC grain by forming twins. Although at room temperature this interface is not wetted, it is unclear whether such a special interface can be wetted at the fabrication temperatures although it is known that in general solid-liquid interface energies are lower at higher temperatures [3,4].

Conclusions

A twin boundary is observed between α-SiC and β-SiC and it is found that the twinning occurs on $(\bar{1}11)$ plane of β-SiC and $(10\bar{1}\bar{2})$ plane of α-SiC. This and the other special interfaces shown in Fig. 1 were not wetted by intergranular films and this can be understood qualitatively in terms of special interfaces which cannot be wetted by thin films energetically.

The results also show that SiC-SiC grain boundaries do have intergranular films (Fig. 1(a) and Fig. 2(a)) provided that they do not have special orientation relationship and liquid phases are available at fabrication temperatures. These are different from theoretical expectations raised by Clarke [1] that SiC grain boundaries would not be wetted by intergranular films because the refractive index of SiC is very high. However, given possible additional contributions to the repulsion of grains by steric forces by, for example, electric double layers [10], it is possible to rationalise the formation of intergranular thin films in SiC materials.

References

[1] D.R. Clarke, J. Am. Cer. Soc., **70**, p15 (1987).
[2] H. Schmid & M. Rühle, J. Mat. Sci., **19**, p615 (1984).
[3] D.R. Clarke, J. de Physique **46** Coll. C4, p51 (1985).
[4] D.R. Clarke, In Ceramic Microstructures '86 Eds: J.A. Pask and A.G. Evans, p569 (1987).
[5] K.M. Knowles & S. Turan, Mat. Sci. For., **207-209**, p353 (1996).
[6] S. Turan & K.M. Knowles, Ins. Phys. Conf. Ser., **153**, p483 (1997).
[7] L.S. Sigl & H.-J. Kleebe, J. Am. Cer. Soc., **76**, p773 (1993).
[8] S. Turan & K.M. Knowles, J. Microscopy, **177**, p287 (1995).
[9] S. Turan & K.M. Knowles, J. Am. Cer. Soc., **79**, p2892 (1996).
[10] D.R. Clarke, T.M. Shaw, A.D. Philipse & R.G. Horn, J. Am. Cer. Soc., **76**, p1201 (1993).

Materials Science Forum Vols. 294-296 (1999) pp. 317-320

Interplay between Planar Defects and Threading Dislocations in GaAs-on-Si

A. Delimitis[1], Ch.B. Lioutas[1], K. Michelakis[2] and A. Georgakilas[2,3]

[1] Aristotle University of Thessaloniki, Physics Department, GR-54006 Thessaloniki, Greece

[2] FORTH, Institute of Electronic Structure and Lasers, Microelectronics Research Group (MRG), P.O. Box 1527, GR-71110 Heraklion, Crete, Greece

[3] University of Crete, Physics Department, P.O. Box 2208, GR-71003 Heraklion, Crete, Greece

Keywords: Transmission Electron Microscopy, Molecular Beam Epitaxy, Planar Defects, Heteroepitaxy

Abstract

GaAs-on-Si films grown by Molecular Beam Epitaxy (MBE) on vicinal (100) Si substrates were examined by means of Transmission Electron Microscopy in order to study the dependence of threading dislocations' density on the formation of planar defects. We found that the threading dislocations' density slightly changes in the mid-range angles (1.5° - 6°) and is in the order of 10^8 cm^{-2}. The dislocation density is minimised significantly for tilting angles below 1°. However a large number of planar defects appears for very small and large angles. The appearance of microtwins in a narrow zone is characteristic for 0.5° tilting angle while the anisotropic growth of stacking faults characterises films grown on large angle tilted Si substrate.

1. Introduction.

Heteroepitaxial layers of GaAs on silicon [1] gained much attention as they provide the possibility of manufacturing monolithic devices having the common used silicon substrates with the III-V elements. On the other hand, the mismatch on the lattice parameters, the difference in the thermal expansion coefficients between Si substrate and GaAs overgrown film leads to the formation of extended crystal defects, that seriously affect the properties of the obtained devices. It has been proposed [2] that misoriented (100) Si substrates towards [011] or (111) directions provide the optimum conditions for minimising the structural faults (threading and misfit dislocations, antiphase domains (APDs), stacking faults, twins) with the tilting angle being in the range of 4° - 4.5°, in order to form double atomic layer steps. This method is used particularly for the elimination of antiphase domains [1,3] since these defects affect dramatically the electrical and optical properties of GaAs thin films and decrease the yield performance of such as devices.

In this paper we present a systematic electron microscopy study of the influence of the Si substrate tilting angle on the structural characteristics of GaAs-on Si thin films and the interrelation of threading dislocations and extended planar defects.

2. Sample preparation and experimental details

We used 3-inch diameter silicon wafers tilted from (100) towards [011] direction, with tilting angles spanning the range of 0° to 9°. GaAs-on-Si samples were grown by Molecular Beam Epitaxy (MBE), using the standard two-step procedure [1,4]. A pre-exposure of Si to As_4 at 400°C took place before growth of the films for prelayer formation in several deposition temperatures. Finally, over 2 μm thick films were grown with a structure of the type (Si substrate)-GaAs/AlAs/GaAs.

Electron microscopy studies of the films were done both parallel to growth direction [100] (plane-view) and towards [011] and [0$\underline{1}$1] directions, with cross-sectional observations (XTEM). Samples appropriate for TEM were done using mechanical polishing and low voltage accelerated (3 - 4 KeV) Ar+

ion beam milling without any cooling treatment. In the case of plane view samples, we used a sequential ion beam milling from both sides of the specimen, in order to have transparent areas from the free surface of GaAs film down to the interface GaAs/Si in successive layers. In every case we examined two sets of XTEM samples (towards [011] and [0$\underline{1}$1] directions) in order to determine the existence of any anisotropy in the growth of structural defects.

3.Results and Discussion

Electron Microscopy observations revealed the existence of threading dislocations in almost all tilting angles. The dislocation network, as expected, arises from the interface GaAs/Si and in many cases reaches the near-surface region, crossing all over the film. From XTEM images it was concluded that they have no preferential direction of crossing and their density becomes smaller as they traverse from GaAs/Si interface to GaAs free surface. Table 1 summarises the threading dislocations' density, found in the order of 10^8 cm^{-2}, as measured from plane-view and XTEM images.

TABLE 1

Sample	*Tilting angle*	*Dislocation Density* $[10^8 cm^{-2}]$
SIGAS-1	0.5° off	-
SIGAS-2	1.0° off	2.1
SIGAS-3	1.5° off	6.07
SIGAS-8	3.0° off	8.8
SIGAS-4	4.5° off	5.53
SIGAS-5	7.5° off	4.5
SIGAS-6	9.0° off	5.03

Fig. 1 shows typical bright field (BF) XTEM image from sample grown on Si substrate with cut-off angle 4.5° (SIGAS-4) viewed along [0$\underline{1}$1] direction with **g** vector [400]. The edge type misfit dislocations' network is presented as a system of bright and dark fringes, located exactly at the interface of substrate and film. Planar view observations verified [3] the existence of two networks of misfit dislocations, perpendicular to each other. The distance between the dislocations in the two networks, measured from weak beam dark field images as well as from the satellite electron diffraction spots, is found equal to 9.4 nm, in agreement with the lattice mismatch between GaAs and Si.

The existence of extended planar defects is notable in both small and large tilting angles of Si substrate. Significantly, figs. 2(a) and (b) show typical XTEM images from film grown on Si substrate with 0.5° tilting angle (SIGAS-1) observed along [0$\underline{1}$1] and [011] directions respectively. The main features on theses images are: (a) the presence of extended planar faults that lie in characteristic crystallographic directions and (b) the negligible number of threading dislocations. The extra spots in Selected Area Electron Diffraction image, that are denoted with white arrows in fig. 2(c), reveal that these observed planar faults are twin planes. Observations along [0$\underline{1}$1] and [011] directions confirmed the isotropic distribution of twins in {111} planes. Fig. 3 shows the {111} tetrahedron and the electron beam directions for the images on fig. 2. It is obvious that in every case, only two sets of these planes are projected along the electron beam (ACO and ACB or OAB and OCB). The presence of other two sets is revealed from the contrast that is visible under specific imaging conditions. The black arrowheads in fig. 2(b) show twins in these planes. Fig.2 also shows that the dominant feature in these GaAs films is the appearance of microtwins restricted in a 300 nm thick zone starting from the GaAs/Si interface. However we rarely found in very thick areas of the specimens several cases of twin planes crossing the GaAs film throughout the free surface.

The appearance of extended planar defects is also the main characteristic in samples grown on Si substrates with large tilting angles. Fig. 4 shows a typical BF XTEM image from GaAs film grown on Si substrate with tilting angle 7.5° (SIGAS-5), observed along [0$\underline{1}$1] direction. A wide area of planar defects is clearly shown, expanding in the whole film thickness. In most cases, the faults end at the free surface of

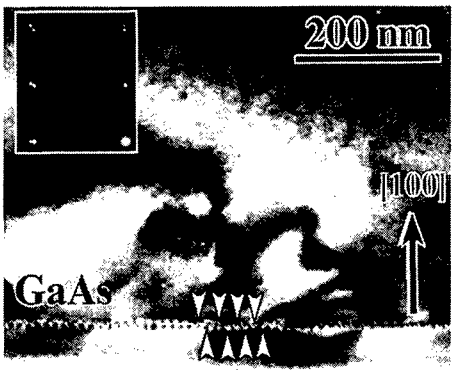

Fig.1 BF XTEM image from sample SIGAS-4 (Si substrate 4.5° tilted) viewed along [0$\underline{1}$1] direction. Arrows indicate the network of misfit dislocations on GaAs/Si interface.

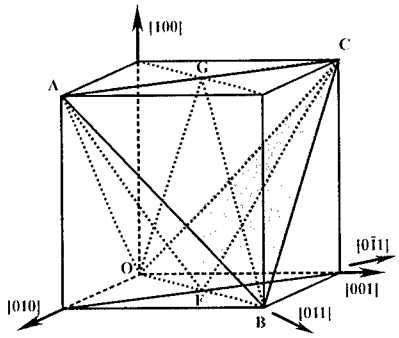

Fig.3 The {111} tetrahedron and the electron beam directions for XTEM images.

Fig.4 BF XTEM image from sample SIGAS-5 (tilting angle 7.5°) viewed along [0$\underline{1}$1] direction. Black arrows on the free surface of the film show the position of the steps created form planar faults grown preferably on (111) planes.

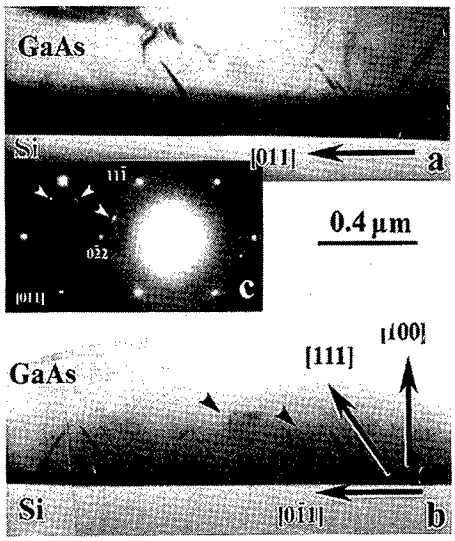

Fig.2 BF XTEM images from sample SIGAS-1 (tilting angle 0.5°) with the electron beam along [0$\underline{1}$1] and [011] directions for (a) (b) respectively.(c) Selected Area Electron diffraction pattern with extra spots revealing the microtwinning.

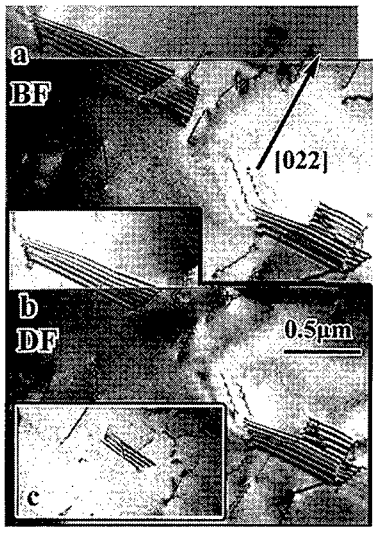

Fig.5 BF (a) and DF (b) Plane view TEM images from sample SIGAS-5 (tilting angle 7.5°). α-fringes contrast reveal that the planar faults in fig.4 are staking faults. (c) BF plane view TEM from an area close to the GaAs/Si interface.

the film and correspond to characteristic steps, denoted by black arrowheads on fig. 4, that increase significantly the free surface roughness. Fig. 4 shows as well the preferential growth of the planar defects on one of the characteristic {111} crystallographic planes. The observation of the specimen along [0$\underline{1}$1] presents nearly the same steps but the projection of the planar faults is not confined on particular crystallographic direction. We consequently conclude the anisotropic growth of planar faults that lie on (111) planes (ABC plane in fig. 3). Scanning Electron Microscopy and Atomic Force Microscopy images show the formation of different size hollows on the free surface of the film which approximately have the same orientation. This morphology could explain the presence of the surface steps in the two XTEM observations. Furthermore figs. 5(a) and (b) show typical BF and DF plane-view images of SIGAS-5 film that present the planar faults' situation near the free surface of the film. α-fringes contrast reveal that we have to deal with staking faults that are parallel only to [0$\underline{1}$1] direction. Plane-view TEM images (fig. 5(c)) from the same specimen, after sequential Ar^+ ion milling, show that the size as well as the density of the stacking faults are reduced as the distance from the surface of the film increases and they are negligible near the GaAs/Si interface.

4. Conclusions.

Electron microscopy studies of the structural properties of GaAs thin films grown by MBE on (100) Si substrates tilted towards [011] direction showed a clear dependence between the linear and planar defects. The presence of extended planar faults leads to a reduction of threading dislocations' density which, is more remarkable for very small Si substrate tilting angles. It is well known that both linear and planar faults may exist already from the early stages of the GaAs film growth [5] and consequently they have the possibility to dominate preferably the structural character of the film [6]. Thus the neutralisation of remaining misfit stresses during growth by the expansion of misfit dislocation segments and the resulting interactions of moving threading dislocations with the planar faults could be proposed in order to explain the observed decrease of threading dislocations' density. On the other hand the character of the planar defects seems to depend on the tilting angle. Small tilting angles allow the isotropic appearance of microtwins on the equivalent {111} planes that are mainly restricted in a narrow zone near the GaAs/Si interface. This formation of twins is consistent with the development of small islands with {111} facets in the early steps of the film growth[7]. Nevertheless it is interesting to point out that this growth model is preferable for small tilting angles, while there are no results supporting the same mechanism for mid-range angles. Larger steps on the tilted surface of Si substrate, in large tilting angles, enforce the presence of stacking faults which are preferably grown on (111) plane only and extend throughout the film .

Acknowledgements

This work gained financial support from the research program PENED (95)-1623 of G.S.R.T.

References

[1] A. Georgakilas, P. Panayotatos, J. Stoemenos, J.-L. Mourrain, A. Christou, J. Appl. Phys. **71**, 2679 (1992)

[2] E. Kaxiras, O.L. Alerhand, J. Wang and J.D. Ioannopoulos, Mater. Sci. Eng. **B14**, 245 (1992)

[3] M. Kayambaki, R. Callec, G. Constantinidis, Ch. Papavassiliou, E. Löchtermann, H. Krasny, N. Papadakis, P. Panayotatos and A. Georgakilas, J. Cryst. Growth **157**, 300 (1995)

[4] A. Georgakilas, J. Stoemenos, K. Tsagaraki, Ph. Komninou and N. Flevaris, P. Panayotatos and A. Christou, J. Mater. Res. **8**(8), 1908 (1993)

[5] A. Vila, A. Cornet, J. R. Morante and P. Ruterana, Inst. Phys. Conf. Ser. No. 134, pp. 353-356 (1993)

[6] T. Yodo, M. Tamura, M. Tomita and M. Wazawa, Jpn. J. Appl. Phys. **34**(4B), L491 (1995)

[7] F. Ernst and P. Pirouz, J. Appl. Phys. **64**(9), 4526 (1988).

Materials Science Forum Vols. 294-296 (1999) pp. 321-324

Structural Evolution with Temperature of MBE Au/Ni Multilayers

C. Dressler, P. Bayle-Guillemaud and J. Thibault

CEA / Département de Recherche Fondamentale sur la Matière Condensée/ SP2M,
17 rue des Martyrs, F-38054 Grenoble, France

E-Mail:jthibault@cea.fr

Keywords: Quantitative HREM, Evolution with Temperature, Au-Ni, Metallic Multilayers

Abstract: Ni films grown on (001) Au are expected to be unstable for a thickness lower than one atomic plane. Nevertheless they were found to grow coherently until 5 Ni mls. The thermal stability of these Ni coherent thin films is investigated.

1. Introduction

Despite the large misfit between Au and Ni (15%), Ni can grow coherently up to 5 monolayers (mls) on (001)Au by MBE [1]. This is due to an intermixing occurring during growth. The stability with temperature of these multilayers has been investigated by HREM: an anisotropic chemical decomposition upon annealing occurs until the layer remains strained. This has been confirmed by in-situ X-rays experiments [2]. The very early stages of the transformation has been observed by in-situ HREM experiments. The evolution of Au/Ni multilayers and Au/Ni alloys grown by MBE [2] were studied showing that the multilayered structure has no influence on the phenomenon. The present paper will report the HREM study of the phenomenon observed on multilayers which is particularly clear for initial samples containing (4Ni/20Au) repeating sequences. HREM was performed on a Jeol 4000EX at 400 kV (Cs = 1 mm) and in-situ experiments were done in a Jeol 3010 at 300 kV (Cs = 0.6 mm).

2. Evolution between 180°C and 300°C of 4 mls Ni on (001)Au

2.1 T < 150°C

The initial sample is shown on fig. 1a with the corresponding distortion profile (fig 1b). They are identical to the ones found in [1]: the Ni layer is no longer confined on 4 atomic planes but is extended on 10 planes: an intermixing between Au and Ni occurs during growth which induces partial stress relaxation and permits Ni to grow on (001) Au without dislocations. This was shown also to occur by molecular dynamics simulations [2]. The image contrast is inhomogeneous revealing the strain inhomogeneity on both sides of the Ni layer. No observable evolution was detected in samples treated at a temperature lower than 150°C.

2.2 2 mn at T> 180°C

Some change occurs at that temperature. The layer appears more straight and the contrast on both sides of the layer becomes more homogeneous. Some atomic planes exhibit a stronger white intensity on areas laterally limited. The distribution of these platelets is hazardous.

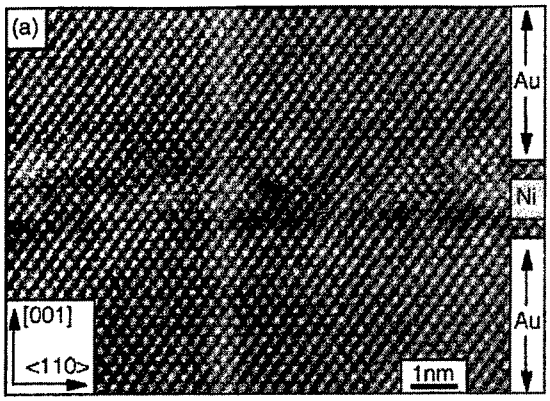

Fig 1 a) HREM image of Ni (4 mls)/Au before heat treatment

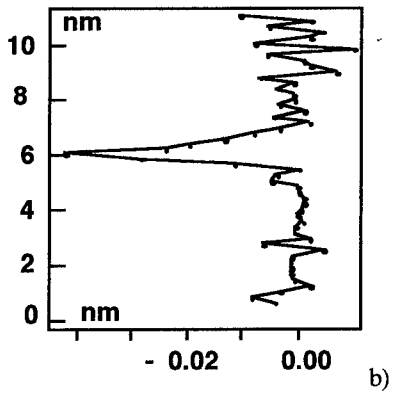

b) distortion profile

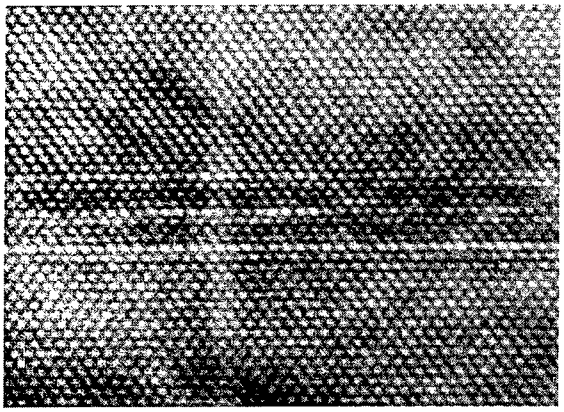

Fig 2 a) HREM image of Ni (4 mls)/Au after 2 mn at 250°C

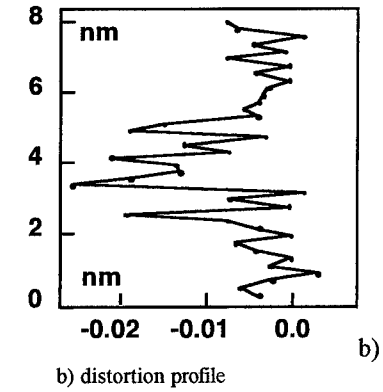

b) distortion profile

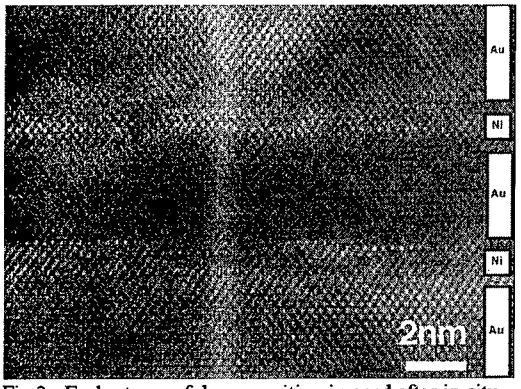

Fig 3 : Early stages of decomposition imaged after in-situ heating at 200°C

2.3 2 mn at T = 250°C and 300°C.

The contrast change is clearly established at 250°C (fig. 2a). Periodic oscillations of four (002) atomic planes parallely to the growth direction can be well recognized. The contrast of these oscillations is enhanced at 300°C and the lateral extension of the platelets is wider at 300°C. The oscillations are coherent laterally over 20 nm at 250°C and 30 nm at 300°C. But domains of 60 nm width can be found. Figure 2b shows the distortion profile. At a temperature higher than 300°C the oscillations disappear: Ni likely diffused into the 100 nm thick Au substrate.

3. The very early stages of the transformation : in-situ electron microscopy.

The very early stages of the phenomenon were studied by in-situ microscopy (fig. 3). The transformation takes place inhomogeneously along the layer. A platelet-like contrast appears only

on one atomic plane. This sustains clearly the observations made at 180°C. The time and temperature ranges in which the transformation begins in the microscope are similar to those in the ex-situ experiments despite a difference of 20°C which may be attributed to the temperature calibration. Thus it seems that the thin film condition for in-situ experiment has no basic significant consequence on the phenomenon.

4. Image interpretation of the contrast oscillations : Ni or Au rich planes ?

Since the HREM imaging is a non linear process, it is necessary to simulate the images in order to validate a structural model by a comparison between experimental and simulated images. In the present case, the contrast oscillations may be due to either Ni or Au rich planes. Two models of Ni profiles which are the most plausible are presented here. Firstly three Au rich planes (fig. 4a) are embedded into an Au_{1-x}-Ni_x ($x = 0.3$), whereas in fig. 4b three Ni rich planes are embedded in Au rich planes. These two cases will illustrate the difficulty of interpretation. The contrast variation in both cases is shown to vary on a subtle manner (fig. 4a, b). Thus the only way to discriminate is to make an experimental through focus series of a sample with a thickness ramp. Fig. 4 c and d show two images obtained at a focus respectively around -30 nm and -70 nm in an area around 25 nm thick. The features of these images are similar to the ones given by the simulation of the Ni profile given on fig 4b. Thus a Ni planar enrichment is likely to occur.

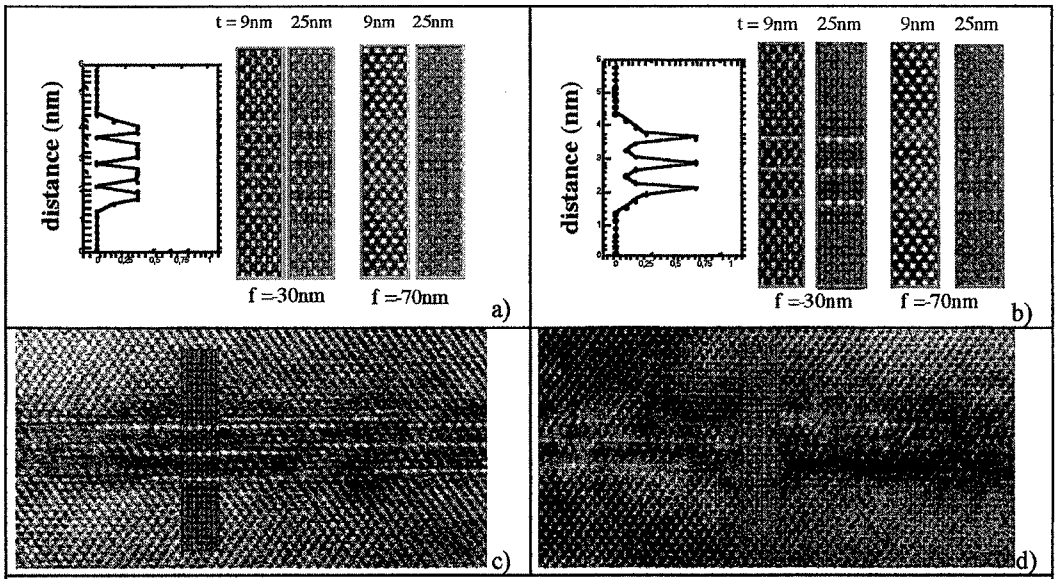

Fig 4 : HREM simulations of two different Ni profiles for two different defocusing distances and two different thicknesses t = 9 nm and t = 25 nm. The motif appearing in (a) at t=25 nm and f= -70nm appears in (b) for f = -30nm. The HREM experimental images c and d correspond to f = -30nm and f = -70nm and a thickness around 25nm.

5. Discussion

The Ni-Au system has a large miscibility gap, and no ordered phase exists. Thus the occurrence of a periodic structure has to be discussed. From X-rays experiments this structure is stable at 250°C for several days. One must add also that the observed transformation is anisotropic and no longer occurs as soon as the Ni layer is fully relaxed [3].

5.1 Nucleation

Nuclei made of Ni platelet precipitate first, which induces a large volume change. In this case platelet nucleation is favored even in the case of coherent precipitate [4]. No long period fluctuation

has been observed in the early stages as required by a spinodal decomposition [5] although a lot of experimental results reviewed in [6] claimed that it takes place in AuNi bulk alloys along the three [001] axes. Our results look quite similar to what have been observed in Al-Cu alloys [7] where the Guinier Preston zones were shown to be the nuclei of the ordered Al_2Cu phase. In our case, the in-situ experiment shows that the initial enrichment is planar, the platelets being inhomogeneously distributed. Afterwards these platelets begin to grow in thickness exhibiting a new phase with a periodic structure. In fact this type of nucleation is sustained by numerical simulations where a strong softening in tension of Ni along the <001> direction [8a,b, 9a] is shown to occur. Furthermore this local enrichment in platelets on (001) planes has been detected by diffuse X-ray scattering to occur even above the miscibility gap [10].

5.2 Stability of the 3Au/Ni phase.

From the equilibrium bulk phase diagram, no ordered phase is expected to be stable in AuNi. Nevertheless numerical simulations [8, 9] show that the Au_nNi_n superlattice along [001] is energetically favorable over the disorder alloy. Furthermore Ozolins et al showed [9a] that the Au_nNi_n superlattice along [001] deviates strongly from the Vegards law: the a parameter of the tetragonal cell varies abruptly as soon as the Ni content is larger than 10% to reach a value slightly lower than the a(Au) parameter. They found a (3Au/Ni) = 0.406 nm and c(3Au/Ni) = 0.752 nm. Furthermore in [10b] the authors show that the enthalpy of formation for 3Au/Ni [001] superlattice is not too much unfavorable and thus the phase might be stabilized by epitaxial stresses.

6. Conclusion.

Experimentally we found that after heat treatment of 28Au/4Ni multilayers an anisotropic decomposition occurs in the Ni areas and that a metastable phase 3Au/Ni-like superlattice can be stabilized on the Au (001) substrate. This results are well sustained by numerical simulation except the fact that the pure phase has not been detected. This might be due to an entropic effect or to a kinetic effect: the diffusion in the temperature range used is extremely low and only few exchange over one atomic distance is expected. The observation of long time heat treated samples may help to see if the pure phase is stabilized.

Acknowledgments : G. Abadias, B. Gilles, A. Marty made the MBE samples, and the X-rays experiments with I. Schuster. They are all are thank for their close collaboration.

[1] P. Bayle, T. Deutsch, B. Gilles, F. Lançon, A. Marty and J. Thibault, *Ultramicroscopy*, 56, 1994, 94.
[2] T. Deutsch, P. Bayle, F. Lançon, J. Thibault, *Jour. of Physics: Cond. Matter*, 7, 1995, 6407.
[3] C. Dressler, G. Abadias, P. Bayle-Guillemaud, A. Marty, I. Schuster, J. Thibault, and B. Gilles, *Appl. Phys. Let.* 72, 1998, 2241.
[4] J. W. Christian, *The Theory of Transformations in Metals and Alloys*, 1975, Pergamon Press, Oxford
[5] J. Cahn, Trans. Metall. Soc. AIME, 242, (1968), 166.
[6] J Woodilach, B.L. Averbach, *Acta. Met*, 16, 1968,. 255.
[7] H. Fujita, C. Lu, *Materials Transactions, JIM*, 33, 1992, 897.
[8] a)T. Deutsch, 1995, PhD Thesis, Université Joseph Fourier, b) T. Deutsch, A. Pasturel, in "Stability of Materials" (1996) NATO-ASI Sub-Series B355 Physics. p381.
[9] V. Ozolins, C. Wolterton, A. Zunger, Phys. Rev. B57, 1998, a) p4332, b) p4816, c) p 6427.
[10] T. B. Wu, J. B. Cohen, Acta. Met. 31, (1983) 1929.

Materials Science Forum Vols. 294-296 (1999) pp. 325-328

Variation of Interfacial Structure and Chemistry of Topotactic {111}MgO-Cu Interfaces with the Oxygen Chemical Potential

S. Laurent[1], D. Imhoff[2], C. Colliex[2], M.J. Hÿtch[1], J. Devaud[1], S. Hagège[1] and M. Backhaus-Ricoult[1]

[1] Centre d'Etudes de Chimie Métallurgique, CNRS, 15 Rue G. Urbain, F-94407 Vitry, France

[2] Laboratoire de Physique des Solides, CNRS, Université Orsay, F-91106 Orsay, France

Keywords: Metal-Oxide Interfaces, Interfacial Electronic States, Bonding, Oxygen Activity Dependency, MgO-Cu

Abstract

Atomic structure and electronic states of flat polar {111} MgO-Cu interfaces brought to equilibrium at different oxygen activities are studied by HREM and EELS. For high oxygen activity (10^{-8} at 900°C) the final magnesia plane at the interface is composed of oxygen and is fully occupied. Copper at the interface adopts a Cu_2O-like electronic state with a large transfer of charge across the interface. Lattice deformations due to interfacial dislocations are highly localised within the first two copper planes. At lower oxygen activities (10^{-12} at 900°C) no visible charge transfer for copper is detected across the interface, interfacial copper remains in its metallic state. HREM imaging reveals perturbations in the copper lattice close to the interface which can be explained by a lattice relaxation due to reduced occupancy of the oxygen end plane.

Introduction

Many metal-oxide interfaces are thermodynamically stable within a wide range of oxygen activities determined by the redox-equilibria of the metal and the oxide. Even though the same metal and oxide phase are in contact, the interface structure may vary with oxygen activity. This has been examined by studying a unique and well defined interface (crystallographic orientation and interface position kept constant), which was brought to equilibrium at different oxygen partial pressures. Modification by impurities of the interfacial structure and chemistry was avoided by forming the interfaces by internal reaction at high temperature within a solid matrix. Thermodynamic equilibrium, with different oxygen partial pressures, was achieved by annealing for a long time at temperatures close to the metal melting point and ensuring, by comparison of different annealing times, that no further shape changes occurred.

In the present work Cu-MgO {111}//{111} interfaces were chosen as the model system. Numerous results have already been reported on this system, see for example [1,2,3,4,5], including high resolution electron microscopy (HREM), atom probe and electron energy loss spectroscopy (EELS). For 950°C, $a_{O2}=10^{-8}$ the authors in [5] report ELNES features different from our results, which they interpret in terms of a small charge transfer of 0.18e and a reflection of the MIG states. However, a systematic study on the influence of oxygen chemical potential on metal-oxide interfaces is missing and is the aim of our present work [6,7]. The interfaces are produced by internal oxidation of (Cu,Mg) alloys at different oxygen partial pressures and investigated by HREM and EELS in order to reveal the atomic and electronic structure at the interface.

Experimental procedure

A copper 3% magnesium alloy was oxidised at 900°C for 300 to 1000 hours at different oxygen activities, established by a Rhines pack, $a_{O2}(Cu/Cu_2O) = 10^{-8}$ or a buffering CO/CO_2 gas mixture

(3% CO), $a_{O2} = 10^{-12}$. Oxidised samples were cross-sectioned, mechanically polished and ion-milled in a cold stage to electron transparency.
The thin foils were investigated with a conventional transmission electron microscope (CTEM JEOL 2000 FX) in order to identify the morphology and the orientation of the precipitates. HREM was performed on a TOPCON 002B microscope (200kV, Cs=0.4 mm, equipped with CCD camera and on-line diffractogram analysis). EELS was carried out on a dedicated scanning transmission microscope VG HB 501 STEM (100kV, field emission gun, GATAN parallel EELS spectrometer). Images were taken close to the Scherzer focus. Bragg filtered images and geometric phase images were used to reveal local lattice perturbations and to identify easily the position of the interface and interfacial dislocations [8]. The occupancy of the final magnesia plane at the interface was investigated by comparison of image simulations (produced using the EMS software package) with the experimental HREM images.
In the VG STEM, EELS spectra were acquired for 2-5 seconds for the characteristic O-K, Cu-L and Mg-L absorption edges. Typical working parameters were a probe size of 1.5 nm, a collection semi-angle of the spectrometer of 16 mrad and an energy dispersion of 0.1 - 0.2 eV/channel. Line spectra were acquired at many different probe positions across the interface. The characteristic signals were extracted from the acquired spectra by removal of the intrinsic dark current of the array of photo-diodes and by background subtraction with a power law approach. Details on the experimental procedure and the spectra treatment are reported elsewhere [7,9].

Experimental results and interpretation
For the investigated oxygen activities, internal oxidation of the (Cu,Mg) alloys yields mainly MgO cubo-octahedra in topotactic orientation with the copper matrix. The cubo-octahedra are limited by $\{111\}_{MgO}//\{111\}_{Cu}$ and $\{001\}_{MgO}//\{001\}_{Cu}$ facets. The relative facet size varies with the oxygen activity leading to the formation of almost octahedral precipitates at high oxygen activity and to increasing truncation at low oxygen activity, see [10,11].

$\{111\}_{MgO}//\{111\}_{Cu}$ interfaces in equilibrium with $a_{O2}=10^{-8}$ at 900°C
A typical $\{111\}_{MgO}//\{111\}_{Cu}$ interface brought to equilibrium at 900°C and $a_{O2}=10^{-8}$ is shown in Fig. 1a with a close-up in Fig. 1b. The interfaces are flat on an atomic scale over large distances. Steps of diatomic (Mg-O) height occur only occasionally or close to precipitate corners. High resolution imaging indicates that the interface is semi-coherent with interfacial dislocations occurring every seven planes in copper to accommodate the 14% lattice mismatch, see the phase image in Fig. 1c. While the magnesia lattice remains completely rigid, deformations in the copper lattice extend from the interface over two lattice planes. This means that interfacial strain is very localised and small in size. Comparison of the experimental HREM images with image simulations with different magnesia end planes, a fully occupied oxygen plane, a half-filled oxygen plane and a completely filled magnesium plane shows that the distance between planes at the interface are consistent with a Mg-O-Cu bonding at the interface. While the terminating lattice plane in magnesia can be clearly identified as being occupied by oxygen atoms, no precise oxygen occupancy (0.5 - 1) can be obtained from this type of analysis.
By EELS the typical modifications in the edge fine structures (ELNES) at the interface can be identified, see Figures 2a, 2b and 2c. A large charge transfer across the interface can be identified, yielding at the interface Cu-L features characteristic of copper in the Cu^{1+} state (appearance of the L_3 white line) in a Cu_2O-like environment. Features of the O-K edge are also modified at the interface; edge enlargement and the presence of a low energy shoulder confirm bonding of oxygen to Cu^{1+}. The Mg-L edge at the interface is not modified compared to bulk MgO. A semi-quantitative analysis of the different bond contributions in terms of experimental cross-section ratios in the spatial difference mode indicates approximately one monolayer of Cu_2O at the interface [7]

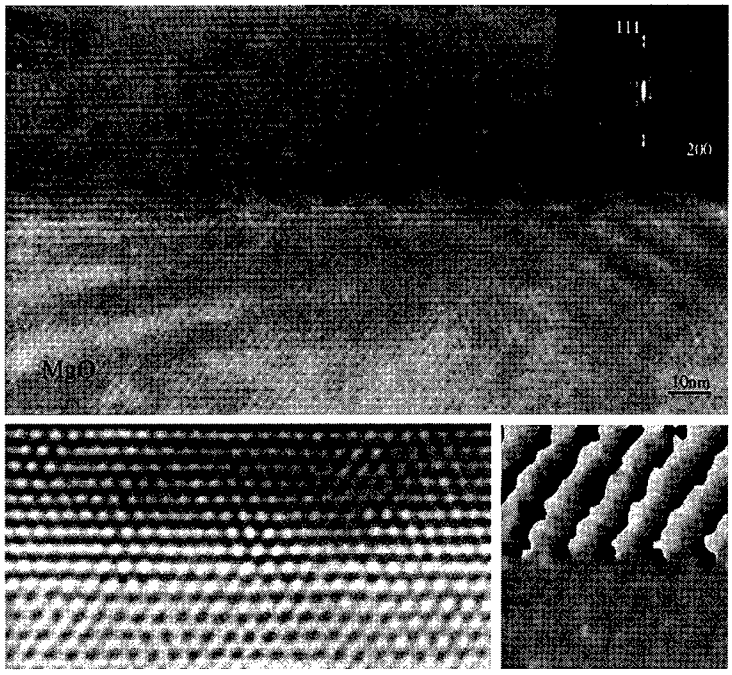

Fig. 1: (111)MgO//(111)Cu interface at $a_{O2} = 10^{-8}$ a) HREM image with corresponding b) power spectrum, c) Bragg filtered image and d) phase image

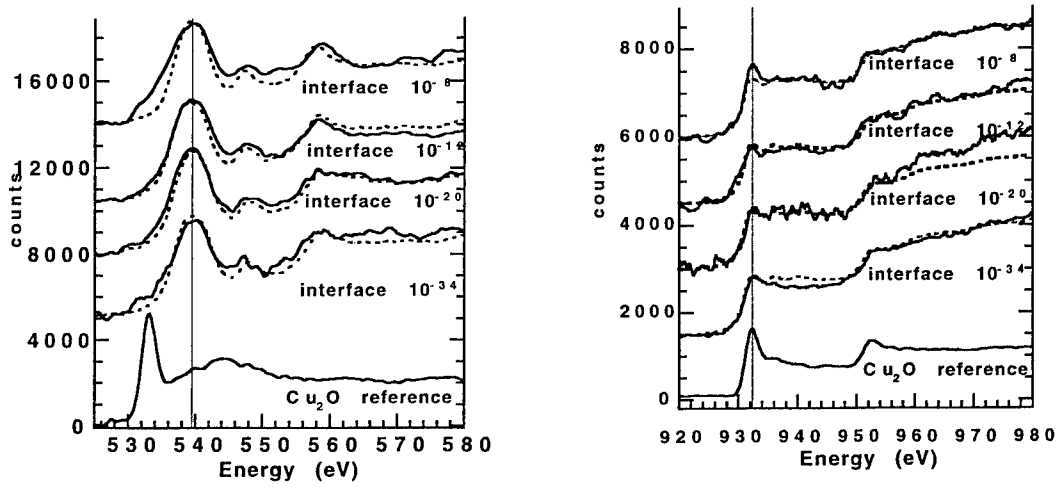

Fig. 2: ELNES of a) Cu-L and b) O-K of the (111) interface at $a_{O2} = 10^{-8}$, 10^{-12}, 10^{-20} and 10^{-34} and the corresponding Cu or MgO matrix (dotted line). In addition, a bulk Cu_2O spectrum is shown.

$\{111\}_{MgO}$//$\{111\}_{Cu}$ interfaces in equilibrium with $a_{O2}=10^{-12}$ at 900°C

As in the precedent case, the interface is flat at an atomic level, however, lattice deformations close to the interface within the copper are much more important and extend over several atom layers, see Fig.3. Near edge fine structures at the interface show almost no modifications compared to bulk copper and bulk magnesia (Figure 2) and indicate thereby that no visible charge transfer occurs across the interface

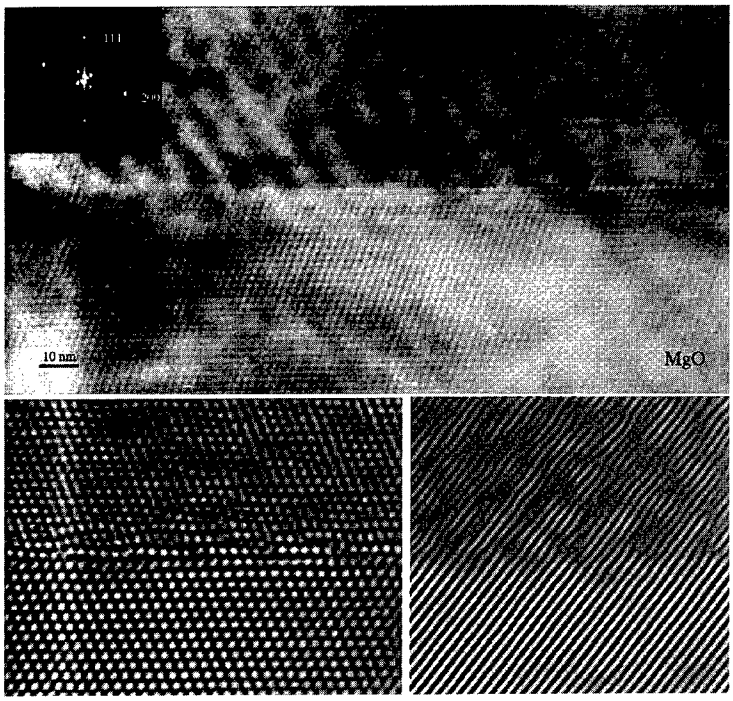

Fig. 3: (111)MgO//(111)Cu interface at $a_{O2} = 10^{-12}$ a) HREM image with corresponding b) power spectrum, c) Bragg filtered image and d) phase image

Discussion

From the above observations it is concluded that interfacial structure and electronic interfacial states strongly depend on the equilibrium oxygen activity.

For high oxygen activity, the final plane in magnesia in contact with copper is occupied by oxygen. An occupancy of 0.5 would correspond to electron neutrality in contact with uncharged copper metal. However, from ELNES semi-quantification of Cu-L and O-K edges [7] it can be seen that the planar occupation is more close to 1 and that an important charge transfer from copper to oxygen compensates the charge of the additional oxygen ions. The full occupancy of the final oxygen plane explains that under these conditions a very flat unperturbed {111} interface is found.

For lower oxygen activity the final oxygen plane in magnesia is apparently no longer completely filled. Since no large charge transfer is visible between copper and oxygen in the interfacial ELNES the final oxygen occupation must be more closely to 0.5. This is supported by the fact that the more important lattice deformation is detected close to the interface, which may be provoked by an important local relaxation of the atoms in the neighbourhood of the half-filled oxygen plane.

Studies on $\{001\}_{MgO}//\{001\}_{Cu}$ interfaces [6] and at lower oxygen activities confirm these results.

[1] M.Backhaus-Ricoult, S.Hagège, Phil Mag A67 (1993) p. 1471
[2] R.F.Chen et al , Ultramicroscopy 54 (1994) p 179
[3] W.Mader, B.Maier, Colloque de physique C1-51 (1990), p. 867
[4] H.Jang, D.N.Seidmann, K.L.Merkle, Interface Science 1 (1993) p.61
[5] D.A.Muller, D.A.Shashkov, R.Benedek, L.H.Yang, J.Silcox, D.N.Seidmann, Phys. Rev. Lett. 80 (1998) p. 4741
[6] S.Laurent, D.Imhoff, M.Hÿtch, J.Devaud, S.Hagège, M.Backhaus-Ricoult, Colloque de Métallurgie (1998)
[7] D.Imhoff, S.Laurent, C Colliex, M.Backhaus-Ricoult, EJPS (1998) p.
[8] M.Hÿtch, Microsc. Microstr. Microanal. 8 (1997), p.41-57
[9] D.Imhoff, S.Laurent, C.Colliex, M.Backhaus-Ricoult, EJPS (1998) p.
[10] M.Backhaus-Ricoult, NATO Conf proc. on Materials Joining, Bled (1998)
[11] S.Laurent, M.Backhaus-Ricoult, ibid Proc. iib (1998)

Materials Science Forum Vols. 294-296 (1999) pp. 329-332

Microstructure of Al/α-Al_2O_3 Interface Fabricated by Surface Activated Bonding at Room Temperature

T. Akatsu[1,3], N. Hosoda[1], T. Suga[1] and M. Rühle[2]

[1] Research Center for Advanced Science and Technology (RCAST), The University of Tokyo, Meguro-ku, Komaba 4-6-1, Tokyo 153, Japan

[2] Max-Planck-Institut für Metallforschung, Seestraβe 75, D-70174 Stuttgart, Germany

[3] Present address: Max-Planck-Institut für Mikrostrukturphysik, Weinberg 2, D-06120 Halle/Saale, Germany

Keywords: Surface Activated Bonding, TEM, Al, α-Al_2O_3

Abstract

Surface activated bonding (SAB) has been developed as a joining method of dissimilar materials at room temperature and widening its applicability. In this study, Al (111) and α-Al_2O_3(0001) were bonded via SAB and the interface formation was investigated by observing the microstructure of the interface, in order to study the mechanism of the interface formation. It was revealed that the interface formed between γ-Al_2O_3 surface layer formed during Ar bombardment of α-Al_2O_3 surface and the Al surface protrusions. In the Al crystal near the interface, many microtwins were found, which are considered to have formed due to not only the deformation but also the rearrangement of the Al atoms on the Al_2O_3 surface.

Introduction

Surface activated bonding (SAB) has been developed as a room-temperature joining method of similar and dissimilar materials without heating at all [1,2]. The method is expected to solve the problems caused due to the high bonding temperature in conventional bonding procedures, such as thermal residual stresses and formation of brittle reaction layer. The process of SAB is simple; Surfaces to be bonded are activated by Ar bombardment and brought into contact in vacuum. As previous studies revealed, SAB makes it possible to join a variety of combinations of dissimilar materials, such as different metals, metal-ceramic and semiconductors. On the other hand, the investigation of interface formation at room temperature has not been made in details, which is, however, necessary for further understanding and developing of SAB. First of all, understanding of the atomistic structure of the interface is inevitable. In the present report, Al and α-Al_2O_3 , already shown to form a strong interface via SAB [3], were chosen as a typical metal-ceramic system, and the interfacial microstructure was examined in the atomic level by high resolution transmission electron microscopy (HREM).

Experiment

α-Al_2O_3 samples produced by Shinkoh-sha, the purity being higher than 99.9938wt%, were cut into 5mm x 5mm plates. The sample surfaces had been already mechano-chemically polished and heat-treated in vacuum, the surface roughness being less than Ra 2.5 nm. Al samples were cut out from an Al single crystal of a purity of 99.999% into cubes of $5mm^3$, so that one surface of the cubes were parallel to the (111) planes with an accuracy within ±1 degree. The (111) surface of Al was first polished using emery sheets of increasing fineness up to #1500, and then buff-polished using alumina abrasive up to 1 μm. The sample cubes were next annealed at 753K for 1 hour under

a vacuum of ca. $5x10^{-4}$ Pa, and finally electrolytically polished in a 20% alcohol solution of perchloric acid. Following this treatment, the polished surface was macroscopically flat. Fig.1 shows an AFM micrograph of the Al surface after electrolytic polishing. This surface clearly has a roughness with a maximum height difference of about 8nm and spatial distance of about 5 to 50nm. With this preparation, this microscopic roughness was unavoidable and taken as a given preliminary condition of the surface.

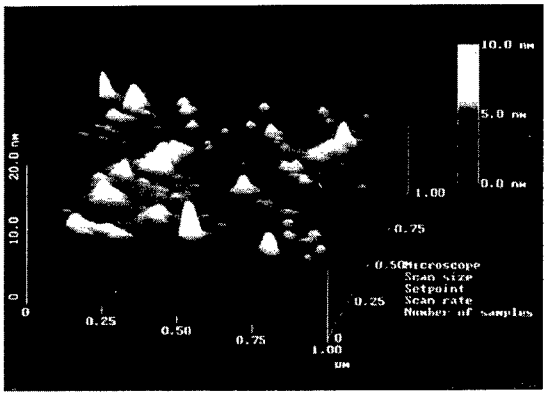

Fig.1 AFM picture of Al surface after electrolytic polishing.

The bonding was conducted throughout in a UHV bonding system. The details of the structure of the system was described in somewhere already [3]. After being set into the UHV system, the samples were sputter-cleaned with a saddle-field type cold cathode fast atom beam (FAB) at the acceleration voltage and current of 1.5kV and 15mA, respectively, in the background vacuum of $2\text{-}5x10^{-6}$ Pa. α-Al_2O_3 samples were irradiated for 5min, while Al samples for 15min, after which no contaminants were observed by Auger electron spectroscopy (AES) but assumably implanted Ar was slightly detected. After the surface irradiation, the samples were transferred into another chamber of a vacuum of ca. 10^{-7} Pa, and brought into contact and held for 1 min under load of ca. 40MPa, with the crystallographic relationship of :

(111) Al || (0001)α-Al_2O_3, [$1\bar{1}0$]Al || [$10\bar{1}0$]α-Al_2O_3, and [$11\bar{2}$]Al || [$11\bar{2}0$]α-Al_2O_3,

misalignments within ±2 degrees being unavoidable. TEM samples were prepared in a way described in the reference [4] and finally ion-thinned carefully using liquid nitrogen. For high-resolution TEM observations, JEM4000EX was used.

Results and Discussion

Fig. 2 is a cross-sectional TEM of the interface. The α-Al_2O_3 surface is flat on the order of 1nm, while the Al side shows a wave-like configuration. Bonding along the interface between the two crystals appears to be interrupted by areas of non-bonding regions. Namely, regions of bonding around several tens of nm long are interrupted by gaps of 5 to 10nm in length. As was shown in Fig. 1, the Al pre-bonding surface had a similar microscopic roughness. It is therefore conjectured that the wave-like configuration of the interface arose from the original Al surface roughness. As far as observed by TEM, all the protrusions of Al were bonded to α-Al_2O_3. Therefore, the heads of the protrusions must have been deformed.

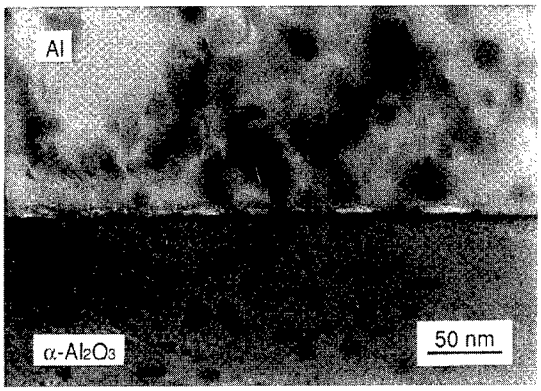

Fig.2 Wave-like configuration of the interface.

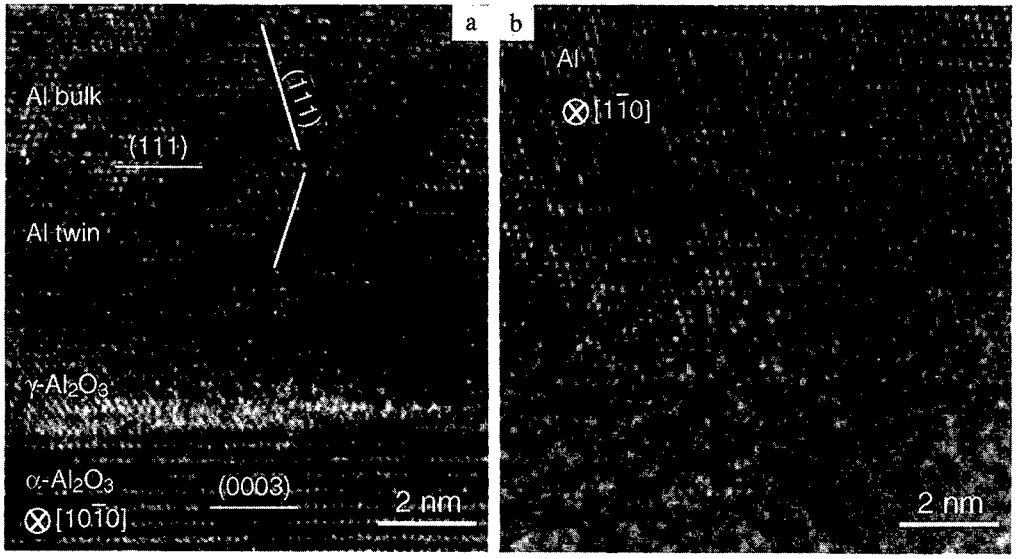

Fig.3 High resolution micrographs of a bonded region; (a) taken in the [$10\bar{1}0$] zone axis of α-Al_2O_3, (b) taken exactly at the same region in the [$1\bar{1}0$] zone axis of Al.

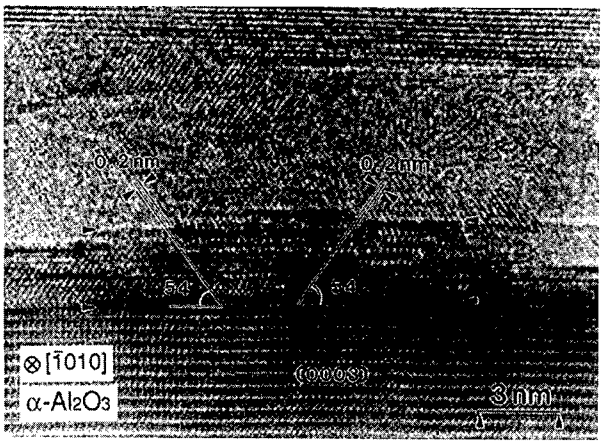

Fig.4 High resolultion micrograph of a non-bonding region, showing γ-Al_2O_3 on the α-Al_2O_3 surface.

Fig. 3a shows a TEM picture of one of the bonded regions at a higher resolution taken in the [$10\bar{1}0$] zone axis of the α-Al_2O_3. As mentioned above, there is a misalignment between the crystals of a couple of degrees, causing the less clear lattice image of the Al bulk. It has recently been found that γ-Al_2O_3 may form under a similar condition [5]. In the present case, the lattice image of γ-Al_2O_3 can be seen all along the α-Al_2O_3 surface even at non-bonding regions (Fig.4). The Al region bonded onto this formed γ-Al_2O_3 exhibits a twin structure of that of the bulk, within ca. 5nm from the interface. As a result, many microtwins parallel to (111) planes were observed along the border with the original bulk. Fig.3b was taken exactly at the same bonded region in the [$1\bar{1}0$] zone axis of Al. In Fig.3b, the lattice image of α-Al_2O_3 cannot be seen any more. The Al lattice image continues to the interface, but shows no twins. Therefore, the Al side within a few nm from the interface contains both the original and twinned structures and are associated with many microtwin planes along the border with the original bulk. The microstructure of the interface may be summarized as follows; The surface of α-

Al_2O_3 was changed to γ phase due to the Ar FAB irradiation. On to this, Al protrusions were bonded. The Al side 5nm from the interface was composed of the structure of the bulk and that of a twin.

The change in the crystal orientation must have been caused by the plastic deformation of the heads of the protrusions on the Al surface as they were pressed to the α-Al_2O_3 surface during the bonding. However, in order to explain the appearance of the twin structure near the formed interface parallel to the interface plane, the influence of the Al_2O_3 should be taken into consideration. In fact, the twined region is well aligned to the Al_2O_3 crystal as seen in Figs.3a. In addition, the preferential crystallographic orientation with the substrate was studied with the Al film grown on the similarly prepared α-Al_2O_3 basal plane[6]. In this case, two preferential orientations were found:

(111) Al ‖ (0001)α-Al_2O_3, [$1\bar{1}0$]Al ‖ [$10\bar{1}0$]α-Al_2O_3, and $\pm$[$11\bar{2}$]Al ‖ [$11\bar{2}0$]α-Al_2O_3.

Obviously, one of them is that which was taken for the bonding in the present report. It is true that the orientation relationship taken for bonding was closer to it, even though there was a misalignment of a couple of degrees between the crystals. It is, therefore, conjectured that this preferential orientation could appear with ease. However, it is still noteworthy that the twin structure formed first due to the deformation, followed by rearrangement of the Al atoms so that the preferential orientation would be achieved. This fact indicates that the interface formation between Al and Al_2O_3 via SAB occurs not only due to the deformation but also due to the rearrangement of the Al atoms on the Al_2O_3 surface even at room temperature.

Summary

The microstructure of the Al(111)/α-Al_2O_3(0001) interface via surface activated bonding (SAB) was investigated using HREM. The Ar sputtering process caused the formation of γ-Al_2O_3 on α-Al_2O_3. The interface formed between the γ-Al_2O_3 and the Al protrusions. It was found that the Al atoms near the interface rearranged so that the preferential orientation with the Al_2O_3 would be achieved, causing many microtwins parallel to (111) planes in the Al region near the interface. This indicates that the SAB bonding process takes place by rearrangement of the atoms around the interface even at room temperature.

Acknowledgment

T. Akatsu was financially supported by Japanese Science Promotion Society (JSPS).

References

[1] T. Suga, Y. Takahashi, H. Takagi, B. Gibbesch and G. Elssner, 1992, *Acta metall, mater.*, **40** Suppl., S133-137.

[2] T. Suga, K. Miyazawa and H. Takagi, 1990, *J. Japan Inst. Metals,* **54** [9], pp-935-943

[3] T. Akatsu, G. Sasaki, N. Hosoda and T. Suga, 1997, *J. Mat. Res.,* **12** [13], pp.852-856

[4] A. Strecker, U. Salzberger, and J. Mayer, 1993, *Prakt. Metallogr.,* 30, **48**.

[5] to be published.

[6] not published.

Materials Science Forum Vols. 294-296 (1999) pp. 333-336

Ball Milling Driven Formation of Interfaces in Powders of Super α_2-Ti_3Al Alloy

Th. Kehagias[1], Ph. Komninou[1], J.G. Antonopoulos[1], Th. Karakostas[1], G. Nouet[2] and V. Pontikis[3,1]

[1] Department of Physics, Aristotle University, GR-54006 Thessaloniki, Greece

[2] LERMAT, UPRESA-CNRS 6004, 6 Bd du Maréchal Juin, F-14050 Caen Cedex, France

[3] Laboratoire des Solides Irradies, CEA-CNRS URA 1380 Ecole Polytechnique, F-91128 Palaiseau Cedex, France

Keywords: Mechanical Alloying, Ordered Structures, Amorphisation, Deformation Twinning, TEM

Abstract

Powders of the multiphase super α_2-Ti_3Al alloy are processed in a vibrating frame ball mill, in native atmosphere. The structure of the powder particles is investigated by Transmission Electron Microscopy, as a function of the duration of the ball milling process. The phenomena associated with this process include an order-disorder transformation and a gradual amorphisation of the α_2-Ti_3Al phase, that later recrystallises into new structures, the first belonging to the Rhombohedral system, with lattice parameters close to those of α-alumina and the second belonging to the Cubic system with an f.c.c. unit cell that is very rich in Ti. This is explained by a mechanism of oxygen incorporation driven by the continuous deformation of the powder particles, that resembles to high temperature oxidation of Ti_3Al aluminides. The new phases continue to deform by mechanical twinning, forming (0001) and $(1\bar{1}1)$ twins that exhibit a defected character.

Introduction

Ternary Ti-Al-Nb alloys are commonly used in high temperature applications, due to the excellent mechanical behaviour that they present in detrimental environments [1]. Mechanical alloying is often utilised for manufacturing these type of alloys, since conventional metallurgical methods can not always accomplish a fine dispersion of the alloy elements. Composite metal alloy powders with refined microstructures could be produced with the use of ball milling. Furthermore, the application of this repeated fracturing, welding and refracturing method on prealloyed powders allows the fabrication of nanostructured and amorphous materials [2].

In our study, we investigate the influence of ball milling on the microstructural elements of the composite super α_2-Ti_3Al alloy powders, as a function of the duration of the process, by conventional and high resolution electron microscopy (CTEM, HREM). Particularly, we examine the evolution of the existing phases of the alloy and the formation of new phases that are not yet clearly explained, since they seem to be strongly dependent on the ball milling parameters [3]. We have conducted our experiments in native atmosphere, in order to compare the oxidation behaviour of the alloy with the ball milling process, that appear to produce similar microstructures [4]. In addition, we investigate the formation of mechanical twin interfaces induced in the alloy phases by the continuous deformation process and we analyse their defected character.

Experimental

The as-received super α_2-Ti_3Al alloy is manufactured in the Interdisciplinary Research Centre (IRC) in Birmingham (UK), by rotating disk atomisation, with a nominal composition of 63 Ti, 21 Al, 12 Nb, 3 V and 1 Mo (at %). The as-received powders were ball milled in a vibratory ball mill, "Pulverisette O" Fritsch, for continuous time periods lasting from 2 to 180 hours. A WC ball of 1 kg (ball to powder ratio 100:1) was used for the ball milling. In order to have TEM specimens, the ball milled powders were mixed with epoxy raisin and then were mechanically polished and finally ion-etched. Microscopic observations were carried out in a Jeol JEM 120CX TEM microscope operating at 120 kV and a Topcon 002B microscope operating at 200 kV with a point to point resolution of 0.18 nm.

Results

X-ray diffraction (XRD) analysis shows that the as-received powder particles of the alloy consist mainly of two ordered phases, the α_2-Ti_3Al (h.c.p.) phase with a DO_{19} superlattice structure and the B2-

$Ti_2Al(Nb,Mo,V)$ (b.c.c.) phase [5]. The particles present a spherical morphology with an average diameter of 100 μm containing several grains of the order of 15 μm. In Figure 1, a random grain boundary (GB) between two α_2-Ti_3Al grains of the as-received material is depicted, showing also antiphase domain boundaries (APBs) that are commonly observed in ordered structures. Primarily, ball milling induces a gradual destruction of the DO19 superlattice structure and an order-disorder α_2-Ti_3Al to α-Ti_3Al transformation, whereas particles sizes diminish to 15 μm. At 36 h of ball milling, the powder particles consist of a mixture of polycrystalline α-Ti_3Al and polycrystalline B2-Ti_2AlNb (Figure 2). As the process continues, the disordered α-Ti_3Al becomes partially amorphous, while the B2-Ti_2AlNb phase exhibits a nanocrystalline morphology. At 84 h of ball milling, the electron diffraction analysis depicts the absence of the $20\bar{2}0$ reflection of α-Ti_3Al, indicating its partial amorphisation (Figure 3a). Simultaneously, nuclei of a new structure appear within the amorphous material (Figure 3b). This new structure crystallises in the Rhombohedral system, with space group R3 or $R\bar{3}$ and lattice parameters a=0.504 nm and $\alpha=56.4^{o}$. The equivalent description in the Hexagonal system results in lattice parameters a=0.476 nm and c=1.267 nm that are very close to those of α-alumina. However, the XRD intensities differ from those of α-alumina, implying that there is a mixture of Al and Ti in the lattice sites and the new phase could be more precisely described as Ti-rich α-alumina. The following mechanism could explain the formation of this new phase: The oxygen of the atmosphere creates a native oxide around the powder particles, which is progressively incorporated into the material through the ball milling. Due to the local rise of temperature, the embedded oxygen reacts with the Ti and Al atoms forming nuclei of stable crystalline oxides. The Ti-rich α-alumina product of this ball milling driven oxidation mechanism is also formed during high temperature oxidation of Ti_3Al aluminides, where the Nb content facilitates its formation [4]. By further ball milling the nuclei of the new Ti-rich α-alumina phase grow into particles with an average size of 0.5 μm. The new phase continue to deform by mechanical twinning. In Figure 4, a particle of the new phase is depicted, containing a K_1=(0001), η_1=<1$\bar{1}$00> twin interface. A set of pure edge <0001> dislocations is decorating the twin in order to absorb the strain energy, that results from a small deviation of the twin plane from the basal plane. The diffraction pattern with the [$\bar{1}2\bar{1}0$] common zone axis oriented parallel to the electron beam corresponds to Figure 4c, where the twin plane is on edge-on position. The occurrence of interfaces in the Ti-rich Al_2O_3 is very low, since the metallic character of the original phases has weakened due to the emergence of the new ceramic-like phase that presents different mechanical behaviour. Consequently, for the present conditions, plastic deformation by dislocations slip does not occur in this phase, that deforms with the growth of few mechanical twins. The same type of deformation twin is reported in pure α-alumina after single point scratching [6]. At 180 h of ball milling, particles of another new phase with an f.c.c. unit cell that is very rich in Ti (≅95%) appear. The excess Ti can be explained by the decomposition of α-Ti_3Al, followed by the reaction of Al with oxygen in order to form the α-alumina phase. In Figure 5a, a HREM image of a perfect ($1\bar{1}1$) twin viewed along the [110] common zone axis is depicted, whereas in Figure 5b a defected area of the same twin, containing a step with a $5d_{1\bar{1}1}$=1.23 nm height, is shown. The crystallographic analysis of this phase resulted in a lattice parameter a=0.426 nm, that is very close to the parameter of the f.c.c. TiN (a=0.423 nm). It should be noticed that an f.c.c. pure Ti phase with a lattice parameter of a=0.432-0.442 nm is reported to occur in Ti-Al and Ti-Ni multilayers [7].

Conclusion

The ball milling process induces severe morphological and structural changes to the powder particles of the multiphase super α_2-Ti_3Al alloy. As a function of ball milling time, an order-disorder α_2-Ti_3Al to α-Ti_3Al transformation occurs, followed by partial amorphisation of the latter phase. Recrystallisation of the amorphous phase results in the emergence of a new ceramic-like and a new metallic phases, the first being described as Ti rich α-alumina and the second as f.c.c. TiN or f.c.c. Ti. These new phases are attributed to a ball milling driven oxidation mechanism that constrains Al to form alumina and discharges Ti into a high energy metastable f.c.c. phase. These phases continue to deform by mechanical twinning, resulting in the formation of (0001) and ($1\bar{1}1$) twins exhibiting a defected character.

Acknowledgment

This work is supported by the Greek Secretariat of Research and Technology program PENED 94-1504. The authors wish to thank the IRC Deputy Director Dr. M.H. Jacobs for providing the original material.

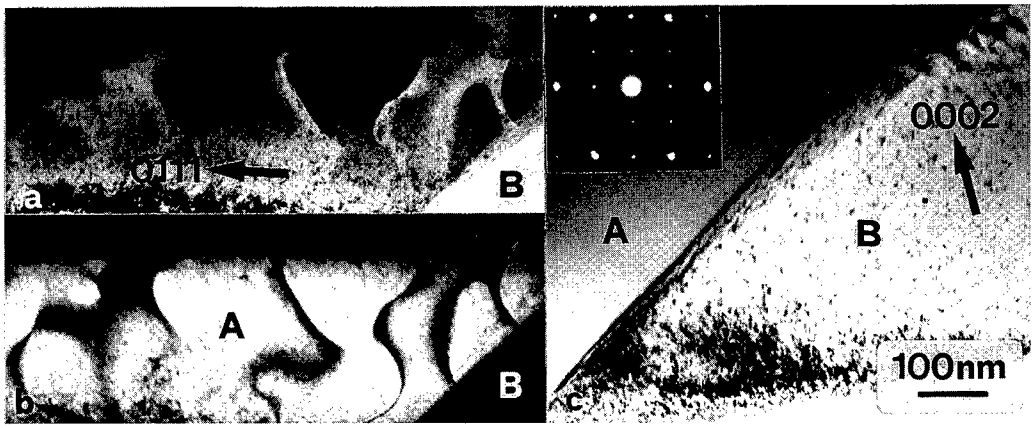

Figure 1. a) Bright field (BF) image of APBs in the ordered α_2-Ti_3Al phase of the as-received material. b) Corresponding dark field (DF) image with the $01\bar{1}1$ superlattice reflection. c) A random GB between two crystals of the α_2-Ti_3Al phase, where crystal B is viewed with the 0002 reflection while crystal A is out of contrast; the inset diffraction pattern presents a typical zone axis of the DO_{19} superlattice structure.

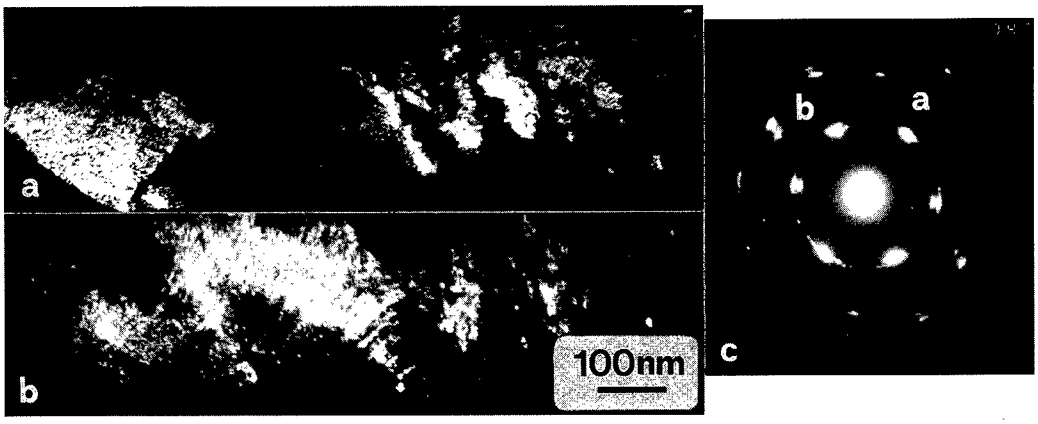

Figure 2. a,b) DF images of the structure after 36 h of ball milling, depicting a homogeneous mixture of polycrystalline α-Ti_3Al and B2-Ti_2AlNb. c) Corresponding diffraction pattern, showing the disappearance of the superlattice reflections; the marked reflections correspond to $20\bar{2}0$ and 0002 of α-Ti_3Al and 011 of B2-Ti_2AlNb.

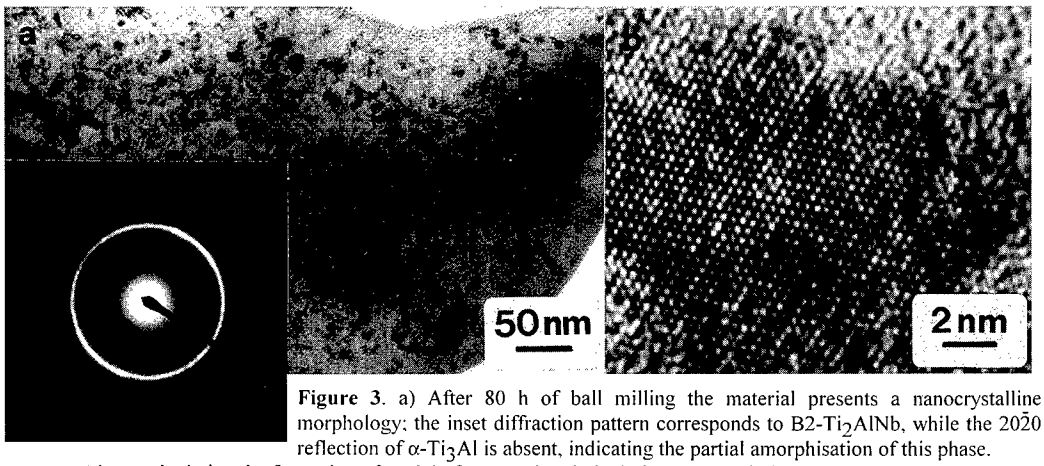

Figure 3. a) After 80 h of ball milling the material presents a nanocrystalline morphology; the inset diffraction pattern corresponds to B2-Ti_2AlNb, while the $20\bar{2}0$ reflection of α-Ti_3Al is absent, indicating the partial amorphisation of this phase. b) HREM image depicting the formation of nuclei of a new Rhombohedral structure within the amorphous α-Ti_3Al.

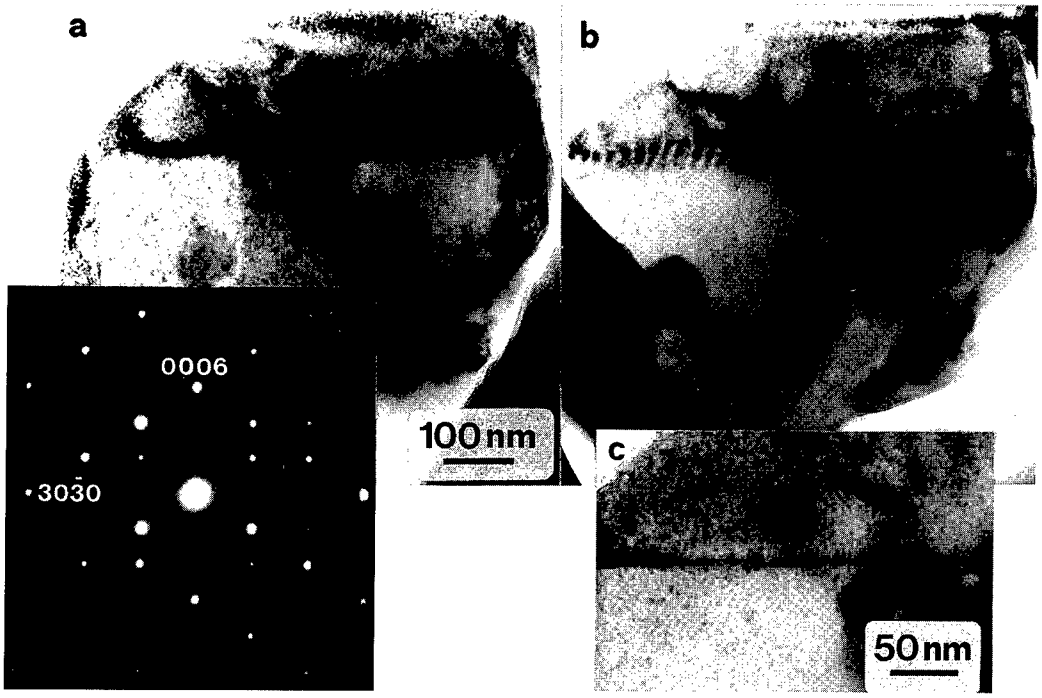

Figure 4. a) A particle of the new phase after 108 h of ball milling, containing a K_1=(0001) twin. b) A set of pure edge basal dislocations is present in the twin interface. c) The same twin in edge-on position; the inset diffraction pattern corresponds to this orientation, where the $[\bar{1}2\bar{1}0]$ common zone axis is oriented parallel to the electron beam.

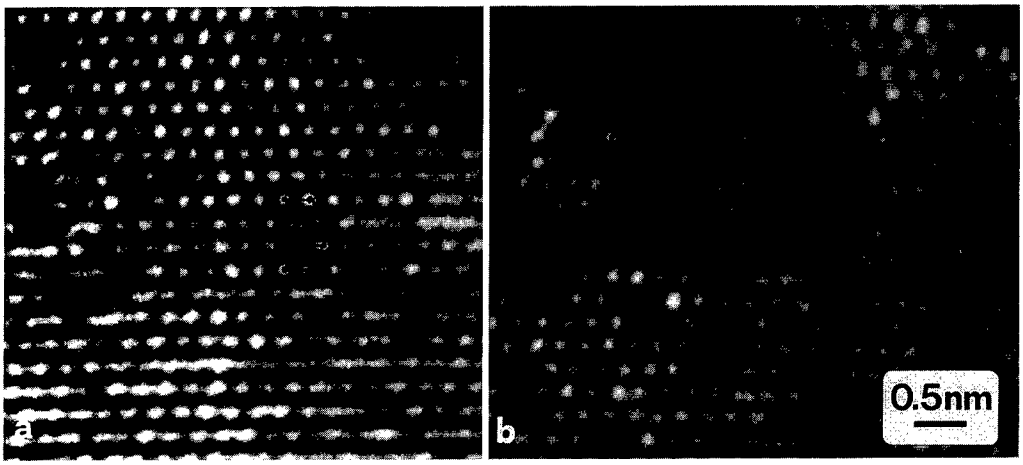

Figure 5. HREM images of the $(1\bar{1}1)$ twin of the new f.c.c. metallic phase viewed along the [110] common zone axis. a) Perfect twin orientation. b) Defected area of the same twin containing a step with a $5d_{1\bar{1}1}$=1.23 nm height.

References

1. M. Oehring, T. Klassen and R. Bormann, *J. Mater. Res.*, **8** (1993) 2819.
2. C.C. Koch, *Nanostruct. Mater.*, **2** (1993) 109.
3. C. Suryanarayana, G.E. Korth and F.H. Froes, *Metall. Mater. Trans. A*, **28A** (1997) 293.
4. T.K. Roy, R. Balasubramaniam and A. Ghosh, *Metall. Mater. Trans. A*, **27A** (1996) 3993.
5. G. Itoh, T.T. Cheng and M.H. Loretto, *Mater. Trans. JIM*, **35** (1994) 501.
6. I. Zarudi, L.C. Zhang and D. Cockayne, *J.Mater.Sci.*, **33** (1998) 1639.
7. R. Ahuja and H.L. Fraser, *J.Electr.Mater.*, **23** (1994) 1027.

Materials Science Forum Vols. 294-296 (1999) pp. 337-340

Nanoscopic Analysis of a Ag-Cu-Ti/Sapphire Brazed Interface

T. Ichimori, Ch. Iwamoto and S. Tanaka

Tanaka Solid Junction Project, ERATO, Japan Science and Technology Corporation,
1-1-1 Fukuura, Kanazawa-ku, Yokohama 236-0004, Japan

Keywords: TEM, Active Brazing, Reaction Product, Interface Structure, Ti-Free Phase

Abstract

Transmission electron microscopy was employed to investigate the detailed nanoscopic structure of a sapphire/Ag-Cu-Ti brazed interface. Sapphire substrates with various plane directions were brazed by a Ag-Cu-Ti alloy, and their cross sections were investigated in terms of interface structure and orientation relationships between phases. The reaction phases formed during brazing were identified by nano-probe compositional analysis and electron diffraction. The typical interface structure was Ag-Cu eutectoid/Ti_3Cu_3O (1-2-μm-thick layer)/TiO (10-50-nm-thick layer)/sapphire, which generally existed at the interface in all the samples investigated. Al was present as solute in the reaction phases.

However, the interface structure was multiple, which can be due to the local deviation of titanium and oxygen activities. In some regions where TiO was formed as discrete precipitation, an atomically-flat Ti_3Cu_3O/sapphire was present without TiO interlayer. Occasionally, a reaction phase without titanium concentration, Cu-Al-O, existed in contact with the sapphire substrate, which suggests a direct reaction between copper and sapphire.

1. Introduction

Active brazing is one of the most important methods for joining ceramics to metals or to other ceramics, and for the improvement of the C/M joints, clarification of the interface structure and its formation process is essential. Interface designing and processing in nanometer scale is becoming very important today, as a result of the downsizing requirement in industrial technology. Consequently, nanoscopic analysis of brazed interfaces, which provides detailed information about interface reaction/formation and stability is a key point in structural studies. One good example is that the atomic structure of Si_3N_4 brazed by a Ag-Cu-Ti alloy was revealed to be closely related to its high mechanical strength, where the atomically-wavy Si_3N_4/TiN interface was formed by chemical reaction and epitaxial growth, which provided anchoring points at the interface [1].

On alumina/titanium-containing alloy system, various reaction products have been reported to date, such as titanium oxides, titanium aluminates, titanium coppers, and titanium copper oxides [2-5], where the variety can be due to the different brazing condition used in each experiment. Using these results, macroscopic trends such as the formation processes and rate-controlling steps of reactions have been explained through thermodynamics and reaction kinetics[2-7], but in order to understand the actual reaction at the reaction front and the resulting detailed structure of interfaces, nanoscopic TEM analysis is required. Although there have been few TEM studies reported on this system, Santella et al. identified the reaction products of the dual layered structure as TiO and Ti_3Cu_3O by TEM [8]. However, questions still remain as to the details of the morphology, the identity of the nanometer-sized phases in the reaction layers, and the formation processes and stability of the interfaces.

In this experiment, by means of TEM with EDS/EELS compositional analysis, we investigated a sapphire/Ag-Cu-Ti brazed interface with the intention of clarifying the nanostructure of the interface, identification of the nanometer sized reaction phases, the orientation relationships between alumina and/or reaction phases.

2. Experimental

99.99% purity sapphire (corundum, single crystal of α-alumina) substrates were polished parallel to a variety of low-indexed planes such as (0001), $(10\bar{1}0)$ and $(11\bar{2}0)$. The dimension of each substrate was 10mm x 2mm x 0.5mm

thick. They were stacked with a Ag-Cu-Ti alloy sheet (100 μm thick), whose nominal composition was 66.7Ag-28.4Cu-4.9Ti (in mass %) and its eutectic point was 1051K. The stacks were brazed in a vacuum higher than $5x10^{-5}$Pa at 1173K. The duration of the heating was set as 300 sec to investigate the initial reaction at the interface. No pressure was applied during brazing. The heating rate was controlled at 5 deg/min and the cooling rate was about 20 deg/min (furnace cooling). The resultant brazed joints were cross-sectioned with a low-speed saw and mechanically polished on a lapping disk.

To acquire electron transparency, we employed the focused ion beam technique on a scanning ion microscope, SMI9200 (Seiko Instruments). By this method, since the ion beam is directed normal to the specimen thickness, thickness uniformity on alumina, braze metal and reaction phases is almost preserved.

TEM observation and EDS/EELS analysis were performed on a JEM-2010 (JEOL) and a HF-2000 (Hitachi) at an accelerating voltage of 200 kV. Nano-probe analysis was carried out on a HF-2000, equipped with a field emission electron source, the smallest probe diameter of which was 0.5nm.

3. Results and Discussion

3.1 Ag-Cu eutectoid/Ti_3Cu_3O/TiO/sapphire

Fig.1 shows the typical structure of a sapphire/brazed alloy interface. A reaction layer of 1-2 μm thickness existed between the sapphire substrate and the Ag-Cu eutectic metal. At a larger magnification, another reaction layer of 10-50 nm thickness was observed next to sapphire, which is shown in Fig.2. Using EDS/EELS and electron diffraction, they were identified as Ti_3Cu_3O(diamond cubic) and TiO(fcc). Al was present as solute in both reaction phases. Hence, the typical structure was Ag-Cu eutectoid/Ti_3Cu_3O (1-2-μm-thick layer)/TiO (10-50-nm-thick layer) /sapphire, which is independent of the surface direction of the sapphire substrates. These reaction products and the dual layered structure agree with the results reported by Santella et. al. [8]. No definite orientation relationship has been observed between the phases in the samples studied so far.

TiO grains were irregularly-shaped but usually had a tendency to develop along the substrates, forming an elongated shape. Since they were not regularly oriented with respect to sapphire or Ti_3Cu_3O, it can be surmised that the nucleation sites are present at some rugged points on the sapphire surface, and developed in arbitrary directions, but growth in the direction normal to the substrate was suppressed because of the gradient of the titanium activity in the melt alloy. This could be the reason for the complex microstructure and slight faceting of the TiO grains. Thermodynamical calculations explain the formation of various titanium oxides, and from the free energy changes TiO and Ti_2O are expected [3]. Our experiment supports the results of this calculation, considering the population of these phases, since we observed some grains in the thin reaction layer which can be identified as Ti_2O. Some Ti_2O grains were oriented to fulfill the relationship:

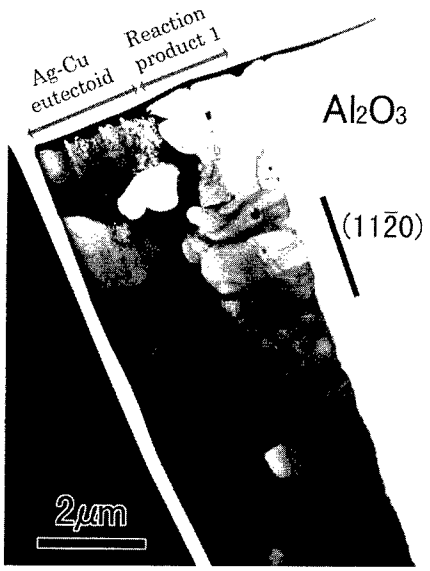

Fig.1 The typical microstructure of a sapphire/Ag-Cu-Ti interface. A 1-2-μm-thick Ti_3Cu_3O layer is formed between the sapphire substrate and the Ag-Cu eutectoid.

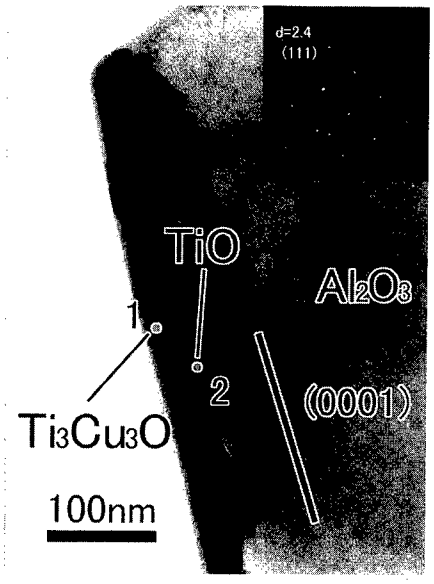

Fig.2 A 10-50nm-thick TiO layer existed between the substrate and the Ti_3Cu_3O layer. TiO grains were irregulary-shaped and slightly faceted.

$(1\bar{1}04)$sapphire//$(10\bar{1}0)Ti_2O$. It is a lattice matching relation between these fringes, which is observed in many grain boundaries and interfaces and considered to be a stable structure.

3.2 Atomically flat $(11\bar{2}0)$sapphire/Ag-Cu-Ti interface

In $(11\bar{2}0)$sapphire/braze alloy joints, the thin TiO layer was not formed from time to time. In Fig.3, irregularly-shaped TiO grains were present at intervals, rather than in the form of a continuous layer. Here, Ti_3Cu_3O was directly joined to sapphire without a TiO layer between them. The stacking sequence is Ag-Cu eutectoid/Ti_3Cu_3O/ sapphire. Ti_3Cu_3O/sapphire interface is atomically flat over micron order length. Still no special orientation relationship was observed between the two phases, however, this is because the orientation of the Ti_3Cu_3O grain was modified during recrystalization.

In our former work on SiC/Ag-Cu-Ti *in situ* wetting experiment[9], Ti segregated near the substrate and the substrate was dissolved parallel to its low-indexed plane, atom by atom; subsequently TiC nucleated and grew epitaxially on the SiC substrate. It is likely that the same mechanism occurred in this system when Ti_3Cu_3O was formed next to the sapphire substrate. In the present study, the sapphire substrate may have dissolved parallel to $(11\bar{2}0)$, atom by atom, creating an atomically flat sapphire surface. Ti_3Cu_3O is considered to be formed during the cooling process when titanium activity was lower. The large grains and flat boundaries of Ti_3Cu_3O suggest this phase had been recrystallized. TiO was found only at those locations where the interface flatness was disturbed. From this consideration, it is likely that Ti_3Cu_3O was formed before TiO was precipitated. It is also presumed that TiO formation was difficult to be on flat surfaces of sapphire, where nucleation sites were not present.

Fig.3 An atomically-flat Ti_3Cu_3O/sapphire interface where a continuous TiO layer is not present.

3.3 Ti-free reaction product

Occasionally, a complex structure with many reaction products was observed in $(11\bar{2}0)$sapphire/Ag-Cu-Ti interface. In a multi-layered interface structure shown as in Fig.4, EDS analysis was performed on the grains numbered 1-5. Grain 1 is Ti_3Cu_3O and grain 2 is TiO. Grain 3 is similar to grain 2 with the exception that it had a slightly higher Al content. Thus, grain 3 can be Ti-Al-O compound, but the identity of which is unclear. Grain 5 is alumina. The EDS spectrum of grain 4 is shown on the bottom of Fig.4. It contained copper, aluminum and oxygen, but titanium was scarcely present. Here, the stacking sequence of the phases is Ag-Cu eutectoid/Ti_3Cu_3O/TiO/Cu-Al-O/sapphire. Fig.5 is the magnified image of the Cu-Al-O/sapphire interface. The crystal structure of Cu-Al-O can be rhombohedral, and the planes on the image are indexed as in the figure, where the beam direction is parallel to both $[10\bar{1}0]$sapphire and $[11\bar{2}0]$Cu-Al-O. No Cu-Al-O

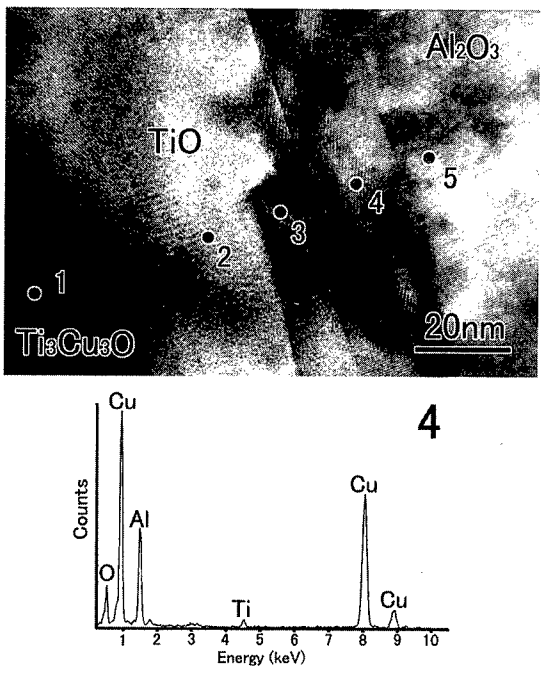

Fig.4 Multi-layered structure of a $(11\bar{2}0)$sapphire/Ag-Cu-Ti interface. Grain 4 is a Ti-free phase, the EDS spectrum of which is shown on the bottom.

compounds which agree with this structure have been reported so far. (The details will be reported elsewhere.) Although titanium-free phase is unpredictable from the thermodynamical point of view, nonequilibrium condition can occur at a solid/liquid interface, where complicated reactions for minimizing local instabilities are always under. One possible reason for the presence of this Ti-free phase is that lattice mismatch is negligible between (0003) planes of Cu-Al-O and sapphire, resulting in this quasi-stable Cu-Al-O/sapphire interface. This phase was possibly formed by the direct reaction between copper and sapphire without Ti intervention.

3.4 Multiple structure of the interface

The structure was not uniform in all the samples although they were brazed in one batch. Fig.6 illustrates, schematically, the multiple interface structure, where three different structures are depicted. The typical structure observed generally for all the samples is shown in the middle, and the two less frequently observed structures are shown on the right and left. The reason for these multiple structures can be attributed to the local fluctuations of titanium and oxygen activities. The reaction products contained some aluminum, which is considered to exist as solute or substitute.

Although such multiple interface structures were observed only in the case of $(1\bar{2}10)$sapphire/Ag-Cu-Ti samples, it is still not clear if the phenomenon is correlated with the surface direction of the substrate. We feel that the fluctuation in local chemical conditions is a more significant factor.

4. SUMMARY

The structure of sapphire/Ag-Cu-Ti alloy brazed interfaces was investigated by TEM and nanoprobe EDS/EELS analyses. The typical reaction products were confirmed as TiO and Ti_3Cu_3O, and multiple (three types) interface structures were discovered. Al was present as solute in the reaction phases. The typical interface structure was Ag-Cu eutectoid/Ti_3Cu_3O (1-2-μm-thick layer)/TiO (10-50-nm-thick layer)/sapphire, which existed generally at the interface in all the samples investigated. In another structure, the TiO layer was missing, creating Ag-Cu eutectoid/Ti_3Cu_3O (1-2-μm-thick layer)/sapphire structure, where an atomically flat interface was formed. The other structure is an interface where a reaction phase without titanium concentration was discovered next to the sapphire substrate, which indicates a direct reaction between copper and sapphire without Ti intervention.

For each structure, the reaction process can be different, which leads to a different interface structure. This multiple structure could be dependent on the local condition of Ti and O activities in the melt alloy.

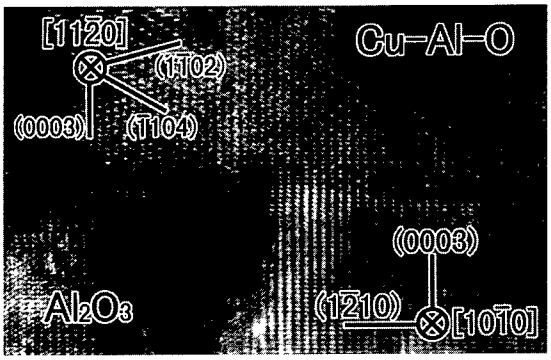

Fig.5 Magnified picture of Cu-Al-O/sapphire interface. (0003) fringes of the two phases are continuous without mismatch. Cu-Al-O has rhombohedral symmetry.

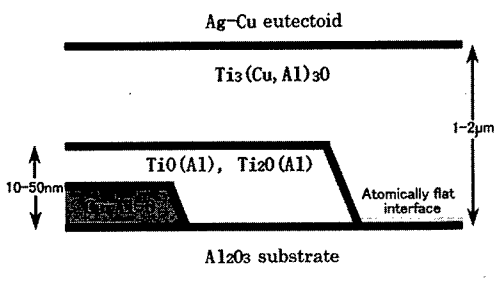

Fig.6 A schematic illustration of the multiple interface structure, where three different structures are shown. The typical structure is in the middle, while other uncommon structures are depicted on the right and left.

REFERENCES

1. Iwamoto, C. and Tanaka, S.-I., J. Am. Ceram. Soc., **81** (1998) 363.
2. Bang, K.-S. Liu,et.al., Welding. Res. Suppl., March (1994) 54-s.
3. Chidambaram, P. R. et.al.., Metall. Trans. A, **25A** (1994) 2083.
4. Byun, W. and Kim, H., Scripta Metall. Mater., **31** (1994) 1543.
5. Xiao, P., Derby, B., and Penfold, J., et.al., Acta mater., **45** (1997) 273
6. Nicholas, M. G., Br. Ceram. Trans. J., **85** (1986) 144.
7. Kritsalis, P., Coudurier, L. and Eustathopoulos, N., J. Mat. Sci., **26** (1991) 3400.
8. Santella, M. L., Horton, J. A. and Pak, J. J., J. Am. Ceram. Soc., **73** (1990) 1785.
9. Iwamoto, C. and Tanaka, S.-I., Appl. Surf. Sci., to be published

Materials Science Forum Vols. 294-296 (1999) pp. 341-344

Si/Si Interface Bonded at Room Temperature by Ar Beam Surface Activation

H. Takagi[1], R. Maeda[1], N. Hosoda[2] and T. Suga[2]

[1] Mechanical Engineering Laboratory, AIST. MITI., 1-2 Namiki, Tsukuba, Ibaraki, 305-8564, Japan

[2] Research Center for Advanced Science and Technology, Univ. of Tokyo, 4-6-1 Komaba, Meguro, Tokyo 153-8904, Japan

Keywords: Silicon, Wafer Bonding, Room Temperature Bonding, Ar Beam Etching, TEM

Abstract: Si wafers are successfully bonded at room temperature by Ar beam surface etching in ultra high vacuum. The bonding interface was investigated by transmission electron microscope (TEM). Residual strain originated from surface roughness is observed in the interface region. The residual strain is relaxed by low temperature annealing. An amorphous-like intermediate layer exists at the interface. The layer is different from the oxide layer which often observed at Si/Si interface prepared by the conventional wafer bonding. It is supposed that damages by Ar atom impact formed this layer, because thickness of the layer changes according to kinetic energy of Ar beam. This layer is quite instable. Low temperature annealing or electron beam irradiation during TEM observation cause re-crystallization of the layer. Therefore, the residual stress and the intermediate layer are observed only in the specimens which is not subjected any heat treatments.

Introduction

Wafer bonding technology was developed to produce high performance semiconductor substrates, such as silicon-on-insulator and lightly-doped silicon layer on heavily-doped silicon substrate [1,2]. The applications have extended to silicon micro mechanical structures and III-V semiconductors [3,4]. In these new applications, high temperature annealing causes many problems. We have developed a new bonding method which utilizes Ar beam sputter etching in vacuum. This treatment enables bonding at room temperature [5]. In addition, for the bonding of very flat specimens such as Si wafers, external bonding load is not necessary [6,7]. This method realize a very low damage bonding.

Microstructures of the Si/Si bonding interface have been investigated relating to sample preparation method. By the conventional hydrophilic wafer bonding, using HNO_3 or $H_2SO_4 + H_2O_2$ treatment, a thin oxide or suboxide layer is formed at bonding interface. Stability of the oxide layer during heat treatment depends on the oxide concentration in wafers [8,9]. On the other hand, by the hydrophobic wafer bonding, using HF treatment, such oxide layer does not grow [10]. Therefore, microstructures of the interface depend on both surface pretreatment and post-bonding annealing. In our room temperature wafer bonding method, the interface is formed without any heat treatment. Wafer surface after Ar beam etching is expected to be quite clean. At the same time, incident Ar atoms cause various effect in surface region. It is expected that these differences in bonding process affect on micro structures of the interface. In this work, we perform TEM observation of Si/Si interface prepared by Ar beam surface activation and investigate its micro structures and influence of Ar beam etching.

Experimental

For bonding experiments, small pieces cut from 4 inch, (100), CZ grown, n-type, 10-20 Ωcm, Si wafers were used [5]. These specimens were washed by the same procedure with that of the usual hydrophilic bonding in order to remove surface contaminant and small particles [1-3]. After setting in a vacuum chamber [5] and evacuation to 2×10^{-6} Pa, the surfaces of specimens were etched by Ar fast atom beam (FAB 110, Atom Tech Ltd. U.K.) and immediately mated in the vacuum. Etching time was 60 to 300 s, corresponding to etching depth of 2 to 10 nm. Beam incident angle was 45 °. Applied voltage of the Ar beam source was varied from 600 to 1800 V. Measured strength by tensile tests shows no dependence on Ar beam energy, and fracture from the silicon bulk is observed. Bonding strength equivalent to conventional wafer bonding with high temperature annealing is achieved without

any heat treatment.

Specimens for TEM observation were prepared by the ion thinning technique. Usually, during ion thinning process, temperature of a specimen raises up to 100°C. In most cases, this heating does not affect on the microstructures of a specimen. However, some changes can occur in our specimens even at the temperature because they are bonded without any heat treatment. Therefore, we used liquid nitrogen cold stage to avoid the heating of specimens. During the ion thinning process, specimen temperature was kept under 0 °C. For observation, we used JEM 2010 (JEOL, Japan) 200kV TEM system.

Results and Discussion

Fig.1(a) shows TEM image of Si/Si interface bonded at room temperature. This image was taken using (400) diffraction perpendicular to bonding interface. Many contours near the bonding interface are observed in the image. They indicate residual strain in the direction perpendicular to bonding interface. It is supposed that the strain is introduced to compensate surface roughness before bonding and achieve intimate contact at the interface. After annealing at 400 °C for 2 hours, these contours disappear as shown in Fig.1(b). The residual stress is relaxed by low temperature annealing. Therefore, only at the interface bonded at room temperature, we can observe those contours which illustrates local residual strain.

In high resolution TEM image, an intermediate layer is observed as shown in Fig.3. In the layer, lattice images disappear. The layer is in an amorphous state or contains high density defects. It looks like the oxide layer observed at Si/Si interface by the conventional hydrophilic wafer bonding [8,9]. However, as shown in Fig.2, thickness of the layer increases when Ar beam energy increases. It is often pointed that Ar beam bombardment causes Ar atom implantation into the specimen and generates crystal defects. Implantation depth can be estimated form kinetic energy and incident angle of Ar beam. For the applied voltage of 600 V, estimated kinetic energy of Ar atom is about 500 eV [11]. Similarly, for 1200 V and 1800 V applied voltage, kinetic energy is about 1000 eV and 1500 eV, respectively. Estimated depth well corresponds to a half of thickness of the intermediate layers [12]. These considerations imply that the layer is formed by impact of Ar atoms during etching procedure.

The bonding interface is expected to be in the middle of the layer, but in the images in Fig.2 nothing is observed there. This means that interatomic bonds formed at the interface are similar to those in bulk. After the strong bonds formation, it becomes quite difficult to identify the bonding interface in the region where high density defects exist.

By low temperature annealing, this layer recrystallized. Fig.3(a) shows Si/Si interface after annealing at 400 °C for 2 hours. The specimen was bonded after 1000 eV Ar beam etching. Thickness of the intermediate layer becomes smaller than that before annealing, shown in Fig.2(b). It is expected that the recrystallization have some relation to the residual stress relaxation shown in Fig.2. After

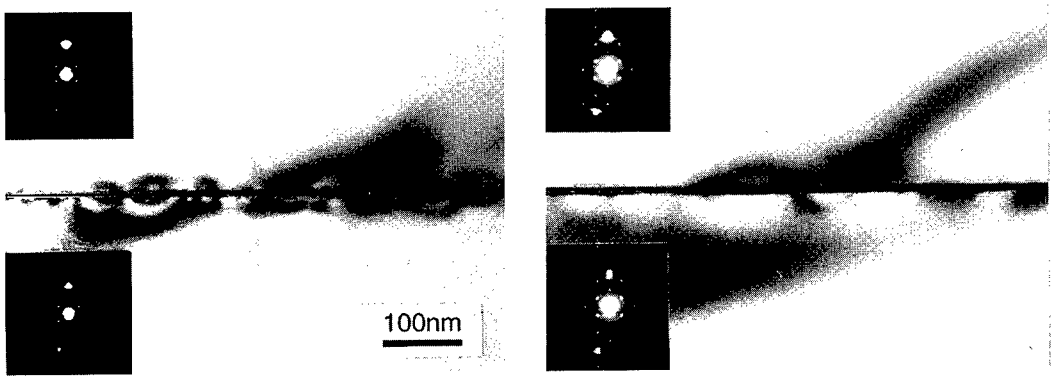

(a) (b)

Fig. 1. TEM images of Si/Si interface bonded at room temperature (a), and after 400°C annealing (b). Contours in (a) indicate existence of residual stress in the direction perpendicular to bonding interface. The stress is relaxed after annealing (b).

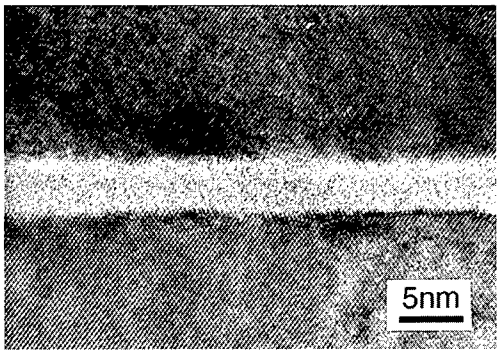

(a)

Fig. 2. (left) High resolution TEM images of Si/Si interface bonded after Ar beam etching. Kinetic energy of Ar beam is 500 eV (a), 1000 eV (b), and 1500 eV (c).

Fig. 3. (below) Si/Si interface bonded after annealing. The specimen is bonded by 1000 eV Ar beam etching. An amorphous-like intermediate layer shrinks by 400 °C annealing (b), and disappears by 700 °C annealing.

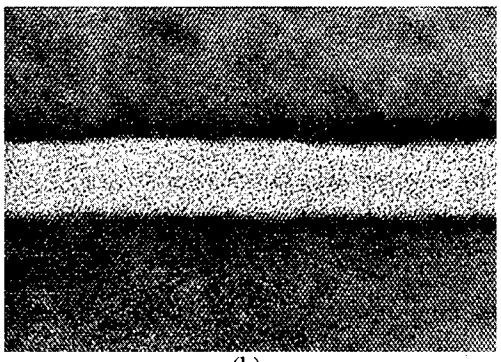

(b)

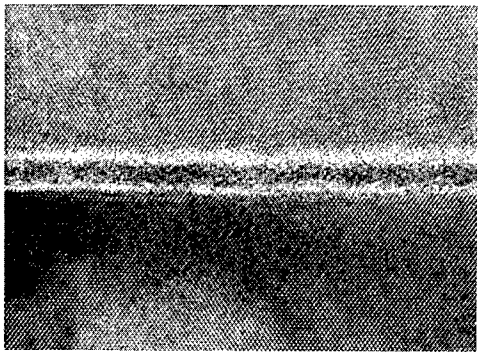

(a)

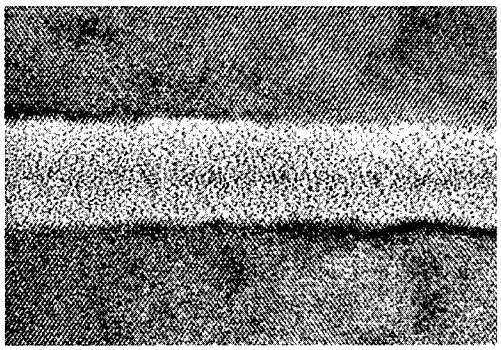

(c)

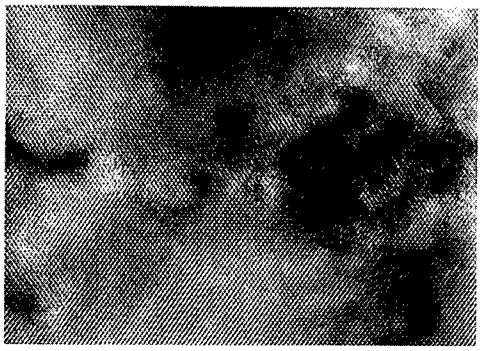

(b)

annealing at 700 °C for 2 hours, the intermediate layer disappears. Compared to oxide layer at the interface by conventional bonding, the layer disappears at much lower temperature.

Fig.4 shows EDS analysis of the bonding interface. In the intermediate layer, Ar is detected as shown in Fig.4(a) whereas only Si is detected at bulk part, Fig.4(b). This confirms the implantation of Ar atoms in the intermediate layer. During the analysis, recrystallization of the intermediate layer was caused by convergent electron beam irradiation, as shown in Fig.4(c). It is assumed that high density defects in this layer enhanced recrystallizations at low temperature.

These results mean that the amorphous-like intermediate layer is not a oxide layer but a damaged layer formed by Ar atom implantation. The layer is quite unstable and easily recrystallized. In other words, the layer is in an active state. It is expected that the layer plays some role in bond formation at room temperature. On the other hand, these defects often affect the various properties of the interface. The condition of the Ar beam etching should be determined carefully considering each application.

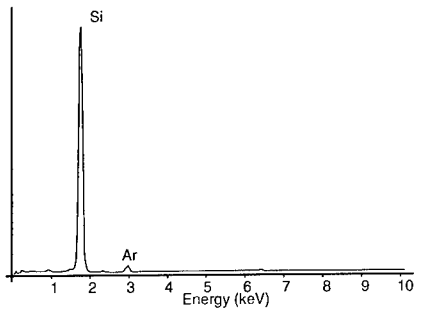

(a)

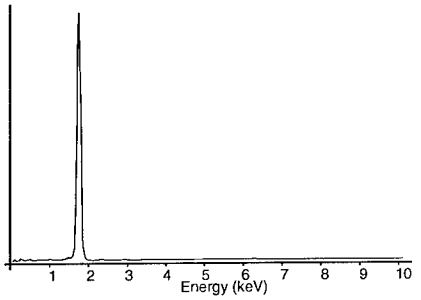

(b)

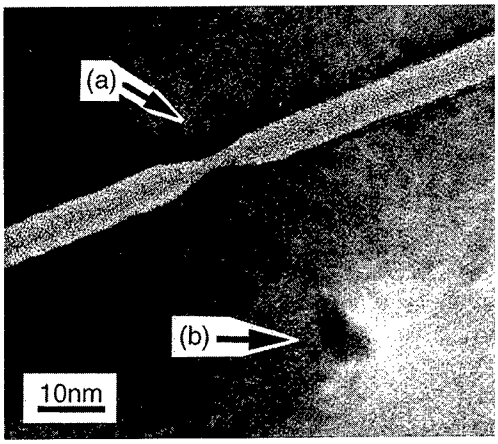

(c)

Fig. 4. EDS analysis of the intermediate layer at bonding interface (a) and bulk material (b). Each analyzed parts are indicated in (c). After convergent electron beam irradiation for analysis, the intermediate layer shrinks and recrystallization is observed.

Summary

We have investigated Si/Si interface bonded at room temperature by Ar beam surface activation. Contours which indicate residual strain in the direction perpendicular to the interface are observed near the bonding interface by TEM. An amorphous-like thin layer exists at the interface. It is assumed that the layer contains high density defects formed by Ar atom implantation. Recrystallization of the layer occurs at a low temperature, and at the same time it causes residual stress relaxation. These features are observed only in the interface prepared without any heat treatment.

References

[1] W.P.Maszara, G.Goetz, A.Caviglia, J.B.McKitterick, J. Appl. Phys. **64**(1988), p. 4943.
[2] K.Furukawa, A.Nakagawa, Appl. Surf. Sci. **41/42**(1989), p. 627.
[3] M.A.Huff, A.D.Nikolich, M.A.Schmidt, J. Microelectromech. Syst., **2**(1993), p. 74.
[4] J.J.Dudley, M.Ishikawa, D.I.Rabic, B.I.Miller, R.Mirin, W.B.Jiang, J.E.Bowers, E.L.Hu, Appl. Phys. Lett., **61**(1992), p. 3095.
[5] H.Takagi, K.Kikuchi, R.Maeda, T.R.Chung, T.Suga, Appl. Phys. Lett., **68**(1996), p. 2222.
[6] H.Takagi, R.Maeda, T.R.Chung, N.Hosoda, T.Suga, Jpn. J. Appl. Phys., to be published.
[7] U.Gösele, H.Stenzel, T.Martini, J.Steinkirchner, D.Conrad, K.Scheerschmidt, Appl. Phys. Lett., **67**(1995), p. 3614.
[8] K.Y.Ahn, R.Stengl, T.Y.Tan, U.Gösele, P.Smith, Appl. Phys. A, **50**(1990), p. 85.
[9] L.Ling, F.Shimura, J. Electrochem. Soc., **140**(1993), p. 252.
[10] H.Himi, M.Matsui, S.Fujino, T.Hattori, Jpn. J. Appl. Phys, **33**(1994), p. 6.
[11] J.Franks, A.M.Ghander, Vacuum, **24**(1974), p. 489.
[12] L.J.Huang, W.M.Lau, H.T.Tang, W.N.Lennard, I.V.Mitchell, P.J.Schultz, M.Kasrai, Phys. Rev. B, **50**(1994), p. 18453.

Materials Science Forum Vols. 294-296 (1999) pp. 345-348

Reactions at Ceramic-Metal Interfaces in Capacitor-Discharge Joined Ceramics

S. Turan

Anadolu University, Department of Ceramic Engineering, Yunusemre Campus, TR-26470 Eskisehir, Turkey

Keywords: Transmission Electron Microscopy, Interfaces, Joining, Coating, Titanium, Zirconia, Reaction Layers

Abstract

A capacitor-discharge joining technique has been used to fabricate zirconia-$Al_xNi_yY_z$-zirconia (ZrO_2) joints. In addition, the surface of the ZrO_2 tiles were sputter coated with Ti and joined using Al as an interlayer material. An investigation of the interfacial structure of the joints using transmission electron microscopes (TEM) revealed that there is a distinct reaction layer containing small particles between the ceramic substrate grains and the foils used as interlayers.

Introduction

Ceramic joining techniques enable the production of more complex shapes than can presently be achieved in monolithic ceramics. Several techniques available for joining ceramics can be classified into two groups: (i) mechanical joining and (ii) chemical joining, such as active-metal brazing, diffusion bonding and ceramic adhesives. The use of ceramic adhesives gives high temperature stability but relatively low mechanical strength, while diffusion bonding and brazing both necessitate heating the ceramics parts for relatively long periods of time, which is not only expensive but which can alter the properties of the ceramic.

Yuschenko et al. [1] and Turan et al. [2] have shown that capacitor-discharge joining technique is capable of joining ceramics using thin metal foil interlayers. The principal of the technique has been previously explained [2]. Briefly, a metallic foil is sandwiched between two ceramic pieces with the foil in contact with two copper electrodes capable of carrying the discharge from a capacitor. When the capacitor is discharged while simultaneously applying pressure to the joint, the resulting high energy pulse vaporizes the interlayer which then bonds to the ceramics on either side of the foil. The technique is extremely fast and because it does not involve any heating, the ceramic parts remain unaffected.

Alumina and zirconia ceramics have been joined using Al and Ti foils as interlayers [2]. However, bond strengths of the joints were either very low or widely scattered. This is beleived to be due to uneven wetting of metal or lack of reactions at interfaces. Therefore, in order to optimise the mechanical properties of the joints, sputter-coating of the ceramic surfaces with metal films prior to joining was also investigated. This paper reports on the interfacial microstructures of the joints examined by TEM.

Experimental procedure

The surface preparation of the ceramics and shear testing procedure of the joints have been previously described [2]. 3 mol% Y_2O_3-stabilised zirconia were cut into 10x10 mm or 10x5 mm tiles of $\approx$ 4 mm thickness from the bulk materials. Some tiles of zirconia surfaces were sputtered with Ti. Then, one 10x5 face of a tile was bonded to the centre of the 10x10 mm tile face. Al or amorphous $Al_xNi_yY_z$ alloys was then sandwiched between the two ceramic pieces and connected to the copper contacts through which the discharge from a 47 μF capacitor charged to 2 kV would subsequently be passed.

Specimens for TEM were prepared by cutting thin slices perpendicular to the width of the joint, further thinning the slices by polishing of both sides and completing thinning by ion-beam milling. TEM examination was carried out in a JEOL 4000EX-II and in a Philips CM30 TEM attached with an ultra-thin energy dispersive X-ray analyser (EDX).

Experimental results and discussion

TEM observations showed that there was an ≈ 200-250 nm thick reaction layer between zirconia grains in the substrate and the interlayer foil (Fig. 1(a)). EDX analysis in Fig. 1(b) showed that this thin layer contained Y, Al, O and Zr and was depleted in Ni, whereas the adjacent layer did contain Ni in addition to Y, Al and Zr and a smaller amount of O (Fig. 1(c)).

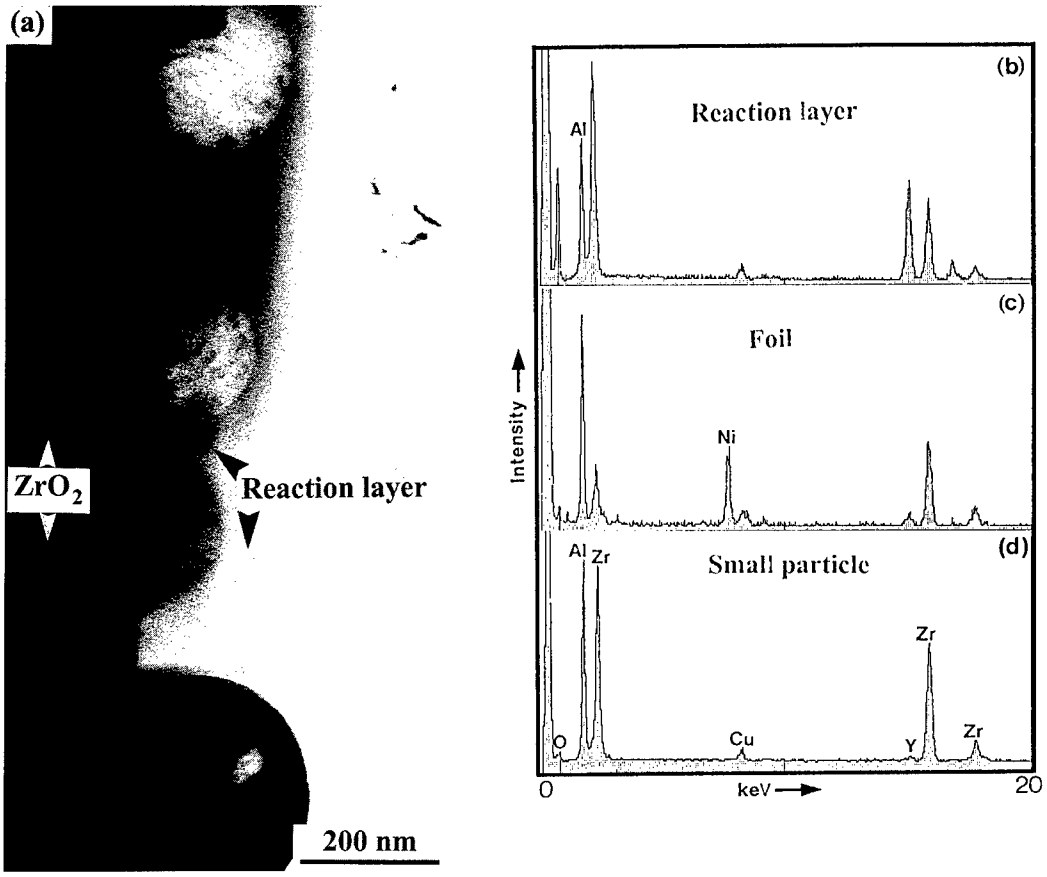

Figure 1 (a) Bright-field TEM image of a typical reaction layer between a zirconia substrate and an $Al_XNi_YY_Z$ interlayer. EDX spectra from (b) the reaction layer, (c) the $Al_XNi_YY_Z$ interlayer foil and (d) a small spherical particle in the reaction layer.

In order to identify the possible reactions, Ellingham diagrams were considered for all the elements involved when joining ZrO_2 substrates [2]. It was found that, of the interlayer constituents, it is thermodynamically favourable for only Y to react with zirconia according to reaction (1).

$$3ZrO_2 + 4Y \rightarrow 2Y_2O_3 + 3Zr \qquad (1)$$

TEM micrographs also showed that the reaction layer contained small circular crystalline particles (e.g., Fig 1(a)). In order to establish their composition, EDX spectra were collected from these particles (Fig. 1(d)). Al and Zr peaks, with very small O and Y peaks, were observed. It is proposed that the Y and O peaks arose from the surrounding reaction layer, because elemental mapping using a scanning transmission electron microscope found no evidence for either Y or O in the particles [3]. Therefore, it can be suggested that these small particles are Zr_XAl_Y compounds formed in a reaction (1) between the zirconia substrate and Y and Al in the original foil.

According to reaction (1), the small particles in the reaction layer in zirconia-$Al_xNi_yY_z$ system should be pure Zr metal, but EDX analysis detected Al as well (Fig. 1(d)). Al should not reduce zirconia because their oxides have very similar formation energies [2], but it is possible that a lower melting point Zr_xAl_y liquid formed, the presence of which increased the reaction rate between Al and Zr. No attempt to determine the exact structure and the composition of these small particles has been carried out since there are many different intermetallic phases in the Al-Zr system [4].

TEM observations on Ti-sputtered zirconia when joined using Al foil showed that there is an amorphous layer and that the layer also contains small spherical particles (Fig. 2(a)) similar to the observations of zirconia ceramics joined using $Al_xNi_yY_z$ amorphous foils (Fig. 1). This reaction layer contained Al, Zr and O and a small amount of Y and was depleted in Ti, whereas the small particle did contain Ti in addition to Al, Zr and a smaller amount of O in comparison to the reaction layer (Fig. 2 (b) and (c)).

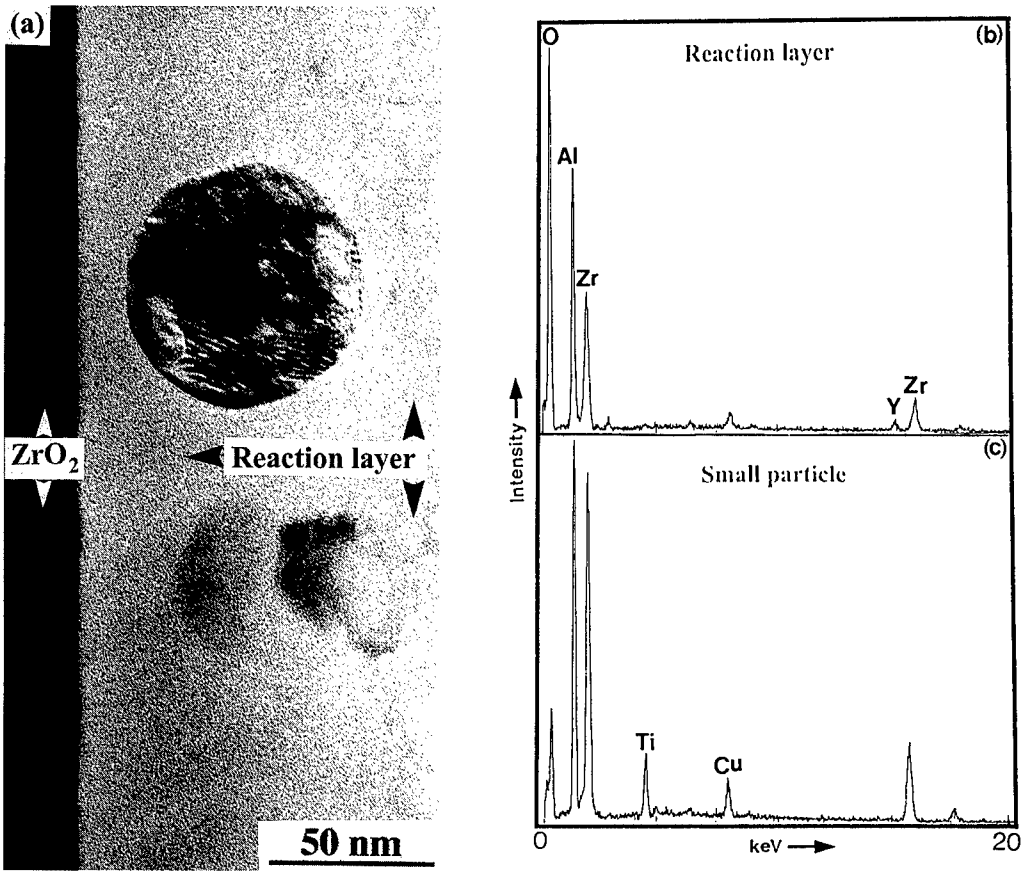

Figure 2 (a) Bright-field TEM image of a typical joint of zirconia sputter-coated with Ti and joined using Al. EDX spectra from (b) the reaction layer and (c) a small spherical particle in the reaction layer.

In this case, it is surprising to see such particles as a result of a reaction because neither Al nor Ti would be expected to react with zirzonia under normal conditions [2]. Although thermodynamical arguments would suggest that Ti should reduce ZrO_2 to form TiO, it was shown to be thermodynamically more favourable to form Ti-O solutions since O_2 in ZrO_2 is relatively mobile and is also interstitially soluble in α-Ti up to 34 at% [5]. Any distinct reaction layer between ZrO_2 and Ti foil has not been observed in our work (not shown here), but there was an interdiffusion between ZrO_2 and Ti [2]. This is in good agreement with the work of Santella and Pak [5].

The question that needs to be considered is whether or not interfacial reactions of the kind seen in the present work are beneficial to the integrity of the bond, and whether Y in particular plays a special role. It has also been suggested [6] that the formation of new phases at interphase boundaries should be avoided because the mismatch between thermal expansion coefficients and between crystallographic structures can lead to significant stresses. Recent studies have shown that the mechanical properties of such interphase boundaries can be controlled by interfacial reactions and that the mechanical integrity of the interface between Ni and Al_2O_3 was reduced by the formation of spinel during diffusion bonding [7]. In another study [8], a reaction product some 5 μm thick was observed when alumina was diffusion bonded at 1100 °C for 30 minutes under a 3 MPa compressive stress using a 1 mm thick Ta+Ti interlayer (0.67:0.33) and it was concluded that the thickness of the reaction layer had little effect on the interface fracture energy [8]. Finally, it was noted that a chemical reaction across the interface was necessary to achieve a good bond, but that excessive reactions decreased the bond strength [9].

In the light of the experimental results obtained in this work and of the above summary of the literature, it is surmised that the presence of a reaction layer (providing that it is not too thick) can be beneficial when joining ceramic by the capacitor-discharge technique. This is supported by the result that the highest shear strengths were obtained when there was a distinct reaction layer between the substrate and the foil, as was the case when using $Al_xNi_yY_z$ foils, whereas in the absence of a distinct reaction layer in the zirconia-Ti system, lower shear strengths were obtained [2]. In addition, it seems that the presence of Y facilitates reactions between the substrate and the foil, again improving bond strengths.

The mechanical strengths obtained from the zirconia samples coated with Ti and joined with Al foils were slightly less than those obtained when $Al_xNi_yY_z$ foil was used [2,3]. It is also found that if the surface of zirconia sputtered with Ti and joined with Al foil, the shear values were better than when only Al was used and similar values when only Ti was used. Therefore, it can be said that in the case of ZrO_2-Al joints, sputtering has improved the mechanical strength. However, it is unclear whether this increment is due to the increased wetting by sputtering or due to Ti facilitating reactions at the interfaces.

Conclusions

Reaction layers between the polycrystalline zirconia substrate and amorphous $Al_xNi_yY_z$ interlayers were observed. Bonded zirconia substrates contained small circular particles (identified as Zr_xAl_y) within this reaction layer. These observations suggest that there is a reaction between Y in the interlayer foils and zirconia substrates. Such reactions are thermodynamically favourable, and the small Zr_xAl_y particles are probably the remnants from such reactions. It is clear that Y is beneficial in promoting reactions which result in chemical bonding between the metal and the ceramic.

Reaction layers between zirconia and Al interlayers when the surface of zirconia sputter coated prior to joining were also observed, but there was no distinct reaction layer between zirconia and a Ti foil. Mechanical shear testing of ceramic joints made after sputtering the surfaces showed that the strength of the joints were better than the joints made without sputtering.

References

[1] K.A. Yushchenko, V.S. Nesmikh and I.V. Dubovetskii, In *Advances in Joining Newer StructuralMaterials*, p109 (1990).
[2] S. Turan, I.A. Bucklow & E.R. Wallach, J. Am. Cer. Soc., in press.
[3] S. Turan, D. Özkaya, I.A. Bucklow and E.R. Wallach, in preparation.
[4] T.B. Massalski (Ed.), Binary alloy phase diagrams Vol;1, p187, Am. Soc. Metals, Ohio (1980).
[5] M.L. Santella and J.J. Pak, Welding Research Supplement, 165-s (1993).
[6] J.T. Klomp, *Joining of Ceramics*. Ed. by M.G. Nicholas, Chapman and Hall, London (1990).
[7] K.P. Trumble and M. Rühle, *Acta metall. mater.*, **39**, p1915 (1991).
[8] A. Bartlett and A.G. Evans, *Acta metall. mater.*, **41**, p497 (1993).
[9] R.E. Tressler, T.L. Moore and R.L. Crane, *J. Mat. Sci.*, **8**, p151 (1973).

Fax: 00-90-222-3353616 **e-mail:** stur@mmf.mm.anadolu.edu.tr

Materials Science Forum Vols. 294-296 (1999) pp. 349-352

The Structure of Threading Dislocations Generated at the GaN/Al_2O_3 Interface

P. Ruterana, V. Potin and G. Nouet

Laboratoire d'Etudes et de Recherches sur les Matériaux, UPRESA CNRS 6004, Institut des Sciences de la Matière et du Rayonnement, 6 Boulevard du Maréchal Juin, F-14050 Caen Cedex, France

Keywords: Gallium Nitrides, Transmission Electron Microscopy, Edge Dislocations, Mosaic Growth, Subgrain Boundaries, Dislocation Core Structure

Abstract: Due to the large misfits involved, the nitride layers deposited on (0001) sapphire grow in a mosaic mode. This microstructure may not only be due to growth errors as it has been argued previously. The threading dislocations which are mainly of **a** type exhibit 5/7 and 8 atom rings cores. They form subgrain boundaries and many of them are connected to the 60° interface misfit dislocations. This can be one explanation of the rotation of individual islands around the c growth axis.

Introduction

GaN layers for optoelectronic applications are epitaxially grown on sapphire, which exhibits a misfit of 14%. This results in the formation of layers containing high densities of defects (10^9 – 10^{10}) which are mainly : **a, a + c** and **c** threading dislocations which originate at the interface and propagate through the active GaN layers [1, 2]. It is a consequence of the three dimensional growth mode in these highly mismatched systems [3,4]. When the islands come into coalescence, they are misoriented either by rotations around the c axis, or by tilts of this c axis. In their work on GaN layers grown on sapphire, Ning et al [3] have argued that the mosaic growth can only be explained by growth errors on top of hexagonal (0001) surfaces. In many ways, the above argument may not be the only mechanism. Actually due to the large misfits, the three dimensional growth mode is predominant and it can be supposed that the islands start to relax before coalescence takes place. Therefore, each island comes in touch with its neighbour bringing along its shape, and interface dislocations. During the growth on top of the (0001) surface, the 14% lattice mismatch between GaN and sapphire is releaved by the formation of misfit dislocations which always have a screw component. It is worth to remember that if the relaxation is to be completed, 60° misfit dislocations in the interface are to be found at an average distance of less than 2 nm. Notwithstanding the high densities of the threading defects, these layers are used to fabricate very efficient optoelectronic devices such as LED's and laser diodes [5] implying that these defects do not have a high electrical activity. However, the laser diodes made in these layers exhibit short life times meaning that the defects do become electrically active under devices operation.

In this work, we determine the connection of the threading dislocations to the interface and next investigate their atomic structure .

Experimental procedure

The analyzed samples were 1 to 2 μm thick GaN layers grown at 800°C by molecular beam epitaxy on the (0001) sapphire substrates [6]. The specimens for electron microscopy were prepared in the conventional way by mechanical polishing followed by ion milling down to electron transparency. The ion milling was always carried out with the specimen hold at the liquid nitrogen temperature in

order to minimize the ion beam damage. Cross section and planar view observations were carried out in order, first to determine the type of the threading dislocations, and next to analyze their atomic structure. The experimental micrographs were recorded in the 002B Topcon microscope operated at 200 kV, its point to point resolution is 0.18 nm. Models of the 1/3 $[11\bar{2}0]$ dislocation were generated by applying the displacement field calculated by anisotropic elasticity [7]. The resulting supercells were used in the electron microscopy software (EMS) for image simulations and comparison with the experimental micrographs [8].

Results

The mosaic growth is mostly visible in rather bad quality samples in which the dimension of the islands can be as small 100 nm (fig. 1), in this case the density of the threading dislocations is in the high 10^{10} cm^{-2} . The rotation of the island is only around **c** as there is no contrast between them when the area is imaged along [0001] zone axis. Therefore the limiting dislocations which make the subgrain boundaries are of edge type.

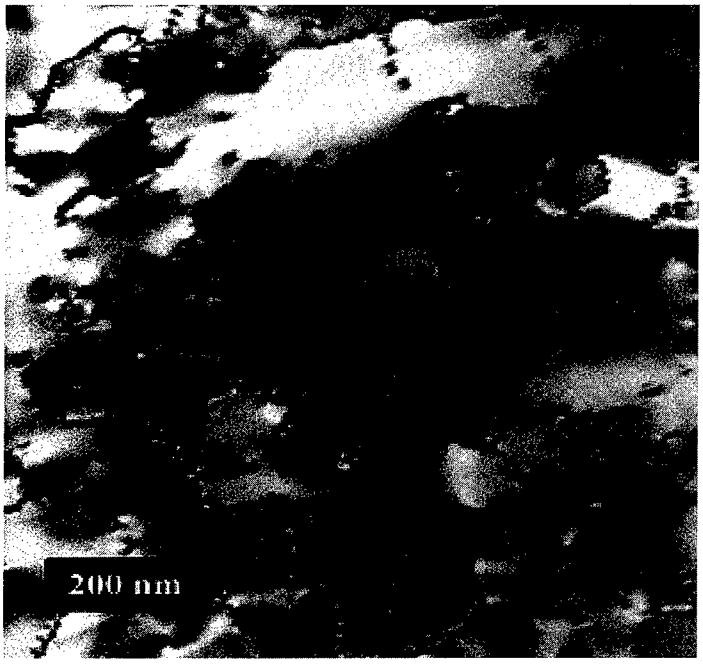

Fig.1 Planar view micrograph slightly off the [0001] axis, mosaic structure of the GaN film

In the interface areas, after a Fourier filtering by selection of the fringes perpendicular to the interface, the additional lattice fringes in the interface show that the misfit dislocations are present (fig.2). They are regularly spaced by 17.2 Å, which means that in this area, the layer is completely relaxed by 60° dislocations. So the interfacial and threading dislocations are mainly of **a** type and this is agreement with previous observations which showed that more than 90 % of the threading dislocations are **a** and **a+c** [2]. Moreover, we have recently shown that the **c** dislocations are mainly due to occurence of impurities at the interface [4]. Thus the mosaic growth is mostly due to coalescence of island which are rotated around the **c** axis.

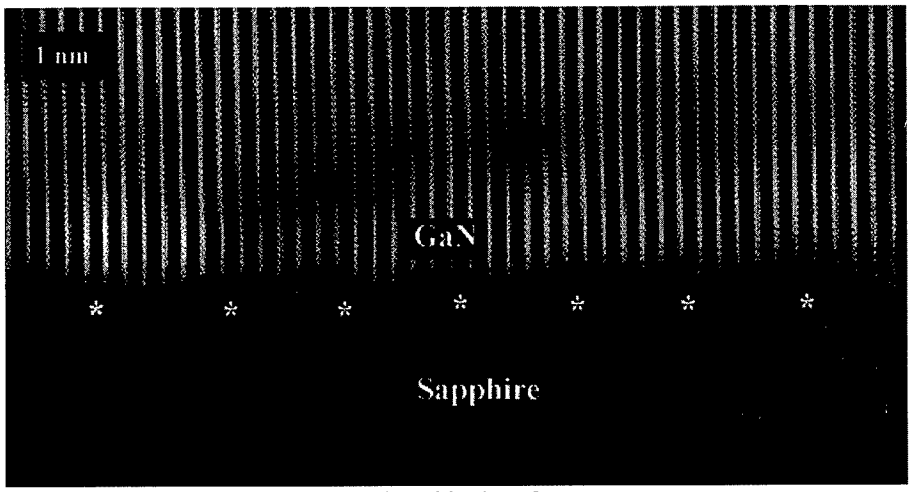

Fig.2 Misfit dislocations at the GaN/sapphire interface

It is then very important to see if there is some connection between the threading dislocations and the misfit ones in the interface. In good layers the average rotation angles measured are between 0 and 1.5°, for 0.5° rotation angle, the average distance of 60° dislocations in sub grain boundaries would be 18 nm instead of the 1.7 nm in the interface. Therefore, it is possible that most of the misfit dislocations do not give rise to threading dislocation. However, as can be seen on figure 3, there appears to be a direct connection, as pointed out by the additional moiré fringes which show the location of threading dislocation and most of them are linked by a dislocation line in the interface between GaN and the sapphire substrate.

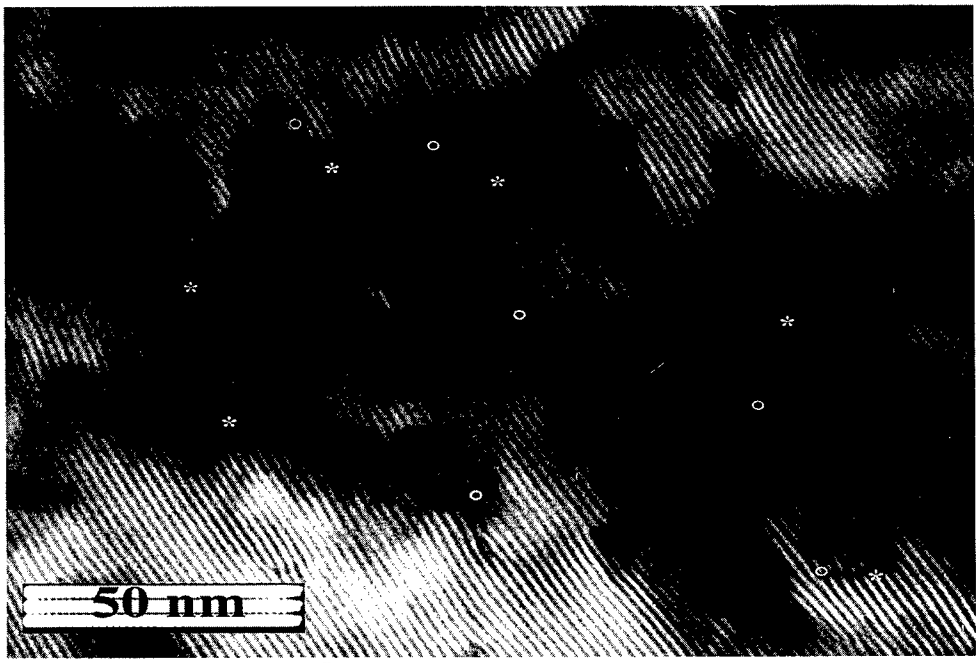

Fig.3 Moiré image along the $10\bar{1}0$ systematic row, each two threading dislocations joined by an misfit one are marked by a white star and circle

HREM observations along the **c** zone axis show mainly two atomic configurations for the core of the edge threading dislocations. As shown in figure 4, they can have 5/7 atoms cycles, but 8 atom rings configurations have also been observed in agreement with recently published experimental and theoretical results [10,11].

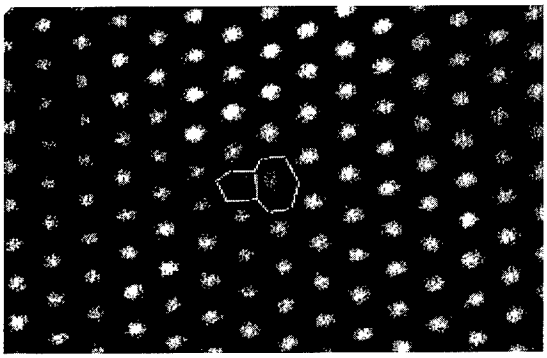

Fig.4 A 5/7 atom rings core of an edge dislocation in GaN, view along [0001]

Summary

In this work, it is shown that most of the edge dislocations in subgrain boundaries are connected to misfit dislocations in the GaN/sapphire interface. Their atomic structure can have 5/7, as well as 8 atom cycles. Their connection to the 60° interface dislocations is a direct evidence for the contribution of screw component of the misfit dislocation in the rotation of the individual islands around the **c** axis and subsequent mosaic growth of the epitaxial layers.

Ackowledgement
Professor Morkoc of the Virginia Commonwealth University in Richmond and his group are gratefully acknowledged for providing us with the samples as well as for fruitfull discussions.

1. F.A. Ponce, D.P. Bour, W. Götz, N.M. Johnson, H.I. Helava, I. Grzegory, J. Jun and S. Porowski, Appl. Phys. Lett., **68**, 917 (1995).
2. P. Vermaut, P. Ruterana, G. Nouet, A. Salvador and H. Morkoç, Int. Phys. Conf. Ser., **146**, 289 (1995).
3. X.J. Ning, F. R. Chien, P. Pirouz, J. W. Wang and M. A. Khan, J. Mater. Res. **3**, 580 (1996)
4. P. Ruterana, P. Vermaut, G. Nouet, A. Salvador, and H. Morkoç Mater. Res. Soc. Internet Journal of Nitride Semiconductor Research, Vol. **2**, paper 42 (1997)
5. S. Nakamura, M. Senoh, S. Nagahama, N. Iwasa, T. Yamada, T. Matsushita, K. Kiyoku and S. Sugimoto, Jpn. J. Appl. Phys. **66**, L 74 (1996).
6. M.E. Lin, S. Strite, A. Agarwal, A. Salvador, G.L. Zhou, N. Teragush, A. Rockett, and H. Morkoc, Appl. Phys. Lett. **62**, 702 (1993)
7. R. Bonnet, Acta Met. **29**, 437 (1981)
8. P. Stadelmann, Ultramicroscopy, **21**, 131 (1987).
9. P. Ruterana, P. Vermaut, V. Potin, G. Nouet, R. Bonnet and M.Loubradou, Mater. Sci. Eng. **B** , in press
10. P. Ruterana, V. Potin, G. Nouet, Mat. Res. Symp. Proc. Vol **482**, 459 (1998)
11. J. Elsner, R. Jones, P.K. Sitch, V.D. Porezag, M. Elsner, Th. Frauenheim, M.I. Heggie, S. Obert and P.R. Briddon, Phys. Rev. Lett. **79**, 3672 (1997)

Author for correspondence: P. Ruterana, fax: 33 2 31 45 26 60, mail: ruterana@lermat8.ismra.fr

Materials Science Forum Vols. 294-296 (1999) pp. 353-356

Disclinations at Grain Boundary Triple Junctions: Between Bollmann Disclinations and Volterra Disclinations

P. Müllner

Max-Planck Institut für Metallforschung, Seestrasse 92, D-70174 Stuttgart, Germany
E-Mail: peter.muellner@po.uni-stuttgart.de

Keywords: Disclinations, Triple Junctions, Grain Boundary

Abstract

We discuss the question whether Bollmann's classification of triple junctions into *I*- and *U*-lines corresponds to a physical reality. We describe a virtual multiple junction of only small angle boundaries in two ways: First, by using Bollmann's *I/U*-line scheme (***Bollmann disclinations***) and second, by an elasticity approach (rotational Volterra cuts, ***Volterra disclinations***). Depending on the number of boundaries, the multiple junction is found to be an *I*-line or a *U*-line. We conclude that the Bollmann disclination is a real crystallographic defect that is essentially different from the Volterra disclination.

1. Introduction

There have been proposed several concepts how to categorize triple junctions in different classes [1, and refs. there]. The most general concept is Bollmann's *I/U*-line scheme [2,3] which is applicable to a junction between any random grain boundaries. Corrosion experiments provide evidence for the phyisical validity of the classification into *I*- and *U*-lines [4]. Nevertheless, there has been a long standing debate as to whether Bollmann disclinations (*U*-lines) exist at all [5,6] and recently, the concept has been dismissed [7]. The aim of the present paper is to contribute to this discussion and, in particular, to emphasize some characteristics of the Bollmann disclination. This is done by describing a virtual multiple junction of n small angle tilt boundaries using two concepts: Bollmann's *I/U*-line scheme (Eqns. B) and the concept of Volterra cuts [8] (Eqns. V).

2. Background

Bollmann [2,3] describes the structures of a tripple junction by a circuit transformation **D:**

$$\mathbf{D} = \mathbf{CBA}\,, \qquad (1B)$$

where **A**, **B**, and **C** are unimodular transformations describing the boundaries. If now the circuit transformation **D** is the identity **I**, the triple line is an *I*-line. It may instead be a unimodular transformation **U** unlike the identity. In this case, the triple line is a *U*-line or *triple line disclination* or ***Bollmann disclination***. There is an infinite number of choices for **A**, **B**, and **C** which all describe correctly the bicrystallography of the boundaries. However, the „nearest-neighbour relation" (NNR) has been defined which transforms a unit cell of one crystal into the nearest corresponding unit cell in the neighboring crystal. The general validity of the NNR as the physically unique description of a boundary may be argued [7]. However, small angle tilt boundaries are made up by walls of edge dislocations with the smallest possible dislocation content [9] and, thus, correspond to the NNR.

We distinguish between the *Bollman dislcination* and the *Volterra disclination*: The Bollmann disclination is defined in the context of crystallography alone, *i.e.* in terms of

misorientations. A ***Volterra disclination*** is an elastic line defect with a rotational displacement field. The displacement field is described by the Frank vector $\underline{\omega}$ which represents a rotation [8].

A terminated tilt grain boundary is associated with a Volterra disclination and vice versa (except for perfect disclinations [8]). Thus, a multiple junction may be decomposed into N terminated boundaries with N Volterra disclinations. The Frank vector $\underline{\omega}_J$ of the junction Volterra disclination is simply the vector sum of the Frank vectors of the individual Volterra disclinations:

$$\underline{\omega}_J = \sum_{i=1}^{N} \underline{\omega}_i \,. \qquad (1V)$$

In an unstrained system, the vector sum has to vanish (*i.e.* $\underline{\omega}_J = \underline{\mathbf{0}}$), and thus, there is no Volterra disclination at the junction. While the Bollmann concept applies to any boundary configuration, the Volterra concept applies in this simple form only to tilt boundaries.

3. A thought experiment

We now do a thought experiment: We consider <100> small angle tilt boundaries in a primitive cubic lattice. We successively build a number of multiple lines *without causing strains or stresses*. In a first step, we cut a wedge with a wedge angle $\alpha = \pi/R$ (R being an even integer) out of a cylinder (Fig. a). We take a second wedge with exactly the same shape, however with slightly different orientation and insert the second wedge into the gap which was left in the cylinder (Fig. b). The transformation $\mathbf{A}_1$ from the original cylinder orientation to the new wedge orientation shall be a counterclockwise rotation around the cylinder axis by the „small" angle $\varphi_1 = \varphi = \pi/(2R)$. We end up with two crystals, namely grain O and grain I and two grain boundaries A_1 and A_{e1} with the corresponding transformations and Frank vectors $\mathbf{A}_1 = \mathbf{A}$ and $\mathbf{A}_{e1} = \mathbf{A}^{-1}$, $\underline{\omega}_1 = \underline{\omega} = -\varphi\underline{\mathbf{e}}$ ($\underline{\mathbf{e}}$ is the unit vector along the cylinder axis out of the plane of drawing, Fig. b) and $\underline{\omega}_{e1} = -\underline{\omega}$, respectively. The boundary A_1 shall be symmetric. A_1 and A_{e1} meet at the cylinder axis which can be considered as a „double junction" and we may apply the concept of a multiple junction:

$$\mathbf{D}_1 = \mathbf{A}_{e1}\mathbf{A}_1 = \mathbf{A}_1^{-1}\mathbf{A}_1 = \mathbf{I} \qquad (2B)$$

$$\underline{\omega}_{J1} = \underline{\omega}_1 + \underline{\omega}_{e1} = \underline{\mathbf{0}} \,. \qquad (2V)$$

Thus, at the double junction, there is neither a Bollmann disclination nor a Volterra disclination.

In a second step, we create a second wedge-shaped grain II next to grain I. The transformation from the grain I orientation to the grain II orientation shall be a counterclockwise rotation by the angle $\varphi_2 = \varphi$, *i.e.* $\mathbf{A}_2 = \mathbf{A}$ and $\underline{\omega}_2 = \underline{\omega}$. We have now three grains (O, I, and II) with three grain boundaries (A_1, A_2, and A_{e2}) meeting at the triple line. The transformation and Frank vector of A_{e2} are $\mathbf{A}_{e2} = (\mathbf{A}_2\mathbf{A}_1)^{-1} = (\mathbf{A})^{-2}$ and $\underline{\omega}_{e2} = -(\underline{\omega}_1 + \underline{\omega}_2) = -2\underline{\omega}$, respectively. We obtain:

$$\mathbf{D}_2 = \mathbf{A}_{e2}\mathbf{A}_2\mathbf{A}_1 = (\mathbf{A})^{-2}\mathbf{A}\mathbf{A} = \mathbf{I} \qquad (3B)$$

$$\underline{\omega}_{J2} = \underline{\omega}_1 + \underline{\omega}_2 + \underline{\omega}_{e2} = \underline{\mathbf{0}} \,. \qquad (3V)$$

Again, there is neither a Bollmann disclination nor a Volterra disclination at the triple junction.

We continue with this procedure n times, thereby producing n wedge-shaped grains (I, II, ...N, Fig. d) all sharing the same (n+1)-fold junction. There are n+1 boundaries (A_1, A_2, ... A_n, and A_{en}) with the transformations $\mathbf{A}_i = \mathbf{A}$ (i = 1..n) and $\mathbf{A}_{en}$, and the Frank vectors $\underline{\omega}_i = \underline{\omega}$ (i = 1...n) and $\underline{\omega}_{en}$, respectively. The multiple junction is described by:

$$\mathbf{D}_n = \mathbf{A}_{en}\mathbf{A}_n \ldots \mathbf{A}_1 = \mathbf{A}_{en}(\mathbf{A})^n \qquad (4B)$$

$$\underline{\omega}_{Jn} = n\underline{\omega} + \underline{\omega}_{en} \qquad (4V)$$

We now consider the special case with $n = R$ (Fig. e). For the boundaries A_i ($i = 1..R$) this specification does not matter, i.e. $\varphi_i = \varphi$, $\mathbf{A}_i = \mathbf{A}$, and $\underline{\omega}_i = \underline{\omega}$. However, the misorientation between R and O is a rotation around <100> by $R\varphi = \pi/2$ which is a symmetry rotation. Therefor, the boundary A_{eR} is a perfect Σ=1 boundary with $\mathbf{A}_{eR} = \mathbf{I}$ and $\underline{\omega}_{eR} = \underline{\mathbf{0}}$. The junction is described by:

$$\mathbf{D}_R = \mathbf{A}_{eR}(\mathbf{A})^R = (\mathbf{A})^R = \mathbf{U} \neq \mathbf{I} \qquad (5B)$$

$$\underline{\omega}_{JR} = R\underline{\omega} + \underline{\omega}_{eR} = -\pi/2\underline{\mathbf{e}} \neq \underline{\mathbf{0}}, \qquad (5V)$$

where **U** is a 90° rotation. In this case, the junction is a *U*-line, there is a Bollmann dislination and a Volterra disclination. The Volterra disclination has a strong stress field [8]. Recalling that there are no stresses introduced by the above proceedure, we see that *there is a discrepancy*!

4. Discussion

It can be shown [10], that the alleged discrepancy is due to an incorrect neglection of a perfect Volterra disclination. The boundary A_{en} plays a key role: With increasing but still small n ($n < R/2$), the dislocation content of A_{en} increases proportionally to n. A_{en} is characterized by $\varphi_{en} = -n\varphi$, $\mathbf{A}_{en} = (\mathbf{A})^{-n}$, and $\underline{\omega}_{en} = -n\underline{\omega}$. Thus, $\mathbf{D}_n = \mathbf{I}$ (Eqn. 4B) and $\underline{\omega}_{Jn} = \underline{\mathbf{0}}$ (Eqn. 4V), *i.e.* there is neither a Bollmann nor a Volterra disclination. However, if $n > R/2$, the tilt angle of A_{en} is not $\varphi_{en} = -n\varphi$ but $\varphi_{e,n>R/2} = (\pi/2 - n\varphi)$ because the latter has the smaller magnitude and smaller dislocation content [12]. The corresponding transformation and Frank vector are $\mathbf{A}_{e,n>R/2} = \mathbf{U}(\mathbf{A})^{-n}$ (as above, U is a 90° rotation) and $\underline{\omega}_{e,n>R/2} = -\varphi_{e,n>R/2}\underline{\mathbf{e}} = -(\pi/2)\underline{\mathbf{e}} + n\underline{\omega}$, respectsively. The transition from the description $\varphi_{en} = -n\varphi$ to $\varphi_{e,n>R/2} = (\pi/2 - n\varphi)$ at $n = R/2$ corresponds physically to the formation of a perfect lattice disclination with $\underline{\omega}_{\text{lattice}} = (\pi/2)\underline{\mathbf{e}}$. Since a perfect lattice disclination is not associated with a boundary, there is no further transformation and the correct multiple line description is:

$$\mathbf{D}_{n>R/2} = \mathbf{A}_{e,n>R/2}(\mathbf{A})^n = \mathbf{U}(\mathbf{A})^{-n}(\mathbf{A})^n = \mathbf{U} \neq \mathbf{I} \qquad (6B)$$

$$\underline{\omega}_{J,n>R/2} = n\underline{\omega} + \underline{\omega}_{e,n>R/2} + \underline{\omega}_{\text{lattice}} = n\underline{\omega} - (\pi/2)\underline{\mathbf{e}} - n\underline{\omega} + (\pi/2)\underline{\mathbf{e}} = \underline{\mathbf{0}}. \qquad (6V)$$

Thus, for $n > R/2$, *there is a Bollmann disclination* with **U** independent of n, *but there is no junction Volterra disclination.* In variance with the result of Bollmann [12], a Bollmann disclination does not have a stress field. The validity of Eqns. (6) might be argued for the case $n \approx R/2$ [7]. However, when $n \approx R$, all boundaries are small angle boundaries and their structure certainly is made up by dislocation walls corresponding to the NNR. Nevertheless, one can extend the argumentation to any multiple junction - including triple junctions of high angle boundaries - when assuming that in equilibrium there is only one physical form of a given boundary [10].

5. Conclusions

(i) The *I*/*U*-line scheme is a reasonable classification for multiple junctions at which only small angle boundaries meet. The distinction between *I*- and *U*-lines is physically justified.

(ii) The Bollmann disclination is a real defect. It is a crystallographic defect unlike the Volterra disclination which is an elastic defect.

(iii) The Bollmann disclination has no stress field.

References

[1] A.H. King and V. Singh, Mater. Sci. Forum 207-209 (1996), p. 257.
[2] W. Bollmann, Phil. Mag. A 49 (1984), p. 73.
[3] W. Bollmann, Phil. Mag. A 57 (1988), p. 637.
[4] G. Palumbo and K.T. Aust, Mater. Sci. Engng. A 113 (1989), p. 139.
[5] G. Palumbo and K.T. Aust, Mater. Sci. Engng. A 205 (1996), p. 254.
[6] L. Priester and D. Yu, D., Mater. Sci. Engng. A 205 (1996), p. 255.
[7] G.P. Dimitrakopulos, Th. Krakostas, and R.C. Pond, Interf. Sci. 4 (1996), p.129.
[8] A.E. Romanov and V.I. Vladimirov, Dislocations in Solids, Vol. 9, edited by F.R.N. Nabarro (Amsterdam: Elsevier 1992), p. 191.
[9] W.T. Read and W. Shockley, Phys. Rev. 78 (1950), p. 275.
[10] P. Müllner, to be published.
[11] F.C. Frank, Phil. Mag. (ser. 7) 42 (1951), p. 809.
[12] W. Bollmann, Mater. Sci. Engng. A 136 (1991), p. 1.

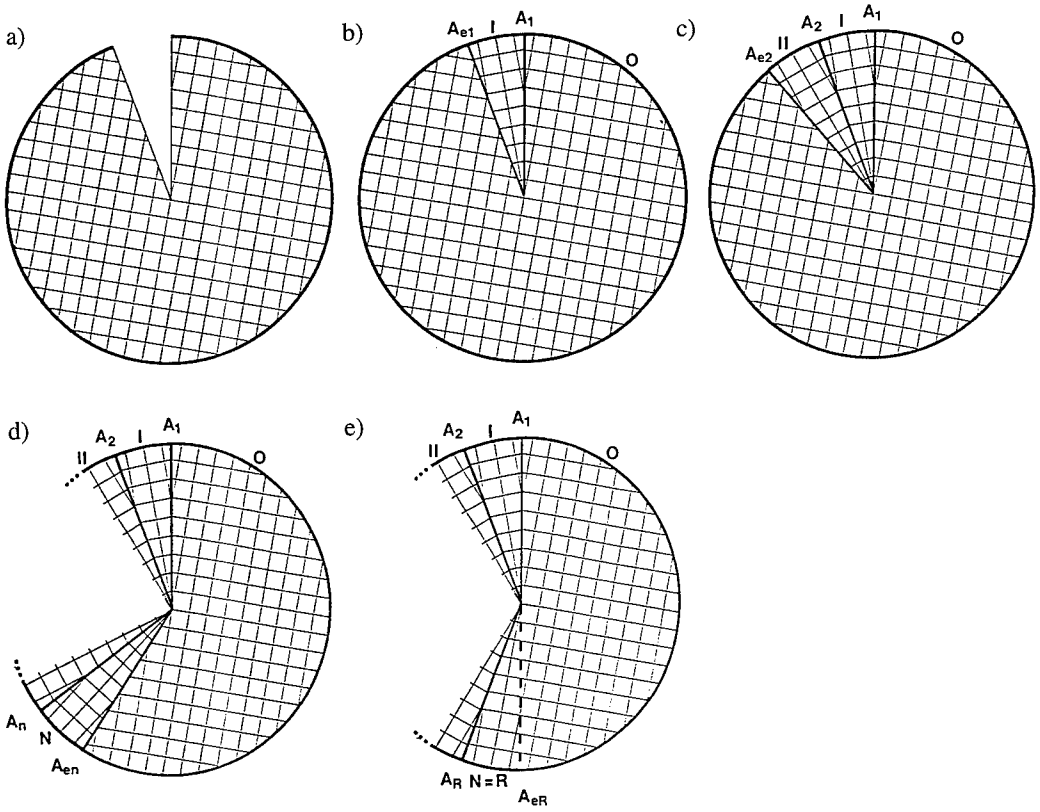

Fig.: Schematics of the thought experiment: A wedge is cut from a single crystal cylinder (a) and replaced by an other wedge of the same shape but different orientation (b), forming two grain boundaries (A_1 and A_{e1}). A second wedge is replaced by an other wedge (c). There three grain boundaries (A_1, A_2, and A_{e2}). The procedure is repeated n times (d) resulting in n+1 grains (O, I, II,...N) and n+1 grain boundaries (A_1, A_2, ... A_n, and A_{en}). In the special case with $n = R$ (e), the grain boundary A_{eR} is a Σ=1 boundary which has no substructure. It is shown that this is a Bollmann disclination.

Materials Science Forum Vols. 294-296 (1999) pp. 357-360

Quantitative Analysis of Co Silicide/SiC Interfaces

M. Lamy and J. Thibault

CEA / Département de Recherche Fondamentale sur la Matière Condensée/ SP2M,
17 rue des Martyrs, F-38054 Grenoble, France
E-Mail: mlamy@cea.fr and jthibault@cea.fr

Keywords: Quantitative HREM, ESI, Co-Silicide, SiC

Abstract : The structure of the interfaces between Co silicide and (0001) SiC has been characterized mostly by high resolution electron microscopy and electron spectroscopic imaging. It has been found that, in general, there is no simple and systematic relationships at the silicide/ceramic interface and that there is no noticeable interdiffusion: the interfaces are chemically abrupt over 1.5 nm.

1. Introduction

The purpose of this study is to determine the atomic structure of the interface between the eutectic $CoSi_2$-CoSi and SiC(6H) in order to understand the joining at the silicide/ceramic interface which was prepared by a high temperature treatment at which the eutectic was melted on the (0001)SiC plane.

2. Experimental techniques

In the present study, optical and electron microscopy have been used. Samples for transmission electron microscopy (TEM) observation were prepared on a standard way by mechanical thinning followed by ion milling (Gatan Duo-Mill).

2.1 Quantitative HREM

High resolution electron microscopy (HREM) was performed using a JEOL 4000EX (Cs = 1mm). Quantitative analysis of the distortion between atomic planes were made using the method describe in [1]. In order to reduce the noise, the image was firstly projected along the direction of the atomic planes parallel to the interface. The distance d_i (in pixels) between two intensity maxima which corresponds to the local lattice parameter is then measured: this gives the profile of the interplanar distances with an accuracy of ± 0.0025 nm. In order to avoid a systematic error propagation in the determination of two neighboring maxima, the profile can be smoothed by a weighted averaging over 3 neighboring distances but as a consequence the interface is expected to be slightly enlarged.

2.2 Chemical mapping

Electron spectroscopic imaging (ESI) was performed on a JEOL 3010 (LaB_6 filament) running at 300 kV (Cs=0.6mm, Cc=1.2mm) and equipped with a Gatan imaging filter (GIF). The maps are obtained using the method where three windows [2] are selected from an Electron Energy Loss Spectrum (EELS): one image is recorded with electrons having suffered energy loss after the edge and two images are recorded with the electrons having lost energy before the edge. This method permits to extract the true signal from the background. The resolution [3],[4] depends strongly on the imaging conditions in the microscope (objective aperture), and in the GIF (slit width). In our case for a 16 mrad objective aperture and a 20 eV slit, the resolution of the method is between 1 and 1.5 nm.

3. The interface at the micrometric scale

3.1 Evolution of the SiC surface during heat treatment

During heat treatment, the (0001)SiC surface suffers a transformation. Although the SiC surface was very well polished before the preparation, the final surface is no longer flat: some SiC grains grow on top of the original flat (0001) surface (fig. 1). Most often these grains have a hexagonal structure with the same orientation as the (6H)SiC substrate but in one specimen, grains with a cubic structure were found with the relationship : <11-20>SiC//<111>SiC and (0001)SiC//(200)SiC. Furthermore, just below the interface, SiC often exhibits an area whose thickness can reach 1 μm with many stacking faults. This area (fig. 2) is actually made of a mixing of (6H)SiC areas and cubic SiC areas whose thickness is in between 20 and 50 (111) planes.

3.2 $CoSi/CoSi_2$ characterization

A planar view of a $CoSi/CoSi_2$ 150 μm thick has been first characterized by optical microscopy (fig. 3). The silicide is made of a $CoSi_2$ matrix with CoSi grains whose morphology is various and depends on their size: they have either a large dendritic structure with an average size of 0.1 mm or a small round shape 1 μm to 10 μm in diameter. The chemical composition was checked by EDX in a JEOL SEM. The morphology of the eutectic is not a typical one: this might be attributed to the fact that the two phases are growing independently during solidification. Figure 4 shows a cross-section image of the interface obtained by conventional TEM. The $CoSi_2$ matrix and the small CoSi grains are clearly visible. Generally, CoSi grains are faceted crystals on the SiC surface but some others are dispersed in the $CoSi_2$ matrix. The $CoSi_2$ matrix is made of only a few grains 1 mm large. No other phase has been detected. No simple and systematic crystallographic orientation between $CoSi_2$ or CoSi and SiC has been detected by electron diffraction.

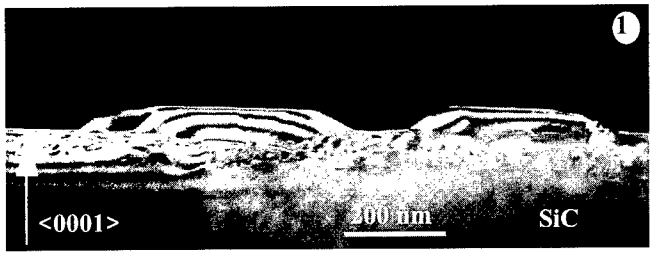

Fig. 1: SiC surface after heat treatment : SiC grains have grown on the initially flat (0001) SiC surface.

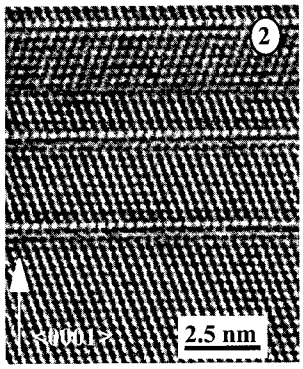

Fig. 2: Faulted area just below the interface.

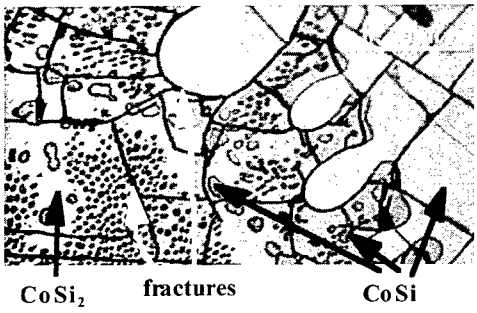

Fig. 3: Optical micrograph of a planar view of the eutectic film showing the different shapes of the CoSi grains in the $CoSi_2$ matrix.

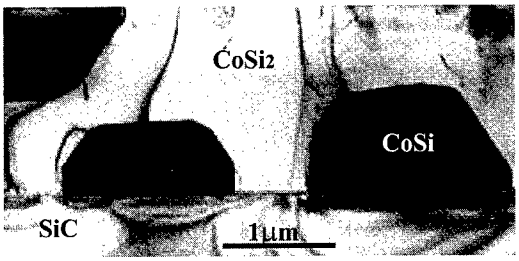

Fig. 4: TEM micrograph of the eutectic film: the CoSi small grains are either embedded in the $CoSi_2$ matrix or at the SiC surface.

Fractures occur when the film thickness is large (fig. 3) whereas no fracture is detected for films whose thickness is of a few microns (fig. 4). In the latter case dislocations are found in the $CoSi_2$ matrix and at the interfaces between $CoSi_2$ and CoSi. The fractures are due to the difference in the thermal expansion coefficients between silicides 13 10^{-6} °C $^{-1}$ and SiC 5 10^{-6} °C $^{-1}$ over the 20°C-1000°C temperature range.

4. The interface at the nanometric scale

Fortunately, a simple crystallographic orientation between $CoSi_2$ and SiC was once observed: <100>$CoSi_2$//<11-20>SiC and (010)$CoSi_2$//(0006)SiC (fig. 5a). HREM image of this particular $CoSi_2$/SiC interface and the profile of $CoSi_2$ and SiC interplanar distance are shown in figure 5. The difference between the (010) interplanar distance in $CoSi_2$ and the (0006) interplanar distance in SiC is clearly shown but there is no noticeable variation of the lattice parameter on both sides up to the interface: the distances are the ones in the bulk: $d_{010}(CoSi_2) = 0.268$ nm and $d_{0006}(SiC) = 0.251$ nm. Nevertheless a strong variation in the interplanar distance profile is clearly visible and takes places only over one atomic plane located just between the last $CoSi_2$ plane and the first SiC plane. A similar distortion is often found in the measurement of the SiC interplanar distances even with $CoSi_2$ out of a special zone axis (fig. 6a and b). This effect is due to the variation of the mean inner potential and has been checked by simulations of HREM images as a function of thickness and defocusing distance (fig. 7). The images of a simple geometrical model (fig. 7a) with the <100>$CoSi_2$//<11-20>SiC relationship have been simulated: the interplanar distance at the interface being the average distance between $d_{002}(CoSi_2)$ and $d_{0006}(CoSi_2)$. Figure 7b shows the theoretical profile. Fig. 7c, 7e and 7g are the simulated images obtained for a sample thickness of 4.9nm and for defocusing distances respectively of -30nm, -50nm, -70nm. The corresponding interplanar distance profiles are shown 7d, 7f, 7h. For f=-30nm, the atoms are imaged in black in SiC whereas they are white in $CoSi_2$. For f=-50nm, atoms are black and for f=-70nm atoms are white. It is clear that the interplanar distortion depends strongly on the imaging conditions and cannot be interpreted directly as a true variation of the interplanar distance. The true profile is obtained only for f=-70nm.

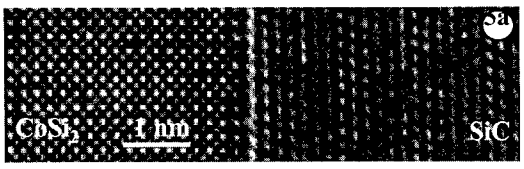

Fig. 5a: HREM image of a $CoSi_2$/SiC interface. $CoSi_2$ is viewed along [001] and SiC along [11-20].

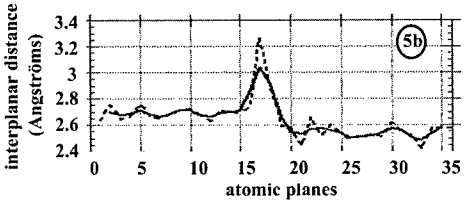

Fig. 5b: Interplanar distance profile extracted from (5a): raw profile (dotted line) smoothed profile (black line).

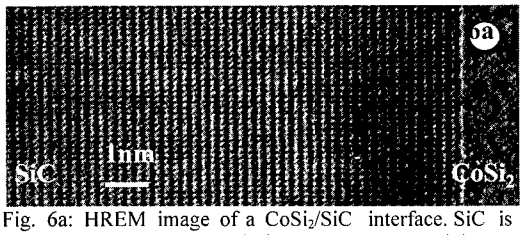

Fig. 6a: HREM image of a $CoSi_2$/SiC interface. SiC is viewed along [1-100], $CoSi_2$ is not along a special zone axis

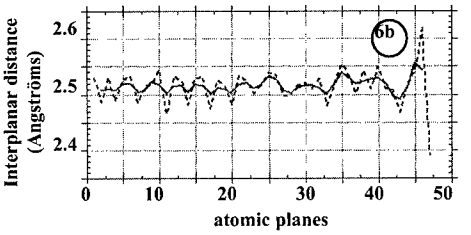

Fig. 6b: Interplanar distance profile extracted from (6a): raw profile (dotted line) smoothed profile (black line).

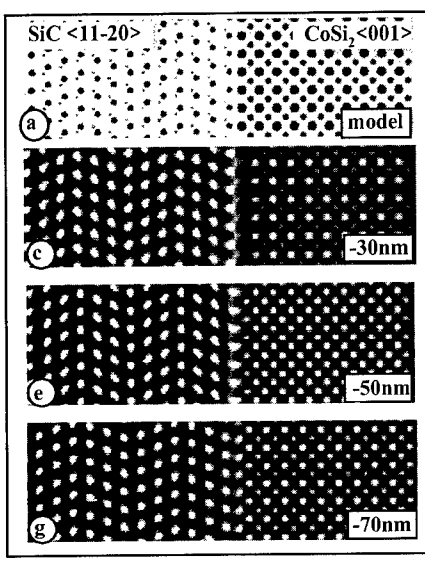

Fig. 7: a) Geometraical model of a SiC/CoSi2 interface.
b) interplanar distance profile.

Fig. 7: c) HREM image simulation.
f = -30nm, t = 4.9nm.
d) interplanar distance profile.

Fig. 7: e) HREM image simulation
f = -50nm, t = 4.9nm.
f) interplanar distance profile.

Fig. 7: g) HREM image simulation
f = -70nm, t = 4.9nm.
h) interplanar distance profile.

Fig. 8a: Cobalt map of the $SiC/CoSi_2$ interface.

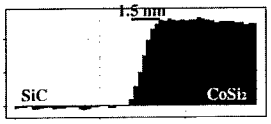

Fig. 8b: Profile of Co concentration across the interface averaged over the frame width in figure 8a.

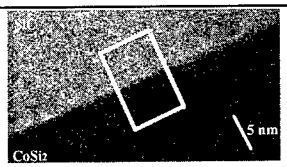

Fig. 8c: Carbon map of the $SiC/CoSi_2$ interface.

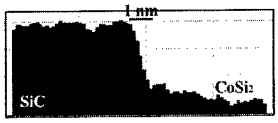

Fig. 8d: Profile of C concentration across the interface averaged over the frame width in figure 8c.

Fig. 8a shows the cobalt chemical map of one interface $SiC/CoSi_2$ and fig. 8b shows the Co profile across the interface averaged on the frame in figure 8a. The cobalt map was performed using the L23 edge at 779 eV. The carbon map was performed using the K edge at 284 eV. Due to contamination, the C map is more noisy than the Co map (fig. 8c). Moreover, the carbon profile (fig. 8d) shows the presence of carbon even on $CoSi_2$. The $SiC/CoSi_2$ and SiC/CoSi interfaces exhibit the same features: there is no noticeable long distance diffusion of cobalt and carbon.

5. Conclusion

The $CoSi_2$-CoSi / SiC interface exhibits no special crystallographic relationship. Furthermore, in general, the interface plane in $CoSi_2$ or CoSi is not a particular one. The chemical abruptness of the interface is of the order of (or better than) 1.5 nm. Although the SiC surface may be strongly affected during heat treatment, this seems to have no noticeable consequence on the further silicide/SiC interface structure.

[1]R. Bierwolf, M. Hohenstein, F. Phillip, O. Brandt, GE. Cook, P. Ploog, Ultramicroscopy, **49** (1993) 273.
[2] R. F. Egerton, (1986) Electron Energy Loss Spectroscopy in Transmission Electron Microscope, Plenum Press, New-York.
[3] O. L. Krivanek, M. K. Kundmann, and K. Kimoto, Jour. of Microscopy, **180** (1995), 277.
[4] R. F. Egerton, P. A. Crozier, Micron, **28** (1997), 117-124.

Materials Science Forum Vols. 294-296 (1999) pp. 361-364

Non-Equilibrium Grain Boundaries in Ultrafine-Grained Materials Processed by Severe Plastic Deformation

R.K. Islamgaliev and R.Z. Valiev

Institute of Physics of Advanced Materials, Ufa State Aviation Technical University, K. Marx 12, Ufa RU-450000, Russia

Keywords: Ultrafine-Grained Materials, Grain Boundaries

Abstract Structure of ultrafine grained materials processed by severe plastic deformation was investigated by TEM, XRD and Raman scattering. Special attention is focused on investigations of diffraction contrast at grain boundaries observed by TEM. Uniform elastic strain distribution with maximum in near grain boundary areas is revealed.

Introduction

Recent studies have shown that severe plastic deformation (SPD) leads to formation of ultrafine-grained (UFG) structure in bulk samples of various metals, alloys and intermetallics [1]. Special methods of mechanical deformation were developed for this purpose such as torsion straining (TS) under high pressure, equal channel angular (ECA) pressing and multiply forging. The SPD technique has a number of advantages as compared to other methods for processing of UFG metals, namely, condensation in inert atmosphere or ball milling. In particular, SPD enables fabrication of bulk samples free of residual porosity and impurities which can be successfully used for thorough investigations of achieved properties, including mechanical testing and forming. In addition, the SPD procedure can be applied for formation of nanostructures in various metallic materials using both starting monolithic ingots and powders. Moreover, many of the processed materials have extraordinary properties due to their unusual structure associated with both a small grain size less than 100 nm and non-equilibrium grain boundaries (GB) having long stress fields.
The aim of this work is to reveal the features of the GB defect structure in order to develop a structural model of UFG materials processed by SPD. Special attention is focused on investigation of internal stresses and elastic strain distribution at GBs testifying the presence of high density of the GB dislocations and disclinations.

Experimental

Pure Cu (99,98%), Ni (99,98), Ge and Si were used for investigations. Processing of UFG structures was performed by TS under high pressure and ECA pressing [1]. The structure of UFG samples was examined by JEM-2000EX, JEM-200CX and JEM-100B transmission electron microscopes. X-ray diffraction (XRD) studies were carried out with Hilger and XRD7 (Seifert-FPM) powder diffractometers. Raman scattering were performed at room temperature in backscattering geometry. The spectra were excited by the 532 nm line of Nd-ion laser and 488 line of Ar-ion laser.

Results and Discussion

SPD leads to formation of UFG structure in different materials, where an attained grain size and a level of elastic strains depend on scheme of deformation, processing regimes and phase compositions of materials [1]. Usually the TS under high pressure results in formation of a mean grain size of 20-150 nm, while ECA pressing provides a grain size of 200-300 nm. Typical micrograph of UFG Cu processed by ECA pressing (Fig.1) contains rather homogeneous and equi-axed structure. Data of the direct estimation of grain misorientation parameters show a significant fraction of high angle grain boundaries in the structure of samples [2].

XRD analysis shows that lattice parameters determined for UFG samples (Table) agree well in all cases with the value for coarse-grained samples given in ICDD PDF-2 database. A significant decrease of the intensity of the peaks and their broadening due to a very small grain size and a high level of internal elastic strains are the features of the XRD pattern for the as-prepared samples (Fig.2). A mean grain size and a value of elastic strains determined by the Williamson-Hall method for some UFG materials are presented in Table. Significant anisotropy of line broadening of the type $\beta_{hhh} < \beta_{h00}$ for as-deformed Cu sample was noticed . Therefore, the evaluation should be done separately from two pairs of peaks 111-222 and 200-400. By using the measurement with Cu radiation the following values were found : hhh: e = 0.04%, D = 71 nm, h00: e = 0.08%, D = 50 nm.

Table. Lattice parameters, strains, a mean grain size for some UFG materials.

Material	a (nm)	ε (%)	d (nm)		
			TEM	XRD	Raman scattering
Cu	0,36149(4)	0,06	107	50	-
Ni	0,3523(1)	0,15	114	81	-
Ge	0,5657(1)	0,7	24	10,4	9,0
Si	0,5429(1)	0,55	17	7	5,5

The Raman spectra of the single Ge and Si crystals have revealed the symmetrical profiles with a maximum at 301 cm^{-1} and 521 cm-1, respectively [3]. An increase of the full width at half maximum (FWHM), a decrease of the peak intensity, as well as their asymmetry and shift to lower frequencies are observed for the as-prepared samples. For example, the values of FWHM were equal to 14.0 cm^{-1} and 14.2 cm^{-1} for NC Ge and Si. In addition, a peak shift of 2.0 cm^{-1} and 2.5 cm^{-1} for NC Ge and Si was revealed as well.

According to model [4], a better fit of the calculated peak to the experimental data is observed for a mean crystallite size 9 nm and 5.5 nm for NC Ge and Si, respectively. However, there exist extra intensities in the measured spectra. Similar additional peaks were revealed also in NC samples of Ge and Si [5] processed by other techniques, where they were attributed to the GB defect structure. At the same time, a significant distinction of a mean grain size determined by various techniques: TEM, XRD and Raman scattering (Table) is observed. One can note the following possible reasons resulting in mentioned difference: the presence of subgrains; the difference of character of grain size averaging; specific features of different methods allowing to determine a size of various grain areas: TEM determines a size of whole grain including both a grain interior and the GB defect structure, while XRD and Raman scattering allow to calculate a size of a grain interior with perfect crystal lattice.

In addition, appearance of a widened diffraction contrast of thickness fringes on images of GBs in the as prepared samples was revealed by TEM in UFG materials processed by SPD. This contrast being a typical feature of non-equilibrium grain boundaries with a higher energy and long-range stresses was observed in different UFG materials [1]. In order to determine an elastic strain distribution at GBs a

method based on the study of the thickness fringes width dependence on a tilt of goniometer was developed [6]. This method is based on the analysis of additional scattering of electron beam on elastically distorted crystal lattice near GBs. The presence of high elastic strains in UFG materials processed by SPD lead to widening of thickness fringes on the images of GBs. At the same time, the dependence of the thickness fringes width on the goniometer tilt has as a rule three stages: the increase of a visible contour width with increasing of the goniometer tilt, its constant value and its consequent decrease. With that, the second stage is typical for images of thickness fringes in UFG materials processed by SPD (Fig.3). This circumstance is favorable in order to determine a value of elastic strains for separate thickness fringes using the following equation:

$$\varepsilon = \frac{\Delta\varphi \sin\beta}{2}$$

where: ε - a value of elastic strains for planes of crystal lattice corresponding to vector of reciprocal lattice **g**; $\Delta\varphi$ - the interval of goniometer angles (in radians) with constant thickness fringes width (Fig.3); β - an angle between a direction of **g** and a projection of goniometer tilt axis (Fig.3b).

This approach used for investigation of a grain presented on Fig.3a revealed uniform elastic strain distribution near GBs. It was shown, that elastic strains in UFG Cu processed by ECA pressing has a maximum in near GB area on the distance from GB about 10 nm (Fig.4). Moreover, the value of maximum was found 5 times higher than a mean value determined by XRD analysis of peak broadening (Fig.2) (Table) [7].

The obtained results are important for development of a structural model of UFG materials processed by SPD [8]. The given model is based on the concept of non-equilibrium GBs containing high density of extrinsic GB dislocations and partial disclinations. Dislocations and disclinations create fields of long range elastic stress. These fields near GBs and triple junctions are responsible for elevated energy and dilatation of crystal lattice. With that, high internal stresses lead to formation of elastically distorted regions of a crystal lattice near GBs. A decrease in a mean grain size to 10-20 nm results in elastic distortions of crystal lattice in the whole grain.

Concluding remarks

Different techniques show that the structure of UFG materials processed by severe plastic deformation is characterized by both a small grain size and high elastic strains originated from defect grain boundaries. The investigations of diffraction contrast at grain boundaries for ultrafine grains indicate uniform elastic strain distribution in near grain boundary areas due to excess density of grain boundary dislocations. Such non-equilibrium grain boundaries are responsible obviously for unusual mechanical behavior of UFG metals, namely: high strength, unusual fatigue behavior, low temperature and high strain rate superplasticity which was demonstrated recently in some UFG materials processed by SPD [1].

References

1. R.Z.Valiev, I.V.Alexandrov, R.K.Islamgaliev, NATO ASI. Series V.50 (1997), p.121.
2. O.V.Mishin, V.Yu.Gertsman, R.Z.Valiev, G.Gottstein, Scripta Mater. 35 (1996), p.873.
3. R.K.Islamgaliev, R.Kuzel, E.D.Obraztsova, J.Burianek, F.Chmelik, R.Z.Valiev, Mat.Sci.Eng. A249 (1998), p.152.
4. I.H.Campbell, P.M.Fauchet, Solid Stat Commun. 58 (1986), p.739.
5. E.D.Obraztsova, NATO ASI. Series E. 260 (1994), p.483.
6. R.K.Islamgaliev, R.Z.Valiev, Solid State Physics 37 (1995), p.3597.
7. R.K.Islamgaliev, F.Chmelik, R.Kuzel, Mat.Sci.Eng. A237 (1997), p.43.
8. R.Z.Valiev, Nanostructured Materials 6 (1995), p.73.

Figure 1. Typical microstructure of UFG Cu processed by ECA pressing.

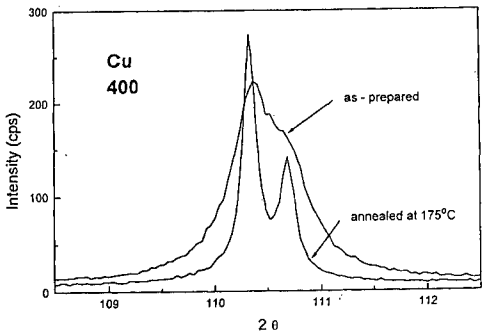

Figure 2. Comparison of XRD profiles of the 400 dif-fraction line for UFG Cu and for the sample annealed at 175°C.

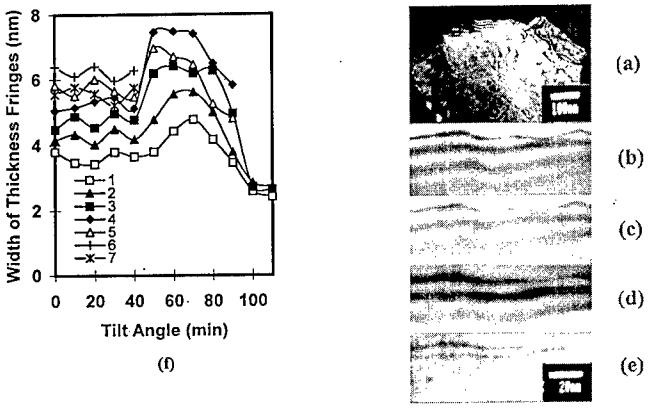

Figure 3. The dependence of the thickness fringes width on a grain tilt: (a) dark field image of a grain in the spot (111); (b), (c), (d), (e) micrographs illustrated the dependence of the thickness fringes width on a goniometer tilt 30, 50, 80, 100 min (f) - the dependence of thickness fringes width on a grain tilt, where (1-7) - numbers of contours.

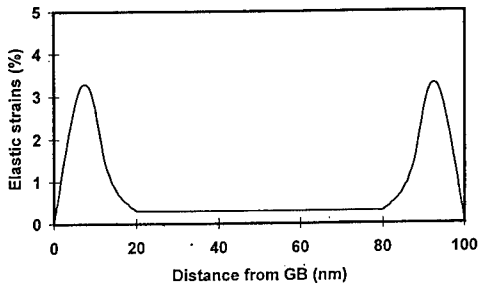

Figure 4. Elastic strain distribution in ultrafine grain.

Materials Science Forum Vols. 294-296 (1999) pp. 365-368

Structural Characteristics of Twin Boundaries in Deformed Polycrystalline Zirconium

Ph. Komninou[1], G. Nouet[2], Th. Kehagias[1], A. Serra[3] and Th. Karakostas[1]

[1] Department of Physics, Aristotle University, GR-54006 Thessaloniki, Greece

[2] LERMAT, UPRESA-CNRS 6004, 6 Boulevard du Maréchal Juin, F-14050 Caen Cedex, France

[3] Department de Matematica Aplicada III, Universitat Politecnica de Catalunya, ETSE Camins, Jordi Girona Salgado 31, E-08034 Barcelona, Spain

Keywords: Deformation Twin, Twinning Dislocation, Zirconium, HREM

Abstract

Deformation twins in thin foils of deformed polycrystalline α-Zr are observed along $[1\bar{2}10]$ viewing direction, by High Resolution Electron Microscopy (HREM). The elements of the twinning mode are $K_1=(10\bar{1}2)$ and $\eta_1=[10\bar{1}\bar{1}]$. The interface consists of steps separating perfect and defected segments. The perfect areas present a corrugated structure of the boundary plane, while the defected areas have dislocation character associated with steps of various heights. The shorter step corresponds to the so-called $b_{2/2}$ twinning dislocation. Computed models of the relaxed structures of both, the perfect boundary and the $b_{2/2}$ twinning dislocation, are constructed using many-body potential calculations based on two different potentials. The resulting atomic positions are utilised for simulations of the HREM images. These images are compared with the experimental ones. The results show that one of the potentials used leads to a better image matching for the observed perfect twin boundary.

Introduction

The study of the atomistic structure of the twin interfaces in hexagonal close packed metals (hcp) is an important issue for the understanding of the deformation mechanism of these materials [1,2]. Deformation twins grow by the motion of twinning dislocations along the twin-matrix interface, associated with steps of various heights. The Burgers vectors and the corresponding steps can be predicted by topological theory and circuit mapping method, using as reference space the dichromatic complex [3]. The atomistic relaxed structures of the perfect twin boundaries and the twinning dislocations can be calculated by computer simulation using either many-body interatomic potentials or pair potentials [4-7]. There are recent experimental results on the atomic structure of twin boundaries and their defect content in Zn and α-Ti [8, 9].

In this work, we present HREM observations of the $(10\bar{1}2)$ twin boundary in thin foils of deformed bulk polycrystalline α-Zr. We present an interface without defects and one containing a $b_{2/2}$ dislocation in end-on orientation. We also give results of theoretical investigations of these twin structures using two many-body interatomic potentials of the Finnis-Sinclair form suggested for Zr. The relaxed models deduced from these calculations are used to produce simulated HREM images for comparison with the experimental ones.

Experimental

Thin foils of polycrystalline Zr were annealed for 1 h at 750° C in vacuum at 2×10^{-3} Pa, followed by cold rolling at room temperature. The latter process resulted in a thickness reduction of 10%. Specimens for HREM observations were prepared by electropolishing at 12 V and -40° C, using a solution of 10% Perchloric acid in Methanol. Prior to the introduction of the specimens into the microscope, ion-beam thinning was performed for a few minutes in order to remove the thin oxide

layer of the free surfaces. The observations were performed in a Topcon 002B electron microscope, operating at 200 kV with a point to point resolution of 0.18 nm and Cs = 0.4 mm.

Results

The HREM images of the perfect and the defected boundaries, observed along [$1\bar{2}10$], are shown in Figs .1a and 2a respectively. In the boundary plane of Fig.1a no strain induced contrast is observed, since it does not present any defected structure. For the imaging conditions pertaining, the dark dots in the image correspond to columns of atomic sites. A careful observation of this image leads to the conclusion that the atomic columns do not have a mirror symmetry on the boundary but they are arranged on a corrugate surface. The same type of boundary appears in Fig. 2b, where two corrugated planes separate the disturbed area, that is a characteristic configuration of a dislocation core associated with a step. The step height equals to $2d_{(10\bar{1}2)}$, where $d_{(10\bar{1}2)}$ is the interplanar spacing of the ($10\bar{1}2$) planes and thus the dislocation is a $\mathbf{b}_{2/2}$. For the determination of its Burgers vector, a closed circuit SABCDEF is constructed around the defect and is used for mapping into the reference space [10]. For Zr, at room temperature and c/a= 1.593, this is determined to be $\mathbf{b} = 0.0835\ [\bar{1}011]$.

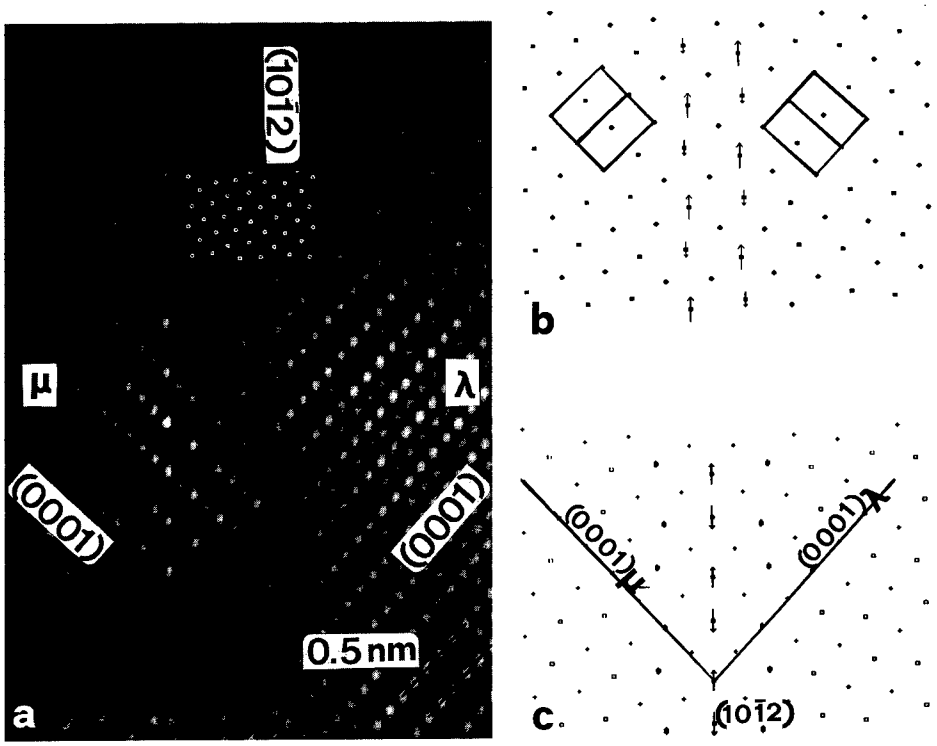

Figure 1. a) Experimental HREM micrograph of a ($10\bar{1}2$) twin boundary in polycrystalline α-Zr viewed along [$1\bar{2}10$]. In the inset, the simulated HREM image is superimposed on the experimental depicting the good matching between them. The defocus is -79nm, the specimen thickness is 6.5nm and the columns of the atomic sites are dark as it is defined from the overprinted atomic positions. b,c) relaxed atomic arrangement of the ($10\bar{1}2$) twin boundary in Zr projected along [$1\bar{2}10$] derived by the Igarashi and the Ackland potential respectively. The vertical arrows show the sign and magnitude of the hydrostatic component of stress **p** and mean (↑) tension and (↓) compression.

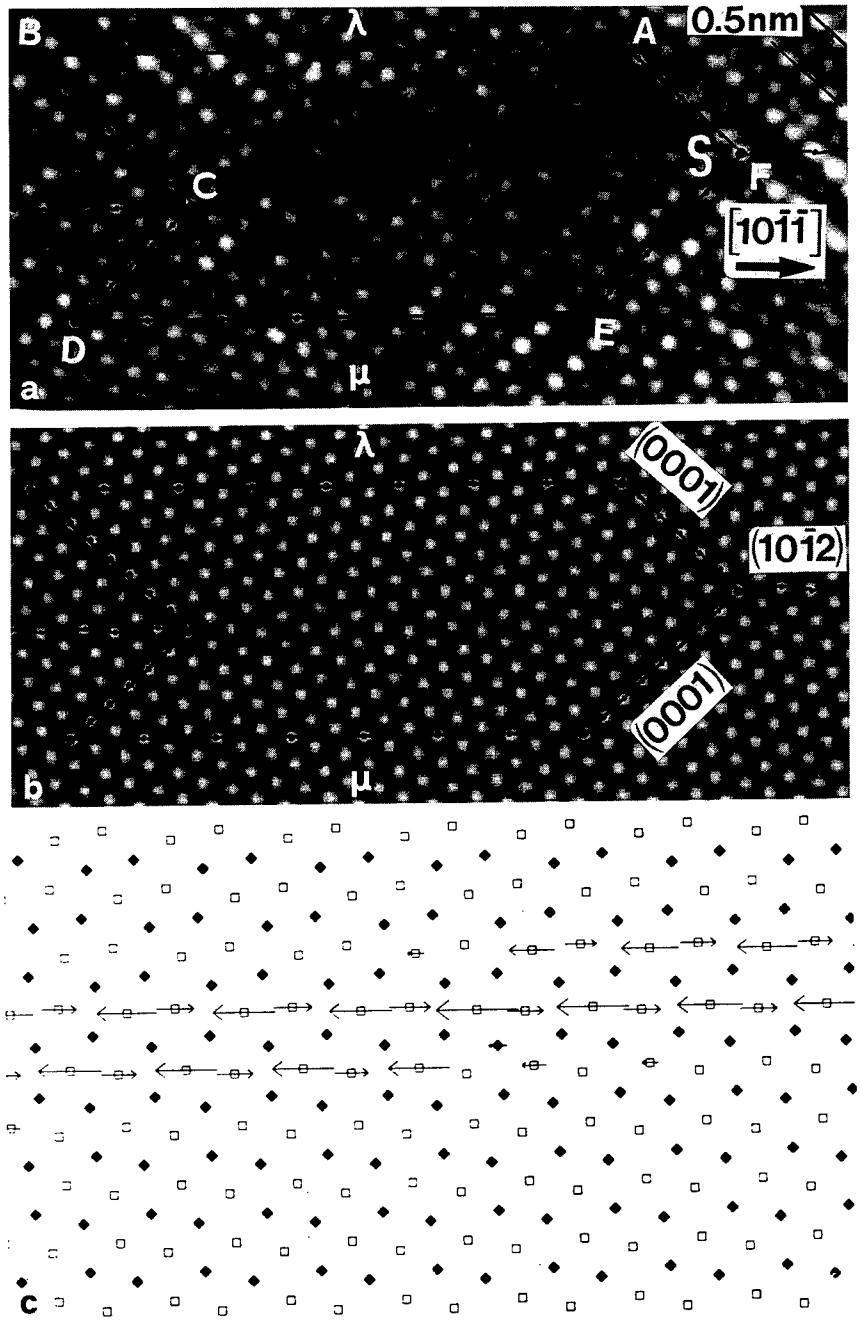

Figure 2. a) Experimental HREM micrograph of a twinning dislocation in a (10$\bar{1}$2) twin boundary in polycrystalline Zr, viewed along [1$\bar{2}$10]. The step height associated to the defect equals to $2d_{(10\bar{1}2)}$, where $d_{(10\bar{1}2)}$ is the spacing of the (10$\bar{1}$2) planes. A closed circuit SABCDEF is constructed around the defect. b) Simulated HREM image of the twinning dislocation. The defocus is -39nm, the specimen is thickness 5.2nm and the atomic columns are white. c) Relaxed model associated with a twinning dislocation derived by the Igarashi potential. The atomic positions of this computational cell were used for the image simulation in (b).

In order to simulate these interfacial structures a theoretical investigation has been undertaken and is summarised in the following: For the study of the perfect boundary plane a crystal with periodic boundary conditions along the two directions parallel to the boundary and fixed outer region in the direction normal to the boundary, containing about 300 atoms, has been relaxed by the method of conjugate gradients. The $b_{2/2}$ twin dislocation has been simulated in a crystal containing about 1500 atoms with periodic boundary conditions along $[1\bar{2}10]$ direction and fixed boundaries in the other two directions. The $(10\bar{1}2)$ twin boundary has two stable configurations related by a shift along the $[10\bar{1}\bar{1}]$ direction. The relaxed models from these many-body interatomic potential calculations are illustrated in Fig. 1b,c. They have comparable energies and a small energy barrier between them. The difference in energies is potential dependent. Thus, the Igarashi et al. [11]potential gives the corrugated boundary plane as the most stable, Fig. 1b, whereas the Ackland potential gives the 'flat' one, Fig. 1c. In real hcp metals both boundaries could coexist because the core of the $b_{2/2}$ twin dislocation, which is spread along the interface, adopts the form of the second stable configuration, i.e. for Zr, the Igarashi potential reproduces a corrugated boundary with a $b_{2/2}$ dislocation with a flat surface as core. For the Ackland potential the boundary is flat and the core of the $b_{2/2}$ is corrugated. Fig 2c is an example showing the configuration received from the Igarashi potential. It is clear that the width of the core and easy movement of the dislocation depends on the difference in energies for the two configurations and the barrier between them, recpectively.
The atomic positions taken from the computational cells of Figs. 1b,c, 2c were used to simulate the HREM images by the EMS software package [12]. Comparison between the experimental and the simulated images leads to the conclusion that the relaxed boundary structure derived from the Igarashi potential gives a better fitting with the experimental perfect twin boundary image, as it is deduced from Fig. 1a where, in the inset, the corresponding simulated image is superimposed on the experimental. The same result is derived for the perfect parts of the defected boundary of Fig. 2a. In the area of the dislocation core the condition is not clear. In the experimental image, Fig. 2a, the core does not look to be a flat surface, while in the model, Fig. 2c, does. The simulated HREM image of Fig. 2b, that was created from the computational cell of the relaxed $b_{2/2}$ model using the Igarashi potential, Fig. 2c, corresponds with the experimental HREM image of Fig. 2a, only in the perfect areas of the twin.

Acknowledgment
This work is supported by the Greek Secretariat of Research and Technology program PENED 94-1504.

References

1. J.W. Christian and S. Mahajan, *Prog. in Mat. Sci.*, **39** (1995) 1-157
2. R.C. Pond, D.J. Bacon, A. Serra and A.P. Sutton, *Metall. Trans. A*, **22**, (1991) 1185
3. R. C. Pond, *Dislocation in Solids*, Vol. **8**, ed. F.R.N. Nabarro (Amsterdam; North-Holland) (1989) 1.
4. A. Serra, D.J. Bacon, *Phil. Mag. A*, **54** (1986) 793
5. A. Serra, R.C. Pond and D.J. Bacon, *Acta metall. matter*. Vol **39** (1991) 1469-1480
6. A. Serra and D.J. Bacon, *Mat. Sci. Forum*, Vols **126-128** (1993) 69-72
7. S.Hagege, M.Mori and Y.Ishida, *J. Physique* **51**, *Colloque C1*, suppl. no.1 (1990) C1-161
8. T Braisaz, P. Ruterana, G. Nouet and R.C. Pond, *Phil. Mag. A*, **75** No 4 (1997) 1075
9. T. Braisaz, P. Ruterana, G. Nouet, A. Serra, Ph. Komninou, Th. Kehagias and Th. Karakostas, *Phil. Mag. Lett.*, **74** No 5 (1996) 331.
10. R.C. Pond, *Interface Sci.*, **2** (1995) 299
11. M. Igarashi, M. Khantha and V. Vitek, Phil. Mag. A, 63 (1993) 603
12. P.A. Stadelmann, *Ultramicroscopy*, **21** (1987) 131

Materials Science Forum Vols. 294-296 (1999) pp. 369-372

Shape Changes of Nanosized Liquid Pb Inclusions in Al at Elevated Temperatures

L. Kjeldgaard and E. Johnson

Ørsted Laboratory, Niels Bohr Institute, University of Copenhagen,
Universitetsparken 5, DK-2100 Copenhagen Ø, Denmark

Keywords: Nanosized Inclusions, TEM

Abstract

We present transmission electron microscopy (TEM) results from an experimental study of the morphological changes of liquid Pb and (Pb,Bi) inclusions embedded in an Al matrix. Such inclusions are insoluble up to the bulk melting point of aluminium. We use rapidly solidified samples which gives inclusion sizes in the range from 20 to 250 nm. The experiments consist of heating cycles of the liquid inclusions from the melting point of around 600 K up to around 800 K and back to their solidification. The solid Pb and (Pb,Bi) inclusions are topotactically aligned with the Al matrix, with an incoherent boundary. The shape is a cuboctahedron with hexagonal {111} facets and square {100} facets. We have found a hysteresis in the morphology of the liquid inclusions. Immediately after melting the (100) planes bulge outwards and become rounded whereas the (111) planes remain flat until the temperature reaches 750–800 K where the inclusions rapidly become spherical. During subsequent cooling the inclusions were retained their spherical shape until solidification. Since atomic and vacancy mobility is high at all temperatures above the melting point we suggest that diffusion cannot be rate controlling. The experiments were made with inclusion and host material of various purities to test the possibility that the presence of impurities in the interfaces was rate controlling.

Introduction

The study of solids can be divided into several fields. At one end of the size scale there is what is now known as cluster physics. At the other end of the size scale we find what people in general connect with materials science – the study of bulk materials. In between these two size scales we have nanosized clusters embedded in a bulk material, the so-called inclusions. These inclusions do not behave quite like free clusters in the form of large precipitates, but they are also too small to behave as the bulk material.

The lead inclusions have in their solid state the shape of a cuboctahedron, where the square faces are the {100} facets and the hexagonal faces are the {111} facets. In our study of the morphological changes of liquid Pb and (Pb,Bi) inclusions embedded in an Al matrix we found that above the melting temperature the {100} facets become round, but the {111} faces remain flat for inclusions larger than a critical size: 40–50 nm, until the temperature reaches a size dependent critical temperature around 750–800 K, where the inclusions become almost spherical. Inclusions below the critical size become spherical directly upon melting. During subsequent cooling the inclusions retain their spherical shape until solidification.

These experimental results raises two important questions:

A. Which of the two observed shapes is the equilibrium shape?

B. What causes the observed hysteresis in the shape of the inclusions?

One might well be able to assume that the answer to **A** brings about the answer to **B**.
The hypothesis that we tested is inspired by the work by Cheng and Wynblatt [1]: the hysteresis might be impurity induced. This would also explain why the inclusions have to be above a critical size r_c in order for the hysteresis to be present: There simply are not enough impurities in the smaller inclusions to inhibit the transition from faceted to round. In that case, the round shape would be the equilibrium shape for all sizes and all temperatures above the melting temperature.
We tested this hypothesis by investigating the behaviour of lead inclusions of a variety of purities ranging from 99.9% pure to 99.9999% pure in matrices of similar purities, and for inclusions of lead with 10 atomic per cent bismuth (effectively 90% pure lead).

Sample Treatment and Experimental Procedures

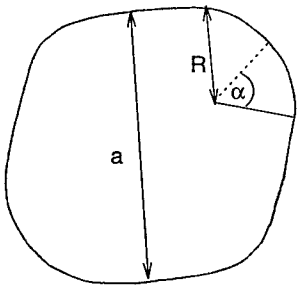

Figure 1: The outline of an inclusion seen from the {110} direction. The measured parameters are the distance between opposite {111} faces a, the radius of curvature of the rounded {100} faces R, and the semi-opening angle α.

Using the Al-Pb system has several advantages: For the concentrations of lead that we use (0.5 or 0.65 atomic per cent) Al and Pb are virtually non-mixing up to the bulk melting point of aluminium. Also, Pb is much better than Al at scattering electrons, so image contrast in a transmission electron microscope (TEM) is maximal. And finally, Pb melts more than 300 degrees below Al, which gives ample opportunity to study the properties of liquid lead in situ.
All samples used were made in France by S. Hagége et al. from rapidly solidified melt spun material. The samples are three mm diameter disks punched out from thin ribbons. The discs were electropolished to perforation, with the edge of the holes thin enough to be electron transparent.
Three samples with different levels of purities for the inclusions and host material alike and one sample of effectively 90% pure lead (10% Bi in the lead) in 99.999% pure aluminium were prepared:

i. Al with 0.5 atomic per cent Pb 99.9999% pure.

ii. Al with 0.65 atomic per cent Pb 99.999% pure.

iii. Al with 0.5 atomic per cent Pb 99.9% pure.

iv. Al with 0.65 atomic per cent Pb and 0.06 atomic per cent Bi.

For the experiments a Phillips CM 20 electron microscope with a single tilt heating holder and a JEOL CX 200 electron microscope with a double tilt Gatan heating holder were used. The inclusions were always studied and photographed from the {110} direction, where two pairs of {111} facets and one pair of {100} facets are seen edge on. The edge on view means that the inclusions are sharply defined and that changes in the shape of the inclusions like bulging can be noticed immediately.
The experiments consist of heating the liquid inclusions from their melting point at around 625 K up to around 800 K and cooling them down to their point of solidification at 550 K.
The first picture was taken of the still solid inclusions a couple of degrees below the bulk melting point (T_m = 600 K for lead). The temperature was then increased 10 or 15 K and kept there for

5-10 minutes to let the sample equilibrate and the microscope stabilise before the next picture was taken. This was repeated until the inclusions became round at about 750–800 K. After the inclusions had become round, the temperature was decreased and pictures taken in steps of 15–20 K.

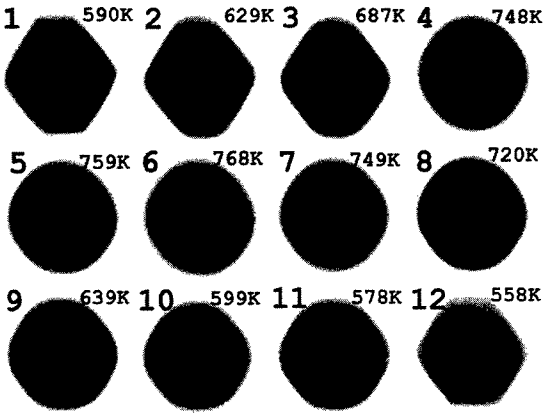

Figure 2: A heating cycle. The figure is read left to right, top to bottom, as indicated with the numbers top left of each image. Top right of the images the temperature is shown.

The parameters measured were the radius of curvature and the distance between opposite {111} facets as shown in Fig.1.

Results

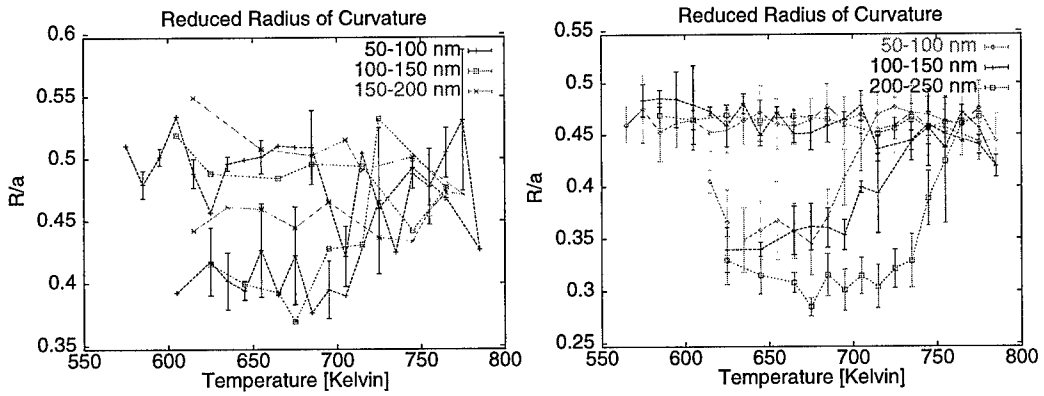

Figure 3: Left: 99.9999% pure Al–Pb alloy. The 50–100 nm bin contains 5 inclusions, the 100–150 nm bin 1, and the 150–200 nm bin 1. Right: 99.999% pure Al–Pb alloy. The bins are 50–100 nm (14), 100–150 nm (2), and 200–250 nm (3)

.

The figures display the evolution of the radius of curvature of the inclusions during a heating cycle. An example of such a heating cycle is given in Fig. 2. As we can see, the radii of the inclusions are low before the rounding temperature has been reached (about one third of the size of the inclusions) and gets larger (up to half the size of the inclusions) when the rounding

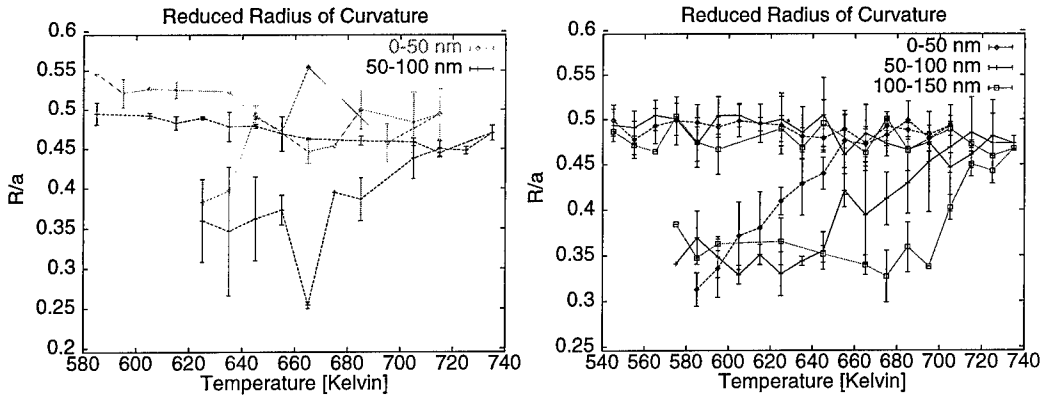

Figure 4: Left: 99.9% pure Al–Pb alloy. The bins are 0–50 nm (5) and 50–100 nm (11). Right: Al–(Pb,Bi) alloy. The bins are 0–50 nm (9), 50–100 nm (18), and 100–150 nm (6).

temperature is passed, and during cooling. The radius of curvature graphs shown in Figs. 3 and 4 are read from the bottom left to top right and back to the top left, and show the evolution of the radius of curvture in units of the size of the inclusions during the heating cycles.

Discussion

In the more impure samples the grain sizes were markedly smaller both for the matrix and for the precipitates. This effect of impurities can be seen as evidence of heterogeneous solidification as opposed to the conjectured homogeneous solidification by Gråbæk and Bohr[2]. Also Cantor and co-workers have found evidence of heterogeneous solidification[5].

We have recorded a hysteresis effect in all the experiments made with inclusions larger than 50 nm, independently of the purity of the samples. But the *size* of the hysteresis is conditional to the impurity content of the samples. Looking closely at the results in Figs. 3 and 4, we see that the hysteresis ranges from 0.4 to 0.5 for the very pure samples and from 0.35 to 0.5 for the "dirty" samples.

We can conclude that the higher the impurity content in the inclusions, the larger the hysteresis. So, impurities have a limiting influence, but since we do observe a hysteresis even for the very pure particles, the hysteresis cannot be due to impurities alone.

References

[1] W.-C. Cheng and P. Wynblatt, *Coupled compositional and roughening phase transitions at the surface of a Pb–Bi–Ni alloy*, Surface Science, 302 (1994), pp. 185–191.

[2] L. Gråbæk and J. Bohr, *Melting, growth, and faceting of lead precipitates in aluminum*, Physical review B, 45 (1992), pp. 2628–2637.

[3] J. C. Heyraud and J. J. Métois, *Equilibrium shape and temperature: Lead on graphite*, Surface Science, 128 (1983), pp. 334–342.

[4] L. Kjeldgaard, *Investigation of the Morphological Changes of Microscopic Liquid Pb Inclusions in an Aluminium Matrix*, PhD thesis, Ørsted Laboratory, Copenhagen University, June 1998.

[5] K. I. Moore, D. L. Zhang, and B. Cantor, *Solidification of Pb particles embedded in Al*, Acta Metallic Materials, 38 (1990), pp. 1327–1342.

Materials Science Forum Vols. 294-296 (1999) pp. 373-376

Grain Boundaries and Propagation of Slip Bands

J. Gemperlová[1], A. Jacques[2], M. Polcarová[1], J. Brádler[1], V. Novák[1] and A. George[2]

[1] Institute of Physics AS CR, Na Slovance 2, CZ-18221 Praha 8, Czech Republic

[2] Laboratoire des Physique des Matériaux, Unité associée du CNRS 155, Ecole des Mines, parc de Saurupt, F-54042 Nancy, France

Keywords: Bicrystals, Grain Boundaries, Dislocations

Abstract. Deformation experiments were performed on three different Fe-4at%Si bicrystals. Synchrotron radiation topography *in situ* and *post mortem* was used to investigate the influence of grain boundaries (GB) on slip transmission and to study the interaction of slip dislocations with the GB. It was found that the GB forms a strong barrier in all cases and the slip transfer cannot be fully explained by geometric relations of Burgers vectors and slip planes in the two grains. To explain the results of experiments the internal stresses near the GB due to accumulated slip dislocations produced in one grain and stopped at the GB and image forces due to the grain boundary were calculated. The structure of GB has been studied by conventional TEM.

Introduction

Grain boundaries significantly affect various properties of materials as their atomic structure and chemical composition differ from those of a regular lattice. They influence the plastic deformation by restraining slip dislocations from transmission and/or by activation of slip systems in the neighborhood of the GB different of those observed inside the grains. Among high angle GBs low Σ coincidence boundaries are an important group. In a polycrystal their frequency may attain up to 30% [1]. Three types of bicrystals with grain misorientation $\Sigma3$, $\Sigma9$ and $\Sigma15$ were studied. The directions of Burgers vectors (BVs) and of slip planes are parallel in both grains of a $\Sigma3$ bicrystal, this is the case of easy slip transfer. In $\Sigma9$ bicrystals the slip planes have a common intersection line with the GB, the BVs are not parallel and the slip propagation is therefore more difficult. There is no common intersection line of slip planes and the GB in $\Sigma15$ bicrystal and the slip propagation is difficult even from the geometric point of view. To study the pure effect of GB not affected by differences in macroscopic resolved shear stresses in both grains, the bicrystal should be oriented for single slip with the same Schmid factors in both grains. The direction of loading axis was parallel to the GB. The experiments have been confined to the cases of zero additional stresses due to plastic and elastic incompatibilities [2], which may affect the transmission of slip bands.

In Fe-4at%Si the macroscopic slip planes are not necessarily crystallographic planes. They are determined by the $\psi(\chi)$ curves [3] which depend on the temperature and deformation type (tension or compression). At room temperature they are essentially planes of maximum resolved shear stress (MRSS) and differ from them only by few degrees. Dislocations are not dissociated except for a slight core extension, which is responsible for a low mobility of screw segments [4].

The X-ray topographic techniques were used to study the propagation of slip bands across the GB, as they are very sensitive to small lattice distortions [5,6].

Experiments

The specimens observed *post mortem* were deformed by compression in the Instron machine. Those followed *in situ* were deformed by tension or by compression in a deformation stage designed to fit the goniometer at the synchrotron radiation (SR) source. Successive stages of slip band development were recorded in dependence on the applied stress to find out the strength of the barrier for the slip transmission across the GB. White beam and monochromatic synchrotron radiation topography was applied to observe whole specimens for both *in situ* and *post mortem* experiments. The experimental details of deformation by tension are presented in [7,8] and those of deformation by compression in this proceeding [9]. The choice of orientations was limited by requirements on the deformation axis and on suitable reflections. The geometric orientations of specimens are summarised in the table below.

type of bicrystal	axis/angle of rotation	GB plane	inspected surface	tensile axis	primary slip system
Σ3	[110]/70.5°	$(\bar{1}1\bar{2})_A / (1\bar{1}\bar{2})_B$	$(20\bar{1})_A / (201)_B$	$[152]_A / [15\bar{2}]_B$	$[111]_A / (110)_A$
Σ9	[110]/38.9°	$(1\bar{1}4)_A / (\bar{1}14)_B$	$(110)_A / (110)_B$	$[2\bar{2}\bar{1}]_A / [2\bar{2}1]_B$	$[1\bar{1}1]_A / (1\bar{1}\bar{2})_A$
Σ15	[201]/48.2°	$(11\bar{2})_A / (1\bar{1}\bar{2})_B$	$(201)_A / (201)_B$	$[\bar{1}52]_A / [15\bar{2}]_B$	$[111]_A / (\bar{1}10)_A$

Results and discussion

As the specimen state has not changed after the stress relaxation, the results of *in situ* experiments can be compared with those obtained on specimens studied after deformation. The differences in the slip patterns observed in specimens deformed by tension and by compression (narrower slip bands at greater distance from each other, rarely observed fans and groups of slip bands, slip transmission observed more frequently) are discussed in detail in [9]. The results differ from those in fcc or diamond like materials. The GB forms a strong barrier for slip transmission also in the case of the most favourable geometry in the Σ3 bicrystals. For some Σ3 specimens, transmission through the GB of thin slip bands was observed (Figs.1 and 2). Generally, stronger slip bands or groups of them are formed in one grain before extending to the other grain (Figs. 3 and 4). The head of the slip band near the GB was described by a macrodislocation situated at the centre of the group (~ at a distance of 1μm from the GB). The magnitude of its BV was estimated comparing the topographs with the simulated images. It attains a value of 100nm (~ hundreds of unit BV) before the slip band transition occurs. This yields a certain evaluation of the barrier formed by the GB.

The bands behind the GB originate more likely from new dislocation sources than from transmitted dislocations. There are several reasons to explain these observations. In ideal bicrystals (exact coincidence, planar crystallographic boundary) internal stresses due to accumulated slip dislocations stopped at the GB and image forces representing long range interaction between GB and lattice dislocation are present. The GB structure in real bicrystals, moreover, contributes to impede the slip transmission. GB dislocations compensate the deviation from exact coincidence, steps due to the fact that the GB plane is not exactly the crystallographic one and small precipitates may be present at the GB and/or different regimes of deformation further influence the transfer.

The stresses exerted by the slip bands in the first deformed grain were considered together with the applied stress to predict the slip system in the second grain [6]. It has been found that MRSS for the primary slip system predicted by the applied stress remains the highest. This is valid even if the secondary slip system is more favourable from the geometric point of view in the Σ15 bicrystal. MRSS induced in the second grain by a slip band in the grain A as well as the normals of MRSS planes depend on the distance from the boundary. This result explains the bending of slip bands

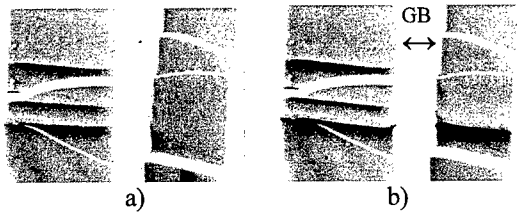

Fig.1. White beam SR topographs of a Σ3 bicrystal before (a) and after (b) GB transmission. Rarely observed easy slip transmission of single slip bands through the GB in a Σ3 bicrystal. The GB slows down the slip

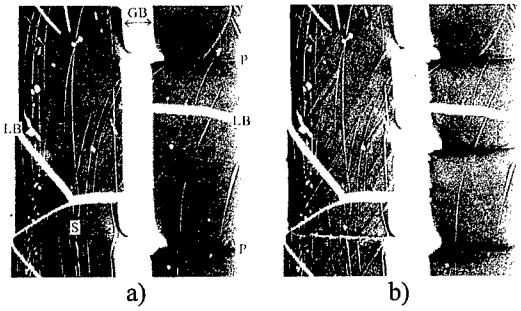

Fig.2. White beam SR topographs of a Σ3 bicrystal. a) The individual slip bands of primary slip system develop in the right grain and stop at the GB, b) The slip continues in the left grain starting from the GB. LB - low angle boundary, P - primary slip system, S - secondary slip system.

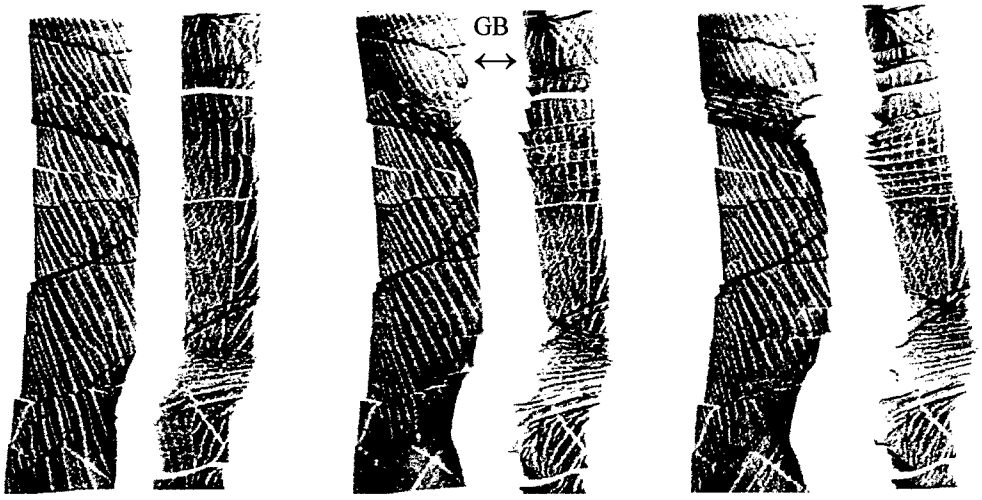

Fig.3. *In situ* white beam SR topographs of a Σ15 bicrystal. Slip band development during compression deformation at the stress levels 133MPa, 155MPa and 158MPa, respectively.

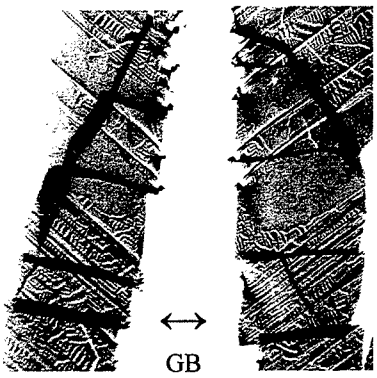

Fig.4. White beam SR topographs of a Σ9 bicrystal deformed by compression. Strong slip bands and groups of them developed and slip transfer through the GB occurred.

near the grain boundary in *bcc* metals.

The image forces are probably the most important for slowing down the dislocation motion when the dislocations are approaching the GB (Fig.1). They occur in bicrystals when elastic anisotropy is taken into account. The effect has been treated theoretically [10,11]. For Σ3, Σ9 and Σ15 bicrystals the primary dislocations are repulsed from the GB, the forces at a distance of 1μm have values 106.7E4Nm^{-1}, 16.8E4Nm^{-1} and 70.2E4Nm^{-1}, respectively [7]. They are comparable with the other driving or frictional forces. The image force has the highest value for the Σ3 bicrystal where easy transfer is expected. It compensates the external stress at a distance 4nm (~ 16 BVs).

When an interruption during the deformation occurs, the applied force is kept constant, the stress decreases and the material relaxes. We expect that the dislocations near the GB rearrange, the fans are produced (they may be very small), the stress spreads along the GB and at any spot is not high enough to initiate the slip transfer. High local stresses are important for the slip propagation. It is necessary to increase the applied force to continue the deformation.

To elucidate the influence of GB structure on impeding the slip bands at the GB, the grain boundary dislocation (GBD) structures were studied by TEM in bicrystals Σ3 (112)[110], 70.53° previously used for deformation experiments [12,13]. The misorientation angle and axis were measured in the area of observation by an improved Kikuchi line technique [14]. The additional deviation from exact coincidence was compensated by a honeycomb network, one side of which is formed by a rather dense system of parallel dislocations having the dislocation lines almost parallel to the tilt axis in all investigated cases. Contrast experiments in various reflections with generally only one-grain reflecting strongly indicated that these dislocations are edge. The BVs of other two sides were determined using simple dislocation contrast criteria and the node condition (the sum of BVs meeting at the node is zero). The structure of GBD network and the density of dislocations may change significantly along a GB. The TEM observations confirm that the local structure of the GB, especially the high density of GBDs, may be the cause of the impeding slip dislocations.

The authors acknowledge the financial supports of GA of ASCR (the grant contract No. A1010702), GA of CR (the grant contract No. 202/98/1281) and PICS (No 477). The authors are grateful to J. Baruchel from ESRF Grenoble for his help during the experiments.

References

[1] T. Watanabe, J. de Physique 49 (1988), C5-507.
[2] J. Gemperlová, V. Paidar and F. Kroupa, Czech. J. Phys. B 39 (1989), 427.
[3] B. Šesták and J. Blahovec, Phys. Stat. sol. 40 (1970), 599.
[4] V. Vitek, Cryst. Lattice Defects 5 (1974),1.
[5] M. Polcarová and J. Brádler, J. appl. Crystallogr. 21 (1988), 169.
[6] J. Gemperlová, M. Polcarová and J. Brádler, J. appl. Crystallogr. 24 (1991), 316, 324, 331.
[7] M. Polcarová, J. Gemperlová, J. Brádler, A. Jacques, A. Georges and L. Priester, Phil. Mag. A 78 (1998), 105.
[8] A. Jacques, A. George, S.G. Roberts, M. Polcarová, J. Brádler and J. Gemperlová, Interface Science 4 (1997), 339.
[9] M. Polcarová et al, these Proceedings
[10] J. Gemperlová, Phys. Stat. sol. 30 (1968), 261.
[11] M. Condat and H.O.K. Kirchner, Phys. Stat. sol.(b) 144 (1987), 137.
[12] A. Gemperle, T. Vystavěl and J. Gemperlová, Proc. MCEM, High Tatras 1995, 211.
[13] T. Vystavěl, A. Gemperle and J. Gemperlová, Proc. EUREM, Dublin 1996.
[14] A. Gemperle and J. Gemperlová, Ultramicroscopy 60 (1995), 207.

Materials Science Forum Vols. 294-296 (1999) pp. 377-380

Comparison of Tension and Compression Deformation of Fe-Si Bicrystals – X-Ray Topography Observation

M. Polcarová[1], A. Jacques[2], J. Brádler[1], F. Vallino[2], J. Gemperlová[1] and A. George[2]

[1] Institute of Physics AS CR, Na Slovance 2, CZ-18221 Praha 8, Czech Republic

[2] Laboratoire des Physique des Matériaux, UMR CNRS 7556, Ecole des Mines, parc de Saurupt, F-54042 Nancy, France

Keywords: Plastic Deformation, Bicrystals, Fe-4at%Si, X-Ray Diffraction Topography

Abstract. Compression deformation experiments were performed on three types of Fe-4at%Si bicrystals with different mutual orientation of Burgers vectors and slip planes in the two grains corresponding to the easy, more difficult and difficult slip transfer. Synchrotron radiation topography *in situ* and *post mortem* were used to investigate the slip transfer. The results were compared with similar experiments made on the same bicrystals deformed by tension. Explanation for the differences in the slip pattern, namely the GB transmission, is suggested.

Introduction

The influence of grain boundaries (GBs) on plastic deformation, namely the interaction of slip dislocations with the GBs, has been studied experimentally and theories explaining the observed effects have been developed (see e.g. [1-3]). Although it is generally accepted that the GBs slow down the slip bands movement, the details of the interaction are not yet fully understood. The experiments described here should contribute to a better understanding of the processes at the GB. They are part of a project involving different materials and modes of plastic deformation, various experimental methods and theoretical treatment of the problem. The present experiments concerning deformation by compression follow those dealing with tension deformation described in a recent paper [4]. Comparison of the results of both deformation modes and an attempt to explain the observed differences are given.

Experiments

All experiments were performed on bicrystals, where the GBs are well defined. The material was Fe-4at%Si. Three types of bicrystals with different mutual orientation of operating slip systems were chosen: $\Sigma 3$ – both Burgers vectors (BVs) and slip planes in the two grains are parallel, the dislocation transmission through the GB should be easiest; $\Sigma 9$ – BVs are not parallel, the intersections of slip planes with the GB are parallel, the dislocation transmission is more difficult; $\Sigma 15$ – neither BVs nor the intersections of slip plane with the GB are parallel, the dislocation transmission is most difficult. In all cases the external force was along equivalent crystallographic directions parallel to the GB, the Schmid factor of the slip systems in both grains was the same. No additional stresses due to the elastic incompatibility were present, therefore the pure effect of the GB could be studied. The specimens (size $3\times3\times10$ mm^3 or $4\times4\times12$ mm^3) were prepared from the same bicrystals as those used for the tension experiments [4]. They were inspected either *in situ*, under the applied stress, or *post mortem*, after the deformation. X-ray diffraction topography was used to investigate the slip pattern. Although the resolving power of this method is only approx. 3 – 5 μm, it is very useful due to its high sensitivity to slight lattice distortion and its capability to

reveal different kinds of crystal defects at the same time. By comparing the experimental images with the simulated ones some parameters characterizing the defects can be determined.
The experiments were performed using the synchrotron radiation at LURE, Orsay, and at ESRF, ID19 station, Grenoble. The bicrystals were not perfect, they contained subgrain low angle boundaries. Therefore white beam or monochromatic beam and rocking the specimen over the range of subgrain misorientation had to be applied. The topographic image was followed using an X-ray sensitive camera and registered on a Kodak SR film or Ilford L4 Nuclear Plates.

Results

Although the topographs were taken using diffracting planes parallel in the two grains the images of the grains are mutually shifted. This is due to a misorientation of the grains (< 3°) additional to that describing the low Σ special GB. The enlarged parts of the topographs shown here are arranged in such a way that the images of adjacent grain regions fit together.

In Fig.1 topographs typical for Σ3 bicrystals deformed by compression are shown. The nearly horizontal black-and-white lines are images of the slip bands. The curved black or white bands and stripes are images of low-angle subgrain boundaries. The irregular black-and-white curved lines are due to the magnetic domains. The steps at the GB are caused by the elastic strain around the heads of slip bands. The origin of the contrast was explained and the images simulated assuming that the dislocations accumulated at the GB can be substituted by a macrodislocation with a multiple Burgers vector [5]. The size of the steps is proportional to $(bl)^{1/2}$, where b is the magnitude of BV and l is the distance of the image from the specimen. By comparing the experimental and simulated images the number of dislocation accumulated at the GB can be estimated.

The Σ3 specimens deformed by compression differ from those deformed by tension in several aspects.

- Slip bands of the primary slip system are mostly straight, well developed and separated from each other. Small groups of few bands can be observed occasionally. Fans and groups similar to those observed in specimens deformed by tension as well as slip bands of the secondary slip system can be seen only exceptionally near the ends of the specimens where the deformation is no more homogeneous.
- Slip transfer over the GB is observed frequently.
- A great variety of the size of the steps at the GB is observed. Large steps giving evidence of a great number of accumulated dislocations can be seen mainly in those cases where the slip bands end and no slip continuation can be seen behind the GB. Little or negligible steps are visible at the spots where the slip is transferred over the GB. It follows that at least part of the dislocations has crossed the GB.
- The dislocation transmission through the GB was confirmed by observation *in situ*. The large step at the head of the slip band at the GB strongly diminished after the slip appeared in the other grain.

In Fig.2 a topograph of a specimen cut from a Σ9 bicrystal is shown. The slip bands are inclined by 54.7° to the GB and perpendicular to the surface. They are straight and narrow. Slip transfer over the GB is observed in several cases only. Comparing with the results on bicrystals deformed by tension we find that slip transfer over the GB occurs also by narrow well-defined individual bands or by small groups of only few bands. As the stress grows up the slip bands become stronger and more GB transfers appear.

A topograph of a specimen of Σ15 bicrystal is shown in Fig.3. The slip planes are approx. perpendicular to the GB and inclined by 50.8° to the surface, but in opposite directions in the two grains. The slip bands occurred evidently first in the grain A and stopped at the GB. The slip

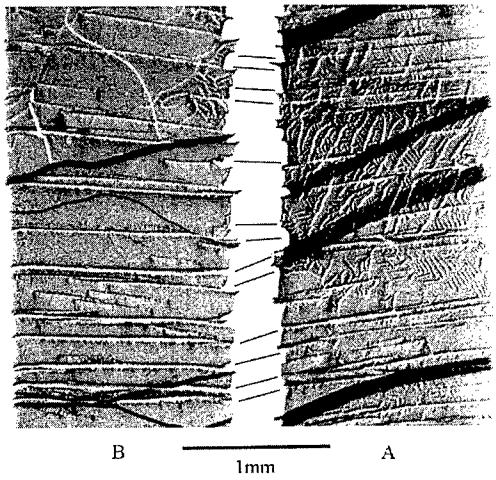

Fig.1 White beam reflection topograph of a Σ3 bicrystal after deformation by compression taken at LURE, Orsay. Diffracting planes {402} parallel to the surface, Bragg angle ϑ=65°, wavelength λ=0.116nm. Corresponding slip bands in the grains A and B are marked.

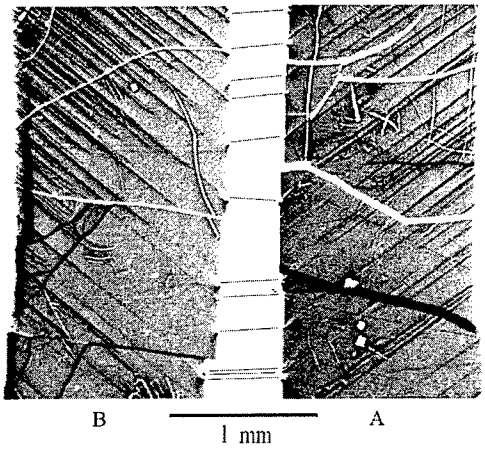

Fig.2 White beam reflection topograph of a Σ9 bicrystal after deformation by compression taken at LURE, Orsay. Diffracting planes {110} parallel to the surface, Bragg angle ϑ=65°, wavelength for the main reflection 330 λ=0.122nm, higher harmonics are present. Corresponding slip bands in the grains A and B are marked.

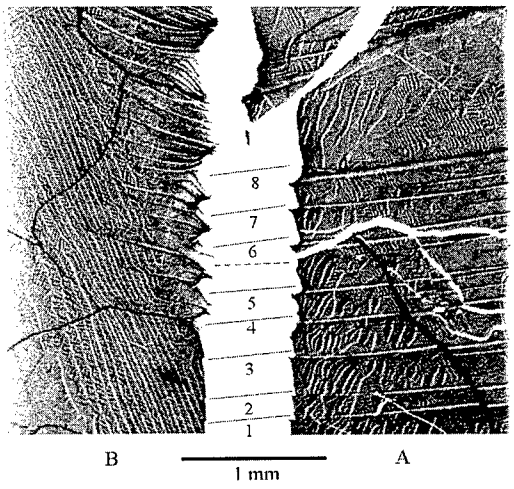

Fig.3 White beam reflection topograph of a Σ15 bicrystal after deformation by compression taken at LURE, Orsay. Diffracting planes {402} parallel to the surface, Bragg angle ϑ=65°, wavelength λ=0.116nm. Corresponding slip bands in the grains A and B are marked.

continues in the grain B by a high number of fine bands. The curved shape of images of some of them near the GB does not show the real shape of the bands, it is an effect of the contrast formation. *In situ* observation confirms that a strong stress has to be formed at the GB before the slip occurs in the other grain. Unlike the Σ3 bicrystals the dimensions of the steps do not diminish but even grow up after the slip transfer.

Observation of Σ15 bicrystals shows very different effects related to the slip transfer over the GB:

- well defined narrow slip bands appear in one grain and stop at the GB, single slip bands or small groups of few bands then continue behind the GB; this was not observed in specimens deformed by tension;
- in other specimens extended groups producing large stress at the GB develop and initiate mass slip transfer similarly as in bicrystals deformed by tension;
- gradual fanning of the slip bands frequently observed in the specimens deformed by tension was not found.

Summary

The differences in the slip patterns observed in the specimens deformed by tension and by compression common for the three types of bicrystals can be summarised in the following points. In compression the slip bands are narrower and at a greater distance from each other. Fans and groups of slip bands appear only rarely. Slip transfer over the GB is observed more frequently.
These effects can be explained by the properties of the two types of deformation. When a specimen is deformed by tension its cross-section is smaller in the neighbourhood of a slip band. Therefore the local stress is higher and so is the probability of new slip bands formation. An opposite effect appears during the compression deformation. Near a slip band the cross-section of the specimen is larger, the local stress higher and new slip bands tend to be formed further.
The compression experiments confirm the earlier conclusion [4] that the GB forms a strong barrier for the slip transfer even in the geometrically favourable case of Σ3 bicrystals. The reasons of this effect connected with both the structure of low Σ and lattice defects present in real GBs are discussed in detail in [6].

The authors acknowledge the financial supports of GA of ASCR (the grant contract No. A1010702), GA of CR (the grant contract No. 202/98/1281) and PICS (No 477).

References

[1] D.A. Smith, J. de Phys. **43** (1982), C6-225.
[2] A. George, Rev. Phys. Appl. **23** (1988), 479.
[3] W.A.T. Clark, R.H. Wagoner, Z.Y. Shen, T.C. Lee, I.M. Robertson and K. Birnbaum, Scripta Metall. **26** (1992), 203.
[4] M. Polcarová, J. Gemperlová, J. Brádler, A. Jacques, A. George and L. Priester, Phil. Mag. A **78** (1998), 105.
[5] M. Polcarová, J. Gemperlová and J. Brádler, J. Appl. Cryst. **23** (1991), 331.
[6] J. Gemperlová, A. Jacques, M.Polcarová, J. Brádler, V. Novák and A. George, this Proceeding

Materials Science Forum Vols. 294-296 (1999) pp. 381-384

Characterisation of (340)/(010) Asymmetrical Grain Boundary

J. Erhart[2] and V. Paidar[1]

[1] Institute of Physics, AS CR, Na Slovance 2, CZ-18221 Praha 8, Czech Republic

[2] Department of Physics, Technical University of Liberec, Hálkova 6, CZ-46117 Liberec, Czech Republic

Keywords: Grain Boundary Structure, Computer Simulation, Visualisation

Abstract Structures of the (340)/(010) asymmetrical grain boundary with the [001] rotation axis in the bcc lattice are discussed. Four low energy atomic configurations of this boundary were found by computer simulation. Local properties such as atomic volume and pressure were determined in order to find atomic sites, which might be important for solute segregation. A new method for visualisation of crystal defect structures based on atomic coordination is proposed.

1) Introduction

The properties of grain boundaries depend on their atomic structure, which is determined by the coordinates of a large number of atoms in the boundary core. An indispensable part of their investigation is computer simulation that is widely used for the interpretation of experimental observations. The boundary structure is currently described by so called structural units that can be understood as compact atomic polyhedra forming the perturbed region [1,2] or as short-period elements into which large-period grain boundary structures can be decomposed [3,4]. A hierarchical relationship of structural elements for the symmetrical grain boundaries in cubic lattices has a geometrical nature valid independently of particular material type [5].

The approach that elucidates the relationships among boundaries of different types, given by geometrical macroscopic degrees of freedom, is not sufficient for characterization of the grain boundary properties, which depend on the local parameters associated with particular atomic sites, such as impurity atom segregation. It is thus important to look for simple methods to identify the atomic sites possessing extremum values of these parameters.

In this paper we will present four low energy configurations of the (340)/(010) asymmetrical grain boundary in the bcc crystals and discuss how such structures can be visualised. A new simple method based on the atomic coordination enabling to find the atomic sites in the boundary core with exceptional properties will be introduced.

2) The structures of the (340)/(010) grain boundary

The results of the systematic modelling of Σ5 asymmetrical grain boundaries with the [001] rotation axis in the bcc lattice will be published elsewhere. The details of relaxation procedure used to find stable and metastable configurations of the grain boundary structure, corresponding to local energy minima, were described in [6]. Four different structures of the (340)/(010) grain boundary are depicted in the projection parallel to the [001] rotation axis in Fig. 1. The atomic positions on two alternating (001) planes are distinguished by circles and squares. The planes parallel to the interface are (010) and (340) in the lower and upper grains, respectively. For an asymmetrical grain boundary, the position of the interface plane cannot be univocally determined. In principle, a local quantity characterizing the deviation from the perfect crystal can be chosen and the interface plane

can be identified by the atomic site with the extremum value of this quantity. The sites with large atomic volume are denoted in Fig. 1 by full triangles pointing down and those with large negative local pressure by full triangles pointing up. The overlap of two triangles pointing down and up forms a hexagonal star. These two quantities indicate lattice dilatation, i.e. the lattice sites suitable for large impurity atoms. On the other hand, the atomic sites which are compressed, i.e. possessing large positive pressure, are marked by heavy crosses.

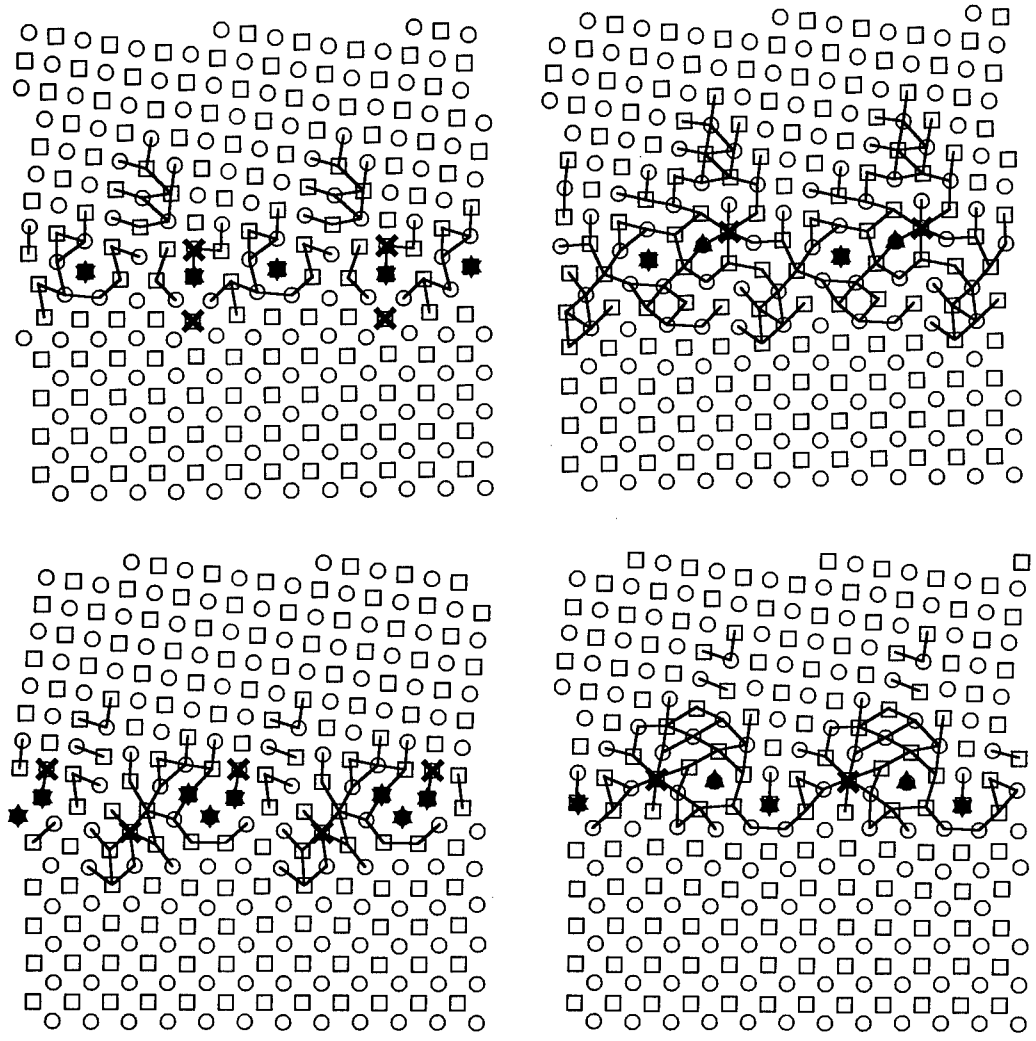

Fig. 1. Four structures of the (340)/(010) Σ5 [001] asymmetrical grain boundary. The atomic positions are marked by open circles and squares; full triangles and crosses denote the sites with extremum values of local volume and pressure.

3) Visualisation of the interface core

The purpose of our method is to select atomic bonds which would describe space nature of the interface core. A number of neighbouring atoms, and a radius of the sphere where the neighbours are counted, are used as input parameters. The criterion for the bond selection is the

magnitude of coordination number. If it is different from the prescribed value, the bonds are depicted in the figure of the boundary structure. The number 8 of the nearest neighbours in the bcc lattice was used in our case. When the sphere radius is smaller than the separation of the nearest neighbours of the perfect lattice, only the contracted bonds are depicted providing that their number is different from 8. For certain value of the radius between the first and second neighbours, a layer where the interatomic bonds are selected is relatively narrow. The width of the depicted region increases when the radius approaches the separation of the second neighbours. Crossing this atomic separation, all the nearest neighbour bonds in the perfect lattice far from the interface are visible. For the radii of 0.91 and 1.09 in the units of bcc lattice parameter, the bond pattern is in certain sense reversed. Only a small number of bonds is selected for 0.91 while practically all the bonds excluding only a small number of significantly extended ones is presented for 1.09 (see Fig. 2). It is seen that the grain boundary core is localized at the interface plane, where the sites with the largest atomic volume and the largest negative pressure are situated, but also penetrates into both grains along the most close packed planes of the {110} type. Consequently, the core is wider in the upper grain with the [340] normal. The radius of 0.91 was chosen for all four atomic configurations shown in Fig.1.

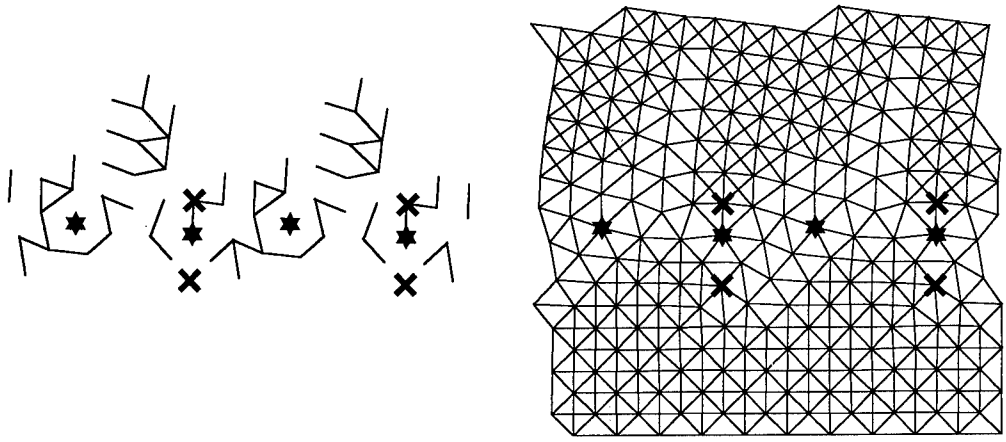

Fig. 2. Patterns of selected atomic bonds for the sphere radii of 0.91 and 1.09.

A standard way of presentation of the grain boundary structures is shown in the left-hand part of Fig. 3. The perfect bcc lattice is composed entirely of identical tetrahedra with four edges formed by the nearest neighbour bonds and two edges by the second neighbour bonds. If only the nearest neighbour bonds are depicted, the tetrahedra are projected as squares. However, for the sphere radius greater than 1.00, the in plane second neighbour bonds appear as square diagonals.

In addition to a distorted square network, a topologically different pattern, namely trigonal prisms, can be found in the boundary core. In fact, all the structures shown in Fig. 1 can be presented as composed of capped trigonal prisms periodically repeated on the interface plane. Three capped trigonal prisms corresponding to one period of the (340)/(010) boundary are shown in Fig. 3. Notice that the same pattern is obtained in a reversed form for the sphere radius of 1.27. The narrow channels of missing bonds depicted in Fig. 2 are suppressed with increasing radius value, and the diagonals appear even in heavily distorted squares leaving thus only triangles of capped trigonal prisms.

It should be emphasized that the symmetry and topological character of the grain boundary core are important for the relationship among various types of boundary structures, however, for many interface properties, a quantitative knowledge of local characteristics is indispensable. Since

the atom energy, local volume and pressure are determined by the interaction with the surrounding atoms, the atom coordination has an essential meaning even for metallic bonding. This is apparently the reason why the simple method introduced above turned out to be quite efficient.

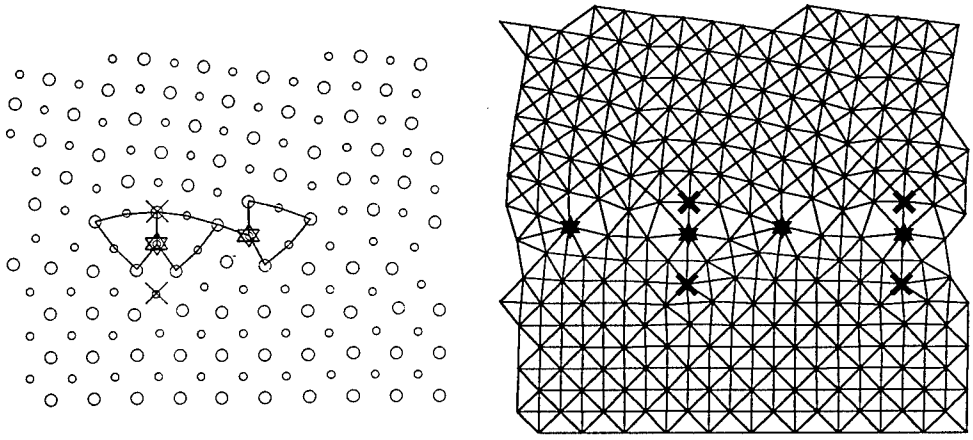

Fig. 3. Comparison of the grain boundary structure presentation by the capped trigonal prisms and by the pattern of selected atomic bonds for the sphere radius of 1.27.

4) Conclusions

Grain boundary properties such as segregation of impurities are sensitive to the local parameters associated with particular atomic sites at the interface. It has been shown that these sites can be identified by a simple visualisation method based on the atomic coordination that is closely related to bonding nature in the perturbed region of boundary core.

Acknowledgements This work was supported by the Grant Agency of the Academy of Sciences of the Czech Republic (A1010708/1997) and by the International Collaboration COST Action 517 (OC 517.40).

References

[1] M.F. Ashby, F. Spaepen and S. Williams, *Acta Metall. 26* (1978) 1647.
[2] R.C. Pond, D.A. Smith and V. Vitek, *Scripta Metall. 12* (1978) 699.
[3] A.P. Sutton and V. Vitek, *Phil. Trans. R. Soc. Lond. A 309* (1983) 1.
[4] G.J. Wang, A.P. Sutton and V. Vitek, *Acta Metall. 32* (1984) 1093.
[5] V. Paidar, *Acta Metall. 35* (1987) 2035.
[6] J. Erhart and I. Trubelík, *Phys. Stat. Sol. (a) 179* (1993) 329.

Materials Science Forum Vols. 294-296 (1999) pp. 385-388

Interface Dislocations in TiAl

V. Paidar[1], S. Zghal[2] and A. Couret[2]

[1] Institute of Physics, AS CR, Na Slovance 2, CZ-18221 Praha 8, Czech Republic

[2] Centre d'Elaboration de Matériaux et d'Etudes Structurales, CNRS, BP 4347, F-31055 Toulouse, France

Keywords: Intermetallics, TiAl, 120° Rotation Interface, Misfit Dislocations

Abstract The interfaces of lamellar structure in γ-phase TiAl are analysed. The misfit between 120° rotation domains with the ordered $L1_0$ lattice on the (111) plane, and the arrays of interface intrinsic dislocations observed by transmission electron microscopy are investigated. It is shown that a triangular dislocation network of screw Shockley partials can accommodate the observed misfit.

1. Introduction

The interfaces of lamellar structure in TiAl base alloys have a strong effect on plastic deformation and other mechanical properties [1], and deserve thus a special attention. Between six variants of the $L1_0$ tetragonal lattice with respect to a chosen (111) plane, four different types of interfaces parallel to (111) can be distinguished (for more details see e.g. [2,3]):

- translation faults, e.g. antiphase boundary, with 0° misorientation
- 120° rotation domain boundary
- true twin boundary for 180° rotation
- pseudo-twin boundary corresponding to 60° rotation

In this paper, we will investigate only the interface of the second type, which is not coherent contrary to the true twin where the atomic planes in contact are in perfect coincidence due to mirror symmetry. The theoretical evaluation will be compared with the experimental observations.

2. Analysis of 120° interface misfit

The γ-phase of TiAl is slightly tetragonal with the c/a ratio close to 1.02. Consequently, the atomic spacing in the <110] directions parallel to the close packed atomic rows composed solely of either Ti or Al atoms is different from the spacing of the <101] atomic rows with the alternating Ti and Al atoms. For $c/a = 1+x$, each (111) plane of the reference cubic lattice is extended in the $L1_0$ structure by the factor of $1+2x/3$ in the <112] direction perpendicular to the <110] direction, along which the atomic spacing is $a/\sqrt{2}$. Since the $[\bar{1}10]$ directions of the lower and upper domain are not parallel, the atomic positions can be in coincidence only along the $[10\bar{1}]_L = [01\bar{1}]_U$ direction where the atomic spacing is extended by the factor of $1+x/2$.

Contrary to the f.c.c. lattice, where the angles between <110> directions in the equilateral triangles are $\pi/3$ (60°), the apex angle of the isosceles triangles in the $L1_0$ structure is smaller, $\pi/3-\phi$, and hence the other two angles must be larger than $\pi/3$, $\pi/3+\phi/2$ (Fig. 1). If $[10\bar{1}]_L = [0\bar{1}1]_U$, the misfit can be fully compensated by a single shear on the interface plane of the magnitude 2ϕ parallel to the coinciding direction (Fig. 1a). However, the atomic spacing can be equal also along the perpendicular $[1\bar{2}1]_L = [\bar{2}11]_U$ direction and the misfit is then compensated by the perpendicular shear again of 2ϕ (Fig. 1b).

A rotation of 2ϕ of the upper domain with respect to the lower one about the interface normal is required for the transition between two configurations depicted in Fig. 1. Therefore, an intermediary configuration is reached by a half rotation of ϕ. The deviation of crystallographic direction parallel to the interface in the neighbouring domains far from the interface varies from 0 to 2ϕ for the single shear with the $[10\bar{1}]$ coincidence, and from -2ϕ to 0 for the perpendicular single shear with the $[1\bar{2}1]$ coincidence. After the rotation of ϕ, the maximum deviation for the intermediary double shear is only one half, i.e. ϕ. Hence the angle between the corresponding crystallographic directions, depicted in Fig. 1 for two single shears, is equal only to $\phi/2$ when the misfit is compensated by the double shear. In other words, the deviation angle between the close directions such as $[\bar{1}10]_L$ and $[10\bar{1}]_U$ is not $3/2\phi$ as in the case of one of the single shears in Fig. 1 but only $\phi/2$ for the double shear composed of two perpendicular contributing shears of equal magnitude ϕ. It is important to emphasize that the misfit between the 120° rotation domains is still the same, but if accommodated by the double shear, the deviations of respective crystallographic directions and resulting strains are smaller.

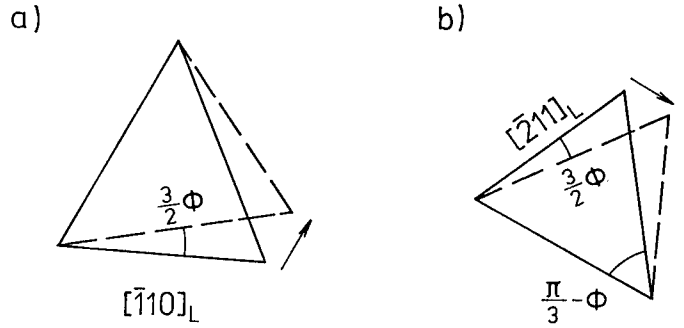

Fig. 1. Misfit between the (111) planes on the 120° rotation interface. It can be accommodated either by shear parallel to $[10\bar{1}]_L$ or to $[1\bar{2}1]_L$ as depicted in a) and b). The upper and lower domains are distinguished by the full and dashed isosceles triangles, respectively.

For $x = 0.02$ we get $\phi = 0.0115$, i.e. 0.66°, since $\phi = x/\sqrt{3}$. This angle is in a relatively good agreement with the measured deviation between $[\bar{1}10]$ and $<10\bar{1}]$ [4] which is $\phi/2$ as explained above and which was found to be 0.2°-0.3°, i.e. 0.0035- 0.0052, in Ti-49.3at.%Al where the *c/a* ratio was measured to be slightly smaller than 1.02.

3. Experimental observations and their interpretation

The samples for transmission electron microscopy observations were prepared from polysynthetically twinned crystals of Ti-49.3at%Al provided by Prof. Yamaguchi's group (Kyoto University, Japan). For other details on experimental procedure see [3].

The observed network of interface dislocations on the (111) plane is shown in Fig. 2 under several diffraction conditions which allow us to evaluate the directions of Burgers vectors for all three sets of dislocations. The dislocation structure can be analysed the most easily in the images c, e and g, which were taken with the three diffraction vectors of the <202> type lying in the interface plane. The observation plane in these cases is parallel to the interface. As it is seen in the images a and b, which were taken with the diffraction vector of the <111> type, the interface dislocations form a triangular grid. This grid composed of the intrinsic dislocations is relatively regular in the whole observed area, but is perturbed in some places apparently by the extrinsic dislocations. It can be deduced from the contrast fringes that the observed interface dislocations are partial dislocations. One set of dislocations is invisible on each of the images c, e and g similarly as in the images d, f

and h, taken with the diffraction vector of the <113> type. For example, the dislocations d_1 are invisible in images c and d, hence their Burgers vector is parallel to the $[\bar{1}2\bar{1}]^I$ direction in the lower domain and we can assume that these dislocations are Shockley partials $\mathbf{b}_1=1/6[\bar{1}2\bar{1}]^I$. Using **g.b** criterion in a similar way for the other two sets of dislocations, it can be shown that their Burgers vectors are $\mathbf{b}_2=1/6[\bar{2}11]^I$ and $\mathbf{b}_3=1/6[11\bar{2}]^I$. It follows from the analysis of dislocation line directions that all three sets of dislocations are nearly screws. The measured average separation of the neighbouring dislocations is about 25 nm.

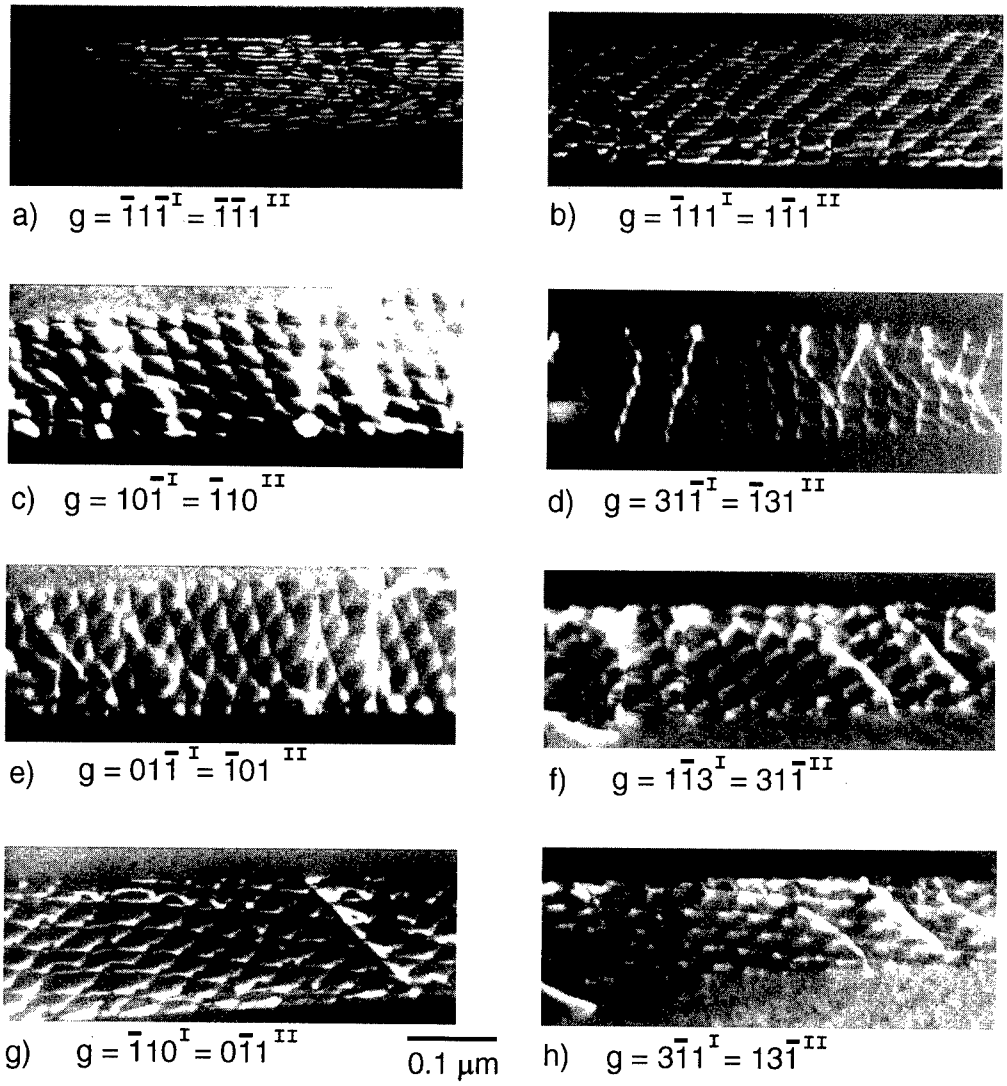

Fig. 2. Week-beam images of dislocation network in the 120° interface taken with different diffraction vectors.

A triangular net can be decomposed into three equilateral hexagonal nets as depicted in Fig. 3. It can be shown that three arrays of parallel screw Shockley partials create triangular regions of stacking faults alternating with the perfect lattice in agreement with the fringe contrast observed experimentally.

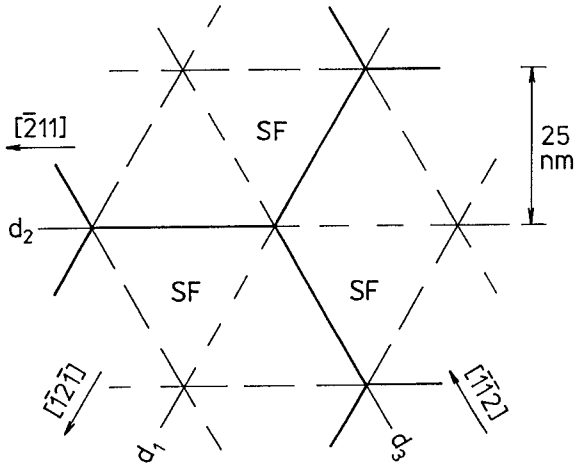

Fig. 3. Triangular dislocation network composed of three equilateral hexagonal nets distinguished by full lines, and long- and short-dashes. SF denotes stacking fault regions.

The misfit due to the screw dislocations of equilateral triangular network is three times that of each component hexagonal net which can be calculated according to expression [5] $\psi = \frac{1}{2S}\sum_i l_i b_i$, where b_i are magnitudes of screw Burgers vectors, l_i are lengths of respective dislocation segments and S is area of one network cell. For the lattice parameter of 0.4 nm, the Burgers vector of Shockley dislocations is about 0.1633 nm, the length of dislocation segments for dislocation separation of 25 nm is about 28.9 nm, and the area of hexagons is 2165 nm^2. Finally, the resulting misfit $\psi = 0.0098$ is about 15% smaller than the expected value $\phi = 0.0115$.

4) Conclusions

It has been shown that the deviation of atomic bonds across the 120° rotation interface is smaller if the adjoining domains are not in coincidence orientations neither in the <101] nor in <121] directions but when the rotation angle is in between these two positions. This result agrees not only with the deviation angle derived from the Kikuchi lines but also with the dislocation structure observed by weak-beam technique.

Acknowledgements This work was supported by the Grant Agency of the Academy of Sciences of the Czech Republic (A1010817/1998) and by the international collaboration programs (ME190 and ME264/1998).

References

[1] M. Yamaguchi and H. Inui, in R. Darolia, J.J. Lewandowski, C.T. Liu and M.V. Nathal (eds.), *Structural Intermetallics*, TMS, Warrendal, 1993, p. 127.
[2] D.M. Dimiduk, Y. Sun and P.M. Hazzledine, in J. Horton, I. Baker, R.D. Noebe and D.S. Schwartz (eds.), *High-Temperature Ordered Intermetallic Alloys VI*, Mat. Res. Soc. Symp. Proc., Vol. 364, Pittsburgh, 1995, p. 599.
[3] S. Zghal, S. Naka and A. Couret, *Acta Mater. 45* (1997) 3005.
[4] H. Inui, M.H. Oh, A. Nakamura and M. Yamaguchi, *Phil. Mag. A 66* (1992) 539.
[5] C. Rey and G. Saada, *Phil. Mag. 33* (1976) 825.

Materials Science Forum Vols. 294-296 (1999) pp. 389-392

Auger Spectroscopy of TiAl Interface Diffusion Specimens

D.E. Luzzi[1], D. Imamura[2], H. Inui[2], E.P. George[3], L. Heatherly[3], H. Yasuda[4], H. Mori[4] and M. Yamaguchi[2]

[1] Dept. of Materials Science and Engineering, Univ. of Pennsylvania, Philadelphia, PA 19104-6272, USA
E-Mail: luzzi@lrsm.upenn.edu

[2] Dept. of Materials Science and Engineering, Kyoto Univ., Kyoto 606-01, Japan

[3] Metals and Ceramics Div., Oak Ridge National Lab., Oak Ridge, TN 37831-6093, USA

[4] Res. Ctr. for Ultra-High Voltage Electron Microscopy, Osaka Univ., Osaka 565, Japan

Keywords: Interface Diffusion, TiAl, Auger Electron Spectroscopy

ABSTRACT

The utility of polysynthetically-twinned (PST) TiAl, which contains a high density of parallel, atomically-flat interfaces within a set of identical crystallographic orientations, as a potential model system for a detailed investigation of interface diffusion is explored. Macroscopic PST crystals were grown in an optical float zone furnace. Thin films were cut from oriented crystals and polished with <110> and <112> directions normal to the film. After sputter cleaning, Ag was deposited on one side of the TiAl thin films. Auger spectra were obtained from these films over a wide range of sputter/anneal conditions. The Al and Ti concentrations were analyzed as well as the important impurity elements, S, Ar, C, N and O. Ag diffusion on the interfaces was confirmed. Using the present data and existing knowledge of the microstructure and crystallography of PST TiAl, the potential of this material for providing a detailed understanding of the atomistic mechanisms of interface diffusion is analyzed.

INTRODUCTION

The limited tensile ductility of fully lamellar polycrystalline TiAl alloys [1, 2] obscures evidence that the lamellar interfaces in this alloy are susceptible to environmental embrittlement at room temperature as seen in experiments on polysynthetically twinned (PST) TiAl single crystals [3]. Promising signs have been reported that the segregation of certain ternary additions to the interfaces can mitigate this environmental embrittlement [4], but with a penalty in other properties. There is also growing evidence that under the moderate stress states expected in service, interface sliding will be the rate controlling creep mechanism in TiAl alloys [5, 6]. At the present time, little is known about the interface diffusion or segregation properties of the lamellar interfaces in TiAl alloys, and almost nothing is known about the effects of these properties on the strength and deformation behavior of these lamellar interfaces.

Yet TiAl is a remarkable alloy system in which to develop an understanding of the relationship between interface atomic structure and properties. The lamellar interfaces are fully ordered and atomically flat with high macroscopic symmetry, which enables the imaging of the atomic structure and the mapping of compositional variations by electron microscopy (EM) techniques. The relatively short periods of the interface structures are ideal for computer-based atomistic modeling. Crystal growth techniques have been developed which allow large PST crystals to be grown in which all lamellar interfaces are parallel. At the same time, the introduction of field emission TEMs and the development of interatomic potentials that enable the effective treatment of bond covalency provide the experimental and theoretical tools with which to carry out an effective analysis of diffusion in this interesting alloy. In the present paper, initial Auger electron spectroscopy results are presented which primarily concern the determination of the experimental conditions under which interface diffusion in PST TiAl can be studied by Auger electron spectroscopy using the penetration method.

EXPERIMENT

Polysynthetically-twinned (PST) Ti-49.3%Al crystals were grown by directional solidification in an optical float zone furnace at Kyoto University. Using back Laue x-ray diffraction, spark cutting and precise mechanical polishing, 3 mm ϕ parallel-sided disks with a thickness less than 50 μm were produced. The disks were oriented with the <111> directions in the plane of the disks and the <112> directions lying in the lamellar interface planes and perpendicular to the plane of the disks.

The thinned disks were washed using acetone and ethanol. The disks were mounted in a sputter deposition system at Osaka University with a 1 mm collimating aperture centered on each disk. The central 1 mm ϕ area of each disk was sputter cleaned using Ar ions and Ag was then sputter deposited on the disks to a thickness of approximately 1 μm. The disks were mounted on an in-situ heating holder within an Auger spectroscopy system at the Metals and Ceramics Division of Oak Ridge National Laboratory. The orientation was such that the side of the disks containing Ag, the source side, was mounted **away** from the electron beam and sputter gun of the Auger system.

Some initial data on Ag diffusion was obtained. However, it was found to be necessary to characterize the sputter and annealing behavior of the TiAl. Therefore, after cleaning some specimens of Ag, sputter/anneal cycles were run at a variety of temperatures. Auger spectra were obtained over an energy range from 50 eV to 1450 eV. This range includes the low energy Al LMM peak, the Ti LMM peaks and the Al KLL peaks. It also includes the important impurity peaks of, in increasing energy, S, Ar, C, N and O.

RESULTS AND DISCUSSION

An initial Auger spectrum was recorded of a specimen at room temperature prior to any processing but after the UHV chamber was baked. The differential spectrum is shown in Figure 1. The peaks due to carbon, titanium, oxygen and aluminum are labeled; the low energy peak due to aluminum is not visible due to the impurity surface layer. This impurity layer, which exists around

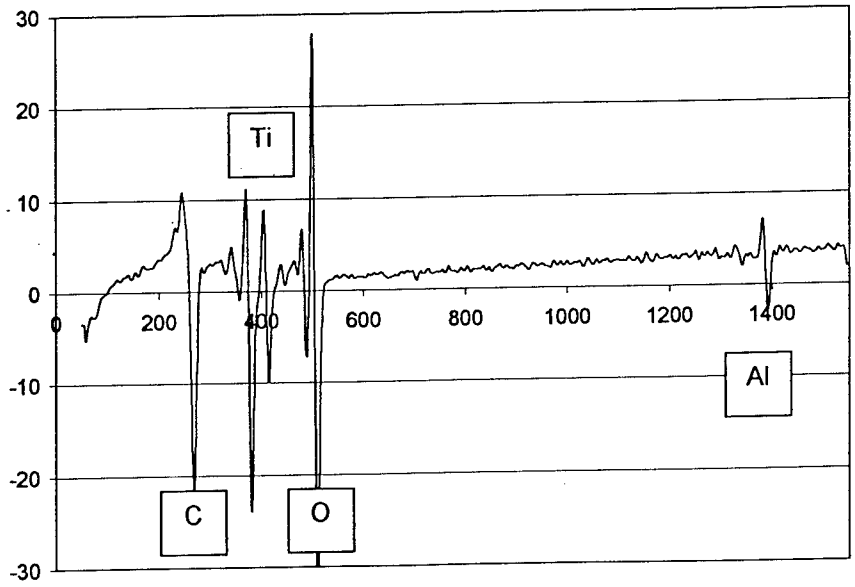

Figure 1 Auger spectrum of the diffusion specimen prior to sputtering or annealing. This spectrum was recorded from the back side of the specimen.

the deposited diffusant on the source surface provides a barrier to short circuit surface diffusion. Ten minutes exposure to a 5 keV Ar^+ beam and an anneal at 600 °C removed virtually all of the surface C and O as well as the residual Ar from the sputtering treatment. (see Figure 2). Strong preferential sputtering of Al from the surface is indicated by the sharp increase in intensity of the low energy surface Al peak after annealing.

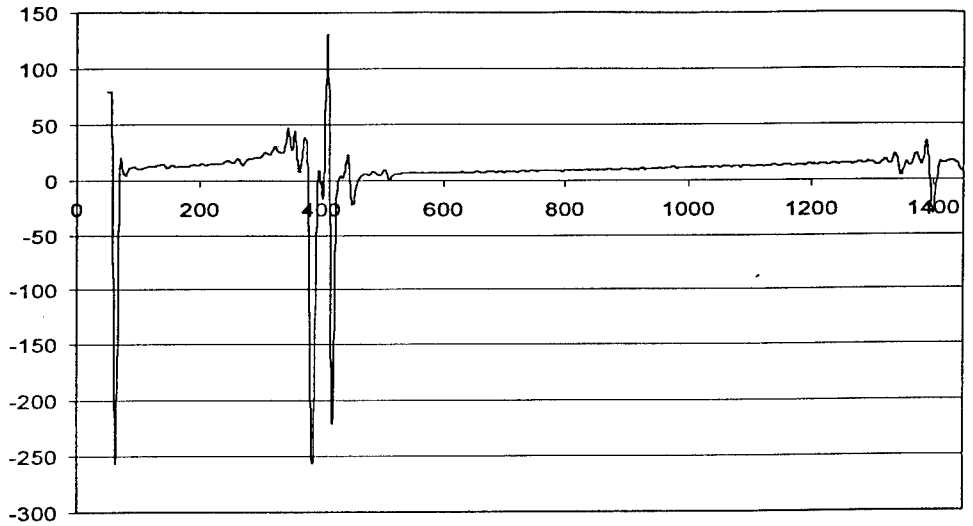

Figure 2 Differential Auger spectra after sputtering and annealing at 600°C.

In Figure 3, the compositions of Ti and Al at the surface are presented as a function of annnealing temperature after room temperature sputtering. The concentrations were adjusted using sensitivity values for Ti and Al in TiAl which were obtained from an in-situ fracture specimen at room temperature [7]. The data at 200, 400 and 500 °C were recorded after the specimen had been held at the respective temperature for 1 hour. The data at 600 °C was obtained after the specimen reached the temperature, after an additional thirty minutes and after an additional two hours. The data at 700 and 800 °C were obtained upon reaching these temperatures and after additional 30 minute anneals at 800 °C. The data of Figure 4 are consistent with the diffusion of Al from the bulk to the surface to restore the surface to the bulk composition.

The preferential loss of aluminum from the surface was greatly reduced when sputtering was done at elevated temperatures. Only a minor difference was found between the differential spectrum recorded after sputtering for ten minutes at 550 °C and that shown in Figure 3.

The Auger data indicate that the intrinsic sputtering and annealing behavior of the TiAl surface will have to be considered in any interface diffusion analysis that relies upon the measurement of the accumulation of diffusant on the surface. In the temperature range over which interface diffusion is much larger than bulk diffusion, measurements can rely upon a comparison of the diffusant surface peak to the Ti peak as there will be little recovery in the Al surface composition. At higher temperatures, the high energy Al peak can be used as a reference peak to normalize the surface accumulation of diffusant atoms. This peak is much less sensitive to the composition of Al atoms within the surface layer.

CONCLUSION

Polysynthetically twinned TiAl single crystals is an excellent model system for the systematic study of interface atomic structure/diffusion relationships. However, the presence of two elemental bulk species leads to preferential sputtering changing the composition of the surface

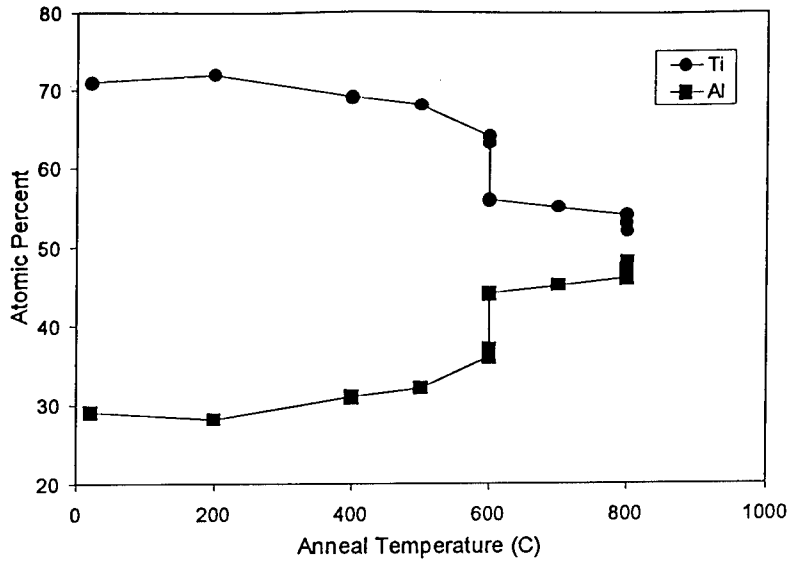

Figure 3 Corrected concentrations of titanium and aluminum on the (112) surface as a function of annealing temperature. Prior to annealing, the specimen was sputtered for 10 m with 5 keV Ar^+ ions at room temperature. The compositions were corrected using sensitivity data from a virgin in-situ fractured specimen of similar bulk composition.

layer. Therefore, these effects must be included in order to obtain reliable measurements of interface diffusion of solute by the surface accumulation method.

ACKNOWLEDGEMENTS

This research program is supported by the National Science Foundation, Division of Materials Research under grant DMR96-15228, program manager Dr. Bruce MacDonald and through the Oak Ridge National Laboratory SHARE Program, program administrator, Dr. Neal Evans. One of the authors, DEL, is grateful to the National Science Foundation International Programs Office for support in Japan through grant INT94-14511.

REFERENCES

1. Chan, K.S. and Y.-W. Kim, *Strain Rate and Environmental Effects on Fracture of a Two-Phase TiAl Alloy.* Metallurgical Transactions, 1993. **24A**: p. 113.
2. Kim, Y.-W. and D.M. Dimiduk, in *Structural Intermetallics 1997*, M.V. Nathal, *et al.*, Editors. 1997, TMS: Warrendale. p. 531.
3. Oh, M.H., *et al.*, *Environmental Effects on the Room Temperature Ductility of Polysynthetically Twinned (PST) Crystals of TiAl.* Acta Metallurgica et Materialia, 1993. **41**: p. 1939.
4. Oh, M.H., *et al.*, *Environmental Effects on the Room Temperature Ductility of PST Crystals of Binary and Some Ternary TiAl Compounds*, in *High-Temperature Ordered Intermetallic Alloys V*, I. Baker, *et al.*, Editors. 1993, MRS: Pittsburgh. p. 1001.
5. Hsiung, L.M. and T.G. Nieh, in *Structural Intermetallics 1997*, M.V. Nathal, *et al.*, Editors. 1997, TMS: Warrendale. p. 129.
6. Yamamoto, N. and K. Maruyama, private communication.
7. George, E.P., unpublished data.

Materials Science Forum Vols. 294-296 (1999) pp. 393-396

On the Possibility to Predict Dislocation Structures of Low Σ Symmetric Grain Boundaries

A. Gemperle, T. Vystavěl and J. Gemperlová

Institute of Physics AS CR, Na Slovance 2, CZ-18221 Praha 8, Czech Republic

Keywords: Grain Boundary, Grain Boundary Dislocation, Bicrystal

Abstract. Dislocation structures of vicinal grain boundaries Σ5 $[001](310)_A$ in Cu and Σ3 $[101](1\bar{2}\bar{1})_A$ in Fe-4at%Si are described. A method of theoretical prediction of GBD structures in GBs from Σ3 to Σ11 is proposed. It uses analogies in basic DSC vector configurations that exist between the two described cases and other low Σ symmetric boundaries.

Introduction

Various properties of metals and alloys are significantly influenced by grain boundaries (GB). Studies of e.g. grain boundary diffusion, migration and sliding have shown that the GB microstructure plays a decisive role. Low Σ coincidence boundaries are an important group of high angle GBs. In a polycrystal their frequency may attain up to 30% [1]. Exact coincidence is observed rarely, generally there is some deviation from it. According to the secondary grain boundary dislocation (GBD) model [2] this deviation is accommodated by GBDs. For mixed deviations (tilt and twist) the network of GBDs is complex and inherently anisotropic [3]. This anisotropy must be considered e.g. in studies of diffusion along the GB [4,5].

The experimental analysis of complete dislocation structure is difficult, time consuming, and for deviations larger than about 3° in many cases even impossible. In this paper an attempt is made to outline a procedure for approximate theoretical prediction of this structure. It is based on an analysis of experimentally determined misorientation and on analogies between DSC vector configurations with respect to GB planes of symmetrical low Σ boundaries.

Discussion of experimental results

A general deviation of a bicrystal from exact coincidence may be decomposed in a rotation around the GB plane normal (twist) and a rotation on an axis lying in the boundary plane (tilt) [3].

Fig. 1a to Fig.1d show the dislocation structures of four Σ5 $[001](310)_A$ boundaries in Cu. The common features of these structures are as follows: the twist component is accommodated by a hexagonal network formed from screw dislocations $\frac{a}{10}[\bar{1}30]_A$ (1 in the schematic drawing Fig.1e) and mixed dislocations $\frac{a}{10}[\bar{1}\bar{2}5]_A$ and $\frac{a}{10}[2\bar{1}\bar{5}]$ or $\frac{a}{10}[\bar{1}\bar{2}\bar{5}]_A$ and $\frac{a}{10}[2\bar{1}5]$ (2 and 3 in Fig.1e). The direction of dislocation 1, $\mathbf{l}_1$, and the common mean direction of 2 and 3, $\mathbf{l}_2$ - $\mathbf{l}_3$, lie for all deviations within 10° in $[\bar{1}30]_A$ and $[001]_A$ respectively. The hexagons are mostly elongated in $[\bar{1}30]_A$ direction. The tilt deviation is to a certain degree accommodated by the edge components of 2 and 3 (rotation on [001] by about 1/3 of the twist angle). The main part of the additional tilt is produced by an array of parallel $\frac{a}{10}[310]_A$ edge dislocations. Their line direction may be any direction in the plane of the boundary and the corresponding tilt is a rotation on their direction.

Fig. 2a to Fig. 2d show the dislocation structures of three Σ3 $[101](1\bar{2}\bar{1})_A$ grain boundaries in Fe-4at.%Si. Both components of the deviation are accommodated by a hexagonal network containing edge dislocation $\frac{a}{3}[1\bar{2}\bar{1}]_A$ (1 in the schematic drawing Fig. 2e, f) and mixed dislocations $\frac{a}{3}[112]_A$, $\frac{a}{3}[\bar{2}1\bar{1}]_A$ (2 and 3 in Fig. 2e, f). The common mean direction $\mathbf{l}_2$ - $\mathbf{l}_3$ agrees within 10° with $[101]_A$. The edge components of 2 and 3 produce a tilt rotation on $[101]_A$ axis. The edge dislocations accommodate the main part of the tilt deviation by a rotation on their line direction, which may be any one in the boundary plane. For large tilt to twist ratios the hexagons of the net are very elongated and strongly deformed with the line direction of 1 approaching $[101]_A$ (Fig. 2a, b, c). Calculations of rotations, caused by hypothetical dislocation nets of the type found for Σ3 in Fe-Si, according to the formulas in [6] have shown that for increasing twist to tilt ratios the directions of 2 and 3 approach a straight line lying in $[101]_A$. A set of parallel $\frac{a}{6}[11\bar{1}]_A$ screw dislocations is needed to eliminate long range shear stresses. Experimental evidence for such a set is given in [7] for Σ3 grain boundary in Fe.

Prediction of the dislocation structure

According to the results of the discussion we expect that both types of experimentally investigated dislocation structures may contain dislocations of four Burgers vectors. Three of them are composing a hexagonal net. This hexagonal net may be composed either of mainly screw dislocations and the fourth Burgers vector is forming a set of parallel edge dislocations (structure type I) or it is composed of one edge dislocation and two mainly screw dislocations, the fourth Burgers vector is forming a set of parallel screw dislocations (structure type II).

Possible grain boundary planes for symmetric grain boundaries up to Σ11 were found using data from [8]. Basic DSC vectors were calculated by the method outlined in [9]. It is based on a matrix formed from three smallest non-coplanar diffraction vectors common to both grains. Only the basic DSC vectors were considered for formation of dislocation structures. The character of the Burgers vectors (screw, mixed or edge) with respect to the boundary planes was determined. Reactions between basic DSC vectors, which result in another basic DSC vector, were found by inspection. If there is only one possibility, this combination was expected to form the hexagonal net. In the case the hexagonal net belongs to structure type I or II, it was verified whether the fourth vector also corresponds to the correct structure type. In some cases two different reactions between basic vectors will be possible. We suppose that the hexagonal net containing three mainly screw dislocations will be preferred.

The proposed structures are presented in the Table. It is found that in all cases except for Σ5 $[001](120)_A$ and Σ9 hypothetical geometric configurations belong to structure type I or II.

The definitive form of the GB dislocation structure predicted for special deviations from coincidence is designed in such a way that the rotation produced by it corresponds to the experimental value and the structure produces no long-range shear stresses in the boundary plane. The formulas from [6] are used for calculation of the rotation due to the hexagonal net and the simple formula $\theta = b/d$ (b is Burgers vector, d is dislocation spacing) is used for the set of parallel dislocations.

The authors acknowledge the financial supports of GA of ASCR (the grant contract No. A1010702), GA of CR (the grant contract No. 202/98/1281).

References

[1] T. Watanabe, *J. de Physique* 49 (1988), C5-507.
[2] A.P. Sutton, *Int. Metals Reviews* 29 (1984), 327.

[3] T. Vystavěl, V. Paidar, A. Gemperle and J. Gemperlová, *Interface Science* 5 (1997), 215.
[4] A.N. Aleshin, S.J. Prokofjev and L.S. Schwindlerman, *Scripta Metall.* 19 (1985), 1135.
[5] E. Budke, C. Herzig, S.J. Prokofjev and L.S. Schwindlerman, *Mater. Sci. Forum*, 207-209 (1996), 465.
[6] C.Rey and G. Saada, *Philos. Mag.* 33(1976), 825.
[7] L.M. Clarebrough and C.T. Forwood, *Phys. Stat. Sol. a* 105 (1988), 131.
[8] H. Mykura, *Grain Boundary Structure and Kinetics*, ASM, Metals Park, OH (1980), p. 445.
[9] C.T. Forwood and L.M. Clarebrough, *Electron Microscopy of Interfaces in Metals and Alloys*, Adam Hilger, Bristol 1991, p.137.

Table. Predicted basic elements of the GBD structures (all vectors are for grain A)

		GB plane		sets of dislocations forming hexagonal net	independent set of parallel dislocations
Σ3	[101] 70.53°	$(11\bar{1})_A$	*bcc*	three pure screw $\frac{a}{3}$<112>	pure edge $\frac{a}{6}[11\bar{1}]$
			fcc	three pure screw $\frac{a}{6}$<112>	pure edge $\frac{a}{3}[11\bar{1}]$
		$(1\bar{2}\bar{1})_A$	*bcc*	pure edge $\frac{a}{3}[1\bar{2}\bar{1}]$ and two mainly screw $\frac{a}{3}$<112>	pure screw $\frac{a}{6}[11\bar{1}]$
			fcc	pure edge $\frac{a}{6}[1\bar{2}\bar{1}]$ and two mainly screw $\frac{a}{6}$<112>	pure screw $\frac{a}{3}[11\bar{1}]$
Σ5	[001] 36.87°	$(310)_A$	*bcc*	mainly edge $\frac{a}{5}$[210] and two mainly screw $\frac{a}{10}$<531>	mainly screw $\frac{a}{5}[1\bar{2}0]$
			fcc	pure screw $\frac{a}{10}[\bar{1}30]$ and two mainly screw $\frac{a}{10}$<521>	pure edge $\frac{a}{10}$[310]
		$(120)_A$	*bcc* *fcc*	not predictable; vectors have not mainly edge or screw character	
Σ7	[111] 38.21°	$(3\bar{2}\bar{1})_A$	*bcc*	pure edge $\frac{a}{7}[3\bar{2}\bar{1}]$ and two mainly screw $\frac{a}{7}$<321>	pure screw $\frac{a}{14}[35\bar{1}]$
			fcc	pure edge $\frac{a}{14}[3\bar{2}\bar{1}]$ and two mainly screw $\frac{a}{14}$<321>	pure screw $\frac{a}{14}$[563]
Σ9	[101] 38.94°	$(21\bar{2})_A$ $(\bar{1}41)_A$	*bcc* *fcc*	not predictable with basic DSC vectors	
Σ11	[101] 50.48°	$(\bar{1}31)_A$	*bcc*	pure screw $\frac{a}{11}[32\bar{3}]$ and two pure screw $\frac{a}{11}$<714>	pure edge $\frac{a}{22}[\bar{1}31]$
			fcc	pure screw $\frac{a}{22}[32\bar{3}]$ and two pure screw $\frac{a}{22}$<714>	pure edge $\frac{a}{11}[\bar{1}31]$
		$(32\bar{3})_A$	*bcc*	pure edge $\frac{a}{11}[32\bar{3}]$ and two mainly screw $\frac{a}{11}$<714>	pure screw $\frac{a}{22}[\bar{1}31]$
			fcc	pure edge $\frac{a}{22}[32\bar{3}]$ and two mainly screw $\frac{a}{22}$<714>	pure screw $\frac{a}{11}[\bar{1}31]$

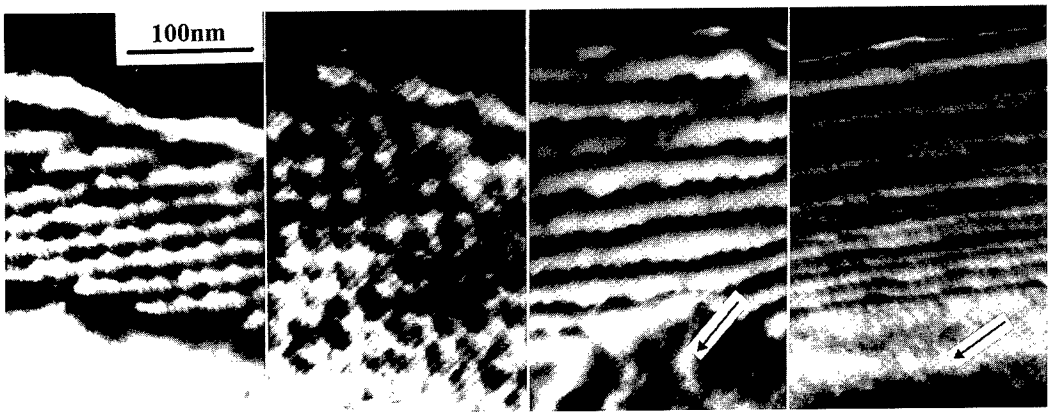

a) b) c) d)

Fig. 1 Dislocation structures of Σ5 [001](310)$_A$ boundaries in Cu. a) 1.07° tilt, 0.40° twist, dark field $\bar{2}02_A$ reflection, b) 1.11° tilt, 0.21° twist, dark field $0\bar{2}0_B$ reflection, c)1.69° tilt, 0.36° twist, dark field $00\bar{2}_A$ reflection, d)1.60° tilt, 0.55° twist, dark field $1\bar{1}1_A$ reflection, e) schematic representation of the network. Direction of faint edge dislocation 4 in c), d) is marked by arrows.

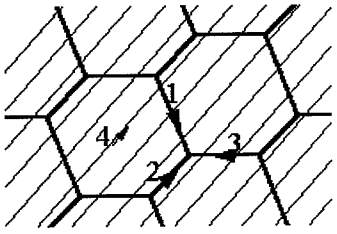

e)

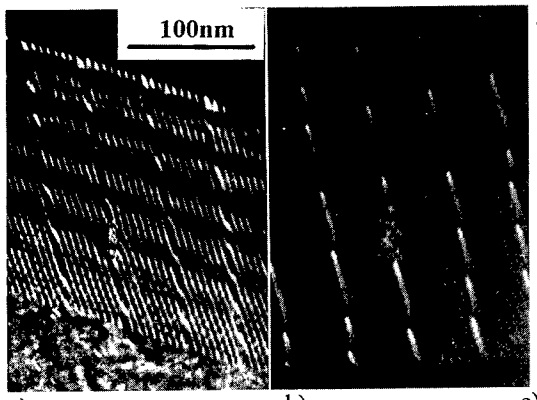

a) b)

e)

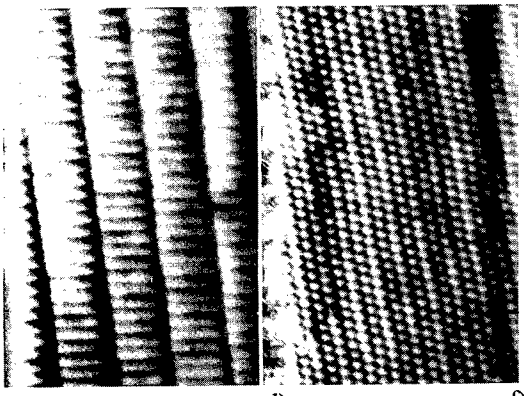

c) d)

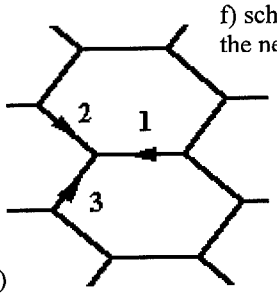

f)

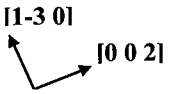

Fig.2 Dislocation structures of Σ3 [101] $(1\bar{2}\bar{1})_A$ boundaries in Fe-4at%Si.
a) 2.80° tilt, 0.14° twist, weak beam $\bar{1}0\bar{1}_A$ reflection,
b) same area as a) in weak beam $\bar{2}\bar{1}\bar{1}_A$ reflection,
c) 1.32° tilt, 0.20° twist, dark field $\bar{2}00_B$ reflection,
d) 1.86° tilt, 0.65° twist, dark field $\bar{2}00_B$ reflection,
e) schematic representation of the network in a) and b),
f) schematic representation of the network in d)

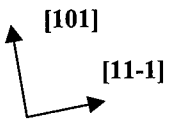

Materials Science Forum Vols. 294-296 (1999) pp. 397-400

Dislocation Interaction with a Σ=3 Grain Boundary Observed by *in-situ* TEM

T. Vystavěl[1], A. Jacques[2], A. Gemperle[1], J. Gemperlová[1] and A. George[2]

[1] Institute of Physics AS CR, Na Slovance 2, CZ-18221 Praha 8, Czech Republic

[2] Laboratoire de Physique des Matériaux, URA CNRS 7556, Ecole des Mines, parc de Saurupt, F-54042 Nancy cedex, France

Keywords: Dislocation, Grain Boundary, Plasticity

Abstract. Dislocation interaction with a Σ = 3 grain boundary in bcc Fe-4at% Si was investigated by *in-situ* TEM. The dislocations, whose Burgers vector belongs to the grain boundary plane, cross slip out of their slip band, and do not form stress concentrations. No slip transfer through the grain boundary has been observed yet.

Introduction

Grain boundaries (GBs) are known to act as strong obstacles to plastic deformation. The difficulty of the transmission of dislocations through an interface is expected – and observed - to depend on geometrical parameters i.e. the differences in the Burgers vectors of dislocations in one and the other grain, and in the respective intersection of slip planes with the GB. The slip system is common in both grains in studied bicrystals and the transmission of slip bands is thus expected to be easy, as observed in fcc germanium [1]. However, recent observations made by X-ray Topography, either *post mortem* on strained specimens or *in-situ* at LURE and ESRF on Fe-4at% Si [2-4], show that even in this case slip lines may be stopped at the GB, and a minimum stress concentration can be necessary to promote transmission. *In-situ* TEM was then expected to give a new insight into the details of the interaction of dislocations with a GB.

Experiments

The experiments were performed on symmetric tilt bicrystals of Fe-4at% Si containing a Σ = 3 GB (70.54° rotation around the common [110] axis, $(\bar{1}\,1\,\bar{2})_A / (1\,\bar{1}\,\bar{2})_B$ GB plane). The departure from exact coincidence position was a few tenths of a degree. Samples 5.5×1.7×0.1 mm^3 in size with a $[10\,1\,\overline{30}]_A / [7\,\bar{4}\,1]_B$ tensile axis and a $[3\,\bar{1}\,1]_A / [113]_B$ foil normal were cut and prepared by mechanical thinning and electropolished until a hole was formed. Special care was taken to select the specimen so that the GB intersects the hole edge in a zone where it is parallel to the tensile axis (Fig.1). In these cases the stress conditions are well defined [5]. The dislocations of the most favoured slip system have $[\bar{1}\,1\,1]_A / [\bar{1}\,1\,\bar{1}]_B$ Burgers vector, and are expected to glide on the plane near $(0\,1\,\bar{1})_A / (1\,0\,\bar{1})_B$. A secondary slip system may also be activated with Burgers vectors $[1\,1\,\bar{1}]_A / [1\,\bar{1}\,\bar{1}]_B$, in planes $(011)_A / (101)_B$. As the Burgers vector of the dislocations of the primary slip system belongs to the GB plane, dislocations trapped at the GB are in a screw orientation. The specimens were strained at room temperature in a double tilt tensile holder in a 300 kV JEOL microscope at LTPCM, Grenoble. The observations were made in simultaneous bright field conditions, using 121_A and $\bar{1}10_B$ diffracting vectors. After the experiment, the specimens were cut and the final configuration was investigated with a JEOL 120 kV microscope and the Burgers vectors of dislocations were analysed.

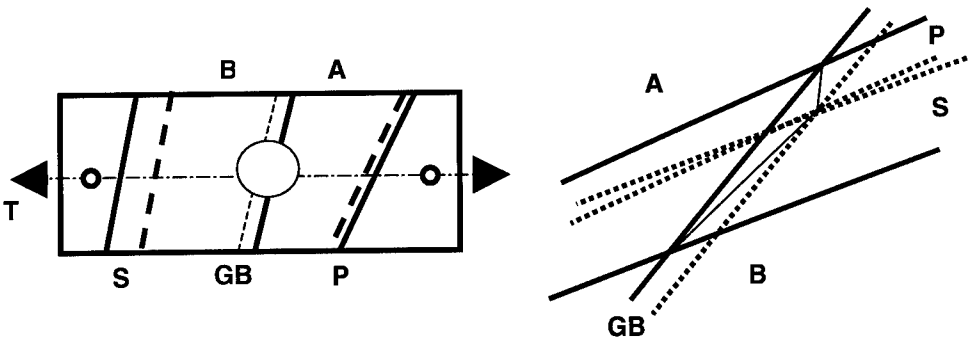

a) b)

Fig.1 a) Specimen shape (P, S and GB are intersection of the primary and secondary slip planes and the GB with the specimen surface. Full line at upper surface, dashed line at lower surface, T is tensile axis). b) Lines of intersection of the primary and secondary slip systems with the GB plane. A and B are the two grains.

Results

The specimen contained originally no or very few dislocations, except the GB dislocations required to accommodate the deviation from coincidence of the GB. It was thus necessary to increase the load on the specimen until a slip band appeared, either coming from the thicker part of the specimen, or formed at a small crack in the neighbourhood of the hole. (In some cases this load increase led at one moment to the arrival of a slip band, which instantaneously obscured the zone under view, making further observations impossible).

A first example of a slow event is shown Fig.2: A slip band appears in grain A in the field of view, which was originally dislocation-free (2a). The slip traces left at the intersection of the slip plane and the surfaces make an average angle of 30 degrees with the GB plane. This and the direction of the dislocations trapped (within the resolution of BF TEM) at the GB shows that they move in the primary slip plane. Instead of being confined to a single or very near parallel planes, as observed in fcc materials [1], the dislocations are more or less scattered on several microns. The dislocation movements are very jerky, i.e. involve nearly instantaneous displacements over a few micrometers followed by long periods of immobility. Some cross slipping dislocations and short lived sources can be seen, but the overall activity within the slip bands remains very low, except after load increases. After some time it can be seen in Fig.2b, that the slip band has extended into the thinnest part of the foil. New dislocations, either coming from the thick part of the specimen, or formed at sources in the immediate vicinity of the GB, arrive near the GB and stop at short distance from it (about 0.25 μm). They do not further advance into the GB, but are seen to cross slip into a plane nearly parallel to the GB until they move out of the field of view. The experiment was stopped before any transmission occurred.

Fig.3 shows the most interesting part of the second experiment. A slip band was formed in grain B. It met the GB, and widened by (double) cross slip. The slip traces left by incoming dislocations on the edge of the slip band are curved in the vicinity of the GB: once again, the dislocations seem to be repelled from the tip of the slip band. Another slip band formed of dislocations of the secondary slip system in grain B has reached the GB, coming from the thicker part of the specimen (a very difficult transmission is expected in this case). At one moment (Fig.3), new dislocations appear at the GB: they have no associated traces in grain B and ill visible traces in grain A. Inspection of the thicker part of the specimen showed that a very dense slip band had been formed in grain A, corresponding at the GB with the band in grain B. New dislocations had then been remitted by cross slip from this band.

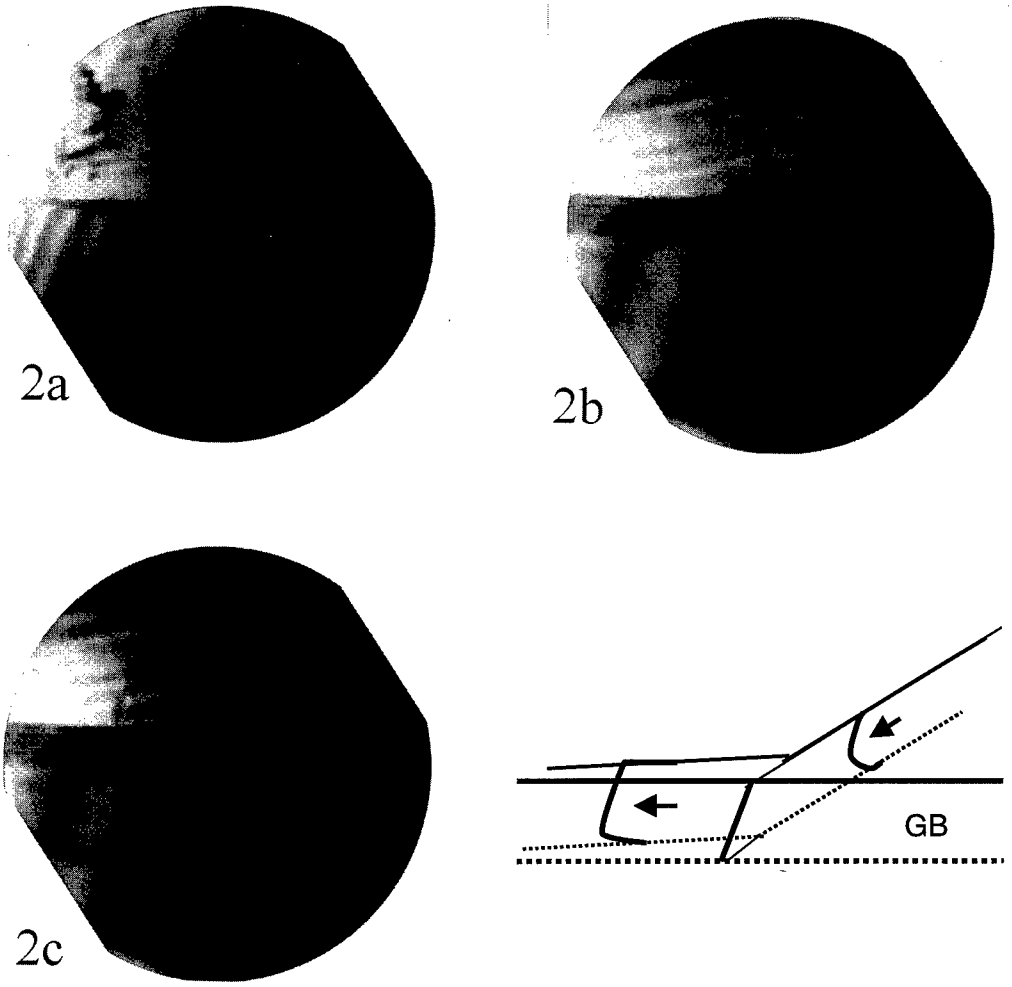

Fig.2 Slip band formation in grain A a) first dislocation appear, b), c) cross slip of a group of dislocations, d) schematic drawing of cross slip of primary dislocations along the GB. Scale marker 0.5μm.

The micrographs of Fig.4 taken after the experiment show in more detail the interaction of dislocations of the primary and the secondary slip systems observed in Fig.3 with the GB. Two points can be stressed: first, the primary screw dislocations remain straight, and did not glide in the GB plane, as they could; second, there is no disturbance of the underlying set of GB dislocations, and so no indication of interaction between grain and grain boundary dislocations.

Conclusions

The most striking results of the experiment are:

- When a slip line meets the GB, the first dislocations are trapped in or near the interface, without interaction with GB dislocations.

- The trapped dislocations exerce a backward force on the new incoming dislocations, either stopping them or pushing them to the sides of the slip band. (The apparent short range of this force is due to surface effects).
- Easy cross slip in bcc metals leads to a spreading of the tip of a slip band and the stress concentration which might overcome the GB resistance loses its edge.
- The experiments did not give evidence of transmission of dislocations through the GB. This confirms the evident difficulty of transmission, even in the easiest case, observed on massive specimens.

The authors are grateful to B. Doisneau and L. Guetaz for their help during *in-situ* observations. The authors also acknowledge the financial supports of GA of ASCR (the grant contract No. A1010702), GA of CR (the grant contract No. 202/98/1281) and PICS (No. 477).

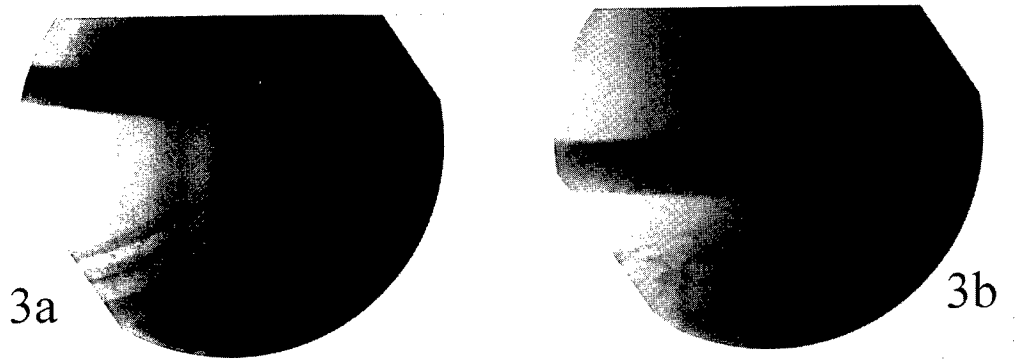

Fig. 3 a) Slip band in grain B stopped at the GB, b) arrival of dislocations from the grain A at the GB. Scale marker 0.2 μm.

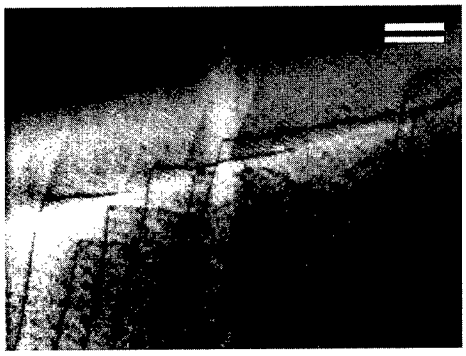

Fig.4. Interaction of individual dislocations of primary and secondary slips systems with the GB. $\mathbf{g} = 1\ \bar{1}\ 0_B$. Scale marker 0.2 μm.

References

[1] X. Baillin, J. Pelissier, J.J. Bacmann, A. Jacques, A. George, *Phil. Mag.* A, **55** (1987), 143.
[2] M. Polcarová et al, *Phil. Mag.* A, **78** (1998), 105
[3] A. Jacques, A. George, S.G. Roberts, M. Polcarová, J. Brádler and J. Gemperlová, *Interface Science* 4 (1997), 339.
[4] M. Polcarová et al, this Proceedings
[5] A.Coujou, Ph. Lours, N.A. Roy, D. Caillard and N.Clement, *Acta Metall.*, **38** (1990), 825.

Materials Science Forum Vols. 294-296 (1999) pp. 401-404

TEM Study of Twin Segments in Annealed Copper

O.V. Mishin[1,2] and X. Huang[2]

[1] On leave from the Institute for Metals Superplasticity, Ufa, Russia

[2] Materials Research Department, Risø National Laboratory, DK-4000 Roskilde, Denmark

Keywords: Twin Boundaries, Grain Boundary Planes, Copper

Abstract

Misorientations and grain boundary planes of twin boundaries are determined by the TEM technique in annealed copper with a nearly random texture. Straight segments on the long sides of twins are associated with {111} planes. The potential of TEM and SEM methods for determination of GB planes is discussed.

Introduction

The idea of grain boundary (GB) engineering [e.g.1], i.e. manipulation of fractions of CSL boundaries has been intensively exploited in the past 20 years. It has been also recognized that the inclination of GB planes may be important in GB engineering [e.g.2].

For investigations of GB planes, conventional TEM techniques [e.g.3-5] have been used for a long time. Unfortunately, most TEM works consider a quite limited number of boundaries. In recent years, scanning electron microscopy with the EBSD technique has been employed for studies of grain boundary planes and GB misorientations [e.g.6-10]. Inspections of mutually perpendicular sections or parallel sections before and after polishing allows one to reveal the inclination of boundary planes in bulk samples. The latter method gives larger statistics since large sample areas can be inspected and it has been used in a number of studies [7-10]. Some possible problems associated with the use of this method are considered herein. For extended planar boundaries such as twin boundaries, a relatively simple TEM technique [e.g.11,12] can be used for determination of GB planes. Our new results of a TEM investigation of GB planes of twin boundaries are presented in this work along with a discussion of the potential of the TEM and SEM techniques.

Experimental

High purity copper was 50% cold rolled and annealed at 773K for 2h to produce a nearly random texture and high fractions of Σ3 boundaries [13]. Misorientations and GB planes of twin boundaries were determined by the TEM method [12,14]. A technique [14] allows a rapid recognition of GB planes and involves tilting a foil such that a boundary has a minimum image width. The minimum image width of straight segments of twin boundaries was obtained at a tilt position where one of the <011> zone axes was parallel to the incident electron beam. The angle between the traces of a twin boundary and the closest {111} plane indicates the angular deviation of the GB plane from the {111} plane.

Results

Twin boundaries in one of the investigated regions are shown in Fig.1. Indexes correspond to GB planes of the long straight segments of twin boundaries.

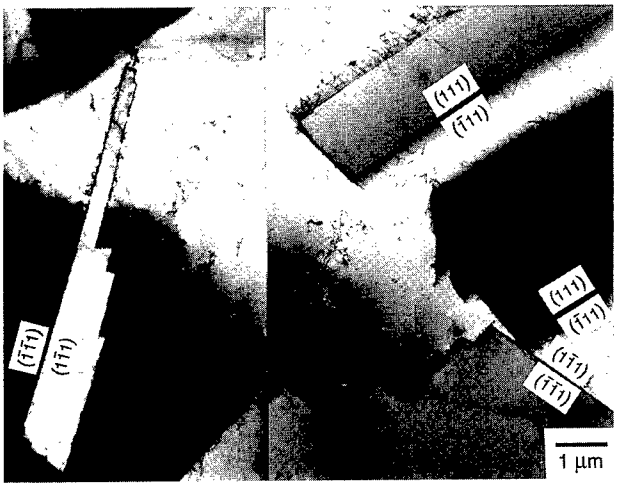

Fig. 1. Twin boundaries in annealed copper.

All misorientations at twin boundaries were very close (<3°) to the exact Σ3 relationship, this is typical of TEM experiments [e.g.15]. In fact, the deviation for only 5 boundaries exceeds 2°. Following [9,10,15], all deviations were normalized to the maximum allowable deviation according to the Brandon criterion for a Σ3 boundary, i.e. $\Delta\theta_c$=8.66°. Fig.2 shows the distribution of the normalized deviations.

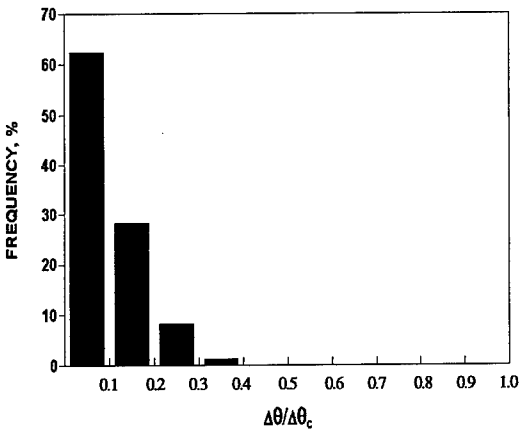

Fig. 2. Normalized deviations from the exact Σ3 relationship.

There were many steps at twin boundaries (see Fig.1). A thorough investigation of several foils indicated that the size of such steps varied from several nanometers to several microns. At some boundaries, more than ten steps were observed within relatively short GB lengths.

In this communication we do not consider GB plane indexes on the short sides of island or peninsular lammelar twins and on steps. Extremely short lengths of many of them did not permit precise measurements of angular deviations from the traces of low index planes. Some relatively coarse facets revealed different GB plane inclinations.

When straight long side segments of 75 boundaries were inspected, all their GB planes were within 3° from the exact {111} planes both in matrix and twin grains, i.e. were symmetrical tilt (coherent) twin boundaries (see Fig.1).

Potential of TEM and SEM techniques

Here we consider some aspects of the TEM and SEM approaches for measuring GB planes. In many TEM techniques, a large number of micrographs must be analysed to index GB planes. Therefore, the statistics of TEM works are not as high as can be achieved by SEM, where large specimen areas are investigated. In particular, many GB traces can be inspected using serial sectioning [e.g.7-10]. The latter procedure includes recording the co-ordinates of the boundary position before and after removing a layer of known thickness. The angle β between the GB trace and a reference axis (Fig.3a) is used for calculations of GB plane indexes [8]. It is considered that a plane which connects two GB images before and after sectioning (Fig.3b) is a true GB plane. However, the GBs are not necessarily planar. Therefore, the large population of GBs, where GB planes have been investigated in a SEM, are twin boundaries [6-10]. These boundaries are easily recognized by their straight morphology along long sides of twins.

Some SEM findings claim that long straight twin boundaries in many cases were asymmetrical tilt boundaries with different grain boundary plane indexes on both sides of the boundary, while coherent {111}/{111} boundaries constitute only 9-30% from all twin boundaries [6-10]. Most of the TEM works [e.g.3-5], however, recognize that these straight twin boundaries have {111}/{111} GB plane indexes, whereas different GB planes can be associated with steps (facets) or short sides of twins [3,4]. The latter results were also obtained in our experiment. Obviously, there is a certain discrepancy in the recognition of coherent twin boundaries when GB planes are studied by TEM and SEM methods.

It is important to note that during serial sectioning, the inclination of the GB plane within the removed layer is only assumed. According to [9], the thickness of this layer is expected to be at least 20 μm. Over such a distance, several steps of different size can be easily found at twin boundaries (Fig.1). Through faceting, twins can form quite different configurations even though twin boundaries appear as planar interfaces in the 2D section [16]. If such steps appear in the sectioning direction, the angle β does not reflect the actual inclination of the GB plane (Fig.3c). The inclination of GB plane of each facet can be substantially different from that calculated from the angles β between GB traces in two inspected sections. Certainly, after sectioning it is already impossible to know whether such facets existed in the removed layer.

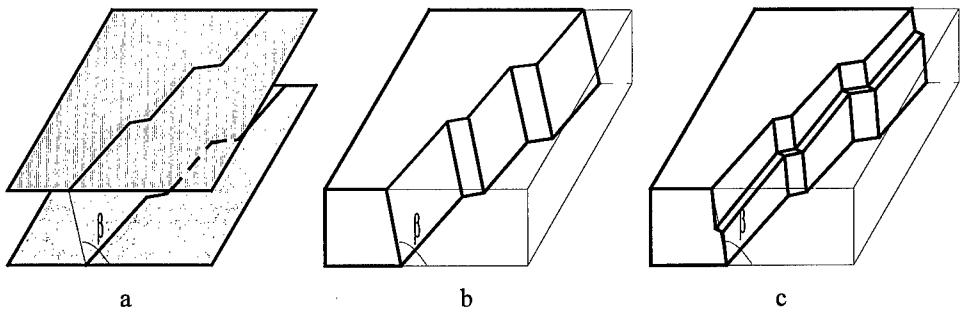

Fig.3 Reconstruction of a twinned region from GB traces after serial sectioning: (a) GB traces on the surface before and after sectioning; planes without (b) and with a facet (c) in the sectioning direction. In (b) angle β is related to the true GB plane, whereas in (c) it does not reflect the actual inclination of the GB plane.

Whereas a proper determination of the GB planes is conditioned by the absence of steps in the sectional direction (see also [17]), different indexing results can be obtained in their presence. The situation seems better, when GB traces are investigated in two mutually perpendicular sections [e.g.6], however, again certain caution is necessary, since fine steps can hardly be resolved in a SEM, in particular at low magnifications. Alternatively, one-grain-thick specimens can be studied at high magnifications. For example, Lin and Pope investigated 20 twin boundaries in such Ni_3Al specimens [18]. They found that 18 (90%) boundaries were either symmetrical {111}/{111} (65%) or {112}/{112} (25%) boundaries.

TEM methods avoid such an ambiguous situation with twin facets. First of all, the number and spacing of steps at twin boundaries can be clearly estimated due to better resolution at high magnifications. GB planes are determined in a very thin layer, which is the thickness of the transparent foil area (usually much less than 0.5 μm). Fine steps through the foil thickness can be distinguished, since in this case, no sharp GB image can be achieved by tilting the foil. The differences in resolution of twin steps by TEM and SEM techniques might explain the discrepancy in recognition of GB planes of long straight twin boundaries. Certainly, we do not discount that different fractions of coherent twin boundaries result from differences in material chemistry and thermomechanical prehistory. However, one should be aware that unobserved twin facets may have an effect on the indexing results.

Acknowledgements

The authors are grateful to Dr. D.Juul Jensen for useful discussion and encouragement. Dr. Q.Liu is acknowledged for valuable technical discussions.

References

[1] T. Watanabe, *Res. Mechanica* **11**, 47 (1984).
[2] V. Randle, *Acta Mater.* **46**, 1459 (1997).
[3] S. Dash and N. Brown, *Acta Metall.* **11**, 1067 (1963).
[4] C. M. Sargent, *Trans. AIME* **242**, 1188 (1968).
[5] G. D. Sukhomlin and A. V. Andreeva, *Phys. Stat. Sol. (a)* **78**, 333 (1983).
[6] V. Randle, *Mater. Sci. Techn.* **7**, 985 (1991).
[7] V. Randle, *Acta Crystallogr.* A**50**, 588 (1994).
[8] V. Randle, *Mater. Char.* **34**, 29 (1995).
[9] V. Randle, *J. Mater. Sci.* **30**, 3983 (1995).
[10] M. Caul, J. Fiedel and V. Randle, *Scripta Mater.* **35**, 831 (1996).
[11] J.W. Edington, Practical Electron Microscopy in Materials Science, Philips Techn. Libr., 1975.
[12] X. Huang and Q. Liu, *Ultramicroscopy* (in press).
[13] O. V. Mishin, *Proc. iib' 98, this volume.*
[14] Q. Liu, *Ultramicroscopy* **60**, 81 (1995).
[15] V.Y.Gertsman and K.Tangri, *Phil. Mag. A*, **64**, 1319.
[16] J. Bystrzycki, W. Przetakiewicz and K. J. Kurzudlowski, *Acta Metall. Mater.* **41**, 2639 (1993).
[17] R. L. Fullman, *J. Appl. Phys.* **22**, 456 (1951).
[18] H. Lin and D. P. Pope, *Acta Metall. Mater.* **41**, 553 (1993).

Materials Science Forum Vols. 294-296 (1999) pp. 405-410

Grain Boundary Wetting in Metals: "Self Indentation-Internal Solution" Mechanism

E.E. Glickman

Tel Aviv University, Faculty of Engineering, Israel

Keywords: Non-Mullins Grooving, Finger-Like Profile, Dynamical Dihedral Angle, Surface Tension Imbalance Force, GB Self Diffusion and Deposition, Diffusional Creep, Liquid Diffusion, Wetting Transitions

ABSTRACT

Under the thermodynamic condition of grain boundary wetting (GBW), the imbalance between GB and solid -liquid interphase surface tensions γ_{GB} and γ_{SL} creates a linear force applying at the root of the GB groove and pointing into the solid. The *"indentation"* action of this force is suggested to cause stress- driven self diffusion (diffusional creep) into the GB slab. This process drains the groove and leads to the deposition of the solid atoms along the GB (*"internal solution"*). Assuming that the GB acts as a perfect sink, this *"self indentation -internal solution" (SIIS)* mechanism can account for the non-Mullins morphology and linear kinetics of GBW, the origin of the singular stress field at the wetting front, the expansion of the solid under GBW, the role of external stress, and the GBW transitions with temperature. The mechanism is considered in more detail in [1] where a summary of GBW observations in metals is also given.

I. INTRODUCTION

Many free of stresses solid metals (SM) wetted with liquid metals (LM), which are presaturated with respect to the SM to prevent any gross dissolution and have large enough volume to ensure simultaneous wetting of both GB's and surface, experience penetration of capillary liquid films along GB's[1-6]. This process of GBW is thermodynamically justified when

$$S = \gamma_{GB} - 2\gamma_{SL} \geq 0 \qquad (\text{at } T > T_{WI}) \qquad (1)$$

This happens above a GBW transition temperature T_{WI} because γ_{SL} normally decreases with T much faster than γ_{GB}.

The kinetic mechanism of GBW is not clear; the problem is far even from an adequate experimental formulation because the available kinetic and morphological data are not numerous and rather scattered. A summary of the GBW data for bi- and poly-crystalline metals [1] shows that typically the width h of LM channel observed at GB's is several μm's, linear penetration kinetics apparently prevalent, and the penetration rates V= l/t lie mostly in the range $(10^{-1} \div 10^{-3})$ μm/s. Most of the data (ten systems) reviewed in [1] relate to GBW which proceeds at high normalized temperature $0.65 \leq T/T_M \leq 0.96$ in the presaturated LM's. T_M is the melting point of the SM. In two systems (Al-Ga and Zn-Ga), GBW experiments performed at much lower $0.32 \leq T/T_M \leq 0.43$ show $V \approx (0.1 \div 1)$μm/s and $h \approx (0.1\text{-}1)$ μm.

To explain the GBW mechanism , one needs to understand why, where , and how fast the SM goes from the channel filled then by the LM. Generally, GBW can be viewed as a kind of thermal grooving problem.

Application of the classical Mullins mechanism [7,8], is however not straightforward since for S>0, the equilibrium dihedral angle $\theta_0 = 2\cos^{-1}(\gamma_{GB}/2\gamma_{SL})$ becomes zero, therefore *invalidating the central Mullins postulate of a mechanical equilibrium existing at the groove root.* For this reason, the modified version of the Mullins theory proposed in [5] which accounts for possible GB diffusion of the LM in the solid, but ignores the inevitable lack of mechanical equilibrium at the root under the GBW condition, also does not apply.

Vogel and Ratke first pointed out [5] to that the finger- like shape of a GBW channel clearly differs from that characteristic of Mullins type groove observed in SM-LM couples below T_{WI} [5,8], Fig.1a,b. Additional point which is suggested by the GBW observations in bicrystals [3-6] and deserves in our opinion special consideration is that the *actual* non-zero angle established at the root (θ_d in Fig. 1b) is different from the *apparent* dihedral angle $\theta_A \rightarrow 0$. For example, we found from the tangents to the groove profiles presented in Refs.[3] and [5] that $\theta_d = 110 \pm 15$ deg. and 70 $\pm$ 20 deg., respectively , for Cu-In and Al-In couples; the figures are closer to $\pi/2$ than to zero.

Clarke and Gee [1] speculated that GBW perhaps can be considered in terms of creep cavity growth along GB at high temperatures, no analysis of this kind has been performed yet. The SIIS mechanism outlined in our paper explores in essence the line of attack proposed in [1].

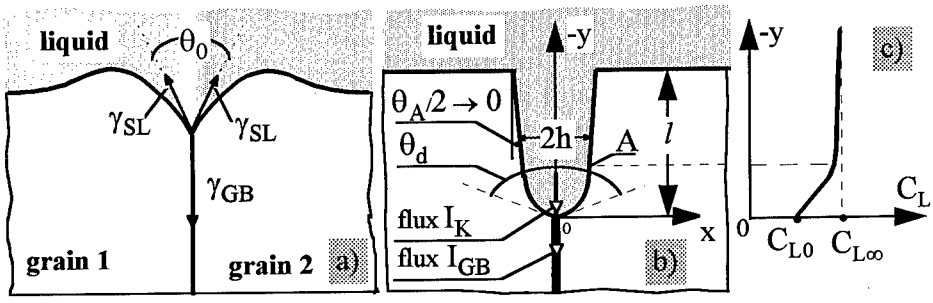

Fig.1 Schematic conceptual profiles: (a) of a Mullins groove, (b) of finger like channel characteristic of GBW, and (c) of solute concentration $C_L(y)$ along the liquid- filled channel.
In **(a):** Walls have convex-up profile (the curvature K>0) everywhere. They intersect at the tip forming the equilibrium dihedral angle θ_0 . Two ridges deposit at the external surface near the groove mouth. In **(b):** Flat walls form the channel with the width 2h and the apparent dihedral angle $\theta_A \to 0$, a non-zero angle θ_d develops at the root. At $y \approx 2h$ from the root, the walls are nearly tangent to convex-down (K<0) section. Regular ridges are not seen. This conceptual profile follows from the microscopical observations of GBW in bicrystals [3-6]. In **(c):** $C_{L\infty}$ and C_{L0} are respectively the solute concentration C_L in equilibrium with a flat surface and with the surface of local negative curvature near the root. In the x direction, $C_L(y)$ across the channel is assumed constant.

II. "SELF-INDENTATION- INTERNAL SOLUTION" MECHANISM of GBW

II-1.THE MODEL

1.Under the GBW condition expressed in the Eq.(1), the equilibrium angle $\theta_0 = 2\cos^{-1}(\gamma_{GB}/2\gamma_{SL})$ is zero and loses its physical meaning because the liquid *phase* has no access to the root. It is reasonable to assume that instead of θ_0 , a minimum "dynamical" angle θ_d which *ensures an intimate contact between the LM phase and the SM* should be established and kept *at the root.* Since the interatomic forces in metals act over a short distance $f \approx (1 \div 2)a$ which is close to an atomic diameter a , a rather large angle θ_d is required to ensure the "intimate contact" between the liquid phase and SM. Assuming that the minimum thickness of a liquid phase g is about $(2 \div 4)a$, the angle $\theta_d = 2tg^{-1}(g/2f)$ should lie in the range $(75 \div 125)$ deg. This naive estimate is in reasonable agreement with the above experimental observations.

2.Regardless of the exact value of θ_d , the balance between the surface tensions γ_{GB} and γ_{SL} at the root does not exist for S>0. An imbalance linear force $F_{YY} = \gamma_{GB}\{1-[\cos(\theta_d/2)/\cos(\theta_0/2)]\}$ applied to the GB-liquid intersection at the root points *into the solid* and produces a corresponding compressive stress

$$\sigma_{YY} = F_{YY}/\delta = \gamma_{GB}\{1-[\cos(\theta_d/2)/\cos(\theta_0/2)]\}/\delta \qquad (2)$$

3.The gradient $\nabla\mu = (\nabla\sigma_{YY}\,\Omega)$ causes a GB diffusion flux I_{GB} of solid atoms from the root *into the GB*, Fig.1b, and their deposition here:

$$I_{GB} = (D_{GB}\delta/kT)\cdot(\nabla\sigma_{YY}\,\Omega) = (D_{GB}\Omega/kT)\cdot(F_{YY}/L) \qquad (3)$$

Here D_{GB}, δ, and Ω are, respectively, the GB self diffusion coefficient, GB width, and atomic volume. L is the characteristic distance between dislocation- like defects which serve as the sinks in the GB structure. The flux I_{GB} drains the groove.

4.Our *primary assumption* is that the GB acts as a *perfect sink* for atoms in that the grains can move apart as the solid material deposits at the GB. This assumption (common in Nabarro-Herring and Coble theories of diffusional creep in pure metals [9]) implies that such stress relaxation processes as differential deposition along GB's, emission of dislocations into the grains, or /and GB migration and sliding are not controlling the overall penetration rate.

5. It is instructive to consider the parallels between the described groove draining process and the diffusional creep of thin metal foils under the action of free surface tension γ_{SV} which causes their "spontaneous" shrinkage in the Udin type zero-creep experiments [10]. As in our approach, in these experiments the stress caused by γ_{SV} is also treated as the uniaxial compressive stress $\sigma_{SV} = \gamma_{SV}/H$, applied to the butt end of the foil , H being here the foil thickness. Once the GB

is assumed to be a perfect sink, σ_{YY} acts as a microscopic analogue of σ_{SV} and causes a continuous shrinkage of the GB slab in the y direction (by diffusional creep process with characteristic "bulk" viscosity $\eta_{YY} \approx kTL^2/D_{GB}\Omega$ [9]).

6.To maintain $\theta = \theta_d$, the flux I_{GB} which tends to sharpen the dihedral angle and eliminate thus the contact between the liquid and solid phases at the root should be coupled with a flux I_K

$$I_K = -2C_{L\infty} D_L h \nabla K \gamma_{SL} \Omega / kT = I_{GB} \qquad (4)$$

I_K represents the diffusion flux of "solid" atoms dissolved in the LM; their concentration along the channel is given by $C_L(y) = C_{L\infty} \exp [K(y) \gamma_{SL} \Omega / kT]$, i.e. considered to be in equilibrium with the local wall curvature K(y), Fig.1c. D_L and $C_{L\infty}$ are, respectively, the diffusion coefficient and equilibrium solubility of SM in LM. The flux $I_K \propto -\nabla K$ points towards the root and restores the angle θ_d provided that the curvature K is more negative near the root than farther from it. This is actually consistent with the observations, Fig.1b.

7.Deepening of the channel occurs due to inevitable divergence of the flux I_K at the point A, Figs.1b,c, where the curved section meets flat walls. I_K depletes the liquid of solute thus causing dissolution of the walls in the curved section , the curved section breaks out from the remained flat surface thus forming ultimately finger-like profile which extends with the velocity V:

$$V = -\mathrm{div}\, I_K = \mathrm{div}\, 2(C_{L\infty} D_L h \nabla K \gamma_{SL} \Omega / kT) \qquad (5)$$

Eqs.(2)-(5) close the problem which , except for the origin of the flux I_{GB} , is essentially identical to that of GB grooving under an arbitrary external GB flux, including the stress- driven flux which drains GB cavities under creep [11,12].The velocity V and the profile can be found by solving Eqs.(4)and (5) with the appropriate boundary conditions. We shall restrict our discussion here to the rough estimates of the channel width 2h and the penetration rate V by using a simple approximation $(1/h)^2 \approx \nabla K$ and $V = -\mathrm{div}\, I_K \approx I_K / h$ [12]. Eqs.(2-5) then yield:

$$h \approx D_L \gamma_{SL} C_{L\infty} L / D_{GB} \gamma_{GB} m \qquad (6)$$

$$V \approx (D_{GB} \gamma_{GB} m)^2 \Omega / D_L \gamma_{SL} C_{L\infty} L^2 kT , \qquad (7)$$

where

$$m = 1 - [\cos(\theta_d/2) / \cos(\theta_0/2)] \qquad (8)$$

II-2. COMPARISON WITH THE EXPERIMENTAL DATA

Eqs(6-8) fit to the V and h observations made at $0.64 \le T/T_M \le 0.95$ and reviewed in [1] if we use $710^{-6} \le L \le 510^{-5}$ cm. For example, a good agreement with the data (T/T_M=0.7, linear kinetics, penetration rate $V = 710^{-2}$ μm/s, h=(3÷5) μm) for rather representative couple, polycrystalline Ni-liquid Bi [13], is obtained at $L = 8 \cdot 10^{-6}$ cm [1].[1] A distance of the order of 10^{-5} cm between dislocations and/or ledges which act as sinks in GB's is quite reasonable, in particular because the GB viscosity $\eta_{YY} \approx kTL^2/D_{GB}\Omega \approx 0.3$ MPa·s calculated with $L \approx 10^{-5}$ cm is still several order of magnitude larger than an ideal viscosity of random high angle GB given by $\eta_{GB} \approx kT / 2\pi D_{GB} \Omega^{1/3}$ which manifests itself in GB internal friction and sliding experiments with diffusional accommodation in pure metals at high temperature.

In summary: the mechanism outlined captures the major morphological features and the linear kinetics of GBW observed *at T above≈ 2/3 T_M* . Furthermore, it enables to understand (i) the origin of a singular stress-strain field observed recently at the GBW penetration front [14], (ii) a volumetric expansion of solids observed during GBW in polycrystalline ceramics and metals [15,16], (iii) an arresting action of small (≈ 1MPa) uniaxial compressive stress which almost stopped GBW in columnar-grain Zn [17], and (iv) fast GB migration which attends GBW and was shown to disobey classical DIGM scenarios [18]. A parabolic GBW kinetics [5] can be attributed within this framework to the stress relaxation controlled regime [19].

The SIIS mechanism offers also a simple explanation of what is called *"GBW transitions" with temperature* [1-6,20,21].We consider them as the changes in the *kinetic regimes* of GBW (Fig.2), rather than as a GB phase transition.

In field I, where $S \ge 0$ and therefore $\theta_0(T) = 0$, the above discussed regime of "complete" GBW (parallel walls) operates. In field II , $S \le 0$; to compensate for $2\gamma_{SL} > \gamma_{GB}$, the GBW morphology with the parallel walls ($\theta_A = 0$) is bound to change to

[1] The relevant parameters used in the calculations: $D_{GB} = 710^{-11}$ and $D_L = 510^{-9}$ m²/s, $\gamma_{GB} = 0.75$ J / m² , $(2\gamma_{SL}/\gamma_{GB}) = 0.9$, $C_{L\infty} = 0.35$, and $\theta_d = \pi/2$

that with $\theta_A>0$ ("partial" GBW). Because $0<\theta_0(T)$ is still below θ_d, the imbalance force $F_{YY}= m\gamma_{GB}$ continues to exist. The SIIS mechanism, which requires only *flat* but not necessarily parallel walls, can continue thus to operate. The angle $\theta_0(T)$ ultimately reaches θ_d at $T= T_{W2}$. At this temperature , the surface tension balance restores at the root, the force F_{YY} thus disappears; the classical Mullins GB grooving mechanism takes over at $T\geq T_{W2}$ (field III) causing dramatic change in the surface morphology, Fig.2, and the penetration kinetics.

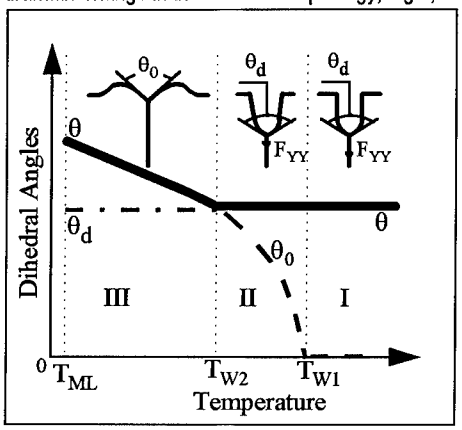

Fig.2 Schematic description of the temperature transitions from complete GBW (field I) to partial GBW (II), and ultimately to Mullins grooving (III).
$\theta_0(T)=2\cos^{-1}(\gamma_{GB}/2\gamma_{SL})$ is the equilibrium dihedral angle, θ_d is "dynamical" angle which ensures wetting at the root. Solid line: the angle θ (T) which actually forms at the root. F_{YY} is the imbalance surface tension force which develops at $\theta_0(T)<\theta_d$ and drains the groove by the GB self -diffusion. T_{ML} is the melting point of the liquid metal.

Low-temperature GBW (penetration rate $(0.1\div1)\mu m/s$ observed at $T/T_M\leq 0.43$ in Al and Zn wetted with Ga [14,17,22]) *is hard to explain within the SIIS mechanism* because the GB diffusivity D_{GB} is far too small. It should be noted that in in-situ TEM experiment [14], Ga definitely was not presaturated with Al. Regarding another studies[17,22] performed in air ambient , information on the Al and Zn content in Ga is not available. Even with precautions taken to ensure initial presaturation , the equilibrium can hardly be kept throughout the time of exposure of Al and Zn to LM because both metals have very high affinity for oxygen and, when dissolved in LM, experience continuous oxidation on its surface at RT. Presumably, fast low-temperature penetration [14,17,22] can be attributed to the corrosive attack of Ga. It is known that even moderate general corrosion rate V_{cor} can lead in SM-LM systems to rather fast GB penetration [23,24].

III. CONCLUSIVE REMARKS

Experimentally, the SIIS hypothesis can be best tested by systematic measurements of the volumetric expansion during GBW , in particular the *directional* expansion expected for bicrystals and bamboo-like polycrystals. Conceptually, kinetics of stress relaxation and the role of LM component diffusion ahead of the groove root remain to be considered.

IV. ACKNOWLEDMENTS

Extensive discussions with Profs. M. Nathan and E. Rabkin are gratefully acknowledged. This work was partially supported by the Grant #96722-97 from the Israel Ministry of Science.

V. REFERENCES

1.E.E.Glickman and M. Nathan, submitted to JAP
2.D. R. Clarke and M. L. Gee, in: "Materials Interfaces" (edited by D. Wolf and S. Yip), p.255, Chapman & Hill, London (1992)
3.B. Straumal, T. Muschik, W. Gust and B. Predel, Acta Metall.Mater., **40**, 939 (1992)
4.B.B. Straumal, W. Gust and D. A. Molodov, Interface Science, **3**, 127 (1995)
5.H. J. Vogel and L. Ratke, Acta Metall. Mater., **39**, 641 (1991)
6.B.Straumal, E. Rabkin, W. Lojkowski, W. Gust and L. S. Shvindlerman, Acta Metall.Mater, **45**, 1931 (1997)
7.W. W. Mullins, J. Appl. Phys., **28**, 333 (1957); Trans.TMS-AIME, **218**, 354 (1960)
8.M. Robertson, Trans. Met. Soc. of AIME, **233**, 1232 (1965)
9. J. Cadek, Creep in Metallic Materials, Academia, Prague (1988), 212
10.E. D. Hondros, Proc. Roy. Soc. A, **275**, 479 (1965)
11.L.M.Klinger, E. E. Glickman, V.E. Fradkov, W.W. Mullins and C. L. Bauer, J. Appl. Phys.,**78** , 3833 (1995);
12.W. W. Mullins, Met. and Mater. Trans., **26A**, 1917 (1995)
13. R. F. Cheney, F. G. Hochgraf , and C. W. Spencer, Trans. TMS-AIME, **221**, 492 (1961)

14.R. C. Hugo and R.G. Hoagland, Scripta Metall. Mater., **38**, 523 (1998)
15.T. M. Shaw and P. R. Duncombe, J. Am. Ceram. Soc., **74**, 2495 (1991)
16. A. F. Lisovskyi, Migration of Metal Melts in Sintered Composite Solids , Naukova Dumka, Kiev (1984), p.256 (in Russian)
17.L. A. Pogosyan, Yu. V. Gorjunov, N. V. Pertzov and V. Yu. Traskin, Proc. Moscow State University, Chemistry, **15**, 589 (1974) (in Russian)
18.E. Rabkin, W. Weygand, B. Straumal, V. Semenov, W. Gust and Y. Brechet, Phil. Mag. Lett.,**73**, 187 (1996)
19.E.E.Glickman and Nathan , to be published
20.E. I. Rabkin, L. S. Shvindlerman and B. B. Straumal, Int. J. Mod. Phys., B **5**, 2989 (1991)
21.B. Straumal and W. Gust, Mat. Forum, **207-209**, 59 (1996)
22.V. Yu. Traskin, Z. N. Skvorzova, V. I. Kukshev, N. V. Perzov and E. D. Schukin ,Sov. J. Colloids , **44**, 62 (1982) (in Russian)
23.V.E. Fradkov, Scripta Metall. Mater, **30**, 1599 (1994)
24.B. S. Bokstein, L. M. Klinger, I. V. Apukhtina, Mater. Sci. Eng., **A 203**, 376 (1995)

For rapid communication:
Tel: 972-2-642-83-42
Fax: 972-3-642-35-08
E-mail: EVGENY@ENG.TAU.AC.IL

Materials Science Forum Vols. 294-296 (1999) pp. 411-414

Tie Lines of the Grain Boundary Wetting Phase Transition in the Zn-Rich Part of the Zn-Sn Phase Diagram

B.B. Straumal[1,2,3], W. Gust[1] and T. Watanabe[3]

[1] Institut Für Metallkunde, Seestr. 75, D-70174 Stuttgart, Germany

[2] Institute of Solid State Physics, Russian Academy of Sciences, Chernogolovka, RU-142432 Russia

[3]Department of Machine Intelligence and Systems Engineering, Faculty of Engineering, Tohoku University, 980-77 Sendai, Japan

Keywords: Contact with Liquid Phase, Zn-Sn System, Grain Boundary Phase Transitions

ABSTRACT

The temperature dependence of the contact angle θ at the intersection of Zn grain boundaries with Zn/liquid Zn-Sn boundaries have been studied. For this purpose, two Zn bicrystals were grown with $<10\bar{1}0>\{1000\}$ tilt boundaries having misorientation angles of $\phi=16°$ (small angle grain boundary) and $\phi=60°$. These boundaries possess different energies. The temperatures T_w of the grain boundary wetting phase transition for these two boundaries were determined and the corresponding tie lines in the two-phase (Sn)+L field of the Zn-Sn phase diagram were constructed. Above T_w the contact angle θ is 0° and a layer of liquid phase substitutes for the grain boundary. The temperature of the wetting transition (T_{w1} = 382±1°C) for the boundary with the high energy ($\phi=60°$) is lower than that (T_{w2} = 386.5±1°C) for the boundary with the low energy ($\phi=16°$). Above the temperature interval where all the grain boundaries become wetted, the solid phase may exist only as isolated single crystalline "islands" in the "sea" of melted phase.

INTRODUCTION

The properties of modern materials, especially those of superplastic, nanocrystalline or composite materials, depend critically on the properties of internal interfaces such as grain boundaries (GBs) and interphase boundaries (IBs). All processes which can change the properties of GBs and IBs affect drastically the behaviour of polycrystalline metals and ceramics [1]. GB phase transitions are one of the important examples of such processes [2]. Recently, the lines of GB phase diagrams began to appear in the traditional bulk phase diagrams [2–4]. The addition of these equilibrium lines to the bulk phase diagrams ensures an adequate description of polycrystalline materials. One of the most important GB phase transitions is the *GB wetting transition.* Consider the contact between a bicrystal and a liquid phase L (Fig.1). If the GB energy σ_{GB} is lower than the energy of two solid/liquid interfaces $2\sigma_{SL}$, the GB is not wetted and the contact angle $\theta>0$. If $\sigma_{GB} > 2\sigma_{SL}$ the GB is wetted by the liquid phase and $\theta=0$. If the temperature dependencies $\sigma_{GB}(T)$ and $2\sigma_{SL}(T)$ intersect, then the GB wetting phase transition proceeds at the temperature T_w of their intersection. The contact angle θ decreases gradually with increasing temperature down to zero at T_w. At $T>T_w$ the contact angle $\theta=0$. The *tie line of the GB wetting phase transition* appears at T_w in the two-phase region *(S+L)* of the bulk phase diagram. Above this tie line GBs with an energy σ_{GB} cannot exist in equilibrium with the liquid phase. The liquid phase forms a layer separating the crystals. A decrease of the contact angle θ down to 0 at T_w was first observed in polycrystalline samples; in later

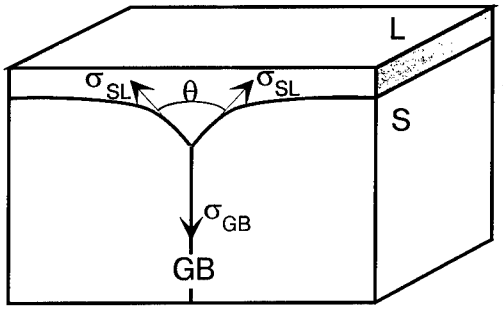

Fig. 1. Bicrystal in contact with a liquid phase. The GB is not wetted: θ>0.

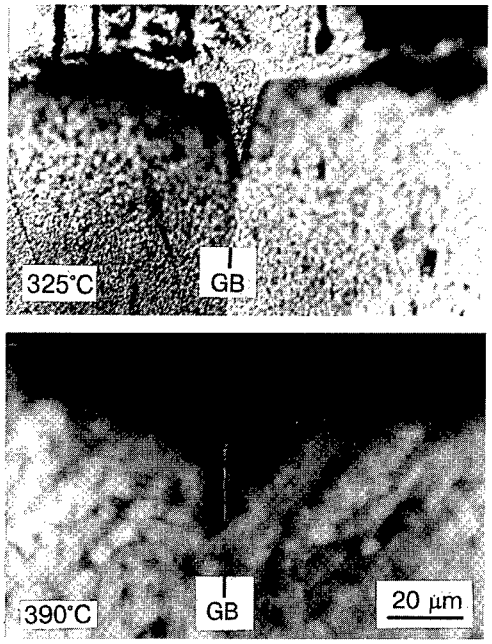

Fig. 2. Optical micrographs of the contact areas between the Zn bicrystal (bottom) and the Sn-rich melt (top) after anneals at 325 and 390°C and subsequent quenching.

measurements bicrystals with individual GBs were also used [2]. The goal of this work was to construct experimentally the GB wetting tie lines in the Zn–Sn system in the field where solid Zn and Sn-rich melt coexist. The investigation of GB phase transition lines in Zn-based binary systems is driven by the technological importance of Zn alloys. For example, Zn–Sn alloys are regarded as a good alternative to Pb-containing solders, the usage of which will be gradually restricted due to the detrimental influence of Pb on the environment [5].

EXPERIMENTAL

There is experimental evidence that the GB wetting phase transition exists in the Zn–Sn system, but the temperature T_w was determined for polycrystalline samples [6, 7]. It is not correct to define the tie lines of the GB wetting transition in the bulk phase diagram using two-phase polycrystals with boundaries of different energies because of the dependence of T_w on GBs energy. The bicrystals with $<10\bar{1}0>$ tilt GBs were grown from Zn of 99.999 wt.% purity by the Bridgman technique, which allows one to grow bicrystals with GBs of all possible crystallographic parameters [8]. The Zn used for the bicrystal growth contained 1.0, 0.5, 0.5 and 1.0 mass ppm (parts per million) of Pb, Cd, Cu and Fe, respectively. At intermediate stages of bicrystal production the single crystalline seeds were chemically polished for 1–5 s in HNO_3 and etched in HCl. They were oriented using Laue back reflection and cut with the aid of spark erosion. Finally, the orientation of the crystallographic axes of the bicrystals were controlled with the aid of Laue back reflection. Flat 38×6×180 mm bicrystals with the flat GB laying parallel to the long axis of the bicrystal and to the $<10\bar{1}0>$ axes of both grains were grown in high purity graphite crucibles in an atmosphere of high purity argon (the oxygen concentration was equivalent to a vacuum of 10^{-3} Pa). Two bicrystals with $<10\bar{1}0>\{1000\}$ tilt GBs having misorientation angles of $\phi = 16\pm0.5°$ (small angle GB, near Σ1 misorientation) and $\phi = 60\pm0.5°$ were produced. After growing, the bicrystals were cut by spark erosion and a diamond disk wire (Struers Minitom) into 4×6×10 mm pieces. For the wetting experi-

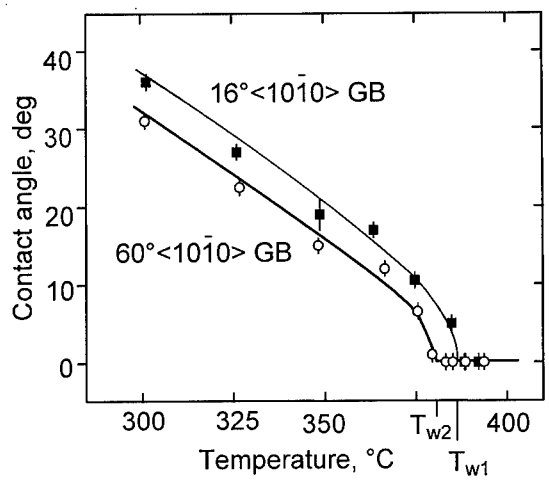

Fig. 3. The temperature dependence of the contact angle θ for the two GBs studied. The wetting temperatures are and T_{w1} = 381±1°C and T_{w2} = 386.5±1°C.

ments the Zn bicrystals were etched for 10–30 s in HNO_3 in order to remove the deformed layer and brought in contact with the liquid Sn of 99.999 wt.% purity at about 240°C in an apparatus made from high purity graphite. The samples had 0.2–0.4 mm thick Sn layers on both sides. The ratio between the length of the Zn bicrystal and the thickness of the Sn-rich layer was selected so that the average sample composition during the subsequent anneal was in the two-phase field of the Zn–Sn phase diagram [9]. The Zn bicrystals coated with the Sn-rich layers were then placed in silica ampules filled with high purity Ar. The samples were then annealed for 50 min at various temperatures between 300 and 394°C and subsequently quenched into water. After that a surface parallel to the $<10\bar{1}0>$ axes of both grains and perpendicular to the GB and solid/liquid interface was ground and polished. The polished surface was etched in HCl for a few seconds. The contact area between the GB and IB was photographed in an Olympus BH optical microscope with magnifications of 500:1 and 1000:1, and the contact angle θ was measured.

RESULTS AND DISCUSSION

Figure 2 shows optical micrographs of the $16°<10\bar{1}0>\{1000\}$ GB for 325 and 390°C. At 325°C the GB is still not wetted by the liquid phase and the contact angle $\theta > 0$. At 390°C the GB is already wetted and $\theta = 0$. The temperature dependences of the contact angles of both GBs studied are shown in Fig. 3. The contact angle θ decreases in both cases with increasing temperature. At all temperatures below T_{w1} the contact angles for the GB with $\phi = 60°$ are lower than those for the GB with $\phi = 16°$. This means the energy σ_{GB2} is really lower than σ_{GB1} as was presumed during the selection of the GB misorientation parameters. At the temperature T_w the GB wetting phase transition happens: at $T>T_w$ the contact angle $\theta = 0$. Both GBs studied have different temperatures of the wetting phase transition: T_{w1} = 381±1°C for the 60° GB with a high energy and T_{w2} = 386.5±1°C for the 16° GB with a low energy. Figure 4 shows the Zn–Sn bulk phase diagram along with the tie lines T_{w1} and T_{w2} of the GB wetting transition for the GBs studied. The borders of bulk phase fields are represented by thick lines and the GB wetting tie lines by thin lines. The values of the contact angle θ change in the temperature interval studied (down to 120°C below from T_w) from 30–40° to 0°. In the same interval lie the θ values in Zn–Sn polycrystals [7]. In the Al–Sn system θ increases up to 80° with decreasing temperature, but in the interval about 120°C below T_w the contact angles are also below 50° [3]. Using the value of σ_{SL} = 150±30 mJ/m^2 for the Zn–Sn system at 200°C [10], one can estimate the energy for our GBs at 250°C as σ_{GB} = 280±60 mJ/m^2. The absolute difference (σ_{GB1}–σ_{GB2}) is about 4 mJ/m^2 and lies well below the accuracy of the σ_{SL} value.

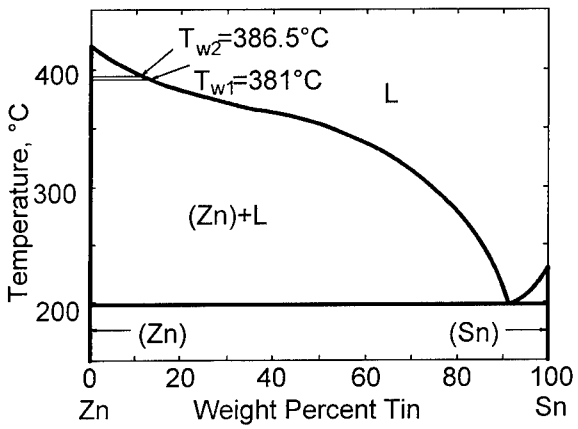

Fig. 4. The Zn–Sn bulk phase diagram (thick solid lines) [9] along with the tie lines of the GB wetting transition (thin solid lines) at T_{w1} = 381±1°C for the 60° tilt GB and T_{w2} = 386.5±1°C for the 16° tilt GB.

The tie lines of the GB wetting transition lie in the temperature interval, where the solubility of Sn in the liquid phase decreases very rapidly with decreasing temperature. In systems like Al–Sn [3] or Al–Cd [11] the GB wetting temperatures also coincide with the temperatures where the liquidus line has a low concentration slope. This is not surprising because in this case the difference between the liquidus and solidus concentrations decreases very fast with increasing temperature. The same is true for the surface tension of the solid/liquid interface σ_{SL}. Therefore, it is possible that $2\sigma_{SL}$ will be lower than σ_{GB} above a certain temperature. The most important feature of the GB phase transition is that below T_w the GBs can exist in equilibrium with the melt. Above T_w conversely the same GBs cannot exist in contact with the melt having the equilibrium liquidus concentration. The melt will penetrate along the GBs.

ACKNOWLEDGMENTS

This work has been partially supported by the Volkswagen Foundation (under contract I/71 676), Russian Foundation for Basic Research (grant 96-02-17483), INCO-COPERNICUS Network PL97-8078, PECHINEY Corporation and Heiwa Nakajima Foundation. We thank Prof. L. Shvindlerman, Dr. V. Sursaeva and S. Protasova for helpful discussions.

REFERENCES

[1] T. G. Langdon, T. Watanabe, J. Wadsworth, M. J. Mayo, S. R. Nutt, and M. E. Kassner, Mater. Sci. Eng. A 166 (1993) p. 237.
[2] B. B. Straumal and W. Gust, Mater. Sci. Forum 207–209 (1996) p. 59.
[3] B. Straumal, D. Molodov, and W. Gust, J. Phase Equilibria 15 (1994) p. 386.
[4] B. Straumal, T. Muschik, W. Gust, and B. Predel, Acta metall. mater. 40 (1992) p. 939.
[5] W. Müller, Metallische Lotwerkstoffe, DVS-Verlag, Düsseldorf (1990) p. 166 [in German].
[6] W. A. Miller and W. M. Williams, Canad. Metall. Quart. 2 (1963) p. 157.
[7] A. Passerone, N. Eustathopoulos, and P. Desrè, J.Less-Common Metals 52 (1977) p. 37.
[8] T. Watanabe, M. Yamada, M. Shima, and S. Karasima, Phil. Mag. A 40 (1979) p. 667.
[9] T. B. Massalski et al. (editors), Binary Alloy Phase Diagrams, ASM International, Materials Park, Ohio (1990, 1993) p. 3417.
[10] N. Eustathopoulos, Int. Met. Rev. 28 (1984) p. 189.
[11] J. H. Rogerson and J. C. Borland, Trans. Am. Inst. Met. Engrs 227 (1963) p. 2.

Corresponding author: D. Sc. Boris Straumal, e-mail straumal@issp.ac.ru and straumal@song.ru
web site http://www.issp.ac.ru/libm/straumal, fax +7 095 238 23 26 or +7 095 111 70 67

Materials Science Forum Vols. 294-296 (1999) pp. 415-418

Structure of Triple Line in Reactive Ag-Cu-Ti/SiC Wetting System

M. Nomura, T. Ichimori, Ch. Iwamoto and S. Tanaka

Tanaka Solid Junction Project, ERATO, Japan Science and Technology Corporation,
1-1-1 Fukuura, Kanazawa-ku Yokohama 236-0004, Japan

Keywords: Wetting, Chemical Reaction, Brazing, Interface, Titanium Silicide, TEM, SIM

Abstract

The structure around a wetting triple line in the specimen of 900-second-wetting was studied in an Ag-Cu-Ti/SiC reactive system. Preceding reaction products consisting of upper and lower double layers were observed in front of brazing metal front line. The upper layer characterized as Ti_5Si_3 had intervals and thickness beyond 20 nanometers. The lower layer had thickness less than 10 nanometers. Only lower layer was observed at the top of reaction layer exceeding the upper layer.

Introduction

One of the most important factors to characterize an interface structure which strongly affect the material properties is the interface formation mechanism. To design the interface structure for better material properties, well-understanding of the interface formation mechanism is required. Our group has focused attention on the brazing metal/ceramics reactive wetting which continuously forms the interface due to the spread of the molten brazing metal on the ceramics via chemical reactions, and the triple line where the interface is formed has been studied. The existence of a reaction layer preceding the metal front line and the structural change of the reaction layer as a function of wetting time have been reported in the Ag-Cu-Ti/Si_3N_4 system [1]. In this paper, we will report on the nanostructure around a triple line in an Ag-Cu-Ti/SiC system.

Experimental

A reactive brazing alloy with a composition of 67.7mass%Ag-27.4mass%Cu-4.9mass%Ti was melted and spread on the surface of a 6H-SiC single crystal substrate under a vacuum of 10^{-3} Pa in a vacuum chamber equipped with a heating system, where the surface of the substrate is a crystallographic basal plane . After the brazing metal spreading in 900 seconds, the specimens were

cooled down in the vacuum chamber, and wetting triple lines on the specimens were observed using a scanning ion microscope (SIM), SMI9800 (Seiko Instruments Inc.). Then the specimens were cut and ground into thin plates and then etched finely using a focused ion beam apparatus (FIB), SMI9800 (Seiko Instruments Inc.) into suitable thickness for transmission electron microscope (TEM) observation. Cross-sectional structures around the triple line were observed using the TEM equipped with a cold emission gun (FE-TEM), HF-2000 (Hitachi Ltd.). An energy-dispersive X-ray spectroscopy (EDX) analyzer equipped with the FE-TEM was sometimes used to characterize the reaction products.

Results and discussion

Complex structure was observed around the triple line in the Ag-Cu-Ti/SiC reactive system as shown in **Fig. 1**. The structure could be divided into three regions. The left area in the figure, having a zebra pattern due to eutectic structure, is the image of solidified brazing metal, the right light gray area shows the unwetted surface of SiC substrate, and the middle dark gray area shows the reaction product. The structure suggests that in the Ag-Cu-Ti/SiC system, the reaction product lies in front of the metal front line as in the Ag-Cu-Ti/Si_3N_4 system [1]. This implies that there is a possibility that the contact angle which has been measured as a parameter for wettability is that on the reaction product in the Ag-Cu-Ti/SiC system.

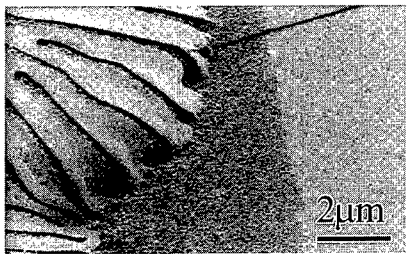

Fig. 1 Surface SIM image around the wetting triple line

By cross-sectional observation of the preceding layer using TEM, double layered structure was observed as shown in **Fig. 2** a) and an upper layer had intervals as shown in **Fig. 2 b)**. The upper layer is considered to be a Ti_5Si_3 because Ti and Si were detected from the upper layer as the main components by EDX analysis, and its diffraction pattern coincided with that of Ti_5Si_3. In the Ag-Cu-Ti/SiC and Ti/SiC systems, Ti_5Si_3, TiC and Ti-Si-C ternary compounds have been reported as reaction products at the interface [2,3]. From a lower layer, Ti and a little Si were detected by EDX analysis, thus two cases i.e. TiC or Ti-Si-C ternary compounds are considered, for the lower layer.

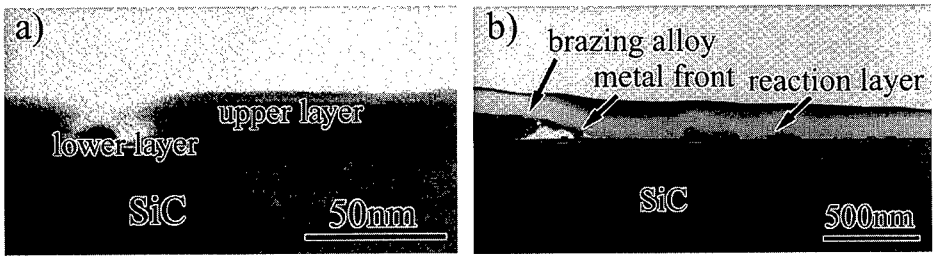

Fig. 2 Reaction products lying in front of the brazing metal front line
a): upper and lower double layered structure, b): intervals of the upper layer

Morphological features of the structure around the triple line in the Ag-Cu-Ti/SiC system are intervals of the upper layer and thin thickness of the lower layer less than 10 nanometers. In the Ag-Cu-Ti/Si_3N_4 system, almost the same double layered structure has been observed. However, the upper Ti_5Si_3 layer had no intervals and the lower TiN layer was a few times thicker than the lower layer in the Ag-Cu-Ti/SiC system at the rear of the metal front line [1]. This fact indicates that the amount of dissolved SiC which supplies component materials of reaction products was less than that of Si_3N_4. It has been reported that reacted interface between the Ag-Cu-Ti alloy and SiC tends to become flat by facing nucleated TiC to the basal plane of SiC [4]. This means that the most resistive plane of SiC for dissolution by the Ag-Cu-Ti brazing metal is the basal plane. In our study, since wetting was performed on the basal plane of SiC, it is considered that one of the reasons why for the low amount of dissolved SiC is the dissolution resistance of SiC basal plane. As for the upper Ti_5Si_3 layer, it had intervals in Ag-Cu-Ti/SiC system. Both in the Ag-Cu-Ti/SiC and the Ag-Cu-Ti/Si_3N_4 systems, no Ti_5Si_3 layer less than 20 nanometer-thick was observed. This fact suggests that there is a critical thickness of Ti_5Si_3, as has been reported for the solid/solid interface[5]. In order to grow beyond the critical thickness, in spite of low supply of component Si by SiC dissolution, it is considered that the upper Ti_5Si_3 was forced to form separately. However, no Ti_5Si_3 layer with intervals has been reported at the interface between metal phase and SiC in Ti/SiC or Ag-Cu-Ti/SiC systems [3,6,7]. Around the triple line, reaction time is very short, therefore it is considered that the separated Ti_5Si_3 layer was formed due to less reaction time for growth, too.

At the top of reaction layer, only lower layer was observed exceeding the upper layer. This suggests that the first step of reactive wetting at 900 seconds in the Ag-Cu-Ti/SiC system is the formation of the lower layer. Next, the Ti_5Si_3 upper layer formed, and then the brazing alloy spread on them.

Conclusions

In a Ag-Cu-Ti/SiC system, the structure around wetting triple line in the specimen of 900 second-wetting was studied and following conclusions were obtained.

1. Preceding reaction products consisting of upper and lower double layers were observed in front of the brazing metal front line.
2. The upper layer characterized as Ti_5Si_3 had intervals and thickness about 20 nanometers. The lower layer had a thickness less than 10 nanometers.
3. Only lower layer was observed at the top of reaction layer exceeding the upper layer.

References

1. M. Nomura, C. Iwamoto and S.-I. Tanaka, Proc. 2nd Int. Symp. on High Temperature Capillarity, (1997) in press
2. T. Iseki, T. Yano and Y.-S. Chung, J. Ceram. Soc. Jpn. Int. Ed., **97** (1989), 697.
3. M. Naka, J. C. Feng, and J. C. Schuster, Metall. Trans., **28A** (1997), 1385.
4. C. Iwamoto and S.-I. Tanaka, Acta Mater., **46** (1998) 2381
5. J. Philibert, Diffusion in Metals and Alloys, DIMETA-88, ed. By F. J. Kedves et al., Sci-Tech Pub., (1989), 995.
6. H. K. Lee, S. H. Hwang and J. Y. Lee, J. Mater. Sci., **28** (1993), 1765.
7. M. Backhaus-Ricoult, Ber. Bunsenges. Phys. Chem., **93** (1989), 1277.

Materials Science Forum Vols. 294-296 (1999) pp. 419-422

Atomic-Level Stresses at Interfaces and their Effect on Solute Segregation

O.C. Hellman and D.N. Seidman

Department of Materials Science and Engineering, Northwestern University, Evanston, IL, 60208 USA

Keywords: Grain Boundary, Segregation, Simulation, Atomic-Level Stress, Ni(Pd)

ABSTRACT

Segregation of a solute species to a grain boundary is known to be dependent on many factors, including strain, chemistry and crystal structure. We attempt to make general statements about the relationship of segregation to the stress calculated on an atomic scale. We find a relationship between local stress and segregation, but also show that the traditional definition for stress at an atomic site is only part of the influence of stress on segregation phenomena.

INTRODUCTION

The goal of this work is to tie together two different aspects of atomistic calculations concerning grain boundaries (GBs). The first is the calculation of stress on a site-by-site basis for each atomic site near a GB. The second is the calculation of preferential segregation of one atomic species to a GB.

The calculation of stresses on an atomic level was first fully developed by Born and Huang [1], who treated the problem in the framework of homogenous deformation of a solid, while Alber et al. [2] show how calculations for stresses at discrete sites relate to continuum elasticity theory. A number of workers [3-6] have developed interatomic potentials for atomistic calculations from which atomic stresses can be calculated and which are consistent with the demands of continuum elasticity theory. In particular, Sutton and Vitek [3] first showed hydrostatic stress maps near GBs using a density-dependent potential, while Foiles [4] presented an elegant derivation of the local stress from the embedded atom method (EAM) potentials [5].

Segregation to grain boundaries has been investigated by simulation for many systems [3, 5, 7-14]. All of these studies point to local elastic effects that cause some GB sites to be preferential sites for a solute atom. Sutton and Vitek [3] point to a qualitative relationship between segregation and local atomic stress for the systems Au(Ag), Cu(Ag) and Cu(Bi). Wang et al. [15] identify a similar relationship for Cu-Ni alloys, using an elegant vibrational approximation to calculate free energy, as outlined by Najafabadi et al. [7]. A paper from the same group [16] treats the relationship between local stress and segregation more rigorously for the case of segregation to an isolated dislocation, which shows a clear dependence of effective concentration at a site on the atomic-level stress. They found, however, that the exact dependence could not be replicated based on local stress alone, even by including a second order term. Here, we develop further the framework for understanding the influence of local stress on segregation behavior.

APPROACH

We use an EAM potential [5] for calculating energies of and forces between atoms, and use Foiles' expression [4] for local stress. A Monte Carlo-based technique for estimating the concentration of a solute on a site-by-site basis, following Seki et al. [8]. Our model alloy is Ni(Pd), as we expect that

the effects of chemistry in this system to be much smaller than the effect of stress (atomic size misfit). The calculation of local stress is performed on a minimum energy structure of a GB of pure Ni. The minimum energy configuration is found by switching between a Metropolis algorithm and a congugate gradient energy minimization algorithm many times, while the temperature used in the Metropolis activation energy calculation is slowly lowered. The segregation calculation is performed at a constant number of atoms, constant GB area, and constant temperature. The GB is constructed between two rigid but floating slabs of atoms. These slabs enforce the crystal orientation of each side of the GB. The GB area is adjusted for the effect of thermal and solute expansion. Two strategies for controlling the ratio of Ni to Pd have been used: a) that of using a fixed number of both species and a Monte Carlo algorithm incorporating swapping of neighboring atoms, and b) that of fixing the chemical potential difference between the two species and allowing for transmutation.

RESULTS

We show results for the case of the Σ =33 / (225) / 58.99° [110] symmetric tilt boundary, chosen because in one boundary it displays a range of different structures; in particular, this GB emits stacking faults to one side, resulting in an asymmetric structure containing both tensile and compressive regions [11]. At the cores of the emitted dislocations, the boundary between tension and compression is especially sharp, whereas the distribution elsewhere is more diffuse. The simulation cell contains 1300 particles, with a GB area of 29.16 Å x 10.15 Å. 84 atoms on each side of the boundary are constrained to be rigid, floating slabs. The structure found for the boundary in this simulation cell is essentially equivalent to that found for a much larger cell (> 4000 atoms), and thus the results of the simulation should not be perturbed by this choice of cell size. Figure 1 shows maps of the regions of tensile and compressive stresses. Figure 2 shows a concentration map for Pd for a simulation of a sample with a bulk concentration of 1.4 at.% Pd. Clearly, sites under tensile stress

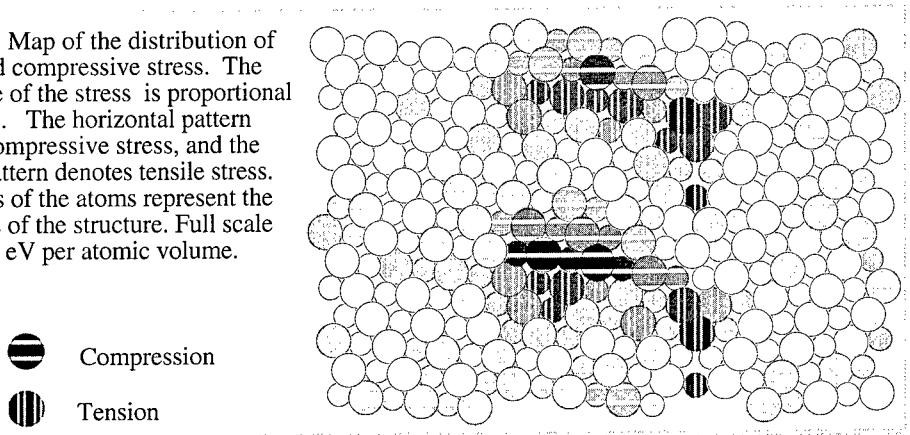

Figure 1. Map of the distribution of tensile and compressive stress. The magnitude of the stress is proportional to shading. The horizontal pattern denotes compressive stress, and the vertical pattern denotes tensile stress. Two sizes of the atoms represent the two layers of the structure. Full scale (dark) is 2 eV per atomic volume.

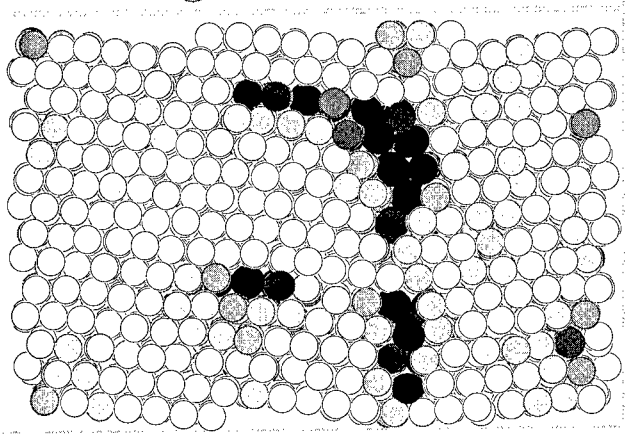

Figure 2. Map of the calculated site-by-site Pd concentration distribution at the grain boundary. Darker shading represents higher Pd concentration. Full scale (black) corresponds to 20 at.% Pd.

are preferential sites for segregation. Figure 3 shows this relationship quantitatively; ln((1-C) / C) is plotted here as a function of the trace of the stress tensor ($\sigma_{xx} + \sigma_{yy} + \sigma_{zz}$) calculated for the pure GB. The scatter in the data is due to the statistics involved in the Monte Carlo method (Fitting parameter Pearson's R = 0.729). To first approximation, the fit is linear, as suggested by Smith et al. [16]. We find that the Pd concentration at each site also shows a dependence on the stress at atoms in the vicinity of that site. We define a "local host stress" σ_h at a site p by summing the magnitude of the stresses at neighboring sites in the direction of site p:

$$\sigma_h = \sum_{i=1}^{n} V_i \left(\sigma_{xy,i} \bullet \hat{r}_i\right)_{\| \hat{r}} \quad , \qquad (1)$$

where the sum is taken over all the neighboring sites within the range of the EAM potential, which is is 4.8Å for the Ni potential. The quantity $\sigma_{xy,i}$ is the local stress at site i, and r_i is the vector from site p to site i. $\|r$ denotes the magnitude of a vector parallel to r, as is common when evaluating the magnitude of a tensor property in a certain direction [17]. This should be valid because of the centrosymmetric nature of the EAM potential. The term V_i is a first-order approximation of the relative importance of each neighbor in accommodating a volume change at site p:

$$V_i = r_i^{-3} \Big/ \sum_{j=1}^{n} r_j^{-3} \quad , \qquad (2)$$

where the sum is over the same neighbors as in Eq. 1. The exponent of minus three reflects the expectation that the nearer neighbors will have to relax more than more distant neighbors to accommodate any volume change at site p. In essence, we approximate atomic relaxation by point dilatation. This construction is similar to that of a "ball and matrix" model [18], except that we use discrete rather than continuum stresses. A plot of ln((1-C) / C) vs. local host stress is shown in Fig. 4. We emphasize that the local host stress for each site is calculated for the pure GB. The fit of the data is not as good as that in Fig. 3 (R = 0.610). However, we find that a further plot (not shown) of ln((1-C) / C) vs. ($\sigma_{xx} + \sigma_{yy} + \sigma_{zz} + \sigma_{host}$) improves the fit of the data (R = 0.752) to better than that in either Fig. 3 or Fig. 4 . If the dependence shown in Fig. 4 were a by-product of the dependence in Fig. 3 (i.e. a correlation effect), then the fit of the data should not improve, but instead be an average of those of Figs. 3 and 4. Thus we conclude that the local host stress is a real contribution to the effect of preferential segregation to certain sites.

Effectively, this is a separation of the stress of segregation into two components: relaxation of the stress at the site which contains the solute atom, and relaxation of the atoms surrounding the solute atom. The results are good despite the facts that we have assumed a simple distribution of relaxation among the neighboring sites, and have arbitrarily used the EAM potential cutoff radius. The results

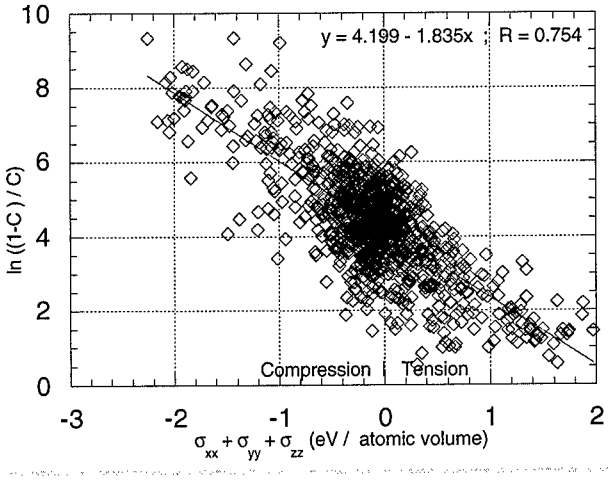

Figure 3. Plot of the Pd concentration versus the local stress on a site-by-site basis.

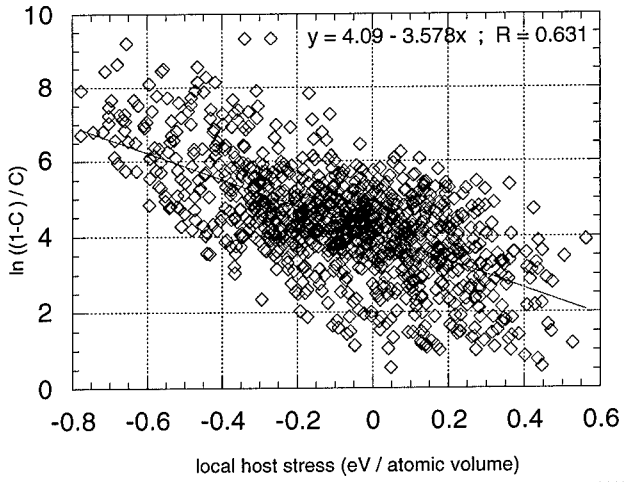

Figure 4. Plot of the Pd concentration versus the local host stress on a site-by-site basis.

should improve with more careful consideration of the atomic-scale relaxations, i.e. by performing the stress calculations in the presence of solute. This is a topic of continuing study.

CONCLUSION

We have shown that segregation to sites at a grain boundary (GB) is a function of the local atomic stress calculated for that site in a pure boundary. We have also shown a quantitative relationship between segregation to a site and the stress at neighboring sites. We have defined a measure of the "host stress" for each site, and shown that it is a contributing factor to the overall effect of stress on segregation. We point out that such calculations depend on a rigorous treatment of the local stress as a tensor property, and that the understanding of the local stress tensor is useful for generalizing the effect of stress on interfacial phenomena such as segregation. We speculate that the calculation could be improved by incorporating a comparison of the local stresses with and without solute at the GB.

Acknowledgements - This research is supported by the National Science Foundation, Division of Materials Research, Grant # DMR-9728986, B.A. MacDonald, Grant Officer.

REFERENCES

[1] M. Born and K. Huang, *Dynamical Theory of Crystal Lattices,* Oxford: Clarendon Press, 1954.
[2] I. Alber, J.L.Bassani, M. Khantha, V. Vitek and G.J. Wang, Phil. Trans. Roy. Soc. A **339**, 555 (1992).
[3] A.P. Sutton and V. Vitek, Acta. Metall. **30**, 2011 (1982).
[4] S.F. Foiles, Phys. Rev. B **32**, 7685 (1985).
[5] M.S. Daw and M.I. Baskes, Phys. Rev. B **29**, 6443 (1984).
[6] J.F. Lutsko, J. Appl. Phys. **64**, 1152 (1988).
[7] R. Najafabadi, H.Y.Wang, D.J. Srolovitz and R. LeSar, Acta Metall. Mater. **39**, 3071 (1991).
[8] A. Seki, D.N. Seidman, Y. Oh and S.M.Foiles, Acta Metall. Mater. **39**, 3167 (1991).
[9] D. Udler and D.N. Seidman, Interface Science **3**, 41 (1995).
[10] J.D. Rittner, D. Udler and D.N. Seidman, Interface Science **4**, 65 (1996).
[11] J.D. Rittner and D.N. Seidman, Acta Mater. **45**, 3191 (1997).
[12] D. Udler and D.N. Seidman, Acta Mater. **46**, 1221 (1998).
[13] X.Y. Liu, W. Xu, S.M. Foiles and J.B. Adams, private communication.
[14] E.S. Machlin and A. Levi, Scripta Metall. **14**, 127 (1980).
[15] H.Y.Wang, R. Najafabadi, D.J. Srolovitz and R. LeSar, Acta Metall. Mater. **41**, 2533 (1993).
[16] R.W. Smith, R. Najafabadi, and D.J. Srolovitz, Acta Metall. Mater. **43**, 3621 (1995).
[17] J.F. Nye, *Physical Properties of Crystals*, Oxford: Clarendon Press, 1957, pp. 24-25.
[18] A.P.Sutton and R.W. Balluffi, *Interfaces in Crystalline Materials*, Oxford: Clarendon Press 1995, pp. 426-27.

Materials Science Forum Vols. 294-296 (1999) pp. 423-426

Segregation and 2D-Compound in a Grain Boundary: An Exotic Behaviour

J. Creuze[1], F. Berthier[1], R. Tétot[1], B. Legrand[2] and D. Tanguy[2,3]

[1] LEMHE, U.A. CNRS 1107, Université de Paris XI, F-91405 Orsay, France

[2] SRMP-DECM, CEA Saclay, F-91191 Gif sur Yvette Cedex, France

[3] SMS, URA CNRS 1884, Ecole des Mines de Saint-Etienne, F-42023 Saint Etienne Cedex 02, France

Keywords: Segregation, Grain Boundary, 2D Compound, Monte-Carlo Simulation, Cu-Ag

Abstract : Using Monte-Carlo simulations coupling atomic displacements and change in chemical identity in the transmutational ensemble, we have studied the segregation isotherms for the different sites of the $\Sigma = 5$ (310) [001] tilt grain boundary in Cu (Ag) system. Even though the Cu-Ag system is characterised by a strong tendency to phase separation in the bulk, a 2D-ordered compound is obtained in the boundary plane for bulk concentration in the domain of the solid solution. The driving forces for segregation and compound formation are analysed and a statistical model is proposed.

1. Introduction

The relation between grain boundary segregation, two dimensional (2D) compound formation and precipitation has been studied in the pioneering work of M. Guttmann [1]. However, at this time, experimental evidences of 2D compounds in grain boundary were very scarce, as well as numerical simulations of grain boundary segregation. Since this time, a lot of Monte-Carlo simulations of grain boundary enrichment have been performed either in the domain of the solid solution in the bulk or for 3D ordered alloys [2]. However, only a few studies have been devoted to link the results of numerical simulations to statistical models on one hand [3] and to analyse the driving forces of grain boundary segregation on the other hand [4]. This is the aim of the present paper, in which we study segregation in a symmetrical grain boundary $\Sigma = 5$ (310) <001> in Cu (Ag) solid solution by atomistic simulation.

We first describe the interatomic potential and the relaxation algorithms (§2). The driving forces of intergranular segregation are then clearly identified in the dilute limit (§3). For more concentrated solid solutions, we obtain an unexpected result (§4) : a 2D ordered compound is stabilised in the grain boundary plane, even though the Cu-Ag system has a strong tendency to phase separate in the bulk ! This behaviour is then analysed within a regular solution model and a simple mean-field approximation (§5).

2. Methods of calculation

The many-body potential employed in this study is derived from the second moment approximation of the tight-binding scheme [5]. It is very similar to the one used in previous studies on surface [6] and on grain boundary structure in Cu-Ag system [7], except that at present the interactions are extrapolated to zero between second and fourth neighbour distances by fifth-order polynomials.

The segregation energy on a site i of the $\Sigma = 5$ (310) <001> grain boundary, ΔE_i^{seg}, is obtained in the dilute Cu (Ag) limit by the following balance [4] :

$$\Delta E_i^{seg} = E_i^{tot}(\text{solute}) - E_{bulk}^{tot}(\text{solute}) \qquad (1)$$

where E_i^{tot}(solute) (resp. E_{bulk}^{tot}(solute)) is the total energy of the system when one solute atom is at the i-site (resp. a bulk site). In each configuration the atomic positions are relaxed using quenched molecular dynamics [8].

For a finite concentration and at a given temperature, we obtain the equilibrium concentration on each site of the grain boundary by Monte-Carlo simulations coupling atomic displacements and change in chemical identity in the transmutational ensemble [8]. This is performed using a box of

7560 atoms with periodic boundary conditions in the three directions [310] (x), [$\bar{1}$30] (y) and [001] (z), see figure 1. This box contains 5 periods along the tilt axis, 4 periods along y and 94 (310) planes on each side of the boundary plane.

3. Segregation driving forces in the dilute limit

In figure 1 we show the most stable structure of the $\Sigma = 5$ (310) <001> grain boundary in pure Cu. It is very similar to the C structure obtained in previous works [9]. A characteristic feature of this structure is the existence of two different (002) planes along the tilt axis, the first one being more compressed than the second one (see figure 1). As a consequence the density of the (310) boundary plane is twice as large as the one of a (310) bulk plane (see figure 1c). Moreover the sites 1 and 1' belonging to this boundary plane are geometrically inequivalent. We then can expect a different segregation behaviour for these two sites.

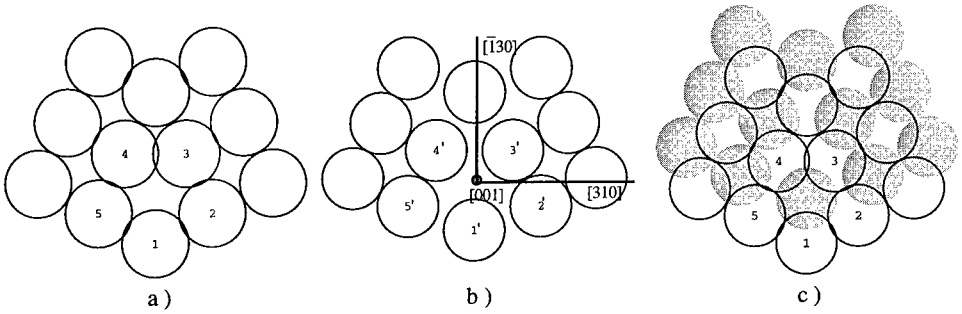

Figure 1: C structure of the $\Sigma = 5$ (310) <001> tilt grain boundary obtained after relaxation. The atoms 1, (2, 5) and (3, 4) belong to the first (002) plane (a), whereas the prime atoms 1', (2',5') and (3', 4') belong to the second (002) plane (b). A superimposition of these two planes along the tilt axis [001] is shown in (c).

We present in table 1 the segregation energies ΔE_i^{seg} obtained in the Cu(Ag) dilute limit for the main sites i of the grain boundary. Let us recall that a negative segregation energy indicates a segregation of the solute (here Ag). We can see that all the quoted sites are favourable to Ag segregation. Moreover, in the boundary plane, the site 1' is much more favourable to Ag occupancy than the site 1. We will see in the next section that this is at the origin of the formation of a 2D compound in the boundary plane.

sites i	1	(2, 5)	(3, 4)	1'	(2', 5')	(3', 4')
ΔE_i^{excess}	- 62	- 16	- 52	+ 57	- 15	- 11
ΔE_i^{size}	- 91	- 116	- 69	- 578	- 87	- 191
$\Delta \tilde{E}_i^{seg}$	- 153	- 132	- 121	- 521	- 102	- 202
ΔE_i^{seg}	- 138	- 131	- 119	- 565	- 99	- 204

Table 1: The various contributions to the segregation energy ΔE_i^{seg} on the different sites i of the grain boundary at T = 0 K in the Cu(Ag) dilute limit. $\Delta E_i^{excess} = E_i^{excess,Ag} - E_i^{excess,Cu}$ is the difference of site energy excess between pure metals, ΔE_i^{size} is the size effect and $\Delta \tilde{E}_i^{seg} = \Delta E_i^{excess} + \Delta E_i^{size}$ is the reconstruction of the segregation energy with the help of its two main components. All the energies are expressed in meV.

By analogy with superficial segregation, we decompose the segregation energy in two parts [10]:

- a first term, $\Delta E_i^{excess} = E_i^{excess,Ag} - E_i^{excess,Cu}$, which is the difference of site energy excess between pure metals. At the surface ΔE_i^{excess} is equal to the difference in surface energy between the two metals and is known to be the leading term for superficial segregation [11].
- a second term, ΔE_i^{size}, which corresponds to the size effect. It is evaluated by considering a virtual impurity which differs from the matrix only by its size, the atomic positions being relaxed by quenched molecular dynamics [12]. This atomistic treatment has shown the inadequacy of the elasticity approach to quantify this effect [13].

In table 1 we show that the segregation energy is very well reproduced by these two effects : $\Delta E_i^{seg} = \Delta E_i^{excess} + \Delta E_i^{size} \approx \Delta E_i^{seg}$. It means that the alloying effect [14], which has been well documented for surface segregation, is negligible in the present case, at least in the infinite dilute limit.

Moreover the size effect, ΔE_i^{size}, is the leading term for intergranular segregation, in contradistinction to superficial segregation, for which ΔE_i^{excess} is the dominant factor. In particular ΔE_i^{size} is at the origin of the large difference in segregation energy between sites 1 and 1' in the boundary plane.

4. Stability of a 2D compound

To obtain the equilibrium intergranular segregation for finite concentration at a given temperature, we have performed Monte-Carlo simulations coupling atomic displacements and change in chemical identity in the transmutational ensemble [8]. In a first time, we have considered a box without grain boundary to obtain the relation between the bulk concentration and the difference in chemical potential $\Delta\mu = \mu_{Cu} - \mu_{Ag}$. This calculation, performed at T = 900 K, leads to a solubility limit $c^{\alpha}_{Ag} = 0.005$.

We present in figure 2a the chemical structure of the grain boundary at T = 900 K for a bulk concentration (in silver) c = 0.0035, i.e. in the domain of the solid solution. We can observe a very large difference between the concentration of sites 1' ($c_{Ag} = 21\%$) and sites 1($c_{Ag} = 2\%$). This leads to the stability of an ordered 2D-compound, localised in the boundary plane itself. The structure of this compound is shown in figure 2b. Let us note that this compound does not have an equivalent in the bulk, due to the double density in the (310) boundary plane.

Let us dwell on the formation of a 2D-compound in a system which has a strong tendency to phase separate in the bulk ! It must not be confused with pre-precipitation of compounds in grain boundaries for systems which present ordered compounds in bulk phase diagram, such as M-S, M-P with M = (Ni, Cu, ...).

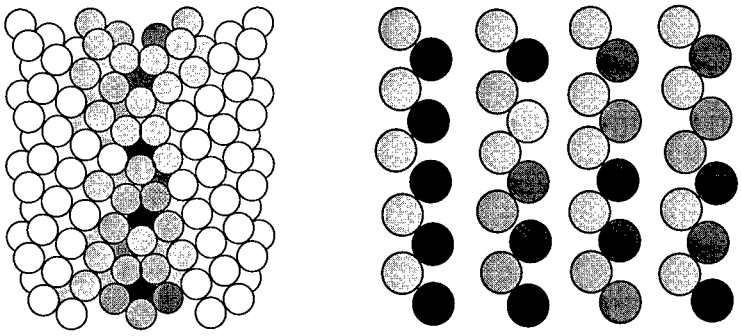

a) b)

Figure 2: Site concentration (in silver) for the Σ = 5 (310) <001> tilt grain boundary for a bulk concentration c = 0.35% at T = 900 K. The superimposition of the two (002) planes is shown in (a). A top-view of the 2D-ordered structure of the (310) boundary plane is shown in (b). The grey scale is such that the black sites are the most Ag-enriched ($c_{max} = 44\%$), whereas the white sites corresponds to $c_i < 0.35\%$.

5. Towards a statistical model

Performing Monte-Carlo simulations at T = 900 K for different $\Delta\mu$, i.e. for different bulk (silver) concentration c in the Cu-rich solid solution, we obtain segregation isotherm for each site i of the grain boundary. The i-site segregation isotherm is defined as the curve giving the i-site concentration c_i as a function of c at a given T. If we consider the bicrystal Ag_cCu_{1-c} as a stacking of p-planes parallel to the grain boundary plane, we can write the well-known relation [10] :

$$\frac{c_p}{1-c_p} = \frac{c}{1-c} \exp\left(-\frac{\Delta E_p^{seg}}{kT}\right) \qquad (2)$$

where c_p is the concentration of the p-plane and ΔE_p^{seg} is the segregation energy in this plane. To apply this formula, obtained within the Bragg-Williams approximation on a rigid lattice, we have to consider the boundary plane as two different planes composed respectively of sites 1 and 1'.

Let us recall that ΔE_p^{seg} is the sum of three contributions [10]:

$$\Delta E_p^{seg} = \Delta E_p^{excess} + \Delta E_p^{size} + \Delta E_p^{alloy} \quad (3)$$

The first two terms have been evaluated in the dilute limit and can be considered as constant as long as the crystallographic structure of the grain boundary is unchanged. The third one, which was negligible in the dilute limit, takes into account the interactions between solute atoms both in the bulk and in the grain boundary . This term is at the origin of a possible dependence of ΔE_p^{seg} with c [10].

Fitting the equation (2) on isotherms obtained by Monte-Carlo simulations for $0.00065 < c < 0.0035$ at T = 900 K yields the values of $\Delta E_i^{seg}(MC)$ shown in table 2. They are in very good agreement with those previously obtained in the infinite dilute limit at T = 0 K (ΔE_i^{seg}), except for the sites 1'. Work is currently in progress to study the influence of the alloying term on $\Delta E_{i'}^{seg}(MC)$. By taking into account this term, we can hope that a simple mean-field statistical approach, based on Eq. (2-3), will be efficient to model grain boundary segregation, as far as the energetic quantities are determined on each site by atomistic calculations.

sites i	1	(2, 5)	(3, 4)	1'	(2', 5')	(3', 4')
$\Delta E_i^{seg}(MC)$	- 120	- 159	- 120	- 346	- 105	- 190
ΔE_i^{seg}	- 138	- 131	- 119	- 565	- 99	- 204

Table 2: Segregation energy for the different sites of the $\Sigma = 5$ (310) <001> grain boundary obtained by Monte-Carlo simulations at T = 900 K for finite concentrations ($\Delta E_i^{seg}(MC)$) and by quenched molecular dynamics in the infinite dilute limit at T = 0 K (ΔE_i^{seg}). All the energies are expressed in meV.

Acknowledgement

We would like to thank J.L. Bocquet (SRMP, Saclay), A. Larère and L. Priester (LEMHE, Orsay) and G. Tréglia (CRMC2, Marseille) for helpful discussions.

References

[1] M. Guttmann, Met. Trans. A **8** (1977) 1383.
[2] D. Farkas, E.J. Savino, P. Chidambaram, A.F. Voter, D.J. Srolovitz and S.P. Chen, Phil. Mag. A **60** (1989) 433.
M. El Azzaoui, J.M. Penisson and V. Pontikis, Interf. Sci. **2** (1994) 79.
S.M. Foiles and D.N. Seidman in *Materials Interfaces: Atomic-level Structures and Properties*, eds. D. Wolf and S. Yip (Chapman & Hall, London, 1992), p. 497.
[3] M. Menyhard, M. Yan and V. Vitek, Acta Metall. Mater. **42** (1994) 2783.
[4] F. Berthier, B. Legrand, G. Tréglia and L. Priester, Mat. Sci. Forum **207-209** (1996) 701.
[5] V. Rosato, M. Guillopé and B. Legrand, Phil. Mag. A **59** (1989) 321.
[6] C. Mottet, G. Tréglia and B. Legrand, Phys. Rev. B **46** (1992) 16018.
[7] F. Berthier, B. Legrand and G. Tréglia, submitted to Phil. Mag.
[8] D. Frenkel and B. Smit, *Understanding Molecular Simulation: from Algorithms to Applications*, (Academic Press, San Diego, 1996).
[9] G.J. Wang, A.P. Sutton and V. Vitek, Acta Metall. **32** (1984) 1093.
A.P. Sutton and R.W. Balluffi, *Interfaces in Crystalline Solids* (Oxford University Press, New York, 1995) p. 405.
[10] F. Ducastelle, B. Legrand and G. Tréglia, Prog. Theor. Phys., suppl **101** (1990) 159.
[11] G. Tréglia, B. Legrand and F. Ducastelle, Europhys. Lett. **7** (1988) 575.
[12] G. Tréglia and B. Legrand, Phys. Rev. B **35** (1987) 4338.
[13] P. Wynblatt and R.C. Ku, *Interfacial Segregation*, eds W.C. Johnson and J.M. Blakely (American Society for Metals, Metals Park, OH, 1979) p. 115.
[14] A. Saúl, B. Legrand and G. Tréglia, Phys. Rev. B **50** (1994) 1912.

Materials Science Forum Vols. 294-296 (1999) pp. 427-430

Intergranular Segregation and Precipitation: Monte-Carlo Simulations

D. Tanguy[1,3], B. Legrand[2] and Th. Magnin[1]

[1] Ecole Nationale Supérieure des Mines de Saint-Etienne, Centre SMS URA CNRS 1884, 158 cours Fauriel, F-42023 Saint-Etienne Cedex 02, France

[2] SRMP/DECM, CEA Saclay, F-91191 Gif-sur-Yvette Cedex, France

[3] PECHINEY CRV, Parc Economique Centr' Alp, BP 27, F-38340 Voreppe, France

Keywords: Grain Boundary Segregation, Precipitation, Monte-Carlo Simulations, Al-Mg

Abstract: Monte-Carlo simulations have been performed to study the relation between intergranular segregation in the solid solution domain of the bulk phase diagram and the intergranular precipitation in the two-phase domain. We have studied the symmetrical tilt grain boundary $\Sigma = 5$ (310) [001] for a model alloy that partly has the characteristics of Al-Mg. We determine the driving forces for segregation at the infinite dilute limit, then we stress the rôle of interactions between segregated atoms in the grain boundary. The main result is the existence of a 3D ordered compound in the solid solution domain, that initiates in the grain boundary and developes over ten to fifteen [310] planes on every side of the boundary. This compound is different from the one stable in the bulk and is likely to prevent its preferential precipitation when the bulk composition raises (or the temperature decreases).

1. Introduction

The properties of the Al-Mg based alloys, which are at the origin of the present work, are limited by intense intergranular segregation. Since ordered compounds are of complex structures in this alloy, high resolution experimental characterisation seems difficult. Therefore, atomic scale simulations are a powerful tool to investigate the driving forces and mechanisms of segregation.

In this work we study the link between segregation defined as the enrichment of the grain boundary with respect to an element when the bulk concentration is in the solid solution domain, and intergranular precipitation which is the preferential location of the precipitates at the interface when the bulk is in the two-phase domain [1]. We will mainly focus on the appearance of a compound in the boundary while C_{bulk} remains in the solid solution.

This kind of modelisation requires the description of the grain boundary structure at the atomic scale. The most powerful algorithm to treat our problem is the Monte-Carlo simulation in the transmutational ensemble, since it combines relaxations and chemical nature changes of the atomic sites [2]. This leads to the optimisation of the grain boundary structure and of its chemistry.

We will first describe the semi-empirical potential [3] which roughly reproduces the characteristics of the Al-Mg alloy (Al rich) which are essential to our problem. They are mainly the existence of a solid solution and of an ordered compound separated by a coexistence region, as well as a critical temperature (Tc) for the order-disorder transition higher than 700K for the compound. Monte-Carlo simulations at T=300K allows us to estimate an isotherm of the model phase diagram. Then we will describe segregation on every atomic site as a function of the bulk concentration for the symmetrical tilt boundary $\Sigma = 5$ (310) [001] in the domain of the solid solution. By increasing the magnesium concentration towards the solubility limit, we will show that an ordered compound appears at the interface.

2. Model

The energetic model used for our study stems from the Tight Binding Second Moment Approximation [3]. Although it is more physically grounded for the transition metals than for Al-

Mg [4] it can be used as a semi-empirical potential, according to its ability to describe correctly a certain number of properties.
The energy of an atom on a site i is:

$$E_i = -\sqrt{\sum_{j,r_{ij}<r_c} \xi_{IJ}^2 \exp\left[-2q_{IJ}\left(\frac{r_{ij}}{r_0^{IJ}}-1\right)\right]} + \sum_{j,r_{ij}<r_c} A_{IJ} \exp\left[-p_{IJ}\left(\frac{r_{ij}}{r_0^{IJ}}-1\right)\right] \quad (1)$$

where r_{ij} stands for the distance between site i and j, respectively occupied by the chemical species I and J: {I,J}={Al, Mg}; r_c is the cut-off radius for the interactions (here beyond the second neighbours) and r_0^{IJ} is the first neighbour distance in the metal I ($r_0^{IJ} = (r_0^{II} + r_0^{JJ})/2$). Therefore the energy depends on three sets of four parameters ξ_{IJ} , A_{IJ} , p_{IJ} ,q_{IJ} which characterise the interactions Al-Al, Mg-Mg and Al-Mg. The parameters of the homoatomic interactions are fitted to reproduce the experimental values of the lattice parameter, the cohesive energy and the bulk modulus, as well as the trend of the universal equation [5].

The heteroatomic interactions are not fitted to the characteristics of the β phase (1173 atoms per unit cell) which is observed experimentally [6]. Instead, we chose to have a Tc higher than 700K which is approximately the temperature of the eutectic, for the simple ordered compound Al_3Mg on the fcc lattice. Three other conditions are needed for the fitting procedure: the lattice parameter and the bulk modulus for the Al_3Mg stoichiometry are taken as the arithmetic average of the pure metals values; furthermore, the compound has to satisfy the universal equation of state. The values of the parameters can be found in [7].

Monte-Carlo simulations were done in the transmutational ensemble at a fixed difference between chemical potentials: $\Delta\mu=\mu_{Al}-\mu_{Mg}$, zero pressure and at T=300K to determine an isotherm of the phase diagram (Figure 1a). The solid solution spreads up to 18%, whereas the two-phase domain (solid solution, ordered phase) lays between 18 and 23%. The precise crystallography of this compound is DO_{22} [8] (Figure 1b). The model phase diagram has then the essential properties to study the evolution of segregation when the bulk concentration is increased up to the limit of the solid solution.

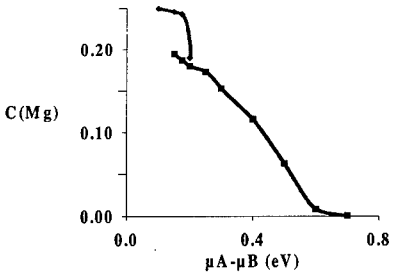

(a)

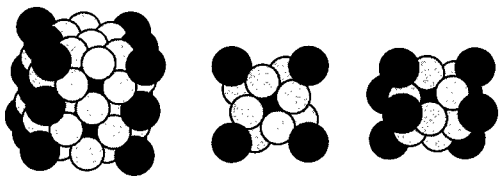

(b)

Figure 1: magnesium concentration as a function of $\Delta\mu=\mu_{Al}-\mu_{Mg}$ at T=300K, showing the stability domain of the solid solution and of the DO_{22} phase (b); DO_{22} and $D1_a$ phases (b).

3. Intergranular segregation

First of all, we have obtained the relaxed structure of the symmetrical tilt grain boundary Σ = 5 (310) [001] by Quenched Molecular Dynamics (QMD). The simulation box contains 4 structural units in the $[\bar{1}30]$ direction, 8 along [001] and 70 planes on every side of the interface. The box

contains only one grain boundary thanks to Möbius periodic conditions [9]. As in the previous work [10], the well known C structure (Figure 2) has the lowest energy.

At the infinite dilute limit, segregation energy maps are calculated by QMD, introducing only one impurity, first on a bulk site, then on every site in the interface [11]. Table 1 shows that sites « 0 » and « 2 » are the most favourable. By analogy with surface segregation, we try to correlate these results with the difference in excess energy, analogous to the difference in surface energy of the pure metals, and with the size effect correlated to local pressure. The agreement between sites under strong tension and sites with important negative segregation energy is good. Since $r_{Mg} \approx 1.13$ r_{Al}, size effect seems to be the dominant driving force when no interactions exists between solute atoms.

Table 1 : segregation energies ($\Delta E_i seg$), difference in excess energy (ΔE_i^{excess}) and local pressures ($p_i \delta\Omega$) on every interface site i (in eV), where $\delta\Omega$ is the difference in atomic volume between Mg and Al.

Site i	0	0'	1	2	3	4
$\Delta E_i seg$	-0,28	-0,02	-0,02	-0,1	-0,05	-0,04
ΔE_i^{excess}	+0,04	-0,06	-0,05	-0,01	-0,01	-0,01
$p_i \delta\Omega$	-0,73	+0,09	+0,07	-0,16	-0,07	-0,03

At higher bulk concentrations, these interactions cannot be neglected anymore and Monte-Carlo simulations are necessary. The segregation profile in the solid solution region of the phase diagram (C_{Mg}=6,3%, T=300K) is presented in Figure 3. Sites « 0 » are highly Mg enriched as predicted by the segregation tendency at the infinite dilution. On the contrary, the sites « 1 » to « 4 » are depleted although they were slightly favourable to Mg segregation in the dilute limit. This is a sign of the importance of the solute interactions. They can be described as the combination of local chemical ordering and relaxation propagation (80% of the « 0 » sites are occupied by big Mg atoms).

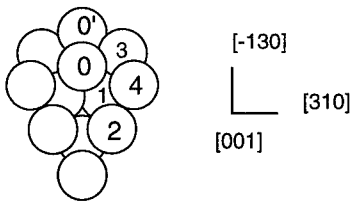

Figure 2: C structure of the Σ=5 (310) [001] tilt grain boundary.

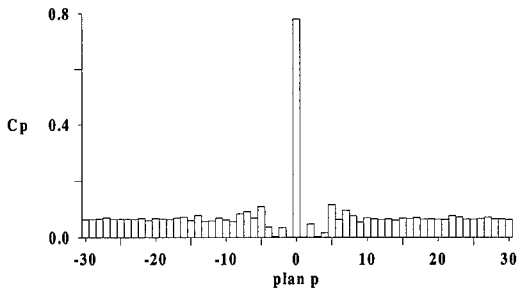

Figure 3: Mg concentration profile in the <310> direction perpendicular to the interface at T=300K and C_{bulk}=6,3%.

4. Intergranular precipitation

By increasing the bulk concentration, we get closer to the coexistence limit, but the composition we consider (C_{Mg}=17,3%) still belongs to the solid solution at T=300K (Figure 1a). Even if the statistics seems limited, the profile shown in Figure 4a confirms the trend observed at the lower concentration. Moreover, planes -5 and 5 are strongly Mg enriched, as well as plane 10 to a lesser extend. This profile corresponds to the precipitation of a $D1_a$ phase (Ni_4Mo) extending over a 3D zone of 10 (310) planes on every side of the boundary.

We have to stress that the $D1_a$ phase (Figure 1b) is not stable in the bulk with the potential we used. Therefore, this phenomenon does not correspond to the pre-precipitation of a bulk compound,

but to the equilibrium formation of an ordered phase specific to the boundary. One has to notice the registry between its unit cell and the coincidence site lattice of the Σ=5 grain boundary.

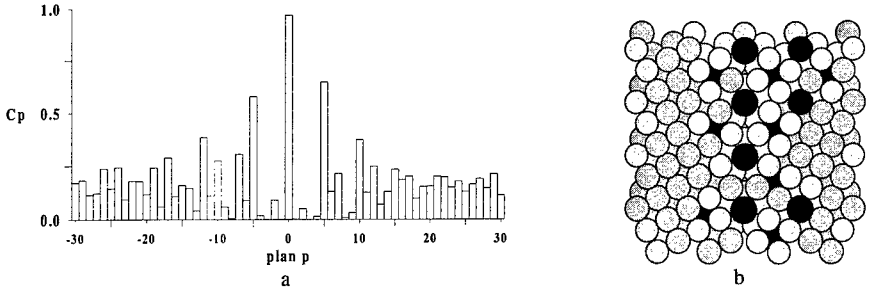

Figure 4 : Mg concentration profile in the <310> direction perpendicular to the interface at T=300K and C_{bulk}=17,3% (a); site concentrations (from the darkest to the clearer : C(Mg) ≥ 60%, intermediate, C(Mg) ≤ 1%) (b).

5. Discussion

By means of Monte-Carlo simulations, combining displacements and changes of chemical nature, this study has shown the existence of a 3D ordered compound extending over 10 planes on each side of the boundary. This phenomenon is surprising due to the fact that it occurs when the bulk is in the solid solution domain on the one hand and that the 3D grain boundary compound ($D1_a$ phase) is not stable in the bulk on the other hand.

One can wonder whether the pre-existing grain boundary compound will prevent preferential precipitation at the interface when C_{bulk} is higher than the solid solution limit or when T decreases. Preliminary results, though not totally converged, confirm this hypothesis. We have stressed the compatibility of $D1_a$ crystallography with the specific geometry of Σ = 5 (310) [001] grain boudary. Thus dependence of the phenomenon described above on the geometry of the interface remains to be studied.

Acknowledgement

The authors wish to thank : J.L. Bocquet, F. Willaime, M. Athènes, Y. Limoge, C. Gallis and C. Schmidt (CEA/SRMP), as well as F. Ducastelle (ONERA), F. Berthier (LEMHE - Orsay) and K. Wolski (EMSE) for the numerous and stimulating discussions concerning interfacial segregation.

References

1. M. Blakely, H.V. Thapliyal, in *Interfacial Segregation*, eds W.C. Johnson and J.M. Blakely (American Society for Metals, Metals Park, OH, 1979) p. 137.
2. S.M. Foiles, Phys. Rev. B **32** (1985) 7685.
3. V. Rosato, M. Guillopé and B. Legrand, Philos. Mag. A **59** (1989) 321.
4. J. Friedel, *The Physics of Metals*, eds J. Ziman (Cambridge University Press, London) 1969, p.340.
5. J.H. Rose, J. Ferrante and J.R. Smith, Phys. Rev. Lett. **47** (1981) 675.
6. M. Hansen, *Constitution of Binary Alloys* (McGraw-Hill, New York, 1958).
7. D. Tanguy and B. Legrand, J. Physique, under press.
8. F. Ducastelle, *Order and Phase Stability in Alloys* (North Holland, Amsterdam, 1991).
9. O.B.M. Hardoin Duparc and M. Torrent, Interface Science **2** (1994) 7.
10. D.A. Smith, V. Vitek and R.C. Pond, Acta Metall. **25** (1977) 475.
11. F. Berthier, B. Legrand, G. Tréglia and L. Priester, Mat. Sci. Forum **207-209** (1996) 701.

Email : tanguy@calcul.emse.fr

Materials Science Forum Vols. 294-296 (1999) pp. 431-434

Segregation of Atomic Probes and Interstitial Impurities in the Grain Boundary Core and Outside Grain Boundaries in 3d, 4d and 5d Metals

V.N. Kaigorodov, S.M. Klotsman, M.I. Kurkin and V.V. Dyakin

Institute of Metal Physics, Urals Division of Russian Academy of Sciences,
RU-620219 Ekaterinburg, Russia

Keywords: Grain Boundary Core, Segregation, Intercrystallite Diffusion, Metals

Abstract. The ^{57}Co atomic probe introduced by diffusion in polycrystalline metals enriches grain boundaries in polycrystalline Cr and W, depletes grain boundaries in Ta, and does not segregate at grain boundaries in Pd, Pt and Au. The isomer shift δ and the width Γ of two components of nuclear gamma-resonance (NGR) spectra used for investigation of segregation of residual interstitial impurities in the grain boundary core (segregation-1) and outside the grain boundary core (segregation-2). In segregation-2 residual interstitial impurities do not have the cubic symmetry and cause formation of similar complexes of point defects. In tungsten interstitial impurities possess the cubic symmetry in segregations-1. The change in the isomer shift δ_1 and the width Γ_1 of components-1 of NGR spectra in Ta, Cr, W, Pd, Pt and Au depends on the difference in valences of the atomic probe ^{57}Co and the matrix. The interaction energy in segregations of different types was determined.

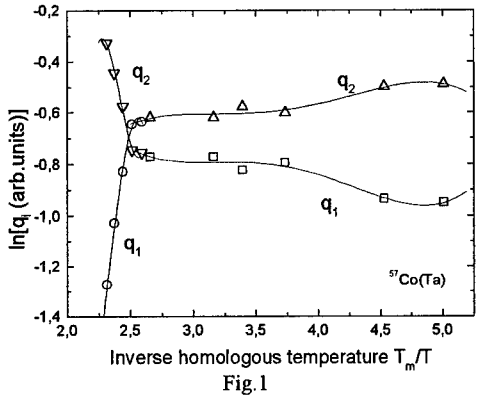

Fig.1

Arrhenius dependencies of the states-1 (q_1) and -2 (q_2) populations measured after isochronous annealings of ^{57}Co(poly-Ta) system.

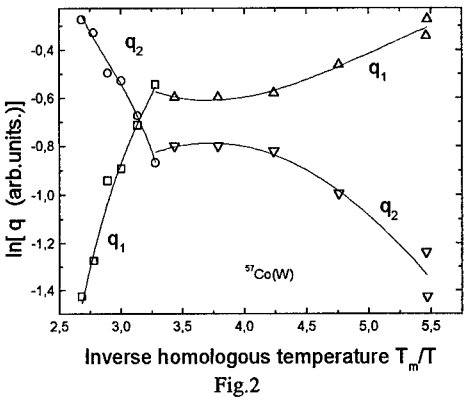

Fig.2

Arrhenius dependencies of the states-1 (q_1) and -2 (q_2) populations measured after isochronous annealings of ^{57}Co(poly-W) system.

I. Introduction. The new method [1,2] for analysis of the structure and the set of physical properties of the grain boundary core in polycrystals made it possible to derive separate information about interstitial impurity segregations localized in the grain boundary core and in adjacent two-dimensional regions of the lattice. This paper reports results of our investigations of the temperature dependencies of the interstitial impurity segregations in the grain boundary core and in the lattice regions adjacent to the grain boundary. Symmetry of segregating point defects were detected.

II. Results and Discussion.

II.1. Segregation of ^{57}Co atomic probes in the matrices studied. The description of the profile of atomic probes in the intercrystalline diffusion zone includes the segregation coefficient s of these atomic probes at grain boundaries. The ratio between the population by atomic probes of two types

of states localized in the intercrystalline diffusion zone at low annealing temperatures is given by the expression [3]:

$$q_1/q_2 = 2s(l/d), \qquad (1)$$

where q_1 and q_2 denote the population of states in and outside the grain boundary core respectively; d is the grain boundary core width; l is the segregation zone width. Figs. 1 and 2 exemplify temperature dependences $\ln q_i(1/T)$ for the ^{57}Co(W) and ^{57}Co(Ta) systems respectively. In ^{57}Co(Cr) and ^{57}Co(W) the coefficient $s>1$, $(q_1/q_2>1)$ and the ^{57}Co atomic probes enriches the GB. In ^{57}Co(Ta) the coefficient $s<1$, $(q_1/q_2<1)$ and the ^{57}Co atomic probes depletes the grain boundaries. In ^{57}Co(Pd), ^{57}Co(Pt) and ^{57}Co(Au) the ^{57}Co atomic probe does not segregate at the grain boundaries.

Tab.1 Segregation enthalpies Q_s (kJ/mole) for AP's-^{57}Co in BCC metals

Solvent	Ta	Cr	W
Q_s	- (5.0±1.2)	9.6±0.75	19.2±3.7

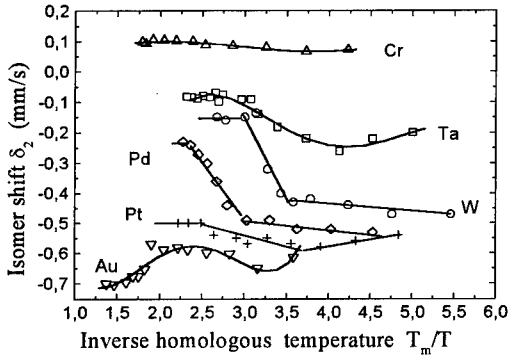

Fig.3

Temperature dependencies of the isomer shifts δ_2 of ^{57}Co in 3d,4d and 5d transition and noble polycrystalline metals. For clarity δ_2 values for different metals are shifted along the vertical axis.

II.2. Segregations-2 of interstitial impurities outside the grain boundary core.

The composition of atomic probe localization regions was determined from dependencies of the isomer shift and the width of the components of emission nuclear gamma-resonance (NGR) spectra on the impurity concentration, which was changed by annealing the samples at consecutively elevating temperatures. The isomer shift δ of the NGR spectra components depends on the density of inner-shell and valence s-electrons on the atomic probe nuclear. The change in the volume of the nearest neighborhood of the atomic probe is the main cause of changes of the isomer shift in metals [4]. The same volume factors largely determine the response of the NGR spectra parameters to appearance of impurity segregations in the intercrystalline diffusion zone of atomic probes. Obviously, most significant changes in the volume of the nearest neighborhood of the atomic probe may be due to interstitial impurities.

Interstitial impurities possess a positive excess charge in metals. Interstitial sites, which are nearest to the interstitial impurities, prove to be squeezed and forbidden for localization of other interstitial impurities [5]. At low homologous temperatures, when interstitial impurities can segregate, they form stable "vacancy– interstitial impurity" complexes [6].

The ^{57}Co atomic probe represented a substitutional impurity in the volume of all the solvents studied. Occupying lattice sites near grain boundaries in the intercrystalline diffusion zone ^{57}Co atomic probes underwent only medium volume changes caused by the increase or the decrease of the interstitial impurities concentration in these regions (segregations-2). The increase in the annealing temperature of the polycrystal was followed by the drop of the interstitial impurities concentration near grain boundaries. This was reflected in the corresponding *decrease in*

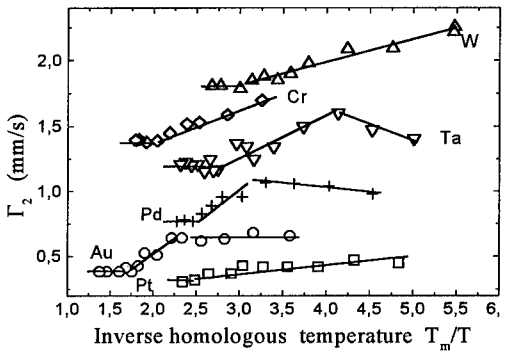

Temperature dependencies of the width Γ_2 of NGRS components-2 of ^{57}Co in 3d,4d and 5d transition and noble polycrystalline metals. For clarity Γ_2 values for different metals are shifted along the vertical axis.

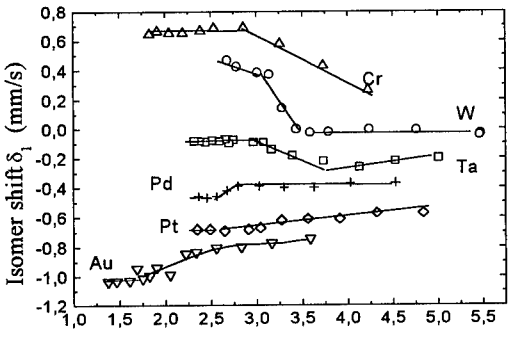

Fig.5

Temperature dependencies of the isomer shifts δ_1 of ^{57}Co in 3d,4d and 5d transition and noble polycrystalline metals. For clarity δ_1 values for different metals are shifted along the vertical axis.

the lattice parameter in the zone of the segregation-2. This decrease was accompanied by compression of the atomic probes and *growth of* δ_2 (Fig.3). The decrease of δ_2 within a narrow interval of low temperatures in Ta, Pt and Au reflected formation of the interstitial impurities segregation. The change of δ_2 was accompanied by changes (opposite in sign) of the width of the NGR spectrum component-2 (Fig. 4), as was found earlier for volume interstitial solid solutions in tungsten [7].

II.3. A new phenomenon arising during the decay of the interstitial impurities segregation-2 in tungsten.

During the high-temperature decay of interstitial impurities segregations-2 in tungsten a narrow and virtually two-dimensional space region near the grain boundary core turned to a diffusion source of point defects: interstitial impurities, vacancy–interstitial impurities complexes, etc. *A new phenomenon occurred, which consisted in expansion of the region with a high concentration of point defects (ERHCD) to the crystallite volume*. The ERHCD in tungsten took place at homologous temperatures, when the equilibrium volume concentration of vacancies was negligibly small. The flow of all point defects contained in the ERHCD caused a flow of substitutional ^{57}Co atomic probes from the grain boundaries to the crystallite volume. The latter flow had a surprisingly low activation enthalpy which was five (!!!) times lower than the volume activation enthalpy. This drop of the diffusion activation enthalpy of substitutional atomic probes was due to two reasons. First, the vacancy formation enthalpy did not contribute to the activation enthalpy of ^{57}Co atomic probes diffusion through ERHCD. Second, the migration enthalpy of atomic probes in the ERHCD decreased twice (!!) thanks to the "point defect wind" [8]. It is known that in tungsten ^{57}Co atomic probe strongly interact with vacancies [9]. Similar strong interaction of the small radius substitutional impurities with self- and impurity interstitials is known cause the radiation induced segregation [8]. Therefore entrainment of these atomic probes by the "point defect wind" appears to be quite natural. Tab.1 gives the parameters of interaction of point defects in the interstitial impurities segregation-2 between one another and with the grain boundaries.

II.4. Segregations-1 of interstitial impurities in the grain boundary core.

The annealing temperature dependencies of isomer shifts of the NGR spectra components-1 (Figs.5,6) proved to be qualitatively different for different solvents. In FCC solvents located in the Ni- and Cu-groups (Pd, Pt, Au) of the Periodic Table, when the excess charge (the difference between the impurity and solvents valences) of ^{57}Co atomic probes was $Z_{21}<0$, *δ_1 dropped with decreasing concentration of interstitial impurities* (Fig. 5) in the segregation zone (with increasing annealing temperature). The drop of δ_1 was followed by the decrease in the width Γ_1 of

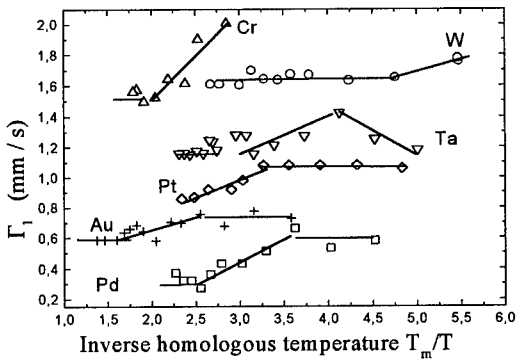

Fig.6

Temperature dependencies of the width Γ_1 of NGRS components-1 of ^{57}Co in 3d,4d and 5d transition and noble polycrystalline metals. For clarity Γ_1 values for different metals are shifted along the vertical axis.

the component-1 of the NGR spectra (Fig. 6), as one might expect when interstitial impurities having a non-cubic symmetry disappeared from the localization region of states-1. The drop of δ_1 caused by the decrease in the density of s-electrons at the atomic probe nuclear means that *the decrease in the interstitial impurities concentration was followed by the increase in the volume occupied by ^{57}Co atomic probes at interstitial sites of the grain boundary core* of these solvents.

These conditions may be realized for ^{57}Co atomic probes in the grain boundary core containing an interstitial impurities (IImp) segregation only if ^{57}Co atomic probes with $Z_{21}<0$ in these solvents are attracted to interstitial impurities ($Z_{IImp1}>0$) and occupy interstitial sites nearest to the residual interstitial impurities. The volume of such interstitial sites is reduced [5] and therefore the drop of the interstitial impurities concentration with elevating annealing temperatures is accompanied by the decrease in the number of these squeezed interstitial sites and the apparent increase in the volume of states-1.

Tab.1. Interaction energies (kJ/mole) between defects.

Solv.	$(E_{IImp})_2$	$(E_{IImp})_1$	$(E_{vIImpC})_2$	$(E_{vIImpC})_1$	E_{vIImpC}
W	7±1	—	38±7	100±12	57
Cr	—	—	23±5	20±3	356
Ta	—	—	30±6	50±9	327
Pd	1.6±0.4	2±1	96±32	50±9.1	—
Pt	—	7±3	23±7	62±30	106
Au	—	3.4±0.35	80±20	64±23	165

$(E_{IImp})_i$-interaction energy of a single IImp with regions of localization states-i; $(E_{vIImpC})_i$ -interaction energy of a complex vacancy-IImp with regions of localization states-i; E_{vIImpC} - interaction energy between partners in a complex vacancy-IImp

Correspondingly, the response of the parameters of the NGR spectra in this system to the drop of the interstitial impurities concentration is similar to the response of the NGR spectra parameters of ^{57}Co atomic probes occupying states-2. When the interstitial impurities concentration dropped (the annealing temperature was raised), the volume of all sites in the grain boundary core structure increased and, correspondingly, the density of s-electrons at the ^{57}Co atomic probe core decreased, while δ_1 dropped. Tab.1 gives interaction energies characterizing interstitial impurities segregations-1 in the solvents studied. The comparison of the data in Tab.2 shows that interaction energies in the core of the grain boundaries W, Ta, and Pt are several times higher than their counterparts outside the grain boundary core.

References.

[1]. S.M.Klotsman, Sov.Phys.Uspech.,**33(1),** (1990), p.55.
[2]. V.N.Kaigorodov, S.M.Klotsman, Phys. Rev. B, **49(14)**, (1994), p.9374; *ibid.*, p.9387; *ibid.*, p.9395.
[3]. S.M.Klotsman, M.I.Kurkin, V.N.Kaigorodov, V.V.Dyakin, Phys.Metals & Metallogr., **82(4),** (1996), p.419.
[4]. I.Deszi, U.Gonser, G.Langouche, Phys.Rev.Letters, **62(14),** (1989), p.1659.
[5]. E.S.Sirkin, S.B.Fedoseev, FTT, **34(5),** (1992), p.1367.
[6]. P.Ferguson, K.H.Westmacott, R.M.Fisher, U.Dahmen, Mater.Sci.&Technol.,**1(1),**(1985), p.53,
[7]. S.M.Klotsman, M.I.Kurkin, V.N.Kaigorodov, V.V.Dyakin, Phys.Metals&Metallogr., **85(2),** (1998), p.135; ibid., p.212; ibid., p.342,
[8]. N.Q.Lam, H.Wiedersich, Nucl.Instrum.Meth.B., **18(4-6),** (1987), p.471.
[9]. S.M.Klotsman, S.A.Matveev, S.V.Osetrov, A.N.Timofeev, Phys.Metals&Metallogr., **83(6),** (1997), p.647.

Materials Science Forum Vols. 294-296 (1999) pp. 435-438

Segregation in Advanced Steels

M. Militzer[1] and A. V. Krajnikov[2]

[1] The Centre for Metallurgical Process Engineering, The University of British Columbia, Vancouver, BC, Canada V6T 1Z4

[2] Institute for Problems of Materials Science, National Academy of Sciences, Kiev, UA-252180, Ukraine

Keywords: Auger Electron Spectroscopy, Interstitial Free Steels, Segregation Kinetics, Segregation Anisotropy

Abstract Surface segregation kinetics has been studied in two commercial as hot-rolled interstitial free steels. Auger electron spectroscopy (AES) investigations in the temperature range 853 - 923 K reveal substantial C segregation in both steels as well as S and P segregation in competition with C. The results of scanning AES indicate segregation anisotropy, however, no evidence of preferential segregation from grain boundaries has been found.

Introduction Many researchers have investigated grain boundary and surface segregation in steels by Auger electron spectroscopy (AES) with an emphasis on grain boundary embrittlement [1-4]. For advanced steels, e.g. interstitial free (IF) steels, segregation mechanisms are also of interest as they are associated with the texture development. IF steels are increasingly being used in automotive applications because of their excellent formability characteristics which have improved over the years by optimizing the texture through industrial rolling. While embrittlement may be an issue in IF steels, it is usually difficult to reveal the grain boundary by in-situ fracture. As an alternative, scanning AES can be employed to obtain information on preferential segregation from grain boundaries by mapping the surface segregation kinetics in polycrystalline material. This approach had first been applied to an Fe-3at%Ni alloy embrittled by Sb segregation [4]. Further, these studies indicated an apparent anisotropy of surface segregation. Anisotropy of segregation has been studied in detail at surfaces and grain boundaries of Fe-6at%Si single crystals and bi-crystals, respectively [5, 6]. Segregation anisotropy may play a key role in the development of textures.
The present study examines surface segregation kinetics in polycrystalline, commercial IF steels. The goal of this initial work is to evaluate the segregating species, the temperature dependence of segregation as well as the potential for preferential segregation from grain boundaries and segregation anisotropy.

Experimental Surface segregation was studied by AES in two as-hot rolled commercial IF steels, both with a mean ferrite grain size of approximately 15 μm (equivalent area diameter). Table 1 summarizes the chemistries of the steels representing two common microalloying strategies to scavenge residual C and N; i.e. by Ti (steel A) or by a combination of Ti and Nb (steel B). Both steels are overstabilized; i.e. there are more Ti and Nb atoms in the material than C and N atoms.

Table 1: Chemical composition (in at%) of the steels.

Steel	C	Mn	P	S	Si	Ti	Nb	Al	Sn	N
A	0.009	0.108	0.018	0.014	0.020	0.069	0.005	0.068	0.001	0.016
B	0.014	0.194	0.020	0.019	0.016	0.043	0.019	0.106	0.003	0.012

The segregation kinetics to the free surfaces of the polycrystalline samples were investigated with a JAMP-10S scanning Auger microprobe in the temperature range of 853 to 923 K with fresh specimens being employed for each test. The segregation levels were characterised by the relative Auger peak height ratios, i.e. I_i/I_{Fe} where I_i is the peak to peak height of the segregating element i and I_{Fe} is the peak to peak height of Fe (LMM 703 eV). The Auger peak height ratios were monitored at two surface areas one with an intersection of a grain boundary and a second one located at the centre of the grain. In addition, two-dimensional distributions of the segregants across the surface were recorded with qualitative scanning AES. Details of the specimen preparation and the AES experiments are identical to those described previously [4].

Results and Discussion The AES results for the two different surface locations suggest that, in all investigated cases, there is no evidence for preferential segregation from grain boundary areas. This finding is confirmed by scanning AES. The kinetic results shown in Figs. 1 and 2 represent the quantitative AES measurements made at the grain centre surface location.

Fig. 1 illustrates the temperature dependence of the surface segregation kinetics in steel A. At 853 K, C segregation dominates whereas segregation of S remains low. By increasing the temperature to 873 K, S segregation is sufficiently fast to prevent substantial segregation of C. Increasing the temperature further to 923 K results in a more complex segregation behaviour since P segregates simultaneously with S. The segregation competition of S and P with C which segregated initially is clearly confirmed. The segregation rate of S appears to be lower than that observed at 873 K which may be attributable to S-P segregation competition, which is frequently observed in iron alloys [7, 8]. However, the total amount of P and S atoms segregated at 923 K is significantly higher than for the same holding times at 873 K, and can be estimated using the different sensitivity factors for the Auger signals of P and S.

Fig. 2 shows the surface segregation kinetics in steel B with a similar temperature trend of the segregating species, as observed in steel A. At lower temperature (853 K) competition of S and C dominates whereas at higher temperature (903 K) the segregation competition of S and P is clearly observed with C segregation being marginal. The scanning AES maps shown in Figs. 3 and 4 confirm these findings for both steels and also indicate segregation anisotropy. Certain surface facets are occupied by S whereas the other facets are covered by the competing segregant; i.e. C at lower temperatures (Fig. 3) and P at higher temperatures (Fig. 4). This segregation competition is similar to that reported for S and Sb in Fe-3at%Ni [4]. However, the facet size in the IF steels is coarser than the actual grain structure of the material indicating that a few neighbouring grains exhibit the same surface composition, suggesting that these grains have a similar orientation.

Even though the general temperature trends of segregation concluded from Figs. 1 and 2 are consistent with the scanning AES maps, details of the observed segregation kinetics may be affected by variations in the orientation of the surface location from measurement to measurement [9]. Further studies are initiated to quantitatively correlate segregation with surface orientation by combining AES with transmission electron microscopy and orientation image microscopy.

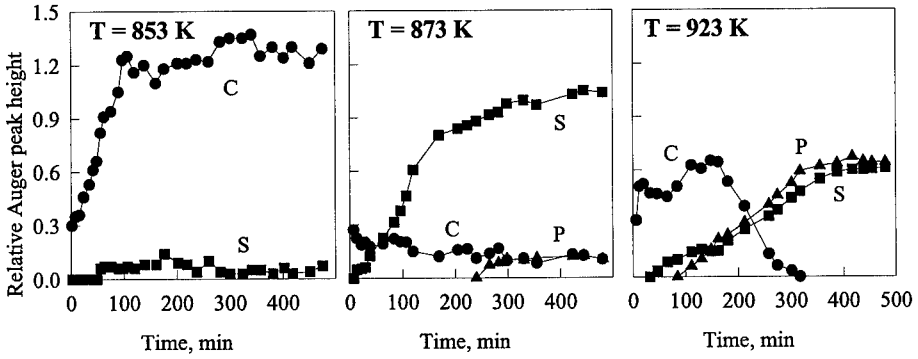

Figure 1: Surface segregation kinetics in steel A.

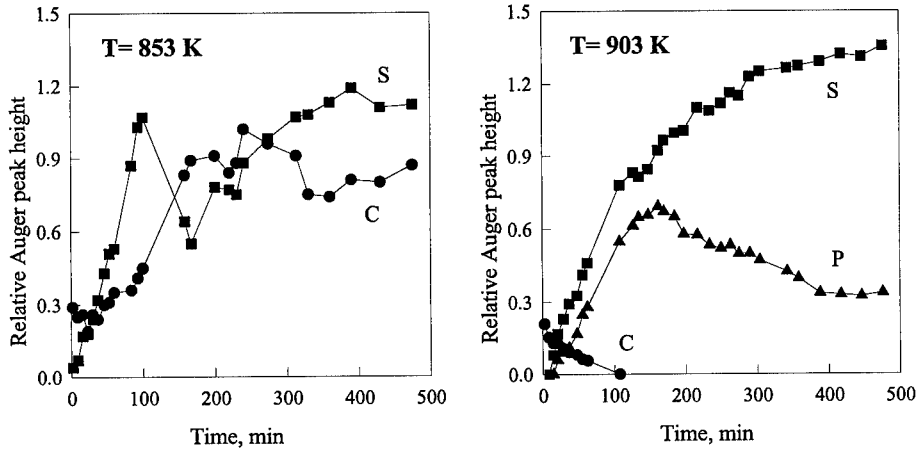

Figure 2: Surface segregation kinetics in steel B.

Conclusions Surface segregation in as-hot rolled IF steels appears to be independent of the microalloying strategy. At approximately 873 K, a transition is observed from C-S competition at lower temperatures to P-S competition at higher temperatures. The relatively strong segregation of C suggests that even though the steels are overstabilized, a sufficient amount of C remains in solution. Further, scanning AES indicates segregation anisotropy which may be a key factor in the texture development. To gain further insight into this subject, additional studies will be conducted to quantitatively correlate segregation and surface orientation and to evaluate the effect of thermomechanical processing on segregation.

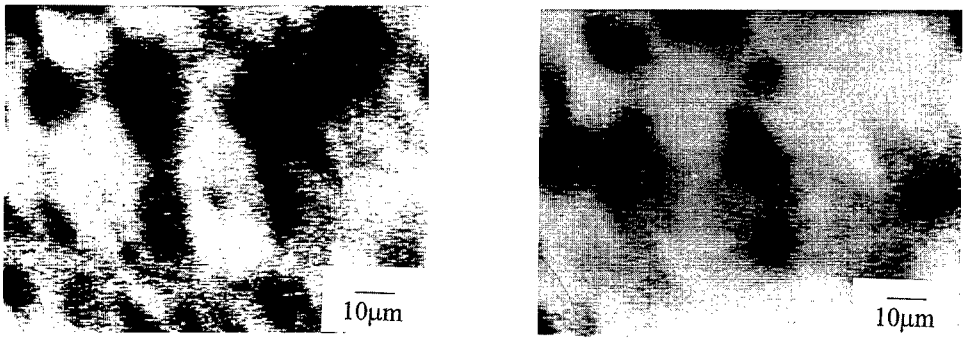

S **C**

Figure 3: Scanning AES maps of S and C for steel A after 2 hours holding at 873 K.

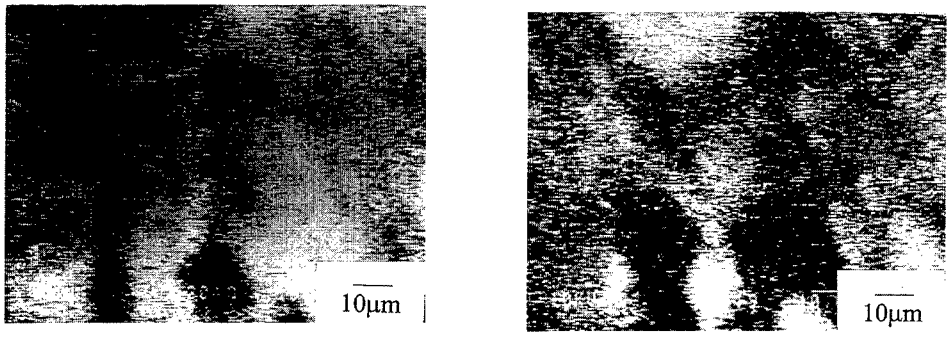

S **P**

Figure 4: Scanning AES maps of S and P for steel B after 5 hours holding at 903 K.

References

[1] M.P.Seah and C. Lea, Phil. Mag. 31 (1975) p. 627.
[2] H.J. Grabke, Steel Res. 57 (1986) p. 178.
[3] M. Mackenbrock and H.J. Grabke, Steel Res. 62 (1991) p. 371.
[4] A.V. Krajnikov, M. Militzer and J. Wieting, Mater. Sci. Techn. 13 (1997) p. 877.
[5] P. Lejcek, J. Adamek, A.V. Krajnikov and M. Militzer, Czech. J. Phys. 47 (1997) p. 429.
[6] P. Lejcek and S. Hofmann, Acta Metall. Mater. 39 (1991) p. 2469.
[7] Y. Im and S. Danyluk, Metall. Trans. A 18 (1987) p. 19.
[8] M. Es-Souni and A. Mosser, Scripta Metall. 22 (1988) p. 1469.
[9] D.R. Batchelor, M. Dalton and G.J. Tatlock, Surf. Interface Anal. 24 (1996) p. 875.

Correspondence should be sent to: militzer@cmpe.ubc.ca

Materials Science Forum Vols. 294-296 (1999) pp. 439-442

Segregation at Interphase Boundaries in Oxide-Dispersion Strengthened Ferritic Steels

A.V. Krajnikov[1], H.M. Ortner[2], V.M. Yurchenko[3] and A.N. Demidik[1]

[1] Institute for Problems of Materials Science, Krzhizhanivsky Street, 3, Kiev, UA-252180, Ukraine

[2] Technical University of Darmstadt, Petersenstrasse, 23, Darmstadt, D-64287, Germany

[3] Physics and Technology Institute, R. Luxemburg Street, 72, Donetsk, UA-340050, Ukraine

Keywords: ODS Ferritic Steel, TiO_2 Dispersoids, Interphase Boundaries, Interfacial Segregation

Abstract: Alloying elements distribution in the vicinity of matrix - TiO_2 dispersoid interphase boundaries in an oxide dispersion strengthened Fe-Cr ferritic steel is studied by Auger electron spectroscopy. Pronounced Cr segregation resulting in formation of a wide enrichment zone at the interface is observed and described as diffusion process in the field of long-range elastic stresses.

Introduction Oxide - dispersion strengthened (ODS) ferritic steels are considered as promising construction materials for fast neutron reactor cores. Since mechanical properties of the ODS steels depend strongly on parameters of the dispersoids, a knowledge of dispersoid - matrix interphase structure and chemistry is of primary importance. The present paper is aimed at the study of alloying element distribution in the vicinity of TiO_2 dispersoids - ferritic matrix interphase boundaries in Fe-Cr ferritic steels strengthened by TiO_2 and the elucidation of reasons for chemical inhomogeneity formation.

Experimental The material under investigation was a Fe - 13wt.%Cr - 2wt.%Mo ferritic steel strengthened by 2.2 wt.% of disperse TiO_2. Other details concerned with alloy preparation are given elsewhere [1,2]. The alloy was annealed at 700°C for 1 - 450 h. Interfacial segregation was studied by Auger electron spectroscopy (AES). AES samples were *in-situ* fractured in an UHV chamber at liquid nitrogen temperature and Auger spectra were recorded from the surface of dispersoids and ferritic matrix adjacent to the dispersoids. Surface chemistry of more than 20 interfaces was studied. The ratios of the intensity of an element i peak (I_i) to the intensity of either the Fe peak (I_{Fe}) or the Ti peak (I_{Ti}) were considered as a measure of the surface concentration of element i in the matrix and dispersoid respectively. In-depth element distributions were studied by ion beam sputtering with argon.

Results and Discussion Two different types of the TiO_2 particles depending on Cr behaviour are found to occur in the steel. In the first case (Fig. 1,a), Cr atoms penetrate into the dispersoid to the measured depth of 30 nm. The value of I_{Cr}/I_{Ti} reaches 0.5 and is practically unchanged during sputtering time except for a very thin subsurface layer. In the second case (Fig. 1,b), Cr is enriched near the subsurface layers only. The thickness of the enriched zone is estimated to be approximately 4 nm; the I_{Cr}/I_{Ti} ratio reaches the value of 0.8 at the surface but decreases quickly with distance from the interface. However, a background signal of Cr appears to be recorded even after rather prolonged sputtering. In both considered cases, remarkable peaks of Fe are also detected. Since diameters of the studied dispersoids are usually comparable in size with the diameter of the primary electron beam, the presence of Fe is probably connected with a partial overlap of the electron beam with the matrix.

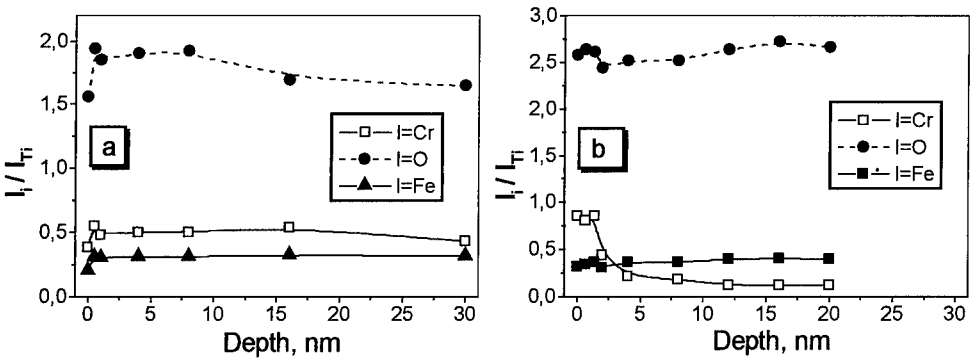

Fig. 1 In-depth alloying elements distribution in subsurface layers of the TiO_2 dispersoid illustrating two observed types of Cr behaviour: a - Cr is distributed homogeneously to the full depth studied; b - Cr is accumulated mainly in subsurface layers

The Cr enrichment first appears at some interfaces after 1 h annealing at 700°C. After 20 - 50 h annealing, most of the dispersoids show similar behaviour; further increase of annealing time does not give rise to any qualitative changes. Evidently, Cr diffusion progresses and involves more and more dispersoids with increasing time. In contrast to Cr, the Fe and O profiles are rather constant giving evidence that these elements are distributed more or less homogeneously in both types of the dispersoids (Fig. 1). S and C also segregate to the interfaces of both types of the TiO_2 particles. The enrichment of both, C and S, is practically independent on annealing time. The small width of the S segregation zone confirms its monolayer behaviour (Fig. 2). The C enrichment zone is very thin in the dispersoids but it appears to be wider in subsurface layers of the matrix. None of those enrichments affect the interaction of Cr with the TiO_2 dispersoids.

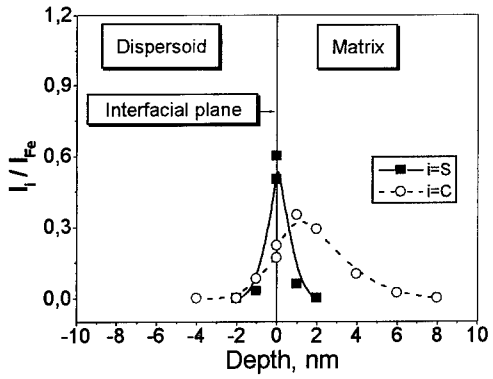

Fig. 2 S and C in-depth distribution in the vicinity of the TiO_2 - ferritic matrix interphase boundary

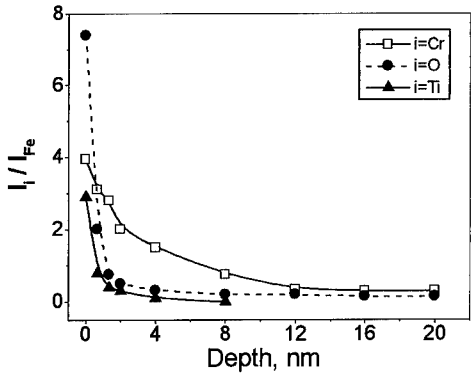

Fig. 3 In-depth distribution of alloying elements in subsurface layers of the ferritic adjacent to the TiO_2 - matrix interface matrix

Typical Auger profiles for subsurface layers of the matrix are given in Fig. 3. Practically in all the cases studied, rather a wide enrichment zone of Cr is observed at the matrix surface. The width of this zone usually ranges between 2 and 4 nm and reaches 8 nm at most. The value of I_{Cr}/I_{Fe} varies between 5 and 10. A certain Ti and O segregation is also observed in subsurface matrix layers with a

typical width of less than 1 nm. These elements are concentrated within the dispersoids and no systematic evidence confirms their out-diffusion, as was previously assumed in [1].

The observed changes in interfacial chemistry are mainly connected with the Cr redistribution. Being, in principle, rather a weak segregant in Fe, Cr shows a tendency to segregate to the interphase boundaries of the studied samples and form either a wide enrichment zone or even three-dimensional $Cr_xTi_yO_z$ structures. As follows from TEM data [1], long-range elastic stresses occur at certain interphase boundaries in hot-extruded samples of the ODS steel and disappear after prolonged annealing at 700°C. Since elastic stresses are known to influence solute segregation behaviour [3], the observed Cr segregation is suggested to be caused by the long-range elastic stresses and proceeds as a stress relaxation process. Then, the Cr behaviour can be simulated as one-dimensional diffusion in the field of long-range elastic stresses.

Solute segregation kinetics induced by both short- and long-range impurity - interface elastic interactions has been discussed theoretically in [4]. Based on this work, the following equation in dimensionless form is obtained for the solute concentration as a function of time and distance:

$$n(\xi,\tau) = n_e(\xi) + \frac{\xi^4}{\left[15U_0\tau+\xi^5\right]^{4/5}}\left\{1 - n_e\left[\left(15U_0\tau+\xi^5\right)^{1/5}\right]\right\} \qquad (1)$$

where $n=C/C_o$, $\xi=x/a$, $\tau=t/t_g$, $t_g=a^2/D$ and $U(\xi)=U(x)/T$ are the dimensionless parameters. $C(x, t)$ and C_o are the concentration to be found and the bulk concentration respectively; a is the lattice parameter; d is the sample size; x is the distance from the interfacial plane $x = 0$; $U(x)= U_0/x^3$ is the potential energy of induced elastic interaction [5]; D, t and T are the diffusion coefficient, time and temperature, and t_g is a characteristic time to attain an equilibrium at the interface. $n_e(\xi)$ is given by:

$$n_e(\xi) = \left(1 - (a/d)\int_{\xi_0}^{\infty}\left[\exp(-U(\xi)) - 1\right]d\xi\right)\exp(-U(\xi)) \qquad (2)$$

The following values of model parameters are used for calculations: T=973 K, a=0.3 nm, d=100 nm and $D_{Cr}=3\times10^{-17}$ m^2/s [6]. $U_0\approx13$ is estimated on the basis of experimental data. Relative Cr concentration, n_{Cr} calculated by Eq. 1 and plotted as a function of distance for a set of annealing times is shown in Fig. 4. Quick and intensive enrichment in a thin subsurface layer is seen in Fig. 4. The thickness of the enriched zone increases with time and reaches approximately 7 interatomic layers or 2 nm at most. The experimentally measured thickness ranges usually between 2 and 4 nm showing a rather good correlation between the experimental and calculated data. At distances $x > 2$ nm, the calculated curves exhibit a certain depletion (Fig. 4). The depleted zone becomes deeper and wider with increasing annealing time. Nevertheless, no depletion in subsurface layers was found to occur by AES. The reason of this discrepancy seems to consist in a small predicted value of the depletion, namely not more than 3 % rel., and, therefore, insufficient to be detected by AES.

The Cr concentration as a function of annealing time is simulated by Eq. 1. It is found that the calculated curves behave differently in enriched and depleted zones. In the vicinity of the interface plane, n_{Cr} quickly increases and reaches its equilibrium level. At large distances, first the concentration profile practically coincides with the bulk concentration. A certain depletion appears after 10^4 s annealing only. However, the equilibrium level of concentration is not reached even after 10^7 s. At intermediate distances, a transition from the bulk concentration level to the depleted equilibrium level is predicted to occur during a few hours of annealing. Summarizing, the depletion rate strongly depends on the distance: All changes at a distant region proceed much slower as compared with a near-interface zone.

In general, the discussed segregation process quickly reaches its steady state in the vicinity of dispersoids and leads to a quick and intensive enrichment of a few subsurface layers accompanied by a rather slow and moderate depletion of distant layers. No serious changes in the Cr profile caused by the given segregation mechanism are predicted to occur with increasing annealing time. Therefore, the described process does not affect dispersivity of the strengthening phase. The latter conclusion agrees well with the experimental observations [2].

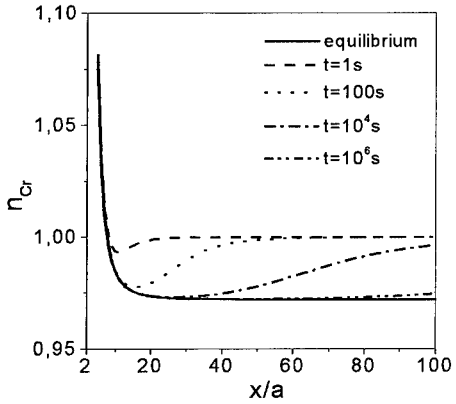

Fig. 4 Calculated Cr interfacial concentration normalised to its bulk concentration is plotted as a function of distance (x/a) from the interface to the matrix for a set of annealing times (t) and compared to calculated Cr equilibrium concentration

Conclusions In ODS ferritic steels strengthened by TiO_2 dispersoids, Cr atoms display strong multilayer segregation to the matrix - dispersoid interphase boundaries. The Cr segregation is caused or/and enhanced by long-range elastic stresses around the dispersoids and proceeds as stress relaxation process. A steady state of the segregation process is reached quickly in the vicinity of the interfaces and this suppresses further changes in chemical element distribution. The Cr redistribution does not cause distinct depletion of distant regions of the matrix. Since the TiO_2 dispersoids exhibit a pronounced defect structure, the observed intensive accumulation of the segregated Cr atoms at the interfaces is accompanied by Cr diffusion into the dispersoids followed by formation of three-dimensional $Cr_xTi_yO_z$ compounds.

Acknowledgements This work was partially supported by NATO under grant No. HTECH.LG 950452. A. V. K. gratefully acknowledges financial support from the Deutscher Akademischer Austauschdienst (DAAD).

References

[1] H.M. Ortner, N. Reger, S. Weinbruch, A.N. Demidik, N.V. Graivoronskii and A.V. Krajnikov. In: Proc. 14th Int. Plansee Seminar on Refractory Metals & Hard Materials. Eds.: G. Kneringer, P. Roedhammer and P. Wilhartitz, Plansee Metal AG, Reutte, Austria, vol. 4 (1997) p. 168.
[2] A.V. Krajnikov, A.N. Demidik and H.M. Ortner, Mater. Sci. Eng. (A), 234-236 (1997) p.357.
[3] S. Onaka and M. Kato. Mater. Sci. Eng. (A), 146 (1991) p.217.
[4] E.P. Feldman and V.M. Yurchenko, Poverhnostj. Fizika, Himiya Mehanika (in Russian) No12 (1990) p.138.
[5] A.M. Kosevich, Backgrounds of Mechanics of Crystalline Lattice. Nauka: Moscow (in Russian), (1972).
[6] J. Kaur, W. Gust and L. Kozma, Handbook of Grain and Interphase Boundary Diffusion, Siegler Press: Stuttgart, (1989).

Correspondance should be sent to: avk@ipms.kiev.ua

Materials Science Forum Vols. 294-296 (1999) pp. 443-448

Effect of Character of Grain Boundaries on Non-Equilibrium Segregation of B in a Nickel Base Superalloy

M.C. Chaturvedi, H. Guo and N.L. Richards[1]

Department of Mechanical and Industrial Engineering, University of Manitoba, Winnipeg, Canada R3T 5V6

[1] Bristol Aerospace Ltd., Winnipeg, Canada R3G 2S4

Keywords: Random, CSL and Low Angle Boundaries, Orientation Imaging, Electron Back Scatter Diffraction, SIMS Analysis, Inconel 718, HAZ Microfissuring, GB Liquation

Abstract

Boron was observed to segregate heterogeneously to the grain boundaries of Inconel 718 during cooling from the solution heat treatment temperature. That is, in the same area only a few grain boundaries were segregated while others were not. The examination of a water-quenched Inconel 718 by SEM, orientation imaging microscopy based on electron back scatter diffraction, and by SIMS suggested the heterogeneity in segregation of B to be due to the variation in the character of different GBs. It was found that the high angle random boundaries were invariably segregated with B, high Σ CSL boundaries were occasionally segregated, and low Σ CSL and low angle boundaries were seldom segregated. A direct correlated between segregation of B on GBs and their liquation during thermal cycling was also observed.

Introduction

Inconel 718 is a high temperature superalloy and is one of the most widely used material in the fabrication of jet engine turbine blades and vanes. The alloy is generally considered to be weldable, however, it does suffer from extensive microfissuring along grain boundaries in heat-affected zones (HAZ) in electron beam welds. It is well established that this HAZ microfissuring is associated with the liquation of grain boundaries caused by the constitutional liquation of NbC[1] and Laves phase[2] present on them. Recently, however, the segregation of solute atoms, present as impurities or tramp elements, to the grain boundaries during pre-weld heat treatment, has been also suggested to be the cause of GB liquation leading to the formation of microfissures along GBs in the HAZ. In a previous study on cast Inconel 718, Huang, Chaturvedi and Richards[3,4], using secondary ion mass spectrometry (SIMS) have shown that B can segregate to the grain boundaries on cooling from the pre-weld solution heat treatment temperature by non-equilibrium mechanism. The segregation of boron lowers the melting point of the grain boundary material. Therefore, if the extent of segregation, which depends upon the cooling rate from the solution heat treatment temperature, is large enough, the segregated GB in HAZ will liquate during the thermal cycle associated with welding resulting in the formation of microfissures[5]. An example of liquation and the formation of microfissures in the HAZ around an EB weld of Inconel 718 is shown in Figure 1. The liquation of GBs, as evidenced by the formation of resolidified products, is seen to be heterogeneously distributed.

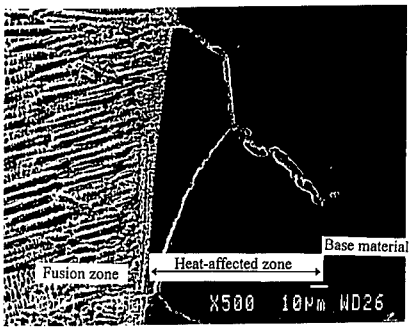

Fig. 1. Fusion zone, heat affected zone and base metal in electron beam welded Inconel 718. A few GBs in the HAZ are seen to be liquated.

The atomic size of boron is such that its segregation would cause a considerable lattice distortion. Therefore, it is likely that the character of GB, or the degree of misfit in the GB, will influence the extent of segregation. That is, a large angle GB is likely to have a greater degree of segregation as compared to a low angle GB. Therefore, a study was initiated to determine the relationship between the character of GBs and non-equilibrium segregation of B on them. The results of this study are presented is this Communication.

Experimental Methods

To eliminate the effects of the presence of NbC and Laves phases, an alloy whose composition was identical to a commercial Inconel 718, with the exception of C, S, P and B, was prepared by normal commercial practice. The C, S and P were extremely low and the concentration of B was 43 ppm. The chemical composition of the alloy was (wt%): Ni-19Cr-19Fe-5Nb-3Mo-0.5Al-1.0Ti-0.0043B. This alloy was prepared by Special Metals Corporation of New Hartford, USA, and supplied in the form of 12.5 mm thick plates. 12.5 x 12.5 mm sections of plate were swaged, with intermediate annealing at 1200°C followed by water-quenching into 6 mm dia. bars. 100 mm long cylindrical specimens were given a final solution heat treatment at 1050°C and then water-quenched. These specimens were subjected to thermal cycling in a Gleeble 1500 thermo-mechanical simulator. Metallographic samples were sectioned from these and prepared by normal mechanical and electro-polishing technique, followed by a light electrolytic etch in a 10% solution of oxalic acid and water. An important aspect of microstructural examination was that the SEM microstructural characterization of grain boundary liquation, determination of character of grain boundaries by Orientation Imaging Microscopy (OIM) using electron back scatter diffraction (EBSD), and the boron segregation analysis by SIMS were conducted on the same areas of samples to establish a correlation between the intergranular liquation behaviour, the segregation of boron on GBs and the character of GBs. The thermally simulated samples were first examined in optical microscope to determine the extent of grain boundary liquation. Then the areas containing liquated grain boundaries were identified by microhardness indentations. The identified areas were then examined in a JEOL-840 SEM equipped with a Noran 5500 EDS and a TSL-OIM system. The specimens were then given a light polish to remove the etched surface, making sure that microhardness indentations remained. The repolished specimens were used to determine the character of grain boundaries in the previously identified areas. The grain boundaries were characterized as low angle boundaries (<15°C), coincident site lattice boundaries (Σ3 to Σ49) and non-special geometry or

random boundaries. The same regions of the samples were then analyzed for B segregation by a Cameca-4f SIMS using $^{10}B^{16}O^-$ signal on mass 42. The equipment parameters were: Raster: 250-300 μm, image field: 250 μm, primary beam: O_2^+, primary ion beam current: 3-5 μa, primary ion beam voltage 10 KV.

Experimental Results and Discussion

The 6 mm dia. specimens were given a final solution heat treatment at 1050°C followed by water quenching. The solution treated alloy was basically single phase with a grain size of about 200 μm. The solution treated sample was thermal cycled in a Gleeble 1500 system by heating to 1200°C at a heating rate of 150°C /S, held there 1-5 seconds and then cooled by compressed air-jet at about 250°C/S to room temperature. The thermal cycled samples exhibited heterogeneity in the grain boundary liquation and grain boundary microfissuring. A typical SEM of thermal cycled sample is shown in Fig. 2. It is seen that GBs 1 and 2 liquated but GB3 did not. The micrograph features a very small area of the sample. This, combined with the resistance heating of the sample in Gleeble 1500, ensures that the temperature gradient in the region would be almost nil. Therefore, the heterogeneity in grain boundary liquation must be due to the difference in the melting point of the grain boundary material which could be due to a difference in the level of segregation of B on them, rather than due to a difference in their temperatures. The interrelationship between the segregation of B and character of grain boundaries in terms of high and low angle boundaries, and CSL boundaries is presented next.

Segregation of B on High and Low Angle Grain Boundaries:

A typical region containing different types of grain boundaries is shown in Fig. 3a. The OIM and SIMS B ion images are shown in Fig. 3b and 3c, respectively. In the OIM image L_1, L_2, L_3 and L_4 are low angle boundaries. The SIMS image shows that while L_1, L_2 and L_3 do not have any B on them, L_4 has a small amount of B on it. However, as seen in Fig. 3a, none of them liquated. R_1, R_2 and R_3 boundaries are random and show signs of liquation (Fig. 3a). The OIM image suggests the presence of B on them in the form of discrete particles. It is likely that the segregated B atoms combined with other elements on liquation of these GBs and formed discrete particles of borides seen in Fig. 3c.

Fig. 2 SEM micrograph of a thermal cycled sample showing heterogeneous nature of GB liquation.

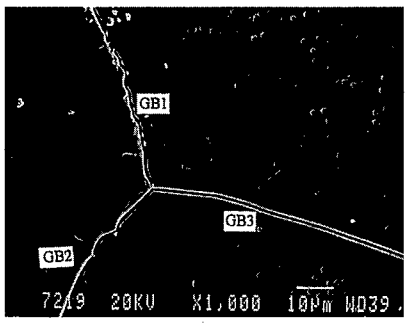

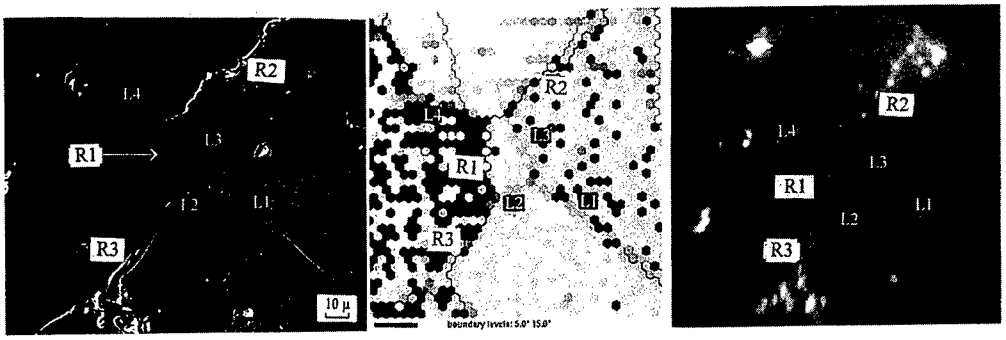

Fig. 3 SEM micrograph of a thermal cycled specimen (a), the corresponding OIM image (b), and SIMS B-ion image (c)

Segregation of B on CSL Boundaries:

Fig. 4a is the SEM image of an area containing CSL boundaries. The corresponding OIM image is shown in Fig. 4b and SIMS image in Fig. 4c. It is seen that the CSL boundary, whose Σ value was 41C, did not liquate (Fig. 4b) and had practically no B on it (Fig. 4c). However, Random boundaries liquated and had segregated B on them.

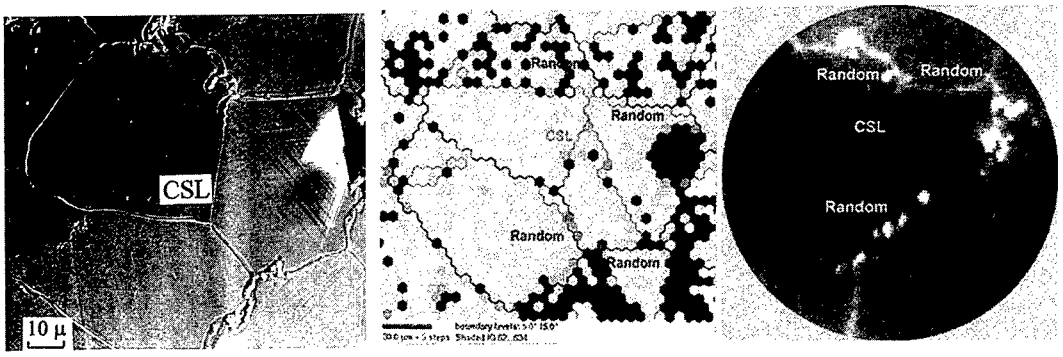

Fig. 4. SEM micrograph showing liquated random and non-liquated CSL boundary (a), the corresponding OIM image (b) and B-ion image (c)

A total of 255 boundaries in a number of samples were examined. It was found that the segregation tendency of boron on different grain boundaries was as follows:

Random GBs > High Σ CSL GBs > Low Σ CSL GBs < Low angle GBs:

The liquation tendency of grain boundaries also exhibited the same trend. That is, the high angle random boundaries invariably liquated, high Σ CSL boundaries occasionally liquated, and low Σ and low angle boundaries never liquated. This can be explained on the basis of the ability of grain boundaries of different characters i.e. of different interfacial energies, to accommodate boron atoms. Random or high angle random boundaries have the highest interfacial energy, therefore, they can most easily accommodate boron atoms. CSL boundaries in general are relatively low energy interfaces, however, the interfacial energy of high Σ CSL boundary is higher than that of a low Σ CSL boundary. Therefore, a high Σ CSL boundary can accommodate larger number of boron atoms as compared to low Σ CSL and low angle boundaries.

Conclusions:

- Non-equilibrium segregation of B occurred mainly on high angle random boundaries and seldom on low angle boundaries.
- Very low levels of boron segregation were found in the CSL boundaries and as the Σ value decreased, the tendency for boron segregation and grain boundary liquation reduced.
- A close relationship was observed between the B segregation and the character of grain boundaries. The order of segregation varied as follows:

  Random GBs > High Σ CSL GBs > Low Σ CSL GBs > Low Angle GBs

- Intergranular liquation was found to occur mainly on non-special grain boundaries in thermal cycled specimens because of high level of B segregation on them, which lowered the local melting temperature and led to their liquation.

Acknowledgments:

The authors would like to thank the Consortium of Manitoba aerospace industries and Natural Science and Engineering Research Council of Canada for the financial support and to Dr. G. McMahon for the SIMS analysis.

References:

1. R. Vincent, Acta. Metall. 33, (1985), p. 1205.
2. B. Radhakrishnan and R.G. Thomson, Metallography, Vol. 19, (1988), p. 453.
3. X. Huang, M.C. Chaturvedi and N.L. Richards, Metall. and Mater. Trans. A, Vol. 27A, (1996), p. 785.
4. X. Huang, M.C. Chaturvedi and N.L. Richards, Acta. Metall., Vol. 45, (1997), p. 3095.
5. M.C. Chaturvedi, W. Chen, A. Saranchuck and N.L. Richards, Proc. Int. Symp. on Superalloys 718, 625, 706 and Various Derivatives June 15-18, 1997, Ed. E.A. Loria, TMS, Warrendale, Pennsylvania, P. 743.

Materials Science Forum Vols. 294-296 (1999) pp. 449-452

Competition between Segregation of Sulfur and Precipitation of hBN

V. Hays, R. Le Gall and G. Saindrenan

Laboratoire génie des matériaux, ISITEM, La Chantrerie,
BP 80604, F-44306 Nantes Cedex 03, France

Keywords: Segregation, Precipitation, Hexagonal Boron Nitride, Sulfur, Stainless Steel

Abstract. We have studied the sulfur segregation at the interface of austenitic stainless steel-hexagonal boron nitride by Auger spectrometry, SEM and TEM. Sulfur segregation does not occur at the metal-ceramic interface when the epitaxial relation (0001) hBN || (111) austenitic stainless steel exist, because boron and nitrogen atoms are in interstitial positions at the (111) steel surface. But sulfur can segregate at the interface when there is no epitaxial relation

Experimental

The 304N austenitic stainless steel investigated in this work is an industrial material manufactured by Ugine S.A. in the form of a thin plate (thickness 1 mm). Its chemical composition is given in Table 1. The sulfur concentration (50 ppm) is higher than the solubility limit at room temperature especially in the presence of manganese. Manganese sulfide precipitates are detected by SEM and microanalysis. The initial boron content was 5ppm but it was increased to 100ppm by ion implantation.

TABLE 1
Chemical composition of the stainless steel wt%.

C	Si	**S**	P	**Mn**	Ni	Cr	Mo	Sn
0.021	0.485	**0.005**	0.023	**1.33**	6.6	17.5	0.179	0.005
V	Cu	Co	Ti	Nb	Al	B	N	
0.073	0.077	0.149	0.002	0.004	0.001	0.0005	0.142	

The Auger specimens were cut into $3x1x0.5mm^3$ then homogenized for 10 hrs at 1000°C in evacuated quartz capsules. The AES system consists of a Riber ISA model ASC2000 analyzer with a cylindrical mirror analyzer and a coaxial gun. The specimens were spot welded to a strip of tantalum which is used as a resistive heater. The temperatures were measured using type K thermocouples spot welded to the specimens. The residual pressure was maintained below $5x10^{-8}$ Pa. Typical parameters for Auger measurements are : 3 keV primary energy, 0.1 μA primary beam current, and ~1 μm primary beam diameter.
Extraction was made in a solution of three acid (HNO_3, HF, Hcl) and gave a BN thin film which floated to the top of the solution and a metallic residue which settled to the bottom. The BN thin coating on stainless steel and the thin film alone were characterized by X-ray diffraction (Philips θ-2θ diffractometer, Cu Kα radiation), scanning electron microscopy (S440/ISIS SEM) and transmission electron microscope (CM30 Philips 300 kV) with a Si-Li detector and a Link energy both dispersive analyzer.

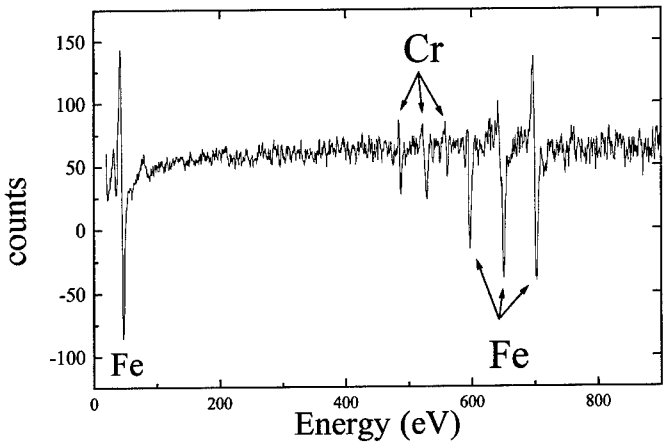

Figure 1. Auger spectrum of stainless steel clean surface.

The Auger spectra were recorded, and peak to peak heights were measured in the derivative mode (Fig. 1). On the Auger spectra of a clean stainless steel surface, only iron and chromium peaks are significantly detectable, the nickel peaks do not appear. The peaks at 529 eV and 650 eV were chosen as characteristic peaks for chromium and iron respectively.

Before heating, the samples were sputtered to produce identical initial conditions. The Auger spectra were recorded during each run.

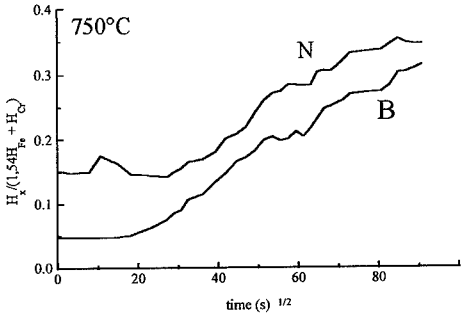

Figure 2 : hBN precipitation at the stainless steel surface at 750°C

Results

The hBN film comes from a precipitation of boron and nitrogen during an anneal at 750°C (Fig. 2). Selected area diffraction (Fig. 3) shows a ring pattern characteristic of polycrystalline material in which the $\vec{c}$ axis of most of the grains are parallel to the electron beam direction (the film was perpendicular to the electron beam). All the crystallites which contribute to the diffraction pattern are disoriented in the perpendicular plane to the $\vec{c}$ axis, because the reflections of the (00ℓ) plane and those corresponding to the planes which form an angle near 90° with the $\vec{c}$ axis are missing.

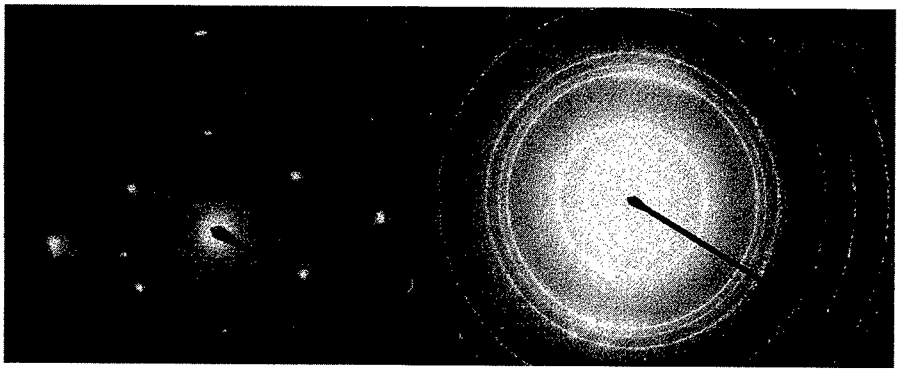

Figure 3 : electron diffraction from hBN film

An electron backscattered pattern (EBSP) analysis performed on the stainless steel covered with an hexagonal boron nitride film shows that the hBN film is thicker when the steel grains have an (111) orientation.
A crystallographic relation is possible between the hBN film and the (111) grains, because the hBN's basal-plane lattice parameter (2.504 Å) is nearly the same than the (111) plane in austenite lattice (2.54 Å). This should promote the nucleation of hBN with the following epitaxy relation : $(0001)_{hBN} \parallel (111)_{fcc}\ [0001]_{hBN} \parallel [110]_{fcc}$. This model was previously proposed by Fujita et al [1] and is analogous to graphite layers on the (111) surface of nickel proposed by Shelton et al [2].

The superficial segregation of sulfur can inhibit the hBN precipitation, by AES, a competition between sulfur segregation and hBN precipitation is observed. If the sulfur is already on the steel surface, the sulfur prevents the hBN precipitation, probably by a mechanism of site occupation (Figure 4). But if the hBN precipitates first onto the steel surface, it does not prevent the sulfur segregation, in this case the sulfur segregates under the hexagonal boron nitride thin film, at the interface.

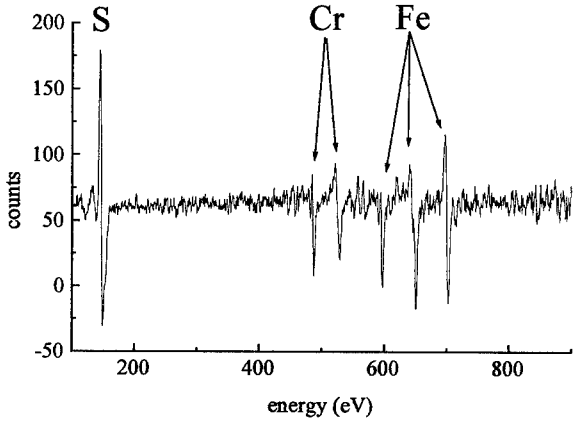

Figure 4 : sulfur segregation

Sulfur does not seem to diffuse in the hBN bulk, because it is not detectable on all AES spectra taken from different grains (fig. 5 a)) ; whatever the hBN thickness. It is detected in a similar to time that substrate peaks (fig 5 b)) that means that the hBN thickness is thin and that the sulfur located at the interface.

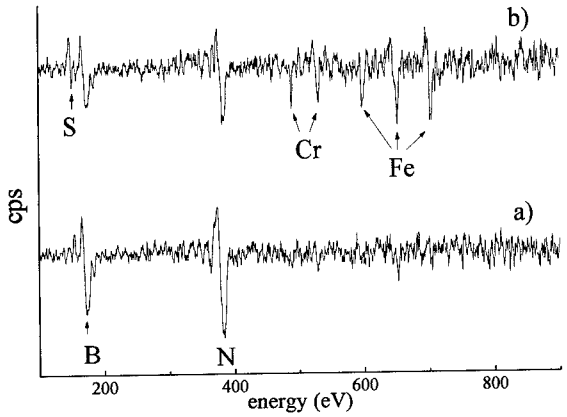

Figure 5 : AES spectra of hBN at stainless steel surface

Conclusion

Sulfur segregation does not occur at the metal-ceramic interface when the epitaxial relation (0001) hBN || (111) austenitic stainless steel exists, because the boron and nitrogen atoms are in interstitial positions at the (111) steel surface. But sulfur segregation occurs at the interface when there is no of epitaxial relation with the substrate.

1 D. Fujita, T. Homma, Thin Solid Films 181 (1989) 267.

2 J. C. Shelton, H. R. Patil, J.M. Blakely, Surf. Sci. 43 (1974) 493.

Materials Science Forum Vols. 294-296 (1999) pp. 453-456

Mechanisms of the Intergranular Segregation of Boron in (B2) FeAl Alloys

A.-S. Gay, A. Fraczkiewicz and M. Biscondi

Ecole des Mines, Centre SMS, 158 Cours Fauriel, F-42100 St. Ettienne, France

Keywords: Iron Aluminides, Boron, Non-Equilibrium Segregation, Equilibrium Segregation

ABSTRACT Small boron additions reduce the intergranular brittleness of some intermetallics, thanks to their intergranular segregation. Two different origins of this segregation were identified in FeAl (B2) alloys, containing 40 or 46 at. % Al. Its very fast kinetics, low level and almost no temperature dependence suggest a non-equilibrium mechanism, based on an interaction between boron atoms and the flux of migrating thermal vacancies. Still, an equilibrium segregation is also stable : its low level (few at. % B) may be explained be strong repulsive interactions between segregated boron atoms. Thanks to the cooperation of the two mechanisms of the segregation of boron, its reinforcing effect is efficient quite independently of the applied heat treatment.

INTRODUCTION

Small boron additions are a well-known, experimental way to improve the fracture behavior at room temperature of many intermetallic alloys : in the B-doped alloys, the fracture changes to an intragranular mode, while it is intergranular brittle in the « pure » materials. The boron effect on fracture mode was first observed in the $L1_2$ Ni_3Al alloys [1] ; later, an analogue phenomenon was reported in the B2 FeAl materials [2]. As some intergranular enrichment in boron was also measured by the Auger Electron Spectroscopy method [3], a hypothesis of the boron segregation was immediately put into consideration. Still, until now, no systematic study of the origins and mechanisms of this segregation is available in the literature.

The purpose of this work is to characterize the boron segregation in the B2 FeAl, from the kinetic and thermodynamic point of view, with an attempt of estimation of the importance of the equilibrium and non-equilibrium segregation mechanisms. This last hypothesis seems to be very probable, as (i) the FeAl alloys are known to retain strong concentrations of quenched-in vacancies [4], (ii) our previous results show a strong influence of boron additions on the kinetics of thermal vacancy migration [5].

I EXPERIMENTAL TECHNIQUES

The B2 FeAl alloys, containing 40 or 46 at. % Al (here-after : Fe40Al and Fe46Al, respectively), were prepared in our laboratory by cold-crucible melting. The « pure » or B-doped (40 to 2000 appm) alloys were studied. No thermomechanical treatment was given ; this choice, caused by high brittleness of the « pure » alloys, explains the large grain size (500 μm) of all the materials studied.

A two-stage heat treatment [4] was applied to the samples. The first annealing (950°C/1hour), which was finished by an air quenching, allowed to retain a maximum concentration of thermal vacancies. The second, a low temperature annealing, should allow to eliminate the excess vacancies, as well as to promote the intergranular segregation of boron.

The intergranular segregation of boron was studied by the Auger Electron Spectrometry method (AES), in the direct mode, on the *in situ* open intergranular fracture surfaces, with the

spectrum quantification by an internal standards method [6]. To obtain a satisfactory statistics of AES measurements, about 10 different regions were analysed.

II RESULTS

II.1 Isothermal segregation at 400°C.

The effect of the bulk concentration of boron (Cv) on its intergranular concentration (Cj) was studied by AES in Fe40Al alloys (fig. 2), quenched from 950°C and annealed for 24 h at 400°C.

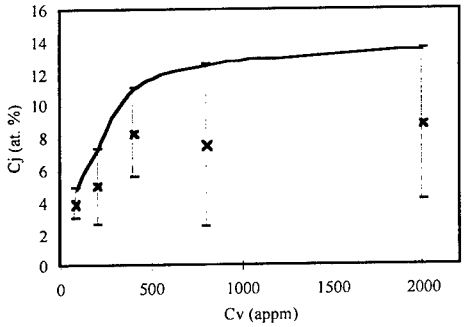

Fig. 1 . Effect of the bulk boron content (Cv) on its intergranular concentration (Cj) after an isothermal annealing (400°C/24h). Fe40Al alloys, previously quenched from 950°C.

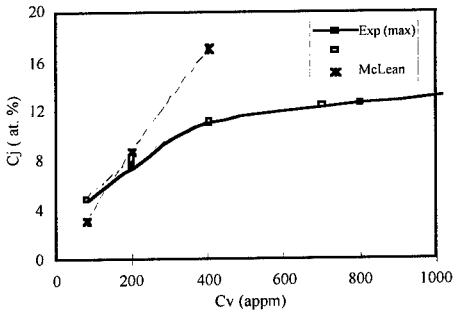

Fig. 2. The relation Cj = f(Cv) for the boron in solid solution in the Fe40Al alloys. The experimental curve was fitted with the McLean and Fowler models of the equilibrium segregation.

The maximum values of intergranular concentration of boron grow with Cv to reach a saturation value for Cv = 800 appm ; a value corresponding to the solubility limit of boron in Fe40Al alloy [7]. This behaviour is in conformity with the general description of intergranular segregations, which admit that only elements in solid solution are concerned. However, the saturation level of the boron segregation, observed in FeAl alloys, is rather low, when compared to the equilibrium segregation models (recently revieved by Faulkner [8]), which consider the C_j° value as equal to 1 atomic monolayer. Neverthless, the measured values of C_j are conform to those measured in the FeAl alloys by other authors [9, 10], giving the C_j value of about 5 at. % : the slight difference observed cas easily be explained by differences in methods of the quantification of the Auger spectra.

The experimental $C_j = f(C_v)$ curve was compared to two models of the equilibrium segregation (fig. 2). The McLean model [8] is clearly unsatisfactory to describe our experimental results ; it is not really surprising if one realises that this model considers the saturation of the grain boundaries (GB) equal to one monolayer, much higher than the experimental one. In fact, the low level of the observed GB saturation may indicate that repulsive interactions between segregated atoms exist, as it was quantified by the Fowler model of equilibrium segregation [8]. In this model, the energy of segregation E_s depends on actual intergranular concentration C_j by a relation : $E_s = E_s^\circ - wC_j/C_j^*$, where E_s° is the energy of segregation for the first segregated atom, and w is the interaction parameter.

For the studied case, a good fit was obtained when the Fowler model was used, with E_s° = 0,4 eV/at and the interaction parameter w = 2 eV. Therefore, the isotherm of the boron segregation in the Fe40Al alloys may be described by an equilibrium segregation model, when strong repulsive interactions between segregated atoms are taken into consideration.

II.2 Effect of time and temperature on the intergranular segregation of boron

The effect of the temperature of annealing (during 24 hours) on the intergranular boron concentration in the Fe46Al-400B alloy is shown on fig. 3. No significant differences in the Cj value are observed in a very large domain of temperatures, going from 300 to 950°C. It should be noted that the equilibrium segregation models predict a strong decrease of intergranular segregation level when the temperature grows.

The intergranular boron concentration as a function of the time of annealing at 400°C, in the Fe40Al-200 B alloy, is presented on fig. 4. Already during the quench (time of annealing = 0), a significant level of the intergranular segregation of boron is established. Then, during the annealing, its level grows slightly in the first 24h of the applied heat treatment ; however, a longer heat treatment results in clear decreasing of the segregation level.

Both the very fast kinetics, allowing an important segregation in the quench conditions, and the existence of the desegregation phenomenon during a long heat treatment, suggere a non-equilibrium mechanism of boron segregation. Moreover, the independence of the segregation of the annealing temperature, reinforce this hypothesis.

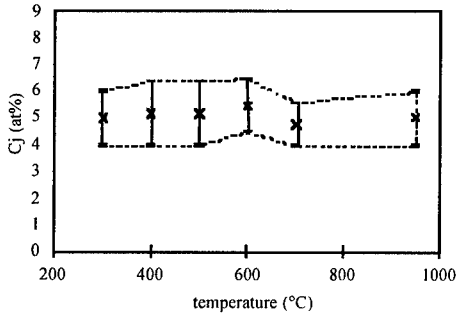

Fig. 3 : Effect of the temperature of annealing on the intergranular boron concentration. Annealing during 24 hours, after the air-quench from 950°C. Fe46Al-400 appm of B.

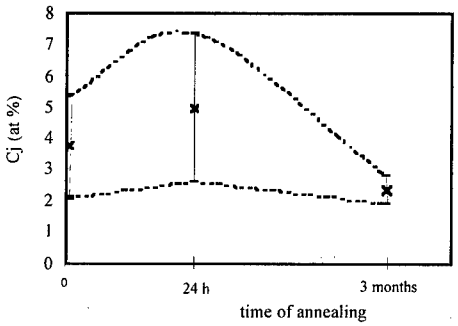

Fig. 4 : Effect of the time of annealing at 400°C on the intergranular boron concentration. Fe40Al-200 appmB.

II.3 Discussion : origins of the intergranular segregation of boron

The experimental results presented in II.1 and II.2 show in fact that the two possible mechanisms of intergranular segregation (equilibrium and non-equilibrium) are active in the case of the boron segregation in FeAl alloys. The relative efficiency of these mechanisms is a function of the thermal history of the material.

During the high-temperature quench of the FeAl alloys, and at the beginning of their low-temperature annealing, the main process which takes place is the migration of thermal vacancies and their elimination to the sinks, e.g., grain boundaries (GB). The migrating vacancies may form complexes with the boron atoms : this effect was already observed by a clear acceleration of the kinetics of vacancy migration in B-doped FeAl alloys [5]. In these conditions, the fast migration of boron/vacancies complexes to the GB will provoke an intergranular enrichment in B, observed as a (non-equilibrium) boron segregation.

When a low-temperature annealing is given to an alloy, two oposite processes take place. At the beginning of annealing, the vacancies elimination, started during quench, continue. As the boron atoms are transported with the vacancies, the intergranular concentration of boron increases, compared to its after-quench value (fig. 4). However, when the annealing is sufficiently long to

achieve the thermal vacancies migration, the desegregation process starts. In fact, the boron atoms, transported to the GB by the migrating thermal vacancies, are not in their equilibrium positions in the intergranular region : therefore, a flux of boron atoms leaving the GB region to return to their equilibrium, matrix sites, is created. This effect is clearly observed in the 3-months annealed sample (fig. 4). However, it is worth noting, for the studied case, that even after a very long annealing, which should let reach, *in principle*, the equilibrium state of the material, a low level of segregation, very probably of equilibrium type, is still stable. Even in these conditions, when the intergranular boron level is lower then after the « standard » 24 hours annealing, the boron does not loose its efficiency as to the grain boundaries reinforcement : the fracture surfaces of the studied alloys after the 24h-annealing and after the 3-months-annealing are quite similar.

The aim of the study of the $C_j = f(C_v)$ relation in isothermal conditions (fig. 1 and fig. 2) was to show the equilibrium aspects of the boron segregation ; arbitrarily, the 24-hours annealing was estimated as being sufficient to allow the equilibrium. Unfortunately, our later experiments have shown that an important part of a non-equilibrium segregation is still present in the so-treated samples. Therefore, the numerical values of the energy of segregation calculated in these conditions are obviously over-estimated, as they consider the segregation level higher than the equilibrium one. Still, this calculation stays interesting, as it shows that some repulsive interaction between segregated atoms may be at the origin of the low-level of GB saturation in boron.

III CONCLUSIONS

1. The intergranular segregation of boron in the FeAl (B2) alloys is characterized by a low level (<12at. %), very fast kinetics and independence of the annealing temperature. These parameters indicate the existence of a non-equilibrium mechanism of segregation. This hypothesis was confirmed by experimental observation of desegregation process after a long low-temperature annealing. The thickness of enriched intergranular layer is slightly higher than 1 nm : this value, too high for an equilibrium segregation, reinforce the assumption of a non-equilibrium segregation.
2. A low-level equilibrium segregation of boron is also stable in the FeAl alloys. The low-level of grain boundary saturation can be explained by strong repulsive interaction between segregated boron atoms. Therefore, the boron segregation in the FeAl alloys may be described by the Fowler model, but not by the Mclean model, which neglects the interactions between segregated atoms.

BIBLIOGRAPHY

1. C.T.Liu, C.L. White, J.A. Horton, Acta Metall., 33, 1985, 213
2. M.A. Crimp, K. Vedula, Mat.sci.Eng., 78, 1986, 193
3. A. Choudhury, C.L. White, C.R. Brooks, Acta Metall., 40, 1992, 57-68
4. J. Rieu, C.Goux, Mem.Sci.Rev. Metall., LXVI, 1969, 869
5. A.S. Gay, A. Fraczkiewicz, M. Biscondi, J. de Phys., 6, 1996, C2-153
6. M.T. Simonetta-Perrot, C. Lorenzon, M. Biscondi, Surf. and Interface Anal., 21, 1994, 316
7. A.-S. Gay, Ph.D. thesis, St-Etienne 1998
8. R.G. Faulkner, Int.Mat.Rev., 41, 5, 1996, 198
9. C.T. Liu, E.P. George, Scripta Metall., 24, 1990, 1285
10. I. Baker, O. Klein, C. Nelson, E.P. George, Scripta Metall., 30, 1994, 863

Materials Science Forum Vols. 294-296 (1999) pp. 457-460

Ordered Monolayer Overstructures Formed on Cu Surfaces Through Segregation

E.C. Viljoen, J.Y. Wang, W.J. Erasmus, J.J. Terblans and J. du Plessis

Department of Physics, University of the Orange Free State, ZA-9300 Bloemfontein, South Africa

Keywords: Surface Segregation, Segregation Kinetics, Darken Model, Copper, Tin, Antimony, Silver

Abstract

The segregation kinetics of the metal dopants Sn, Sb and Ag in copper matrices were determined for three different low index orientations. In the Cu(Sn) and Cu(Sb) systems ordered submonolayer coverages were obtained following a $t^{1/2}$ dependence close to equilibrium values. The kinetics were found to be more complex in the case of Cu(Ag), where a relative high self interaction parameter led to a two step kinetic process. The diffusion parameters were determined in all cases by the appropriate Darken model fits and the results do suggest an orientation dependence of the diffusion coefficient D in the near surface region.

1 Introduction

Until a few years ago, no unified model existed for describing both segregation kinetics and equilibrium values using well established concepts. One such an unified model was proposed previously[1] and since then a number of model segregation systems have been investigated to test the validity of the model. We report on three of these systems, all having a copper matrix. As will become clear, the Darken model describes complex segregation behaviour quite well. In addition, some evidence, although not conclusive, was obtained that suggests that the diffusion coefficient D in the near surface region may be orientation dependent - contrary to the usual theoretical result presented in textbooks [2].

2 Experimental

The experimental detail has been described elsewhere [3]. An important point is that the thermocouple could not be spotwelded to the crystal surface. This may result in systematic differences in the obtained values of D. The experimental results (in terms of surface concentration against time) are given in figure 1 for the three systems.

3 Results and discussion

The rate of increase in the various layers is given by a system of coupled rate equations[1]:

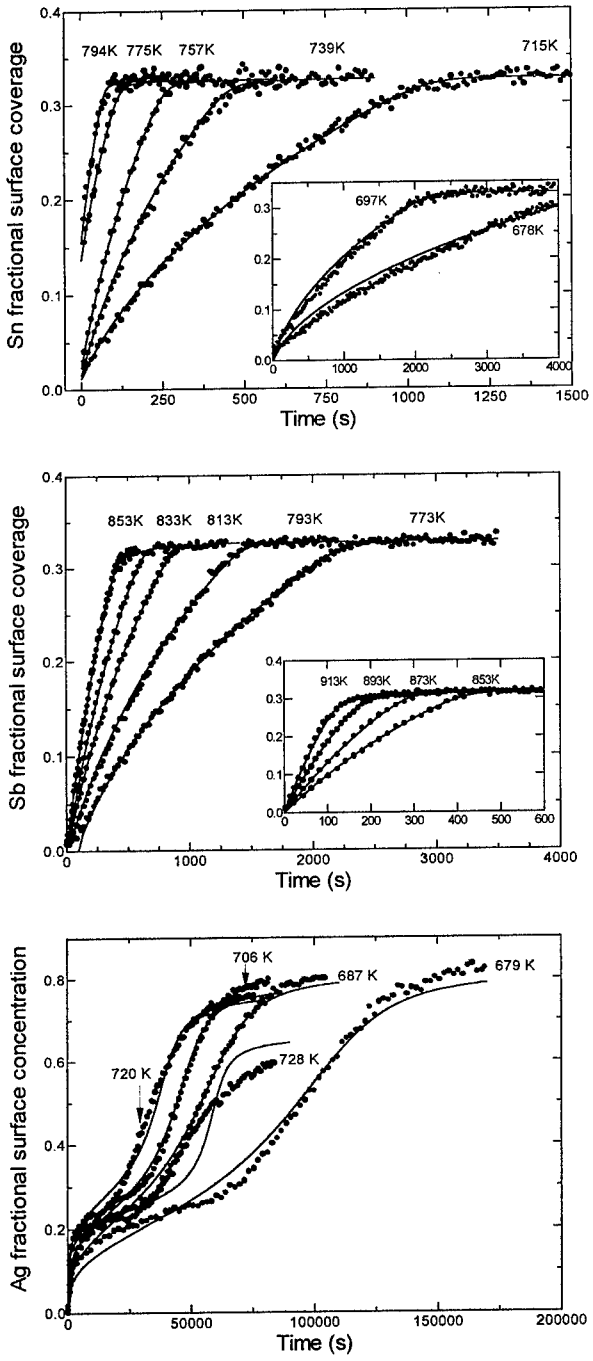

Figure 1: Surface segregation kinetics for (111) orientations for the systems Cu(Sn), Cu(Sb) and Cu(Ag). The solid lines are the best fits of the Darken equations.

$$
\begin{aligned}
\frac{\partial X_1^{\phi}}{\partial t} &= \frac{M_1^{B\leftarrow\phi} X_1^{B_1}}{d^2}\left[\Delta G + RT\ln\left(\frac{X_1^{B_1}\left(1-X_1^{\phi}\right)}{X_1^{\phi}\left(1-X_1^{B_1}\right)}\right)\right] \\
\frac{\partial X_1^{B_1}}{\partial t} &= \frac{M_1^{B} X_1^{B_2}}{d^2}\left[RT\ln\left(\frac{X_1^{B_2}\left(1-X_1^{B_1}\right)}{X_1^{B_1}\left(1-X_1^{B_2}\right)}\right) - RT\ln\left(\frac{X_1^{B_1}\left(1-X_1^{B_2}\right)}{X_1^{\phi}\left(1-X_1^{B_1}\right)}\right)\right] \\
&\vdots \\
\frac{\partial X_1^{j}}{\partial t} &= \frac{M_1^{B} X_1^{j+1}}{d^2}\left[RT\ln\left(\frac{X_1^{j+1}\left(1-X_1^{j}\right)}{X_1^{j}\left(1-X_1^{j+1}\right)}\right) - RT\ln\frac{X_1^{j}\left(1-X_1^{j-1}\right)}{X_1^{j-1}\left(1-X_1^{j}\right)}\right]
\end{aligned}
\tag{1}
$$

where

$$
\begin{aligned}
M_1^B &= \text{mobility of species 1} \\
&= D/RT \text{ (for an ideal solution)}
\end{aligned}
$$

Solutions of these equations, for appropriate values of diffusion coefficient D yielded the solid lines in figure 1. It is clear that the Darken model provides a very good fit of all the data. It follows the time dependence right up to equilibrium and even yields values for the segregation energy ΔG. This parameter is not very sensitive for the high segregation energies for the Cu(Sn) and Cu(Sb) systems. However, in the case of Cu(Ag) a fit of the equilibrium surface coverage against temperature yielded fits of ΔG and the interaction parameter Ω_{12}. Using these values in the kinetic calulations, only the diffusion coefficient D had to be adjusted to fit the complex Cu(Ag) segregation kinetics.

The Arrhenius plots are given in figure 2. As stated above, systematic differences may give rise to the differences in the diffusion coefficient as measured for the different orientations. The results for the more complex Cu(Ag) system are not conclusive, but for the two systems Cu(Sn) and Cu(Sb) the diffusion coefficient (100) direction is markedly higher than for the other two directions. Infrared calibration is now being used to eliminate any systematic temperture errors and further theoretical research is being undertaken to account for the (possible) orientation dependence of D in the near surface region.

References

[1] J. du Plessis and G.N. van Wyk, J Phys Chem Solids 49 (1988), p. 1441;1451;50 (1989), p. 237;247;251

[2] See for example: *Introduction to diffusion in semiconductors*, B. Tuck, IEE Monograph Series 16 (Peter Peregrinus Ltd)

[3] J. du Plessis and E.C. Viljoen, Appl Surf Sci 100/101 (1996), p. 222

[4] (a) S.K. Sen, M.B. Dutt and A.K. Barua, Phys. Stat. Sol. A 32 (1975), p. 345 (b) V.A. Gorbachev, S.M. Klotsman, Ya A. Rabovskiy, V.K. Talinsky and A.N. Timofeyev, Phys. Met. Metalogr. 4 (1973) p. 226 (c) S. Hofmann and J. Erlewein, Scripta Metal. 10 (1976), p. 857

[5] (a) R.C. Weast (ed.), *Handbook of Chemistry and Physics*, 65th edition (CRC Press, Inc., Florida) (b) D.B. Butrymowicz, J.R. Manning and M.E. Read, J. Phys. Chem. Ref. Data 3 (1974), p. 2544

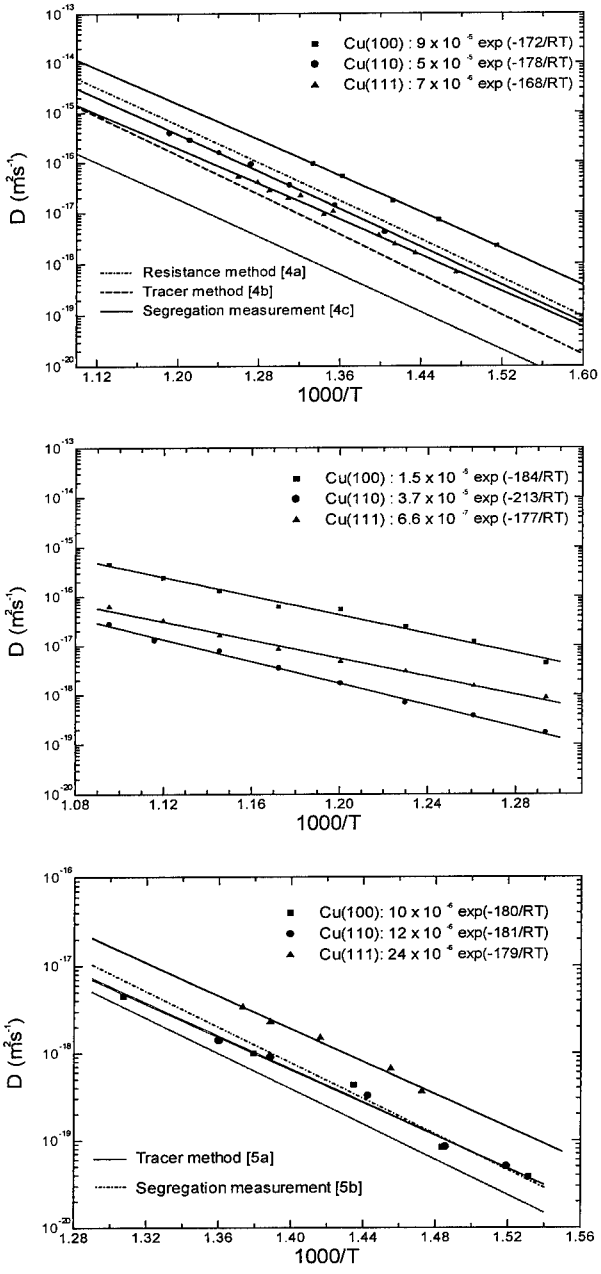

Figure 2: Experimental diffusion coefficient D values for the various low index surfaces for the systems Cu(Sn), Cu(Sb) and Cu(Ag).

Materials Science Forum Vols. 294-296 (1999) pp. 461-464

The Effect of N on the Segregation Kinetics of Mo in a Fe-3.5%Mo-N(100) Single Crystal Studied by Constant Temperature Heating Method

E.C. Viljoen[1], W.A. Jordaan[1], C. Uebing[2] and J. du Plessis[1]

[1] Department of Physics, UOFS, ZA-9300 Bloemfontein, South Africa

[2] Max-Planck-Institut für Eisenforschung, D-40074 Düsseldorf, Germany

Keywords: Surface Segregation, Segregation Kinetics, Darken Model, Molybdenum, Nitrogen

Abstract

The segregation kinetics of molybdenum in a nitrogen atmosphere was studied at temperatures between 773K and 873K. It was found that the rate of segregation of the molybdenum is only slightly enhanced by the presence of the nitrogen. The increase in molybdenum surface coverage as a function of time was fitted with the Darken equations, yielding a segregation energy of $\Delta G_{\mathrm{Mo}} = 28.3$ kJ/mol and an interaction parameter $\Omega = -60$ kJ/mol. The diffusion parameters of molybdenum in the first 20 layers of a iron matrix were determined as $D_0 = 7 \times 10^{-3}$ m^{2}s^{-1} and $E = 290$ kJ/mol.

1 Introduction

The Darken model that describes bulk-to-surface segregation, has been used with much success to determine the bulk diffusion coefficient D and segregation energy ΔG of species in a binary alloy [1, 2, 3]. This binary description is now extended to include a gas layer of atoms of a third kind. This leads to a system that has:

1. a gas layer consisting of atoms of species 2 that absorb on the surface,
2. a surface layer of atoms of species 1, 2 and 3 with fractional concentration given by $X_1^\phi, X_2^\phi, X_3^\phi$, and
3. bulk layers consisting of atoms of specie 1 and 3 where X_j^i is the fractional concentration of specie i in layer j.

In such a system, atoms of species 1 will only segregate to the surface at elevated temperatures if (a) the segregation energy, ΔG_1, is high or (b) ΔG_1 is low, but there exists an attractive interaction Ω that lowers the total energy. This interaction can be either between the different species or a self interaction between atoms of the segregating species.

The rate of increase in the various layers is given by a system of coupled rate equations [4]:

$$\frac{\partial X_1^\phi}{\partial t} = \frac{M_1^{B\leftarrow\phi} X_1^{B_1}}{d^2}\left[\Delta G + RT\ln\left(\frac{X_1^{B_1}\left(1-X_1^\phi\right)}{X_1^\phi\left(1-X_1^{B_1}\right)}\right)\right]$$

$$\frac{\partial X_1^{B_1}}{\partial t} = \frac{M_1^B X_1^{B_2}}{d^2}\left[RT\ln\left(\frac{X_1^{B_2}\left(1-X_1^{B_1}\right)}{X_1^{B_1}\left(1-X_1^{B_2}\right)}\right) - RT\ln\left(\frac{X_1^{B_1}\left(1-X_1^{B_2}\right)}{X_1^\phi\left(1-X_1^{B_1}\right)}\right)\right]$$

$$\vdots$$

$$\frac{\partial X_1^j}{\partial t} = \frac{M_1^B X_1^{j+1}}{d^2}\left[RT\ln\left(\frac{X_1^{j+1}\left(1-X_1^j\right)}{X_1^j\left(1-X_1^{j+1}\right)}\right) - RT\ln\frac{X_1^j\left(1-X_1^{j-1}\right)}{X_1^{j-1}\left(1-X_1^j\right)}\right] \quad (1)$$

where

$$\begin{aligned} M_1^B &= \text{mobility of species 1} \\ &= D/RT \text{ (for an ideal solution)} \\ \text{and } \Delta G &= \Delta G_1^0 + \Omega X_2^\phi. \end{aligned}$$

In the experimental set up a Fe-3.5%Mo(100) crystal is inserted into an Auger electron spectroscopy system with base pressure of $< 10^{-9}$ torr. The crystal is first cleaned *in situ* by cycles of sputtering at 700K and annealing at 900K to remove the oxide layer. Thereafter, at a temperature T, the increase in Auger peak to peak heights (APPH's) is monitored as a function of time t in the presence of N_2 at 5×10^{-7} torr. The APPH's are converted to surface concentration X^ϕ using sensitivity factors [5], Shimizu backscattering factors [6] and TPP-2 escape depths [7]. This data can be fitted by the system of equations 1, the fit parameters being the diffusion coefficient D and the segregation energy ΔG.

2 Results and Discussion

In Fig. 1 the increase in the fractional surface coverage of Mo and N in the presence of N_2 at 821K is shown. Contrary to what is expected, the N concentration is not instantaneously

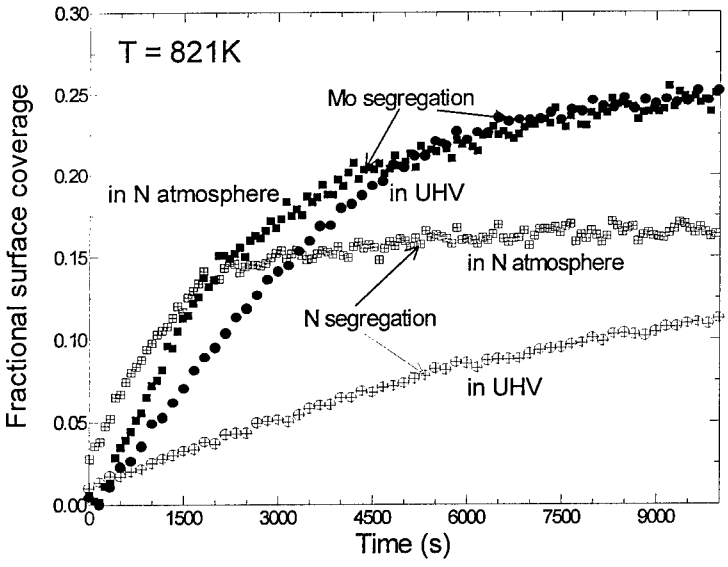

Figure 1: The increase in fractional surface coverage of Mo and N at 821K in (a) the presence of N_2 at 5×10^{-7} torr and (b) UHV.

high, but increases with increase in Mo concentration. The reason for this is the low sticking coefficient of N at elevated temperatures. Mo is needed to stabilize N on the surface [8, 9].

Also shown in Fig. 1 is the increase in Mo and N concentration when the crystal is annealed at 821K in UHV. The rate of increase in the N concentration, due to the 3ppm N present in the iron crystal, is much lower than in N_2 atmosphere. However, the Mo segregation rate is nearly the same and the presence of N in the ambient only slightly enhances it. This indicates that there exists an interaction between Mo and N, but that this interaction is not so large that N is needed on the surface before Mo will segregate.

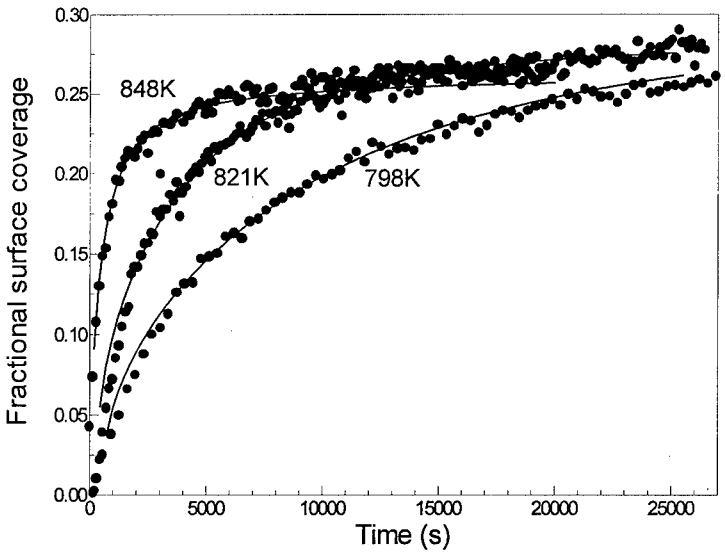

Figure 2: The increase in Mo surface concentration as function of time t at temperatures T = 789K, 821K and 848K. The solid lines are the best fits of the Darken equations.

The increase in Mo surface concentration at temperatures between 773K and 873K is shown in Fig. 2. At lower temperatures the Mo segregation kinetics is very slow, leading to the contamination of the surface by impurities before equilibrium Mo coverage is reached. At temperatures higher than 873K, N desorbs from the surface, changing the Mo segregation rate.

The solid lines on the graph are the best fits of the Darken equations 1, yielding a segregation energy ΔG_{Mo} = 28.3 kJ/mol and an interaction parameter Ω = -60 kJ/mol. The value of the segregation energy compares well with ΔG_{Mo} = 20 kJ/mol determined previously [10]. The interaction parameter is needed because the time dependance of Mo segregation deviates from the usual $t^{1/2}$ relation. However, the value is much larger than the interaction between Mo and N indicated in Fig. 1. This may indicate a self interaction between the Mo atoms increasing the segregation energy as the surface concentration increases. Another possibility is that, because the Mo diffusion length of 10-20 layers is in the same order of magnitude as the surface roughness, there is a deviation from the model $t^{1/2}$ behaviour.

The diffusion coefficient D of Mo obtained by the Darken fits of the data in Fig. 2 is shown on the Arrhenius plot in Fig. 3. A linear regression yields $D_0 = 7 \times 10^{-3}$ m^{2}s^{-1} and E = 290

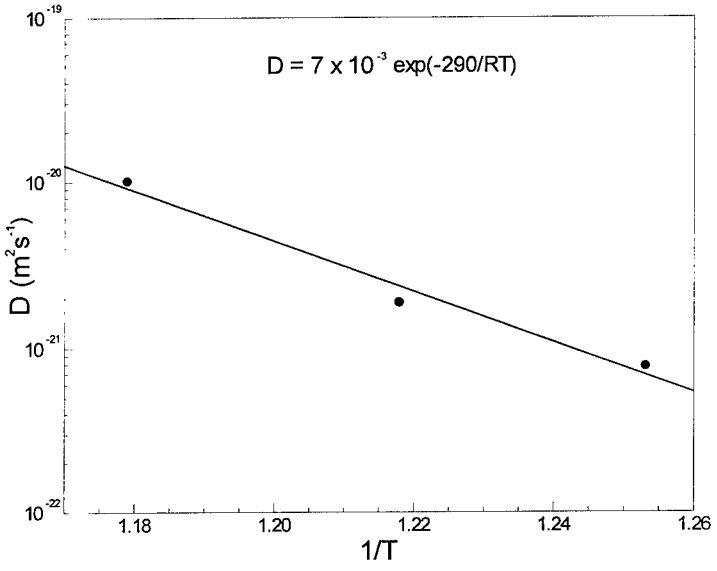

Figure 3: The Arrhenius plot of the D values obtained by the Darken fits in Fig. 2.

kJ/mol. These are not the bulk diffusion parameters of Mo in a Fe matrix, but rather indicates the diffusion of Mo through the first 20 Fe layers in a Fe(100) crystal. Since Mo is necessary to stabilize N on the surface, these parameters will play a significant role in any N layer formation on the surface.

References

[1] J. du Plessis and P.E. Viljoen, Surf. Sci. Let. 276 (1992), p. L7

[2] E.C. Viljoen, J. du Plessis, H.C. Swart, and G.N. van Wyk, Surf. Sci. 342 (1995), p. 1.

[3] J. du Plessis and E.C. Viljoen, Appl. Surf. Sci. 100-101 (1996), p. 222.

[4] J. du Plessis and E. Taglauer, Surf. Sci. 260 (1992), p. 355.

[5] L.E. Davis, N.C. MacDonald, P.W. Palmberg, G.E. Riach, and R.E. Weber, editors, *Handbook of Auger electron spectroscopy*, Physical Electronics Industries, Eden Prairie, 1976.

[6] R. Shimizu, Jap. J. Appl. Phys. 22 (1983), p. 1631.

[7] S. Tanuma, C.J. Powell and D.R. Penn, Surf. Interf. Anal. 17 (1991), p. 911.

[8] B. Eltester and C. Uebing, Surf. Sci. 347 (1996), p. 39.

[9] E.C. Viljoen, C. Uebing, Surf. Rev. and Letters, 4 (1997), p. 601.

[10] E.C. Viljoen, B. Eltester and C. Uebing, Surf. Rev. and Letters 3 (1996), p. 1421

Materials Science Forum Vols. 294-296 (1999) pp. 465-468

Surface Segregation on Fe-25%Cr-2%Ni-0.1%Sb Single Crystals

E. Clauberg, C. Uebing, H. Viefhaus and H.J. Grabke

Max-Planck-Institut für Eisenforschung Postfach 140444, D-40074 Düsseldorf, Germany

Keywords: Antimony, Auger Electron Spectroscopy (AES), Iron, Low Energy Electron Diffraction (LEED), Low Index Single Crystal Surfaces, Surface Segregation

Abstract

Surface segregation was investigated on (100) oriented Fe-25%Cr-2%Ni-0.1%Sb-N,S single crystals. For temperatures up to 500°C, cosegregation of nitrogen and chromium is observed; the corresponding LEED pattern exhibits a (1×1) structure. In the temperature range between 500°C and 650°C, nitrogen and a large amount of chromium are replaced by segregating antimony and nickel. A depth profile showed that the enrichment of antimony and nickel is restricted to one monolayer. The LEED pattern taken of an antimony saturated surface is the result of a highly defective surface structure. For temperatures higher than 650°C or long annealing times, antimony is replaced by segregating sulphur; the corresponding LEED pattern yields a c(2×2) structure.

Introduction

Segregation phenomena greatly affect the material properties of steels. Both impurity elements and alloying elements may segregate to the surface or to the grain boundaries at elevated temperatures. Some elements mutually enhance their segregation; this phenomenon is referred to as cosegregation. Antimony is a tramp element and has a strong tendency to grain boundary segregation and even more to surface segregation in steels. The question if antimony and nickel cosegregate to the grain boundaries in steels and iron alloys has been explored by several authors [1, 2, 3, 4]; however, the investigations yielded contradictory results. Chromium has been reported to intensify the enhancing influence of nickel on antimony segregation to the grain boundaries [5].

In this work, surface segregation of nickel and antimony will be investigated. A Fe-25%Cr-2%Ni-0.1%Sb single crystal that contains the impurities nitrogen and sulphur as additional segregating species is investigated by means of Auger electron spectroscopy (AES) and low energy electron diffraction (LEED). Apart from the question if antimony and nickel enhance their respective tendency to surface segregation, this system is of special interest as it can be considered as a model for the interdependent behaviour of various segregating species.

Experimental

The ferritic Fe-25%Cr-2%Ni-0.1%Sb single crystal (concentrations are given in weight percent) was produced by the vertical Bridgman technique. The nitrogen content of the material was determined as 55 weight ppm by chemical bulk analysis. Since irregularly distributed precipitates

were present in the material after growing, the crystal was annealed in an argon atmosphere at 1300°C for 3 days. As a result of this treatment, the precipitates were still present but uniformly spread within the material. The crystal was spark-eroded into slices which were ground and polished mechanically until a mirror-like finish was obtained. Surface analysis was conducted in a Varian AES-LEED system that is described in detail elsewhere [6]. After introduction into the UHV system, the samples were cleaned by sputtering and heating cycles. For the calculation of the Auger peak height ratios (PHR) that will be referred to in the next section, the following Auger peaks were used: Fe($L_3M_{23}V$), Sb($M_5N_{45}N_{45}$), N($KL_{23}L_{23}$), Cr(L_3VV) and Ni($L_3M_{45}V$).

Results and discussion

The experiments were performed on (100) oriented surfaces in the temperature range between 450°C and 750°C. Prior to most experiments, the samples were sputter-cleaned at room temperature. At lower temperatures up to 500°C, cosegregation of nitrogen and chromium is observed. Final N/Fe PHR of 1.0±0.1 and Cr/Fe PHR of 1.8 are attained independent of the conditions of enrichment, indicating that there is saturation of the surface with the compound CrN. A typical Auger spectrum of a surface covered with CrN is shown in Fig. 1 (a). The corresponding LEED pattern shows a sharp (1×1) structure after sufficient annealing time (15 h at 500°C). These results are in accordance with investigations performed on Fe-Cr-N single crystals with lower chromium and nitrogen contents [7].

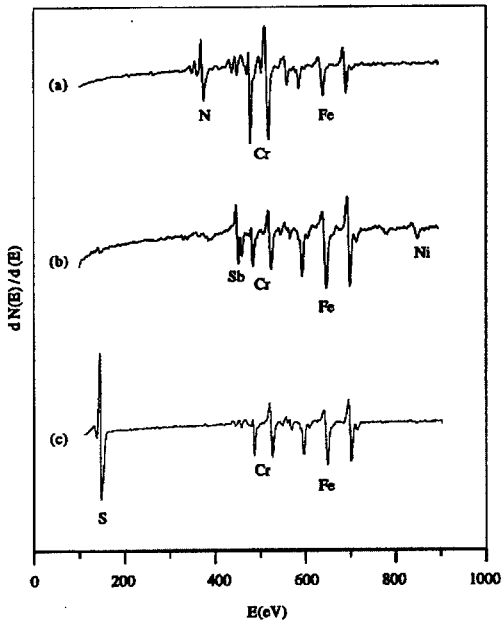

Figure 1: Auger spectra of the sample surface covered with different segregating species; (a) Saturation with CrN, 500°C; (b) Saturation with Sb, 620°C; (c) Segregation of sulphur, 700°C

In the temperature range between 500°C and 650°C, antimony segregates to the surface accompanied by nickel and replaces nitrogen and a large amount of chromium. A final Sb/Fe PHR of 0.8 is reached over the whole temperature range, indicating that there is saturation of the surface with antimony. The amount of nickel that can be detected on the antimony saturated surface varies depending on the temperature of antimony enrichment and the pretreatment of the sample; the maximum Ni/Fe PHR ranges between 0.1 and 0.2. Nickel can only be detected on the sample surface in the presence of segregated antimony; thus, antimony probably enhances the tendency of nickel to segregate. The question if nickel enhances antimony surface segregation as well cannot be explored with the material under investigation as surface saturation with antimony occurs under all conditions.

A depth profile of the antimony-nickel segregation layer was taken to gain information on the structure of the segregation layer. A problem with the interpretation of the depth profile is that the detection limit for antimony is high since the major antimony peak overlaps with the small chromium peaks; a Sb/Fe PHR below 0.3 cannot be reliably detected. The depth profile yielded the result that the Ni/Fe and Sb/Fe peak height ratios fall below the detection limit after a few minutes of sputtering time corresponding to the removal of half a monolayer. Thus, it can be concluded that the enrichment of antimony and nickel is mainly restricted to one surface layer.

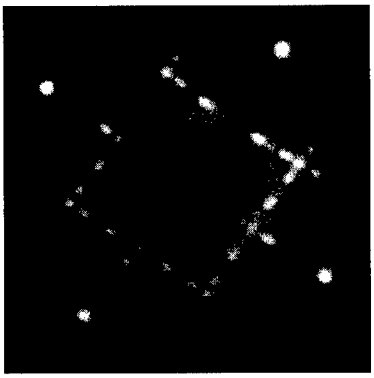

Figure 2: LEED pattern of antimony saturated surface after 15 h of annealing at 620°C, Ni/Fe PHR=0.15, E=82eV

A LEED investigation of the antimony saturated surface yielded the complex pattern shown in Fig. 2. This pattern can be derived from a c(2×2) structure in which the reflexes are splitted. The pattern can be compared to the pattern obtained for the (100) surface of Fe-4%Sb single crystals [8]; in this case, splitting of the reflexes to a smaller degree is found and interpreted as the result of a defective c(2×2) structure. From the LEED pattern discussed here, it can be concluded that the surface contains even more defects.

For temperatures higher than 650°C, antimony is replaced by segregating sulphur. An Auger spectrum of a sulphur covered surface is shown in Fig. 1 (c). The corresponding LEED pattern shows a c(2×2) structure. When LEED patterns are recorded during the displacement of antimony by sulphur, it can be observed that the splitted reflexes move closer to each other with increasing sulphur enrichment and finally unify.

References

[1] J. Bernadini, P. Gas, Scripta Met. 22 (1988) 1165

[2] H. J. Grabke, C. L. Briant, Scripta Met. 22 (1988) 1169

[3] A. Wirth, I. Andreoni, G. Gregory, Surface and Interface Analysis 9 (1986) 157

[4] R. Mast, Ph. D. Thesis, The University of Dortmund, 1996

[5] C. L. Briant, A. M. Ritter, Acta Met. 32 (1984) 2031

[6] H. Viefhaus, M. Rüsenberg, Surf.Sci. 159 (1985) 1

[7] C. Uebing, H. Viefhaus, H. J. Grabke, Appl. Surface Science 32 (1988) 363

[8] M. Rüsenberg, H. Viefhaus,Surf. Sci. 172 (1986) 615

Materials Science Forum Vols. 294-296 (1999) pp. 469-472

First-Principles Theory of Coherent Precipitation in Size-Mismatched Alloys

C. Wolverton

National Renewable Energy Laboratory, Golden, CO 80401, USA

Keywords: First-Principles Theory, Precipitation, Coherency Strain, Al-Cu, Al-Mg

Abstract. A first-principles thermodynamic approach for studying coherent precipitation in size-mismatched alloys is presented. The approach takes into account both strain and interfacial energies, incorporates the effects of finite temperature, and can treat systems with length scales of ~200Å, all with first-principles accuracy. The method is applied to coherent precipitation in Al-Cu and Al-Mg alloys, where the coherent precipitation sequence is experimentally well-studied, but still controversial. This theoretical approach should aid in understanding the strengthening mechanism underlying precipitation hardening in these materials.

The strengthening of alloys relative to pure metals has been a subject of technological and scientific interest for centuries. In precipitation hardening, small amounts of a solute element are added to the pure metal at high temperatures (where there is solubility between the two metals), and the alloy is quenched down in temperature and aged so that the solute atoms begin to precipitate out of the matrix. [1, 2, 3] The aged alloy is made stronger because dislocation motion through the crystal is impeded by the precipitate itself and also by the elastic strain field surrounding the precipitate. Since coherent precipitates involve no dislocations between the precipitate and matrix, and hence have a large strain field surrounding them, they are very effective at strengthening in alloys. To understand the mechanism of this strengthening, one must first understand the atomic scale structure (e.g., size, shape, ordering) of the coherent precipitates, which requires knowledge of both the strain and interfacial free energies of the precipitate. Hence, the shape, size, and atomic structure of coherent precipitates have been the subject of intense experimental study. [1, 2, 3]

The study of coherent precipitation with a first-principles theoretical approach is problematic because: (1) The length scale of coherent precipitates is often ~100Å or more, (2) highly strained, atomically-relaxed configurations result from the coherency strain between precipitate and matrix, (3) finite-temperature free energies are needed (as opposed to T=0 energetics), and (4) substitutional disorder in both matrix and precipitate must be treated. Here, we present a first-principles total energy theory which overcomes the above difficulties and hence is capable of directly examining the structure, energetics, and thermodynamics of coherent precipitation in size-mismatched alloys. This theoretical approach should aid in understanding the strengthening mechanism in these alloys. The method used here to describe the energetics of coherent configurations involves mapping first-principles local density approximation (LDA) alloy energetics onto an effective Hamiltonian, the mixed-space cluster expansion (CE): [4, 5] For a single, underlying parent lattice (in this case, fcc) one defines a configuration, σ, by specifying the occupations of each of the N lattice sites by an A-atom or a B-atom, with $\hat{S}_i = \pm 1$ assigned to each of the N sites. The formation energy (the energy with respect the the compositional average of the alloy constituents) of any configuration σ is then given by

$$\Delta H(\sigma) = \sum_{\mathbf{k}} J(\mathbf{k})|S(\mathbf{k},\sigma)|^2 + \sum_f D_f\, J_f\, \overline{\Pi}_f(\sigma) + \frac{1}{4x(1-x)} \sum_{\mathbf{k}} \Delta E_{\mathrm{CS}}^{\mathrm{eq}}(\hat{k},x)|S(\mathbf{k},\sigma)|^2 \qquad (1)$$

where the J's are the interaction energies ("effective cluster interactions"), f is a symmetry-distinct figure comprised of several lattice sites, D_f is the number of figures per lattice site, and the "lattice-averaged product" $\overline{\Pi}_f$ is defined as a product of the variables $\hat{S}_i$, over all sites of the figure f averaged over all symmetry equivalent figures of lattice sites.

The mixed-space CE of Eq. (1) is separated into three parts: (1) The first summation includes *all pair figures* with arbitrary separation, conveniently summed using the reciprocal-space concentration-wave formalism. $J(\mathbf{k})$ and $S(\mathbf{k},\sigma)$ are the lattice Fourier transforms of the real-space pair interactions and spin-occupation variables. (2) The second summation includes only *non-pair figures*, f. (3) The third summation involves $\Delta E_{\rm CS}(\hat{k},x)$, the *coherency strain energy*, defined as the strain energy of bulk A and B required to maintain coherency along an interface with orientation $\hat{k}$. In practice, this may be calculated by the energy change when the bulk fcc solids A and B are deformed from their equilibrium cubic lattice constants $a_{\rm A}$ and $a_{\rm B}$ to a common lattice constant $a_\perp$ in the direction perpendicular to $\hat{k}$.

$$\Delta E_{\rm CS}(\hat{k},x) = \min_{a_\perp}\left[(1-x)\Delta E_{\rm A}^{\rm epi}(\hat{k},a_\perp) + x\Delta E_{\rm B}^{\rm epi}(\hat{k},a_\perp)\right]. \qquad (2)$$

where $\Delta E_{\rm A}^{\rm epi}(\hat{k},a_\perp)$ is the energy required to deform A biaxially to $a_\perp$. [6] (A detailed discussion of the calculation of coherency strain from first-principles total energies including anharmonic elastic strain terms, and its parameterization for arbitrary wavevector, is given in Ref. [7].)

The mixed-space CE Hamiltonian for fcc Al-Cu and Al-Mg has been constructed using fully-relaxed, full-potential, linearized augmented plane wave (LAPW) total energies. Total energies of 41 (33) ordered compounds were used to fit the values of the interaction energies of Eq. (1), $J(\mathbf{k})$ and J_f for Al-Cu (Al-Mg). A large number of pair (~40-50) as well as three- and four-body interactions where used to fit the LAPW energetics. All compounds were relaxed to their energy-minimizing geometry with respect to volume, unit cell vector lengths, and cell-internal coordinates. These ordered compounds included short-period superlattices for a variety of orientations (e.g., [100], [111], [110], etc.), special quasi-random structures [8] which mimic the random alloy, isolated substitutional Cu and Mg impurities, and other structures. Additionally, for the Al-Cu system, the energies of several supercells were evaluated which were specifically relevant to the precipitation sequence in this alloy: Dilute $Al_{16-p}Cu_p$ (p=1,2) supercells of {100} monolayers and bilayers of Cu (both for 100%Cu and <100% Cu). LAPW epitaxial energies of the alloy constituents for 5 different orientations ([100], [111], [110], [201], and [311]) were used to compute the strain energies $\Delta E_{\rm CS}^{\rm eq}(\hat{k},x)$. The mixed-space CE Hamiltonian of Eq. (1) thus contains interfacial and strain energies, both determined from a first-principles quantum-mechanical approach. With this Hamiltonian, one can compute the energy of any configuration (not only ordered compounds), even 100,000-atom cells or larger with the accuracy of fully-relaxed, full-potential LAPW total energies. Furthermore, the form of the Hamiltonian is sufficiently simple so that it can be used in a mixed-space Monte Carlo algorithm to deduce thermodynamic properties of coherent fcc-based configurations.

The calculated $T = 0$ K coherency strain energies alone give some indications of preferred orientation, shape, and structure of the GP zones (coherent conglomerates of solute atoms). In the dilute limit ($x_{\rm Al} \to 1$) Cu (or Mg) is highly strained and Al is unstrained, and therefore the coherency strain values reflect the elastic response of elemental Cu and Mg when strained biaxially to $a_{\rm Al}$. The two elements show very different elastic response: In dilute Al-Cu alloys, the strain energies are ~200-240 meV/Cu atom, except for the {100} direction which is elastically extremely soft [$\Delta E_{\rm CS}(100) = 52$ meV/Cu atom], meaning that Cu is easily distorted to $a_{\rm Al}$ along the {100} direction. This soft elastic response along {100} is correlated with the small fcc/bcc energy difference in Cu. [7] The strong directional selectivity leads to an energetically strong preference for Cu to form {100} planar-type precipitates, as has been well established

by a variety of experimental measurements. The strain energies in Al-Mg are not only generally smaller than Al-Cu (reflecting the relative softness of Mg compared to Cu), but the strain is also much more isotropic in Al-Mg [$\Delta E_{CS}(\hat{k}) \sim$ 90-100 meV/Mg atom, for all directions except $\Delta E_{CS}(111) = 150$ meV/Mg atom]. One would expect, at least for very large precipitates (which are dominated by the strain contribution), a more spherical precipitate structure, again which agrees well with measured data.

We have subjected the Al-Cu mixed space CE of Eq. (1) to Monte Carlo simulations, using fcc unit cells with sizes of 16^3-60^3=4192-216,000 atoms (with corresponding length scales of ~50-170Å), 100-1000 spin flips/atom for taking thermal averages, and the canonical (fixed composition) ensemble. We describe the results of our Monte Carlo simulations for a 2-at.%Cu cell, starting at high temperature and cooling down to low temperature: At high temperature, there is a solid solution where Cu is soluble in Al. We find a short-range clustering tendency in this solid solution, in agreement with diffuse scattering measurements. [2] By monitoring the specific heat as the temperature of the Monte Carlo simulation is lowered, one may determine the metastable coherent fcc phase boundary. One advantage of this theoretical approach is that the Hamiltonian is constrained to only fcc-based configurations; hence the equilibrium, incoherent phase boundary between Al + Al_2Cu is not seen, and the metastable coherent phase diagram is exposed. We find evidence of a single thermodynamic transition at $T_c \sim 300$°C. By performing simulations at a variety of compositions (up to x_{Cu}=25%), we are able to determine that the coherent phase boundary for dilute compositions represents a two-phase field between the Al-rich solid solution and a metastable Al_3Cu phase, which is an Al_3Cu_1 (100) superlattice consisting of two (100) planes of Cu separated by three planes of Al. In other words, we predict that the fcc coherent phase diagram of Al-Cu has an ordered Al_3Cu ground state. [The stability of this structure is also confirmed from direct LAPW calculations (i.e., it has a lower energy at the Al_3Cu composition than any other structure or two-phase mixture of structures of the 41 considered compounds).] This (100) structure corresponds to the traditional model of GP2, a coherent precipitate formed in the latter stages of aging in Al-Cu alloys.

By examining the output of the Monte Carlo cells inside the coherent two-phase region, we can ascertain the precipitate shape and structure. The output of two typical Monte Carlo runs is shown in Fig. 1. Depending on different initial conditions and Monte Carlo cell sizes, we find either Cu monolayers (Fig. 1a) or two Cu monolayers separated by three Al layers (Fig. 1b). Interestingly, these two structures correspond to the "traditional model" of the two types of GP zones in Al-Cu, GP1 and GP2, respectively. We find roughly disc-shaped zones (although some {010} and {011} faceting can be seen in Fig. 1). Also, our calculations indicate that the composition of the zones is 100% Cu. The mixed-space CE Hamiltonian also provides the decomposition of the zone energies into strain and interfacial contributions, and we have used this decomposition make some statements about the nucleation of GP2 zones from GP1. [9]

Work at NREL was supported by the Office of Energy Research (OER) [Division of Materials Science of the Office of Basic Energy Sciences (BES)], U. S. Department of Energy, under contract No. DE-AC36-83CH10093.

References

[1] A. Guinier, Solid State Physics **9**, 293 (1959).

[2] J. B. Cohen, Solid State Physics **39**, 131 (1986).

[3] H. Zandbergen, S. J. Andersen, and J. Jansen, Science **277**, 1221 (1997).

[4] D. B. Laks, L. G. Ferreira, S. Froyen, and A. Zunger, Phys. Rev. B **46**, 12587 (1992).

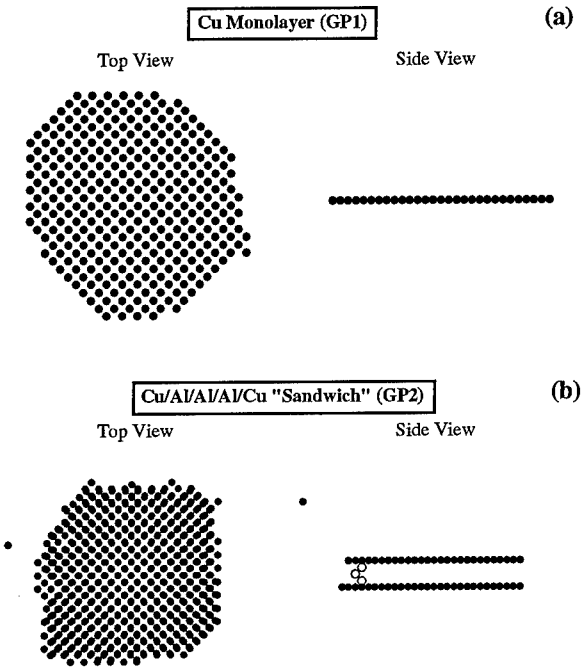

Fig. 1. Predicted precipitate shapes from the mixed-space cluster expansion Hamiltonian combined with Monte Carlo simulations. Shown are two typical zone structures found, corresponding to (a) an {001} Cu monolayer, and (b) a Cu/Al/Al/Al/Cu structure, corresponding to GP1 and GP2 of the traditional model. Only Cu atoms (black) are shown, and for clarity, three Al atoms (white) are shown for the GP2 zone in order to emphasize the three Al layers between the two Cu layers.

[5] V. Ozoliņš, C. Wolverton, and A. Zunger, Phys. Rev. B **57**, 6427 (1998).

[6] When the precipitate consists of an *ordered phase*, rather than a GP zone, the strain energy of the CE between precipitate and matrix can be substantially improved by attenuating the strain energy in Eq. (1) by a decreasing function of the magnitude of the wavevector (V. Ozoliņš, C. Wolverton, and A. Zunger, unpublished). We have used such an attenuating function for the Al-Mg CE, but not for Al-Cu, as we find that this function provides no significant differences in our results for this system.

[7] V. Ozoliņš, C. Wolverton, and A. Zunger, Appl. Phys. Lett. **72**, 427 (1998).

[8] A. Zunger, S.-H. Wei, L. G. Ferreira, and J. E. Bernard, Phys. Rev. Lett. **65**, 352 (1990).

[9] C. Wolverton, Phys. Rev. Lett. (submitted, 1998).

Materials Science Forum Vols. 294-296 (1999) pp. 473-476

Embedded Lead Inclusions in Aluminium, Aluminium-Silicon Eutectic Alloys and Silicon

S. Hagège, L. Haas, P. Ochin, A. Dezellus, Ph. Plaindoux and J.C. Rouchaud

Centre d'Etudes de Chimie Métallurgique, UPR CNRS 2801, F-94407 Vitry-sur-Seine, France

Keywords: Pb, Al, Si, Monotectic Alloys, Equilibrium Morphology, Interfacial Energy, Twins, Melt Spinning, TEM

Abstract : Small inclusions of Pb have been embedded in pure Al, AlSi composites and pure Si by rapid quenching. Inclusions in aluminium are topotactic truncated octahedra undergoing large overheating and undercooling during in situ TEM thermal treatment. In the composite AlSi there is a definite tendancy for the inclusions to appear only in the aluminium phase. In pure silicon they are topotactic truncated octahedra with a smaller aspect ratio than in Al. They appear also on single and multiple twins with compound morphology. No overheating has been detected whereas undercooling is size dependent and can reach 80°C.

Introduction

Rapid solidification of binary monotectic alloys produces a fine dispersion of small inclusions embedded in a matrix. The thermal behaviour of these inclusions can be monitored in-situ in a TEM thin foil and in this process they can reach their equilibrium shape easily. Therefore, their orientation, morphology and atomic structure at the heterophase interfaces of the different facets can be unambiguously associated with the lowest energy configuration.

The aluminium-lead binary system has produced numerous experimental results over the past few years [e.g.1-3] provoking a great interest in the fundamental aspects of melting and solidification, interfacial energy for heterophase interfaces and influence of impurity traces on the structure and morphology of interfaces. The two main experimental routes to obtain an homogeneous distribution of fine inclusions in the matrix for monotectic alloys are rapid quenching from the homogeneous melt (melt spinning) and ion implantation[1-3]. Some tentatives by mechanical alloying [4] or ultrasonic field [5] have been also reported in the literature.

One natural extension of this approach was to keep aluminium as a matrix and substitute lead by another metal with a comparable binary phase diagram (Bi[6] , Cd[7] , In[8] , Tl[9]). The next step was to introduce a third element to be incorporated within the inclusion, or segregated at the matrix inclusion interface (Cd-Mg[10], Pb-Bi[11], Pb-Cd[12]). Then the effect of silicium on the nucleation of Pb inclusions in Al has been observed for very low concentrations[13]. For other fcc matrices, Cu, Ni [14] were shown to contain topotactically aligned lead inclusions. Zinc specified the role played by a hexagonal matrix[15]. Very recent work showed even the role of quasicrystalline lattice on the orientation of lead inclusions[16] Lead in diamond structure, as in silicon, has already been tried by ion implantation[17], giving preliminary results on the orientation and thermal behaviour of the inclusions with the remaining difficulty of avoiding amorphisation of the matrice during implantation

Melt spinning of silicon faces several problems related to the rf frequency inducing the melt of the alloy, and to the silica nozzle spraying the liquid alloy onto the spinning wheel. These technical difficulties can be overcome by alloying the silicon to a non miscible metal and lowering the melting temperature of the system by choosing an eutectic composition. As an alternative way of obtaining a fine scale precipitation of lead in silicon, the eutectic Al-Si alloy, containing a small amount of Pb, is rapidly quenched, thus producing particles of pure lead in a composite system. Finally, drastic improvements of the experimental set up and fine tuning of the injection conditions allow pure and lead alloyed silicon to be rapidly quenched [18].

The purpose of this contribution will be to give a first insight of the structure and morphology of lead inclusions in silicon and compare these results to pure aluminium matrix and composite aluminium-silicon composite matrix. The presence of lead inclusions on single and multiple twins in silicon grains indicates experimental evidence of relative energies between the two structures.

Experimental Procedure

The alloys of composition $AlPb_{0.5at\%}$, $(Al_{88}Si_{12})Pb_{0.5at\%}$, $SiPb_{0.5at\%}$ were prepared by rf induction melting. The ingots were rapidly quenched using the planar flow technique. AlPb and AlSiPb samples are produced in long ribbons, 1 cm wide and 20 μm thick following the quenching conditions employed. For equivalent experimental conditions, high concentrations of silicon produce needle like flakes of 1 to 2 mm in width. In order to control and limit the loss of lead during the homogeneisation of the melt at high temperature, the chemical composition of the quenched material was verified by ICP-AES (inductively coupled plasma - atomic emission spectroscopy). TEM thin foils were prepared by electropolishing for AlPb alloys and ion milling for all the compositions containing silicon. TEM observations were made using a heating stage at 200 kV.

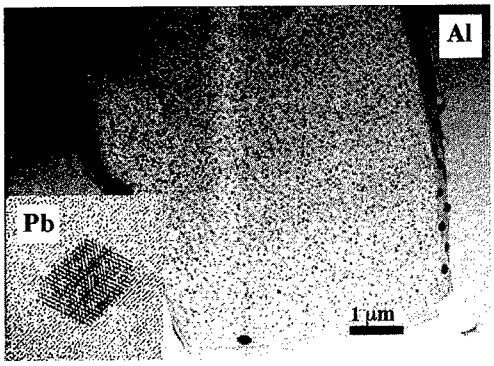

Figure 1. Pb inclusions in pure aluminium

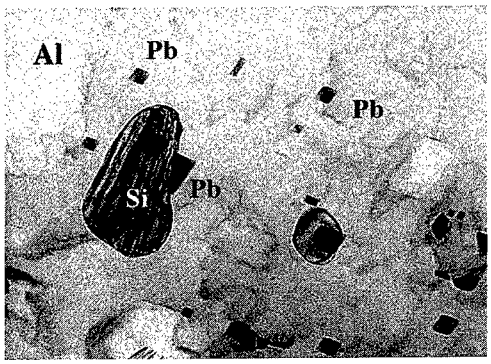

Figure 2. Pb inclusions in the eutectic Al-Si alloy

Lead inclusions in aluminium :

Despite the 20% misfit in parameters between the two fcc structures, lead inclusions in the grains of polycrystalline aluminium are truncated octahedra, topotactically oriented in a matrix found to be almost free of defects (Fig. 1). On heating, most of the particles within the grains remain solid well above the melting point of bulk lead (T_b). This "overheating" effect is size dependent, the smaller inclusions staying in the solid state up to 100°C above T_b. This effect is in fact shape dependent : the smallest inclusions have an aspect ratio ($\gamma_{100}/\gamma_{111}$) which is larger than the average, 1.15, and are often seen as pure octahedra, limited only by (111) facets, without truncation or other defects. Solidification of the inclusions follows the same pattern in reverse, with the smallest particles still liquid as low as 50°C below T_b. Inclusions on $\Sigma 3$ twins are themselves twinned, and their global morphology is based on the interpenetration of two (eventually truncated) octahedra[3]. On general grain boundaries, inclusions are generally single crystals, oriented topotactically with one grain and faceted in this grain, while the interface facing the other grain is curved without any sign of faceting.

Lead inclusions in the aluminium-silicon eutectic system :

Rapidly quenched aluminium silicon alloys at the eutectic composition (12at% Si) cannot reach the equilibrium morphology usually found for oriented growth for instance. Our alloys are therefore aluminium based composites with an homogeneous dispersion of silicon grains, usually twinned, but without particular shape or preferential orientation with the matrix. A wide range of compositions has been explored (5 to 85at% Si) in order to follow the evolution of the global morphology of the composite with respect to the distribution of lead inclusion throughout the composite.

When lead is included in the composition of the alloy, the inclusions are only found within the aluminium phase. Their structure, morphology and thermal behaviour are very similar to those observed in pure aluminium. No lead inclusion has ever been found in the silicon phase of the composite alloy. On relatively rare occasions, a lead particle is found at the aluminium silicon interface but does not even protrude into the silicon phase (Fig. 2). This clearly indicates a definite tendency for lead to segregate, in the liquid phase, in aluminium and not in silicon . This is a consequence of the non homogeneity of the melt at the temperature at which the alloy is maintained before quenching (approx. 100°C above the liquidus)

Even if the composite is gradually enriched in silicon, lead is always confined to the aluminium phase. For the most Si enriched alloys that we have been able to quench in the traditionnal set up, the aluminium phase is found as an amorphous film between the silicon grains. These films still contain crystalline lead; however, in these extreme cases, lead inclusions no longer have a particular shape and are seen as a fine dispersion of nano-crystallites.

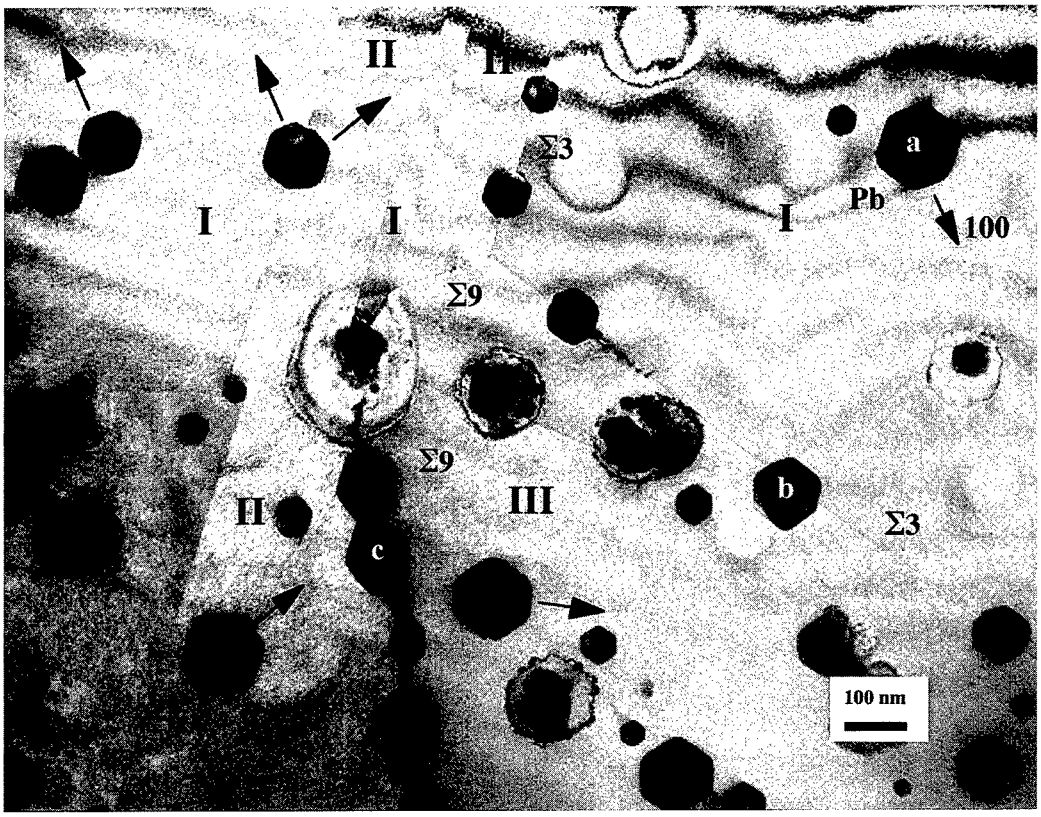

Figure 3. Inclusions in a multiple twinned silicon grain. [100] directions are indicated in every orientation I,II and III. Note the shape of the inclusions inside a grain (a) on Σ3 (b) and Σ9 (c) twins

Lead inclusions in silicon :

Rapid quench of silicon with an improved experimental set up and conditions reported elsewhere[17], produces polycrystalline flakes with a grain size ranging from 5 to 20 μm. Most of the grain are twinned creating networks of multiple twin boundaries with "singular" triple junctions. For SiPb alloys inclusions are found all over the sample, first on general grain boundaries and general triple junctions, then within the grains and along the twins (Fig. 3). The morphology of these inclusions varies according to the localisation in the specimen. Related to the general tendancy for lead to segregate in grain boundaries, specimen have an increasing brittleness for high lead content

Structure and morphology of the inclusions embedded in a silicon grain :

Lead inclusions in silicon have a cuboctahedral shape; the extent of the (100) truncation is always significant and leads to an aspect ratio larger than one but still smaller than the one found in aluminium (Fig 3). Almost no perfect octahedra were found even among the smallest size. They are topotactically oriented with the matrix (the misfit is now 10% but the ratio is reversed (a_{Si}/a_{Pb} = 1.10; a_{Al}/a_{Pb} = 0.83). Thermal behaviour shows no overheating of the lead inclusions. They all melt within 3-5°C above T_b. There is a definite size dependent undercooling, ranging from 50°C below T_b for the 100nm range inclusions, to 85°C for the smallest ones (approx. 20nm). For long annealing above T_b, when lead is liquid,the inclusions have a tendancy to smooth their (100) truncation.

Inclusions on single twins (Σ 3), multiple twins (Σ 3^n) and triple junctions in silicon :

Inclusions on Σ3 twin boundaries are very regular in shape. They are always twinned and correspond to the overlap of two truncated octahedra sharing a common (111) facet (Fig. 3). The extent of the overlap, or the volume ratio between the two components of the twinned lead particle, varies from one perfect symmetrical morphology to a tiny crystal of lead twinned to a larger grain on the other side of the silicon twin boundary. Whatever their shape, they all exhibit a continuity at the twin boundary. In other words, the extent of the common (111) facet lying on the (111) twin boundary in silicon is the same for the two elements of the lead inclusion. One interesting feature of the more symmetrically twinned lead particles is the presence of a re-entering angle made of (111) facets opposite a protruding angle made of (100) facets.

On multiple twins there is a high density of similarly twinned inclusions varying in faceted shape and overall symmetry. Most of the time they are seen to be continuously distributed along the interface indicating a preferential "complete wetting" of the multiple twins in silicon by lead (Fig. 3).

Acknowledgements : These results are part of an ongoing research project on the structure, morphology and thermal behaviour of nanosized inclusions with U. Dahmen (NCEM - LBL Berkeley, USA) and E. Johnson (Niels Bohr Institute - Copenhagen, Danemark). They are gratefully acknowledged for their collaboration.

References :

[1] K.L. Moore, K. Chattopadhyay and B. Cantor, Acta Metal. Mater. **38** (1990), 1327 and following works

[2] E. Johnson et al, MRS Proc. **157** (1990), 247 and L. Gråbæk, J. Bohr, H.H. Andersen, A. Johansen, E. Johnson, L. Sarholt-Kristensen, and I.K. Robinson, Phys. Rev. **B45** (1992), 2628.

[3] S. Q. Xiao, E. Johnson, S. Hinderberger, A. Johansen, K. K. Bourdelle and U. Dahmen, J. Microscopy, **180** (1995), 61 and U. Dahmen, E. Johnson, S.Q. Xiao and A. Johansen, J. Surface Analysis, **3** (1997), 185.

[4] F. Zhou, H.W. Sheng and K. Lu, J. Mater. Res. **13** (1998), 249

[5] F. Chen and G. Shu, J. Mater. Sc. **17** (1998), 259.

[6] N.B. Thoft, J. Bohr, B. Buras, E. Johnson, A. Johansen, H.H. Andersen and L. Sarholt-Kristensen, J. Phys. D : Appl.Phys. **28** (1995) 539

[7] D.L. Zhang, K. Chattopadhyay and B. Cantor, J. Mater Sc. **26** (1991), 1531.

[8] H.W. Sheng, J. Xu, L.G. Yu, X.K. Sun, Z.Q. Hu and K. Lu, J. Mater. Res **11** (1996), 2841.

[9] E. Johnson, A. Johansen, N.B. Thoft, H.H. Andersen and L. Sarholt-Kristensen, Phil. Mag. Let. **68** (1993), 131.

[10] D.L. Zhang and B. Cantor, Mat. Sc. Eng. **A128** (1990), 209.

[11] F. Faudot, U. Dahmen and S. Hagège, unpublished results.

[12] S. Hagège and U. Dahmen, Phil. Mag. Let. **74** (1996), 259 and E. Johnson, V.S. Tuboltsev, A. Johansen, U. Dahmen and S. Hagège, Nucl. Instr. Methods B **127/128** (1997), 727.

[13] D.L. Zhang and B. Cantor, Scripta Metal. Mater. **24** (1990) 751.

[14] R. Goswami and K. Chattopadhyay, Acta Metall. Mater. **43** (1995) 2887.

[15] R. Goswami and K. Chattopadhyay, Phil. Mag. Let. **68** (1993), 215.

[16] A. Singh and A.P. Tsai, Phil. Mag. Let. **77** (1998), 89.

[17] V.S. Tuboltsev, E. Johnson, U. Dahmen, A. Johansen, L. Sarholt and S.Q. Xiao, Materials Science Forum **269-272** (1998), 345

[18] A. Dezellus, Ph. Plaindoux, P. Ochin and S. Hagège, Mat. Sc. Let. (1999) to appear.

Materials Science Forum Vols. 294-296 (1999) pp. 477-480

The Effect of Grain-Boundary Structure Formation on β-Precipitation in Aged Al-Mg Alloys

L.I. Kaigorodova

Institute of Metal Physics, Ural Division Russian Academy of Sciences

Keywords: Aluminum-Magnesium Alloys, Transmission Electron Microscopy, Age, Thermomechanical Treatment, Phase, Grain-Boundary Precipitates, Recrystallization, Mechanical Properties

Abstract. *Microstructure and mechanical properties evolution during long-term natural aging has been studied by means of optical and transmission electron microscopy as well as tensile tests and corrosion resistance measurements. It was found that the sharp decrease of plasticity and corrosion resistance during aging results from film like grain - boundary β′ - and β - phases precipitation. Special thermomechanical and thermocyclic treatments have been worked out to produce a desired grain - boundary structure that affect the grain - boundary precipitation and alloys properties. The results have been demonstrated that grain - boundary precipitation of Al - Mg alloys can be controlled by prior deformation and recrystallization. The creation of special boundaries with a high density of coincident sites or low - defect faceted boundaries remain free of precipitation during subsequent aging. "Pure" grain boundaries provide stable ductility and corrosion resistance.*

Result and discussion. Transmission electron - microscopic studies of Al - Mg alloys during long - term natural age showed the formation of ordered Guinier-Preston (G.P.) zones. Electron microscopic patterns show a deformation - induced ripple contrast. Such contrast is typical of spherical particles. When the aging period is increased to five years, the contrast enhances due to enlarged sizes of G.P. zones. The corresponding electron diffraction pattern in Fig.1a shows the presence of superstructural 100 and 110 reflections, which indicates the ordering of internal structure.

The formation of ordered G.P. zones was preceded by appearance of a modulated structure with the concentrational waves along the $<001>_{Al}$ directions.

This decomposition inside grains is accompanied by grain-boundary precipitation. The grain-boundary precipitates can be represented by metastable β′ particles but, more frequently, by the stable β phase (Al_2Mg_3). After two or more years of aging, the grain-boundary precipitates form a continuous film(Fig.1b).

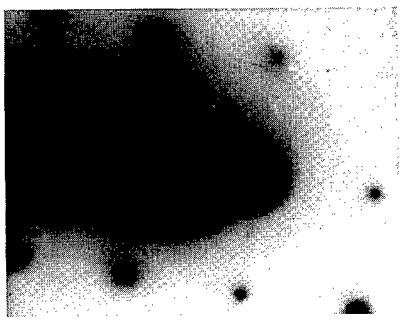

a

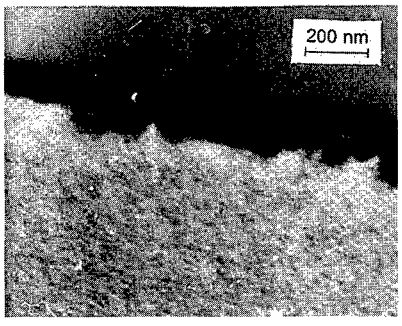

b

Fig.1. Al-11 wt. % Mg alloy after natural aging for one year: (a) electron diffraction pattern , zone axis $[001]_{Al}$; (b) bright-field image of a grain-boundary with precipitates.

It was found a sharp decrease of plasticity and corrosion resistance during aging. Short-term heating of aged specimens to 150 or 200°C results in the dissolution of G.P. zones inside grains (recovery after aging), whereas the particles at grain boundaries remain unchanged. The plasticity and corrosion resistance do not reach the initial values after such a treatment, although the G.P. zones completely dissolve. Hence, decrease of this properties during aging results from filmlike grain-boundary precipitation.

It follows from the above that, in order to improve the ductility and stress corrosion resistance of Al-Mg alloys, it is necessary to prevent or at least decrease grain-boundary precipitation. The mode of precipitation is known to correlate with the peculiar structure of grain boundaries. Hence, attention was attracted to the formation of special low-energy boundaries with a high density of coincident sites and to effect of these boundaries on the precipitation and properties during subsequent aging. In addition, the influence of small addition of Be, Ti and Zr on the formation grain boundaries, nucleation and growth of precipitates inside grains and at their boundaries was studied

In order to study the possibility of obtaining polycrystalline structures with a given physical state of grain boundaries, the effect of deformation parameters and rates of heating to the quenching temperature on the structure and properties of quenched and aged Al-Mg alloys were examined. It was found that the rapid heating of deformed alloys by inserting a sample into a furnace, preliminarily heated to the quenching temperature of 460°C and holding it there for 1 h, results in a course-grained structure, irrespective of the deformation mode.

Slow heating to 460°C at a rate below 50 K/h favors the formation of various structures, from polygonized to completely recrystallized ones, depending on the mode of prior deformation. A markedly developed subgrain structure with a subgrain diameter of 1 μm and misorientation angle of 1° was observed in Al-Mg alloy with additions of Be, Ti and Zr deformed by 16-25%. The 50% deformation results in a completely recrystallized fine-grained structure with an average grain size not exceeding 20 - 25 μm.

Stronger deformation causes the variation in grain size, with the maximal grain sizes increasing to 50 - 100 μm. In the binary Al - 10 wt % Mg alloy, the subgrain structure is less stable and can be obtained only during slow heating to 350°C. The variation in grain size becomes pronounced even after 50% deformation. It was concluded that small additions of beryllium, titanium, and zirconium in the Al-Mg alloy stabilize its grain-boundary structure upon slow heating.

During further natural and artificial aging, sub-boundaries and most of the high-angle boundaries (formed after 50% deformation) remain free of precipitates. With 80% deformation, the proportion of such boundaries essentially decreases.

An analysis of precipitation-free boundaries showed that these are special boundaries with misorientation angles close to 21° or 37°.

The grain-boundary state is known to depend on both misorientation and content of lattice defects. During recrystallization and boundary migration through the deformed matrix, the boundary can become even less equilibrium due to the absorption of lattice dislocations. It was studied the effect of boundary migration rate on the nucleation of grain-boundary precipitates in the Al-11 wt. % Mg alloy with Be, Ti and Zr additions. To obtain different recrystallization conditions, specimens were deformed by 50 to 90% and recrystallized at 380 to 480°C.

Annealing of 90% deformed specimens at 480°C for 3 h resulted in intense grain growth. The rate of boundary migration calculated from changes in grain sizes was 10^{-2}μm/s. The misorientation angle and misorientation axis showed that these boundaries were random and predominantly planar.

Identically annealed specimens deformed by 50% showed variation in grain sizes. In this case, the boundaries of coarse grains were planar, but those of fine grains were curved and subdivided into separate segments (Figs.2a and b, respectively).

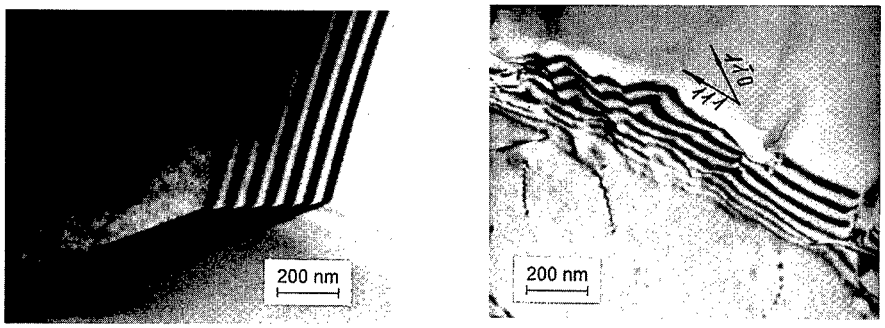

Fig.2. Microstructure of a deformed Al-11 wt. % Mg alloys with Be, Ti and Zr annealed at 480°C for 3 h: (a) triple junction of grains with planar boundaries and (b) faceted boundary.

Upon decreasing the annealing temperature to 380°C, only primary recrystallization was observed in specimens treated for 3 h. Irrespective of the amount of deformation, the rate of boundary migration did not exceed 10^{-5} μm/s. Most boundaries are segmental. The specific morphology of boundaries and their crystallographic analysis indicate that they are faceted. In this case, the segments corresponding to loosely packed crystallographic planes are subdivided into separate close-packed sections of different orientations.It is known that the facet structure are typical of the equilibrium boundaries in pure polycrystalline aluminum and they are special boundaries [1].

Increasing the time of annealing at 380°C to 30 h can hardly eliminate faceted boundaries. The stability of this morphology verifies the low-energy state of these boundaries.

The type of grain structure affects the morphology and distribution of precipitates formed upon subsequent aging. At planar random-type boundaries with misorientation angles greater than 15°, grain-boundary particles precipitate as laths up to 10 μm long (Fig. 3a). When the misorientation angle is 5° to 10°, a set of closely arranged lenticular particles is observed (Fig.3b). Faceted boundaries remain predominantly free of precipitates during aging(Fig.3c).

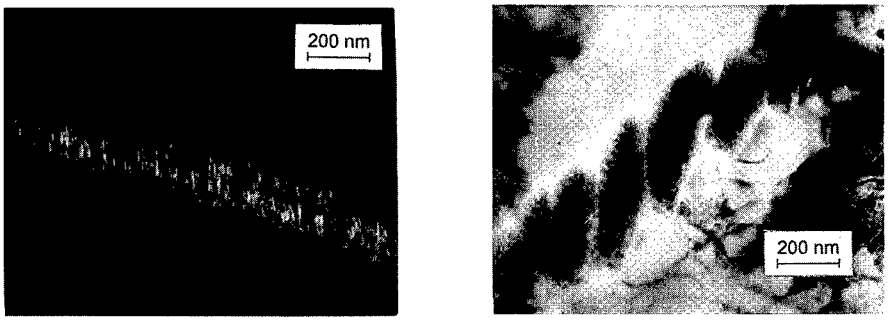

a б

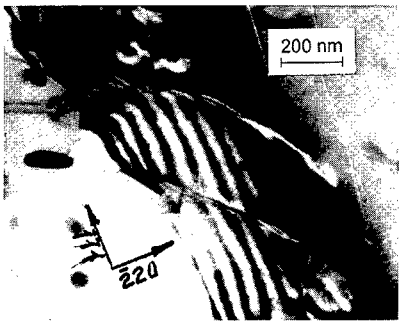

c

Fig.3. Microstructure of deformed Al-11 wt. % Mg alloy annealed at 480°C for 1 h and aged at 180°C for 12 h:
(a) Laths of the β phase nucleated at a planar high-angle boundary, dark-field image in the $(880)_\beta$ reflection;
(b) Lenticular particles of the β phase nucleated at a low-angle boundary, bright- field image; and
(c) Faceted high-angle boundary free of precipitates, bright field image.

The obtained results demonstrate that grain-boundary precipitation during natural aging of Al-Mg alloys can be controlled by prior deformation and recrystallization modes that produce special grain-boundary structure. One can obtain special boundaries with a high density of coincident sites or low-defect faceted boundaries. Both types of boundaries remain free of precipitates during subsequent aging.

The suppression of grain-boundary precipitation using slow heating of deformed alloys Al-Mg improves their corrosion and plastic properties. For example, the stress-corrosion endurance of the Al-Mg alloys with small additions Be, Ti and Zr, aged at 175°C for 16 h after conventional quenching, can hardly exceed 20 days, whereas after slow heating, this characteristic reaches two months. In the latter case, the elongation is 7-8%.

References

1.Andreeva, A.V. and Fionova, L.K., Low-Energetic Grain Boundaries in Aluminum, *Fiz. Met. Metalloved.,* 1981,vol. 52., no. 3, pp.593-602.

Materials Science Forum Vols. 294-296 (1999) pp. 481-484

Physical Mechanisms of the Non-Equilibrium Phase Transitions in Amorphous Solids

T.V. Ischenko and S.V. Demishev

Low Temperatures Laboratory, General Physics Institute,
Vavilov street 38, RU-117942 Moscow, Russia

Keywords: Non-Equilibrium Phase Transition, Explosive Crystallization, Solid State Amorphization, Phase Boundary Movement

Abstract: A theoretical approach to the non-equilibrium phenomena in disordered solids including explosive crystallization and solid state amorphization is proposed. We consider the special excited metastable states at the phase boundary as a "driving" force of the non-equilibrium phase transition. The decay of these metastable states leads to the appearance of the fundamental scales hierarchy in the sample structure that can by verified experimentally. A possible schemes of the formalisation of the proposed physical mechanisms in a different models are discussed.

1. Introduction

The problem of the non-equilibrium phase transitions in disordered materials covers such non-equilibrium processes as solid state amorphization (SSA) and explosive crystallization (EC). It is known from experiments [1] that under certain conditions the process of the non-equilibrium phase transformation may become very fast and involve a new physical mechanisms, that makes complicated to build a consistent theory of this regime. In spite of a lot of experimental data the detailed theory of these non-equilibrium phenomena is missing. In this work we will formulate a possible general approach to the description of the SSA and EC processes based on the universal microscopic mechanisms.

2. Explosive crystallization.

Experimentally the EC mode may be induced by deposition of the local energy impulse in the amorphous sample when an impulse amplitude and an initial sample temperature exceeds critical value. The typical rate of the phase boundary movement in this process is about v_{ex}=1-10 m/s [1], whereas the temperature profile associated with the phase boundary can be considered as a thermal domain with the temperature much higher than that of the initial state and with the sharp front. Optic experiments on a laser nanosecond impulse excitation have shown that special metastable quasi metallic excited states exist on the phase boundary [2]. Moreover, the excitation of these metastable states can be considered as a necessary condition of the non-equilibrium EC mode [3].

Over the past decades the explanation of the explosive crystallization has been given on a phenomenological level, without going into the details of the microscopic mechanisms and nowadays this theory remains rather controversial. First of all, there is a serious discrepancy between the observed growth rates for such non-equilibrium processes and those obtained by extrapolating from the equilibrium growth rates to the appropriate temperatures of the non-equilibrium processes [4,5]. The detail analysis show that it is necessary to enhance the concentration diffusivity, D_N, by 10^4-10^5 times [1,4,5], and hence to introduce some extra physical mechanism to drive the non-equilibrium process. Moreover, the explosive crystallization should be considered as an adiabatic fast process [1,3-5] and the renormalisation of the thermal diffusivity is required [4,5]. In order to agree with the experimental data the thermal diffusivity D_T must be multiplied by a factor of 10^{-5}-10^{-6} [4,5].

Following the above consideration a new theoretical model of the EC process has been proposed in Ref. [4,5]. This model is based on the three main assumptions.

(i) The characteristic microscopic spatial scale of the non-equilibrium process is given by the medium range order length L_{MRO}~1 nm.

(ii) The energy at the non-equilibrium phase boundary is stored in localised phonon modes, which causes damping of the thermal diffusion.
(iii) The interaction of electrons with the high energy localised phonon states results in simultaneous excitation of the electrons and the quasi-metallic metastable state is formed at the phase boundary. The excitation of electronic states leads to the anomalous diffusion regime with the enhanced coefficient of the concentration diffusivity.

The idea of the non-equilibrium process driven by the special metastable states means that the processes of the crystallisation and energy transfer at the phase boundary are synchronised [4,5]. Consequently the simple analysis of the energy transfer allows to predict the possible structure of the sample which undergo the non-equilibrium phase transition. In semiconductors the characteristic time of life of the metastable state is about $\tau \sim 10^{-9}$ s and the velocity of the EC front is $v_{ex} \sim 1$ m/s. These data taken together with the equilibrium values of the thermal diffusivity $D_T^0 = 10^{-5} \div 10^{-6}$ m^2/s allow to define three characteristic spatial scales for an non-equilibrium process

$$L' = v_{ex} \cdot \tau \approx 1\,\text{nm} \qquad (1)$$

$$L'' = \left(D_T^0 \tau\right)^{1/2} \approx 10 \div 100\,\text{nm} \qquad (2)$$

$$L''' = D_T^0 / v \approx 1 \div 10\,\mu\text{m} \qquad (3)$$

The first length L' is of the same order of magnitude as the medium range order length found in the X-ray diffraction experiments and L' also provides an estimate of the localisation radius for phonon states. This is the minimal physical length which is essential for the non-equilibrium process and which is essentially related to the basic microscopic structural units in the disordered sample. The second length L'' defines the region where the non-equilibrium localised phonon states relax to the equilibrium phonon gas and hence can be considered as a "physical width" of the non-equilibrium phase transition front. This length will give a size of the physical inhomogenities in the sample which undergoes a non-equilibrium phase transition. The last parameter L''' is a maximal coherence length in a diffusion controlled process. This length will manifest itself as a typical crystallite size which is formed after explosive crystallisation.

The presence of the spatial scales given by equations (1)-(3) in the structure of the samples which undergo EC is in agreement with the available experimental data [6]. Consequently we can conclude that for the non-equilibrium process a well-defined scales hierarchy is characteristic:

$$L' \approx L_{MRO} < L'' < L''', \qquad (4)$$

that is in contrast with the equilibrium process. Indeed, in the equilibrium diffusion controlled process of phase transition the parameter L' is about atomic distance a; the thermal field is almost homogeneous and $L'', L''' \to \infty$. As a result instead of relation (4) we get $L' \approx a << L'', L'''$ that is typical for standard process of nucleation and growth.

3. Solid state amorphization.

Traditionally the area of SSA includes solid state reactions, mechanical allowing by continuos milling of a two-component mixture, disordering due to ion implantation or exposure to radiation, hydrogenation and phase transitions under high-pressure [7]. The "energy source" for the amorphization originates from stresses which are formed on the interphase boundary [7,8]. When stresses are allowed to relax the amorphous solid is formed.

The role of stresses in the SSA by ion implantation had been clearly demonstrated in Ref.[8] According to the data [8] the ion bombardment leads at first to increasing of the stresses in the layer, and at some dose of radiation the amplitude of stresses reaches its maximum. The point where the maximum stress value is reached is found to be exactly coincide with the beginning of formation of amorphous phase and further growth of amorphous layer is accompanied by subsequent decrease of the amplitude of stress field [8].

However the stress analysis is insufficient for the description of SSA. According to the Ref.[9] the SSA under high pressure requires a formation of the special intermediate quasi-metallic metastable state which evolves into amorphous phase. It is interesting that the structure studies of the samples obtained by

SSA under high pressure have given evidence of the presence of the scales hierarchy (1)-(4), characteristic for a non-equilibrium process [10].

Following this consideration we assume that in general, the SSA occurs when a highly excited metastable solid is allowed to relax, and this phenomenon can be described as a non-equilibrium phase transition based on the same physical mechanisms as explosive crystallisation.

Nevertheless the theoretical model of SSA should have a specific point, as long as amorphization requires the creation of the medium range order. The validity of the relation (4) assumes that all characteristic lengths of the non-equilibrium process are well-defined, i.e. the dispersion of each parameter L', L'', L''' is not so large. This is in agreement with some models of the amorphous state [4,7], where amorphous network is described as an aggregate of more ordered "rigid" regions of size $\sim L_{MRO}$ separated by more disordered "soft" parts of the random network and the loss of the long-range order is associated with the special structural elements in amorphous network. These elements those we will further call structure forming defects (SFD) act as soft regions in the rigid covalent network and allow to vary an angle and a distance of bonds adjacent to SFD, that makes possible the loss of the long-range order.

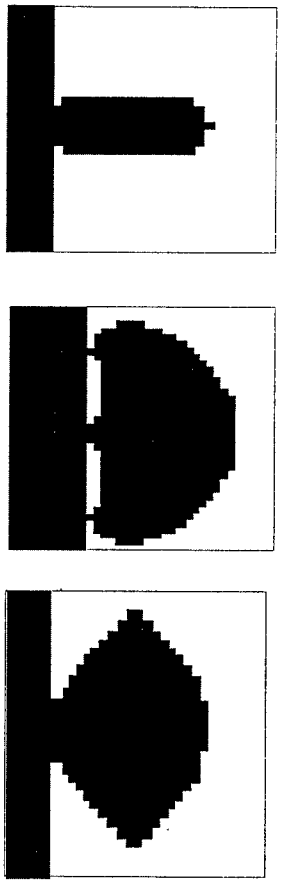

Fig.1. Examples of the EC waves near the excitation threshold. Excited metastable states are shown in black.

Obviously, exact structure of SFD may be different in each amorphous solid, depending on its chemical content. If the concentration of SFD in each moment is $N(t)$ we can immediately write for the correlation length

$$L_{MRO}=N(t\to\infty)^{-1/3}, \qquad (5)$$

that is, it should be given by a stationary value of the SFD concentration (the case of crystal corresponds to $N\approx 0$). Thus, the problem of SSA becomes eqivalent to the problem of the generation of specific defects in a process of decay of the excited metastable state. In general case, the decay of this state may result in $L_{MRO}=\infty$ (crystall) or $L_{MRO}<\infty$, in the latter case amorphous solid is formed.

4. Possible formalisms.

The above qualitative picture based on the idea that a non-equilibrium phase transition in amorphous solid goes via intermediate metastable excited state can be formalised in a different way.

In the case of EC it is natural to take into account the presence of the medium range order and the localised phonon states. Consequently the discrete models, genetically connected to the cellular automata may take an advantage. In this model the sample volume consists of the cells having characteristic size L_{MRO} and each of the cell may acquire one of three possible states: amorphous, crystalline or metastable excited. The change of the phase state is controlled by the energy exchange between the localised phonon states in the nearest neighbourhood of a cell as well as of the local surrounding.

This program of the study of EC have been realised in Ref. [5]. It was find out that even this simple model allows to describe quantitatively the threshold characteristics of EC and predicts a variety of the possible EC waves, some of which have been probably observed experimentally. Some examples of the calculated EC waves are shown in fig. 1, and more details can be found in [5]. Note, that this approach is valid only for scales $x < L''$ and the characteristic times of the energy exchange are controlled by the localised modes.

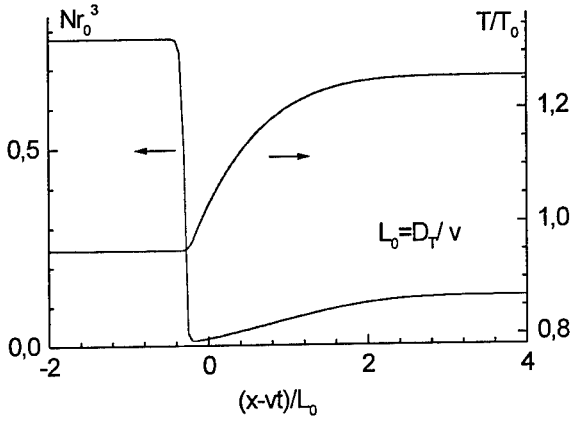

Fig. 2 The wave solution of the non-linear SSA model [7]. In this model r_0 gives the characteristic interaction length of the SFD, T_0 denotes the temperature of the equilibrium phonon gas.

An alternative approach was applied to the description of SSA [7]. We have considered a set of non-linear master equations describing the generation and annihilation of SFD and energy transfer. The non-linearity appears as a result of interaction of the SFD via stress field [7]: in a stressed sample the probability of the creation of the SFD increases [7,8]. We have found that in the model of SSA proposed in [7], one of the possible solutions is a SSA wave (analogous to EC wave) with a sharp SFD concentration front travelling through the excited metastable solid (fig. 2). When the SSA wave passes, the vibronic energy of the system decreases and the excessive energy of the metastable state is stored in the interacting SFD. As a result an amorphous solid, having excessive energy with respect to a crystal is formed.

For the solution shown in fig. 2 the concentration profile is much more sharp than the thermal profile. This is typical for the scales region $x > L''$, where the continuos model [7] is valid. Nowadays little is known about the microscopic kinetics of SSA which is essential for the region $x < L''$. More experimental work is required to clarify the physical mechanisms of SSA at the scale 1-10 nm.

5. Conclusions.

The new approach to the description of the non-equilibrium phase transitions in disordered solids predicts a hierarchy of the characteristic scales (1)-(4) which will appear in the structure of a solid after the transition. The corresponding specific structures have been already observed [6,10] and may serve as an indication that the disordered solid originated or have undergo a non-equilibrium phase transition. The proposed qualitative mechanism can be formalised in a different way using continuos or discrete models. Depending on a particular scale which is essential for the process described by a formal model, the parameters of the model (thermal and concentration diffusivites, etc.) may be renormalised with respect to the equilibrium case. The physical reason of this renormalisation is the excitation of the metastable states at the phase boundary.

References

[1] V.A.Shklovskii, V.M.Kuzmenko, Uspekhii Fiz. Nauk, 157 (1989), p.311.
[2] Zh.I.Alferov et al, Pis'ma v ZhTF, 9 (1983), p.1373.
[3] P.S.Peercy *et al.*, Appl.Phys.Lett., 53 (1988), p.203.
[4] F.V.Pirogov, S.V.Demishev, Latvian Journal of Physics and Technical Sciences, N3 (1992), p. 31.
[5] S.V.Demishev, T.V.Ischenko at al., J.Non-Cryst.Solids, 163(1993),13; J.Phys.:Cond.Matt., 7(1995),9173
[6] O.Bostanjoglo, Phys.Stat.Sol.(a), 70 (1982), p.473.
[7] S.V.Demishev, T.V.Ischenko et al., Fiz.Tv.Tela, 37 (1995), p.608; J.Phys.: Cond.Matt., 9(1997), p.9199.
[8] C.A.Volkert, J.Appl.Phys., 70 (1991), p. 3521.
[9] E.G.Ponyatovskii, O.I.Barkalov, Material Science Reports, 8 (1992), p. 147.
[10] S.V.Demishev *et al.*, Physics-Uspekhi, 62, (1994), p. 195.

For correspondence: Fax: +007-(095)-1358129
e-mail: tan@lt.gpi.ru

Materials Science Forum Vols. 294-296 (1999) pp. 485-488

Metastable and Equilibrium Decomposition of the Eutectoid β-Phase in the Cu-In System

A. Das[1], W. Gust[2], S.K. Pabi[1] and I. Manna[1]

[1] Dept. of Metallurgical & Materials Engg., I.I.T., Kharagpur, W.B. IN-721302, India

[2] Institut für Metallkunde, Universität Stuttgart, Seestr. 75, D-70174 Stuttgart, Germany

Keywords: Eutectoid Transformation, Cu-In System, Moving-Boundary Reaction, Pre-Precipitation

Abstract The β-phase in the Cu-In system is known to decompose into α and δ below 847 K through a eutectoid transformation controlled by interphase boundary diffusion. The present study with the Cu-20.15 at.% In eutectoid alloy investigates the morphology, identity and origin of a duplex microstructure in the prior β region ahead of the eutectoid reaction front. A detailed investigation through optical, scanning and transmission electron microscopy and X-ray diffraction analysis indicates that the prior β region undergoes a time dependent pre-precipitation of a transient phase through a static boundary mode. The latter precedes/accompanies the moving boundary eutectoid transformation initiated at the prior β grain boundaries.

Introduction

According to the Cu-In phase diagram, the high temperature β-phase undergoes eutectoid transformation into α and δ on cooling below 847 K [1]. A number of studies on the kinetics of eutectoid change in the Cu-In system has earlier inferred that interface diffusion through the reaction front (RF) is the rate controlling mechanism of the former change [2,3]. Spencer and Mack [4] have, however, reported that the parent β-phase undergoes a gradual conversion to the equilibrium structure during eutectoid transformation below 820 K. This gradual development of the microstructure cannot be attributed to interface diffusion. If volume diffusion governs eutectoid decomposition of β, quenched-in excess vacancies should accelerate such a process. However, the present authors have concluded through a detailed kinetic analysis that on quenching and aging β decomposes through a moving boundary transformation controlled by interphase boundary diffusion [2]. In the present study, a detailed microstructural characterization through optical (OM), scanning (SEM) and transmission electron microscopy (TEM) has been attempted to investigate the true mode of isothermal decomposition of β in the quenching and aging routines.

Experimental

The Cu-20.15 at.% In alloy was prepared by vacuum induction melting appropriate amounts of elemental Cu and In (99.999% pure). The cast ingot was homogenized at 933 K in evacuated and argon filled silica capsules for a period of 14 days before quenching in ice-brine mixture. Isothermal transformation was carried out by reheating the samples to different predetermined temperatures under similar protection for different lengths of time followed by quenching in iced brine. The isothermally treated samples were polished and etched using a CrO_3 based reagent for SEM and OM studies. A JEOL SEM operating at 15 kV and a REICHERT MEF-2 OM were used to monitor the microstructural development during the decomposition of β. For TEM studies, the specimens were electroploished in a solution of concentrated HNO_3 in CH_3COOH maintained at 233 K under an operating voltage of 8-10 V. A PHILIPS CM-12 TEM operating at 80 kV was used for a detailed investigation of the microstructural evolution. X-ray diffraction (XRD) studies were carried out with a PHILIPS PW-1710 X-ray diffractometer using cobalt radiation.

Results and Discussion

Figure 1 reveals a typical SEM micrograph showing the growth of a eutectoid colony at 750 K after 2 h. It is interesting to note that the microstructure on either side of the RF bears a close resemblance, except for a differential contrast across the RF such that the colonies growing away on either sides of an original grain boundary appear more prominent or in relief in contrast to the less distinct structure in the prior β-regions. This microstructure may immediately suggest that the prior-β region undergoes transformation to equilibrium α+δ structure in two distinct ways: one initiating at the grain boundaries and the other occurring throughout the matrix grains. Earlier, Spencer and Mack [4] reported that the β-phase in Cu-In may undergo a gradual transformation below 820 K that occurs through the β-matrix on continued isothermal aging. Figures 2a and b record an isothermal growth of eutectoid colonies along the three boundaries meeting at a junction at 750 K as a function of time. It is relevant to note that the microstructure ahead of the eutectoid colony does not reveal any easily distinguishable transformation product resembling the eutectoid transformation products in the early stages of the transformation (Fig. 2a). It is, however, interesting to note that the prior β gradually developes a microstructure bearing close resemblance to that within the eutectoid colony in the course of time at a given isothermal temperature. The microstructural similarity between the eutectoid transformation products and prior β region across the RF evidenced in Fig. 1 is precisely the same as revealed in Fig. 2b. Thus, it appears that the isothermal growth of the eutectoid colonies in the present alloy is accomplished by a moving boundary mechanism and accompanied by a parallel route of decomposition of β in the area ahead of the RF. Careful experimentation with a Cr_2O_3 based color tinting solution has enabled an easy and unambiguous distinction between the eutectoid colony (blue) and prior β regions (orange) in terms of their respective colors and indicates a possible structural difference between these regions. A close comparison among the different stages reveals that the eutectoid colonies nucleate on the grain boundaries and grow away from the latter with an increase in time (t). However, both OM and SEM seem inadequate to resolve the transient microstructural change in prior β. Hence a detailed TEM study has been undertaken to resolve this aspect.

Figure 3 illustrates a TEM micrograph of β quenched from the solution treatment temperature in iced brine. Here, the dark network seen in the microstructure has subsequently been confirmed as precipitates by dark field imaging. The inset shows a selected area diffraction pattern obtained from a β-grain. An analysis of this pattern using only the major spots indicates that prior β has a body centred cubic (bcc) structure with a lattice parameter of 3.01 Å. Weaker spots coming from the precipitates are indicative of a hexagonal structure with a large lattice parameter and have a possible orientation relationship with the β-phase. These precipitates cannot be attributed to an equilibrium transformation and appears to be a transitional phase. It may be mentioned that the presence of extra lines has earlier been reported in the XRD pattern of quenched β [5]. It was suggested that the extra lines could arise from the presence of metastable decomposition products in prior β. Following isothermal treatments for a longer time, these metastable precipitates seem to grow, preferably along their longitudinal directions. Figure 4 presents a typical microstructure formed at 750 K after 15 min of aging. The selected area diffraction pattern obtained from the matrix (inset) conforms to a bcc structure indicating that the prior β region retains its crystal structure. On further transformation, the metastable precipitates continue to grow and subsequently assume a lamellar morphology before being consumed by the transformation proceeding from the grain boundaries to produce the equilibrium α+δ structure. It is now important to note that the results from the TEM investigation do not indicate any structural transformation of β to the equilibrium products ahead of the eutectoid RF. It may be mentioned that the microstructural features discussed so far are not characteristic of 750 K alone. Similar microstructural evolution in the β-phase has been confirmed at other temperatures [6]. X-ray diffraction is a convenient tool for identification of the phases evolved in a given solid state phase transformation. However, the present system poses difficulty in that respect as the crystal structure of δ is not yet established.

Moreover, β is difficult to index as there is a considerable tendency of peak overlapping of all the coexisting phases, i.e., β, α and δ. Figure 5 shows the XRD pattern obtained in solution treated and isothermally aged (at 750 K for 45 min) conditions indicating that β is present in the partially transformed sample. Therefore, it appears that the structural transformation of β to δ is accomplished only by the eutectoid transformation that initiates and grows from the grain boundaries.

On the basis of the present OM, SEM, TEM and XRD observations, a possible sequence of decomposition of prior β may now be proposed. The precipitation and growth of metastable phases in prior β indicates that a continuous process of solute rejection is operative during isothermal treatments in the present study. As the precipitation appears confined only within the prior β-region and is not associated with thermally activated motion of an interphase boundary, the process is presumably controlled by volume diffusion. This may further be assisted by the presence of quenched-in excess vacancies due to the quenching and aging routine adopted in this study. As the matrix retains the bcc structure of β throughout the precipitation stage, the transient phase change in prior β could easily be differentiated from eutectoid transformation.

Conclusions

- On quenching the β phase in the Cu-20.15 at.% In alloy, metastable precipitates appear in the microstructure.
- Isothermal decomposition of prior β is preceded or accompanied by a thermally activated and time dependent growth of these transient precipitates during which the prior β matrix retains its crystal structure.
- The eutectoid transformation initiating at the prior β grain boundaries follows a moving boundary mode and replace the metastable precipitates with an equilibrium α+δ structure.

References

[1] T.B. Massalski et al. (ed.), Binary Alloy Phase Diagrams, ASM International, Materials Park, Ohio, 1990, Vol. 2, p. 1425.
[2] M.K. Bhatia and S.P. Gupta, Z. Metallkd. 85 (1994), p. 192.
[3] I. Manna, A. Das, S.K. Pabi and W. Gust, Defect Diff. Forum 143-147 (1997), p. 1551.
[4] C.W. Spencer and D.J. Mack, J. Inst. Metals 82 (1953-54), p. 81.
[5] W. Hume-Rothery, G.V. Reynor, P.W. Reynolds and H.K. Packer, J. Inst. Metals 66 (1940), p. 191.
[6] A. Das, Ph.D. thesis, Indian Institute of Technology, Kharagpur, India, 1997.

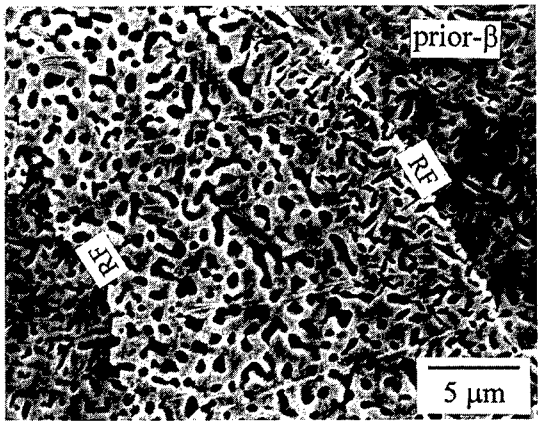

Fig. 1. SEM micrograph illustrating the growth of eutectoid transformation in Cu-20.15 at% In alloy after 2 h at 750 K. Note the structural resemblance between the eutectoid colonies and the prior-β region across the reaction front (RF).

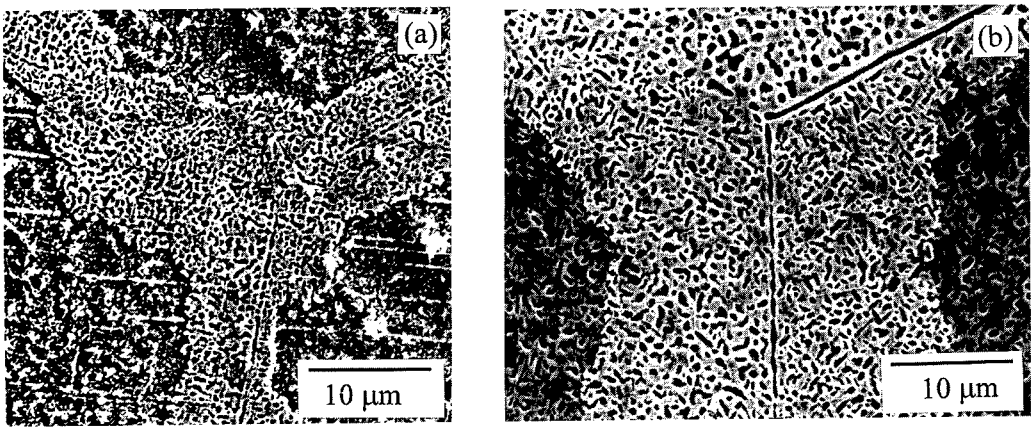

Fig. 2. SEM micrographs illustrating the progress of eutectoid change at 750 K after (a) 1 h and (b) 2 h. Note the gradual development of duplex structure in the prior β matrix ahead of the RF.

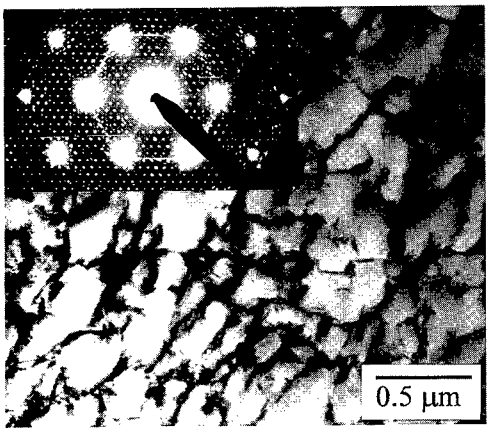

Fig. 3. TEM micrograph of a β-grain quenched from 933 K in iced brine showing precipitate network. Inset: Selected area diffraction pattern obtained from the β-grain.

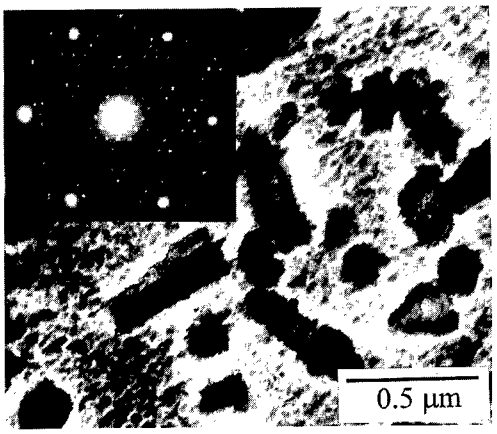

Fig. 4. TEM micrograph showing growth of metastable precipitates in the prior β matrix at 750 K after 20 min. Inset: Selected area diffraction pattern obtained from the prior β grain.

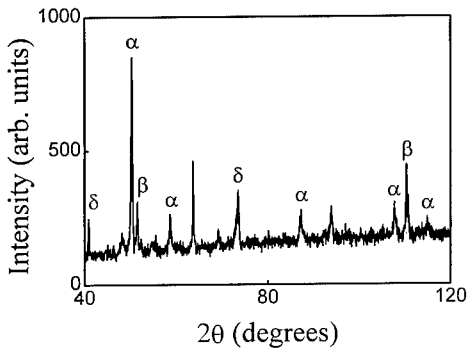

Fig. 5. The XRD pattern obtained in a specimen isothermally aged (following homogenization and quenching to room temperature) at 750 K for 45 min. Note the presence of β in the sample.

Materials Science Forum Vols. 294-296 (1999) pp. 489-492

Electronic Structure and Doping Effect of the $\Sigma 11(11\bar{3})/[110]$ Grain Boundary in Ni

L.G. Wang[1] and C.Y. Wang[1,2]

[1] Central Iron and Steel Research Institute, Beijing CN-100081, China

[2] China Center of Advanced Science and Technology (World Laboratory), P.O. Box 8730, Beijing CN-100080, China

Keywords: Grain Boundaries, First-Principles Calculations, Electronic Structure, Impurities

Abstract The first-principles discrete variational method is employed to study the effect of boron and phosphorus impurities on the electronic structure of the Ni$\Sigma 11(11\bar{3})/[110]$ grain boundary. The calculated results show that boron slightly decreases the bonding between the host Ni atoms but, on the other hand, it forms a strong bonding state with its Ni neighbours. Phosphorus strongly decreases the bonding between the host Ni atoms. The calculated environment-sensitive embedding energies show that boron has a strong site-competition ability and can successfully drive out phosphorus from the grain boundary region.

1. Introduction

Grain boundaries (GBs) belong to one of the most common extended defects in crystalline solids. They strongly affect, and to a great extent control, the physical and mechanical properties of materials. Intergranular embrittlement is usually associated with the segregation of impurities on the GBs [1,2]. It was found that impurities in ppm concentrations can result in a dramatic influence on the ductility and strength [3]. So it has become increasingly important to gain a microscopic understanding of the effect of impurities on the GB cohesion for developing technologically important materials.

Theoretical studies based on the first-principles calculations play an important role in gaining the insight into the microscopic mechanism of the GB cohesion at the electronic and atomic scale. Because the first-principles electronic structure calculations have been limited by the complexity of GB structures, the polyhedral atomic-cluster model in which only the impurity atom and a limited number of GB atoms are included has been used to represent the local environment of GBs doped with impurities in these calculations [4-11]. Briant and Messmer [4] first studied the effect of impurities on the GB cohesion in Ni based on the polyhedral model by performing a series of multiple-scattering calculations. Their results showed that if B is in the interstices of a Ni GB, a covalent-like bond is formed between the impurity and the host metal atoms and, at the same time, the strength of the metal-metal bonds accross the interface does not decrease. But the impurity-host bonds are favored at the expense of the metal-metal bonds when the GB is doped with S. Since then much of effort has been devoted to investigation of GB segregation in the past 15 years [5-11]. But the microscopic mechanism of influence of impurities on the GB cohesion is not yet completely known and more studies are desirable.

In the present paper, we investigate the effect of boron and phospohorus impurities on the electronic structure of the $\Sigma 11(11\bar{3})/[110]$ GB in Ni by employing the first-principles discrete variational method (DVM) and the polyhedral model. Based on the calculated results, we discuss the behavior of these impurities when they segregate on the GBs in Ni.

2. Theoretical method and atomic configuration

The discrete variational method (DVM) [12,13] is a numerical method within the framework of density-functional theory (DFT) using the local-density approximation (LDA), and has been

successfully used in many studies of electronic structure of metals [14] and alloys [13] as well as of grain boundaries in metals [10,11] and in intermetallic compounds [6,7]. In this paper, this method is employed to study the electronic structure and doping effect of the GBs in Ni. Details of the calculations can be found in [11].

In order to study the interaction between atoms, the interatomic energy between atoms l and m is given by [6,7]

$$E_{lm} = \sum_{n} \sum_{\alpha\beta} N_n a^{*}_{n\alpha l} a_{n\beta m} H_{\beta m \alpha l}, \tag{1}$$

where N_n is the occupation number for the eigenstate ψ_n, $a_{n\alpha l} = \langle \phi_{\alpha l}(r) | \psi_n(r) \rangle$, and $H_{\beta m \alpha l}$ is the Hamiltonian matrix element connecting the atomic orbital β of atom m and the atomic orbital α of atom l.

The atomic configuration of the $\Sigma 11(11\bar{3})/[110]$ GB in Ni is set up by a self-consistent convergent MD simulation using a first-principles interatomic potential developed by us [15]. It is shown in Fig. 1(a), where a periodic structure unit is constructed using two atomic polyhedrons. Fig. 1(b) shows the cluster which is used in our calculations.

We relax the GB atomic configuration after the impurity atom is located at the interstitial site (site 18 in Fig. 1(b)), and keep the GB symmetry during the relaxation. The equilibrium atomic configurations can be obtained by minimizing the total energy (binding energy) of the GB cluster. The electronic structure calculations are performed for these equilibrium atomic configurations. We get the equilibrium lattice constants equal to 3.600 Å, 3.618 Å and 3.856 Å for the clean GB and for the GBs doped with B and P, respectively. The equilibrium lattice constant of 3.600 Å for the clean GB obtained here agrees quite well with the experimental value of 3.5238 Å[16] for the bulk crystalline Ni.

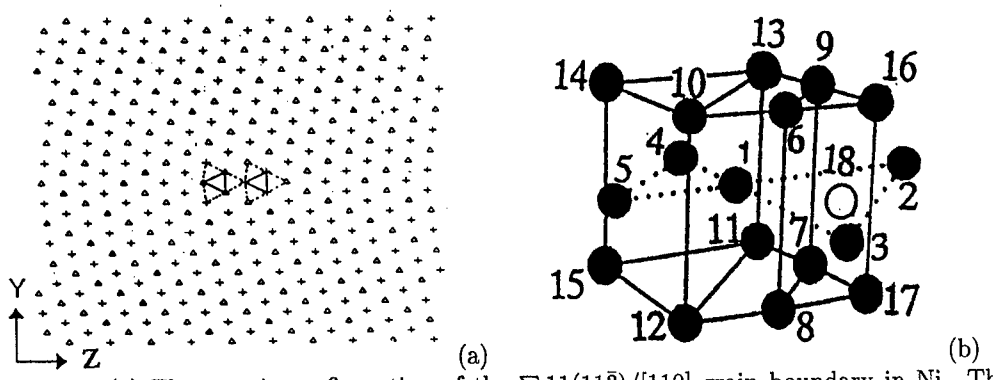

Figure 1. (a) The atomic configuration of the $\Sigma 11(11\bar{3})/[110]$ grain boundary in Ni. The symbols Δ and + represent the atoms on the stacking (...ABAB...) layers along the [110] tilt axis (X axis). (b) The polyhedral atomic-cluster model. The open circle and the filled circles stand for the impurity atom (B or P) and the Ni atoms, respectively.

3. Results and discussion

3.1. Charge density

The charge density difference is obtained by subtracting the charge density of the clean GB from the charge density of the doped GB, so that the impurity-induced charge redistribution in the GB region can be seen more clearly. In Figs. 2(a) and 2(b) we show the charge density difference of the GBs plotted in the Y-Z plane which contains the impurity atom and the host metal atoms Ni1, Ni2, Ni3, Ni4 and Ni5. High values of the charge density difference located close to the atomic sites are truncated. We can see that the charge density in the GB doped

with B is similar to that of the clean GB, but it decreases in the interstices of the GB with P. It implies that B does not strongly influence the cohesion between the host metal atoms, but P does. The charge density in the region where the impurity atom (B or P) is located increases due to the presence of the impurity atom. This effect can be regarded as the impurity acting as a 'bridge' [6].

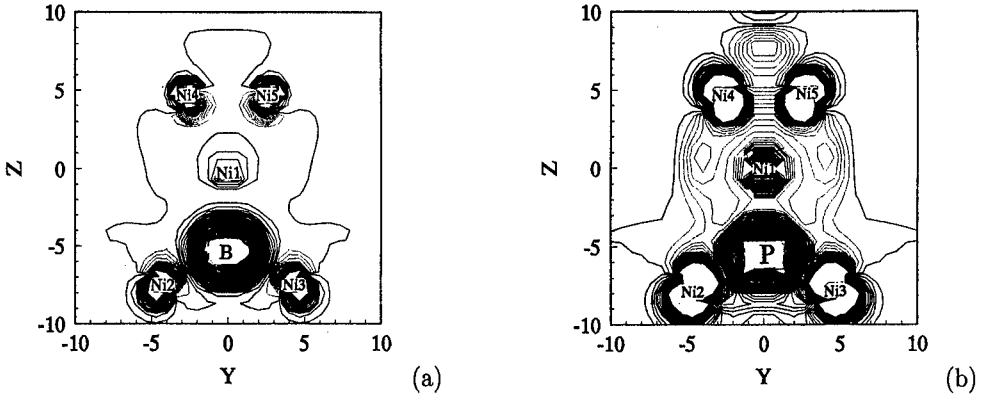

Figure 2. The charge density difference between the doped GB and the clean GB: (a) for the GB doped with B, (b) for the GB doped with P. The contour spacings are 0.002 $e/(au)^3$. Solid lines represent a gain of charge, dotted lines a loss of charge.

3.2. Density of states

The densities of states (DOS) of the clean GB, of the doped GBs and of the crystalline Ni (we used a cluster with 19-Ni atoms to simulate the crystalline Ni) are shown in Fig. 3. The DOS of Ni1 and Ni2 when the GB is doped with B are very similar to those of the clean GB. It follows that the influence of the boron impurity on the host metal atoms, for example Ni1 and Ni2, is not very strong. This is consistent with the analysis of the charge densities. However, we can see that the DOS of Ni1 and Ni2 atoms are strongly influenced by the phosphorus impurity. In this case, the DOS of Ni1 and Ni2 are moved towards higher energies and the bandwidths become narrower compared with those of clean GB or of the GB doped with B. The DOS near the Fermi level is also increased strongly. These effects induced by P decrease the bonding tendency between the host metal atoms and the stability of the GB. On the other hand, the hybridization of orbitals and the covalent bonding between the phosphorus impurity and the host metal atoms are also weakened because they depend on the energy levels of orbitals of the phosphorus atom and the host metal atoms. It turns out that the bonding tendency between the impurity atom and Ni1 (in the GB plane) and between the impurity atom and Ni2 (across the GB plane) is different for the case doped with B or P. This shows

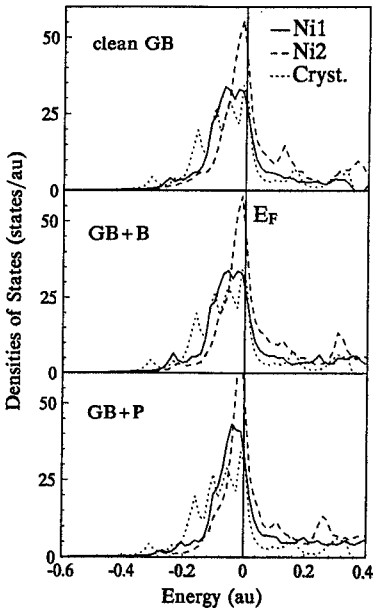

Figure 3. The densities of states of Ni1 atom and Ni2 atom in the clean GB and the doped GB comparing with the densities of states of the crystalline Ni.

a directional character of bonding. Our findings are consistent with the results obtained by Krasko et al. [9] in the Fe GBs doped with B, C, P and S.

3.3. Interatomic interaction energy

The interatomic energies defined by Eq. (1) are given in Table 1. We can see that the interaction between the host metal atoms is weakened by the presence of segregants (B and P) in the GB. The effect of boron is relatively small in comparison with a strong decrease of the interatomic interaction due to phosphorus. The interaction between the pairs of host metal atoms close to the impurity atom is weakened more strongly. These results are in agreement with the analysis of the charge density and DOS.

Table 1. The interatomic energies (in eV) between the host metal atoms in the clean GB and in the GBs with the B or P impurities.

pairs of atoms	clean GB	GB + B	GB + P
1-4	-1.63	-1.55	-1.28
1-6	-1.20	-1.14	-1.01
1-13	-1.50	-1.47	-1.21
4-5	-2.13	-2.10	-1.73
6-9	-1.82	-1.63	-1.30
7-9	-1.57	-1.30	-1.06

3.4. Characteristics of segregation

Our earlier calculations [10] had shown that B strongly segregates towards the GBs in Ni and can successfully drive out the other impurities, such as N, H, O, P and S, from the GBs. From the present results, we can see that B forms strong bonds with the neighboring host metal atoms and does not substantially diminish the interactions between them. However, the bonds between P and the host metal atoms are favored at the expense of the electrons in the metal-metal bonds. These findings agree with the results obtained by Briant and Messmer [4]. We conclude that the effect of impurities on the GB cohesion is closely associated with (i) the decrease of the interaction between the host metal atoms due to the presence of impurities, (ii) the bonding between the impurity atom and the host metal atoms, and (iii) the site-competition ability of impurity atoms.

Acknowledgements

The authors thank Dr. Mojmir Šob for fruitful discussions. This work was supported by the National Natural Science Foundation of China.

References

[1] D. Y. Lee, E. V. Barre, J. P. Stark, H. L. Marcus, Metall. Trans. 15A (1984), p. 14115.
[2] J. Komedo, C. J. McMahon Jr., Metall. Trans. 12A (1981), p. 31.
[3] C. L. Briant, Metallurgical Aspects of Environmental Failures, Materials Science Monographs No. 12, Elsevier, New York, 1985.
[4] C. L. Briant, R. P. Messmer, Phil. Mag. B 42 (1980), p. 569.
[5] M. E. Eberhart, D. D. Vvedensky, Phys. Rev. Lett. 58 (1987), p. 61.
[6] F. H. Wang, C. Y. Wang, J. L. Yang, J. Phys.: Condens. Matter. 8 (1996), p. 5527.
[7] F. H. Wang, C. Y. Wang, Phys. Rev. B 57 (1998), p. 289.
[8] G. S. Painter, F. W. Averill, Phys. Rev. Lett. 58 (1987), p. 234.
[9] G. L. Krasko, G. B. Olson, Solid State Commun. 76 (1990), p. 247.
[10] L. G. Wang, C. Y. Wang, Mater. Sci. Eng. A 234-236 (1997), p. 521.
[11] L. G. Wang, C. Y. Wang, Comput. Mater. Sci. 11 (1998), p. 261.
[12] D. E. Ellis, G. S. Painter, Phys. Rev. B 2 (1970), p. 2887.
[13] D. E. Ellis, G. A. Benesh, E. Bykom, Phys. Rev. B 16 (1977), p. 3308.
[14] D. Guenzburger, D. E. Ellis, Phys. Rev. B 45 (1992), p. 285.
[15] C. Y. Wang, T. Yu, W. H. Duan, L. G. Wang, Phys. Lett. A197 (1995), p. 449.
[16] C. J. Smith, ed., Metal Reference Book, 5th Ed., Butterworths, London, 1976, p. 186.

Materials Science Forum Vols. 294-296 (1999) pp. 493-496

Mean-Field Analytical Calculation of the Segregation Profile Around Grain Boundaries in Binary Alloys

I.P. Antoniades and G.L. Bleris

Solid State Section, Physics Department, Aristotle University of Thessaloniki, Thessaloniki, GR-54006, Greece

Keywords: Grain Boundary Segregation, Surface Segregation, Σ5 Grain Boundary, CSL, Cu_3Au, MC Simulation

Abstract: We derive a mean field equation for a [001] twist grain boundary. For the description of the one-site probability function we use the CSL symmetry and the DSC lattice with two order parameters one corresponding to the direction of the CSL supercell lattice vector and one to direction [001] (normal to boundary). We then present a new analytical method to obtain an asymptotic analytical solution to the mean-field equation for the disordered state ($T>T_C$) for a *general* pair potential decaying exponentially for arbitrary range interactions. The solution describes the segregation profile around the grain boundary (decay lengths and amplitudes) and can also be applied to free surfaces. The method reveals several more pertinent length scales (compared to a simple NN or NNN interaction) whose relative amplitudes vary differently with temperature giving a richer description for the shape of the segregation profile depending on the strength of average interactions between planes on the same side and on either side of the boundary. Either no fit to experimental data is required (if one knows the potential) or a fit to a known profile at a specific temperature can provide the potential parameters and then profiles can be calculated for all other temperatures. The profile obtained is found to be very sensitive to interatomic interaction, a feature also captured by a MC simulation we performed for a twist Σ5 boundary in Cu_3Au which at the same temperature gave qualitatively completely different results for a rigid and a relaxed lattice.

Introduction:

The phenomenon of segregation around free surfaces (FS) or grain boundaries (GB) in binary alloys has attracted a lot of interest both from an experimental and theoretical point of view due to its importance in the physical properties of materials. Several experimental techniques have been applied since the past decade to measure the degree of segregation in the first (or second) plane from the GB (or FS). More recently, in the case of an FS, concentrations can be measured for several planes from the surface giving information on the decay length Λ, and shape of the segregation profile (SP) towards the bulk [1]. For temperatures T greater than the critical temperature of order-disorder transition T_C, several experimental results (on Au-Cu, Cu-Ni systems) agree that Λ, as well as the excess concentration δc, decrease with increasing temperature, whereas Λ diverges at $T=T_c$ as $(T-T_c)^{-1/2}$.

Several theoretical (mean-field, cluster-variation, even first principles) as well as numerical studies (Monte Carlo (MC), free energy minimisation) have also been applied capturing qualitatively the main features of experimental findings [2-5]. However, there is recently a controversy concerning the exact shape of the SP: whereas most of the theoretical/numerical results support an *oscillating* profile [1,3] -planes 0,2,4... showing an excess concentration of one species whereas 1,3,5... a depletion- some others show monotonic exponentially decaying SPs [5]. Other authors have reported the existence of a monotonic profile with a gaussian decay shape or even more complicated profiles [e.g. 2,4]. In our own MC numerical study with a Finnis-Sinclair potential for a Σ5 twist boundary in Cu_3Au, we get a more complicated shape where more than one equally important length scales seem to be present (see last section). In [5] is argued that in theoretical studies the exact shape depends strongly on the potential used. In experimental studies, on the other hand, it also appears that the shape is sensitive to the experimental techniques and sample

preparation (e.g. impurity content). In addition, it must be pointed out that all analytical studies resort to a NN or at most NNN interaction ignoring long-range forces which maybe very important. In a study by Mecke and Smith [6], where a linearised mean-field equation using NN and NNN interactions was solved analytically, an oscillating profile was obtained for a (100) Cu_3Au FS and, qualitatively, experimental features for the decay length and amplitude were captured. The authors point out that their interaction parameters were selected so that they give the correct critical temperatures and equilibrium Cu_3Au bulk structure at T=0, i.e. no adjustment was necessary to fit experimental results. However, one can argue that including longer range interactions or even using a different ratio of NN vs. NNN interaction parameters that fit bulk properties equally well may result in a completely different SP.

In this study, we first offer a new, more general analytical solution to the mean-field equation for *arbitrary range* interactions using *any* exponentially decaying pair-potential and for $T>T_c$. We obtain a fully analytical solution of the linearised equation giving the excess concentrations in planes parallel to a GB or an FS. By this we hope to offer a theoretical tool that will aid the clarification of some of the matters we mentioned above. Secondly, we present some first MC results for segregation around a Σ5 twist GB in Cu_3Au contrasting the behaviour of the SP between a rigid and relaxed lattice.

One-site probability function around a GB

A general and well-known theory to fully describe the function $p(r)$, defined as the probability of finding an atom of species A at position r, is the method of *Static Concentration Waves* (SCW) by Khachaturyan [7] in which an LRO parameter is assigned to every independent sublattice of the ordered alloy structure. Each sublattice is associated with a specific direction in k-space and all the equivalent vectors that form a *star* together with the original (group theory). The method has the advantage that it can produce mean-field equations as well as incorporate higher-order expansions of the entropy term using arbitrary interaction potentials. We applied the same principle in the case of a GB assuming, as an approximation, the existence of only two independent directions in k-space. We derived empirically that within CSL theory for a GB with $\Sigma=(p^2+q^2)/a$, one such direction is $k_1=2\pi[p,q,0]/d$ and the other $k_2=2\pi[001]/R$, R being the lattice parameter and d the size of the primitive DSC lattice cell. The first vector arises due to the periodicity of the CSL, whereas the second arises because the 3D periodicity of the perfect lattice is broken by the GB. Next, we divide the GB into 'slices' each one consisting of two planes, one on either side of the GB, and equidistant from it. Thus, we express the probability to find an atom of species A at position r on slice m from the GB as

$$p_m(r) = c_m + \frac{1}{4}\eta_{1m}\exp(-ik_1 r) + \frac{1}{2}V(001)\eta_{2m}\exp(-ik_2 r) \qquad (1)$$

where c_m is the average concentration at 'slice' m and η_{1m}, η_{2m} the order parameters. The stoichiometry A_3B is assumed. Other stoichiometries can be described similarly with different constants in front of the last two terms. Inserting (1) into a mean-field expression of free-energy and minimising with respect to concentrations and order parameters one easily derives the mean-field equation from which equilibrium values of all variables can be determined as functions of temperature. We do not report the full equation here due to shortage of space.

Segregation profiles for $T>T_c$:

For temperatures above the critical temperature of the bulk, the disordered state appears with both order parameters equal to zero. The mean-filed equation becomes:

$$T\ln\frac{1-c}{c}-T\frac{\delta c_m}{c(1-c)}=\sum_{m'=0}^{\infty}\left(cV_{mm'}+U_{mm'}+\delta c_m V_{mm'}\right)-\mu \quad (2)$$

where we have expended the logarithmic term on the left side up to first order with $c_m=c+\delta c_m$, and $\delta c_m/c<<1$ since we are interested in the asymptotic behaviour of the SP. $V_{mm'}$ is the average exchange potential ($=V_{AA}+V_{BB}-2V_{AB}$) between slices m and m'. $U_{mm'}=V_{AB}-V_{BB}$ is the 'magnetic field' and μ the chemical potential difference between A and B (assumed constant in all planes). Eq. (2) is an infinite linear system in δc_m each equation involving infinite sums of all the variables and the potentials.

The trick for an analytical solution is to express the interactions between different species as inverse Laplace transforms in (m-m') and do the same for the excess concentrations δc_m. In the fcc, the interactions between odd-odd/even-even and odd-even slices are different. Therefore, $V_{mm'}$ are expressed differently in odd and even slices and so are the δc_m. Plugging into (2) we can readily replace all sums with integrals in complex space and end up with an integral equation where the only unknown is the Laplace transform of the excess concentrations. The solution of the integral equation is exact when the Laplace transform of the average potential has a finite number of poles (of any order). For the purposes of this paper we give only a sketch of the procedure involved:

- The integrals are evaluated using complex analysis.
- In order for the final solution to be independent of slice number m, the condition is that a secular equation, resulting from the evaluation of the determinant of a 2x2 matrix, is satisfied. The equation is a polynomial of degree N in the decay rate of the SPs. N is determined by the number and order of the poles of the interactions.
- The roots, ρ_i of the secular equation are computed numerically. Half of them are larger than unity and are rejected because they do not correspond to decaying profiles. The rest are plugged back into the equation to obtain an $N/2$x$N/2$ algebraic linear system which can immediately be inverted to give the coefficients (amplitudes) R_{1i}, R_{2i} in front of each length scale.
- The final solution is:

$$\delta c_m=\begin{cases}\sum_{i=1}^{N/2}R_{1i}\rho_i^{\,m}, & \text{m even}\\ \sum_{i=1}^{N/2}R_{2i}\rho_i^{\,m}, & \text{m odd}\end{cases} \quad (3)$$

Discussion and Conclusions

In short, knowing the FTs of the pair interactions as a function of interplanar distance analytically (or numerically), one can determine the SP at any temperature. If the FTs are known numerically, the numerical values can be fitted to any number of functions of interplanar distances that are exponential decays, or products of exponential decays with positive powers and/or trigonometric functions. This way one can produce a fit for almost any pair-potential with arbitrary accuracy and solve for the SP.

The advantages of this method are: First, the fact that it uses arbitrary range interactions: Such interactions vary differently with distance for AA, BB, AB pairs and thus give rise to SPs containing several length scales. The amplitude of these length scales varies differently with temperature resulting in a great variety of shapes for the SPs, as has been extensively observed both experimentally and computationally in many alloy systems. All the existing length scales arise naturally in this method contrary to NN or NNN models where only one or two scales appear. Secondly, the method can incorporate the effect of atomic relaxations by using the relaxed atomic positions as input for the calculation of the FTs of interplanar interactions. The latter is, of course, only an approximation, because it assumes that configurational relaxation is independent of the

atomic relaxation process. Thirdly, by obtaining the solution (3) for the linearised system (2), one can proceed to obtain a better approximation to the solution of the non-linear mean-field equations by a simple perturbation technique. In fact, one can include higher order terms in the entropy expansion, thus incorporating atomic site correlations as well. The higher-order approximation could give a more accurate quantitative prediction of the concentration in the first one or two planes from the surface or GB, where the linear approximation is not accurate.

In Fig. 1 we show three characteristic profiles (excess concentration vs. Plane number) around a GB in Cu_3Au using a Rose potential [8]. The resulting profiles contain 30 length scales but only a couple are important for the asymptotic decay length towards the bulk. $\tau=(T-T_c)/T_c$. In Fig. 2a,b we show results of MC simulations around the same GB in Cu_3Au for an unrelaxed and a relaxed lattice in respect. Notice that for the same temperature the profiles change dramatically between the relaxed and unrelaxed case.

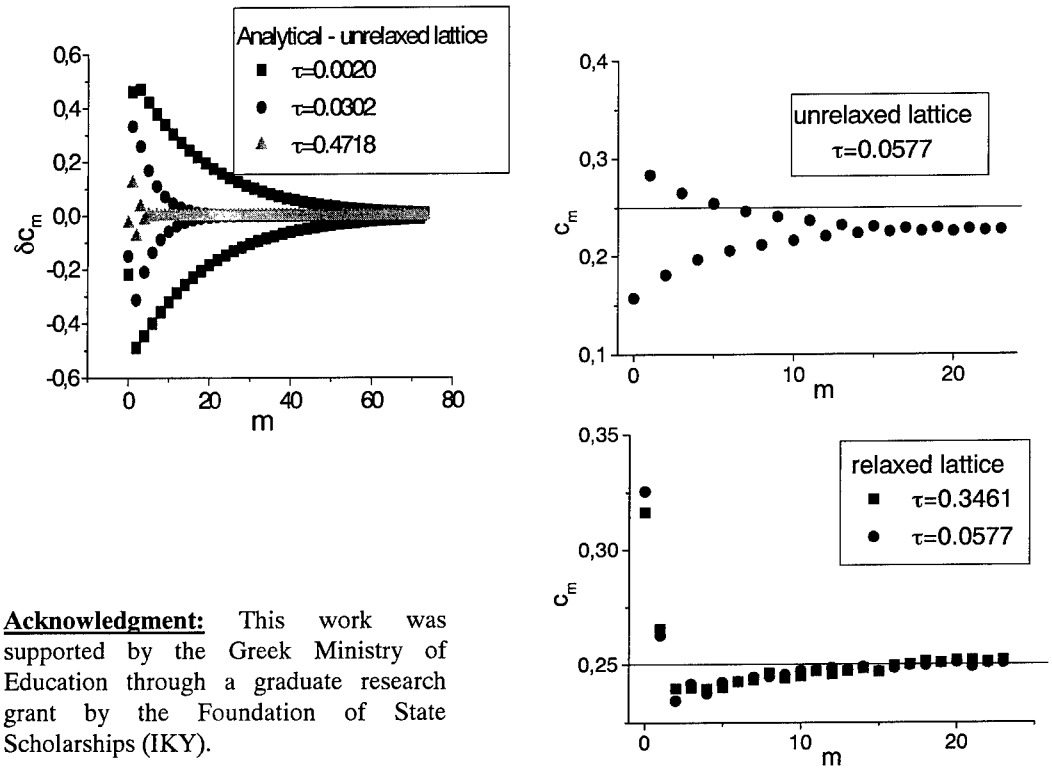

Acknowledgment: This work was supported by the Greek Ministry of Education through a graduate research grant by the Foundation of State Scholarships (IKY).

References

[1] H. Reichert and H. Dosch, *Surf. Sci.*, **345** (1996), p. 27.
[2] J. L. Moran-Lopez et al., *Phys. Rev. Lett.*, **54**, 10 (1985), p. 1936.
[3] C. Seok and D.W. Oxtoby, *J. Phys. Condens. Matter.*, **9** (1997), p. 87.
[4] V. Drchal et al., *Phys. Rev. B*, **54**, 10 (1996), p. 8202.
[5] S. Quanasser, L.T. Wille and H. Dreysse, *Phys. Rev. B*, **55**, 21 (1997), p. 14245.
[6] K. R. Mecke and S. Dietrich, *Phys. Rev. B*, **52**, 3 (1995), p. 2107.
[7] A. G. Khachaturyan, *Phys. Stat. Sol.* (b), **60**, 9 (1973), p. 9.
[8] N. X. Chen, M. Li, S. J. Liu, *Phys. Lett. A*, **195** (1994), p. 135.

Materials Science Forum Vols. 294-296 (1999) pp. 497-500

Moving Interfaces in Shape Memory Alloy Bicrystals

V. Novák and P. Šittner

Institute of Physics, Academy of Sciences of the Czech Republic,
Na Slovance 2, CZ-18221 Prague, Czech Republic

Keywords: Martensitic Transformation, Phase Interfaces, Interactions with Grain Boundaries

Abstract Interactions of moving β_1/β'_1, β_1/γ'_1 austenite/martensite interfaces with grain boundaries in CuAlNi bicrystals were investigated by thermomechanical cycling in compression and experimental stress-strain-temperature data were compared with the data of component single crystal grains. In situ optical observations of the surface of transforming crystals during the stress-strain test suggest that the $\beta_1 \rightarrow \beta'_1$ transformation is favored on the expense of the $\beta_1 \rightarrow \gamma'_1$ transformation in the bicrystal. The reason is that even a grain boundary fully complying with the strain compatibility conditions hinders the macroscopic shape change of adjacent grains accompanying the phase transformation into a single martensite phase. As a result, complex internal stress state suitable for the $\beta_1 \rightarrow \beta'_1$ transition arises in the transforming bicrystal.

INTRODUCTION

Mobile internal interfaces act as deformation carriers [1] in solids exhibiting thermoelastic martensitic transformations [MT] - Shape Memory Alloys [SMA]. The mobile interfaces can be of various sorts: i) phase interfaces, ii) interfaces between two variants of the same phase or common twin interfaces. They have characteristic structure and physical properties. Unique thermomechanical behavior of SMA's - reversibility of inelastic strains and memory effects – is inherently associated with the mobility of these interfaces. Interfaces moving in SMA polycrystals have to interact with other immobile interfaces - grain boundaries [GB]. While SMA single crystals may show up to 25% recoverable strain, polycrystals of the same alloy yield usually less than 3% of recoverable strain[2]. GB's are also weakest points of the SMA's often required to work under cyclic thermomechanical loads in many engineering applications. It is, therefore, of interest to investigate not only properties of individual mobile interfaces in SMA's but also their interactions with stationary grain boundaries on bicrystals with well defined GB's. Available data in the literature [3,4] clearly show that non-isoaxial strain-incompatible CuAlNi bicrystals often suffer severe intergranular damage during stress induced martensitic transformation due to the elastic and transformation anisotropy of SMA's. In the present paper, we investigate single crystals and isoaxial strain-compatible bicrystals made of CuAlNi SMA. Mobile interfaces activated by the

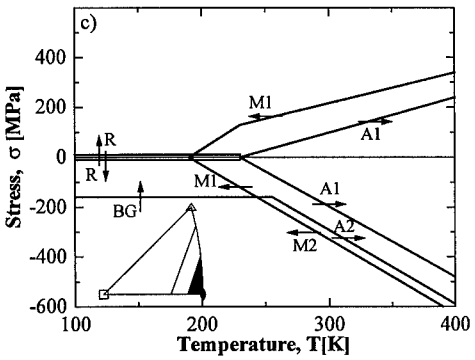

Figure 1: Non-equilibrium stress-temperature diagram of [011] CuAlNi single crystal. Solid lines show transformation conditions at which various phase transformations take place: M1 $\beta_1 \rightarrow \gamma'_1$, A1 $\gamma'_1 \rightarrow \beta_1$, M2 $\beta_1 \rightarrow \beta'_1$, A2 $\beta'_1 \rightarrow \beta_1$, BG $\beta'_1 \rightarrow \gamma'_1$ and R is reorientation in the $\rightarrow \gamma'_1$ phase.

applied stress or thermal change in single crystal and bicrystal are followed by videorecording steps moving on the surface of the transforming specimens. Dynamic information about interactions of mobile interfaces with GB's is presented and thermomechanical responses of the bicrystal and component grain single crystal are compared.

EXPERIMENTAL

Specimens used for thermomechanical experiments were prepared from Cu-14.3Al-4.1Ni [wt.%] shape memory alloy. Near [011] oriented single crystals and bicrystals were grown by seeded Bridgman technique. Specimens for compression tests (10mm x 3mm x 3mm) were machined from as grown crystals and electrolytically polished. Specimens with the GB parallel and perpendicular to the [0.052, 0.707, 0.707] load axis were cut from the symmetrical tilt bicrystal [0.052, 0.707, 0.707]/180°, GB plane (0.477, -0.643, 0.602). The specimens were given a standard thermal treatment by annealing at 900 °C for 2 hours in an argon atmosphere and quenching into the ice water. Following such solution treatment, the specimens have shown at room temperature a bcc - $D0_3$ ordered austenite crystal structure that transformed into a martensite phase upon cooling and/or external loading. The stress-free transformation temperatures measured by a differential scanning calorimeter Perkin-Elmer DSC-7 as martensite start, M_s= -65°C and austenite finish, A_f= -25°C.

Compression stress/strain tests at constant temperature, thermal cycling tests at constant applied stress as well as complex thermomechanical tests were performed in an INSTRON 1362 testing machine equipped with a heating/cooling chamber consisting of an electrical furnace and a cooling system by nitrogen gas vapors. Experiments were performed in position or load control mode and temperature range [-70°C, 20°C]. Surface observations were performed in situ by a an optical microscope with Nomarski interference contrast and videorecorded: i) at low temperatures, upon thermal cycling the compressed specimen in an cooled alcohol liquid, ii) at room temperature, upon straining the specimen in compression.

RESULTS

Depending on the test temperature, two different martensitic phases can be stress induced by compression from the [011] oriented CuAlNi single crystal ($D0_3$ ordered bcc β_1 austenite phase). At high temperature, martensite β'_1 (18R monoclinic structure) and, at low temperatures, martensite γ'_1 (2H orthorhombic structure) were observed [1,5]. In our recent work[5], non-equilibrium stress-temperature diagram for the [011] CuAlNi crystal loaded in tension/compression was presented (fig. 1). The stress-temperature conditions at which individual solid transitions are denoted as solid lines in the diagram. Each of the transformations is carried out by the motion of interfaces of distinct type and mobility. This affects the behavior of the crystal in stress-strain test (compare σ–ε curves due to the $\beta_1 \rightarrow \beta'_1$ (T=20°C) and $\beta_1 \rightarrow \gamma'_1$ (T=-20°C) in figure 2a). The $\beta_1 \rightarrow \beta'_1$ ($\beta_1 \rightarrow \gamma'_1$) transformations can be recognized from the curves according to the temperature independent transformation strains, $\varepsilon^{tr} = 0.03$ ($\varepsilon^{tr} = 0.025$), and width of stress hysteresis, Δh=70MPa (Δh=200MPa), respectively. The aim of the present work was to check whether an addition of a single grain boundary to the SMA single crystal affects essentially its strain response. With such a goal, a symmetrical near [011]/180° tilt bicrystal was studied: i) in stress free thermal cycles, ii) in thermal cycles with constant compressive stress applied parallel to the GB, iii) in stress-strain compression tests at constant temperature.

Thermally induced transformations Martensitic phase induced by cooling under small or no applied stress in CuAlNi single crystal is always an ortorhombic 2H phase ($\beta_1 \rightarrow \gamma'_1$) as can be read from the σ-T diagram (fig. 1). Looking at the surface of transforming single crystal, big γ'_1 particles arranged in a selfaccommodated manner (strains of individual particles mutually compensate each other) can be seen. The only change of this pattern resulting from a presence of the GB in cooled bicrystal (fig. 3c) is that the γ'_1 particles on both sides of the GB tend to align with the GB plane. In the case of such an arrangement, there is no strain mismatch at the grain boundary – no additional closing domains (variants) need to appear at the GB. In the case of small compressive stress ($\sigma \sim$-100MPa) applied parallel to the GB plane during cooling (fig. 3d), complex interactions of moving interfaces corresponding to γ'_1 particles with the GB plane were observed. Either small closing martensite domains appear at the GB plane when a growing martensite variant arrives to it or new martensite variants are induced in the adjacent grain across the GB plane.

Stress induced transformations Both $\beta_1 \rightarrow \beta'_1$ ($\beta_1 \rightarrow \gamma'_1$) transformations proceed in the [011] single crystal compressed at room temperature (figs. 2a, 3a). Stress-strain curves of the single crystal and bicrystal in

compression are compared in figures 2a,2b. Load axis orientation is the same in single crystal and in the both component grains of the bicrystal – i.e. close to the [011] axis.

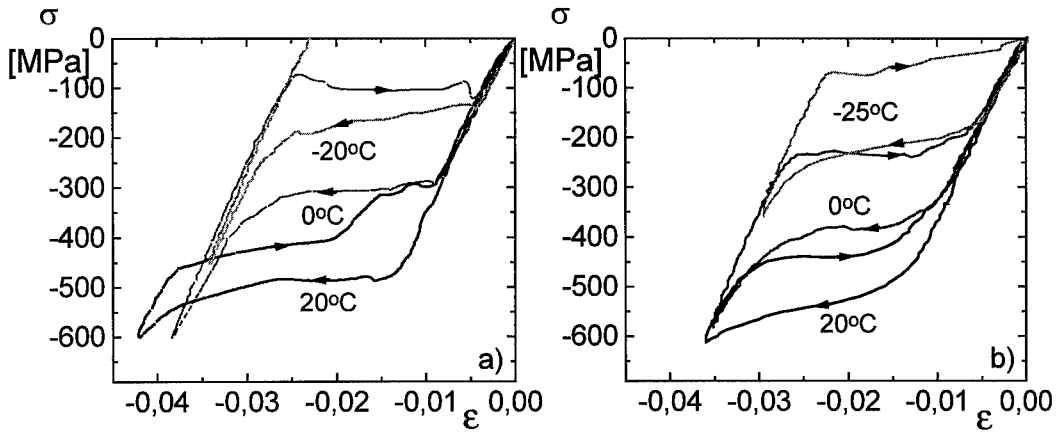

Figure 2: Stress-strain curves of [011] oriented CuAlNi single crystal (a) and bicrystal (b) at three different temperatures. Load axis is parallel to the GB plane and [011] direction in both bicrystal grains.

There is a mirror symmetry of the crystal structure across the GB plane. Such a load geometry assures compatibility of strains in the GB plane – i.e. no additional stresses should theoretically arise as a result of the presence of the GB. Nevertheless, response of the bicrystal shows the following remarkable differences from the single crystal's case: i) transformation stresses of the bicrystal are higher, ii) transformation strains are reversible at temperatures as low as T=-25°C (in the single crystal case, only down to the T=-10°C), iii) stress-strain curves are smooth, iv) $\beta_1 \rightarrow \beta'_1$ and $\beta_1 \rightarrow \gamma'_1$ transitions cannot be distinguished based only on the experimental values of transformation strains and hysteresis widths. Indeed, looking in situ at the surface of the compressed bicrystal (fig. 3b), mainly two active $\beta_1 \rightarrow \beta'_1$ transformation systems were observed. Single $\beta_1 \rightarrow \gamma'_1$ transformation systems active in each grain appeared only in very late stages of the test in spite of the theoretical compatibility of strains in the symmetrical bicrystal. On the other hand, the $\beta_1 \rightarrow \gamma'_1$ transformation appeared early and massively in the compression test of the bicrystal with the GB perpendicular to the load axis. This can be due to an orientation effect (called martensite formation anisotropy in the paper [1]) but also due to the fact that perpendicular GB allows shape change of component grains in a larger extent that the parallel GB does .

CONCLUDING REMARKS

Thermomechanical tests and in situ optical observations of martensitic transformations in CuAlNi [011] oriented single crystals and isoaxial strain-compatible bicrystals suggest that:

- grain boundary poses a severe limit on the macroscopic shape change of component grains during the martensitic transformation even in the case of the isoaxial strain-compatible bicrystal.
- while martensitic transformations into distinct γ'_1 and β'_1 martensite phases can be clearly distinguished on transforming single crystals at low and high temperatures, respectively, in a bicrystal case, no abrupt change in the transformation mode with decreasing test temperature was observed. Multiple variant $\beta_1 \rightarrow \beta'_1$ transformation seems to be favored in the case of the bicrystal transformation. Likely reason is a complex internal stress state that arises in the bicrystal due to the hindering effect of the GB on the macroscopic shape change associated with the transformation.
- grain boundary does not essentially affect nucleation of martensite, neither in stress induced transformations nor in thermally induced transformations.
- grain boundary stops effectively growing martensite variants but the transformation often proceeds by nucleation of new variants across the boundary in the adjacent grain.

Acknowledgment Support of the Grant Agency of the Academy of Sciences of the Czech Republic under contract No. A1020621 is greatly acknowledged

REFERENCES

[1] K.Otsuka and K.Shimizu, Int. Met. Rew. 93,(1986),p.93
[2] K.Bhatacharya and R.V.Kohn, Acta Mater.,44,(1996),p.529
[3] S.Miyazaki, T.Kawai and K.Otsuka, Scripta Met. 16, (1982),p.431
[4]K.Takezawa,T.Izumi,H.Chiba and S.Sato, Journal de Phys. Col. C4, (1982),P.819.
[5] V.Novák, P.Šittner and N.Zárubová, Mat. Sci. Eng. A234 (1997), p. 414.

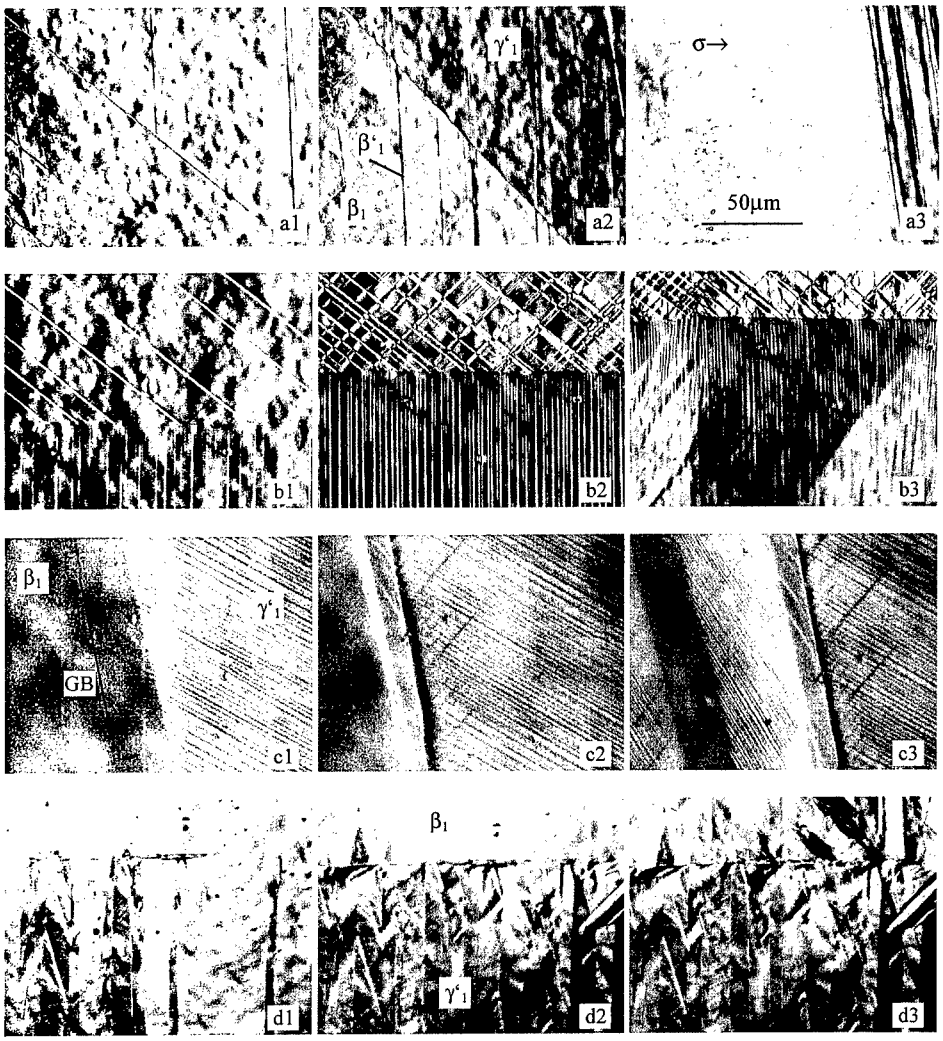

Figure 3: In situ optical surface observation of austenite-martensite transformation – three pictures taken from four video sequences a-d, transformation proceeds from left to right: a) single crystal, compression stress induced transformation, b) bicrystal, compression stress induced transformation, c) bicrystal, thermally induced transformation by cooling, d) bicrystal, thermally induced transformation by cooling under compressive stress σ~-100MPa. Load axis parallel to the GB plane in all cases.

Materials Science Forum Vols. 294-296 (1999) pp. 501-504

Grain Boundary Migration in Fe-3%Si

M. Furtkamp[1], G. Gottstein[1], D.A. Molodov[1] and L.S. Shvindlerman[2]

[1] Institut für Metallkunde und Metallphysik, RWTH Aachen,
Kopernikusstr. 14, D-52056 Aachen, Germany

[2] Institute of Solid State Physics, Russian Academy of Sciences,
Chernogolovka, Moscow RU-142432, Russia

Keywords: Grain Boundary Migration, Fe-3%Si, Compensation Temperature, Shape of the Migrating Grain Boundary

Abstract. Grain boundary (GB) migration was studied on Fe-3%Si bicrystals, using both the reversed-capillary technique and the method of constant driving force. The reduced mobility of the completely dragged motion was determined using the reversed-capillary geometry with samples of commercially pure material. On high purity Fe-3.5%Si bicrystals with [001] tilt boundaries with different angles the reduced mobility of the free moving boundary was determined in the temperature range from 944° C to 1104° C, using in most cases the constant driving force technique. In-situ observation of the fastest migrating boundary confirmed the results obtained by conventional methods. For the free motion the activation enthalpy and the pre-exponential factor of the reduced mobility were determined for the different types of tilt boundaries studied. Activation enthalpy and logarithm of the pre-exponential factor are linearly related, i. e. comply with the compensation effect. The obtained results were in good accordance with literature data of GB mobility in Fe-3%Si bicrystals. From the measured values and the literature data a compensation temperature of 1113° C ± 50° was found, i. e. slightly below the eutectic temperature of 1200° C of the system Fe-Si. For the reversed-capillary technique experimentally observed shapes of the moving GB were compared to theoretically predicted shapes. It was found that a better fit is obtained when taking into account the drag effect by impurities. It was shown that owing to this drag effect for the reversed-capillary technique, contrary to the constant driving force technique, a scaling behavior of the shape of the boundary in the course of migration is impossible. Thus displacement-independent geometry factors used for calculation of the mobility can only be approximations in the case of a free motion.

1. Introduction

The importance of electrical steel containing about 3 weight % silicon as a transformer core material is well known, also the role of Goss texture ({110}<001> orientation) for achieving the best magnetic properties of Fe-3%Si. The Goss texture is obtained by secondary recrystallization of rolled sheet. Obviously, Goss oriented grains are capable of growing fast. A key issue in this context is the GB mobility and its dependence on temperature and on GB structure.
The aim of this work is to elucidate the effect of impurity drag and misorientation on the mobility of freely moving [100] tilt boundaries of different misorientation angles of Fe-3%Si.

2. Experimental

The GB mobility was studied with bicrystal experiments using both the reversed-capillary technique (fig. 1 (a)) and the constant driving force technique (fig. 1 (b)). All experiments were performed by annealing in vacuum < 10^{-4} mbar. The mobility m is calculated from the experimental data by

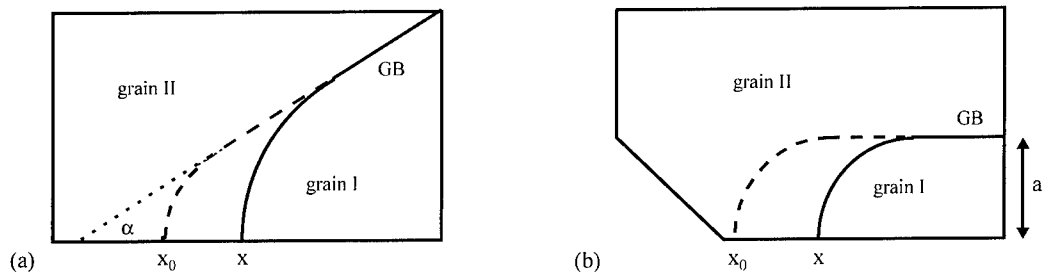

Fig. 1 Bicrystal geometries: (a) reversed-capillary geometry, (b) constant driving force technique

$$m = \frac{x^2 - x_0^2}{2 \cdot t \cdot f(\alpha) \cdot \sigma} \tag{1}$$

in the case of the reversed-capillary technique, and by

$$m = \frac{(x - x_0) \cdot a}{t \cdot \sigma} \tag{2}$$

in the case of the constant driving force technique where x, and x_0, respectively, is the position of the GB after and before the annealing experiment, respectively, t is the annealing time, $f(\alpha)$ is the so-called geometry factor depending on the angle α (see fig. 1(a)), a is the width of the shrinking grain (see fig. 1 (b)), and σ is the GB energy. Because the value of σ is not known for all grain boundaries the reduced mobility $A = m \cdot \sigma$ instead of the mobility is calculated. In the case of free GB migration and in the case of a motion dragged by impurity atoms the temperature dependence of the reduced GB mobility is given by

$$A = A_0 \cdot \exp(-H / kT) \tag{3}$$

with the activation enthalpy H and the pre-exponential factor A_0 of the reduced mobility. So, H and A_0 are determined from an Arrhenius plot ln A vs. $1/T$ in the ranges of free and dragged motion, respectively. Such data also allow one to identify the transition from dragged to free migration.

To study GB motion under the influence of impurity drag, bicrystals with large angle grain boundaries of various misorientations were produced from Fe-3%Si of commercial purity. Successive annealing experiments were performed using the reversed-capillary technique [1].
Fig. 2 shows the temperature dependence of the reduced mobility for a typical case. In the range from 780° C to 940° C dragged motion was observed. An increase in mobility by about an order of magnitude indicated the change to free migration at 1000° C.
The activation enthalpies derived for the range of dragged motion were roughly the same for the different large angle boundaries (200 - 240 kJ/mol). They corresponded with the value 220 kJ/mol reported by Tsurekawa [2] for the dragged motion of [110] tilt boundaries of Fe-3%Si in accordance with the impurity drag theory.
Free GB migration was studied with bicrystals of high purity Fe-3%Si, using only pure [100] tilt boundaries of three different misorientation angles (37.6°, 34.3°, and 13.8°). The composition of the material is given in table 1. The samples were prepared at the Institute of Solid State Physics in Chernogolovka, Russia, by the electron-beam floating zone technique [3]. In these experiments mostly the constant driving force technique (fig. 1 (b)) was applied.

Si	Mg	Cu	Ni	Pb	Al	Mn	Cr	Zn	C	N	Co
3,5	0,0004	0,0001	0,005	0,0001	0,0001	0,0005	0,003	0,0003	0,005	0,004	0,0001

Table 1. Composition of the high purity Fe-3%Si

The temperature dependence of the reduced mobility found in these experiments is shown in fig. 3 [4, 5]. Contrary to the dragged motion now different activation enthalpies were found for the different boundaries: 265, 377, and 698 kJ/mol for the 37.6° (≈ Σ 5), 34.3°, and 13.8° boundary, respectively.

To check if the migration was a uniform and not a „stop and go" motion, in-situ experiments were conducted with the most mobile boundary ([100] 37.6°) using an X-ray interface continuous tracking device (XICTD) described elsewhere [6]. Within the resolution of the XICTD a uniform motion was observed in the experiments. The reduced mobilities according to these observations showed good agreement with the results for the same boundary obtained by stepwise annealing.

This confirmed that free migration was observed in both experiments.

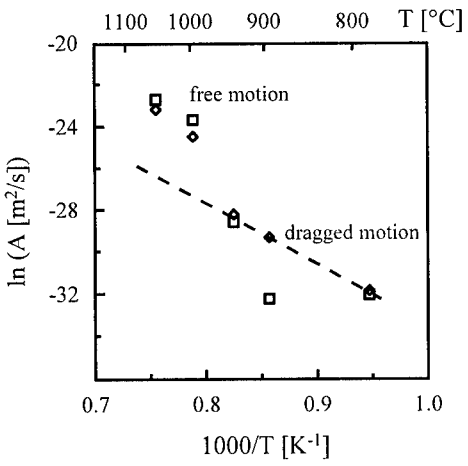

Fig. 2 Temperature dependence of reduced mobility of a GB in commercially pure Fe-3%Si
□ top surface; ◇ bottom surface of the sample; dashed: regression line (780° C to 940° C) [1].

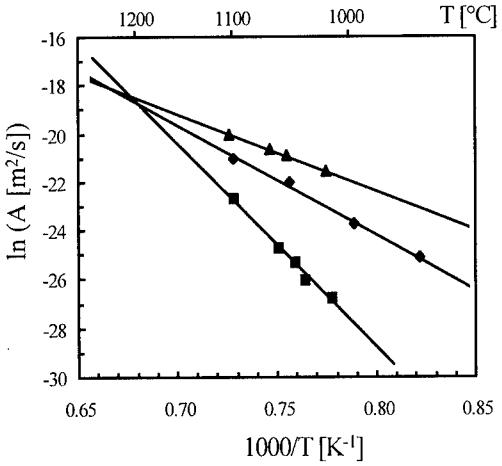

Fig. 3 Temperature dependence of reduced mobility for [100] tilt boundaries of high-purity Fe-3%Si with tilt angles 13.8° (■), 34.3° (◆), and 37.6° (▲) [4, 5].

3. Compensation effect

In thermally activated processes of various kinds a linear relation

$$H = \alpha \cdot \ln A_0 + \beta \qquad (4)$$

has been observed between the logarithm of the pre-exponential factor A_0 and the activation enthalpy H with constants $\alpha = k \cdot T_c$ and β [7]. An equivalent formulation in the case of GB migration is that at the so-called compensation temperature T_c all boundaries which comply with eq. (4) have the same reduced mobility.

In fig. 4 the data derived from fig. 3 are plotted together with the data reported by Lejček [5, 8, 9] and Tsurekawa [2, 5]. The constants α and β of eq. (4) are 11.5 ± 0.4 and 235 ± 7, respectively, for A_0 in m^2/s and H in kJ/mol. The corresponding compensation temperature is T_c = 1386 K ± 49 K, and at T_c the reduced mobility amounts to $A = 1.65 \cdot 10^{-9}$ m^2/s.

Recently it was proposed to attribute the compensation effect to a phase transformation from the ground state to the activated state [7] where the activated state is a metastable state of the alloy. In this context it is remarkable that the observed compensation temperature is only slightly below the eutectic temperature of 1473 K in the iron - silicon system [10].

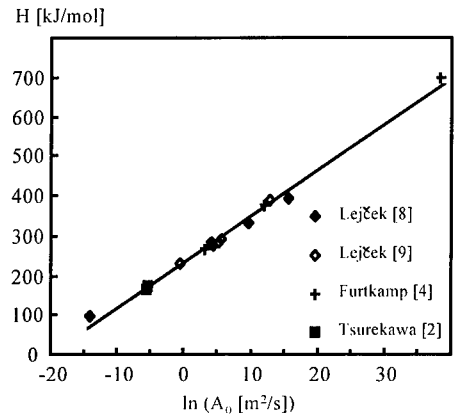

Fig. 4 Compensation plot for data of GB migration in Fe-3%Si

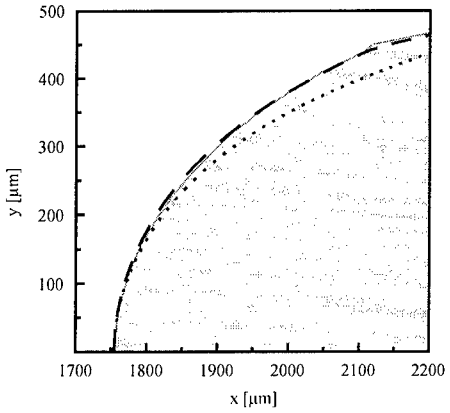

Fig. 5 Experimentally observed (shaded area) and theoretically predicted GB shape (dashed line: accounting for drag effects; dotted line: disregarding drag effects) [11]

4. Displacement-dependence of the geometry factor in the reversed-capillary geometry

To check the reliability of the reversed-capillary technique the experimentally observed shape of the moving GB was compared to theoretical predictions [11]. As shown by the example in fig. 5 the experimentally observed shape is approximated much better when the impurity drag effect is taken into account. It is obvious that the drag effect necessarily influences the shape of the boundary, and a shape invariance during free boundary migration is impossible with the reversed-capillary technique. Consequently, the geometry factor $f(\alpha)$ used in eq. (1) for the determination of the mobility depends on the GB displacement. The traditionally used displacement-independent factors are only rough approximations which degrade the accuracy of the experimental data. For this and other reasons [11] the constant driving force technique generally is superior to the reversed-capillary technique.

References:

[1] M. Furtkamp, doctoral thesis, Aachen, 1998.
[2] S. Tsurekawa, T. Ueda, K. Ichikawa, H. Nakashima, Y. Yoshitomi, and H. Yoshinaga, Mater. Sci. For. **204 - 206**, 221 (1996).
[3] V. N. Semenov, B. B. Straumal, V. G. Glebovsky, and W. Gust, J. Crystal Growth **151**, 180 (1995).
[4] M. Furtkamp, G. Gottstein, D. A. Molodov, V. N. Semenov, and L. S. Shvindlerman, Acta Mater., in press
[5] M. Furtkamp, P. Lejček, and S. Tsurekawa, Interface Science **6**, 59 (1998).
[6] U. Czubayko, D. Molodov, B.-C. Petersen, G. Gottstein, and L. S. Shvindlerman, Meas. Sci. Technol. **6**, 947 (1995).
[7] Y. L. Maksimova, B. B. Straumal, V. Y. Fradkov, and L. S. Shvindlerman, Phys. Met. Metall. **56**, 133 (1983).
[8] P. Lejček, V. Paidar, J. Adámek, and S. Kadecková, Interface Science **1**, 187 (1993).
[9] P. Lejček and J. Adámek, J. Physique IV **5**, C3-107 (1995).
[10] O. Kubaschewski, Iron - Binary Phase Diagrams, Springer Verlag 1982.
[11] M. Furtkamp, G. Gottstein, and L. S. Shvindlerman, Interface Science, in press.

Materials Science Forum Vols. 294-296 (1999) pp. 505-508

Cooperative Effects of Interfaces Motion in Coarsening Cellular Structures

S.B. Goryachev

Laboratoire de Métallurgie Physique, URA CNRS n 234, Bât. C6, Université de Lille I, F-59655 Villeneuve d'Ascq, France

Keywords: Cellular Structures, Coarsening, Interfaces Motion, Cooperative Effects, Kinetics, Hydrodynamics, Stochastodynamics

Abstract. Coarsening of cellular structures (physical systems consisting of homogeneous domains separated by distinct boundaries) is a well-studed effect. During this process the large cells "eat up" the small ones and the mean cell size increases. If we have a good look at an experimental picture of any cellular structure we can see a size correlation of adjacent cells. Near a small cell the probability to find another small cell is grater then a large one, and vice versa. In other words, we observe space-correlated fluctuations of the cell interface density $\rho(\mathbf{x}, t)$. In this paper the phenomenon is consistently analysed. It is shown that the equation for ρ has the form of a diffusion-reaction equation with a negative diffusion coefficient and with ρ playing the role of concentration. Its analysis reveals the effect of macroscopic patterning in the cell medium, being the result of competition between two stochastic processes: interfaces disappearance (annihilation) and interfaces "uphill diffusion" (collective motion in the direction of $\nabla\rho$).

Introduction. There are many physical systems consisting of homogeneous domains separated by distinct boundaries, so-called cellular structures: ordered domains in alloys, magnetic domains, gas bubbles in soap froth and in lipid monolayers, grains in polycrystals, etc. [1]. We have here a simple situation (Fig. 1) [2], when the system volume V being the sum of the

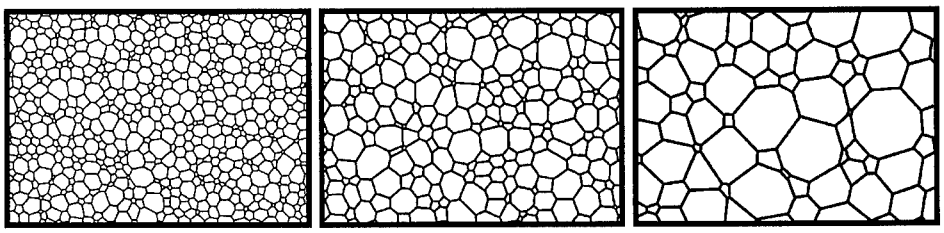

Fig. 1. Configurations of coarsening soap froth. Short-range ordering of cells is easily observable. Near a small cell the probability to find another small cell is grater then a large one, and vice versa, near a large cell the probability to find another large cell is grater then a small one.

volumes of all cells, the volume specific energy and the interface specific energy E are constant. The internal energy of the system $\mathcal{E}$ is completely defined by the cell interface area Σ. It is easy to see that for any two neighbouring cells the volume decrease of the smaller one (down to complete disappearance) and the simultaneous volume increase of the greater one diminish Σ. This permanent topological possibility to decrease $\mathcal{E} = E\Sigma$ makes the system intrinsically unstable. The mean cell size increases during this process, named "coarsening" (large cells "eat

up" small ones). If we have a good look at Fig. 1 we can see a strong size correlation of adjacent cells. Near a small cell the probability to find another small cell is grater than a large one, and vice versa. In other words, we observe here space-correlated fluctuations of a mesoscopic cell interface density $\rho(\mathbf{x},t)$. This is a macroscopic cooperative effect of cells interaction and motion. To analyse it a multilevel description of the cellular structure evolution are used in this paper. The coarsening are consistently analysed at micro-, meso- and macroscopic levels by the methods of kinetic, hydrodynamic and stochastodynamic theories, respectivly.

Kinetic theory (microscopic level). To get a cell dynamics equation let us approximately consider each cell as an elastic sphere shell embedded in an elastic environment which represents the average effect of cell-cell interaction. Then the structure configuration may be described through the cell centre coordinates and the cell radii. For a weakly nonhomogeneous structure we can approximately calculate the cell velocity and the cell size change rate as [1]

$$\mathrm{d}\mathbf{x}/\mathrm{d}t = Da\nabla\kappa/d, \tag{1}$$

$$\mathrm{d}a/\mathrm{d}t = -D(1/a-\kappa) + Da^2\triangle\kappa/(2d), \tag{2}$$

where $d = 2,3$ is the structure dimensionality; $D = ME$ and M is the interface mobility. The term $1/a$ is related to the effect of interface surface tension of the cell itself and the term $\kappa(\mathbf{x},t)$ - to the effect of interface surface tension of adjoining cells (the elastic environment). The quantity $\kappa(\mathbf{x},t)$ is a local characteristic - an *interface curvature self-consistent mean field.* We see that the cells move in a coordinate-size space $\{\mathbf{x},a\}$ in the process of coarsening. These movements are conveniently described by a continuity equation (kinetic equation) [1]

$$\partial f/\partial t + \partial(f\mathrm{d}\mathbf{x}/\mathrm{d}t)/\partial\mathbf{x} + \partial(f\mathrm{d}a/\mathrm{d}t)/\partial a = 0 \tag{3}$$

for the probability distribution function $f(\mathbf{x},a,t)$ in the cell coordinate-size space with a normalisation condition (conservation law of the total volume of all cells of the system)

$$(\Omega_d/V)\int \mathrm{d}\mathbf{x}\int \mathrm{d}a a^d f = 1, \tag{4}$$

where $\Omega_d = 2\pi(d-1)/d$. The mesoscopic quantities of the structure are easily expressed as the integrals of $f(\mathbf{x},a,t)$: $n(\mathbf{x},t) = \int f\mathrm{d}a$ is the mean number of cells per unit volume; $\bar{a}(\mathbf{x},t) = \int af\mathrm{d}a/n$ is the mean cell size and $\rho(\mathbf{x},t) = (\Omega_d d/2)\int a^{d-1}f\mathrm{d}a$ is the mean cell interface density. For macroscopically homogeneous structure [3] the solution of Eq. 1 - Eq. 4 has a universal scaling form

$$f_0(a,t) = \alpha\rho^{d+1}\varphi(\beta a\rho), \tag{5}$$

where α and β are constants [1], and all macroscopic system variables obey simple scaling laws: $\bar{a}(t) \propto \kappa^{-1}(t) \propto \rho^{-1}(t) \propto t^{1/2}$, $n(t) \propto t^{d/2}$.

Hydrodynamic theory (mesoscopic level). To get the hydrodynamic equation let us use the well-known Enskog method. Namely, let us multiply Eq. 3 by $\Omega_d d a^{d-1}/2$, Eq. 1 by $\Omega_d d a^{d-1} f_0/2$, Eq. 3 by $\Omega_d a^d$ and integrate them by a. We obtain, respectively, the *equation of cell medium continuity* , an analogue of *Darcy's law* in hydrodynamics and an equation similar to the *state equation* in gas dynamics [1]:

$$\partial\rho/\partial t + \nabla(\rho\mathbf{v}) = -D[\alpha_1\rho^3 - \alpha_2\rho^2\kappa - \alpha_3\triangle\kappa], \tag{6}$$

$$\mathbf{v} = (D/2)\rho^{-1}\nabla\kappa, \tag{7}$$

$$\rho^3\kappa = \beta_1\rho^4 - \beta_2\rho\triangle\kappa + \beta_3\nabla\kappa\nabla\rho. \tag{8}$$

The set of three hydrodynamic equations Eq. 6-Eq. 8, containing three hydrodynamic quantities of the cell medium: the density $\rho(\mathbf{x},t)$, the velocity $\mathbf{v}(\mathbf{x},t) = (\Omega_d d/\rho)\int_0 a^{d-1}(\mathrm{d}\mathbf{x}/\mathrm{d}t)f\mathrm{d}a$, and the curvature $\kappa(\mathbf{x},t)$, forms a closed set. The role of quantities $\rho(\mathbf{x},t)$, $\kappa(\mathbf{x},t)$ and $\mathbf{v}(\mathbf{x},t)$ are completely analogous to the role of gas density, pressure and velocity in viscous gas dynamics. By substituting Eq. 7 and Eq. 8 in Eq. 6, the set can be reduced to an evolution equation

$$\partial\rho/\partial t = -\gamma_1 D\rho^3 - \gamma_2 D\triangle\rho, \tag{9}$$

where $\alpha_1, \alpha_2, \beta_1, \beta_2, \gamma_1, \gamma_2$ are calculated constants [1].

Stochastodynamic theory (macroscopic level). To analyse the dynamics of macroscopic spatial perturbations of the cell medium, let us introduce a relative value of deviation of the interface density from its mean macroscopic value $\psi(\mathbf{x},t) = \delta\rho(\mathbf{x},t)/\rho(t) << 1$, where $\rho(t)$ is the uniform solution of Eq. 9. Substituting $\rho(\mathbf{x},t) = \rho(t) + \delta\rho(\mathbf{x},t)$ in Eq. 9 and coming to new variables $\partial\tilde{t} = 3\gamma_1 D\rho^2(t)\partial t = -\partial \ln\rho^3(t)$ and $\partial\tilde{\mathbf{x}} = \rho(t)\partial\mathbf{x}$, we obtain

$$\partial\psi/\partial\tilde{t} = -\delta\mathcal{F}/\delta\psi \tag{10}$$

with $\mathcal{F}\{\psi\} = \int \mathrm{d}\tilde{\mathbf{x}}[\mathcal{A}\psi^2 + \mathcal{C}(\tilde{\nabla}\psi)^2]/2$, $\mathcal{A} = 1$ and $\mathcal{C} = -\gamma_2/(3\gamma_1)$. As all mesoscopic quantities, ψ is a fluctuating quantity. But on writing Eq. 10 we have neglected these fluctuations. Eq. 10, after taking into account the fluctuations, becomes Langevin stochastic equation with $\mathcal{F}\{\psi\}$ being a *stochastodynamic potential.* The noise ζ is Gaussian noise, with $<\zeta>= 0$ and the correlation function $<\zeta(\tilde{\mathbf{x}},\tilde{t})\zeta(\tilde{\mathbf{x}}',\tilde{t}')>= 2\theta\delta(\tilde{\mathbf{x}}-\tilde{\mathbf{x}}')\delta(\tilde{t}-\tilde{t}')$, where θ is calculated constant [1]. The forms of evolution Eq. 10 and of the noise ζ guarantee that the steady-state probability distribution functional is given by Boltzmann formula $P\{\psi\} \propto exp[-\mathcal{F}\{\psi\}/\theta]$.We see that our system is rated in the class of so-called potential systems with potential $\mathcal{F}\{\psi\}$ having Landau-Ginzburg form and the quantity ψ plays the role of an *order parameter.* It is not surprizing because in general sense the system is in perfect analogy to a thermodynamic system with a nonconserved order parameter ψ. So the forms of evolution Eq. 10 and of potential $\mathcal{F}\{\psi\}$ are dictated by simple symmetry macroscopic considerations. Instead of the thermal noise in thermodynamic systems we have here the stochastic noise, created by the continuous process of cells annihilation. From Eq. 10 we see that the modes $\psi(\tilde{\mathbf{k}},\tilde{t})$ with $\tilde{k} > \sqrt{-\mathcal{A}/\mathcal{C}}$ are unstable. This is an indication that highest order terms of the expansion of $\mathcal{F}\{\psi\}$ in powers of $\tilde{\nabla}\psi$ must be considered for analysis of the system stability. Potential $\mathcal{F}\{\psi\}$ has necessarily the general form $\mathcal{F}\{\psi\} = \int \mathrm{d}\mathbf{x}[\mathcal{A}\psi^2 + \mathcal{C}(\tilde{\nabla}\psi)^2 + \mathcal{D}(\tilde{\triangle}\psi)^2]/2$ with $\mathcal{D} > 0$ [1]. The coefficient $\mathcal{D}$ can be found from experiments, computer simulations or by a direct calculation as we have made above for $\mathcal{A}$ and $\mathcal{C}$. There are two possible scenarios of system evolution [1]. If $\mathcal{D} > \mathcal{C}^2/(4\mathcal{A})$ the system is in a *modulated state* (short-range ordering, Fig. 1) and the structure function

$$\tilde{S}(\tilde{\mathbf{k}}) = \theta/(\mathcal{A} + \mathcal{C}\tilde{k}^2 + \mathcal{D}\tilde{k}^4). \tag{11}$$

has a maximum at $\tilde{k} = \tilde{k}_{\mathcal{C}} = \sqrt{-\mathcal{C}/(2\mathcal{D})} = 2\pi/\tilde{\xi}$, where $\tilde{\xi}$ is a correlation length (Fig. 2). If $0 < \mathcal{D} < \mathcal{C}^2/(4\mathcal{A})$, the system is in a *patterned state* (long-range ordering, Fig. 3) and forms stationary one-, two-, ... or d -dimensional space-periodical configuration with wavelength $\tilde{\xi}$ [1].

Conclusions. We see that in the process of coarsening the macroscopic cell interface density $\rho(t)$ decreases with time as $\rho(t) \propto t^{-1/2}$ and the mesoscopic density $\rho(\mathbf{x},t) = \rho(t)[1 + \delta\rho(\mathbf{x},t)/\rho(t)]$ also decreases (Fig. 1). The competition of two stochastic processes of the cells annihilation and of the cells collective motion creates space-correlated fluctuations of $\rho(\mathbf{x},t)$. These fluctuations are the adjacent domains of size ξ with $\rho(\mathbf{x},t)$ greater or smaller than $\rho(t)$ (Fig. 1 and 3). In other words, they are the domains in which the cells have the mean size $\bar{a}(\mathbf{x},t)$ greater or smaller than the macroscopic mean value $\bar{a}(t)$. The amplitude of relative fluctuations $\delta\rho(\mathbf{x},t)/\rho(t)$ and the domain size (characteristic wavelength of fluctuations), divided by

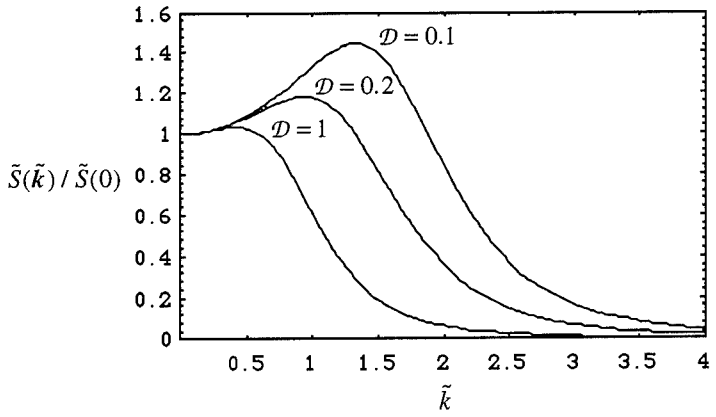

Fig. 2. Scaled structure function $\tilde{S}(\tilde{\mathbf{k}})/\tilde{S}(0) = 1/[1 + (\mathcal{C}/\mathcal{A})\tilde{k}^2 + (\mathcal{D}/\mathcal{A})\tilde{k}^4]$ of relative interface density fluctuations $\psi(\mathbf{x}, t) = \rho(\mathbf{x}, t)/\rho(t) - 1$ for the cellular system in modulated state. The value and the position of the maximum characteristic for short-range ordering depends on the value of $\mathcal{D}$.

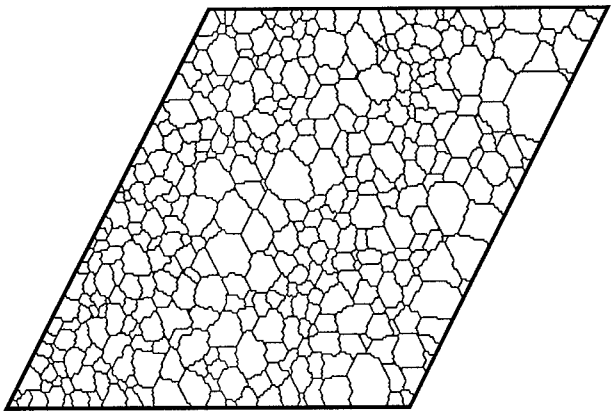

Fig. 3. Configuration of cellular structure in patterned state observed in grain growth simulation. Periodical fluctuations of relative interface density in horizontal direction are clealy visible.

the mean cell size $\xi/\bar{a}(t) \propto \xi\rho(t) = \tilde{\xi}$ stay constant. These domains can be short-range ordered (Fig. 1) or long-range ordered (Fig. 3) in space. The short-range ordering of cell interface density fluctuations resembles the fluid density fluctuations ordering in the well-known phenomenon of critical opalescence. The long-range ordering of cell interface density fluctuations resembles the effect of spinodal decomposition in thermodynamic systems.

References

[1] S.B. Goryachev, cond-mat/9710131; Mod. Phys. Lett. B11 (1997), p.949 and references therein.

[2] J. Stavans, Physica A194 (1993), p.307.

[3] M. Hillert, Acta Met. 13 (1965), p.227.

[4] P. Paillard, Ph.D. Thesis, Paris XI University (1994); Scripta Met., to be published.

Materials Science Forum Vols. 294-296 (1999) pp. 509-512

Experimental Determination of Nickel Grain Boundary Mobility During Recrystallization

R. Le Gall, G. Liao and G. Saindrenan

Lab. Génie des Matériaux, ISITEM, rue C.Pauc, BP 90604, F-44306 Nantes Cedex 03, France

Keywords: Recrystallization, Grain Boundary Mobility, Nickel

Abstract. We have studied the grain boundary migration during primary recrystallization of cold-worked nickel by *in-situ* heating scanning electron microscopy. The rate of grain boundary migration during recrystallization was plotted against the driving force for recrystallization deduced from calorimetric measurements. It was shown that boundary velocity evolution agrees with the Cahn, Lücke, and Stüwe theory of impurity drag. Values of the mobility and of the interaction energy between a moving boundary and sulfur are deduced from the experimental results.

Introduction

The solute drag theory proposed by Cahn [1], Lücke, and Stüwe [2] gives a good semi-quantitative account of the effects of solute atoms on boundary migration. This theory is based on the fact that segregation can occur at a moving grain boundary (GB), so when the boundary moves, an impurity atmosphere is assumed to be carried along with the boundary [3]. The rate of grain boundary migration (GBM) will, therefore, be reduced by the necessity for impurity atoms to diffuse.

This theory predicts that GBM rate V has the following relation with the driving force P and the solute concentration, C:

$$P = \frac{V}{M} + \frac{\alpha C V}{1+\beta^2 V^2} \tag{1}$$

Here, M is the mobility, C is the solute concentration, α and β are parameters defined as :

$$\frac{\alpha}{\beta^2} = \frac{2N_v E_0^{\,2} D}{kT\delta} \tag{2}$$

where $N_v = 4/a^3$ is the number of atoms per unit volume, a is the lattice parameter, k is the Boltzmann constant, E_0 is the interaction energy between the grain boundary and a solute atom (E_0 is negative assuming solute adsorption at the GB), D is the diffusion coefficient for motion of solute atoms in the vicinity of the moving boundary.

The purpose of the present work is to investigate quantitatively the rate of GBM during primary recrystallization of cold-rolled nickel to determine the nickel boundary mobility and the interaction energy E_0 between sulfur and GB since sulfur strongly segregates at nickel GB.

Experimental procedures

The material used in this study is a 270 polycrystalline nickel from Wiggins Alloys whose purity is better than 99.98%.

The samples were cold rolled to different deformation ratios (ε=0.25~1.12). All the isothermal annealings were carried out at 728K by means of an in-situ heated Scanning Electron Microscopy (SEM). The details can be seen in a previous paper [4]. Individual grains were chosen so that there was no impingement of grains and no overlap of adjacent recrystallized grains. The average radius of individual grains was measured using image analysis. The migration velocity of each grain was taken from the initial slope of the curve, displacement-time. The measured velocity was thus the average of measurements taken from at least twenty grains from two different samples. One of the great

advantage of this in-situ technique is to distinguish newly recrystallized grains from initial ones especially at low deformation ratios.

Results

In-situ SEM observations of the grain boundary migration . Fig. 1 shows pictures taken during isothermal annealing at 728K for a specimen deformed at ε=0.8; for the sake of simplicity only one grain has been isolated here.

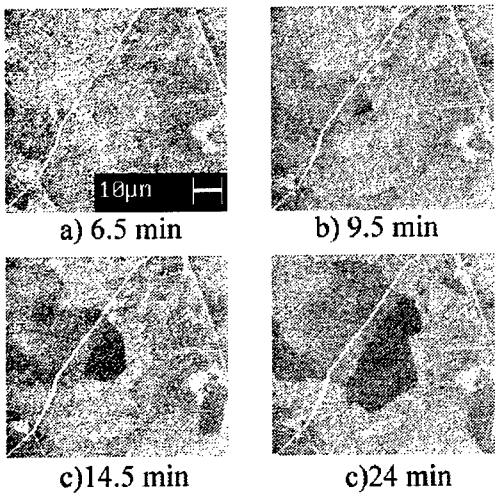

Figure 1 : SEM micrographs of a cold rolled nickel specimen deformed at ε=0.8 isothermally annealed at 728K.

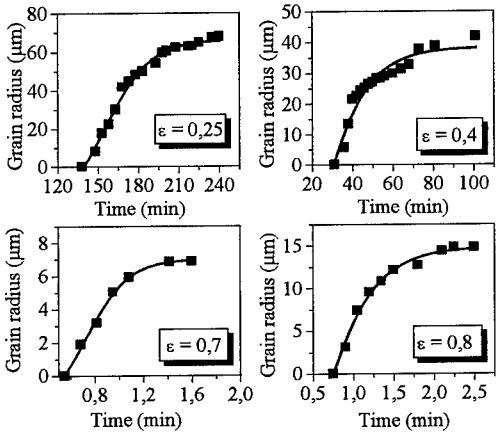

Figure 2 : Typical individual grain growth versus annealing time at 728K. Each curve represents the growth process of a grain.

Grain boundary migration. Fig. 2 illustrates typical displacement-time curves of individual grains. The curves are quite linear at the beginning of grain growth.

We assume that the driving force for recrystallization is the stored energy during cold rolling of nickel, as was previously measured by calorimetry [5].The measured driving forces are listed in table 1 as a function of deformation. Thus, the evolution of GBM rate versus driving force is shown in fig.3.

Table 1 : Experimental results

Deformation ratio, ε	0.25	0.4	0.5	0.6	0.7	0.8	1.12
Measured stored energy, P [MJ m^{-3}]	2.28	3.47	4.87	5.88	6.95	8.05	11.3
Measured boundary rate, V [10^{-8} m s^{-1}]	2.6	8.9	11.7	24.7	33.1	52.5	72.8

By fitting our experimental values shown in fig. 3 to the theoretical equation (1) of Cahn, we obtain the following relation (3):

$$P = (138 \pm 9) \times 10^{11} V + \frac{(49 \pm 12) \times 10^{12} V}{1 + (65 \pm 33) \times 10^{12} V^2} \qquad (3)$$

P is in J m^{-3} and V in m s^{-1}.

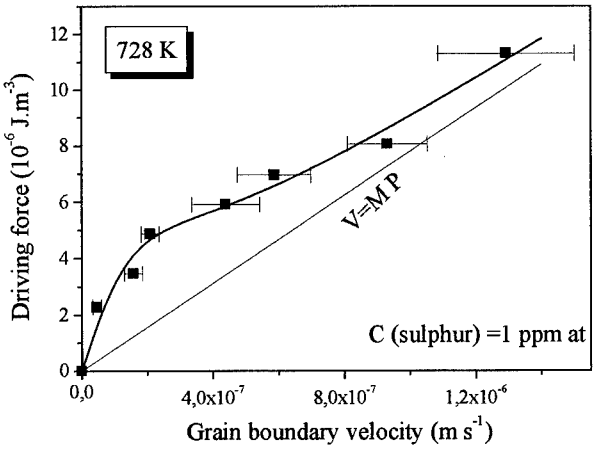

Figure 3 : Grain boundary migration versus driving force. The velocity is the average of at least 20 grains for each point ; the driving force is the stored energy measured by differential calorimetry.

There is a good agreement between the predictions of the solute drag theory and our experimental results from which we can estimate the mobility of the boundary and calculate the interaction energy between sulfur and the GB.

Discussion

Impurity drag . Previous experiments on sulfur segregation have demonstrated that there is a strong attractive interaction between the nickel GB's and sulfur.

Estimation of boundary mobility M. The value of grain mobility M extracted from the experimental law (3) is : $M = (7.25\pm0.4) \times 10^{-14}$ m^4 s^{-1} J^{-1}

New experiments at different temperatures of recrystallization are however needed to obtain the activation energy and the preexponential factor according to the classical equation :

$M = M_0 exp\ (-\Delta G/RT)$.

On the other hand, it can be compared to the mobility calculated using the model of Turnbull [6] proposed for the GBM rate. The mobility M is :

$$M = \frac{D_{JDG}}{RT} \cdot \frac{V_{at}}{d} \qquad (4)$$

where D_{JDG} is the grain boundary self-diffusivity, V_{at} is the atomic volume, d is the interatomic jump distance, R is the gas constant, and T is the absolute temperature.

By taking $D_{JDG}=4.85\times10^{-14}$ m^2.s^{-1}, extrapolated according to the measurement of Bokshtein et al [7] for 99,97% nickel between 823 and 1373K : $\delta D_{JDG}=4\times10^{-15}.exp(-1.378\times10^{4}/T)$ m^2.s^{-1}, with $\delta=5\times10^{-10}$m; $V_{at}=6.59\times10^{-6}$ m^3/mol for nickel ; $d=\frac{a\sqrt{2}}{2}=2.48\times10^{-10}$ m for nickel, we obtain the value of the mobility for nickel at 728K according to equation (4): $M = 2.13\times10^{-13}$ m^4.s^{-1}.J^{-1}

This theoretical value has the same magnitude as our measured value, although it is three times larger than the measured one ($M=(7.25\pm0.4) \times 10^{-14}$ m^4 s^{-1} J^{-1}).

Interaction energy E_0 between sulfur and nickel. The values of α and β enable us to calculate the interaction energy E_0 according to relation (2). We estimate the interaction width δ to be 13×10^{-10} m. The atomic volume of nickel is $N_v=9.17\times10^{28}$ m^{-3}. If one takes the bulk heterodiffusivity of sulfur in nickel or in the GB, the values E_0 obtained are abnormal [8].

However, it is now well established that a moving GB increases the vacancy concentration in the vicinity of the boundary [9,10], leading to the heterodiffusion of impurities in the vicinity of the boundary to be undoubtedly higher. Therefore, a better estimation of the heterodiffusion constant value can be obtained using the heterodiffusion constant in a material supersaturated with vacancies. Ferhat *et al* [11] have determined the apparent heterodiffusion constant of sulfur in nickel samples quenched from 1423K, where the vacancy concentration was estimated to be 2.15×10^{-6}. By extrapolating their results to 728K we obtain $D=3\times10^{-15}$ m^2s^{-1}, and with this value of the diffusion constant, the interaction energy becomes : E_0= - 0.84 ±0.23 eV at^{-1}

Although we do not have any more precise information about the vacancy concentration in the vicinity of a migrating GB, this value is probably more reasonable. Despite that, it can be compared with the value of the segregation energy of sulfur in nickel GB, 1 eV at^{-1} [12].

Conclusions

The behavior of GBM during recrystallization of cold rolled nickel has been studied with *in-situ* heated SEM. The conclusions from this work can be stated as follows:

The experimental relationship between GB velocity and driving force has been obtained according to the solute drag theory of Cahn, Lücke and Stüwe ; it allows us to measure the value of the mobility of GB's for polycrystalline nickel at 728K : $M=(7.25\pm0.4)\times10^{-14}$ m^4 s^{-1} J^{-1}. This value is comparable with the theoretical one calculated according to the model of Turnbull.

The interaction energy between sulfur atoms and a moving GB in nickel is also deduced from our results (E_0= - 0.84 ±0.23 eV at^{-1}); it could be compared with the segregation energy (1 eV at^{-1}) of sulfur in the GB of nickel.

References

1. J.W. Cahn, Acta Metall ,10 (1962),pp. 789-798.

2. K. Lücke and H.P. Stüwe , Acta Metall, 19 (1971), pp.1087.

3. R.L. Fullman, Metal Interfaces, ASM, Cleveland, 1952.

4. G. Liao, R. Le Gall and G. Saindrenan, Mater. Sci. Technol, 14 (1998), pp. 411-416

5. R. Le Gall, G. Saindrenan and D. Roptin, Annales de Physique, 20 (C3) (1995),pp. 101-108.

6. D. Turnbull, Trans. AIME, 191 (1951), pp. 661.

7. S.Z. Bokshtein, S.T. Kishkin, Y.M. Mishin and I.M. Razumovskii, Dokl. Akad. Nauk. SSSR, 280 (1985), pp.1125-1128.

8. G. Liao, (Ph.D. thesis, Université de Nantes ,1998),pp.116.

9. K. Lücke and G. Gottstein, Acta Metall, 29 (1981), pp.779-789.

10. H. Gleiter, " Vacancy Drag - Acta Metall, 27 (1979), pp.1749-1754.

11. F. Ferhat, G. Saindrenan and D. Roptin, Journal de phys, 25 (1990), pp.269-275.

12. A. Larère, M. Guttmann, P. Dumoulin and C. Roques-Carmes, Acta Metall, 30 (1982), pp.685-693

Materials Science Forum Vols. 294-296 (1999) pp. 513-516

Grain Structure Evolution in 1-d Rods and 2-d Strips of Polycrystalline Aluminium

V.G. Sursaeva and S.G. Protasova

Institute of Solid State Physics, Russian Academy of Sciences,
RU-142432, Chernogolovka, Moscow distr., Russia

Keywords: "Bamboo" Structure, "Columnar" Structure, Triple Junction Motion, Grain Boundary Motion, Aluminium

ABSTRACT

The paper presents data on the motion of grain boundary system with individual triple junction in aluminium and data on the grain structure evolution in one-dimensional (1-D) rods ("bamboo" structure without triple junctions) and two-dimensional (2-D) strips ("columnar" structure) of polycrystalline aluminium. Influence of triple junction motion on the grain growth in polycrystalline aluminium is discussed.

INTRODUCTION

Triple junctions and grain boundaries are the main structural elements of polycrystals. However, little studies have been carried out so far on the triple junction influence during grain growth of polycrystalline materials. The first data available on triple junction mobility were obtained for Zn tricrystals [1]. It was shown that triple junction can drag the boundary motion and that its role and properties should be taken into consideration in theories of grain growth.

The main goal of the current work is the determination the triple junction influence on the grain growth in 1-D "bamboo" structure and 2-D "columnar" structure.

EXPERIMENTAL

Experiments were carried out using rods with the 1-D "bamboo" structure, strips with 2-D "columnar" structure and tricrystals with triple junction. All samples were made of Al 99.999%. The term "bamboo" structure is used for the description of a system in which two dimensions are smaller than the third one (Fig.1a). Each grain in this structure has only two neighbours along the sample axis. Rods have a square cross section 1×1 mm^2 .The rods were cut from rolled aluminium polycrystals and single crystals (ε = 75%). They were annealed at 823 K for 0.5 hour to obtain the initial "bamboo" structure. 2-D "columnar" structure labels a system where grain boundaries are perpendicular to the sample plane and where sample thickness is of the order of the mean grain size. The third dimension remained homogeneous (Fig. 1b). Strips thickness is 1 mm. They were cut from rolled aluminium polycrystals and single

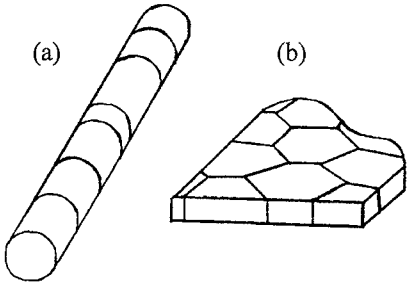

Fig. 1. The schematic view of: (a) 1-D "bamboo" structure, (b) 2-D "columnar" structure.

crystals (ε = 75%). Strips were annealed for 0.5 h at 823 K to obtain the "columnar" structure. Thus, the initial material, both rods with "bamboo" and strips with "columnar" structures, received the same heat and mechanical treatment. Sample preparation scheme is shown in Fig.2. Finally rods and strips were annealed at the same conditions at 773 K for 0.5, 1.5, 3 and 6 h.

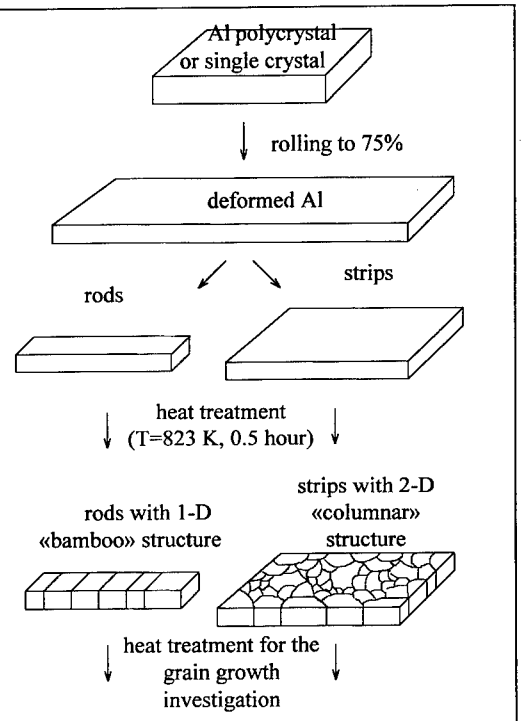

	Mean grain growth velocity, mm/s		
initial state of samples	«bamboo» structure	«columnar» structure	
		in cluster	the whole
polycrystal	4.54×10^{-5}	1.41×10^{-5}	6.06×10^{-6}
single crystal	3.03×10^{-5}	5.56×10^{-6}	5.56×10^{-6}

Fig.2 Scheme for obtaining rods with "bamboo" structure and strips with "columnar" structure

To study the kinetic of the grain growth in the 1-D rods and 2-D strips the mean grain size was measured for each annealing time. It is known that grain boundaries are etched to a different degree depending on their crystallography. The low angle grain boundaries produce a weak contrast and it is practically impossible to reveal them during metallographic investigations using optical microscope in bright field conditions. But we can not ignore these low angle grain boundaries in our consideration, because it may lead to incorrect results. There are some papers, where this question was discussed. Therefore we decided to use dark field conditions and inclined beam with a large aperture. Rotating of the microscope stage varies the angle of incidence of the light beam on the specimen surface. This causes a variation in intensity of the grain colouring and permits to obtain data on the grain boundary distribution in specimen, including the low angle grain boundaries [2]. Determination of grain misorientations was performed using selected area channelling pattern technique (SAC) in the scanning electron microscope (SEM).

The Al tricrystals with triple junction were grown by a directed crystallization technique (Fig. 3). A graphite crucible in a high purity argon atmosphere was used. The orientation of three adjacent grains in each sample was also determined by SAC technique. In order to study the triple junction motion we fix the displacement and the angles in a vertex of the half-loop.

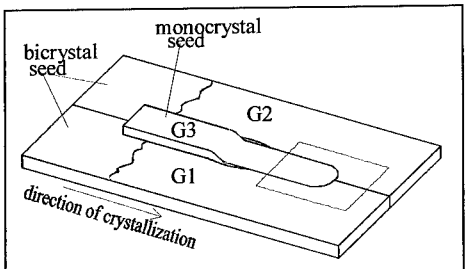

Fig3. The scheme of Al tricrystal growth; the square with thin line indicates the used tricrystal. G1, G2, G3 are grains with different crystallography.

Al <111> tricrystals contain <111> tilt grain boundaries with different misorientation angles. We used tricrystals with <111> tilt grain boundaries, because these boundaries in Al bicrystals have a high mobility [3]. We assumed that <111> tilt triple

junctions would have a high mobility too. The experiments on triple junction mobility were carried out in the temperature range 380°C–510°C.

We also supposed that driving forces for grain boundary migration in bicrystals, in system with individual triple junction, in "bamboo" structure and "columnar" structure can be: difference in surface tension between two grains ($p \approx 10^4$erg/cm^3 [4]) and decreasing of grain boundary energy ($p \approx 10^3$–10^4 erg/cm^3 [5, 6]).

RESULTS AND DISCUSSION

1. Triple junction mobility.

Experimental data on triple junction migration in Al <111> tricrystals are obtained for the first time. Triple junction mobility may be calculated using the expression for boundary and triple junction kinetics as shown in [1]. As we did not observe sharp change in angle at the triple junction vertex, we used the formula of triple junction mobility A for boundary kinetics:

$$A = \frac{a \cdot V}{2\theta} = A_0 e^{-\frac{H}{kT}},$$

where a is the width of consumed grain, V is triple junction motion velocity, 2θ is vertex angle, A_0 is pre-exponential factor, H is activation enthalpy.

The obtained data on triple junction mobility for Al tricrystals are shown in Table 1. Activation enthalpy for the different triple junction differs one from another by one order of magnitude. Triple junction mobility differs by two orders of magnitude. These differences are determined by triple junction crystallography. Triple junction crystallography determines also the temperature, at which they become mobile. So, as the triple junction mobility varies with the change of temperature triple junctions enter into recrystallization process at different stages. It is resulted in changes not only of mean grain size, but also of grains shape during grain growth. Interval of triple junction motion velocity is shown in Fig. 4.

Table 1. Crystallography and activation parameters of triple junction mobility in Al <111> tilt tricrystals. T_m is melting point.

	H, eV	<111>			A_0, m^2/s	T, °C	T/T_m
		φ_{1-2}	φ_{2-3}	φ_{1-3}			
T1	4.14	8°	56°	56°	8.60×10^{19}	440 – 460	0.76
T2	2.60	5°	25°	20°	1.74×10^{11}	380 – 420	0.70
T3	0.36	30°	20°	10°	3.93×10^{-6}	470 – 510	0.80

2. "Columnar" structure.

We investigated grain growth in Al strips with 2-D structure. The data on grain growth in "columnar" structure are shown in Fig. 2. It was found that there are grains with different normal orientation to their surface. Grain boundaries spatial arrangement is far from random one. There is <111> microtexture in Al. The clusters of like-textured grains can be recognised readily. There are many low angle grain boundaries, fewer large-angle grain boundaries and only isolated special grain boundaries into the clusters. Large angle grain boundaries divide mainly grains with normals

to the strips surface <110> and <100>. Mean grain size growth velocity in clusters is higher than in specimen as a whole. It can be associated with the fact, that triple junction with a configuration *large angle/low angle/large angle* tilt grain boundaries are significantly more mobile then those with other configurations. Migration of such triple junctions resulted in increase of cluster area. Intervals of change in mean grain size growth velocity are shown in Fig. 4. All data were obtained at the same driving forces.

3. "Bamboo" structure.

There are no triple junctions in rods. Low angle boundaries are not observed in them. Mean grain size growth velocity in rods is lower than migration velocity of individual grain boundary in Al [3] (Fig. 4). However mean grain size growth velocity in "bamboo" structure is about one order of magnitude higher than in 2-D structure (Fig. 2). Triple junctions are absent in 1-D rods and do not drag the motion of the grain boundary in "bamboo" structure.

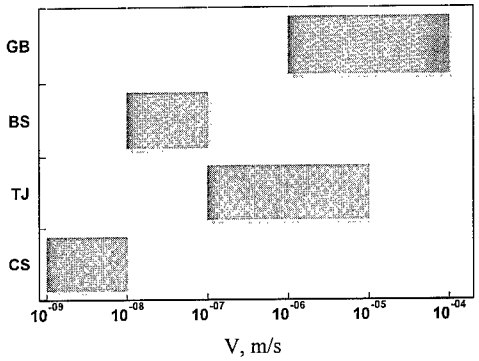

Fig.4. Interval of change: GB-individual grain boundary migration velocity; BS-mean grain size growth velocity in "bamboo" structure; TJ-triple junction motion velocity; CS- mean grain size growth velocity in "columnar" structure. All data were obtained at the same driving forces.

CONCLUSIONS

1. Triple junctions have a considerable influence in the processes of grain growth.
2. Grain growth velocity in 1-D system without triple junctions is higher than in 2-D strips, obtained by the same preprocessing.
3. Grain growth velocity in 2-D system with triple junctions ("columnar" structure) is determined by drag of triple junctions.

ACKNOWLEDGEMENTS

The authors are grateful to Prof. L.S. Shvindlerman for fruitful discussions. The work was partially supported by the Russian Foundation for Basic Research and Copernicus Network PL97-8078.

REFERENCES

[1] L.S. Shvindlerman, G. Gottstein, U. Czubayko and V.G. Sursaeva, Proceedings of ReX'96,
[2] V.G. Sursaeva, S.G. Protasova, W. Lojkowski, J. Jun, Proceeding of ICTPM'97, in press.
[3] G. Gottstein, D.A. Molodov, U. Czubayko, L.S. Shvindlerman, Journal De Physique IV, Coll.C3, v. 5, april (1995).
[4] J.L. Walter, C.G. Dunn, Trans. AIME, 215, (1959), p. 46
[5] B.B. Rath, H. Hu ,Trans. AIME, 245, (1969), p. 1577
[6] B.B. Rath, H. Hu, Nature and Behaviour of Grain Boundaries, New-York - London, (1972), p. 405

Corresponding author: Dr.V.Sursaeva, e-mail sursaeva@issp.ac.ru, Fax 096 576 41 11

Materials Science Forum Vols. 294-296 (1999) pp. 517-520

Effect of Triple Junctions on Grain Boundary Migration

V.G. Sursaeva[1], U. Czubayko[2], G. Gottstein[3] and L.S. Shvindlerman[1]

[1] Institute of Solid State Physics, Russian Academy of Sciences, Chernogolovka, Moscow Distr., RU-142432 Russia

[2] Hahn-Meitner-Institut, Berlin GmbH, Gliwnickerstr. 100, D-14109 Berlin, Germany

[3] Institut für Metallkunde und Metallphysik, RWTH Aachen, Kopernikusstr. 14, D-52056 Aachen, Germany

Keywords: Grain Boundary, Triple Junctions Motion, Steady State Motion, Zinc

Abstract

The paper is dedicated to the steady state motion of the grain boundary systems with the triple junctions. The main features of one of the systems where steady state motion is possible are considered. In the experimental part the results of the experiments on the tricrystals of Zn are described. In particular, it was demonstrated that the vertex angle θ at the triple junction can deviate distinctly from the equilibrium value, when a low mobility of the triple junction drags the grain boundary motion. A transition from triple junction kinetics to grain boundary kinetics was observed. There is experimental evidence that in TJ motion pre-exponential factor changes linearly with the activation enthalpy. This behaviour is referred to as compensation effect.

The Effect of Triple Junctions

Despite the triple junctions along with grain boundaries are the main structural elements of polycrystals, the influence of triple junctions on grain boundary migration was not treated at all experimentally and hardly investigated theoretically. It is usually assumed in all studies of grain boundary migration and grain growth that triple junctions do not drag boundary migration and that their role is reduced to preserving the equilibrium angles where boundaries meet. However, the movement of triple junctions, induced by boundary migration, might involve additional dissipation of energy, in other words, a triple junction might have a finite mobility. A theoretical consideration of triple junction motion was reported in [1]. It is stressed that the steady-state motion of such a system can only be measured for a very limited set of geometrical configurations. One of them is shown in Fig. 1.

This problem of joint grain boundary - triple junction motion was solved in a quasi-two-dimensional approximation, assuming a uniform grain boundary model (i.e. both the surface tension σ and the mobility m_b are the same for all grain boundaries and independent of boundary orientation), and some very important features of the kinetics of the motion of such systems were derived. In particular, it was shown that the steady-state motion of the system as a whole is indeed possible.

Fig.1 The shape of the grain boundary system with triple junction in the course of steady-state motion

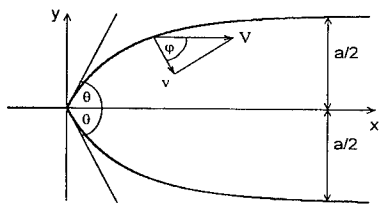

The behaviour of the system can be described by dimensionless criterion Λ that determines the drag influence of the triple junction on the migration of the grain boundary system

$$\Lambda = \frac{m_{tj} a}{m_b} = \frac{2\theta}{2\cos\theta - 1} \qquad (1),$$

where m_{tj} is the mobility of the triple junction, 2θ is the vertex angle and a the width of the consumed grain (Fig. 1).

For large values of Λ (Λ»I) the junction does not drag the migration, and the angle θ tends to attain the equilibrium value $\pi/3$. In this case the velocity V of the system movement as a whole is independent on the mobility of the triple junction and is determined by the boundary mobility and the driving force (corresponding to the width of the grain) [1]: $V = \frac{2\pi m_b \sigma}{3a}$. When Λ « I, the steady state velocity V is controlled by the mobility of the junction: $V=\sigma m_{tj}$. In this case the angle θ tends to zero.

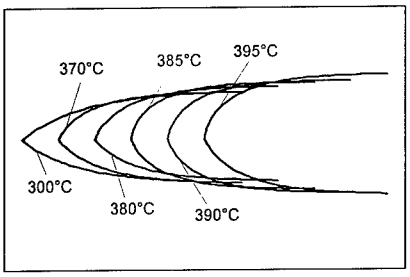

Fig. 2. The evolution of the form of the grain boundary system with increasing temperature.

The shape of the grain boundary system in the steady-state motion (Fig.2) was predicted for both uniform grain boundary model and the case when the system is symmetric relative to the x-axis, i.e. the grain boundaries I and 2 are the same, but different from boundary 3:

$\sigma_1 = \sigma_2 = \sigma \neq \sigma_3; m_{b1} = m_{b2} = m_b \neq m_{b3}$.

For the latter situation the velocity of triple junction can be expressed as

$$V = m_{tj}(2\cos\theta - \sigma_3) \qquad (2)$$

and the steady-state value of the angle θ is

$$\frac{2\theta\sigma}{2\sigma\cos\theta - \sigma_3} = \frac{m_{tj} a}{m_b} = \Lambda \qquad (3).$$

Table.1.Kinetic parameters of the system with individual triple junction.

N TJ	Grain Boundary Kinetics		Triple Junction Kinetics	
	H_{GB} [eV]	Log(A_{0GB} [m^2/s])	H_{TJ} [eV]	log(A_{0TJ} [m^2/s])
TJ 1,Fig.3	0,6 ± 0,2	-5,0 ± 1,5	1,8 ± 0,6	5,6 ± 4,4
TJ 2	2,3 ± 0,4	7,3 ± 3,4	4,0 ± 0,4	22,0 ± 6,5
TJ 3	5,0 ± 0,5	28,9 ± 3,9	10,1 ± 2,4	69,3 ± 18,7
TJ 4	5,1 ± 0,4	29,6 ± 2,7	5,1 ± 0,4	29,8 ± 2,9
TJ 5	2,4 ± 0,6	8,6 ± 4,3	3,2 ± 0,8	15,6 ± 6,4
TJ 6,Fig.4	11,5 ± 1,3	77,5 ± 9,6	14,4 ± 2,3	109,5 ± 17,6

The criterion parameter Λ defines the drag influence of the triple junction on the migration .The value of the criterion parameter Λ, which defines, by which kinetics - grain boundary or triple

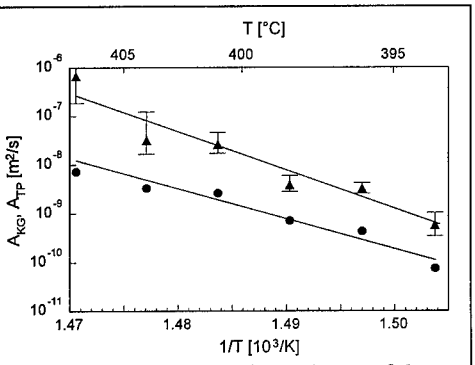

Fig.3. The temperature dependence of the mobility TJ6.

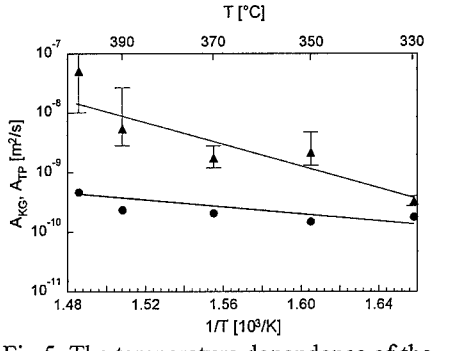

Fig.5. The temperature dependence of the mobility TJ1.

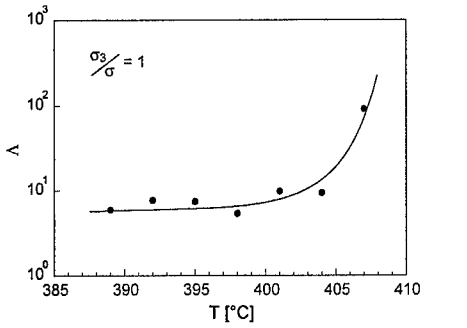

Fig. 4. Temperature dependence of the criterion Λ for a symmetrical triple junction TJ6:14° <01$\bar{1}$0>, 16° <01$\bar{1}$0>, 30° <01$\bar{1}$0>

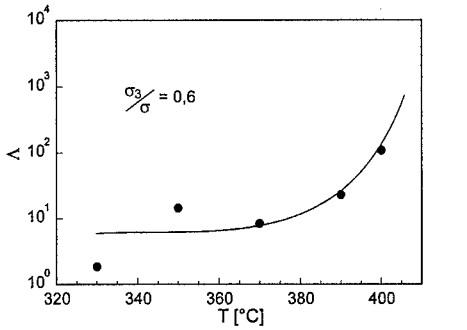

Fig. 6: Temperature dependence of the criterion Λ for a symmetrical triple junction TJ1:82° <01$\bar{1}$0>, 81° <01$\bar{1}$0>,3^0

junction - the motion of the system is controlled, can be estimated on the basis of the given approach. As can be seen at relatively "low" temperatures, the motion of the system is governed by the mobility of the triple junction, whereas at "high" temperatures the motion is controlled by the mobility of the high-angle grain boundary.(Fig.3-6). Also, the transition from triple junction to boundary kinetics was observed [2]. Similar results were obtained on grain boundary systems with another set of grain boundary [3].

For all triple junctions the velocities V and the angles θ were found to be constant for a given temperature over the entire investigated temperature range. Evidently, the assumption of a steady state motion of the entire grain boundary system was justified. θ increased with increasing temperature. In particular for the symmetrical triple junction the change of θ was drastic (Fig.2). In accordance with the temperature dependence of θ, the criterion Λ, determined by Eqs. (3) was found to be constant for a given temperature, but increased with increasing temperature (Fig. 2). At low temperatures θ was on the order of unity and increased with rising temperature up to 3 orders of magnitude (Fif.4,6). For the calculation of Λ for symmetrical triple junctions (TJ5,TJ6) the ratio σ_3/σ was determined under the assumption that for temperatures near the melting point the value of θ reaches the thermodynamic equilibrium value.

For the first time two different regimes of coupled triple junction grain boundary motion were observed, indicated by a change of the angle θ with temperature. At low temperatures, where Λ is on the order of unity (Fig. 4,6), the motion of the boundaries is dragged by the hardly mobile triple

junction. Accordingly, the angle θ is smaller than predicted by the equilibrium of grain boundary surface tensions, and the motion of the entire boundary system is controlled by the mobility of the triple junction. With increasing temperature the triple junction becomes more mobile compared to the grain boundary mobility as indicated by an increasing value of Λ (Fig. 4,6). Such temperature dependence of θ can not be explained in terms of a different temperature coefficient of the grain boundary surface tension. Firstly, the temperature coefficient of the surface tension is much higher for high angle grain boundaries than for low angle boundaries. Thus, the change of θ for TJ1 and TJ3 should be opposite to that observed in experiment, i.e. the angle θ would have to decrease with increasing temperature. Secondly, the order of change of θ is too large to be explained by thermodynamic reasons in terms of different temperature coefficients of the surface tension, in particular for TJ5 and TJ6, which comprise nearly identical boundaries [3]. Consequently, the temperature dependence of θ for all triple junctions must result from the change of the kinetics of motion, reflected by the temperature dependence of Λ (Fig. 4,6). The current investigation unambiguously proves the existence of a specific mobility of triple junctions, which usually differs from the mobility of the adjoining grain boundaries. As a consequence, the transition temperature between the two kinetic regimes, where m_b is comparable with the reduced mobility of triple junction, changes with grain size. For a large grain size a, as characteristic for grain growth experiments, the mobility of grain boundaries is comparable to the mobility of triple junctions at relatively low temperatures, while for a very small grain size, as typical for ultrafine grained materials, the situation is opposite and there is circumstatial evidence that the surprising thermal stability of nanocrystalline systems is due to insufficient junction mobility.

Acknowledgements.

The authors express their gratitude to the Russian Foundation for Fundamental Research and the Deutsche Forschungsgemeinschaft N438 113/130/0 for financial support.

References.

[1] A.V. Galina, V.E. Fradkov and L.S. Shvindlerman, Phys. met. metall., 63, (1987), p.165.
[2] L.S. Shvindlerman, et.al., in "Recrystallization and Related Phenomena", ed. By Terry R-McNelly, Monterey, Institute of Advanced Studies,(1997),p.255.
[3] U. Czubayko, et.al., Acta mater., to be published.

Corresponding author: Dr.V.Sursaeva, e-mail sursaeva@issp.ac.ru, Fax 096 576 41 11

Materials Science Forum Vols. 294-296 (1999) pp. 521-524

The Role of the Triple Junctions During Grain Growth

V.G. Sursaeva, S.G. Protasova and A.Yu. Tuflin

Institute of Solid State Physics, Russian Academy of Sciences, Chernogolovka, RU-142432, Moscow, Russia

Keywords: Grain Boundary, Triple Junction, Grain Boundary Migration, Triple Junction Migration, Compensation Effect, Compensation Temperature T_c, Aluminium, Zinc

Abstract

Experimental data on triple junction (TJ) motion in Al and Zn are presented. There is experimental evidence that during TJ motion the pre-exponential factor changes linearly with activation enthalpy. The TJs impact on the kinetics of microstructure evolution during grain growth is outlined.

Introduction.

Grain growth studies in polycrystals provide only an average grain boundary (GB) mobility, i.e. a mobility averaged over a large number of GBs. If all GBs and TJs were alike, this would be correct. As will be shown below, this is far from reality. GBs and TJs movement is strongly affected by crystallography and temperature interval of motion. Such dependencies cannot be obtained from experiments on polycrystals, but only from systems with individual GBs and TJs.

Theories on grain growth and microstructure evolution assume the existence of free GBs whose motions don't interact with each other. This implies that TJs that are a main part of a grain boundary network, do not affect the kinetics of microstructure evolution.

Experimental.

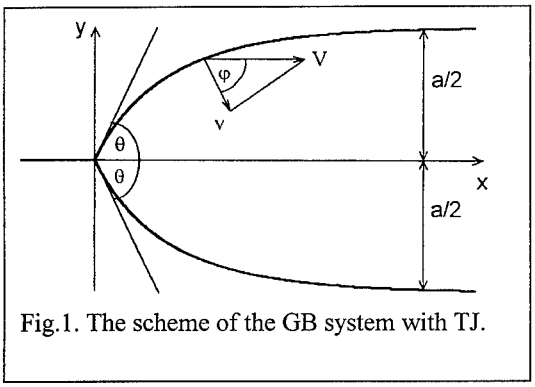

Fig.1. The scheme of the GB system with TJ.

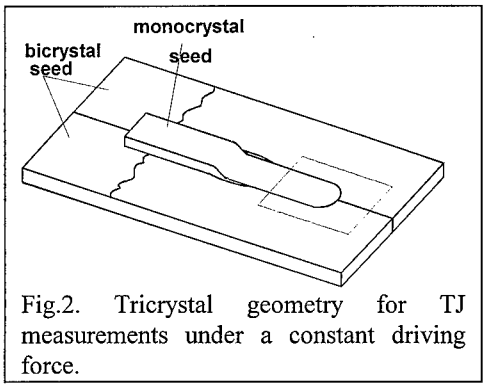

Fig.2. Tricrystal geometry for TJ measurements under a constant driving force.

Investigations conducted under reproducible experimental conditions. The major requirements for a proper experiment on system with individual TJ are a controlled driving force, a continuous monitoring of TJ displacement and a good reproducibility of TJ crystallography.

We used a continuous method to determine the successive boundary positions with time. It has the advantage to provide a real time TJ monitoring without forcing the grain boundary to stop. For Zn samples, the contrast difference under polarized light due the discontinuity in crystal orientation at the TJ was used [1]. Al samples required a special dark field set up including a large aperture inclined beam connected to an optical microscope. During experiment boundary displacement and angles at triple junction are recorded. Zn experiments were carried out in the temperature range (0.87÷1) T_m K, Al experiments were carried out in the temperature range

(0.7÷0.8) T_m K. Tricrystals Zn (99,999 at %) and Al (99,999 at %) were grown by a directional crystallization technique [1,7]. TJ motion under a constant driving force **p** was investigated in aluminium and zinc tricrystals. The driving force was provided by the surface tension of a curved GB. **p** per unit volume is given by $\mathbf{p}=\sigma/\mathbf{2a}$, where σ is the GB surface tension, and **a** - the width of the grain to be consumed. (Fig.1). (Fig.2) Pure <111> tilt TJs with different tip misorientation were studied in Al.. Crystal seeds and fabricated tricrystals orientations were measured using Selected Area Channeling Pattern technique based Scanning Electron Microscopy. Owing to the constant driving force, the TJ was expected to displace at a constant rate, and this was actually observed. Velocity was determined from displacement and time measurement. During isothermal experiments temperature remained constant within 0.3°C. To avoid thermal grooving and oxidation, the sample was set under argon atmosphere during measurement.

Results and discussion.

The main structural elements of polycrystals-grain boundaries and triple junctions. Grain boundaries motion has been widely studied, whereas no experimental literature on triple junctions migration is available so far. A theoretical consideration of triple junction motion was reported in [2]. The steady-state motion of a system with an individual triple junction can be precisely measured for a given configuration as shown in Fig.1.System behavior is discussed in terms of the parameter Λ, which describes the drag influence of the triple junction on the grain boundary system migration:

$$\Lambda = \frac{m_{TJ} a}{m_{GB}} = \frac{2\theta}{2\cos\theta - 1} \qquad (1),$$

where m_{TJ} and m_{GB} are respectively triple junction and grain boundary mobility; 2θ the vertex angle and a the width of the consumed grain. (Fig 1). For $\Lambda >> 1$ the triple junction does not drag the migration, and the angle θ tends to $\pi/3$. In this case the velocity V of the system (with an individual triple junction) motion is independent of the triple junction mobility. V is determined by the driving force and the grain boundary mobility [2].

$$V = \frac{2\pi m_{GB} \sigma}{3a} \qquad (2).$$

When $\Lambda << 1$, the steady state velocity V is controlled by the triple junction mobility, θ tends to zero.

$$V = \sigma m_{TJ} \qquad (3).$$

The value of the criterion parameter Λ, which defines by which kinetics - grain boundary or triple junction - the motion of the system is controlled, was derived using Eqs.(1). The current observations in Zn demonstrate that triple junction does not always act as pinning center. In some cases, the transition from triple junction to grain boundary kinetics occurs (Table 1). System motion is then controlled by grain boundaries mobility only.

Compensation effect.

So-called compensation effect was repeatedly observed in various thermally activated processes but most distinctly in processes related to interfaces and grain boundaries

$$H = \alpha \ln A_0 + \beta \qquad (4),$$

where α and β are constants, H the activation enthalpy, A_0 the pre-exponential factor.

The consequence of linear dependence between the activation enthalpy and the logarithm of the pre-exponential factor in the mobility equation $A = A_0 \exp(-H/kT)$ is the existence of the so-called compensation temperature

$$T_c = \alpha/k \qquad (5).$$

In concept of [3] the compensation temperature is the equilibrium temperature for a virtual phase transformation. Above a compensation temperature the process with the highest activation enthalpy has the highest rate, while for $T<T_c$ the process with the lowest value of H proceeds fastest.

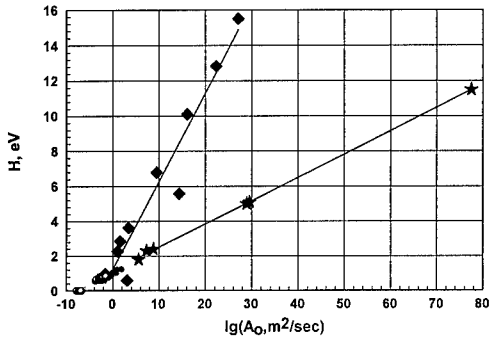

Fig 3.The dependence of migration activation enthalpy on the preexponential mobility factor for the investigated GBs[1,4] and TJs (Table 1). ●-GB[1,4], o-GB[1,4],★- TJ1-TJ6 (Table 1). ◆- TJ7-TJ16 (Table 1).

The compensation lines lgA_0 for the mobility <11$\bar{2}$0> individual tilt grain boundaries in Zn, <01$\bar{1}$0> individual tilt boundaries in Zn [4] and mobility for individual triple junctions in Zn [5] are given on Fig. 3.

The corresponding temperature of compensation for tilt grain boundaries [4] and triple junctions TJ1 - TJ6 (Table 1) is 350°C. The corresponding temperature of compensation for triple junctions TJ7-TJ16 (Table 1) above melting point T_m. Compensation effect controls the kinetics of the processes. We suppose that the compensation temperature divides the temperature range into two regimes. Below T_c triple junction drag the system motion, vice verse, above T_c triple junction do not drag and grain boundary kinetics defines the processes.

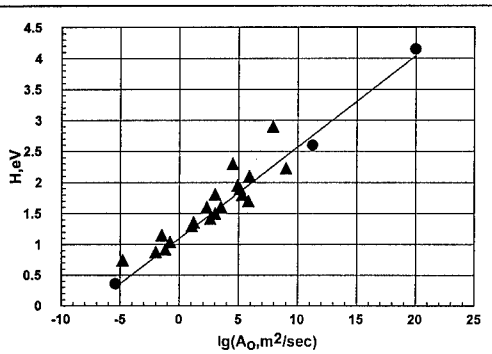

Fig.4. The dependence of migration activation enthalpy on the pre-exponential mobility factor for the investigated▲-<111> tilt GBs [7,8] and ●- <111> tilt TJs.

For triple junctions TJ1 - TJ6 (Table 1) there are two regimes, above 350°C grain boundaries determine the system motion, below T_c=350°C triple junction determine the system motion. For triple junction TJ7-TJ16 (Table 1) $T_c >> T_m$,, there is one kinetics regime: triple junctions drag system motion. There is not transition from one regime to another.

The dependence of migration activation enthalpy a pre-exponential mobility factor for the investigated <111> tilt GBs [7,8] and currently investigated <111> TJs (Table 1) is shown in Fig.4. There is the linear dependence for GBs and TJs. T_c(for GB) = 450°C. T_c(for TJ) = 380°C. We suppose that at high temperatures (T > 380°C) i.e. above the compensation temperature T_c., TJs exhibit highest mobility, then GBs and do not drag GBs motion, so TJs show highest activation enthalpy, while at low temperatures (T<380°C), GBs with the lowest activation enthalpy can exhibit the highest mobility, but TJs drag the GBs.

At last, the compensation effect opens up possibilities to look at the grain growth from two point view (quite different perspective): grain boundary and triple junction.

Table.1.Kinetic parameters of the system with individual triple junction.

Probe	$T/T_{MELTING}$	Grain Boundary		Triple Junction		Ref.	Λ
		H_{GB} [eV]	$LogA_{0_{GB}}$	H_{TJ} [eV]	$LogA_{0TJ}$		
TJ1	0,87	0,6	-5,0	1,8	5,6	[6]	1-100
TJ2	0,91	2,3	7,3	4,0	22,0	[6]	
TJ3	0,93	5,0	28,9	10,1	69,3	[6]	1-1000
TJ4	0,94	5,1	29,6	5,1	29,8	[6]	
TJ5	0,90	2,4	8,6	3,2	15,6	[6]	1-100
TJ6	0,96	11,5	77,5	14,4	109,5	[6]	1-100
TJ7	0,93	5,6	14,3			Current	~1
TJ8	0,94	15,5	27,1			Current	~1
TJ9	0.94	12.8	22.3			Current	~1
TJ10	0.92	2.9	1.6			Current	~1
TJ11	0.94	101.0	16.1			Current	~1
TJ12	0.88	1.0	-1.6			Current	~1
TJ13	0.88	2.3	1.0			Current	~1
TJ14	0.93	3.6	3.4			Current	~1
TJ15	0.87	0.6	3.1			Current	~1
TJ16	0.96	6.8	9.5			Current	~1

Conclusions.

1. A linear relation between the activation enthalpy and the logarithm of pre-exponential factor was observed for all system with the individual triple junctions in Al and Zn. This is referred to as compensation effect.
2. Compensation effect controls the kinetics of grain growth in polycrystals.

Acknowledgements.

The authors express their gratitude to Prof. L.S.Shvindlerman for fruitful discussion and to the Russian Foundation for Fundamental researches for financial support.

References.

[1] A.V.Antonov,Ch.V.Kopetskii,L.S.Shvindlerman,V.G.Sursaeva,Sov.Phys.Dokl.,18,(1974),p.736.
[2] A.V.Galina, V.E. Fradkov, L.S.Shvindlerman, Phys. Met. Metall.,63,(1987),p.165.
[3] G.Gottstein, L.S.Shvindlerman,Interface Science, in press.
[4] Ch.V.Kopetskii, V.G.Sursaeva,L.S.Shvindlerman,Sov.Phys.Solid.State 21,(1979).p.238.
[5] L.S.Shvindlerman, G.Gottstein, U.Czubayko,V.G.Sursaeva
in: Proc. of Intern.Conf.on Recrystallization and Related Topics, Monterey, Cal.,USA. (1997),p.255.
[6] V.G.Sursaeva, U.Czubayko, G.Gottstein, L.S.Shvindlerman, in this issue.
[7] E.M.Fridman, Ch.V.Kopezki, L.S.Shvindlerman, Z.Metallkde, **66**, (1975),p.533.
[8] V.Yu.Aristov,V.L.Mirochnik, L.S.Shvindlerman,Sov.Phys.Solid State **18**, (1976),p.137.

Corresponding author: Dr.V.Sursaeva,e-mail sursaeva@issp.ac.ru, Fax 096 576 41 11

Materials Science Forum Vols. 294-296 (1999) pp. 525-528

The Propagation of Crystalline-Amorphous Interface: Experiment and Model

Y. Lereah[1], S. Buldyrev[2] and H.E. Stanley[2]

[1] Faculty of Engineering, Tel Aviv University, IL-69978 Tel Aviv, Israel

[2] Center for Polymer Studies, Physics Department Boston University, Boston MA 02215, USA

Keywords: In situ Electron Microscopy, Crystallization, Amorphous Alloys, Pattern Formation, Diffusion Limited Aggregation, Eden Model

Abstract The dynamic of propagating interface was studied by time resolved electron microscopy. The system is binary amorphous Ge-Al alloy which was heated and crystallized in Transmission Electron Microscope. The crystallization of this alloy reveals a unique structure compsed of Al crystals in which Ge precipitate in branched morpholgy. The crystallization process was computer simulated by combining Eden model for the Al growth and Diffusion Limited Aggregation (DLA) model for the Ge growth. A comparison of experimental and model results are presented for both: the general pattern and the interface propagation.

In the field of pattern formation, two principal models are used to create aggregates: the Eden model, in which no diffusion plays no role, and the Diffusion Limited Aggregation (DLA) model, in which is the determining feature [1]. The Eden aggregate is characterized as a compact cluster with rough surface; the DLA aggregate exhibits its characteristic branching. Both models have recently undergone intensive study, in some modification of the principal rules governing their generation.

In the last 15 years we have studied various aspects related to the crystallization of amorphous Ge:Al thin films. The details of the preparation of the films were described elsewhere [2]. Briefly: thin films, 200A thick, of Al-Ge alloys containing about 50% of each element, were prepared by simultaneous evaporation of Al and Ge from two electron guns. The substrate is a microscope slide covered by soluble material that enable the separation of the film from the substrate. The films were examined in a Transmission Electron Microscope (TEM), Philips EM300, and the amorphous ones were selected for crystallization studies. These films were heated to a temperature above 250°C in the TEM during observation, using a commercial heating holder. At this temperature crystallization occurs. The crystalline phase consists of colonies each of them composed of a large Al crystal that contained subgrain boundaries. In these Al crystals Ge precipitates to create a core with multi-twinned structure and branched morphology. The velocity of the crystalline front is as slow as few A per second. Such slow velocities enable video recording (by large angle camera: Gatan model 673) at variety of magnifications. This procedure enables to study the dynamic of the crystallization process. Moreover, the process can be stopped at any time, simply by stop heating the film. Such a procedure is extremely useful for studding the interface by various methods of microscopy and analysis such as Conventional Transmission Electron Microscopy (CTEM), Electron Diffraction,

analysis. From these experimental studies [2,3,4,6] combined with theory [5,6] and computer simulation [6] we concluded that two processes are involved in the crystallization of the alloy: 1.Diffusionless growth of Al in the amorphous phase, and 2.Diffusion control growth of the Ge core inside the Al crystal.Both interfaces are coupled with a fixed (averaged, in time and space) distance between them for each crystallization temperature. The crystallization rate is limited by diffusion of Ge atoms through this Al rim. Accordingly, the observed velocity of the process can be in the range of few atoms per second. These experimental findings were computer simulated by considering: 1.Random mixture of Al and Ge as the amorphous phase. 2.Eden model for the Al crystal growth. 3.DLA model for the Ge growth. 4.Limited solubility of Ge in the Al crystals. A comparison between the experimental and the model patterns is seen in Fig. 1. The propagation of the interface between the crystalline Al and the amorphous phase was investigated by further experimental and model studies. It was found that the propagation of the crystalline interface is dominated by three rates: 1.Transferring Al atoms from the amorphous phase to the crystalline phase (T_{al}). 2.Diffusing of Ge through the Al as solid solution (D). 3.Transferring the Ge atoms from the Al solid solution to the crystalline Ge. (T_{ge}). While the ratio T_{Ge}/D determine the average thickness of the Al rim, the ratio T_{Al}/D determines the fluctuations in the Al rim thickness. Fig. 2 demonstrates a sample in which the ratio T_{Al}/D is extremely high. Fig. 3 demonstrates the equivalent model results.

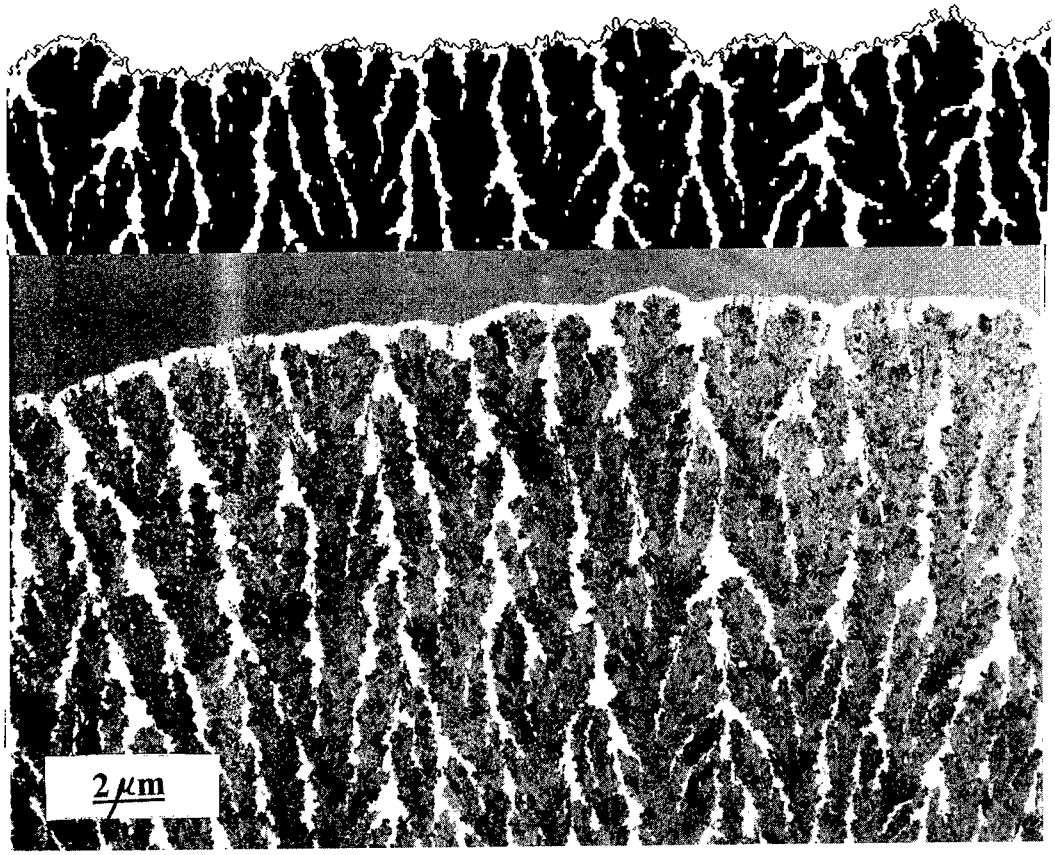

Figure 1. A general view of the crystallized area: branched Ge inside compact Al embedded in amorphous phase. The upper part is the computer simulation of model.

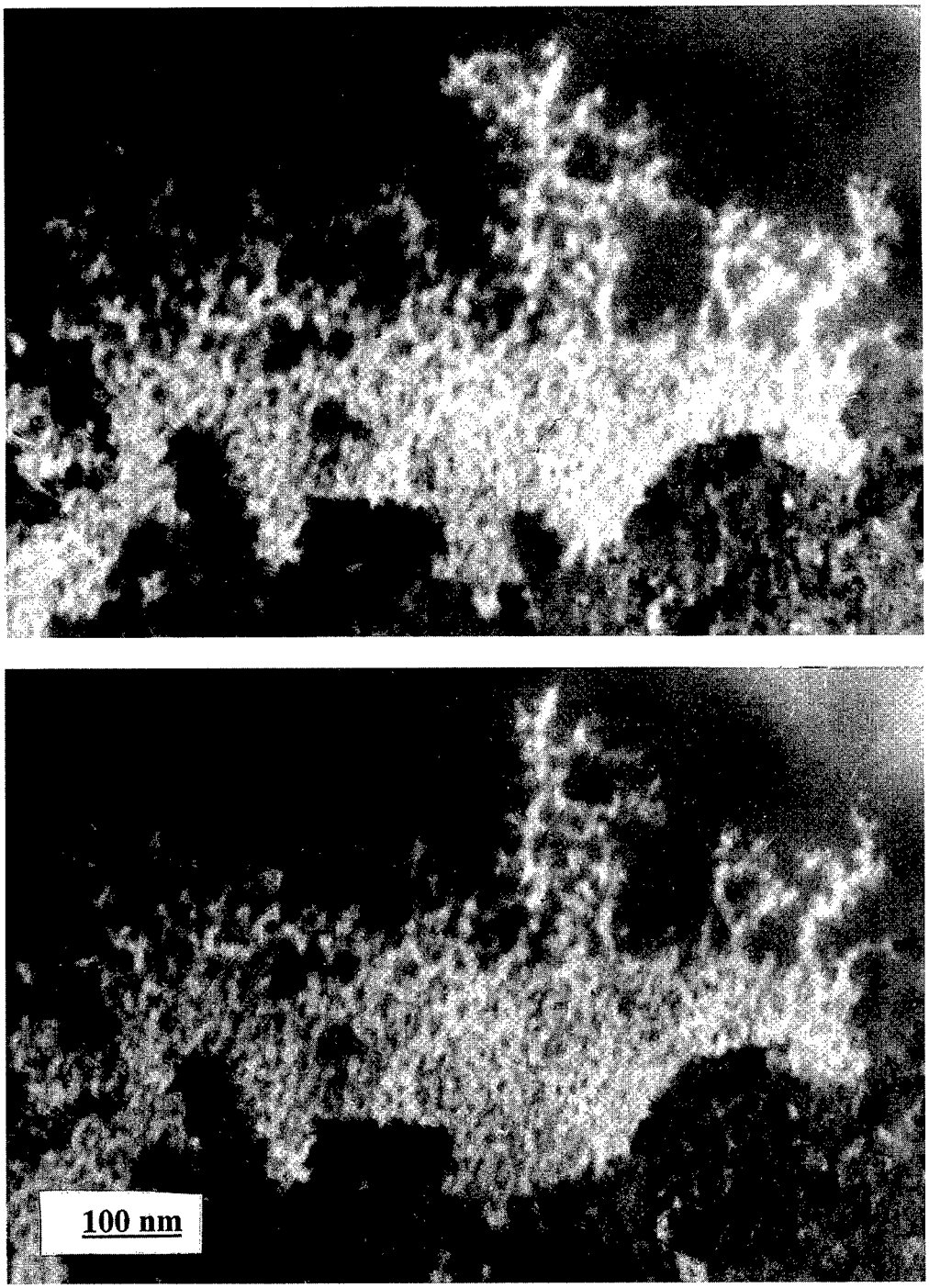

Figure 2. Time sequence of the 'Crystalline Al - Amorphous phase' interface. A transition between a zone in which T_{Al} dominats to a zone in which D dominats is clearly seen.

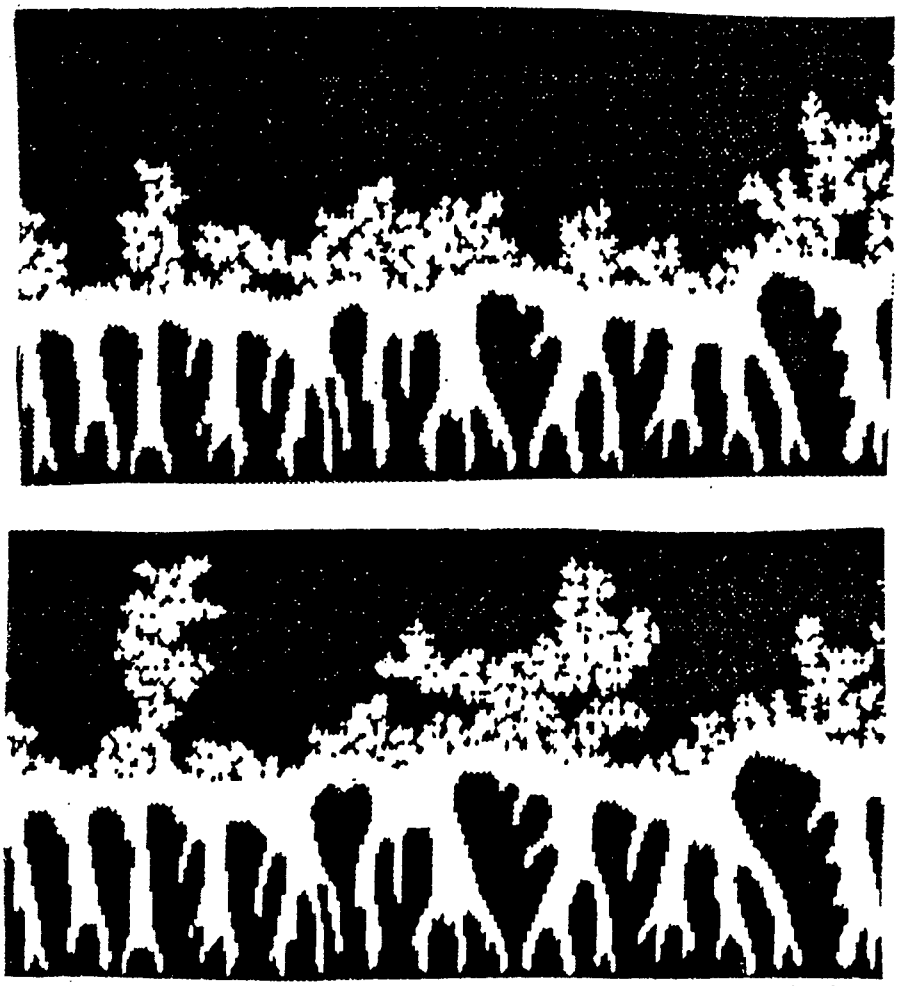

Figure 3. The results of the model, compare with the experimental results in Figure 2.

Acknowledgment: It is a pleasure to acknowledge Guy Deutscher for stimulating discussions during the early stages of this work. This work is supported by the U.S. - Israel Binational Scientific Foundation grant no. 94-00333

References

[1] see for example "On Growth and Forms" Edited by H.E.Stanley and N.Ostrowsky Martinus Nijhoff publishers (1986)
[2] Y. Lereah, E. Grunbaum and G. Deutscher Physical Review A 44 8316 (1991)
[3] Y. Lereah, J.M. Penisson and A. Bourret Applied Physics Letters 60 1682 (1992)
[4] Y. Lereah, I. Zarudi, A. Bourret and J.M. Penisson J. of Electron Microscopy 44 79 (1995)
[5] S. Alexander, R. Bruinsma, R. Hilfer, G. Deutscher and Y. Lereah, Physical Review Letters 60 1514 (1988)
[6] Y. Lereah, I. Zarudi, E. Grunbaum, G. Deutscher, S. Bulderyv and H.E. Stanley, Physical Review E 48 649 (1994)

Materials Science Forum Vols. 294-296 (1999) pp. 529-532

The Effect of Annealing Texture on Orientation Correlations in Copper

O.V. Mishin[1,2]

[1] Materials Research Department, Risø National Laboratory, DK-4000 Roskilde, Denmark

[2] On leave from the Institute for Metals Superplasticity, Ufa, Russia

Keywords: Texture, Grain Boundary Misorientation Distribution, Orientation Correlation, Copper

Abstract

The effects of annealing texture on the grain boundary misorientation distribution and orientation correlations are studied. The dominance of the $\Sigma 3^n$ ($n \geq 1$) boundaries in the condition with a weak texture is related to the orientation correlation "matrix/twin". The influence of the orientation correlation is significantly reduced in the presence of an extremely strong texture. In this case, the misorientation distribution is determined by the relationships between orientations belonging to dominant and minor texture components.

Introduction

The misorientation distributions of annealed f.c.c. materials with low and medium stacking fault energy are frequently orientation correlated. The correlation "matrix/twin" produces significant fractions of $\Sigma 3^n$ ($n \geq 1$) misorientations. The percentage of such boundaries can vary from ~25% to 70% after static recrystallization and grain growth [e.g.1]. The fractions of $\Sigma 3^n$ ($n \geq 1$) boundaries between adjacent grains exceed the corresponding fractions in the distributions of all possible [2,3] or randomly selected [4] misorientations. The influence of the orientation correlation is believed to be controlled by the crystallographic texture. Previous works on copper have shown that the proportion of twin boundaries can be manipulated through the texture strengthening during recrystallization and grain growth [5-7]. The influence of texture on the orientation correlation in annealed copper is demonstrated in this work.

Experimental

A nearly random texture and a strong cube texture (in states A and B, respectively) were generated through different thermomechanical treatments in high purity copper (for details see [6,7]). Local orientations were measured using the electron back-scatter diffraction (EBSD) technique in a SEM. In the present work, 304 orientations were determined in three different regions in sample A. This provided better statistics than that presented earlier [6]. In sample B, 234 orientations were collected in four regions. In all, 708 and 509 misorientations between adjacent grains were analyzed in samples A and B, respectively.

To investigate the effect of possible orientation correlations, the distributions of GBs between adjacent grains were compared with those of all mutual misorientations. The misorientations were calculated between all crystallites regardless of whether or not the crystallites were neighbours in the microstructure. Each of N orientations was compared with all other orientations in the inspected

region, which gave N(N-1)/2 mutual misorientations. The uncorrelated distributions of mutual misorientations were drawn from the cumulative numbers of all mutual misorientations collected from all regions studied in each sample. The CSL boundaries were categorized using the Brandon criterion $\Delta\theta_c = 15°\Sigma^{-1/2}$ [8].

Results

The orientations of measured grains are shown in Fig.1. No strong texture can be distinguished in sample A (Fig.1a). A cube texture dominates in sample B (Fig.1b) Almost 65% of grains had orientations within 15° from the ideal cube {001}<100> orientation. Also, a minor twin-to-cube component {212}<122> was present in this sample.

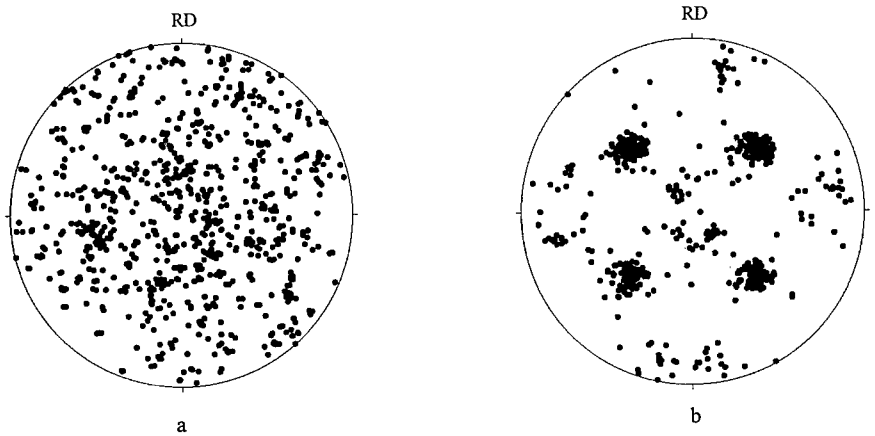

Fig. 1. Microtextures: state A (a) and state B (b).

The distribution of misorientations is given in terms of distributions by misorientation angles (Fig.2) and misorientation axes (Fig.3) within the standard stereographic triangle (SST) divided into the zones according to Mackenzie [9].

In the strongly textured sample B, there was a significantly higher frequency of low-angle boundaries compared to "textureless" sample A. In sample A, the total fraction of the $\Sigma 3^n$ ($n \geq 1$) boundaries significantly exceeds the corresponding fraction revealed in state B (Fig.4). Also, in sample B, many $\Sigma 3$ boundaries had larger deviations from the exact twin relationship than in state A, where such boundaries occurred only between matrix grains and their twins (details are given in [11]). The distribution of all mutual misorientations in state A (Fig.2c) is similar to the random Mackenzie distribution [10]. In state B, the distribution of mutual misorientations is similar to the distribution of misorientations between next neighbours (compare Fig.2b and Fig.2d) .

Discussion

The influence of annealing texture on the GB character distribution and triple junction distribution in these conditions has been previously discussed [6]. Multiple twinning is active in state A, therefore many twin and twin related $\Sigma 3^n$ ($n \geq 1$) boundaries are formed. In state B, progressing grain growth causes strengthening of the cube texture and the impingement of cube oriented grains [7]. Other grains, including island twins, tend to shrink and disappear. Consequently, the fraction of low-angle boundaries increases at the expense of high-angle boundaries.

The occurrences of low-angle boundaries between nearest neighbours are determined primarily by the volume fractions of grains with nearly identical orientations. The fractions of these

boundaries in the distributions of misorientations of nearest neighbours and all mutual misorientations are similar in both states (see Fig.1). However, in strongly textured copper, low-angle boundaries between the nearest neighbours tend to have smaller misorientation angles than those in the distributions of all mutual misorientations (Fig.2b,d).

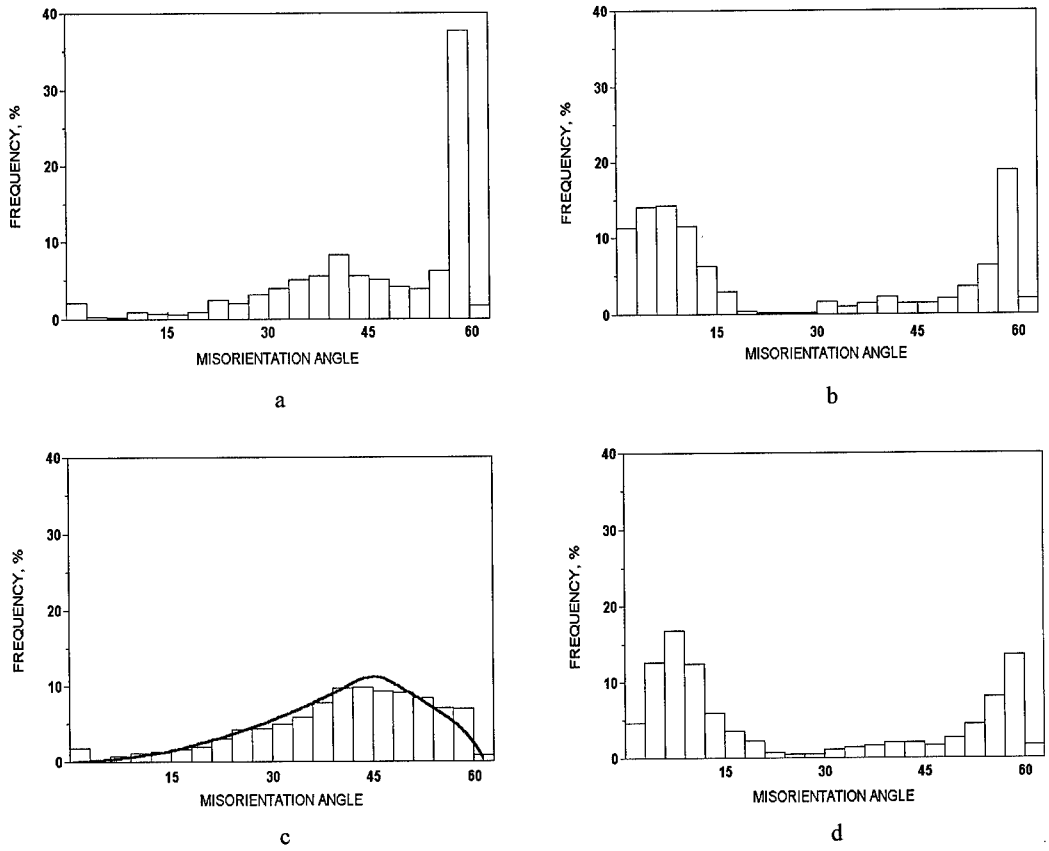

Fig.2. Distributions by the misorientation angles in sample A (a,c) and sample B (b,d); misorientations between nearest neighbours (a,b) and all mutual misorientations (c,d). Solid line (c) corresponds to the misorientation distribution in the random aggregate [10].

The distribution of all mutual misorientations in sample A is close to the Mackenzie distribution calculated for a random polycrystalline aggregate. This reflects a nearly random texture in this sample, i.e. all available orientations appear in approximately equal proportions. In the microstructure with the "matrix/twin" correlation, crystallites with these orientations are connected not randomly, but in such a way that they form Σ3 boundaries between neighbours.

The frequencies of Σ3 (41.5%), Σ9 (5.2%) and Σ27 (2.0%) boundaries formed between adjacent grains exceed (Σ3, in particular greatly) the corresponding random fractions. Even in the strongly textured material, where only the cube and its twin components were distinguished, Σ3 boundaries between nearest neighbours appear more frequently than would be expected excluding any orientation correlation. The prevalence of twin boundaries between adjacent grains over their frequencies in the distribution of all mutual misorientations is, nevertheless, essentially reduced in the presence of an extremely strong texture. The fraction of Σ9 boundaries in the distribution of

neighbours is not much different from the distribution of all mutual misorientations. The Σ27 boundaries constitute low fractions in both these distributions.

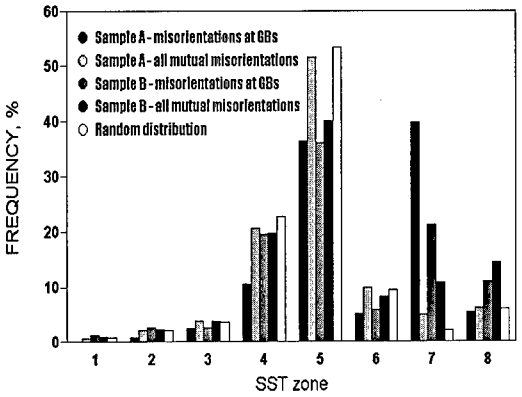

Fig. 3. Distribution of misorientation axes within the SST subdivided into zones according to [9].

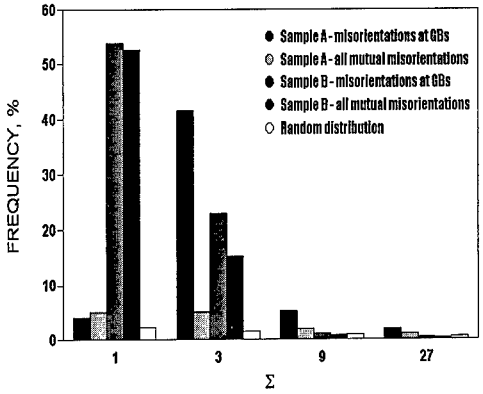

Fig. 4. Distribution of grain boundaries by Σ value (Σ ≤ 27).

In sample B, the misorientation distribution of nearest neighbours resembles the uncorrelated distribution of all mutual misorientations. Since in a strongly textured material orientations of available grains occupy a very limited orientation space, there is little opportunity to realize possible orientation correlations.

Conclusion

The misorientation distribution of nearest neighbours in f.c.c. materials prone to annealing twinning is influenced by the "matrix/twin" orientation correlation. Such a correlation was prominent in a weakly textured material of this class even though all mutual misorientations demonstrated no predominance of $\Sigma 3^n$ boundaries. The influence of the orientation correlation in these materials may be significantly reduced in the presence of an extremely strong texture. The uncorrelated distribution of all mutual misorientations in this case resembles the distribution of nearest neighbours. Both of these distributions are determined primarily by the crystallographic texture (dominant cube and its twin component).

References

[1] V. Y.Gertsman, J. A. Szpunar, *Scripta Mater.* **38**, 1399 (1998).
[2] V. Y. Gertsman and K. Tangri, *Scripta Metall. Mater.*, **33**, 1037 (1995).
[3] F. Heidelbach, H.-R. Wenk, S. R. Chen, J. Pospiech and S. I. Wright, *Mater. Sci. Eng.* **A215**, 39 (1996).
[4] V. Randle, *Phil. Mag.* A, **67**, 1301 (1993).
[5] P. Fortier, W. A: Miller and K. T. Aust, *Acta mater.* **45**, 3459 (1997).
[6] O. V. Mishin, *Scripta Mater.* **38**, 423 (1998).
[7] O. V. Mishin and G.Gottstein, *Mater. Sci. Eng.* A **249**, 71 (1998).
[8] D. C. Brandon, *Acta Metall.*, **14**, 1479 (1966).
[9] J. K. Mackenzie, *Acta Metall.* **12**, 223 (1964).
[10] J. K. Mackenzie, *Biometrika*, **45**, 229 (1958).
[11] O. V. Mishin, J. Mater. Sci. (in press).

Materials Science Forum Vols. 294-296 (1999) pp. 533-536

Normal and Abnormal Grain Growth in Tungsten Polycrystals

B.B. Straumal[1,2], W. Gust[1], V.G. Sursaeva[2], V.N. Semenov[1,2] and L.S. Shvindlerman[1]

[1] Institut für Metallkunde, Seestr. 75, D-70174 Stuttgart, Germany

[2] Institute of Solid State Physics, Russian Academy of Sciences, Chernogolovka,RU-142432 Russia

Keywords: Normal Grain Growth, Abnormal Grain Growth, Tungsten

ABSTRACT

The grain growth has been studied in high-purity flat W polycrystals at 2000°C in vacuum. The onset of abnormal grain growth proceeds without inhibition of the normal grain growth. After appearing of the large abnormal grains the areas with small "normal" grains exist very long. The polycrystal has a bimodal grain structure, both normal and abnormal grains continue to grow. The orientations of individual grains were determined with aid of the electron backscattering diffraction method in the contact area between the abnormally growing large grains and normal matrix. In samples of a larger thickness the abnormal grain growth do not appear in the time period studied. The influence of the formation of new grain boundaries with a high mobility on the onset of abnormal grain growth and similarities with the abnormal grain growth in Al alloys are discussed.

INTRODUCTION

The formation of very large grains or a large scatter of the grain size in a material due to the onset of the abnormal grain growth can deteriorate drastically the properties of the material. The studies of individual grain boundaries (GBs) in bicrystals show that the GB mobility m can differ by many orders of magnitude, depending the GB misorientation and the impurity concentration [1]. Theoretical calculations and computer simulation of grain growth in polycrystals predict that if the mobility ratio between "slow" and "fast" GBs reaches a certain amplitude (about 5) the transition from normal to abnormal grain growth can occur [2, 3]. Recently the transition from normal to abnormal grain growth in pure Al and Al–Ga alloys in dependence on Ga content, integral concentration of impurities, temperature and sample thickness was studied [4–6]. It was shown that a decreasing thickness of the sample diminish drastically the onset time of the abnormal grain growth. Below a certain temperature the abnormal grain growth do not appear [6]. This barrier temperature decreases with increasing purity of Al [6]. It is important to prove whether these regularities established for Al, having a low-melting temperature and face-centred cubic lattice, are general enough. Therefore, the goal of this work was to investigate the grain growth in a metal with a high melting point and a body-centred cubic lattice. As an object for this investigation W polycrystals were chosen. In this material the drastic influence of the GB misorientation on the GB wetting behaviour was recently demonstrated [7].

EXPERIMENTAL

Tablets of pure W compact (diameter 10 mm, height 5 mm) produced by Metallwerk Plansee GmbH were used. They were cutted with the aid of spark erosion in order to produce the specimens of different thickness h (0.8 mm and 2 mm). The samples were than annealed at 2000°C in vacuum

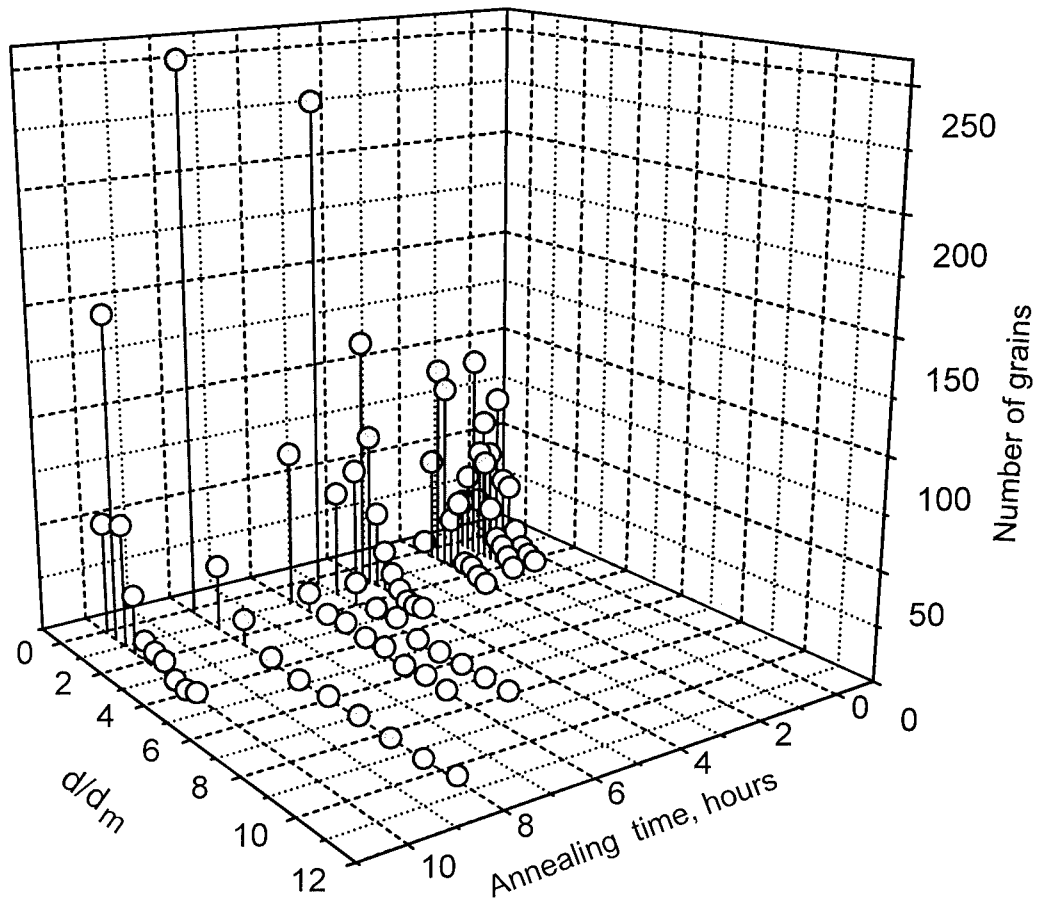

Fig. 1. Size distributions for various annealing times at $T = 2000°C$ for $h = 0.8$ mm, d is the grain size and d_m is the mean grain size.

of 10^{-8} Pa during various times from 0.5 to 10 h. For each anneal a separate sample was used. Already after 0.5 h the W polycrystals revealed the fully recrystallized structure without deformed matrix. After annealings the microstructure of the W polycrystals was investigated with the aid of scanning electron microscopy, optical microscopy and the electron back scattering diffraction technique. The microstructure was photographed and the mean grain size d was determined on 400–500 grains with aid of an intersection method using the optical microscopy.

RESULTS AND DISCUSSION

Figure 1 displays the distributions of the grain size d for various annealing times t at $T = 2000°C$ for $h = 0.8$ mm. For each t the grain size is normalized to the mean grain size d_m. Figure 2 shows the time dependence of d_m in W polycrystals having different thickness h. At low t the normal grain growth proceeds. After $t = 5$ h very large grains appear in the polycrystal. The size distribution becomes bimodal. The transition from normal to abnormal grain growth happens. The onset of abnormal grain growth proceeds without inhibition of the normal grain growth. After appearing of the large abnormal grains the areas with small "normal" grains exist very long. The increase of

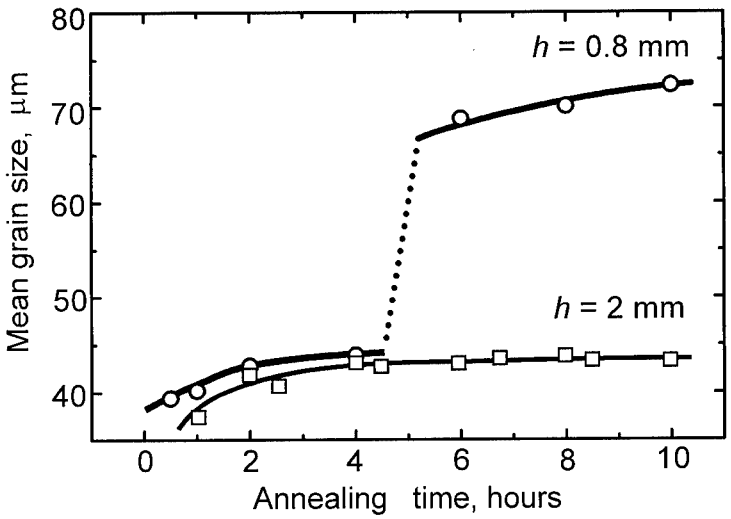

Fig. 2
Time dependence of the mean grain size in W polycrystals having different thickness *h*.

the mean grain size is accompanied by an increase of the grain size variation. It is also the sign of the abnormal grain growth. In the thicker sample the normal grain growth remains not interrupted, at least in the time interval studied. The transition to the abnormal grain growth do not proceed.

Figure 3 shows the inverse pole figure for a W polycrystal annealed at 2000°C for 10 h having a thickness h = 0.8 mm. The sample has an orientation texture. The axes <110> and <112> of about 50% of grains are nearly parallel to the normal direction (ND) to the sample surface. The analysis of microstructure demonstrates that the grains of <110> ND and <112> ND orientation are not randomly distributed but are clustered. Each cluster contains 5 or 6 grains separated by high-angle GBs.

Secondary recrystallization plays a very important role in defining the microstructure and texture of many technologically important materials [8]. In these materials the secondary recrystallization begins after the suppressing of the normal grain growth by pores or fine particles of a second phase. Such an inhibition of the normal grain growth was assumed to be a necessary condition for the secondary recrystallization [9]. In our experiments, normal grain growth is inhibited only at 350°C (see Figs 1 and 3). If abnormal growth proceeds, d is propotional to the square root of the annealing time until the onset of the abnormal growth (see Fig. 3). Therefore, in our case the inhibition of normal growth is not necessary for the beginning of abnormal growth. The present theory [2] predicts different conditions for the onset of abnormal growth in 3-dimensional and the 2-dimensional polycrystals. Computer modelling of the grain growth revealed that the transition from the normal to the abnormal grain growth can start if the scatter of GB mobilities in the polycrystal is high enough, and the mobility of certain GBs is somewhat higher than the mean GB mobility [2, 3]. It was also shown that this barrier difference of GB mobilities is less in case of the 2-dimensional grain growth (all grains intersect both surfaces of the platelete) than in case of the 3-dimensional growth (only a part of grains contacts the free surface) [2, 3]. Recently it was observed in Al – 1 wt. % Ga alloy that the onset time of abnormal grain growth increases with increasing thickness of the sample [5]. The size of the grains growing abnormally fast was larger than the sample thickness and the grain size of the "normal" fine-grained matrix was smaller than the sample thickness. Therefore, it could be supposed that the transition from the normal to the abnormal grain growth is triggered by the transition from 3-dimensional growth to the 2-dimensional one. The indication for that was also that the fine-grained matrix was very fast consumed by the "abnormal" grains. In this work the increase of the sample thickness suppresses

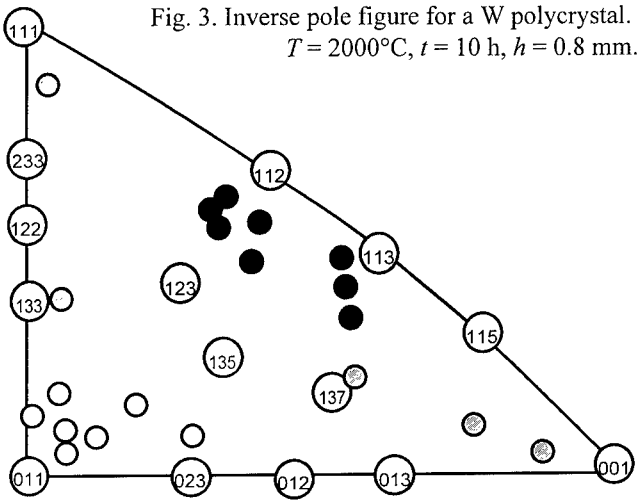

Fig. 3. Inverse pole figure for a W polycrystal. $T = 2000°C$, $t = 10$ h, $h = 0.8$ mm.

also the onset of the abnormal growth. But the abnormally large grains are nevertheless much smaller than the sample thickness. In other words, even after the onset of the abnormal growth the conditions for 3-dimensional growth are still valid. Therefore, the transition from normal to the abnormal grain growth in W is not triggered by the transition from 3-dimensional growth to the 2-dimensional one. The continuation of the normal grain growth in the fine-grained matrix after the onset of the abnormal grain growth confirms this conclusion.

The W polycrystals studied possess a clustered structure containing both small-angle GBs with low mobilities and high-angle GBs with high mobilities. Threfore, we can suppose that the barrier difference in mobilities needed to trigger the abnormal growth can be reached in case of W as a result of the GB misorientaion "summation" which proceeds during the gradual dissappearance of the smaller grains in the fine-grained matrix. Another reason for the transition to the abnormal growth can be the difference of the surface energies of grains having different orientations. In the W polycrystals studied the texture is rather pronounced. If the number of grains contacting with the free surface is large enough, the difference in the surface energies among neighboring grains can also trigger abnormal grain growth. In this case abnormal grain growth should begin earlier in thinner polycrystals even if the grain structure is still 3-dimensional.

ACKNOWLEDGMENTS

This work has been partially supported by the Volkswagen Foundation (under contract I/71 676), INTAS (grant 93-1451), NATO Linkage Grant HTECH.LG.970342 and INCO-COPERNICUS Network PL97-8078. We would like to thank V. Klassen for helpful discussions.

REFERENCES

[1] G. Gottstein, L. Shvindlerman, Acta metall. mater. 41 (1993), p. 3267.
[2] C. H. Wörner, P. M. Hazzledine, Mater. Sci. Forum 113–115 (1993), p. 379.
[3] A. D. Rollett, D. J. Srolowitz, M. P. Anderson, Acta metall. 37 (1989) p. 1227.
[4] V.Sursaeva, B.Straumal, S.Risser, B.Chenal, W.Gust, L.Shvindlerman, phys. stat. sol. (a) 149 (1995) p. 379.
[5] B.Straumal, V.Sursaeva, S.Risser, B.Chenal, W.Gust, Mater. Sci. Forum 207 (1996) p. 557.
[6] B. B. Straumal, W. Gust, L. Dardinier, J.-L. Hoffmann, V. G. Sursaeva, L. S. Shvindlerman, Materials & Design 19 (1998) p. 293.
[7] V.Glebovsky, B. Straumal, V. Semenov, V. Sursaeva, W. Gust, Plansee Sem. 13 (1993) p. 429.
[8] G. Gottstein, Rekristallisation metallischer Werkstoffe, DGM, Oberursel (1984).
[9] V. Novikov (ed.) Grain Growth and Control of Microstructure and Texture in Polycrystalline Materials, Springer, Berlin (1996).

Corresponding author: D. Sc. Boris Straumal, e-mail straumal@issp.ac.ru and straumal@song.ru
web site http://www.issp.ac.ru/libm/straumal, fax +7 095 238 23 26 or +7 095 111 70 67

Materials Science Forum Vols. 294-296 (1999) pp. 537-540

Effect of Surface Diffusion on the Contact Formation and Adhesion of Atomically-Clean Surfaces of Lead, Tin and Pb-Sn Eutectic Alloy

J. Maniks and F. Muktepavela

Institute of Solid State Physics, University of Latvia, 8 Kengaraga St., Riga LV-1063, Latvia

Keywords: Atomically-Clean Surfaces, Surface Diffusion, Sintering, Adhesion

Abstract

The role of sintering on contact formation and adhesion of polycrystalline lead, tin and Pb-62%Sn alloy in the temperature range 0.4-0.6 T_m has been investigated. Atomically-clean surfaces were obtained by the method of controllable internal rupture. Pronounced surface diffusion was observed on free surfaces for all metals investigated. However, contribution to the contact formation and adhesion strength from sintering was found to be essential for Pb-Sn alloy only.The effect of interface energy and grain boundary grooving on sintering is considered.

Introduction

Low-temperature sintering is important for a wide range of problems in solid state bonding and compacting of materials. Sintering-promoting factors, such as mechanoactivation, nanostructured state, surface cleanliness, etc. are of special interest. In this paper we report the experimental results on contribution of the surface diffusion to contact formation and adhesion of atomically-clean surfaces of polycrystalline lead, tin and Pb-62%Sn alloy.

Experimental

The materials investigated were tin, lead (99,99%) and Pb-62%Sn alloy. The lead and tin samples had coarse grains (50-100μm), while Pb-Sn eutectic was finer grained (2-3μm). Atomically-clean surfaces were obtained by the method of internal rupture based on creation of cavities of a controlled shape and size in the bulk of solids during deformation of specially manufactured heterogeneous systems[1]. In the present study a modified scheme of extrusion for this purpose was used (Fig.1). The punch of special configuration was covered with the metal to be investigated under conditions of complete wetting. Then it was placed into the container with die and subjected to extrusion by loading the punch. When the punch tip enters the die, the effusion rate of metal exceeds the punch moving rate that causes internal rupture in the metal under investigation. Further extrusion expands the zone of internal rupture. Since the interface between the punch and the metal is formed under conditions of complete wetting, it remains vacuum-tight during extrusion, and space of internal rupture is isolated from the ambient atmosphere. In such way closed tubes with atomically-clean internal surface were obtained. Length of the tubes was about 200 mm, diameter - 8-14 mm and wall thickness 1 mm.

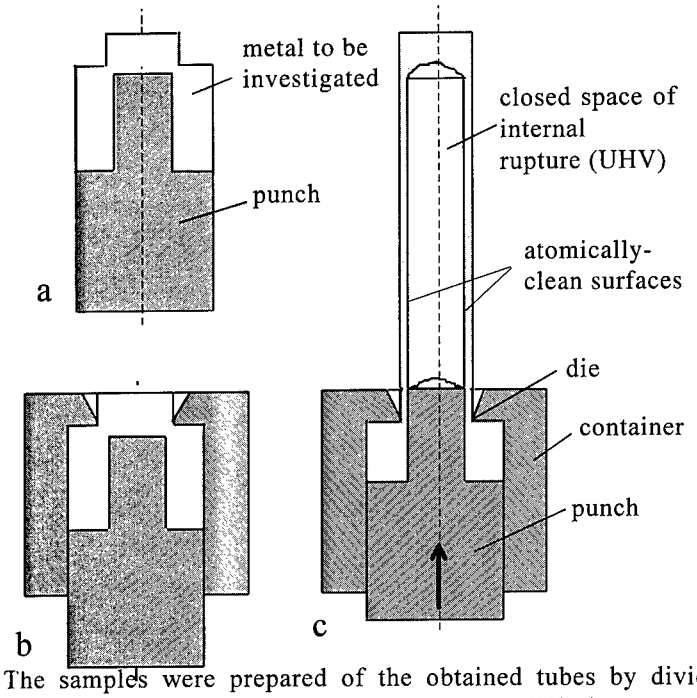

Fig.1. Obtaining of atomically-clean surfaces and closed UHV space by the extrusion method;

(a) punch covered with the metal to be investigated,

(b) and (c)- formation of the internal rupture space and obtaining of atomically-clean surfaces during extrusion;

The samples were prepared of the obtained tubes by dividing them into vacuum-tight fragments by a cold welding method. The diffusion processes on free (non-contacted) surfaces during annealing the samples in the range of 10^2 - 10^6s was studied. The effect of elastic stress on diffusion mass-transport was investigated by applying a bending force to the samples. For the adhesion investigation surfaces of internal rupture were contacted by flattening the obtained tubes at a pressure of 0.2 HB, where HB-Brinell hardness of the metal. Initial contact of the asperities created a series of contact spots and voids at the interface. The effect of sintering on the contact formation and adhesion was evaluated by the dependence of the adhesion strength on the contact duration under zero applied load in the range of 10^2 - 10^6s. Kinetics of the adhesion under compression load was also investigated.

Results

Diffusion mass transport on free surfaces. Annealing of closed tubes at 0.4-0.6 T_m during 10^6s resulted in smoothing of the surfaces, grain boundary grooving and formation of the thermal etching figures, so giving evidence for pronounced diffusion on free surfaces of internal rupture (Fig.2). The first signs of thermal etching on the clean surfaces of tin and lead at the room-temperature were observed during some hours. Equilibrium structures for tin and lead were formed during about two months, but for Pb-Sn alloy - during about 48 hours. Maintaining of the samples under the bending load showed promoted diffusion mass transport on the stressed surfaces, especially, in the near-boundary zones with width up to ~10 μm. More intense smoothing of the surfaces, grain-boundary sliding and migration for stressed samples compared to non-loaded ones was observed.

Effect of surface diffusion on the adhesion. Despite the fact of extensive surface diffusion, negligible increase in the adhesion strength was observed during annealing of the Pb/Pb and Sn/Sn joints under zero applied load at 0.5 T_m for up to10^6s (Fig.3). Increase in the adhesion strength after long-time keeping the samples at 0.6T_m was less than ~3%. Microscopic studies showed non-healed voids of 3-10 μm at the interface. Such defects in

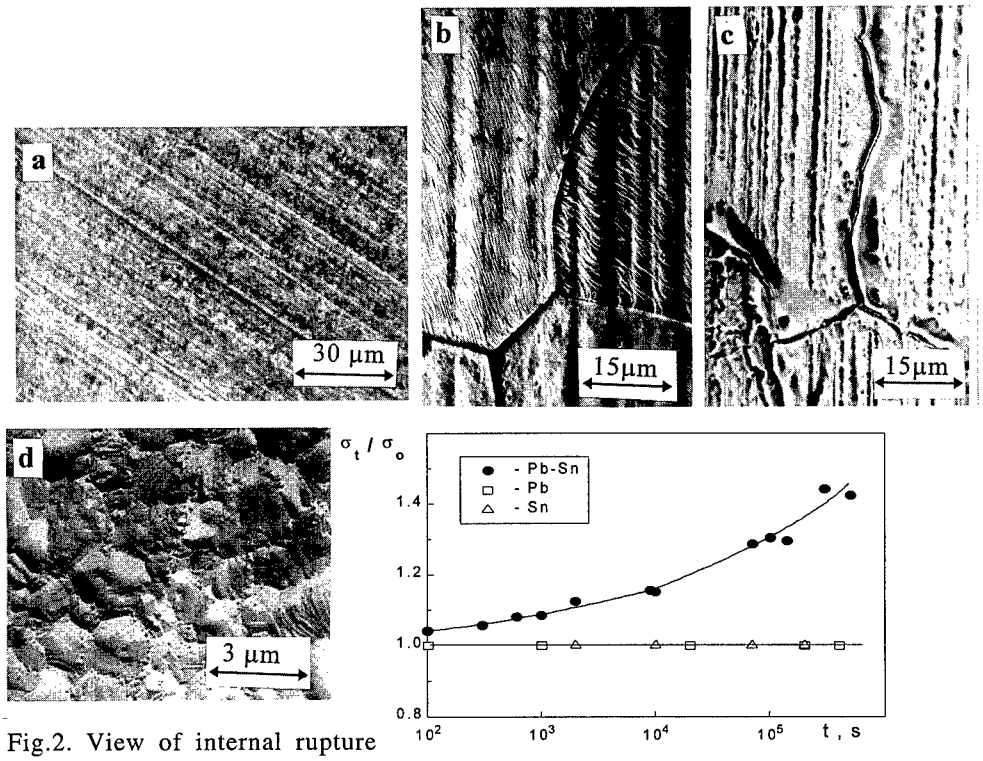

Fig.2. View of internal rupture surfaces: (a)Sn, as-obtained, (b) Sn, annealed for 2 months, (c) Sn, annealed for 1 month under elastic stress, (d)Pb-Sn, annealed for 24 hours.

Fig.3.Adhesion strength of atomically-clean surfaces of tin, lead and Pb-Sn alloy as a function of annealing time under zero load at 290K; σ_0 -strength of as-obtained joints.

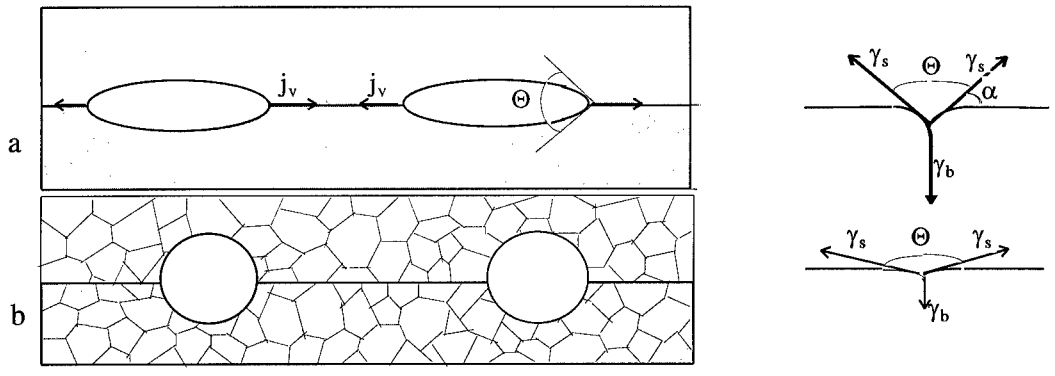

Fig.4. Schematic illustration of the effect of grain boundary on the healing of pores on contact interface of coarse-grained material with grain size greater than the pore (a) and on interface of fine-grained material (b).

the contact zone were detected even after exposure for one year. Surface diffusion-induced increase in adhesion strength was found to be essential for Pb-Sn alloy only. The structural investigations showed marked mass-transport to the periphery of the contact spots as well as effective healing of the voids at contact interface.

Kinetics of the adhesion under compression load. A marked temperature- and time-dependent increase in adhesion strength under the compression load for all materials investigated was observed. Activation energies were 44 kJ/mol for lead and 42 kJ/mol for tin and Pb-Sn alloy. Kinetics of the adhesion obeys the known relation $\sigma = \sigma_0 t^n$, where n is a constant (0.09,0.13 and 0.24 for lead, tin and Pb-Sn alloy, respectively) [2,3].

Discussion

Generally, matter is expected to be surface diffusion-transferred from the point of least curvature to the point of greatest, this being the sharp neck of the voids and contact spots at the bonding interface. For the present analysis, we consider that an interface obtained by mechanical contacting is a planar grain boundary with high concentration of voids. No migration of such boundary is known to occur under annealing even at comparatively high temperatures [4]. The presence of a planar grain boundary at the contact interface can lead to restriction of the sintering for pure lead and tin due to grain boundary grooving at the intersection of the boundary with interfacial voids and contact spots as shown in Fig.4. In the case of high ratio of grain boundary to surface energy (as for Pb and Sn) the grooves are characterized by sharp dihedral angle, that limits spheroidization of the interfacial voids and growth of the contact spots. Healing of the interfacial ensemble of voids in Pb and Sn by grain boundary diffusion is also negligible because direction of vacancy flows $\mathbf{j}_v$, emitted from the neighboring voids, are opposite. The situation in the case of Pb-Sn eutectic is quite different. Significant contribution in healing of large voids in fine-grained alloy from vacancy flow through developed boundary network is expected as shown in Fig.4(b). As it is well known from the thermodynamics, this process depends on adhesion work W_a. Adhesion work is defined as $W_a = \gamma_s^A + \gamma_s^B - \gamma_b^{AB}$, where γ_s^A , γ_s^B are surface and γ_b^{AB}, phase boundary energies. Phase boundary energy for Pb-Sn alloy (0.04 J/m^2) is of an order lower compared to grain boundary energy for pure tin (0.16 J/m^2) or lead (0.21 J/m^2). The effect of phase-boundary grooving becomes negligible due to low phase boundary energy, and surface diffusion-promoted increase in contact area can occur. Growth of the eutectic structure in the healing zone was observed due to consistent surface and grain boundary diffusion of both Pb and Sn.

The effect of contact duration on adhesion strength is ascribed mainly to the creep-induced increase in contact area [3]. However, activation energies obtained in the present study were close to those for vacancy migration or grain boundary diffusion, and some contribution from the stress-promoted diffusion at the interface under such conditions is supposed. In summary, the results obtained show that surface diffusion-induced sintering of atomically clean surfaces of metals becomes significant if definite structural and energetic conditions at the interface are met. Such conditions are fulfilled for Pb-Sn eutectic characterized by fine grained structure and low interfacial energy.

References

1.J.Maniks, Vacuum,46 (1995)1439-1444.
2.J.Maniks, A.Simanovskis, J.Adhes. Sci. Technol., 10 (1996) 541-557.
3.D.Maugis, Wear, 62(1980)349-386.
4.L.N.Larikov, Healing of the defects in metals, Kiev, Naukova Dumka, 1980 (in Russian).

Materials Science Forum Vols. 294-296 (1999) pp. 541-544

Radiotracer Diffusion of Ni and Ag in Ag and Ni Grain Boundaries and Oriented Ag/Ni Interphase Boundaries

Chr. Minkwitz[1], Chr. Herzig[1], B. Straumal[2] and W. Gust[2]

[1] Institut für Metallforschung, Universität Münster,
Wilhelm-Klemm-Str. 10, D-48149 Münster, Germany

[2] Institut für Metallkunde, Universität Stuttgart, Seestr. 75, D-70174 Stuttgart, Germany

Keywords: Grain Boundary, Interphase Boundary, Radiotracer Diffusion

Abstract

Grain boundary and interphase boundary diffusion has been investigated in the system Ag/Ni using the radiotracer serial sectioning technique. Ni segregation in Ag grain boundaries is strongly temperature dependent leading to the conclusion that Ni atoms are located mainly in the bulk planes adjacent to the grain boundary. From interphase boundary diffusion measurements in (110) oriented Ag/Ni interphase boundaries it can be deduced that the structure of this interphase boundary is incoherent.

Introduction

Diffusion in grain boundaries (GB) and interphase boundaries (IB) is strongly affected by their structure and chemistry. In this work the influence of both factors has been investigated. First, segregation of ^{63}Ni in Ag GBs was studied by comparative measurements in the type-B and –C kinetic regime. These results were necessary [1] for the evaluation of IB diffusion coefficients of ^{110m}Ag diffusion in (110) oriented IBs of Ag/Ni bycrystals. Moreover, ^{110m}Ag GB diffusion in Ni polycrystals was measured.

To study the influence of the orientation of the single crystals forming an IB, it is prerequisite to produce bycrystals with well defined sharp interfaces. Therefore a system with low mutual solid solubility of the IB forming components and a miscibility gap in the phase diagram is favourable, e.g. the systems Ag-Ni. The ratio of the lattice constants a_{Ag}/a_{Ni} is almost exactly 7:6. For cube-on-cube oriented bycrystals of Ag and Ni this leads to a coincidence of every 6th Ag with every 7th Ni atom (Fig.1) in the interplane. The misfit between these coincident atoms is equalised by misfit dislocations and relaxation. The misfit dislocations form a superlattice being parallel to the orientation of the Ag and Ni single crystals and with a periodicity of $6a_{Ag}$. For a (110) oriented IB this leads to an anisotropic density of misfit dislocations, which in <100>-direction is higher (by a factor $2^{1/2}$) than in <110>-direction. In previous investigations on the IB diffusion of Ag in Ag/Cu IBs it has been shown, that a higher density of misfit dislocations leads to a faster IB diffusion [2].

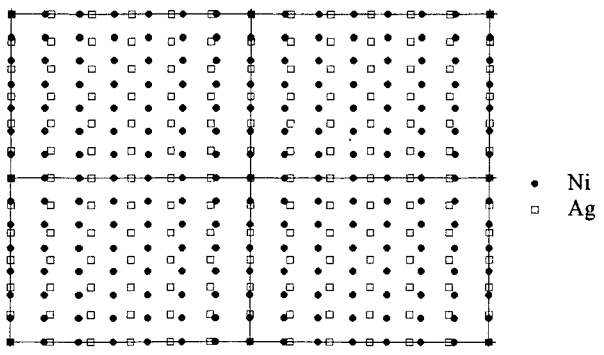

Fig. 1:
Onview on the unrelaxed structure of a (110) IB in Ag/Ni

Experimental procedure

Ag and Ni samples, single- and polycrystals, were produced from high purity (5N) ingots. Single crystals of Ag and Ni were grown from the melt and slices of 4 mm were cut with (110) surface orientation. The single crystals were etched, polished and diffusion-bonded with cube-on-cube orientation. From these bycrystals samples were cut perpendicular to the IB with <100> or <110> orientation of the surface.

All samples were pre-annealed at the temperature of the later diffusion annealing. The radiotracer materials, ^{63}Ni and ^{110m}Ag, were evaporated onto the samples. All annealings were performed under high vacuum ($p \approx 10^{-3}$ Pa). The sectioning of the diffusion profiles was done on a microtome; the slices were dissolved and their radiation detected with a high sensitive Liquid Scintillation Counter (LSC).

Results and discussion

Grain Boundary diffusion of ^{63}Ni in Ag polycrystals. Measurements were performed in Harrisons type-B and -C kinetics. In the B-kinetic regime superposition of grain boundary diffusion (D_{GB}) and volume diffusion ((D) into the adjacent bulk makes it impossible to calculate the GB diffusion coefficient D_{GB} independently. From type-B measurements on GB solute diffusion only the triple product $s\delta D_{GB}$ can be evaluated, with s being the GB segregation coefficient and δ the GB width:

$$s \cdot \delta \cdot D_{GB} = 1.308 \cdot \left(\frac{D}{t}\right)^{1/2} \left(-\frac{\partial \ln \bar{c}}{\partial y^{6/5}}\right)^{-5/3} \qquad (1)$$

Measurements were performed in the range 821 K to 989 K. The detected decrease in the tracer concentration $\bar{c}$ was up to 4 decades (Fig.2a). In the type-C kinetic regime this decrease was only about 1-2 decades due to the negligible bulk diffusion from the GB (Fig.2b). In such a condition the

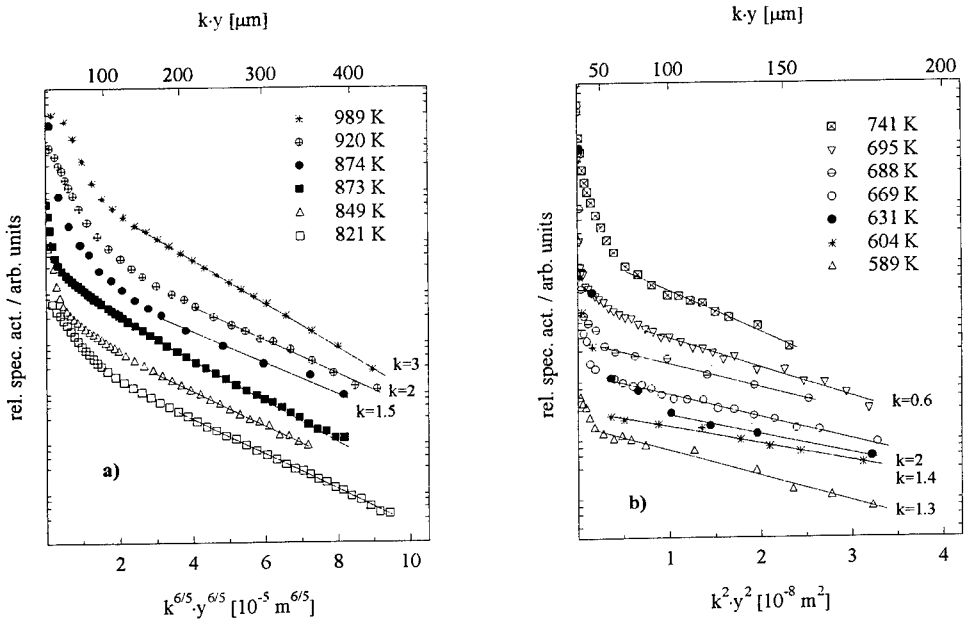

Fig.2: GB diffusion of ^{110m}Ag in Ni polycrystals according to different kinetic regimes
a) type-B b) type-C

GB diffusion coefficient D_{GB} can directly be calculated from the slope $\partial \ln \bar{c} / \partial y^2$. The resulting Arrhenius relations for ^{63}Ni GB diffusion in Ag polycrystals are:

$$s \cdot \delta \cdot D_{GB} = 1.9 \cdot 10^{-15} m^3 s^{-1} \cdot \exp\left(-69.2 kJmol^{-1} / RT\right). \quad (2)$$

$$D_{GB} = 3.1 \cdot 10^{-6} m^2 s^{-1} \cdot \exp\left(-110.1 kJmol^{-1} / RT\right). \quad (3)$$

From the comparison of D_{GB} (multiplied with δ=0.5nm) with $s\delta D_{GB}$ (Fig.3) the segregation factor s was evaluated :

$$s = 1.2 \cdot \exp\left(40.9 kJmol^{-1} / RT\right). \quad (4)$$

The characteristic features of the present results are : the strong segregation (segregation enthalpy H_S=40.9 kJ/mol) and the slow GB diffusion of Ni in Ag as compared with the Ag GB self-diffusion [3]. These facts can be explained by the high surface tension σ_{Ni} of Ni, which is remarkably higher than that of Ag, and by a repulsive vacancy–Ni solute interaction. From this it can be concluded that Ni does not segregate in the GB core, but in the adjacent bulk planes [4].

Grain Boundary diffusion of ^{110m}Ag in Ni polycrystals. Measurements were performed in the type-B kinetic regime from 973 to 1253 K. The profiles were of the same quality as for GB diffusion of ^{63}Ni in Ag polycrystals (Fig.2a). The Arrhenius relation is :

$$s \cdot \delta \cdot D_{GB} = 5.6 \cdot 10^{-15} m^3 s^{-1} \cdot \exp\left(-120.5 kJmol^{-1} / RT\right). \quad (5)$$

The values of $s\delta D_{GB}$ for Ag GB diffusion in Ni (Fig. 4) are higher than those of Ni GB self diffusion [5], while the activation enthalpy is nearly the same. The very low solid solubility of Ag in Ni is expected to lead to a strong Ag segregation in Ni GBs. Taking this into account, it can be estimated that the Ag mobility in Ni GBs is less than that of Ni.

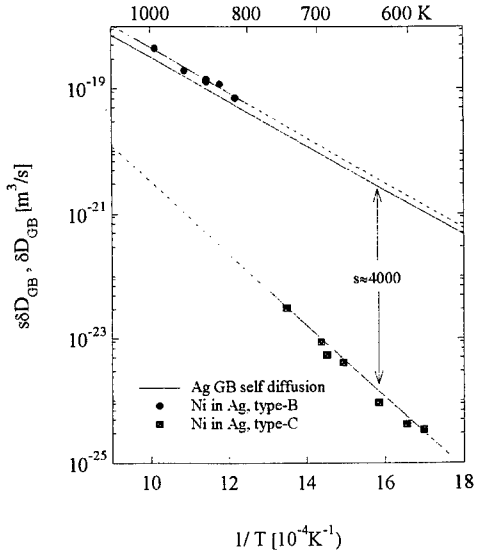

Fig. 3: Arrhenius plot of $s\delta D_{GB}$ (upper) and δD_{GB} (lower curve)

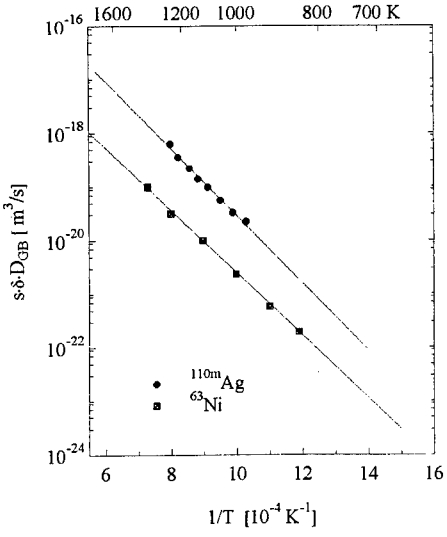

Fig 4 : Arrhenius plot of ^{110m}Ag GB diffusion compared with GB self-diffusion in Ni [5]

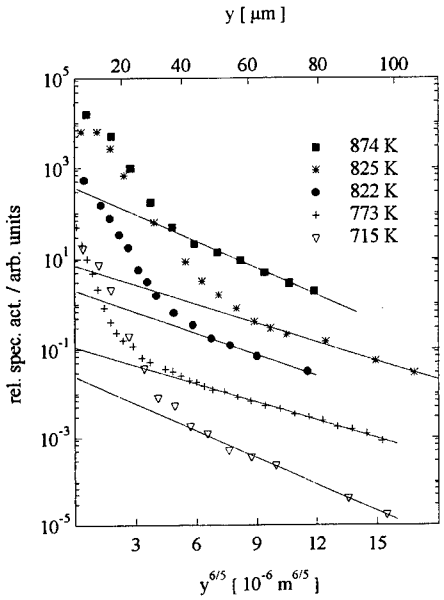

Fig. 5: Penetration profiles for IB diffusion of ^{110m}Ag in Ag/Ni (110) bycrystals.

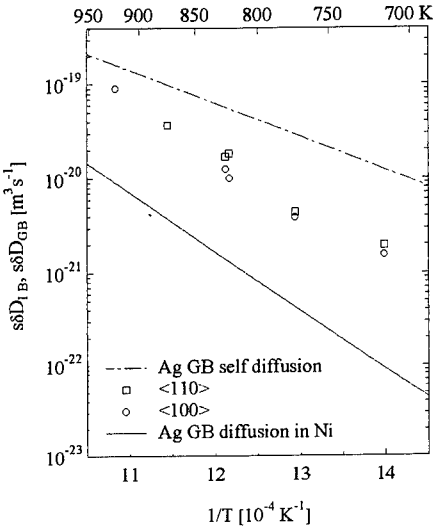

Fig. 6 : Arrhenius plot of ^{110m}Ag IB diffusion in Ag/Ni bycrystals and comparison with GB diffusion of Ag in Ag and Ni.

IB diffusion of ^{110m}Ag in (110) oriented Ag/Ni IB. Measurements were performed from 715 K to 923 K (Fig.5). In [1] it was shown that IB diffusion coefficients can be evaluated e.g. from the Suzuoka solution if the volume diffusion coefficient is replaced by an effective volume diffusion coefficient D_{eff} depending on volume diffusion and segregation of the tracer material in both bycrystal materials. In the case of Ag diffusion in Ag/Ni bycrystals the quantitative evaluation of D_{eff} is more simple, because it turns out that the terms related to diffusion of Ag in Ni can be neglected.

From the Arrhenius plot (Fig. 6) it can be seen that in the presently investigated IB nearly no diffusional anisotropy can be observed. Diffusion of ^{110m}Ag in <100>-direction is equal to or even slower than in <110>-direction which is in disagreement to the results found in Ag/Cu IBs []. This can be explained by the larger misfit in lattice constants of Ag/Ni when compared with Ag/Cu leading to an incoherent structure of the IB in the present case because of a very high misfit dislocation density. Thus, at higher temperatures a completely incoherent IB appears to be more favourable than a semi-coherent structure of the (011) Ag/Ni phase boundary.

References

[1] I. Kaur, Y.M. Mishin, W. Gust: in *Fundamentals of grain and interphase boundary diffusion*, John Wiley & Sons Ltd., Chichester, 1995

[2] J. Sommer, Chr. Herzig, T. Muschik, W. Gust: Acta mater. **44** (1996) 327

[3] J. Sommer, Chr. Herzig: J. Appl. Phys. **72** (1992) 2578

[4] A. Rolland, B. Aufray: Surf. Sci. **162** (1985) 530

[5] S. Frank, J. Rüsing, Chr. Herzig : Intermetallics **4** (1996) 601

Materials Science Forum Vols. 294-296 (1999) pp. 545-548

Germanium Tracer Diffusion in a Series of Symmetrical Near Σ=7, Θ=38.2° [111] Tilt Grain Boundaries of Aluminum

T. Surholt[1], D.A. Molodov[2] and Chr. Herzig[1]

[1] Institut für Metallforschung, Universität Münster,
Wilhelm-Klemm-Str. 10, D-48149 Münster, Germany

[2] Institut für Metallkunde und Metallphysik, RWTH Aachen,
Kopernikusstr. 14, D-52074 Aachen, Germany

Keywords: Tilt Grain Boundaries, Grain Boundary Diffusion, Orientation Dependence

Abstract - Grain boundary (GB) diffusion was measured in a series of Al bicrystals with symmetrical near Σ=7, Θ=38.2° (12-3) [111] tilt GBs. The actual orientations of the bicrystals were precisely measured with the Kossel technique. The tilt angles Θ ranged from 34.15° to 41.41°. Grain boundary diffusion parallel to the tilt axis was measured in the type-B kinetic regime at five temperatures in the range 518 - 680 K. A characteristic non-monotonic behaviour of the resulting dependence of the GB diffusivity $s\delta D_{GB}$ on the tilt angle Θ was observed for all five investigated diffusion temperatures. At the ideal Σ=7, Θ=38.2° (12-3) [111] tilt GB the GB diffusion is minimal; with increasing deviation from the CSL (coincidence site lattice) GB the diffusivity increases and reveals a broad maximum at about Θ=38.2°±3°. The opposite dependencies are observed for the Arrhenius parameters $(s\delta D_{GB})_0$ (pre-exponential factor) and Q_{GB} (effective activation enthalpy of GB diffusion), which were calculated from the temperature dependence of $s\delta D_{GB}$. At the ideal Σ=7 CSL GB the Arrhenius parameters are maximal. Due to the rather small GB segregation of Ge in Al, the orientation dependence of $s\delta D_{GB}$, $(s\delta D_{GB})_0$ and Q_{GB} qualitatively reflects the orientation dependence of D_{GB}, D_{GB0} and H_{GB}. The orientation dependence of the GB diffusion supports the CSL GB diffusion model.

Introduction

A number of studies have been made to relate grain boundary (GB) properties to the structure of GBs. Whereas the structure dependence of GB energy seems to be fairly well known [1,2], the situation concerning the orientation dependence of GB diffusion remains still less clear. One issue is the possible continuous relationship between GB diffusion and the tilt angle Θ. The tilt angle Θ with respect to a given symmetry axis is one of the three macroscopic parameters describing the orientation of adjacent grains. Investigations of self-diffusion along a series of symmetrical [001] Ag tilt GBs [3] and of Ag diffusion along a series of [001] Au tilt GBs [4] reveal a continuous variation of δD_{GB} (δ: GB width) with the tilt angle Θ. These results were interpreted in terms of the structural unit model for diffusion [5]. The measurements, however, were made in comparatively large steps in the variation of Θ. Therefore, possibly existing cusps at the Σ=5 CSL GB might have been overlooked. In contrast, the other issue is the existence of cusps of $s\delta D_{GB}$ and peaks of the Arrhenius parameters at CSL GBs, which were observed in diffusion measurements of Zn along symmetrical [001] and [111] tilt GBs in Al [6]. It should be pointed out, however, that these studies were carried out, in fact, under conditions of chemical diffusion and the observed minima in $s\delta D_{GB}$ vs. Θ might be related to the structural dependence of the solute GB segregation factor s which is included in the GB diffusion parameter for solute diffusion. The obstacles of both contradictory GB structure related diffusion considerations can be overcome by using a series of very well oriented bicrystals with orientations in a narrow range near special GBs of high coincidence. Therefore, applying the radiotracer- and serial sectioning technique the orientation dependence of ^{71}Ge diffusion along symmetrical [111] Al tilt GBs close to the ideal Σ=7, Θ=38.2° (12-3) [111] tilt GB was studied.

Experimental

The Al bicrystals were grown in a graphite mold by directional crystallization using high purity (nominal 99.999%) oriented Al single crystals. The orientations of the grains of each bicrystal were very precisely determined applying a modified Kossel technique. All three macroscopic parameters describing the grain orientations were determined.

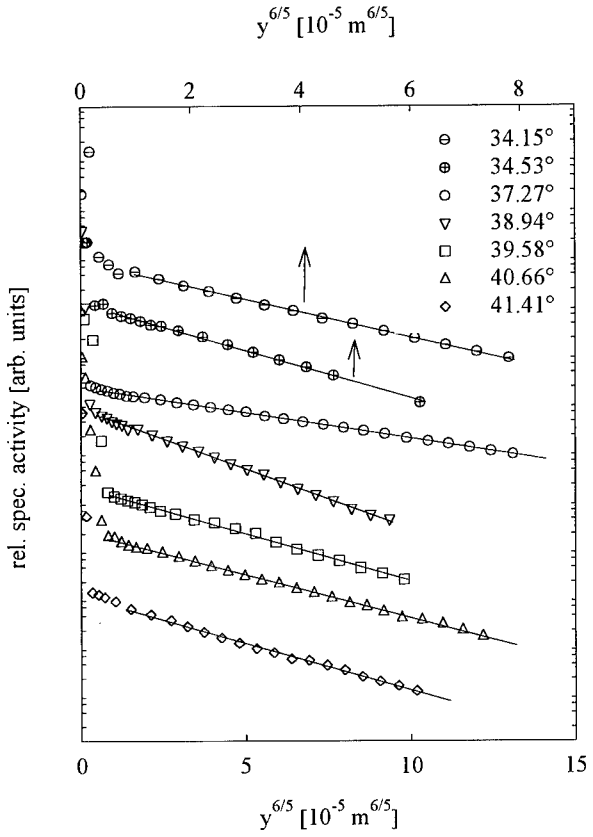

Fig. 1: Tracer penetration profiles of ^{71}Ge diffusion in symmetrical near Σ=7, Θ=38.2° [111] tilt GBs at T=518 K for t=151440 s.

Cylindrical diffusion samples were cut from the bicrystals by spark erosion. One front (111) surface of each specimen was mechanically polished by standard metallographic procedures and finished by chemical polishing. They were annealed in argon atmosphere first at 723 K for two days and furthermore under the conditions of the intended diffusion anneals in order to achieve quasi-equilibrium GB segregation of spurious impurities and to prove the stability of the GB. The radioisotope ^{71}Ge was produced by the reaction ^{70}Ge(n,γ)^{71}Ge in the reactors of GKSS, Geesthacht, Germany and of the Forschungszentrum Jülich, Germany. To avoid hold-up effects due to oxide film on the Al surface, the oxide layer was removed by ion sputtering under high vacuum conditions. The radiotracer ^{71}Ge was evaporated *in situ* on the polished and sputter-cleaned (111) surface of each sample subsequent to the ion sputter process. The temperatures of the diffusion anneals were measured with Ni/NiCr thermocouples and controlled within ±1 K. After the diffusion annealing the specimen were reduced in diameter to eliminate the effect of radial diffusion and sectioned on a microtome. The intensity of the decays of the ^{71}Ge in each section was detected with a liquid scintillation counter of very low background.

Results

For all studied temperatures in the range 518 - 680 K the conditions of type-B kinetic regime were fulfilled. Accordingly, the resulting penetration profiles were plotted as $\ln \bar{c}$ vs. $y^{6/5}$ and their GB diffusion related tails were approximated by straight lines. Typical diffusion profiles are shown in Fig.1. The GB diffusion parameter $s\delta D_{GB}$ was determined from the slope of the GB related diffusion profiles, using Suzuoka's equation for GB diffusion from an instantaneous source [7]. The dependence of $s\delta D_{GB}$ on the tilt angle Θ is shown in Fig. 2 for four temperatures. The temperature dependence of $s\delta D_{GB}$ is presented in Fig. 3 in Arrhenius co-ordinates. The dependence of the resulting Arrhenius parameters on the tilt angle Θ is shown in Fig. 4. The GB diffusion depends

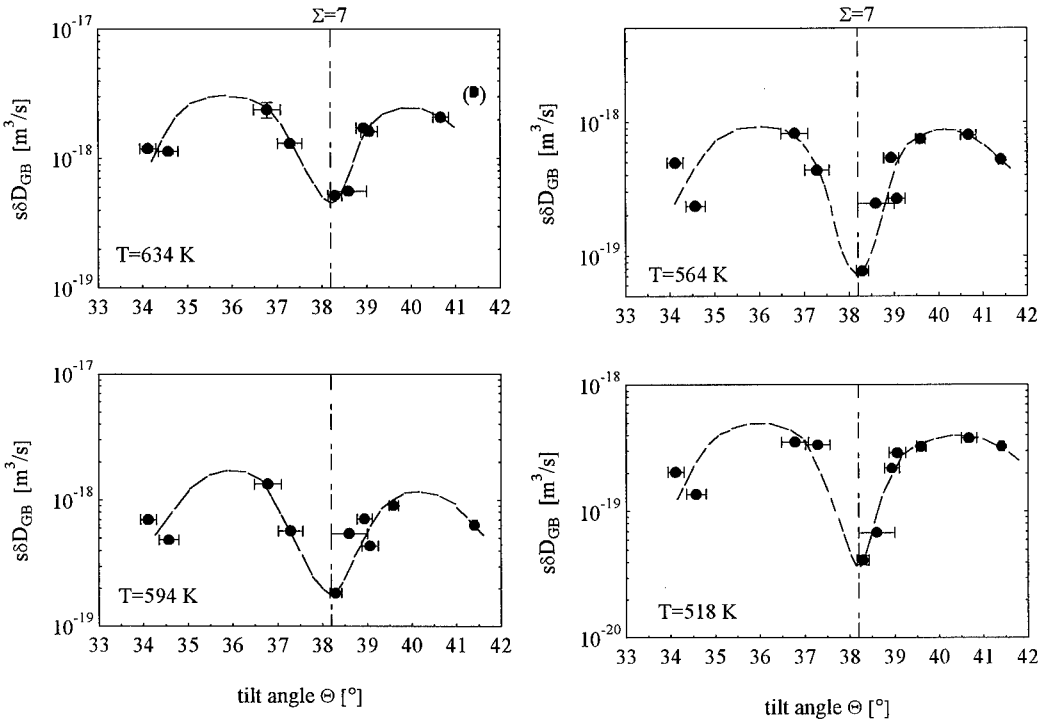

Fig.2: Dependence of the diffusion parameter $s\delta D_{GB}$ of ^{71}Ge diffusion along near Σ=7, Θ=38.2° (12-3) [111] Al tilt GBs on the tilt angle Θ at different temperatures. Point in brackets was not taken into account

strongly on the tilt angle Θ. At the position of the ideal Σ=7 CSL GB, $s\delta D_{GB}$ adopts a minimum and increases with increasing tilt angle deviation from the ideal Σ=7 GB symmetrically on both sides of the CSL GB, Fig. 2. The Arrhenius parameters Q_{GB} and $(s\delta D_{GB})_0$, on the other hand, adopt a maximum at the ideal Σ=7 GB and decrease with increasing tilt deviation from the ideal Σ=7 GB symmetrically on both sides of the CSL GB, Fig. 4.

Discussion

Since the solute GB diffusion of Ge in Al bicrystals was studied in the type-B kinetic regime, the orientation dependence of Ge GB segregation effects on the measured GB diffusion parameter $s\delta D_{GB}$ and determined Arrhenius parameters $(s\delta D_{GB})_0$ and $Q_{GB}=H_s+H_{GB}$ (H_s: GB segregation enthalpy, H_{GB}: activation enthalpy of GB diffusion) must be considered. The estimation of the segregation enthalpy following the semi-empirical relation of Seah [8] reveals $-H_s < 8$ kJ/mol. Since this estimation refers to general large angle GBs, the value of H_s for high coincidence near Σ=7 tilt GBs is expected to be smaller. Therefore, the observed variation of Q_{GB} in Fig. 4, which exceeds ≈20 kJ/mol, cannot be explained by segregation effects alone. The orientation dependence of $s\delta D_{GB}$, Q_{GB} and $(s\delta D_{GB})_0$ therefore reflects at least to a larger part the tilt angle dependence of D_{GB}, H_{GB} and D_{GB0}.

The observed minima of the Ge diffusion parameter in Al GBs and maxima in the Arrhenius parameters at the ideal Σ=7 GB can be explained in terms of the CSL model. Following Straumal et al. [9], GBs of high coincidence and, therefore, of highly ordered atomic structure - in comparison to

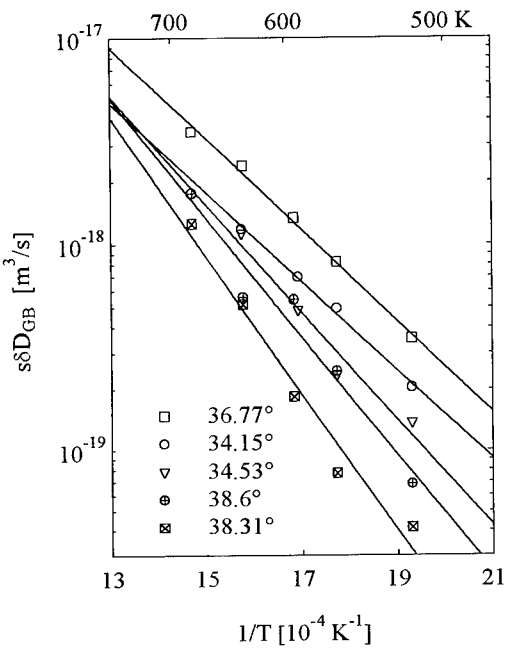

Fig. 3: Temperature dependence of ^{71}Ge diffusion along near Σ=7 [111] Al tilt GBs in Arrhenius co-ordinates.

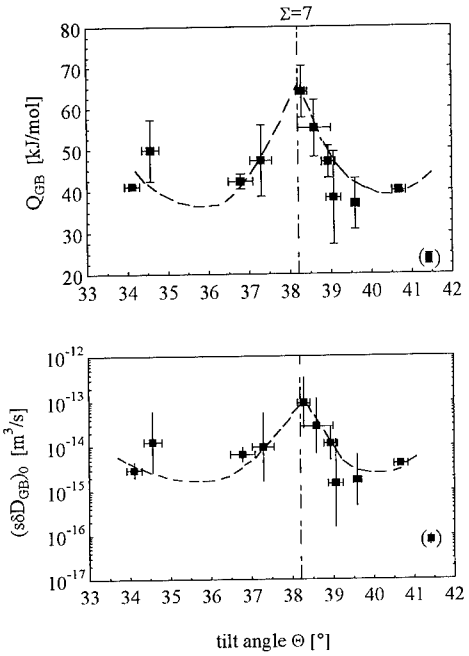

Fig. 4: Dependence of Q_{GB} and $(s\delta D_{GB})_0$ of ^{71}Ge diffusion along near Σ=7 [111] Al tilt GBs on the tilt angle Θ. Point in brackets was not taken into account.

general large angle GBs - yield minima in the diffusivity and maxima in the Arrhenius parameters due to the larger mean formation and migration enthalpies of vacancies in comparison to general large angle GBs of low coincidence and lower degree of perfection. Small deviations from the ideal Σ=7 GB in the tilt angle Θ are compensated by dislocations which are additionally inserted in the GB structure [10]. These intrinsic GB dislocations obviously offer additional paths of "easy" atomic motion and enhance the diffusion flux along the GBs. With increasing deviation ΔΘ from the ideal Σ=7 GB and, therefore, increasing density of the additionally inserted GB dislocations the diffusivity increases and the Arrhenius parameters decrease.

References

[1] D. Wolf, Acta metall. 38 (1990), p. 791.
[2] T. Mori, T. Ishii, M. Kajihara and M. Kato, Phil. Mag. Lett. 75 (1997), p. 367.
[3] J. Sommer, Chr. Herzig, S. Mayer and W. Gust, Defect Diff. Forum 66-69 (1989), p. 843.
[4] Q. Ma and R.W. Balluffi, Acta metall. mater. 41 (1993), p. 133.
[5] R.W. Balluffi and A. Brokman, Scripta metall. 17 (1983), p. 1027.
[6] A.N. Aleshin, V.Y. Aristov, B.S. Bokshtein and L.S. Shvindlerman, phys. stat. sol. (a) 359 (1978), p. 1256.
[7] I. Kaur, Y. Mishin and W. Gust, *Fundamentals of Grain and Interphase Boundary Diffusion*, Wiley and Sons, Chichester, 1995.
[8] M.P. Seah, J. Phys. F. 10 (1980), p. 1043.
[9] B.B. Straumal, L.M. Klinger and L.S. Shindlerman, Acta metall. 32 (1985), p. 1355.
[10] T. Schober and R.W. Balluffi, Phil. Mag. 21 (1970), p. 109.

Materials Science Forum Vols. 294-296 (1999) pp. 549-552

Equilibrium Sites Occupied in the Grain Boundary Core During Intercrystalline Diffusion of ^{57}Co in Metal Polycrystals

V.N. Kaigorodov and S.M. Klotsman

Institute of Metal Physics, Urals Division of Russian Academy of Sciences,
RU-620219 Ekaterinburg, RF

Keywords: Grain Boundary Core, Equilibrium Positions, Intercrystalline Diffusion, Metals

Abstract. Only two types of states are occupied in metal polycrystals during intercrystalline diffusion of atomic probes. The states-1 are localized in the grain boundary core of metal polycrystals. The states-2 are localized in lattice regions adjacent to grain boundaries. In 4d and 5d metals ^{57}Co atomic probes represent small-radius impurities and occupy interstitial sites in the grain boundary core of these metals. In 3d metals ^{57}Co atomic probes are no longer small-radius impurities and therefore occupy only the substitutional sites in the grain boundary core structure.

I. Introduction. The structure and properties of grain boundary core have still been the subject of intensive studies, because grain boundaries are significant for the properties of ordinary polycrystals and materials of the new class, namely three-dimensional nanocrystalline materials. The new method [1,2] for examination of the structure and the set of physical properties of the grain boundary core in polycrystals provides information about the type and properties of equilibrium sites occupied by atomic probes during intercrystalline diffusion, giving spectral data about occupied states. This paper reports results of the study into the types of states occupied by ^{57}Co atomic probes (AP's) in metal polycrystals.

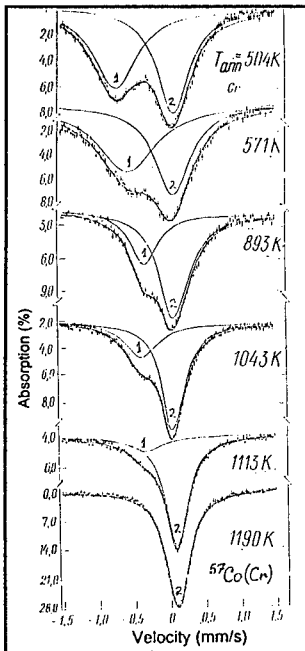

Fig.1

NGR spectra of ^{57}Co in poly-Cr, obtained after annealings at various temperatures.

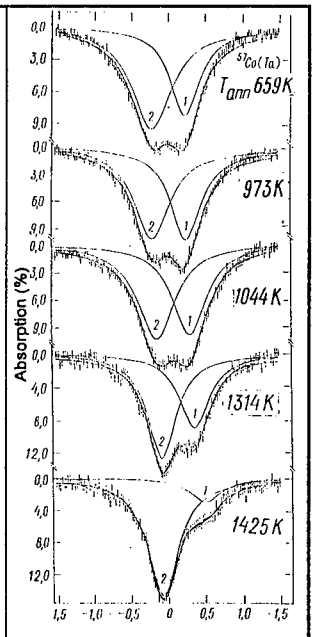

Fig.2

NGR spectra of ^{57}Co in poly-Ta, obtained after annealings at various temperatures.

II. Materials and Methods.

The polycrystalline foils with the crystallite size of about 10^{-4} m were obtained by rolling of single crystals of metals and their subsequent recrystallization. The impurity concentration of these foils was measured on an IMS-3f microanalyzer (Cameca, France) by the SIMS method. It proved to be the same as in the initial single crystals. ^{57}Co atomic probes with specific activity of 300 GBq/mg were deposited on the foil surface by an electrolytic method. The samples underwent diffusion annealings at successively increasing temperatures in an oilless dynamic vacuum of (10^{-5}-10^{-4}) Pa. After the first annealing unused remainders of the diffusion source were removed from the sample using a selective etching. Then a polishing

etching was applied to remove the sample's layer whose thickness was much greater than the depth of volume diffusion at the given temperature. During all the subsequent annealings atomic probes were only redistributed between states in the intercrystalline diffusion zone of the samples prepared by this method. Emission nuclear gamma resonance (NGR) spectra were taken on a constant-velocity spectrometer after each annealing. The absorber (potassium ferrocyanide having the surface density of 2.5 g/m^2) and the sample were held at room temperature.

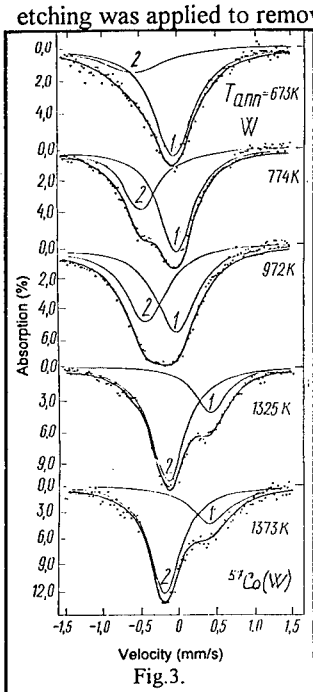

Fig.3.

NGR spectra of ^{57}Co in poly-W, obtained after annealings at various temperatures.

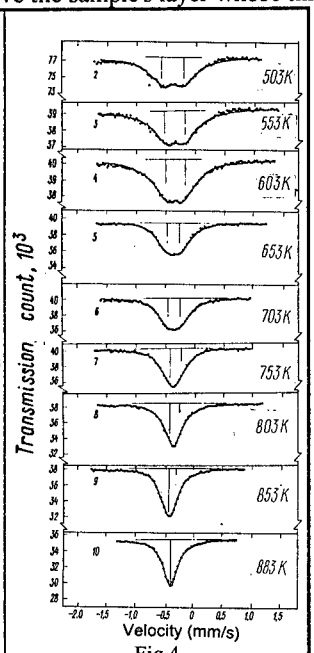

Fig.4

NGR spectra of ^{57}Co in poly-Pt, obtained after annealings at various temperatures.

III. Results and Discussion. In terms of our method [1,2], a single sample undergoes isochronous annealings at temperatures below the foil recrystallization temperature. In this case the same system of grain boundaries is preserved in the sample. Figures 1 to 4 show typical emission NGR spectra taken after annealings at successively increasing temperatures.

III.1. Types of occupied states in the intercrystalline diffusion zone of ^{57}Co in metal polycrystals and their manifestation in NGR spectra. Only two components are present in emission NGR spectra of all the polycrystalline cubic-lattice metals examined by the new method [1, 2] with ^{57}Co atomic probes. One of these components – the component-1 – decreases rapidly with increasng high temperatures of annealing (in the "intrinsic" interval). This component is due to ^{57}Co atomic probes occupying states localized in the GB core. The other component – the component-2 – increases with increasing high temperatures of annealing (in the "intrinsic" interval). It is caused by ^{57}Co atomic probes occupying states-2 localized outside the grain boundary core. The component-2 remains almost the only one after annealing at the highest temperature, when the component-1 is no longer registered in emission NGR spectra. Thus, among several different states existing in the structure of the grain boundary core and in the immediate vicinity to the grain boundary core, only two discrete types of states are occupied during diffusion of ^{57}Co atomic probes in polycrystalline metals – Al (3sp); V, Cr and Cu (3d); Nb, Mo, Rh, and

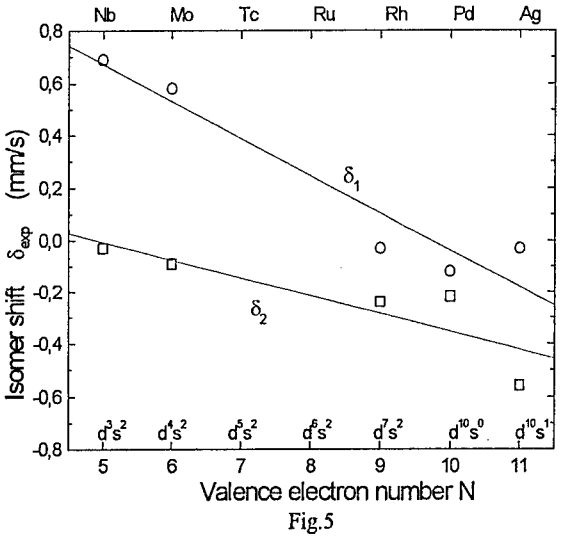

Fig.5

Dependencies of the isomer shifts δ_1 and δ_2 of the NGRS components on the valence electron number N for polycrystalline 4d metals after annealings in the «intrinsic» temperature interval

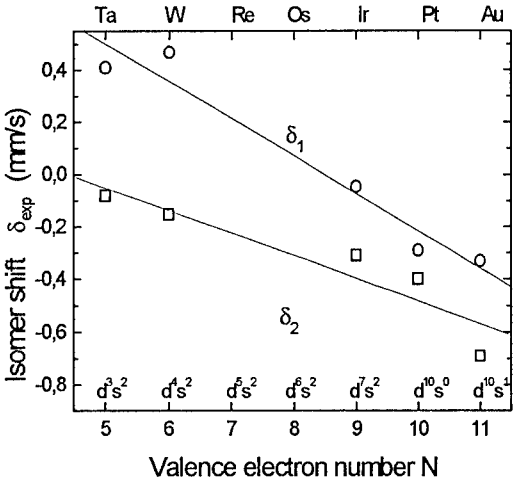

Fig.6

Dependencies of the isomer shifts δ_1 and δ_2 of the NGRS components on the valence electron number N for polycrystalline 5d metals after annealings in the «intrinsic» temperature interval

Thus, among several different states existing in the structure of the grain boundary core and in the immediate vicinity to the grain boundary core, only two discrete types of states are occupied during diffusion of ^{57}Co atomic probes in polycrystalline metals – Al (3sp); V, Cr and Cu (3d); Nb, Mo, Rh, and Pd (4d); Ta, W, Ir, Pt and Au (5d) – examined by our method [1-5]. One of these types is represented by states-2 localized at lattice sites outside the grain boundary core. The other type of states occupied during intercrystalline diffusion – states-1 – is localized in the grain boundary core. The parameters of the component-2, such as the isomer shift, the width of NGRS components and the Debye temperatures, coincide with the corresponding parameters of volume NGR spectra.

III.2. Two qualitative criteria of states-1 localized in the GB core of 5d and 4d matrices where ^{57}Co atomic probes are small-radius impurities. The main criterion, which distinguishes states-1, is the decrease in their occupancy when a single sample with a fixed number of atomic probes in the diffusion zone undergoes isochronous annealings (in the "intrinsic interval"). The component-1 vanishes in the emission NGR spectra (Figs 1 to 4) with growing annealing temperature. One more qualitative criterion of states-1 occupied by ^{57}Co atomic probes appears in 5d and 4d matrices, where the ^{57}Co atomic probes is a small-radius impurity ($R_{Co} < R_{solv}$). In these solvents the isomer shift δ_1 of states-1 is larger than the isomer shift δ_2 of states-2 (Figs 5 and 6). These conditions may arise for ^{57}Co in the grain boundary core of pure metals and in emission NGR spectra only if *^{57}Co atomic probes in the grain boundary core of 4d and 5d matrices are more compressed than at lattice sites of the corresponding matrices*.

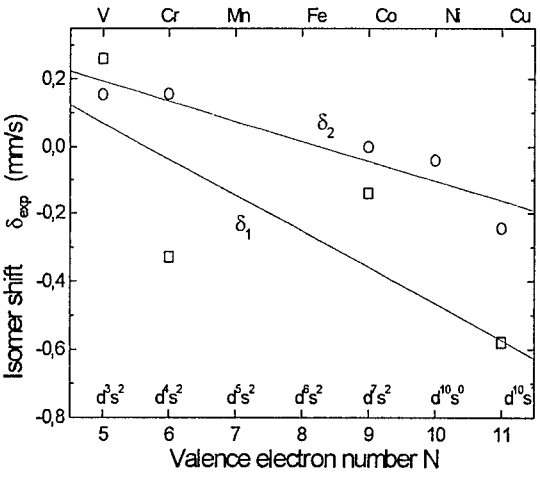

Fig.7

Dependencies of the isomer shifts δ_1 and δ_2 of the NGRS components on the valence electron number N for polycrystalline 3d metals after annealings in the «intrinsic» temperature interval

III.3. Two qualitative criteria of states-1 localized in the GB core of 3d matrices where ^{57}Co atomic probes are not small-radius impurities. Similar to 4d and 5d matrices, the main criterion distinguishing states-1 in 3d metals is the decrease in the populatuion of these states when a single sample with a fixed number of atomic probes in the diffusion zone undergoes isochronous annealings in the "intrinsic interval". The component-1 vanishes in emission NGR spectra with growing annealing temperature. But the other criterion of states-1 in 3d metals differs qualitatively (Fig.7): the isomer shift δ_1 of states-1 is smaller than the isomer shift δ_2 of states-2. In chromium, iron and copper ^{57}Co

atomic probes are not small-radius impurities ($R_{co} \cong R_{matrix}$). Therefore in these solvents ^{57}Co atomic probes can occupy only substitutional sites both in the lattice and in the grain boundary core.

A low atomic density in the grain boundary core is fully reflected in NGR spectra of the corresponding systems: $^{57}Co(Cr)$, $^{57}Co(Fe)$ and $^{57}Co(Cu)$. *The increase in the volume of sites in the structure of the grain boundary core as compared to the volume of lattice sites in 3d metals causes a decrease in the density of both inner-shell and collective s-electrons at the core of ^{57}Co atomic probes occupying sites in the structure of the grain boundary core*.

References.

[1]. S.M. Klotsman, Sov. Phys. Uspech., **33(1),** (1990), p.55.
[2]. V.N. Kaigorodov, S.M. Klotsman, Phys. Rev. B, **49(14)**, (1994), p.9374; *ibid.*, p.9387; *ibid.*, p.9395.
[3]. V.N. Kaigorodov, S.M. Klotsman, S.N. Shlyapnikov, Phys. Metals & Metallogr.,**75(3),** (1995), p.252.
[4]. M.S. Dudarev et al., Phys. Metals & Metallogr., **79(5),** (1995), p.565.
[5]. S.M. Klotsman, M.I. Kurkin, V.N. Kaigorodov, V.V. Dyakin, Phys. Metals & Metallogr., **82(4),** (1996), p.252.
[6]. V.N. Kaigorodov, S.M. Klotsman, M.I. Kurkin, V.V. Dyakin, D.V. Zherebtsov, Phys. Metals & Metallogr., **84(3),** (1997), p.277.
[7]. S.M. Klotsman, M.I. Kurkin, V.N. Kaigorodov, V.V. Dyakin, Phys. Metals & Metallogr., **85(2),** (1998), p.135; ibid., p.212; ibid., p.342.
[8]. V.N. Kaigorodov, .S.M. Klotsman, D.V. Zherebtsov, Phys. Metals & Metallogr., **86(1),** (1998), p.100.

Correspondence: e-mail: klotsman @ imp.uran.ru

Materials Science Forum Vols. 294-296 (1999) pp. 553-556

Models for Grain Boundary Diffusion in Thin Films Under Stress Fields in Different Kinetic Regimes

A. Ostrovsky, N. Balandina and B. Bokstein

Department of Physical Chemistry, Institute of Steel and Alloys,
Leninsky prospect 4, Moscow, Russia

Keywords: Diffusion, Grain Boundary, Stress, Thin Films

Abstract. Models describing the grain boundary (GB) diffusion in thin polycrystalline films for the B- and C- regimes under a stress field are reviewed. A new model is proposed which describes the GB diffusion in the C-regime under stress field for the case of a finite source on the surface which is in contact with the diffusant. Analytical solutions for the source and sink surface kinetics are obtained. The results of the calculations are discussed.

Introduction. A mechanical stress field can influence both the diffusion coefficient and the driving force that is connected with the chemical potential gradient [1]. It has been shown that the value of the stresses in thin metallic films may be as much as 1 GPa and they are usual tensile [2]. Analysis of experimental data on GB diffusion and stress in thin films was performed in [3]. Methods of the stress estimation were suggested. It was shown that the greater the mean value of stresses, the greater the GB diffusion coefficient.
The diffusant flux in an infinitely dilute solution with regard to stress is

$$j = -D(\nabla c - cV\nabla\sigma_{ii}/3RT), \quad (1)$$

where D is the diffusion coefficient, R is the gas constant, T is the absolute temperature, c is the diffusant concentration, V is its partial molar volume, σ_{ii} is the first invariant of the stress tensor. It was proposed that the partial molar volume does not depend on the coordinate.
The diffusion coefficient depends on stress [4]:

$$D(\sigma)=D_0\exp(-[E^0-\sigma_{ii}\Omega/3]/RT), \quad (2)$$

where D_0 is the pre-exponential factor of D, E^0 is the activation energy for the stress-free diffusion, and Ω is the activation volume. Its value is close to the molar volume [5] in face-centred cubic metals.

Model of GB diffusion under a stress field. Let us consider the diffusion in an array of uniformly spaced parallel GBs for a specimen of finite dimension in the direction of diffusion. The GBs are assumed to be homogeneous slabs with constant thickness δ and perpendicular to both film surfaces. They are supposed to be centred at $(n+1/2)d_s$, where n=0, ±1, ±2 and d_S is the GB spacing. The film of the thickness h has a strong adherence to the substrate at y=h and it contacts with the diffusion source at y=0.
The stress of the thin film is in x- and y- directions. The stress tensor components are $\sigma_{xx}=\sigma_{zz}=\sigma$, $\sigma_{yy}=\sigma_{xy}=\sigma_{xz}=\sigma_{yz}=0$. The first invariant of the stress tensor is $\sigma_{ii}=\sigma_{xx}+\sigma_{yy}+\sigma_{zz}=2\sigma$. The stress gradient acts only along the y-axis. The balance equations for bulk and GB diffusion are the following

$$\frac{\partial c}{\partial t} = D(\sigma)\left(\frac{\partial^2 c}{\partial x^2}+\frac{\partial^2 c}{\partial y^2}-\frac{2V}{3RT}c\left(\frac{\partial^2\sigma}{\partial y^2}+\frac{2V}{3RT}\left(\frac{\partial\sigma}{\partial y}\right)^2\right)\right), \quad (3)$$

$$\frac{\partial c_b}{\partial t} = D_b(\sigma)\left(\frac{\partial^2 c_b}{\partial y^2}-\frac{2V}{3RT}c_b\left(\frac{\partial^2\sigma}{\partial y^2}+\frac{2V}{3RT}\left(\frac{\partial\sigma}{\partial y}\right)^2\right)\right)+\frac{2}{\delta}D(\sigma)\left.\frac{\partial c}{\partial x}\right|_{x=(d_s\pm\delta)/2}, \quad (4)$$

where D_b and c_b are the GB diffusion coefficient and the GB concentration, respectively. The initial diffusant concentration everywhere is zero.

Equations 3 and 4 need the boundary conditions on both interfaces and the determination of the stress depth distribution function. Also, depending on the GB diffusion kinetics, this problem can be solved by using different simplifications.

B-regime. Numerical solution and experimental results. In [6] this problem was solved numerically for the B-regime after Harrison [7]. It was assumed that the source is constant: $c(x,0,t)=c_0$. The stress distribution function was linear

$$\sigma_{ii}(y) = \overline{\sigma}_{ii} + \Delta\sigma_{ii}(y/h - 1/2), \quad (5)$$

where $\overline{\sigma}_{ii}$ is the mean value and $\Delta\sigma_{ii}$ is the difference between the values at the source and sink film surfaces. In this case the non-dimensional parameters $S=\overline{\sigma}_{ii}V/(3RT)$ and $G=\Delta\sigma_{ii}V/(3RT)$ describe the effect of stress on GB diffusion.

It was shown that the homogenous (G=0) film tension (S>0) accelerates the resulting diffusion flux. If the film is stretched in every plate along its thickness (G<S/2, S>0), the stress gradient decreases the diffusion flow compared to the homogenous strain (G=0, S>0), but it accelerates if compared with the free stress case (G=0, S=0). In the case of different (G>S/2) sign stress distribution the flux slows down even compared to the stress-free case.

The conclusions from the model are in accordance with our experimental investigation of the stress effect on GB diffusion in Cu-Ni thin films [8]. This is the only work with simultaneous measurements of stress and GB diffusion parameters system. It was shown that for stretched Ni films the GB diffusion coefficients were less than for stress-free films. The stress distribution function for this system was also estimated from the experimental stress measurements and GB diffusion data.

C-regime. Infinite diffusion source. At low temperatures the volume diffusion coefficient is negligibly small compared to the GB diffusion coefficient. This condition allows us to substantially simplify Eqs. 3 and 4. Now we must solve only Eq. 4 without the volume diffusion coefficient containing term. This problem is very current because as it was shown [3, 6] that the lower the temperature of diffusion experiments, the greater the stress effect on GB diffusion. Also the stress relaxation is much slower during the diffusion annealing at low temperatures.

A model describing the GB diffusion in thin polycrystalline films in the C-regime under a stress field was proposed in [9]. The analytical quasi-steady solution for the conditions of linear stress distribution, rapid surface diffusion and constant source was obtained as

$$\overline{c}_S/c_0 = L\left(1 - \exp[-2t_b ML^{1/2}\ln L/(L^2 - 1)]\right), \quad (6)$$

where $\overline{c}_S$ is the average sink surface concentration, $L=\exp(G)$, $M=\exp(S)$, and $t_b=\delta D_b^0 t/(\delta_S h d_S)$ is the non-dimensional time, where D_b^0 is the GB coefficient for stress-free diffusion, δ_S is the effective thickness of the sink surface. It was supposed that the surface diffusion coefficient is much larger than the GB diffusion coefficient, as it is usually for the C-regime [10].

The parameter S, which is a non-dimensional mean stress value, is the kinetic parameter of the problem. It directly influences the effective GB diffusion coefficient and the velocity of the surface saturation. The parameter G, which is a non-dimensional stress gradient related term, is the thermodynamic parameter of the problem. It influences the diffusant chemical potential directly and determines the level of surface saturation.

It was shown that the stresses in a non-homogeneous ($G\neq 0$) stretched (S>0) film decrease the saturation concentration at the sink surface compared to the homogeneous film, and that the greater the stress gradient, the less the saturation concentration. The saturation concentration $\overline{c}_S^{sat}=c_0 \exp(G)$.

The homogenous (G=0) film tension leads to a saturation time decrease compared to the stress free-case and the greater the stress value, the less the saturation time. The effective GB diffusion coefficient may be expressed in this case as $D_b^{ef}=D_b \exp(S)$.

It was shown by using the experimental surface saturation plots from the literature [11, 12] that the difference in the value of the GB diffusion activation energy which can be determined from this model and the stress-free model [13] is about 12 $kJmol^{-1}$.

It is important to note that this quasi-stationary model is only true if G≤0, because in the opposite case the sink surface capacity will be exhausted before the stationary state is achieved and we must solve the non-quasi-stationary problem.
Now following Hwang and Balluffi's [13] approach, let us consider the more realistic finite diffusion source.

C-regime. Finite diffusion source. In the case of a finite diffusion source we can write the boundary condition on the source interface (y=0) as

$$\partial \bar{c}_{S0} / \partial t = -\delta j_y / \delta_{S0} d_S . \quad (7)$$

Here $\bar{c}_{S0}$ is the average source surface concentration and δ_{S0} is the effective thickness of the source surface. It was also supposed that the surface diffusion coefficient is much higher than the GB diffusion coefficient and thus the concentration c_{S0} on the sink surface can be approximated by an average value $\bar{c}_{S0}$ which is a function of time only, i.e. $c_{S0}(x,h,t)=\bar{c}_{S0}(t)$. The initial condition at the source surface is $\bar{c}_{S0}(0)=c_0$. The same boundary condition on the sink surface (y=h) is given by

$$\partial \bar{c}_S / \partial t = \delta j_y / \delta_S d_S . \quad (8)$$

If the GB capacity is much smaller than the surface capacity, under these conditions according [13] a quasi-steady state may be attained in the GB. A quasi-steady state is realised when the change of the GB concentration profile depends on the surface concentrations only. In this case the divergence of the GB diffusion flux is equal to zero. This corresponds to a situation in which at every time enough material is transported to the accumulation surface causing a significant change in concentration, and the GB concentration changes rapidly to maintain a quasi-stationary profile through out diffusion. Consequently, from Eq. 4, we can obtain the next solution

$$c_b = [\bar{c}_S \mathrm{sh}(GY) + \bar{c}_{S0} \mathrm{sh}(G(1-Y))]/\mathrm{sh}(G) . \quad (9)$$

Here Y=y/h is the non-dimensional penetration depth. The concentration distribution in quasi-stationary state does not depend on GB diffusion coefficient. In the absence of stresses the parameter G is equal to zero and Eq. 10 describes the well-known linear y-dependence.
The solutions of Eqs. 1, 2, 7, 8 and 9 system are

$$\bar{c}_S/c_0 = L\left(1-\exp[-2t_b(L+1)ML^{1/2}\ln L/(L^2-1)]\right)/(L+1), \quad (10)$$

$$\bar{c}_{S0}/c_0 = \left(1+L\cdot\exp[-2t_b(\delta_S/\delta_{S0})(L+1)ML^{1/2}\ln L/(L^2-1)]\right)/(L+1). \quad (11)$$

Equation 10 for the sink surface differs from the one for a constant source (Eq. 6) by a factor of 1/(L+1) in the saturation value and by a factor (L+1) in the exponent. In the absence of stresses Eqs. 10 and 11 transform to the Hwang-Balluffi equations [14]. The solutions of Eqs. 10 and 11 are illustrated in Figs. 1 and 2. In all calculations it is assumed that $\delta_{S0}=\delta_S$.

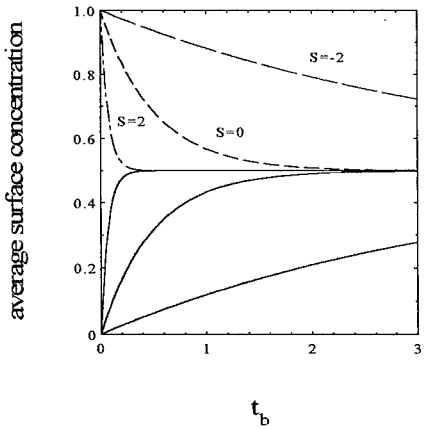

Fig.1. Kinetic plots for the source (dashed lines) and sink (solid lines) surfaces (stress gradient-free film).

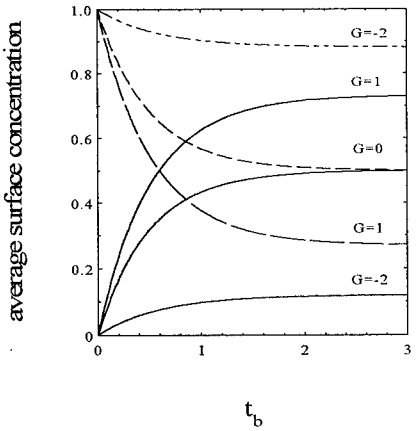

Fig.2. Kinetic plots for the source (dashed lines) and sink (solid lines) surfaces (on average stress-free film).

In Fig. 1 it is suggested that the stress gradient (G=0) in the film is equal to zero. From Fig. 1 we can see that the homogenous film tension (S>0) leads to a acceleration of GB diffusion and to a decreasing saturation time. The homogenous film compression (S<0) leads to a decrease in the GB diffusion rate and to an increase in the saturation time. The saturation level in this case is half of the initial surface concentration. In the case of constant source [9] the saturation concentration for a stress gradient-free film was always equal to the initial surface concentration.
In Fig. 2 it is suggested that the average stress level in the film is equal to zero (S=0). From Fig. 2 we can see that if the stress and concentration gradient have the same sign (G<0) then it decreases the saturation concentration on the sink surface and increases on the source surface. If the stress and concentration gradient have different signs (G>0), then it decreases the saturation concentration on the source surface and increases on the sink surface.
We can see from Eqs. 10 and 11 that the sink and surface saturation concentrations correlate as $\bar{c}_S^{\,sat}/\bar{c}_{S0}^{\,sat}=\exp(G)$ and in the sum give us the initial surface concentration.

C-regime. Processing of the experimental data. This model allows us to receive stress and GB parameters of a system both from the sink surface concentration plots and source ones. It may be convenient for the organisation of an experiment.
From the saturation concentration we can calculate the parameter L

$$L=\bar{c}_S^{\,sat}/\bar{c}_{S0}^{\,sat},\ L=(c_0-\bar{c}_{S0}^{\,sat})/\bar{c}_{S0}^{\,sat} \text{ or } L=\bar{c}_S^{\,sat}/(c_0-\bar{c}_S^{\,sat}) \tag{12}$$

for the case of finite source and

$$L=\bar{c}_S^{\,sat}/c_0 \tag{13}$$

for the case of constant source. We can plot ln L vs. (V/3RT) and from the slope receive exactly the value of $\Delta\sigma_{ii}$.
We note that according to Eqs. 7, 10 and 11 we can plot in a linear form A vs. t where A is now (after L determination) the known parameter of our problem. We can do the GB diffusion experiments on two sets of specimens (such it was in [8] for the B-regime). One set is the fully stress-free and the second one is with stress. This we can receive, for example, by using a different film deposition technique [3]. From the diffusion measurements in stress-free films we can calculate by linear fitting the values $\delta D_b^0/\delta_S$ or $\delta D_b^0/\delta_{S0}$ from the sink or surface kinetic curves consequently. From the diffusion measurements in stressed films we can calculate values $M\delta D_b^0/\delta_S$ or $M\delta D_b^0/\delta_{S0}$. In the case L=1 we must do the extreme transformation in Eqs. 7, 10 and 11 $2\ln L/(L^2-1)\rightarrow 1$. After comparing the results of the two sets of measurements we can plot ln M vs. (V/3RT) and from the slope we can receive exactly the value of $\bar{\sigma}_{ii}$.

Conclusion i) A model describing the GB diffusion in thin films under a stress field for the C-regime in the case of a finite source on the surface is proposed. **ii)** The analytical solutions for the kinetic of the source and sink surfaces are analysed. **iii)** A method for the determination of the stress and GB diffusion parameters from surface accumulation curves is proposed.

References

[1] J. Philibert, Diffusion and Mass Transport in Solids, Édition de Physique (1991).
[2] K.L. Chopra, Thin Film Phenomena, McGraw-Hill, New York (1969).
[3] N. Balandina, B. Bokstein, A. Ostrovsky et. al., Defect Diff. Forum 129-130 (1996), p. 151.
[4] B.S. Bokstein, Diffusion in Metals, Moscow, Metallurgia (1978) (in Russian).
[5] H. Mehrer, Defect Diff. Forum 129-130 (1996), p. 57.
[6] N. Balandina, B. Bokstein, A. Ostrovsky et al., Defect Diff. Forum 143-147 (1997), p. 1499.
[7] L.G. Harrison, Trans. Faraday Soc. 57 (1961), p. 1191.
[8] N. Balandina, B. Bokstein, A. Ostrovsky, Defect Diff. Forum 156 (1998), p. 181.
[9] A. Ostrovsky, Defect Diff. Forum 156 (1998), p. 249.
[10] N. A. Gjostein, Diffusion, edited by H. I. Aaronson, American Society for Metals, Metals Park, Ohio (1973).
[11] S. Danyluk, G.E. McGuire, K.M. Kollwad et. al., Thin Solid Films 25 (1974), p. 483.
[12] P.H. Holloway, G.E. McGuire, J. Electrochem. Soc. 125 (1978), p. 2070.
[13] J.C.M. Hwang, R.W. Balluffi, J. Appl. Physics 50 (1979), p. 1339.

Materials Science Forum Vols. 294-296 (1999) pp. 557-560

Grain Boundary Self-Diffusion of Alloy 800 as Affected by Sulphur, Phosphorous and Carbon

J. Lindemann, K. Hennesen, C. Derder, R. Mast, H. Viefhaus and H.J. Grabke

Max-Planck-Institut für Eisenforschung, Max-Planck-Str. 1, D-40237 Düsseldorf, Germany

Keywords: Alloy 800, Grain Boundary Diffusion, Solution of Suzuoka, Radioactive Tracer Method, Residual Activity, Bulk Diffusion, Phosphorous, Sulphur, Segregation, Creep Process, Creep Cavities, Minimum Creep Strain Rate

Abstract

Using a radioactive tracer method the bulk and grain boundary diffusion of ^{59}Fe was determined in industrial Alloy 800 and melts of Alloy 800 with additional P and S in the temperature range 800 to 1000 °C. The use of the approximation of Suzuoka was confirmed by autoradiographs. In Alloy 800H the activation energy of grain boundary diffusion of ^{59}Fe is (209 ± 17)kJ/mol. Dissolved elements especially P increase the activation energy of the grain boundary diffusion of Fe by their segregation to the grain boundaries.

In addition the influence of the grain boundary diffusion on the growth of creep cavities was investigated in the same materials, and the chemical composition of the creep cavities and grain boundaries were analysed by Auger electron spectroscopy (AES). For Alloy 800 + 0.088 wt-%P an enrichment of about 14 at-%P was observed at the grain boundaries. The addition of P clearly enhances the creep strength of Alloy 800; this can probably be explained by precipitation of $Cr_{23}C_6$ on the grain boundaries during the creep process.

Introduction

Alloy 800 is an austenitic Fe-Ni-Cr steel which combines relatively high creep strength with resistance against hot gases and combustion products. Under stress conditions at high temperatures, a possible reason for the failure of Alloy 800 is intergranular creep fracture initiated by the formation and growth of creep cavities at the grain boundaries. Therefore, not only the Fe-diffusion in Alloy 800 was investigated but also the creep process of Alloy 800.

Special grades of Alloy 800 known as 800H, 800HT and 800LC differ in the concentrations of these elements. These industrial specifications have been investigated, and in addition further melts containing P or S were prepared and studied. The chemical composition of the materials is shown in Table 1.

TABLE 1: Chemical composition (wt-%) of the investigated materials and obtained grain sizes (µm)
Fe: remainder

	Ni	Cr	Ti	Al	C	P	S	Mn	grain sizes
Alloy 800H	30.2	19.7	0.34	0.29	0.074	0.010	<0.001	0.78	90 - 110
Alloy 800HT	30.4	19.6	0.51	0.45	0.090	0.010	<0.001	0.73	110 - 130
Alloy 800LC	32.1	19.9	0.48	0.31	0.016	0.017	0.004	0.69	70 - 90
Alloy 800+ P	29.8	19.6	0.35	0.30	0.069	0.088	0.002	0.70	35 - 45
Alloy 800+ S	29.7	19.7	0.35	0.30	0.069	0.014	0.041	0.70	35 - 45

Recrystallization annealing was conducted at 1150 °C for 30 min with a subsequent water quenching was chosen. For the stabilisation of the grain sizes and to reach equilibrium segregation, the materials were aged at 800 °C for 100h; the grain sizes are also listed in Table 1.
From these materials samples were prepared for diffusion, segregation and creep measurements. For diffusion measurements cylindrical samples (∅=11.9mm, h=4.0mm) were coated electrolytically with Fe^{59} as radioactive tracer. After the diffusion annealing (800 to 1000 °C) thin layers of the specimens were successivly abraded and the residual activity was determined to obtain penetration profiles of the tracer. Auger-measurements were carried out with fracture samples to check if grain boundary segregation of elements takes place. Therefore cylindrical notched specimens were cooled to about -120 °C, then fractured by impact in the UHV chamber of the spectrometer and analysed. Creep experiments were conducted at constant temperature (800°C) under constant load (σ= 60, 80, 100 MPa) using creep samples prepared according to DIN 50118.

Results and discussion

a) Diffusion measurements

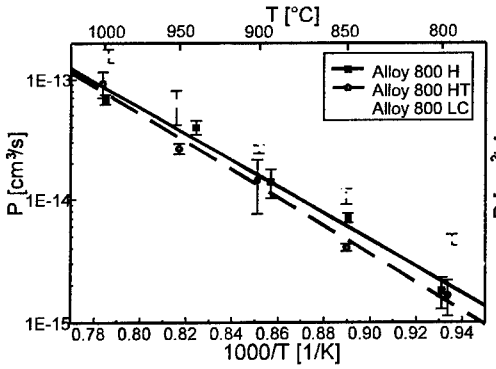

Fig 1a: Arrhenius-plot of grain boundary diffusion coefficients of Fe in Alloy 800H, Alloy 800HT and Alloy 800LC

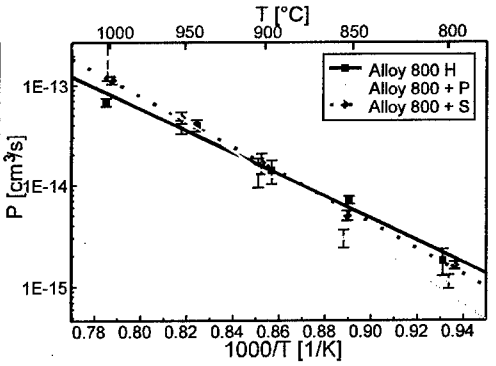

Fig 1b: Arrhenius-plot of grain boundary diffusion coefficients of Fe in Alloy 800H, Alloy 800+P and Alloy 800+S

The residual activity β-counts of the diffusion samples can be related to the tracer concentration in the given layer using the approximation of Borg and Birchenall [1]. To distinguish between volume and grain boundary diffusion regions autoradiographs were taken in different penetration depths. A depletion of the radiotracer above the grain boundaries was observed [2]. To obtain grain boundary coefficients D_{gb} from the penetration profiles the approximation of Suzuoka [3,4] was used; this evaluation method considers the depletion of the tracer on the surface.
The measured grain boundary coefficients $P=k\cdot\delta\cdot D_{gb}$ (k: segregation factor; δ=0.5 nm grain boundary width) for Fe in Alloy 800 are plotted in Fig. 1a,b as Arrhenius-plots. The following relations for the triple product P were determined:

Alloy 800H $P\left(cm^3s^{-1}\right)=(3.1\pm1.8)\cdot10^{-5}cm^3s^{-1}\cdot\exp\left(-(209\pm17)kJ\cdot mol^{-1}/RT\right)$

Alloy 800HT $P\left(cm^3s^{-1}\right)=(8.9\pm4.2)\cdot10^{-5}cm^3s^{-1}\cdot\exp\left(-(221\pm14)kJ\cdot mol^{-1}/RT\right)$

Alloy 800LC $P\left(cm^3s^{-1}\right)=(1.3\pm0.5)\cdot10^{-5}cm^3s^{-1}\cdot\exp\left(-(194\pm11)kJ\cdot mol^{-1}/RT\right)$

Alloy 800+S $P\left(cm^3s^{-1}\right)=(9.9\pm2.4)\cdot10^{-4}cm^3s^{-1}\cdot\exp\left(-(242\pm7)kJ\cdot mol^{-1}/RT\right)$

Alloy 800+P $P\left(cm^3s^{-1}\right)=(9.8\pm7.3)\cdot10^{-2}cm^3s^{-1}\cdot\exp\left(-(288\pm22)kJ\cdot mol^{-1}/RT\right)$

The diffusion coefficients of Fe in Alloy 800 closely fit together with measurements in similar Fe-Ni-Cr alloys [5]. The dissolved elements P, S and C increase the activation energy of grain boundary diffusion of Fe and so delay the grain boundary diffusion in Alloy 800 at least in the low temperature range. This can be explained by the grain boundary segregation of the dissolved

elements. The relatively high activation energy in undoped Alloy 800 is caused by the high C-content, which can be derived since the same value was obtained for measurements in α-iron doped 140 ppm C [6].

b)Segregation measurements

Surface active elements should influence the grain boundary diffusion of Fe in two ways. They vary the activation energy for interchange of sites and they cover the Fe atoms at the grain boundaries. Therefore, grain boundary diffusion coefficients are decreased by k: $P=k\cdot\delta\cdot D_{gb}$.
Analysing the 5 materials, dimpled fracture was observed exclusively in Alloy 800LC and predominantly in Alloy 800H and HT; any possible enrichment at the grain boundaries is not observable in these alloys. Alloy 800+P shows mainly intergranular fracture (Fig. 5); Auger spectra taken on the grain surfaces clearly demonstrate the enrichment of P (Fig. 2). The P-concentration at the grain boundaries is in the range of 14 at-% of a monolayer. In Alloy 800+S both intergranular fracture and dimpled fracture was found. Fig. 3 shows an enrichment of Ti, S and C with constant peak-to-peak-height-ratio. By TEM/EDX measurements and diffraction pattern these enrichments were identified as precipitation of $Ti_4S_2C_2$ (Fig. 6).

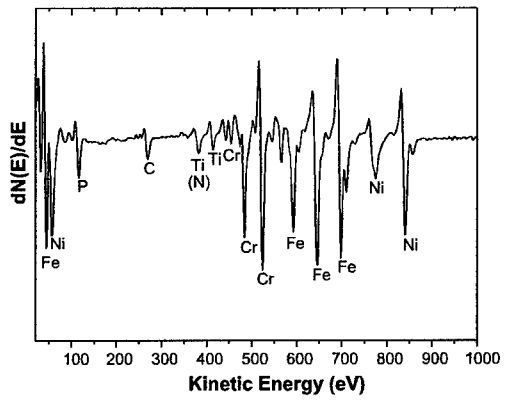

Fig. 2: Auger-analysis of a grain boundary in Alloy 800 + 0.09 wt-% P

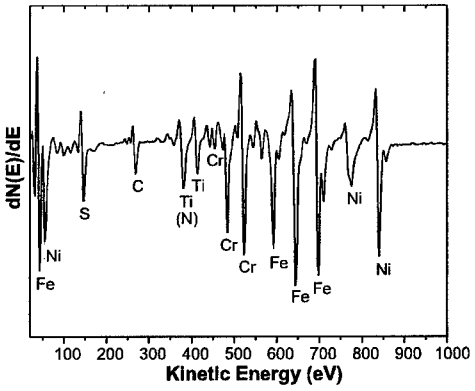

Fig. 3: Auger-analysis of a grain boundary in Alloy 800 + 0.04 wt-% S

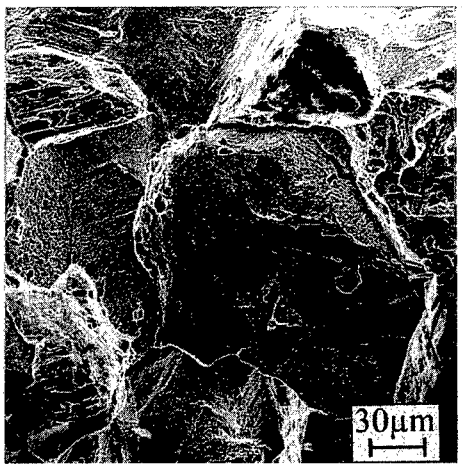

Fig. 5: SEM of a typical intergranular fracture in Alloy 800 + 0.09 wt-% P

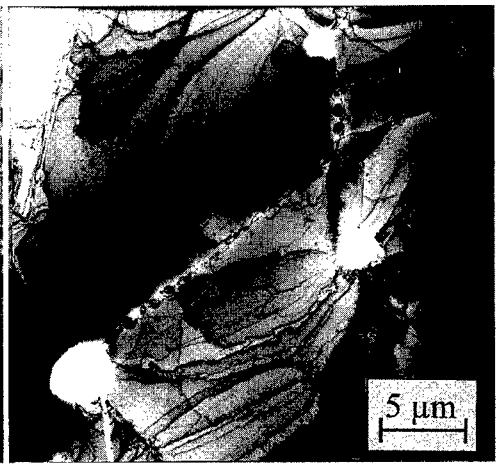

Fig. 6: $Ti_4C_2S_2$-precipitation at grain boundary facet in Alloy 800 + 0.04 wt-% S ;TEM (bright field)

c) Creep measurements

Creep experiments showed that the addition of P clearly enhances the creep strength of Alloy 800. It decreases the minimum creep strain rates up to two orders of magnitude, enhances the creep rupture time, and decreases the creep rupture strain (Table 2, Fig. 7). After creep rupture the samples were analysed with AES and TEM. Addition of P reduces the creep cavity formation; in the creep cavities and at the grain boundaries in Alloy 800+P $Cr_{23}C_6$-precipitates and P-segregation were observed. By the fcc-structure of the $Cr_{23}C_6$ precipitates at the grain boundaries the coherence to the matrix seems to be increased. However, the main reason for the better creep strength of Alloy 800+P is the precipitation of platelet phosphides in the matrix (Fig. 8). In the creep cavities of the other materials no enrichment of any element was observed; addition of S enhances the creep cavity formation.

TABLE 2: minimum creep strain rates ε'_{min} [1/s] obtained at 800 °C and different stresses σ

	Alloy 800H	**Alloy 800HT**	**Alloy 800LC**	**Alloy 800+S**	**Alloy 800+P**
σ= 100 MPa	1.8 E-05	1.5 E-05	3.0 E-05	1.4 E-05	1.3 E-07
σ= 80MPa	4.2 E-06	3.1 E-06	7.8 E-06	3.5 E-06	9.7 E-09
σ= 60 MPa	2.8 E-07	3.1 E-07	1.4 E-06	3.9 E-07	2.8 E-09

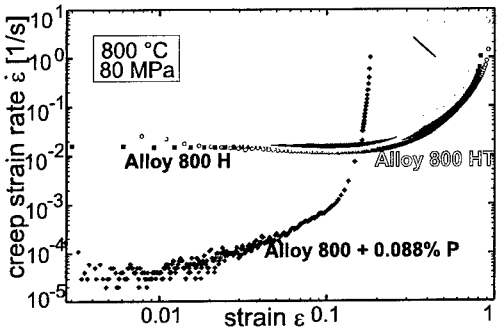

Fig 7: Creep strain rates of Alloy 800 at 800°C and σ=80 MPa

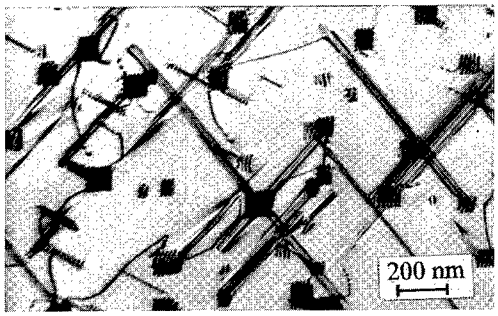

Fig.8: Precipitates (platelets phosphides) in Alloy 800 +0.09wt% P; TEM (bright field)

Conclusions

S and especially P enhance the activation energy of grain boundary diffusion of Fe in Alloy 800. In Alloy 800+S this is due to precipitation of $Ti_4S_2C_2$ at the grain boundaries. In Alloy 800+P, P segregates to the grain boundaries and $Cr_{23}C_6$ enriches at the grain boundaries.
Addition of P clearly enhances the creep strength. This is due to fcc-structured $Cr_{23}C_6$ precipitation at the grain boundaries and due to precipitation of phosphides in the matrix.
No connection between grain boundary diffusion and creep cavity formation could be observed: addition of S enhances and P reduces the creep cavity formation.

References

[1] R.J. Borg, C. Birchenall, Trans. Met. Soc. AIME, 218 (1960) 980.
[2] J. Lindemann, K. Hennesen, R. Mast, H. Viefhaus, H.J. Grabke; Proceedings NIM Münster March 1998; GDMB Clausthal-Zellerfeld (1998) 115.
[3] T. Suzuoka, J. Phys. Soc. of Japan, 19 (1964) 839.
[4] T. Suzuoka, Trans. Jap. Inst. Met., 2 (1961) 25.
[5] J. Rothman, L.J. Nowicki, G.E. Murch; J. Phys. F 10(3) (1980) 383.
[6] H. Hänsel, L. Stratmann, H. Keller, H.J. Grabke; Acta Met., 33 (1985) 659.

Materials Science Forum Vols. 294-296 (1999) pp. 561-564

Grain-Boundary Diffusion of Bi in Cu Bicrystals

R. Monzen and T. Okamoto

Department of Mechanical Systems Engineering, Kanazawa University,
2-40-20 Kodatsuno, Kanazawa 920-8667, Japan

Keywords: Boundary Diffusion, Cu Bicrystal, Bi, [011] Twist Boundary, [001] Symmetric Tilt Boundary, [001] Twist Boundary, Boundary Energy

Abstract–The diffusion of Bi along various [011] and [001] twist and [001] symmetric tilt boundaries of Cu has been investigated as a function of the misorientation angle. For the three types of grain boundary, a close correlation is found between the diffusivity of a boundary and the energy of the boundary. The minimum of the boundary diffusivity occurs where the cusps of the boundary energy exist. The larger the degree of disorder in the atomic arrangement at a boundary, the higher is the boundary diffusivity. The diffusion in the [011] twist boundaries takes place more easily than that in the [001] twist boundaries.

1. Introduction

It has been well established that grain-boundary diffusion is dependent strongly upon the character of individual boundaries. For example, boundary diffusion has been reported to be easy on random boundaries but difficult on coincidence-site boundaries with low values of Σ, such as 3 and 5 [1-4]. It is often presumed that the atomic arrangement along high-Σ boundaries is more random and disturbed than that along low-Σ boundaries. However, since the Σ values are independent of the inclination of boundary plane, they may only be a rather qualitative parameter to characterize the grain boundaries.

On the other hand, Watanabe [5] has pointed out that the boundary character should be more obviously expressed using grain-boundary energy rather than the Σ values. An excellent correlation exists between the boundary energy and a quantity characterizing a boundary-induced phenomenon. In fact, we see such a correlation for the diffusion penetration depth of Zn in [011] symmetric tilt boundaries of Al, reported by Herbeuval *et al.* [1].

The boundary diffusion along [001] symmetric tilt [2,3,6,7] and twist [3] boundaries in fcc metals, such as Al and Cu, also was examined as a function of the misorientation angle by several investigators. However, the misorientation dependences of the diffusivities in [001] tilt boundaries are different from each other. In this study, we have investigated the diffusivity of Bi in various [001] symmetric tilt and [001] and [011] twist boundaries of Cu from observations of the intergranularly fractured surfaces of Bi-doped Cu bicrystals. The segregation of Bi on grain boundaries of Cu is well known to result in embrittlement [8,9]. For the three types of grain boundary, a good correlation has been found between the boundary energy and the boundary diffusivity.

2. Experimental

Cu bicrystals containing different [011] and [001] twist and [001] symmetric tilt boundaries with misorientation angles of θ=13~89°, θ=10~44° and θ=14~80°, respectively, were grown in a graphite mold by the Bridgman method using two-seed crystals. Hereafter, the bicrystal with the misorientation angle θ and its grain boundary will be called θ bicrystal and θ boundary, respectively. The

bicrystals were spark-cut into tensile specimens (5mm×10mm×30mm) with a straight boundary oriented perpendicular to the tensile axis. After confirming the misorientation angles, they were packed into alumina tubes with a mixture of Cu (10 parts), Al_2O_3 (10 parts) and Bi (1 part) powders and were Bi-doped at 1223 K for 48 h in an Ar atmosphere. After tensile tests were performed at room temperature, the intergranular-fracture surfaces were observed using a scanning electron microscope (SEM) and an optical microscope.

3. Results and Discussion

Figure 1 shows optical micrographs of the fracture surfaces of Bi-doped Cu bicrystals with (a) θ=31° and (b) θ=62° [001] symmetric tilt boundaries. The brittle and ductile regions are evidently seen on the fracture surfaces. It is clear that the 62° boundary has a lower diffusivity than the 31° boundary does. From Fig. 1(b), it also is noted that the diffusion along the tilt axis of [001] is much faster than along the direction normal to it.

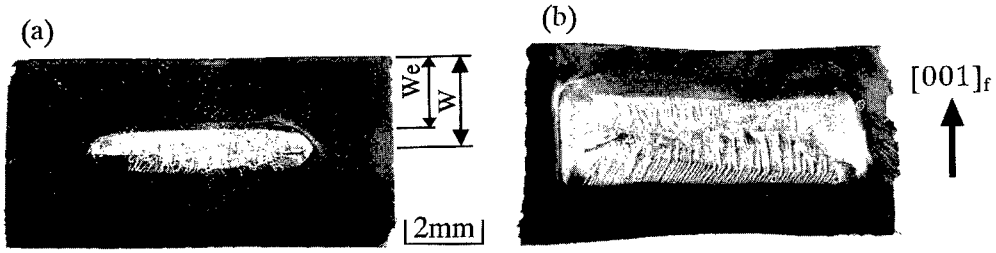

Fig. 1: Optical micrographs of the intergranularly fractured surfaces of Bi-doped Cu bicrystals with (a) θ=31° and (b) θ=62° [001] symmetric tilt boundaries.

The fraction of brittle fracture surface W_e/W, defined in Fig. 1, was measured by SEM. In Fig. 2, the values of W_e/W are given against the misorientation angle θ for [011] twist boundaries. About five bicrystal specimens were tensile tested for each experimental value. The grain-boundary diffusivity of Bi in Cu bicrystals depends strongly on the misorientation angle or boundary character. The cusps at θ=51° (Σ11), θ=59° (Σ33C), θ=71° (Σ3) and θ=83° (Σ57B) are clearly seen. To our knowledge, no experiments have been reported on the effect of θ on the diffusion in [011] twist boundaries.

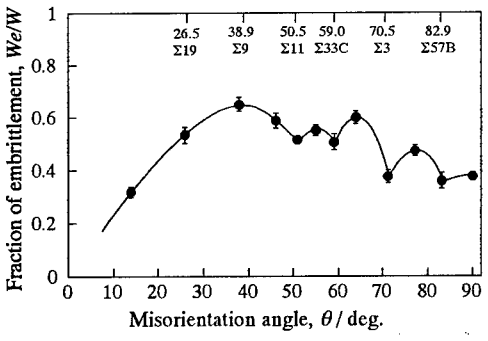

Fig. 2: Fraction of the brittle relief W_e/W on the fracture surface morphology, plotted against the misorientation angle θ for [011] twist boundaries.

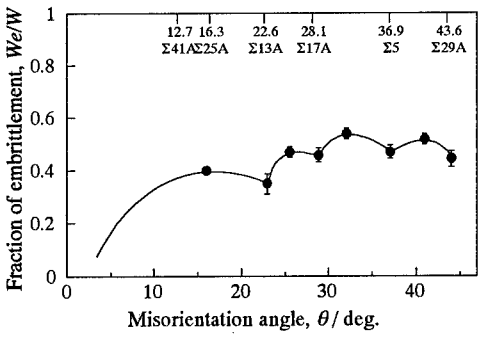

Fig. 3: W_e/W plotted against the misorientation angle θ for [001] twist boundaries.

Figure 3 is the $W_e/W-\theta$ curve for the [001] twist boundaries. Since transgranular fracture occurred in 10° and 13° bicrystals, data on these bicrystals are not included in this figure. The existence of cusps at θ=23° (Σ13A) and possibly θ=44° (Σ29A) is noticed, as observed by Biscondi [3] who measured the diffusivity of Zn in boundaries of Al. In addition, two more cusps at θ=28° (Σ17A), θ=37° (Σ5) are found. Furthermore, comparison with Fig. 2 reveals that, in general, Bi atoms diffuse more readily along the [011] twist boundaries than along the [001] twist boundaries. This is contrast to the result by Biscondi [3] that diffusion along [011] symmetric tilt boundaries is slower than that along [001] tilt boundaries.

Figure 4 shows the diffusivity in [001] symmetric tilt boundaries against the misorientation angle. // and ⊥ are for the diffusion directions parallel and perpendicular to the tilt axis. Transgranular fracture occurred in 80° bicrystals. The dependence of W_e/W on θ is not monotonous; there are four cusps at θ=28° (Σ17), θ=37° (Σ5), θ=53° (Σ5) and θ=62° (Σ17). The variation of the diffusivity with θ does not follow the same tendency as the diffusion of Zn [2,3], Ni_{63} [6] and Bi [7] in [001] symmetric tilt boundaries of Al, Ni and Cu, respectively. Aleshin *et al.* [2] measured the diffusivity of Zn in Al boundaries with θ=10~45° and found minima at θ=23.5°, 28.5° and 37°. The boundary diffusivity–θ curve reported by Biscondi [3] showed no clear cusps. The dependence of penetration on θ in Ref.[6] was monotonous and revealed no cusps. Yukawa and Sinnott [7] measured the penetration depth of Bi in Cu boundaries parallel to the tilt axis of [001]. The penetration was found to be more difficult for 22°, 25°, 63° and 72° boundaries close to Σ13 (θ=23°), Σ17 (θ=62°) and Σ25 (θ=74°) boundaries in comparison with other high-angle boundaries. From Fig. 4, it is also noted that Bi atoms diffuse more rapidly along the direction parallel to the tilt axis. The anisotropy decreases as the misorientation angle increases, and it exists up to $\theta\cong$30°. This is analogous to the results previously obtained by diffusion measurements of Zn [3], Ag_{110} [10] and Ag_{110} [11] into [001] symmetric tilt boundaries of Al, Cu and Ag, respectively. Furthermore, comparison with Fig. 3 shows that the tilt boundaries have higher diffusivities than the twist boundaries. This is in agreement with the result reported by Biscondi [3] that diffusion in [001] symmetric tilt boundaries is much faster than in [001] twist boundaries.

A larger degree of disorder in the atomic arrangement along a grain boundary leads to a larger boundary energy. Thus, grain-boundary diffusion in a high-energy boundary is expected to occur more easily than that in a low-energy boundary. In fact, the shapes of the curves in Figs. 2 to 4 are generally similar to those of the boundary energy γ–θ curves for Cu reported by Miura *et al.* [12] and Mori *et al.* [13]. The γ–θ curves show cusps at θ=51° (Σ11), θ=59°(Σ33C), θ=71° (Σ3) and θ=83° (Σ57B), θ=13° (Σ41A), θ=23° (Σ13A), θ=28° (Σ17A), θ=37° (Σ5) and θ=44° (Σ29A), and θ=28° (Σ17), θ=37° (Σ5), θ=53° (Σ5), θ=62° (Σ17) and θ=74° (Σ25) for [011] and [001] twist [12] and [001] symmetric tilt [13] boundaries, respectively. Therefore we conclude that, the smaller the degree of disorder in the atomic arrangement at a boundary, the lower is the boundary diffusivity.

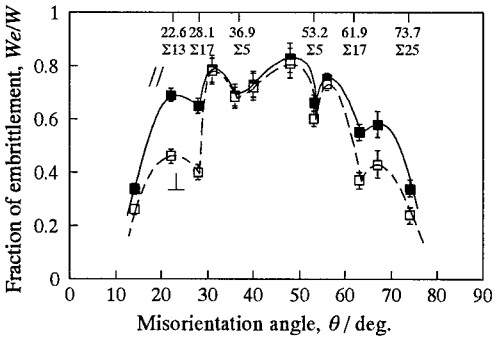

Fig. 4: W_e/W plotted against the misorientation angle θ for [001] symmetric tilt boundaries.

Grain boundaries may also be described in terms of the grain-boundary free volume V_f, which is the expansion in volume caused by the creation of a grain boundary in a perfect crystal [14]. Such an expansion provides excess opening for grain-boundary diffusion. Thus, it is inferred that, the larger

the V_f value, the larger is the W_e/W value. However, the W_e/W values are inconsistent with the calculated values of V_f for the [001] symmetric tilt [15] and twist [16] boundaries of Al and Cu. For example, the W_e/W value for the 53° ($\Sigma 5$) tilt boundary is larger than that for the 62° ($\Sigma 17$) tilt boundary as seen in Fig. 4, indicating that V_f for the former should be larger than that for latter. However, the calculated V_f values show the opposite trend; V_f=0.16 and 0.23 for the former and latter, respectively.

4. Summary

The diffusion of Bi along various [001] symmetric tilt and [001] and [011] twist boundaries of Cu has been measured by observing the intergranular-fracture surfaces of Bi-doped Cu bicrystals. The results obtained are as follows:

(1) The diffusivity of a boundary is found to show a close correlation with the energy of the boundary. The boundary diffusivity becomes minimum at θ=28° ($\Sigma 17$), θ=37° ($\Sigma 5$), θ=53° ($\Sigma 5$) and θ=62° ($\Sigma 17$), θ=23° ($\Sigma 13A$), θ=28° ($\Sigma 17A$), θ=37° ($\Sigma 5$) and θ=44° ($\Sigma 29A$), and θ=51° ($\Sigma 11$), θ=59° ($\Sigma 33C$), θ=71° ($\Sigma 3$) and θ=83° ($\Sigma 57B$) for [001] symmetric tilt and [001] and [011] twist boundaries, respectively. A lower-energy boundary has a lower diffusivity.

(2) The diffusion along the [011] twist boundaries occurs more readily than that along the [001] twist boundaries.

References

[1] I. Herbeuval, M. Biscondi and C. Goux, Mém. Sci. Rev. Métall. 70 (1973), p. 39.
[2] A. N. Aleshin, B. S. Bokshtein and L. S. Shvindlerman, Sov. Phys. Sol. State 19 (1977), p. 2051.
[3] M. Biscondi, in Physical Chemistry of the Solid States: Applications to Metals and Their Compounds (edited by P. Lacombe), Elsevier Science Publishers, Amsterdam (1984), p. 225.
[4] X. M. Li and Y. T. Chou, Acta Mater. 44 (1996), p. 3535.
[5] T. Watanabe, Trans. Japan Inst. Metals, Suppl. 27 (1986), p. 73.
[6] W. R. Upthegrove and M. J. Sinnott, Trans. Amer. Soc. Metals 50 (1958), p. 1031.
[7] S. Yukawa and M. J. Sinnott, Trans. Amer. Inst. Mining Eng. 215 (1959), p. 338.
[8] A. Fraczkiewicz and M. Biscondi, J. Phys. Paris 46 (1985), p. 497.
[9] M. Menyhard, B. Blum and C. J. McMahon Jr, Acta Metall. 37 (1989), p. 549.
[10] S. R. L. Couling and R. Smoluchowski, J. Appl. Phys. 25 (1954), p. 1538.
[11] R. E. Hoffman, Acta Metall. 4 (1956), p. 97.
[12] H. Miura, M. Kato and T. Mori, J. Phys. Paris 51 (1990), p. 263.
[13] T. Mori, T. Ishii, M. Kajihara and M. Kato, Phil. Mag. Lett. 75 (1997), p. 367.
[14] H. B. Aaron and G. F. Bolling, Surf. Sci. 31 (1972), p. 27.
[15] D. A. Smith, V. Vitek and R. C. Pond, Acta Metall. 25 (1977), p. 475.
[16] P. D. Bristowe and A. G. Crocker, Phil. Mag. A 38 (1978), p. 487.

Corresponding author: R. Monzen, Fax: +81-76-234-4679, E-mail: monzen@t.kanazawa-u.ac.jp

Materials Science Forum Vols. 294-296 (1999) pp. 565-568

Computer Programs for Simulation of Growth Multiphase Diffusion Layers

S. Gut

University of Mining and Metallurgy, Al. Mickiewicza 30, Kraków, Poland

Keywords: Diffusion, Computer Simulation, Carburizing, Nitriding

ABSTRACT: A mathematical model of processes taking place during a thermo-chemical heat treatment is presented. The paper focuses on the analysis of phenomena which occur when a diffusing element forms with an alloy a phase diagram with solid solutions. It was assumed that the concentration of elements on the phase boundaries in the diffusion layer are consistent with the phase diagram. The effect of the surface reactions and of the diffusion coefficient values on the kinetics of the growth of various phases is discussed in the light of solutions of Fick's second law. Using computer simulation a process of new phases formation on the surface is analyzed.

1. INTRODUCTION

During a thermo-chemical treatment changes in the chemical composition in the sub-surface layers of alloys are affected by the surrounding atmosphere. Diffusion layer structure, the mechanism and the kinetics of diffusion processes observed for a given alloy depend mainly on the alloy - diffusing element phase diagram. For a technologist it is very important to know not only the phase composition of the diffusion layer but also the concentrations of the diffusing element in each phase. The determination of the distribution of the elements following a thermo-chemical treatment by using an analytical solution of Fick's second law can only be achieved in very simple cases [1]. Predicting results of a thermo-chemical treatment is then possible only by applying numerical methods.

2. MATHEMATICAL MODEL OF DIFFUSION PROCESSES IN MULTIPHASE DIFFUSION ZONE

The concentration distribution of the diffusing element across the diffusion layer is given by an equation known in the literature as Fick's second law:

$$\frac{\partial c}{\partial t} = \frac{\partial}{\partial x}\left(D(x)\frac{\partial c}{\partial x} \right) \qquad (1)$$

where: c – the concentration, x – the distance, t – the time,
D – the diffusion coefficient.

In a case of thermo-chemical treatment this equation can be solved with two type of boundary conditions :

1. concentration of the diffusing element on the surface of the alloy is constant and equals the concentration of the element in the atmosphere remaining in an equilibrium with the alloy
2. the flux of atoms from the atmosphere to the alloy J, is proportional to the difference between their activity in the atmosphere a_a and in the alloy a_s:

$$J = \beta (a_a - a_s) \tag{2}$$

where: β - atmospheric transfer coefficient

The latter condition is of more practical use since it enables an evaluation of the effect of the surface reaction rate on the kinetics of the growth of the layer.
The following assumptions have been made in the mathematical model of the formation of the diffusion layer:

- the flux of the atoms from the atmosphere to the alloy is equal to the flux of atom diffusing into the alloy (a boundary condition of the third kind)

$$J = \beta (a_a - a_s) = -D\frac{\partial c}{\partial x} \tag{3}$$

- phases of a higher concentration, i.e. β, γ, are formed when the concentration on the surface exceeds the solubility limit in the phase of the lower concentration
- the kinetics of processes taking place at the interphase boundaries in the solid phase is driven by the diffusion, hence the location of the interphase boundary can be determined from the difference of fluxes of the diffusing element at that boundary [2]

$$\left(c^{\beta} - c^{\alpha}\right)\frac{d\xi}{dt} = -D^{\beta}\frac{\partial c^{\beta}}{\partial x} + D^{\alpha}\frac{\partial c^{\alpha}}{\partial x} \tag{4}$$

where: c_α , c_β - the concentrations of the element in the α and β phases at the interphase boundary,
ξ - the α/β interface location

Having regard to such initial and boundary conditions, the concentration distribution across the diffusion layer, the thickness of individual phases within the layer and the concentration on the alloy surface have been calculated using numerical methods. Calculations have been made using the finite difference method [3]. An application running under Microsoft Windows 95™ has been created to simulate these processes by numerical methods. The application has a friendly user interface for both data input and a visual presentation of results. The input data are: diffusion coefficients and solubility limits in existing phases, as well as the temperature and the activity of the atmosphere. The results (the distribution of the elements in the diffusion layer, the thickness of layers and the elements' concentrations on the surface) are displayed on the screen. The paper demonstrates the use of the application to predict the concentration profiles and the layer growth rate during carburizing and nitriding of steel.

3. DESCRIPTION OF COMPUTER PROGRAMS

To simulate the steel carburizing process a computer program running under Windows 95 ™ has been created (available at http://galaxy.uci.agh.edu.pl/~gut). The carbon distribution across the carburized layer has been determined by numerical methods. Fick's second law has been solved by using the finite difference method (Equation 1). The calculations take into account the dependence of the carbon diffusion coefficient values on the carbon concentration and the presence of alloy elements in austenite. For any given process of steel carburization, the program enables the user to monitor the effect of the following:

- the diffusing saturation time on the distribution of carbon across, the diffusion layer, and on the kinetics of the layer build-up,
- the surface reaction rate on the thickness of the diffusion layer, and on an element's concentration at the surface of the steel,
- the temperature on the rate of the diffusion layer's growth,
- mass increase of the treated object as a function of the treatment time.

The following parameters are used as input for the calculations:

- the chemical composition of the steel subjected to carburization process and the carbon transfer coefficient,
- the changes in temperature and in the carbon potential of the atmosphere as a function of the treatment time.

Both the data and the calculation results are displayed on the screen by graphing the following parameters as a function of the treatment time:

- the temperature and the carbon potential of atmosphere,
- the carbon concentration on the steel surface,
- the thickness of the carburized layer up to the following concentrations - 0.3%C, 0.35%C and 0.4%C,
- both the carbon distribution and the hardness gradient across the carburized layer (the hardness gradient is determined assuming that the samples are quenched directly upon removal from the carburizing chamber and any effect on the hardness arising from the alloy's elemental composition or quenching rate is ignored).
-

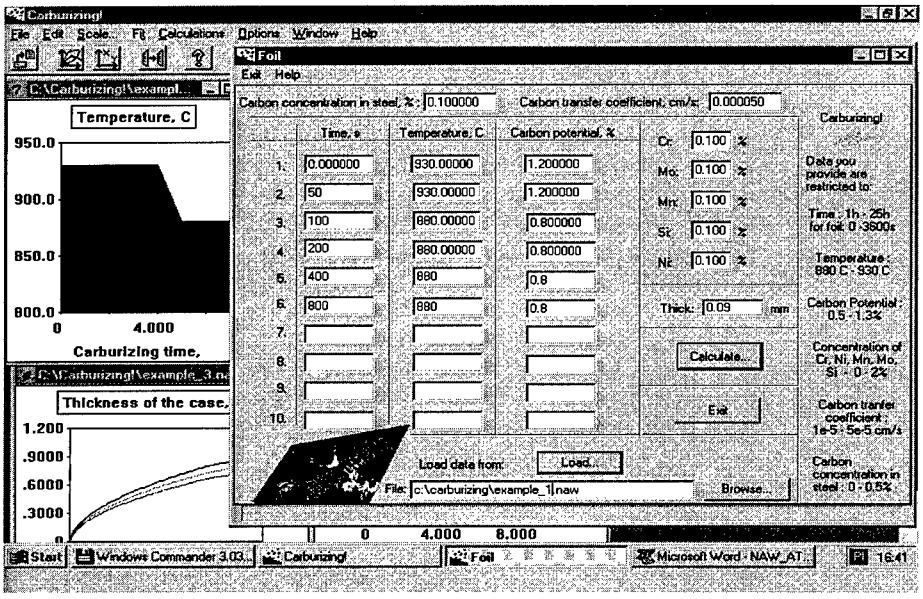

Fig. 1 Data input dialog

The program can be used to optimize the steel carburization process. This can be achieved by selecting appropriate parameter values which will lead to the desired carbon concentrations throughout the diffusion layer. The calculations may be performed for semi-infinitive samples as well as for samples of simple shapes, i.e., a cylinder, plate or foil. In the latter case, we can

use the process of carburizing a foil with a small carbon content to determine the carbon transfer coefficient from the atmosphere to steel by measuring the kinetics of the carburizing process. Fig. 1 illustrates the data input dialog box.
Second program - "Nitriding!" can be used to predict the distribution of nitrogen in the nitrided layers of steel and for the visual presentation of the calculation results [4]. The results (the distribution of the elements in the diffusion layer, the thickness of layers and the elements' concentrations on the surface) are displayed on the screen (Fig. 2). This application can be an excellent teaching aid in a course of materials science for students majoring in mechanical engineering or material sciences.

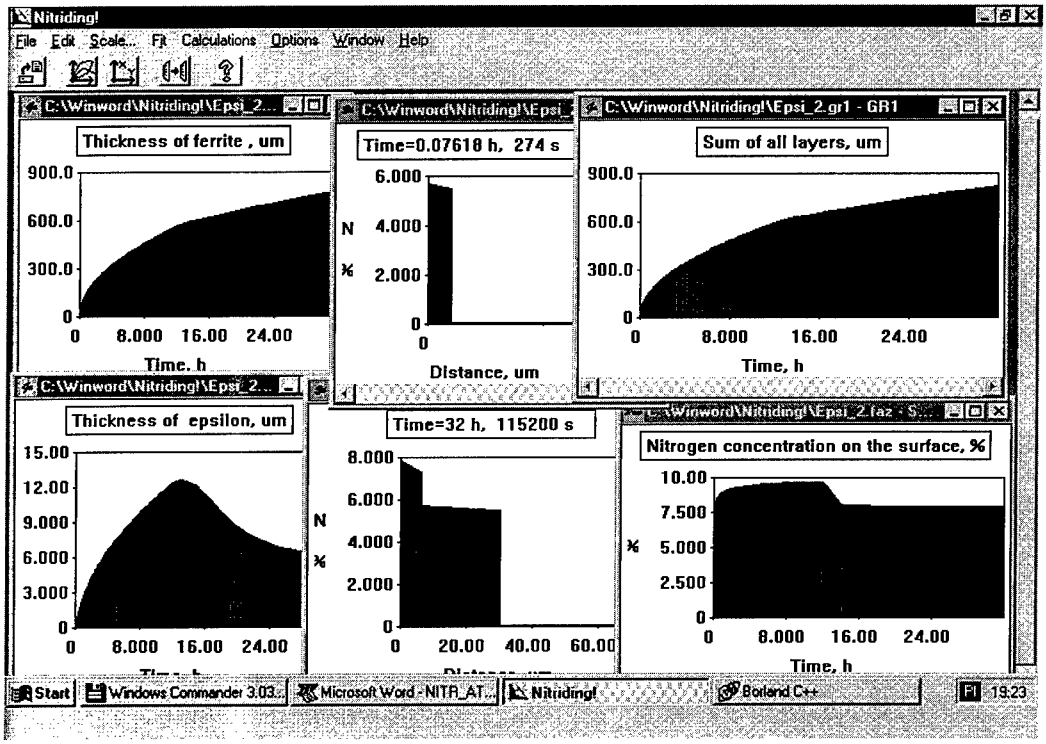

Fig. 2 Distribusion of nitrogen across nitrided layers, layers thickness and nitrogen concentration on the surface (available at http://galaxy.uci.agh.edu.pl/~gut).

Acknowledgments This work was supported by Polish State Committee for the Scientific Research under grant No. 7 T08D 032 13.

REFERENCES

1. W. Jost, Diffusion in Solids, Liquids, Gases, Academic Press 1965.
2. J. Kirkaldy, D. Young, Diffusion in the Condensed State, Institute of Metals 1986.
3. S. Smith, Numerical Solutions of Partial Differential Equations, Elsevier 1975.
4. S. Gut, Inzynieria Materialowa 4(1998),p.1096

Materials Science Forum Vols. 294-296 (1999) pp. 569-572

Short-Circuit Diffusion of ^{51}Cr and ^{59}Fe in Nickel-Aluminium Intermetallics

J. Čermák, I. Stloukal, J. Růžičková and A. Pokorná

Institute of Physics of Materials, AS of the Czech Republic,
Žižkova 22, CZ-61662 Brno, Czech Republic

Keywords: Nickel Aluminides, Nickel, Grain Boundary Diffusion, Grain Boundaries

Abstract

Tracer grain-boundary diffusion (GBD) of ^{51}Cr and ^{59}Fe in Ni_3Al modified by iron, chromium and zirconium was studied in the temperature interval from 773 K to 1273 K using the serial sectioning method.

It was found that additions of Fe and Cr up to about 6 at pct. do not alter the activation enthalpy Q_b of chromium GBD, whereas the alloying of Ni_3Al with Zr (up to 1.6 at pct) leads to a significant increase in Q_b for chromium GBD.

The values of Q_b for iron GBD in the same materials are smaller than activation enthalpies of Cr GBD and, they slightly increase with increasing concentration of either Fe, or Cr. A decrease in Q_b for Fe GBD in Zr-doped alloys with increasing Zr concentration was observed. An interpretation of obtained results is proposed, based on the atomic size effect and on the different affinity between Zr and Cr and between Zr and Fe atoms.

INTRODUCTION

Intermetallics based on nickel-aluminium play important role in many industrial applications. The excellent properties of these materials, such as high temperature strength, high corrosion resistance, high thermal and electrical conductivity and low density, make them very attractive materials for the structural applications. However, it is also known that these intermetallics are very brittle which limits severely their applications. This disadvantageous property may be effectively suppressed by (micro)alloying [1] or by directional solidification [2]. Fe or Cr are frequently used alloying elements that improve the mechanical characteristics of Ni_3Al-based intermetallics. They increase, to a certain degree, the strength and ductility and, moreover, Cr increases the oxidation resistance by a formation of protective chromium oxide films on the free surface [3] and on the grain boundaries (GBs). Zr addition improves high-temperature strength via solid solution hardening [4].

The study of GBD in polycrystalline intermetallics, together with the study of some other characteristics of GBs may shed some light to understanding the fracture mode. In the present work, the GB diffusivities $P = \delta D_b$ of iron and chromium are measured in pure and Fe-, Cr- and Zr-doped Ni_3Al intermetallic compounds.

EXPERIMENTAL

The experimental alloys were prepared from pure Ni (4N7), Al (5N), Fe (3N5), Cr (3N) and Zr (3N) by melting in the induction furnace under the protective argon atmosphere.

The ingots were annealed in vacuum at 1523 K for 1 hour to achieve the homogeneous structure. The chemical composition of the individual alloys was obtained by SEM Phillips equipped with EDAX analyser with absolute accuracy of ± 0.5 at.%. The measured compositions are summarized in Table 1.

Table 1. Chemical composition of experimental alloys in at. pct.

Alloy	x_{Al}	x_{Fe}	x_{Cr}	x_{Zr}
undoped	24.7	-	-	-
3Fe	22.8	3.9	-	-
6Fe	23.1	6.1	-	-
3Cr	23.2	-	2.9	-
6Cr	22.6	-	5.9	-
05Zr	22.9	-	-	0.7
1Zr	22.3	-	-	1.6

The diffusion samples were spark cut from ingots and their surfaces were metallographically polished. The thin layers containing ^{51}Cr and ^{59}Fe radioactive isotope were deposited on the polished front surface using the vacuum evaporation technique. After that, the diffusion annealings were carried out at six temperatures T chosen in interval from 773 K to 1273 K. The respective diffusion times t were estimated in order to keep the type-B kinetics of GBD.

The GB diffusivities P were measured using serial sectioning method. The thickness of individual layers, taken off by grinding, was measured by precise weighing and their relative activity of both β^- and γ radiation of ^{51}Cr and ^{59}Fe was measured by $\alpha/\beta/\gamma$ low-level counter CANBERRA 2400.

RESULTS AND DISCUSSION

Examples of measured penetration profiles $c = c(x, t)$, obtained for Cr diffusion at temperature $T = 848$ K and the diffusion time $t = 259.2$ ks, are shown in Fig.1. The symbol c stands for the mean diffusant concentration in the depth x under the surface. The GB diffusivities P were evaluated from the slopes of straight lines fitted to the tail part of the curves in coordinates $\log c$ vs $x^{6/5}$ [5]. Coefficients of volume diffusivities D_v needed for the P evaluation were taken from the literature [6,7]

$$D_v^{Cr\ in\ Ni_3Al} = (1.1 \pm 0.3) \times 10^{-1} \exp\left\{-(366 \pm 3)\ kJ/mol/RT\right\} \quad m^2/s \qquad (1)$$

$$D_v^{Fe\ in\ Ni_3Al} = 1.3 \times 10^{-2} \exp(-335\ kJ/mol/RT) \quad m^2/s \quad . \qquad (2)$$

The temperature dependence of calculated GB diffusivities P is Arrhenius-type: $P = P_o \exp(-Q_b/RT)$. The Arrhenius parameters P_o and Q_b are listed in Table 2.

Table 2. Arrhenius parameters.

Alloy	^{51}Cr -log P_o m^3 / s	^{51}Cr Q_b kJ / mol	^{59}Fe -log P_o m^3 / s	^{59}Fe Q_b kJ / mol
undoped	11.58 ± 0.24	198.3 ± 4.4	12.11 ± 0.31	176.5 ± 6.3
3Fe	11.09 ± 0.46	203.8 ± 8.4	11.80 ± 0.34	185.2 ± 6.8
6Fe	11.81 ± 0.41	192.2 ± 7.7	11.75 ± 0.24	193.0 ± 4.6
3Cr	12.26 ± 0.31	188.9 ± 7.1	11.85 ± 0.72	186 ± 14
6Cr	11.49 ± 0.82	194 ± 14	11.90 ± 0.40	191.7 ± 7.8
05Zr	9.74 ± 0.37	232.4 ± 6.9	12.77 ± 0.36	166.9 ± 7.3
1Zr	10.30 ± 0.71	220 ± 12	12.92 ± 0.51	159.7 ± 9.7

As can be seen in Fig.2, the Q_b for ^{51}Cr GBD does not depend on concentration of either Cr nor Fe. The addition of Zr, however, induces an increase in Q_b. In the case of ^{59}Fe GBD, the additions of Cr and Fe increase slightly Q_b, the admixture of Zr on the other hand, reduces Q_b. For pure Ni_3Al, the inequality $Q_b^{Fe} < Q_b^{Cr}$ in activation enthalpies of Fe and Cr GBD was observed.

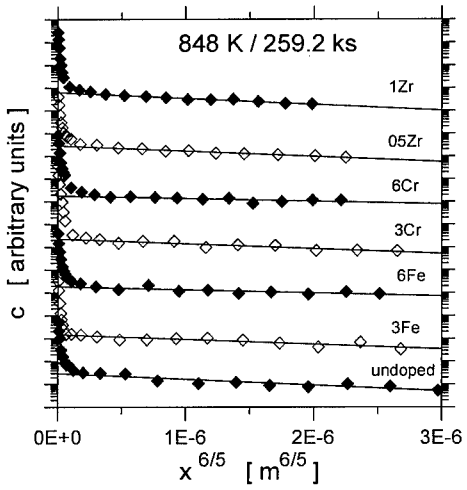

Fig.1 Examples of penetration profiles.

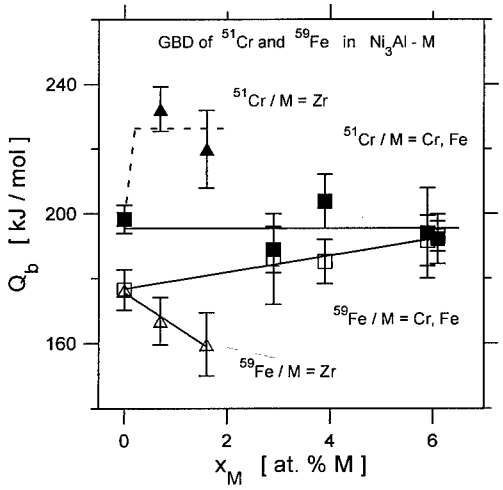

Fig.2 Concentration dependence of Q_b. Open symbols – ^{59}Fe, full symbols – ^{51}Cr.

It is also obvious that the values of Q_b obtained for ^{51}Cr and ^{59}Fe GBD in present paper for pure Ni_3Al, are lower in comparison with the value Q_b = (244.3 ± 7.6) kJ / mol measured in

[8] for Ni GBD in pure stoichiometric Ni_3Al. This may be explained by the fact that diffusing Cr and Fe atoms do not have to keep the atomic order since they can occupy both Ni and Al sublattices [9] and no extra contribution to migration enthalpy due to the creation of antisite defects is needed.

The cause of the inequality $Q_b^{Fe} < Q_b^{Cr}$ consists most likely in different affinity of the both elements to components of the respective alloys. This difference in behaviour of otherwise similar atoms of Cr and Fe can be illustrated by their GBD characteristics measured in pure Ni. It can be shown [10] that the Fe and Cr GBD diffusivities P and activation enthalpies Q_b in close packed FCC structure of Ni-Fe-Cr are very close to those, measured in present paper for Ni_3Al, and that the relations between the relevant GBD characteristics of Fe and Cr are the same in both cases.

The addition of large Zr atoms to Ni_3Al causes a certain dilatation of the lattice which facilitates the GBD of Fe – see the decrease in Q_b. In the case of Cr GBD, however, the same addition of Zr leads to an increase in Q_b. This is, most likely due to an interaction between Cr and Zr atoms. This explanation may be indirectly supported by the fact that the activation enthalpies Q_v^{Cr} of Cr volume diffusion in β-Zr [11,12] is greater than Q_v^{Fe} [11,13,14]. At the same time, the addition of Cr to β-Zr increases the activation enthalpy Q_v^{Zr} [11], whereas the dependence of Q_v^{Zr} on Fe additions [11] is very weak.

ACKNOWLEDGEMENTS

This work was supported by The Grant Agency of the Academy of Sciences of the Czech Republic, grant number 106/96/0261.

REFERENCES

[1] T. Takasugi, O. Izumi & N. Masahashi, *Acta Metall*, **33** (1985), p.1259.
[2] T. Hirano, *Acta Metall. Mater.*, **38** (1990), p.2667.
[3] C.T. Liu, & V.K. Sikka, *J. of Metals*, **38** (1986), p.19.
[4] J.H. Westbrook, & R.L. Fleischer, *Intermetallic Compounds, Vol. 2 - Practice*, John Wiley & Sons, Chichester-New York-Brisbane-Toronto-Singapore, 1995, p. 35.
[5] I. Kaur, & W. Gust, *Fundamentals of Grain and Interphase Boundary Diffusion*, Ziegler Press, Stuttgart, Germany, 1988, p. 65.
[6] S.B. Jung, Y. Minamino, H. Araki, T. Yamane, K. Hirao, & S. Saji, *Defect and Diffusion Forum*, **98-98** (1993), p.859.
[7] Y. Minamino, T. Yamane, S. Saji, K. Hirao, S.B. Jung, & T. Kohira, *J. of Japan Institute of Metals*, **58** (1994), p.397.
[8] J. Čermák, J. Růžičková, I. Stloukal, & A. Pokorná, *Scripta Mater.*, **37** (1997), p.31.
[9] S. Ochiai, Y. Oya, & T. Suzuki, *Acta Metall.*, **32** (1984), p.289.
[10] J. Čermák, *Mat. Sci. Eng.*, **A148**, (1991), p.279.
[11] R.V. Patil, G.P. Tiwari, & B.D. Sharma, *Phil. Mag. A*, **44** (1981), p. 717.
[12] L.I. Nicolai, & R.H. de Tendler, *J. Nucl. Mater.*, **87** (1979), p.401.
[13] R.H. Zee, *J. of Physics - Condens. Matter*, **1** (1989), p.5631.
[14] J. Trampenau, & C. Herzig, *J. of Physics - Condens. Matter*, **2** (1990), p.9345.

Materials Science Forum Vols. 294-296 (1999) pp. 573-576

The Effect of Solubility of the Diffusant on its Grain-Boundary Penetration in Aluminium Bicrystals

S. Gut[1], K. Przybylowicz[2] and I. Suliga[1]

[1] University of Mining and Metallurgy, al. Mickiewicza 39, PL-30-059 Krakow, Poland

[2] Kielce Technical University, al. 1000-lecia P.P. 7, PL-25-314 Kielce, Poland

Keywords: Reactive Diffusion, Oxygen, Aluminium Bicrystals

Abstract: Diffusion of various elements differing in the solubility in aluminium was carried out in aluminium bicrystals with a tilt grain boundary (GB) and common direction <100>. Correlation of GB penetration has been looked for with various properties of the diffusing atoms (solubility, atomic size, reactive diffusion). The strongest correlation has been stated with the limit of solubility of the elements in aluminium. GB diffusion of oxygen atoms has been stated in aluminium bicrystals and oxide wedge was formed at the grain boundary.

Introduction

Some aspects of GB diffusion have been investigated very poorly, though their role in science and technology is significant. These are e.g. the effect of atomic size, solubility and reactive diffusion. An investigation of these problems is, however, very difficult because some conditions must be fulfilled. For example, as for the atomic size effect, the diffusing atoms should belong to the same group in the periodic system (to eliminate the effect of valency) and have similar solubility in the matrix metal. Analogically, in the case of solubility effect the diffusing atoms should have the same valency and atomic size but a different solubility. If two or more factors change in experiment, drawing conclusions are difficult or impossible.

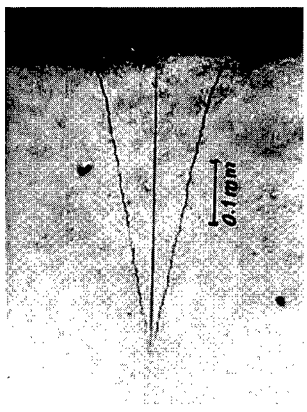

Fig.1. GB diffusion of Cu in an Al bicrystal,
$\Theta = 45^\circ$, $T = 400^\circ C$, $\tau = 185$ h. [1]

The other essential factor in GB diffusion experiments is the revealing of the diffusion front, possibly at the same or close concentration of the diffusant. Our experiments on GB diffusion in aluminium bicrystals have shown the possibility of etching a very distinct diffusion front of copper, silver or zinc. Figure 1 shows a GB diffusion contour of copper in an aluminium bicrystal with <100> tilt boundary, misorientation angle $\Theta = 45^\circ$, at the temp. $T = 400^\circ C$, time $\tau = 185$ hrs.

The concentration of copper along the contour line is 0.05 wt.% [1]. Very similar contours were revealed in experiments on silver diffusion in a low angle GB of aluminium bicrystal ($\Theta = 7^\circ$) [2]. Our investigations have shown that copper atoms with the smaller atomic diameter penetrated deeper than silver atoms.

Effect of solubility of the diffusant

The experiments have been carried out on <100> bicrystals of aluminium with tilt boundaries and various misorientations [3]. As diffusing atoms the following elements were chosen: Au, Co, Ti, Ni, Cr and components of austenitic steel (Fe, Cr, Ni). The covering of aluminium specimens with mentioned elements and revealing the diffusion front proved very difficult. After many unsuccessful trials a comparative method was used. One side (perpendicular to the common direction) of each specimen has been covered with one of the mentioned elements or austenitic steel and other with copper together with one of these elements. The magnetron sputtering method has been applied. The assumption has been made that if the insoluble elements do not diffuse along the GB, they should not change the geometry of diffusion front of copper (the shape of the GB diffusion contour which could be revealed distinctly (Fig. 1). A two - stage annealing has been applied: first at 550° C for 5 h and second at 400° C for 192 h. The parameters of the geometry of diffusion front have been given in Table 1.

Table 1. Geometrical parameters of the GB diffusion contours.

Diffusant Cu+Me	Depths of GB diffusion y_g ,μm	Depths of volume diffusion y_v ,μm	Solubility limit in Al, at. %	Atomic radius, nm
Au	225	297	0.048	0.288
Co	320	352	0.108	0.251
Ni	114	291	0.110	0.240
Ti	269	310	0.159	0.295
Cr	431	388	0.880	0.250
Cu	234	345	2.54	0.256

A correlation of GB penetration has been looked for with various properties of the diffusing atoms. The strongest correlation was stated with the solubility limit of the elements in Al. The higher the solubility, the stronger the influence on GB diffusion of copper in Al. No correlation has been stated between intermetallic phases formation and GB penetration. These problems are very complex and require further investigation.

GB diffusion of oxygen in aluminium bicrystal

It is thought that solubility of oxygen in aluminium is negligibly small and because of the high affinity of oxygen to aluminium an Al_2O_3 layer is formed even at low temperatures. No information is available on the diffusion of oxygen along grain boundaries in aluminium. The problem is not easy to be investigated because even at high temperatures the aluminium oxide layer is very thin, what makes difficult to reveal the grain boundary diffusion wedge. Hence, a special method must be applied. In our experiments a method of aluminium matrix solution in HCl acid has been used. After the metal solution, an insoluble oxide wedge set up at the GB could be observed and measured in the scanning electron microscope. The specimen was cut off from an aluminium bicrystal with tilt GB, common direction <100> and misfit angle Θ = 45°. The surfaces perpendicular to the <100> direction were ground on abrasive papers, etched in acid and electropolished. Then the specimen was put to powdered magnetite and subjected to a two-stage annealing: first 5 h at 500° C and second 192 h at 400°C. The aim of the first annealing was the creation of a thicker layer of oxide and moving away the GB wedge from the surface. After annealing, the specimen was included in acrylic resin and immersed in water solution of HCl (1:1).

Removing of the metal matrix revealed a thin strip in the place of the GB which could be seen even by the unaided eye.

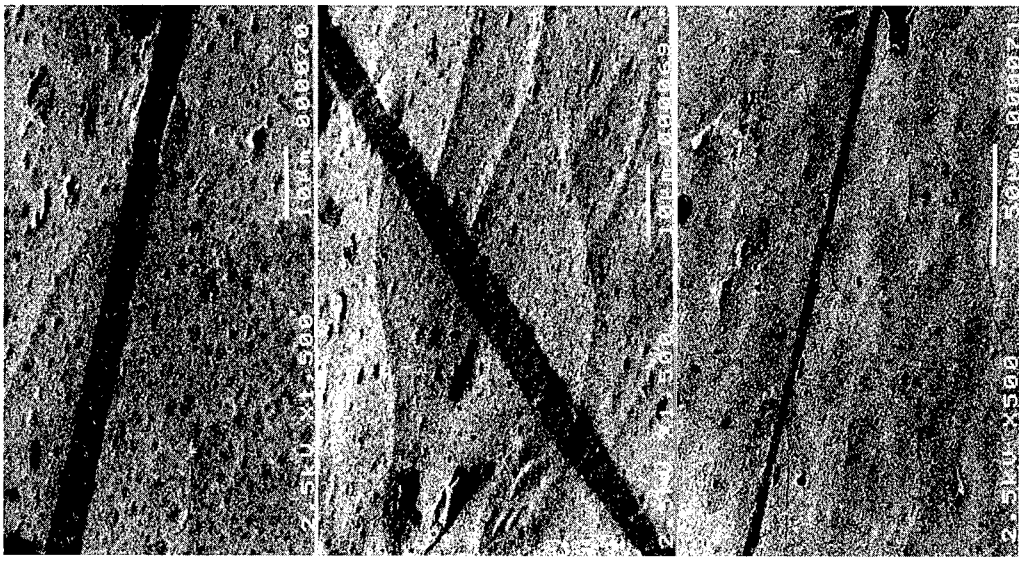

(a) (b) (c)

Fig 2. Scanning electron micrographs of the GB diffusion wedge; (a) and (b) are side views and (c) is perpendicular to the surface view.

Observation by means of electron scanning microscopy has shown that the strip has a wedge shape. In Figs. 2 (a, b) both surfaces of that wedge can be seen and Fig. 2 (c) shows the view of the wedge in the direction perpendicular to the surface. It can be seen from the micrographs that the height of the edge is about 5 μm and its width at the base is about 4 μm. So the vertex angle of the GB diffusion wedge is about 50 degrees.

Trials to determine the chemical composition of the wedge were also performed using Kevex analyser. Only the content of aluminium and iron in the wedge could be stated, because the peaks of aluminium and oxygen were overlaped.

The revealing of the diffusion wedge rises the question what is the mechanism of its formation. The only explanation is to assume that oxygen atoms diffuse through defects in the aluminium oxide layer (dislocations and grain boundaries). Such defects can be created in the region of aluminium GB also in the oxide layer. An analogic mechanism was proposed by Przybylowicz et al. [4] in the case of the formation of borides during the boronizing process. It has been assumed that the boron atoms can diffuse into the matrix along the boundaries of the FeB needles. This assumption has been confirmed experimentally using the carbon isotope C^{14} as a tracer of diffusion paths (it is insoluble in borides as well as boron) [5]. In this experiment boronized specimens have been subjected to carburizing, and then the distribution of the C^{14} atoms in the borides was tested by an autoradiographic method. The ununiform distribution of C^{14} patterns along the GBs was interpreted as a confirmation of the hypothesis. A further confirmation was given by Wierzchon [6] who had shown that also nitrogen atoms can diffuse through a boronized layer without changing its structure but creating nitrides under it.

Comparing the shape of the GB diffusion contour for copper (Fig. 1) and oxygen obtained nearly at the same conditions, it is easy to state that the height of the wedge for oxygen diffusion is about 100

times less than for copper diffusion. It can be explained with a very low GB diffusion coefficient of oxygen in aluminium oxide, which probably is the controlling factor in the formation of the GB diffusion wedge.
The Arrhenius equation for GB diffusion of oxygen in α - Al_2O_3 in the temperature range 1450 - 1700° C is as follows [7]:

$$D_g = 1.1 \quad 10^{-7} \exp (- 456.1 \text{ kJmol}^{-1}/ \text{RT}) \text{ [m}^2\text{/s]} \qquad (1)$$

Data are not available for the low temperature range. Extrapolating Eq. (1) to a temperature of 400°C one may evaluate an extremally low coefficient $D_g \approx 10^{-43}$ m^2/s, whereas for GB diffusion of copper in aluminium $D_g = 7.2 \ 10^{-9}$ m^2/s [1]. Hence the thickness of the oxide diffusion layer should be negligibly small. The constitution of a small oxide wedge may testify that activation energy for the low temperature range is larger, than for high temeprature range. According to Tomizuka [8] such a suggestion is possible to accept.

Conclusions

1. The strongest correlation has been stated between the solubility limit of the diffusing element and its GB penetration depth.
2. The height of the GB diffusion wedge for oxygen is about two orders of magnitude less than that for copper.
3. The described experiment has yielded probably the first evidence of a reactive diffusion of oxygen along GBs in aluminium. The GB diffusion wedges may increase the cohesion forces between the various phases contacting in composites or other multi-phase materials.

References

[1] K. Przybylowicz, Arch. Hutn. 9 (1964), p.347
[2] K. Przybylowicz, in: Diffusion in metalischen Werkstoffen, Leipzig (1970), p.212
[3] K. Przybylowicz, S. Gut, I. Suliga, Zeszyty Naukowe Politechniki Swiętokrzyskyskiej. Kielce, Mechanika 55 (1995), p. 268
[4] K. Przybylowicz, IV Int. Conf. on "Carbides, Nitrides, Borides", Kolobrzeg (Poland), (1987), p. 203
[5] B. Kastner, K. Przybylowicz, I. Grygoruk, Härterei Technische Mitteilungen , 34 (1979), p.173
[6] T. Wierzchoń, Tworzenie się warstwy borków żelaza na stali w warunkach wyładowania jarzeniowego, Wydawnictwa Politechniki Warszawskiej (1986)
[7] R. Pampuch, Constitution of Properties of Ceramic Materials, Państwowe Wyd. Naukowe-Elsevier, Warsaw - Amsterdam (1991)
[8] C.T. Tomizuka, Acta Met. 6 (1958) p. 660

Materials Science Forum Vols. 294-296 (1999) pp. 577-580

Site Preference of ^{57}Co in $Fe_{72}Al_{28}$ After Grain Boundary Diffusion

O. Schneeweiss and S. Havlíček

Institute of Physics of Materials, Academy of Sciences of the Czech Republic,
Žižkova 22, CZ-61662 Brno, Czech Republic

Keywords: Grain Boundary Diffusion, ^{57}Co, Mössbauer Spectroscopy, Iron Aluminides, Intermetallics

Abstract

The location of diffused ^{57}Co atoms in single crystal and polycrystalline samples of $Fe_{72}Al_{28}$ was investigated by means of Mössbauer spectroscopy. From the detailed analysis of spectra it was found that an important part of the atoms diffusing along grain boundary interfaces occupies positions different from those in bulk. During the volume diffusion, there is a strong site preference for the regular iron position in the Fe_3Al superstructure with four Al atoms in the nearest neighbourhood.

Introduction

The mechanical properties of some intermetallic compounds, like iron or nickel aluminides, are very sensitive to the properties of grain boundaries. Therefore detailed information about their crystallographic structure and chemical composition has great importance.

Grain boundaries in materials distinct from the bulk crystal and their properties differ from those of a regular crystal lattice [1, 2]. According to both experimental and theoretical studies the structure of grain boundaries is crystal-like. By means of computer simulations of the structure of numerous grain boundaries a structural unit model of the atomic structure of grain boundaries was developed (e.g., [3]). In this model, a grain boundary is composed by repeated structural units that represent particular arrangements of limited groups (clusters) of atoms.

Grain boundaries are usually channels of fast diffusion in comparison with the bulk of crystal. The most probable diffusion mechanism in grain boundaries is also the vacancy mechanism [4]. Several types of grain boundary vacancies are to be expected in accordance with lowered symmetry of a respective cell. The grain boundary diffusion experiments using Mössbauer isotopes can yield some interesting information about basic problems of grain boundary properties.

Iron aluminides based on Fe_3Al ($D0_3$) and FeAl (B2) have important magnetic and mechanical properties [5, 6] very sensitive to additional alloying and the state of grain boundaries [7, 8]. The alloy $Fe_{72}Al_{28}$ is ferromagnetic in an equilibrium state, with bcc structure and $D0_3$ superstructure at room temperature. The Curie temperature T_c = 623 K, and the critical temperatures of $D0_3 \rightleftharpoons$ B2 and B2 $\rightleftharpoons$ A2 phase transformations are about 823 K and 1223 K, respectively [9]. Magnetic moments and T_c of the Fe–Al alloys (in ordered $D0_3$ or B2 states) rapidly decrease with increasing content of Al above 25 at.%. For $\sim$ 30 at.% Al the T_c is about 300K [9].

Several studies document the strong influence of mechanical treatment on magnetic properties of Fe-Al alloys with 25 to 50 at.% Al, e.g., [10, 11]. An explanation of the changes in magnetic behaviour of Fe-Al alloys due to plastic deformation was proposed by Chin [5]. Therefore a

very precise sample preparation must be guaranteed for the Mössbauer spectroscopy on Fe-Al alloys. Beside the influence of mechanical treatment, important difference in vapour pressure of Al and Fe at high temperatures, and high affinity of Al to oxygen and nitrogen must be taken into account by vacuum and protective atmosphere high temperature annealing, respectively. The aim of the present work is to characterize locations that ^{57}Co atoms prefer during grain boundary diffusion in $Fe_{72}Al_{28}$ intermetallic alloy in comparison with the grain bulk.

Experimental

The samples were prepared in the form of 1mm thick plates cut using spark erosion from a single crystal and from a fine grain polycrystal. From the polycrystal a 50μm thin foil for transmission experiments was manufactured as well. Surfaces of the samples were carefully ground, polished and cleaned, and annealed in a vacuum furnace in vacuum about 10^{-3} Pa at 973 K for 1 hour with subsequent cooling rate 120 K/h down to room temperature. After the annealing, cleaning by Ar ions was carried out. The aim of the procedure of sample and surface treatments was to remove all traces of plastic deformation produced during cutting and grinding of the plates. The structure of the surfaces of both samples was investigated by optical metallography and ^{57}Fe CEMS. Content of Al was 28.4 $\pm$ 0.5 at.% according EDX analysis. These samples were used as matrices for the preparation of ^{57}Co sources. A thin layer of ^{57}Co was deposited on their surfaces in a few drops of cobalt(II) chloride in 0.1M HCl that were dried using an infrared radiation. Diffusion anneals were carried out in a vacuum resistance furnace.

Emission ^{57}Fe Mössbauer spectra were taken at room temperature using $Na_4Fe(CN)_6{\cdot}10H_2O$ with iron enriched to about 90% of ^{57}Fe as absorber. Standard transmission ^{57}Fe spectrum of the polycrystalline foil and CEMS spectra were taken using ^{57}Co in Cr as a source.

Results and discussion

The transmission spectrum of the polycrystalline foil was used as a basis for analysis of the other spectra. The spectrum of the polycrystalline foil consists of two component represented by sextets. The first sextet with magnetic splitting B_{hf} = 2.3 T and isomer shift δ= 0.18 mm/s can be ascribed to the iron atoms at A and C sites of $D0_3$ superstructure. Iron atoms at these sites have four aluminium atoms in the nearest neighbourhood at D sites. The other four nearest neighbour sites (B) are occupied namely by Fe and partially by Al atoms when Al content is larger than the stoichiometric concentration 25 at.%. The second component with $B_{hf} \approx$ 12.9T and $\delta \approx$ 0.12 mm/s corresponds to iron atoms in the B sites.

Volume diffusion in the single crystal sample was induced by annealing at 1273 K for 20 hours. Two components were identified in its spectrum. The main component agrees with that in the polycrystalline foil spectrum which represents the iron atoms at A and C sites of $D0_3$ superstructure. The second component (broad sextet with mean B_{hf} = 34.5T) was ascribed, according to our previous experiences [12], to a surface layer containing deposited ^{57}Co atoms. In comparison with the spectrum of the polycrystalline foil a component corresponding to iron atoms in the B sites was not found. It means that ^{57}Co did not occupy B sites of the $D0_3$ superstructure.

Annealing of the polycrystalline sample at 903 K for 24, 48, and 96 hours was applied to obtain grain boundary diffusion characteristics. Volume diffusion is negligible at this low temperature. In the spectrum of the polycrystalline sample (see Fig.1) both components found in the single crystal sample were also identified. Neither here a component of ^{57}Co atoms in the B sites was found. However, a new dominating component of intensity 64% appeared in this spectrum, which was described by sextet with B_{hf} = 5.1 T, δ= 0.44 mm/s and quadrupole splitting σ = 1.15 mm/s. The results derived from the spectrum of sample after annealing for 24 hrs

show that of ^{57}Co atoms in grain volumes occupy preferentially the A and C sites of the $D0_3$ superlattice. The large values of quadrupole splitting and isomer shift of the grain boundary component indicate, that the corresponding atoms are placed in a surrounding with lower symmetry and lower s-like electron density. It matches models of grain boundaries where a part of the atoms at interfaces have different topological and chemical nearest neighbourhood in comparison with the grain bulk [2].

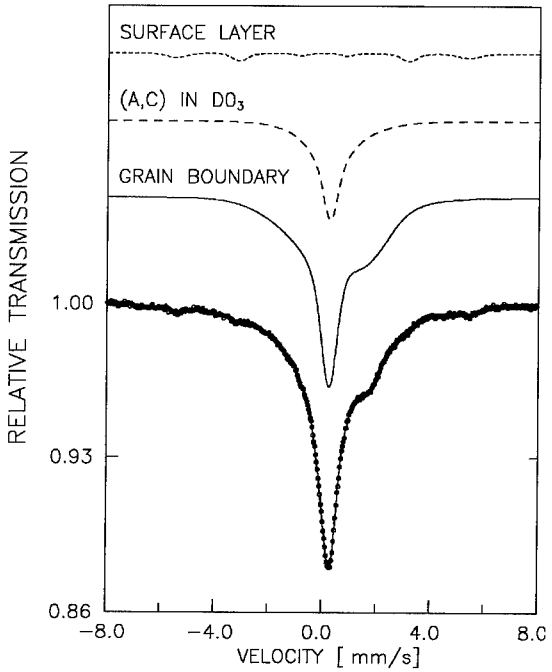

Figure 1. The Mössbauer spectrum of $Na_4Fe(CN)_6{\cdot}10H_2O$ using ^{57}Co in $Fe_{72}Al_{28}$ after annealing at 903K for 24hrs in vacuum. The fitted experimental data (below) are shown together with labelled components of the fitted function.

Further annealing steps of both, single crystal and polycrystal samples cause a decrease of the surface layer component intensity and in the spectrum of the polycrystalline sample also decreased the intensity of the grain boundary component from 64% to 57% and 50%. This is in agreement with grain boundary diffusion model assuming that the grain boundaries enriched by ^{57}Co atoms also act as a source for diffusion into volumes of grains (e.g., [13, 14]). A scheme of this process is drawn in Fig. 2. A progress of constant concentration contours were calculated for time of annealing t and $2t$, like in our experiments. As follows from this simple model, the part of diffusing atoms in the bulk increases much more rapidly than the grain boundary part, and its intensity is less attenuated by absorption effect.

Conclusion

Following conclusions can be derived from the above comparison of locations of ^{57}Co atoms diffused in the single crystal and the polycrystal of $Fe_{72}Al_{28}$ intermetallic alloys:

- ^{57}Co atoms prefer A and C sites in the $D0_3$ superstructure during volume diffusion in the $Fe_{72}Al_{28}$ alloy. These positions are occupied by iron atoms with four iron and four aluminium atoms in the nearest neighbourhood in the ordered $D0_3$ structure. No indications about ^{57}Co atoms on B or D sites of the $D0_3$ structure were detected.

- A component representing ^{57}Co atoms placed at grain boundary interfaces was identified in the spectrum of the polycrystalline sample. The intensity of this component changes with annealing time in agreement with a model which describes the grain boundary as a source of ^{57}Co atoms for volume diffusion.

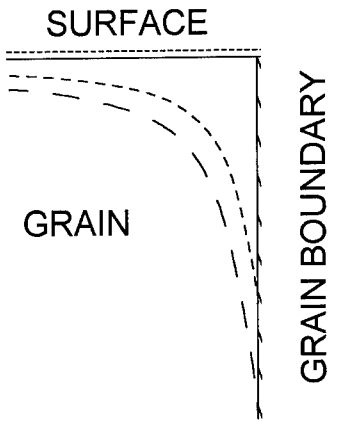

Figure 2. Constant concentration contours by diffusion near a grain boundary. The short dashed and long dashed curves correspond to contours for time of annealing t and $2t$, respectively.

Acknowledgment
This study was supported by the grant No. 106/97/1044 of the Grant Agency of the Czech Republic.

References

[1] T. Watanabe, Mater. Sci. Forum 46 (1989) 25.
[2] P. Lejček and S. Hofmann, Crit. Rev. Sol. State Mater. Res. 20 (1995) 1.
[3] A.P. Sutton and R.W. Balluffi, *Interfaces in Crystalline Materials*, (Oxford University Press, Oxford), 1995, p. 10.
[4] I. Kaur and W. Gust: *Fundamentals of Grain and Interphase Boundary Diffusion*, (Ziegler Press, Stuttgart), 1989, p. 1.
[5] G.Y. Chin, in: *Advances in Materials Research*, Vol. 5, edited by H. Herman, (Wiley, New York), 1971, p. 217.
[6] C.T. Liu, in: *Mater. Res. Soc. Symp. Proc.*, Vol. 288, (MRS, Pittsburgh), 1993, p. 3.
[7] V.K. Sikka, in:*Processing, Properties, and Applications of Iron Aluminides*, edited by J.H. Schneibel and M.A. Crimp, (TMS, Warrendale), 1994, p. 3.
[8] O. Schneeweiss, T. Žák, Y. Jirásková, J. Magn. Magn. Mater., 103 (1992) 250.
[9] G. Inden, Bull. Alloy Phase Diagrams 2 (1982) 412.
[10] G. Rassmann and H. Wich, Z. angew. Physik 13 (1961) 172.
[11] K. Oki, S. Towata, M. Tamiya and T. Eguchi, Transaction Japan Inst. Metals, 22 (1981) 771.
[12] O. Schneeweiss, J. Pavlovský, S. Havlíček, and T. Žák, Nanostructured Materials, 4 (1994) 815.
[13] L.A. Girifalco: *Atomic Migration in Crystals*, (Blaisdell Publishing Company, New York), 1964, p. 117.
[14] Y. Adda and J. Philibert: *La diffusion dans les solides*, (Inst. Nat. Sci., Techn. Nucleaires, P. Univ. France, Saclay), 1966, p. 667.

Materials Science Forum Vols. 294-296 (1999) pp. 581-584

Extraction of the Segregation Term from the Triple Product of Grain Boundary Diffusion: Reconsideration of Experimental Data

B. Bokstein[1], A. Ostrovsky[1] and J. Bernardini[2]

[1] Department of Physical Chemistry, Institute of Steel and Alloys, Leninsky prospect 4, RU-117936 Moscow, Russia

[2] Laboratoire de Métallurgie associé au CNRS, Faculte des Sciences St Jérôme, F-13397 Marseille Cedex 20, France

Keywords: Grain Boundary, Diffusion, Segregation, Non-Linear Segregation, Migration, Copper, Silver

Abstract. The practical possibility of the segregation parameter determination by using the nonlinear segregation effect on grain boundary (GB) diffusion is illustrated based on the example of silver-copper GB diffusion measurements. The segregation and migration parameters of silver in copper are estimated and the results are compared with the results of previous investigations.

Introduction. It is well-known that the apparent activation enthalpy Q_{gb} of solute GB diffusion in kinetic regime B after Harrison [1] includes the segregation enthalpy H_s [2, 3]. Today there are three practical possibilities for the GB segregation parameter estimation from the GB diffusion measurements:

1) Simultaneous measurements in type B (the result is the triple product of GB diffusion $P=s\delta D_b$, where s is the GB enrichment ratio $s=c_b/c$, here c_b and c are GB and bulk concentrations consequently, δ is the GB diffusion width, D_b is the GB diffusion coefficient) and type C (the result is D_b) diffusion kinetics. With assumptions about the value and temperature behaviour of the GB diffusion width one can obtain the enrichment ratio s. Since the mid-eighties [4] there have been about ten experimental works in this direction, mostly in the scientific group of Prof. Chr. Herzig, see review in [5].

2) Simultaneous solute GB diffusion measurements in the pure metal and in the saturation solid solution formed from the metal and the solute. In this case $P^{alloy}=s^{alloy}\delta D_b^{alloy}$ is determined for the alloyed system, where the concrete form of s^{alloy} one can write from the assumption GB segregation isotherm. With assumption about the relation between D_b and D_b^{alloy} one can receive the segregation coefficient b ($b = \exp[-H_s/RT]$, here H_s the segregation enthalpy, R is the gas constant, T is the absolute temperature). This method was proposed and applied to the Cu-Ag system in [6].

3) Simultaneous GB diffusion measurements for self- (result is δD_b^{self} (s=1)) and solute diffusion. With assumption about the relation between D_b^{self} and D_b one can calculate s. This is a semi-qualitative but useful method, because one can compare results deducted from the different sources. The review of these results are in [7].

In the last two decades several theoretical works dealing with the effects of nonlinear segregation (saturation of GB, interaction of species in GB, non-homogeneity of GB) on GB diffusion were performed [8-12]. A common point in them is that the nonlinear segregation leads to the nonlinear GB penetration plots and this feature could be used for the segregation parameter extraction from the only penetration plot in kinetic regime B. Recently, a new method, based on such a profile's shape analysis, was proposed [12], but up to now it has never been applied to experimental results. In this paper it is illustrated how this method can be used for the processing of the experimental plots based on the example of Ag-Cu [6] penetration plots.

Processing of the penetration plots. The solution for the GB saturation effect was proposed in Ref. [12]. Both definite GB solubility and definite bulk solubility were taken into consideration:

$$\theta_b = bc/(1-\theta+bc), \quad (1)$$

here θ_b and θ are the fractions of occupied sites in the boundary and bulk, which are taken as the ratios of the GB or bulk concentration to the GB (c_{b0}) or bulk (c_0) solubility.
In the dilute bulk solution when θ <<1 this equation transfers to McLean [13] equation for dilute bulk solution

$$\theta_b=bc/(1+bc) \quad (2)$$

or to the truncated BET isotherm [14]

$$\theta_b=k\theta/(1+k\theta), \quad (3)$$

here $k=bc_o$. One can estimate the k parameter theoretically as $\exp[(10\pm6)kJmol^{-1}/RT]$ [15]. In practice the values for this parameter vary from 1.8 to 6.8 [16].
In an dilute GB solution when $\theta_b<<1$ one can obtain the Henry isotherm $\theta_b=bc$ and $s= bc_{b0}$. Note that in simultaneous type B-type C and self- solute GB diffusion measurements one can not determined the segregation enthalpy H_s but only the effective enthalpy $H_s+H_{sol}^{gb}$, where H_{sol}^{gb} is the enthalpy of the GB solubility. Therefore, the s values determined from such measurements are lower than the b values that are directly measured by, for example, AES-measurements, deducted from the simultaneous pure metal – alloy GB diffusion measurements or calculated by present method. One can see that there is a possibility for the separate determination of c_{b0}, b and δD_b from type B-type C diffusion measurements by using this nonlinear segregation approach.
The parameter k values can be calculated in the case of an isotherm described by Eq. 1 as

$$k=1+4qc_0(Dt)^{0.5}/[\bar{c}_{nonlin}d(1-q)\pi^{0.5}], \quad (4)$$

here d is the mean grain size, $\bar{c}_{nonlin}$ is the mean layer concentration in the nonlinear part of GB penetration plots, D is the bulk diffusion coefficient, t is the annealing time, q is a parameter which is the mean layer concentration function.
We can calculate $q(\bar{c}_{nonlin})$ from the Eq. 5

$$P_{nonlin}/P=-0.5q^2(1-q)^2/[\ln(1-q)+q], \quad (5)$$

here P_{nonlin} is 'the effective triple product' in the nonlinear part of GB penetration plots when concentration is $\bar{c}_{nonlin}$. In the lack of the segregation k=1, q=0, ln $(1-q)\rightarrow -q-q^2/2$ and $P_{nonlin}=P$ at the whole GB concentration range.
This solution was received for the conditions of kinetic regime B after Harrison when $\alpha=(s\delta/2(Dt)^{0.5})<<1$, $\beta=(s\delta D_b/2D^{1.5}t^{0.5})$ >>1. Although Eq. 5 was obtained in the quasi-stationary Fisher's [17] approximation, it is suggested that one can use this equation for the real experimental penetration plot processing.

GB diffusion of silver in polycrystalline copper. Nonlinear experimental penetration plots for Ag GB diffusion in copper are shown in Fig. 1 [6]. Several effects can lead to the nonlinear penetration plots such as i) direct volume diffusion from the surface, ii) measurements in the transition B-C regime [18], iii) GB motion [5], iv) diffusion along sub-boundaries [19, 20] and so on.
In our case only GB part of the penetration plots are shown on the Fig. 1 because the volume diffusion penetration depth $(Dt)^{0.5}$ is enough small (see Table 1).
From the values presented in table 1 it is seen that the conditions of the B-regime ($\alpha<<1$, $\beta>>1$ calculated from the data published in [6]) are fulfilled. It was shown earlier that the Sb GB solubility in copper changes from 6.7 to 8.5 mol. % at the temperature interval 673-1073 K, while the corresponding bulk solubility changes from 4.1 to 6.0 mol. % [21]. The parameter b varies from 50 to 100, and it means that $c_{b0}<<bc_0$. If this relation is the same in our case then α values are much less than unity.
In [6] simultaneous measurements for pure copper and Cu(Ag) alloy were carried out. It was shown that the upward curvature of the penetration plots in alloyed system is much less than in pure copper and it means that such structural defects as sub-grain boundaries and GB distribution on diffusivity are absent or not dominated.
Note that the curvature of these plots decreases with the increase in temperature, as it is expected for the case of a nonlinear segregation effect. In [6] it was shown that supposing a McLean-like

segregation isotherm the comparison of Ag-Cu and Ag-Cu(Ag) measurements leads to a segregation coefficient b

$$b=1.2\ \exp[(37\pm13)\text{kJmol}^{-1}/RT]. \quad (6)$$

In the following section it is illustrated how the method proposed in [12] can be applied to processing of the experimental results and the segregation parameters are recalculated uniquely using Ag-Cu penetration profiles. The results of these calculations are presented also in Table 1. Due to strong Ag segregation, its low solubility and diffusivity one must deal with a constant diffusant source [6] for T=584 K, 617 K, 665 K. Therefore $\bar{c}(y=+0)=c_0$, where y is the diffusion direction. With this assumption one can convert the diffusant concentration from arbitrary activity units to atomic percents, as it required for the application of the method. At the highest experimental temperature (804 K) both solubility and diffusivity increase about one order of magnitude, while segregation decreases about one order of magnitude. It leads to the exhaustive source at y=0 and to indefiniteness of the concentration. In the calculations the mean grain size value 150 μm was used [22]. The values of $k=bc_0$ were received by fits to the overall penetration plots and the values of P_{nonlin} were calculated by using LeClair-Whiplle [5] equation. The bulk solubility values were taken from Ref. [23].

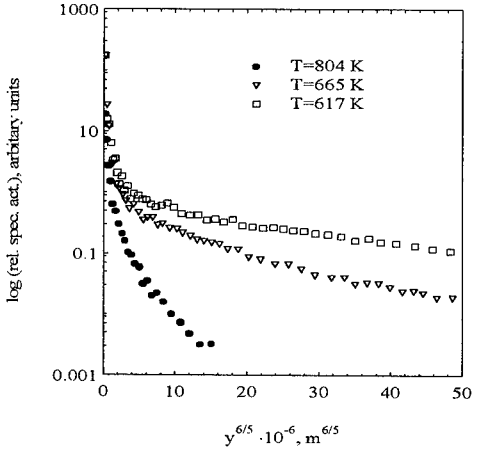

Fig. 1. Typical tracer penetration profiles for Ag GB diffusion in Cu

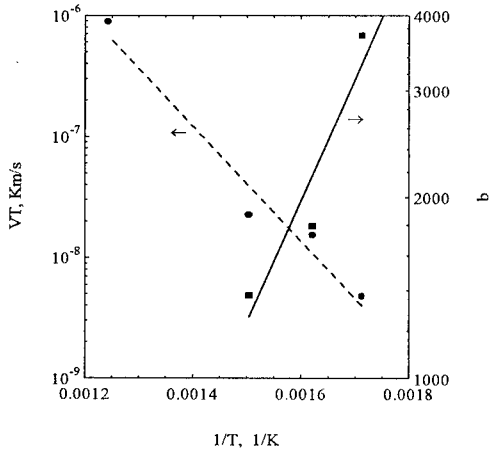

Fig. 2. Arrhenuis plots of Ag GB segregation and GB migration in Cu

Table 1

Silver grain boundary diffusion, segregation and migration in copper

T, K	$[(Dt)^{0.5}]^{1.2}$, $m^{6/5}$ [6]	α/c_{b0}	β	P, m^3s^{-1} [6]	c_o, at. % [23]	bc_o	b, 10^3	$-H_s$, $kJmol^{-1}$	$q_4, 10^5$, m^{-1}	V, ms^{-1}
584	$2.6\cdot10^{-9}$	8.6	$1.0\cdot10^{7}$	$3.7\cdot10^{-22}$	0.12	4.5 ± 1.9	3.75	39 ± 2	1.6	$8.2\cdot10^{-12}$
617	$8.6\cdot10^{-9}$	2.1	$7.6\cdot10^{5}$	$6.1\cdot10^{-22}$	0.19	3.4 ± 1.2	1.89	38 ± 2	1.7	$2.5\cdot10^{-11}$
665	$5.5\cdot10^{-9}$	1.9	$6.4\cdot10^{5}$	$5.5\cdot10^{-21}$	0.32	4.4 ± 1.5	1.37	39 ± 2	1.04	$3.4\cdot10^{-11}$
804	$1.1\cdot10^{-8}$	0.3	$8.7\cdot10^{3}$	$5.6\cdot10^{-20}$	1.1	-	(0.3)	-	1.45	$1.1\cdot10^{-9}$

The Arrhenius fitting of these results leads to

$$b=1.2^{+14}_{-1.1}\ \exp[(39\pm13)\text{kJmol}^{-1}/RT]. \quad (7)$$

At T=804 K the value of b in Table 1 was estimated with the help of Eq. 7. One can see that two methods of b determination give us comparable results both with each other and with Auger electron spectroscopy value, which was estimated at less than 40.4 $kJmol^{-1}$ [24]. Moreover, there is the possibility of segregation enthalpy determination only from the one penetration plot in kinetic regime B, since from the theory the pre-exponential factor of b must be equal to the unit. In the Table 1 the segregation enthalpy values were determined by this assumption. One can see that in this case $H_s=-(39\pm2)\text{kJmol}^{-1}$.

In above paragraphs the possibility of GB migration was not considered, although for Ni GB diffusion in Cu it was shown that a certain fraction of GBs moves during diffusion [25]. According to the Güthoff approach [5] one can determine GB migration velocity V as $V=q_4^2P$, where the parameter q_4 is obtained as $-\partial \ln \bar{c} / \partial y$ from the region, where the GB migration is dominating. Although this model doesn't take into consideration non-linear segregation one can try to extract the parameters of migration from the first several points of each plot. Of course, in this crude way only effective migration parameters can be obtained, because with the concentration increasing there is increase not only of GB migration but also of GB segregation nonlinearity. The results of the migration parameter calculations are listed in Table 1. In Fig. 2 one can see Arrhenius plots for Ag GB migration and GB segregation in Cu. The Arrhenius relation for the effective GB migration is

$$VT = 0.55^{+4.61}_{-0.49} \exp[-(91\pm12)\text{kJmol}^{-1}/RT]. \quad (8)$$

This result correlates well with the conclusions of previous investigations [5], where it was shown that the activation energy of the GB migration is close to the activation energy of GB self-diffusion. The activation energy for the GB self-diffusion in Cu polycrystal with the same (5N) purity is 85±3 kJmol^{-1} [26] in good agreement with Eq. 8.

Conclusions. i). The possibility to determine segregation parameters only by using penetration plots obtained in the B-kinetic regime is shown based on the example of Ag GB diffusion in Cu **ii).** The segregation and migration enthalpies of Ag in Cu are determined as $-(39 \pm 2)$ kJmol^{-1} and (91 ± 12) kJmol^{-1}, respectively. **iii).** The obtained results correlate well with the previous experimental data.

Acknowledgement. We are grateful to Dr. Zs. Tokei for valuable discussions. One of us (A. O.) was supported by Young Scientist's Grant from Russian Ministry of General and Professional Education.

References

[1] L.G. Harrison, Trans. Faraday Soc. 57 (1961), p. 1191.
[2] B.S. Bokstein, I.A. Magidson, I.L. Svetlov, Phys. Met. Metallogr. 6(6) (1958), p. 81.
[3] G.B. Gibbs, Phys. Stat. Sol. 16 (1966), p. K27.
[4] D.L. Beke, I. Gödény, F.J. Kedves, Trans. Jap. Inst. Metals 27 (1986), p. 649.
[5] I. Kaur, Y. Mishin, W. Gust, *Fundamentals of Grain and Interphase Boundary Diffusion,* 3d edition, John Wiley & Sons Ltd, Chichester (1995).
[6] J. Bernardini, Zs. Tökei and D.L. Beke, Phil. Mag. A 73 (1996), p. 237.
[7] J. Bernardini, Defect Diff. Forum 66-69 (1990), p. 667.
[8] G. Martin, B. Perraillon in *Grain Boundary Structure and Kinetics*, American Society for Metals, Metals Park, Ohio(1980).
[9] B.S. Bokstein, V.E. Fradkov, D.L. Beke, Phil. Mag. A 65 (1992), p. 277.
[10] Yu.M. Mishin, Chr. Herzig, J. Appl. Phys. 73 (1993), p. 8206.
[11] B.S. Bokstein, A.S. Ostrovsky, A.O. Rodin, Phil. Mag. A 72 (1995), p. 829.
[12] B. Bokstein, A. Ostrovsky, Defect Diff. Forum 156 (1998), p. 51.
[13] D. McLean, *Grain Boundaries in Metals*, Claderon Press, Oxford (1957).
[14] M.P. Seah, E.D. Hondros, Proc.Roy. Soc A 295 (1973), p. 191.
[15] E.D. Hondros, M.P. Seah, S. Hofmann, P. Lejcek in *Physical Metallurgy* (Eds. R.W. Cahn, P. Haasen,), Elsevier Science BV (1996).
[16] M.P. Seah, J. Phys. F: Metal. Phys. 10 (1980), p. 1043.
[17] J.C.Fisher, J. Appl. Phys. 22 (1951), p. 74.
[18] I.A. Szabó, D.L. Beke and F.J. Kedves, Phil. Mag. A 62 (1990), p. 227.
[19] D.L. Beke, I. Gödeny, G. Erdélyi, F. J. Kedves, Phil. Mag. A 56 (1987), p. 659.
[20] A. Ostrovsky, K Vieregge, Chr. Herzig, Z. Metallk. in press (1998).
[21] B.S. Bokstein, G.S. Nikolsky, A.N. Smirnov, Phys. Met. Metall. 72 (2), p. 142.
[22] Zs. Tokei, private communication.
[23] M. Hansen, K. Anderko, *Constitution of binary alloys*, McGraw-Hill Book Company (1958).
[24] M. Menyhard, Mater. Sci. Forum 126-128 (1993), p. 205.
[25] Zs. Tökei, J. Bernardini, and D.L.Beke, *Interface Science and Materials Interconnection,* Proceedings of JIMIS-8, Trans. Jap. Inst. Metals (1996), p. 475.
[26] T. Surholt, Chr. Herzig, Acta Mater. 45 (1997), p. 3817.

Materials Science Forum Vols. 294-296 (1999) pp. 585-588

Kinetics of the Bi Segregation at Grain Boundaries in Polycrystalline Cu

L.-S. Chang[1], E. Rabkin[2], B.B. Straumal[1,3], B. Baretzky[1] and W. Gust[1]

[1] Max-Planck-Institut für Metallforschung and Institut für Metallkunde, Seestr. 92, D-70174 Stuttgart, Germany

[2] TECHNION-Israel Institute of Technology, Department of Materials Engineering, IL-32000 Haifa, Israel

[3] Institute of Solid State Physics, Chernogolovka, Moscow District, RU-142432 Russia

Keywords: Grain Boundaries, Segregation Kinetics, Dislocation-Pipe Diffusion

Abstract

The kinetics of Bi segregation at grain boundaries (**GBs**) in polycrystalline Cu-25 at.ppm and Cu-50 at.ppm Bi alloys has been investigated at different temperatures. In the two-phase region of the Cu–Bi phase diagram the kinetics of the Bi segregation can be described by a model of enhanced diffusion along dislocations, while in the single-phase region it obeys the classical McLean model. This enhanced pipe diffusion can be explained by the precipitation of a Bi-rich liquid phase along the dislocations in the two-phase region. From this dislocation-pipe model a linear relationship between Bi segregation and annealing time was derived.

Introduction

The thermodynamics of GB segregation in the Cu–Bi system has been investigated in a number of works (e.g. [1–4]), however, the kinetic aspects of segregation were rarely addressed [5, 6]. In other systems some attempts have been made to explain the segregation kinetics in the framework of volume diffusion [7, 8] and dislocation-pipe models [9, 10]. However, the fundamental understanding with regard to the applicability of the different kinetic models is still lacking. Moreover, the question about the phase state (single phase or two phases) of the specimens has been widely ignored.

Recently, the bulk solidus line at the Cu-rich side in the Cu–Bi phase diagram has been determined [11] and a GB solidus line has been suggested [4]. These lines provide the knowledge about the state of the bulk and of the GBs in dilute Cu–Bi alloys. Besides, the extraction of Bi from the bulk to the surface of the Cu–Bi alloys has been revealed and investigated with the help of scanning force microscopy and Auger electron spectroscopy (AES) [12]. It was supposed that the enhanced diffusion of Bi atoms occurs along the dislocation lines. It is very plausible that the same process contributes also to the Bi enrichment at GBs. In this work the kinetics of the Bi segregation at GBs in Cu has been investigated in order to clarify the applicability of the different kinetic models.

Experiment and Results

Cast polycrystalline Cu containing 25 and 50 at. ppm Bi was cut into pieces of 3×3×15 mm³. In order to investigate the kinetics of Bi segregation at GBs in the single-phase and two-phase region the temperatures of 850 and 600°C were chosen according to the Cu–Bi phase diagram [11]. All specimens were homogenized at 1000°C for 24 h. In order to be able to measure the initial value of the Bi enrichment a further homogenization was performed at 850°C for the specimens annealed at 600°C. No second homogenization was performed for specimens annealed at 850°C. The homogenized specimens were annealed at 850 and 600°C for different time. The details of the heat treatment are listed in **Table 1**. After annealing the specimens were quenched in water in order to preserve the Bi enrichment at GBs. Then the Bi concentration in the GB was measured by means of AES on *in situ* fractured specimens. Further experimental details may be found in Ref. [13].

Table 1 The details of heat treatment.

Bulk conc.	1st Homogenization		2nd Homogenization		Annealing	
at. ppm Bi	T,°C	t, ks	T,°C	t, ks	T,°C	t, ks
25.....	1000	86.4	–	–	850	0.9/1.8/3.6/10.8/14.4/86.4
	1000	86.4	850	604.8	600	0.3/0.6/0.9/1.8/3.6/86.4/172.8/864
50.....	1000	86.4	850	604.8	600	0.3/0.9/86.4/172.8/2592

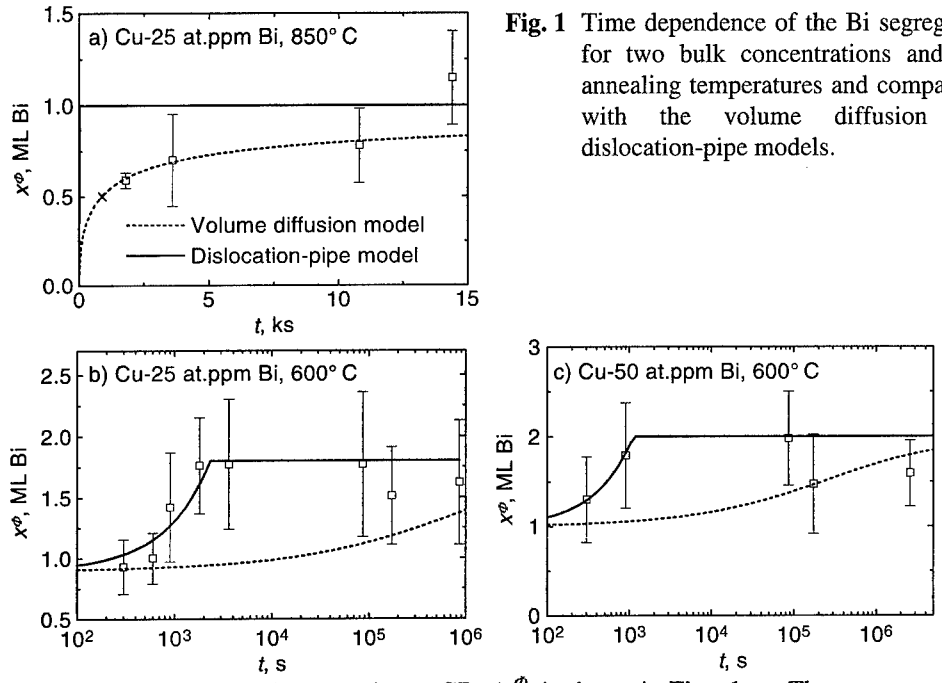

Fig. 1 Time dependence of the Bi segregation for two bulk concentrations and two annealing temperatures and comparison with the volume diffusion and dislocation-pipe models.

The time dependence of the Bi segregation at GBs (x^Φ) is shown in **Figs. 1a-c**. The square symbols designate the Bi segregation averaged over 15-20 GBs in one polycrystalline specimen. The error bars are determined from the distribution of the Bi enrichment. The cross indicates that a specimen could not be broken. The Bi concentration is given in monolayers (MLs). One ML is defined in this work as 9.3 atoms/nm². The threshold value of the Bi enrichment for embrittlement is about 0.5 ML, therefore, the cross was set to 0.5 ML. The equilibrium Bi enrichment at GBs in Cu–25 at. ppm Bi was achieved in this work after annealing for 4 h (14.4 ks) at 850°C (**Fig. 1a**) and after 0.5 h (1.8 ks) at 600°C (**Fig. 1b**). For Cu–50 at. ppm Bi the annealing time for saturation was 0.25 h (900 s) at 600°C (**Fig. 1c**).

Discussion

For the interpretation of our data we firstly used the volume diffusion model of McLean [7]. The McLean equation can be written as followed

$$\frac{x^\Phi(t)-x^\Phi(0)}{x^\Phi(\infty)-x^\Phi(0)}=1-\exp\left(\frac{4Dt}{s^2\delta^2}\right)\operatorname{erfc}\left(\frac{2\sqrt{Dt}}{s\delta}\right) \quad (1)$$

where $x^\Phi(t)$, D, δ and s are the Bi concentration at GBs for the annealing time t, the volume diffusion coefficient, the GB thickness and the Bi segregation factor ($s = x^\Phi(\infty)/x^B$ where x^B is the bulk concentration), respectively. The results are drawn as dashed lines in **Figs. 1a-c**. It is clearly seen that only for Cu–25 at. ppm Bi at 850°C (**Fig. 1a**) the model fits to the experimental data. In this case the specimens are in the single-phase region (Cu-rich solid solution) of the Cu–Bi phase

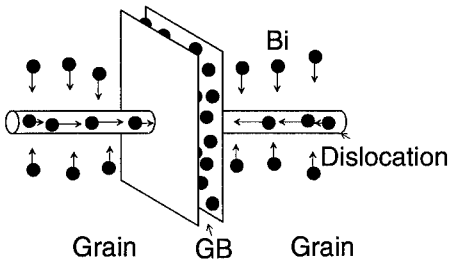

Fig. 2 Schematic view of the dislocation-pipe model.

diagram. Cu–25at. ppm Bi alloys contain so little Bi at GBs after an annealing at 1000°C for 24 h that the GB is not brittle. Therefore $x^{\Phi}(0)$ was set to zero in **Fig 1a**.

To address the discrepancy between the experimental data and the volume diffusion model, we developed a new dislocation-pipe model. A schematic view illustrating the principles of this model is shown in **Fig. 2**. To simplify the model we assume: a) The dislocation-pipe diffusion coefficient ($D^{\perp}$) is much larger than the volume diffusion coefficient. The same assumption has been made by Arabczyk et al. [8] with $D^{\perp}/D \approx 10^5$. b) The bulk flux of Bi atoms into the dislocation is equal to that along the dislocation to the GB. c) The effective diffusion zone around the dislocation is much smaller than the distance between dislocations. d) The dislocation-pipe diffusion is stopped after reaching the previously measured saturation value of the Bi enrichment at GBs [4]. From these assumptions it can be seen that the rate determining process is the volume diffusion of Bi in solid Cu, not the dislocation-pipe diffusion. Starting from the cylindrical Fick's diffusion equation and with some further simplifications we obtain

$$x^{\Phi}(t) - x^{\Phi}(0) = \frac{\rho^{\perp} x^{B} dDt}{\alpha\delta} \qquad t < t_{sat}$$
$$x^{\Phi}(t) = x^{\Phi}(\infty) \qquad t \geq t_{sat} \tag{2}$$

where $\rho^{\perp}$, d and t_{sat} are the dislocation density (= $10^{11}/m^2$), grain size (= 500 μm) and the time for Bi saturation at GBs, respectively. α is a numerical constant between 2 and 4. A detailed description of the derivation of Eq. (2) can be found in Ref. [13]. The results from Eq. (2) are drawn as solid lines. These solid lines agree well with experimental data in **Figs. 1b** and **c** for the specimens which are in the two-phase region (Cu-rich solid solution + liquid) of the phase diagram except that in **Fig. 1a**.

The kinetics of the Bi enrichment at GBs in both regions of the phase diagram cannot be described by only one model. However, the parameters used in the two models are the same in both regions of the phase diagram: The volume diffusion coefficient has been explicitly determined and has the same value in both models. The specimens in both regions have similar grain size and dislocation density due to the same homogenization treatment. However, in the two-phase region of the phase diagram the precipitation of a Bi-rich liquid phase along dislocation lines is possible. This can explain the applicability of these two models in different regions. The Bi enrichment in dislocations enhances the atom flux along the dislocation to such an extent that the assumptions of the dislocation-pipe model become satisfied. According to this model the dislocation diffusivity can be estimated as follows

$$D^{\perp} r_0^2 = (D^{\perp} r_0^2)_0 \exp(-\frac{Q^{\perp}}{RT}) \tag{3}$$

where $(D^{\perp} r_0^2)_0 = 3.47\times10^{-22}$ m^4/s is the pre-exponential factor, $Q^{\perp} = 94.4$ kJ/mol is the activation energy, r_0 is the dislocation core radius, R is the gas constant and T is the absolute temperature.

In the framework of the suggested concept the time needed for approaching the equilibrium GB segregation level can be estimated. This can be done with the help of a temperature-time-enrichment

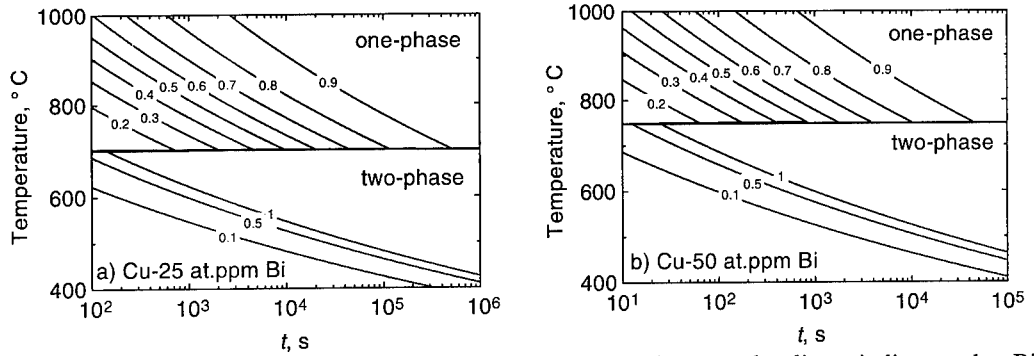

Fig. 3 Temperature-time-enrichment diagram. The number on the lines indicates the Bi enrichment as fraction of the saturated value $\{= [x^{\Phi}(t)-x^{\Phi}(0)]/[x^{\Phi}(\infty)-x^{\Phi}(0)]\}$.

(TTE) diagram. **Figure 3** shows the TTE diagrams for Cu–25 at. ppm Bi and Cu–50 at. ppm Bi. To calculate these diagrams the volume diffusion model and the dislocation-pipe model are used for the single-phase and two-phase regions, respectively. Each curve in the diagram is a contour curve with a constant enrichment level. The number on the lines indicates the Bi enrichment as fraction of the saturated value. The horizontal line in the middle of the diagram shows the bulk solidus temperature which can possibly be regarded as the dislocation solidus temperature, too. This line indicates the frontier between two different kinetic mechanisms: volume diffusion (above) and dislocation-pipe diffusion (below). Consequently, the kinetics in the two-phase region may be even faster than that in the single-phase region, although the annealing temperature in the latter case is higher.

Conclusions

The kinetics of the Bi segregation at GBs in polycrystalline Cu can be described by the volume diffusion model and the dislocation-pipe model in the single-phase and two-phase regions of the Cu–Bi phase diagram, respectively. The enhanced dislocation-pipe diffusion is explained by the precipitation of Bi-rich liquid phase along dislocation lines. Accordingly, the dislocation diffusion coefficient is estimated and a TTE diagram is constructed.

Acknowledgments

This work has been supported by the Deutsche Forschungsgemeinschaft (contract Gu 258/12-1) and partially supported by the Russian Foundation for Basic Research (grant 97-02-16830), NATO Linkage Grant HTECH.LG.970342 and INCO-COPERNICUS Network PL97-8078.

References

[1] A. Joshi and D.F. Stein, *J. Inst. Metals* **99** (1971), p. 178.
[2] E.D. Hondros and D. McLean, *Phil. Mag.* **29** (1974), p. 711.
[3] M. Menyhard, B. Blum and C.J. McMahon Jr., *Acta metall.* **37** (1989), p. 549.
[4] L.-S. Chang, E. Rabkin, B.B. Straumal, S. Hofmann, B. Baretzky and W. Gust, *Defect Diff. Forum* **156** (1998), p. 135.
[5] W.C. Johnson, A. Joshi and D.F. Stein, *Metall. Trans. A* **7** (1976), p. 949.
[6] A. Fraczkiewicz and M. Biscondi, *J. Physique* **46** (1985), p. C4-497.
[7] D. McLean, *Grain Boundaries in Metals*, Oxford, Clarendon Press (1957), p. 116.
[8] E.D. Hondros and M.P. Seah, *Inter. Metals Rev.* **22** (1977), p. 262.
[9] W. Arabczyk, M. Militzer, H.-J. Müssig and J. Wieting, *Surf. Sci.* **198** (1988), p. 167.
[10] M. Militzer, Y.N. Ivashchenko, A.V. Krajnikov, P. Lejcek, J. Wieting and S.A. Firstov, *Surf. Sci.* **261** (1992), p. 267.
[11] L.-S. Chang, B.B. Straumal, E. Rabkin, W. Gust and F. Sommer, *J. Phase Equilibria* **18** (1997), p. 128.
[12] L.-S. Chang, E. Rabkin, B. Baretzky and W. Gust, *Scripta mater.* **38** (1998), p. 1033.
[13] L.-S. Chang, Ph.D. thesis, *University of Stuttgart* (1998), p. 50.

Materials Science Forum Vols. 294-296 (1999) pp. 589-592

Direct Atomic Observation of Reactive Wetting Front on Silicon Carbide

Ch. Iwamoto[1,2] and S. Tanaka[1]

[1] Tanaka Solid Junction Project, Japan Science and Technology Corporation, 1-1-1, Fukuura, Kanazawa-ku, Yokohama 236-0004, Japan

[2] Present adress: High Voltage Electron Microscope Laboratory, Engineering Research Institute, School of Engineering, University of Tokyo, 2-11-16, Yayoi, Bunkyo-ku, Tokyo 113-8656, Japan

Keywords: HRTEM, *In Situ* Experiment, Interface, Solid/Liquid Reaction

Abstract

Defect formation mechanism in the reaction product during reactive wetting was examined in SiC/Ag-Cu-Ti molten alloy system using *in situ* high resolution transmission electron microscopy. The orientational relationship between SiC and the reaction product TiC governed the orientation of the TiC, and various defects were formed depending on the TiC nucleation site on the SiC while the nucleated TiC grew and impinged. The mechanism was discussed from the crystallographic point of view.

Introduction

The reaction between a solid material and a molten alloy with the production of a reaction phase is the basis for important bonding processes such as brazing. The reaction process is gradually revealed at an atomic scale in the SiC/Ag-Cu-Ti system[1-4]. Direct observation of the reaction in the system at high temperature indicated that during the reaction, SiC dissolution and nucleation of the reaction product TiC were repeated [3, 4]. In this process, the nucleation site of SiC behaved like a template for TiC and the crystallographic orientational relationship between SiC and TiC governed the orientation of TiC [4]. As the nucleated TiC grew and came into contact with each other, several defects were formed in TiC.

The strength of the bonded material are related to the characteristics of the reaction phase such as thickness, morphology and defect pattern. In order to control the strength of the bonded material, it is important to understand the defect formation mechanism in the reaction product.

In this study, we directly observed a dislocation formation process in the reaction product in SiC/Ag-Cu-Ti molten alloy system. The formation mechanism was discussed from the crystallographic viewpoint.

Experimental

The substrate used was a 6H-SiC single crystal wafer. The SiC wafer was cut ($2\times2mm^2$) using a low-speed cutter, mechanically ground and thinned using an Ar^+ beam. An Ag-Cu eutectic foil and a Ti foil were used as brazing alloy. These foils were cut into approximately $30\times30\mu m^2$ sizes using a scalpel. The Ag-Cu eutectic foil, which was overlapped by the Ti foil, was carefully placed on the thinned SiC wafer. The samples were mounted on a hot stage holder (JEOL) of a high resolution transmission electron microscope (JEOL JEM-2010) and heated to the nominal temperature of approximately 1073K. The specimen was observed at an accelerating voltage of 200kV.

During heating, images were recorded using a fiber-optically coupled TV (Gatan) system with a time resolution of 1/60 sec. The [1 $\bar{2}$10] axis of SiC, which is parallel to the [1 $\bar{1}$0] direction of TiC, was adjusted to be parallel to the direction of the incident electron beam.

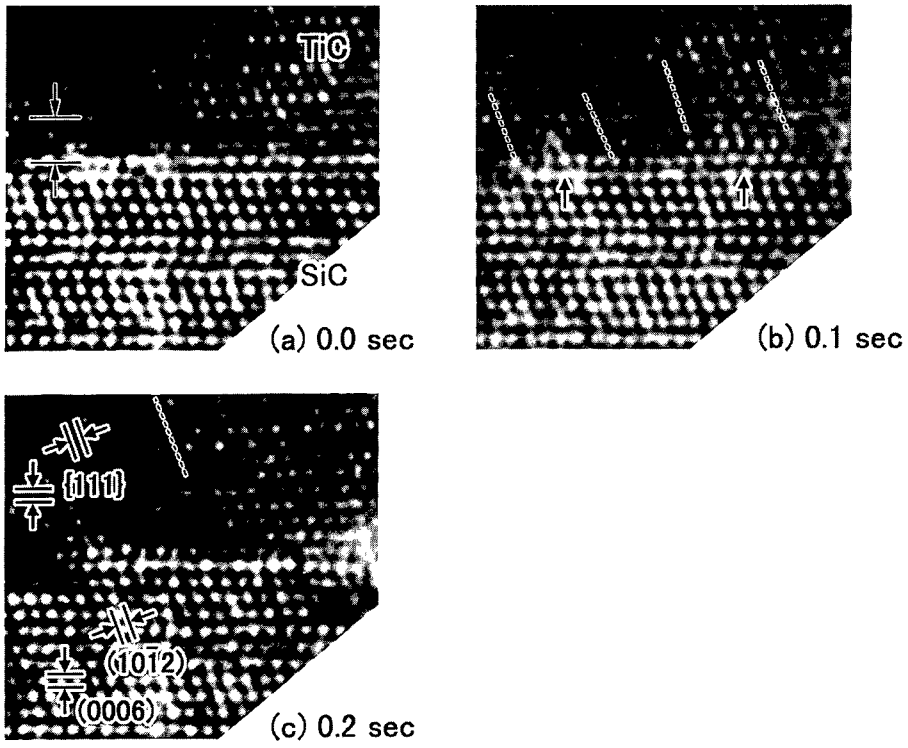

Fig. 1 Formation process of a dislocation in TiC during the reaction between SiC and molten Ag-Cu-Ti alloy. (a)An obscure contrast region which indicates the instability of the lattice is observed at the region between the SiC and TiC. (b)TiC nucleate on the basal planes of SiC which are denoted by two arrows and join with TiC which has already been formed during the reaction. (c)A dislocation remains in TiC standing off from the SiC/TiC interface.

Experimental results and discussion

The high resolution observation revealed that two different processes were repeated during the reaction; dissolution of SiC, and nucleation and growth of a reaction product [3, 4]. Figure 1 shows the formation process of the defect in reaction product TiC during the reaction. The molten alloy spreads from top to bottom in the image. An obscure contrast region which indicates the instability of the lattice was observed at the region between the SiC and TiC in Fig. 1(a). In this region, dissolution of SiC and Ti supply from the Ag-Cu-Ti molten alloy to produce TiC may take place. From this region, TiC nucleate on the basal planes of SiC which is denoted by two arrows and join with TiC which has already been formed during the reaction (Fig. 1(b)). An obscure contrast region is still observed between two arrows. Then, the obscure contrast disappeared and a dislocation, standing off from the SiC/TiC interface, remains in TiC.

The reason for the formation of the defect was considered from the crystallographic viewpoint. In the reactive wetting process in SiC/Ag-Cu-Ti molten alloy, the nucleation site of SiC behaved like a mold for TiC and the crystallographic orientational relationship between SiC and TiC governed the orientation of TiC. Depending on the nucleated TiC orientation, a characteristic boundary is produced, as the growing TiC come into contact with each other [4]. In this experiment, TiC nucleates on the basal plane of SiC and the orientation of TiC is similar to that of the TiC which is already formed during the reaction. Thus, the nucleated TiC is considered to produce a defect free single crystal TiC with the already formed TiC.

The misfit between TiC and SiC at the interface is small. The spacing of the $(10\ \bar{1}2)$ plane of SiC is 0.2511nm and that of the (111) plane of TiC is 0.2499nm. The misfit is about 0.48% and does not seems to be the reason for the defect formation in the observed region. Thus, the shift of the surface atomic structure parallel to the basal plane of SiC is considered to be the reason for the defect formation.

The basal plane of 6H-SiC consists of stacked polar planes which are formed by either C or Si atoms. The atomic sites on the polar planes differ in position by d/3 (d denotes the spacing between atoms which exist on the basal plane) parallel to the basal plane between each polar plane. Figure 2 depicts one of the probable model which may explain the experimental results. In this structural model of the interface between SiC and TiC[5], C atoms serve as a bridge between two lattices. Lattice relaxation at the interface is not considered. Since the resolution of the high magnification image was not enough, we could not determine a unique structure experimentally. In this model, TiC (A), TiC(B) and TiC(C) nucleate different polar planes. At the interface between TiC (A) and TiC (C), atomic sites differ in position by d/3 and two lattices may become strained so as to form coincident atomic sites. Similarly, at the interface between TiC (B) and TiC (C), and the interface between TiC (A) and TiC (C), two lattices may become strained. Consequently, triple junction among the TiC (A), TiC(B) and TiC(C) lattices, a difference in position of d/3+d/3+d/3=d exists and the difference may be relaxed by the formation of lattice dislocation which is observed in Fig. 1(c). These considerations suggest that although the nucleated TiCs have the same orientations,

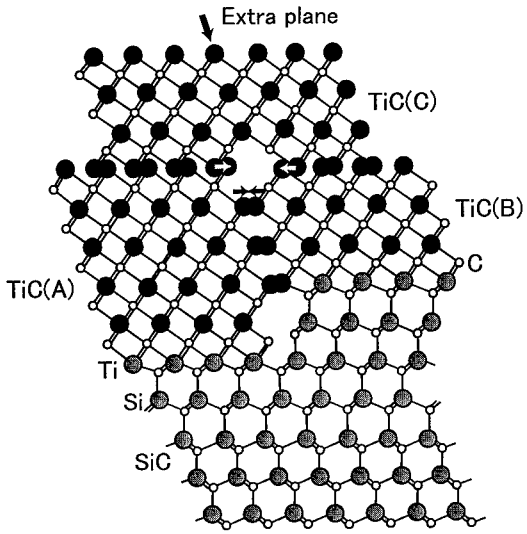

Fig. 2 Dislocation formation model around SiC/TiC interface. TiC (A), TiC(B) and TiC(C) which nucleate different polar planes join each other and produce a lattice dislocation which is observed in Fig. 1(c).

defects are formed by the shift of the atomic sites parallel to the interface. In order to control the defect formation around the interface, the control of TiC orientation is not enough during the solid/liquid reaction.

Conclusions

Defect formation mechanism in the reaction product during reactive wetting was examined in SiC/Ag-Cu-Ti molten alloy system using an *in situ* high resolution transmission electron microscope. It was considered that not only the orientation variation but also the position variation of each nucleated TiC was controlled by the surface structure of the SiC and resulted in the production of defects in TiC after reaction.

Acknowledgments

We would like to thank Professor H.Ichinose for the stimulating discussion and interest in this work.

References

[1] T.Yano, H.Suematsu and T.Iseki, *J. Mater. Sci.* **23** (1988) p.3362-3366.

[2] C.Iwamoto and S.-I.Tanaka, *Acta Materialia.* **46**, 7 (1998) p.2381-2386.

[3] C.Iwamoto, H.Ichinose and S.-I.Tanaka., *Philosphical Magazine A* in print.

[4] C.Iwamoto and S.-I.Tanaka, *Philosphical Magazine A* in print.

[5] F.R.Chien, S.R.Nutt, J.M.Carulli, Jr.N.Buchan, Jr.C.P.Beetz and W.S.Yoo, *J.Mater. Res.*, **9**, 8, (1994) p.2086-2094.

Materials Science Forum Vols. 294-296 (1999) pp. 593-596

Cellular Precipitation at Different Sites in Copper Based Alloys

D. Hamana and Z. Boumerzoug

Research Unit in Materials Physics and Applications, University of Constantine, Algeria

Keywords: Discontinuous Precipitation, Grain Boundary, Interphase Boundary, Lamellar Structure, Coarsening

Abstract. The reaction of discontinuous (cellular) precipitation which is of diffusional nature, takes place at static or migrating boundaries and advances into grain interiors. The development of this reaction at grain and interphase boundaries which provide diffusivity paths in solids is explained by different mechanisms. This investigation has been carried out to study the different sites of cellular precipitation in Cu-Sb, Cu-Ag and Cu-In systems by utilizing optical and scanning electron microscope and X-ray diffraction. An overview of various sites of discontinuous precipitation like grain boundaries, different interphase boundaries and dislocations in the grain interiors is given. Moreover a change in the development sequence of the first (which gives fine lamellar structure) and the second (which gives coarse lamellar structure) discontinuous reactions is presented.

Introduction

In discontinuous precipitation, also known as cellular precipitation, a supersaturated α' phase decomposes into a new β phase and an α phase structurally identical to α' but depleted in solute. The transformed zone is separated from the original phase by an interface called the reaction front in which all the diffusion processes that are involved in the reaction take place. Generally, the reaction fronts are migrating grain boundaries that act as fast diffusion paths, allowing the required composition change at temperatures too low for appreciable volume diffusion [1]. The moving boundary plays a crucial role in providing the primary route of solute transport [2-4]. It is generally believed that only the large angle matrix grain boundaries can support the process of heterogeneous precipitation and the concurrent boundary migration required for discontinuous precipitation [5] Initiation of the reaction depends crucially on the structure and properties of individual grain boundaries and their ability to nucleate grain boundary precipitates [3]. However, recent studies have demonstrated that under certain conditions the precipitate/matrix type of phase boundaries may be equally capable of initiating discontinuous precipitation as grain boundaries [6-8]. Besides a discontinuous coarsening (DC) or secondary cellular reaction is observed in a number of alloy systems [7,9]. Generally the product of the secondary cellular reaction has a coarse lamellae structure which gradually replaces the fine lamellar structure of the primary cells. All these results confirm the complexity of the precipitation and coarsening and explain the need of a further detailed study of such processes of phases transformation.
The aim of this work is to show the existence of different sites of discontinuous precipitation and to follow the coarsening reaction process in a Cu-9 wt. % Sb, Cu-6.5 wt % Ag and Cu -15 wt % In alloys.

Experimental procedure

The alloys were prepared from copper and indium of 99,999 wt % purity and silver and antimony of 99,99 wt % purity by melting under vacuum ($1,3 \times 10^{-1}$ Pa) in an alumina crucible. Cylindrical specimens about 3 mm thick were then cut from the casting and encapsulated in silica tubing under vacuum. The samples were homogenised 600 °C for 7 days, water quenched and aged at different

temperatures for various times. The decomposition of the supersaturated solid solution was followed mainly by optical and electron scanning microscopy, and X-ray diffraction.

Experimental results and discussion

Typical microstructure of cellular precipitation in the Cu - 9 wt % Sb alloy from grain boundary during ageing at 573 K is shown in Fig. 1. In the latter one can notice a structure with a larger interlamellar spacing and consisting of equilibrium α phase and a solute rich precipitate phase ε (Fig. 1a) with different direction in two adjacent grains. There is no indication of continuous or general precipitation in the observed microstructure. Moreover diffraction peak position and microhardness value in different regions of the supersaturated solid solution are not changed during ageing. An other site of initiation of discontinuous precipitation is observed in the grain interior, not far from a grain boundary (Fig. 2a). This type of cellular precipitate which has been observed by Saheb et al in Cu - 15 wt % In alloy [10] , can not be the emergence of a cell formed at the surface of the grain boundary in the volume interior, because successive polishing alternated with microscopic observations show that the cell has not a contact with the grain boundary (Fig. 2b). It is most probably the result of a nucleation and growth at a structural defect as dislocations. Matrix/eutectic boundary (Fig. 3a) and matrix/cell interface (i.e. the initial position of the moving grain boundary) (Fig. 3b) can also be the sites for discontinuous precipitation. The nucleation and the growth of cells in the adjacent grains 1 and 2 is followed by a new cell formation at the initial position of the moving high-angle grain boundary (Fig. 3b) which can also become a second reaction front and permits the formation of a new cell in grain 2 after the nucleation and growth of the first cell in the grain 1 This important and unexpected result, can not yet be explained by all proposed mechanisms. Generally the formation of a cell with two-phase aggregate occurs across a moving boundary, advancing into a supersaturated solid solution. The lamellar coarsening in Cu - 9 wt % Sb alloy is observed during the first stage of ageing at 573 K in undeformed alloy, when coarser lamellae nucleate at grain boundary of the supersaturated solid solution (Fig. 4a) and at a hole (Fig. 4b).The microstructural evolution in the same regions (Fig. 4) shows that after this reaction, finer lamellae appear at the reaction front of the coarser structure. This reversed sequence of lamellar structure development which has been observed recently by Hamana and Boumerzoug [11] is also difficult to explain. The fact that the interlamellar space is first higher then slower is certainly due to the rate growth variations. Generally coarsening reactions transform fine two phase microstructures produced by discontinuous precipitation into coarser structures of the same two phases. Morphologically the reaction is characterised by the migration of the boundary between two fine lamellar colonies resulting from the first reaction from one colony into the other and leaving behind a coarser lamellar structure of the same two phases. In all studies of discontinuous coarsening it has been found that the coarsening reaction proceeds at a much slower rate than the discontinuous precipitation reaction preceding it, that it results in a coarser lamellar spacing and that in those cases where the phase compositions were determined, those resulting from the coarsening reaction are closer to equilibrium than those resulting from the first reaction [12]. A reduction of the interfacial energy "depleted matrix/solute-rich phase" can explain the discontinuous coarsening [7].In our case a coarser lamellar space is observed in the first formed cells (Fig. 1) and with increasing ageing time, at the reaction front of these cells a new two-phase product with a finer lamellar space is formed (Fig. 4).
The same observations has been practically done for the two other studied alloys (Cu-6.5 wt % Ag and Cu-15 wt % In) (Fig. 5).

Conclusion

The study of the discontinuous precipitation in Cu-based alloys has shown that cellular precipitation can occur at different sites as large angle boundaries, eutectic/supersaturated solid solution interface, defects in the grain interior and unexpected original grain boundary position. However, on the contrary of the generally observed discontinuous reactions, coarse cellular structure appears before the fine one which develops at the reaction front of coarse cell.

References

[1] I.G. Solorzano, W. Gust, Materials Science Forum, 94-96 (1992), p. 659.
[2] W. Gust in "Phase transformations", Serie 3, N°11, Vol. 1, Spring Res. Conf. (University of New York, 1979) p. II-27.
[3] D.B. Williams, E.P. Butler, Int. Met. Reviews, 3 (1981) p. 158.
[4] M. Frisel, I. Manna and W. Gust, Colloque de Physique, 51 (1990) p. C1-381.
[5] R.D. Doherty, in "Physical Metallurgy", edited by R.W. Cahn and P. Hoasen (North-Holland Physics, Amsterdam, 1983) p. 1002.
[6] I. Manna, S. K. Pabi, W. Gust, J. Mater. Sci., 26 (1991) p. 4888.
[7] D. Hamana, Z. Boumerzoug, Z. Metallkd. 7 (1994) p. 85.
[8] D. Hamana, Z. Boumerzoug, N. Saheb, Phil. Mag. Let. 72 (1995) p. 369.
[9] R.A. Fournelle, Acta Metall. 27 (1979) p. 1135.
[10] N. Saheb, Z. Boumerzoug, D. Hamana, Scripta Met. Mater., 32 (1995) p. 1453.
[11] D. Hamana, S. Nebti, Z. Boumerzoug and A. Boutefnouchet, Phil. Mag. A, 67 (1993) p. 1143.
[12] W. Gust, R.A. Fournelle, Anais do 7° CBECIMAT, UFSC, (Florianopolis, SC Dezembro de 1986) p. 273.

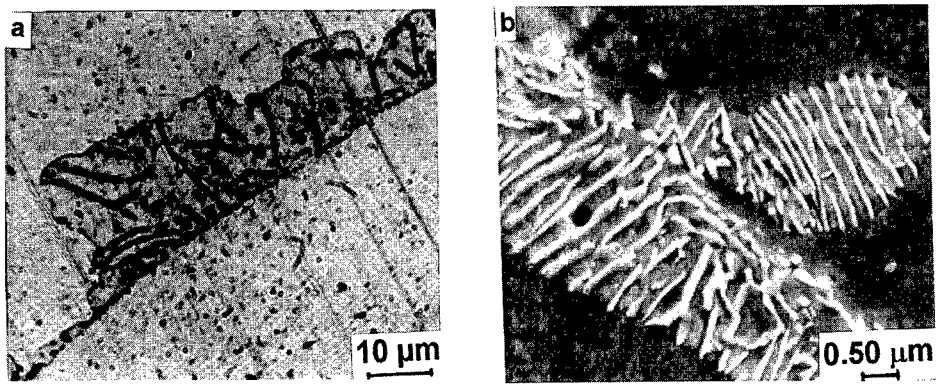

Fig. 1 Microstructure of Cu - 9 wt % Sb alloy homogenised, quenched and aged at 573 K for 30 h showing coarse cellular reaction at the earlier stages (a) with different lamellae orientation in adjacent grains (b).

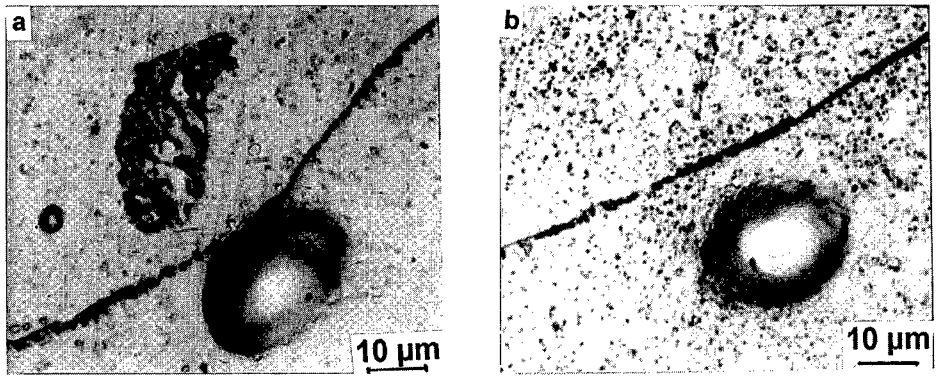

Fig. 2 Microstructure of Cu - 9 wt % Sb alloy homogenised, quenched and aged at 573 K for 411 h showing a cell formation in the grain interior (a and b).

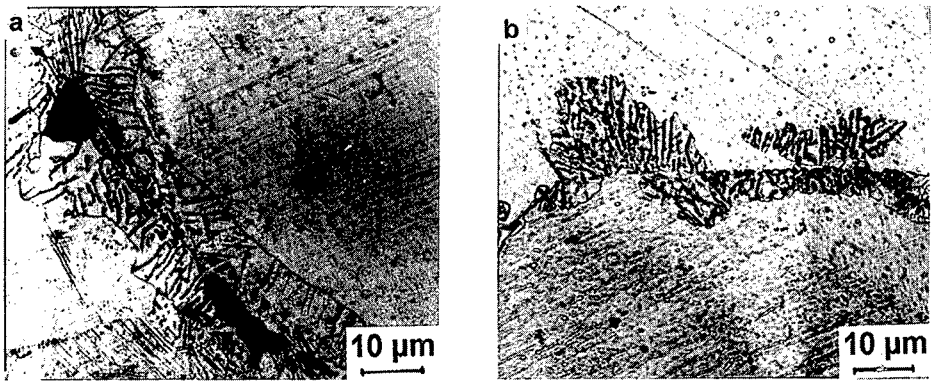

Fig. 3 Microstructure of Cu - 9 wt % Sb alloy homogenised, quenched and aged at 573 K for 168 h showing a coarse cellular precipitation at eutectic/supersaturated solid solution boundary (a) and a cellular precipitation at original grain boundary position/supersaturated solid solution interface (b).

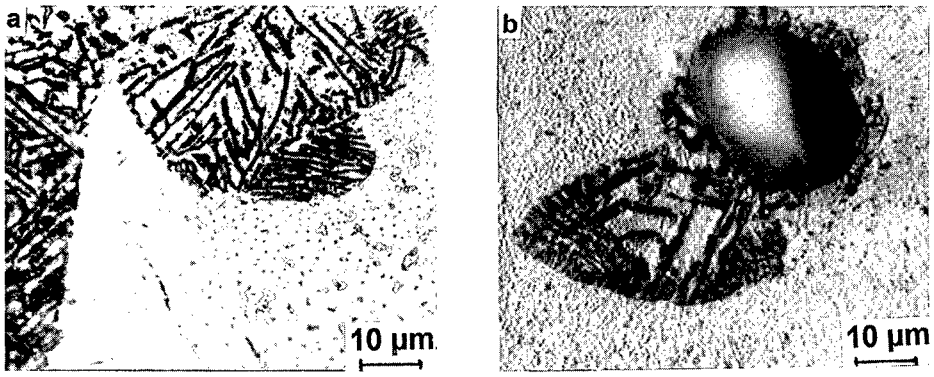

Fig. 4 Microstructure of Cu - 9 wt % Sb alloy homogenised, quenched and aged at 573 K for 280 h showing the fine cell structure at the reaction front of a coarse cell (a and b).

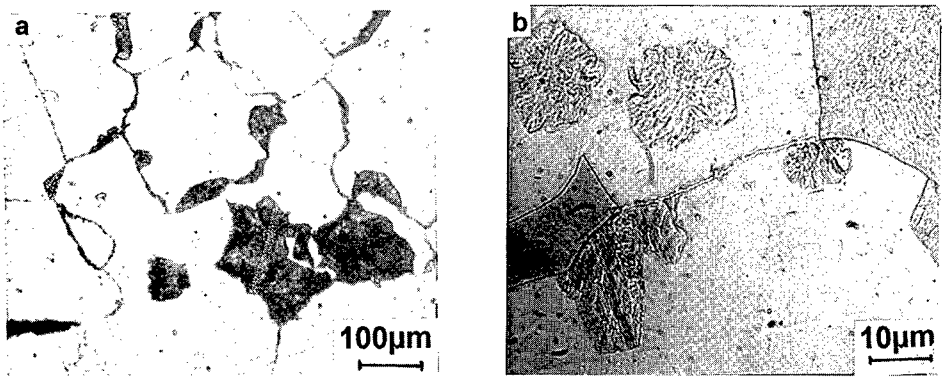

Fig. 5 Microstructures of homogenised, quenched and aged at 573 K for 30 h Cu – 6.5 wt % Ag alloy (a) and at 673 for 2 h Cu – 15 wt % In alloy (b) showing precipitation in the grain interior and at the eutectic/matrix interphase boundary.

Materials Science Forum Vols. 294-296 (1999) pp. 597-600

Topotaxial Reaction Fronts in Complex Ba-Ti-Si Oxide Systems Studied by Transmission Electron Microscopy

D. Hesse, A. Graff, S. Senz and N.D. Zakharov

Max-Planck-Institut für Mikrostrukturphysik, Weinberg 2, D-06120 Halle/Saale, Germany

Keywords: Interfaces, Solid State Reactions, Titanates, High-Resolution TEM, Reaction Mechanisms

Abstract

Processes and interface structures occurring during $BaTiO_3$ sintering in the presence of the sintering aid SiO_2 are studied by model experiments. The formation of fresnoite $Ba_2TiSi_2O_8$ and different Ti-rich barium titanates by solid state reactions proceeding at the (001)$BaTiO_3$/SiO_2 interface is followed by XRD and TEM. High resolution transmission electron microscopy (HRTEM) permits the structure to be studied of the various solid-solid reaction fronts involved. The observations indicate, e.g., a certain topotaxial reaction mechanism at the $Ba_4Ti_{13}O_{30}$/$BaTiO_3$(001) and $Ba_6Ti_{17}O_{40}$/$BaTiO_3$(001) reaction fronts, which comprises the outdiffusion of barium, the indiffusion of titanium and oxygen, and a restacking of the $BaTiO_3${111}planes.

1. Introduction

Complex reactions between $BaTiO_3$ and SiO_2 generally occur during the sintering processes of $BaTiO_3$ ceramics, if the sintering aid SiO_2 is applied [1-3]. Phases forming and processes or structures occurring during these complex reactions, have, however, not been studied in detail. Recently, spinel oxide reactions of medium complexity have successfully been evaluated, and certain topotaxial reaction mechanisms have been derived, after investigating the structure of the involved reaction fronts by high resolution cross-sectional electron microscopy. Interrelations between the structure of the reaction front, the mechanism of the interfacial reaction, and the overall kinetics were established [4-7]. In view of this rather successful approach investigations of more complex reactions in the $BaTiO_3$-SiO_2 system are now under way. After describing details of phase formation and orientation relationships in Refs. 8 and 9, we now report on recent results concerning the structure of the involved reaction fronts.

2. Experimental

Thin amorphous SiO_2 films of 100 nm thickness were electron-beam deposited onto polished $BaTiO_3$(001) single-crystal surfaces (10x10x1mm^3) in high vacuum, maintaining an oxygen pressure of 10^{-2} Pa and a substrate temperature of 500 °C. After deposition, the samples were annealed in air in a laboratory furnace for 2 h and 8 h, respectively, at temperatures between 700 and 1300 °C. Thin-film X-ray diffraction (θ-2θ scans and pole figures) was performed in a Philips X'Pert MRD equipped with a Cu tube and an open Eulerian cradle. Specimens for TEM were prepared by mechanical and ion beam thinning following standard procedures. TEM/SAED and EDX investigations were performed in a Philips CM20T, whereas a JEOL 4000 EX was applied for HRTEM.

3. Results

3.1. Phase formation and crystallographic orientation

Starting at a reaction temperature of 700 °C, solid state reactions between the SiO_2 film and the $BaTiO_3$ substrate were observed to occur. At 700 and 800 °C, $Ba_2TiSi_2O_8$ (fresnoite) islands originate at the $BaTiO_3/SiO_2$ interface and grow through the SiO_2 film to the surface of the latter, where they continue to grow in lateral direction (Fig.1). This reaction obviously follows the overall scheme

$$2\ BaTiO_3 + 2\ SiO_2 \rightarrow Ba_2TiSi_2O_8\ (\text{fresnoite}) + TiO_2. \quad (1)$$

From XRD, SAED and HRTEM the orientation relation

$$(120)_F \text{ or } (210)_F \parallel (001)_{BT};\ [001]_F \parallel [100]_{BT} \text{ or } [010]_{BT} \quad (2)$$

was deduced („F" - fresnoite; „BT" - $BaTiO_3$) [8]. After about 2 h at 800 °C, large fresnoite grains have formed, with small amorphous regions remaining. At higher temperatures, fresnoite loses its orientation (2) and turns polycrystalline assuming a fiber texture [9]. A marker experiment [9], with platinum islands steadily marking the position of the initial $BaTiO_3/SiO_2$ interface, showed that during the fresnoite formation both in- and out-diffusion processes occur. Reactions of the released TiO_2 (*cf.* Eq.1) with the $BaTiO_3$ substrate result in the formation of Ti-rich phases. For example, $Ba_4Ti_{13}O_{30}$ and $Ba_6Ti_{17}O_{40}$ form at temperatures above 1000 °C according to the overall reactions

$$4\ BaTiO_3 + 9\ TiO_2 \rightarrow Ba_4Ti_{13}O_{30}, \quad (3)$$

$$6\ BaTiO_3 + 11\ TiO_2 \rightarrow Ba_6Ti_{17}O_{40}. \quad (4)$$

The Ti-rich phases form grains of a distinct crystallographic habit. They are located between the fresnoite grains, but they are in contact with the $BaTiO_3$ substrate (Fig.2). The Ti-rich phases („TRP") proved [8,9] to grow according to the orientation relation (*cf.* [10])

$$(001)_{TRP} \parallel (111)_{BT};\ [010]_{TRP} \parallel [110]_{BT}. \quad (5)$$

Other Ti-rich phases also grow, the lattice parameters of which, however, do not correspond to either of the Ti-rich Ba-Ti-O phases known from the JCPDS files [11]. The characterization of these phases by SAED and PEELS is in progress. In terms of the present paper they will be named „new titania-rich" („NTR") phases. Structurally, these NTR phases are very similar to $Ba_4Ti_{13}O_{30}$ and $Ba_6Ti_{17}O_{40}$. For example, they are characterized by stacked planes and typical stacking faults (*cf.* Fig.3) parallel to the $BaTiO_3\{111\}$ planes, on the very analogy of the (001) planes of $Ba_4Ti_{13}O_{30}$ and $Ba_6Ti_{17}O_{40}$. Their crystallographic orientation follows a relation most similar to Eq.5.

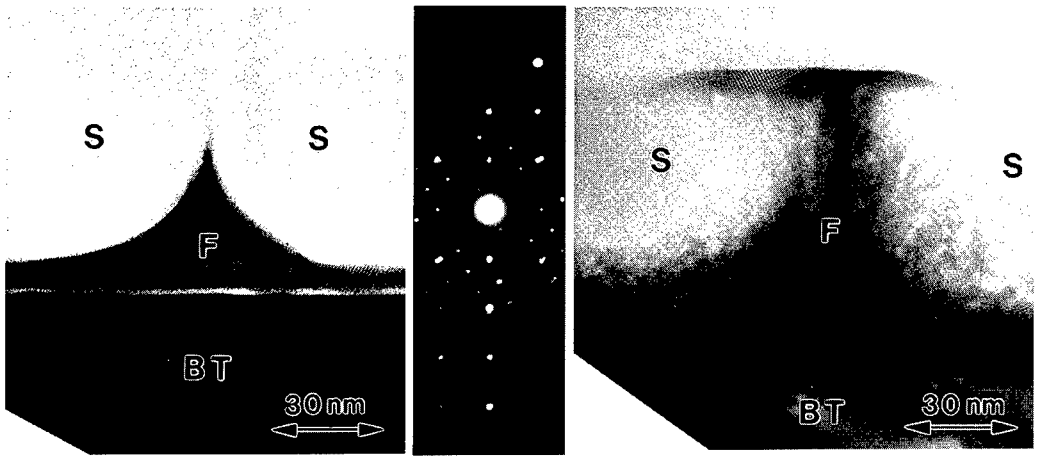

Fig.1 Cross section TEM images demonstrating two growth stages of fresnoite islands (F) grown into the SiO_2 film (S) on the $BaTiO_3$ substrate (BT). The inset shows a fresnoite diffraction pattern together with some $BaTiO_3$ substrate reflections. Beam direction is $[100]_{BT} = [001]_F$.

3.2. Grain morphology

In TEM cross-sectional micrographs the TRP grains (including the NTR grains) are easy to recognize, because most of them have an elongated, distinctly plate-like shape (Figs. 2 and 3). The plate surfaces („PS"), seen edge-on in the figures, are formed by the $(001)_{TRP}$ planes. In accordance with Eq.5, the latter are parallel to the $\{111\}_{BT}$ planes of the substrate thus forming an angle of 54.7° (or 125.3°, resp.) with the $BaTiO_3(001)$ substrate surface. As Fig.3 also shows, the TRP grains contain stacking faults, most of which are parallel to the $(001)_{TRP}$ planes.

3.3. Reaction fronts

Figure 4 shows a cross section HRTEM image of a typical TRP/$BaTiO_3$ reaction front located under a TRP grain. Clearly visible are the plate surface („PS") and the $(001)_{TRP}$ planes, both making an angle of 125.3° with the „actual" $BaTiO_3(001)$ substrate surface („ASS"). Due to the reaction, the actual substrate surface most probably moved down from the initial position of the $BaTiO_3$ substrate surface. The proper reaction front is formed by the end faces of broad stacks of (001) planes separated by ledges („L"). The stacks, in turn, consist of bundles of individual (001) planes, which clearly suggest to have moved into the $BaTiO_3$ substrate. Taking into account that the formation of the TRP (NTR) phase *within* the $BaTiO_3$ substrate obviously proceeds in a stress-free manner, the following reaction mechanism has been derived: The grains of the Ti-rich phases, i.e. $Ba_4Ti_{13}O_{30}$, $Ba_6Ti_{17}O_{40}$, or one of the NTR phases, grow into the $BaTiO_3$ substrate along the $(111)_{BT}$ planes. Along the latter, Ba ions are outdiffusing and Ti and oxygen ions are indiffusing, whereas at the reaction front the $(111)_{BT}$ planes are rearranged into $(001)_{TRP}$ planes by corresponding atomic-scale steps. The nature of the latter may be deduced from a detailed evaluation of the structures. The lattice of $BaTiO_3$ consists of regularly stacked BaO_3 and Ti layers parallel to the $\{111\}$ plane. If Ba ions are removed from two neighbouring BaO_3 planes, and a Ti ion is allowed to occupy a corresponding site in the Ti layer in between, a Ti-rich lattice may form out of the $BaTiO_3$ lattice. Details are under investigation.

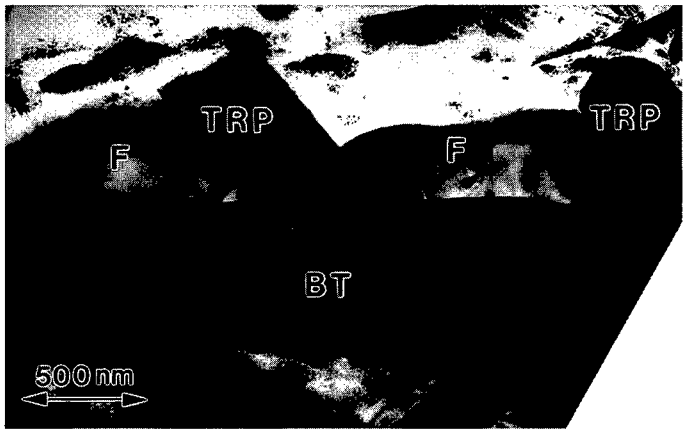

Fig. 2 Cross section TEM image showing two grains of Ti-rich phases (TRP) grown in between the fresnoite grains (F) on the $BaTiO_3$ substrate (BT). Beam direction is $[1\bar{1}0]_{BT} = [010]_{TRP}$.

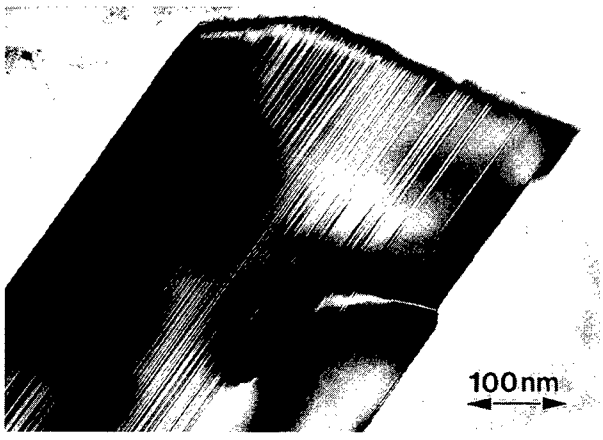

Fig.3 Cross section TEM image of a Ti-rich grain with a large number of stacking faults on the $(001)_{TRP}$ planes. Beam direction is $[010]_{TRP}$.

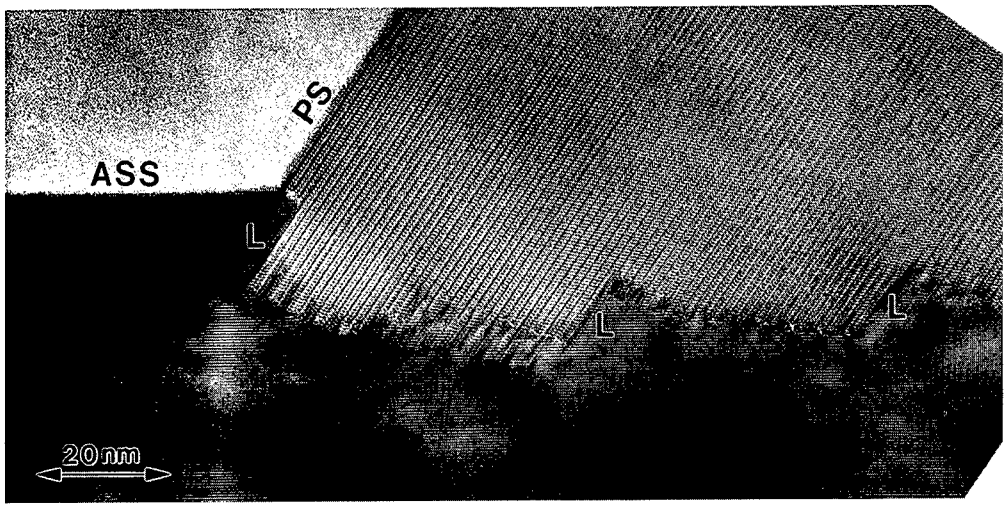

Fig.4 HRTEM cross section image of the reaction front under a Ti-rich grain. Beam direction is $[1\bar{1}0]_{BT} = [010]_{TRP}$.

4. Conclusions

Sintering processes of $BaTiO_3$ ceramics with SiO_2 as the sintering aid have been modeled by single-crystal investigations. At temperatures above 700 °C and 1000 °C, respectively, fresnoite $Ba_2TiSi_2O_8$ and various Ti-rich phases ($Ba_4Ti_{13}O_{30}$, $Ba_6Ti_{17}O_{40}$ and other new phases) form by solid state reactions. Fresnoite forms by the diffusion of Ba and Ti out of the $BaTiO_3$ substrate, and of Si into it. At low temperatures (700 and 800 °C), fresnoite obviously nucleates at the $BaTiO_3$ surface and grows topotaxially in a near-coincidence site lattice orientation, whereas at higher temperatures the nuclei are more or less randomly oriented. The Ti-rich phases (TRP) always grow well oriented. They are formed by a topotaxial reaction involving the barium outdiffusion and the titanium and oxygen indiffusion along the $(001)_{TRP}$ planes as well as a well-ordered restructuring of the $\{111\}_{BT}$ planes into the $(001)_{TRP}$ planes at the reaction front.

Acknowledgement

The authors are grateful to Professor H.-P.Abicht for numerous fruitful discussions and helpful comments, as well as to Professor U.Gösele for his continuous support.

References

[1] H.-P.Abicht, H.T.Langhammer, and K.-H.Felgner, J.Mater.Sci. **26** (1991) p.2337.
[2] K.H.Felgner, U.Nilius, H.T.Langhammer, and H.-P.Abicht, J.Mater.Chem. **2** (1992) p.575.
[3] H.F.Cheng, T.F.Lin, C.T.Hu, and I.N.Lin, J.Am.Ceram.Soc. **76** (1993) p.827.
[4] D.Hesse, Solid State Ionics **95** (1997) p.1.
[5] H.Sieber, D.Hesse and P.Werner, Phil. Mag. A **75** (1997) p.889.
[6] H.Sieber, P.Werner and D.Hesse, Phil. Mag. A **75** (1997) p.909.
[7] A.Graff, S.Senz, N.D.Zakharov and D.Hesse, *accepted by* Z.Phys.Chem. (1998).
[8] S.Senz, A.Graff, W.Blum, D.Hesse and H.-P.Abicht, *accepted by* J.Am.Ceram.Soc. (1998).
[9] S.Senz, A.Graff, W.Blum, H.-P.Abicht, and D.Hesse, *submitted to* Proc. 9th World Ceramic Congress & Forum on New Materials CIMTEC'98, Florence/Italy, June 14-19, 1998.
[10] V.Krasevec, M.Drofenik, and D.Kolar, J.Am.Ceram.Soc. **70** (1987) p.C-193.
[11] JCPDS data base on CD-ROM, Int. Centre for Diffraction Data, Newton Square, PA (1995).

Materials Science Forum Vols. 294-296 (1999) pp. 601-604

Evidence for Slow Self-Diffusion Along Special CSL Grain Boundaries from the Kinetics of Discontinuous Ordering in Fe-50 at.%Co

E. Rabkin[1], V. Semenov[2], E. Bischoff[3] and W. Gust[3]

[1] Department of Materials Engineering, TECHNION-Israel Institute of Technology, Haifa IL-32000, Israel

[2] Institute of Solid State Physics, Russian Academy of Sciences, Chernogolovka, Moscow district, RU-142432 Russia

[3] Max-Planck-Institut für Metallforschung und Institut für Metallkunde, Seestr.92, D-70174 Stuttgart, Germany

Keywords: Discontinuous Ordering, Grain Boundary Self-Diffusion, Special Grain Boundaries

Abstract The kinetics of the discontinuous ordering reaction has been studied in a polycrystal of Fe-50 at.% Co alloy, in which the orientations of individual grains have been determined by orientation imaging microscopy. The majority of the grain boundaries exhibiting a low reaction rate can be characterized as special coincidence site lattice (CSL) boundaries with a low value of the inverse density of coincident sites Σ. The inactivity of the special grain boundaries is attributed to the low value of the self-diffusion coefficient. It is demonstrated that the low-Σ grain boundaries exhibit a low diffusivity irrespective of their inclination and tilt or twist character.

Introduction

The dependence of the grain boundary (GB) self-diffusion coefficient on the misorientation angle of adjacent grains is still a subject of controversy. According to Sutton and Balluffi [1], this dependence is monotonic, exhibiting breaks at the misorientations of delimiting GBs, which are composed of the structural units of the one type. There are experiments on self-diffusion in Ag bicrystals [2] and on the Ag heterodiffusion in Au bicrystals with symmetrical tilt GBs [3] which support this point of view. However, recently it was demonstrated that the GB diffusion coefficients of Au in Cu and Ge in Al exhibit sharp cusps only 3-4 degrees in width at the special misorientations of Σ5<001> and Σ7<111>, respectively [4, 5]. This correlates with the sharp minima of GB diffusivity for Zn diffusion along the GBs in Al [6]; however, in the latter case it is very probable that the anisotropy of GB segregation is responsible for the observed effect. Also for the GB diffusion of Au in Cu and Ge in Al the role of GB segregation cannot be excluded, though it is probably not so severe as in the case of Zn diffusion in Al. Therefore, it should be concluded that up to now an unambiguous evidence for the GB diffusivity cusps at the low-Σ special GBs is absent. Another important factor which is often ignored is the inclination of the GB plane. The variation of the misorientation angle for symmetrical tilt GBs is associated also with the variation of the orientation of the GB plane, the low-Σ GBs often corresponding to the low-index planes with a high value of the interplanar spacing. Therefore, from the experiments on bicrystals mentioned above [4-6] it is impossible to conclude whether the misorientation or GB inclination is responsible for the observed cusps.

In a series of previous works we have demonstrated that the kinetics of the discontinuous ordering (DO) reaction provides information about the self-diffusion in GBs [7-9]. During the DO reaction, the ordering process in the quenched disordered alloy occurs in the wake of migrating GBs. The coherency strain model of DO has been formulated, which led to the following expression for the GB velocity, v:

$$v = AM^{1/5}\tau_b^{-4/5} \qquad (1)$$

where A=const, and M and τ_b are the GB mobility and the relaxation time for the long-range order parameter in the GB region, respectively. The latter is approximately inversely proportional to the GB self-diffusion coefficient. According to Eq. (1), the self-diffusion along the GB provides the main contribution to v. In this work we have not only characterized the low-diffusivity GBs by their misorientational degrees of freedom, but also developed a semi-quantitative method for the estimation of the effect of the GB inclination and GB type (tilt or twist) on the GB self-diffusion.

Experimental

The experimental details are given elsewhere [7, 9]. Instead of as-cast Fe-Co samples employed earlier [7-9], rolled samples were used. During rolling a thickness reduction of 40% was achieved. Subsequently, the samples were annealed at 1400 °C for 4 h (in the region of stability of the face-centred cubic phase) in a vacuum of 10^{-6} Pa. This procedure resulted in large grains (1.5 mm) and decreased the density of subgrain boundaries. The sample was DO-treated at 400 °C for 1, 2 and 3 h. Between the DO treatments the sample was disordered at 900 °C for 24 h. After each DO treatment the specimen was mechanically polished and electrolythically etched, and a complete map of the selected area (6×2.4 mm^2) on the specimen (marked by a notch) has been assembled from the optical micrographs. The thickness of the layer removed from the surface in each polishing/etching cycle was estimated from the increase of the size of the notch: 150±20 μm. The comparison of three maps depicting the microstructure at different depths allowed us to exclude from consideration the GBs inclined to the surface at small angles. Only columnar grains were analyzed.

Results and Discussion

In Fig. 1 the typical microstructure developing during the DO reaction is shown. Three GBs meeting at the triple junction exhibit different reaction rates. In Fig. 2 the orientation imaging microscopy map of the selected area of the specimen after the last DO treatment at 400 °C for 3 h is presented. The microstructure is characterized by a large number of Σ3 twins, which are inactive during the DO reaction. Each numbered grain was characterized by the crystallographic indexes of the normal and x-directions. The maximal width of the reaction zone for some of the GBs is given in Table 1. It can be clearly seen from this table that besides the Σ3 twins, the Σ5<001> and Σ17<001> GBs exhibit a low reaction rate. From the microstructure observed on three subsequent cross-sections we concluded that these Σ5 and Σ17 GBs were approximately columnar, because they preserved their shape and relative position on the cross-sections. This is demonstrated in Fig. 3, in which three shapes of the Σ5 GB (between grains 15 and 16) are shown. In this figure, also the projection of the common rotation axis <010> on the cross-section surface is shown. This axis is inclined to the surface by an angle of approximately 60.5 degrees. It can be seen from Fig. 3 that the Σ5 GB is of a mixed tilt-twist type, and the relative fraction of the tilt and twist components varies along the GB. There is one point at the GB at which it is of a pure tilt character. However, no correlation can be found between the width of the reaction zone (which is at the resolution limit of the optical microscope) and the relative amount of the tilt/twist component. The same is true also for the Σ17 GB. Therefore, at least for these GBs we can conclude that the self-diffusion coefficient exhibits a local cusp at the special misorientations, and that this cusp is insensitive to the inclination of the GB and the relative fraction of the tilt or twist component. It is obvious from Table 1 that the DO reaction zone width does not increase linearly with annealing time. For many of the GBs the zone width is even less after the 3 h annealing than after the 2 h one. This may be connected with the local lattice rotations in the vicinity of the GBs during the high-temperature disordering annealings, which decrease the GB energy and the deviation from the exact special misorientation for the near-CSL GBs [10]. It should be also noted that in accordance with the previous studies [7-9] the Σ19 GB exhibits one of the highest reaction rates.

Conclusions

The Σ3, Σ5 and Σ17 GBs exhibit the local cusps on the dependence of the GB self-diffusion coefficient on the misorientation angle. For the Σ3 GBs the width of the cusp is approximately 9°.

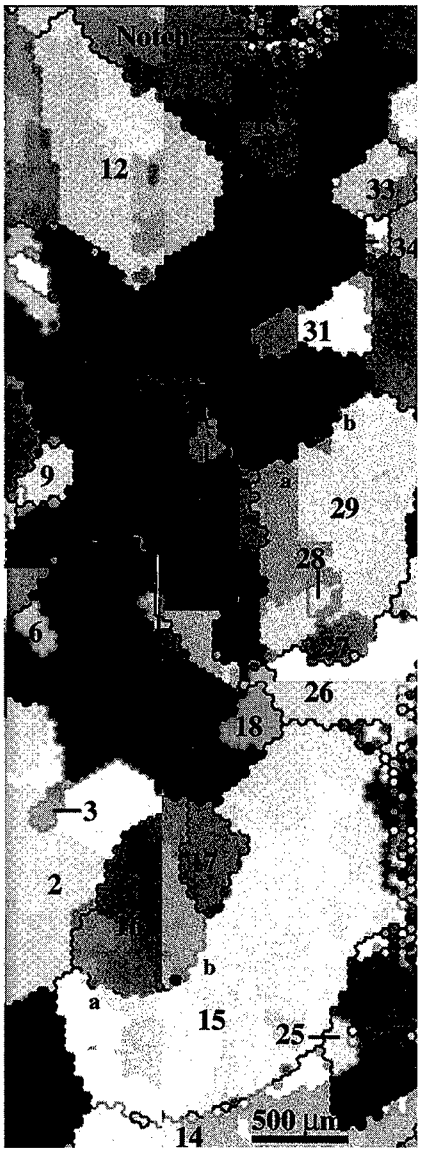

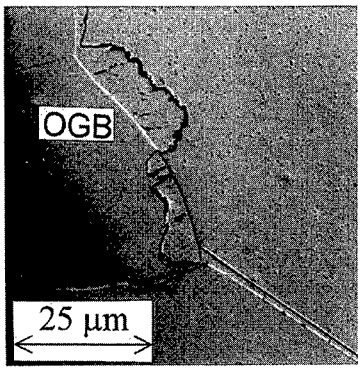

Figure 1. The typical microstructure observed in the light microscope after annealing at 400°C, 1 h. OGB=original position of the GB.

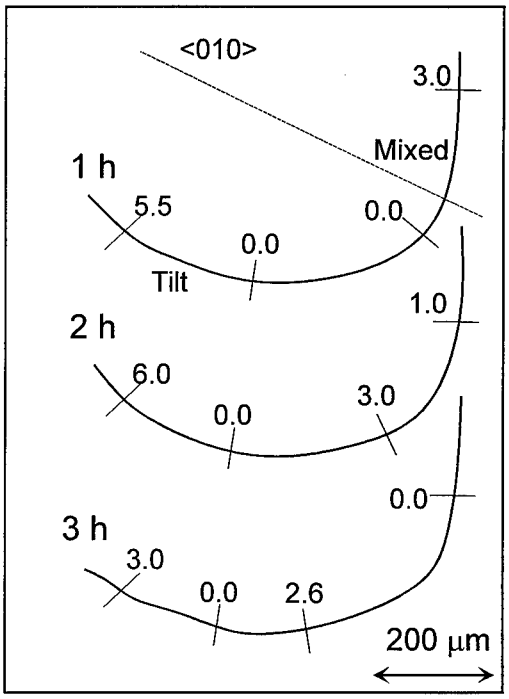

Figure 3. The successive shapes of the GB between grains 15 and 16 (close to the Σ5<001> special misorientation) after three annealing/ polishing cycles. The numbers indicate the width of the DO reaction zone in μm.

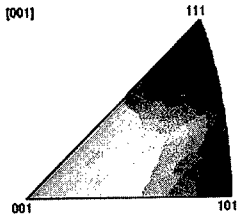

Figure 2. The orientation image microscopy map of the selected area of Fe-50 at.% Co specimen after annealing at 400 °C for 3 h. Special GBs are marked by red lines.

The Σ5 and Σ17 GBs exhibit the low diffusivites irrespectively of their inclination and the relative fraction of tilt and twist components in the misorientation.

Acknowledgements
E.R. wishes to thank the support of the Alexander Goldberg Memorial Research Fund. V.S. wishes to thank the Alexander von Humboldt Foundation for the support of his stay in Stuttgart.

References

[1] A.P. Sutton and R.W. Balluffi, *Interfaces in Crystalline Materials*, Clarendon Press, Oxford (1995).
[2] J. Sommer, Chr. Herzig, S. Mayer and W. Gust, Defect Diff. Forum **66-69** (1989) 843.
[3] Q. Ma and R.W. Balluffi, Acta metall. mater. **41** (1993) 133.
[4] E. Budke, Chr. Herzig, S. Prokofjev and L.S. Shvindlerman, Materials Sci. Forum **207-209** (1996) 465.
[5] T. Surholt, Chr. Herzig and D. Molodov, Acta mater., in press.
[6] A.N. Aleshin, B.S. Bokstein and L.S. Shvindlerman, Sov. Phys. Solid State **19** (1977) 2051.
[7] V. Semenov, E. Rabkin, E. Bischoff and W. Gust, Acta mater. **46** (1998) 2289.
[8] E. Rabkin, V. Semenov and W. Gust, Scripta mater. **37** (1997) 245.
[9] E. Bischoff, V. Semenov, E. Rabkin and W. Gust, Materials Sci. Forum **273-275** (1998) 243.
[10] C.B. Thomson and V. Randle, Acta mater. **45** (1997) 4909.

Table 1. The DO reaction rate at some of the GBs. Δ is the angular deviation from the exact special misorientation.

Grains Nos.	θ<*hkl*>	Σ, Δ	DO zone width, μm		
			1 h	2 h	3 h
Slow GBs					
15-16 a	33.9°<3 17.6 –1>	5, 6.9°	5.5	6.0	3.0
15-16 b	34°<3.2 25.4 –1>	5, 5.4°	3.0	1.0	0.0
5-8 a	28.7°<23.1 2.7 –1>	17, 3.5°	3.2	13	8.1
5-8 b	28.7°<23.1 2.7 –1>	17, 3.5°	13.6	5.5	7.2
8-23 a	38.3°<14.3 –1.9 1>	5, 5.6°	2.6	7.7	3.8
8-23 b	37.8°<16.7 –2.2 1>	5, 5.4°	0	0	0
1-2	53.9°<1 7.2 6.6>	11, 6.5°	9.4	5.5	1.0
Σ3 twins					
22-29 a	60.6°<–1.4 1 1.5>	3, 9.5°	0	2.8	3.4
22-29 b	60.6°<–1.4 1 1.5>	3, 9.5°	2.3	0	4.3
2-3	58.2°<1 1 –1>	3, 1.9°	0	0	0
4-18	56.7°<–1 –1.1 1>	3, 3.5°	0	0	0
8-21	59.9°<–1 1 1>	3, 0.2°	0	0	0
28-29	59.6°<1 1 1>	3, 0.4°	0	0	0
5-6	59.4°<1 –1 1>	3, 1°	0	0	0
Rapid GBs					
8-29	33.4°<–1.5 –1 –1.8>		25.5	54	37.4
26-27	47.7°<–6.9 12 1>	15, 4.3°	10.2	20.4	19.1
22-23	29.7°<1.7 –2 1>		11.9	43.4	37.4
8-22	27.0°<–1 1 1.5>		14.0	22.6	23.0
4-17	34.1°<1.6 2.1 1>		12.8	34	29.8
13-34	27.1°<1 –10.6 –9.6>	19, 2.3°	21.3	35.7	22.1

e-mail: mtrerab@vmsa.technion.ac.il
HomePage: http://www.technion.ac.il/technion/materials/rabkin.html

Materials Science Forum Vols. 294-296 (1999) pp. 605-608

Distribution Function for the Activation Volume of the Discontinuous Precipitation Reaction in the Cu – 7.5 at.% In Alloy

M. Zenotchkin[1], D. Kolesnikov[1], J. Jun[1], W. Lojkowski[1] and W. Gust[2]

[1] High Pressure Research Center, Polish Academy of Sciences, Warsaw, Poland

[2] Institut für Metallkunde, University of Stuttgart, Germany

Keywords: Discontinuous Precipitation, Grain Boundary Diffusion, High Pressure, Activation Volume

Abstract

The effect of pressure and temperature on the distribution function for the activation energy and activation volume of the discontinuous precipitation reaction in a Cu – 7.5 at.% In alloy has been studied. For each pressure and temperature the distribution functions for the activation energy and activation volume for the grain boundary (GB) diffusivity were determined. It was found that the average activation volume increases from 0.75 to 1.5 atomic volumes, when the temperature is increased from 310 to 370°C. At each temperature the activation energy and activation volume vary within 15% to 30% around the average.

Introduction

During the discontinuous precipitation (DP) reaction a solid solution of two metals A and B, dissociates in such a way that lamellae of a B rich phase separate layers of an A rich phase. DP can be easily studied by metallographic methods and provides a way to investigate the grain boundary kinetics [1, 2]. The rate of GB migration v, the interlamellar spacing λ and the GB diffusivity $s\delta D_B$ can be related by the equation [2]:

$$s\delta D_b = \frac{\lambda^2 v R T}{8(-\Delta G)} \qquad (1)$$

where : s is the segregation factor, δ is the grain boundary width, D_B is the GB diffusion coefficient, λ - the interlamellar spacing, R is the gas constant, T is the absolute temperature, and ΔG is the Gibbs free energy change of the DP reaction.

The purpose of the paper is to determine the activation energy and activation volume of the DP reaction in the Cu – 7,5 at.% In alloy and draw conclusions for the GB migration mechanism during the DP reaction. The GB migration mechanisms can be divided into two groups:

- Jumps of atoms across the interface take place by the vacancy mechanism.
- "Shuffling of atoms", where there is a small movement of several atoms [3].

High pressure investigations permit to discriminate between the above two mechanisms [4-7]. The crucial parameter is the activation volume V^*:

$$V^* = -kT\left(\frac{\partial \ln(s\delta D_b)}{\partial P}\right)_T \qquad (2)$$

where P is the pressure and k is the Boltzman constant. In this expression the effect of pressure on pre-exponential factors was neglected. In the case of vacancy mechanism, a significant deceleration of the GB migration rate is expected and V^* is in the range 0.7 – 1.0 Ω, where Ω is the atomic volume. On the other hand, there are experimental results where $V^* < 0.2\ \Omega$ [7, 8]. Gleiter and Lissowski [3] proposed a vacancy-less diffusion mechanism, where atoms move a distance smaller than the atomic distance but the interatomic bonds rearrange. They called this mechanism as "shuffling of atoms". The latter mechanism can be interpreted as a process where bonds between atoms jump. It follows that the GB migration mechanism is an open issue that can be studied using high pressure annealing. In the present study we measured the pressure and temperature effect on the distribution function for the GB migration rate. This is an intermediate approach between the study of average properties of GBs in polycrystals and the study of individual bicrystals.

Experimental

Cylindrical ingots of the Cu – 7.5 at.% In alloy of 1 cm length and 0.8 cm in diameter were homogenized for two days at 900 K and then for 500 h at 965 K. After homogenization annealing the ingots were quenched into water. The samples were cut from the ingots using a wire saw. For the determination of the activation energy the samples were aged in evacuated silica ampoules in a standard furnace and subsequently quenched in water. The annealings at high pressure were carried out in an apparatus with a limit pressure of 1.5 Gpa, using high purity argon as pressure medium. The pressure was measured with a manganin coil with an accuracy of 0.01 GPa. The temperature was controlled with an accuracy of 1 K. After polishing, the microstructure of the samples was studied by means of optical and scanning electron microscopy. The rate of GB migration during the DP reaction was measured for about 400 GBs for each sample.

Results

Figure 1 shows typical microstructures developed during the DP reaction. There is a decrease of the reaction rate at high pressure. We suppose that GBs corresponding to a given fraction have an identical structure from the point of view of diffusivity. In other words: constant fraction = constant structure. For each fraction we calculated the activation energy and the activation volume:

$$Q_i^* = -k\left(\frac{\partial \ln(s\delta D_b)^i_{F=const}}{\partial (T^{-1})}\right)_P \qquad (3)$$

$$V_i^* = -kT\left(\frac{\partial \ln(s\delta D_b)^i_{F=const}}{\partial P}\right)_T \qquad (4)$$

i denotes GBs with an equal fraction of the maximum migration rate.

Figure 2 shows the distribution function for the activation energy and Fig. 3 for the activation volume at 310, 340 and 370°C, respectively. The activation energy for all the GBs is within the following range of values:

$$140 \text{ kJ/mol} < Q^* < 155 \text{ kJ/mol}.$$

As far as the activation volume is concerned, its value is within the following range:

$$0.72\ \Omega < V^* < 0.87\ \Omega \text{ at } 310°C$$
$$0.77\ \Omega < V^* < 1.07\ \Omega \text{ at } 340°C$$
$$1.35\ \Omega < V^* < 1.60\ \Omega \text{ at } 370°C$$

Discussion and conclusions

The activation energies for the DP reaction found in the present study are in good agreement with the literature data. The activation energy at atmospheric pressure for the DP reaction in Cu – 7.5% In was 151 kJ/mol [8]. During the analysis of the results we neglected the pressure effect on the driving force for the reaction, since the volume changes cannot exceed a few percents. Furthermore, the changes in the reaction energy under pressure influence the reaction rate in a linear way [Equ.(1)]. On the other hand, the effect of pressure on the GB kinetics is exponential.

The effect of pressure on the DP reaction was previously studied by Dudler and Gleiter [9], Itkin et al. [10] and Friesel et al. [11]. They observed a decrease of the activation volume with increasing temperature, which is opposite to the present results. It has to be pointed out, however, that in the present study for each experimental point from 300 to 400 GBs were investigated. This speaks for the reliability of the present results.

As far as the GB migration mechanism is concerned, only the value for the temperature of 310°C agrees with the single-vacancy mechanism. The high activation volume at 370°C may be explained by a multi-vacancy mechanism. We observe a variation of the activation volume in the range 15 - 30% around the average, depending on the temperature. This variation must reflect the influence of the GB structure on the degree of relaxation of the vacancy structure.

References

[1] A. Bögel, W. Gust, Z. Metallk. **59**, (1968), p. 296.
[2] J. Petermann, E. Hornbogen, Z. Metallk. **59**, (1968), p.814.
[3] H. Gleiter, A. Lissowski, Z. Metallk. **62**, (1971), p.237.
[4] W. Lojkowski, Defect Diff. Forum **129–130** (1996) p. 269.
[5] V. Sursaeva, W. Lojkowski, S. Protasova, Int. Conf. "Texture and Properties of Materials", Ekaterinburg , Sept. 28 - Oct. 5, 1997 p. 1407.
[6] W. Lojkowski, Y. Minamino, S. Hozumi, J. Wyrzykowski Joint XV AIRAPT & XXXIII EHPRG Int.Conf. „High Pressure Science & Technology", Warsaw, Sept. 11-15, 1995.
[7] D.A. Molodov, J. Swiderski, G. Gottstein, W. Lojkowski, L.S. Shvindlerman, Acta Metall. Mater. **42**, (1994), p.3397.
[8] B. Predel, W. Gust, Mater. Sci. Eng. **16**, (1974) p.3397.
[9] R. Dudler, H. Gleiter, Z. Metallk. **73**, (1982), p. 677.
[10] M. V. Itkin, I. A. Osipienko, T. V. Shrina, O.A. Shmatko, Fiz. Met. Metallov. **65**, (1988), p. 1027.
[11] M. Friesel, W. Lojkowski, W. Gust, B. Predel, Defect Diff. Forum **75,** (1991), p.229.

Acknowledgements

The authors are grateful to Dr.P. Zi ϕa for fruitful discussions. The support of the Polish Committee for Scientific Research and of the Internationales Buro of the BMBF (contract pol-161-96) is gratefully acknowledged.

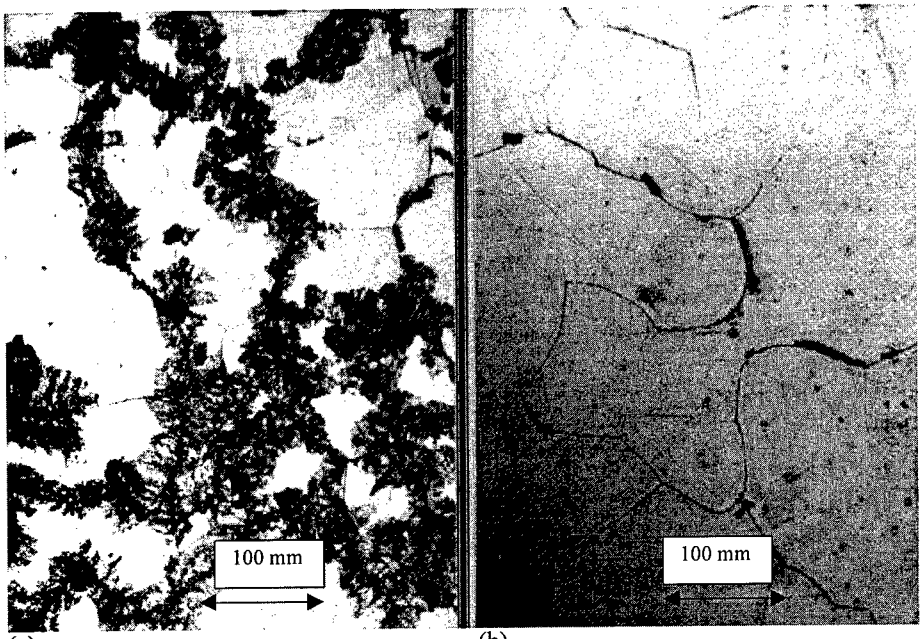

(a) (b)

Figure 1. Optical micrographs of DP zones in the Cu – 7.5 at.% alloy after at 370 °C for one hour under atmospheric pressure (a) and 1 GPa (b).
Magnification 200 x.

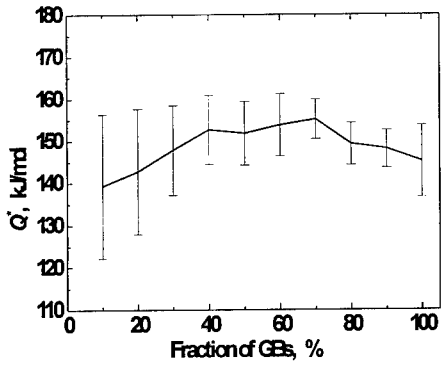

Figure 2. Distribution function for the activation energy of the DP reaction in the Cu –7.5at% In alloy at atmospheric pressure.

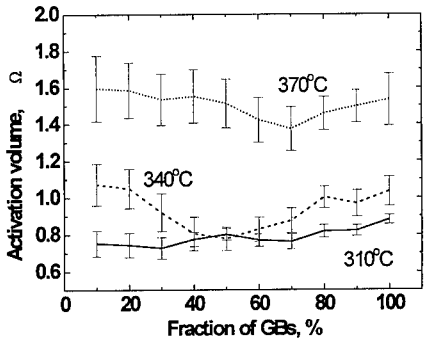

Figure 3. Distribution function for the activation volume for GB migration during the DP reaction in the Cu –7.5at.% In alloy at three temperatures.

Materials Science Forum Vols. 294-296 (1999) pp. 609-612

Growth of bcc Fe-Co Precipitate Particles at Boundaries in Cu Bicrystals

R. Monzen and T. Echigo

Department of Mechanical Systems Engineering, Kanazawa University,
2-40-20 Kodatsuno, Kanazawa 920-8667, Japan

Keywords: Growth Kinetics, Boundary Particles, Cu-Fe-Co Bicrystal, Activation Energy, Boundary Diffusivity, [001] Twist Boundary, [001] Symmetric Tilt Boundary

Abstract–The kinetics of the coarsening of bcc Fe-Co boundary particles has been examined for various [001] twist and symmetric tilt boundaries in Cu-Fe-Co bicrystals aged at 673, 698 and 723K. The particle growth obeys the $r^4=Kt$ law (where r is the average particle radius, K is a constant and t is the aging time), irrespective of misorientation angle and aging temperature. The measured activation energy Q and calculated pre-exponential factor D_0 of grain-boundary diffusivity against misorientation curves display several cusps and these curves are similar to the grain-boundary energy against misorientation angle curve. A lower-energy boundary has a lower diffusivity with a larger value of Q and a larger value of D_0.

1. Introduction

The diffusion-controlled coarsening of precipitates on grain boundaries has been studied theoretically by several investigators [1-4]. They have shown that the average particle radius r increases with the one-fourth power of aging time t. This result was derived from the presumption that solute atoms diffuse on two-dimensional grain boundaries.

On the other hand, some experimental studies have also been conducted on the growth of boundary particles. For example, using Cu-Fe-Co alloy bicrystals aged at 873K, Fujii *et al.* [5] investigated the growth of bcc Fe-Co precipitate particles on [011] symmetric tilt boundaries with misorientation angles of θ=5~50.5°. The development of precipitate-free zones (PFZs) during aging also was examined. They found that the power n for $r^n=Kt$ (where K is a constant) varied systematically from 3 to 5 with increase in the misorientation from 10° to 50.5°, while the relationship $d^2 \propto t$ held between the width d of PFZs and aging time t for all the bicrystals examined. The change in the n values was interpreted reasonably by taking into account the relative contribution of bulk diffusion and dislocation pipe diffusion towards the particle growth.

More recently, we studied systematically the coarsening of bcc Fe-Co boundary particles for various [011] twist [6] and symmetric tilt [7] boundaries in bicrystals of a Cu-Fe-Co alloy aged at 723, 748 and 773K lower than the temperature of 873K, adopted by Fujii *et al.* [5]. We showed that, except for some specific tilt and twist boundaries in bicrystals aged at 773K, the relationship $r^n=Kt$ with n=4 held, and for the special boundaries, n lay between 3 and 4. Furthermore, it was found that, for the two types of grain boundary, there was a close correlation between the activation energy Q for the particle growth and the grain-boundary energy. In this work, as an extension of these studies, the coarsening of bcc Fe-Co particles is investigated for various [001] symmetric tilt and twist boundaries in Cu-Fe-Co bicrystals aged between 673 and 723K. In addition, the values of Q are evaluated as a function of the misorientation angle.

2. Experimental

Bicrystals, 1mm thick, of a Cu-1.4mass%Fe-0.6mass%Co alloy having various [001] twist and symmetric tilt boundaries with misorientation angles of θ=10~44° and θ=9~80° were grown by the

Bridgman method using two-seed crystals. Hereafter, the bicrystal with the misorientation angle θ and its grain boundary will be called θ bicrystal and θ boundary, respectively. The bicrystals were aged at 673, 698 or 723K for 40~216h after solutionizing at 1253K for 1h. The size of bcc Fe-Co precipitate particles formed on grain boundaries was measured by means of a transmission electron microscope (Hitachi H-800; 200kV) after making thin foils. For each boundary and aging condition, about 30 particles were observed.

3. Results

Coherent fcc Fe-Co particles in grain interiors were too small to be detected by transmission electron microscopy in the present study. As a result, PFZs could not be identified on both sides of all the grain boundary examined. On the other hand, bcc Fe-Co particles were formed on all the boundaries. The boundary particles were nearly spherical (lens like), independent of misorientation angle, aging temperature and time. This was confirmed by observing the same particles from several different orientations. This observation is consistent with the result previously obtained for [011] twist [6] and symmetric tilt [7] boundaries.

Figure 1 shows the mean particle radius r as a function of aging time t for a 25° boundary in bicrystals aged at 673, 698 and 723K. An almost linear relationship exists between log r and log t, indicating that r is nearly proportional to $t^{1/n}$. From the slope of the straight line drawn by the least-squares method, n can be obtained for each boundary and aging temperature. The calculated values of n for [001] twist boundaries are listed in Table 1. For all the boundaries, n is very close to 4 regardless of aging temperature. $n \cong 4$ also was obtained for all the [001] symmetric tilt boundaries. The value of $n=4$ is accordant with the theoretically derived value [1-4].

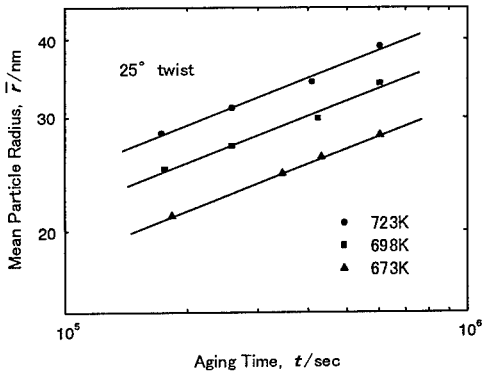

Fig. 1: Variation in the mean particle radius with aging temperature for a 25° twist boundary in bicrystals aged at 673, 698 and 723K.

Table 1: Calculated n value for each [001] twist boundary in bicrystals aged at 673, 698 and 723K.

Misorientation Angle (degrees)	n		
	Aging Temperature (K)		
	723	698	673
10	3.8	4.0	4.0
13	3.8	4.1	4.1
16	4.0	4.2	4.1
23	3.9	4.2	4.2
25	4.0	4.1	4.1
28	3.9	4.1	4.1
32	3.9	4.0	4.0
37	3.8	4.1	4.1
41	4.0	4.0	4.2
44	3.9	4.1	4.2

The kinetics of particle growth on high angle-grain boundaries is given as [3]

$$r^4-r_0^4=Kt, \tag{1}$$

where

$$K=\frac{8\sigma CD_0\omega\Omega^2<\mu(\phi)>^4}{3GRT\nu(\phi)}\exp(-\frac{Q}{RT}). \tag{2}$$

Here σ is the particle-matrix interfacial energy per unit area, C is the solute concentration, ω is the width of the grain boundary, Ω is the molar volume of the particle, D_0 is the pre-exponential factor of grain-boundary diffusivity, Q is the activation energy of grain-boundary diffusion, G is a constant related to the alloy system, $<\mu(\phi)>$ and $\nu(\phi)$ are constants which depend on the volume fraction ϕ, and RT has its usual meaning. Based on Eq. 2, $\log(KT/C)$ was plotted against $1/T$. K was calculated by the least-squares method from plots of r^4 against t. Also, C=70, 80 and 90mol/m^3 were adopted at 673, 698 and 723K, respectively [8]. For all the boundaries, a straight line could be drawn and the activation energy Q was estimated from its slope. Figures 2 and 3 give the values of Q against the misorientation angle θ for [001] twist and symmetric tilt boundaries, respectively. In these figures Q is plotted downwards. Depending on the misorientation angle, the Q values for the twist and tilt boundaries vary between 1.0×10^5 and 1.3×10^5J/mol and between 0.9×10^5 and 1.3×10^5J/mol, respectively.

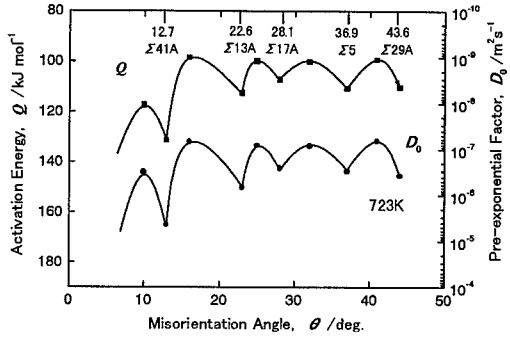

Fig. 2: Measured activation energy Q and pre-exponential factor D_0 plotted against the misorientation angle for [001] twist boundaries.

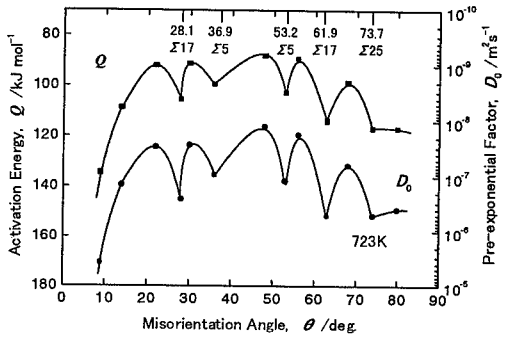

Fig. 3: Measured activation energy Q and pre-exponential factor D_0 plotted against the misorientation angle for [001] symmetric tilt boundaries.

4. Discussion

The activation energy of grain-boundary diffusion is known to be about 50 to 70% of that of bulk diffusion [9]. Since the activation energies Q in Figs. 2 and 3 are much smaller than that (about 2.2×10^5J/mol) of the bulk diffusion of Fe or Co in Cu, they can be reasonably identified as the activation energies for boundary diffusion of solute. Furthermore, the Q values in Fig. 2 are in general larger than those in Fig. 3. This is in agreement with the observation by Biscondi [10] that diffusion of Zn along symmetric tilt boundaries in Al occurs more easily than that along twist boundaries.

The Q values in Fig. 2 exhibit a non-monotonic dependence on the misorientation angle; four cusps exist near θ=12.7° (Σ41A), θ=22.6° (Σ13A), θ=28.1° (Σ17A) and θ=36.9° (Σ5). The dependence of Q on θ does not show the same tendency as the grain-boundary diffusion of Zn in [001] twist boundaries of Al reported by Biscondi [10]. The boundary diffusivity–θ curve revealed no clear cusps. On the other hand, there are cusps neat θ=28.1°, 36.9°, 53.2°, 61.9° and 73.7° in Fig. 3. The

misorientation dependence of Q is not similar to that of the diffusivity of Zn in [001] symmetric tilt boundaries of Al [10,11]. The diffusivity–θ curve reported by Biscondi [10] showed no apparent cusps. Aleshin et al. [11] measured the activation energy of diffusion for boundaries with θ=10~45° and found minima at θ=23.5°, 28.5° and 37°. However, it is expected that boundary diffusion in a high-energy boundary is faster than that in a low-energy boundary since atoms at the former is considered to be more irregularly arranged. Actually the position of the cusps in Figs. 2 and 3 agrees with that of the energy cusps of the [001] twist [12] and tilt [13] boundaries in Cu. Thus it is concluded that a higher-energy boundary has a higher diffusivity.

Using Eq. 2 and the values of Q in Figs. 2 and 3, the pre-exponential factor D_0 was calculated for all the boundaries. In this calculation, we used the following numerical values: σ=3.3J/m^2 [14], G=0.34 [3], ω=0.5nm, Ω=7.1×10^{-6}m^3/mol, $<\mu(\phi)>$=1.0338 [3] and $\nu(\phi)$=18 [3]. D_0 was independent of the aging temperature. The calculated values of D_0 at 723K are shown against the misorientation angle θ in Figs. 2 and 3, where D_0 is plotted downwards. For the two types of grain boundary, the D_0 values depend strongly on the misorientation. The values for the twist boundaries are in general larger than those for the tilt boundaries. Also these values are smaller than that (~10^{-4}m^2/s) for bulk diffusion of Fe or Co in Cu. Furthermore, it is interesting that, the larger the Q value, the larger is the D_0 value.

5. Conclusions

The growth of bcc Fe-Co precipitate particles on different [001] twist and symmetric tilt boundaries has been examined using Cu-Fe-Co alloy bicrystals aged at 673, 698 and 723K. The aging time t dependence of the mean particle radius r can be represented by r^n=Kt, where K is a constant. The power n is 4 independent of misorientation angle and aging temperature. This value is in agreement with the growth theories of grain-boundary particles [1-4]. For the two types of grain boundary, an excellent correlation is found between the calculated pre-exponential factor D_0 and measured activation energy Q of grain-boundary diffusivity and the grain-boundary energy. A boundary with a higher energy has a higher diffusivity and is described by a smaller value of Q and a smaller value of D_0.

Acknowledgment–We would like to thank the Industrial Research Institute of Ishikawa whose transmission electron microscope was used for the microscopic observation.

References

[1] M. V. Speight, Acta metall. 16 (1968), p. 133.
[2] H. O. Kirchner, Metall. Trans. 2 (1971), p. 2861.
[3] A. J. Ardell, Acta metall. 20 (1972), p. 601.
[4] R. D. Vengrenovitch, Acta metall. 30 (1982), p. 1079.
[5] T. Fujii, M. Moriyama, M. Kato and T. Mori, Phil. Mag. A 68 (1993), p. 137.
[6] R. Monzen and T. Hasegawa, Phil. Mag. Lett. 76 (1997), p. 69.
[7] R. Monzen and T. Echigo, J. Japan Inst. Metals 61 (1997), p. 1206.
[8] G. Tammann and W. Oelsen, Z. Anorg. U. Allg. Chem. 186 (1930), p. 38.
[9] H. Gleiter and B. Chalmers, Prog. Mater. Sci. 16 (1972), p. 77.
[10] M. Biscondi, in Physical Chemistry of the Solid States: Applications to Metals and Their Compounds (edited by P. Lacombe), Elsevier Science Publishers, Amsterdam (1984), p. 225.
[11] A. N. Aleshin, B. S. Bokstein and L. S. Shvindlerman, Sov. Phys. Solid State 19 (1997), p. 2051
[12] T. Mori, H. Miura, T. Tokita, J. Haji and M. Kato, Phil. Mag. Lett. 58 (1988), p. 11.
[13] T. Mori, T. Ishii, M. Kajihara and M. Kato, Phil. Mag. Lett. 75 (1997), p. 367.
[14] T. Fujii, M. Kato and T. Mori, Mater. Trans., Japan Inst. Metals 32 (1991), p. 229.

Corresponding author: R. Monzen, Fax: +81-76-234-4679, E-mail: monzen@t.kanazawa-u.ac.jp

Materials Science Forum Vols. 294-296 (1999) pp. 613-616

Theoretical Investigation of the Thermal Stability of Nanoscale Layered Systems

M. Bobeth[1], M. Hentschel[1], G. Diener[2], W. Pompe[1] and A. Ullrich[1]

[1] Institut für Werkstoffwissenschaft, Technische Universität Dresden, D-01026 Dresden, Germany

[2] Institut für Theoretische Physik, Technische Universität Dresden, D-01062 Dresden, Germany

Keywords: Multilayer, Stability, Agglomeration, Decomposition, Simulation, Cahn-Hilliard Theory

Abstract The stability of multilayers at elevated temperatures is investigated by simulating the evolution of the concentration profiles within the framework of the Cahn-Hilliard theory. For immiscible binary systems, a permanent layer thickness coarsening perpendicular to individual layers occurs by dissolution of the thinnest layers. With advancing layer coarsening, this one-dimensional coarsening mechanism slows down strongly. Comparatively rapid multilayer decomposition is caused by lateral inhomogeneities in individual layers. Possible mechanisms of the formation of 'holes' consisting of one phase in layers of the other phase are proposed and subsequent hole growth is studied within a two-dimensional model.

1 Introduction

The concentration profiles and atomistic structure in artificial multilayers change during annealing at elevated temperatures due to diffusion processes. The knowledge of failure mechanisms and stability limits of multilayers is of great interest for practical applications. On the other hand, multilayer decomposition can lead to new desired morphologies as for example a nanodisperse structure. The present work analyses the compositional evolution in multilayers during annealing within the framework of the Cahn-Hilliard-Theory (CHT) [1]. Although the CHT is a continuum theory, it approximately describes characteristic features of the composition evolution also on the nanoscale (see e. g. the comparison of the CHT with Monte Carlo simulations of phase separation in [2]). Also in the limiting case of atomically abrupt phase boundaries, the approach permits elucidation of the morphological development of phase boundaries driven by the reduction of interface energy.

In the following, multilayers with coherent phase boundaries consisting of two immiscible components A and B are considered. According to the CHT [1], the Gibbs free energy of the system is given as functional of the concentration (mole fraction) c of component B

$$F[c]=\int dV\left[f(c)+\kappa(\nabla c)^2\right] \tag{1}$$

where $f(c)$ is the Gibbs free energy density of a uniform system and κ is the gradient energy coefficient. In general, the concentration $c(\mathbf{r})$ depends on position $\mathbf{r}$. The interdiffusion flux in the system is supposed to be given by $\mathbf{j}=-M\,\nabla(\delta F/\delta c)$ where M is the atomic mobility. Together with the conservation law $\partial c/\partial t+\Omega\nabla\cdot\mathbf{j}=0$, the evolution equation of the concentration profile results as

$$\frac{\partial c}{\partial t}=\nabla\cdot\Omega M(c)\nabla\left[\frac{df}{dc}-2\kappa\nabla^2 c\right] \tag{2}$$

where Ω is the atomic volume supposed to be equal for both species [3]. For simplicity, the concentration dependence of the mobility is ignored in the following.

2 One-dimensional instability mechanism

During annealing, the concentration profile in as-deposited periodic multilayers evolves comparatively rapidly to intermediate states which can approximately be described by the stationary periodic solutions of Eq. 2. In one dimension, one obtains the following equation determining the concentration profile $c(x)$ for fixed period length $d = d_a + d_b$ and mean composition c_m (cf. Fig. 1a)

$$\frac{df(c)}{dc} - 2\kappa \frac{d^2c(x)}{dx^2} = \mu . \tag{3}$$

The chemical potential for interdiffusion μ has to be constant for stationary states. For the case where $f(c)$ is a polynomial of fourth power, $f(c) \propto (c_\beta - c)^2 (c - c_\alpha)^2$, solutions of Eq. 3 can be obtained analytically [4, 5, 6]. An example of the resulting concentration profile is shown in Fig. 1a. The phase boundary between layers is defined at the concentration $c_0 = (c_a + c_b)/2$ where c_a and c_b are the concentrations in the middle of the two layers of thickness d_a and d_b. The interface width is defined by $\xi = (c_b - c_a)\left[dc/dx\right]^{-1}$ at $c = c_0$. In the limiting case $d_a, d_b >> \xi$, the well-known common tangent construction with $c_a = c_\alpha$ and $c_b = c_\beta$ applies [1]. However, for small layer thicknesses, the layer compositions can differ from the corresponding bulk phases, $c_a > c_\alpha$ and $c_b < c_\beta$.

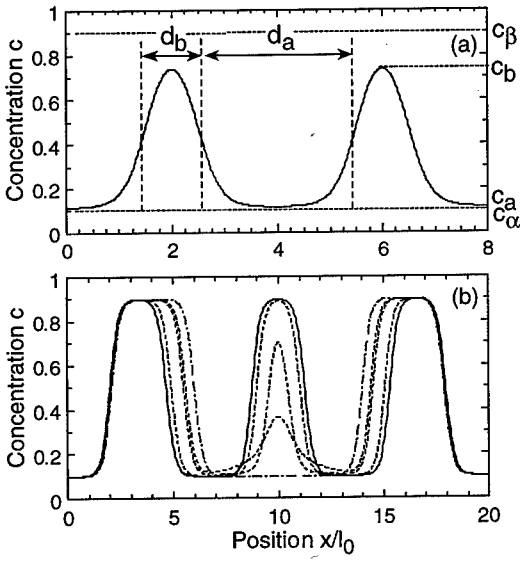

Fig. 1: a) Stationary periodic concentration profile and b) layer coarsening by dissolution of the thinnest layer; $c_\alpha = 0.1$, $c_\beta = 0.9$ (t = 0, 1190, 1290, 1290.2, 1292 t_0).

A homogeneous composition with concentration c_m within the region of the spinodal ($f''(c_m) < 0$) is known to be unstable against composition fluctuations with sufficiently large wavelengths, larger than $\lambda_0 = 2\pi\sqrt{2\kappa/|f''(c_m)|}$. This follows from the linearised Eq. 2. Similarly, the nonlinear Eq. 3 possesses solutions only for sufficiently thick individual layers, larger than some critical value $d_b^{\min}$ ($d_b < d_a$). Thin layers $d < d_b^{\min}$ rapidly dissolve during annealing due to the predominance of interface energy and subsequently thicker precipitates can form. $d_b^{\min}$ is of the order of the interface width and depends slightly on the period length d [6].

The stationary periodic solutions of Eq. 3 (Fig. 1a) are unstable with respect to small one-dimensional thickness fluctuations [4]. In the course of annealing, thicker layers will thicken at the expense of thinner layers. Such an example is plotted in Fig. 1b as numerical solu-

tion of Eq. 2. Note the rapid dissolution of the layer after a long time of layer thinning when the thickness becomes comparable with the interface width. The length and time units are given by $l_0 = \sqrt{\kappa / f_0}$ and $t_0 = \kappa / (\Omega M f_0^2)$, where the unit of energy density was chosen as $f_0 = f((c_\alpha + c_\beta)/2)$. Then, l_0 is comparable with the interface width ξ in the present model. Simulations and analytical estimates [4] reveal that the layer coarsening considered above extremely slows down with increasing thicknesses. Thus, for thicker individual layers, two-dimensional instability mechanisms discussed in the following are especially important.

3 Two-dimensional instability mechanisms

Planar phase boundaries (PB) between individual layers are in principle stable against infinitesimal morphological perturbations, in contrast for example to the surface of a cylinder. Despite this stability, observations indicate the decomposition of individual layers, which starts presumably by the formation of a 'hole' in a layer, i.e. the penetration of say phase a (dark) into layers of phase b (bright), which grows rapidly afterwards (cf. Figs 2 to 4). In the following, possible mechanisms of hole formation are considered.

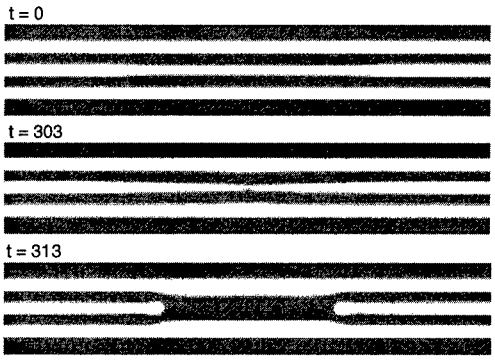

Fig. 2: Hole formation at the thinnest place in an individual layer (sample size 128 x 24; length and time units l_0 and t_0).

Lateral thickness variations lead to a laterally nonuniform layer thinning of thinnest layers in the course of layer coarsening discussed above. Thus, individual layers should dissolve at first at their thinnest places. In this way, holes in layers could nucleate. On the other hand, diffusion processes tend to compensate lateral thickness variations. Thus, the present mechanism of hole formation should be effective for very thin layers and large wavelengths of layer thickness fluctuations. Such an example is shown in Fig. 2 as numerical solution of Eq. 2.

Another effective hole formation mechanism is presumably connected with the grain structure of multilayers which depends on the material system, layer thicknesses and deposition technique. For systems with large lattice misfit, individual layers typically consist of small grains comparable with the layer thickness. In coherent systems with small lattice misfit, columnar grains extending through the whole multilayer can form. The grain boundaries (GB) between such columnar grains could be favoured sites where holes in individual layers develop.

For conventional polycrystalline films, grain boundary grooving has been proposed as mechanism of film decomposition [7]. In a similar manner, different grain boundary energies within the two phases of a coherent multilayer could cause shrinkage of grain boundaries with higher energy as shown schematically in Fig. 3. In this way, a hole or a series of holes could be formed when the corresponding grooves meet each other in the course of grooving.

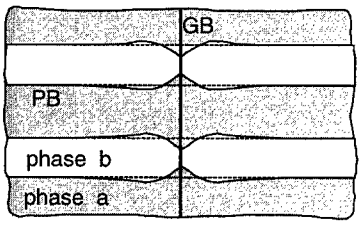

Fig. 3: Hole formation by 'grain boundary grooving' in multilayers with columnar grains.

After the formation of holes, their subsequent growth occurs comparatively rapidly driven by reduction of interface energy. Depending on the geometry of the layer, different scenarios have been observed in simulations of the composition evolution via Eq. 2. The typical mechanism of layer coarsening,

which has been proposed for lamellar eutectics [8], is the lateral recession (dissolution) of a layer accompanied by thickening of adjacent layers (Fig. 2, t = 313). However, for very thin layers (Fig. 4a) or in the case of multiple hole formation (Fig. 4b), a fusion of the bulges of the receding layers can occur. The subsequent morphological development can become rather complex and requires simulations in three dimensions which is beyond the scope of the present paper. For example, for very thin layers the cut off of cylinders during the lateral recession of individual layers has been found (see also the cylinder formation in Fig. 4a). Due to the Rayleigh instability, cylinders decompose further into spheres.

4 Conclusions

Morphological changes in coherent multilayers with columnar grains at elevated temperatures are driven by the reduction of the interface energy of phase boundaries and grain boundaries. Layer thickness coarsening in one dimension strongly slows down with increasing layer thicknesses (cf. also [4]). A special kind of grain boundary grooving in multilayers has been proposed as a mechanism of hole formation in individual layers. Simulations suggest subsequent hole growth and morphological development to depend sensitively on the initial individual layer thicknesses of the multilayer. A high stability of multilayers is expected in the absence of grain boundaries as for coherent single crystal and amorphous films.

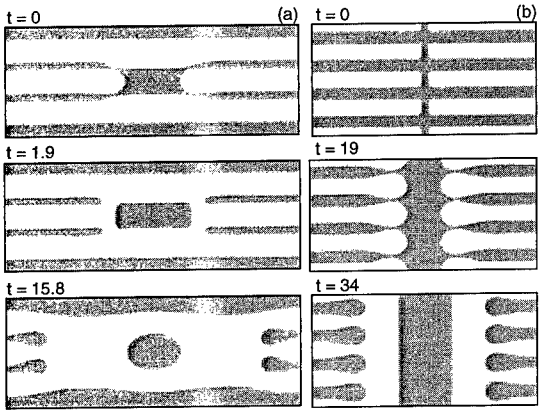

Fig. 4: Single (a) and multiple (b) hole growth with subsequent layer fusion (sample size: a - 64 x 24, b - 64 x 32; length and time units l_0 and t_0).

Another instability mechanism, which was not included in the present analysis, is due to mechanical stresses within individual layers (cf. for example [9]). Furthermore, rapid interface diffusion along grain boundaries and, in the case of semi- or incoherent systems, also along phase boundaries has to be taken into account in further studies.

Acknowledgement: This work was supported by the Deutsche Forschungsgemeinschaft, Sonderforschungsbereich 422.

References

[1] J.W. Cahn and J. E. Hilliard, J. Chem. Phys. 28 (1958), p. 258.
[2] M.K. Miller, J.M. Hyde, M.G. Hetherington, A. Cerezo, G.D.W. Smith, and C.M. Elliott, Acta metall. mater. 43 (1995), p. 3385.
[3] F. Spaepen, Mat. Res. Soc. Symp. Proc. 37 (1985), p. 295.
[4] J.S. Langer, Annals of Physics 65 (1971), p. 53.
[5] T. Tsakalos and M.P. Dugan, J. Mater. Sci. 20 (1985), p. 1301.
[6] M. Hentschel, M. Bobeth, G. Diener and W. Pompe, to be published.
[7] D.J. Srolovitz and M.G. Goldiner, J. Met. 3 (1995), p. 31.
[8] L.D. Graham and R.W. Kraft, Trans. Met. Soc. AIME 236 (1966), p. 94.
[9] N. Sridhar, J.M. Rickman and D.J. Srolovitz, J. Appl. Phys. 82 (1997), p. 4852.

e-mail: bobeth@tmfs.mpgfk.tu-dresden.de

Materials Science Forum Vols. 294-296 (1999) pp. 617-620

In situ HRTEM Observation of Solid-Liquid Interfaces

H. Saka[1], S. Arai[2], S. Tsukimoto[1] and K. Sasaki[1]

[1] Department of Quantum Engg, Nagoya University, Nagoya 464-8603, Japan

[2] CIRSE, Nagoya University, Nagoya 464-8603, Japan

Keywords: Heating Experiment, Alumina, Al, Al-Si Alloy

Abstract

The processes of melting and freezing of alumina, Al and Al-Si alloy have been observed directly in a conventional transmission electron microscope (CTEM). The solid-liquid and solid-solid interfaces in these materials have been observed at an atomic level. The liquid phase nucleated preferentially at the surfaces of the Al particles at the melting. The liquid phase then propagated into the interior of the Al particles at the expense of the solid. The solid-liquid interface of alumina showed the atomically flat interface. The layer-by-layer growth of alumina on the solid-liquid interface was observed. The solid-liquid interface in an Al-Si alloy was atomically flat, while the solid-solid interface was atomically rough. When Al melted, the surface of Si particle showed characteristic reconstructed structures.

Introduction

The process of freezing and melting of a solid is one of the most attractive phenomena in the physics of condensed materials. In the initial stage of freezing and melting, there is the nucleation process of the solid and liquid. It is well known that all substances can be made to supercool under suitable circumstances, while superheating never takes place under normal conditions. This cannot be explained by the theory of homogeneous nucleation, which predicts approximately equal degrees of superheating and supercooling. In order to explain the asymmetry, it is assumed that melting always begins at the surface, which can act as its own heterogeneous nucleating site [1]. Surface-nucleation models of melting [2] have also been applied successfully to explain the reduced melting points. In order to study the process of freezing and melting of a solid, we have developed the experimental technique to stabilize the liquid in a transmission electron microscope (TEM), by which the liquid is stably sustained on [3] or embedded in [4] a rigid solid substrate. The experimental technique we had developed gave the direct experimental evidence for the surface melting of small crystalline particles [5] embedded in a solid substrate.

The refinement of our method modified the stability of the sample realized the observation of the solid-liquid interface in an atomic resolution using high resolution transmission electron microscopy (HRTEM). An *in situ* heating experiment using newly developed heating holder [6] in a TEM was performed to observe the surface melting of free Al particles. Also, the HRTEM was applied to observe the atomic structure and the dynamics of solid-liquid interfaces of alumina (α-Al_2O_3) [7] and an Al-Si alloy [8].

Experiments

The newly developed heating holder [6] for our experiment uses a fine tungsten wire with the diameter of 25 μ m as the heating element. The powdered specimens with the diameter of which ranged from 100 to 500nm for Al and Si particles and about 1 μ m for the alumina were put directly on to the heating wire. For the observation of solid-liquid interface of Al-Si alloy, particles of Al and Si were mixed together and mounted on the heating holder [9].

The specimens were heated by applying the direct electric current onto the heating wire and examined between room temperature and the melting temperature of the particles in a Hitachi H-9000NAR electron microscope operating with the accelerating voltage of 300kV. The processes of

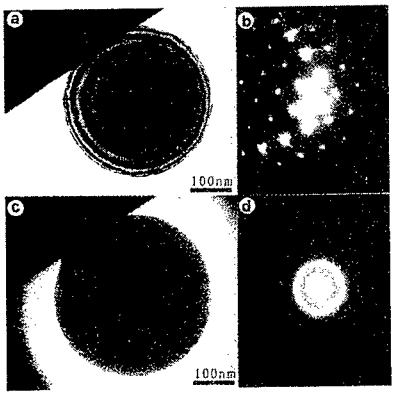

Fig. 1 Typical electron micrographs of an Al particle and the corresponding electron diffraction at room temperature and after melting.

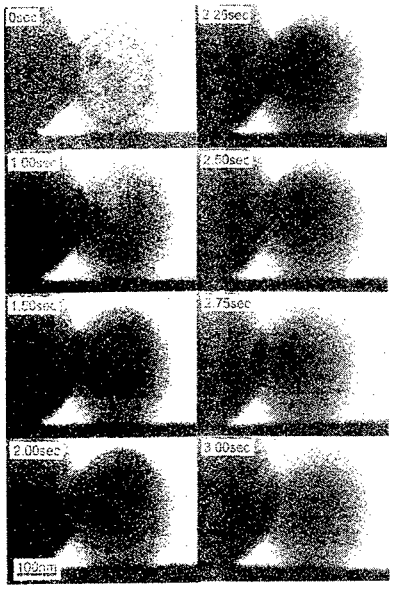

Fig. 2 A sequence of the melting process of an Al particle reproduced from a video tape.

lie on the isothermal contour surface.

The melting takes a few seconds for completion, however, frame-by-frame analysis confirmed that the freezing process completed within the period of two successive frames, i.e., less than 1/30s. This is due to the nonequilibrium condition of freezing caused by the supercooling

Melting and solid-liquid interface of alumina

At around 2000K, fine hemispherical droplets were formed on the surface of alumina. These droplets increased their diameter, or they melting and freezing were continuously recorded using a TV camera. The vacuum pressure of the specimen chamber during the experiment was about 2×10^{-5}Pa.

Results and Discussion

Melting and freezing of Al particles

Figure 1a and 1b shows a typical electron micrograph of an as-received particle of Al and the corresponding electron diffraction, respectively, taken at room temperature. The particle is almost spherical with the diameter of 370nm. Figure 1c and 1d shows an electron micrograph and a diffraction pattern, respectively, of the same particle shown in Fig. 1a but after it has melted. The equi-thickness contours have disappeared and the diffraction pattern now shows only halo-rings. It is noted that the area of the projected image of the Al particle after melting is larger by 2% than before melting. This difference corresponds to the volume expansion of about 14%. This is good agreement with volume change of Al upon melting. The surface of the particle seems to be covered with the thin layer of native surface oxide that sustains the shape and inhibits the evaporation of the liquid Al.

Figure 2 shows a sequence of the processes of melting reproduced from a video tape. The area which shows equi-thickness contours shrinks towards the center of the particle, i.e., the liquid phase nucleates at the surface. The solid-liquid interface in Al does not show any anisotropy; it must

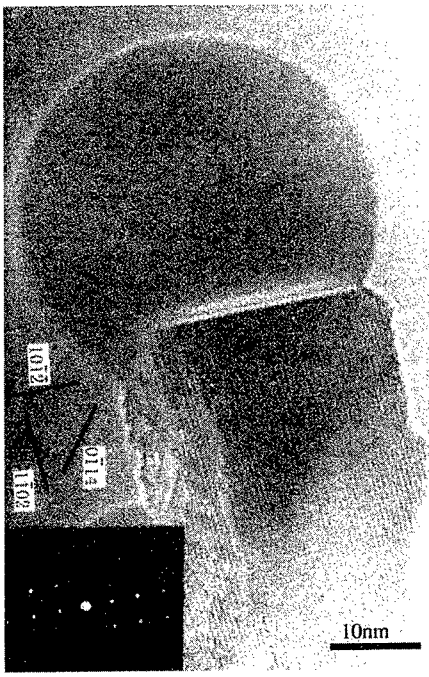

Fig.3 The alumina whisker formed under the liquid droplet. The inset of electron diffraction pattern indicates the whisker is the alumina single crystal.

fused with each other. Thus, the diameter of the droplet increased to about 50nm; and then an alumina whisker started to form under each droplet (Fig. 3). The sample was tilted ± 10 degree to detect lattice fringes or diffraction contrast in the droplet; however, any contrast has never been observed. That means that the droplet was the liquid alumina.

Figure 4 is the series of video recorded images which reveal the formation of one monolayer on the solid-liquid interface between the droplet and the whisker. The formation of the monolayer was initiated by the nucleation of the cloud-like contrast on the interface (Fig. 4b), and then it elongated along the solid-liquid interface (Fig. 4c). The lattice fringes perpendicular to the interface corresponding to that in the whisker were formed (Fig. 4d) during the elongation. These processes are thought to be the formation of a monolayer island with atomic steps on both sides. The monolayer island extended continuously, adding new lattices on both edges until the interface was completely covered by the new monolayer (Fig. 4e).

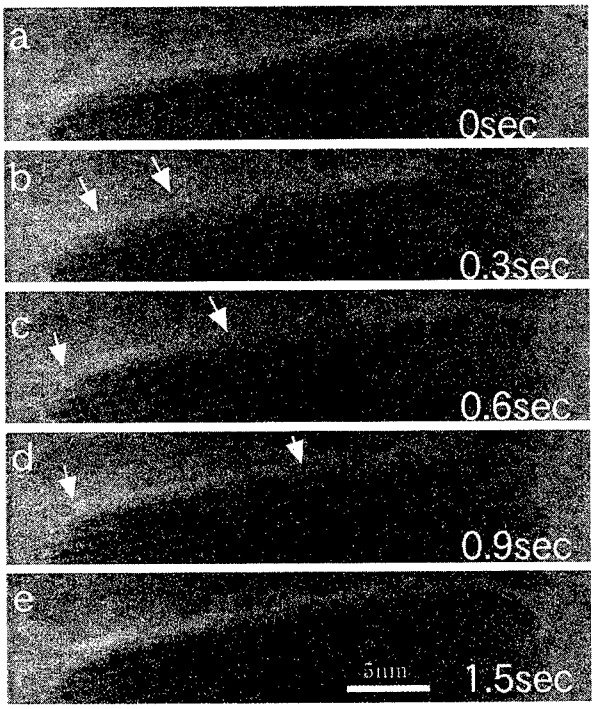

Fig.4 Time resolved video images of solid-liquid interface. The formation of the monolayer was initiated by nucleation of the cloud-like contrast (b). The extended cloud formed the lattice fringes perpendicular to the interface (d). The monolayer extended continuously, and covered the interface completely (e).

It has been reported that the surface of a solid can already liquefy far below bulk melting temperature for many substances [10]. The temperature at which the present experiment has been done was 90% of the bulk melting temperature of alumina [11]. The surface of alumina could also have a liquefied layer in our experiments. The tips of the sharp edge of the sample at which the surface has steep curvature will have large surface energy. In order to reduce the curvature of the surface, i.e., to reduce the surface energy, the liquefied surface layer will be attracted and accumulated at the tip of the sharp edge of the sample, and tend to form hemispherical liquid droplets.

The fine particle of molten aluminum oxide can be undercooled approximately 500K [12]. The melting temperature of fine particle decreases monotonically with decreasing particle size [2]. In counter-word, increase of the particle size, increase the melting temperature. When the size of droplet reached to a certain size, in our case 50nm, the melting temperature of the droplet will be equal to the sample temperature; then the droplet starts to solidify on the solid-liquid interface, which initiates the growth of the alumina whisker.

Solid-liquid interface in an Al-Si alloy

The mixed Al and Si particles were contacted and fused with each other during heating experiment as shown in Fig. 5. In this figure, the lower part denoted by Si is single-crystalline Si, while upper part denoted by Al is Al-rich liquid phase.

The behavior of the Al-Si interface during melting and freezing was observed at an atomic

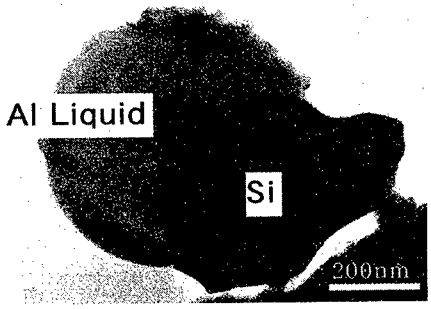

Fig. 5 The Al and Si particle fused each other during heating experiment.

resolution (Fig. 6). When Al gets molten (at 950K), the interface of solid Si/liquid Al is perfectly straight on atomic scale (Fig. 6a). When Al froze, the interface of solid Si/solid Al became atomically rough as shown in Fig. 6b. This behavior of Si-Al interface is quite reversible.

Another point to be noted in Fig. 6 is that when Al is molten, the surface of Si becomes very clean and faceted on atomic scale. That is, the surface of Si is reconstructed. By contrast, while when Al is frozen, the surface of Si gets covered with a surface layer (presumably an oxide layer) and is not atomically faceted any longer. Such a reconstruction takes place only after the surface of Si is wetted with molten Al. This can be seen in Fig. 6c. In Fig. 6a, although Al is molten already, the surface Si is not wetted by Al as yet. Thus, the surface of Si is covered with an oxide layer. On the other hand, in Fig. 6c, the liquid Al wets the Si surface. After wetting the surface of Si with liquid Al, the characteristic reconstruction, which usually takes place only in an ultra-high-vacuum condition, takes place in a conventional vacuum (10^{-5}Pa). This is in good agreement with observation made on Au-deposited Si by Kamino et al [13].

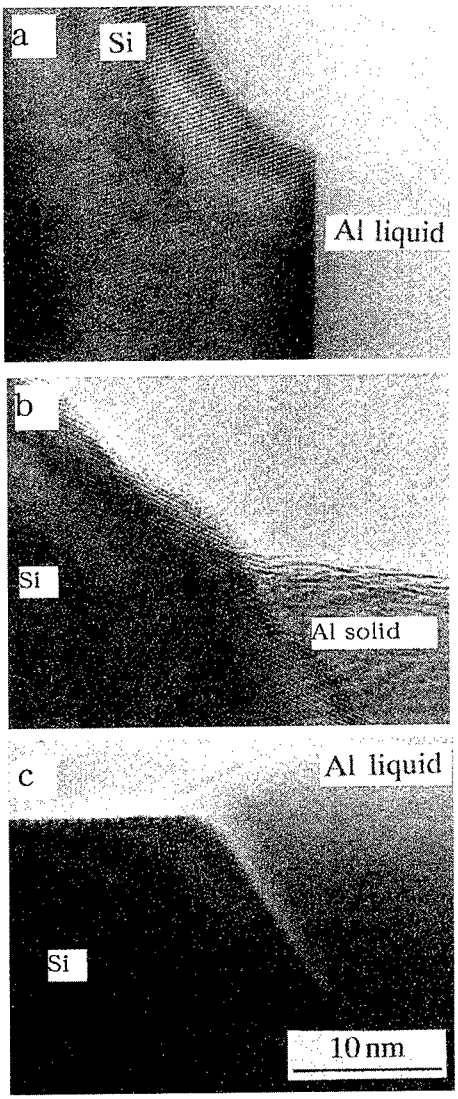

Fig. 6 The behavior of the Al-Si interface. The solid Si/liquid Al interface is atomically flat (a,c), while solid Si/solid Al interface atomically rough (b). The surface of Si wetted by Al liquid is reconstructed, while the surface not wetted by liquid Al is covered with a surface layer.

Conclusions

In situ HRTEM using newly developed heating holder allow us to observe the solid-liquid interface in an atomic resolution. The surface melting of free Al particles was observed as predicted by the surface-nucleation models [2] of melting. The solid-liquid interfaces of alumina [7] and an Al-Si alloy [8] were observed by *in situ* HRTEM in an atomic resolution. The atomically flat interfaces were observed on the solid-liquid interfaces of alumina and an Al-Si alloy. The layer-by-layer growth of alumina and the surface reconstruction of Si were observed.

References

[1] J.W.Christian, "The Theory of Transformations in Metals and Alloys", (Pergamon Press. Oxford 1965).
[2] P.R.Gouchman, and W.A. Jesser, Nature **269** (1977), p.481.
[3] H.Saka, A.Sakai, T.Kamino and T.Imura, Phil. Mag. **A52** (1985), L29.
[4] H.Saka, Y.Nishikawa and T.Imura, Phil. Mag. **A57** (1988), p.895.
[5] H.Saka, Y.Nishikawa, and T.Imura, Phil. Mag. Lett. **55** (1987), p.163.
[6] T.Kamino and H.Saka, Microsc. Microanal. Microstruct. **4** (1993), p.127.
[7] K.Sasaki and H.Saka, Mat. Res. Soc. Symp. Proc. **466** (1997), p.185.
[8] S.Arai, S.Tsukimoto and H.Saka, Proc. 4th Spec. Symp. Adv. Mat. Nagoya Japan (1998) p.39.
[9]. M.Takagi, J. Phys. Soc. Jpn. 9 (1954), p.359.
[10] D.Nenow and A.Trayanov, J. Crystal Growth, **79** (1986), p.801.
[11] Binary Alloy Phase Diagrams, ed. T.Massalski, J.Murray, L.Bennett and H.Baker, (American Society for Metals 1986), p.144.
[12] J.Weber, C.Anderson, D.Merkley and P.Nordine, J. Am. Cer. Soc. **78** (1995), p.577.
[13] T. Kamino, T. Yaguchi, M. Tomita, and H. Saka, Phil. Mag. **A75** (1997), p.105.

Materials Science Forum Vols. 294-296 (1999) pp. 621-624

Grain Boundary Modification During Long-Term Creep in Silicon Nitride

F. Lofaj[1], H. Gu[2], A. Okada[3] and H. Kawamoto[3]

[1] Institute of Materials Research of SAS, Watsonova 47, SK-04353 Kosice, Slovakia

[2] Ceramic Superplasticity International Research Project, JST, Japan Fine Ceramic Center (JFCC), 2-4-1 Mutsuno, Nagoya 456, Japan

[3] JFCC, 2-4-1 Mutsuno, Nagoya 456, Japan

Keywords: Tensile Creep, Crystalline Secondary Phases, Ytterbium Oxynitride, Transformation, Ytterbium Disilicate, Epitaxial Growth, Silicon Nitride

Abstract *The microstructure changes in the commercial silicon nitride SN88M after tensile creep at the temperatures 1250°C-1400°C under the stresses of 140 - 430 MPa and lasting up to 10 000 hours were investigated. Creep induced changes in the grain boundary phases were studied by X-ray diffraction (XRD), high resolution transmission electron microscopy (HREM) a. nd scanning transmission electron microscopy with electron energy loss spectroscopy (STEM/EELS). XRD revealed the transformation of the ytterbium oxynitride crystalline phases at the multigrain junctions in the as-received materials into disilicates in the whole volume during creep tests. This change was confirmed by EELS. Epitaxially grown layers of silicon nitride were observed at the junctions of silicon nitride grains and transformed phase due to the Yb-rich precipitates segregated at the original facets. The reaction of the oxynitride with amorphous silica leading to the reduction of the amount of silica at the grain boundaries and formation of new silicon nitride epitaxially reprecipitated on the original grains is proposed as the mechanism for the observed grain growth and phase changes during creep.*

Introduction

Practical use of silicon nitride ceramics in the advanced gas turbines is hampered by insufficient knowledge of the processes controlling lifetime and reliability during long-term operation. Since the long-term durability of the rotating parts at high temperatures is ultimately controlled by creep, a detailed characterization of creep behavior of the corresponding materials is an essential part of the US, Japanese and European projects of the development of ceramic engines [1-2]. The objectives of the creep studies carried out within currently running Japanese national project "Research and Development of Ceramic Gas Turbines (300 kW class)" are to accumulate data on creep behavior and creep lifetime of the most prospective silicon nitride materials for design purposes and for the development of a life prediction method up to 10 000 hours [1]. Preliminary data indicate that tensile creep deformation in these materials is essentially controlled by cavitation [3]. Grain boundary sliding and viscous flow of the residual glassy phase are considered to be the basic mechanisms responsible for continuous cavitation and resulting creep strain. Because these mechanisms depend on the amount and properties of the residual amorphous boundary phases which are always present in the ceramics prepared via liquid phase sintering, any change in the composition and/or amount of the glass during the long-term tests at high temperatures in oxidizing atmosphere may introduce significant changes in creep behavior of these materials. This possibility is generally omitted in creep studies and only recent studies pointed out the significance of the oxidation processes accompanying creep deformation [4,5].

Therefore, the objective of the current work is to investigate the changes in the grain boundary phases in the high performance SN 88M silicon nitride after the long-term tests in order to determine their role in the long-term creep deformation.

Experimental Procedure

Material Characterization Commercially available self-reinforced silicon nitride designated as SN 88M, which is produced by NGK Insulators, Ltd., (Nagoya, Japan) was investigated. The microstructure of this material has bimodal grain size distribution with large grains of β-Si_3N_4 (diameter 5-10 μm, length 50-80 μm) distributed in the fine grained (0.5 - 0.8 μm) β -Si_3N_4 matrix. The crystalline $Yb_4Si_2N_2O_7$ phase with a minor content of $Yb_2Si_2O_7$ were identified by X-ray diffraction at the grain boundaries.

Tensile Creep Testing Creep tests were performed on dog-bone tensile specimens with a rectangular gage cross section of 2.5 mm x 4 mm and a gage length of 20 mm. Creep experiments were conducted in nine testing machines (model HT 300, Toshin Kogyo Co., Ltd., Tokyo, Japan) at 1250°C, 1300°C, 1350°C and 1400°C in air under tensile stresses ranging from 130 to 430 MPa. Additional details of the creep machines and testing procedure are described elsewhere [5].

Microstructure Study Thin foils for TEM and STEM studies were cut parallel to the direction of the applied stress from eight specimens after tests lasting from 255 hours to 11 114 hours. TEM studies were carried out at 100 kV, 200 kV and 400 kV accelerating voltages (Models JEM 100 CX II, JEM 2010 and JEM-4000 FX, respectively), STEM study was done at 100 kV (HB 601 UX, Vacuum Generator Microscopes). The phase and chemical compositions were investigated by X-ray diffraction, energy disperse X-ray analyzer (EDX) and electron energy loss spectroscopy (EELS).

Results and Discussion

X-ray diffraction patterns of the as-received material and those taken from the bulk of the creep tested specimens are compared in Fig. 1. After long-term creep, $Yb_2Si_2O_7$ is the major secondary phase while $Yb_4Si_2N_2O_7$, which was the major secondary phase in the as-received material, almost disappeared. The transformation from ytterbium oxynitride toward ytterbium disilicate depends on the testing temperature and duration of testing. At 1350°C this transformation is completed within the whole bulk within 500 hours while at 1250°C a considerably longer time is required. Note that the resulting compositions in both cases are very similar. Furthermore, additional experiments revealed that heating in air at the temperatures around 800°C transforms the oxynitride phase at the surface into disilicate. These results indicate that the oxynitride phase is less stable at the elevated temperatures in air and the system "Si_3N_4-$Yb_2Si_2O_7$-residual glass" is thermodynamically more favorable than the system "Si_3N_4-$Yb_4Si_2N_2O_7$-residual glass" in the as-received material. Fig. 2 (A) shows the EELS spectra taken from three crystalline pockets in the as-received material. Although the normalized ratios of Yb:Si:N:O vary in the pockets, $Yb_4Si_2N_2O_7$ phase is very probable in the first two pockets and $Yb_2Si_2O_7$ in the last pocket in the as-received material. This is consisten with the XRD results indicating minor content of disilicate and oxynitride as the major secondary phase. Fig. 2 (B) shows the spectra in triple junctions in the specimen tested under the stress of 200 MPa at 1250°C for 11 114 hours. Very low content of nitrogen indicate that only $Yb_2Si_2O_7$ is possible in the pockets. Fig. 3 is a bright field STEM micrograph of the interface between β-Si_3N_4 grain and $Yb_2Si_2O_7$ phase in the same specimen. The original surface of silicon nitride grain is decorated by small (~6 nm) dark precipitates and an additional layer of Si_3N_4 is formed on the original surface. EELS measurements revealed high

Fig. 1. The comparison of the phase composition in the as-received material and after tensile creep at 1250°C and 1350°C for 500 h and more than 11000 hours, respectively. As received material contains usually $Yb_4Si_2N_2O_7$ phase in the pockets among the β Si_3N_4 grains whereas $Yb_2Si_2O_7$ phase is found after creep.

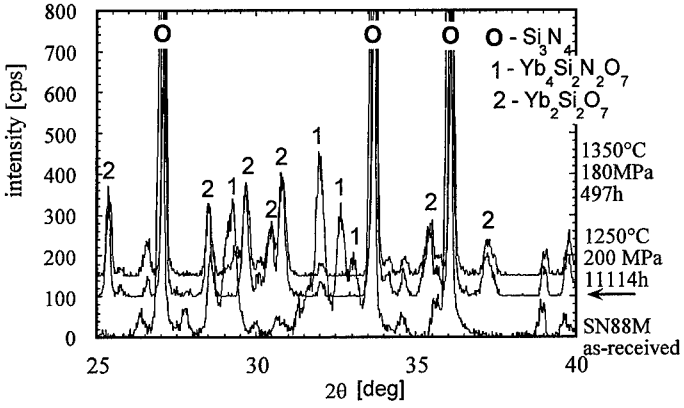

Fig. 2. EELS spectra of the interstitial pockets filled with crystalline secondary phases in the as-received material - (A) and after creep at 1250°C for 11 000 h under the stress of 200 MPa - (B).

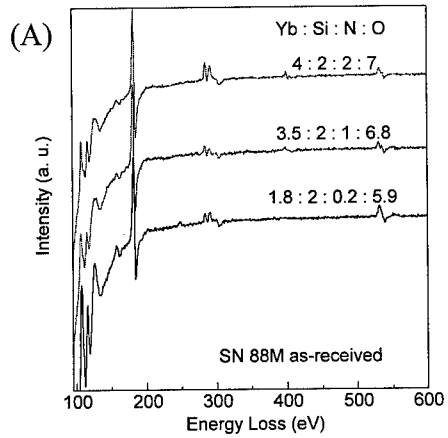

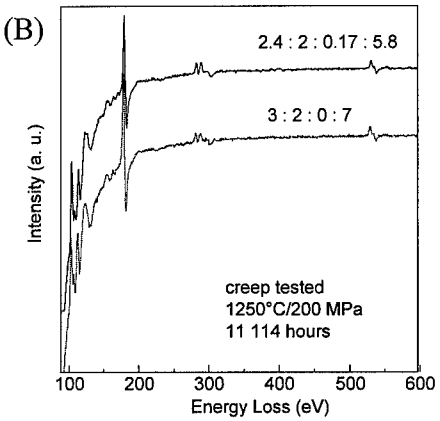

Fig. 3. STEM image of the interface between silicon nitride and disilicate grain after creep.

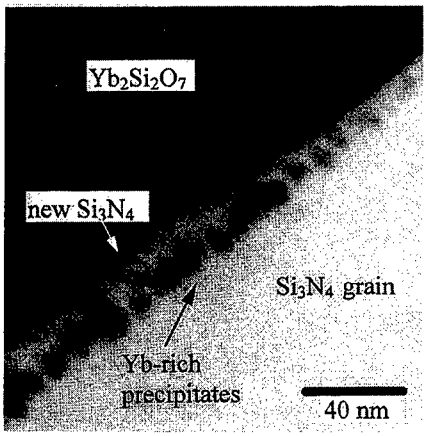

Fig. 4. HREM micrograph of similar interface between silicon nitride and $Yb_2Si_2O_7$.

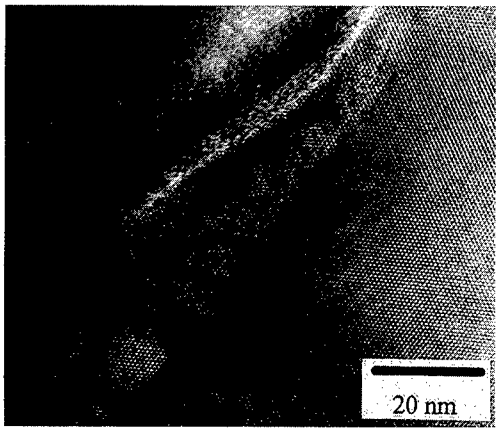

concentration of Yb in the precipitates whereas the new grown layers contain only silicon and nitrogen. This suggests the layers consist of silicon nitride. HREM study of the same specimen (Fig. 4) revealed that the layers are epitaxially deposited on the facets of the original silicon nitride grains.

Two possible mechanisms for the transformation of the Yb-oxynitride into Yb-disilicate are considered:

$$2\ Si_3N_4 + 2\ Yb_4Si_2N_2O_7 + 9\ O_2 \longrightarrow 2\ SiO_2 + 4\ Yb_2Si_2O_7 + 6\ N_2 \qquad (1)$$

and

$$2\ Yb_4Si_2N_2O_7 + 7\ SiO_2 \longrightarrow 4\ Yb_2Si_2O_7 + Si_3N_4\ . \qquad (2)$$

Eq. 1 assumes oxidation with the formation of SiO_2 and the release of nitrogen whereas Eq.2 suggests that SiO_2 is consumed to form new Si_3N_4. Results of STEM and HREM studies support Eq. 2 as the the mechanism because very low amount of the residual glassy phase was found at two grain junctions and the epitaxially grown new silicon nitride layers were observed. Thus, new mechanisms for the formation of silicon nitride and reduction of the amount of residual glass are proposed.

Conclusions

The transformation of the ytterbium oxynitride secondary phases at the pockets in the advanced silicon nitride SN 88M into ytterbium disilicate phase was observed in the creep tested specimens. The transformation is possible in a limited extent already in the as-received material and it starts at app. 800°C in the surface layers of the specimen. The mechanism proposed for the transformation assumes that amorphous silica at the grain junctions is consumed during reaction with ytterbium oxynitride and ytterbium disilicate and new silicon nitride are formed. Reduction of the content of the amorphous phase seems to result in improving the creep resistance of SN 88M [6]. Epitaxial precipitation of new silicon nitride on grain facets which was observed by HREM confirms a possibility of the proposed mechanism.

Acknowledgment The work was partially sponsored by COST-510 Project A9 and VEGA Grant No. 2/5162/98. HREM study at QMW (London, UK) was supported by British Council Academic Link Program and the help of Dr. M. Reece is highly appreciated. The support for the stay of F. Lofaj at JFCC provided by STA (Japan) and JFCC is heartily acknowledged.

References

[1] T. Kamei *et al.*, Proc.1995 Yokohama Int. Gas Turbine Congress, (1995), p. I-143.
[2] V. Parthasarathy *et al.*, Proc. 6 Int. Symp. Ceramic Materials & Components for Engines, Nissei Ebro, Co., (1998), p. 259.
[3] F. Lofaj *et al.*, J. Am. Ceram. Soc. **80** [6] (1997), p.1619.
[4] A.A. Wereszcak *et al.*, J. Am. Ceram. Soc. **78** [8] (1995), p.2129.
[5] F. Lofaj *et al.*, Proc.1995 Yokohama Int. Gas Turbine Congress, (1995), p. III-37.
[6] F. Lofaj *et al.*, Engineering Ceramics '96: Higher Reliability through Processing, Kluwer Academic Publ., (1997), p. 337.

Contact address:
František Lofaj,
Institute of Materials Research of SAS Watsonova 47, 043 53 Košice, Slovakia;
tel: +421-95/ 63-381-15, ext. 236 fax: +421-95/ 63-371-08
e-mail: lofaj@saske.sk

Materials Science Forum Vols. 294-296 (1999) pp. 625-628

Grain Boundary Intersecting a Free Surface: Structural Evolution Toward Equilibrium

C.S. Becquart[1] and V. Pontikis[2]

[1] Laboratoire de Métallurgie Physique, URA CNRS 234, Bât. C6, Université Lille I, F-59655 Villeneuve d'Ascq Cédex, France

[2] Laboratoire des Solides Irradiés, CEA-CNRS UMR 7642-Ecole Polytechnique, F-91128 Palaiseau Cédex, France

Keywords: Grain-Boundaries, Structure, Surface, Mobility, Atomistic Simulations

Abstract By using computer simulation, we study early stages of the evolution toward thermal equilibrium of a Σ=5 (210)[001] tilt axis grain boundary that intersects an initially flat (100) free surface in copper. The calculations rely on an adapted, phenomenological n-body potential that satisfactorily reproduces static and dynamical properties of copper. We report detailed features of elementary diffusion mechanisms that occur at the neighbourhood of the grain boundary-surface intersection.

Introduction

Because of their importance in determining key properties of materials, such as mechanical behaviour and corrosion resistance, grain boundaries have been extensively studied by both experiments and computer simulations [1]. These studies have shown that at grain boundaries the formation energy of defects decreases with respect to the bulk and is thus responsible for the large values of intergranular diffusivity observed. Thereby, a satisfactory explanation is given of the role of grain boundaries as 'short-circuits' for diffusion.

The enhanced mobility of atoms at interfaces might be of particular importance in determining thermal grooving and intergranular corrosion, damage phenomena that are both initiated at the crossing between a grain boundary and a free surface. To our knowledge, grooving has never been studied at the atomistic scale given that mean field approaches are better adapted to the natural, macroscopic scale of this phenomenon [2][3]. The present work is a preliminary investigation of the initial stages of grooving and of the very beginning of the evolution toward equilibrium of a system with a high angle grain boundary intersecting a low-index free surface.

Computational procedure

The simulations were performed using Molecular Dynamics (MD) with an adapted, phenomenological n-body potential that satisfactorily reproduces static and dynamical properties of copper [4]. The code used was a slightly modified version of CDCMD: a user oriented code developed at the University of Connecticut by J. Rifkin to do Monte Carlo and MD simulations (a version in C-programming language is available in [5]). The newtonian equations of motion are integrated by using a fifth order Gear predictor-corrector algorithm with a time step $0.5\ 10^{-15}$ s at a temperature T=900 K ($T_{melting} \cong 1200$ K for the potential here used). Canonical equilibrium trajectories of 300 000 time steps have been generated under these conditions representing a total duration of 0.15 ns.

The initial configuration was obtained as follows: (i) the grain boundary (GB) was geometrically setup by means of the coincident-site lattice (CSL) theory. Two computational cells have been used with dimensions 6[210]x3[$\bar{1}$20]x4[001] (referred to as the 'small array') and 6[210]x3[$\bar{1}$20]x8[001] (referred to as the 'big array'). Two kinds of calculations have been made that differ in the border conditions applied: one used periodic boundary conditions (PBC) along the three space directions and has served as a reference state for the intergranular mobility while in the

other PBC have been suppressed along the [001] direction, thus creating a pair of parallel free surfaces intersecting the interface normal to the tilt axis (ii) the relaxed structures at T=0 K are then obtained by minimizing the total energy [6] (iii) the studied systems have been slowly brought to the required temperature by annealing stages which lasted 1000 MD steps, the temperature increasing by δT=100 K at each stage. The appropriate lattice parameter at the target temperature, previously determined for the perfect bulk, has been used. Simulations with free surfaces have been performed at T=600 K and T=900 K for the small array and at T=900 K for the big array. For the former system an additional calculation with full PBC has provided the reference state for the interfacial diffusivity.

As the system is heterogeneous, a local analysis is required for the interfacial diffusivity to be investigated. This is however difficult a task because the smaller the volume element considered in such an analysis, the larger are the associated statistical errors. Therefore, instead of estimating the diffusion coefficient, we have determined what we will refer hereafter to as the 'site mobility'. To this end, the computational box was divided into small volumes, ΔV, and the identity of the atoms contained in each has been determined. Atomic mean square displacements (MSD) are then computed versus the delay, τ, for each elementary cell and average values have been computed over N_{conf} equilibrium configurations of the studied system (configurations were recorded every 20 time steps) and the n_{at} atoms contained in each cell. How active diffusion is, depends on the considered cell, and is estimated by computing the amplitude of MSD for the atoms it contains:

$$M = \frac{1}{N_{conf}} \sum_{N_{conf}} \frac{1}{n_{at}} \sum_{i \in \Delta V} \delta r_i^2(\tau) \qquad (1)$$

Results

The results presented here are preliminary and qualitative as the system is very small. However, they exhibit some interesting features. In Figs. 1a and 1b, two-dimensional plots of the 'site mobility' of the atoms along directions parallel and normal to the tilt axis are given for the two kinds of systems studied, that with a pair of parallel free surfaces intersecting the boundary plane (Fig. 1a) and the reference case of the infinitely extended grain boundary (Fig. 1b). The minimum value on the 'site mobility' scale (0.07 Å^2) corresponds to the vibrational MSD of the atoms at T=900 K. The influence of the free surface is visible from Fig. 1a where the region of high 'site mobility' values is shown to increase in size on approaching the free surface. Far from the surface, the grain boundary mobility is still important in all directions, while in the case of the infinitely extended GB (Fig. 1b) the mobility perpendicular to the grain boundary plane is negligible. The surface is though a very important perturbation that adds in a non-linear manner to the perturbation introduced in the crystal by the GB. One can also conclude that if the simulations were to reproduce far from the free surfaces the properties of a perfect GB the size of the simulated system should be further increased. In addition to the above, Fig. 1 shows also that the 'site mobility' close to the GB is anisotropic. Indeed atoms located at the grain boundary and close to free surfaces are more mobile along the direction perpendicular to the tilt axis (the active sites are " darker " and more connected) than along the direction parallel to it. This is in agreement with previous computer simulations [7], that, unlike experiments [8], showed that the diffusion perpendicular to the tilt axis is faster than parallel to it: $\frac{D_{//}}{D_{\perp}} < 1$. This persistent contradiction between simulations and experiments needs to be elucidated and motivates for future investigations of intergranular diffusivity.

Another point worth mentioning is that at the two temperatures studied and in all cases (with or without (100) free surfaces for both the small and the big array), the grain-boundary exhibits the allotropic phase transition previously observed by Guillopé [9]. This structural change is illustrated by the atomic density profiles drawn along the direction [210] normal to the GB plane (Fig. 2). The fine structure of the peaks in the neighborhood of the interface has changed and after the transition has occurred, the central GB plane contains twice as many atoms as it does at low temperatures.

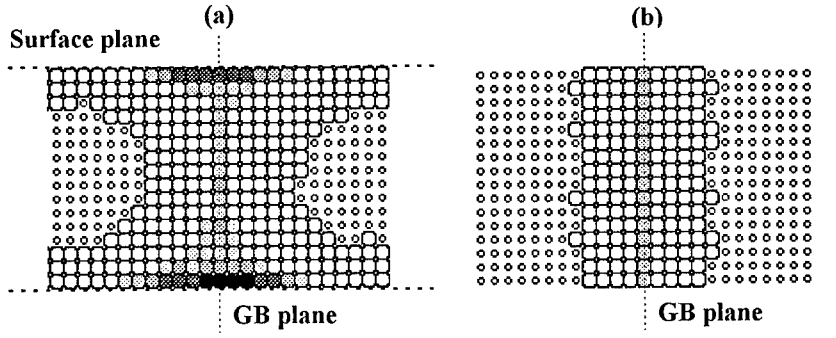

Component along the direction perpendicular to the tilt axis ([$\bar{1}$20] direction)

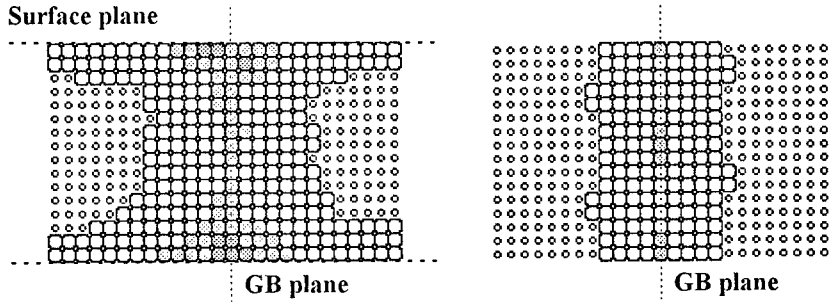

Component along the direction parallel to the tilt axis ([001] direction)

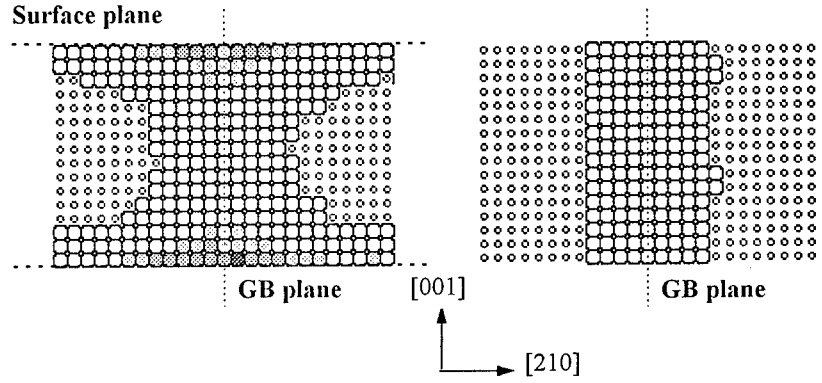

Component along the direction perpendicular to the grain boundary plane ([210] direction).

Fig.1: Snapshots of the mobility close to the grain boundary at 900K for a delay $\tau = 0.5\ 10^{-12}$ s. **(a)** big array with (001) free surfaces intersecting the boundary; **(b)** small array with PBC on (for purpose of comparison, the image was duplicated along the flexion axis)

0.07 Å^2 < ○ <; 0.07 Å^2 < □ < 0.376 Å^2; 0.376 Å^2 < ▨ < 0.682 Å^2; 0.682 Å^2 < ▩ < 0.988 Å^2

0.988 Å^2 < ■ < 1.294 Å^2; 1.294 Å^2 < ■ < 1.6 Å^2

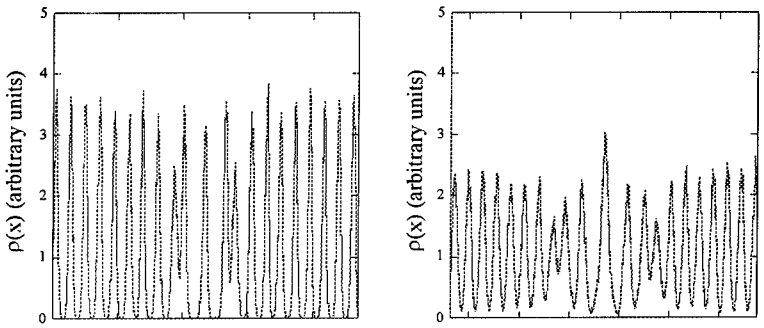

Fig. 2 Atomic density profile perpendicular to the GB plane. Left: T = 400K, Right: T = 900K. x // [210]. Abscissae are given in arbitrary units.

For the thinnest slab (small array) with (001) free surfaces, an unexpected behaviour is observed at T=900 K: the system undergoes spontaneously small shears parallel to the interface. These fluctuate as a function of the time elapsed as does the interface which oscillates between different positions and different atomic configurations. This behaviour, intimately related to finite size effects, can be suppressed by using PBC in all three directions, or equivalently by increasing the dimension of the system along the tilt axis (a factor two increase is sufficient). At low temperatures however, T< 600 K, the shear is not observed. An explanation of this behaviour is given elsewhere [6].

Discussion and conclusions

The purpose of this work is to study the properties of a grain boundary that intersects a free surface and the transient structural aspects of its evolution toward equilibrium (thermal grooving). The results presented here permit us to conclude that atoms located close to the intersection between free surfaces and grain boundaries display an enhanced mobility with respect to the bulk and to a perfect grain boundary. During the evolution toward the equilibrium shape of the bicrystal, these atoms will eventually move out leaving a groove behind them. Although preliminary and qualitative, as the system studied is very small, these results are important in guiding work in progress devoted to the study of the energetics of point defects close to the emergence line of a grain boundary at a free surface. These may serve as an input to mean field approaches, the only capable to describe the evolution toward equilibrium under control of the balance between surface and grain boundary tensions.

Acknowledgments

One of the author (C. S. Becquart) wishes to thank C. Domain of EDF and A. Legris of the LMP of the university de Lille for their help with this work.

References

[1] A.P. Sutton and R.W. Balluffi, in « Interfaces in Crystalline Materials », Clarendon Press, Oxford (1995).
[2] Wen Zhang and J.H. Schneibel, Comp. Mater. Sci. **3**, 347 (1995).
[3] W. Mullins, in « Metal Surfaces », ASM, (1962).
[4] B. Loisel, D. Gorse, V. Pontikis and J. Lapujoulade, Surface Sci. **221**, 365 (1989); B. Loisel, J. Lapujoulade and V. Pontikis , Surface Sci. **256**, 242 (1991).
[5] http://www.ims.uconn.edu/centers/simul/index.htm#xmd.
[6] P. Gregoriadis, Th. Karakostas, Ph. Komninou and V. Pontikis, this conference.
[7] R.E. Hoffman, Acta Met. **2**, 419 (1954).
[8] M. Guillopé, G. Ciccotti and V. Pontikis, Surface Sci. **144**, 67 (1984).
[9] M. Guillopé, J. Phys. **47**, 1347 (1986).

Materials Science Forum Vols. 294-296 (1999) pp. 629-632

Grain Boundary Migration in Fe-Si Alloy Bicrystals

S. Tsurekawa[1] and H. Nakashima[2]

[1] Department of Machine Intelligence and Systems Engineering, Graduate School of Engineering, Tohoku University, Sendai 980-8579, Miyagi, Japan

[2] Department of Molecular and Material Sciences, Graduate School of Engineering Sciences, Kyushu University, Kasuga 816-8580, Fukuoka, Japan

Keywords: Grain Boundary Migration, Fe-3%Si Alloy, Solute Drag, Grain Boundary Diffusion, Misorientation

ABSTRACT

Migrations of <110> tilt boundaries in Fe - Si alloy bicrystals have been investigated by Sun and Bauer technique as a function of misorientation angle, driving force, temperature and Si content. Two distinct regions with different migration behaviour are observed on temperature - dependence of mobility: a drastic change in mobility occurs at a critical temperature. The critical temperature depends on the driving force and also the grain boundary (GB) character. The activation energy for grain boundary migration (GBM) is *ca.* 2/3 of that for Fe bulk self - diffusion in the higher temperature region, suggesting that the boundary motion is governed by GB diffusion. On the other hand, the activation energy increases up to *ca.* 220 kJ/mol in the lower temperature region, being in agreement with that for Si intrinsic - diffusion in α-Fe. This agreement shows that GB is most likely to move dragging Si atmosphere. Also, it is of great interest that the mobility for coincidence boundary, particularly Σ9 GB, is higher than that for a random boundary in the lower temperature region, but reverse is the case in the higher temperature region. In addition, the mobility depends on Si content in the lower temperature region; it increases with decreasing Si content, whereas such dependence is scarcely observed in the higher temperature region. These results obtained here will be discussed from the viewpoint of the interaction between GB and solute atoms.

1. INTRODUCTION

Silicon steel has sharp preferred orientation of the secondary recrystallization texture, so - called Goss texture of {110}<001>. The formation of the oriented grains in a polycrystalline material is believed to result from preferred GBM with a specific orientation relation between two adjacent grains. From the experiments conducted so far, it has been pointed out that Σ9 and Σ5 GBs may play an important role in the Goss texture formation during the secondary recrystallization in silicon steel [1, 2]. The GBM behaviour may depend on such various factors as misorientation angle, temperature, driving force, impurity, etc. Then, for clarifying the mechanism of GBM, it is necessary to observe the single GBM in a well characterized orientation controlled bicrystal. However, in most of investigations concerning the boundary migration in silicon steel, polycrystals have been used [3], and then it seems to be difficult to monitor the individual boundary motion.

Recently, an independent research on the GBM with bicrystals has been performed by Lejeck *et al.*[4, 5], Nakashima *et al.*[6-8] and Furtkamp *et al.*[9, 10]. In the present paper, therefore, we will mainly review our results to obtain an information on GBM in Fe-Si based alloy.

2. EXPERIMENTAL PROCEDURES

2.1 Preparation of bicrystals

The starting material was a vacuum melted Fe-3%Si alloy rod, 10mm in diameter, whose impurity contents were minimized as far as we could comparing with those in commercial alloy. To prepare the bicrystals with <110> symmetric tilt boundaries, oriented single crystals were grown using the r. f. floating zone technique, and the partly remelted and roted by 180°, followed by slow solidification. The details of the preparation method of the bicrystals are the same as those reported by Kurishita *et al.*[11]. The chemical composition of the r. f. melted bicrystal is also given in refrences[6][7].

2.2 Experimental Technique

2.2.1 Sun and Bauer method

For measuring the boundary mobility, Sun and Bauer method [12] was employed in the present study, as illustrated in Fig. 1, to provide a driving force for the migration of a single bounday. The angle α at which the GB meets the surface B in Fig. 1 is directly related to the magnitude of the driving force, *i. e.*, the driving force increases with decrease in angle α. Furthermore, the driving force decreases as the hyperbola-like boundary migrates under course of an experiment.

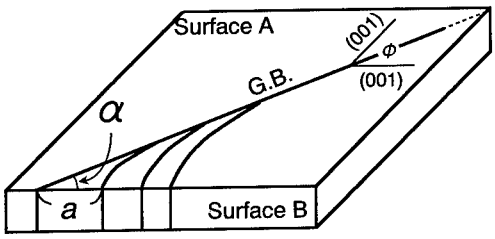

Fig.1 Illustration of Sun and Bauer method.

According to Sun and Bauer [12], the relation between the displacement, a, of the boundary along the surface B and time, t, should be described by

$$a^2 = k\,t, \quad k = 2M\gamma_b f(\alpha), \qquad (1)$$

where M is the mobility of the GBM, γ_b the GB energy and $f(\alpha)$ the magnification factor which is functionally related to the angle α[12]. The details of the preparation procedures of specimens are given in references [6, 7].

2.2.2 Interrupt annealing test

Samples for GBM measurements were pre-heated at 1070K and rapidly heated to the desired temperatures and then held for various periods under a vacuum of about 2 mPa. The range of annealing temperatures used here was 1200 to 1625K (0.68 to 0.92T_m: T_m is the absolute melting temperature of material). To prevent formation of an oxide film on the specimen surface during annealing, Zr foils were placed near the specimen as an oxygen getter. After cooling, the specimens were etched in a solution of HF, HNO_3, and H_2O in a volume ratio of 1:8:10, and then subjected to optical microscope or scanning electron microscope observation to determine the position of the migrated boundary. Further, cumulative anneals were conducted on each specimen, with the mechanical polishing and the annealing to remove the strain between successive annealing.

3. RESULTS AND DISCUSSION

3.1 Time-dependent GBM

The square of GB displacement are plotted against time in Fig. 2 [6, 7]. For comparison, the results obtained by a *in-situ* synchrotron x-ray topographic observations [8] are shown in Fig. 2. The values of displacement were normalized by the magnification factor $f(\alpha)$ [12], because the angles α were different among the specimens, and a_0 in the vertical axis is the distance which boundary travelled during the heating up period. The relationship between the square of the boundary displacement and time is found to be divided into two or three distinct regions with different slopes of the straight lines. The slope of the straight lines in Fig.3 implies the product of the mobility and the GB energy. According to the Sun and Bauer method, the driving force successively decreases with increasing boundary displacement. Assuming that the variation of the GB energy due to change in orientation of GB plane during migration is negligible, the change in the slope of the straight line indicates a change in the mobility with decrease in driving force.

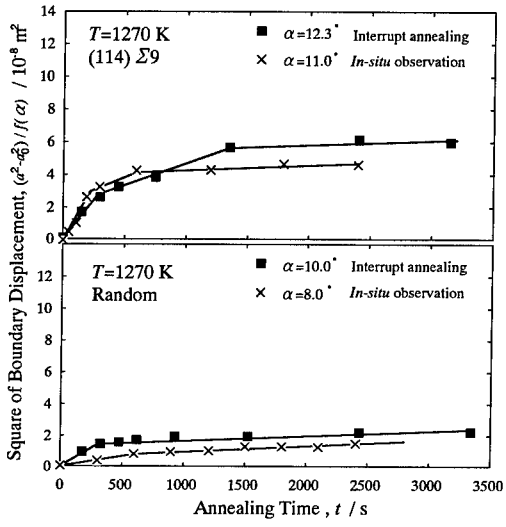

Fig.2 Variations of the square of GB displacement with time at 1270K.

3.2 Driving force dependence of GBM rate

Figure 3 [6, 7] shows a variation of the GB

velocity with driving force at 1270K and 1320K for (221) Σ9 GB (ϕ=141°). It is seen that a drastic change in GBM velocity occurs at a critical driving force, and the critical driving force decreases with increasing temperature.

These interesting phenomena agree qualitatively with the prediction from the solute drag theory proposed by Cahn [13] and Lücke and Stüwe [14]. The theories say that under a smaller driving force, *i. e.*, slow GB motion, a GB should move dragging a solute atmosphere, which is similar to the Cottrell atmosphere around a moving dislocation, whereas under a higher driving force, *i. e.*, quick boundary motion, the breaking away of the GB from the solute atmosphere occurs and then the GB can migrates independently of solute atoms.

3.3 Temperature dependence of grain boundary migration rate

Figure 4 [6, 7] shows the Arrhenius plot of the mobility M (= $\Delta a^2 / 2f(\alpha)\Delta t\, \gamma_b$) for (221) Σ9 coincidence and random GBs. Here, the misorientation and temperature dependences of the grain boundary energy γ_b were estimated from the reference [15] and [16], respectively.

As shown in Fig. 5, an abrupt change in mobility occurs and then three regions of different migration behaviour are observed. The transition temperature depends on the driving force, such that the temperature decreases with increasing driving force, and the transition is much steeper in Σ9 boundary than that in random boundary. The activation energies for GBM are less dependent on GB misorientations; in the higher temperature region the energies for Σ9 and random GBs are 175±10 kJ/mol and 165±20kJ/mol, respectively, which are *ca.* 2/3 of that for Fe atom bulk self-diffusion of 270 ±13 kJ/mol [17], while in the lower temperature region the energies increase to 220±20kJ/mol for both cases, which is consistent with that for intrinsic-diffusion of Si in α-Fe, 220 kJ/mol [18]. The results obtained here are also agreement well with the prediction by Gordon and Vandermeer theory [19] based on solute drag mechanism. Also, it is of great interest that the mobility for Σ9 boundary is higher than that for a random boundary in the lower temperature region , however, the reverse is the case in the higher temperature region.

In addition, the mobility depends on Si content in the lower temperature region; it increases with decreasing Si content, whereas such dependence is scarcely observed in the higher temperature region [20].

From the results obtained here, in the lower temperature region, we see that the rate controlling process of the migration should be intrinsic-diffusion of Si in α-Fe, suggesting that the GB may drag Si atmosphere formed around the GB due to the elastic interaction between the GB and solute atoms. Further, the fact that Σ9 boundary migrates faster than random boundary in the lower temperature region may come from the difference in GB segregation between them; an enrichment

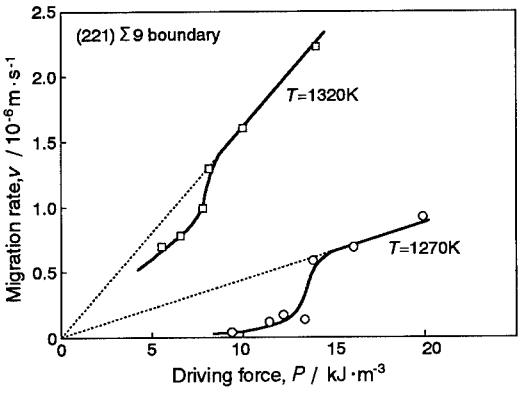

Fig. 3 Relationship between GBM velocity,v, and driving force, P, at 1270K and 1320K for Σ9 GB.

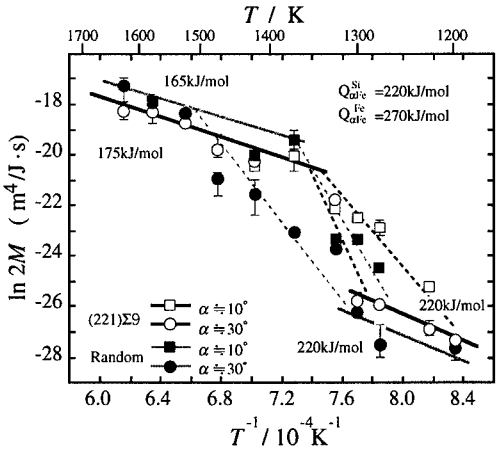

Fig. 4 Temperature dependence of the mobility for Σ9 and random GBs under a large driving force (□,■) and a small ones (○,●).

of Si atoms at $\Sigma 9$ GB is probably lower than that at random GB.

On the other hand, the remarkable increase in the mobility in the higher temperature region suggests the breakaway of the boundary from a solute atmosphere. The activation energy obtained in this region was approximately 2/3 of that for self-diffusion in α-Fe. Therefore, the GB motion would probably be governed by GB diffusion. The cusps in the curve showing the relation between the GB diffusivity and misorientaion are often observed at low Σ GBs [21, 22], suggesting that the GB diffusion in random GB is faster than that in $\Sigma 9$ GB, which causes the random GB to migrate faster than $\Sigma 9$ GB in the high temperature region.

The observed transition of the GBM mechanism was also seen in Pb [23] and NaCl [24]. Nevertheless, some researchers have been considered that the transition in migration behaviour might occur owing not to the breakaway of the boundary from the solute atmosphere but to change in the GB structure [25]. If the assumption is true, the transition should occur at constant temperature irrespective of the magnitude of driving force. As shown in Fig. 4, however, the transition temperature is found to depend obviously on driving force. Consequently, we conclude that the solute drag concept is reasonable to explain the transition of GBM behaviour.

From the experimental results, we confirm that the transition of GBM mechanisms from the solute drag control to the GB diffusion control is of great importance for development of the Goss texture, because the mobilities for $\Sigma 9$ and random GBs are large difference in the transition region; particularly the mobility for $\Sigma 9$ GB around 1300K is *ca.* two or three order of magnitude higher than that for random GB. In practice, the secondary recrystallization to achieve the Goss texture is being empirically conducted at around 1300K, and the sharp Goss texture scarcely obtains in pure Fe for which such transition of GBM mechanism should not take place.

References

[1] J. Harase and S. Shimizu, J. Jpn. Inst. Met., **54**, 1 (1990).
[2] Y. Yoshitomi, K. Iwayama, T. Nagashima, J. Harase and N. Takahashi, Acta Met., **41**, 1577 (1993).
[3] For example, Y. Ushigami, Y. Suga, N. Takahashi, K. Kawasaki, Y. Chikura and H. Kii, J. Mater. Eng., **13**, 113 (1991).
[4] P.Lejcke, V. Paidar, J. Adamek and S. Kadeckova, Interface Science, **1**, 187 (1993).
[5] P.Lejcke and J.Adamek, J. Physique IV, Colloque C3, suppl. J. Physique III, **5**, C3-107 (1995).
[6] S.Tsurekawa *et al.*, Mater. Sci. Forum, **204-206**, 221 (1996).
[7] H.Nakashima, T.Ueda, S.Tsurekawa, K.Ichikawa and H.Yoshinaga, TETSU-TO-HAGANE, **82**, 238 (1996).
[8] K.Ichikawa *et al.*, TETSU-TO-HAGANE, **82**, 471 (1996).
[9] M.Furtkamp, G.Gottstein, D.A.Molodov, V.N.Semenov and L.S.Shvindlerman, (To be published)
[10] M.Furtkamp, P.Lejcke and S.Tsurekawa, Interface Sci., **6**, 59 (1998).
[11] H. Kurishita, A. Oishi, H. Kubo and H. Yoshinaga, J. Jpn. Inst. Met., **47**, 546 (1983).
[12] R. C. Sun and C. L. Bauer, Acta Met., **18**, 635 (1970).
[13] J. W. Cahn, Acta Met., **10**, 789 (1962).
[14] K. Lücke and H. P. Stüwe, Recovery and Recrystallization of Metals, Ed. by L. Himmel, p. 171, Interscience, New York, (1993).
[15] D. Wolf, Phil. Mag., **62**, 447 (1990).
[16] E. D. Hondors, Technique of Metals Reserch, Ed. by R. Bunshah, Vol. 6(A), Chapter 8A, John Wiley &Sons, New York (1970).
[17] J. Cermark, J. Kucera, B. Million and J. Krumpos, Kov. Mater., **18**, 537 (1980).
[18] Metal Data Book, Ed. by Jpn. Inst. Met., Maruzen, (1993).
[19] P. Gordon and R. A. Vandermeer, Trans. AIME, **224**, 917 (1962).
[20] K. Ichikawa, Master Thesis, Kyushu Univ., 53 (1996).
[21] C. W. Haynes and R. Smoluchowski, Acta Met., **3**, 130 (1955).
[22] C. Jurisch, Ph. D. Thesis, Freiburg, Sachsen, (1969)
[23] J. P. Drolet and A. Galibois, Met. Trans. **2**, 53 (1971).
[24] R. C. Sun and C. L. Bauer, Acta Met., **18**, 639 (1970).
[25] C. J. Simpson, W. C. Winegard and K. T. Aust, Grain Boundary Structure and Properties, Ed. by G. A. Chadwick and D. A. Smith, Academic Press, (1976).

Materials Science Forum Vols. 294-296 (1999) pp. 633-636

Interface Structure Effects on the Fracture of Hard Thin Films

N.R. Moody, A. Strojny[1], D. Medlin, J. Schneider, A. Talin[2]
and W.W. Gerberich[1]

Sandia National Laboratories, Livermore, CA, USA

[1] University of Minnesota, Minneapolis, MN, USA

[2] Motorola, Tempe, AZ, USA

Keywords: Interface Structure, Interfacial Fracture, Tantalum Nitride Films, Aluminum Nitride Substrates, Aluminum Oxide Substrates

ABSTRACT

In this study we combined nanoscratch testing with a multi-layer aluminum oxide and aluminum nitride single substrate system to determine the effects of interface composition and structure on susceptibility to fracture of hard, thin tantalum nitride films. Nanoscratch tests showed that the film on aluminum oxide and on aluminum nitride portions of the substrate failed readily along the tantalum nitride film-substrate interface regardless of substrate composition. Most importantly, the fracture energies were essentially equal on both substrate materials. These results strongly suggest that a sputter deposited interface structure controls susceptibility to fracture.

INTRODUCTION

Thin tantalum nitride films are often used in microelectronic applications because of their long term stability and low thermal coefficients of resistance. However, they are high heat generators that when combined with a high structural defect content and high compressive residual stresses can alter interface structure and properties over long service lives. [1] This has motivated replacing aluminum oxide substrates currently in use with aluminum nitride. [2] However, nanoindentation and nanoscratch tests show that films on polycrystal aluminum nitride exhibit significantly less resistance to fracture than films on single crystal aluminum oxide. [1,2] In contrast, high resolution TEM shows that films on aluminum nitride substrates exhibit a similar several atom layer transition in structure from substrate to film to that observed on aluminum oxide substrates. (Fig. 1) We have therefore used continuous nanoscratch testing and a single multi-layer substrate system to determine the effects of interface composition and structure and substrate properties on interfacial fracture of thin tantalum nitride films. Nanoscratch testing measures properties at the submicron scale while the multi-layer single substrate eliminates sample-to-sample differences and constrains aluminum nitride ductility. When combined with atomic force and high resolution transmission electron microscopy, the results define the relationships between structure, properties and interfacial fracture on a submicron scale.

MATERIALS AND PROCEDURE

A special substrate for this study was created by growing a 50-nm-thick epitaxial layer of aluminum nitride using pulsed laser deposition on the middle one-third of a (0001) single crystal of aluminum oxide. [3] (Fig. 2) This served to constrain ductility in the aluminum nitride. The aluminum nitride and aluminum oxide basal planes were parallel but the aluminum nitride film had rotated 30° with respect to the oxide substrate such that the aluminum nitride $[1\bar{1}00]$ were parallel to the $[11\bar{2}0]$ aluminum oxide. The sample was then transferred to a deposition chamber, heated to 170°C in vacuum for two hours to drive off moisture, and given a RF backsputter for 15 s to remove contaminants and expose fresh material. With a vacuum of 1.3×10^{-5} Pa (10^{-7} torr), the film was

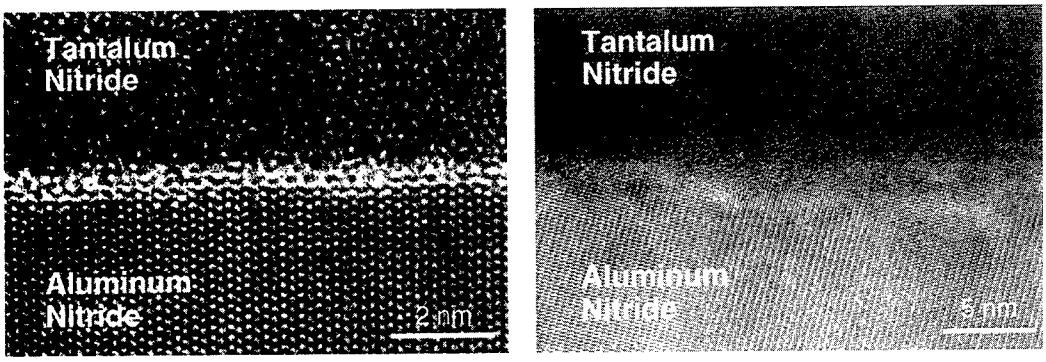

(a) (b)

Fig. 1. HRTEM shows that the tantalum nitride film-substrate interface in (a) aluminum oxide and in (b) aluminum nitride systems is characterized by a several atom layer transition zone between the crystalline substrate and amorphous film. The structures differ in orientation leading to a difference in appearance.

reactively sputtered onto the substrate using a tantalum target, argon as a carrier gas, and controlled additions of nitrogen at a rate of 0.3 nm/s to give a final thickness near 425 nm.

RESULTS AND DISCUSSION

Film properties were determined using nanoindentation [1,2]. These tests showed that the elastic moduli of the films, aluminum oxide and aluminum nitride substrates were essentially equal at 350 GPa. In contrast to previous work on individual substrates where hardness was significantly higher for aluminum oxide compared to aluminum nitride [1,2], there was no measurable difference in hardness as indentations probed through to the aluminum nitride and aluminum oxide substrate regions of the multi-layer system. As a consequence, results can be compared directly.

Resistance to fracture was determined using nanoscratch tests [1,2]. The nanoscratch tests revealed no significant difference in fracture behavior between films deposited on aluminum oxide or aluminum nitride-on-aluminum oxide portions of the substrate. Failures on both portions occurred consistently at loads near 100 mN and were characterized by formation of large circular spalls at the point of fracture as shown in Fig. 3. The fracture surfaces under the spalls are distinctly interfacial in character with no evidence of tantalum nitride remaining on the surfaces within the limits of energy dispersive spectroscopy. Beyond the initial point of fracture, the indenter penetrated the substrate.

Atomic force microscopy profiles traces across the spalls showed that the film thickness remained constant at 425 nm whether the spalls formed on the aluminum oxide or aluminum nitride portions of the substrate. Moreover, there was no indication of failure between the aluminum nitride and aluminum oxide. This shows that fracture occurs along the tantalum nitride film-substrate interface. Furthermore, the results strongly suggest that sputter deposition creates a preferred path for failure characterized by tantalum-aluminum and aluminum-nitrogen bonds on all portions of the substrate.

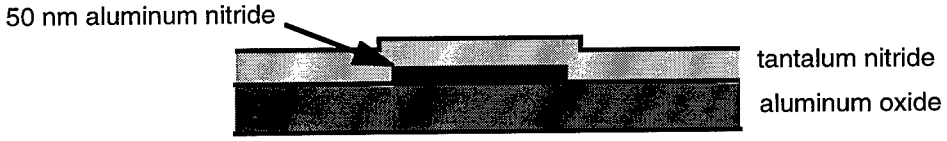

Fig. 2. Schematic showing the multi-layer substrate created by depositing 50 nm epitaxial layer of aluminum nitride on single crystal aluminum oxide onto which is sputter deposited tantalum nitride.

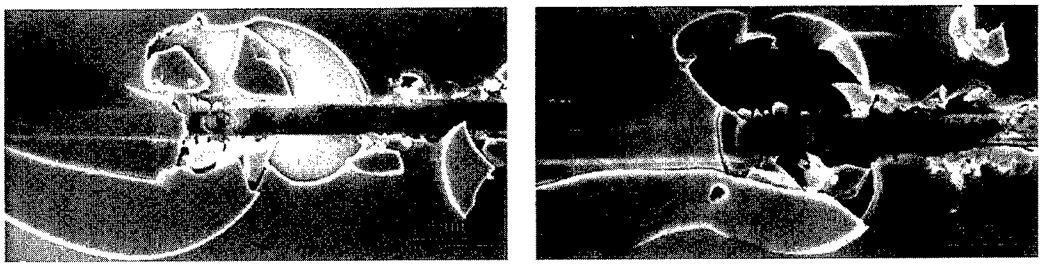

(a) (b)

Fig. 3. Scratch fractures on both (a) aluminum oxide and (b) aluminum nitride occurred by formation of large circular spalls at the point of fracture.

Two scratches on each portion of the film triggered buckles that ran back along the scratch track lengths as shown in Fig. 4. Treating these buckles as uniform-width blisters provides an estimate of residual stresses following the analysis of Hutchinson and Suo. [4] This gives a calculated compressive residual stress that ranges from -5.0 to -7.3 GPa with an average value of -6.4 GPa. This is slightly higher than found in previous work on aluminum oxide and aluminum nitride substrates [1], but it is in reasonably good agreement with values observed in other oxide, carbide, boride, and nitride film systems [5-7].

The circular spalls that form during the scratch tests are more prevalent and more uniform in character than the blisters. With the average residual stress calculated from the one-dimensional blisters and stresses applied during test, the energy stored in each film at fracture is estimated as follows [1,4],

$$G_o = \frac{(1-\nu^2)\sigma_r^2 h}{2E} + \Sigma\left(\frac{(1-\nu^2)\bar{\tau}_{ij}^2 h}{2\mu} + \frac{(1-\nu^2)\bar{\sigma}_{ij}^2 h}{2E}\right) \quad (1)$$

where G_o is the elastic strain energy stored in the film, h is the film thickness, E is the elastic modulus, ν is Poisson's ratio, μ is the shear modulus of the film, σ_r is the residual stress in the film, and $\bar{\tau}_{ij}$ and $\bar{\sigma}_{ij}$ are the average applied elastic shear and normal stresses in the film at `fracture. [1] The energies expended for fracture, $\Gamma_{I\text{-}II}$, are then determined from the stored energies using the circular blister analysis of Hutchinson and Suo. [1,6] These energies are comprised of mode I opening and mode II shear contributions. The mode I contributions give the interfacial fracture energies, Γ_I.

The circular spall data are given in Table I. This table shows the normal and tangential loads at fracture, P_{cr} and L_{cr}, and fracture areas, A, are essentially the same regardless of the portion of the

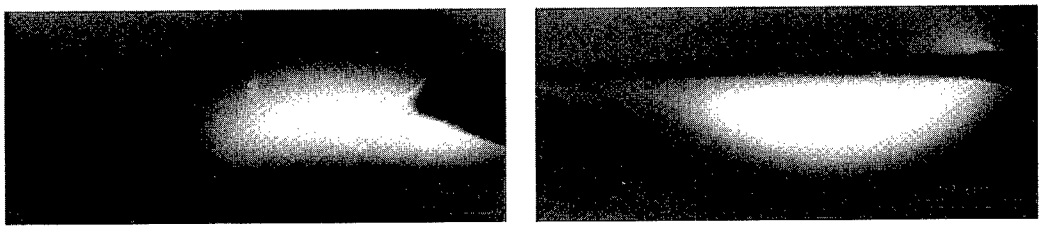

(a) (b)

Fig. 4. Two scratches on both the (a) aluminum oxide and (b) aluminum nitride portions of the substrate triggered blisters that ran back along the scratch tracks.

Table I.Circular spall data from scratch tests of thin tantalum nitride films on aluminum oxide and aluminum nitride portions of the multi-layer substrate.

Film/Substrate	A (μm^2)	Pcr (mN)	Lcr (mN)	σ_{res} (GPa)	G_{stored} (J/m^2)	Γ_{I-II} (J/m^2)	Γ_I (J/m^2)
Ta_2N/Al_2O_3	67	84	45	-6.4	33.3	11.9	3.4
$Ta_2N/AlN/Al_2O_3$	68	99	43	-6.4	33.4	12.1	3.4

substrate in which they occurred. Moreover, the fracture energies are essentially identical at an average value of 3.4 J/m^2 and equal to values determined previously on aluminum oxide substrates [1]. These results further support the observations suggesting that the interface controls susceptibility to fracture in this film system through structure and composition. The data also suggest that earlier results on individual aluminum nitride substrates giving very low fracture energies were due to the effects of substrate plasticity that were not included in the analyses and are not present in tests of films on much harder aluminum oxide.

CONCLUSIONS

In this study, nanoscratch testing was combined with a multi-layer aluminum oxide and aluminum nitride single substrate system to determine the effects of interface composition and structure on susceptibility to fracture of hard, thin tantalum nitride films. The substrate was comprised of a 50-nm-thick epitaxial layer of aluminum nitride deposited on a portion of a single crystal of aluminum oxide. Onto this substrate system, 425 nm of tantalum nitride was sputter deposited. The nanoscratch tests showed that the film on both substrate materials failed readily along the tantalum nitride film-substrate interface regardless of interface composition. More importantly, the tests showed that the fracture energies were essentially equal on both substrate materials. In contrast to previous results on individual substrates, the results from this study show that the susceptibility to fracture of sputter deposited tantalum nitride films on aluminum oxide and aluminum nitride substrates is essentially the same. Moreover, the results strongly suggest that a sputter deposited interface controls susceptibility to fracture in these film systems through structure and composition.

ACKNOWLEDGMENTS

The authors gratefully acknowledge the support of the U.S. DOE through Contract DE-AC04-94AL85000. A. Strojny and W. W. Gerberich also acknowledge the support of the U. S. DOE through Contract DE-FG02-96ER45574.

REFERENCES

[1] N. R. Moody, R. Q. Hwang, S. K. Venkataraman, J. E. Angelo, D. P. Norwood, and W. W. Gerberich, Acta mater. 46 (1998) p. 585.
[2] N. R. Moody, D. Medlin, D. Boehme, and D. P. Norwood, Engng. Fract. Mech., accepted for publication.
[3] D. Feiler, R. Williams, A. Talin, H. Toon, and M. Goorsky, J. Crystal Growth 171 (1997) p. 12.
[4] J. W. Hutchinson and Z. Suo, in Advances in Applied Mechanics, Academic Press Inc., New York, vol. 29 (1992), p. 63.
[5] D. F. Cardinale, D. G. Howitt, K. F. McCarty, D. L. Medlin, P. B. Mirkarimi, and N. R. Moody, Diamond and Related Materials 5 (1996) p. 1295.
[6] K. Messaoudi, A. M. Huntz, B. Lesage, C. Haut, and J. L. Lebrun, and V. Ji, in Corrosion-Deformation Interactions, The Institue of Metals, London (1997) p. 319.
[7] P. J. Burnett and D. S. Rickerby, Thin Solid Films 157 (1988) p. 233.
[8] A. G. Evans, M. Ruhle, B. J. Dalgleish, and P. G. Charalambides, in Metal-Ceramic Interfaces. Pergammon Press, Oxford (1990) p. 345.

Materials Science Forum Vols. 294-296 (1999) pp. 637-640

Sliding Mechanism of FCC/BCC Interphase Boundaries

H. Miyamoto[1], T. Mimaki[1] and S. Hashimoto[2]

[1] Department of Mechanical Engineering, Faculty of Engineering, Doshisha University, Kyotanabe, 610-0321, Japan

[2] Department of Engineering Physics and Mechanics, Graduate School of Engineering, Kyoto University, Kyoto, 606-8501, Japan

Keywords: Interphase Boundary Sliding, Bicrystal, Two-Phase Steel, Superplasticity

Abstract

Sliding mechanism of fcc/bcc interphase boundaries was discussed based on our results of two-phase γ(fcc)/α(bcc) stainless steel bicrystals and reported results of two-phase α(fcc)/β(bcc) Cu-Al and α(fcc)/β(bcc)Cu-Zn bicrystals; those results were obtained by a simple shear tests. Common features were obtained as follows; the stress exponent n of power low creep, $v \propto \tau^n$,was approximately 2 , subboundary development was observed in the soft bcc phase adjacent to the interphase boundary and the activation energy of the interphase boundary sliding (IBS) was estimated to be average self-diffusion coefficient of the soft bcc phase. These common features of IBS indicate that mechanism of IBS could be essentially identical in the fcc/bcc interphase boundary ,that is, IBS proceeds with lattice dislocation glide of the soft bcc phase rate-controled by a climb of pile-up dislocations arrested along the interphase boundary. Shear stress - sliding rate relation of the fcc/bcc interphase boundary could be explained by a single constitutive equation constructed based on the model of the sliding mechanism.

1.Introduction

It is well known that grain boundary sliding (GBS) and interphase boundary sliding (IBS) play important roles in superplastic deformation. A number of superplastic deformation models based on the GBS have been proposed [1-5]. Those models are mainly of a single phase crystal , and few models of the two-phase have been reported[6-8], although superplasticity has been mainly realized by the two-phase alloys in which the hard second phase prohibits the grain growth of the soft matrix.

Questions arise if the mechanism of IBS is the same of that of the GBS and how much is the difference of the sliding resistance between the interphase boundary and the homophase grain boundary. Chandra et al have concluded from the scratch marker offset that the sliding resistance of α(fcc)/β(bcc)-interphase boundary is lower than those of the α/α、β/β-homophase boundary in the superplastic deformation of α/β-two phase brass[9], while some authors have reported vice versa[10,11]. It is very arduous to evaluate the intrinsic sliding resistance of those boundaries because of the complicated stress distribution, grain boundary triple point etc.

Those difficulties led some authors to conduct creep tests employing bicrystals with a plane and a well defined grain boundary [12]or interphase boundary[13-18]. It was revealed that a creep curve of those homophase bicrystals shows the "slide hardening" which means that the sliding rate decreases with increasing sliding displacement, while that of two-phase bicrystal shows "slide softening" [16-17]. Furthermore, the sliding rate of the two-phase bicrystal was found to be much higher, by a factor of 10^2-10^3, than those of homophase boundary[16]. Eberhardt et al applied a model of GBS in superplasticity to IBS and described quantitatively the sliding rate of α/β brass bicrystals in which the sliding proceeds by lattice dislocation glide of soft β(bcc)-phase, rate-controled by climb of pile-up dislocations in the vicinity of the interphase boundary in their pioneering work[14].

In the present paper, our experimental results of the IBS of two-phase γ(fcc)/α(bcc) stainless steel bicrystals is reviewed in comparison with the reported results of two-phase α(fcc)/β(bcc) Cu-Al and α(fcc)/(bcc)β Cu-Zn bicrystals, and then the sliding mechanism of the fcc/bcc interphase boundary is discussed.

2. Behaviour of IBS , microscopic and macroscopic aspects of the IBS

The γ/α two-phase bicrystals were prepared by a solid state diffusion bonding method employing Fe-30%Cr (α-phase) and Fe-15Cr%-15%Ni (γ-phase) alloy single crystals. Simple shear tests were carried out in a flowing argon gas atmosphere at 1100℃. The specimens were set so that the interphase boundary was parallel to a load axis. Details of experimental procedures including preparation of the two-phase interphase bicrystals were reported elsewhere [16,17]. A creep curve (sliding displacement vs. testing time) shows a constant sliding rate v and a subsequent rapid increase of sliding displacement with increasing time. **Figure 1** shows a relation between applied shear stress τ and the constant sliding rate v; this relation could be analyzed through the power law creep of $v \propto \tau^n$, where the stress exponent n was estimated to be approximately 2. The experimental results of α/β-brass bicrystal [14] and α/β Cu-Al bicrystal [18] are also shown in **Fig.1**. Those three kinds of bicrystal show an approximate equivalent stress exponent n, thus it is implicated that the IBS proceeds by the same sliding mechanism.

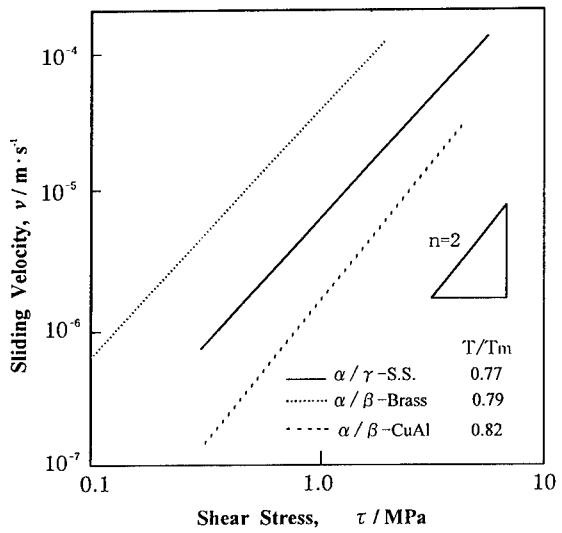

Fig.1 Relation between shear stress and sliding rate in γ/α stainless steel[17], α/β brass bicrystal [14] and α/β Cu-Al bicrystal [18]. Normalized test temperature by the melting points, T/Tm are norted.

Local plastic deformation in the α-phase adjacent to the interphase boundary was observed by optical microscopy (**Fig.2**), and thickness t of the deformed layers was estimated to be approximately 10～100 μm from the scratch marker whereas no plastic deformation in the γ-phase neighboring to the interphase was observed. It was confirmed from vickers hardness tests that plastic flow stress of the α-phase is lower than that of the γ-phase over around 650℃, and values of vickers hardness of the α-phase and γ-phase were 3 and 10 respectively at 1373K (**Fig.3**). Subboundary development was observed in the α-phase neighboring to the interphase boundary whereas recrystallization was not observed in both the α- and γ-phase. Those details of microscopic aspect of IBS are reported elsewhere[16].

Fig.2 Optical micrograph of the interphase boundary after the sliding test. Curved scratch marker shows the local plastic deformation of the α-phase adjacent to the interphase boundary.

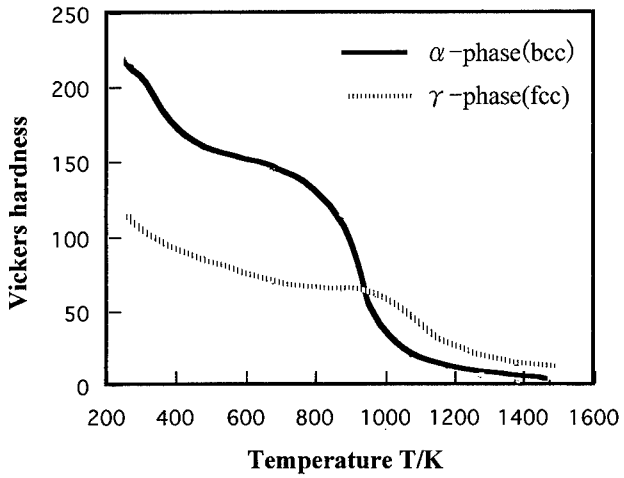

Fig.3 Dependence of Vickers hardness of the α- and γ-phase on temperature.

The activation energy of the IBS was measured by a temperature change test, and it was estimated to be approximately 267kJ/mol. The present value is close to the activation energy of self-diffusion of α-Fe, which was reported to be 239kJ/mol, although the exact value of activation energy for self-diffusion of the present alloy compositions is not available. Thus, one can say that IBS could be rate-controled by the self-diffusion of the α-phase. The present result is consistent with some reports that the activation energy of the superplastic deformation is close to that of self-diffusion of matrix β(bcc)-phase in α/β brass [6] and α(bcc)-phase in γ/α-duplex stainless steel[19], in both cases IBS contributes to the total amount of strain.

3. Mechanism of IBS

In a high temperature deformation and creep, a relation between stress and strain rate has been usually analyzed through the power low, $\varepsilon \propto \tau^n$, as was mentioned in the previous section. Mechanism of the deformation has been discussed by the value of stress exponent n. Under relatively low stress and high temperature, the deformation behaviour shows Newtonian viscous flow as diffusional creep is predominant, thus stress exponent n should be equal to 1 whereas under relatively high stress and low temperature, a creep rate-controled by recovery is predominant, and n should be equal to 3. Under the appropriate stress and temperature, alloys of fine grained structure show superplasticity, n is empirically 2.

So far, some authors have described the constitutive equations of superplastic flow based on models in which GBS proceeds by dislocation glide rate-controled by climb of pile-up dislocations in the vicinity of grain boundary[4,20,21]. Eberhardt et al[14] have applied these models to the IBS of α/β brass bicrystals and described quantitatively the applied shear stress and sliding rate (= shear strain rate) relation as follows.

$$v = \frac{Db^3\lambda}{l_d kT\mu h_c^2}\tau_a^2 \qquad (1)$$

where D is the bulk-diffusion coefficient of vacancy of α-phase, b is the length of burgers vector, λ is the average period of asperity in the interphase boundary which was observed by an optical microscope, k is the Boltzmann constant, μ is shear modulus, h_c is climb distance by which pile-up dislocation could overcome the obstacles and $l_d=(b/2\pi)\ln(R/b)$ where R is the radius of a cylinder around a dislocation for which the vacancy concentration is equal to that of thermal equilibrium. Substituting our experimental result, and assuming R is approximately $\lambda/2$ and that thickness of α-phase layer adjacent to the interphase boundary, where local plastic deformation was observed, could be $10\sim100\,\mu$m, one can obtain climb distance of pile-up dislocation, h_c is $17\sim54$nm (**Fig.4**). It could be said that h_c is of the order of $1/10\sim1/100$ of grain diameter in fine grained structure and climb distance of pile-up dislocation is localized quite adjacent to the interphase

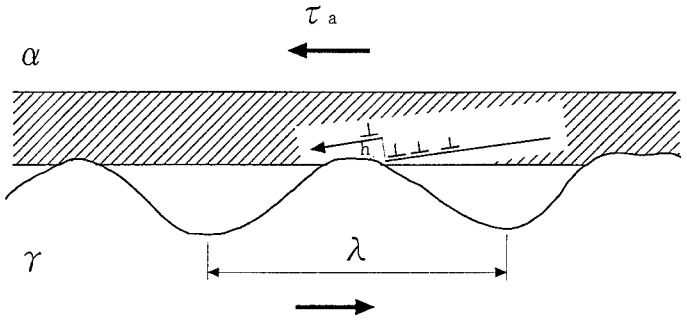

Fig.4 Schematic diagram of the interphase boundary sliding accommodated by plastic deformation of a thin layer of the the α-phase on top of the asperities.

boundary. Although hc is difficult to verify by experiment, the above suggestion is consistent with experimental observations by TEM that showed little dislocations inside the grains even after a considerable amount of strain was applied in the superplastic deformation[22].

3.Summary

Sliding Mechanism of fcc/bcc interphase boundary was discussed. Common features of the sliding observed in the γ(fcc)/α(bcc) two-phase stainless steel, α(fcc)/β(bcc) Cu-Al and α(fcc)/β(bcc) Cu-Zn bicrystals indicates that the sliding mechanism is essentially identical in fcc/bcc interphase boundary ; sliding should proceed by the glide of lattice dislocation in the soft bcc phase, rate-controled by climb of pile-up dislocations in the close vicinity of the interphase boundary. Shear stress - sliding rate relation of those IBS can be explained by a single constitutive equation derived from a model of the mechanism.

References

[1]T.H.Alden , Acta metall. 17(1969), p.1435.
[2]M.F.Ashby and R.A.Verall; Acta metall. 21(1973), p.149.
[3]R.C.Gifkins, Metall.Trans. 7A(1976), p.1225.
[4]R.C.Gifkins, J.Mater. Sci. 13(1978), p.1926.
[5]A.Geckinli, Metal Sci. 17(1983), p.12.
[6]M.Suery and B.Baudelet, Phil. Mag.41(1980), p.41.
[7]D.G.Partrige, D.S.MaCdarmaid and A.W.Bowen, Acta Metall, 33(1985), p.571.
[8]S.Hashimoto, H.Miyamoto and S.Miura, "*Aspects of high temperature deformation and fracture in crystalline materials*" , eds. Y.Hosoi, H.Yoshinaga, H.Oikawa and K.Maruyama, The Japan Institute fo Metals, p.115
[9]T.Chandra, J.J.Jonas and D.M.Taplin, J.Mater. Sci. 13(1978), p.2380.
[10]P.Shariat, R.Vastava and T.Langdon, Acta Metall.30(1982), p.285.
[11]R.V.Vastava and T.G.Langdon, Acta Metall. 27(1979), p.251.
[12]P.Lagarde and M.Biscondi, Can. Metall. Quart. 13(1974), p.245.
[13]A.Eberhardt and M.Suery , Scripta Met. 9(1975), p.1231.
[14]A.Eberhardt and B.Baudelet, Phil.Mag. 41(1980), p.843.
[15]T.Takasugi and O.Izumi, Acta Metall. 28(1980), p.465.
[16]S.Hashimoto, F.Moriwaki, T.Mimaki and S.Miura, " *Superplasticity in Advanced Materials* ", eds. S.Hori, M.Tokizane, and N.Furushiro, The Japan Society for Reserch on Superplasticity ,p.23,.
[17]S.Hashimoto, H.Miyamoto and T.Mimaki, J. Jpn. Inst. Met. 62(1998), p.255 (in Japanese).
[18]A.Eberhardt, M.Suery and B.Baudelet, Proc. ICSMA 4(1976), p.388.
[19]T.H.W.Hayden, R.C.Gibson , H.F.Merrick and J.H.Brophy, Trans. ASM, 60(1967), p.3.
[20]A.Ball and M.Hutchison, Metal Sci. J. 3(1969), p.1.
[21]A.Arieli and A.K.Mukherjee, Mater.Sci.Eng. 45(1980), p.61.
[22]K.Tsuzaki, H.Matsuyama, M.Nagao and M. Maki, J. Jpn. Inst. Met.54(1990), p.878 (in Japanese).

Materials Science Forum Vols. 294-296 (1999) pp. 641-644

Mechanical Properties of Interphase Boundaries in Austenitic-Ferritic Steel

W.A. Świątnicki and W. Zieliński

Faculty of Materials Science & Engineering, Warsaw University of Technology,
Narbutta 85, PL-02524 Warsaw, Poland

Keywords: Interphase Boundaries, Slip Transmission Across Interphase Boundaries, Hall-Petch Relationship, *In situ* TEM Straining

ABSTRACT

The influence of interphase boundaries (IBs) on mechanical properties of two phase austenitic-ferritic steel has been studied. It was assumed that the mechanical behaviour of the material depends on the IB reaction to the internal stresses created during loading. This reaction can be interpreted as a mechanical property of the boundary. In order to determine the microscopic mechanism of such reactions the *in situ* TEM straining experiments have been performed. It was shown, that the macroscopic mechanical behaviour of the steel depends on the mechanical properties of the IBs.

INTRODUCTION

Several models have been developed to explain the relationship between the yield stress and the grain size of single-phase materials (see f. ex. reviews [1,2]). These models generally assume that in polycrystals the yield stress is attained when the plastic deformation is transferred from one grain to another across the boundary. Thus many studies have been carried out to reveal the microscopic mechanisms of the slip transfer across the grain boundaries and to establish the structural conditions at which it takes place [3,4]. On the contrary few studies concerned the mechanisms of the slip transfer across the interphase boundaries (IBs) [5]. For this reason the role of interphase boundaries in the mechanical properies of two-phase materials is not as well known as the role of GB in single phase polycrystals. The aim of this work is to study the influence of the density and the crystallography of interphase boundaries on mechanical properties of a two-phase austenitic-ferritic steel.

MATERIAL AND EXPERIMENTAL

The material used in the study is an austenitic-ferritic steel of composition given in Table 1:

Table 1.

C	Cr	Ni	Mn	Si	P	S	Mo	N	Fe
0.03%	26.5%	6.0%	0.24%	0.21%	0.005%	0.014%	0.04%	295ppm	balance

Two variants of thermo-mechanical treatment (A and B) given in the Table 2 were applied to the initially ferritic structure in order to produce two series of specimens (A and B) with different types of orientation relationships (ORs) between α and γ phases. The quantitative description of the obtained microstructures was carried-out with use of modern stereological methods and is presented in a separate paper [6]. The interphase boundaries were examined in a Philips EM300 Transmission Electron Microscope (TEM) operating at 100kV. The crystallography of IBs (phase's misorientation and interface plane orientation) was determined by the analysis of diffraction spot and Kikuchi line patterns obtained by TEM. The interactions of lattice dislocations with interphase α/γ boundaries were investigated by *in situ* straining experiments in TEM with use of a standard simple tilt tensile

holder. Dislocation's Burgers vector and line orientation were determined by checking of the vanishing conditions and by trace analysis. The mechanical properties of the steel were determined by hardness and microhardness measurements and by tensile tests performed at room temperature.

Table 2: Scheme of the thermo-mechanical treatments

Treatment	A	B
Step 1	cold rolling up to 50%	annealing 1260°C-30mn in vacuum, oil quenching,
Step 2	annealing 1260°C-30mn in vacuum, oil quenching	cold rolling up to 50%
Step 3	annealing at 960-1150°C for 1 to 3h, slow cooling to 960°	
step 4	annealing 960°C-1h, oil quenching	

RESULTS

The A treatment led to the precipitation of γ phase in form of elongated grains in the ferritic matrix. With the B treatment a fully recrystallised, duplex microstructure with equiaxed α and γ grains was obtained. In both states the ferritic matrix is fragmented into subgrains separated by low angle dislocation boundaries. The density S_V of α/α and γ/γ grain boundaries is lower than the density of α/γ interfaces which varies from $140mm^{-1}$ up to $1100mm^{-1}$ in each state depending on the annealing parameters in the third step of heat treatment. The last step of the heat treatment allowed obtaining the same volume fraction of austenite and ferrite of about 50%.

The analysis of the IBs structure revealed that in the state A most of the γ grains are oriented close to the Kurdiumov-Sachs (K-S) or Nishiyama-Wassermann (N-W) relationships with respect to the ferritic matrix. In the state B the recrystallisation that occurs during γ growth destroys the habitual N-W and K-S orientation relationships between γ and α phases. This gives rise to the random misorientation between phases. It means that the main difference between two states results in the IBs structure which can be considered as special in the state A (where IBs fulfil special ORs) and random in the state B (for which IBs deviate from special ORs).

The mechanical tests performed on samples with different grain size revealed, that the yield strength and hardness increase with the density of interphase boundaries according to the Hall-Petch (H-P) relationship:

$$\sigma_{pl} = \sigma_0 + kd^{-1/n} \qquad (1)$$

where: σ_{pl} is the flow stress for given strain, σ_0 is a parameter proportional to friction stress for moving dislocations, k is a stress intensity factor proportional to the mean stress concentration at which the slip transfer from one grain to the other occurs, d is the mean intercept length of the grains, n is a constant usually equal to 1 or 2.

It was shown, that the similar relation can be applied for hardness H in two phase materials [6,7]:

$$H = H_0 + K_H(S_V/2)^{1/n} \qquad (2)$$

where $S_V=2/d$, H_0 and K_H are proportional to σ_0 and k respectively and have the similar meanings. The careful analysis of the obtained data has shown, that the best fit is obtained for n=1 with the values of parameters in H-P equation given in Table 3 as shown on Fig. 1. The interface sensitivity of mechanical parameters is more pronounced in the B state than in A state, i.e., the parameter K_H for the B state is higher than for the A state. Taking into account the usual meaning of this parameter in H-P equation one can assume that the slip propagation from one phase to the other across the interphase boundary occurs at lower stress level in A state than in B state.

To verify this hypothesis the *in situ* straining experiments have been performed. The examples of slip transfer across the boundaries with special (K-S) and random misorientations are given in Fig. 2 and Fig. 3 respectively.

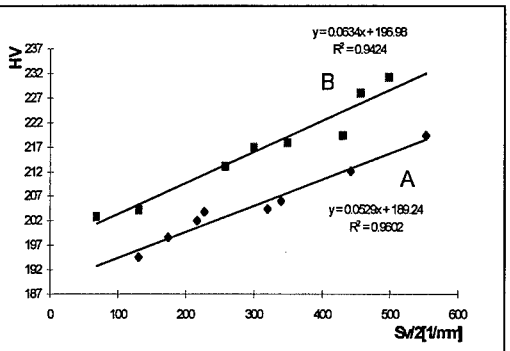

Fig.1. Hall-Petch plot for state A (with special ORs) and state B (with random ORs)

Table 3: Parameters of the Hall-Petch equation for two states A and B of the steel investigated (Eq.2 with n=1)

Values of parameters in H-P equation	A	B
H_0 [MPa]	189.2	197.0
K_H [MPa m]	52.9 10^{-6}	63.4 10^{-6}

It was found that in the case of special K-S and N-W relationships the transfer of plastic deformation from austenite to ferrite across the interphase boundary frequently occurs by direct slip transmission (according to the definition given in [8]). As it is visible in Fig.3. the slip lines are quite straight and they follow the direction of the dislocation pile-up in austenite.

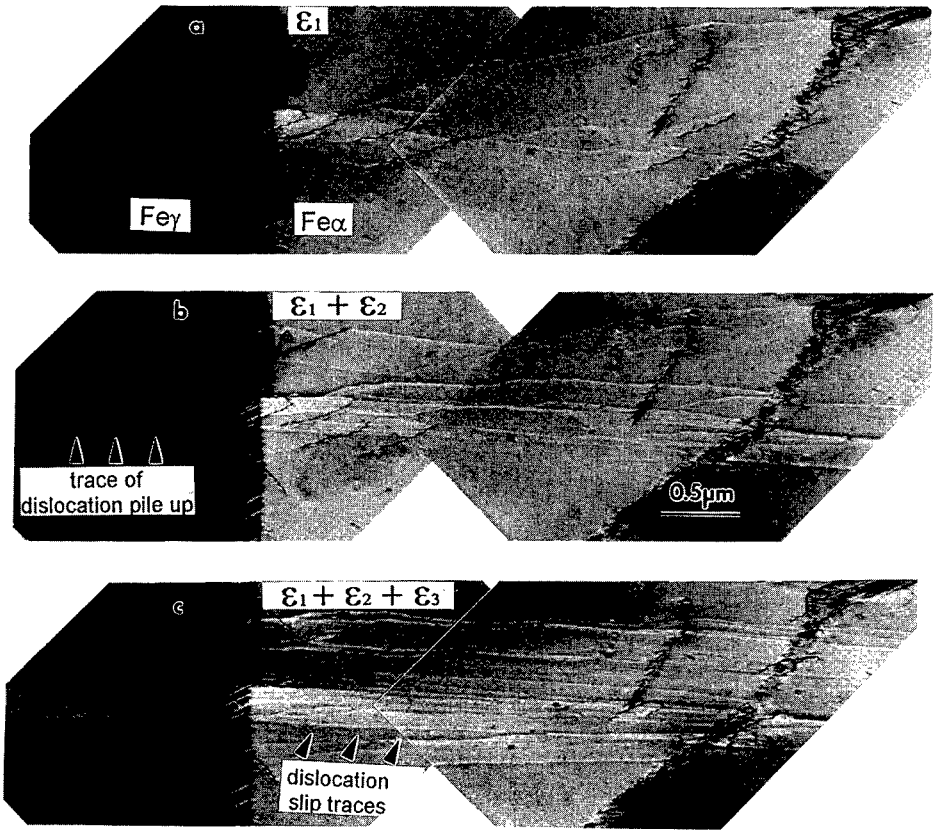

Figure 2. Various stages of dislocation activity in ferrite during the slip transfer through a special interphase boundary deviated by 2° from K-S relation. a) ε_1 , b) $\varepsilon_1 + \varepsilon_2$, c) $\varepsilon_1 + \varepsilon_2 + \varepsilon_3$.

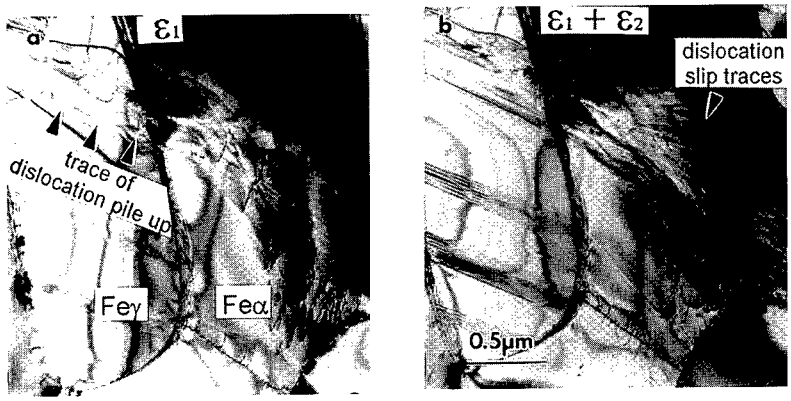

Figure 3. Two stages of dislocation activity in ferrite during the slip transfer through a randomly oriented interphase boundary (deviated by 24° from K-S relation). a) ε_1 , b) $\varepsilon_1 + \varepsilon_2$.

In the case of random OR (Fig.3) the stress concentrations resulting from dislocation pile-ups in austenite relax by creation and evolution of dislocation loops in the neighbouring α grain. This mechanism seems to require higher stresses than the direct slip transmission observed in the case of special ORs. For these reasons in the A steel with special ORs the process of slip transfer across the IBs may occur easier than in B steel with random misorientations.

CONCLUSIONS

The character of OR distribution influences the mechanical behaviour of a two-phase steel. In particular the steel exhibiting special ORs between phases displays lower strength and hardness than the steel with randomly disorientate phases. This results from different slip transfer mechanisms through interfaces with different ORs. It follows that it is possible to control the mechanical properties of a two-phase material by appropriate change of the OR distribution which determine the contribution of different microscopic mechanisms of stress relaxation that occur at interfaces.

ACKNOWLEDGEMENTS

The authors are very grateful to Professor M. W. Grabski and to Professor L. Priester for helpful discussions. This work was supported by the Warsaw University of Technology and by the Franco-Polish collaboration contract n° 76549.

REFERENCES

1. J.C.M. Li, Y.T. Chou, Metall.Trans. **1** (1970) p. 1145
2. J.P. Hirth, Metall.Trans. **3** (1972) p. 3047
3. M.W. Grabski, J.Physique (France) **46**, C4 (1985) p. 567
4. T.C. Lee, I.M. Robertson, H.K. Birnbaun, Philos. Mag. A, **62** (1990) p. 131
5. L. Guetaz, J.-M. Penisson, Mater. Sci. Eng., A **175**, (1994) p. 141
6. G. Żebrowski, J. Krzyczkowska, W.Świątnicki, K.J.Kurzydłowski, accepted for publication in Mater. Sci. and Technology (1998)
7. K.J. Kurzydłowski, J.J. Bucki, Acta Metall. Mater., **41** (1993) p. 3141
8. A. P. Sutton and R. W. Balluffi, Interfaces in Crystalline Materials, Clarendon Press, Oxford 1995, p. 739

Materials Science Forum Vols. 294-296 (1999) pp. 645-648

Sliding Characterization of Coincidence, Near-Coincidence and General Boundaries in Zinc

A.D. Sheikh-Ali[1,2] and J.A. Szpunar[1]

[1] Department of Mining and Metallurgical Engineering, McGill University, 3610 University Street, Montreal, PQ, Canada, H3A 2B2

[2] Institute for Metals Superplasticity of Russian Academy of Sciences, 39 Khalturina, Ufa, Bashkortostan, RU-450001, Russian Federation

Keywords: Zinc Bicrystals, Tilt Grain Boundaries, DSC-Lattice, Grain Boundary Sliding, Grain Boundary Migration, Grain Boundary Dislocations, Intragranular Slip, Lattice Dislocations

Abstract - Observations of grain boundary sliding along symmetric tilt coincidence $\Sigma=9\{11\bar{2}2\}$ and three boundaries deviated at different angles from coincidence misorientation have been made in zinc bicrystals. The coincidence boundary and boundaries whose deviation does not exceed ~6 degrees slide and migrate in a coupled manner predicted by the DSC-dislocation model. The boundary whose deviation exceeded ~6 degrees slides without migration and with a significantly lower rate in contrast to the previous boundaries except the coincidence one. The sliding along the coincidence boundary is activated at higher stresses only in the presence of intragranular slip. These results enable to distinguish special, near-special and general boundaries. It is emphasized that the ability of a boundary to slide and migrate in a fixed ratio is an important criterion for its specialness.

1. Introduction

Grain boundary sliding (GBS) is quite sensitive to the grain boundary structure especially in crystallographic regions close to coincidence misorientations. It has been established that GBS along coincidence and near-coincidence boundaries is significantly retarded in comparison with general boundaries [1,2]. Other investigations have revealed the effect of the coupling of GBS and boundary migration for some coincidence boundaries with low-index planes in Al and Zn [3-6]. It has been demonstrated that boundary migration accompanying sliding in a fixed ratio is the result of the motion of DSC-dislocations with steps [7]. Until now, only one study concerning the effect of misorientation on the sliding-migration behaviour has been published [4]. However, in this study the angular deviations from the exact coincidence are within the crystallographic region of specialness.

In this paper, the novel results of the study of sliding behaviour of a few symmetric tilt $<10\bar{1}0>$ boundaries deviated on different angles from $\Sigma=9\{11\bar{2}2\}$ coincidence misorientation in zinc bicrystals are presented. Obtained results are analyzed in terms of behaviour of grain boundary dislocations.

2. Experimental Details

Zinc bicrystals having symmetrical tilt boundaries of four different misorientations: 56.4±0.5°, 54.2±0.5°, 50.9±0.5° and 48.3±0.5° around the $<10\bar{1}0>$ axis have been used. The geometry of the bicrystals investigated are shown in Fig. 1. These boundaries deviate at different angles from "exact" $56.25°<10\bar{1}0>\Sigma=9$ coincidence misorientation. A $56°<10\bar{1}0>$ boundary has almost the coincidence misorientation angle. It is worth noting that in HCP metals, except for rotation about [0001], exact coincidence is obtained only when $(c/a)^2$ is a rational number [8]. For a given ideal coincidence misorientation, the nearest rational number $(c/a)^2$ is 7/2 [9]. The bicrystal plate used for obtaining specimens with $56°<10\bar{1}0>$ boundary have been grown by the vertical Bridgman method with seeding from the bottom of the graphite mould and single crystal [10]. Specimens with the other boundaries have been obtained from bicrystal plates which are grown by the horizontal Bridgman method from the zinc melt using bicrystal seeds. The initial purity of zinc was 99.996%. The technique of preparation of the specimens is described in detail in [11]. All specimens were tensile strained under creep conditions at T=553K ($0.8T_{melt}$) and at value of the stress σ=0.44 MPa, which corresponded to the value of shear stress along the boundary τ=0.22 MPa. In addition, bicrystals with a 56° boundary also strained at two values of tensile stress: σ=0.46 MPa and σ=0.48 MPa, which corresponded to τ=0.23 MPa and τ=0.24 MPa, respectively. The values of GBS and migration were determined respectively by the shift of marker lines and by spacing between the initial and subsequent boundary traces on the surface. Following Hauser and Chalmers [12] the

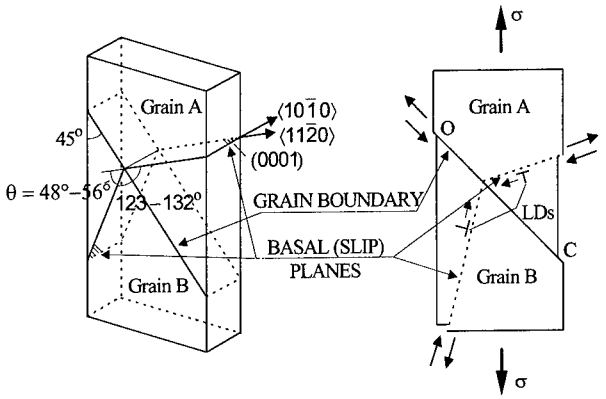

Fig. 1. Geometry of bicrystalline specimens and schematic of slip.

bicrystals investigated can be defined as incompatible ones. Fig. 1 displays the geometry of intragranular slip and GBS during the tension of bicrystals. This scheme enables to determine the direction of shear stresses and signs of edge lattice dislocations slipping in basal planes under the applied stresses. The ends of the boundary are designated as Points O and C.

3. Results

Bicrystal with the 48° boundary. Fig. 2(a) shows, that during sliding, the shear of neighboring crystals takes place in a narrow boundary area and is not accompanied by boundary migration. After long-term testing, macroscopic spatial non-uniformity of GBS is observed in this bicrystal: the sliding value increases from Point O to Point C. Although, after testing during 1.5 min. this sliding variation is unmarked (fig. 3(a)).

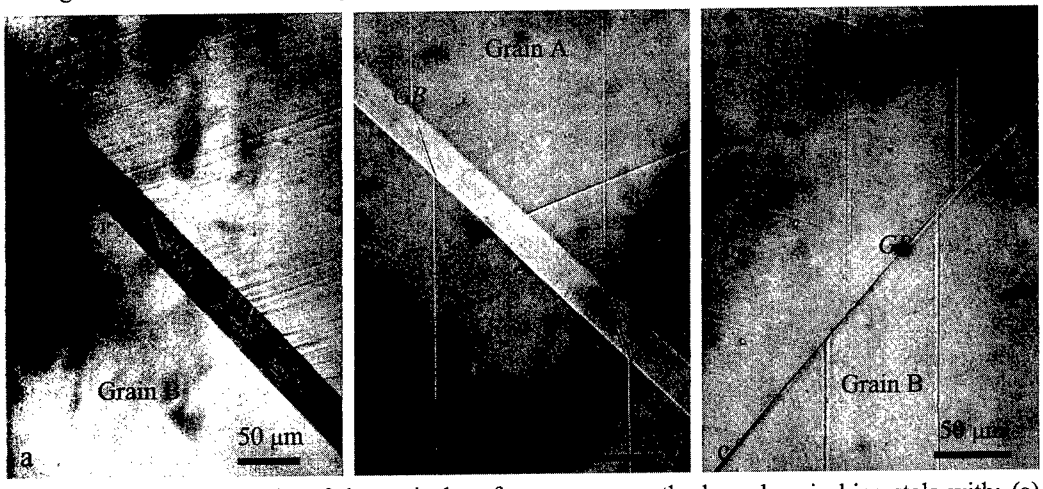

Fig. 2. Optical micrographs of the typical surface areas near the boundary in bicrystals with: (a) 56°, (b) 51° and (c) 48° boundaries. (a) σ=0.48 MPa and t=2.2 min.; (b), (c) σ=0.44 MPa and t=1.5 min. (a), (b) front and (c) rear faces of bicrystals.

Bicrystals with 51° and 54° boundaries. In these bicrystals, GBS and boundary migration act simultaneously, which is proved by the deflection from the original direction of marker lines and retaining their straightness in the region wherein migration takes place (fig. 2(b)). Migration occurs in the direction of Grain A. A significant macroscopic spatial non-uniformity of GBS and boundary migration is observed: values of GBS S and migration M increase from one end of the boundary to to the other (fig. 3(a)). For the bicrystal with the 51° boundary tested at σ=0.44 MPa during 1.5 min., S increases from 9.6 to 37 μm along the boundary length L=4 mm. For bicrystal with the 54° boundary with the same length and tested at the same conditions, S increases from 2.7 to 18 μm. A correlation between the M and S values is observed. Mean ratios of M/S equal to 1.09 for the 51° boundary and 0.96 for the 54° boundary at standard deviations σ_n=0.07 and σ_n=0.05 respectively.

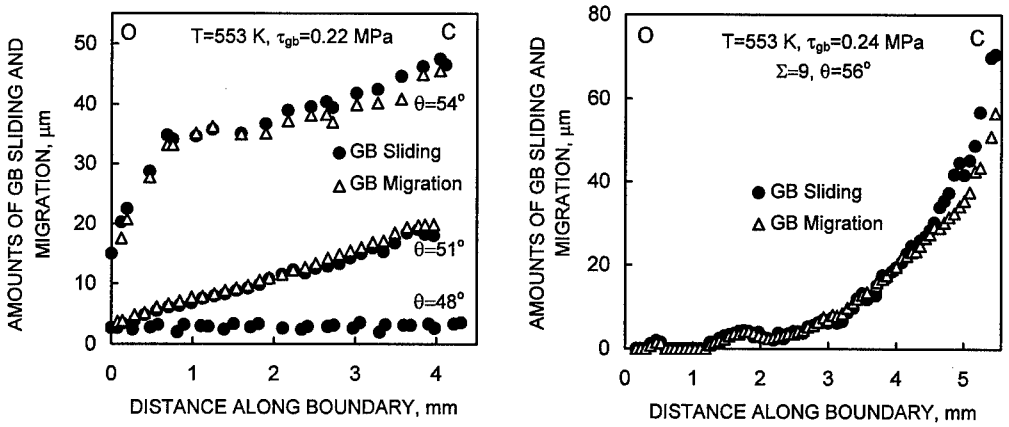

Fig. 3. Variation of magnitudes of sliding and migration along the boundary for bicrystals containing: (a) 48°, 51° and 54° boundaries after testing at σ=0.44 MPa during 1.5 min., and (b) 56° boundary after testing at σ=0.48 MPa during 2.2 min.

Bicrystals with the 56° boundary. Grain boundary sliding does not occur at σ=0.44 MPa. At σ=0.46 MPa sliding and migration operate only in a small portion of the boundary near the Point C. At σ=0.48 MPa, GBS and migration occurs along the most part of the boundary. These two processes occur in a coupled manner as in the case of 51° and 54° boundaries. In the bicrystal tested at σ=0.48 MPa and t=2.2 min., S gradually increases from 0 near Point O to 71 μm at Point C along the boundary length L=5.5 mm. Mean ratio of M/S equals to 0.97 while σ_n = 0.16.

Comparison between the sliding rates of different boundaries. The rate of GBS at Point C of 51° and 54° boundaries is 6 and 15 times that of the 48° boundary respectively (Fig. 3(a)). The sliding rate at Point O of 54° boundary is 5.6 times that of the 48° boundary. The GBS rates at Point O for the 51° and the 48° boundaries are similar. These data can be reproduced as the misorientation dependence of sliding and migration rates (Fig. 4).

4. Discussion

The misorientation dependence of rates of sliding and migration in Fig. 4 can be divided into three regions wherein the sliding behaviour of boundaries is different. We can define these regions as the regions of existence of coincidence, near-coincidence and general boundaries. Let us consider in detail the behaviour of boundaries of different regions. The coincidence 56° boundary does not slide at all at σ=0.44 MPa. At higher stresses (σ=0.48 MPa), it does not slide at Point O and in the adjacent boundary portion (Fig. 3(b)). However for other boundaries, a certain amount of sliding is reached in O. According to the concept suggested in [13] GBS at Point O is fully provided by grain boundary dislocations (GBDs) generated at grain boundary dislocation sources. In the remaining part of the boundary including Point C, GBS is contributed both by these GBDs and that are produced as a result of interaction between lattice dislocations and the boundary. Consequently, for 56° boundary, there is no emission of GBDs from boundary dislocation sources and GBS is completely provided by glissile GBDs originated from the interaction between lattice dislocations and the boundary. In the other boundaries, GBS is contributed by GBDs of the both origin. The simultaneous operation of GBS and migration is the result of the motion of glissile GBDs with steps, which preserve low-energy boundary structure [3-7]. For all boundaries which slide and migrate, the ratio between sliding and migration is practically the same and close to 1. According to the concept of the DSC-lattice, this ratio is determined by the ratio between the Burgers vector and the step height of the DSC-dislocation. Knowing this ratio and direction of boundary migration, the parameters of the DSC-dislocation responsible for the sliding-migration process can be determined. In the case of the $\Sigma=9\{11\bar{2}2\}$ boundary GBDs has the Burgers vector $b=4/27<11\bar{2}3>$ (Fig. 5). Generation of these GBDs at dislocation sources is impossible for the coincidence boundary probably due to its perfect structure which seems to be free from grain boundary facets or/and steps. With increasing angular deviation from the coincidence misorientation, the density of structural GBDs compensating for this deviation increases. It appears that these structural dislocations considerably facilitate the generation of glissile GBDs, which results in very rapid GBS at small

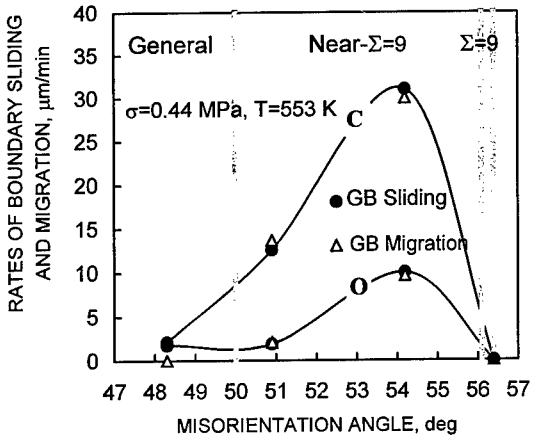

Fig. 4. Misorientation dependence of the sliding and migration rates in boundary Points O and C.

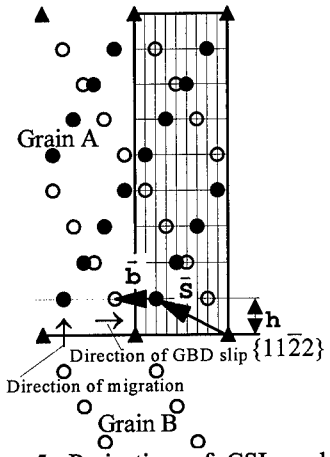

Fig. 5. Projection of CSL and DSC-lattice on the (10$\bar{1}$0) plane. b and S are the Burgers and step vectors of glissile GBD, respectively.

angular deviations. One can try to explain the decrease of GBS rate at further angular deviations which corresponds to the high density of structural GBDs supposing that they impede the motion of glissile GBDs. Motion of 4/27<11$\bar{2}$3> dislocation preserves structure of Σ=9 and near-Σ=9 boundaries. Further increases in the angular deviations cause the transition to the region of general boundaries. At a certain density of structural GBDs, the energy of the boundary reaches some critical value after which retention of atomic structure during GBS is not profitable. The DSC-dislocations are not generated and the boundary does not migrate during sliding. Sliding along such a boundary changes its structure. For the description of GBS along the general boundary, one can use the glissile non-DSC dislocations without steps and with infinitesimal Burgers vectors.

5. *Conclusions*

Grain boundary sliding along symmetric tilt coincidence 56°<10$\bar{1}$0>Σ=9{11$\bar{2}$2} and near-coincidence 54° and 51° boundaries is accompanied by regular boundary migration. The magnitudes of sliding and migration are close. The symmetric tilt 48° boundary which can be defined as a general one does not migrate during sliding. The rates of sliding along near-coincidence boundaries are significantly higher than along the general boundary. The sliding along the coincidence boundary is activated at a higher stress value and only in the presence of intragranular slip. For the other boundaries, the intragranular slip is not a prerequisite for sliding.

Acknowledgements-The authors are grateful for Dr. Y. Kazarov for growing a bicrystal with coincidence 56°<10$\bar{1}$0> boundary. The pure zinc used for growing the other bicrystals was kindly supplied by Noranda Inc.

References

[1] M. Biscondi and C. Goux, *Mem. Sci. Rev. Met.* **65** (1968), p. 167.
[2] T. Watanabe, M. Yamada, S. Shima and S. Karashima, *Phil. Mag.* **A40** (1979), p. 667.
[3] T. Takahashi and R. Horiuchi, *Grain Boundary Structure and Related Phenomena* (edited by Y. Ishida), Suppl. 27, p. 707. Trans. JIM (1986).
[4] H. Fukutomi, T. Iseki, T. Endo and T. Kamijo, *Acta Metall. Mater.* **39** (1991), p. 1445.
[5] A. D. Sheikh-Ali , F. F. Lavrentyev and Y. G. Kazarov, *Acta Mater.* **45** (1997), p. 4505.
[6] A. D. Sheikh-Ali and J. A. Szpunar, *Mater. Sci. Eng.* **A245** (1998), p. 49.
[7] S. E. Babcock and R. W. Balluffi, *Acta Metall.* **37** (1989), p. 2357.
[8] C. A. Bruggeman, G. H. Bishop and W. H. Hartt, *in Nature and Behavior of Grain Boundaries,* edited by H. Hu, New York, Plenum Press (1972), p. 83.
[9] R. Bonnet, E. Cousineau and D. H. Warrington, *Acta Crystall.* **A37** (1981), p. 184.
[10] Y. G. Kazarov and F. F. Lavrentyev, *The preprint of the Institute for Low Temperature Physics and Engineering,* UkrSSR Academy of Sciences, Kharkov, 1991, No18, 18 p.
[11] A. D. Sheikh-Ali and R. Z. Valiev, *Scripta Metall. Mater.* **31** (1994), p. 1705.
[12] J. J. Hauser and B. Chalmers, *Acta Metall.* **9** (1961), p. 802.
[13] A. D. Sheikh-Ali, *Acta Mater.* **45** (1997), p. 3109.

Materials Science Forum Vols. 294-296 (1999) pp. 649-652

Local Stress in Highly Strained Coherent InGaAs Islands

S. Kret, C. Delamarre, J.Y. Laval and A. Dubon

Laboratoire de Physique du Solide UPR5 CNRS, ESPCI 10, rue Vauquelin, Paris, France

Keywords: 2D Deformation Map, HREM, GaInAs, Quantum Dots, 3D Islands

Abstract : The 2D-3D transition of the growth mode of highly strained $In_xGa_{1-x}As$ layers on {100} GaAs was observed by HREM. Local deformations were measured by image processing of HREM {110} projections. ε_x and ε_z deformation mappings of $In_xGa_{1-x}As$ islands are shown. By comparing with theoretical calculation for a homogeneous solid, local indium segregation is expected towards the top of the island. The stress distribution between islands was studied during the growth up to plastic deformation.

Introduction : Molecular beam epitaxy (MBE) of highly strained $In_xGa_{1-x}As$ layers (with x>0.25) on {100}GaAs led to a 2D-3D transition with formation of coherent islands when the number of GaInAs deposited layers was comprised between 8 and 30 [1,2]. Quantitative measurements of local lattice distortions were carried out in order to understand the process of formation of such islands and their subsequent electronic properties.

We have reviewed the different techniques for measurements of 3D stress distribution in heterostructures [3]. Measurements on GaInAs islands were done first in plan-view TEM by contrast simulation using dynamic diffraction theory [4]. Tillman et al. [5] then drew average relaxation profiles along z via image processing by location of the intensity maxima in HREM projections. We improved the image processing method of HREM micrographs to obtain 2D deformation maps.

Experimental : Highly strained InGaAs layers were grown by MBE on nominal {100} GaAs. Cross-sections for HREM were prepared by mechanical polishing and argon ion-milling. Electron microscopy was performed with a Philips CM 20 UT operating at 200 kV with a 0.19 nm point resolution, on {110} GaAs projections. The size of the digitized areas ranged from 60x60 to 100x100 nm with 4 pixels/Å sampling and 8-bit dynamics.

The image processing algorithm includes Wiener Fourier filtering, with local noise estimation as well as high- and low-frequency suppressing [6,7]. This filtering procedure conserves the information of the crystal deformation and improves the signal to noise ratio. The location of the intensity maxima of the image dots with subpixel resolution was done by the fitting of 4 parabolas tilted by 45° and which intersected the pixel with maximum intensity [6]. The lattice parameters for the reference area (substrate) were determined by minimization of the total differences between calculated and experimental lattice points by applying Newton's optimization method. Contrast maxima, in both reference and deformed areas, were related to a common origin. For each experimental lattice point, displacement vectors u_x and u_z were calculated using extrapolated positions from the reference region. Each point was corrected by replacing the original value with an average weighted with its neighbours. The influence of neighbouring points defined by a kernel matrix with a radius corresponding to 5 to 6 spacings of the discrete lattice.

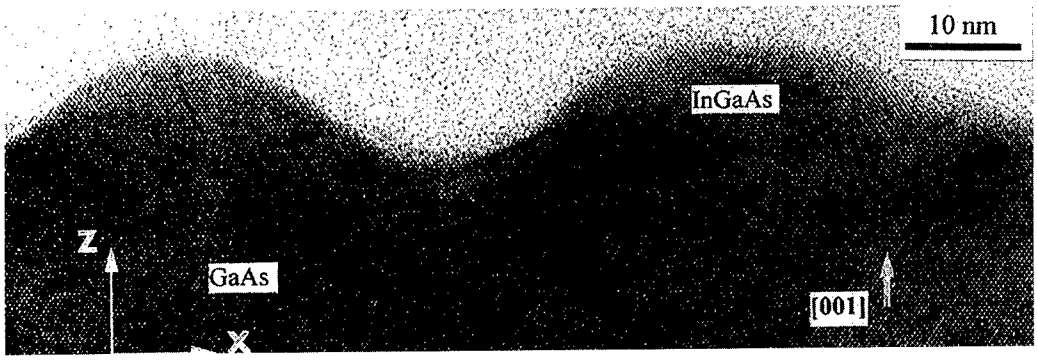

Fig. 1 : Cross-sectional {110} HREM image of two adjacent InGaAs islands

Results : Fig. 1 represents a cross-sectional {110} HREM image of two adjacent InGaAs islands created during the 2D-3D transition of the MBE growth mode. They correspond to the deposition of 23 monolayers. The thickness of the foil was about 10 nm. The islands were 50 to 60 nm long and 10 nm high. They were approximately sinusoidal and partially facetted along {311} planes. For processing, only islands with a symmetric shape and a homogeneous contrast were selected to make sure they corresponded to the median cross-section and exhibited a uniform thickness. Fig. 2 shows the deformation maps along the x and z axes. The interface position of $In_xGa_{1-x}As/GaAs$ corresponds to z = 0 on the vertical axis. The spacing between isolines is $\Delta\varepsilon$=0.002, i.e. 1 picometer in displacement. A relaxation is observed at the top of the island (ε_x = 0.027, ε_z = 0.045) whereas a compression is found in the troughs. Consequently, the parameter is lower in the troughs (ε_x = -0.007) than in the substrate.

Our results were compared with calculations based on the theory of a homogeneous solid with a sinusoidal undulating surface [8]. For both limits:biaxial compression (bulk material) or uniaxial compression (complete relaxation of the thin film along y parallel to the electron beam), the concentration in indium should be much higher within the islands than in the troughs.

In Fig. 3, we can see how the stresses increase when islands meet. ε_x goes from - 0.002 (Fig. 3a) to –0.025 (fig. 3b) which corresponds to a stress of $\cong$ 3.5 GPa. In Fig. 4, plastic deformation is observed when 35 ML of GaInAs are deposited. Dislocations are formed in the troughs to relax plastically the loci with highest stresses at the junction between adjacent islands.

Conclusion : By image processing of HREM micrographs a very precise mapping of the deformation field of highly strained $In_xGa_{1-x}As/GaAs$ coherent islands was obtained. The limit of detection was about $\Delta\varepsilon$ = 0.002. A complete relaxation was found at the top of the island whereas a lattice compression was observed between adjoining islands. By comparing ε_x (x,z) and ε_z (x,z) experimental maps with the ones calculated from Gao's theory related to a homogeneous solid [8], a local enrichment in indium within islands was expected. The increase of the stresses when islands draw closer was shown. When the number of deposited layers became $\geq$ 35 ML the plastic deformation occurred with the formation of dislocations in the troughs.

References

[1] S. Guha, A. Madhukar and K. C. Rajkumar, Appl.Phys.Lett. **57**, (1990), 2110
[2] C. Delamarre, J.Y. Laval, L.P. Wang, A. Dubon, G. Schiffmacher, J. Cryst. Growth, **177** (1997) 6-16

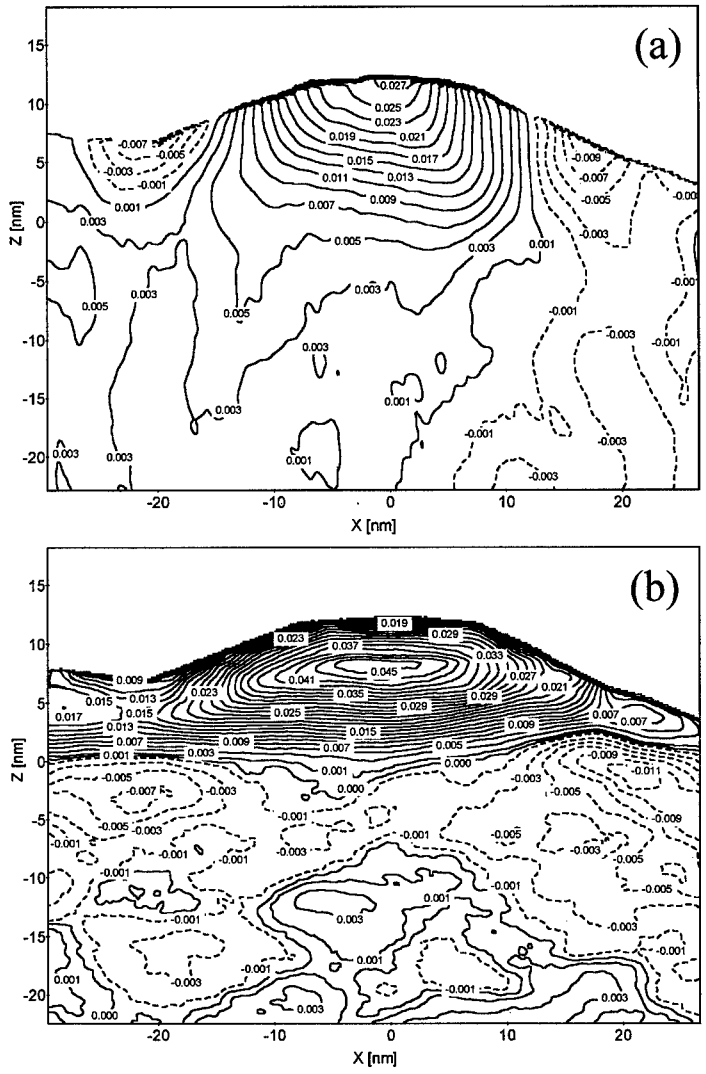

Fig. 2 : 2D deformation maps of a InGaAs island a) ε_x (x,z) b) ε_z (x,z)

[3] S. Kret, C. Delamarre, J.Y. Laval, A. Dubon, Phil Mag Letters, **77**, n° 5 (1998), 249-256
[4] Y. Androussi, A. Lefebvre, T. Benabbas, P. François, C. Delamarre, J.Y. Laval, A. Dubon, J. Cryst. Growth **169**, (1996), 209-216
[5] K. Tillman, D. Gerthsen, P. Pfundstein, A. Forster. and K. Urban, J.Appl.Phys. **78 ,** (1995) 3824
[6] A. Rosenauer, S. Kaiser, T. Reisinger, J. Zweck W. Gebhard and D. Gerthsen, Optik, **101,** (1996) ,1
[7] R. Bierwolf, M. Hohenstein, F. Phillipp, O. Brandt, G.E. Crook and K. Ploog, Ultramicroscopy, **49,** (1993) 273
[8] H. Gao, J. Mech. Phys. Solids, **39** (1993) 2983

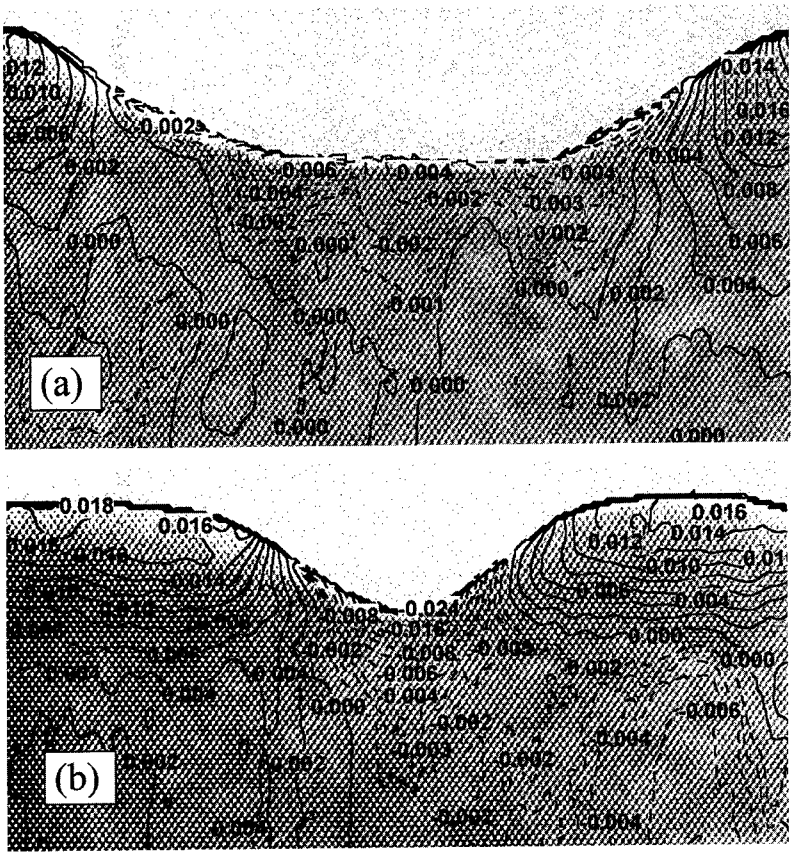

Fig. 3 : Evolution of stresses in between adjoining islands
a) negligible stress b) islands abut : stresses become high

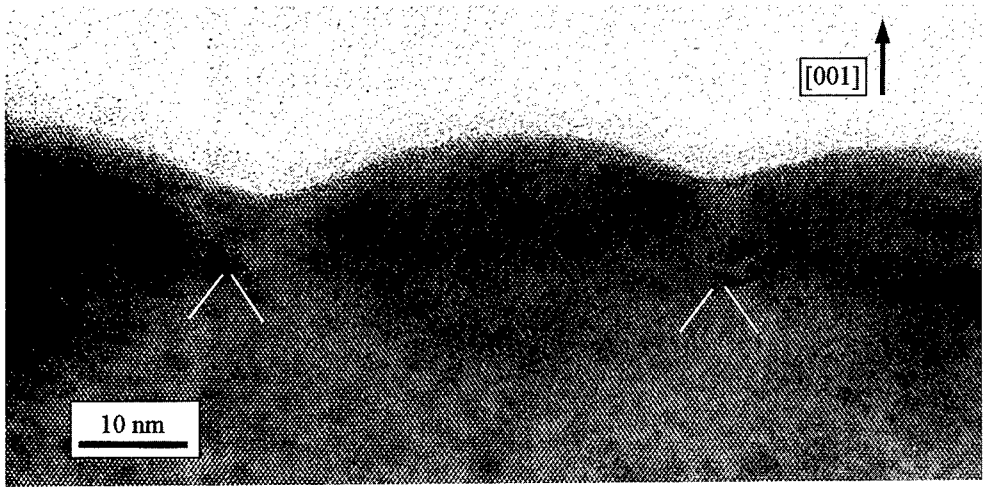

Fig. 4 : Plastic relaxation : formation of dislocations in between islands (GaInAs = 35 ML)

Materials Science Forum Vols. 294-296 (1999) pp. 653-656

Interface Effect on Dislocation Structure of Deformed Radiation-Hardened Layered LiF Crystals

T.S. Orlova and B.I. Smirnov

A. F. Ioffe Physico-Technical Institute, Russian Academy of Sciences,
Polytechnicheskaya 26, RU-194021 St. Petersburg, Russia

Keywords: X-Ray Irradiation Hardening, Interface, Dislocation Structure

Abstract Interface effect on the evolution of dislocation structure accompanying plastic deformation of layered LiF crystals under single-slip condition has been experimentally studied. The samples were prepared with X-ray irradiation of layers of LiF single crystals, interfaces between the irradiated ("hard") and unirradiated ("soft") regions being located along the specimen axis.

It was found that plastic deformation under compression occurs by means of nucleation and development of slip bands in "soft" regions followed by their penetration into "hard" regions. When screw dislocations intersected the interface their density in the irradiated region increased sharply (up to by a factor of three). In edge slip bands, the dislocation etch pit densities were approximately the same in different regions. Influence of the irradiation time and of irradiated region size on the yield stress has been studied, too. The obtained results can be explained by a difference in parameters of double cross slip and multiplication of dislocations before and after intersecting the interface.

Introduction

To understand the role of interfaces on evolution of dislocation structure during plastic deformation and hardening of solids, it is very useful to perform experiments under physically identical and controllable conditions. In single crystals, many uncertainties in the interpretation of the experimental results are removed when deformation occurs in only one slip system of crystallographic planes. For alkali-halide crystals, a method of plastic deformation under such single slip was proposed in [1]. This method is based on hardening samples by X-ray irradiation with the exception of a special, crystallographic oriented zone in which single slip occurs. Additional hardening of some part of the single-slip zone results in formation of interfaces between parts of the same materials but with different mechanical properties. It is significant that for a such interface there are no interfacial stresses and misfit dislocations.

In the present work we studied the yield stresses and evolution of dislocation structure of radiation-hardened layered LiF crystals under deformation along single system of crystallographic planes. Depending on the orientation of the single-slip zone relative to the interface, either screw or edge dislocations crossed the interface.

Experimental

A large LiF crystal, grown by the Kyropoulos method and containing approximately 0.002 wt.% Mg, was cleaved into samples of 3.6 x 4 x 20 mm dimensions along the [100], [010] and [001] directions, respectively.

To investigate single slip in layered crystals, the samples were irradiated with X-rays (using a X-ray tube with a silver anode) in two stages. At the first stage, except for a specially protected 2

mm high zone intended for deformation by single slip on the (011) plane, the sample bulk was subjected to X-irradiation as described elsewhere [1,2]. At the second stage, different series of compositions of irradiated and unirradiated regions were obtained with the aid of special lead screens (Fig.1). From viewpoint of dislocation physics, the difference of samples 2 and 3 from samples 4 and 5 lies in the fact that in the first case the boundary between the irradiated and unirradiated regions is parallel to the edge components of the dislocations while in the second case it is parallel to the screw components of the dislocations. The degree of hardening of the irradiated regions of total width $d_i \approx 1$ mm could be varied by changing the irradiation time t. In addition, for variant 4, samples with a constant irradiation time t=3 h but different d_i value from 0 to d_0, where d_o is transverse size of the sample, were obtained.

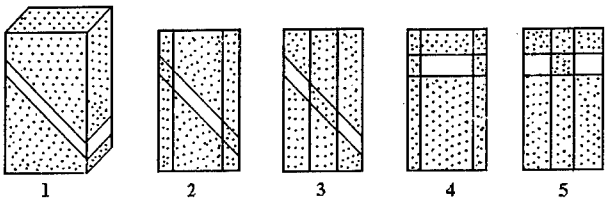

Fig.1. Arrangements of hardened parts (marked by dots) in samples after the first (1) and second (vertical bands in 2-5) stages of irradiation.

In most experiments, the samples were deformed by single slip along (011) system of planes under compression at a constant rate of 10^{-4} s^{-1}. In a number of cases, however, the samples were subjected to tension or symmetric cyclic loading. The dislocation structure of deformed crystals was revealed by selective etching and examined with optical and electron microscopes.

Experimental results and discussion

To estimate this radiation hardening under our specific experimental conditions, first the dependence of the yield stress τ_y of completely irradiated crystals on the irradiation time t was determined. It was found that for $t \geq 0.5$ h $\tau_{yi}=\tau_{yo}+\alpha t$, where $\tau_{yo}=3$ MPa and $\alpha=1.25$ MPa/h. It follows that the radiation hardening $\Delta\tau_i=\alpha t$. Investigation of mechanical properties of layered crystals showed that their stress-strain diagrams are of the same shape as that in single slip, i.e. they consist of two stages: plateau of flow with stress $\tau=\tau_y=$const and stage of linear hardening. At the same time, the yield point τ_y depends on the dimensions and the irradiation dose of the radiation-hardened regions.

Fig. 2 shows the dependence of τ_y on the irradiation time of these regions with their constant dimension $d_i \cong 1$ mm. These $\tau_y(t)$ dependences can be described by a linear function

$$\tau_y=\tau_{yo}+kt\,, \qquad (1)$$

where $k_2=k_4=k_5=0.46$ MPa/h for samples 2, 4, and 5, respectively, and $k_3=0.36$ MPa/h for sample 3. The expression (1) can be written in the form

$$\tau_y=\tau_{yo}+k_\alpha\Delta\tau_i\,, \qquad (1a)$$

where $k_\alpha=k/\alpha$.

Fig. 3 displays τ_y versus the total width d_i of the irradiated region for samples of type 4 with the same irradiation time t=3 h. To a first approximation, this dependence can also be described by a linear function

$$\tau_y=\tau_{yo}+\beta d_i/d_o\,, \qquad (2)$$

where $\beta=5$ MPa, or

$$\tau_y=\tau_{yo}+d_i/d_o\,(\tau_y-\tau_{yo}). \qquad (2a)$$

Thus, in layered crystals under compression, the yield stress depends on the volume fraction of hardened layers and on degree of their hardening with respect to the initial state as described by Eqs. (1a) and (2a).

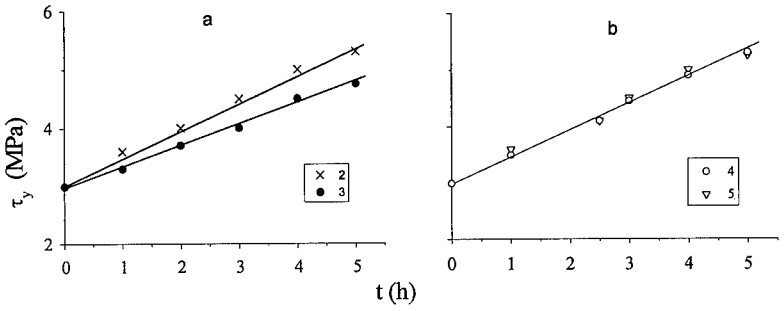

Fig.2. The yield point τ_y versus the irradiation time for samples of the type 2, 3 (a) and 4, 5 (b) for $d_i \cong 1$ mm.

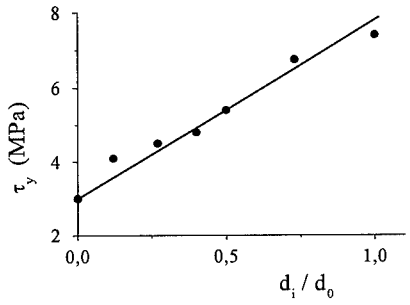

Fig.3. The yield point of samples of type of 4 versus the width of the hardened region in the single-slip zone.

These equations are similar to so-called mixture rule [3]. According to this rule, the yield point of a layered composition consisting of two materials (1 and 2) with equal elastic module, the yield points τ_1 and τ_2, and cross-sections S_1 and S_2, is described as follows

$$\tau(S_1+S_2)=\tau_1 S_1+\tau_2 S_2, \quad (3)$$

or

$$\tau = \tau_1 + \frac{S_2}{S_1 + S_2}(\tau_2 - \tau_1). \quad (4)$$

Investigation of the evolution of dislocation structure in the layered crystals under compression showed that the plastic deformation in them occurs by means of nucleation and development of slip bands in "soft" regions followed by penetration into the hard regions. This penetration into the hard regions occurs due to the formation of interfacial dislocation pileups of the same sign in slip lines and bands, which give rise to significant internal stresses.

When screw dislocations run to the interface, the width of their slip band decreases after intersecting the interface. This can occur both by means of a gradual decrease of the width away from the interface and as a result of the separation of the band into a series of separate narrow bands (Fig. 4 (a)). At the same time, the density ρ_s of screw dislocations increases sharply when the interface is crossed (Fig. 4 (b)). For example, in Fig. 4 (b) $\rho_{s0}=4.1\text{x}10^7$ cm^{-2} and) $\rho_{si}=1.3\text{x}10^8$ cm^{-2}.

A completely different picture is observed when edge dislocations run to the interface. In this case, in intersecting the interface the width of the edge slip bands does not change, and the density ρ_e of edge dislocation components also remained approximately constant (Fig. 4(c)). In Fig.4(c) $\rho_{ei} \approx \rho_{e0}=7.5\text{x}10^7$ cm^{-2}

The evolution of dislocation structure during plastic deformation under compression can be represented as follows. Under stresses $\tau \approx 2/3\tau_{y0}$ a process of motion and multiplication of separate dislocations starts in the "soft" region and leads to the formation of slip lines which stop at an interface. For $\tau \cong \tau_{y0}$ these slip lines grow laterally into slip bands which stop at the interface creates high internal stresses in the neighbouring "hard" regions. On reaching τ_{yi}, these internal stresses cause the dislocation, i.e. the slip bands, to break through into this "hard" region. To remove the high internal interfacial stresses, the displacements on two sides of the interface must be practical equal. The crucial role of internal stresses as a result of the pileups formation at the interface is supported by our results on tension-compression loading of these layered crystals. It was found that in this case plastic deformation at $\tau < \tau_y$ occurs practically only in the unirradiated regions. This can be explained by the fact that for a different sign of the deformation, dislocation pileups of different

sign form at the interface. They may mutually compensate the high local stresses from one another, preventing the dislocation from penetrating into the "hard" regions.

The expansion of the slip bands occur as a result of double cross-slip and multiplication of screw dislocation. When these dislocations move to the interface and intersect it, they continue to move and multiply in the "hard" region, forming new slip bands with local shear $\gamma_{yi} > \gamma_{y0}$. Naturally, in order for the total displacement on the both sides of the interface to be equal to one another, the total width of the slip bands in the "hard" region must be less than in the "soft" one. This explains the experimentally observed decrease in the width of the narrow bands and the formation of 'gaps" in the wide bands after they cross into the irradiated region (Fig. 4a and 4b). According to [4], for the same band formation mechanism ρ_{si} should be much greater than ρ_{s0}, as we did observe experimentally, in this case, in the same screw slip band.

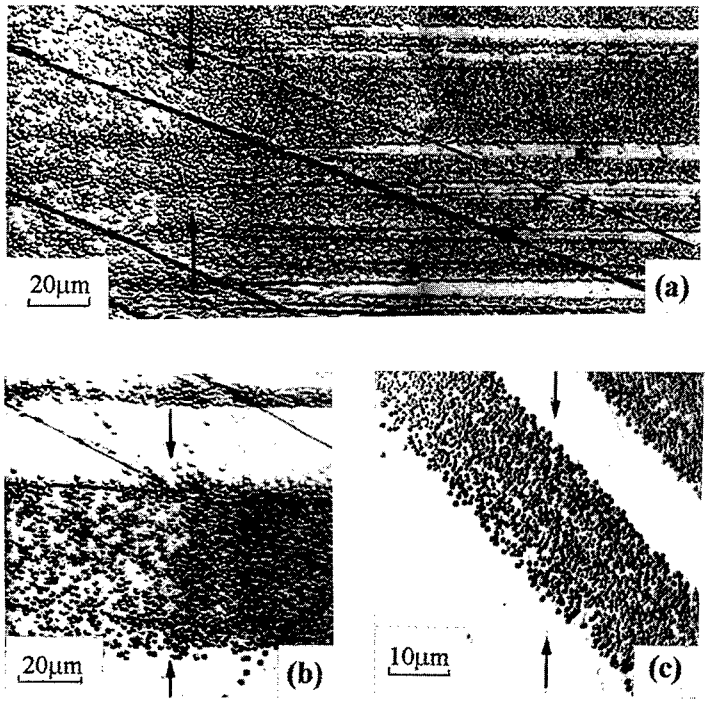

Fig.4. Dislocation structure of single-slip bands near the interface (marked by arrows) between irradiated and unirradiated regions of the crystal with screw (a, b) or edge (c) dislocations crossing the interface. The unirradiated region is on the left.

When edge dislocation run to the interface (Fig. 4c), after crossing it they can continue to move without multiplication because the latter process requires screw components of dislocations. Such screw components can be formed only as a result of buckling of the edge components. The fact that edge dislocation can move significantly without the buckling probably explains the absence of a pronounced difference in density of dislocation etch pits in edge slip bands on each side of the interface. It should be noted that the presence of the interface can also lead to much lower value of the ration ρ_e/ρ_s in both "soft" and "hard" regions than in unirradiated or completely irradiated crystals, where $\rho_e \gg \rho_s$ [4].

Thus, the changes in the flow stress and the evolution of dislocation structure in radiation-hardened layered LiF crystals under loading are explained on the basis of the dislocation mechanism of the formation and expansion of slip bands.

References

[1] B.I. Smirnov, Sov. Phys. Solid State 10 (1968) p. 2117
[2] B.I. Smirnov, Dislocation Structure and Hardening of Crystals, Nauka, Leningrad, 1981
[3] A. Kelly, Strong Solids, Clarendon Press, Oxford, 1973
[4] B.I. Smirnov, T.S. Orlova, T.V. Samoilova, Phys. Solid State 39 (1997) p.1072

Materials Science Forum Vols. 294-296 (1999) pp. 657-660

Ab Initio Tensile Tests of Grain Boundaries in SiC

M. Kohyama

Department of Material Physics, Osaka National Research Institute, AIST,
1-8-31, Midorigaoka, Ikeda, Osaka 563-8577, Japan

Keywords: Density-Functional Theory, First-Principles Molecular-Dynamics Method, Interfacial Fracture, Tensile Strength, Coincidence Boundary, Electronic Structure, SiC

Abstract

Ab initio tensile tests, namely, first-principles calculations of the tensile strength and fracture have been applied to a coincidence boundary in SiC for the first time, using the first-principles molecular-dynamics method beased on the density-functional theory. The non-polar interface of the $\{122\}\Sigma=9$ boundary has been dealt with. The stable configuration contains reconstructed five-membered and seven-membered rings and interfacial C–C and Si–Si wrong bonds. This interface is very strong because of the reconstruction, although the C–C and Si–Si bonds have large effects. The back bond of the C–C bond is broken first because of the short bond length and large strength of the C–C bond. Then the interfacial Si–C bonds are broken, and the Si–Si bond is broken. The *ab initio* tensile test is a powerful tool to investigate the intrinsic strength and fracture of interfaces through the behavior of electrons.

1. Introduction

Grain boundaries in SiC dominate various properties of SiC ceramics. It is of great importance to investigate the mechanical properties of grain boundaries in SiC at the atomic level. In covalent materials, it is essential to clarify the behavior of interfacial bonds, in other words, the behavior of both electrons and atoms at grain boundaries under various tensile or shear stresses. Currently, it is possible to apply *ab initio* calculations to such complex problems [1] by using the first-principles molecular-dynamics (FPMD) method [2] based on the density-functional theory. We have performed "*ab initio* tensile tests", namely, first-principles calculations of the tensile strength and fracture of a conincidence boundary in SiC for the first time.

2. Theoretical Method

We deal with the non-polar interface of the $\{122\}\Sigma=9$ boundary in SiC [3,4]. We construct a 64-atom supercell, which contains two equivalent interfaces with a distance of about $\frac{8}{3}a_0$. Total energy, atomic forces and averaged stresses [5] can be efficiently obtained using the FPMD method in the framework of the *ab initio* pseudopotential method. We use the conjugate-gradient technique for electronic minimization [6] and the TM-type optimized pseudopotentials [7]. A plane-wave cutoff energy of 60Ry is used. We use the equilibrium lattice constant by the present theoretical method. Two special $\mathbf{k}$ points per irreducible part are used.

Initially, the stable configuration is obtained through relaxation from the four-fold coordinated model observed experimentally [8]. In the tensile tests, uniaxial tensile strain is introduced into the stable configuration. First, the cell is stretched in a small increment in the direction normal to the interface, and the atomic positions are changed by uniform scaling.

Second, all the atoms are relaxed until all the atomic forces are less than 0.1eV/Å. Third, the total energy and stress tensor are calculated. This cycle is iterated until the interfaces are broken. This procedure corresponds to a real tensile test at T=0K [9].

3. Results

In the stable configuration of the non-polar interface [4], all the interfacial bonds are well reconstructed. Two sets of five-membered and seven-membered rings constitute one period, and C–C and Si–Si bonds are contained. Bond lengths and bond charges of such wrong bonds are rather similar to those in diamond and Si, which indicates that the wrong bonds possibly have peculiar effects on the strength and mechanical properties. The C–C bond is 3.6% longer than that of diamond, and the Si–Si bond is 4.4% shorter than that of Si. The distortions of the other bonds range from –2.9% to +2.9% and from –22.4° to +27.9°. Here the bond lengths of bulk SiC, diamond and Si are the equilibrium values by the present theoretical method.

Fig. 1 shows the stress–strain curve in the present tensile test. Tensile stresses along the ⟨411⟩ and ⟨011⟩ directions parallel to the interface are also generated. Strictly speaking, the cell sizes along these two directions should be adjusted in each step so as to remove such stresses. This effect should not be so serious at least qualitatively in the present case, because such stresses are not so large as compared with the stress along the ⟨122⟩ direction.

In the configuration of the strain of 0%, there remain small compressive stresses, which seem to be caused by the initial ridig-body translation optimized by the tight-binding calculations [3] and by some errors associated with the limited number of **k** points.

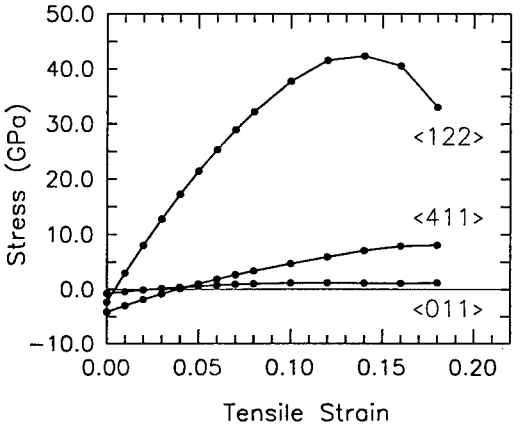

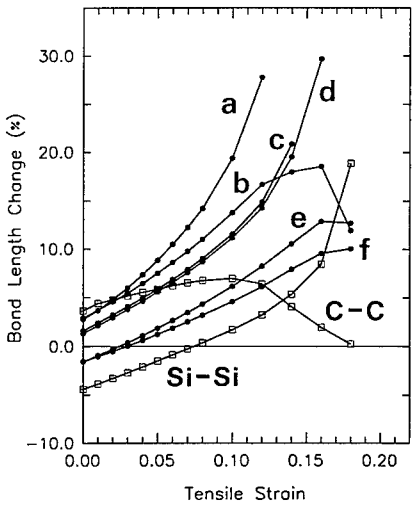

Figure 1 (left). Stress–strain curve of the non-polar interface of the Σ=9 boundary in SiC.
Figure 2 (right). Bond-length changes in the tensile test. The bond-length changes of the interfacial Si–C, C–C and Si–Si bonds specified in Fig. 3(a) are shown against the bulk bond lengths of SiC, diamond and Si, respectively.

The increase of the tensile stress along the ⟨122⟩ direction is decelerated at the tensile strain of 12% in Fig. 1. This means that the interface starts to be broken at this point, where the tensile stress exceeds about 41GPa. This maximum tensile stress is very much larger than the experimental values of SiC ceramics. Note that fracture occurs from the weakest defects

or cracks in usual ceramics. The present system contains no defects other than the interface. It can be said that the present interface is very strong because of the reconstruction of all the interfacial bonds. By the tensile stresses from 0% to 3%, we have calculated the Young's modulus of this interface, which is 505GPa. It can be said that this value is similar to the bulk SiC value, which also means the large strength of the interface. Note that this value itself is larger than the experimental value of bulk SiC. This shoud be caused by the present constraint in the tensile test and by the typical tendency of the present theoretical method for SiC.

Fig. 2 shows the bond-length changes at the interface. It is clear that the fracture starts at the back bond of the C–C bond, indicated by "a" in Fig. 2. Then the two interfacial Si–C bonds, indicated by "c" and "d" in Fig. 2, are broken. Finally, the Si–Si bond is broken. The reason why the fracture starts at the back bond of the C-C bond should be that the C–C bond has short bond length and large strength.

Fig. 3 shows the break of the back bond of the C–C bond. At the strain of 10%, the bond stretchings of the C–C bond and the back bond are +7.0% and +19.4% against the bond lengths of bulk diamond and SiC, respectively. At the strain of 12%, the back bond is suddenly stretched into +27.8%, while the C-C bond shrinks into +6.4%. The C-C bond shrinks much more hereafter. Thus, the back bond has been broken at this point, although the bond charge remains only a little. At the strain of 14%, the bond charge of the back bond disappears.

Fig. 4 shows the break of the two interfacial Si–C bonds. At the strain of 14%, the stretchings of the bonds "c" and "d" are 20.9% and 19.5%, respectively, and there remain the bond charges. At the strain of 16%, these bonds are greatly stretched into 34.2% and 29.7%, respectively, and the bond charges almost disappear or are greatly reduced. At the strain of 18%, there exist no bond charges. The bond "b" shrinks due to the break of the bond "d".

Fig. 5 shows the break of the Si–Si bond. At the strain of 16%, the bond stretching of the Si–Si bond is 8.5% against the bond length of bulk Si, and there remains the bond charge. At the strain of 18%, the Si–Si bond is suddenly stretched into 18.9%, and the bond charge is greatly reduced. It should be noted that the C–C bond is not broken in the present test.

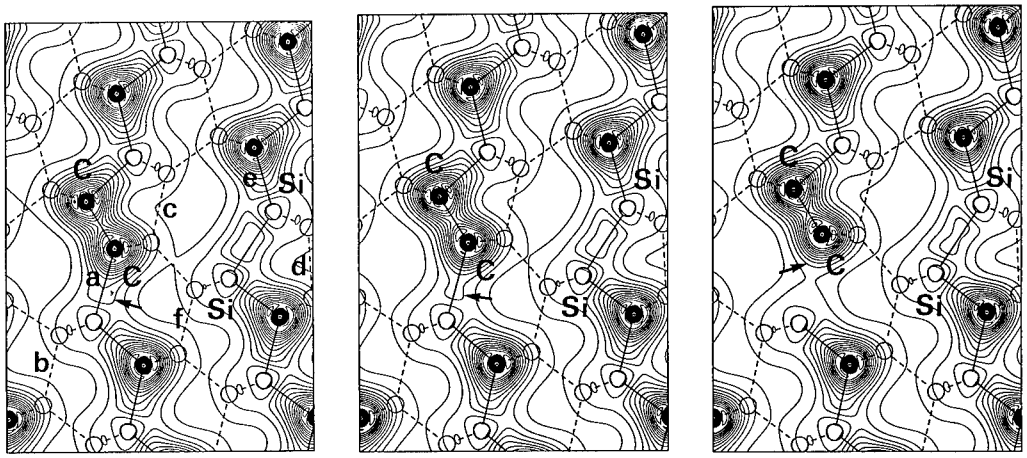

(a) $\varepsilon = 10\%$ (b) $\varepsilon = 12\%$ (c) $\varepsilon = 14\%$

Figure 3. Breaking of the back bond of the C–C bond. Atomic configurations under each tensile strain ε are shown. Arrows indicate the contours of the same value of valence density at the bond "a". Solid or dashed lines indicate bonds of which the stretching is less than 30%. Small letters in Fig. 3(a) indicate the bonds of which the length changes are shown in Fig. 2.

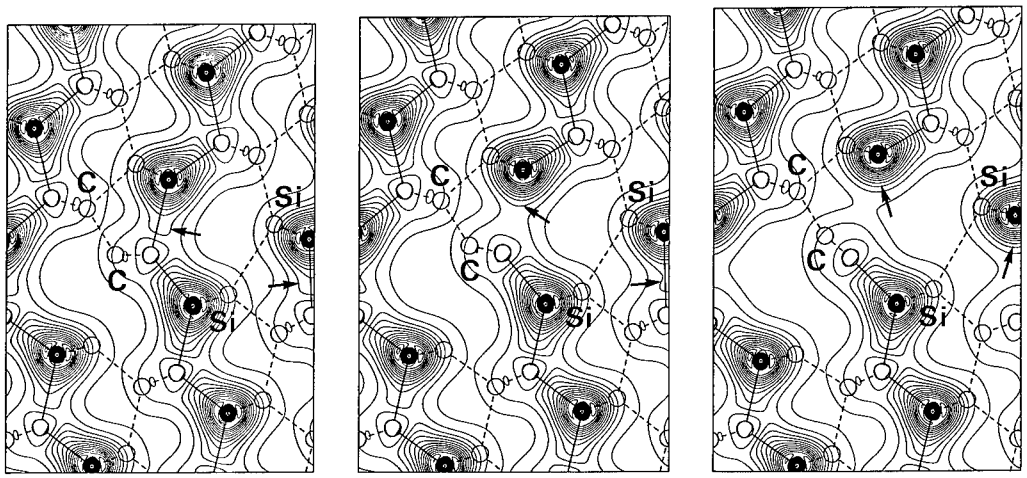

(a) $\varepsilon = 14\%$ (b) $\varepsilon = 16\%$ (c) $\varepsilon = 18\%$

Figure 4. Breaking of the two interfacial Si–C bonds. Arrows indicate the contours of the same value of valence density at the bonds "c" and "d". The charge density is shown on the (011) cross section different from those in Figs. 3 and 5.

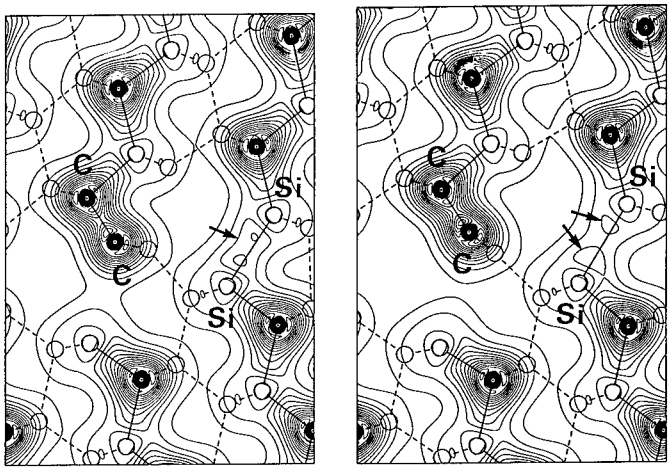

(a) $\varepsilon = 16\%$ (b) $\varepsilon = 18\%$

Figure 5. Breaking of the Si–Si bond. Arrows indicate the contours of the same value of valence density at the Si–Si bond.

The present kind of tests can clarify the intrinsic strength and fracture of each interface or defect, which cannot be easily examined experimentally. Similar tests of the polar interfaces containing only C–C or Si–Si bonds [4] are of great interests, which are now in progress.

References

[1] C. Molteni *et al.*, Phys. Rev. Lett. **76**, 1284 (1996).
[2] R. Car and M. Parrinello, Phys. Rev. Lett. **55**, 2471 (1985).
[3] M. Kohyama *et al.*, J. Phys. Condens. Matter **2**, 7809 (1990); **3**, 7555 (1991).
[4] M. Kohyama, to be published.
[5] O.H. Nielsen and R.M. Martin, Phys. Rev. B **32**, 3780 (1985).
[6] M.C. Payne *et al.*, Rev. Mod. Phys. **64**, 1045 (1992).
[7] N. Troullier and J.L. Martins, Phys. Rev. B **43**, 1993 (1991).
[8] K. Tanaka, M. Kohyama and M. Iwasa, submitted.
[9] V.B. Deyirmenjian *et al.*, Phys. Rev. B **52**, 15191 (1995).

Materials Science Forum Vols. 294-296 (1999) pp. 661-664

Temperature Dependence of Mechanical Behavior of Copper Bicrystals with Dispersed B_2O_3 Particles

H. Miura[1], T. Sakai[1], H. Tamura[1] and G. Gottstein[2]

[1] Department of Mechanical and Control Engineering, University of Electro-Communications, Chofu, Tokyo 182, Japan

[2] Institut für Metallkunde und Metallphysik, RWTH Aachen, D-52056, Germany

Keywords: Grain-Boundary Fracture, Liquid Particles, Bicrystal, High Temperature

ABSTRACT

The high temperature mechanical behavior of orientation controlled Cu bicrystals with dispersed B_2O_3 particles, which behave liquid-like at the temperature over 773K, was studied. Most of the bicrystals having high-angle boundaries fractured intergranularly, though all of the bicrystals with low-angle boundaries fractured transgranularly. The ductility of the former bicrystals tended to decrease with increasing temperature and misorientation angle. These results were explained by the occurrence of grain-boundary sliding and grain-boundary migration in relation with the state change of B_2O_3 from solid to liquid with increasing temperature.

INTRODUCTION

Dispersion of solid particles is very effective to raise strength of materials according to the Orowan mechanism. Therefore, high-temperature mechanical behavior of dispersion-hardened materials containing solid (hard) inclusions have been studied by many investigators(1-4). The hard-solid inclusions are known also to obstacle grain-boundary sliding(GBS) and apparently improves the creep strength of materials at high temperatures. However, unfortunately, the suppression of GBS generates stress concentrations around the particles, and thus, promotes preferential nucleation of voids and cracks. Miura et al. have found that the dispersed solid particles weaken the strength of some special boundaries which can slide easily(3,4). Therefore, dispersion strengthening of materials is sometimes bad for the strength as well as ductility, contrary to the expectation.

Recently, Srolovitz et al.(5) have derived theoretically that dislocations are attracted to inclusions regardless of their phase condition at sufficiently high temperatures where stress relaxation can occur by interfacial diffusion at the particle/matrix interface. This suggests that the effect of dispersion on high-temperature strength is independent of state and volume properties of the reinforcing phase. However, these studies about the effect of liquid particles on the high-temperature mechanical behavior are limited only for when they are dispersed in a matrix. There are virtually no studies about the effect of grain-boundary liquid particles on the mechanical behavior.

For this purpose, in the present paper, Cu bicrystals with dispersed B_2O_3 liquid particles were investigated.

EXPERIMENTAL PROCEDURE

Bicrystals of a Cu-0.15wt.% B alloy with [001] twist boundaries were grown using seed crystals by the Bridgman method. The twist angles were 10°, 20° and 30°. According to Monzen and Suzuki(1996), grain-boundary sliding(GBS) takes place more easily with increasing grain-boundary energy, i.e. in the order of $10° < 20° \leqq 30°$ boundary. These bicrystals were internally oxidized by the powder pack method at 1223K for 24h to obtain Cu-B_2O_3 alloy bicrystals. After a degassing treatment at 1223K for 24h in vacuum in a graphite mold, the bicrystals specimens of 14.8mm gage length and 1x4mm^2 cross section were spark cut by electric discharge machining having planar boundaries inclined 45° with respect to the tensile axis so as GBS takes place easily. Tensile tests were conducted in vacuum at various temperatures between 673 and 1073K on an Instron-type testing machine at an initial strain rate of 4.2 x $10^{-4}s^{-1}$. After the tests, the fracture surfaces were observed using a scanning electron microscope (SEM).

RESULTS AND DISCUSSION

Figures 1 show the samples of true stress-true strain curves of (a) 10° and (b) 20° bicrystals. In all flow curves, after the yielding, work hardening takes place and becomes to fracture with rapid drop in stress. The temperature dependence of fracture strain differs much depending on the misorientation of the bicrystals.

Figure 2 summarizes the result of temperature dependence of fracture strain. Open and filled symbols indicate transgranular and intergranular fracture, respectively. All the specimens of 10° bicrystal fractured transgranularly, and temperature dependency of the fracture strain can not be seen. On the other hand, most of the 20° bicrystal specimens and all the 30° bicrystal specimens fractured intergranularly and brittlely, and their fracture strain rapidly decreases with

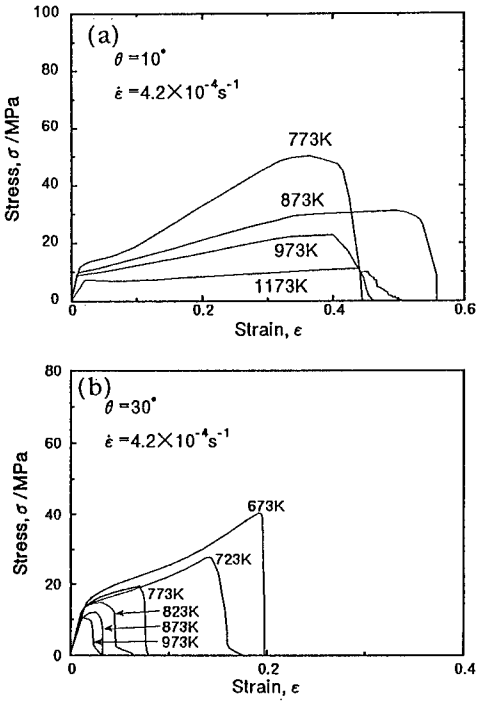

Fig. 1. Stress vs. strain curves of (a) 10° and (b) 30° bicrystals deformed at a strain rate of 4.2x10^{-4}s^{-1}.

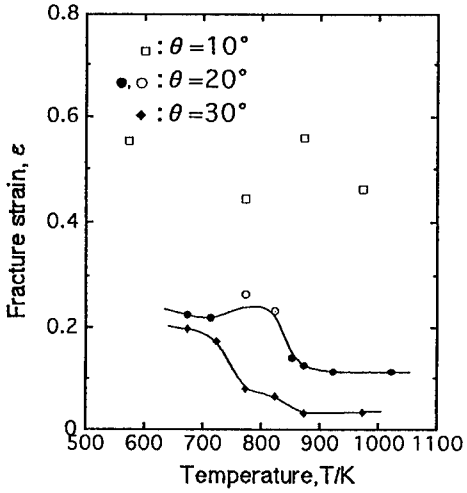

Fig. 2. Temperature dependence of fracture strain. Open and filled symbols indicate transgranular and intergranular fracture, respectively.

increasing temperature. Lower ductility of 20° and 30° bicrystals compared with that of 10° bicrystal should attribute to the occurrence of intergranular fracture. The fracture strain becomes smaller in the order of 10°, 20° and 30° bicrystals at all the temperatures. This is because that the GBS, which provides stress concentration sites to promote voids around solid particles at lower temperatures and induces grain-boundary migration(GBM) at higher temperature, takes place more easily in the order of 10°, 20° and 30° boundaries. The loss of strength at higher temperature must be caused by densifier of the liquid particles on grain boundary by grain-boundary dragging of in-grain particles. Onaka et al. have reported that B_2O_3 particles in copper matrix behave fully liquid like about over 773K(6). Therefore, the observed change in the fracture strains of 20° and 30° bicrystals around 800K should be due to the state change of B_2O_3 particles on the grain boundaries from solid-like to liquid-like.

Figures 3 show the SEM photographs of grain-boundary fracture surfaces of 20° bicrystal deformed at (a) 713K and (b) 873K, respectively. The feature in Fig. 3 (b) shows relatively flatter appearance compared with that of Fig. 3 (a). This should be also the result of characteristic change of B_2O_3 particles from solid-like to liquid-like. That is, the liquid particles can not suppress GBS, though solid particles work to it effectively. In fact, particles sheared by GBS(Fig. 3 (b)) and parallel relief lined formed by solid particle dragging(Fig. 3 (a)) are seen. Therefore, the characteristic difference of the feature of the fracture surfaces in Figs. 3 should be due to the loss of viscosity of B_2O_3 and to the extensive occurrence of GBS at higher temperature.

Figure 4 shows the photograph of GBS and GBM observed in 30° bicrystal deformed to a strain of ε=0.02 at 773K. GBS, which can be recognized from the displacement of scratched marker, took place even at the yield

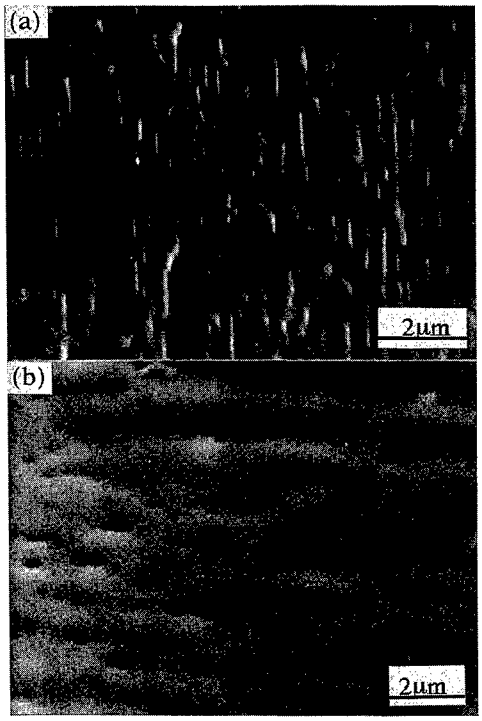

Fig. 3. Scanning electron micrographs of grain-boundary fracture surfaces of 20° bicrystals deformed at (a) 713K and (b) 873K.

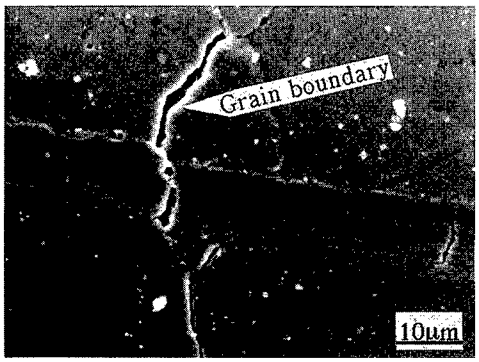

Fig. 4. Scanning electron micrographs of grain-boundary sliding and grain-boundary migration in the 30° bicrystal deformed at 773K to ε=0.02.

strain. What is more interesting in Fig. 4 is that a large scale of GBM occurred to serrate the grain boundary and cracks were nucleated along migrated grain boundary. We believe that the occurrence of GBM accompanied by GBS weakened the grain boundary, as mentioned above. That is, the densifier of liquid particles on grain boundary by dragging and their shearing by GBS lowers the joining strength of copper grain boundary and leads to the boundary cracking at lower strain.

SUMMARY

The ductility of Cu-B_2O_3 bicrystals strongly depended on grain-boundary character and temperature. Densifier of liquid particles on grain boundary induced by grain-boundary migration and grain-boundary sliding would play an important roll on the grain-boundary cracking at the small strain. Therefore, dispersion of liquid particles on grain boundary is harmful to the strength at high temperature where grain-boundary sliding and migration are operative.

Acknowledgement

The authors acknowledge financial support by Grant-in-Aid for Scientific Research from Ministry of Education, Science and Culture under Grant No. 10750512, and the raw material supplement from Nippon Mining and Metals Co. Ltd., Kurami Works, Japan.

References

(1) R.Raj, Acta Metall., 26 (1978), p.341.
(2) G.Gonzalez-Doncel, and O.D.Sherby, Acta Metall. Mater. 41(1993), p. 2797.
(3) H.Miura, T.Sakai, N.Tada, M.Kato, and T.Mori, Acta Metall. Mater. 41 (1993), p.1207.
(4) H.Miura, T.Sakai, N.Tada, and M.Kato, Phil. Mag. A, 73 (1996), p. 871.
(5) D.J.Srolovitz, R.Petkovic-Luton, and M.J.Luton, Phil. Mag. A. 48 (1983), p.795.
(6) S.Onaka, K. Hasegawa and H.Miura, Phil. Mag. A. 74 (1996), p.531.

Correspondent address: miura@mce.uec.ac.jp/Tel.81-424-43-5409/Fax.81-424-84-3327

Materials Science Forum Vols. 294-296 (1999) pp. 665-668

The Structure of Grain Boundaries and the Processes of Failure in the Ferrite-Pearlitic Steels

A.M. Shammazov[1], N.K. Tsenev[1], V.D. Suhanov[1] and B.E. Selsky[2]

[1] Ufa State Petroleum Technical University, 1 Kosmonavtov str., Ufa, RU-450062, Russia

[2] Bashkirian Scientific-Research & Design Institute of Petroleum Machine-Building, 95 Tsurupa str., Ufa, RU-450000, Russia

Keywords: Intergranular Boundaries, Impact Bending Tests, Fatigue, "Knife-Like" Boundaries, Ferrite Grains

Abstract: Influence of a structure with intergranular grain boundaries on mechanical properties and development of impact and fatigue failure processes were considered on an example of St3 steel. Fractographic studies showed that a brittle component is observed during impact fracture when the presence of "knife-like" boundaries inside the ferrite grains take place, the rate of growth of fatigue cracks increases.

At present it is known that intergranular boundaries play an important role in the formation of mechanical and many other physical properties in metallic materials [1-3]. However, this influence is not a synonymous one and depends on specific features of grain boundary structure and its change during external influence [3-5].

Special interest has been aroused by studies of the influence of microstructure and grain boundary structure on development of failure processes. The study of these problems is important for establishment of interrelation between structure of metals and failure parameters. The revealed regularities will allow to develop and create new methods of technical diagnostics and evaluation of residual service life resources for continuously used equipment working in unsteady regimes.

In this connection, the purpose of this work is to investigate the influence of grain boundary structure on development of failure processes using the example of low carbon (ferrite-pearlitic) sheet steel St3. The ferrite-pearlitic steel St3 has been widely used for construction of reservoirs. Dozens of years reservoirs have been working in unsteady regimes that results in change of steel structure and its mechanical properties. It is obvious, that in perspective the data obtained may be used in the development of corresponding methods for evaluation of fatigue crack life of reservoirs, thus allowing to prevent accidents of hard level pollution in time.

Material and methods of investigation

The ferrite-pearlitic steel St3 (Fe-0,17%C-0,5Mn-0,2%Si0,3%P-0,04%S) was taken for these investigations. On the example of the St3 steel the influence of intergranular boundary structure on the character of failure at impact fracture, and development of fatigue cracks were studied. For this purpose, three types of samples were produced: 1) initial (in the as-received state), which are characterised by a high level of lattice dislocations inside the ferrite grains; 2) samples with a cellular structure; 3) samples containing 'knife-like" intergranular boundaries inside the ferrite grains (Fig.1). The intergranular boundaries, which are characterized by high angle misorientations (more than 20°), long range and straight, or smoothly bent, very thin and perfect boundaries; were called "knife-like" boundaries [5].

Samples with a cellular structure and "knife-like" intergranular boundaries were produced by low cyclic bending deformation. This method was described in [4].

Impact bending tests were performed using samples of 7.5x10 mm in cross-section, having a "V" notch stress concentrator. A pendulum impact testing machine of MK-30M type with computer

estimation of impact strength value was used for this purpose. For impact bending tests, 5 samples on one spot were used. A pendulum pile-driver with a maximum impact load of 300 J was used for the test.

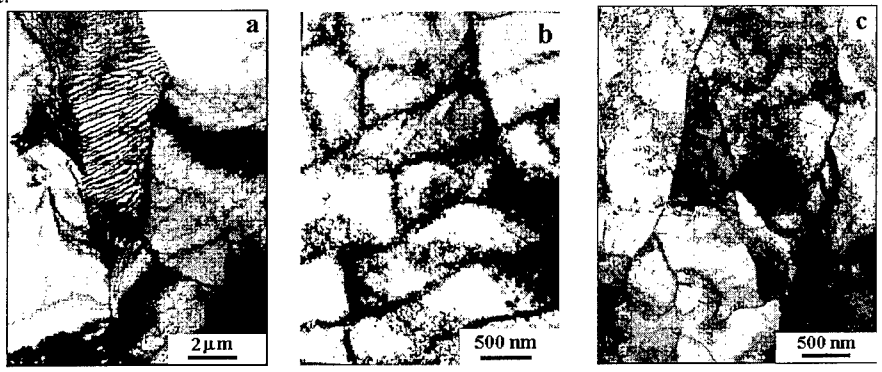

Fig. 1. TEM microstructure of the St 3steel.
a- initial state; b -a cellular structure; c - the structure with "knife-like" grain boundaries.

Estimation of mechanical properties of the St3 steel during tensile tests of the samples was carried out on an universal dynamometer of an Instron type at $\varepsilon = 8 \bullet 10^{-3}$ c $^{-1}$ and T = 293 K. Fatigue tests of samples with 10x10 mm in cross section, having two "V"-notches at constant early stress $\sigma = 0{,}9\sigma_T$ and frequency of 5 Hz were carried out on the universal dynamometer "Shenk".
A fractographic analysis of fracture surfaces after impact and fatigue tests was performed by a scanning electron microscope JSM-840.

Experimental results and discussion

Influence of intergranular grain boundaries on mechanical properties and failure character of samples out of the St3 steel.

In table 1 there are given values of mechanical properties obtained during tensile and impact bending tests of samples in the initial state, having a cellular structure and containing "knife-like" boundaries.

Table 1

Mechanical Properties of the St3 steel with a different structure inside the ferrite grain.

Structure of the St3 steel	Initial $\rho = 2 \bullet 10^9 - 8 \bullet 10^{10}$ cm^{-2}	With a cellular structure	Fragmented with "knife" type boundaries
Yield strength - σ_{02}, MPa	268	250	298
Ultimate strength - σ_s, MPa	430	450	560
Elongation - δ, %	26	24	18
Impact strength a_K, J/cm^2	185	157	78

From table 1, it is seen that in samples with "knife-like" boundaries during uniaxial tension, the yield limit and ultimate strength values are considerably higher than in St3 steel samples with initial structure and those with a cellular structure. At the same time, the impact strength and elongation

values of the St3 steel with "knife like" boundaries are noticeably lower. It should be also noted, when speaking about steel with a cellular structure, that the yield limit value is less when compared to the initial structure, and as for the ultimate strength value: it is higher. The experimental results obtained demonstrate a noticeable influence of the dislocation structure and intergranular boundaries in ferrite grains on mechanical properties at uniaxial tension and impact bending tests.
A fractographic analysis of the fracture surface of the St3 steel after impact bending tests allowed us to determine specific features of the influence of intergranular boundaries in the ferrite grains on a microrelief of fracture surface. One should note that for all samples, irrespectively of their boundary structure, it is a characteristic feature to have tough fracture which relief is formed by an aggregate of separate pits (see Fig.2). However, a depth of pits and their size depend on structure of a steel. Thus, a depth of pits at impact bending tests of samples with a cellular type of structure, having a fracture in surface, is considerably bigger than in comparison to the samples with the initial structure and containing "knife-like" boundaries. This points to a big plastic deformation in local areas of the samples with a cellular structure. One of the very important results revealed during failure of St3 steel samples containing "knife-like" boundaries, is the appearance of specific features common to a brittle fracture, namely, spalling facets and groove patterns (see Fig.2,c).

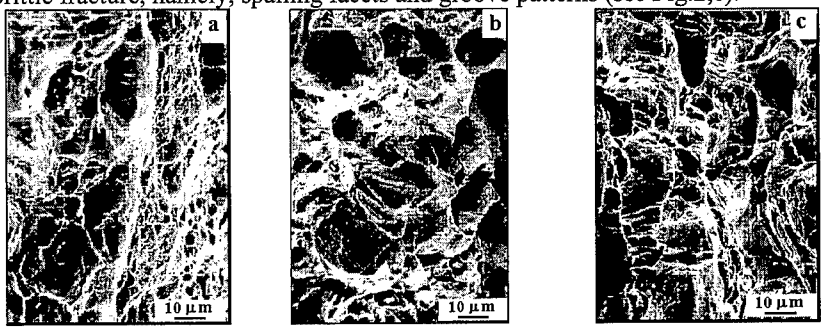

Fig. 2. Scanning electron microscope (impact fracture).
(a)-initial state; (b) -a cellular structure; (c) - the structure with knife-like grain boundaries

Now lets consider the influence of the intergranular structure in the grain interior on microrelief of the surface after fatigue failure of the investigated St3 steel.
The analysis of the fatigue fracture development in samples out of the St3 steel showed that microrelief of the surface after fatigue failure has two very distinct areas: a developing fatigue crack area, and the break-away area. One of the very important properties is a ratio of fatigue fracture area to common failure area of the sample. Knowing this value, one can consider resistance of fatigue crack to growth and declination of metal to brittle failure. The ratio data obtained from the fatigue area to the whole failure area of the sample is presented in table 2.

Table 2.

Development of fatigue cracks at low cyclic deformation.

St3 steel samples	Area of fatigue fracture, S_y, mm^2	Total area, S, mm^2	Ratio, S_y /S	Total number of cycles before complete failure
Initial state $\rho = 2 \bullet 10^9 - 8 \bullet 10^{10}$ cm^{-2}	20,08	50,3	0,41	39200
with a cellular structure	22,5	49,8	0,45	27800
Fragmented structure with "knife-like" boundaries	26,0	50,0	0,52	10300

From the data given in table 2 it is seen, that this ratio has its maximum value in samples containing "knife-like" boundaries. With all that, the total amount of cycles until complete failure has its lowest value. A fractographic analysis showed that during fatigue failure of initial St3 steel samples and samples containing a cellular structure and "knife-like" boundaries, a width of fatigue microgrooves increases, and makes up 0,34 μm, 0,42 μm and 1,3 μm, correspondingly (Fig.3).

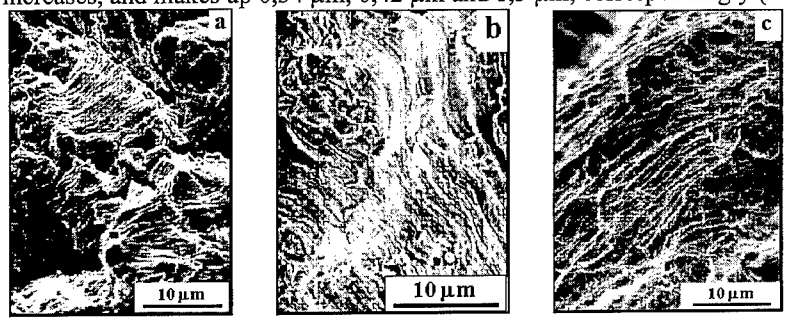

Fig. 3. Scanning electron microscope (fatigue cracks).
(a)- initial state; (b) -the cellular structure; (c)- the structure with "knife-like" grain boundaries

The data obtained show that the highest rate of growth of fatigue cracks is observed in samples with "knife-like" intergranular boundaries inside the ferrite grains. Thus, by use of the experimental research, the influence of intergranular boundaries within the ferrite grains of the steel on development failure processes was shown. It is dangerous, when concerning the questions of failure development, to have "knife-like" boundaries. "Knife-like" boundaries, apparently, is a hard-to-overcome barrier for dislocation sliding. During external influence (impact or unsteadily applied deformations), a sharp increase in dislocation density to a critical value occur in the vicinity of these boundaries. The latter leads to the formation and development of microcracks. This is, obviously, is the reason for the appearance a brittle component at impact bending tests and an elevated rate of development of fatigue cracks in samples with "knife-like" boundaries.

Conclusion

1. It is shown that mechanical properties (σ_{02} and σ_s) of the St3 steel containing "knife" type boundaries at uniaxial tension are considerably higher when compared to steels with a cellular structure and elevated dislocation density ($\rho = 2 \bullet 10^9 - 8 \bullet 10^{10}$ cm^{-2}) inside the ferrite grains.
2. Experiments showed that the presence of "knife-like" intergranular boundaries in the ferrite grains of the St3 steel leads to the appearance of a brittle component at impact bending tests and elevated rate of growth of fatigue cracks .

References

[1] Ch. V. Kopetsky, A.N. Orlov, L. K. Fionova. Grain Boundaries in Pure Metals, Moscow, Nauka, 158 p. (1997) (in Russian).
[2] O.A.Kaibyshev, R.Z.Valiev. Grain Boundaries and Properties of Metals.Moscow, Metallurgiya, 1987.- 216 p. (in Russian).
[3] R.Z.Valiev, O.A.Kaibyshev, G.F.Korznikova, N.K.Tsenev. Physika Metallov i Metallovedeniya v.62, ¹1 (1986), p.180.
[4] N.K. Tsenev, I.R. Kuzeev, V.A. Baryshev, A.M. Gallyamov, B.E. Selsky, Mater. Sci. Forum 207-209.(1996), p. 685.
[5] V.V. Rybin. Large Plastic Deformation and Metal Failure, Moscow, Metallurgia, 224 p, (1986) (in Russian).

Materials Science Forum Vols. 294-296 (1999) pp. 669-672

Mechanical Properties and Deformation Behavior of the Interfaces of Dissimilar Metals

F. Muktepavela and J. Maniks

Institute of Solid State Physics, University of Latvia, 8 Kengaraga St., Riga LV-1063, Latvia

Keywords: Metal Interfaces, Mechanical Properties

Abstract

Bimetallic joints with clean interfaces, obtained by a special cold welding method, are used as a model of phase boundaries for investigation their strength, deformation behavior, fracture mode and relaxation processes at the interface. Pairs of well-soluble and insoluble metals as well as pairs forming chemical compounds and eutectics were choosen for investigation. It has been shown that differences in the mechanical behavior of the interfaces are related to differences in phase boundary energy and other thermodynamic parameters as well as to mechanoactivation of both chemical interaction and structure formation.

Introduction

In the modern technologies for production of composites, superplastic and nanostructured materials, using active plastic deformation at relatively low temperatures, the strength characteristics of resulting phase boundaries comprise an important problem [1]. The properties of interface, in turn, are dependent of adhesion and structure forming processes running under particularly nonequilibrium conditions. Relaxation processes can develop by several mechanisms including chemical interaction, structural reconstruction and healing of pores. In the case of heterogeneous materials, formation of new phases can appear. However, investigations of the boundary properties and accommodation processes in the bulk of the fine-grained material are hindered by the difficulty of such experiments. Investigations of the bimetallic joints, obtained under conditions of large plastic deformation at room temperature can be employed to determine interface properties. The purpose of the present work is to investigate the mechanical properties of phase boundaries obtained in deformed state by a special cold welding method of dissimilar metals. To eliminate influence of impurities on the reliability of the results, the phase boundaries were obtained by contact of atomically-clean surfaces.

Experimental

The cold welding procedure of sheet specimens was carried out by two-side indentation of flat punches with a welding area of 23x3 mm [2]. A hard foil was located between the samples to be welded and this sandwich was subjected to indentation until a

crack in the foil arose and the newly formed clean surfaces of the metals to be welded were brought into contact. Secondary Ion Mass Spectroscopy method was used to determine the cleanliness of the interface. Strength properties of the bimetallic joints were determined by shear test. Fractographic and structural investigations were carried out by use of optical and electron microscopes.

Results and discussion

Pairs of metals selected for investigation differed by the type of physical and chemical interactions in the equilibrium state. However, as one can see from Table 1, this fact had no significant influence on the results of joint strength at 293K. But analyzing strength data for the joints at low temperatures and taking into consideration the results of fractographic studies, it is possible to show important differences between the systems and complicated role of mechanoactivation processes. As one can see, Cu/Sn, Al/Sn and Zn/Sn systems at 78K exhibit brittleness of phase boundaries or boundary regions. At the same time, the character of fracture of Pb/Sn and Cd/Sn systems has been modified from superplastic viscous flow along the boundary at 293K to brittle fracture of tin at 78K. This show that phase boundaries formed under the conditions of active plastic deformation is essentially a region of material with its own properties.

It was determined using SIMS, SEM and precision microhardness methods that phase composition and structure of boundary zone differ qualitatively from those of bulk metal [3]. It may be due to formation of non-equilibrium structure during deformation and subsequent development of the relaxation processes. One should note that, during formation of the solid phase joints, the deformation of subsurface layers is as high as 90-100 % , and in case of separate microasperities this value is even higher, so dislocation density near the interface reaches a limiting value very soon. Then, as it well known [4] , annihilation and rearrangement of dislocation followed by appearance of large number of point defects take place. So, conditions for abnormally high rate of mass transfer processes appear in the phase boundary region, and an energetically favourable structure can be formed. In case of insoluble (Ni/Ag, Al/Cd, Al/Pb, and Fe/Pb) and a well soluble (Ni/Cu) systems under investigation, some boundary blurring was observed indicating solid solution formation in a thin ($< 0.02\mu m$) layer. The effect of boundary hardening is peculiar to these pairs, and hence bimetallic joints' strength corresponds to a softer metal. For systems forming chemical compounds at high temperatures, for example, Ni/Sn, Cu/Sn, formation of non-stoichiometric intermetallic compounds appeared to be an energetically favorable boundary relaxation mechanism at 293K. In that case, intermetallic compounds in the Cu/Sn system are responsible for low temperature brittleness of phase boundaries. Formation of an interface similar to an intraeutectic one was observed for Al/Sn, Zn/Sn, Cd/Sn and Pb/Sn contacts. Strength characteristics obtained for these joints represent well-known effects of brittleness of Al-Sn, Zn-Sn and superplasticity of Cd-Sn and Pb-Sn eutectics after plastic deformation. The grain boundary sliding is known to be the main mechanism of plastic deformation for these eutectics. It is accompanied by formation of the pores, micro- and submicrocracks at the boundary. However, stability of such defects on the phase boundaries of different eutectics significantly differs. It is greatly affected by the development of the accomodation processes during deformation. For investigation of the peculiarities of Al/Sn and Pb/Sn phase boundary sliding, the experiments on pore closure in Pb-Sn, Al-Sn eutectics and their components (Pb, Sn) by plastic flow at uniform compression were carried out. The results show, that the local plastic deformation during pore closure in Al-Sn eutectic, tin and lead, on the contrary

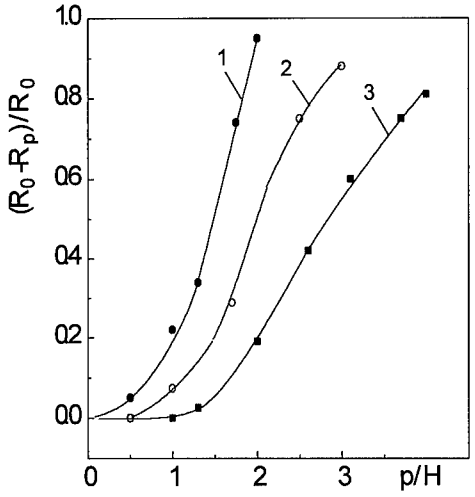

Fig.1. Pore closure as a function of the normalized pressure; 1- Pb-Sn eutectic, 2- Al-Sn eutectic, 3-Sn single crystal.

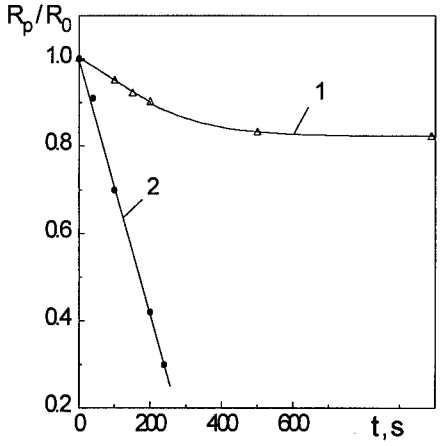

Fig.2.The effect of the loading time upon the relative change of the pore size; 1-lead, 2-Pb-Sn eutectic at p/H=0.17, where p-applied uniform pressure, H-hardness.

to that for Pb-Sn eutectic, is followed by a marked strengthening (Fig.1). The work-hardening coefficient for Al-Sn eutectic at the stage of a developed pore closure was found to be K=16, but at the final stage this was comparable to that of Sn or Pb single crystal samples (K=30). Such strengthening is typical for the dislocation mechanisms of plastic deformation. For superplastic Pb-Sn eutectic grain boundary sliding does not occur by the dislocation gliding but by the viscous flow (Fig.2). Viscosity coefficient equals 10^8 P, that points to fast kinetics of mass-transfer processes or to quasiliquid state of phase boundary. Fractographic investigations of the Pb/Sn joints showed the signs of intensive interfacial mass-transfer at 0.4 - 0.7 T_m which was directed to the healing of pores and smoothing of the interface. Development of dissolution-precipation processes on local areas of the interface was observed. Estimates show very high values of diffusion coefficient that are typical for liquids ($\sim 10^4$ cm^2/s), however, they agree with viscosity coefficient given above.Development and intensity of mass-transport on the Pb/Sn phase boundary depends on the extent of preliminary deformation. Strengthening of the boundary under annealing was observed. Transition of the phase boundary into stable state is more prolonged than the recrystallization processes in both lead and tin. Intensive development of the diffusion-promoted accomodation processes on the Pb/Sn interface is accounted for low phase boundary energy (0.04 J/m^2).

Nothing similar occurs on the Al/Sn phase boundaries. Sliding along the phase boundaries in this case is accompanied by pore accumulation and formation of narrow stable cracks due to high phase boundary energy (0.4 J/m^2).

TABLE 1

The Strength (σ) and Rupture Mode of Solid-phase Joints of Dissimilar Metals at 293 K and 78 K

	293 K		78 K	
Joint	σ, MPa	Fracture mode	σ, MPa	Fracture mode
Ni/Cu	260	ductile, inside Cu	370	ductile, inside Cu
Ni/Ag	160	ductile, inside Ag	325	ductile, inside Ag
Zn/Cd	115	ductile, inside Cd	52	brittle, inside Cd
Cu/Cd	100	ductile, inside Cd	50	brittle, inside Cd
Fe/Cd	100	ductile, inside Cd, brittle, inside Fe	56	brittle, inside Cd
Al/Cd	90	ductile, inside Cd	54	brittle, inside Cd
Cu/Sn	65	ductile, inside Sn	12	brittle, along interface
Zn/Sn	62	ductile, inside Sn	10	brittle, along interface
Al/Sn	63	ductile, inside Sn	10	brittle, along interface
Ni/Sn	57	ductile, inside Sn	40	brittle, inside Sn
Cd/Sn	55	ductile, along interface	35	brittle, inside Sn
Ni/Ca	33	inside Ca	-	-
Fe/Pb	31	ductile, inside Pb, brittle, inside Fe	39	ductile, inside Pb, brittle, inside Fe
Al/Pb	28	ductile, inside Pb	45	ductile, inside Pb
Pb/Sn	15	superplastic, along interface	35	brittle, inside Sn
Zn/In	10	ductile, inside In	15	ductile/brittle, inside In
Al/In	9	ductile, inside In	15	ductile/brittle, inside In

In summary, for most bimetallic systems, such as Ni/Ag, Ni/Cu, Al/Cd, Al/Pb, etc. strengthening of the interfaces was observed. The interfaces in such systems as Cu/Sn, Al/Sn,Zn/Sn exhibit low-temperature brittleness. For the Pb/Sn and Cd/Sn joints superplastic flow along the interface at 293K was observed. It has been shown that the difference in the mechanical behavior of the bimetallic interfaces is determined by termodinamic characteristics (phase boundary energy, solubility) as well as by mechanoactivation of the accomodation processes.

References

1.R.Valiev, R.S.Mishra, J.Grosa and A.K.Mukherjee, Scr.Mater. 34 (1996)p.1443.
2.F.Muktepavel and G.Upit, J.Mater.Sci.,19 (1984)p.599.
3.M.A.Vasiliev and F.O.Muktepavel, Metallofizika, 71(1978)p.12(in Russian).
4.V.E.Panin, V.A.Likhachov and Yu.V.Grinjaev, Structural Levels of the Plastic Deformation and Fracture, Novosibirsk, Nauka,1986 (in Russian).

Materials Science Forum Vols. 294-296 (1999) pp. 673-676

Models of Intergranular Fracture – Decohered Boundaries

A.G. Crocker[1], G.E. Smith[1], P.E.J. Flewitt[2] and R. Moskovic[2]

[1] Department of Physics, University of Surrey, Guildford, UK

[2] BNFL Magnox Generation, Berkeley Centre, Gloucestershire, UK

Keywords: Intergranular and Cleavage Fracture, Cavitated and Decohered Grain Boundaries, Low Temperature Fracture, Scanning Electron Microscopy, Polycrystalline Ferritic Steel, Two-Dimensional Theoretical Modelling

Abstract

The proportion of intergranular fracture in steels, which occurs at low temperatures in the brittle cleavage fracture regime, may be influenced by the presence of cavitated grain boundaries which have formed previously at higher temperatures. An illustrative example in a ferritic steel is provided. Two-dimensional models of the process help to elucidate the mechanisms involved.

Introduction

When polycrystalline materials fail, intergranular fracture competes with several other mechanisms including transgranular cleavage and ductile fracture. The proportion of intergranular fracture which occurs in practice depends on many physical and material parameters including, for example, temperature, applied stress, grain size, grain shape, preferred orientation, the number of cleavage planes available, relative grain boundary and cleavage surface energies and the size and distribution of potential crack nuclei, such as precipitate particles and inclusions. In recent years, the present authors have developed theoretical models to investigate the influence of these parameters and have compared the predictions with available experimental results.[1-3] In some cases, there have been major discrepancies which have stimulated new experimental work which has revealed that the fracture process is far more complex than normally assumed. For example the models, which are based on the assumption that a single cleavage plane may operate in each grain, predict that at low temperatures far more grain boundary fracture is required than is actually observed. This suggests that cleavage on several planes and accommodating plastic deformation must occur in many grains and preliminary results are tending to confirm this.

The present paper addresses a different aspect of the problem. At higher temperatures, ~$0.4T_m$, intergranular fracture often occurs by the nucleation and growth of cavities on grain boundaries.[4] This damage develops within the creep regime leading to creep failure of components when subjected to an external stress. It can also arise from either stress relief or reheat cracking within the heat affected zone (HAZ) of weldments which are subject to internal stresses either alone or combined with external stresses.[5] The cavities form predominantly on those grain boundaries oriented normal to the maximum principal stress axis and as creep strain accumulates so the cavitational damage progressively increases until it ultimately links to form micro-cracks. Although failure at higher temperatures has been studied extensively, there has been little consideration of the contribution that a small number of cavitated grain boundaries may have on the proportion of intergranular fracture for materials, such as ferritic steels, when fractured at temperatures below the upper shelf which correspond with the brittle cleavage fracture regime.

An Illustrative Experimental Example

A specimen was removed from a CrMoV steel weldment (nominal composition wt%: 0.58Cr, 1.3Mn, 0.3Si, 0.3Mo, 0.2Ni, 0.09V, 0.1C, 0.01S and 0.01P) where stress relief cracks had formed at grain boundaries, which are the prior austenitic boundaries within the HAZ. The coarse grained microstructure in the zone was tempered martensite. The area selected was remote from the cracking but contained a distribution of cavitated grain boundaries which had not linked to form cracks. The specimen was fractured at a temperature of 77K and examined in a scanning electron microscope operated in the secondary imaging mode. Figure 1 shows grain boundary facets that contain a distribution of cavities together with intergranular facets which do not contain such damage. The latter therefore correspond to brittle intergranular fracture. Although in this steel, traditionally, the proportion of intergranular fracture is much lower than cleavage fracture, Fig. 1 provides an example where intergranular fracture is promoted by the presence of the cavitated grain boundaries.

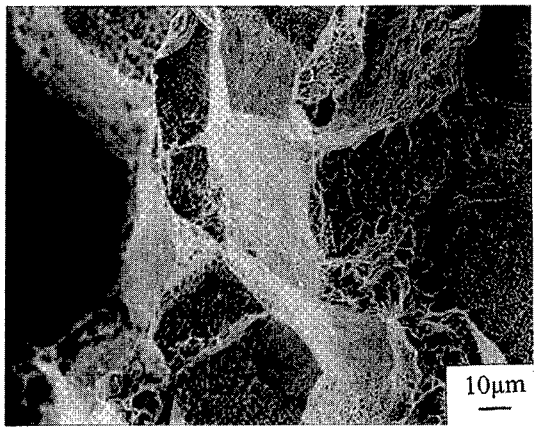

Figure 1. A scanning electron fractograph of the surface of a CrMoV steel fractured at 77K showing cavitational damage on about 30% of the grain boundaries and related brittle intergranular fracture.

Theoretical Modelling

The effect of cavitated boundaries on the proportion of grain boundary failure which occurs in polycrystalline materials tested in the cleavage fracture regime is being investigated using theoretical models. In this work it is assumed that all cavitated boundaries have been weakened to the extent that they are decohered. Also, in the preliminary study reported here, two-dimensional models have been adopted. These were based on 100 regular hexagonal cells, arranged in 5 x 20 arrays to simulate the shape of the HAZ around a weld. Two cases were considered in which edges of the hexagons were parallel to either the long axis or the short axis of the model. More realistic models were then generated by displacing the centres of the cells randomly and constructing Wigner-Seitz cells around them. In order to do this for the cells on the perimeter, a mantle of a further 54 cell centres had to be placed around each model. This resulted in arrays with 349 grain boundaries. The magnitudes of the displacements were restricted so that the resulting distorted cells remained as hexagons, rather than being transformed into other polygons. Examples showing selected areas of the resulting structures with about 35 cells are shown in Fig. 2 for the two cases.

Each cell in the models was assumed to have two orthogonal crystallographic directions along which cleavage could occur. These were distributed randomly and in Fig. 2 are indicated by crosses within the cells. Note that the crosses are located at the displaced centres of the original regular

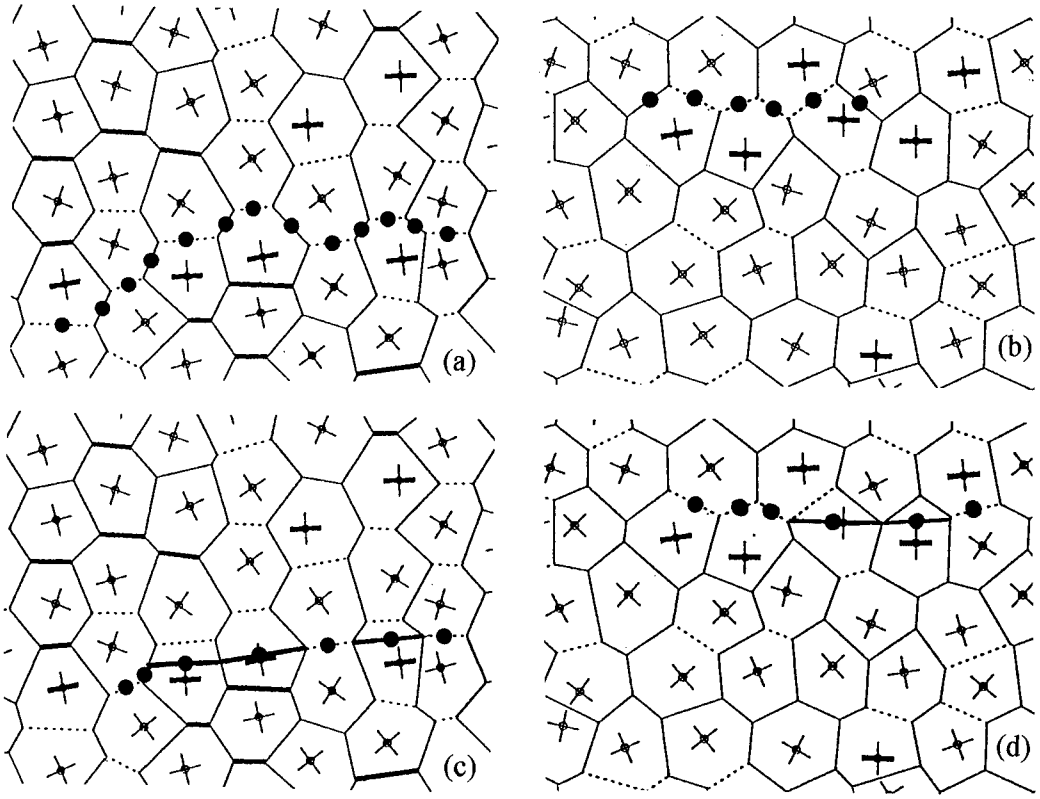

Figure 2. Brittle cracks propagating in the two types of 2-dimensional theoretical model adopted. In (a) and (b) intergranular fracture is favoured and in (c) and (d) cleavage fracture. About 35 of the 100 cells in the models are shown in each case. The stress axis in vertical and the notation used is explained in the text. About 13% of the grain boundaries are decohered, less than in Fig. 1.

arrays of cells and not at the centres of gravity of the distorted cells. Assuming that the principal stress axis is parallel to the short axis of the model, some of the lines forming these crosses are favourably oriented for cleavage fracture and these are shown bold. About 22% of the cells in the models have one of these bold lines.

A proportion of the boundaries was then selected as being decohered. Initially this was done entirely randomly but later a bias was adopted in favour of boundaries perpendicular to the principal stress axis to within about 10^0. In Fig. 2a, about one-third of the boundaries are likely candidates to be selected for decoherence or grain boundary failure whereas the remainder are less likely. Of the favoured boundaries, the biased-random procedure selected about 40%, those indicated by broken lines, as being decohered and a further 30%, those indicated by bold lines, as being well-oriented for grain boundary failure. Thus in this example 13.5% of the 349 grain boundaries are decohered. At this percentage, all of these boundaries are isolated from each other. Indeed simulations have shown that the proportion of decohered boundaries has to increase to about 19% before any linkage of the decohered boundaries occurs. However most of the decohered boundaries have 1, 2, 3 or even 4 next-nearest neighbour boundaries which are also decohered.

In Fig. 2b, because of the orientation of the parent hexagons, the boundaries are less well-aligned for decoherence or grain boundary failure but for comparative purposes, the case shown has been selected to have 12.6% of decohered boundaries, approximately the same as in Fig. 2a. Nevertheless

only three other boundaries, none of which are visible in the region shown in Fig. 2b, have been selected as being well-oriented for grain boundary failure. The most striking difference between the two models however is that decohered boundaries have already started to link together in Fig. 2b, there being a pair at the bottom left and a chain of 4 at the top centre. Indeed when the amount of decoherence was increased to about 21% this chain had increased in length to 8 cell boundaries.

The models have been used to investigate how the pre-existing cracks, in the form of individual or groups of decohered boundaries, could propagate under the influence of an applied stress parallel to their short axes. Two mechanisms are available: (i) intergranular failure along grain boundaries which have not decohered and (ii) cleavage. Figs. 2a and 2b show examples in which the former is favoured energetically. In Fig. 2a, seven decohered boundaries have been linked together by six grain boundary cracks, all 13 elements being indicated by dots. However, all six of the cracked grain boundaries are shown as fine lines and are not therefore particularly well-oriented for failure. In Fig. 2b, the stress concentrations at the ends of the sequence of four decohered boundaries could cause additional grain boundary failure, as indicated, but again these boundaries are not well-oriented. Figs. 2c and 2d show the same regions as Figs. 2a and 2b but illustrate examples in which cleavage is favoured energetically. In Fig. 2c three decohered boundaries, a partial grain boundary crack and three cleavage cracks, indicated by transgranular bold lines with dots, are linked. In Fig. 2d, four decohered boundaries and two cleavage cracks are linked in the sequence although the last join on the right is not exact.

Discussion

It has been demonstrated experimentally that intergranular fracture at low temperatures can be promoted by the presence of cavitated grain boundaries. The mechanisms involved have been investigated using theoretical models based on two-dimensional arrays of cells and the results suggest that cleavage fracture will normally occur. However, this depends on the local geometry of the grain boundaries, the crystallographic orientations of the grains and the relative fracture surface energies for cleavage and grain boundary failure. In some cases local stress concentrations around clusters of decohered boundaries can favour intergranular failure. Also the amount of this grain boundary failure increases as the amount of decohesion increases. More sophisticated two-dimensional models are being developed and preliminary results support the findings summarised here. In three-dimensional models there would of course be additional constraints but it is considered that the results would again be similar.

Acknowledgement

This paper is published with the permission of BNFL Magnox Generation.

References

[1] A.Crocker and G.Smith, Mater. Sci. Forum, 207-209 (1996), p. 593.
[2] A.Crocker, G.Smith, P.Flewitt and R.Moskovic, in *Mechanisms and Mechanics of Damage and Failure*, J. Petit (ed), EMAS, Warley, (1996), vol. 1, p. 233.
[3] G.E.Smith, A.G.Crocker, P.E.J.Flewitt and R.Moskovic, in *Damage and Failure of Interfaces*, H-P. Rossmanith (ed), Balkema, Rotterdam, (1997), p. 229.
[4] A.N.Kumar, in *Advances in Fracture Research*, B.L.Karihaloo (ed), Pergamon, (1997), p. 77.
[5] A.Dhooge and A.Vinckier, Int. J. Pressure Vessels and Piping, 27 (1987), p. 239.

Address for correspondence: a.crocker@surrey.ac.uk 01483 259501

Materials Science Forum Vols. 294-296 (1999) pp. 677-680

Competition between Sensitisation and Environmentally Induced Grain Boundary Damage in 304 Stainless Steel

A. Harabasz, K. Wolski, T. Magnin and M. Biscondi

Ecole Nat. Sup. des Mines de Saint-Etienne, Centre SMS, Département Mécanique physique et Interfaces, CNRS URA 1884, 158 cours Fauriel, F-42023 Saint-Etienne, France
E-Mail: harabasz@emse.fr

Keywords: Sensitisation, 304 Austenitic Stainless Steel, Environmental Effect, Slow Strain-Rate Test, Grain Boundary Fracture

ABSTRACT

Macroscopic fracture properties of 304 H are reviewed through slow strain-rate tests in the range [450;610]°C, either in vacuum or in oxidising environment. Experiments are conducted to correlate the observed grain boundary damage of tensile specimens with key microstructural features. Microstructural unstability of 304 H, associated with sensitisation, which occurs during straining at a temperature at least equal to 480°C, is responsible for a strong internal intergranular embrittlement and involves both carbides precipitation and heterogeneity of a dechromised zone. At 480°C, where the detrimental effect of this internal damage is minimised, we show on notched specimens that the observed grain boundary weakness can be released by the way of an oxidising environment. Consequently, our study suggests that understanding of in-service failures of this stainless steel should integrate competition between sensitisation and environmentally induced grain boundary damage.

INTRODUCTION

The good creep ductility properties of austenitic stainless steels at elevated temperatures justify their extensive use in heat resistant structural components in power generating and chemical industries. However, it does not prevent them from failures involving reheat cracking **[1]** or stress relief treatments under oxidising environment **[2]**. In this context, slow strain-rate tests **(SSRT)** at elevated temperatures in controlled atmospheres allowed to reproduce an intergranular embrittlement detected on austenitic zone of bimetallic welds **[3]**. These tests are also relevant to study operative fracture mechanisms of 304 H stainless steel around 0.5 T_f, in view of relative contribution of sensitisation and environment.

EXPERIMENTAL

The materials used in this work are two types of commercial 304 H stainless steels with similar compositions (18% for Ni, 8% for Cr and 0.08% for C) but different grain size (200 μm for steel H1, 50 μm for steel H2). Cylindrical specimens for tensile tests are machined in two different series, (i) smooth ones, with a gage length of 22 mm and a diameter of 5 mm, (ii) notched ones, derived from the previous, varying by a notch located in the middle of the gage length, which reduces the diameter to 4 mm. All SSRT were performed with a crosshead speed of 45 μmh^{-1}, which gives a strain-rate of $5.5x10^{-7}s^{-1}$ for smooth specimens, but corresponds to a faster one for notched specimens because of strain localisation (homogeneous plastic strain on gage length is no more representative because confined around the notch). A radiant heating furnace allows to raise straining temperature in the range [450;610]°C. Temperature is controlled by a welded K-type thermocouple wire. Specimens are fractured, either under secondary vacuum ($5x10^{-5}$ mbar), or in an oxidising environment (air + 4%CO_2 + 8%H_2O). The results of SSRT are plotted as $\sigma = f(\varepsilon)$ for smooth specimens and as $\sigma = f(t)$ for notched specimens.

RESULTS

Influence of straining temperature (tests on smooth specimens, under vacuum).

Stress strain curves (as well as microfractographs) of tests conducted up to rupture at four temperatures (450,480,530,610°C) are presented in fig.1. Maximum stress and elongation to rupture monotonically decrease with increasing temperature (cf. fig.1a). At the lowest temperature of 450°C, the final fracture region exhibits a fully transgranular ductile mode, covered by dimples (cf. fig.1b) and is associated with an important necking. The two highest straining temperatures (530 and 610°C) lead to an important intergranular damage of specimens, resulting both in intergranular cracking extended to the whole gage length and opened grain boundaries on fracture surface (cf. fig.1d). At the medium temperature (480°C), the number of cracks on gage length decreases and a mixed mode of fracture is observed (cf. fig.1c).

fig.1: influence of straining temperature on stress strain curves and fractographic features, after SSRT on smooth specimens of 304 H (steel H1) under vacuum.

fig.1a. : stress strain curves from SSRT ($5.5x10^{-7}$ s^{-1}) at 450, 480, 530, 610°C.

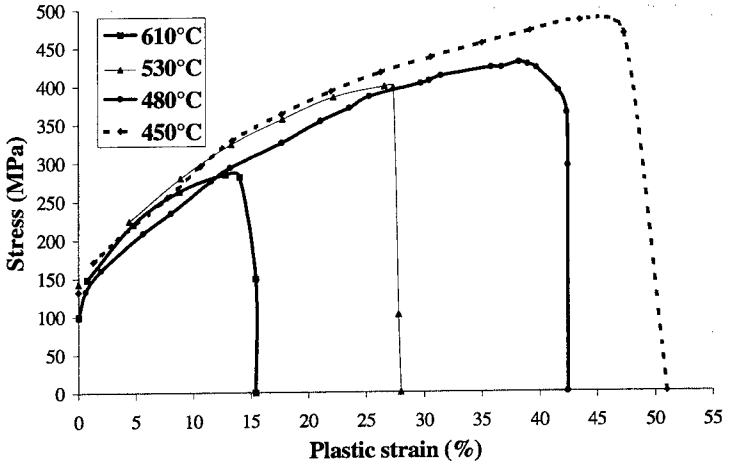

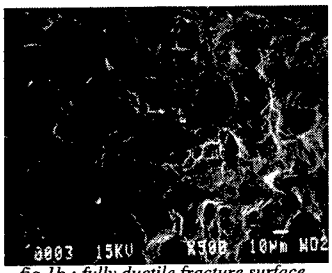

fig 1b : fully ductile fracture surface after SSRT at 450°C.

fig.1c : mixed fracture surface after SSRT at 480°C.

fig 1d : fully intergranular fracture surface after SSRT at 610°C.

Influence of heat treatment previous to SSRT at 610°C (tests on smooth specimens under vacuum).

An additional heat treatment (100 hours at 800°C), done before testing at 610°C, seems to restore the ductility of the material (cf. fig.2), delaying rupture until necking takes place. However, fracture mode remains intergranular and high magnification fractography reveals a continuous precipitation of large carbides (1 micron) on opened grain boundaries.

Influence of heat treatment previous to SSRT at 480°C on smooth specimens.

Tests at 480°C are conducted on smooth specimens after a heat treatment at 700°C for 25 hours. No significant influence is observed, neither on stress strain curves (cf. fig.3), nor on fractographic features.

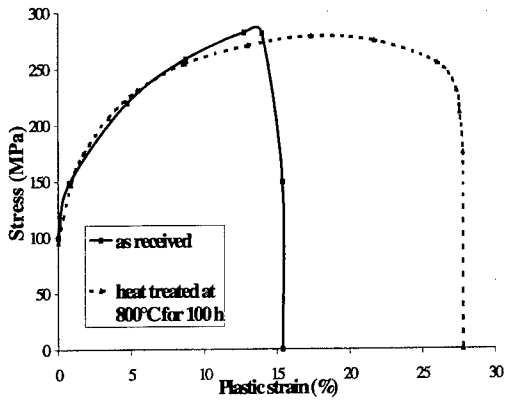

fig.2 : effect of heat treatment (800°C,100h) previous to SSRT at 610°C (smooth specimens of steel H1 under vacuum, $5.5x10^{-7}$ s^{-1}).

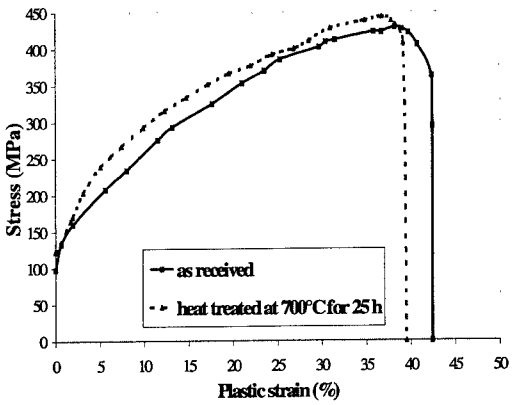

fig.3 : influence of previous heat treatment (700°C,25h) on SSRT at 480°C (smooth specimens of steel H1, $5.5x10^{-7}$ s^{-1}).

Influence of environment during SSRT at 480°C on notched specimens.

Influence of environment was investigated on notched specimens for steels, H1 and H2, by comparing stress strain curves and fractographic surfaces between vacuum and oxidising environment (cf. fig.4). Both steels exhibit marked embrittlement under oxidising environment: (i) life time is reduced by 30% (cf. fig.4a and b), (ii) an intergranular outlying ring appears, surrounding a ductile zone in the centre (cf. fig.4c). This ductile zone extends to the whole surface with tear arrest markings, for test in vacuum (cf. fig.4d). For each steel, stress level is similar in both environments, until fracture under oxidising environment occurs (higher stress for steel H2 is due to its finer grain size).

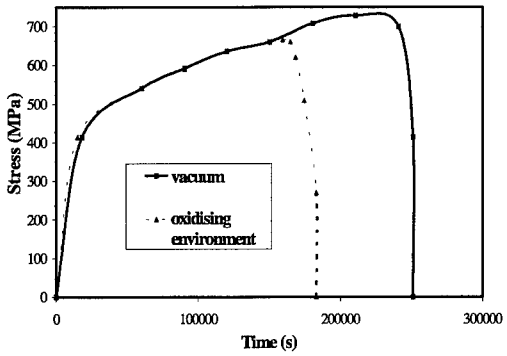

fig.4a : stress time curves for notched specimens of steel H2 (grain size of 50μm).

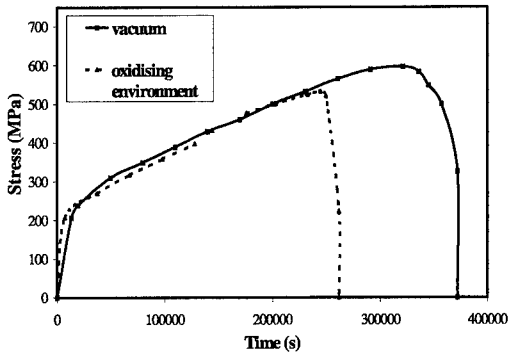

fig.4b : stress time curves for notched specimens of steel H1 (grain size of 200μm).

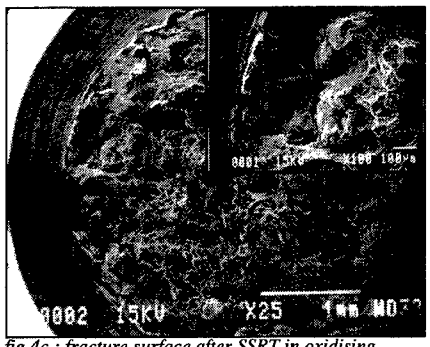

fig.4c : fracture surface after SSRT in oxidising environment (steel H1)

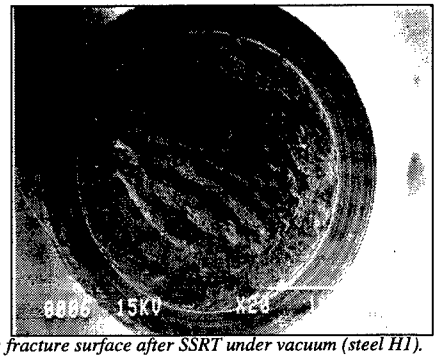

fig.4d : fracture surface after SSRT under vacuum (steel H1).

fig.4: influence of environment on SSRT at 480°C on notched specimens of 304 H with a crosshead speed of 45 μmh^{-1} .

DISCUSSION

Correlation between microstructural unstabilities and grain boundary (g.b.) damage.

Tests on smooth specimens, ranging from 450°C to 610°C, show a transition in fracture mode at 480°C (cf. fig.1), where randomly located intergranular damaged facets border transgranular ductile areas, which gives rise to a mixed mode. This fracture mode is replaced on the one hand, by a fully intergranular one when SSRT are conducted above 480°C and, on the other hand, by a fully ductile one below 480°C. As shown in fig.5, SSRT done under time-temperature conditions within sensitisation field results in intergranular fracture, in contrast with the ductile fracture for that outside and mixed one for that at the border. Therefore, microstructural unstability responsible for the loss in aqueous corrosion properties should be logically involved in the intergranular damage observed after SSRT. It must be underlined that sensitisation is featured both by carbides precipitation and concomitant dechromisation. The presence of mentioned carbides was experimentally confirmed by TEM observations after extraction of replicas from fractrured surfaces of specimens tested at 610°C.

Furthermore, our results indicate that suppressing, at least partly, the dechromised zone, allows to increase the elongation to rupture (cf. fig.2). In fact, the non-sensitising heat treatment of 100 hours at 800°C (cf. fig.5), usually acting as healing treatment after sensitisation, leads here to an exhausting carbides precipitation without dechromised zone. Consequently, further local dechromisation during test at 610°C is alleviated. Because similar strain hardenings are observed, the increased elongation to rupture can't be attributed to a microstructural softening of matrix but rather to the expected change in g.b. neighbourhood. In agreement with previous works on creep properties of 304 stainless steel **[5]**, it is suggested that a

localised deformation process along inclined g.b. promotes the intergranular cracking of g.b. perpendicular to the tensile axis. Without the heat treatment, testing at 610°C generates a deeply dechromised zone whose ability to shearing hastens fracture.

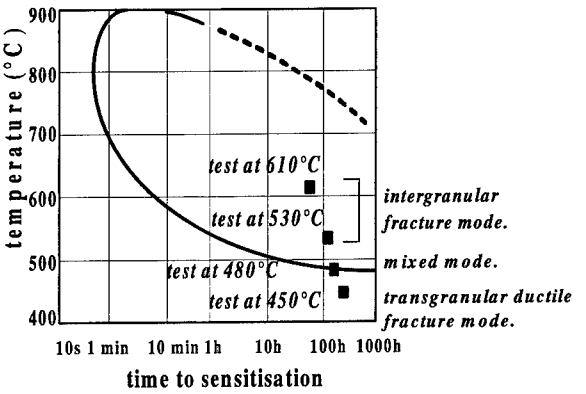

fig.5 : time-temperature sensitisation curve for 304 H (0.08%C), obtained by corrosion test [4], together with square marks indicating temperature, time of rupture and fracture mode for SSRT.

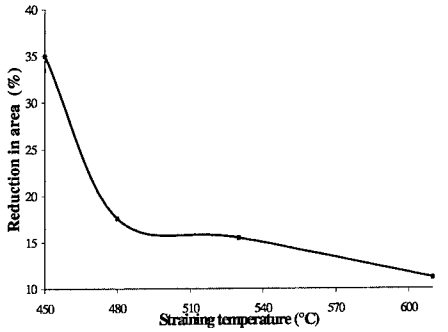

fig.6 : reduction in area as a function of straining temperature. a significant drop at 480°C underlines the transition in fracture mode.

Synergetic effects between straining temperature,sensitisation and environment around 480°C.

The transition around 480°C featured by the mixed mode of fracture, is underlined by the drop of reduction in area above this temperature (cf. fig.6) and a singularity in strength hardening of the corresponding curve (cf. fig.1a). During testing, specimens of 304 remain at the border of sensitisation field and consequently, two modes of fracture operate simultaneously, giving rise to a mixed one. This behaviour persists, even with a strong sensitising heat treatment at 700°C, and therefore suggests that a synergetic effect between sensitisation and straining temperature is needed to generate a fully intergranular fracture mode.

On notched specimens, localised deformation results in a faster strain-rate and a shorter time exposure to temperature. Consequently, it leads to a fully ductile fracture after SSRT under vacuum. Tear arrests markings observed on fracture surface are associated with the repeated re-initiation of cracks. In fact, propagating cracks are arrested by a plastically resistant matrix which leads to blunting of notch. Moreover, at 480°C, we just saw that sensitisation has less weight in g.b. damage, which allows environment to become the releasing parameter for a g.b. embrittlement featured through an intergranular ring and a decreased elongation to rupture. In oxidising environment, peripheral intergranular cracks serve to initiate the final fracture which occurs without blunting, in contrast with the test under vacuum. Intergranular cracking only occurs in oxidising environment at the tip of the notch, where (i) a potential interaction between strain and environment is confined, (ii) a triaxial stress state substitutes an uniaxial one.

CONCLUSIONS

1. Slow strain-rate tests at $5.5 \times 10^{-7} s^{-1}$ lead to grain boundary embrittlement of 304 H, when performed above 480°C, which is the lowest limit of sensitisation field.
2. On smooth tensile specimens, an obvious predominance of internal damage is attributed to microstructural change around g.b. coupled with straining temperature: carbides are responsible for an intrinsic weakness resulting in intergranular fracture, worsened and accelerated when dechromisation occurs.
3. An environmentally induced g.b. damage is released on notched specimens under oxidising gaseous environment at 480°C, evidenced by reduced life time and peripheral intergranular cracking.

REFERENCES

[1] A.Dhooge, A.Vinckier, Le Soudage dans le Monde 3/4 (1992) 45-71.
[2] M.Le Calvar, P.M.Scott, T.Magnin, P.Rieux, Corrosion 54 (1998) 101-105.
[3] M.Le Calvar, P.M.Scott, T.Magnin, P.Rieux, J.Paire, T.G.Gooch, Corrosion-Déformation Interactions 96, Ed. Th.Magnin, The Institute of Materials (1997) 506-515.
[4] S.M.Bruemmer, in Proc. of 6th Int. Symposium on Environmental Degradation of Materials in Nuclear Power Systems, Ed. R.E. Gold, E.P. Simonen (1993) 277-285.
[5] H. Kim, F. A. Mohamed, J.C. Earthman, Met. Trans., 22A (1991) 2629-2636.

Materials Science Forum Vols. 294-296 (1999) pp. 681-684

Dependence of Deviation Angle from Σ3(111) Relation on Intergranular Fatigue Cracking in Copper Bicrystals

Y. Kaneko, T. Mochida and K. Kitagawa

Department of Mechanical Systems Engineering, Faculty of Engineering, Kanazawa University, Kanazawa 920-8667, Japan

Keywords: Intergranular Fatigue Cracking, Copper, Coherent Twin Boundary, Σ3 Vicinal Domain

Abstract

In order to investigate the occurrence of the intergranular cracking, the fatigue crack propagatin tests have been carried out on copper bicrystal specimens in which the constituent crystals have several orientation relationships close to Σ3(111) coherent twin boundary. It was found that fatigue crack growth behavior depended significantly on the deviation angle from the Σ3(111) relation. In the specimens having the deviation angles less than 3°, no any intergranular crack growths were observed. When the deviation angle increased up to abount 5°, the fatigue cracks often propagated along the GBs. However at the deviation angles more than 9°, the intragranular cracking became predominant again. Such intragranular cracks propagated along well-developed slip bands. This deviation-angle dependence of the intergranular cracking could be understood in terms of the changes in both the grain boundary character and the development of the slip bands within the constituent grains.

1. INTRODUCTION

Most of the materials used for engineering purpose are fractured due to fatigue loading. Sometimes the fatal fatigue cracks are initiated and propagate along the GBs. In this sense, the GB design against the fatigue fracture should be one of the important purposes for the GB researches. However, the relationship between GB character and the intergranular fatigue cracking has not been studies in detail to the best of our knowledge. In order to understand a mechanism of the intergranular fatigue cracking, local oxidization in the vicinity of the GB has been proposed as one of the important cracking processes [1]. In the fatigue experiments using the copper bicrystals in air and vacuum, Vinogradov et al [2] reported that the intergranular fatigue crack propagating under air environment altered its path from the GB to the grain when the environment is changed to the vacuum. This fact suggests that the GB damage due to air environment may be a dominant mechanism for the intergranular fatigue cracking in the copper.

It has been shown that the GB-related phenomena such as the GB sliding [3], the GB corrosion [4,5] are sensitive to the character of the GB. Hence, one can expect that the magnitude of the abovementioned GB damage during fatigue loading depends also on the character of the GB. Apart from the GB character, it has also been revealed the velocity of the intergranular stress-corrosion cracking was affected strongly by the geometry of the slip systems operated around the crack tip. If the proposed intergranular cracking due to the GB damage is essentially same as the stress-corrosion cracking, the geometrical relationship between the GB and the operative slip system is probably connected with the intergranular fatigue crack propagation. Therefore, both of the GB character and the slip system geometry should be taken into account in order to investigate the properties of the intergranular fatigue cracks.

To solve this problem, the present authors paid attention to the Σ3 coherent twin boundary. In the Σ3 vicinal domain, the GB energy changes rapidly with the deviation angle from the Σ3 relation. Since the geometry of the slip systems contributing to the intergranular fatigue cracking appears insensitive to the slight deviation angle, the effect of the GB character on the intergranular fatigue cracking can be investigates, irrespective of the slip geometry. However, if the deviation angle becomes large enough to alter the cyclic deformation behavior of the constituent crystals, the GB character may no longer play an important role on the intergranular fatigue cracking.

In the present study, the fatigue crack propagation tests have been carried out using the copper bicrystal specimens with various deviation angles from Σ3 relation. The change in the fatigue cracking mode with the increasing deviation angle was investigated from view points of both the GB character and the cyclic deformation property of the constituent grains.

2. EXPERIMENTAL PROCEDURE

Copper bicrystals were grown by the Bridgman method in vacuum. Surface directions of constituent crystals were fixed to [0 1 1] as schematically shown in Fig.1. The tensile axes of these crystals were controlled to have an orientaion relationship close to Σ3(111) coherent twin boundary. The bicrystals were shaped to the single edge notched specimen ($32\times9\times2$ mm^3) and the notch was introduced along the GB. The GB plane was located perpendicular to the tensile axis. In this single-edge notched specimen with this kind of the crystal orientation, the operative slip planes of both grains would have the GB intersections which are parallel to *z*-axis. This geomety of the slip systems is favorable for the slip step dissolution model. We prepared the bicrystals with different deviation angle from the Σ3(111) relation around the [0 1 1] axis. The maximum deviation angle was about 12°. These devitaion angles were calculated using computer-aided Laue X-ray technique.

Fatigue crack growth tests were carried out in air at room temperature in a servo-hydraulic machine. Cyclic loading was applied to the specimen at 10Hz under a load ratio of –0.5 ($=P_{max}/P_{min}$). The load amplitude was raised stepwise until the fatigue crack initiation was detected at the notch tip. During the experiments, the fatigue cracks were observed with an optical microscope.

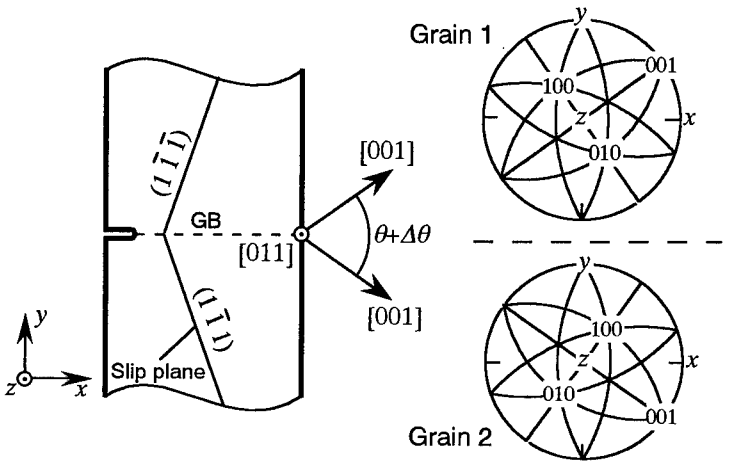

Fig.1 A schematic illustration of the slip geometry in the bicrystal specimen and the stereographic projections of the constituent grains having the Σ3 relationship.

3. RESULTS AND DISCUSSION

With increasing stress amplitude, the fatigue crack began to be nucleated around the notch tip. The fatigue experiments were continued at the constant stress amplitude where the fatigue crack nucleation was detected. The nucleated cracks were grown along the GB or in one of the grains. During the fatigue experiments, such fatigue cracks sometimes changed their paths from the grain boundary to the grain or *vice versa*. It appears that the ratio of the intergranular crack is sensitive to the deviation angle from the Σ3 relationship. Figure 2 shows the relationship between the deviation angle and the ratio of the intergranular crack to the crack length projected to the *x*-axis. According to Fig.2, the behavior of the fatigue cracks could be divided into three regions depending on the absolute value of the deviation angle. In the region where the deviation angle is less than 3° (i.e., $-3°<\Delta\theta<3°$), no any intergranular cracks were detected in the specimen. When the deviation angles were ranged from 3° to 5°, the ratio of the intergranular cracking increased up to 0.3. However, in the specimen having the deviation angle more than 9°, the ratio of the intergranular cracking was

reduced again.

Figure 3 shows the fatigue cracks observed at the above three regions. In the specimen with the deviation angles less than 3°, the fatigue cracks were nucleated and propagated within the one of the constituent grains. The intragranular cracks tended to propagate parallel to the GB plane in a zigzag manner as can be seen in Fig.3a. The SEM observation of the intragranular crack at relatively high magnification revealed that the operative slip system was different at two regions which are divided by the cracking plane. This slip morphology of the intragranular crack is similar to the coarse slip model proposed by Neumann [6].

The intergranular fatigue cracks were accompanied by the characteristic slip band formation in the vicinity of the crack tip: symmetrical formations of two slip bands ($(1\ \bar{1}\ \bar{1})$ plane in Grain 1 and $(1\ \bar{1}\ 1)$ plane in Grain 2) can be recognized in Fig.3b. The referred coarse slip model seems difficult to be applied for the crack propagation in the vicinity of the GB, because one of the required slip activities would be restricted by the GB. The observed slip band formation in the intergranular cracking had the same geometry of slip lines assumed in the slip step dissolution model [7], which was propased originally for stress-corrosion cracking. According to the slip step dissolution model, the intergranular crack growth involves the local embrittlement of the region near the GB and subsequent rupture of that region. Hence, the observed symmetrical slip band formations are compatible with the local oxidization of the GB which was the proposed to cause the intergranular fatigue crack propagation in air [1,2].

When the deviation angles were raised up to about 10°, the intragranular cracking became predominant again as seen in Fig.3c. In such a specimen with large deviation angle, a single kind of the slip bands were remarkably developed. The intragranular cracks were grown along these slip bands. The SEM observation of specimen surface showed that the slip bands were accompanied by the extrusions which are peculiar to the "persistent slip band (PSB)". Thus, the observed slip bands in these specimens can be the PSBs containing a characteristic dislocation substructure. It has been found that the intragranular fatigue cracks in single-slip-oriented specimen are nucleated and grown along the PSB [8,9].

It can be assumed that the present intergranular fatigue cracking is ascribed to the local damage —which is probably oxidization due to air environment — in the vicinity of the GB, because in vacuum the intergranular cracking disappeared on the fatigued copper [2]. In the previous studies on the intergranular corrosion [4,5], the sizes of the resultant GB grooves were closely related to the GB character as referred in Section 1. One can consider that such a GB damage in air environment is also sensitive to the GB energy. Accordingly, the present intergranular cracking at the deviation angle around 5° can be understood in terms of the increase in the susceptibility to the GB damage with increasing deviation angle from the Σ3 relation. However, the reduced ratio of the

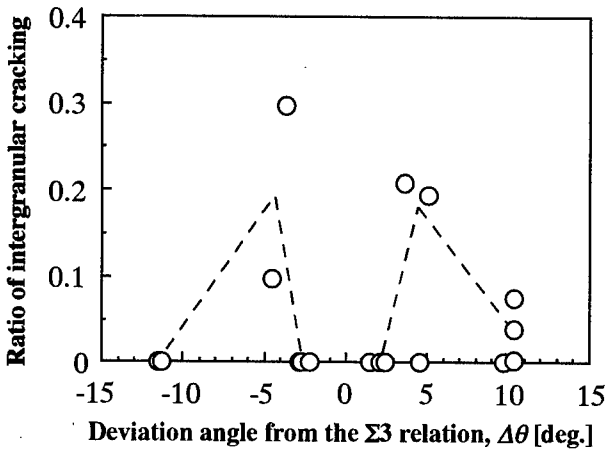

Fig.2 The ratio of intergranular cracking to the crack length projected to x-axis, plotted against the deviation angle from the Σ3 relation.

intergranular cracking at the large deviation angle region appears inconsistent with the increasing damage with increasing deviation angle.

It is likely that the deformation properties of the constituent grains are different between the specimens. On the specimens having a small deviation angle, the tensile axes of both constituent crystals are almost the <1 1 1> multiple-slip orientation. However, the constituent crystals should be no longer the <1 1 1> orientation in the specimen with a large deviation. The behavior of such a constituent crystal was analogous to the single-slip orientation in view of the result that a single kind of the PSBs was preferentially developed. It has been reported that the fatigued <1 1 1> single crystal of copper contained cell dislocation structure within the slip band [10]. This structure is certainly different from the ladder-like structure of the PSB, which is the preferred path for the fatigue crack. Hence, it is reasonable to suppose that the resistance against fatigue crack growth is different between the PSB formed at the large deviation angle and the slip band in the <1 1 1> crystal. In summary, the reduced ratio of the intergranular cracking at the large deviation angle region can be understood if we assume that the PSBs formed at large deviation angles have significantly low resistance against fatigue cracking even with compared to the intergranular fatigue cracking.

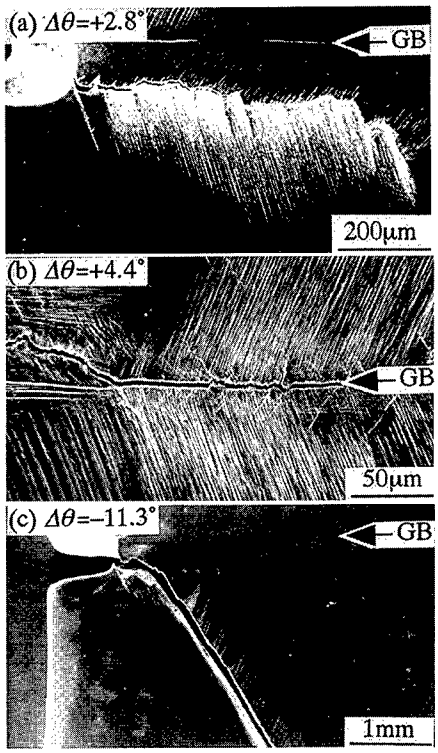

Fig.3 Fatigue crack propagation at several deviation angles from the Σ3 relation.

4. CONCLUSIONS

1. The bicrystal specimens of the deviation angle ranged from 3° to 5° frequently involved the intergranular fatigue cracking, although no any intergranular cracks were detected at the deviation angles less than 3°. This occurrence of the intergranular cracking can be attributed to the change in the GB structure.

2. When the deviation angles were more than 9°, the intragranular fatigue cracking became predominant again. The intragranular cracks of this kind were grown along well-developed slip bands. It is suggested that the intergranular fatigue cracking is governed by both of the grain boundary character and the development of the slip bands within the neighboring grains.

References

1. R.Lombard, H.Vehoff and P.Neumann, *Z.Metallkd*, **83** (1992), 463.
2. A.Vinogradov, T.Mimaki and S.Hashimoto, *Meter.Sci.Eng.*, **A216** (1996), 30.
3. T.Watanabe, M.Yamada, S.Shima and S.Karashima, *Phil.Mag.A*, **40** (1979), 667.
4. G.Hasson, J.-Y.Boos, I.Herveuval, M.Biscondi and C.Goux, *Surf.Sci.*, **31** (1972), 115.
5. M.Yamashita, T.Mimaki, S.Hashimoto and S.Miura, *Phil.Mag.*, **63** (1991), 695.
6. P.Neumann, *Acta Metall.*, **22** (1974), 1155.
7. H.Vehoff, H.Stenzel and P.Neumann, *Z.Metallkd*, **78** (1987), 550.
8. Z.S.Basinski and S.J.Basinski, *Scripta Metall.*, **18** (1984), 851.
9. A.Hunsch and P.Neumann, *Acta Metall.*, **34** (1986), 207.
10. T.Lepistö, V.-T.Kuokkala and P.Kettunen, *Scripta Metall.*, **18** (1984), 245.

Materials Science Forum Vols. 294-296 (1999) pp. 685-688

A Simple Criterion for Occurrence of Intergranular Fatigue Crack Propagation in a Ferritic Stainless Steel

S. Hashimoto[1] and Y. Kaneko[1,2]

[1] Department of Engineering Physics and Mechanics, Graduate School of Engineering, Kyoto University, Kyoto 606-8501, Japan

[2] Now at Department of Mechanical Systems Engineering, Faculty of Engineering, Kanazawa University, Kanazawa 920-8667, Japan

Keywords: Intergranular Fatigue Cracking, Ferritic Strainless Steel, Bicrystal

Abstract Fatigue crack propagation tests have been carried out in bicrystal compact tension (CT) specimens of Fe-30%Cr alloy. A geometrical criterion for the occurrence of intergranular crack propagation was investigated. A bicrystal having a [1 1 0] symmetrical tilt boundary (θ=22°) was prepared by a diffusion bonding. Two kinds of the CT specimens cut from the same bicrystal differs in tensile orientations of constituent grains as schematically shown in Fig.1. A bicrystal specimen in which both grains are oriented to < 1 4 4 > tensile axis showed that the fatigue crack encountering the GB began to propagate along that GB. On the other hand, when one of the constituent grains had a < 1 1 1 > tensile axis, the fatigue crack passed through the GB. This difference in the crack behavior around the GB can be understood in terms of the geometrical relationship between the GB and preferential crack growth directions of the constituent grains. This results suggest that the GB structure is not always a decisive factor determining whether a fatigue crack propagates along a GB or not.

1. INTRODUCTION

In usual polycrystalline materials subjected to cyclic loading, a fatigue crack can be nucleated and frequently propagates along the GBs. Such an intergranular cracking sometimes plays a serious role on the fatigue strength. However, the factors affecting the property of the intergranular crack are still ambiguous. It has been reported in nickel polycrystals [1] and copper bicrystals [2,3] that one of the criteria is the GB character which is determined by a misorientation between the neighboring crystals. A local GB oxidation that may be sensitive to the GB structure has been proposed as a dominant mechanism of the intergranular fatigue cracking [4,5].

However, it appears that the above GB damage under air environment is not so dominant to induce the intergranular fatigue cracking in a material showing high corrosion resistance. In such an environmental and material conditions, a certain criterion probably governs the occurrence of the intergranular fatigue cracking. In addition to the GB character distribution [6], another criterion should be taken into account in designing the GB possessing a high fatigue durability.

In the present study, a criterion for the occurrence of intergranular fatigue crack propagation has been investigated using two kinds of Fe-30%Cr alloy bicrystals. We paid attention to geometrical relationships between the preferential growth directions of intragranular cracking in adjoining grains. In order to diminish the effect of the GB structure, the GBs of these two specimen were set to be exactly the same.

2. EXPERIMENTAL PROCEDURE

Single crystals of Fe-30wt.%Cr alloy were grown by the Bridgman method in argon using the alumina molds. Bicrystals were produced by the diffusion bonding under an appropriate compressive pressure using the single crystals with a flat and smooth bonding plane. The diffusion bonding was done in vacuum at 1373K for 200 hours. We could obtain the bicrystals with very flat GBs. The

bicrystal had a [1 1 0] symmetrical tilt boundary and the angle between the [0 0 1] directions of constituent grains was about 22°.

Two kinds of the CT specimens (Bicrystals A and B) were shaped from the same bicrystal by a spark cutter. Figure 1 shows schematic illustrations of the bicrystal specimens and the stereographic projections of their constituent grains. The loading axes of the constituent grains were different between these specimens, but the GBs contained in them were quietly the same. Broad surfaces of both the specimens were fixed to (1 1 0) plane. Each specimen has the following crystallographic and geometrical features. (A) Both constituent grains of Bicrystal A have equivalent tensile axes of <1 4 4>. The GB plane of Bicrystal A was located normal to the tensile axis. A notch was introduced in Grain 2_A parallel to the GB. (B) Grains 1_B and 2_B of Bicrystal B were oriented to <1 1 1>and <1 4 4>, respectively. The normal of the GB plane was inclined to the tensile axis at 22° in Bicrystal B. The notch was produced at Grain 1_B. For the comparative purpose, the single crystal specimens having [1 $\bar{1}$ 1] and [4 $\bar{4}$ 1] tensile axes were also prepared.

The shaped specimens were annealed in vacuum at 1373K and then quenched in water. Prior to the fatigue test, the specimen surfaces were polished mechanically and electrolytically. Fatigue tests were carried out in air at room temperature in a servo-hydraulic machine. Cyclic loading was applied at 2Hz at the load ratio of 0.1 ($=P_{min}/P_{max}$). During the fatigue crack propagation tests, the load amplitude was gradually reduced in order to maintain a constant crack growth rate of about 10^{-8} m/cycle. The propagating fatigue cracks were observed with an optical microscope.

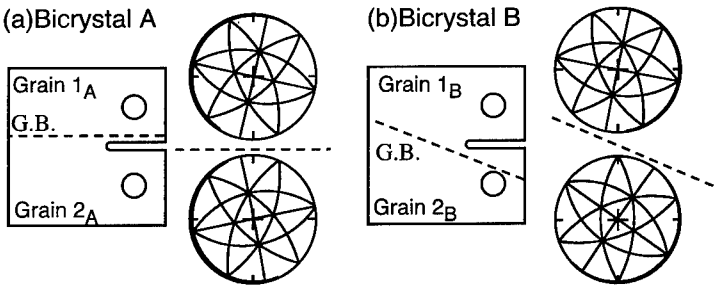

Fig.1 Schematic illustrations showing locations of grain boundaries and stereographic projections of constituent grains in (a) Bicrystal A and (b) Bicrystal B. Both of bicrystal specimens have the same grain boundary.

3. RESULTS AND DISCUSSION

Figure 2 shows the propagating fatigue cracks in the single crystal specimens. It has been found that the intragranular fatigue in the Fe-30%Cr alloy crystals was grown along slip planes [7]; the shear decohesion of the slip plane was the nature of the intragranular fatigue crack growth for this material. Likewise, the present fatigue cracks in the single crystals were grown along several slip planes. We can notice that these intragranular fatigue cracks tended to propagate towards certain directions. The [1 $\bar{1}$ $\bar{1}$] direction was most preferred for the [4 $\bar{4}$ 1] single crystal. The fatigue crack in the [1 $\bar{1}$ 1] single crystal was oriented to directions from [1 $\bar{1}$ $\bar{1}$] to [1 $\bar{1}$ $\bar{2}$]. This preferential direction should be determined by the geometrical relationship between the slip plane and the specimen surface, because the observed fatigue crack corresponds to an intersection of the slip plane with the broad surface.

Fatigue cracks propagated in Bicrystals A and B are presented in Fig.3. The intragranular fatigue cracks were initiated and propagated from the notch tips in Grains 2_A and Grain 1_B, respectively. The trace analyses of the specimens surface provide the following crystallographic features of the fatigue cracks. The fatigue crack in Grain 2_A was grown along (1 $\bar{1}$ 2) slip plane towards the [1 $\bar{1}$ 1] direction. In the same way, the (1 $\bar{1}$ 2)[$\bar{1}$ 1 $\bar{1}$] crack system appears to be operated in Grain 1_B, whereas a kink of the crack is locally seen. This tendency in each constituent grain agrees well with the previous results of the single crystal with the [4 $\bar{4}$ 1] tensile axis. There is no significant effect of the GBs on the cracking path in the region distant from the GBs. The Schmid factor of [1 $\bar{1}$ $\bar{1}$](1 $\bar{1}$ 2) slip system of the [4 $\bar{4}$ 1] tensile axis is almost 0.5, thus the slip bands are easy to be developed along it. Developed slip bands of this kind would be a preferred path of the fatigue crack.

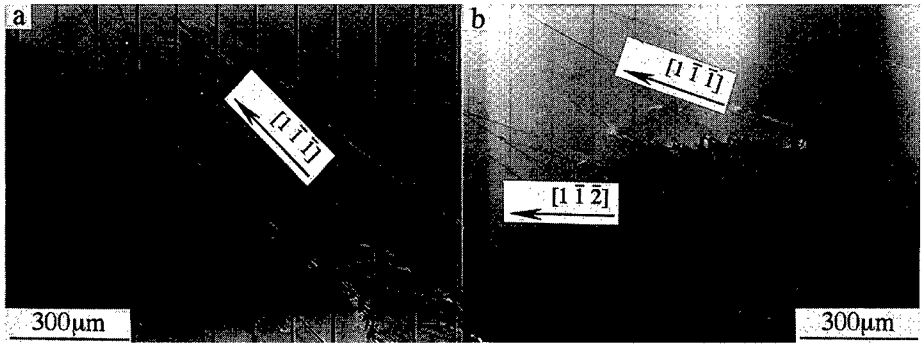

Fig.2 In-situ optical observation of fatigue crack propagation in the single crystals of (a) [4 $\bar{4}$ 1] and (b) [1 $\bar{1}$ 1] tensile axes.

In the further load cycling, these intragranular cracks reached the GBs. The behavior of the fatigue crack encountering the GBs was different between Bicrystals A and B. The fatigue crack in Bicrystal A was captured by the GB and subsequently continued to propagate along it. On the other hand, the fatigue crack passed through the GB in Bicrystal B, although the GBs of both bicrystals are the same. The passed crack propagated within Grain 2_B towards directions from [1 $\bar{1}$ 2] to [1 $\bar{1}$ 1] as indicated in Fig.3, thus never approached the GB again. (The observed crack growth directions in Grain 2_B were almost identical to that obtained in the single crystal.) This result of the crack passage suggests that the GB structure is not always a decisive factor for the occurrence of the intergranular fatigue cracking. In view of the fact that the intergranular cracking was almost absent in Bicrystal B, a structure of the present GB may be essentially strong against fatigue loading under the present experimental condition. One can expect that another criterion for the intergranular cracking should exist for this material.

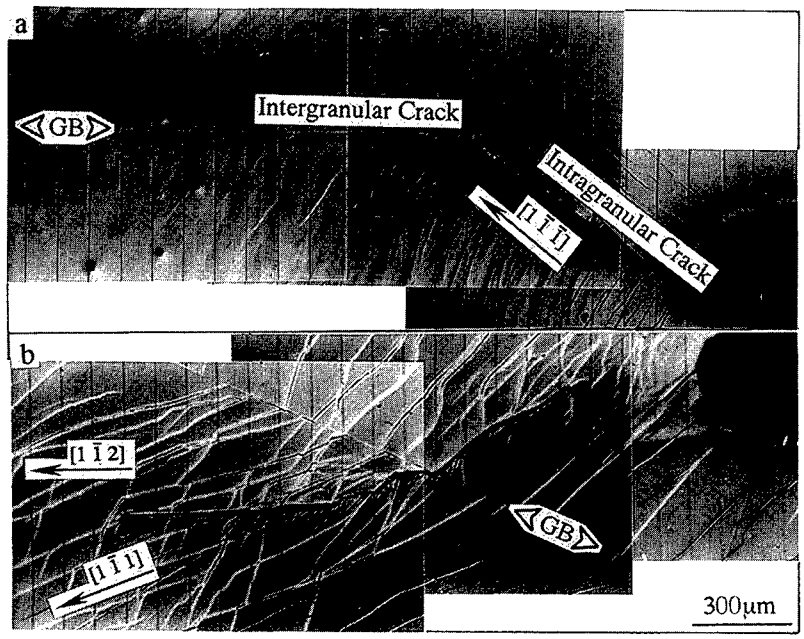

Fig.3 Photographs showing the fatigue cracks in (a) Bicrystal A and (b) Bicrystal B. The intergranular fatigue crack propagation was observed in Bicrystal A. On the other hand, the fatigue crack passed through the GB in Bicrystal B.

It was recognized in the single crystal specimens that each grain has the preferential crack growth direction associated with the highly sheared slip system. These preferential crack propagation directions of the constituent grains are schematically shown in Fig.4. In Bicrystal A, the preferential crack propagation directions of both Grains 1_A and 2_A are oriented towards the GB. On the other hand, Grain 2_B of Bicrystal B shows the preferential crack propagation which is directed out of the GB, while the preferential direction in Grain 1_B is still oriented towards the GB. According to Fig.4, it is easy to understand that the fatigue cracks initiated in Grains 2_A and 1_B propagated towards the GB. Now we consider the intergranular fatigue cracking along the present GB. The shear decohesion of the GB plane — which was found at Σ3(112) twin boundary [8,9] — can not be a cause of the intergranular cracking because the GB plane is approximately {1̄ 4 4}. It has been reported that a local GB oxidation due to air environment is required for the intergranular fatigue crack growth in Fe-Si alloy bicrystals fatigued at elevated temperature [4]. However, it can be assumed for a stainless steel that the local GB damage of this kind at room temperature is minor enough to induce the GB cracking. For this reason, the passage through the GB in Bicrystal B can be interpreted. On the other hand, the fatigue crack was grown along the GB in Bicrystal A, whereas the extent of its GB damage is expected identical to that of Bicrystal B because of the same GB structure. Such a crack propagation along the GB should be understood in the following manner. As illustrated in Fig.4a, the slip band in Grain 1_A does not form such that the fatigue crack leaves the GB: the fatigue crack captured by GB can not leave the GB when the preferential crack directions of the neighboring grains are oriented towards the GB. The intergranular crack in Bicrystal A contained short intragranular cracks actually, but such an intragranular crack easily reverted to the GB.

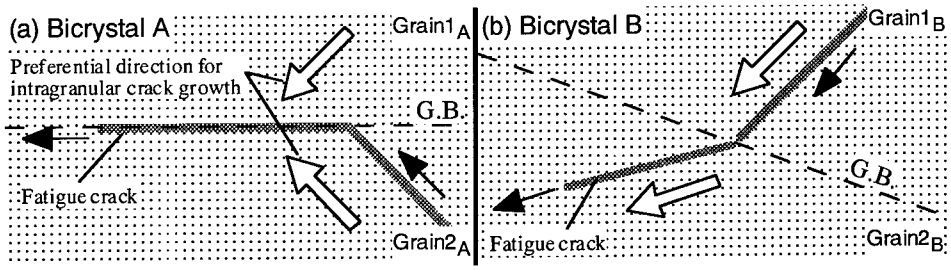

Fig.4 Schematic illustration of a criterion for occurrence of the intergranular fatigue crack growth ((a) intergranular crack growth and (b) crack passage through grain boundary.) Open arrows indicate the preferential crack propagation direction measured in the single crystal specimens. The microscopi c crack directions of the bicrystal specimens are from right to left.

4. CONCLUSION

1. A bicrystal specimen in which both grains are oriented to < 1 4 4 > tensile axis showed that the fatigue crack encountering the GB began to propagate along that GB. On the other hand, when one of the constituent grains had a < 1 1 1 > tensile axis, the fatigue crack passed through the GB.

2. Such a different crack behavior at the GB can be understood in terms of the geometrical relationship between the GB and preferential crack growth directions of the constituent grains.

References

1. L.C.Lim, *Acta Metall.*, **35** (1987), 1653.

2. A.Vinogradov, S.Hashimoto and S.Miura, *Scripta Metall.*, **32** (1995), 427.

3. A.Vinogradov, S.Hashimoto and S.Miura, *Scripta Metall.*, **34** (1996), 775.

4. R.Lombard, H.Vehoff and P.Neumann, *Z.Metallkd*, **83** (1992), 463.

5. A.Vinogradov, T.Mimaki and S.Hashimoto, *Meter.Sci.Eng.*, **A216** (1996), 30.

6. T.Watanabe, *Mater.Sci.Eng.*, **A176** (1994), 39.

7. Y.Kaneko, S.Hashimoto,T.Mimaki and S.Miura, *Strength of Materials, Proceeding of ICSMA10*, (1994), 513.

8. H.Mori, R. Itoh, T.Kozakai and T.Miyazaki, *Scripta Metall.*, **14** (1980), 929.

9. Y.Kaneko, S.Hashimoto and S.Miura, *Phil.Mag.Lett.*, **72** (1995), 297.

Materials Science Forum Vols. 294-296 (1999) pp. 689-692

Image Force on a Lattice Dislocation Due to a Grain Boundary in Hexagonal Metals

O. Khalfallah[1] and L. Priester[2]

[1] Institut de Physique, Université de Constantine, Algérie

[2] Laboratoire d'Etudes des Matériaux Hors Equilibre ISMA, Université Paris Sud, F-91405 Orsay Cedex, France

Keywords: Elastic Interaction, Anisotropy, Image Force, Hexagonal System

Abstract

The image force felt by a dislocation near and parallel to a grain boundary is examined as a function of the grain boundary misorientation and of the dislocation characteristics in hexagonal metals on the basis of the anisotropy theory of elasticity. It is pointed out that there is no image force due to any grain boundary around the c-axis for the basal and the prismatic dislocations. For any misorientation around $[1\bar{1}00]$ or $[11\bar{2}0]$, the dislocations with $b = a/3[2\bar{1}\bar{1}0]$ are attracted to the grain boundary. On the contrary, the dislocations with $b = a[0001]$ are repelled from most grain boundaries around $[1\bar{1}00]$.

I - Introduction

A dislocation at vicinity of a grain boundary in anisotropic materials is submitted to a long range elastic image force due to the misorientation between the two crystals. Theoretical approaches of this interaction have been developped [1-4] and numerical results on the signs and the magnitudes of the image forces between grain boundaries and dislocations have been obtained for cubic systems [5-8].

The image force calculations are based on the theorem of Barnett and Lothe [2] which allows to determine the interaction energy ΔE between the dislocation and the grain boundary, then the image force given by:

$$\mathbf{F}_i = \frac{\left[E^{(I/II)} - E^{(I)}\right]}{d} = -\frac{\Delta E}{d} \qquad [2]$$

where **d** is the distance between the dislocation and the grain boundary plane, $E^{(I)}$ and $E^{(I/II)}$ are the prelogarithmic energy factors for the dislocation in an infinite crystal I and for the dislocation at the interface I/II, respectively. The dislocation line **t** is considered parallel to the grain boundary plane and the image force is the same for any plane belonging to the same zone **t**.

The calculations of the interaction energy ΔE are performed using the intregral formalism [9,10] as already described in the cases of cubic materials [6-8]. It has been shown that the image force depends on several parameters describing the "dislocation -grain boundary" configuration : the misorientation axis [uvw] and angle θ between the two grains, the Burgers vector **b** and the line orientation **t** of the dislocation. According to these parameters, the image force may be attractive

($\Delta E < 0$) repulsive or null. Furthermore, the image force magnitude increases with the anisotropy factor $H = 2\,C_{44} + C_{12} - C_{11}$ [7,8].

The main objective of this study is to investigate the image force effects for hexagonal metals and to compare them to those obtained for cubic metals.

II- Materials and " dislocation-grain boundary " configurations.

The necessary data for the ΔE calculations as well as the anisotropy ratio A_s and the anisotropy factor H.are given in table 1 for different hexagonal metals.

Table 1 : The cristallographical parameters a and c (in Angström) , their ratio a/c, the elastic constants (in GPa), the anisotropy ratio A and the anisotropy factor H (in GPa) of the different metals

Metal	a	c	c/a	C_{11}	C_{12}	C_{13}	C_{33}	C_{44}	C_{66}	A_s	H
Zn	2.66	4.95	1.86	165	31	50	62	40	67	0.59	-5.48
Cd	2.98	5.62	1.88	115	39	40	51	20	37	0.53	-3.57
Y	3.65	5.73	1.57	78	29	20	77	24	24	0.99	0.01
Mg	3.21	5.21	1.62	59	26	21	61	16	17	0.98	0.07
Tl	3.46	5.52	1.59	41	35	29	53	7	3	2.69	0.90
Co	2.51	4.07	1.62	307	165	103	358	75	71	1.06	0.92
Ti	2.95	4.68	1.58	162	92	69	181	47	35	1.33	3.34

The grain boundaries which have been considered are characterized by misorientation axes with simple indices : [0001], $[1\bar{1}00]$ and $[11\bar{2}0]$, the misorientation angles varying from 0 to 180°. The Burgers vectors and the line orientations of the investigated dislocations are given in table 2

Table 2 : Burgers vectors and line orientations of the dislocations in the (0001) basal plane and in the (0110) prismatic plane

Dislocation		**b**	**t**
in (0001)	screw	a/3 $[2\bar{1}\bar{1}0]$	$[2\bar{1}\bar{1}0]$
	edge		$[01\bar{1}0]$
in $(01\bar{1}0)$	edge	a/3 $[2\bar{1}\bar{1}0]$	[0001]
	edge	a [0001]	$[2\bar{1}\bar{1}0]$
	screw	a [0001]	[0001]

III- Results and discussion

III-1) Influence of the metal anisotropy on the interaction energy ΔE

Figure 1 gives an example of the evolution of ΔE with the misorientation angle around a given axis for a given dislocation. This evolution is similar for the grain boudaries around [11$\bar{2}$0] and [1100] whatever the dislocation characteristics.

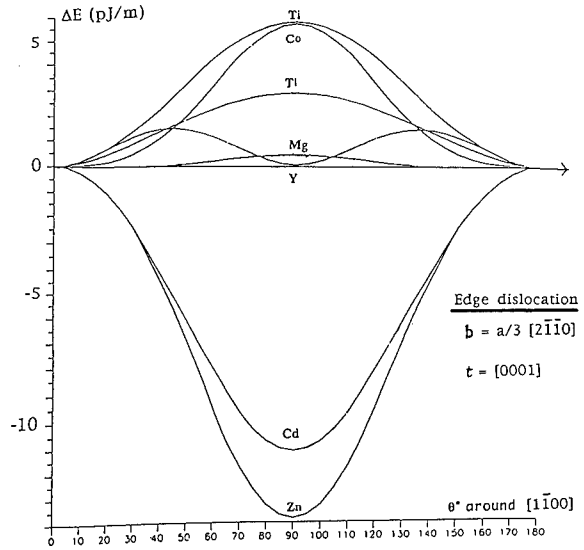

Figure 1 : Evolution, for various metals, of ΔE (in pJ.m^{-1}) in function of θ, the misorientation angle around [1100], for an edge dislocation with ***b*** *= a/3 [2$\bar{1}\bar{1}$0] and* ***t*** *= [0001].*

The curves display a maximum (or minimum) for θ = 90° in agreement with the twofold symmetry of the two misorientation axes.

As previously found for BCC and FCC metals[7,8], the interaction energy is positive or negative according to the sign of the anisotropy factor H. Furthermore, its magnitude increases with the absolute value of H.

III-2) Influence of the geometry on the interaction energy ΔE

The first obvious result is the zero value of ΔE for all the investigated dislocations in any hexagonal metal when the two crystals are rotated around [0001]. This "isotropic" behaviour has two types of explanations :
- If the dislocation Burgers vector and line direction are both in the basal plane of crystal I, they are maintained in the basal plane of crystal II by rotation around the c-axis and then the absence of image force is due to an intrinsic elastic property of hexagonal materials i.e. their elastic isotropy in the basal plane.
- If the dislocation belongs to the prismatic plane, its Burgers vector and/or its dislocation line are parallel to the sixfold symmetry axis, then crystallographic considerations explain the absence of image force. This result is similar to those obtained in the cases of cubic materials for t or b // <100> or to< 111> [7,8].

The evolutions of the interaction energy between one dislocation and any grain boundary around [11$\bar{2}$0] are given in function of the misorientation angle θ in the case of Zn (Fig. 2). When the Burgers vector of the dislocation is equal to a[0001], ΔE is always positive for the edge dislocation and it is only positive for the misorientation angles between 60 and 120°C in the case of the screw dislocation (Fig. 2a). We note that the negative values of ΔE for θ = 0 - 60° and 120 -180° are very small. For the dislocations with the most common vector b = a/3[2$\bar{1}\bar{1}$0], ΔE is always negative indicating an attractive effect of the grain boundary on the

dislocations (Fig. 2b). The curves obtained for the same dislocations in the cases of grain boundaries around [1$\bar{1}$00] in Zn and Cd are similar to those of figure 2. The sign of the interaction energy is inversed for metal with a positive value of H. Then and in particular for Co and Ti, the most common dislocations with b = a/3[2$\bar{1}\bar{1}$0] are repelled from all the grain boundaries around [11$\bar{2}$0] and[1$\bar{1}$00].

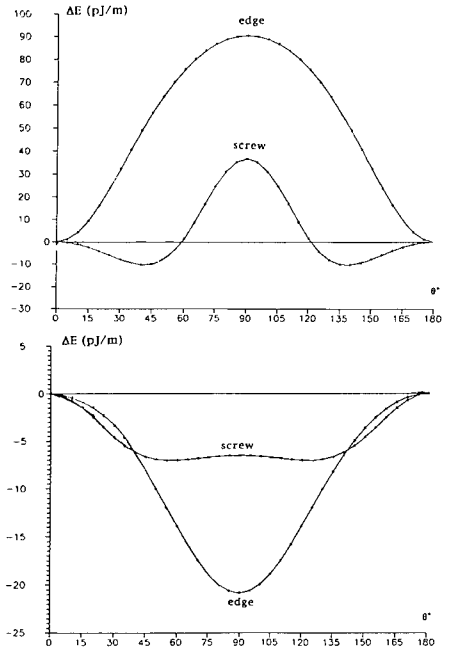

Figure 2 : Evolution of ΔE for an edge and a screw dislocations in the (01$\bar{1}$0)prismatic plane and near grain boundaries around[11$\bar{2}$0] in function of the misorientation θ:
*(a) **b** = a [0001]*
*(b) **b** = a/3[2$\bar{1}\bar{1}$0]*

Conclusion

The magnitude of the image force may become very important as the dislocation approaches the grain boundary. The effect of the image force may be felt up to a limiting distance from the grain boundary, estimated from the comparison between the image force and the friction force, which can reach 100 to 1000 b at room temperature [7,8]. Thus, the image force must not be neglected when considering the interaction between a dislocation and a grain boundary.

Aknowledgements : this work was supported by the European Contract CIPA CT 93 0112

References

1 - J. Gemperlova and U. Saxl, Czech. J. Phys., B 18 (1968) 1085.
2 - D. Barnett and J. Lothe, J. Phys. F 4 (1974) 1618.
3 - J. Lothe, V.L. Indenbom, V.A. Chamrov, Phys. Stat. Sol. 111 (1982) 671.
4 - A.Y. Belov, V.A. Chamrov, V. Indenbom and J. Lothe, Phys. Stat. Sol., 119 (1983) 565.
5 - J. Gemperlova, Phys. Stat. Sol. 30 (1968)261.
6 - O. Khalfallah, M. Condat, L. Priester and H.O.K. Kirchner, Phil. Mag., A 61 (1990) 291.
7 - O. Khalfallah, M. Condat and L. Priester, Phil. Mag. A 67 (1993) 231.
8 - L. Priester and O. Khalfallah, Phil. Mag.A 69 (1994) 471.
9 - H.O.K.Kirchner and J. Lothe, Phil. Mag. A56 (1987) 583.
10 - M. Condat and H.O.K. Kirchner, Phys. Stat. Sol. (b) 144 (1987) 137.

Materials Science Forum Vols. 294-296 (1999) pp. 693-696

Fatigue Crack Growth Across the Interphase Boundaries in Two-Phase Bicrystals

T. Wada and S. Hashimoto

Department of Engineering Physics and Mechanics, Faculty of Engineering, Kyoto University, Kyoto 606-8501, Japan

Keywords: Fatigue Crack Growth Rate, Transgranular Fatigue Crack, Two-Phase Stainless Steel, Bicrystal, Interphase Boundary, Elastic Incompatibility, Slip Transfer

Abstract—Effect of interphase boundaries (IBs) on transgranular fatigue crack growth was examined paying special attention to IB structures, slip behaviors near a crack tip, dislocation transfer across IBs and strain incompatibilities at IBs. Fatigue crack propagation tests were carried out at room temperature in air by employing two kinds of two-phase (α/γ) stainless steel bicrystals; one is elastically compatible and the other is incompatible. It was found that the fatigue crack growth rates, da/dN, changed complicatedly as the cracks grew and the changes in da/dN were strongly influenced by the direction of crack growth across IBs. Crack arrest at IBs occurred on condition that the cracks propagated from the softer γ-phase into the harder α-phase or dislocation transferring across the IBs was restrained due to the crystallographic orientation of crystals. In the incompatible bicrystal, not only deceleration but also acceleration of the crack growth was recognized as the crack approached to the IB. This interesting phenomenon was demonstrated by an analytical calculation of the stress fluctuation owing to the elastic incompatibility at the IB.

Introduction

Fatigue cracks usually propagate in complicated manners since the cracks are affected by various microstructures along their passes. Especially grain boundaries (GBs) have a considerable influence on fatigue crack growth not only intergranularly but also transgranularly. They can act as obstacles to crack transfer as is evidently shown by the fatigue resistance of polycrystals. Some of bicrystal studies [1-5] revealed that a retardation of crack growth at a GB was affected by various crystallographic characteristics, e.g., GB structures, the slip behavior near a crack tip, slip transfer across a GB, crack branching near a GB, and so on. By using pseudosymmetric aluminum bicrystals, Li [1] identified crack branching and splitting in the GB affected zones with deceleration at the GBs and pointed out that the secondary slip activation ahead of crack tips played an important role in increasing crack opening displacement. From the viewpoint of coincidence site lattice (CSL) conceptions, Vinogradov et al. [3-5] examined the fatigue crack behavior in compact tension shaped copper bicrystals containing the Σ3(111), Σ9(221), Σ41(338) or Random [110] tilt boundaries and revealed that a blockage effect of the GBs against crack growth were significantly relevant to the crystallographic orientation relationships.

Several studies have been conducted on interaction between GBs and transgranular crack growth in one-phase bicrystals, whereas there is a great lack of investigation about IBs in two-phase bicrystals. When a crack propagates through an IB between a soft and a hard-phase crystal, the degree of dislocation transfer across them is expected to be more important factor controlling the crack growth rate. The authors have reported the aspects of fatigue crack initiation at the IBs in two-phase (α/γ) stainless steel bicrystals [6]. It was indicated that the elastic incompatibility gave rise to intensive activation of a slip system adjacent to the IB, so that a fatigue crack initiated along the slip system and the fatigue strength of the bicrystal was inferior to that of the component single crystal. In the case of fatigue crack propagation in two-phase bicrystals it is also expected that stress fluctuation due to the strain incompatibilities at the IBs would be of importance and affect change in da/dN near the IBs. The aim of the present work is to examine the physical mechanism responsible for variation of da/dN with crack propagation across IBs by using two-phase (α/γ) stainless steel bicrystals.

Experimental

Two types of bicrystals, consisting of ferritic (α-Fe30Cr) and austenitic (γ-Fe15Cr15Ni) single crystals, were produced by a diffusion bonding method. In the first type of bicrystal, Specimen A, the elastic compatibility is satisfactory fulfilled. Since the primary slip systems in the component crystals are almost parallel to each other, a high degree of the slip continuity across the IB can be expected (see Fig.1). The specimens notched in the α-phase and the γ-phase of the bicrystal are termed Specimens A-α and A-γ, respectively. Specimen A-α was used to investigate the crack transfer phenomenon from α- to γ-phase, and Specimen A-γ vice versa. Since the second type of bicrystal, Specimen B, is elastically incompatible, elastic stresses must be fluctuated near the IB. In contrast to Specimen A, due to the crystallographic characteristics in Specimen B it would be difficult for lattice dislocations to penetrate into the neighboring crystal. The two specimens, Specimens B-α and B-γ, were cut and shaped from Specimen B. The width and thickness of the four specimens are 7mm and 0.8mm, respectively. The IBs are parallel to the stress axis and are located in the middle along the width of specimens. Fatigue crack propagation tests were performed at room temperature in air at a frequency of 10Hz. The applied maximum load was 3.8×10^2 N and the minimum to maximum load ratio, R, was 0.1.

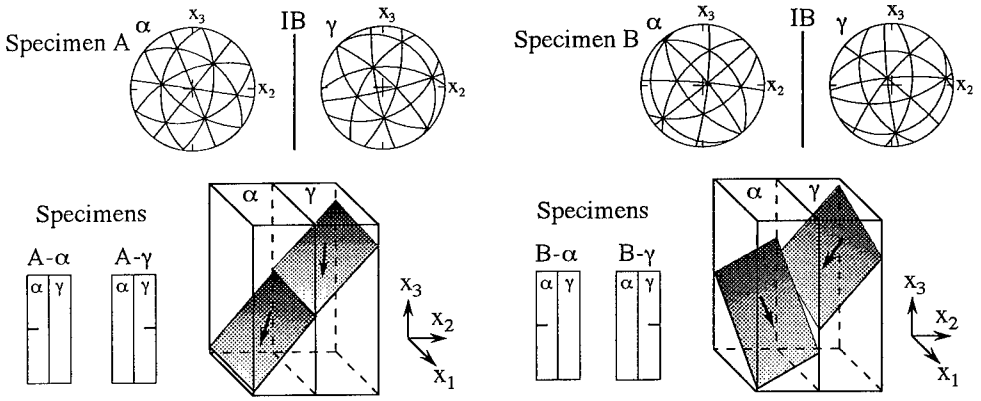

Fig.1. Stereographic projections of the component crystals and schematic illustration of the primary slip systems in Specimens A and B.

Results and Discussion

Figure 2 shows the fatigue crack growth rates, da/dN, vs. the crack length, a, of the four specimens tested. It is clearly shown that the changes in da/dN are complicated and are different depending on the direction of crack growth across the IBs. For all specimens it is thought that the slopes, n, at the *a*-region and *b*-region, as indicated in Fig.2, exhibit the inherent fatigue properties of the component single crystals, since these regions are so far from the IBs that are hardly affected by the IBs. It is recognized that the values of n for the α-phase or the γ-phase in Specimens A-α are equal to those in Specimen A-γ, and also in Specimen B.

In the case of Specimens A-γ, B-α and B-γ, the cracks are arrested at the IBs, as denoted by *c*-region in Fig.2. It is thought that these crack arrests occurred due to the prevention of dislocation emission from the crack tips especially near the IBs which play as obstacles for dislocation movement. In contrast to these specimens, no crack arrest occurred in Specimen A-α, in which there is no *c*-region in the da/dN-a plots. This means that the IB did not act as the barrier to the crack propagation.

The slip behaviors ahead of the crack tips near the IBs in the four specimens are shown in Fig.3. It should be noted that no slip continuities across the IBs are observed in Specimens A-γ, B-α and B-γ. On the other hand a high degree of slip transfer from the α-phase to the γ-phase is observed in Specimen A-α. This observation shows that the degrees of slip continuity must be particularly associated with the crack arrest behaviors at the IBs. In Specimen B, the difficulty of the lattice

dislocations in passing through the IB is attributed to the orientation relationship of the component single crystals. There are no common slip systems which have the same crystallographic orientation. On the contrary the crystallographic orientation of Specimen A is suitable for the primary dislocation transferring across the IB. This property seems to be inconsistent with the crack arrest occurred in Specimen A-γ, while consistent with the crack behavior in Specimen A-α. The reasons for this distinction are that it is severe for the dislocations to transfer from the γ-phase to the α-phase but easy from the α-phase to the γ-phase, since the α-phase is much harder than the γ-phase in the present specimens. This interpretation is confirmed by the slip behaviors at the IBs, as shown in Fig.3.

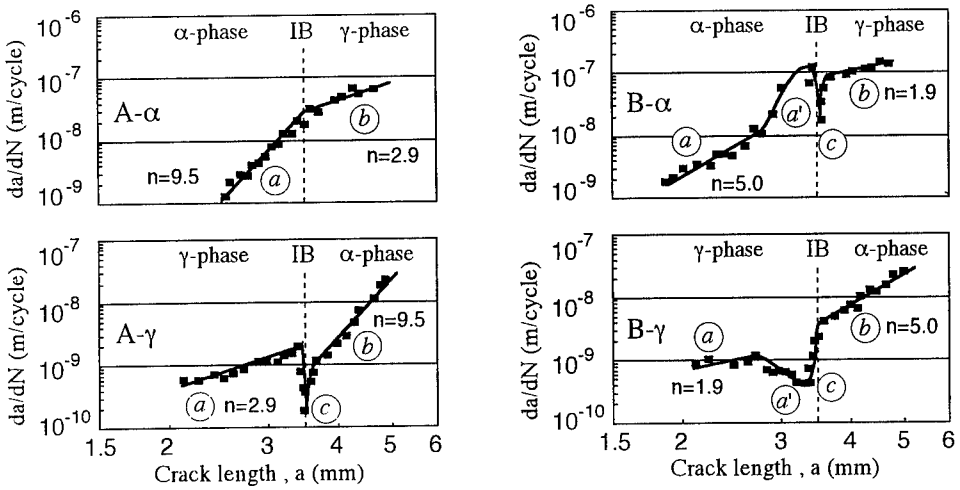

Fig.2. Correlation of the fatigue crack growth rates, da/dN, with the crack length, a, in the four specimens tested. The slopes, n, of the log da/dN - log a plots far from the IBs have definite values and are intrinsic for the component single crystals in each bicrystal.

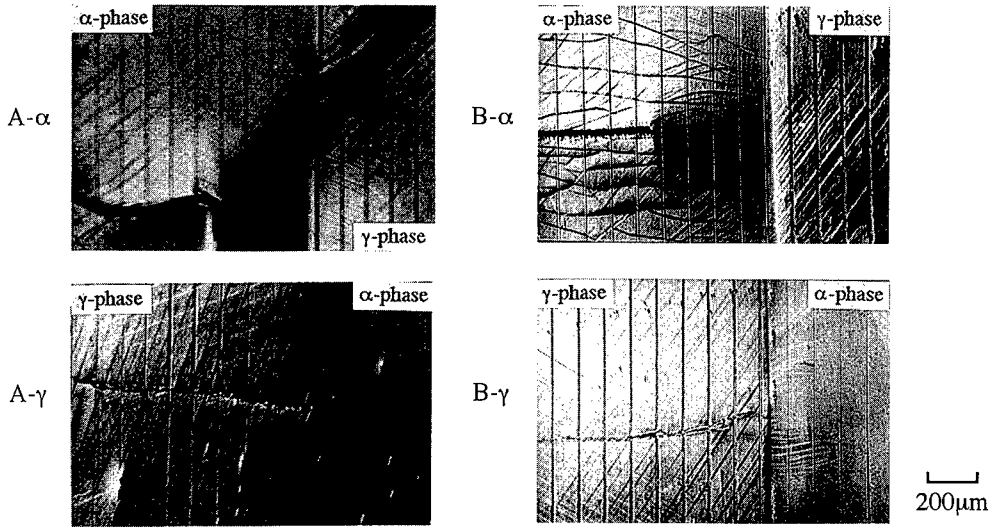

Fig.3. Slip behaviors ahead of the crack tips and the fatigue crack approaching to the IBs in Specimens A-α, A-γ, B-α and B-γ. Only in Specimen A-α the primary dislocations emitted from the crack tip can smoothly transfer into the neighboring grain.

For Specimen B, *a'*-region, where the slope of the crack growth rates are depart from those for *a*-region, exists as shown in Fig.2. As the crack approaches to the IB, acceleration or deceleration of the crack growth takes place in Specimens B-α or B-γ, respectively. However this effect is not observed in Specimen A which is elastically compatible. Therefore this effect is believed to be caused by the elastic incompatibility of Specimen B.

Let us consider a two-phase (α/γ) bicrystal specimen with the planar IB on which the $x_1x_2x_3$ coordinate system is fixed (Fig.1). The x_2-axis and the x_3-axis are identified to the IB normal and the loading direction, respectively. According to [7], the elastic stresses, $\sigma_{ij}^{(\kappa)}$, in each crystal under the applied stress, σ^a, can be expressed as

$$\sigma_{ij}^{(\kappa)}=\sigma^a\delta_{3i}\delta_{3j}+\sigma_{ij}^{b(\kappa)},\ \kappa=\alpha,\ \gamma, \qquad \text{Eq.1}$$

where $\sigma_{ij}^{b(\kappa)}$ are the elastic incompatibility stresses and δ_{ij} is the Kronecker's delta. Here $\sigma_{ij}^{b(\kappa)}$ are assumed to be uniform in each crystal and are determined from the compatibility requirements [8] and the equilibrium condition [6,7]. The analytically calculated values of $\sigma_{33}^{(\kappa)}$ are denoted in Table 1. In Specimen B the stress arises in the α-phase and relaxes in the γ-phase, although there are no such effects in Specimen A. Generally the mode I stress intensity factor, K_I, is proportional to the axial stress, $\sigma_{33}^{(\kappa)}$, and is the dominant factor controlling the crack growth rate, da/dN. Therefore this results of the stress calculation indicate that the increase and the decrease of $\sigma_{33}^{(\kappa)}$ in Specimen B cause the acceleration of the crack growth near the IB in the α-phase and the deceleration in the γ-phase, respectively.

Table 1. Stress distributions in the bicrystals which are calculated analytically.

	Specimen A		Specimen B	
	$\kappa=\alpha$	$\kappa=\gamma$	$\kappa=\alpha$	$\kappa=\gamma$
$\sigma_{33}^{(\kappa)}$	$1.02\sigma^a$	$0.98\sigma^a$	$1.30\sigma^a$	$0.70\sigma^a$

Conclusions

The crack growth behaviors across the IBs in the elastically compatible or incompatible bicrystals were investigated and the following conclusions were derived. Impediment of dislocation emitting from the crack tips near the IBs caused crack arrests at the IBs, while a high degree of slip transfer into the neighboring grain induced no crack arrest at the IB. By the analytical calculation of the elastic incompatibility stress in the incompatible bicrystal, it was found that this long-range stress assisted or impeded the crack growth near the IB. It was revealed that the behaviors of dislocation movement at the crack tips and the stress fluctuation near the IBs due to the incompatibility are the major factors controlling the complicated crack growth manner adjacent to the IBs.

References

[1] C.Li, Metall. Trans. A, 23 (1992), p.3293.
[2] C.Li, P.Zhang and T.Zhang, Mat. Sci. Eng., A183 (1994), p.23.
[3] A.Vinogradov, S.Hashimoto and S.Miura, Scripta Metall., 32 (1995), p.427.
[4] A.Vinogradov, S.Hashimoto and S.Miura, Z. Metalkd., 86 (1995), p.502.
[5] S.Hashimoto and A.Vinogradov, Interface Science, 4 (1997), p.347.
[6] T.Wada, H.Yamada, S.Hashimoto and S.Miura, Interface Science and Materials Interconnection, Proceedings of JIMIS-8 (1996), p.511.
[7] P.Peralta, L.Llanes, J.Bassani and C.Laird, Phill. Mag., A 70 (1994), p.219.
[8] J.D.Livingston and B.Chalmers, Acta Metall. 5 (1957), p.322.

Fax number: +81-75-753-5256
E-mail address: hashimoto@kues.kyoto-u.ac.jp

Materials Science Forum Vols. 294-296 (1999) pp. 697-700

Dynamic Properties of the Grain Boundary Core and Adjacent Lattice Regions in Polycrystals of 3d, 4d and 5d Metals

S.M. Klotsman and V.N. Kaigorodov

Institute of Metal Physics, Urals Division of Russian Academy of Sciences,
RU-620219 Ekaterinburg, RF

Keywords: Grain Boundary Core, Dynamic Properties, Intercrystalline Diffusion, Metals

Abstract.

High-temperature values of the Debye temperature (representing a dynamic parameter) of the grain boundary core and adjacent lattice regions were determined for polycrystals of transition and noble metals. The Debye temperature was almost twice as low as in the regular lattice if "vacancy–interstitial impurity" complexes did not segregate in the polycrystal.

I. Introduction.

Until recently it has been impossible to examine dynamic properties of the grain boundary core in normal polycrystals because it occupied a relatively small volume. A new method [1, 2] for the study of the structure and the set of physical properties of the grain boundary core allowed deriving information about dynamic properties of the grain boundary core and adjacent two-dimensional regions of the lattice in any polycrystals, including bicrystals. This paper reports results of our investigations into dynamic properties of the grain boundary core in ordinary polycrystals of cubic metals.

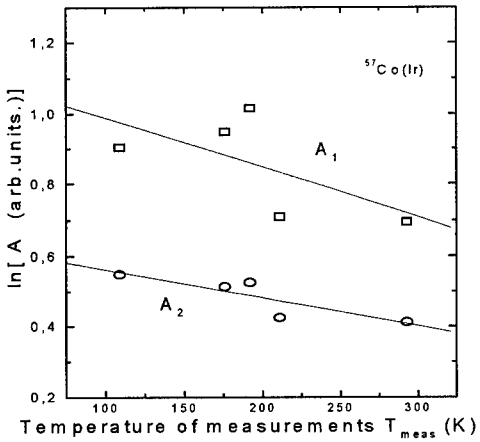

Fig. 1
Temperature dependencies of the areas of NGRS components of ^{57}Co(Ir) system annealed at 953K

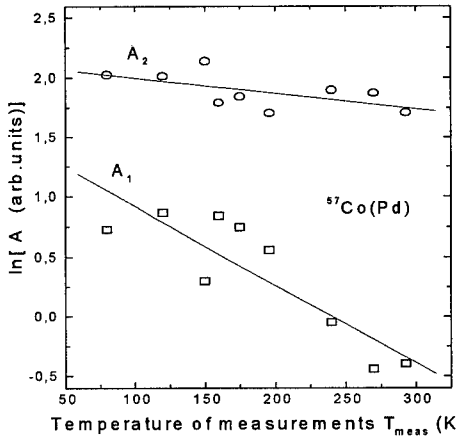

Fig.2
Temperature dependencies of the areas of NGRS components of ^{57}Co(Pd) system annealed at 723K

II. Results and Discussion.

The materials, the techniques of their preparation and the measurement method used have been described elsewhere [3].

Emission nuclear gamma-resonance spectra of polycrystals were shown [1-3] to have two components. The area of the component-1 of these nuclear gamma-resonance spectra decreases only at the temperatures of «intrinsic» interval. This component-1 is due to atomic probes localized in the grain boundary core. The area of the component-2 of the nuclear gamma-resonance spectra of the polycrystals increases only at the temperatures of «intrinsic» interval [3]. This component-2 is caused by atomic probes localized outside the grain boundary core.

Figures 1 and 2 exemplify dependencies of the areas A_1 and A_2 of these two components. The area of the nuclear gamma-resonance spectrum component is proportional to the recoil-free fraction f_i of the14.4 keV gamma line emitted by the atomic probes populating corresponding i-th states in the inter-crystallite diffusion zone. The slopes of the straight lines $\partial \ln A_i/\partial T_{meas} \equiv \partial \ln f_i/\partial T_{meas}$ were calculated for the nuclear γ-resonance measurement temperature $T_{meas} \geq \theta/2$. These values were used to determine the moment $\mu_{AP}(-2)$ of the function of phonon density of the atomic probes states [4], which in the case of the cubic lattice have the form:

Таб.1. Characteristic temperatures T/T_τ of annealing and Debye temperatures θ of bulk and of two regions in the intercrystalline diffusion zone of polycrystalline metals annealed in the «intrinsic» limit.

Solvents	Rh	Pd	Ta	W	Ir	Pt
T/T_τ	—	1.0	0.9	0.93	—	0.85
θ_{vol}, K	430± 30	370± 30	410	400	460	440± 20
$(\theta_2)_{intr}$, K	390± 70	320± 50	420± 30	460± 40	410± 10	460± 50
$(\theta_1)_{intr}$, K	250± 20	140± 10	240	270± 30	310± 50	300± 90

T - temperature of diffusion annealing after which was measured the dependence $\ln A(T_{измер})$, T_τ - temperature at which component-1 of NGR spectra dissapear

$$\partial \ln A_i/\partial T_{meas} = (k/\kappa m_{AP})[\,\mu_{AP}(-2) + (\hbar/kT)^2/12 - (\hbar/kT)^4 \mu_{AP}(-2)/720 + \ldots]\,. \qquad (1)$$

Here

$$\mu_{AP}(n) = \int_0^\infty \omega^n G_{AP}(\omega) d\omega, \qquad \mu_{AP}(0) = 1, \qquad (2)$$

$\mu_{AP}(n)$ - moments of the phonon density of states function $G_{AP}(\omega)$ for cubic lattice with atomic probe, κ is the wave vector of the resonance gamma radiation, m_{AP} is the atomic probe mass, and k and $\hbar$ denote the Boltzmann and Planck constants, respectively.
In the Debye model [4]

$$\mu_{AP}(-2) = 3(\hbar/k)^2[\theta_{AP}(-2)]^{-2}\,, \qquad (3)$$

where $\theta_{AP}(-2)$ is the high-temperature Debye temperature measured using atomic probe.

Force constants F_i at the atomic probe location may be determined from the relationship [4]:

$$[\mu_{AP}(-2)/\,\mu_{solv}(-2)]_i = (m_{AP}/m_{solv})_i \times [1 - 0.675(1 - F_{solv}/F_{AP})_i]. \qquad (4)$$

However, the expression (4) may be used only if one knows the value of $[\mu_{solv}(-2)]$. This quantity in the volume is determined from thermodynamic data (measured specific heat capacity of pure solvent) or from neutron scattering [4]. Unfortunately, similar data for the GB core have been unavailable.

For calculating effective dynamic characteristics of grain boundary core we use in the next the expression based on the Einshtein-Debye model [4]:

$$\partial \ln A_i/\partial T_{meas} = -\,135.63/\theta_i^2\,. \qquad (5)$$

II.2. Relation between dynamic properties of the grain boundary core and the crystallite volume in the "intrinsic" temperature interval.

The values of the "high-temperature" Debye temperature measured by the method described above are presented in Tab.1. One may see that in 4d (Rh, Pd) and 5d (Ta, W, Ir, Pt, Au) metals:

$$(\theta_{AP})_1 \cong 0.6(\theta_{AP})_2 \qquad (6)$$

is fulfilled in the "intrinsic" interval (at the annealing temperature $T \cong T_\tau$ when interstitial impurity segregations disappear at grain boundaries). This result is a consequence of a low symmetry and a large interatomic spacing in the structure of the grain boundary core compared to similar parameters of a regular lattice.

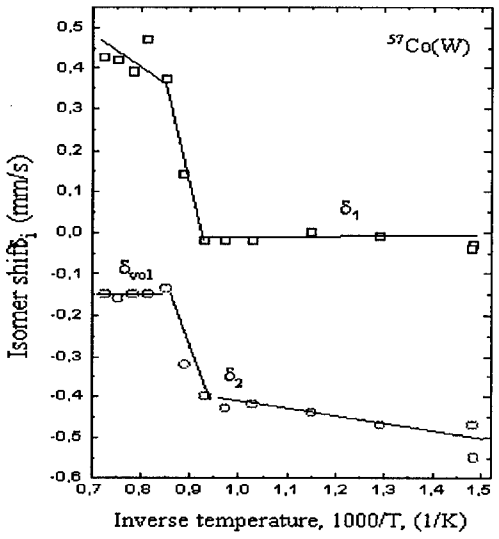

Fig.3
Temperature dependencies of the isomer shifts of the two NGRS components of ^{57}Co(W) system

II.3. Dynamic properties of the grain boundary core and the pumping zone in the "extrinsic" interval.

When atomic probes were introduced in polycrystals at low temperatures, outside the "intrinsic" interval, the grain boundary core composition changed considerably thanks to segregations of interstitial impurities. By way of example, Fig. 3 shows temperature dependences of isomer shifts of both components of nuclear gamma-resonance spectra of ^{57}Co in polycrystalline W. These isomer shifts are due to the temperature dependence of the composition of the atomic probe localization regions. The concentration of interstitial impurities in the segregation zone was shown [5] to change up to 2 at. %.

At temperatures of the interstitial impurity segregation the Debye temperature of the grain boundary core $(\theta_1)_{extrin}$ was almost the same as the "intrinsic" $(\theta_1)_{intrin}$ in W only (Table 2). These complexes decreased the Debye temperature (made interatomic interactions in the grain boundary core weaker) in Ir and Pt and increased the Debye temperature in Pd.

Nearly the same changes in the composition, as those detected in the grain boundary core, caused a considerable drop of the Debye temperature $(\theta_2)_{extr}$ outside the grain boundary core in the lattice regions adjacent to grain boundaries in tungsten, iridium and platinum. In Pd the Debye temperature θ_2 remained unchanged at all temperatures. A stationary region with a high concentration of

Таб.2. Characteristic temperatures T/T_τ of annealing and Debye temperatures θ of two regions in the intercrystalline diffusion zone of polycrystalline metals annealed in the «intrinsic» and «extrinsic» temperature regions.

Solvents	Pd	W	Ir	Pt	Au
T / T_τ	0.57	0.49	—	0.5	0.46
$(\theta_1)_{intr}$, K	140±10	270±30	310±50	300±90	—
$(\theta_1)_{extr}$, K	200±20	250±30	170±40	230±10	330±20
$(\theta_2)_{extr}$, K	290±50	260±30	150±40	290±20	290±30
$(\theta_2)_{intr}$, K	320±50	460±40	410±10	460±50	—

T - temperature of diffusion annealing after which was measured the dependence $\ln A(T_{meas})$, T_τ - temperature at which component-1 of NGR spectra dissapear

point defects (SRHCPD) was formed outside the grain boundary core at low temperatures of intercrystalline diffusion. In the SRHCPD the concentration of vacancies bound into "vacancy–interstitial impurity" complexes was many orders of magnitude higher than the equilibrium concentration [5]. In the "extrinsic" temperature interval of intercrystalline diffusion the Debye temperature of the SRHCPD was equal to the Debye temperature of the grain boundary core:

$$(\theta_1)_{extr.int.} \cong (\theta_2)_{extr.int.}. \quad (7)$$

This result extends to all cubic transition metals with FCC and BCC lattices. One may think therefore that it is due to vacancies bound into "vacancy–interstitial impurity" complexes whose concentration at the given homologous temperatures is 8 to 10 orders of magnitude higher than the equilibrium concentration in the lattice.

II.4. Dynamic properties of the grain boundary core and the crystallite volume in nanocrystalline palladium.

Tab.3. Homologous temperatures T_{diff}/T_m of annealing and Debye temperatures θ of two regions in the intercrystalline diffusion zone of ordinary poly- and nanocrysalline Pd annealed in the «extrinsic» temperature region.

Solvents	Poly-Pd	Nano-Pd
T_{diff}/T_m	0.24	0.25
θ_1 (K)	200±20	235±20
θ_2 (K)	290±50	200±20

Table 3 presents main findings on the dynamic properties of the grain boundary core and the crystallite volume in nanocrystalline palladium [6]. Samples of nanocrystalline palladium were kindly supplied by Prof. H. Gleiter.

The main result ensuing from our study of nanocrystalline palladium is the coincidence of the dynamic parameters of the grain boundary core in ordinary and nanocrystalline palladium. This means that symmetry elements and characteristics of the interatomic spacing in the structure of the grain boundary core are similar in ordinary and nanocrystalline palladium.

References.

[1]. S.M. Klotsman, Sov. Phys. Uspech., **33(1),** (1990), p.55.
[2]. V.N. Kaigorodov, S.M. Klotsman, Phys.Rev.B, **49**,(1994), p.9374; *ibid.*, p.9387; *ibid.*, p.9395.
[3]. V.N.Kaigorodov, S.M. Klotsman, Equilibrium sites occupied in the grain boundary core during intercrystalline diffusion of ^{57}Co in metal polycrystals, **Report on *iib-98***.
[4]. J.M. Grow, D.G. Howard, R.H. Nussbaum, M.Takeo, Phys.Rev., **17(1),** (1978), p.15.
[5]. S.M. Klotsman, M.I. Kurkin, V.N. Kaigorodov, V.V. Dyakin, Phys. Metals & Metallogr., **85(2),** (1998), p.135; ibid., p.212; ibid., p.342.
[6]. V.N. Kaigorodov, S.M. Klotsman, Phys. Rev. B., **46(10),** (1992), p.5928.

Correspondence: **e-mail:** klotsman @ imp.uran.ru

Materials Science Forum Vols. 294-296 (1999) pp. 701-706

Grain Boundary Effects in Nanocrystalline Copper

N.A. Krasilnikov[1] and G.I. Raab[2]

[1] Ulyanovsk State University, ul. L. Tolstoy, 42, RU-432700, Ulyanovsk, Russia

[2] Institute of Physics of Advanced Materials, Ufa State Aviation Technical University, ul. K. Marxa, 12, RU-450000 Ufa, Russia

Keywords: Nanostructured Material, Ball-Milled Powder, Severe Plastic Deformation, Grain Boundaries, Non-Equilibrium State of Material

Abstract. The results of investigations of nanostructured copper with a mean grain size of 75 nm processed by a new method of severe plastic deformation via consolidation of ball-milled powders are given in the paper.

The investigations show that the processed copper has a rather stable nanostructure during annealing and elevated strength properties. A significant influence of deformation temperature on a growth of grain size and a decrease in values of internal stresses was also revealed. Evidently, this is connected with realization of recovery processes on grain boundaries and beginning of recrystallization processes already at low homological temperatures.

The obtained results show that a state of grain boundaries in nanostructured copper is a very important parameter determining properties of nanostructured materials. To explain the experimental data, the structural model of R.Z. Valiev was taken as a basis. According to this model a structure of nanostructured material consists of ultra fine elastically aligned grains characterized by high density of grain boundary dislocations and disclinations. With all that, during annealing a recovery of these defects occurs.

Introduction. Grain boundaries are the most important structural component of metals and alloys which determines the properties of many materials. Investigations show that long range areas of grain boundaries and their state influence strength, plasticity and deformation behaviour of materials as well as their thermal stability of structure and properties [1-3].

In recent years nanostructured materials and their studies have been in the focus of much interest due to rapid development of techniques of their processing and especially methods based on application of severe plastic deformation (SPD) [4]. A specific feature of ultra-fine grained (UFG) materials processed by SPD is a non-equilibrium state of grain boundaries and a presence of long range stress fields in their structure which are attributed to the presence of grain boundary defects whose density is determined by a SPD effect. Long range areas and non-equilibrium state of grain boundaries in nanostructured materials influence on significant change of their properties unlike properties of coarse-grained materials.

The present paper presents original results of investigations of nanostructured copper with a mean grain size of 75 nm processed by severe plastic deformation consolidation of ball-milled powder.

Experimental Procedure. The copper powder (99.99%) was used as a starting material. The ball milling was conducted in argon medium for 150 hours according to the procedure described in [5]. Due to such treatment the internal structure of powder particles became nanostructured.

To process bulk nanostructured samples a two stage technological process was developed. The procedure consists of preliminary vacuum consolidation of powders via upsetting and following

severe torsion straining of precompacts produced in a Bridgmen anvil type set [6]. This resulted in fabrication of samples, 20 mm in diameter and 0.5 mm in thick. The density was measured by the Arkhimed's method using analytical balance with an accuracy of ±1%.
Structural investigations were conducted by methods of scanning and transmission electron microscopy using a scanning electron microscope SEM-100U with an accelerating voltage of 30 kV and a transmission electron microscope Jeol-100B with an accelerating voltage of 100 kV. A diffractometer DRON-4M was used for X-ray structural investigations. The method of harmonic analysis was used to determine sizes of coherent scattering areas and microstresses in the samples under study [7].
The microhardness Hv was determined by the Vicker's method on device PMT-3 under a load of 2 H. The error of measurements was ±5%. Samples were annealed during 15 min in a vacuum furnace and in air. The temperature was hold with an accuracy of ±5% in vacuum and an accuracy of ±3% in air. The measurements of Hv after annealing was made after removal of an oxidized layer.

Experimental Results and Discussion. A two stage technological process for fabrication of bulk samples of high density out of nanostructured copper was developed. The procedure consists of preliminary vacuum consolidation at 500°C and following SPD of the processed precompacts at 150°C in a Bridgemen anvil type set.
The X-ray diffraction pattern of copper powder imposed to ball milling (Fig.1a) is characterised by a set of X-ray peaks typical of pure metals with f.c.c. lattice. However, opposite to the coarse-grained state the X-ray peaks of the nanopowder are significantly widened that testifies a small size of coherent scattering areas D=28 nm and high internal residual microdistortions of a crystalline lattice. The data of X-ray structural analysis shown in Table 1.

Data of X-ray structural investigations of nanostructured copper. **Table 1.**

Sample	initial powder	precompact 500°C-(p/c)	p/c + $SPD_{150°C}$	p/c + $SPD_{350°C}$	p/c+$SPD_{150°C}$ +anneal.750°C
size of coherent scattering areas D, nm	28±3	65±3	75±3	135±3	125±3
microdistortions of crystalline lattice **e**,%	0,12±0,01	0,17±0,01	0,13±0,01	0,06±0,01	0,06±0,01

Preliminary vacuum consolidation of powders at a temperature of 500°C leads to an increase in maxiumum and integral intensities of X-ray peaks (Fig.1b) as compared to the corresponding values of peak intensities for the initial powder. This is attributed to the increase in sizes of coherent scattering areas to 65 nm.
Severe torsion straining of precompacts under high pressure at a temperature of 150°C leads to growth of coherent scattering areas to a value of 75 nm, an increase in the density of samples from 91 to 98% from the theoretical value and a significant growth of maximum and integral intensities of X-ray peaks (111) (Fig.1b). A similar situation has already been observed earlier and it is connected with formation of axial crystallographic texture in a sample material during SPD.
Note the strong influence of SPD temperature on a value of coherent scattering areas and values of internal stresses in the sample. The conducted investigations showed that with decreasing temperature of SPD a size of coherent scattering areas in nanostructured samples becomes smaller (Table 1) and microhardness becomes higher (Fig.2). An increase in the tempertaure of SPD to

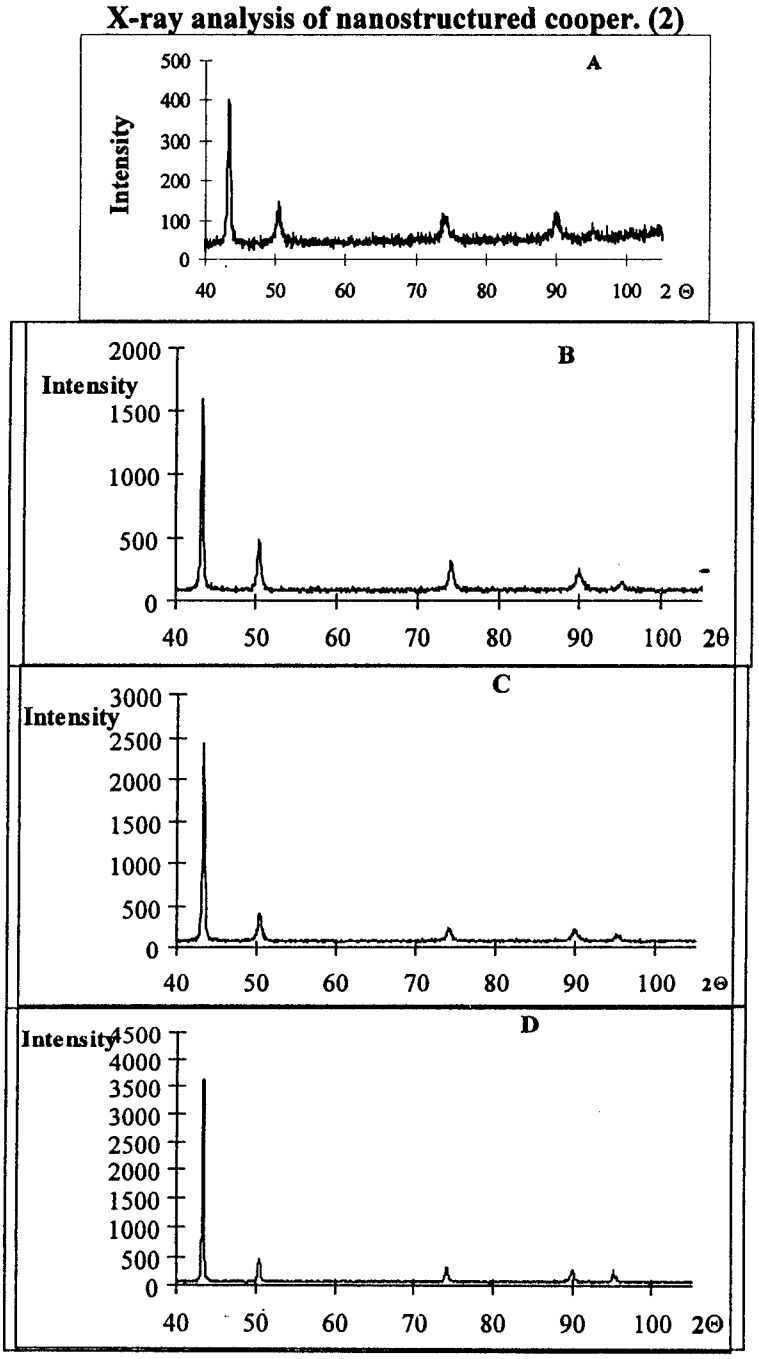

Fig.1. **(a) initial powder; (b) precompact; (c) SPDC at 150°C; (d) SPDC at 150°C and additional annealing at 750 °C.**

350°C leads to a sharp growth of coherent scattering areas to 135 nm and a significant decrease of internal stresses. Apparently, with increasing temperature the intense deformation stimulates dynamic recrystallization processes which lead to a grain growth and a drop in microhardness.

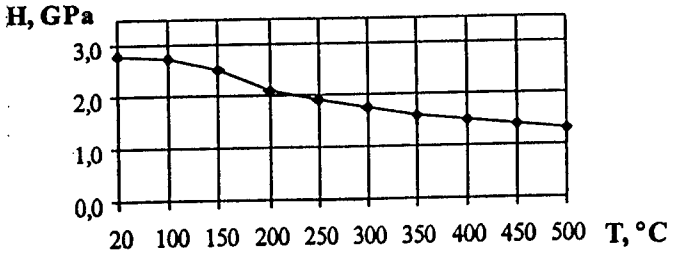

Fig.2. Dependence of microhardness on SPD temperature for a copper sample.

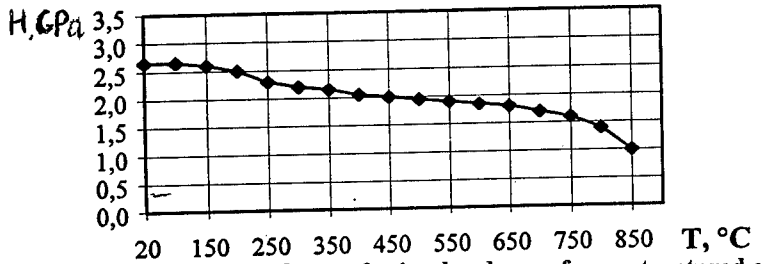

Fig.3. Temperature dependence of microhardness of nanostructured copper.

Annealing at 750°C of the sample imposed to SPD at 150°C leads to almost the same increase in sizes of coherent scattering of areas as deformation at 350°C (Table 1). The observed significant growth of X-ray peak (111) intensity (Fig.1d) can be connected both with the increase in sizes of coherent scattering areas and the decrease in crystalline lattice microdistortions and the evolution of crystalline texture during annealing.

The investigations of the processed nanostructured copper samples show that their microhardness Hv is equal to 2.6 GPa and uniform by sample diameter and thickness within the measurement error limit. This testifies that in the plane of anvils the deformation of the material is homogeneous. Note that a value of Hv for coarse-grained pure copper is 480 MPa.

The annealing temperature dependence of microhardness of the nanostructured copper samples is shown in Fig.3. At the temperature T=200°C some drop in microhardness to a value of 2.5 GPa is observed. Such a behaviour is typical for samples with ultra fine-grained structure processed by other deformation methods [8,9]. Note the high thermal stability of microhardness which has dropped to a value of 2.0 GPa at a temperature of annealing of 400°C. After annealing at 750°C a value of microhardness becomes equal to 1.6 GPa that exceeds the microhardness of coarse-grained copper by 3 times.

The TEM image of a structure of the copper sample after severe torsion straining at 150°C is shown in Fig.4a. It is seen that the structure of the processed samples is high disperse with a grain size of about 70÷75 nm that fits the data of X-ray structural analysis. The electron diffraction pattern taken from a foil area of 0.5 μm^2 (Fig.4a) presents a large number of reflections arranged in circles that testifies the presence of high angle misorientations of grains. Reflections on the diffraction pattern have significant azimuth spreading that indicates the presence of high internal stresses in the structure.

The structure of the sample after annealing at 400°C is shown in Fig.4b. It is seen that the majority of grains have a size of about 75÷85 nm that only slightly exceeds a size of grains in the sample

subjected to annealing. However, the reflections on the electron pattern from this sample (Fig.4b) are more equiaxed that testifies the increase in internal stresses and the transformation of the material to a more equilibrium state as compared the non-annealed samples.

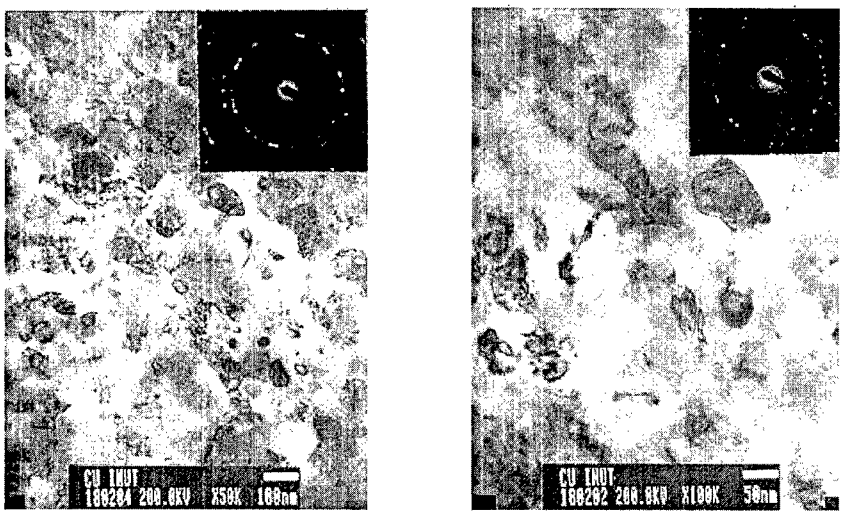

(a) (b)

Fig.4. Structure of the cooper samples observed by TEM: (a)-after SPDC at 150°C; (b)-after additional annealing at 400°C.

The electron microscopic investigations of the material imposed to annealing at 750°C revealed fine ferrite grains with a size of 20 nm the presence of which testifies the presence of iron in the structure of copper. Reflections belonging to b.c.c. lattice are indentified on the electron diffraction pattern taken from an area where ferrite precipitates are present. Most likely this is resulted from ball milled processing of copper powder. At the same time high temperature annealing is responsible for coalescence of iron to crystallites.

According to the developing model [10], material structure after SPD can be presented as combination of elastically aligned grains. High density of grain dislocations and disclinations, which are generators of long range stress field in grain bodies and determine a non-equilibrity of structure, are specific features of their structure. A grain itself does not content dislocations. During the annealing of nanostructured Cu at low temperature there happen a partial annihilation of grain boundary defects, which leads to formation of more regulated grain boundary structure and decrease of internal stresses, and realization of structure recovery nearly without grain growth (fig.4). This process occurs due to transformation of non-equilibrium grain boundaries into more uniform state. A sharp decrease of internal stresses without considerable grain growth at low temperature annealing was revealed for a wide range of materials after SPD [2, 8, 9]. To explain such structural changes, one should consider a of transformation process of grain boundaries, where reconstruction of grain boundary structure is supposed. The latter leads to decrease of grain boundary energy and disappearance of high internal stresses, and is accompanied by a certain grain growth. Obviously, in our case analogous processes in structure occur at annealing of nanostructured Cu. Consequently, the material transforms into more equilibrium state and preserves rather high strength properties. Annealing at temperatures more that 400 °C results in considerable decrease of density of grain boundary defects, re-distribution of internal stresses in grains, and consequently leading to boundary migration and grain growth due to recrystallization process.

Thus, annealing of nanostructured Cu at not high temperatures 0,5 T_m leads to grain boundary structure transformations and decrease of internal stresses in structure, although Cu structure

remains a nanocrystalline one and has high microhardness in the material during such treatment. One of the possible reasons for high stability of the processed nanostructured Cu, probably, is penetration of the tool material (Fe) into the initial Cu powder during ball-milling process.

Conclusion

1. Samples of nanocrystalline copper with high density and a mean grain size of 75 nm were processed by a method of severe plastic deformation consolidation of copper powder after ball milling. The processed nanostructured copper is characterized by high thermal stability of structure and properties which is preserved until a temperature of 750°C.
2. The strong influence of temperature of severe plastic deformation on a growth of grain size and a decrease in internal stresses was revealed. This is evidently connected with realization of recovery processes in grain boundaries and beginning of recrystallization processes during plastic deformation.
3. Specific features of nanostructured copper is a noticeable decrease in strength without grain growth at temperatures to 400°C. This is connected with grain boundary rearrangements occurring almost without migration of grain boundaries and a decrease in internal stresses at these temperatures.

The studies were fulfilled within the frame of Projects RFFI and CRDF. The authors thank Prof.R.Z. Valiev for participation in discussion of results and fruitful comments on conducting investigations.

References.

1. Gleiter H. Materials with ultrafine microstructures. Retrospectives and perspectives, - Nanostructur. Mater., 1992, V.1, p.1-19.
2. Valiev R.Z., Korznikov A.V., Mulyukov R.R. Structure and Properties of Metallic Materials with Submicrocrystalline Structure, - FMM, 1992, No.4, p.70-81.
3. Valiev R.Z. Superplasticity in nanocrystalline metallic materials,- Mater.Sci.Forum, 1997, V.243-245, p.207-216.
4. Ultrafine grained materials produced by severe plastic deformation. Spesial issue. Ed. by R. Z. Valiev. Annales de Chimie - Science des Materiaux, 1996, V.21, p.369-520.
5. Rawers J., Govier D., Doan R. Nitrogen addition to iron powder by mechanical alloying, - Mater.Sci.Eng., 1996, V.A220, p.162-167.
6. Abdulov R.Z., Valiev R.Z., Krasilnikov N.A. Formation of submicrometer-grained structure in magnesium alloy due to high plastic strains, - J.Mater.Sci.Lett. 1990, V.9, p.1445-1448.
7. Alexandrov I.V., Zhang K., Kilmametov A.R., Lu K., Valiev R.Z. The X-ray characterization of the ultrafine-grained Cu processed by defferent methods of severe plastic deformation, - Mater.Sci.Eng., 1997, V.A234-236, p.331-334.
8. Valiev R.Z., Mishra R.S., Mukherjee A.K. The structure of ultra-fine grained nickel produced by severe plastic deformation, - Annales de Chimie - Science des Materiaux 1996., V.21, p.399-404.
9. Gertzman V.Y., Birringer R., Valiev R.Z. Structure and strength of submicrometer-grained copper, - Phys.Stat. Sol. (a), 1995, V.149, p.243-251. 1. Gleiter H. Materials with ultrafine microstructures. Retrospectives and perspectives, - Nanostructur. Mater., 1992, V.1, p.1.
10. Valiev R.Z. Approach to Nanostructed Solids though the Studied of Submicron Grained Policrystals, -Nanostuctured Materials 1995, V6., N1-4, p. 73-82.

Dr.N.A.Krasilnikov, Ulyanovsk State University, ul. L .Tolstoy, 42, 432700, Ulyanovsk, Russia.
Tel: 8-8422-320680, fax: 8-8422-313000, e-mail:nick@sv.uven.ru

Materials Science Forum Vols. 294-296 (1999) pp. 707-710

The Formation of the Grain Boundary Structure, Aging Behavior and Mechanical Properties of Al-Zn-Mg-Cu Alloy

E.I. Selnikhina, L.I. Kaigorodova and A.A. Tkachenko

Institute of Metal Physics, Ural Division Russian Academy of Sciences,
S. Kovalevskaya str. 18, RU-620019 Ekaterinburg, Russia

Keywords: Aluminum-Zinc-Magnesium-Cooper Alloys, Small Additions, Scandium, Zirconium, Recrystallization, Aging, Mechanical Properties

Abstract. *The effects of scandium and zirconium additions on the formation of grain structure, decomposition of supersaturated solid solution and mechanical properties of an Al-Zn-Mg-Cu alloy were studied. The formation of grain structure was shown to be determined by the distribution and volume fraction of fine Al_3Sc and $Al_3[Sc_{1-x}Zr_x]$ particles. Factors that govern the effects of the additions on the kinetics of decomposition of supersaturated solid solution upon natural and artificial aging were discussed. Structural factors responsible for improved mechanical properties of the alloy containing Sc and Zr were established.*

Introduction. Scandium is an efficient refining agent for the cast structure of Al alloys. Its refining ability is much stronger than that of well-known grain refiners, such as Ti, Zr, Ta, V, Nb, Mo, Cr, Mg, ets. Besides, scandium shows very strong antirecrystallization effect on the structure of cold-worked and thermal treated semifinished products.

However, the antirecrystallization ability of scandium decreases substantially after long-term heating during high temperature treatments of commercial semifinished products. This effect is connected with strong tendency to coalescence of Al_3Sc particles [1]. The antirecrystallization ability of scandium can be retained by additional alloying with zirconium. Zirconium slows down the coalescence of fine particles which, in the case of such combined alloying, have the composition $Al_3[Sc_{1-x}Zr_x]$.

The great interest to study the effects of small additions scandium and, particularly, combined scandium + zirconium additions on the formation of grain structure and decomposition of supersaturated solid solution in a high strength Al-Zn-Mg-Cu alloy in order to establish the most common features of the influence of alloying additions on phase transformations in this important alloy and to reveal structural factors responsible for its improved mechanical properties.

Experimental. The methods of optical microscopy, transmission electron microscopy and X-ray diffraction were used. The alloy compositions are given in Table 1.

Specimens of forged semifinished items of all given alloys were solution treated at 738K for 60 min, quenched in water (293K), and naturally and artificially aged. The period of naturally aging was one to two years. Two-stage artificial aging was performed according to the following schedule: 378 K, 8 h + 443 K, 8 h.

Table 1. Chemical composition of forgings of Al-Zn-Mg-Cu alloys (wt %)

Zn	Mg	Cu	Zr	Sc	Fe	Mn	Ti	Si
7,0	2,0	1.2	---	0.24	0.1	0.05	0.02	0.05
7.0	1.9	1.1	0.1	0.22	0.14	0.05	0.02	0.05
6.8	2.0	1.1	---	---	0.1	0.05	0.02	0.05

Results and discussion. *Grain structure.* All given alloys after solution treatment demonstrate fully recrystallized structure. Sc and Zr affect on kinetics of recrystallization.

A comparison of structures of alloys suggests that in the alloy without additions of scandium and zirconium secondary recrystallization occurs (Fig.1a). Alloying, especially combined alloying, suppresses this process, slowing down the migration of grain boundaries and decreasing variation in grain size (Fig. 1b).

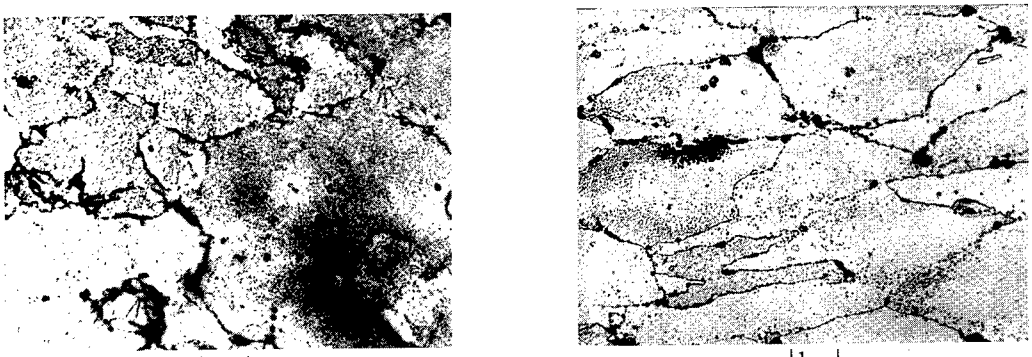

Fig. 1. Microstructures of a quenched Al-Zn-Mg-Cu alloy: (a) grain structure of the alloy without additions of Sc and Zr, × 312; (b) grain structure of the alloy with Sc and Zr; × 312.

To establish the factors responsible for the effect of small additions Sc and Zr on the formation of grain structure in Al-Zn-Mg-Cu alloys, it was studied the decomposition of supersaturated solid solution of Sc and Sc+Zr in Al before deformation. This process is known to occur at the temperature of solution treatment. The structure of the quenched alloy with Sc contains non-uniformly distributed coarse Al_3Sc particles (Fig. 2a). Alloying with Zr decreases the diameter of particles $Al_3[Sc_{1-x}Zr_x]$ and increases precipitation density by an order of magnitude (Fig. 2b).

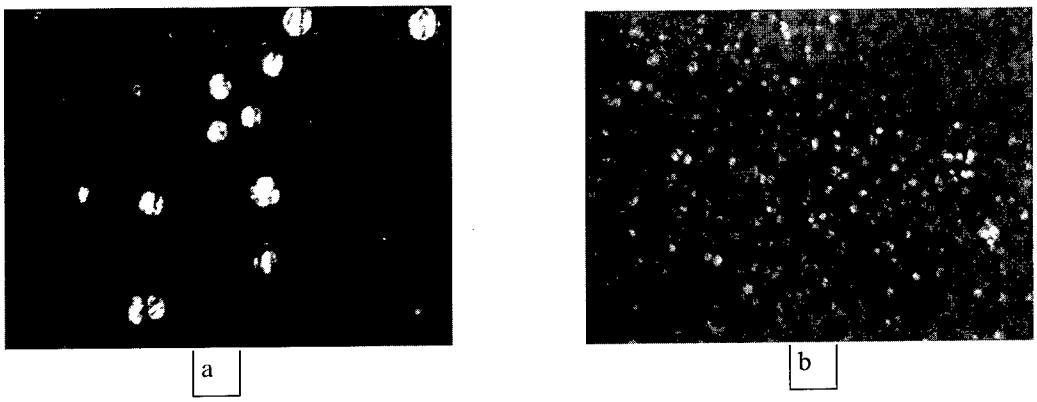

Fig. 2. Microstructures of a quenched Al-Zn-Mg-Cu alloy: (a, b) dark-field images of fine particles of Al_3Sc and $Al_3[Sc_{1-x}Zr_x]$; × 75000.

These results indicate that the recrystallized structure of Al-Zn-Mg-Cu alloys with Sc and Zr additions is due to morphological features of Al_3Sc and $Al_3[Sc_{1-x}Zr_x]$ precipitates. The nonuniform distribution of precipitates in the Sc-containing alloy result in the formation of a grain structure with varying grain size. The intense growth of coarse grains during secondary recrystallization occurs in regions with a reduced density of precipitates. Increasing precipitation density and decreasing nonuniformity of their distribution upon combined alloying suppress grain growth because of the substantially slowed down migration of high-angle grain boundaries. It was found in [2] the particles precipitate before deformation can stabilize the deformation texture.

A strongly developed subgrain structure was observed inside recrystallized grains of alloys with additions (Fig. 3).

Fig. 3. Microstructures of a quenched Al-Zn-Mg-Cu alloy: substructure of the alloy with Sc and Zr; × 10000.

The size of subgrains varies from 1 to 5 micron and misorientation angle is 1 to 3 degrees. These parameters do not depend on the character of precipitate distribution. This suggests that retention of substructure during high-temperature annealing (solution treatment) is due to interaction between subgrain boundaries and impurity atoms of Sc and Zr which are in solid solution.

An analysis of dislocation structure of quenched alloys confirms that a part of the impurity atoms remain in solid solution after precipitation of Al_3Sc and $Al_3[Sc_{1-x}Zr_x]$. This evidenced by the high dislocation density in the alloys with additions. The alloy without additions shows only separate dislocation. The foreign atoms from impurity atmospheres, therefore, hinder the motion of dislocations and their subsequent annihilation. During natural aging the dislocation structure of the alloy without additions changes; dislocation loops appear in it. On the contrary, the dislocation structure in the alloys with additions of Sc and Zr remains unchanged upon aging. This indicates that atoms of Sc and Zr interact with vacancies, suppressing their coalescence in large aggregates, e.g., vacancy discs.

Decomposition of supersaturated solid solution. Natural aging. During natural aging, a metastable phase η′ ($MgZn_2$) precipitates in the Al-Zn-Mg-Cu alloys. Particles of this phase are very fine. This does not allow us to reveal the effect of additions on the nucleation and growth of this phase upon natural aging.

Along with zinc-magnesium phase it was observed the precipitation of an Al-Cu-based phase. Its precipitation is confirmed by following observations. Electron diffraction patterns with a zone axis close to $[001]_{Al}$ exhibit well-pronounced intense streaks along $<001>_{Al}$ directions. Such streaks are typical of the precipitates of the metastable θ″ (Al_2Cu) phase in AlCu alloy [3] and copper-containing Al-Li-Cu [4] and Al-Zn-Mg-Cu [5]. One can observed intensity maximum on these streaks corresponding to reflections of the θ″ metastable phase. Dark-field images demonstrate chains of platelike particles arranged along crystallographic directions close to $<001>_{Al}$. The estimations of the distribution density and average size of these particles show that alloying with Sc and Sc+Zr slows down precipitation of these phases.

These results suggest that upon natural aging, Cu additions in amounts of the 1.0-1.2 wt % not only ensure solid-solution hardening of Al-Zn-Mg-Cu alloys caused by copper dissolution in the matrix, which is well-known [5], but also can strengthen the alloy additionally because of the precipitation of the Al-Cu-based phases. All phases precipitate uniformly inside grains and near grain boundaries. Low-angle and high-angle grain boundaries remain free of precipitates upon natural aging for up to two years.

Decomposition of supersaturated solid solution. Artificial aging. Zinc-magnesium phases (metastable and stable) were found in studied alloys after aging according to the schedule used. No copper-containing phases were observed. This can be due to dissolution of copper in the $MgZn_2$ phase [5].

A comparison of dark-field images of the metastable and stable Mg-Zn phases in alloys of different compositions shows the effect of Sc and Zr additions on kinetics of nucleation and grows of these phases. Alloying with Sc slightly decreases the precipitation density and additional alloying with Zr decreases this parameter by a factor three. The effect of the additions on the precipitation of the stable phase is more

pronounced. The results obtained show that small additions of Sc and, particularly, Sc+Zr decelerate the decomposition of supersaturated solid solution.

After artificial aging, grain boundaries mainly contain particles of the stable η phase. Additions Sc and Zr only have a slight effect on its precipitation density and distribution. The morphology of the particles is controlled by the structure of grain boundaries. Separate platelike precipitates are observed at low-angle and tilt boundaries, whereas particles at twist boundaries appear as long laths (Fig. 4a-c). No zones free of precipitates in the vicinity of grain boundary were observed in all given cases.

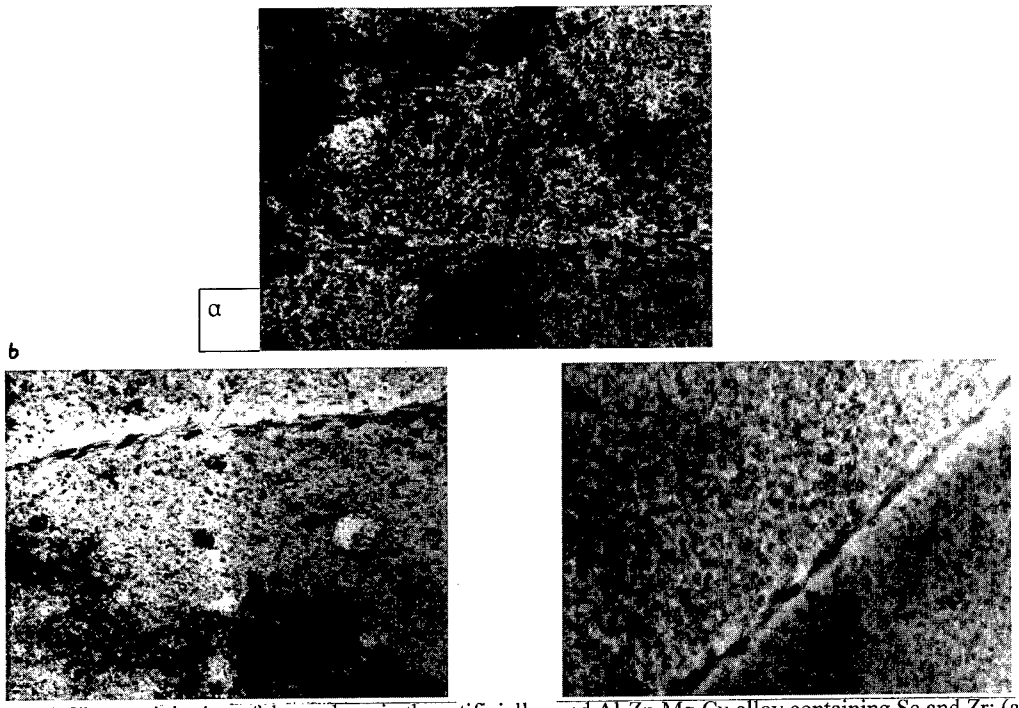

Fig. 4. The precipitation of the η phase in the artificially aged Al-Zn-Mg-Cu alloy containing Sc and Zr: (a) at low-angle boundaries; (b) at tilt boundaries; (c) at twist boundaries; × 75000.

Effect of combined alloying on mechanical properties. The addition of Zr to an Al-Zn-Mg-Cu alloy already containing Sc somewhat decreases the strength property of this alloy (Table 2). This is due to the decreased precipitation density of metastable and stable η′, η hardening phases. The increased plasticity of the alloy with Sc and Zr results mainly from the formation of more homogeneous (in size) grain structure.

Table 2. Mechanical properties of Al-Zn-Mg-Cu forgings after artificial aging

Alloys	Ultimate stress, MPa	Yield stress, MPa	Elongation, %
Alloy with Sc	530-540	480-490	12-16
Alloy with Sc and Zr	510-530	445-485	14-16

References

1. Elagin, V. I., Zakharov, V.V. and Rostova, T. D. Metalloved. Term. Obrab. Met., 1992, No 1, pp.24-28.
2. Kaigorodova, L. I., Tkachenko, E. A., Senatorova, O. G. and Sel'nikhina E. I. Phys. Met. Metallogr., 1995, Vol 80, No 4, pp.454-459.
3. Rioja, R. I. and Laughlin, D. E. Metall. Trans. A, 1977, Vol.8A, No 8, pp.1257-1261.
4. Kaigorodova, L. I., Romanova, R. R., Zhingel, Ya. V. and et all. Phys. Met. Metalloved., 1991, No 1, pp.171-177.
5. Mondolfo, L. F., Aluminium Alloys :Structure and Properties, London: Butterworths, 1976.

Materials Science Forum Vols. 294-296 (1999) pp. 711-714

Grain Boundary Character Dependence of Potential Barrier in Barium Titanate

K. Hayashi, T. Yamamoto, Y. Ikuhara and T. Sakuma

Department of Materials Science, Faculty of Engineering, The University of Tokyo, Tokyo 113-8656, Japan

Keywords: Barium Titanate, Positive Temperature Coefficient of Resistivity (PTCR), Potential Barrier, Coincidence of Reciprocal Lattice Points (CRLP)

Abstract Positive temperature coefficient of resistivity (PTCR) effect is directly measured in bicrystal specimens of Nb-doped $BaTiO_3$ to examine its grain boundary character dependence and to clarify the nature of the potential barrier formed at grain boundaries. The coherency of grain boundaries is evaluated from a geometric method based on the coincidence of reciprocal lattice points (CRLP). Larger PTCR effects were obtained for random grain boundaries rather than coherent boundaries. The formation of the potential barrier is discussed from an analysis of the resistance-temperature characteristics.

1. Introduction

It has generally been accepted that the positive temperature coefficient of resistivity (PTCR) in donor-doped $BaTiO_3$ arises from the potential barrier formed at grain boundaries [1-7]. Several attempts have been made to estimate electric properties of single grain boundaries [1, 2]. These studies revealed the significant difference of the electric properties in individual grain boundaries and further the existence of inactive grain boundaries, where no PTCR effect and nonlinear current-voltage relationships are observed [1, 2]. Recently, present authors' group reported that highly coherent grain boundaries such as a small angle grain boundary and $\Sigma 3$ boundaries do not exhibit PTCR effects [2]. However, the estimation was restricted to special grain boundaries. This study aims to elucidate the grain boundary character dependence of the PTCR effect in general grain boundaries.

2. Experimental Procedure

0.1mol% Nb and 0.05mol% Ba-doped $BaTiO_3$ polycrystals were fabricated through conventional sintering technique [2]. The sinters were sliced and polished into a wafer with 0.25mm thickness. They were annealed at 1350°C for 6h and then cooled down to 900°C with a cooling rate of 50°C/h followed by furnace-cooling to room temperature in air. Samples with mixed-grained structure can be obtained by this annealing, i.e., coarse grains with ~1mm size are present in fine-grained matrix with a size of ~2mm. Bicrystal or single crystal specimens with a size of 0.7 × 0.25 × 0.2 mm were machined from the wafers. The surfaces of the bicrystal specimens were finished to mirror surface. Electrodes were joined on these planes using ohmic Ag paste and Pt wires as shown in Fig. 1. The resistance-temperature (R-T) characteristics were measured at more than 20 specimens with an applied voltage of 0.02V. Crystallographic orientations of individual grains were determined by electron backscatter diffraction (EBSD) analysis attached to scanning electron microscope.

3. Results and Discussion

Figure 2 shows the examples of R-T characteristics measured for the bicrystal samples. The magnitude of PTCR effect, $\log(R_{max}/R_{min})$ (R_{max}: the maximum resistivity above the Curie temperature of about 130°C, R_{min}: the minimum resistivity blow T_C), is quite dissimilar even among the random boundaries.

To evaluate the coherency of low Σ and random grain boundaries, we applied a geometric method based on the coincidence of reciprocal lattice points (CRLP) proposed by Ikuhara and Pirouz [8]. Their hypothesis is that a favored orientation relationship will be achieved by the (near-) coincidence of the reciprocal lattice points (RLPs) from given two crystals. A RLP, *hkl*, corresponding to a reciprocal lattice vector $\boldsymbol{g}(hkl)$, specifies both the orientation of a set of lattice planes (*hkl*), and its interplanar spacing d_{hkl} (= $1/|\boldsymbol{g}|$), and a (near-) coincidence of the PLPs represents the continuity of corresponding lattice planes through two crystals. To formulate the degree of the coincidence, they represent each RLP by a sphere of radius r^* around a point and estimate the volume of the overlapped region v_{gG} between two spheres. Then, the sum of all overlapped volume, $V = \Sigma v_{gG}$ among given RLPs represents the degree of the coincidence.

Figure 3(a) is a plot of calculated overlapped volume V for rotations about [100] and [011] axes in a simple cubic system. In the calculation, RLPs lying within $|\boldsymbol{g}|^2 \leq 3a^{*2}$ with a radius of $0.4a^*$ are considered where a^* is the lattice constant of the reciprocal lattice. The magnitude of PTCR effect is plotted against overlapped volume V in Fig. 3(b). The magnitude of the PTCR effect correlates well with the overlapped volume, i.e., the effect becomes smaller with an increase of the volume. These results indicate that the formation of the potential barrier is closely related to the grain boundary character.

Although the CRLP method is useful to prove the correlation between a property and a geometric character of a grain boundary, it should be stated that the physical basis of the present method is not entirely clear yet. Geometrically, the CRLP corresponds to the degree of the lattice continuity across a grain boundary.

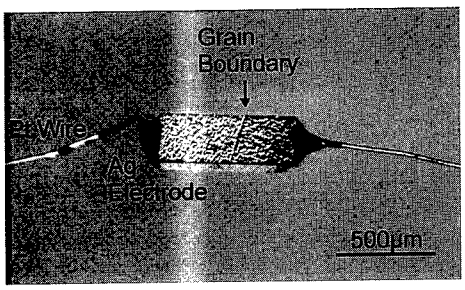

Fig. 1 The optical micrograph of a bicrystal sample connected with electrodes.

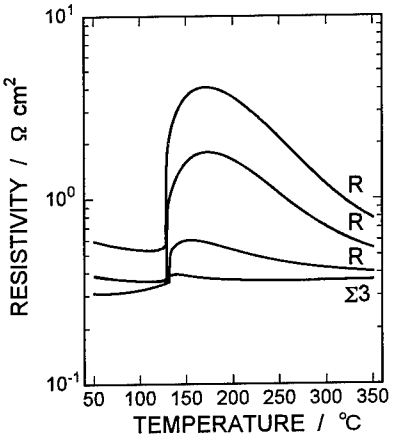

Fig. 2 Examples of resistance-temperature characteristics for bicrystal specimens. Aria resistivity with a thickness of 0.7mm was calculated using the resistivity of single crystal. 'R' denotes a random boundary classified using Brandon's criterion [9].

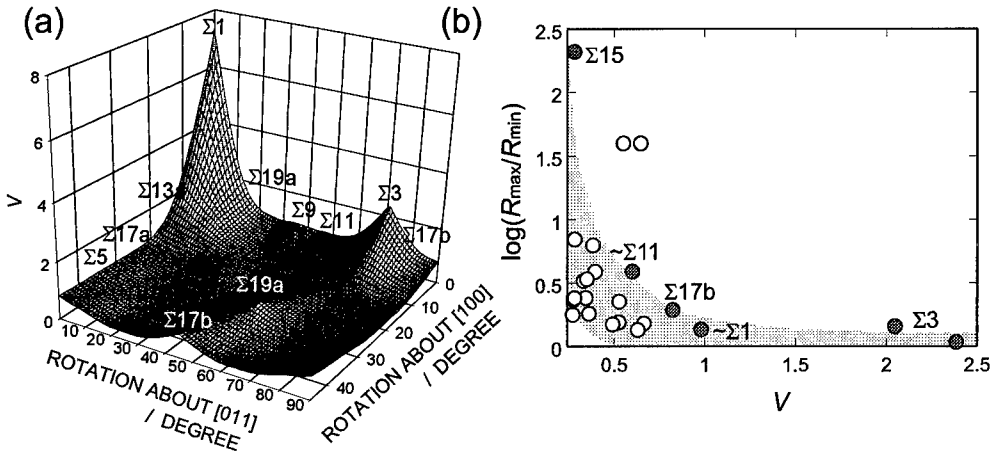

Fig. 3 (a) A plot of overlapped volumes V for rotations about [100] and [011] axes in a simple cubic system. In the calculation, RLPs lying within $|\boldsymbol{g}|^2 \leq 3a^{*2}$ with a radius $r^* = 0.4a^*$ are considered. (b) A plot of the magnitude of the PTCR effect $\log(R_{max}/R_{min})$ against calculated V values. The filled circles denote CSL boundaries classified using Brandon's criterion [9].

In Fig. 3(a), the main peaks appear only at Σ1 and Σ3. The appearance of local maximum at coincidence site lattice (CSL) orientations depends on the consideration range of $|\boldsymbol{g}|^2$ for RLPs. Roughly speaking, the local peaks for Σx appear when the calculation are made among the RLPs lying within $|\boldsymbol{g}|^2 \leq xa^{*2}$. However, the correlation observed in Fig. 3(b) can be obtained by only the RLPs withn $|\boldsymbol{g}|^2 \leq 3a^{*2}$. This suggests that a grain boundary can be characterized by the coincidence of the large d_{hkl} planes. The Σ3 and Σ17b boundaries, in which the orientation relationships can be given by the rotation about <011>, have relatively low magnitude of PTCR effect. Such rotation about low index axis may allow the construction of a grain boundary with large d_{hkl} plane. The large interplanar spacing is one geometric criteria for low interfacial energy [10]. On the contrary, this is not in case to the Σ15 boundary which exhibit the largest magnitude of PTCR effect. This may be one possible explanation of why the correlation can be obtained just by the consideration of the large d_{hkl} planes.

In the Heywang's phenomenological theory [3] for the PTCR effect, a potential barrier is characterized by the two parameters the density of interface states N_S and the energetical depth of the states from the bottom of conduction band E_S.The increase of the parameters results in the increase of the magnitude of PTCR effect. These parameters were estimated from the R-T characteristics using the method proposed by Huybrechts *et al.* [7].

Figure 4 provides a plot of E_S versus N_S estimated with present samples. The increase of N_S is accompanied with the nearly monotonical increase of E_S. The saturation of N_S with the increase of E_S may come from the underestimation due to the narrow PTC region, which is called as *saw-tooth* R-T characteristics [1]. This relationship between E_S and N_S will be interpreted adequately in terms of the formation of potential barrier by the oxidation at a grain boundary as follows.

It is well known that quenched specimens do not exhibit marked PTCR effects [4]. This implies that the potential barrier is formed during cooling from the fabrication temperature to room temperature, and that their formation is governed by diffusional processes [4-6]. Fig. 5 illustrates the simultaneous increase of E_S and N_S with the oxidation of a grain boundary during cooling. At an annealing temperature, the amount of the negatively charged defects such as donors or oxygen vacancies and the positively charged defects such as cation vacancies and acceptors are balanced to maintain the electronic neutrality. During cooling from the annealing temperature, oxygen vacancies will easily annihilate in grain boundaries because of rapid diffusion of the oxygen ions

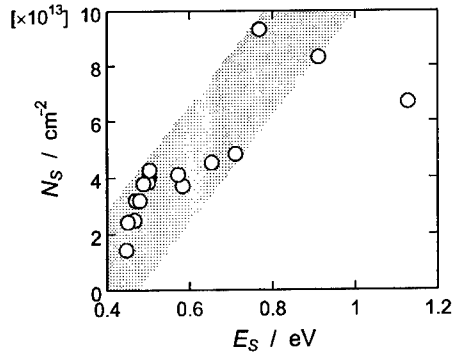

Fig. 4 A plot of the density of the interface states N_S against the energetical depth of the states from the bottom of conduction band E_S estimated from the resistance-temperature characteristics.

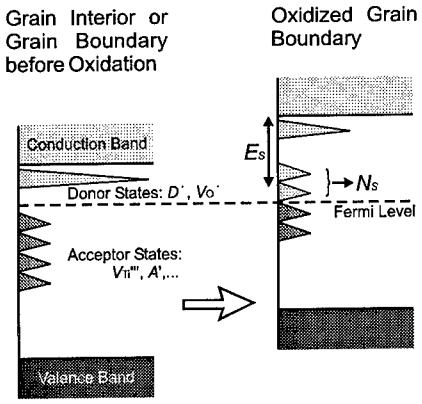

Fig. 5 Schematic band diagrams showing the formation of potential barrier. Hatched states represent the occupied states.

[4]. This will form unoccupied acceptor states, which are again occupied near the Curie temperature because of high dielectric constant [3] and then recognized as N_S. Simultaneously, the Fermi level lowers against the bottom of the conduction band. The energy difference between the bottom of the conduction band and a Fermi level at a grain boundary will correspond to E_S. On the other hand, the defect states will be frozen in grain interior. The energy difference between the Fermi level for the grain boundary and in the grain interior gives the potential barrier height. The grain boundary with higher coherency will not be oxidized due to its low diffusivity [11] and hence no noticeable potential barriers will be formed.

4. Conclusion

Larger PTCR effects are obtained in the grain boundaries with lower coherency. The formation of the potential barrier at a grain boundary may be governed by oxidation and must be affected by the coherency of the grain boundary.

References

[1] M. Kuwabara, K. Morimo, and T. Matsunaga, J. Am. Ceram. Soc. 79 (1996), p. 997.
[2] K. Hayashi, T. Yamamoto, and T. Sakuma, J. Am. Ceram. Soc. 79 (1996), p. 1669.
[3] W. Heywang, J. Am. Ceram. Soc. 47 (1964), p. 484.
[4] G V. Lewis, C. R. A. Catlow, and R. E. W. Casselton, J. Am. Ceram. Soc. 68 (1985), 555
[5] Y.-M. Chiang and T. Takagi, J. Am. Ceram. Soc. 73 (1990), p. 3278.
[6] S. B. Desu and D. A. Payne, ibid., p. 3391.
[7] B. Huybrechts, K. Ishizaki, and M. Takata, J. Am. Ceram. Soc. (1992), p. 722.
[8] Y. Ikuhara, P. Pirouz, Mater. Sci. Forum 207-209 (1996), 121.
[9] D. G. Brandon, Acta. Metal. 14 (1966), p. 1479.
[10] A. P. Sutton and R. W. Balluffi, Acta. Metal. 35 (1987), p. 2177.
[11] X.-M. Li and Y.-T. Chou, Acta. Metal. 44 (1996), p. 3535.

Materials Science Forum Vols. 294-296 (1999) pp. 715-718

Electronic Properties of the Grain Boundary Core in Polycrystals of Cubic Metals

S.M. Klotsman and V.N. Kaigorodov

Institute of Metal Physics, Urals Division of Russian Academy of Sciences,
RU-620219 Ekaterinburg, RF

Keywords: Grain Boundary Core, Electronic Properties, Intercrystalline Diffusion, Metals

Abstract. Local densities of conduction s-electrons in the grain boundary (GB) core of transition and noble metals were determined using two methods. The difference between isomer shifts of components of emission nuclear gamma resonance (NGR) spectra due to ^{57}Co atomic probes occupying states in the lattice sites and the grain boundary core was corrected for the change in the volume of these ^{57}Co atomic probes in the given states. The corrected values of the difference between isomer shifts pointed to a low density of s-electrons at the substitutional and the interstitials sites of the grain boundary core structure. The magnetic ordering temperature of "nearly ferromagnetic" Pd and Pt matrices was proportional to the density of conduction electrons. Different Curie temperatures in the lattice and the grain boundary core of these matrices also suggested a lower (compared to the corresponding lattice sites) density of electrons at interstitial sites of the grain boundary core structure in Pd and Pt.

I. Introduction. Electronic properties of the grain boundary core in metals are difficult to determine by traditional techniques, because conduction electrons largely screen these structural defects. A new method [1, 2] for examination of the structure and the set of physical properties of the grain boundary core in polycrystals allowed receive information about electronic properties of the grain boundary core and adjacent two-dimensional regions of the lattice. Experimental studies [3] on the dependence of isomer shifts of nuclear gamma-resonance (NGR) spectra components on the pressure showed that the decrease in the atomic volume of substitutional ^{57}Co atomic probes in the lattice, which occurred with growing pressure, was followed by the increase in isomer shifts of components of emission NGR spectra. This was due to the rise in the density of inner-shell and conduction s-electrons at the atomic probe nuclear with the pressure build-up. Moreover, a recent study [4] into the state of ^{57}Fe atomic probes at interstitials sites in simple and transition metals revealed that compression of ^{57}Fe atomic probes at lattice interstitials sites also led to the increase in the isomer shift (growth of the density of s-electrons at the atomic probe nuclear) of the corresponding component of the NGR spectrum, such that

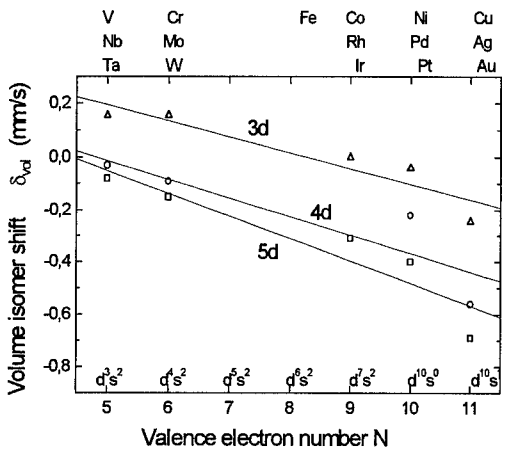

Dependencies of the volume isomer shifts δ_{vol} on the valence electron number for 3d, 4d and 5d transition and noble metals.

$$(\delta_{interst} - \delta_{subst})_{vol} > 0 . \quad (1)$$

This paper reports our findings on the mean density of electrons at the grain boundary core in polycrystals of transition and noble metals.

II. Results and discussion. The materials, the techniques of their preparation and the measurement methods used have been described elsewhere [2].

II.1. Properties of substitutional states-2 localized outside the grain boundary core.

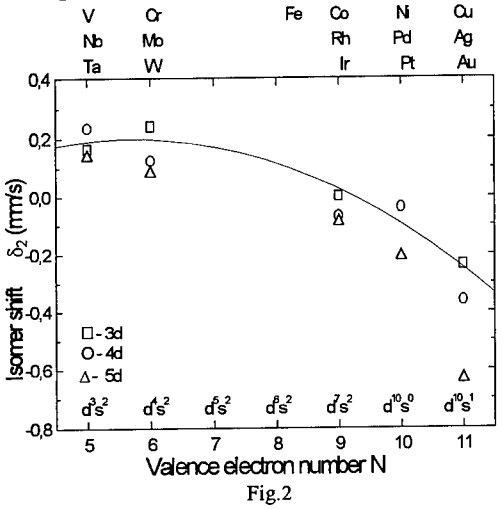

Fig.2

Dependence of the volume corrected isomer shifts δ_2 of states-2 on the valence electron number N.

The systematics of isomer shifts δ_{vol} of volume components of NGR spectra obtained with the help of ^{57}Co atomic probes in metals has been known. Fig. 1 presents the dependence $\delta_{vol}(N)$ for 3d, 4d and 5d matrices. Here N is the number of valence electrons of the solvent metal. This dependence reflects (i) the effect of the variation in the volume of atomic probes at the lattice sites of the corresponding metal on the δ_{vol} value, and (ii) the effect that the increase in the number of valence electrons of the matrix has on the density of s-electrons at the ^{57}Co core and, consequently, on the δ_{vol} value.

Corrections were introduced [5,4] for the change in the volume of ^{57}Fe atomic probes in lattices of different hosts. If such corrections are introduced, the $(\delta_{vol})_{corr}$ values reflect only the electron contribution to the magnitude of isomer shifts.

We used this procedure to calculate corrected $(\delta_2)_{corr}$ values of the isomer shifts δ_2 measured by us (Fig. 2). It is seen that the $(\delta_2)_{corr}$ values are described by a single parabolic dependence in all the metal solvents studied. Therefore the local density of s-electrons at the nuclears of atomic probes occupying substitutional states-2 is nearly the same in homovalent matrices.

II.2. Local density of conduction s-electrons at the grain boundary core determined from the difference between isomer shifts of components of NGR spectra of atomic probes localized in states-1 and -2.

In 4d and 5d transition and noble metals ^{57}Co atomic probes represent small-radius impurities and occupy interstitial sites in the grain boundary core structure (interstitial states-1) [1,2,6]. This statement is supported by the difference of isomer shifts $\delta_{12} = \delta_1 - \delta_2$ of atomic probes in states-1 (δ_1) and states-2 (δ_2). In 4d and 5d metals [1,2,6]:

$$\delta_{12} > 0 . \qquad (2)$$

The positive sign of the difference of isomer shifts δ_{12} is determined mainly by different volumes of atomic probes in states-1 and -2 and testifies to compression of atomic probes occupying interstitial sites at the grain boundary

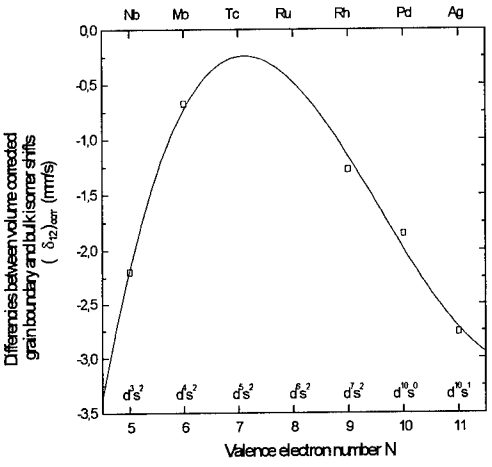

Fig.3

Volume corrected differencies δ_{12} vs. valence electron number N for 4d transition and noble metals.

core of these metals. The density of the grain boundary core structure is lower than that of the lattice. Therefore compression of atomic probes in the grain boundary core and the decrease in the atomic probe volume compared to their volume at the lattice substitutional sites may be realized only *if atomic probes are localized at interstitials sites of the grain boundary core structure* [1,2,6].

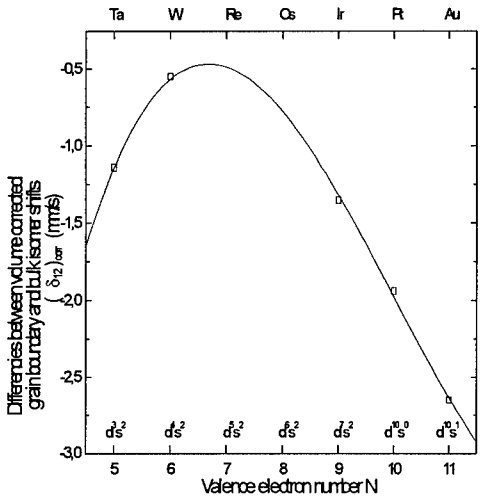

Fig.4

Volume corrected differencies δ_{12} vs. valence electron number N for 5d transition and noble metals.

Let us use the above procedure to obtain information about local electron specific density in the regions of localization of states-1 in the grain boundary core. We need to know the type of sites filled by atomic probes in the grain boundary core and the volume occupied by ^{57}Co atomic probes in the grain boundary core. The volume occupied by ^{57}Co atomic probe in the grain boundary core was estimated using the calculated values [7,8] of the excess volume of large-angle grain boundaries in the metals studied. The volume of octahedral interstitial sites in the fcc lattice and tetraedral sites in bcc lattice, which was increased by the calculated [7,8] excess volume of grain boundaries, was taken as the atomic volume of *interstitial states-1*. The volume of the substitutional sites in the corresponding grain boundary core, which was increased by the calculated [7,8] excess volume of grain boundaries, was assumed to be the atomic volume of *substitutional states-1*. All subsequent estimates were made using the scheme adopted for introduction of volume corrections in isomer shifts [5]. The dependence of the difference $(\delta_{12})_{corr}$, which was corrected for the volume difference in accordance with the scheme described above, on the number of valence electrons N in the matrix of 4d and 5d metals is shown in Fig.3 and Fig.4. As is seen, in 4d and 5d matrices:

$$(\delta_{12})_{corr}^{4d,5d} < 0. \qquad (3)$$

The parabolic behavior found in both cases is due probably to d-band filling effect. Nearly the same behavior was found in [4] volume corrected isomer shifts of ^{57}Fe in the bulk interstitials sites.

The volume corrected difference $(\delta_{12})_{corr}^{3d}$ vs.N presented on Fig.5. The differencies $(\delta_{12})_{corr}^{4d,5d}$ and $(\delta_{12})_{corr}^{3d}$ and in their dependence on N suggests that different types of states-1 having largely different densities of s-electrons are occupied in the grain boundaries core of 4d and 5d matrices and the grain boundaries core of the 3d metals.

II.3. Local density of conduction s-electrons in the grain boundary core determined from magnetic properties of ^{57}Co atomic probes localized in states-1 and -2 in "nearly ferromagnetic" matrices Pd and Pt.

In [9] we described a method for determination of magnetic properties of local regions in a polycrystal: the grain boundary core

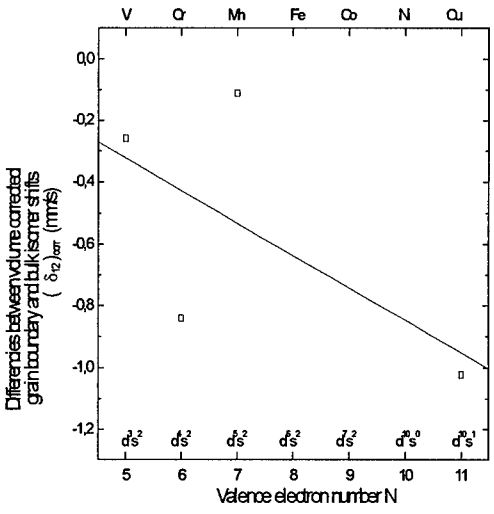

Fig.5

Volume corrected differencies δ_{12} vs. valence electron number N for 5d transition and noble metals.

and adjacent regions of the lattice. Table 1 gives values of the "Curie temperature" T_C measured after Pd and Pt polycrystals were annealed at such high temperatures, at which segregation of residual impurities is absent. It is seen that

$$(T_C)_1 < (T_C)_2 \qquad (4)$$

holds in Pd and Pt. As before, the subscripts 1 and 2 denote localization regions of ^{57}Co AP's in polycrystals.

In "nearly ferromagnetic" metals located at the end of large periods – Pd and Pt – and containing magneto active impurities (MAI's) the Curie temperature:

$$T_C \propto C_{MAI} n^{1/3}. \qquad (5)$$

is proportional to the concentration C_{MAI} and the linear density $n^{1/3}$ of conduction electrons in the matrix [10]:

The mean volume concentration of MAI in Pd and Pt was measured by the SIMS method on an IMS-3f ionic microscope (Cameca, France). It did not exceed 10^{-4} at. fractions in the Pd and Pt polycrystals studied. This value represents a normal level of residual impurities in nominally pure metals. Considering that in Pd and in Pt magneto active impurities did not segregate, one may think the concentration of MAI's in the grain boundary core to be the same as in the volume. Then the observed difference in the Curie temperatures $(T_C)_1$ and $(T_C)_2$ was fully due to different densities of conduction electrons in the said local regions of Pd and Pt lattices:

$$n_1 < n_2 . \qquad (6)$$

Tab.1. Magnetic parameters of the states-1 and -2 in the intercrystalline diffusion zone of the «nearly ferromagnetic» metals.

Solvents	Pd	Pt
C_{MAI} (at.parts)	$(2.8\text{x}10^{-5})^{HP}$ $(1.2\text{x}10^{-4})^{LP}$	$(2.8\text{x}10^{-5})^{HP}$ $(1.4\text{x}10^{-4})^{LP}$
T/T_m	0.4	0.38
T_{C1} (K)	$(25\pm3)^{HP}$ $(42\pm5)^{LP}$	$(80\pm5)^{HP}$ $(100\pm5)^{LP}$
T_{C2} (K)	$(48\pm3)^{HP}$; $(80\pm5)^{LP}$	$(122\pm10)^{HP}$; $(200\pm20)^{LP}$
T_{C1}/T_{C2}	$(0.52)^{HP}$; $(0.52)^{LP}$	$(0.64)^{HP}$; $(0.52)^{LP}$

Acknowledgment. The authors are thankful to Acad. S.V.Vonsovskii for his valuable discussion and support.

References.

[1].S.M.Klotsman,Sov.Phys.Uspech., **33(1),** (1990), p.55.
[2]. V.N.Kaigorodov, S.M.Klotsman, Phys.Rev.B, **49(14)**, (1994), p.9374; *ibid.*, p.9387; *ibid.*, p.9395.
[3]. R.Ingals, Solid.State Com., **14(1),** (1974), p.11.
[4]. B.Keck, R.Sielemann, Y.Yoshida, Phys.Rev.Letters, **71(25),** (1993), p.4178.
[5]. I.Deszi, U.Gonser, G.Langouche, **62(14),** (1989), p.1659.
[6]. V.N.Kaigorodov, S.M.Klotsman, Equilibrium sites occupied in the grain boundary core during intercrystalline diffusion of ^{57}Co in metal polycrystals, Report on *iib-98*.
[7]. D.Wolf, J.Appl.Phys., **68(7),** (1990), p.3221.
[8]. D.Wolf, J.Appl.Phys., **69(1),** (1991), p.185.
[9]. S.M.Klotsman, V.N.Kaigorodov, Magnetic properties of the grain boundary core and lattice regions adjacent to grain boundariesa in polycrystals of 4d and 5d metals, Report on *iib-98*.

Correspondence: **e-mail:** klotsman @ imp.uran.ru

Materials Science Forum Vols. 294-296 (1999) pp. 719-722

Electronic Structure of Σ5[100] Grain Boundary and Doping Effect in Iron

Q. Song[1] and C. Wang[1,2]

[1] Central Iron and Steel Research Institute, Beijing CN-100081, China

[2] International Center for Materials Physics, Academia Sinica, Shenyang CN-110015, China

Keywords: Electronic Structure, Grain Boundary, Doping Effect

Abstract: Based on CSL model and MD relaxation, the atomic structure of Σ5 [100] grain boundary in α–Fe are obtained. By using the tight-binding recursion method, the electronic structure and boron doping effect on Σ5 [100] grain boundary in α–Fe are investigated. The calculated results indicate that the boron enhances the atomic interaction between the host atoms on grain boundary, as well as between the boron and host atoms. The calculation of the energy of impurity segregation to grain boundary shows that the boron has the tendency to segregate onto the grain boundary, and can improve the cohesion of grain boundary.

Introduction

Grain boundary (GB) in materials is closely related with the properties of materials. Many researches reveal that grain boundary may strongly influence the mechanical property of metals and alloys[1-3]. Impurity segregation on GB are sensitively associated with the brittleness and fracture of metals. Light impurity trace elements segregated on GB may enhance or weaken the grain boundary, thus influence the strength of metals. Boron is believed to have the ability of enhancing the grain boundary in some metals[4-6]. In the present paper, by use of the recursion method, the electronic structure and boron doping effect on Σ5 [100] grain boundary in α–Fe are investigated.

Theoretical Method and Calculation Mode

Theoretical Method:

The recursion method[7] is used for calculating the electronic structure of the Σ5[100] of grain boundary in α–Fe. The method is appropriate for studying the local details of system and the electronic effect on atomic defects. The effect of the recursion method is to transform any quantum mechanics model into a chain model expressed by a sequence orthonormal orbitals $\{u_n\}$and two sets of parameters $\{a_n\}$ and $\{b_n\}$. The set $\{u_n\}$ satisfies the recurrence relations, which describes the action of the Hamiltonian **H** on the orbitals. From the recurrence relation, we can obtain the parameters $\{a_n\}$ and $\{b_n\}$, as well as the Hamiltonian matrix in tridiagonal form. The Green operator is defined as:

$$G(E) = \left(E - H^{tri}\right)^{-1} \tag{1}$$

The local Green function can be expressed as a continued fraction[7]. In the linear-combination-of-atomic-orbitals (LCAO) representation, the local density of states (LDOS) can be written as follows:

$$\begin{aligned} n_{\alpha l}(E) &= \sum_n \left|a_{n\alpha l}\right|^2 \delta\left(E - E_n\right) \\ &= -\pi \,\mathrm{Im}\langle \alpha l \left| (E - H)^{-1} \right| \alpha l \rangle \\ &= -(\pi)^{-1} \,\mathrm{Im}\left| E - a_0 - b_1^2 \left[E - a_1 - b_2^2 (E - a_2 - \cdots)^{-1} \right]^{-1} \right|^{-1} \end{aligned} \tag{2}$$

where $|\alpha l>$ is an atomic orbital at site l. Thus, once the a_n and b_n have been determined, the local density of states[8] can be obtained.

The key step in the recursion method is to set up the Hamiltonian matrix. The Salter-Koster integral[9] can be expressed as:

$$E_{sk} = \sum_m f(V_{ij}) V_{ll'm} \tag{3}$$

where $f(V_{ij})$ is a function of the direction cosines of the direction of vector $R_i - R_j$,

$$V_{ll'm} = < lm|H|l'm > \tag{4}$$

is the transition integral, where l, l' are the angular momentum quantum number, and m is the magnetic quantum number. The transition integrals can be given by the Harrison parameter method[10]. Then we can get the $\{a_n\}$ and $\{b_n\}$ and the local density of states $n_{\alpha l}(E)$. The integral density of states is

$$N_l = \int_{-\infty}^{Ef} \sum_{\alpha} n_{\alpha l}(E) dE \tag{5}$$

The structural energy is

$$E_l = \int_{-\infty}^{Ef} E \sum_{\alpha} n_{\alpha l}(E) dE \tag{6}$$

Based on the local electronic theory[7], an analytical expression for describing the interaction between atoms was derived [11]

$$E_{ll'} = \sum_n \sum_{\alpha\alpha'} a^*_{n\alpha l} a_{n\alpha' l'} H_{\alpha l \alpha' l'} = \frac{1}{4} \sum_{\alpha\alpha'} \left[N_{\alpha l + \alpha' l'}(E) - N_{\alpha l - \alpha' l'}(E) \right] H_{\alpha' l' \alpha l} \tag{7}$$

where $a_{n\alpha l} = \langle \Phi_{\alpha l} | \psi_n \rangle$ is the wave vector in the atom orbital representation, $H_{\alpha l \alpha' l'}$ is the interaction matrix elements between atoms. The bond order integral is defined and derived as

$$\begin{aligned} I_{\alpha l \alpha' l'} &= \frac{1}{4} \left[N_{\alpha l + \alpha' l'}(E) - N_{\alpha l - \alpha' l'}(E) \right] \\ &= -\frac{1}{4} (\pi)^{-1} \int_{-\infty}^{Ef} \mathrm{Im} \left[G_{\alpha l + \alpha' l'}(E) - G_{\alpha l - \alpha' l'}(E) \right] dE \\ &= -(\pi)^{-1} \int_{-\infty}^{Ef} \mathrm{Im} G_{\alpha l \alpha' l'}(E) \end{aligned} \tag{8}$$

In this paper, based on the theoretical formulation above, the energy of grain boundary (E_{gb}), the energy of grain boundary segregation (E_{seg}) and the formation energy of the impurity in crystal (E_f^{imp}) can be defined and/or calculated.

$$E_{gb} = \left(\sum_{l'}^{N'} \frac{E_{l'}}{N'} - \sum_{l}^{N} \frac{E_l}{N} \right) / S \tag{9}$$

where E_l and $E_{l'}$ are the structural energy of the crystal and the system containing grain boundary respectively, N and N are the total number of atoms accordingly, S is the effective surface area of atom. The energy of the grain boundary segregation with interstitial form is as follows:

$$E_{seg} = \frac{1}{m} \left[\sum_{l=1}^{N} E_l^{gb} - \left(E_{gb} + N E_l^{cry} + m E_l^{imp} \right) \right] \tag{10}$$

where E_l^{gb} and E_l^{cry} are the energy of atom on site l in grain boundary region with impurities and in crystal respectively. N and m are the total number of atoms in the calculating systems and total

number of impurity atoms respectively. The impurity formation energy is defined as

$$E_f^{imp} = \sum_{l'}^{N'} \frac{E_{l'}}{N'} - \sum_{l}^{N} \frac{E_l}{N} \tag{11}$$

where $E_{l'}$ and E_l are the energy on site l in the region with the impurity and without the impurity respectively. N and N are the number of atoms accordingly.

Calculation Mode

Based on CLS model and self-convergent MD simulation with EAM potential[12], the atomic structure of the Σ5 [100] grain boundary in α–Fe as the calculation model for studying the electronic structure was obtained, as shown in Fig.1.

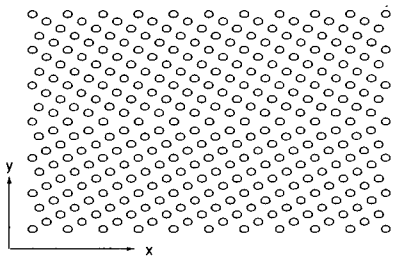

Fig. 1 Atomic structure of Σ5 [100] grain boundary in α–Fe

The calculating system include 2377 atoms. The period of the grain boundary is Tx=3.16a_0 (a_0 is the lattice constant for crystal α–Fe). The electronic configuration of Fe, B atoms are taken as $3d^6 4s^2$, $2s^2 2p^1$ respectively. The Fermi level of the system is determined by neutrality condition of the cluster.

Results and Discussion

Based on the eqs.(7), (9), (10), (11), the energetic parameters of the Σ5 [100] grain boundary are calculated, as listed in table 1. The calculating results of impurity formation energy show that the boron will enter the system with interstitial form, when the distortion energy is considered. From the results of the energy of the grain boundary segregation, it can be seen that the boron has the tendency of segregating to grain boundary, which is in very good agreement with the related experiments[3,14]. The theoretical results of the average interatomic energy between the atoms of the Σ5 [100] grain boundary indicate that the boron possesses the strengthening effect on the interactions between the host atoms in the Σ5 [100] grain boundary region. It means that the brittleness of alloy may be improved by the boron. Meanwhile, the calculating results of the interaction between the impurity and host show that the boron as an alloying element will increase the ability for bonding.

Table 1 The energetic parameters of Σ5 [100] grain boundary

system	$E_f^{imp}(eV)$ intersitical	$E_{gb}(erg/cm^2)$	$E_{seg}(eV)$	$\overline{E}_{Fe-Fe}$(eV)	E_{Fe-Fe}^{acr}(eV)
GB		587.80		-0.212	
doping B	2.18		-2.09	-0.288	-0.328

where $\overline{E}_{Fe-Fe}$ is the average of atomic pairs between host atoms in grain boundary, the E_{Fe-Fe}^{acr} is the energy corresponding to the pairs across the grain boundary in the system.

According to the eqs.(8), the bond order integral between the atoms can be obtained. The calculated results of the bond order integral show that the s-s orbitals between the atoms located in the bottom of the band which corresponds to the orbitals which are in phase and bonding tends to stronger, but

the bond order integral for the all other orbitals, it can be regarded as locating in antibonding state which means that the orbitals are out of phase. The typical result between the boron-iron atoms is shown in table 2.

Table 2 The bond order integral between iron and boron atom for Σ5 [100] grain boundary

	s	p_x	p_y	p_z	d_{xy}	d_{yz}	d_{zx}	$d_{x^2-r^2}$	$d_{3z^2-r^2}$
s	0.1121	0.0000	0.0000	0.0000	-0.0021	-0.0008	-0.0004	-0.0697	-0.0423
p_x	0.0023	0.0000	0.0000	0.0000	-0.0478	-0.0028	-0.0002	-0.0020	-0.0004
p_y	0.1020	0.0000	0.0000	0.0000	-0.0006	-0.0019	-0.0007	-0.0713	-0.0418
p_z	0.0012	0.0000	0.0000	0.0000	0.0022	-0.0512	-0.0009	-0.0011	0.0009
d_{xy}	0.0000	0.0000	0.0000	0.0000	0.0000	0.0000	0.0000	0.0000	0.0000
d_{yz}	0.0000	0.0000	0.0000	0.0000	0.0000	0.0000	0.0000	0.0000	0.0000
d_{zx}	0.0000	0.0000	0.0000	0.0000	0.0000	0.0000	0.0000	0.0000	0.0000
$d_{x^2-r^2}$	0.0000	0.0000	0.0000	0.0000	0.0000	0.0000	0.0000	0.0000	0.0000
$d_{3z^2-r^2}$	0.0000	0.0000	0.0000	0.0000	0.0000	0.0000	0.0000	0.0000	0.0000

Summary

In this paper, the electronic structure and boron doping effect on Σ5 [100] grain boundary in α–Fe is investigated. Some energetic parameters are presented. The theoretical calculation indicate that the boron as the alloying elements has the tendency of segregating onto grain boundary, and is a beneficial factor for strengthening the bonding between the atoms on grain boundary. Thus adding boron can improve the cohesion of grain boundary.

Acknowledgments

This work was supported by the National Natural Science Foundation of China.

Reference

[1] A. K. Vasudevan and J. D. Petrevic, Mat. Sci. Eng. A 155 (1992), p. 1.
[2] L. Goodwin *et al*, Phys. Rev. Lett. 60(1988), p. 2050.
[3] G. S. Paiter and F. W. Averill, Phys. Rev. Lett. 58(1987), p. 234.
[4] M. E. Eberhart, D. D. Vvedensky, Phys. Rev. Lett. 58(1987), p. 61.
[50] M. E. Eberhart, D. D. Vvedensky, Materials Science Forum 46(1989), p. 169.
[6] G. S. Paiter, Phys. Rev. Lett. 70(1993), p. 3959.
[7] V. Heine, Solid State Physics, 35 (1980).
[8] C. M. M. M. Nex, J. Phys. A 11(1978), p. 653.
[9] J. C. Slater and J. F. Koster, Phys. Rev. 94(1954), p. 1498.
[10] W. A. Harrison, Electronic Structure and the Properties of Solid, (Freeman, San Francisco, 1980).
[11] Wang Chongyu *et al*, Mat. Res. Soc. Symp. Proc. Proc., 318(1994), p. 571.
[12] G. Simonelli *et al*, Mat. Res. Soc. Symp. Proc. Proc., 291(1993), p. 567.
[13] M. Hashimoto *et al*, Scripta Metall. 16(1982), p. 267.
[14] M. J. Kelly, Solid State Physics 35(1980), p. 302.

Correspondence: Quanming Song
E-mail: song@fzu.cz

Materials Science Forum Vols. 294-296 (1999) pp. 723-726

Correlation between Superconducting Transport Properties and Grain Boundary Microstructure in $YBa_2Cu_{3-x}O_y$ and $YBa_2Cu_{3-x}O_y/Ag_x$ Ceramics

T.S. Orlova[1], J.Y. Laval[2], A. Dubon[2], C. Nguyen-van-Huong[2] and B.I. Smirnov[1]

[1] A. F. Ioffe Physico-Technical Institute, Russian Academy of Sciences, Polytechnicheskaya 26, RU-194021 St. Petersburg, Russia

[2] Laboratoire de Physique du Solide, CNRS ESPCI, 10 rue Vauquelin, F-75231 Paris Cedex 05, France

Keywords: Grain Boundary, Transmission Electron Microscopy, X-Ray Microanalysis, Superconductors

Abstract The superconducting transport properties (V-I, J_c-B and I_c-T) were correlated with a systematic characterization of the grain boundary microstructure, via TEM observation and local chemical analysis in STEM by EDX on $YBa_2Cu_{3-x}O_y$ (D samples) and $YBa_2Cu_{3-x}O_y/Ag_x$ (S samples) ($0 \leq x \leq 0.4$) ceramics prepared by the citrate gel process. In attempt to substitude Ag for Cu, it turned out that the amount of silver incorporated into the lattice is always less than the nominal concentration x and its maximum value is limited to approximately 0.03 (for x=0.4). Ag was observed mainly as small precipitates in boundaries and grains. The TEM systematic characterization of grain boundaries showed an increase in proportion of clean boundaries in S samples compared to D ones. Specific Ag precipitations of 2-5 nm in size on or near clean boundaries were found in S samples for x=0.4. This is the most likely reason for the improvement of the critical current density J_c in these samples by a factor of 3. It was shown that in samples of both type J_c is controlled by weak links at grain boundaries, which have superconductor-insulator-superconductor (SIS) character in D and superconductor-normal metal-superconductor (SNS) character in S samples. SNS behaviour of S samples was inferred from EDX analysis in STEM to result from a percolation path through 'clean' grain boundaries coated with extremely thin film ($\cong$1 nm).

1. Introduction

In the high-T_c granular superconductors, transport properties are mainly controlled by the grain boundary microstructure unlike T_c which is determined by the crystal structure and oxygen content. Depending on their crystallography and structure, boundaries can be favourable for the passage of supercurrent or can be weak links (reduced J_c regions) in the superconducting current path of a ceramic sample. Recently a large body of research has been directed at investigating the dissipation at a separate boundary of different type (for example [1]). Although studies of separate boundary behaviour highly contribute to understanding polycrystalline transport, they are rather idealistic models of true polycrystalline materials which consist of many boundaries of different types, in parallel and series, simultaneously. So, it is also very important to investigate the relation between transport properties and grain boundary behaviour as a network of boundaries.

One way for changing (increasing) intergrain critical current density of polycrystalline materials is doping with Ag [2, 3]. Small deviations from the stoichiometric composition probably can also lead to a change in structure and distribution of boundaries in a ceramic sample. Distribution of Ag in ceramics and its influence on J_c are subject to contradictory conclusions [4-6] and seem to depend strongly on the processing technology. So, in this work the relation between microstructure and superconducting transport properties was studied in copper deficient $YBa_2Cu_{3-x}O_y$ ceramics and in $YBa_2Cu_{3-x}O_y/Ag_x$ ceramics with silver incorporated in amounts equal to the copper deficiency. The importance of the microstructure of grain boundaries and second phases is underlined by comparing the two types of superconducting behaviour.

2. Experimental

The YBCO ceramics were prepared via the modified citrate gel process [7]. The sol-gel method allows one to achieve highly homogeneous mixing of cations on an atomic scale and produce high-quality powder. In samples of the first type $YBa_2Cu_{3-x}O_y$ ($0 \le x \le 0.4$) (D type) Cu-deficient compositions were obtained. In samples of the second type, $YBa_2Cu_{3-x}O_y/Ag_x$ ($0 \le x \le 0.4$) (substituted S type), Ag was considered as a substituent for Cu. The phases were characterized by powder X-ray diffraction (XRD) using a Philips automated X-ray diffractometer. Microstructure and chemical compositions were analysed with a Jeol 2000 FX TEM equipped with a Link EXL X-ray selective analyser and with an SEM equipped with an EDAX X-ray selective analyser.

The superconducting properties were studied by measuring the resistivity-temperature (R-T) and voltage-current (V-I) characteristics using the four-probe technique. The critical current values I_c were determined at various temperatures using a 1 μV/mm criterion, with and without external magnetic field B. The magnetic field was created by a current-carrying coil and was perpendicular to the transport current.

3. Results and discussion

3.1 XRD, optical microscopy and SEM

X-ray diffraction and SEM analysis showed that both $YBa_2Cu_{3-x}O_y$ (D) and $YBa_2Cu_{3-x}O_y/Ag_x$ (S) samples have an orthorhombic structure. For x=0.1 in samples of both type (D and S), no secondary phase was found. For samples with $x \ge 0.2$, Ag phase (S samples), along with several nonsuperconducting phases such as Y_2BaCuO_5 (211), $BaCuO_2$ (011) and CuO (D and S samples) were registrated. The amount of these nonsuperconducting phases (in D and S samples) and Ag-phase (S samples) increased with increasing x. Second phases such as $BaCuO_2$ and CuO were found at grain boundaries and triple junctions at $x \ge 0.2$ in samples of both type (D and S). These impurity phases were about 1-3 μm in size, the mean distance between them was comparable with respective grain size. It should be noted that the average grain size dramatically decreased with x (Fig. 1). As indicated by SEM, in S samples Ag precipitated as particles of 1-2 μm in size, which were distributed quite uniformly, the mean distance between them being about 10-12 μm for x=0.2 and 5-8 μm for x=0.4. A limited amount of Ag precipitates was observed even at a low Ag content (x=0.1). The nonsuperconducting phases and Ag precipitates appear to stop grain growth during sintering resulting in fine-grain microstructure for $x \ge 0.2$.

3.3 Superconducting properties

It was found that for samples of both type (D and S) the critical temperature was practically unchanged for $0 \le x \le 0.2$ and was equal to about 91.7 K (R=0) with a rather narrow resistivity transition ≤1.5 K. The value of T_c shifted only for x=0.4, namely, T_c=91 K for both D and S samples for the same ΔT. Fig.2 shows measured values of J_c at 77 K versus x. For S samples, J_c increased only slightly with increase in Ag content from x=0 to x=0.2, whereas J_c increased ≅ threefold from J_c=50 A/cm^2 for x=0 to J_c=170 A/cm^2 for x=0.4. For D samples with $x \ge 0.2$, J_c is ≅ twice that obtained for the stoichiometric composition. In samples of both type (D and S), the obtained V-I curves at 77 K exhibited a power-low behaviour. I_c was strongly depressed by low magnetic fields. Such behaviour is characteristic of granular materials which can be described as a collection of superconducting grains connected by weak links [8].

Thus, in all samples I_c was controlled by grain boundary weak links which were characterized from $I_c(T)$ curves. It is known that for a Josephson tunnel (SIS) junction the dependence of I_c on temperature agrees with the equation $I_c=\text{const}(1-T/T_c^*)$ for temperature close to the superconducting transition temperature T_c^* of the intergrain junction [9]. For the SNS-type proximity junctions, close to T_c^* the $I_c(T)$ dependence can be written in the form $I_c=\text{const}(1-T/T_c^*)^2$ [10].

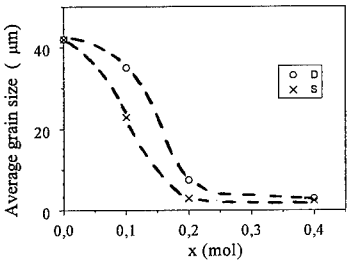

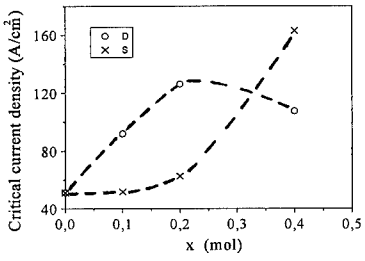

Fig.1. Dependence of the average grain size of D and S samples on x.
Fig.2. Variation of the critical current with x for D and S samples.

To identify the character of weak links we tried to find the dependence of I_c on temperature for T close to the critical temperature T_c of a sample. The obtained dependences of I_c on $(1-T/T_c)$ were plotted on a logarithmic scale in order to determine the value of β in the equation $I_c=\text{const}(1-T/T_c)^{\beta}$ (Fig.3). As can be seen, for D samples $I_c(T)$ corresponds to an SIS junction ($\beta\approx1$). On the other hand, for S samples $I_c(T)$ agrees with an SNS type junction ($\beta\approx2$) for any x value.

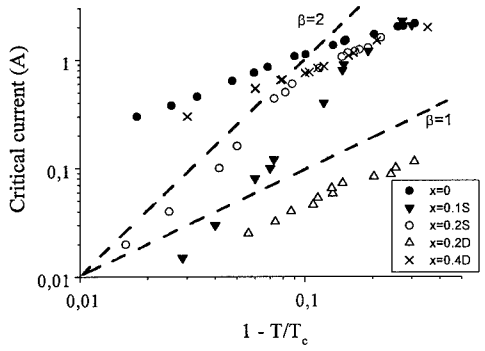

Fig.3. Critical current versus $(1-T/T_c)$ plotted for D and S samples in a logarithmic scale to determine the value of β in the equation $I_c=\text{const}\ (1-T/T_c)^{\beta}$. $\beta=1$ and $\beta=2$ cases are shown by dashed lines.

3.4. Microanalysis by electron microscopy

Localized quantitative chemical analysis was carried out in analytical TEM and STEM by EDX. The incident energy of electrons was 100 keV and 200 keV. The analysis showed (Table 1) that the Ag content (x) of YBCO grains was lower than the nominal amount of Ag, in spite of the sol-gel method which permits highly homogeneous mixing of cations at an atomic scale. As mentioned above, Ag mainly precipitated as small particles (1-2 μm) homogeneously scattered throughout the sample.

In this work a systematic statistical study of grain boundaries was made to correlate their distribution to the observed change in J_c and $I_c(B)$ when x varied from 0 to 0.4. So, 40-50 consecutive boundaries in each sample were characterized by bright field tilting imaging in TEM. The results are shown in Fig.4, where 3 types of grain boundaries were considered. 'Clean' boundaries correspond to boundaries in which no intergranular phase was detected in TEM bright field. In contrast, 'dirty' boundaries exhibit an intergranular phase (thickness >2 nm). At last, 'thin-film-coated' boundaries display a thin phase with a thickness ≤2 nm. In the D samples, the ratio of clean boundaries was found to remain between 27 and 45%. The proportion of clean boundaries decreased with x, whereas the number of dirty ones increased with x.. The observed increase in J_c with x in D samples can be explained by the increase in the proportion of the faceted clean boundaries, which can act as pinning centres (Fig.4). However, one should take into account the fact that clean boundaries are favourable for transmitting the supercurrent only when the orientation crystallographic relationships between adjacent grains are suitable. Usually, no more than 50% of clean boundaries are considered as favourable. Since, according to [11], the percolation threshold is about 12%, a fraction of thin-film-coated boundaries appear to take part in the transmission

Table 1. Average concentration of silver in the grains measured by EDX in TEM and STEM for the substituted samples for all doping levels.

Nominal Ag concentration x	Real Ag concentration
0.1	< limit of detection
0.2	≤0.02
0.4	0.03

of supercurrent for higher values of x. A similar character of the boundary distribution was observed for samples with Ag (S), but the Ag doping resulted in a higher proportion of clean boundaries for x≥0.2 compared to the D samples. Small precipitates of Ag were observed in dirty boundaries for all studied values of x. For high concentrations of Ag (x=0.4) a peculiarity in the structure of clean boundaries was found, namely, about half of the clean boundaries were decorated with small precipitates of 2-5 nm in size on the boundary itself, or close to it (up to 5 nm). The average distance between these precipitates was about 30 nm. An example of such a 'clean' boundary with Ag precipitates is presented in Fig.5. These small Ag precipitates can act as pinning centres which most likely explains the increase in J_c for x=0.4 in S samples.

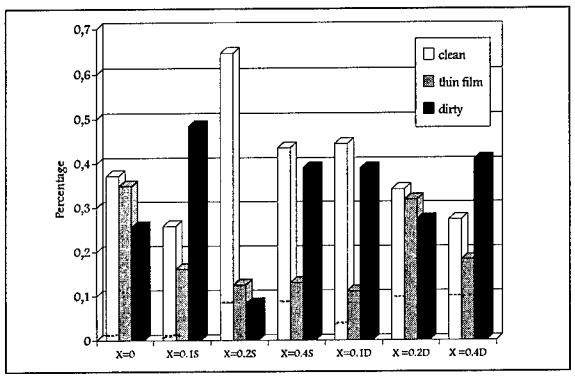

Fig.4. Histogram showing the distribution of clean, thin-film-coated and dirty grain boundaries for a sample of the stoichiometric composition (x=0), D and S samples. The dashed lines show the fraction of faceted clean boundaries among all clean boundaries.

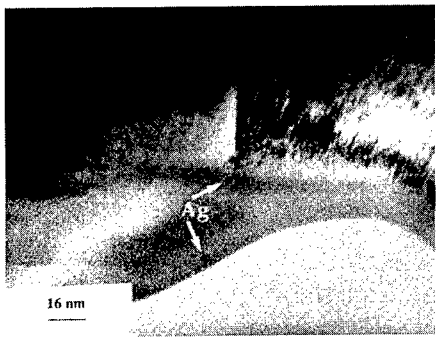

Fig.5. Micrograph of a clean boundary with Ag precipitates (arrows) in TEM for an S sample (x=0.4).

It was not possible to detect any Ag segregation along 'clean' grain boundaries in STEM with a LaB_6 gun. Therefore we did complementary experiments at 200 kV on a Jeol 2010 F electron microscope equipped with a field emission gun. By using a 1 nm probe we could detect 0.5 at.% Ag (x=0.06) on some clean boundaries that was twice higher than the obtained solubility limit of Ag in the grains (x=0.03). This increased Ag segregation on grain boundaries can probably lead to SNS behaviour of weak links in S samples as result of a percolation path through 'clean' boundaries coated with an extremely thin Ag film (≅1 nm).

References

[1] S.E. Babcock and J.L. Vargas, Annu. Rev. Mater. Sci. 25 (1995), p. 193
[2] B. Dwir, M. Affronte and D. Pavuna, Appl. Phys. Lett. 55 (1989), p. 399
[3] S.L. Shinde, J. Morrill, D. Goland, D.A. Chance and T. McGuire, Phys. Rev. B 41 (1990), p. 8838
[4] D.F. Lee, X. Chaud and K. Salama, Physica C 181 (1991), p. 81
[5] J. Joo, J.P. Singh, R.B. Poeppel, A. K. Gangopadhyay and T.O. Mason, J. Appl. Phys. 71 (1992), p. 2351
[6] C. Nguyen-van-Huong, E. Crampin, J.Y. Laval and A. Dubon, Supercond. Sci. Technol. 10 (1997), p. 85
[7] R.S. Liu, W.N. Wang, C.T. Chang. and P.T. Wu, Japan. J. Appl. Phys. 28 (1989), p. L2155
[8] R.L. Peterson and J.W. Ekin, Physica C 157 (1989), p. 325
[9] J. Jung, I. Isaac and A.-K. Mohamed, Phys. Rev. B 48 (1993), p. 7526
[10] P.G. DeGennes, Rev. Mod. Phys. 36 (1964), p. 225
[11] V.K.S. Shante and S. Kirpatrick, Adv. Phys. 20 (1971), p. 325

Materials Science Forum Vols. 294-296 (1999) pp. 727-730

Magnetic Properties of the Grain Boundary Core and Lattice Regions Adjacent to Grain Boundaries in Polycrystals of 4d and 5d Metals

S.M. Klotsman and V.N. Kaigorodov

Instutute of Metal Physics, Urals Division of Russian Academy of Sciences,
RU-620219 Ekaterinburg, RF

Keywords: Grain Boundary Core, Atomic Magnetism, Intercrystalline Diffusion, Metals

Abstract. The Curie temperature and hyperfine magnetic fields at the nuclear of ^{57}Fe atomic probes distributed in the intercrystalline diffusion zone of Rh, Ir, Pd and Pt polycrystals were determined. Magnetic properties of the grain boundary core and those of the lattice regions adjacent to grain boundaries in Rh and Ir are nearly similar. Dimensions of spin-polarized clusters, which appear around every atomic probe in Pd and Pt, are smaller in the grain boundary core than in the regular lattice.

I. Introduction. The structure and properties of the grain boundary core have still been studied intensively, because grain boundaries are significant for the properties of ordinary polycrystals and materials of the new class, namely three-dimensional nanocrystalline materials. The new method [1,2] for examination of the structure and the set of physical properties of the GB core, which is based on intercrystalline diffusion of atomic probes which yields spectral information about the states occupied by the atomic probes, allowed analyzing magnetic properties of two-dimensional regions of polycrystals: the grain boundary core and lattice regions adjacent to grain boundaries. This paper reports results of the investigation of magnetic properties of the grain boundary core and lattice regions adjacent to grain boundaries in polycrystals of 4d and 5d metals.

II. Results and Discussion.

II.1. Areas of the NGR spectra components as a function of the measurement temperature. Manifestation of magnetic ordering in the grain boundary core and adjacent regions of the crystallite lattice.

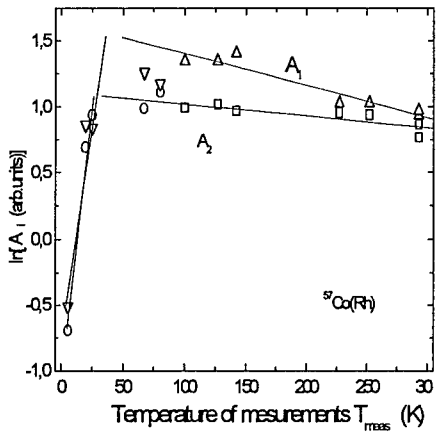

Fig.1
Temperature dependencies of the areas of NGRS components of ^{57}Co(Rh) system annealed at 853K.

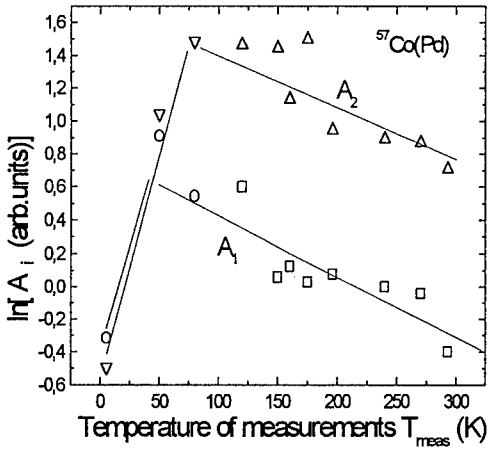

Fig.2
Temperature dependencies of the areas of NGRS components of ^{57}Co(Pd) system annealed at 723K.

The probability of the nuclear gamma-resonance (NGR) is determined by measuring the Debye-Valler factor from the dependence of the areas A_i of the NGR spectra components on temperatures $T_{meas.}$ of measurements of NGR spectra. In the fine absorber approximation the areas A_i of the

emission NGR spectra components are proportional to the recoil free fraction f_i of 14.4 keV gamma line emitted by the atomic probe localized in i-state:

$$A_i \propto f_i = \exp(-k^2\langle x_i^2\rangle) \quad (1)$$

where k is the wave vector of the resonance gamma radiation; $\langle x_i^2\rangle$ the rms shift of the emitting ^{57}Fe

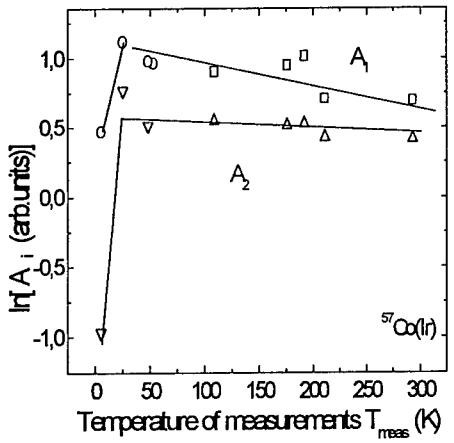

Fig.3
Temperature dependencies of the areas of NGRS components of ^{57}Co(Ir) system annealed at 953K.

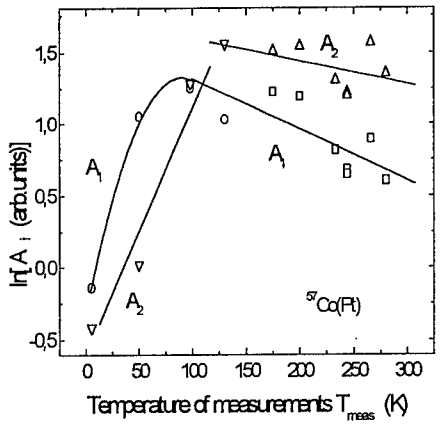

Fig.4
Temperature dependencies of the areas of NGRS components of ^{57}Co(Pt) system annealed at 773K.

atomic probe in the i-th state. Consequently, when the measurement temperature $T_{meas.}$ is reduced and $\langle x_i^2\rangle$ decreases, *the areas A_i of the NGR spectra components cannot decrease*.

By way of example, Figs.1-4 show temperature dependencies of the areas A_i of two components of NGR spectra taken after polycrystalline Rh, Ir, Pd and Pt were annealed at homologous temperatures $\approx 0.4T_{melt}$ (within "intrinsic interval"). The component-1 is due to atomic probes localized in the grain boundary core, while the component-2 is caused by atomic probes localized in adjacent lattice regions [3]. One may see that starting from a certain temperature $T_{meas.}$, *the areas of the NGR spectra component decrease* with decreasing temperature $T_{meas.}$ in the investigated matrices.

II.2. The nature of "anomalies" in $\ln A_i(T_{meas.})$ dependences.

The nature of these anomalies was established by taking NGR spectra at 5.5 K and by use a wide interval of the absorber velocity. The corresponding NGR spectra are given in Figs 5-8. As is seen, the NGR spectra taken under these conditions exhibit 12 more components, which are due to magnetic splitting of nuclear levels of atomic probes. Thus, the observed "anomalies" simply follow from measurements of NGR spectra with a high resolution in a narrow "window" of the absorber velocities.

These "anomalies" have been observed in all polycrystals (Rh, Ir, Pd, Pt, Au) where the ^{57}Fe atomic probe possesses a stable magnetic moment [4]. Such "anomalies" have not been detected in polycrystals Nb, Ta where the atomic probe loses its magnetic moment. For a more detailed discussion of the obtained results let us use the known concepts about the nature of atomic magnetism in strongly dilute solid solutions of magneto active impurities (MAI's) in Rh, Ir, Pd and Pt. The ^{57}Fe atomic probe in Rh and Ir has the local magnetic moment $(M_{Fe})_{Rh,Ir} \cong 3\mu_B$ (μ_B-the Bohr magneton) [4]. If the concentration of MAI's in these matrices is sufficiently high, the paramagnetic state of the ^{57}Fe atomic probe changes to ferromagnetic ordering of magnetic moments of the ^{57}Fe at temperatures $< T_c$-Curie temperature.

In systems like Fe(Pd) and Fe(Pt) a spin-polarized cluster is formed around each MAI [5-7]. The

spin-polarized cluster magnetic moment is approximately equal to (8-12)μ_B. When the MAI concent-

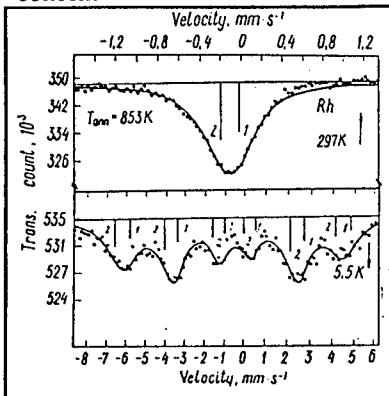

Fig.5

NGR spectra obtained at various measurement temperatures from ^{57}Co(Rh) system

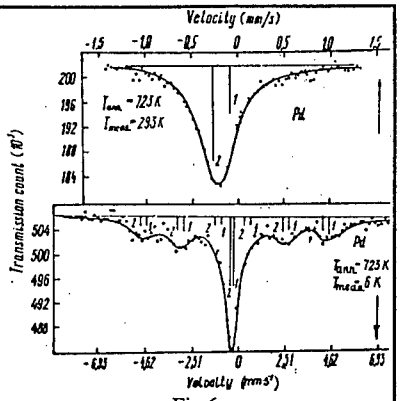

Fig.6

NGR spectra obtained at various measurement temperatures from ^{57}Co(Pd) system

ration ration is less than 100 at. ppm, these spin polarized clusters do not interact with one another. Such dilute solid solutions macroscopically represent a spin glass [7]. When the MAI concentration is greater than 100 at. ppm, spin polarized clusters overlap and their magnetic moments become ferromagnetically ordered. The field at the atomic probe nuclear increases to such an extent that nuclear levels of atomic probe split and a sextet of lines is registered in the NGR spectra. When the temperature of these systems is increased, the exchange interaction between separate spin polarized clusters decreases. As a result, the field at the atomic probe nuclear diminishes and nuclear levels of atomic probes split less. In Figs 6 and 8 one may see paramagnetic components in addition to the classical six lines. The areas $(A_i)_{para}$ are equal in both states-1 and -2.

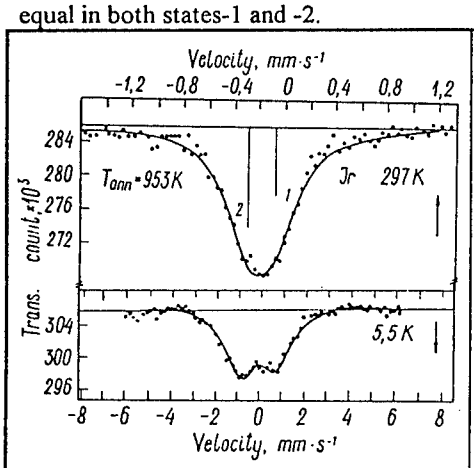

Fig.7

NGR spectra obtained at various measurement temperatures from ^{57}Co(Ir) system

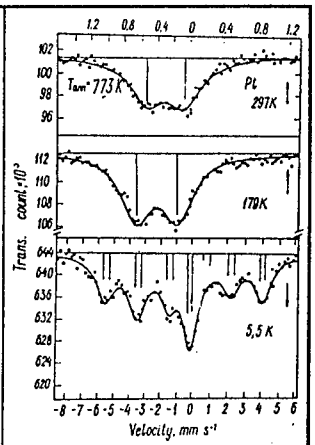

Fig.8

NGR spectra obtained at various measurement temperatures from ^{57}Co(Pt) system

II.3. The dependence of the "anomaly" temperature on the MAI concentration. In systems like Fe(Pd) and Fe(Pt) a macroscopic ferromagnetic order is established at MAI concentrations higher than 100 at. ppm as a result of the spin polarized cluster overlapping [6]. When the spin polarized cluster radius is fixed, the increase in the MAI concentration causes moving of the spin polarized clusters closer together and enhances the spin polarized cluster overlapping. As a result, the long-range ferromagnetic order is preserved at a higher temperature. Hence, in these systems the Curie temperature T_C is related to the concentration C_{MAI} of active magnetic impurities (which determine the number of spin polarized clusters) [6] by the expression:

$$\ln T_C = \text{const} - R(C_{MAI})^{-1/3}. \quad (2)$$

Here $R \propto n^{1/3}$ is the MAI interaction radius and n is the concentration of conduction electrons. At low MAI concentrations the Curie temperature is proportional to C_{MAI} [6]. The spin polarized cluster radius R_{SPC} is proportional to the density n of electron states on the Fermi surface [6].

Tab.1 MAI concentration C_{MAI}, SPC radius R_{SPC}, Curie temperatures T_C and hyperfine magnetic fields H of states-1 and -2 in some transition metals.

Solvents	Rh	Ir	Pd	Pt
C_{MAI} (at.parts)	$2x10^{-3}$	$4x10^{-2}$	$(2.8x10^{-5})^{HP}$ $(1.2x10^{-4})^{LP}$	$(2.8x10^{-5})^{HP}$ $(1.4x10^{-4})^{LP}$
R_{SPC} from (4)	4.5	1.7	$(12)^{LP}$	$(19)^{HP}$ $(11)^{LP}$
T/T_m	0.38	0.35	0.4	0.38
T_{C1} (K)	75±10	23±3	$(25±3)^{HP}$ $(42±5)^{LP}$	$(80±5)^{HP}$ $(100±5)^{LP}$
T_{C2} (K)	75±10	16±3	$(48±3)^{HP}$; $(80±5)^{LP}$	$(122±10)^{HP}$; $(200±20)^{LP}$
T_{C1}/T_{C2}	1	1.4	$(0.52)^{HP}$; $(0.52)^{LP}$	$(0.64)^{HP}$; $(0.52)^{LP}$
H_1 (T)	19	7	$(28±3)^{HP}$;	$(31.5±2)^{HP}$
H_2 (T)	19	7	$(28±3)^{HP}$;	$(32±2)^{HP}$

The value R_{SPC} can be estimated in terms of the percolation theory [9]. If at the Curie point the SPC overlapping attains a critical value, the spin polarized cluster radius is:

$$R_{SPC}=(8.1/4\pi\, C_{MAI})^{1/3} \qquad (3)$$

where $C_{SPC} \equiv C_{MAI}$ denotes the volume density of spin polarized clusters. Tab.1 gives values of the volume concentration C_{MAI} and the corresponding estimated R_{SPC}. It is seen that in Pd and Pt $(R_{SPC})_{Pd,Pt}$ is greater or equal to 10 interatomic spacings, while in Rh and Ir $(R_{SPC})_{Rh,Ir} \cong 1$. This agrees with the nature of the magnetic states of the ^{57}Fe atomic probe in the said matrices. As expected, the Curie temperature increases with growing C_{MAI} in Pd and Pt. The values of magnetic fields H_i at atomic probe nuclears do not differ in the two regions of the atomic probe localization.

II.4. The relationship between the Curie temperatures in the two regions of the atomic probe localization in polycrystals. In Rh and Ir the Curie temperatures of the grain boundary core, $(T_{C1})_{Rh,Ir}$, and the adjacent lattice are nearly the same (Tab.1):

$$(T_{C1})_{Rh,Ir} \cong (T_{C2})_{Rh,Ir} . \qquad (4)$$

In Pd and Pt

$$(T_{C1})_{Pd,Pt} < (T_{C2})_{Pd,Pt} . \qquad (5)$$

In Pd and Pt the MAI concentrations in states-1 and -2 are the same (Fe and Co do not segregate in Pd and Pt). The densities of paramagnetic states in states-1 and -2 are similar too. Therefore the relationship (6) suggests a small spin polarized cluster radius in the GB core and a low density of electron states in regions-1 of the polycrystals.

Acknowledgment. The authors wish to thank Acad. S.V. Vonsovskii for his stimulating discussions and support.

References.

[1]. S.M.Klotsman, Sov.Phys.Uspech., **33(1),** (1990), p.55
[2]. V.N.Kaigorodov, S.M.Klotsman, Phys.Rev.B, **49**, (1994), p.9374; *ibid.*, p.9387; *ibid.*, p.9395.
[3]. V.N.Kaigorodov, S.M.Klotsman, Equilibrium sites occupied in the grain boundary core during intercrystalline diffusion of ^{57}Co in metal polycrystals, Report on *iib-98*.
[4]. T.Beurle, K.Hummler, C.Elaesser, M.Faehnle, Phys.Rev.B, **49(13),** (1994), p.8802.
[5]. B.D.Dunlap, Dash J.G., Phys.Rev., **155(2),** (1967), p.460.
[6]. C.Buesher et al., Phys.Rev.B., **46(2),** (1992), p.983.
[7]. R.A.Webb,G.W.Crabtree, J.J.Williams, Phys.Rev.Letters, **43(11),** (1979), p.796.
[8]. A.Oswald, R.Zeller, P.H.Dederichs, Phys.Rev.Letters, **36(13)**, (1986), p.1419.
[9]. A.L.Efros, Physics and geometry of disordering, Nauka, M., 1982.

Correspondence: e-mail: klotsman @ imp.uran.ru

Materials Science Forum Vols. 294-296 (1999) pp. 731-734

Interfacial Properties of α-SiC in Contact with Molten Metals and Alloys

A. Tsoga, D. Skarmoutsos and P. Nikolopoulos

University of Patras, Chemical Engineering Department, GR-26500 Patras, Greece

Keywords: Wettability, Reactivity, α-SiC Oxidation State, Thermochemical Calculations

Abstract. Under equilibrium conditions thermochemical calculations based on the ideal system Si-C-O-H-Ar showed to predict quit well the nature of the α-SiC-surface. Transition of passive to active oxidation state of α-SiC-surface is expected to occur above 1573K, while at elevated temperatures enhanced Si(g) sublimation results in graphitization of α-SiC surface. Means of wettability the transition of the oxidation state of α-SiC is manifested as a spreading-contracting phenomenon of the metallic drop and as a start of reactivity, when α-SiC is in contact with non-reactive metals or reactive metals, respectively. The presence of Si(l) at the metal-ceramic interface influences both the oxidation state and the graphitization of the α-SiC-surface, leading to improved wettability and suppression of SiC dissolution in reactive metals.

Introduction

SiC finds today a lot of technical applications as an engineering ceramic and as a semiconducting material, for high temperature structural parts as well as for high-frequency and high-power electronic devices. With regard to its commercial viability, techniques are required for joining of SiC to metallic materials. This work attempts to correlate the wetting behavior and reactivity of α-SiC in contact with non-reactive and reactive metals, respectively, with the nature of the α-SiC surface (oxidation state), as this could be predicted by thermochemical calculations simulating the experimental atmospheric conditions. The contribution of alloying of the metallic phases with Si is discussed in terms of alteration of wettability and reactivity conditions in the formed interface.

Experimental

Highly-dense sintered (EKA-SiC HD) α-SiC square plaques were used as ceramic substrates for the wetting experiments. Pure metals Sn, Ag and Ni (Ventron GmbH) were used in rod form. Silicon added for the formation of metal-alloys was of a quality specified for the semiconductor industry. For the measurement of the contact angle, the samples were heated in a horizontal inductive furnace with a graphite susceptor. All experiments were carried out in a flowing argon atmosphere with 700-vpm moisture content and each experiment lasted for about 20 min. Subsequently the samples were examined by X-Ray Photoelectron Spectroscopy (XPS).

Results and discussion

Nature of the α-SiC surface. Thermochemical calculations simulating the experimental conditions were performed in order to predict the oxidation state of α-SiC. The thermodynamic approach is applied on the Si-C-O-H-Ar system, considered to consist of a gas- and a condensed- phase. The gaseous species are considered to form ideal mixtures, where their activities are equal to their partial pressures, while the standard state of the condensed phases was specified as the stable phase of the pure element or compound at the given temperature under 1 atm total pressure. For the calculations the ChemSage software was used, based on the free energy minimization of the system

under the limitation of the mass balance equations. The data needed as input for the program are the standard Gibbs energies of formation of all possible compounds involved in the process provided by the JANAF thermodynamic tables and the initial amounts of the components. SiC and SiO_2 were considered with an activity equal to unity, while the initial amounts of the gas species were chosen in ratios analogous to those measured with the aid of a gas-chromatograph, serially connected to the furnace output, under the same temperature conditions when the furnace is not loaded. The thermochemical estimates were performed considering a closed system.

According to the calculation results under equilibrium conditions, the oxidation state of SiC is mainly determined by the extend of the reactions.

$$SiC(s) + 3H_2O(g) = SiO_2(s) + CO(g) + 3H_2(g) \quad (1)$$

and

$$SiC(s) + 2SiO_2(s) = 3SiO(g) + CO(g) \quad (2)$$

Up to 1373K, the reaction between SiC and the moisture prevailing in the inert-gas furnace atmosphere favors the formation of a passive SiO_2 layer on the SiC surface (Fig.1). Carbon deposition can occur up to 1273 due to gas-phase composition (Fig.1). With increasing temperature up to 1540K, although the presence of a passive SiO_2 layer is still thermodynamically favored (Fig.1), part of it reacts further with SiC according to equation (2) to form gaseous products, mainly CO and SiO (Fig.2). At higher temperatures equation (2) becomes dominant.

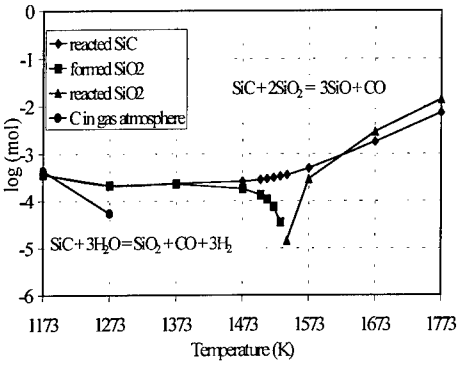

Fig. 1. Calculated equilibrium values of the formed and consumed amounts of the condensed phases varied with temperature

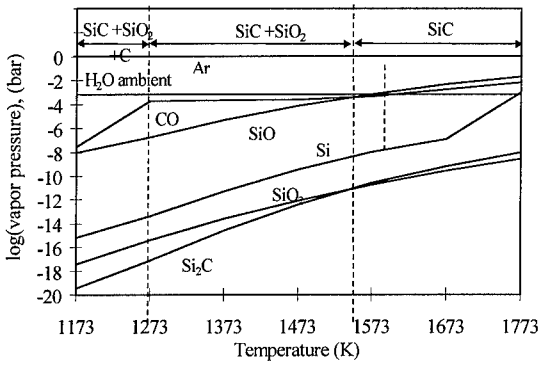

Fig. 2. Calculated equilibrium partial pressures of the gas species and the stable solid phases present at equilibrium in furnace atmosphere with annealing temerature.

Under real conditions the temperature at which the dissociation of the SiO_2 passive layer takes place, depends on the history of the sample, the time that the sample remains at each temperature as well as the ambient partial pressures of the oxidant gaseous species in the furnace atmosphere. The latter could be estimated by the application of Wagner's model [1] on SiC oxidation, considering H_2O as the oxygen carrier [2]. According to the thermochemical calculations, carried out for the specific experimental conditions the temperature where such a transition can occur is above 1573K, when the rates of CO and SiO removal from SiC surface become significant to overcome the ambient pressure of the oxidant (Fig.2). Worth to notice is also the increase of the partial pressure of Si(g) becoming more pronounced at temperatures higher than 1673K (Fig.2). Sublimation of Si can lead, as being discussed later, to graphitization of SiC surface.

Verification of the above results was performed by XPS analysis at the free surface of α-SiC samples after annealing at different temperatures (Fig.3). The measured O_{1s}, C_{1s} and Si_{2p} signals at 300K correspond to a reference, as-received α-SiC surface, after polishing. The low intensity of O_{1s} signal observed for the samples annealed at 1273K is related to the fact that up to this temperature the carbon formation is favored in the furnace atmosphere (Figs. 1 and 2), which is deposited on the

α-SiC surface. The significant reduction of the O_{1s} signal from the SiO_x layer on the SiC surface for samples annealed at 1673 and 1823K is in good agreement with the consideration already made, that the active oxidation of α-SiC starts above 1573K. The increased C-built up on the SiC surface at high temperatures, has been attributed to surface graphitization [3-5]. In accordance to the thermochemical calculations more possible source of this carbon is the Si(g) sublimation.

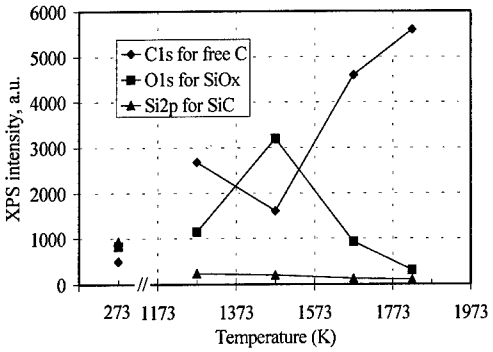

Fig. 3. The variation of three selected XPS peak intensities with annealing temperature at α-SiC surface.

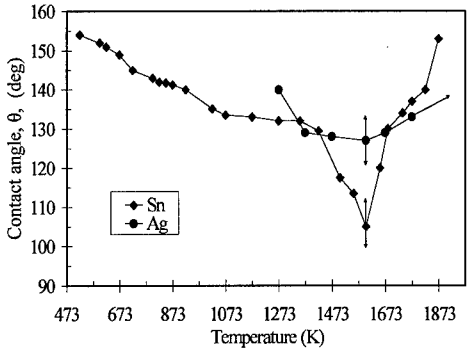

Fig. 4. Temperature dependence of the contact angle, θ, for the systems α-SiC/Sn and α-SiC/Ag

α-SiC in contact with non-reactive and reactive molten metals and alloys. The above results addressing the influence of the experimental atmospheric conditions on the oxidation state of the α-SiC surface was used to explain the wettability and reactivity behavior of α-SiC in contact with non-reactive (Sn, Ag) and reactive (Ni) molten metals and their Si-alloys. Fig.4 shows the temperature dependence of the contact angle, θ, in the systems α-SiC/Sn and α-SiC/Ag. Up to 1600K, in both systems, the contact angle decreases gradually with temperature and compares well with the literature values corresponding to the systems SiO_2/Sn (125° at 1423K) and SiO_2/Ag (142° at 1373K), respectively [6]. Presence of cavities on the debonded metallic interface indicates that the dissociation process of SiO_2 starts already at lower temperature. The pressure of the gaseous products (SiO and CO) formed at the SiC-SiO_2 interface increases with temperature and becomes high enough to overcome the ambient pressure at ~1600K, forcing the liquid drop to instability, observable as a spreading-contracting phenomenon of the metallic phase. The consumption of the SiO_2 film with time under isothermal conditions as well as with increasing temperature suppresses this phenomenon. The higher contact angles measured at T≥1673K (Fig.4) are related to the increasing C-concentration found on the α-SiC surface (Fig.3). The equilibrium angles approach the experimentally measured values in the systems graphite/Sn, θ=155°, at the temperature range 1793-1873K and graphite/Ag, θ=148°, in the range 1373-1673K, under the same experimental conditions. Addition of Si into the Sn- and Ag-melt, were found to improve the wettability with increasing temperature and holding time, while no spreading-contracting phenomenon were observed in the whole temperature range examined. For a silicon content of 17.9at% into Sn and 16.2at% into Ag respectively, contact angle was found to approach an equilibrium value (θ=35°) (Figs 5 and 6) comparable to that corresponding to the α-SiC/Si system [7]. The preferential adsorption of Si at the ceramic-metal interface favors the decomposition of the SiO_2 film which covers the α-SiC surface, according the equation $Si(\ell) + SiO_2(s) = 2SiO(g)$ at a temperature lower than the required for the present experimental conditions, enhanced wettability due to the same character of bonds (covalent bonds) in Si and SiC. Additionally suppression of the spreading-contracting phenomenon at the temperature where transition of the oxidation state of α-SiC occurs is connected to the increase in solubility limits of C and O into the metallic melt, that the presence of Si incorporates.

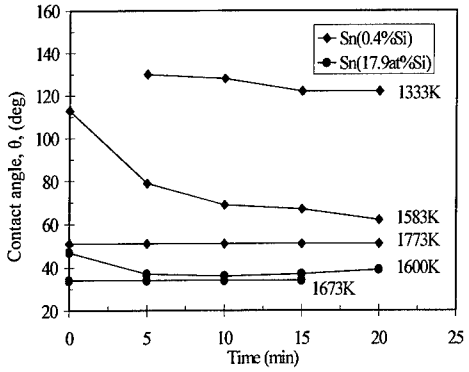

Fig. 5. Time and temperature dependence of the contact angle, θ for the systems α-SiC/(Sn-Si)-alloys

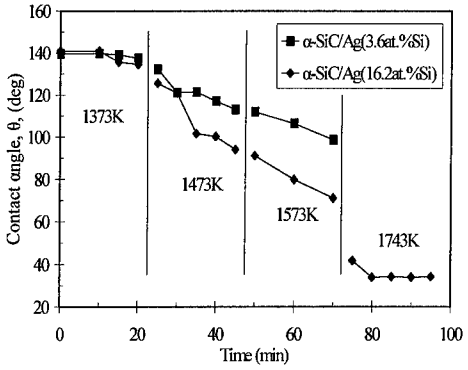

Fig. 6. Time and temperature dependence of the contact angle, θ for the systems α-SiC/(Ag-Si)-alloys

Transition of the oxidation state of α-SiC in contact with a reactive metal is manifested as a start of reactivity as was observed in the α-SiC/Ni system, showed a contact melting at a temperature 135K below the melting point of Ni. The addition of silicon into the nickel matrix (2.1, 37.1 and 47.3 at.%) increases the activity of $[Si]_{Ni}$ resulting the suppression of SiC dissolution into Ni (Table 1) [8]. A silicon content of 47.3 at.% was found to be sufficient to maintain nonreactive conditions between two components giving a contact angle θ=35°, corresponding to that of α-SiC/Si system.

Table 1. Depth of the reaction zone as measured by optical microscopy at the ceramic side in the α-SiC/Ni and (Ni-Si)-alloy systems after wetting experiments at 1773K for different experimental times.

System	Time(min)	Reaction zone (mm)
α-SiC/Ni	15	1.25
/Ni(2.1at.%Si)	30	1.25
/Ni(37.1at.%Si)	45	0.48
/Ni(47.3at.%Si)	20	not observed

References

[1] C. Wagner, J. Appl. Phys. 29 (1958) p.1295
[2] A. Tsoga, S. Ladas and P. Nikolopoulos, Acta mater. 45 (1997) p. 3515
[3] R. Berjoan, J. Rodriguez and F. Sibieude, Surf. Sci., 271 (1992) p. 237
[4] N.S. Jacobson, K.N. Lee and D.S. Fox, J. Am. Ceram. Soc. 75 (1992) p. 1603
[5] L. Muehlhoff, W.J. Choyke, M.J. Bozak and J.T. Yates Jr., J. Appl. Phys. 60 (1986) p. 2842
[6] R. Sangiorgi, M. L. Muolo, D. Chatain and N. Eustathopoulos, J. Am. Ceram. Soc. 71 (1988) p. 742
[7] P. Nikolopoulos, S. Agathopoulos, G. Angelopoulos, A.Naoumidis and H Grubmeier, J. Mater. Sci. 27 (1992) p. 139.
[8] A. Tsoga, P. Nikolopoulos, C. S. Lim, A.Naoumidis and H. Nickel, Proc. COMP'95, Intern. Symp. on Composite Materials, pp 311-315, 18-22 Sept. 1995, Corfu, Greece

Materials Science Forum Vols. 294-296 (1999) pp. 735-738

Grain Boundary Penetration of Liquid Bi in Cu Polycrystals

B. Joseph[1], F. Barbier[1] and M. Aucouturier[2]

[1] CEA-CEREM/SCECF, BP6, F-92265 Fontenay-aux-Roses, France

[2] Laboratoire de Métallurgie Structurale, Université Paris-Sud, F-91405, Orsay, France

Keywords: Grain Boundary, Grooving, Penetration, Embrittlement, Liquid Bi, Polycrystalline Cu

Abstract. This paper deals with intergranular phenomena occurring when copper polycrystals are exposed to liquid bismuth. Grain boundaries (Gbs) exhibit liquid grooving which depends on their crystallographic characteristics. Penetration of Bi is found along the Gbs, ahead of the groove tip. The phenomenon is thermally activated and the time dependence of the Gb penetration is described by linear kinetics. The crystal orientation effect on the intergranular liquid penetration is observed.

1. Introduction

When a solid metal is exposed to a liquid-metal environment, various physico-chemical processes may take place at the solid surface (dissolution, compound formation or preferential attack of grain boundaries). These effects can alter the mechanical properties of the materials and, in some systems, the embrittlement can be so severe that the solid fails instantly [1]. Although the phenomenon of liquid metal embrittlement has been recognized for many years, its explanation has not yet emerged, and its prediction is still lacking. It is therefore appropriate to consider a new work in this area. In particular, the role of liquid penetration into solids and its effect on embrittlement is to be investigated.

This paper reports a study of intergranular penetration and embrittlement of copper polycrystals upon exposure to liquid bismuth. In this system, the embrittling effect has already been mentioned [2-3] and there is evidence that the grain boundaries (Gbs) play a role in the process. In a previous work [4], we have shown that two processes take place during the interaction: (i) intergranular grooving at the solid-liquid interface, (ii) Bi penetration along the path of the boundary ahead of the groove tip. In this investigation, a more complete study of the kinetics of the grain boundary penetration is presented. The influence of the crystallographic parameters of the Gbs on the grooving and the penetration is also discussed.

2. Experimental procedure

Polycrystalline copper (Cu-OFHC, purity 99.95 %) was used. The sheet (2.1 mm thick) was annealed at 800 °C for 1 h under vacuum to obtain an average grain size of 400 μm. Specimens (2x6x35 mm^3) were prepared from this sheet and mechanically polished. They were immersed in liquid bismuth (purity 99.997 %) under argon protective atmosphere. The immersion tests were carried out at a fixed temperature (T = 300 to 600 °C) for times (t) ranging from 5 min to several hours. The composition of the molten phase was adjusted to obtain a Cu-rich liquid bismuth either saturated or undersaturated. In the latter, a slight dissolution of the solid occurred during immersion.

After immersion and cooling, some samples were cut perpendicularly to their length and prepared for examination of the grooving by scanning electron microscopy (SEM). Then, the crystallographic characteristics of the GBs (rotation axis and misorientation angle) were determined by electron back-scattering diffraction (EBSD), and the populations of boundaries in the polycrystals were statistically analysed. Other samples were stressed at room temperature after exposure to liquid bismuth (tensile

test). In one procedure, the stress was applied until the sample failed. The fracture surface was then observed by SEM. In another procedure, the stress was applied to generate incomplete failure, the objective being to promote cracks which reveal the various zones embrittled by the Bi penetration. The samples were all deformed for 10 min at a rate of 0.2 $mm.min^{-1}$, which corresponds to a deformation of about 20 %. Then, they were cut in longitudinal slices and the surfaces were polished. The cracks initiated at the solid-liquid interface and along the polished surface were characterized (number, depth) as a function of time and temperature. A study by EBSD was also performed to determine which types of boundaries were penetrated by the liquid.

3. Liquid grooving at grain boundaries

We have previously shown [4] that, after immersion of Cu polycrystals in liquid Bi, grooves were formed at the intersection of Gbs with the solid-liquid interface. Narrow channels were formed mainly in the case of undersaturated liquid (Fig. 1). In another work [5], we have reported that the kinetics of grooving was described by a parabolic law. In the case of a saturated melt, the groove angles were larger and convex profiles were observed, in agreement with the Mullins theory [6].

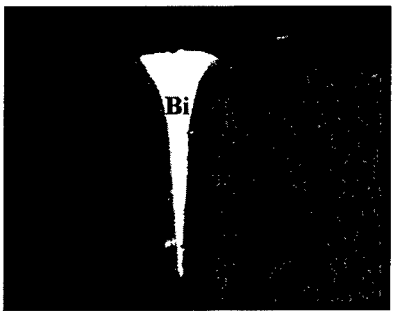

Figure 1. Grain boundary grooving after immersion of a Cu polycrystal in undersaturated liquid bismuth (T = 600 °C, t = 4 h).

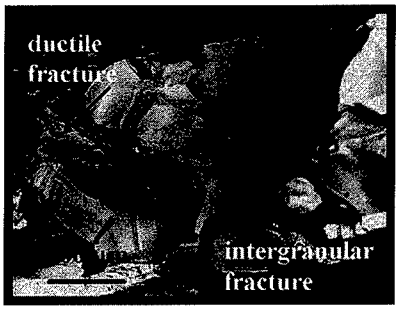

Figure 2. Fracture surface after exposure of a Cu polycrystal in Cu-rich liquid bismuth (T = 600 °C, t = 8h).

The data obtained by EBSD (T = 600 °C, t = 4 h) show that the liquid grooving depends on the crystallographic parameters of Gbs. In undersaturated liquid, nearly all the general Gbs (87 %) exhibited grooves after immersion. Grooves were never observed for twinning boundaries ($\Sigma = 3$) whereas for low angle boundaries, they were sometimes found. On the contrary, in a saturated solution, only 50 % of general boundaries were found with grooving . Thus, the results show the role of the dissolution in the grooving of Gbs. The formation of such narrow channels along Gbs in the presence of an undersaturated solution has already been mentioned in the literature [7-8].

4. Grain boundary penetration of liquid bismuth

After immersion, the Cu polycrystals failed mainly by an intergranular brittle mode when they were stressed until complete rupture. A fracture surface of a polycrystal is presented in Fig. 2. As we reported in [4], Bi is present along triple lines and in the form of particles on the intergranular surface (Fig. 3). Bi is also detected as a segregated film of several monolayers thick on the surface. These observations indicate that liquid Bi has penetrated grain boundaries ahead of the groove tip. The intergranular penetration is thus of importance in the embrittlement.

To investigate the kinetics of the phenomenon, the experimental method used to characterize the depth of the penetrated zones has to be defined. Penetration can be estimated by measuring the depth of the brittle zone on fractured surfaces, but this method does not provide an accurate characterization. In fact, the fracture occurs in regions where the penetration is the largest and thus

the depth is determined by excess. As a consequence, another method has been chosen to quantify the intergranular penetration after the immersion tests. The method consists in straining the sample until incomplete failure, so that the Gbs penetrated by the liquid bismuth open, which reveals the embrittled zones. Then, the characteristics of the intergranular cracks created in the sample (as described in section 2) are determined. In all cases, the immersion times were chosen to obtain an intergranular penetration less than the size of a grain (< 400 μm), in order to prevent connection between penetrated regions (Fig. 4). For all the samples, it was found that the ratio of Gbs exhibiting cracks was equal to 1/8. It was also verified that the depth of cracks did not change with the deformation (only the shape was modified). This demonstrates the relevance of the method proposed to characterize the Bi penetration. In other words, the depth of cracks which defines the loss of cohesion along the Gbs seems to be well related to the intergranular penetration.

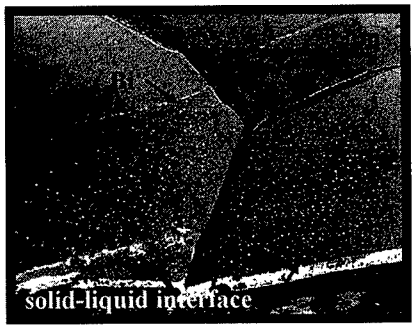

Figure 3. Observation of Bi on the intergranular surface (particles) and along triple lines after fracture of Cu polycrystal.

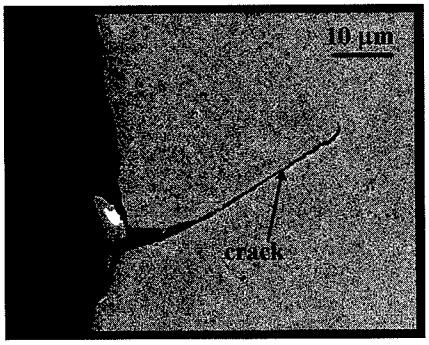

Figure 4. Observation of intergranular crack in Cu polycrystal partially deformed after immersion in Bi.

The time dependence of the penetration depth is shown in Fig. 5 for various temperatures. The kinetics of the phenomenon is clearly expressed by a linear law. The slope of each plot represents the rate of Bi penetration (Vp) along the grain boundaries. Its variation with temperature is described by an Arrhenius plot (Fig. 6). It corresponds to an apparent activation energy equal to 65 ± 10 kJ.mol^{-1}.

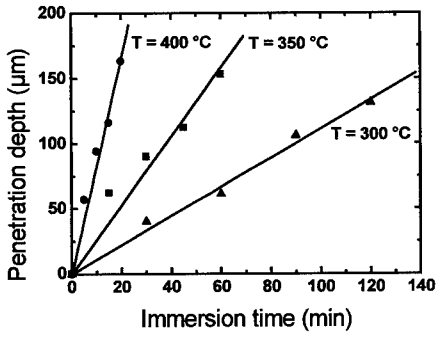

Figure 5. Time dependence of the penetration depth at various temperatures (saturated liquid).

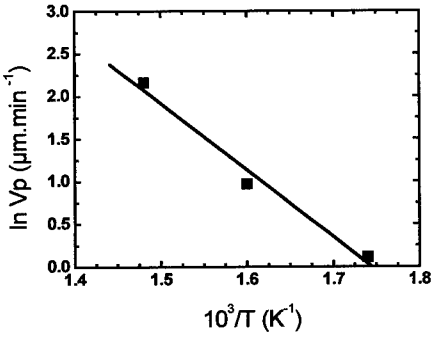

Figure 6. Temperature dependence of the rate of penetration.

The study carried out by EBSD shows the effect of crystal orientation on intergranular penetration (T = 300 °C, t = 1 h). No penetration was found for either coincidence or low angle boundaries,

whereas 25 % of the general boundaries exhibited Bi penetration. Comparison with the results of grooving is not simple because the temperatures of the experiments are not the same. In particular, the shallow depth of the grooves formed at 300 °C (less than 2 to 3 μm) makes a grooving study by EBSD impossible. It seems however that the general Gbs do not all have the same behavior with regard to the penetration.

Finally, the results indicate clearly that the penetration process is much broader than the grooving process as schematically illustrated in Fig. 7. In this example, the average groove depth is about 7 μm, whereas the average penetration is estimated at about 2000 μm. Therefore, the phenomena taking place ahead of the groove tip are of major importance in the embrittlement process.

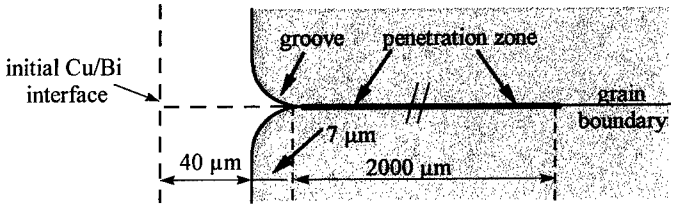

Figure 7. Schematic diagram showing the grooving and penetration processes at the Cu/Bi interface (T = 600 °C, t = 1 h, undersaturated liquid).

To explain the origin of such a rapid penetration, the linear kinetics and the activation energy value of the process must be correlated with a particular mechanism. The penetration might result from the formation of a macroscopic layer along the grain boundary. The nature of this phase is at present not clear but it could be highly disordered and characterized by large atomic displacements. In other studies, authors have reported the existence of a quasi-liquid phase [9] or an amorphous layer [10] to explain anomalous grain boundary properties. Work is being undertaken to prove that the development of such a GB phase may occur in the Cu/Bi system.

5. Conclusion

When Cu polycrystals are exposed to liquid Bi, two processes take place at Gbs. Liquid grooving, which depends on the crystallographic characteristics of the boundaries, is observed. Considerable penetration of Bi, as well, is found along the Gbs, ahead of the groove tip. This phenomenon is thermally activated, and its kinetics is described by a linear law. Crystal orientation effect is also observed. Work is in progress to correlate the intergranular penetration with a particular mechanism.

References

[1] M.H. Kamdar, Treatise on Mater. Sci and Tech. 25 (1983), p. 361.
[2] E. Scheil and K.E. Schiessl, Z. Naturforsch. 4a (1949), p. 524.
[3] E.E. Glikman, Yu. V. Goryunov and I. Yu. Ledovskaya, Soviet Mater. Sci. (1979), p. 446.
[4] B. Joseph, F. Barbier, G. Dagoury and M. Aucouturier, Scripta Mater. (1998, to be published).
[5] B. Joseph, F. Barbier and M. Aucouturier, 41ème Colloque de Métallurgie, 23-25 June 1998, Saclay, France (to be published in J. Phys. IV).
[6] W.W. Mullins, Trans. AIME, 218 (1960), p. 354.
[7] V. E. Fradkov, Scripta Mater., 30 (1994), p. 1599.
[8] B.S. Bokstein, L.M. Klinger and I.V. Apikhtina, Mater. Sci. and Eng., A203 (1995), p. 373.
[9] L.S. Chang, E. Rabkin, B. Straumal, P. Lejcek, S. Hofman and W. Gust, Scripta Mater. 37-6 (1997), p. 729.
[10] P.J. Desré, Scripta Mater. 37-6 (1997), p. 875.

Acknowledgments

The authors wish to thank T. Baudin (Orsay) for his participation in the experiments made by EBSD.

Materials Science Forum Vols. 294-296 (1999) pp. 739-742

Measurement of Grain Boundary Corrosion Current on Copper [110]-Tilt Bicrystals by Scanning Vibrating Electrode Technique

M. Yamashita[1], H. Miyamoto[2], J. Yahashi[2], H. Uchida[1], S. Hashimoto[3] and T. Mimaki[2]

[1] Department of Mechanical Engineering, Faculty of Engineering, Himeji Institute of Technology, Himeji, 671-2201, Japan

[2] Department of Mechanical Engineering, Faculty of Engineering, Doshisha University, Kyotanabe, 610-0321, Japan

[3] Department of Engineering Physics and Mechanics, Graduate School of Engineering, Kyoto University, Kyoto 606-8501, Japan

Keywords: Intergranular Corrosion, Corrosion Current, Bicrystal, Copper, Scanning Vibrating Electrode Technique

Abstract : Intergranular corrosion at [110]-tilt boundaries of high purity copper bicrystals was investigated in an acid solution using the scanning vibrating electrode technique (SVET). Anodic current peaks were observed at the grain boundaries. Cathodic current peaks were measured at small regions in the grain interiors quite adjacent to the $\Sigma 9(114)$ grain boundary. Laser micrographs obtained at the grain boundary showed that 10 μ m-wide terraced embankments parallel to the grain boundary are present extremely close to the V-shaped corrosion groove formed by the intergranular corrosion. This means that cathodic regions where electronation occurs are localized adjacent to the $\Sigma 9(114)$ grain boundary which was preferentially dissolved de-electronation site. On the contrary, little cathodic current peaks were observed at the vicinity of the $\Sigma 3(111)$ and $\Sigma 11(113)$ boundaries. These boundaries, especially the $\Sigma 3(111)$, showed lower corrosion susceptibilities, thus the amount of electron sink by de-electronation is relatively small at these boundary. This could explain the absence of cathodic current peaks at the vicinity of the grain boundaries.

1. Introduction

Localized corrosion often occurs at a grain boundary since the corrosion potential at the grain boundary differs from that at the grain interior. This potential difference is often due to chemical inhomogeneity such as precipitation and impurity segregation at the grain boundary. However, structural irregularity of the grain boundary itself intrinsically controls the grain boundary chemistry, and thus the intergranular corrosion at chemically clean grain boundary in high purity metals still appeals to the interest of electochemists and solid-state physicists. In this paper, intergranular corrosion at [110]-tilt boundaries of high purity copper bicrystals was investigated in an acid solution using the scanning vibrating electrode technique (SVET).

2. Experimental

2. 1 Preparation of bicrystal specimens

Bicrystals with symmetrical [110]-tilt grain boundaries of 99.99998%-purity copper were grown from seed crystals using the Bridgman method under vacuum. Crystallographic orientations of the bicrystals determined by examining back-reflection

X-ray Laue patterns showed that the bicrystals were characterized by the CSL orientation relationships, as shown in Table 1. Specimens were cut perpendicular to the tilt axis by spark cutting, then were annealed and polished by emery papers and diamond paste. The shape and dimensions of the specimens are shown in Fig. 1.

Table 1 Crystallographic characteristics of the bicrystal specimens.

Misorientation about<110>	Σ-value	Grain boundary plane
70.90°	3	(111)
133.40°	11	(113)
143.40°	9	(114)

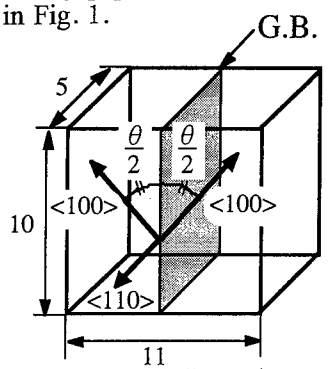

Fig. 1 Shape and dimensions of the bicrystal specimens.

2. 2 Corrosion current measurement

The bicrystals were immersed in a modified Livingston's dislocation etchant of HCl:3cc+CH_3COOH:1cc+H_2O:2696cc at 303±2K, and then the grain boundary corrosion currents were measured by the SVET. The probe of the SVET was W wire with diameter of 0.1mm. The scanning vibrating electrode apparatus is schematically shown in Fig. 2. Laser microscope and scanning electron microscopy (SEM) were used to observe the surface morphology.

3. Results and Discussion

3. 1 Corrosion current distribution at grain boundary

Corrosion current distributions of the bicrystals are shown in Fig. 3 Anodic current peaks were observed at the grain boundaries, therefore de-electronation of electron-donating copper atoms occurs and electrons supplied at the boundaries seek cathodic sites as an electron source. Cathodic current peaks were measured at small regions in the grain interiors quite adjacent to the Σ9(114) grain boundary. Surface observations at the grain boundary showed that 10 μm-wide terraced embankments parallel to the grain boundary are present extremely close to the V-shaped corrosion groove formed by the intergranular corrosion, as shown in Fig. 4(b). This means that cathodic regions where electronation occurs are localized adjacent to the Σ9(114) grain boundary which was preferentially dissolved de-electronation sites. Thus, the Σ9(114) grain boundary is apparently active electron donor and the electron accepters are localized very close to the boundary. This could interpret the previously unexplained observation[1] that the Σ9(114) grain boundary groove grows deeper but not wider with time thus resultantly crevice-like corrosion groove forms. The present SVET experiments revealed a kind of galvanic

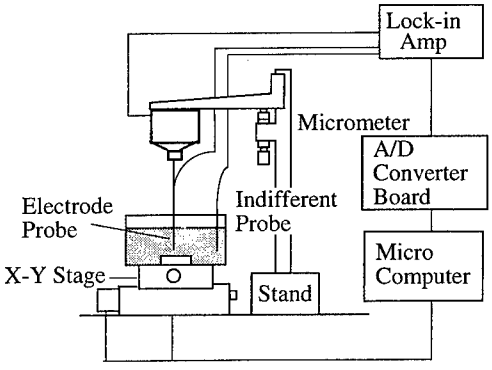

Fig. 2 Schematic illustration of scanning vibrating electrode apparatus.

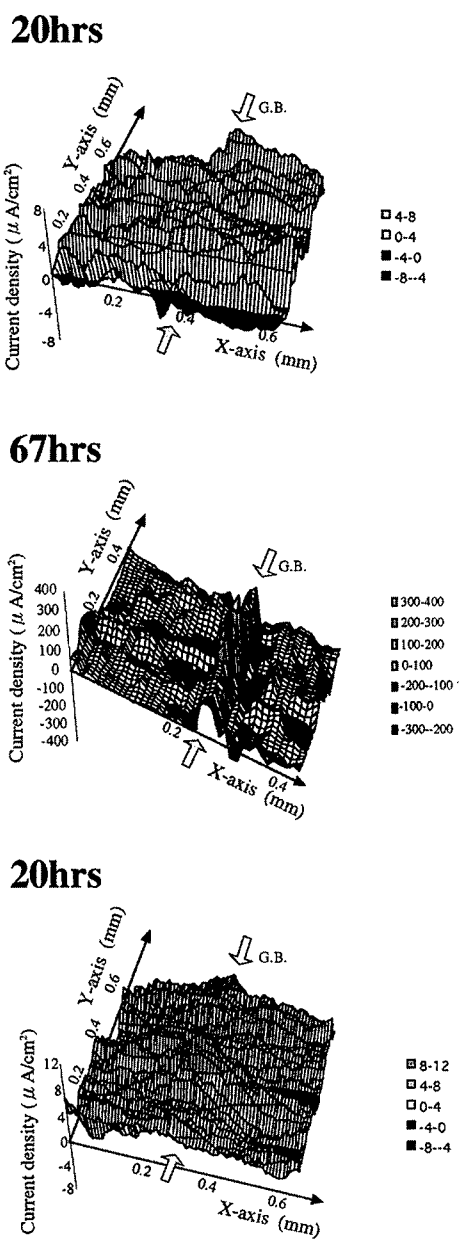

Fig. 3 Corrosion current distributions of the Σ3(111) (a), Σ9(114) (b) and Σ11(113) (c) bicrystals immersed in an acid solution.

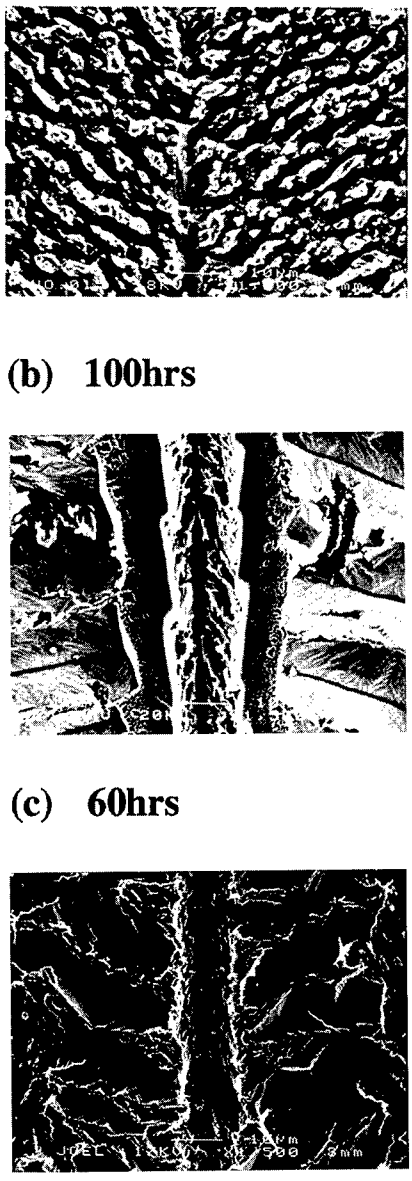

Fig. 4 Scanning electron micrographs of the intergranular grooves at the Σ3(111) (a), Σ9(114) (b) and Σ11(113) (c) bicrystals after immersion in an acid solution.

anode effect of the Σ9(114) grain boundary, which protects grain interiors next to the grain boundary. This cathode localization was observed only in the Σ9(114) bicrystals.

On the contrary, little cathodic current peaks were observed at the vicinity of the Σ3 (111) and Σ11(113) boundaries. The terraced embankments near the grain boundaries were not observed in micrographs shown in Fig. 4 (a) and (c). These boundaries, especially the Σ3(111), showed lower corrosion susceptibilities, thus the amount of electron sink by de-electronation is relatively small at these boundary. This could explain the absence of localized cathodic current peaks at the vicinity of the grain boundaries.

3. 2 Susceptibility to grain-boundary corrosion

Figure 5 shows the time dependences of the depth and width of the intergranular grooves formed in the bicrystal specimens. It is said that the Σ9(114) boundary possesses the highest corrosion rate, whereas the Σ3(111) boundary shows very low susceptibility to corrosion. These susceptibility variation might be dependent upon the structure and energy of the grain boundary[1),2)]. The time dependences indicate that the depth and width of the intergranular groove increase linearly with time except the width at the Σ9(114) boundary. It is considered that the localized cathodic regions adjacent to the Σ9(114) boundary suppress the groove growth in the direction perpendicular to the grain boundary.

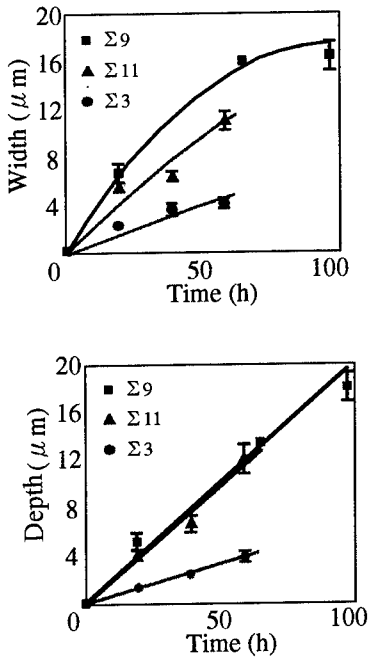

Fig. 5 The time dependences of the depth and width of the intergranular grooves formed in the bicrystals.

4. Conclusion

Anodic current peaks were observed at the copper [110]-tilt grain boundaries. Localized cathodic current peaks were measured quite adjacent to the Σ9(114) grain boundary. Thus, the Σ9(114) grain boundary is apparently active electron donor and the electron accepters are localized very close to the boundary. It is said that the Σ9(114) boundary possesses the highest corrosion rate, whereas the Σ3(111) boundary shows very low susceptibility to corrosion. This susceptibility variation might be dependent upon the structure and energy of the grain boundary.

References

[1]M. Yamashita, T. Mimaki, S. Hashimoto & S. Miura, Phil. Mag. A, 63, (1991), p. 695.
[2]M. Yamashita, S. Hashimoto, T. Mimaki & S. Miura, Mater. Trans. JIM, 32, (1991), p. 885.

Materials Science Forum Vols. 294-296 (1999) pp. 743-746

Oxygen-Induced Intergranular Decohesion in IN718

J.A. Pfaendtner and C.J. McMahon, Jr.

Department of Materials Science and Engineering, University of Pennsylvania, Philadelphia, PA 19104-6272 USA

Keywords: Dynamic Embrittlement, Nickel-Base Superalloy, Intergranular Decohesion, Oxygen, IN718

Abstract

The cracking of IN718 was studied under static loads in air and oxygen and found to undergo oxygen-induced dynamic embrittlement in the same way as in steels with surface-adsorbed sulfur and in bronze with surface-adsorbed tin. When the oxygen supply at the surface is plentiful, the intergranular fracture surface exhibits decohesion with no apparent plasticity, which is consistent with stress-induced oxygen penetration on the nanometer scale ahead of a sharp crack. In one-atmosphere oxygen, cracking was observed to occur at rates on the order of 10^{-5} m/sec. An advancing crack could be abruptly arrested by switching the atmosphere from oxygen to vacuum of less than 10^{-4} torr.

Introduction

Nickel-base superalloys are known to exhibit cycle-dependent transgranular fatigue-crack propagation when tested at low temperatures or under relatively high fatigue cycle frequency [1]. At elevated temperatures, low-cycle-fatigue crack propagation in oxygen-bearing environments becomes time dependent as the cycle frequency decreases, or as the hold time increases (cf. Fig. 1) [2]. A change in fracture mode to smooth, brittle intergranular cracking generally accompanies the transition from cycle-dependent to time-dependent fatigue-crack propagation. In the literature, various reports suggest that this type of brittle cracking is due to some effect of environmental oxygen or water vapor. Based on measurements of grain-boundary niobium segregation and enrichment, Valerio *et al.* [3] proposed that brittle intergranular cracking in alloy IN718 involves the formation of a niobium oxide film on the boundary surfaces. In an investigation on the effect of moisture on the high-temperature cracking behavior of nickel-base superalloys, Hayes *et al.* [4] suggested that the major role of moist air was to increase the kinetics of grain boundary sliding, which was though to be the dominate damage process. Molins *et al.* [5] proposed a cracking mechanism involving the formation of NiO nuclei on the freshly formed crack faces behind a propagating crack, which in turn promotes vacancy formation by cation diffusion to the growing oxide. It was suggested that vacancy injection and migration in the grain boundary ahead of the crack tip may be responsible for the observed embrittlement.

It is the hypothesis of this work that the oxygen-induced intergranular brittle cracking is a manifestation of dynamic embrittlement, a phenomenon responsible for the sulfur-induced cracking in low-alloy steels [6] and the tin-induced cracking of Cu-Sn bronzes [7]. In this case, oxygen would adsorb on the free surface at the crack tip and be driven into the grain boundary by a tensile stress to cause decohesion (cf. Fig. 2).

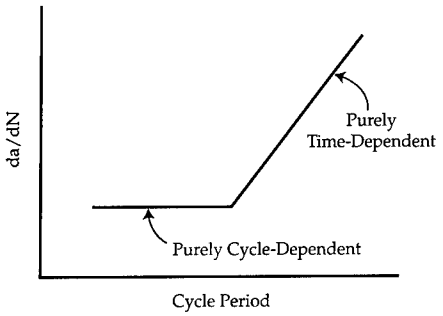

Figure 1. Schematic effect of cycle period, showing the transition from cycle-dependent to time-dependent behavior [1].

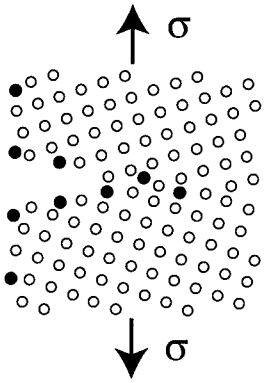

Figure 2. Schematic representation of stress-driven diffusive penetration of a grain boundary by a mobile, surface-adsorbed embrittling element and the progressive decohesion of this boundary [8].

Experimental Procedure

Single-edge-notch (SEN) specimens with dimensions 70 x 10.2 x 10.2 (mm) were cut by electric-discharge machining from an IN718 forging that had been subjected to the following heat treatment: 1040°C 1 hr., 718°C 12 hr., 620°C 12 hr. The specimens were pre-cracked and loaded to a fixed displacement in pure bending in a testing chamber with an atmosphere of laboratory air or pure oxygen. The specimens were heated using two ellipsoidal reflecting infrared lamps to 650°C, as measured by a K-type thermocouple that was spot welded to the specimen. Cracking was detected and monitored by observing drops in load, as recorded by a PC interface. Crack-growth rates were calculated from the load-vs.-time data via a specimen-compliance calibration. The chemical composition of this alloy is given in Table 1.

Table 1. Chemical composition of IN718 (wt.%)

Fe	Cr	Nb	Mo	Ti	Al	Co	Si	Mn	C	B	S	Ni
18.64	18.18	5.15	2.95	1.02	0.48	0.13	0.36	0.06	0.04	0.004	<0.003	Bal.

Results

Subcritical crack growth occurred in two stages, as shown by the load-vs.-time plot in Fig. 3 for constant-displacement testing in air at 650°C. The corresponding crack-growth rates are plotted versus stress intensity (K) in Fig. 4. It can be seen that Stage I cracking corresponds to a regime of K-dependent cracking, where cracking begins at rates less than 10^{-6} m/sec. Stage II cracking is independent of K and was observed to occur at maximum rates in excess 10^{-5} m/sec. Crack growth in IN718 could be turned on and off by switching the test environment from one atmosphere oxygen to vacuum, as illustrated in Fig. 5. The response of the crack-growth rate to changes in the oxygen pressure was very fast, indicating that the oxygen acted locally at the advancing crack tip to cause cracking. This kind of oxygen-induced cracking was found to occur by brittle intergranular decohesion, with the grain-boundary facets appearing smooth to the sub-micrometer level (cf. Fig. 6). Fine striations with a spacing of ~ 0.1 mm were observed on these facets, indicative of step-wise crack advance. Macroscopically, the advancing crack front was observed to be irregular, with many uncracked ligaments remaining behind the crack tip, spanning the crack faces (cf. Fig. 7).

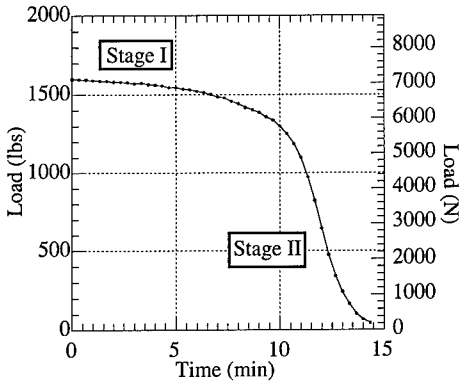

Figure 3. Load relaxation due to cracking in IN718 in laboratory air for a SEN specimen loaded to a fixed displacement at 650°C.

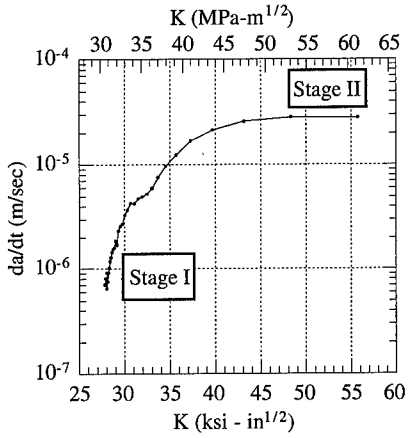

Figure 4. Dependence of crack-growth rate on applied stress intensity for cracking in IN718 at 650°C.

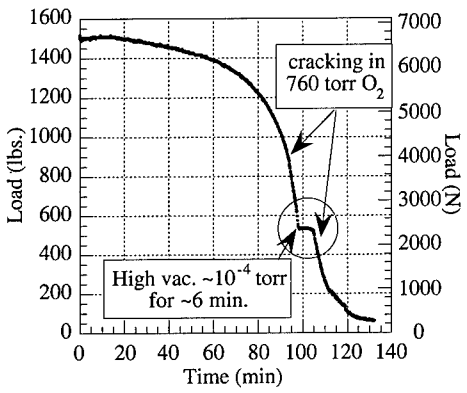

(a)

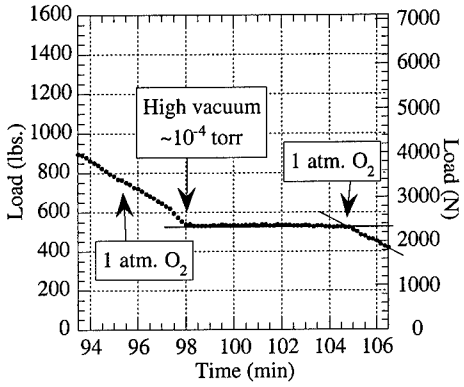

(b)

Figure 5. a) Load relaxation due to cracking in IN718 for a SEN specimen loaded to a fixed displacement in oxygen at 650°C, showing the effect of removal, and then re-admission, of the oxygen to the test chamber. b) blow-up of the region circled in (a) showing the rapid arrest of the growing crack with removal of the oxygen atmosphere.

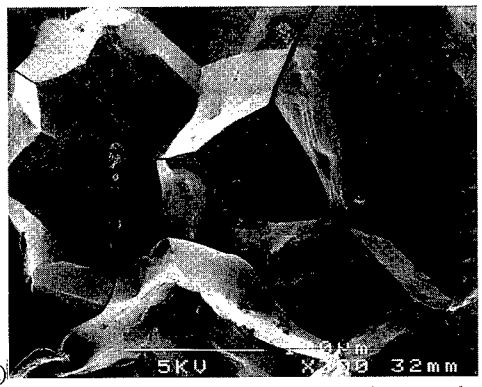

(a)

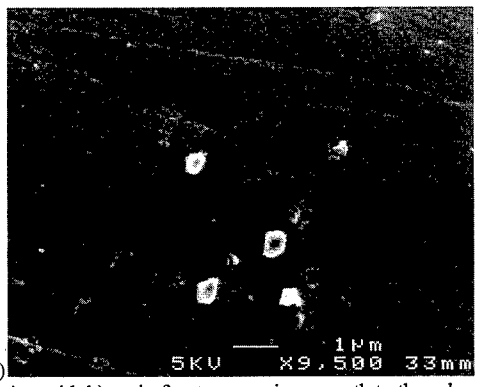

(b)

Figure 6. a) This kind of cracking occurs by intergranular decohesion with b) grain facets appearing smooth to the sub-micrometer level and sometimes exhibiting fine striations.

Figure 7. Interrupted tests demonstrate that high-temperature cracking occurs by fingers of decohesion that advance into uncracked material, with some uncracked ligaments remaining behind. As shown, the crack advanced from bottom to top with regions of intergranular cracking shown in black; all other areas are room-temperature transgranular fracture.

Discussion

The cracking behavior observed in this study is similar to that of previous studies on dynamic embrittlement. Oxygen-induced cracking of IN718 has the same fracture appearance as sulfur-induced cracking of low-alloy steels [6] and tin-induced cracking of Cu-Sn bronzes [9], and occurs at rates that are of the same order of magnitude. The response of crack growth to a changing oxygen pressure is very rapid, suggesting that dynamic embrittlement is a crack-tip phenomenon involving the diffusion-penetration of oxygen in the near-tip grain boundary region. The discontinuous nature of cracking, as indicated by the observed sub-micrometer striations, is thought to be the result of constraint arising from the irregular crack front and ligaments that remain behind the crack front, which are, in turn, a result of the non-uniform cracking rate from point to point. This is considered to be a consequence of the dependence of oxygen diffusivity on grain boundary structure. In a study on dynamic embrittlement of Cu-Sn bicrystals [10], it was observed that cracking occurred by the continuous separation of the grain boundary without the appearance of striations, suggesting that the striations and discontinuous cracking are artifacts associated with polycrystalline materials.

Acknowledgments

This work received support from the National Science Foundation under grant CMS95-03980 and INT-94-14328, and the US-CZ Science and Technology Program grant #95008.

References

[1] M.F. Henry, General Electric Co., unpublished research (1997).
[2] K.-M. Chang, M.F. Henry, and M.G. Benz, *JOM* **42,** 29-35 (1990).
[3] P. Valerio, M. Gao, and R.P. Wei, *Scripta metall. mater.* **30,** 1269-1274 (1994).
[4] R.W. Hayes, D.F. Smith, E.A. Wanner, and J.C. Earthman, *Materials Science and Engineering A* **177,** 43-53 (1994).
[5] R. Molins, G. Hochstetter, J.C. Chassaigne, and E. Andrieu, *Acta metall.* **45,** 663-674 (1997).
[6] D. Bika, J.A. Pfaendtner, M. Menyhard, and C.J. McMahon Jr., *Acta metall.* **43,** 1895-1908 (1995).
[7] D. Bika and C.J. McMahon Jr., *Mater. Res. Soc. Symp. Proc.* **238,** 399 (1992).
[8] D. Bika and C.J. McMahon Jr., *Acta metall.* **43,** 1909-1916 (1995).
[9] E.V. Barrera, M. Menyhard, D. Bika, B. Rothman, and C.J. McMahon Jr., *Scripta metall. mater.* **27,** 205-210 (1992).
[10] R.C. Muthiah, J.A. Pfaendtner, S. Ishikawa, and C.J. McMahon Jr., *submitted for publication* (1998).

Materials Science Forum Vols. 294-296 (1999) pp. 747-750

Antimony, Tin and Selenium Segregation in FeSiC Alloys

M. Jenko[1], M. Godec[1], H. Viefhaus[2] and H.J. Grabke[2]

[1] Institute of Metals and Technology, Lepi pot 11, SI-1000 Ljubljana, Slovenia

[2] Max-Planck-Institut für Eisenforschung, Max-Planck Str. 1, D-40237 Düsseldorf, Germany

Keywords: Sb, Sn, Se, Surface Segregation, Grain Boundary Segregation, Surface Activated Recrystallization, Grain Growth, Core Loss, Texture, Non Oriented Electrical Steel

ABSTRACT The influence of surface active elements e.g. antimony, tin and selenium additions (from 0.025 to 0.1 wt %) into FeSiC alloys on the texture formation was investigated. Measurements of surface segregation of Sb, Sn Se and C were performed under UHV conditions in the temperature range from 25 to 900° C, using high resolution AES and TDS. Maximum equilibrium surface segregation of Sb and Sn of about 0.6 monolayer was estimated at 700° C. At higher temperatures T>800° C, the desorption of antimony from the surface was measured. Sn surface segregation decrease was explained with a higher solubility of Sn in FeSiC alloy . In the temperature range from 25 to 500°C carbon surface segregation of FeSiC alloy with 0.05wt.%Se was measured. The grain boundary segregation of antimony and selenium was negligible. Sn grain boundary segregated layer was estimated to 0.2 monolayer. Surface segregation of Sb, Sn, Se and C causes differences in surface energies and stability of different grains. Controlled surface segregation promotes the selective grain growth and effects on texture formation.

1 INTRODUCTION

The segregation of certain surface active elements e.g. antimony, tin and selenium on the surface and interfaces of iron-base alloys is interesting from different points of view and has been discussed in several papers [1-3]. It is well known that several elements act as severely embrittling impurities in steel and that they segregate to grain boundaries of body centered cubic iron base alloys. A beneficial effect of a small addition, 0.025 –0.1 wt%, into silicon steels on the texture formation as well as on energy losses was also found [1-8]. These surface-active elements segregate on the surface and grain boundaries and affect the texture formation, simply by the enrichment at the free surfaces, i.e. surfaces and grain boundaries. Such enrichment affects the recrystallization producing an increase of the number of ferrite grains with soft magnetic lattice space orientation in the sheet plane and in this way improves electrical properties. Our investigations show a strong correlation between antimony and tin surface segregation and the orientation of the grains in the sheet surface.

2 EXPERIMENTAL

The experimental alloys of compositions given in Table 1 with a minimal content of uncontrolled elements and impurities were prepared from pure base materials in the laboratory. Ingots were hot rolled to a 2.5 mm thick strip, descaled and than cold rolled with the intermediate recrystallization annealing to a final thicknass of 0.15 mm with a final deformation of 60%.

The surface segregation phenomena were investigated *in situ* by AES at a basic vacuum of $5x10^{-10}$ mbar in the temperature range from 25 to 900° C. The surface of the samples was metallographically polished before the AES measurements. The sample was heated up to 900° C for 10 minutes and sputter cleaned, annealed in the temperature range from 450 to 900° C and investigated *in situ* by AES

Table 1: Chemical composition of investigated alloys (wt.%)

Alloy	Si	Al	C	Sb	Sn	Se	P	S
$FeSiC_{Sb}$	1.95	0.95	0.002	0.025-0.1	-	-	<0.0001	0.0010
$FeSiC_{Sn}$	2.00	1.00	0.002	-	0.025-0.1	-	<0.0001	0.0005
$FeSiC_{Se}$	2.00	1.00	0.002	-	-	0.025-0.1	<0.0001	0.0005

and TDS..The antimony surface enrichment of the surface was determined by following the peak height ratio (PHR) of amplitudes between dominant Sb ($M_5N_{4,5}N_{4,5}$) and Fe($LM_{2,3}$) Auger transitions at kinetic energies of 454 eV and 650/703 eV respectivelyThe tin surface enrichment of the surface was determined by following the peak height ratio (PHR) of amplitudes between dominant Sn($M_5N_{4,5}N_{4,5}$) and Fe ($LM_{2,3}$) Auger transitions at kinetic energies of 430 eV and 650/703 eV respectively.

The AES spectrometer was additionally equipped with a Thermal Desorption Spectrometer (TDS) for *in situ* investigation of antimony and tin desorption. The samples were introduced in the UHV system of Auger spectrometer equipped with TDS and heated several times up to 950°C.

Grain boundary segregation of Sb, Sn and Se was also measured by AES method. Cylindrical samples were prepared from the ingots of the same base material notched, encapsulated in quartz tubes, evacuated to about 10^{-6} mbar, normalized for 24 hours at 1000° C, cooled and aged at 550° C for 200 and 500 hours, then introduced into UHV system of the Auger spectrometer at basic vacuum $4x10^{-4}$ mbar and after cooling to aproximately –120° C *in situ* impact fractured. The AES analysis were taken from as many intergranular fractures as possible.

The grain orientation was determined on the polished samples by etch pitting method and by X-ray diffractometry with Mo Kα radiation and ODF function was developed.

3 RESULTS AND DISCUSSION

AES measurements showed different quantity of segregated Sb on the surface of different grains, Fig.1[5]. The Sb surface segregation rate was perceived at the temperatures T>650° C and it increased with the increasing temperature, at T> 850° C Sb segregation rate declined, Fig. 2[6].

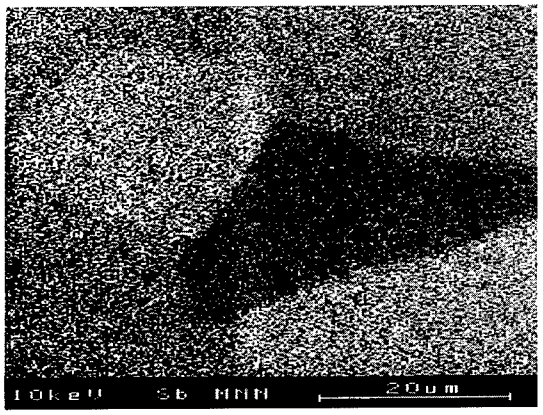

Fig. 1: SAM image of Sb surface segregation on different grains of $FeSiC_{Sb}$ alloy

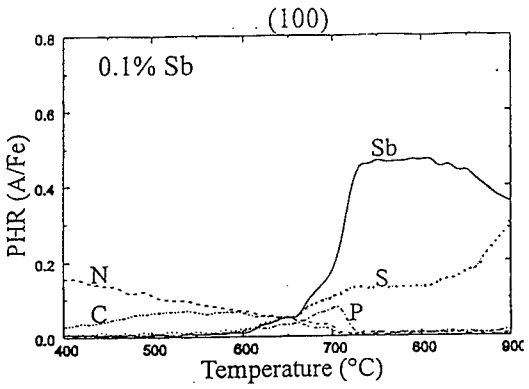

Fig. 2: Temperature dependence of surface segregation on $FeSiC_{Sb}$ alloy

Fig. 3 shows the temperature dependence of surface segregation of Sn, alloying and tramp elements of investigated $FeSiC_{Sn}$ alloy with 0.05 wt% Sn on grains of {100}< 001> and {111} <001> crystallographic orientation. Kinetics studies confirmed the orientation dependence of Sn surface segrgegation[8].

Grain boundaries of FeSi sheet with 0.1wt% Sb were also analyzed by AES after ageing for 200 and 500 hours at 550°C.The fracture facets were almost completely transgranular, only on some areas a decohesion was noticed. AES measurements showed negligible grain boundary segregation of C, Al and Si, but there was no indication of Sb. We supposed that C substituted the Sb on grain boundaries as it is reported in the literature [9].

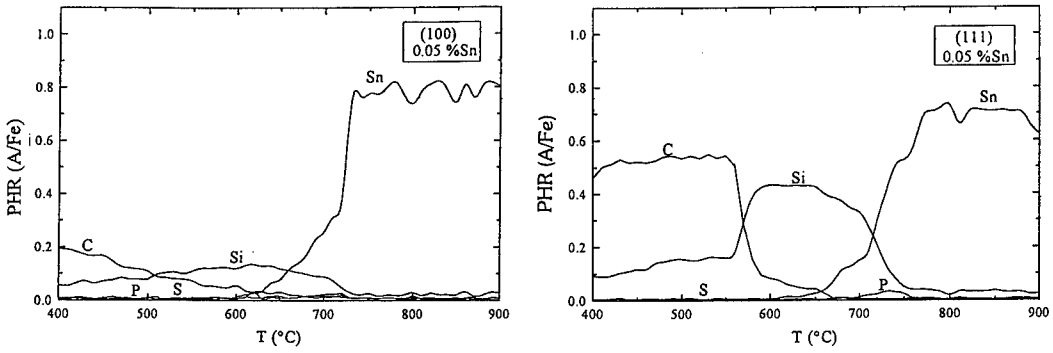

Fig. 3: Temperature dependence of Sn surface segregation, alloying and tramp elements on grains: a) {100}<001> and b) {111} <001>

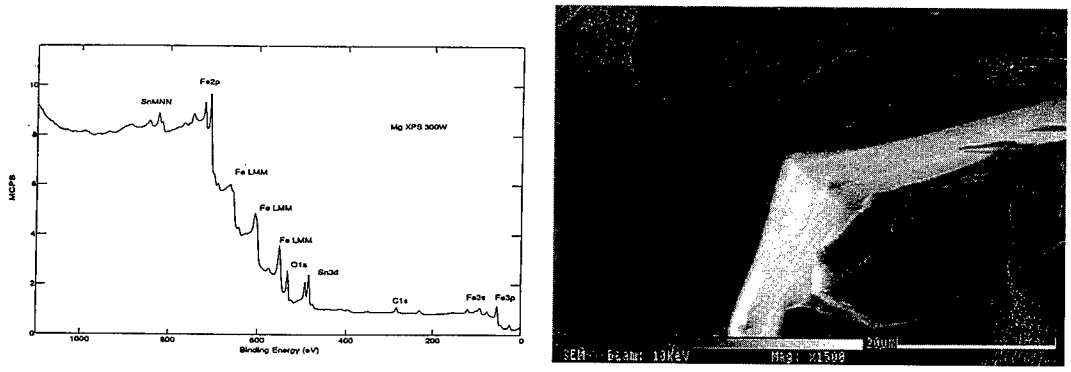

Fig. 4: XPS spectrum of in situ fractured $FeSiC_{Sn}$ alloy with 0.1wt.% Sn and SEM image of intergranular face

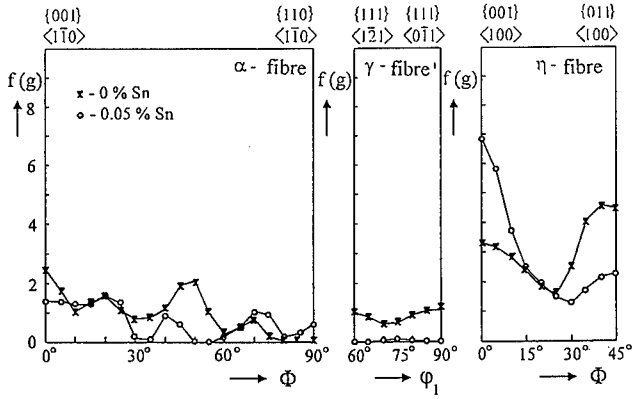

Fig. 5: Texture fibres on surface of $FeSiC_{Sn}$ alloy with 0.05 wt.% Sn and without it.

XPS measurements of *in situ* fractured Fe Si alloy with 0.1wt% Sn confirmed Sn grain boundary segregation Fig. 4[ ].

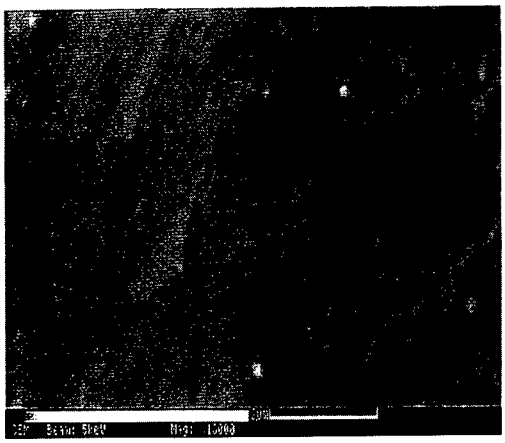

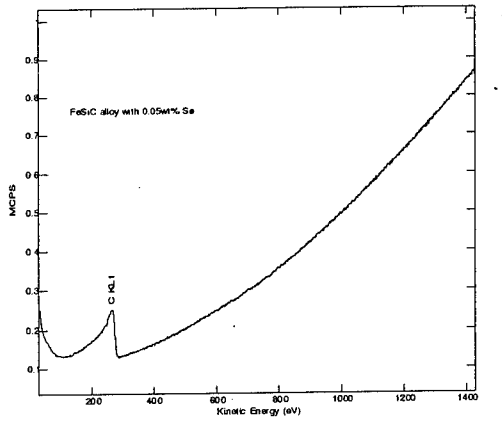

Fig. 6. a) SEM image of C surface segregation of $FeSiC_{Se}$ alloy with 0.05% Se; b) AES spectrum of carbon cluster in (a)

Texture measured on the surface of alloys with Sn showed an increase of (100) planes parallel to the rolling direction by three, compared to the sheet without Sn, Fig. 5.
Our preliminary *in situ* investigation of selenium surface segregation showed at annealing up to 600°C in UHV at the polished surface of FeSiC with 0.05wt% Se the apperance of the segregated carbon in the form of clusters, Figure 5. The phenomenom is important because of its effect on the the thermodynamics of decarburization process of FeSi steels as well as on effect of alloying and/or tramp elements on carbon activity and will be the object our future investigations.

4 CONCLUSIONS

The maximum equilibrium Sb surface segregation of 0.6 monolayer was measured after annealing at 750°C on grains with {111} <001> crystalographic orientation. The maximum equilibrium Sn surface segregation was reached also at 750° C. Grain boundary segregation of C, Al and Si was negligible, there was no Sb indicated in investigated alloys.Grain boundary of Sn was estimated to a 0.2 monolayer. Texture represented as a section through three dimensional orientation distribution space in fixed directions showed that the volume fraction of grains with {100}< 001> increased for three times in Sn sheets when compared to sheet without Sn. We concluded that only a certain level of surface segregation promotes the selective grain growth.
The phenomenom of segregated carbon in the shape of clusters, on the surface of FeSi sheet alloyed with 0.05%Se was found. The effect of segregated carbon on thermodynamics of decarburization process of FeSi steels as well as the alloying and tramp elements affect on the carbon activity will be the object of our future investigations.

5 REFERENCE

1. G.Lyudkovski, P.K.Rastogi, M.L.Bala, Journal of Metals 1(1986)18
2. F.Vodopivec,F.Marinšek,D.Gnidovec, B.Praček, M.Jenko, J. Magn. Magn.Mat. 97, (1991) 281
3. H.J.Grabke, ISIJ International, 29, 7, (1989)529
4. M.Jenko, F.Vodopivec, B.Praček, M.Godec and D.Steiner, J.Mag.Mag.Mat. 133 (1994) 229.
5. M.Jenko, F.Vodopivec, H.J. Grabke, H.Viefhaus, B.Praček, M.Lucas, M.Godec, Steel research 65,11,(1994) 500
6. M.Jenko, H.Viefhaus, M.Lucas F.Vodopivec, M.Godec, D.Steiner Petrovič M.Milun, T.Valla Metals, Alloys,Technologies, 28,4, (1994) 561-565
7. V. Rusenberg, H. Viefhaus, Surf.Sci. 172 (1986) 615
8. M.Godec, Recrystallization and grain growth of non oriented electrical steel sheet microalloyed with tin, Ph.D Thesis, University of Ljubljana, Ljubljana 1997.
9. R.Mast, H.Viefhaus, M.Lucas, H.J.Grabke, Metals, Alloys, Technologies, 30(1996)531

Materials Science Forum Vols. 294-296 (1999) pp. 751-754

Grain Boundaries in Monolayer Liquid Foams

M.A. Fortes and M. Emlia Rosa

Departamento de Engenharia de Materias, Instituto Superior Técnico, Lisboa, Portugal

Keywords: (Grain Boundaries) Topological Defects, Liquid Foams

ABSTRACT

Grain boundaries between two misoriented hexagonal froths of the monolayer type were studied using a device that allows a continuous change of the misorientation angle θ and deformation of the bicrystal by elongation/compression. The boundaries contain topological defects in the form of 5- and 7-sided cells (bubbles), usually in pairs (dislocations). The defect content of a boundary can be predicted by considering the sequence of dangling edges at the surfaces of the two separated crystals and depends on θ and on the inclination, α, of the boundary. As a bicrystal is deformed, the boundary defects move originating a net translation of the boundary and a change of its inclination.

INTRODUCTION

Bubble rafts have been used by several authors as a model system of monoatomic crystals and grain boundaries [1-5]. These rafts consist of identical, nearly spherical bubbles floating on the surface of a detergent solution. We have used a variant of the bubble raft, termed a monolayer foam [6,7], in which the bubbles are sandwiched between the surface of the liquid and an horizontal glass plate at a short distance (around 3mm in the experiments reported). The bubbles are identical hexagonal prisms separated by vertical liquid films the thickness of which depends on the distance of the plate to the liquid surface.

This paper describes experiments with bicrystal monolayer foams formed between two bars at an angle θ (Fig. 1a). Each crystal has a closed packed direction along the adjacent bar (Fig. 1a),

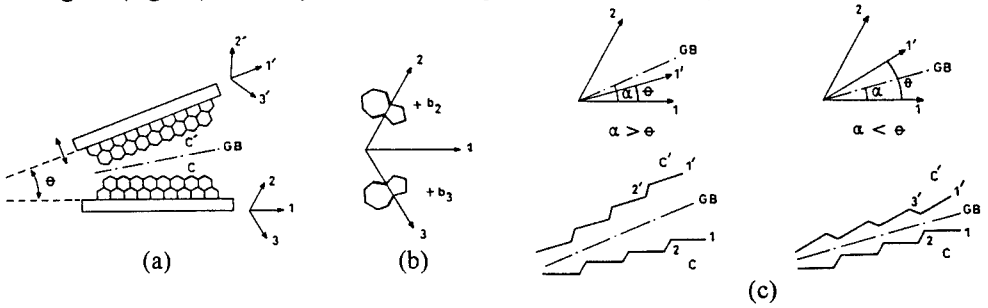

Fig. 1 - a) Experimental device used to produce two foam crystals C and C' of variable θ, with the possibility of deforming the bicrystal. b) The unit vectors $\overline{b}_i$ of the hexagonal network, showing the sign convention for the Burgers' vectors of 5/7 dislocations. c) Ledge-step structure of the surfaces of the two grains meeting at a boundary of inclination α. The orientation of the steps in grain C' depends on whether $\alpha>\theta$ or $\alpha<\theta$.

leading to a bicrystal of misorientation θ with the boundary between the two bars. One of the bars can be rotated and translated in a direction perpendicular to it; this allows a continuous change of θ and deformation of a bicrystal of fixed θ.

STRUCTURE OF GRAIN BOUNDARIES

The boundaries prepared were, in general, not straight, their inclination relative to the close packed directions varying along them. The boundaries are formed by a string of 5- and 7-sided cells separated by 6-cells as in the examples of Figs. 2d and 3. No cells with number of sides different from 5, 6 or 7 were found. The defect cells are usually in pairs of adjacent 5- and 7-cells, but occasionally isolated 5- and 7-cells, in equal numbers, were observed. The 5/7 pairs are dislocations of unit Burgers' vector $\bar{b}$, one of the lattice vectors of the hexagonal lattice. The vast majority of Plateau borders are at the junctions of three cells, but a few could be found in the grain boundaries which are connected to 4 or 5 cells ("free volume"). The close packed rows in general change abruptly their direction at the boundary but, in some cases, when they traverse defect free boundary regions, they look more continuous but slightly distorted. Occasionally, isolated 5/7 pairs are observed inside the crystals under static conditions.

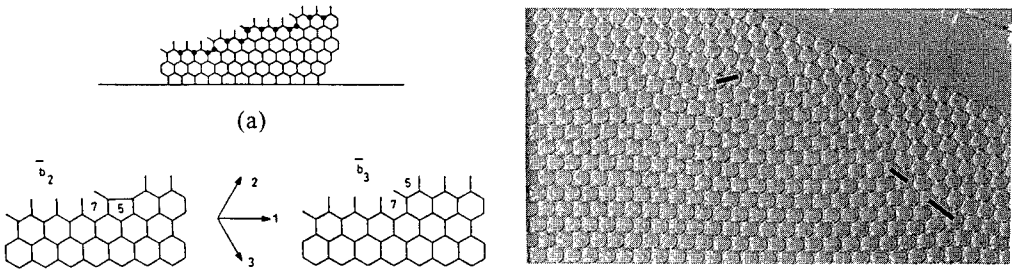

Fig. 2 - a) Dangling edges (d-edges) and saturated vertices (·) at the $5\bar{b}_1 + 2\bar{b}_2$ surface of crystal C. b) Replacement of a 6-cell at a step by a 5-cell, with reduction in the number of d-edges ($\bar{b}_2$ dislocation). c) A $\bar{b}_3$ dislocation forms when the d-edges at a step are connected to a ledge in the opposite crystal surface. d) Grain boundary region in a foam bycrystal ($\theta \cong 20°$) showing dislocations $\bar{b}_2$ and $\bar{b}_3$ and two separated 5- and 7-cells.

The grain boundary dislocations in a straight region of the boundary are of two types, with different orientations of the 5/7 cells in the pair. Consider the three closed packed directions in the two crystals C and C' (Fig. 1a) and define the unit vectors $\bar{b}_1$, $\bar{b}_2$ and $\bar{b}_3$ along these directions in each crystal. The angle θ between $\bar{b}_1$ and $\bar{b}_1'$ in crystals C and C' respectively (the misorientation angle) and the angle α between the grain boundary and direction $\bar{b}_1$ can both be taken in the interval 0, 30° (Fig. 1c).

The dislocations $+\bar{b}_2$ and $+\bar{b}_3$ are shown in Fig. 1b. (The dislocations $-\bar{b}_2$ and $-\bar{b}_3$ have the 5/7 cells in the opposite sides). The two types of dislocations observed in the boundaries with the bars in directions 1 and 1' (and with $\alpha < 30°$) have Burgers' vectors $+\bar{b}_2$ and $+\bar{b}_3$. Even in fairly straight boundary regions the spacing of the dislocations is not usually uniform (Figs. 2d and 3). Relatively long defect free regions are observed in some boundaries. It should be noted that the effective temperature of the foam is close to 0K and equilibrium (minimum free energy) configurations may not form.

The defect content of a boundary can be predicted by considering the surfaces of the two separated crystals and connecting them without introducing cells with number of sides different from 5, 6 or 7. The two surfaces can be described as containing ledges along directions 1 and 1' in the two crystals, separated by steps of orientation $\bar{b}_2$ (in crystal C) and $\bar{b}_2'$ or $\bar{b}_3'$ (in crystal C') depending on the inclination of the boundary (Fig. 1c). Each surface is then characterized by a sequence of dangling edges (d-edges) and saturated vertices, as in Fig. 2a.

To form the boundary we first equalize the numbers of d-edges in a reference length along the boundary. This is achieved by replacing 6-cells at steps by 5-cells as in Fig. 2b. When the d-edges are connected the 5-cell becomes adjacent to a 7-cell and a $\bar{b}_2$ dislocation results.

Steps of orientation $\bar{b}_2$ and $\bar{b}_2'$ can be connected with no defects (Fig. 1c) but steps $\bar{b}_2$ and $\bar{b}_3'$ can not. Dislocations of vector $\bar{b}_3$ are introduced when the steps are connected to opposite ledges as in Fig. 2c. It is possible to derive equations for the density of dislocations of each type as a function of θ and α.

DEFORMATION OF BICRYSTALS

Deformation of the individual crystals caused by translation of the moving bar, at constant θ, occurs mostly by nucleation of fresh dislocations at the surfaces, followed by glide. These dislocations have Burgers' vectors $\pm\bar{b}_2$ or $\pm\bar{b}_3$ at 60° and 120° to the confining bars. In addition to reflections at the bars [7], reflection of glide dislocations at the grain boundary was also observed, particularly if the boundary contains a high density of defects. The grain boundary acts as a source and as a sink for glide dislocations, in the sense that grain boundary dislocations become glide dislocations and vice versa.

The defects at the grain boundary move, inducing a translation of the boundary and a change of its orientation, as shown in Fig. 3: the boundary approaches the fixed bar in tension and moves in the opposite direction in compression, inducing a change in the number of bubbles in the two sides of the boundary (the total number is of course constant). The individual dislocations may move for different distances such that a straight boundary may become zigzaged and vice versa, as in the example shown in Fig. 3. The 5/7 dislocations move by successive T1 (neighbour switching) operations. The edge that "switches" (i.e. the edge that is reduced to zero) is a 6/7 edge adjacent to the 5 cell (marked bold in Fig. 1b) [7]. There are two possibilities which correspond to two directions of motion (e.g. directions ±2 for a $\bar{b}_2$ dislocation). In a boundary with dislocations $+\bar{b}_2$ and $+\bar{b}_3$, elongation (for example) may cause dislocation displacement in directions $\pm\bar{b}_2$ or $\pm\bar{b}_3$, depending on the edge that switches.

CONCLUSIONS

Grain boundaries between two hexagonal foam crystals contain cells with 5 and 7 sides, in equal numbers. The defect content of a boundary can be predicted from the ledge-step configuration at each grain surface. Low defect densities, which are presumably associated with low energy boundaries, occur when there is a favourable "correspondence" of dangling edges and steps at the two surfaces, and this is not directly correlated to coincidence of lattice sites. Most grain boundary defects are 5/7 dislocations with the same Burgers' vectors as those that may occur inside the crystals and may glide into or out of the boundary under stress inducing a translation and a change of inclination of the boundary. The displacement of the individual boundary defects is somehow erratic and occurs in a direction that depends on the orientation of the edge that shrinks to zero length.

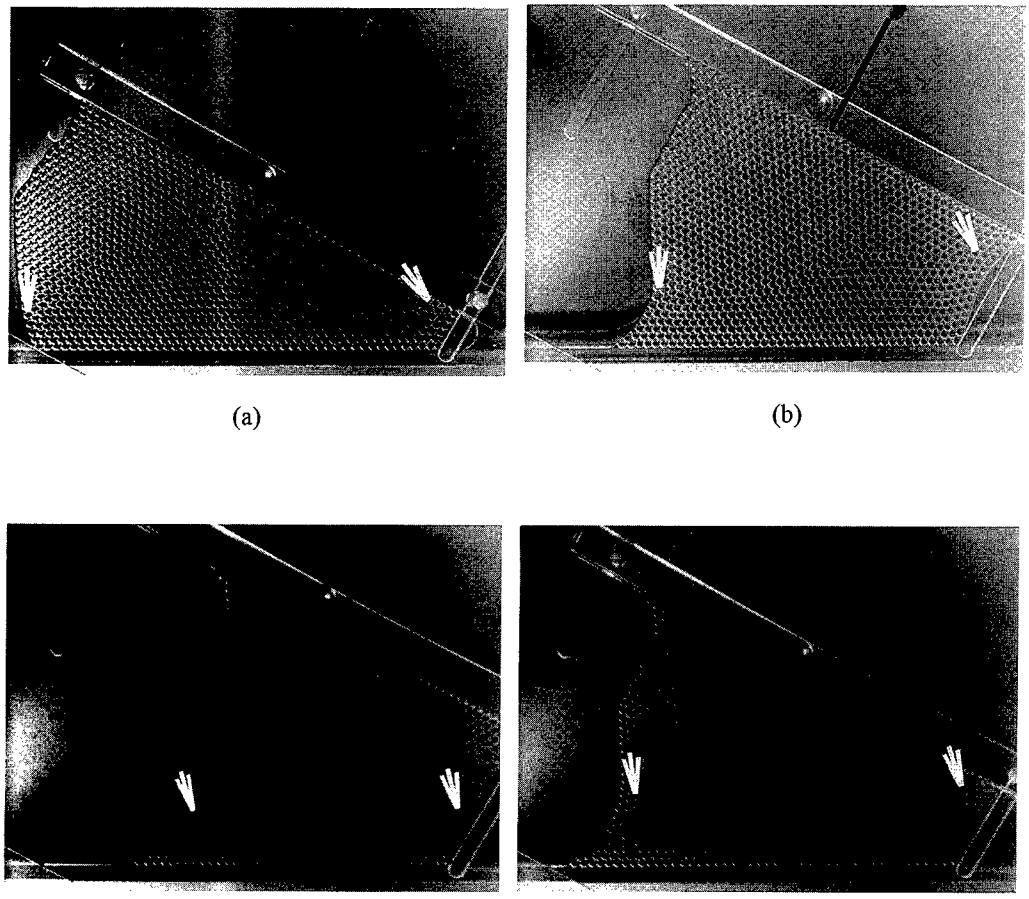

(a) (b)

(c) (d)

Fig. 3 - Sequence obtained by increasing a) to c) and then decreasing (d) the separation of the bars at constant $\theta \cong 30°$.

REFERENCES
1 - L. Bragg and J.F. Nye, Proc. Roy. Soc. (A) 190, 474 (1947).
2 - W. M. Lomer and J. T. Nye, Proc. Roy. Soc. (A) 212, 576 (1951).
3 - E. Fukushima and A. Ookawa, J. Phys. Soc. Japan 8, 609 (1953) ; 9, 44 (1954) ; 12, 139 (1957)
4 - Y. Ishida, J. Mat. Sci. 7, 72 (1972)
5 - M. F. Ashby, F. Spaefen and S. Williams, Acta Metall. 26, 1647 (1978)
6 - M. Fátima Vaz and M. A. Fortes, J. Phys. Cond. Matter, 9, 8921 (1977)
7 - M. Emília Rosa and M. A. Fortes, Phil. Mag. A77, 1423 (1998)

Materials Science Forum Vols. 294-296 (1999) pp. 755-758

Radiation-Induced Grain Boundary Segregation in Austenitic Stainless Steels

E.P. Simonen and S.M. Bruemmer

Pacific Northwest National Laboratory, P.O. Box 999, Richland, WA 99352, USA

Keywords: Grain Boundaries, Segregation, RIS, IASCC

Abstract

Radiation-induced segregation to grain boundaries in austenitic stainless steels has been evaluated for a wide range of solute species, temperatures, irradiation dose and dose rate, and irradiation particle type. The primary findings from measurement and modeling are that major alloying elements (Fe, Ni and Cr) segregate predominately by the inverse-Kirkendall mechanism and undersized minor elements segregate by the interstitial-association mechanism. Several hundred measurements of radiation-induced grain boundary composition have been analyzed and rate theory models of solute-point defect interactions are shown to be useful descriptors of the segregation process. This fundamental study of segregation has aided the definition of grain boundary microchemistry during exposure to neutron irradiation in power reactors and relates to the specific problem of irradiation-assisted stress corrosion cracking.

Introduction

Defect-solute interactions near grain boundaries cause redistribution in solute concentration during irradiation and result in radiation-induced segregation (RIS). [1] RIS depends on both the intensity of the defect flux to the interface and the strength of coupling between the defect flux and solute. The coupling can be associated with relative solute diffusion rates or can be associated with relative solute binding to point defects. During diffusive coupling with vacancies, fast diffusing elements will deplete, whereas slow diffusing elements will enrich. During bound-solute coupling, undersized solutes bind strongly with self interstitials and enrich from interstitial flow to grain boundaries.

This paper outlines a comprehensive study of segregation behavior in irradiated austenitic stainless steels. Previous studies of RIS have emphasized radiation of specific alloys under specific conditions without generalizing to the broad range of radiation. Measured segregation of both major and minor elements is evaluated using a kinetic interpretation with consistent parameter assumptions. From this interpretation, basic science insights into defect-solute interactions near grain boundaries are obtained.

Major Solute Element RIS

Grain boundary microchemistries have been documented in irradiated steels under many conditions of irradiation particle type, temperature, dose and alloy composition for alloys of nearly the same composition. [2-6] Analytical transmission electron microscopy (ATEM) and scanning Auger microscopy have provided the majority of the experimental measurements and have been shown to give comparable results. [4, 7] A convenient method to integrate major alloying elements segregation behavior is by comparing the proportional radiation-induced decrease in Cr with the increase in Ni. This is shown in Figure 1 for grain boundary composition measurements on stainless steels irradiated by heavy ions. The behavior for ions, protons and neutrons are nearly identical and can

be accurately predicted by the inverse Kirkendall mechanism. [2] Controlling parameters for the degree of major alloying element RIS are the relative diffusion rates for Fe, Ni, and Cr which are determined independently from high temperature diffusion experiments.

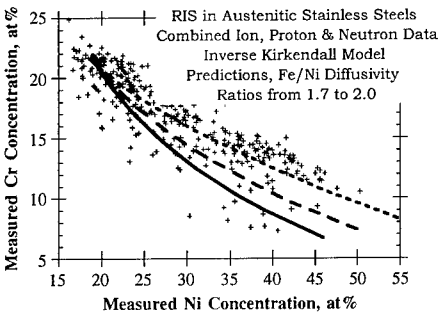

Figure 1. ATEM and SAM Measurements of Radiation-Induced Grain Boundary Cr and Ni Concentrations versus Model Prediction.

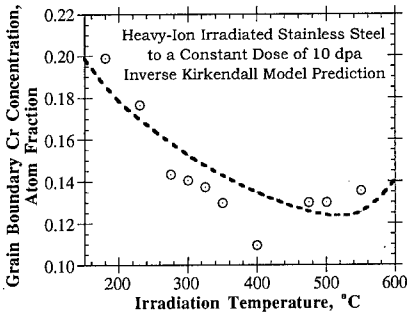

Figure 2. Measurement and Prediction of Cr RIS Temperature Dependence for Ni-ion Irradiated Stainless Steel.

Evaluation of the temperature dependence of Cr depletion can be used to determine the activation energies for vacancy migration and vacancy formation. A maximum in RIS occurs at intermediate temperatures with RIS decreasing at low temperatures because vacancy mobility is reduced and mutual recombination is enhanced. At higher temperatures, RIS decreases because back-diffusion is enhanced. The measured and calculated temperature dependence of the grain boundary Cr concentration for heavy-ion irradiations is shown in Fig. 2. [2] Good agreement has also been documented for proton irradiations. In addition, excellent matches are seen for the dose dependence of Cr, Ni and Fe RIS at 500°C for heavy ions and at 400°C for protons. [2] A vacancy migration energy of about 1.0 eV and a vacancy formation energy of 1.5 eV are in accord with measured segregation behavior. Both of these values are reasonable estimates, although the vacancy-formation energy at a grain boundary must be less than in the matrix (~1.9 eV) as evidenced in self-diffusion experiments at high temperatures. It is clear from these detailed comparisons that major alloying element RIS in stainless steels is controlled by vacancy exchange .

The validated inverse-Kirkendall model has been extended to predict behavior during neutron irradiation of commercial alloys. In order to quantify these predictions, the initial Cr enrichment at grain boundaries due to thermal non-equilibrium segregation (TNES) had to be accounted for. Therefore, the starting grain boundary composition in the inverse Kirkendall model was modified for TNES enrichment of Cr at grain boundaries. Predictions are compared to available ATEM results on LWR-irradiated, austenitic stainless steels in Fig. 3. The measured dose dependence data show that Cr remains enriched to a dose of about 1 dpa. However, predictions reveal that the grain boundary Cr enrichment is eliminated after irradiation exposures less than 1 dpa even for an initial enrichment to 28 at%. The predictions assume that the initial Cr enrichment is compensated by Fe depletion and account for the through-thickness spatial resolution of the analyzing probe.

At intermediate doses, the measured Cr RIS profile with TNES initial enrichment exhibits a "W" shape (enrichment at the interface and adjacent depletion). The prediction agrees with the steep Cr depletion profile that occurs as the boundary is approached, but not with the Cr behavior in the precise boundary plane. [6] The RIS model assumes that atomic jumps into and out of the boundary occur with the same behavior as in the matrix. The delay in the calculated depletion is

simply the time required to deplete the extra Cr atoms associated with TNES enrichment. It is clear that the Cr enrichment is being sustained by a different mechanism probably chemical binding with other solute (e.g., B).

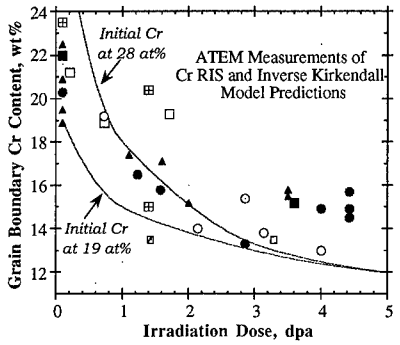

Figure 3. Measured Neutron Cr RIS in Comparison to Inverse Kirkendall Predictions.

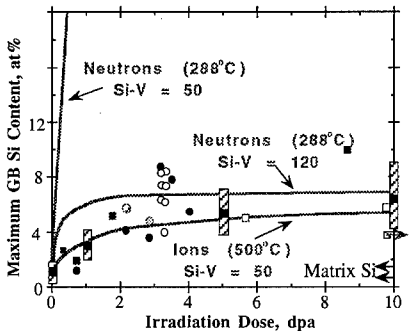

Figure 4. Measured RIS of Si in Comparison to Interstitial Association Model Predictions.

Minor Solute Element RIS

Grain boundary enrichment of undersized minor elements is expected as a consequence of RIS. Of the common undersized elements such as Si, P and S, only Si has been documented to consistently enriched at grain boundaries after irradiation. Si enrichment has been measured in both ion, proton and neutron irradiations. P is often observed to be enriched in irradiated alloys, but the enrichment is often comparable to that in the non-irradiated condition. S enrichment has not been observed in irradiated alloys, most likely because it is incorporated in sulfides and is not available as a solute for segregation.

Radiation-induced segregation predictions and measurements for Si are shown in Fig. 4 as a function of dose (ions and neutrons). The predicted ion-induced segregation assumes a solute interstitial binding energy of 0.4 eV and a constant vacancy-solute capture factor (Si-V) of 50. A comparison of the calculated dose dependency indicates that a factor of 50 is in accord with the measured dose dependency for ions at 500°C but overestimates the measured dose dependency for neutrons at 288°C. The binding energy of 0.4 eV is consistent with a measured binding of 0.42 eV for P (similar size misfit) in stainless steel [8] and the preferred capture factor of 50 is consistent with measurements of fast diffusion of Si in stainless steel by the vacancy mechanism [3]. The failure of the ion calibrated model to predict the dose dependence of neutron-induced segregation of Si is not expected. The calibrated model, i.e., vacancy-solute capture of 50 and binding of 0.4 eV, greatly overpredicts the neutron irradiation data. Similar overpredictions are made attempting to model P where no significant RIS has been observed after LWR irradiations. These discrepancies may be related to matrix interactions limiting the mobile solute in commercial alloys available for RIS.

Summary

Quantitative measurement and mechanistic modeling of grain boundary composition in irradiated austenitic stainless steels has elucidated interactions between solute, point defects and grain boundaries. For inverse Kirkendall RIS of major alloying elements Fe, Cr and Ni, model input parameters have been established by independent experiments. The relative diffusion rates of Fe, Cr, and Ni determined from RIS experiments at low temperatures (less than 500°C) are consistent with diffusion rates determined from high temperature annealing. This is expected based on the

diffusion rate dependency on vibrational frequency as opposed to activation energy. Furthermore, the solute diffusion energies (migration and formation) inferred from inverse Kirkendall segregation at low temperature are consistent with energies determined from solute diffusion measurements inferred from annealing at intermediate temperatures.

The RIS response induced by ions, protons and neutrons all exhibited consistent segregation behavior based on a fixed set of defect-solute parameters. This nearly identical response indicates that the three particle types are creating the same fundamental defect that is influencing RIS to grain boundaries. Although vacancies, interstitials and mobile clusters are expected during irradiation, these experiments indicate that vacancies are the dominant defect affecting the grain boundary Fe, Cr and Ni composition changes. Inverse Kirkendall segregation accounts for observed segregation without any consideration of a contribution from the interstitial association mechanism. The inferred minor contribution from interstitials is expected based on the weak differences in elastic binding for solute of similar atomic size. This is in contrast to Si and P that have large size misfits with the base metal and should interact strongly with self interstitials.

RIS of Si did not exhibit a consistent behavior when comparing ion and proton irradiation of model alloys with LWR neutron irradiation of commercial alloys. These differences in response for minor elements in neutron irradiated commercial alloys suggests that RIS of these elements is subject to complications not included in simple rate theory models. The potential for minor-solute RIS is significant according to interstitial association model predictions, but grain boundary measurements indicate that RIS is effectively inhibited. It is not known if these inhibition mechanisms are intrinsic to complex stainless steels under these irradiation conditions.

Acknowledgments

This research was supported by the Materials Sciences Branch, Office of Basic Energy Sciences, U.S. Department of Energy, under Contract DE-AC06-76RLO 1830. Pacific Northwest National Laboratory is operated for the U.S. DOE by Battelle Memorial Institute.

References

1. J. O. Stiegler, ed., Workshop on Solute Segregation and Phase Stability During Irradiation, J. Nucl. Mater. (1979) p. 83.
2. E. P. Simonen and S. M. Bruemmer, J. Nucl. Mater. 239(1996) p.193.
3. E. P. Simonen and S. M. Bruemmer, in Microstructure Evolution During Irradiation, MRS Symposium Vol. 439 (1996) p. 569.
4. S. M. Bruemmer, L. A. Charlot and E. P. Simonen, 7th Int. Symp. on Environmental Degradation of Materials in Nuclear Power Systems - Water Reactors, eds. S. M. Bruemmer, A. R. McIlree and R. E. Gold, National Association of Corrosion Engineers (1995) p. 971.
5. E. P. Simonen and S. M. Bruemmer, 8th Int. Symp. on Environmental Degradation of Materials in Nuclear Power Systems - Water Reactors, eds. S. M. Bruemmer and A. R. McIlree, American Nuclear Society (1997) p. 751.
6. E. P. Simonen and S. M. Bruemmer, Corrosion 98, National Association of Corrosion Engineers, (1998) Paper 139.
7. S. M. Bruemmer, Corrosion 98 (1998) Paper 138.
8. S. M. Murphy, J. Nucl. Mater., 168 (1989) p. 31.

Materials Science Forum Vols. 294-296 (1999) pp. 759-762

On the Segregation Redistribution in the Fe-Ni Austenite under Thermal and Radiation Effects

V.V. Sagaradze, A.G. Mukoseev, V.A. Shabashov and S.S. Lapin

Institute of Metal Physics, Ural Branch RAS, 18 S. Kovalevskaya Str.,
RU-620219 Ekaterinburg, Russian Federation

Keywords: Fe-Ni Austenite, Phase Transformation, Spinodal-Like Decomposition, Irradiation, Mossbauer Spectroscopy

Abstract.The possibility that two types of phase transformations – the radiation-induced and thermally activated decomposition of austenite to nickel-enriched and nickel-depleted FCC components – take place in the previously thought of as the single-phase high-temperature (773-973 K) range of the Fe-Ni equilibrium diagram was analyzed. The Mössbauer and electron microscopic investigations showed that the purposefully produced concentration-inhomogeneous FCC alloys of iron with 32-34% Ni were fully homogenized in that high-temperature region. This fact indicates to the absence of the thermal decomposition dome in the said areas of the Fe-Ni equilibrium diagram.

INTRODUCTION

The artificial introduction of point defects by irradiation with high-energy particles has been used recently to construct and refine equilibrium diagrams of various alloys. In particular, the authors [1] supplemented the known Fe-Ni equilibrium diagram with two domes of nickel redistribution in the high-temperature range above 773 K (see Fig. 1). The first wider dome is attributed to the spinodal-like decomposition of the FCC phase of the Fe-Ni alloys under irradiation. The second narrower dome is defined as the range of the ordinary equilibrium thermal decomposition of austenite at 673-923 K. The said equilibrium diagram was constructed thanks to low-angle scattering of neutrons [3,4], which revealed some concentration changes in 34Ni annealed at 898 K for 230 days. It is not clear why the low-temperature (683-723 K) nickel redistribution requires ten hours [5,6], while the high-temperature (898 K) decomposition lasts for hundreds of days.

In this work we planned to check the presence or the absence of thermal decomposition in FCC Fe-Ni alloys on equilibrium diagram [1] (Fig.1) not by the nickel redistribution in the FCC (γ) phase but, oppositely, by the kinetics the purposefully produced nickel concentration inhomogeneity is eliminated in this temperature range.

EXPERIMENTAL TECHNIQUE

The subjects of study were pure model FCC iron alloys containing 32.5 and 34.2 wt.% nickel (alloys types 32Ni and 34Ni respectively) and also a reactor austenitic steel 16Cr15Ni3Mo1Ti . The Fe-Ni alloys underwent the forward $\gamma \rightarrow \alpha$ martensitic transformation on cooling to 77 K (32Ni) or as a result of cold deformation (34Ni). The nickel microconcentration inhomogeneity was produced thanks to the reverse $\alpha \rightarrow \gamma$ transformation [5,6]. The nickel concentration variation was registered, as in [7], by the Mössbauer method. The structure was examined using a transmission electron microscope. The foils were irradiated with 1.5-MeV Kr^+ ions to a high damaging dose in an installation, which combined an electron microscope and an ion accelerator [8].

RESULTS AND DISCUSSION

Radiation-induced nickel redistribution of austenite at elevated temperatures

Figure 2 shows the structure of the FCC 16Cr15Ni3Mo1Ti reactor steel irradiated with 1.5-MeV Kr^+ ions at 823 K to the damaging dose of 30 dpa. The structure depicted in Fig. 2 resembles a mosaic pattern made up of dark areas ~150-200 nm in size against a light background and spaced ~300-400 nm from one another. The chromium concentration difference between the chromium-enriched and chromium-depleted areas is as high as 5 wt.% (see Fig.2). A certain order in the arrangement of the radiation-induced concentration inhomogeneous areas at 823 K may be explained by elastic interaction between these areas as is the case with the particles during aging [9].

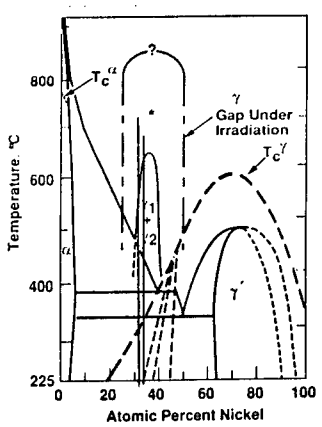

Fig. 1. Fe-Ni phase equilibrium diagram [1]

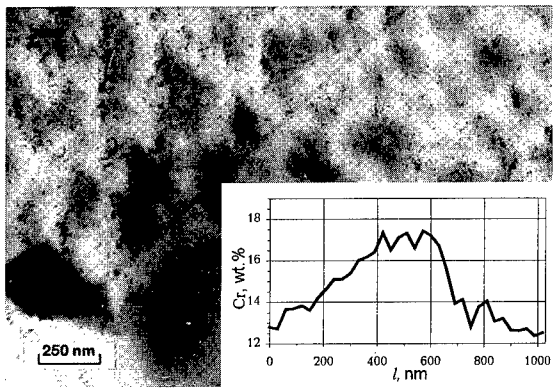

Fig. 2. Structure and distribution of Cr concentration in the 16Cr15Ni3Mo1Ti alloy after irradiation with 1.5-MeV Kr^+ ions at 823 K to the damaging dose 30 dpa

The existence of the radiation-induced dome of redistribution (Fig. 1) at elevated temperatures in the FCC range, which was earlier viewed as single-phase, was reliably proved also for the Fe-35Ni and Fe-35Ni-15Cr alloys [1]. The Fe-35Ni-15Cr alloy, which was exposed to neutron irradiation [1] at 783 K up to the dose of 13 dpa, had relatively large (~100 nm) areas enriched in nickel to 40-45 wt.% and depleted in chromium to 8 wt.%. Those areas were next to nickel-depleted and chromium-enriched ones. The distance between nickel-enriched areas (the oscillation wave length) was ~200 nm. The maximum difference between the concentrations in the enriched and depleted areas was ~16 wt.% for nickel, ~8 wt.% for chromium, and 16% for iron. The Fe-35Ni binary alloy exposed to neutron irradiation (14 dpa, 783 K) had the concentration oscillation wave length of ~200 nm [1].This process may be caused [2] by nonequilibrium segregations due to the Kirkendall inverse effect, which takes place as point defects are moving to sinks (dislocation loops, grain and subgrain boundaries).

To check whether the Fe-Ni equilibrium diagram contains a high-temperature range of the equilibrium decomposition of austenite (the narrow redistribution dome in Fig. 1), we have examined the following issues.

Formation of inhomogeneous Fe-Ni austenite during the $\alpha \rightarrow \gamma$ transformation

Similarly to the procedure adopted by the authors [5,6], the FCC iron alloys with 32% and 34% nickel were decomposed to low- and high-nickel components in the low-temperature two-phase $\alpha+\gamma$ range of the Fe-Ni equilibrium diagram. Nearly 90% martensite was formed during cooling of the 32Ni alloy (the martensite start temperature M_s = 180 K). As the alloy was slowly heated from 573

Fig.3. Structure of the Fe-32Ni alloy after the $\alpha \rightarrow \gamma$ transformation during a slow heating at a rate of 0.2 deg./min. to 823 K (0.2 deg./min.)

K to 753 K, disperse plates of the FCC (γ) phase 20-40 nm thick appeared in the crystals of BCC (α) martensite. The Mössbauer analysis showed [5] that the FCC plates were nickel-enriched to 40% or more, while the BCC matrix encircling those plates was nickel-depleted to ≤25%. When the alloy was heated further, the γ plates grew coarser and a new form of the γ phase – globular austenite – appeared. The globular austenite absorbed the mixture of the nickel-enriched and nickel-depleted γ and α phases. Heating to 823 K (above the $\alpha \rightarrow \gamma$ transformation finish temperature) led to the formation of 100% polyhedral austenite with nickel oscillations in the form of alternating dark and light streaks (Fig. 3).

On the existence of high-temperature decomposition in FCC Fe alloys

The vertical lines in Fig. 1 indicate the 32Ni and 34Ni alloys, which underwent isothermal annealing at 793-823 K representing the range of the conjectured redistribution dome. If the Fe-Ni equilibrium diagram does not contain the region of spinodal decomposition, the concentration inhomogeneity should eliminate at these temperatures. To accelerate diffusive processes, the concentration inhomogeneous samples of the 32Ni and 34Ni alloys underwent cold deformation to 75%.

The Mössbauer spectroscopic examination showed that annealing of the undeformed 32Ni alloy at 843 K for 1 to 7 days caused a gradual decrease in the concentration redistribution but did not provide full homogenization (Fig. 4 a,b,c). When the deformed concentration inhomogeneous 32Ni alloy was annealed even at a lower temperature (793 K) for 48 hours only, full homogenization took place (see Fig. 4 d,e). Annealing of the deformed inhomogeneous 34Ni alloy had nearly the same

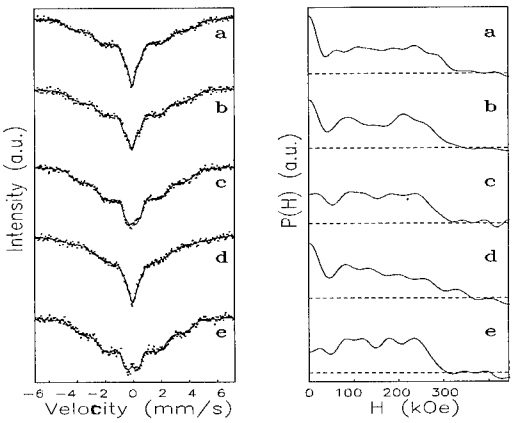

Fig.4. Mössbauer spectra of the 32Ni alloy (298 K) and the corresponding magnetic field density functions P(H). Treatment: a - nickel redistribution: quenching from 1323 K + $\gamma \rightarrow \alpha$ transformation, 77 K + $\alpha \rightarrow \gamma$ transformation, 823 K (0.2 deg./min.); b - as in "a" + annealing, 843 K (24 h); c - as in "a" + annealing, 843 K (168 h); d - as in "a" + deformation (ψ = 75%); e - as in "d" + annealing, 793 K (48 h)

result: the alloy almost fully homogenized in 48 hours at 793 K (Fig. 5 a,b,c). The zero-field paramagnetic component vanished from the Mössbauer spectra and the distributions $P(\overline{H})$ of the annealed 32Ni and 34Ni samples (Figs 4e and 5c). Besides, the high-field component related to nickel-enriched austenite also disappeared with increasing annealing time.

Thus, a relatively intensive homogenization of concentration inhomogeneous FCC Fe-Ni alloys, which takes place in the conjectured high-temperature range of spinodal decomposition (the narrow

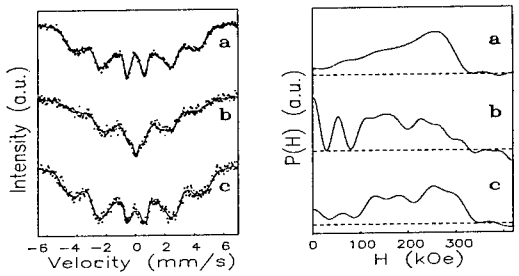

Fig.5. Mössbauer spectra of the 34Ni alloy (298 K) and the corresponding magnetic field density functions P(H). Treatment: a - initial homogeneous austenite; b - nickel redistribution: quenching from 1050 K + $\gamma \rightarrow \alpha$ transformation under deformation, 77 K + $\alpha \rightarrow \gamma$ transformation, 703 K (0.3 deg./min.) + 873 K, 10 min. + cold deformation (ψ = 75%, 298 K); c - as in "b" + annealing, 793 K (48 h)

dome in Fig. 1) calls into question the existence of such range in the Fe-Ni equilibrium diagram.Most probably, this decomposition occurs under irradiation only, has the segregation origin, and represents a radiation-induced rather than radiation-accelerated phase transformation.

CONCLUSION

The study of a Fe-Ni-Cr-based austenitic alloy confirmed the existence of radiation-induced redistribution in austenite at 823 K. This redistribution was accompanied by appearance of three-dimensional oscillations of the composition with the wave length of 300-400 nm.It was shown that high-temperature (773-923 K) phase transformations of FCC iron alloys with 32-34% nickel in the field of radiation defects is not a radiation-accelerated process of equilibrium decomposition of austenite. The alternative process – full homogenization of concentration inhomogeneous Fe-Ni alloys – was realized to prove the absence of thermally activated equilibrium spinodal decomposition.

References

[1] F.A.Garner, J.M.McCarthy, K.C.Russel, J.J.Hoyt, J.Nucl.Mater. **205** (1993), p. 411

[2] A.D.Marwich, R.C.Pillar, E.Horten, Brit.Nucl.Energy Soc. London **1** (1983), p. 11

[3] A.Wiedenmann, W.Wagner, H.Wollenberger, J.Less-Common Metals **145** (1988), p. 47

[4] A.Wiedenmann, W.Wagner, H.Wollenberger, Scripta Metallurgica **23** (1989), p. 603

[5] V.V.Sagaradze, V.A.Shabashov, Phys.Met.Metallography **57** (1984), p. 113

[6] V.V.Sagaradze, A.I.Uvarov, Strengthening of Austenitic Steels, Nauka, Moscow (1989), p. 270

[7] V.V.Sagaradze, V.A.Shabashov, T.M. Lapina, V.L. Arbuzov, Phys. Met. Metallography **78** (1994), p. 414

[8] B.N.Goshchitskii, M.A.Kirk, V.V.Sagaradze, S.S.Lapin, Nanostructered Materials **9** (1997), p. 189

[9] Yu.D.Tyapkin, V.A.Golikov, L.S.Svanidze, Phys.Met.Metallography **43** (1976), p. 562

Materials Science Forum Vols. 294-296 (1999) pp. 763-766

The Effect of Interphase Boundaries on Radiation Resistance of New Low-Activation and Chromium-Nickel Stainless Steels under High-Dose Irradiation up to 200 DPA

S.S. Lapin[1], V.V. Sagaradze[1], B.N. Goshchitskii[1] and M.A. Kirk[2]

[1] Institute of Metal Physics, Ural Branch RAS,
18 S. Kovalevskaya St., RU-620219 Ekaterinburg, Russia

[2] Materials Science Division, Argonne National Laboratories, Argonne, Illinois 60439, USA

Keywords: Microstructure, Swelling, Austenitic Steels, Electron Microscopy, Phase Transformation, Low-Activation Materials

Abstract This paper deals with the evolution of the dislocation structure, phase composition and vacancy voids in new reactor stainless steels over the temperature interval from 550 to 650 °C under irradiation with krypton ions up to high damaging doses (200 dpa). It is shown that the amount of voids formed in stainless steels exposed to irradiation with high-energy particles can be reduced by producing a high density of direct sinks of point defects in the form of α/γ phase boundaries. Compositions of radiation-resistant alloys, including low-activation ones of the Cr13Mn7W2 type having an austenitic-martensitic lath structure, have been proposed.

1. Introduction

Radiation swelling resistance of stainless steels is known [1-5] to be largely determined by the evolution of the structural and phase compositions under irradiation. The formation of voids under irradiation can be retarded by producing a large number of point-defect sinks in the form of dislocations [1] and coherent and incoherent phases [2, 4, 5]. This paper analyzes the structural evolution, including the void concentration variation, in special efficiently alloyed stainless steels having a large amount of point defect sinks in the form of α/γ boundaries, when these steels are exposed to large doses (up to 200 dpa) of irradiation with high-energy particles.

2. Materials, Heat Treatment and Methods

The subjects of study were stainless steels containing a high-plasticity FCC austenite in their structure: austenitic-martensitic Cr16Ni9Mo3 and Cr13Mn7W2 steels having a lath α/γ structure. The compositions of the steels at hand are shown in Table 1. The samples were irradiated at 550-650 °C with 1.5-MeV Kr^+ ions. The structural evolution and phase transformations were studied using transmission electron microscopy. Accelerated ions were fed to the electron microscope [3], making it possible to analyze the same place of the foils during irradiation to 200 dpa.

Table 1: Chemical composition and thermal treatment conditions of the steels studied

No.	Steel type	Thermal treatment conditions	Concentration of alloying elements, mass %						
			C	Cr	Ni	Mo	Mn	Ti	W
1.	Cr16Ni9Mo3	Quenching from 1050 °C, –80 °C for 3 h, 560 °C for 1 h	0.02	15.8	8.9	2.7	-	-	-
2.	Cr13Mn7W2	Quenching from 1050 °C, –80 °C for 3 h, 670 °C for 1.5 h	0.06	12.5	-	-	7.0	-	2.0

3. Results and Discussion

3.1. Cr-Ni-Mo Stainless Steels Having a Martensitic-Austenitic Lath Structure

Ferritic, martensitic and ferritic-martensitic stainless steels having a BCC lattice have been widely used recently as reactor materials. These steels are highly resistant to radiation swelling but are prone to a strong embrittlement under irradiation. The plasticity and the toughness of steels with dominating BCC lattice may be considerably improved if a sufficient amount of a high-plasticity austenite is produced in the structure [6]. To this end, it is necessary [5] that the two-phase steel contains martensite instead of ferrite as the BCC structure and the transformation-hardened FCC austenite with a high density of dislocations (this austenite is the product of the reverse martensitic $\alpha \rightarrow \gamma$ transformation). A lamellar austenitic-martensitic structure having a high density of sinks in the form of closely spaced α/γ phase boundaries and intralath dislocations was produced in the Cr16Ni9Mo3 steel with the martensite start temperature of ~0 °C. This structure appears as a result of the $\gamma \rightarrow \alpha$ transformation (–80 °C, 3 hours) and a partial reverse $\alpha \rightarrow \gamma$ transformation during heating to 560 °C. Thin plates of reverse austenite are formed between martensitic lath α-crystals. In addition to the austenitic-martensitic laths, the structure contains large regions of the retained austenite. Thus, α-martensite and two modifications of austenite – ordinary polyhedral austenite present in quenched austenitic steels and thin-plate austenite located between laths of α-martensite – were compared. Both austenitic components in the form of large light-colored fields of the retained austenite (40%) and thin oblong crystals of the reverse austenite (30%) between martensitic laths (30%) are seen in Fig. 1a. The shear $\alpha \rightarrow \gamma$ transformation, which leads to appearance of transformation-hardened austenite with a high density of dislocations, is followed by diffusion processes responsible for redistribution of nickel between α and γ phases [6] in accordance with the Fe-Ni equilibrium diagram. Reverse austenite is enriched in nickel and its stability is enhanced (M_s drops from 0 to –50 °C). The Cr16Ni9Mo3 steel possesses rather high properties: $\sigma_{0.2}$ = 700 MPa, σ_B = 886 MPa, δ = 27%, and ψ = 70% (T_{test} = 20 °C).

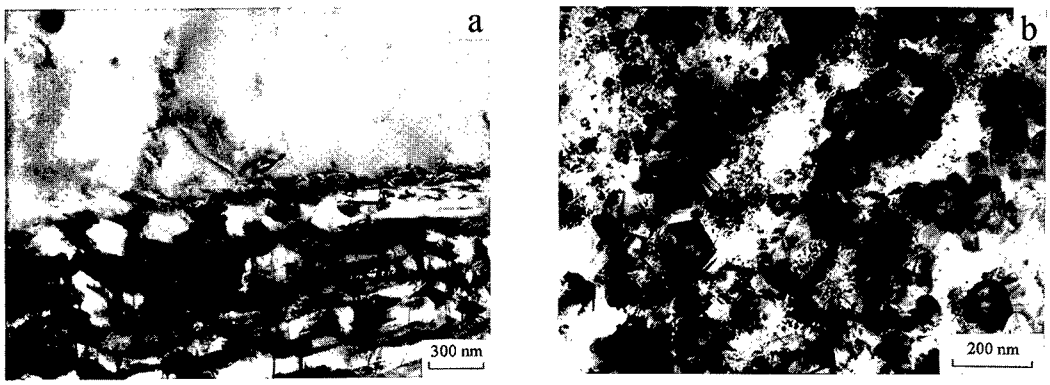

Fig. 1. Austenitic-martensitic lath structure and retained austenite of the Cr16Ni9Mo3 steel in the initial state (a) and after irradiation with Kr^+ ions (~1.5 MeV) up to the dose of 200 dpa at 650 °C (b). The preliminary treatment included quenching from 1100 °C, the $\gamma \rightarrow \alpha$ transformation at –80 °C for 3 hours, and a partial $\alpha \rightarrow \gamma$ transformation at –560 °C for 1 hour

Cascading irradiation of the steel with 1.5-MeV Kr^+ ions to the dose of 80 dpa at 550 °C leads to nucleation of differently oriented fine γ-crystals in the α-phase. Crystals of the γ-phase are 25-50 nm in size and are well seen in austenitic $(002)_\gamma$ and $(111)_\gamma$ reflections. This points to the $\alpha \rightarrow \gamma$ transformation rather than recrystallization of α-martensite. When the irradiation dose is increased to 200 dpa, fine γ-crystals are recrystallized and grow to 60-140 nm in size (Fig. 1b). Vacancy voids

are formed upon nucleation of the γ-phase. However, numerous neutral sinks (grain and twin boundaries) of point defects considerably suppress radiation swelling (~0.2%). The region of the transformation-hardened reverse γ-austenite changes little even after exposure to the dose of 200 dpa. Although the density of dislocations decreases to ~10^{10} cm^{-2}, closely spaced (1000 nm) neutral sinks of point defects in the form of α/γ phase boundaries inhibit nucleation of vacancy voids. Under similar irradiation conditions the polyhedral retained austenite swells considerably (~1%). Voids up to 20 nm in diameter are observed in the regions of the retained austenite after irradiation with 1.5-MeV Kr^+ ions to the dose of 200 dpa at 550 °C. This trend persists at the irradiation temperature of 600 °C. However, when the irradiation temperature is increased to 650 °C, not only the α→γ transformation is accelerated, but also the subsequent recrystallization of γ-crystals formed in the α-phase is enhanced. As a result, voids are progressively formed in the γ-phase plates, although on a lower scale than in large fields of the retained austenite. Large voids 40 nm in size are seen in the former regions of the α-phase and small voids ~10 nm in size are observed in the regions of the transformation-hardened austenite in the lath structure of the Cr16Ni9Mo3 steel after irradiation with 1.5-MeV Kr^+ ions at 650 °C (Fig. 2). The main reasons for the different behavior of the polyhedral austenite and the lath α/γ structure are as follows: 1) Numerous α/γ phase boundaries between alternating austenite and martensite laths (spaced ~100 nm) represent closely spaced sinks of point defects and suppress the void formation. 2) A high density of dislocations in the martensite (up to 10^{11} cm^{-2}) and the transformation-hardened austenite (up to 5×10^{10} cm^{-2}) [6] inhibits swelling too. Moreover, the reverse austenite in the structure of the martensitic-austenitic stainless steel provides for a higher plasticity and improved toughness compared to those of martensitic or ferritic steels.

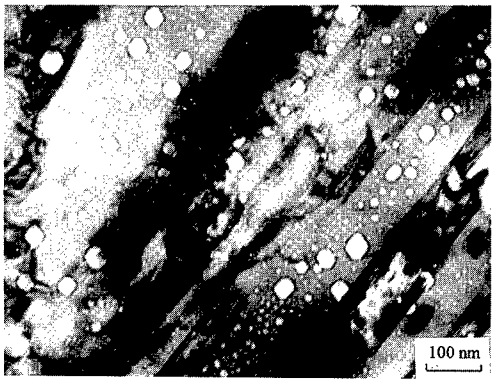

Fig. 2. Structure of the Cr16Ni9Mo3 steel after irradiation with 1.5-MeV Kr^+ ions up to the dose of 200 dpa at 650 °C.

Fig. 3. Structure of the low-activation Cr13Mn7W2 steel after irradiation with 1.5-MeV Kr^+ ions up to the dose of 200 dpa at 650 °C.

3.2. Low-Activation Stainless Steels with a Lath α/γ Structure

The development of low-activation reactor steels and alloys where only "short-lived" isotopes having a short half-life period are formed under neutron irradiation is very important from the ecological viewpoint. These materials would not present any hazard and could be used again, in particular, after they have been stored for 100 years [7]. Manganese could serve as the austenite-forming element in low-activation steels. The Fe-Cr, Fe-V and Fe-Cr-V(W) BCC systems and the Fe-Mn and Fe-Cr-Mn-W FCC systems may be used for development of low-activation steels. The low-activation Cr12Mn20W steel, which was chosen as the prototype [8], contains a large amount of manganese (~20 %). If a martensitic-austenitic lath structure having 15-30 % plastic γ-phase is

used, the manganese content of the steel may be decreased to 6-8 mass %. The composition of the low-activation Cr13Mn7W2 steel is given in Table 1. The steel containing 12.5 mass % chromium and 0.06 mass. % C (Cr13Mn7W2) is virtually a martensitic steel ($M_S \approx 120$ °C, content of δ-ferrite ≤ 5 %). Nearly 75 % α-martensite is formed in this steel after quenching and cold treatment (–80 °C, 3 hours). Note that for the Cr13Mn7W2 steel the α→γ transformation range corresponds to the temperatures of 640-720 °C. This is almost 100 °C higher than for the Cr16Ni9Mo3 steel. Therefore the temperature stability region of the lath structure is larger for the low-activation steel than for the Cr-Ni-Mo steel. A lamellar α/γ structure was produced in the Cr13Mn7W2 steel thanks to the reverse α→γ transformation during heating to 670 °C (holding for 1.5 hour). Under these thermal conditions the lath γ-phase is stabilized, because it is enriched in austenite-forming elements (Mn, C). When the low-activation steel is exposed to irradiation with 1.5-MeV Kr^+ ions to the dose of 200 dpa at 650 °C, its structure undergoes full α→γ transformation and comprises transformation-hardened stabilized γ-grains 0.5 to 2 μm in size. Small voids 10-15 nm in size are uniformly distributed over the whole volume (Fig. 3). However, the structure of this steel does not contain alternating bands with large and small voids, as was observed in the Cr16Ni9Mo3 steel (Fig. 2) at the same irradiation temperature. This fact suggests a relatively long stability of initial α-laths and, consequently, of the whole radiation-resistant martensitic-austenitic structure of the Cr13Mn7W2 steel irradiated at 650 °C. Thus, the thin-plate martensitic-austenitic structure of the low-activation Cr13Mn7W2 steel resists radiation swelling up to the temperature of 600 °C.

4. Conclusions

1. It is shown that at 550 °C the radiation swelling resistance of the thin-plate transformation-hardened austenite is higher than the radiation swelling resistance of the ordinary equiaxial polyhedral austenite. Certain compositions have been developed for radiation-resistant stainless steels of the Cr16Ni9Mo3 type having a lamellar thin-plate structure, which comprises alternating laths of martensite and transformation-hardened austenite with numerous point-defect sinks in the form of α/γ phase boundaries and dislocations.
2. Low-activation stainless steels of the Cr13Mn7W2 type have been proposed. These steels are highly resistant to the vacancy void formation under a large-dose irradiation with high-energy particles (200 dpa at 650 °C).

Acknowledgments
This study has been financially supported by the IPP, USA (Agreement No. 942492402).

References

1. W.G. Johnston, J.H. Rosolowsky, A.M. Turkalo, T. Lauritzen. An experimental survey of swelling in commercial Fe-Cr-Ni alloys bombarded with 5-MeV ions., J.Nucl.Mat. 54(1974) 24-40.
2. V.V. Sagaradze, V.M. Nalesnik, S.S. Lapin, V.M. Alyabiev. Precipitation hardening and radiation damageability of austenitic stainless steels., J.Nucl.Mater. 202 (1993) 137-144.
3. V.V. Sagaradze, S.S. Lapin, M.A. Kirk, B.N. Goshchitskii. Influence of high-dose Kr^+ irradiation on structural evolution and swelling of Cr16Ni15Mo3Ti1 aging steel.,J.Nucl.Mat,1998,in press.
4. I. Shibahara, N. Akasaka, S. Onose. Swelling of advanced austenitic stainless steels developed for the environment of heavy neutron exposure., J.Nucl.Mat. 212-215 (1994) 487-491.
5. V.V. Sagaradze, V.A. Pavlov, V.M. Alyabiev, S.S. Lapin, V.A. Ermishkin, O.V. Antonova. Radiation swelling of steels having a martensitic-austenitic lath structure., Phys. Met. Metallography, 1987, v. 64, No. 5, p. 966-970.
6. V.V. Sagaradze, A.I. Uvarov. Strengthening of Austenitic Steels., Moscow,Nauka, 1989, 270 p.
7. L.I. Ivanov. Problems involved in creation of low-activated radiation-resistant metal materials for atomic and thermonuclear power engineering, accelerators, and aeronautics., In: Constructional Materials For Nuclear Fusion Reactors, Moscow, Nauka, 1993, p. 4-13.

Materials Science Forum Vols. 294-296 (1999) pp. 767-770

The Redistribution of Atoms During Radiation-Induced Martensitic Transformations in Fe-Ni Alloys

T.M. Lapina, V.A. Shabashov, V.V. Sagaradze and V.L. Arbuzov

Institute of Metal Physics, Ural Branch of Russian Academy of Sciences,
18 S. Kovalevskaya St., RU-620219, Ekaterinburg, Russia

Keywords: Iron and Nickel Alloys, Martensitic Transformation, Electron Irradiation, Mössbauer Effect, Deformation, Shear Pressure

Abstract. Using the nuclear gamma resonance (NGR) spectroscopy, a low-temperature (400-500 K) isothermal BCC⇔FCC transformation was found to occur in Fe - (31-32%) Ni alloys subjected beforehand to shear under a high pressure. The phase transformation was stimulated by irradiation with high-energy electrons (E ~ 5.5 MeV, dose F ~ $5 \cdot 10^{18}$ e/cm^{-2}). The BCC+FCC structure of the binary Fe-Ni alloy, which is produced under the deformation pressure, undergoes either the $\alpha \rightarrow \gamma$ or $\gamma \rightarrow \alpha$ radiation-induced martensitic transformation depending on the initial (before strain) state: γ-phase or α-phase.

Introduction. In a submicrograin structure produced by shear-pressure (SP) elastic compression, dispersion and saturation with defects lead to appearance of new highly nonequilibrium phases. Low-temperature (400-500 K) irradiation with high-energy electrons (E ~ 5.5 MeV, dose F ~ $5 \cdot 10^{18}$ e/cm^{-2}) stimulates relaxation processes of a nonequilibrium structure; one of the possible ways of relaxation is phase transformations. Destabilization of the phase composition of the alloy during strong plastic deformation shows how radiation-induced vacancies and interstitial atoms, which facilitate equilibrium diffusion processes [1,2], affect martensitic FCC⇔BCC transformations. A great role in $\alpha \Leftrightarrow \gamma$ transitions is attributed to interphase boundaries, which act as sinks of radiation-induced point defects.

Results and Discussion. Binary iron-nickel alloys types N31 (30.4 at.% Ni) and N32 (31.5 at.% Ni) were chosen for investigations. These alloys were metastable: a heterogeneous mixture of the FCC and BCC phases was formed. When the binary Fe-Ni alloys were cooled in liquid nitrogen, over 80% athermal martensite appeared (M_s < 200 K). The reverse $\alpha \rightarrow \gamma$ transformation temperature A_s > 600 K [3]. A high-pressure (8 GPa) shear strain increased the temperature of the forward FCC→BCC transformation and reduced the temperature of the reverse BCC→FCC transformation. A two-phase alpha/gamma structure having a nonequilibrium weight ratio of the phases and large residual elastic stresses appeared in the binary Fe-Ni alloys subject to this treatment.

Depending on the initial state of the alloys prior to strain – the FCC (gamma) phase produced by water-quenching after high-temperature (1300 K) annealing or the BCC (alpha) phase produced by quenching in liquid nitrogen – different directions of the radiation-induced martensitic transformation were found to occur. Large elastic distortions accumulated during strain determined the phase transformation direction under low-temperature (400-500 K) irradiation with high-energy electrons (E = 5.5 MeV, dose F = $5 \cdot 10^{18}$ e/cm^{-2}). Excess radiation-induced point defects and redistribution of the alloying elements, which was associated with motion of these defects, stimulated relaxation of elastic stresses after a strong plastic deformation. As a result, the alpha+gamma composition was stabilized.

Figure 1 shows Mössbauer spectra (a) and the corresponding effective magnetic field distribution density functions P(H) (a') of the N32 alloy quenched in water and subjected to shear defor-

mation ($\varepsilon = 7$) at a high pressure (8 GPa) to form a strain-induced α-martensite. In accordance with P(H) (see Fig. 1a'), up to 30% α-phase was formed in the structure. Irradiation of the N32 alloy at 473 K ($F = 4 \cdot 10^{18}$ e/cm^2) led to the $\alpha \rightarrow \gamma$ transformation (see the decrease in the P(H) peak corresponding to the α-phase in Fig. 1b'). The amount of the strain-induced martensite decreased gradually when the irradiation dose was increased from $2 \cdot 10^{18}$ to $4 \cdot 10^{18}$ e/cm^2. The reverse $\alpha \rightarrow \gamma$ transformation was observed at temperatures more than 100 K lower than A_s. The transformation was not detected after irradiation of the cooled α-martensite with a coarse-grain structure.

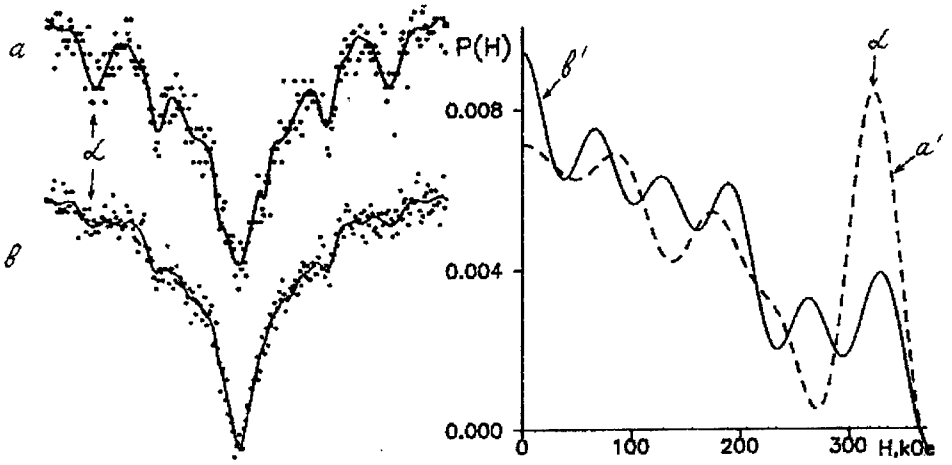

Fig. 1. Mössbauer spectra (a, b) and the corresponding effective magnetic field distribution density functions P(H) (a', b') of the N32 alloy: a, a'- deformation shearing at a pressure of 8 GPa to the strain $\varepsilon = 7$ from the initial γ - phase (quenching in water); b, b' - irradiation $F = 4 \cdot 10^{18}$ e/cm^2 at 473 K.

Figure 2 shows Mössbauer spectra (a) and the corresponding effective magnetic field distribution density functions P(H) (a') of the N31 alloy subject to the deformation shear at a pressure of 11 GPa to strain $\varepsilon = 5$ from the initial α-phase (martensite quenched in liquid nitrogen). In accordance with P(H) (Fig. 2a'), the α-phase volume fraction decreased to 10% during shear-pressure (SP). The reverse direction of the phase transformation (see Fig. 2 b,b'), that is, a partial $\gamma \rightarrow \alpha$ transformation was observed under irradiation at 433 K ($F = 5 \cdot 10^{18}$ e/cm^2) in the N31 alloy subject to the SP deformation from the initial α-phase. The stresses stimulated relaxation through the $\gamma \rightarrow \alpha$ transformation (see the increase in the P(H) peak of the α-phase, Fig. 2b').

Irradiation of the binary Fe-Ni alloys with a BCC+FCC structure, which was produced by SP, led to either the $\alpha \rightarrow \gamma$ or $\gamma \rightarrow \alpha$ isothermal phase transformation depending on the initial (before deformation) structure: γ-phase or α-phase. The amount of the deformation-induced phase decreased upon irradiation. The phase transformations observed under irradiation should be considered as the extension of the phase and structural transformations, which took place in Bridgman anvils under high pressures. «In situ» experiments showed that after high shear pressures were removed, the deformation-induced structures started partially decreasing. These structures continued vanishing upon subsequent irradiation.

For the Fe-Ni alloys the thermodynamic equilibrium temperature of α and γ phases, T_0, was close to the irradiation temperature (400-500 K). Therefore large accumulated elastic distortions determined the direction of the phase transformation during irradiation. The low - temperature

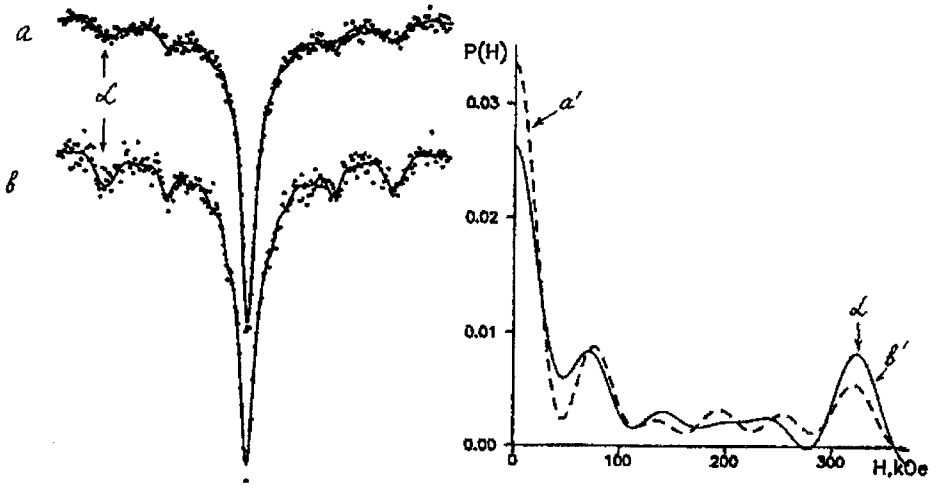

Fig. 2. Mössbauer spectra (a, b) and the corresponding effective magnetic field distribution density functions P(H) (a', b') of the N31 alloy: a, a'- deformation shearing at a pressure of 11 GPa to strain $\varepsilon = 5$ from the initial α-phase (martensite quenched in liquid nitrogen); b, b' - irradiation $F = 5 \cdot 10^{18}$ e/cm^2 at 433 K.

isothermal α⇔γ transformation depended on the mechanism by which residual stresses were relieved. The kinetics of the anomalous α⇔γ transformations in a disperse mixture of phases was determined by the interaction between residual stresses and radiation-induced vacancies. The redistribution of atoms near α/γ phase boundaries, which acted as sinks of radiation-induced vacancies and interstitials, was an additional factor facilitating development of the α⇔γ transitions under irradiation. The radiation-induced BCC⇔FCC transformations in the binary Fe-Ni alloys have been classified as martensitic transformations controlled by the radiation-induced segregation of atoms.

The effective magnetic field at the ^{57}Fe core depended mainly on the number of Ni atoms, which were the nearest neighbors of the Fe atom. The local neighborhoods of the Fe isotope determined the type of the NGR spectra of Fe-Ni FCC alloys with 29 to 36% Ni because of the sign and the value of the paired exchange interaction integrals ($J_{Fe\text{-}Fe}$= -9 MeV, $J_{Fe\text{-}Ni}$= 39 MeV and $J_{Ni\text{-}Ni}$= 59 MeV [4]). It is possible to see the distribution of Ni atoms in γ-regions of the two-phase alloys, for which purpose one needs to separate the FCC component in the field distribution P(H). The comparison of the field distributions in the austenite of the N31 alloy before and after irradiation revealed redistribution of the elements during the radiation-induced FCC→BCC transformation. Figure 3 illustrates distribution of the effective magnetic fields of the residual FCC phase in the N31 alloy after shear deformation at a pressure of 11 GPa ($\varepsilon = 5$) (Fig. 3a) and after exposure to the fluence of $5 \cdot 10^{18}$ e/cm^2 at 433 K (Fig. 3b). These magnetic fields distribution functions were determined by subtracting the BCC component (shown by way of example with a short dotted line in Fig. 3) from P(H) of two-phase alloys (Fig. 2 a',b').

A considerable decrease of the zero-field component in the distribution of the effective magnetic fields P(H) of the irradiated austenite (Fig. 3b) pointed to the formation of the α-phase in nickel-depleted FCC regions. Considering this and also the change of P(H) in the region of medium fields (30÷90 kOe), one may state a more homogeneous distribution of nickel in γ-regions of the irradiated N31 alloy. The drop of the high-field component (~250 kOe) in the distribution P(H) was probably caused by growing martensitic crystals. The fact that the number of low-nickel regions in the FCC structure decreased during the radiation-induced FCC-BCC transformation is indicative of the shear character of this transformation.

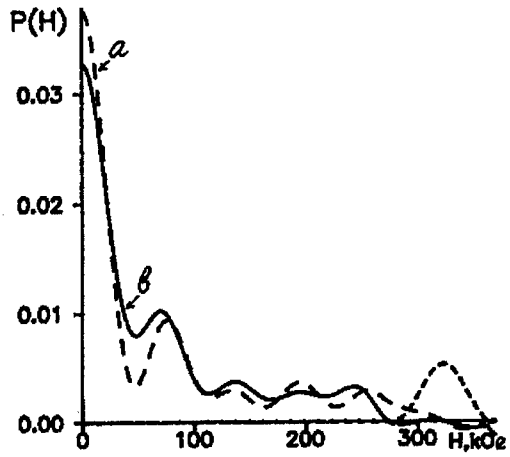

Fig. 3. Effective magnetic field distribution density functions P(H) (a, b) of the FCC-phase N31 alloy:
a - deformation shearing at a pressure of 11 GPa to the strain $\varepsilon = 5$ from the initial α-phase (martensite quenched in liquid nitrogen);
b - irradiation $F = 5 \cdot 10^{18}$ e/cm^2 at 433 K.
The short dotted line denotes effective magnetic field distribution density functions of the BCC-phase (example).

A stress-induced martensite was formed upon implantation of inert gases in stainless steel [5]. The change in the composition under irradiation with $^{+}$Fe and $^{+}$Ni ions has been treated [5] as one more factor responsible for the BCC phase formation. The detection of the weight growth of the α-component during establishment of equilibrium states is a characteristic feature of our study. The experimental data coupled with the above discussion suggests a diffusionless nature of the radiation-induced $\alpha \Leftrightarrow \gamma$ transformations in submicrovolumes of a heterogeneous mixture of the FCC and BCC phases produced by the SP deformation. Thus, radiation-induced point defects, which facilitate diffusion processes, contribute to development of the martensitic transformations. A significant contribution to the $\alpha \Leftrightarrow \gamma$ transformations is due to α/γ interphase boundaries, which participate in relaxation of elastic stresses and radiation-induced redistribution of the alloying elements.

Conclusion. The $\alpha+\gamma$ submicrograin structure of the binary Fe-Ni alloys, which is produced under deformation pressure, exhibits either the $\alpha \rightarrow \gamma$ or $\gamma \rightarrow \alpha$ radiation-stimulated phase transformation depending on the initial (before deformation) structure: γ-phase (austenite quenched in water) or α-phase (martensite quenched in liquid nitrogen).

Acknowledgments
This study has been financially supported by the Russian Fundamental Research Foundation (Project No. 96-15-96515).

References
1. V.V. Sagaradze, V.A. Shabashov, T.M. Lapina, V.L. Arbuzov, Phys. Met. Metallography 78, 6 (1994), p. 88-96.
2. V.V. Sagaradze, T.M. Lapina, V.A. Shabashov, V.L. Arbuzov, Phys. Met. Metallography 83, 5 (1997), p. 121-126.
3. V.V. Sagaradze, A.I. Uvarov, Strengthening of Austenitic Steels., Moscow,Nauka, 1989, 270 p.
4. M Hatherly, K. Hirakawa, R.D. Lowde et al., Proc. Phys. Soc. 84, 2 (1964), p.55-62.
5. I. Sakamoto, N. Hayashi, B. Furubayashi, H. Tanoue, J. Surf. Finish. Soc. Jpn. 39,10 (1988), p.652-655.

Materials Science Forum Vols. 294-296 (1999) pp. 771-774

Modeling the Radiation-Induced Segregation of Undersized Solutes Near Grain Boundaries

V.A. Pechenkin and I.A. Stepanov

SSC RF Institute of Physics & Power Engineering, RU-249020 Obninsk, Kaluga region, Russia

Keywords: Irradiation, Ternary Alloys, Grain Boundaries, Segregation, Silicon, Theory and Modeling

Abstract

A system of diffusion equations is formulated for component and point defect concentrations near grain boundary (GB) in irradiated ternary alloy, in which a minor component has a small atomic size. A possibility of GB migration is taken into account. It is assumed that undersized atoms migrate via interstitial mechanism as nearly stable mixed dumbbells. Radiation-induced segregation (RIS) of Si near both the motionless and moving GBs in Fe-Cr-Ni alloys is modeled by solving the system of equations. A competition between the undersized solute and the major alloy component which tends to segregate at GB is studied by varying the Ni content. It is shown, that the formation of strongly bounded mixed dumbbells consisting of the undersized alloying atom and one of the major component atom can significantly enhance RIS of alloying elements around point defect sinks.

Introduction

Radiation-induced segregation of undersized minor elements can significantly influence on phase stability and swelling in alloys under irradiation. RIS of Si near point defect sinks leads to formation and growth of radiation induced nickel- and silicon-rich γ' and G precipitates in austenitic stainless steels [1,2]. In its turn, voids adjacent to G-phase precipitates are proned to an enhanced growth in comparison with that of isolated voids in a matrix [3-6]. An addition of Fe or Cr undersized solutes to V and some vanadium alloys results in a large swelling enhancement [7,8]. Such an effect can be related to RIS of the solutes near void surfaces [9]. Most of the experimental investigations of RIS in alloys have been performed for grain boundaries. It was found that profiles of major components and an undersized solute near motionless and moving GBs are different in neutron [10] as well as in electron [11,12] irradiated austenitic stainless steels.
In this paper a system of diffusion equations for component and point defect concentrations near a moving grain boundary in irradiated ternary alloy, in which a minor component (solute) has a small atomic size is formulated. Radiation-induced segregation of Si near motionless and moving GBs in Fe-Cr-Ni alloys is compared by numerically solving the system of equations. A competition between undersized solute and a main component, which has a tendency to segregate near GB, is studied by varying the Ni content.

Component and point defect fluxes

A ternary substitutional alloy is considered, in which the minor component A is undersized and forms nearly stable mixed dumbbells with B and C component atoms. At sufficiently high temperatures the

thermal equilibrium is assumed for the nonrandom occupation of interstitials by A-, B- and C- atoms [13]:

$$\frac{C_i^A}{C_i} = \frac{\xi \cdot C_A}{\xi \cdot C_A + C_B + C_C}, \quad \frac{C_i^B}{C_i} = \frac{C_B}{\xi \cdot C_A + C_B + C_C}, \quad \frac{C_i^C}{C_i} = \frac{C_C}{\xi \cdot C_A + C_B + C_C}, \tag{1}$$

where C_i and C_m are the interstitial and alloy component (m=A,B,C) concentrations respectively, $\xi=\exp(E_A^b/kT)$, E_A^b the binding energy of mixed dumbbells AB and AC. As shown in ref. [14], the eq. (1) is valid in a wide temperature range.

The correlation and thermodynamical factors are taken further as unity. In this case the interstitial flux can be written as follows:

$$J_i = j_i^A + j_i^B + j_i^C, \; j_i^m = -d_{mi}\nabla C_i^m. \tag{2}$$

The grain boundary is considered as a plane moving with a given velocity u. It is supposed that the equilibrium point defect (PD) concentrations are maintained at the plane, the latter is assumed to be transparent for component fluxes which are:

$$J_A = -(d_{AV}C_V + \frac{\xi d_{Ai}}{(1+\beta C_A)^2}C_i)\nabla C_A + C_A(d_{AV}\nabla C_V - \frac{\xi d_{Ai}}{(1+\beta C_A)}\nabla C_i) - u \cdot C_A,$$

$$J_B = -(d_{BV}C_V + \frac{d_{Bi}}{1+\beta C_A}C_i)\nabla C_B + \frac{(\xi-1)d_{Bi}}{(1+\beta C_A)^2}C_iC_B\nabla C_A +$$

$$+C_B(d_{BV}\nabla C_V - \frac{d_{Bi}}{1+\beta C_A}\nabla C_i) - u \cdot C_B, \tag{3}$$

$$J_C = -(d_{CV}C_V + \frac{d_{Ci}}{1+\beta C_A}C_i)\nabla C_C + \frac{(\xi-1)d_{Ci}}{(1+\beta C_A)^2}C_iC_C\nabla C_A +$$

$$+C_C(d_{CV}\nabla C_V - \frac{d_{Ci}}{1+\beta C_A}\nabla C_i) - u \cdot C_C,$$

$$J_V = -D_V\nabla C_V + C_V(d_{AV} - d_{CV})\nabla C_A + C_V(d_{BV} - d_{CV})\nabla C_B - u \cdot C_V,$$

$$J_i = -\nabla\frac{\xi d_{Ai}C_A + d_{Bi}C_B + d_{Ci}C_C}{1+\beta C_A}C_i - u \cdot C_i,$$

where d_{mk} are the alloy component diffusivities via vacancy (k=V) and interstitial mechanisms (k=i), D_V is the vacancy diffusion coefficient, $\beta=\xi-1$.

It should be noted that in the case of motionless GB (u=0) and a low undersized solute content ($C_A \cdot (\xi-1) \ll 1$), the set of equations is reduced to one usually used for concentrated ternary alloys (see, ref. [15]). In this case analytical expressions for major component and undersized solute steady-state profiles near PD sinks have been derived in ref. [14].

Diffusion equations for component C_m and point defect C_k concentrations are the following:

$$\frac{\partial C_m}{\partial t} = -\nabla J_m, \quad \frac{\partial C_k}{\partial t} = -\nabla J_k + \eta K - \mu_R D_i C_i C_V - k_{ks}^2 D_k(C_k - C_k^e), \tag{4}$$

where K is the PD generation rate, η is the cascade efficiency, μ_R is the recombination coefficient, k_{ks}^2 is the sink strength for vacancies and interstitials.

Modeling radiation-induced segregation of Si near GB in Fe-Cr-Ni alloys

Experimental data on RIS of major components in Fe-Cr-Ni alloys give evidence that Ni is enriched near various PD sinks, while Cr and Fe are depleted. Therefore, in calculations Fe and Cr were considered as one component with the effective diffusivity $d_{Ck}=(C_{Fe}\cdot d_{Fek}+C_{Cr}\cdot d_{Crk})/(C_{Fe}+C_{Cr})$ and concentration $C_C=C_{Fe}+C_{Cr}$. Diffusion parameters for calculations were taken from ref. [14]. The

mixed dumbbell binding energy known only for dilute Ni-Si alloys [16] (E_{Si}^b=0.23 eV) was considered as a fitting parameter.

Kenic et al. [17] have measured Si and major alloy component profiles near motionless GBs in PCA irradiated at 420°C in FFTF to dose of 9 dpa. The experimental data together with as-calculated and averaged profiles for E_{Si}^b =0.23 eV and E_{Si}^b =0.16 eV are shown in Fig.1. For a correct comparison, averaging was carried out over the electron beam width [17] using the method proposed in ref. [12]. GB velocities are available only for electron irradiated alloys [18]. However, from a comparison of GB migration distances in stainless steels under neutron [10] and electron [18] irradiations it follows, that the magnitudes are comparable at a similar dose. Results of modeling Si segregation near moving GB at u=30 nm/dpa [18] are shown in Fig.2. It should be noted that the effect of GB motion on Si profile is significantly weaker, than that on major component profiles (see ref. [19]).

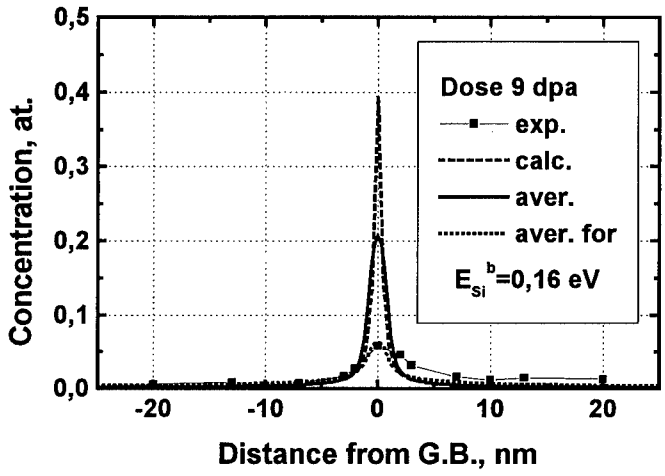

Fig.1. Comparison of as-calculated (E_{Si}^b=0.23 eV) and averaged (E_{Si}^b=0.23 and 0.16 eV) Si profiles across a motionless GB with experimental data from Ref.[17].

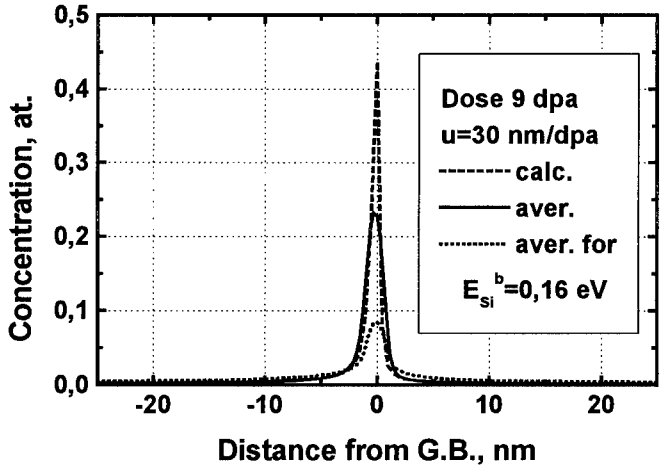

Fig.2. As-calculated (E_{Si}^b=0.23eV) and averaged (E_{Si}^b=0.23 and 0.16 eV) Si profiles across a moving GB.

The model developed allows to get an insight into the competition between undersized solute and alloy component segregating to GBs. In Fe-Cr-Ni alloys such an alloy component is Ni. The influence of Ni content on as-calculated (E_{Si}^b =0.16 eV) and averaged Si concentration at GB in Fe-14Cr-xNi-0.4Si (wt.%) alloy is illustrated in Fig.3. It is seen, that an increase of Ni content reduces significantly the Si concentration at GB.

Conclusions

A model has been developed for calculation the radiation-induced segregation of undersized minor component near moving grain boundaries in a substitutional ternary alloy.
RIS of Si near motionless and moving GB in a Fe-Cr-Ni alloy was modeled. From the results of modeling it follows, that the influence of GB motion on Si profiles is weaker than that on major component profiles. An increase of Ni content reduces significantly the Si concentration near GB due to a competition between Si and Ni in enriching regions near GB.

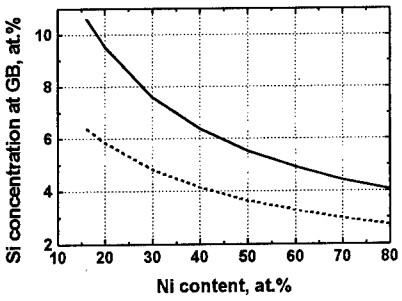

Fig.3. The dependence of as-calculated (solid) and averaged (dash) Si concentration (E_{Si}^{b}=0.16 eV) at motionless GB on Ni content in Fe-14Cr-xNi-0.4Si (wt.%) alloy at 9 dpa.

Acknowledgements

This work was supported by Russian Foundation for Basic Research under Grant №98-02-17400.
The authors would like to thank Prof. Yu.V.Konobeev for useful discussion of the work.

References

[1] P.J. Maziasz, J. Nucl. Mater. 169(1989), p.95
[2] V.A. Pechenkin, G.A. Epov, I.A. Stepanov and Yu.V. Konobeev, Abstracts of the 18th Int. Symp. On Effects of Radiation on Materials, Hyannis, June 27-29, 1996, p.72. To be published in ASTM STP 1325, 1997.
[3] L.K. Mansur, M.R. Hayns and E.H. Lee, Proc. Conf. Phase Stability under Irradiation, AIME, Warrendale, PA, 1981, p.359.
[4] A.S. Bakai, O.V. Borodin, V.V. Bryk, V.N. Voyevodin, V.F. Zelenskij, I.M. Neklyudov, P.V. Platonov and A.A. Turkin, J. Nucl. Mater. 185(1991), p.260.
[5] R.M. Boothby and T.M. Williams, J. Nucl. Mater. 152(1988), p.123.
[6] V.A. Pechenkin and G.A. Epov, J. Nucl. Mater. 233-237(1996) p.1009.
[7] H. Matsui, D.S. Gelles and Y. Kohno, in Proc. 15th Int. Symp. On the Effects of Radiation Materials, ASTM STP 1125(1991), eds. R.E. Kumar and D.S. Gelles (American Society for Testing and Materials, Philadelphia, 1992) p.928.
[8] H. Matsui, K. Fukumoto, D.L. Smith, H.M. Chung, W. Van Wizenburg and S.N. Votinov, J. Nucl. Mater. 233-237(1996), p.92.
[9] Yu.V. Konobeev, V.A. Pechenkin and Rudnev, J. Nucl. Mater. 233-237(1996), p.1070.
[10] D.I.R. Norris, C. Barker, C. Tylor and J.M. Titchmarsh, Proc. Of 15th Int. Symp. on Effects of Radiation on Materials, ASTM STP 1125, Philadelphia, 1992, p.603.
[11] K. Nakata and I. Masaoka, J. Nucl. Mater. 150(1987), p.186.
[12] S. Watanabe, N. Sakaguchi, N. Hashimoto, M. Nakamura, H. Takahashi, C. Namba and N.Q. Lam, J. Nucl. Mater. 232(1996), p.113.
[13] N. Hashimoto, Y. Eda and H. Takahashi, J. Nucl. Mater. 239(1996), p.180.
[14] V.A. Pechenkin and G.A. Epov, J. Nucl. Mater. 207(1993), p.303.
[15] V.A. Pechenkin and G.A. Epov, J. Nucl. Mater. 186(1992), p.269.
[16] A. Bartels, F Dworshak and M. Weigert, J. Nucl. Mater. 152(1988), p.82.
[17] E.A. Kenik, T. Inazumi and G.E.C. Bell, J. Nucl. Mater. 183(1991), p.145.
[18] H. Takahashi, N. Hashimoto and S. Watanabe, Ultramicroscopy 56(1994), p.193.
[19] V.A. Pechenkin and I.A. Stepanov, these Proceedings..

Materials Science Forum Vols. 294-296 (1999) pp. 775-778

Calculation of Radiation-Induced Segregation near Moving Grain Boundaries in Fe-Cr-Ni Alloys

I.A. Stepanov and V.A. Pechenkin

SSC RF Institute of Physics & Power Engineering, RU-249020 Obninsk, Kaluga region, Russia

Keywords: Irradiation, Ternary Alloys, Moving Grain Boundaries, Segregation, Kirkendall Effect, Theory and Modeling

Abstract

A method of calculation of radiation-induced segregation (RIS) and segregation-induced bias (SIB) for a moving plane sink in ternary substitutional alloys is developed. It is assumed that thermal equilibrium concentrations are maintained at the moving plane, which is considered as transparent to alloy component fluxes. Among various drift forces acting on point defects due to RIS, only Kirkendall ones are taken into account. RIS and SIB for a moving plane grain boundary in Fe-Cr-Ni alloys are calculated. It is shown that the dependence of SIB on dose has a maximum at some intermediate dose which depends on the sink velocity. The limiting case of a moving plane nontransparent for alloy component fluxes is also considered. In this case an additional sink velocity arises due to Kirkendall effect. This additional velocity is calculated in dependence on initial one.

Introduction

Under irradiation, a redistribution of alloy components is usually observed near various point defect (PD) sinks (grain boundaries, voids, dislocations and other) as a result of radiation-induced segregation. Due to RIS drift forces on point defects appear near sinks, including Kirkendall ones, related to differences in alloy component diffusivities via vacancy and interstitial mechanisms, as well as drift forces caused by gradients of PD formation and migration energies [12]. This leads to changes of PD sink strengths and to appearance of the segregation-induced bias of sinks to vacancies or interstitials [3,4,5]. The dependence of SIB on alloy composition may be responsible for the observed strong dependence of swelling in Fe-Cr-Ni [6,7] and V-Fe [8] alloys on their composition.
The grain boundary migration is a common feature of the microstructure in irradiated and nonirradiated alloys. A number of physical mechanisms appear to be involved [9]. It was shown, that alloy component profiles across a moving GB are asymmetric in neutron [10] as well as electron [11,12] irradiated austenitic stainless steels. Such an asymmetry means that a moving GB has different SIBs in zones in front and behind the moving GB. A difference in PD fluxes from opposite directions to GB can arise. For Fe-Cr-Ni alloys it means that more vacancies than interstitials will arrive at GB from regions in front of GB and more interstitials than vacancies from regions behind GB. Extra vacancies can destroy the crystal planes in front of GB, but extra interstitials can create new planes behind it. Therefore, the velocity of the moving GB may increase due to a disbalance in PD fluxes caused by the alloy component profile asymmetry. This result could arise in the case when GB is not perfectly transparent for component fluxes. Such an effect is similar to the well known Kirkendall effect for two contacting metals of different component diffusivities via vacancy mechanism. It should be noted that the effect proposed can be operative not only for moving GB, but

also for motionless ones, if asymmetric alloy component profiles are formed near GB under irradiation. Such an asymmetry can be caused by the difference in alloy composition and/or microstructure. In this case a segregation-induced driving force for the GB migration originates.
The objective of this paper is the study of radiation induced segregation near moving GB in an irradiated Fe-Cr-Ni alloy and the estimation of an additive GB velocity arising due to Kirkendall effect.

Model description

A grain boundary is considered as a crystal plane moving with a given velocity v. It is supposed that the thermal equilibrium PD concentrations are maintained at the plane, which is assumed to be transparent to alloy component fluxes. The system of coordinates is rigidly linked to the moving GB. A computational cell of variable length with periodic boundary conditions is used.
A system of diffusion equations for component and PD concentrations near a moving GB in an irradiated ternary alloy has been formulated earlier in Ref. [7] (it can be also obtained from the set of equations formulated in Ref. [13] putting ξ=1). From various drift forces acting on PDs only Kirkendall ones are taken into account.

Modeling RIS near a moving GB in Fe-Cr-Ni alloys

Experimental data on GB migration velocities have been obtained in Ref. [12] for Fe-15.2Cr-20.1Ni alloy (wt.%) irradiated with electrons at 773 K at a dose rate of $5 \cdot 10^{-4}$ dpa/s. Modeling RIS of components near a GB moving with the velocity v_0=30 nm/dpa in this alloy was performed using experimental data by Rothman et al. [14], i.e. with only vacancy mechanism of RIS taken into account. By comparing the GB migration distances in stainless steels under neutron [10] and electron [15] irradiation one can conclude, that they are comparable at similar doses. The method proposed by Marwick [3] was used for SIB calculations.
In Fig.1 the calculated dependence of SIB on dose is shown. This dependence is nonmonotonic for the moving GB and reveals a maximum at about 1.6 dpa. The Ni and Cr profiles across GB at 1.6 dpa and at steady state are shown in Fig.2 and Fig.3. The origin of a SIB maximum is related to a "fast" RIS of components to GB from nearest-to-GB zones and setting steady-state profiles involves the whole cell considered (cell length L=2000 nm). It is seen that the dependence of SIB on dose is a convenient criterion of establishing the steady-state profiles.

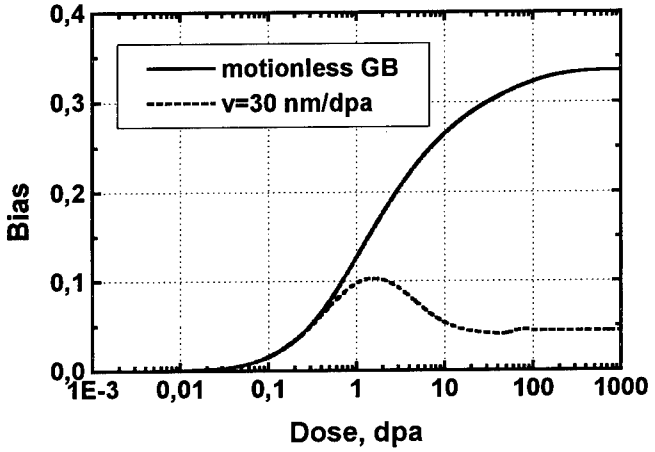

Fig. 1 Dose dependence of SIB for motionless and moving GBs in Fe-15.2Cr-20.1Ni (wt.%), K=5*10^{-4} dpa/s, T=773 K.

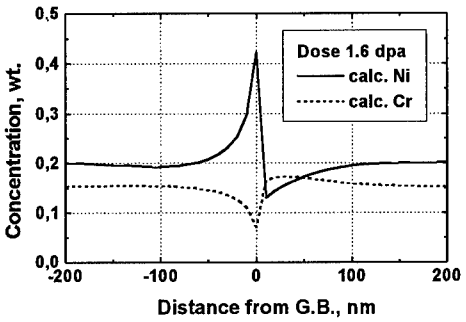

Fig.2. Calculated Ni and Cr profiles near a moving GB (v=30 nm/dpa) at 1.6 dpa.

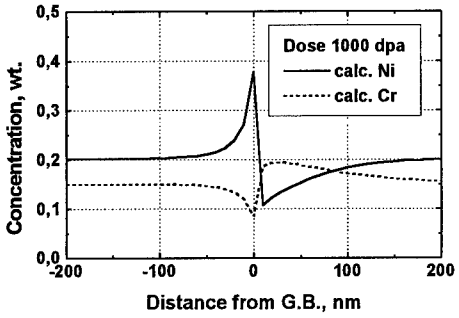

Fig.3. Steady-state Ni and Cr profiles near a moving GB (v=30 nm/dpa).

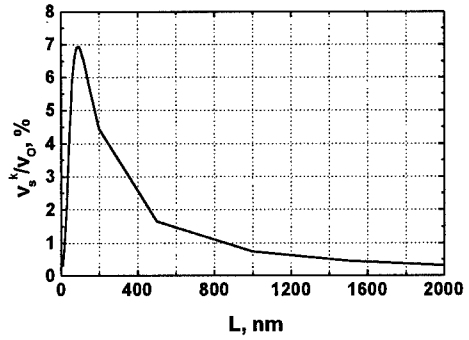

Fig.4. The dependence of relative GB Kirkendall velocity on the length of computational cell.

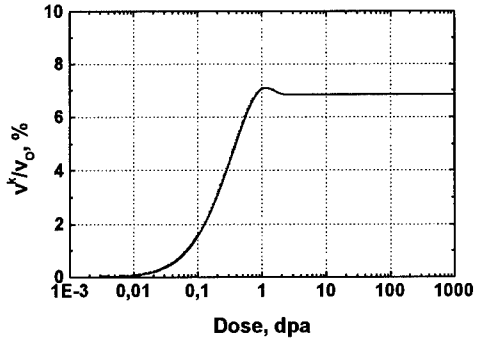

Fig.5. Dose dependence of relative GB Kirkendall velocity.

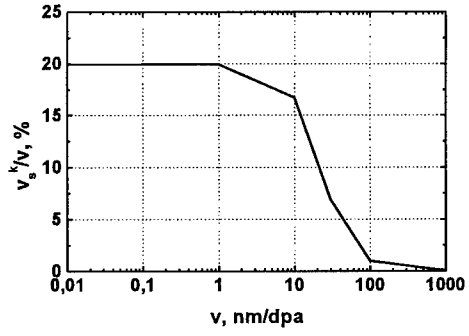

Fig.6. The dependence of relative GB Kirkendall velocity on GB velocity.

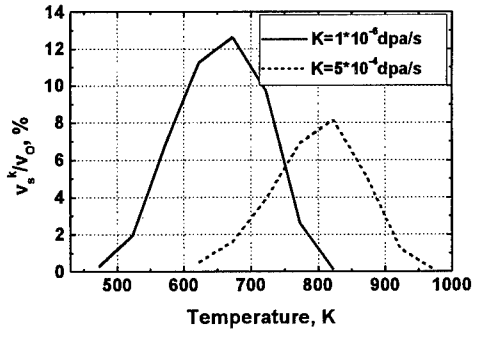

Fig.7. Temperature dependence of relative GB Kirkendall velocity for two different PD generation rates.

An additional GB velocity v^k arising due to Kirkendall effect (see Introduction) was calculated by estimating the extra interstitial flux to GB from the zone behind GB. Note, that this flux is equal to the extra vacancy flux to GB from the zone in front of GB. So, a material continuity near GB is conserved. The dependence of the steady-state relative Kirkendall velocity on the computational cell length L is shown in Fig. 4. It seen that a maximum is located at L=90 nm. The dependence of relative Kirkendall velocity on irradiation dose, GB velocity, temperature and generation rate are shown in Figs 5-7. As it follows from Fig.6, the steady-state relative Kirkendall velocity increases with decreasing GB velocity and reaches a constant value of 20% at low.
Thus, the Kirkendall effect can contribute significantly into the GB migration in irradiated Fe-Cr-Ni alloys.

Conclusions

Modeling the radiation-induced segregation of alloy components near moving grain boundary in a Fe-Cr-Ni alloy was carried out. It was shown that the dependence of segregation induced bias for GB on dose has a maximum at some intermediate dose. GB velocity can increase due to Kirkendall effect caused by the asymmetry of alloy component profiles across a moving GB.

Acknowledgements

This work was supported by Russian Foundation for Basic Research under Grant №98-02-17400.
The authors would like to thank Prof. Yu.V.Konobeev for useful discussion of the work.

References

[1] W.G. Wolfer, J. Nucl. Mater. 114(1983), p.292.
[2] C. Abromeit and G. Martin, ASTM STP 955, F.A. Garner, N.H. Packan and A.S. Kumar, Eds., American Society for Testing and Materials, Philadelphia, 1987, p.822.
[3] A.D. Marwick, J. Nucl. Mater. 135(1985), p.68.
[4] S.I. Golubov, Metallofisika 11(1989), p.10.
[5] V.A. Pechenkin and G.A. Epov, Alushta, USSR, 5(1990), p.104.
[6] V.A. Pechenkin and G.A. Epov, Metally 5(1996), p.87.
[7] V.A. Pechenkin, G.A. Epov, I.A. Stepanov and Yu.V. Konobeev, Abstracts of the 18th Int. Symp. On Effects of Radiation on Materials, Hyannis, June 27-29, 1996, p.72. To be published in ASTM STP 1325, 1997.
[8] Yu.V. Konobeev, V.A. Pechenkin and Rudnev, J. Nucl. Mater. 233-237(1996), p.1070.
[9] A.H. King, International Materials Review 32(1987), p.173.
[10] D.I.R. Norris, C. Baker, C. Taylor and J.M. Titchmarsh, ASTM STP 1125, R.E. Stoller, A.S. Kumar and D.S. Gelles, Eds., American Society for Testing and Materials, Philadelphia, 1992, p.603.
[11] S. Nakata and I. Masaoka, J. Nucl. Mater. 150(1987), p.186.
[12] S. Watanabe, N. Sakaguchi, N. Hashimoto, M. Nakamura, H. Takahashi, C. Namba and N.Q. Lam, J. Nucl. Mater. 232(1996), p.113.
[13] I.A. Stepanov and V.A. Pechenkin, these Proceedings..
[14] S.J. Rothman, L.J. Nowicki and G.E. Murch, J. of Physics F: Metal Physics 10(1980), p.383.
[15] H. Takahashi, N. Hashimoto and S. Watanabe, Ultramicroscopy 56(1994), p.193.

E-mail address: vap@ippe.rssi.ru

Materials Science Forum Vols. 294-296 (1999) pp. 779-782

Interfaces in Rapidly Solidified Zirconia-Yttria

T. Chraska and A.H. King

Department of Materials Science & Engineering, State University of New York at Stony Brook, Stony Brook NY 11794-2275, USA

Keywords: Rapid Solidification, Ceramic Coating, Columnar Grains, Nucleation, Cross-Sectional TEM, Amorphous Interface

Abstract. Rapidly spread and solidified molten droplets (splats) are basic building units of thermal-sprayed coatings. Various interfaces of zirconia-yttria (7%wt. yttria) single splats produced by atmospheric plasma spraying have been investigated using cross-sectional high-resolution transmission electron microscopy. The interface between the substrate and the rapidly solidified splats is of utmost importance for the adhesion of coatings formed by this method though other interfaces also have important effects. Melting and resolidification of the substrate are commonly observed as a result of rapid heat transfer from molten droplets. Possible formation of a thin interfacial layer between the substrate and the splat depends on the substrate material and its temperature. The interfacial layer may be either nanocrystalline or amorphous and is composed of both the substrate and splat material. "Bond coats" of NiCrAlY prevent the formation of this interfacial layer. Rapid solidification, together with good contact at the splat/substrate interface favors copious nucleation followed by growth of narrow columnar grains through the splat thickness, starting at the substrate interface. The zirconia grain width ranges from 30 to 100 nm, while their length is determined by the thickness of the solidified splat and is typically on the order of microns. Boundaries between the columnar grains are clean, without any second phases or amorphous regions, unlike the boundaries in conventionally prepared ceramic materials, although they are occasionally cracked. Growth of narrow columnar grains in splats solidifying on previous splats is very often epitaxial.

Introduction

Plasma-sprayed yttria stabilized zirconia (YSZ) with 6-8wt.% of yttria is considered to be the best thermal barrier coating material [1] for its low thermal conductivity, relatively high coefficient of thermal expansion, very good thermal shock resistance and superior mechanical stability in thermal cycling conditions [2]. In plasma spraying, powder is injected into a high temperature plasma jet and the molten powder particles are accelerated towards a prepared substrate. As the molten droplets impact on the substrate, they undergo rapid spreading and solidification. These solidified lamellae are called splats and are the basic building units of any thermal sprayed coating. To increase the adhesion and thermal compatibility of YSZ coating with a metal substrate, a metallic bonding layer (e.g. NiCrAlY) is usually applied by plasma spraying prior to the ceramic coating [3]. The interface between the bond coat and the ceramic coating plays a key role in determining the overall coatings adhesion. A thin amorphous layer is usually found at the splat/bond coat interface due to the high cooling rates [3-5]. Such a layer is detrimental to the ceramic coating adhesion [3,5]. The splat/splat interface and inherent porosity influence strength, toughness and thermal shock resistance of the whole coating.

Experimental

Yttria stabilized zirconia (YSZ - 7wt. % of Y_2O_3) powder with particle sizes between 10 and 62μm was plasma sprayed in air onto mirror polished stainless steel substrates preheated to approximately 500°C. Only one plasma-gun pass was performed to produce isolated single splats. Some of the substrates were covered with a polished layer of NiCrAlY bond coat, while the remainder were simply type 316 stainless steel.

Cross-sectional samples of YSZ single splats for TEM and HREM examination were prepared by mechanical polishing and ion milling. The mechanical wedge polishing technique employs so called "T-tool" (tripod-like) sample holder and is capable of attaining very small foil thickness so that the necessary ion-milling time is reduced to as little as 15 minutes. High-resolution electron microscopy (HREM) and transmission electron microscopy (TEM) images, and energy dispersive spectroscopy (EDS) investigations were performed on Phillips CM200 FEG and Phillips CM12 electron microscopes.

Results and Discussion

Substrate without bond coat. A typical cross-section bright field (BF) TEM image of a YSZ splat on a stainless steel substrate is shown in Figure 1. The width of narrow columnar grains ranges from 30 to 100nm and the length is almost 2μm. All the grain boundaries are fairly straight as the solidification proceeded in the direction of the heat flow; perpendicular to the substrate. Very good contact at the splat/substrate interface together with a large temperature difference favors copious nucleation at the interface followed by growth of narrow columnar grains through the splat thickness. The only phase detected in the coating is the nontransformable t′ tetragonal phase. At the splat/substrate interface (Fig. 2) we found a thin oxide layer that is composed of elements coming from both the ceramic splat (Zr) and the substrate (Cr, Fe) as determined by EDS. The 30 nm thick oxide interface is partially nanocrystalline and partially amorphous (Fig. 3). This oxide layer was created in two stages, first during the substrate preheating to approximately 500°C carried out in ambient atmosphere forming Cr_2O_3. When the first molten droplets impinge upon the substrate with the surface oxide layer, heat transfer from spreading splat is sufficient to melt the substrate and to enable diffusion of Zr cations into the oxide layer. The resolidified substrate grains (Fig. 2) have the very same composition as the rest of the substrate.

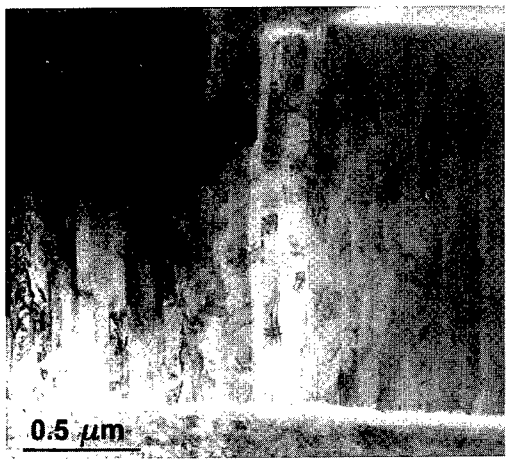

Fig. 1 Cross-sectional bright field TEM image of YSZ splat on stainless steel substrate.

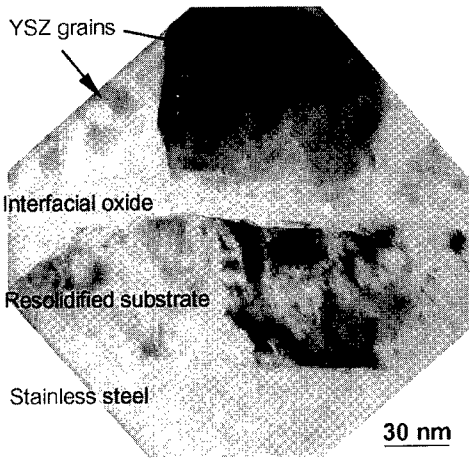

Fig. 2 BF TEM image of splat/substrate interface.

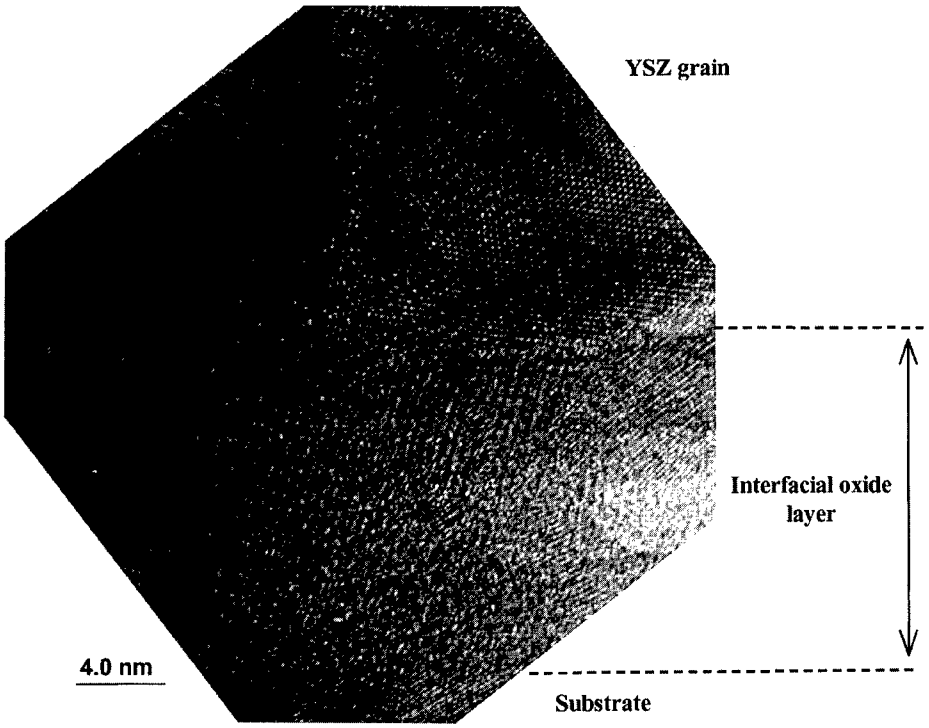

Fig. 3 HREM image of oxide interface layer between a stainless steel susbtrate and a YSZ splat.

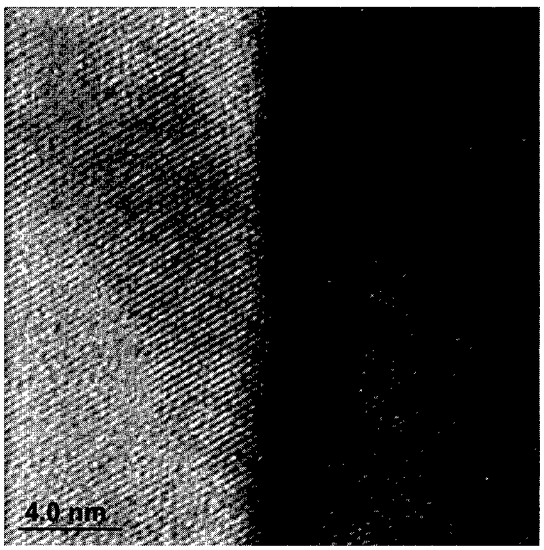

Fig. 4 HREM image of grain boundary between two columnar grains in a YSZ splat

A grain boundary between two columnar grains is shown in Figure 4. One can see that the atomic planes in the left grain extend to the right grain without any disruption so the boundary appears to sustain some form of lattice continuity. In general, the grain boundaries appear to be clean without any second phases or amorphous regions, unlike the boundaries in conventionally prepared ceramic materials. Harmsworth et al. [4], however, reported a glassy phase at the grain boundaries in splats located further away from the substrate. In our study, cooling rates in the substrate vicinity are high enough to prevent any segregation or diffusion. As the originally uniform splat cools down and shrinks in directions parallel to the substrate, cracks develop along some of the grain boundaries and the splat disintegrates into a number of smaller islands.

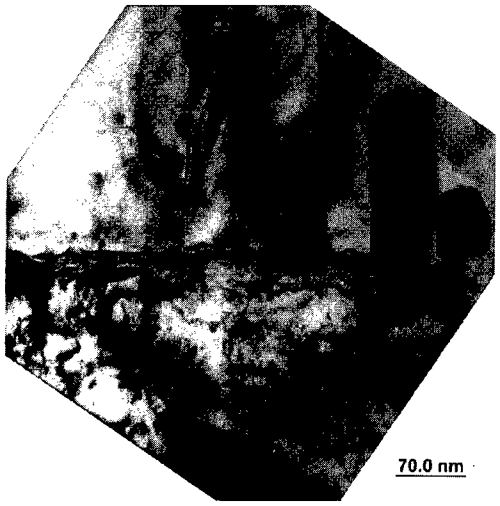

Fig. 5 BF TEM image of a ceramic/bond coat interface.

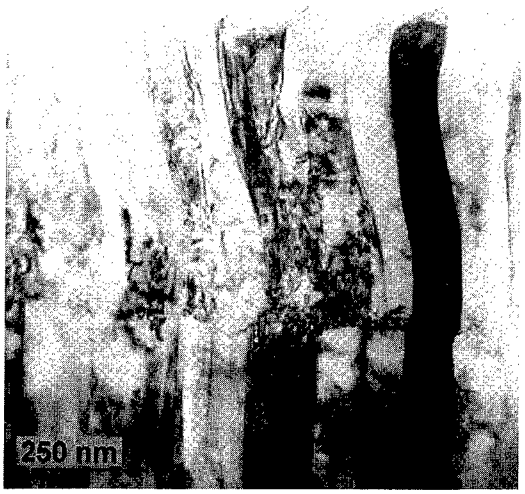

Fig. 6 BF TEM image of two YSZ splats in contact. The splat-splat interface is horizontal.

Substrate with the bond coat. A typical BF TEM image of the bond coat/ceramic interface is shown in Figure 5. In this case, no distinct oxide layer could be detected but only a thin region that is plastically deformed. This result is different from results in Ref. [3,4,5], where an amorphous oxide layer of up to 1μm thickness has been observed. The reason for the different result probably lies in the higher preheating temperature used here. The cooling rates at the interface are not high enough for the formation of an amorphous phase and copious nucleation may occur followed by grain growth. The grain width ranges from 50 to 150nm and the length is 1.5μm. When compared with the values from no-bond-coat splat, one can conclude that the individual columnar grains on the bond coat are wider and the whole splat is thinner. This suggests that the cooling rates in bond coat splat are lower due to the bond coat and its inherent porosity. The lower cooling rate leads to longer spreading times and fewer nucleation sites. The grain boundaries are again clean without any second phases or amorphous regions.

Splat/splat interface. An example of two splats in contact is shown in Figure 6. The columnar grains in the second splat are no longer as straight as in the first splat probably due to the slower cooling rate and the effect of liquid flow during solidification. Most of the columnar grains in the second splat have the same orientation as have the corresponding columnar grains in the bottom splat. This epitaxial growth is enabled by the fact that both splat impinge on the substrate within very short time period as only one plasma-gun pass was performed.

Acknowledgement: This work is performed within the Center for Thermal Spray Research funded by the U.S. National Science Foundation MRSEC Program, grant number DMR 9632570.

References

[1] J. R. Brandon, R. Taylor: Surf. Coat. Technol. Vol. 46 (1991), pp.75-90

[2] N. R. Shankar, H. Herman, S. P. Singhal, C. C. Berndt: Thin Sol. Films Vol. 119 (1984), pp. 159-171

[3] C. Bartuli, L. Bertamini, S. Matera, S. Sturlese: Mater. Sci. Eng. A Vol. 199 (1995), pp. 229-237

[4] P. D. Harmsworth, R. Stevens: J. Mater. Sci. Vol. 27 (1992), pp. 616-624

[5] M. Levit, S. Berger, I. Grimberg, B.-Z. Weiss: J. Mater. Synth. Processing Vol. 2 (1994), pp.11-27

Materials Science Forum Vols. 294-296 (1999) pp. 783-786

Microstructure of Epitaxial (InGa)As on a Borosilicate Glass-Bonded Compliant Substrate

S.E. Babcock[1], K.A. Dunn[1], M. Zhou[1], J.L. Reeves[1], T.F. Kuech[2], D.M. Hansen[2] and P.D. Moran[1,2]

[1] Materials Science and [2] Chemical Engineering, University of Wisconsin-Madison, Madison, WI, 53706 USA

Keywords: Compliant Substrate, CVD, (InGa)As, Wafer Bonded, TEM, SEM

ABSTRACT

A wafer bonding approach to fabrication of a universal compliant substrate for epitaxial growth of high-quality nitride and other materials is described. The compliant substrate consists of an approximately 10 nm thick GaAs template layer that is wafer-bonded to a 0.5 μm thick layer of borosilicate glass that was deposited on a GaAs handle wafer. To test the approach, ~ 2 μm thick films of $(In_{0.45}Ga_{0.55})As$ (3.1 % mismatch with GaAs) were deposited on the substrates. Orientation Imaging Microscopy of a sample cross-section showed that the $(In_{0.45}Ga_{0.55})As$ layer had the same crystallographic orientation throughout the 2 mm long section examined. These results demonstrate that the template layer is successfully transferred to the glass-coated handle wafer by wafer bonding and that epitaxial growth on the template is achieved. Diffraction contrast transmission electron microscopy (TEM) revealed a mismatch dislocation network at the (InGa)As/GaAs interface. The local dislocation spacing varied from place to place and was considerably larger (on the order of ~50-100 nm) than the computed value of about 8 nm. These results suggest that mechanisms of strain relaxation other than mismatch dislocation formation may occur in the compliant substrate.

INTRODUCTION

The lack of substrate materials with suitably matched lattice parameters remains a central issue in the growth of nitride and other compound semiconductor films. The critical thickness (predicted maximum thickness of a dislocation-free layer) is just a few atomic layers for many of these materials when they are grown on conventional (polished single crystal) substrates. However, if the substrate can be thinned to the order of its critical thickness, the strain-relieving dislocations can be forced into the substrate, allowing for growth of defect-free material on top. This concept underlies the various approaches to making compliant substrates that currently are under investigation in a number of different laboratories worldwide. Its implementation generally involves fabrication of a very thin (~ 10 nm or less) single crystal template layer which is supported by, but mechanically de-coupled from, a handle wafer through an intermediate "compliant" layer. Previous probes of the suitability of SiO_2 glass for the compliant layer indicated that the strain relaxation was limited by the high viscosity of the glass at typical growth temperatures [1-4]. The present work explores the use of lower viscosity borosilicate glasses (BSG) as the compliant bonding medium for a GaAs compliant substrate.

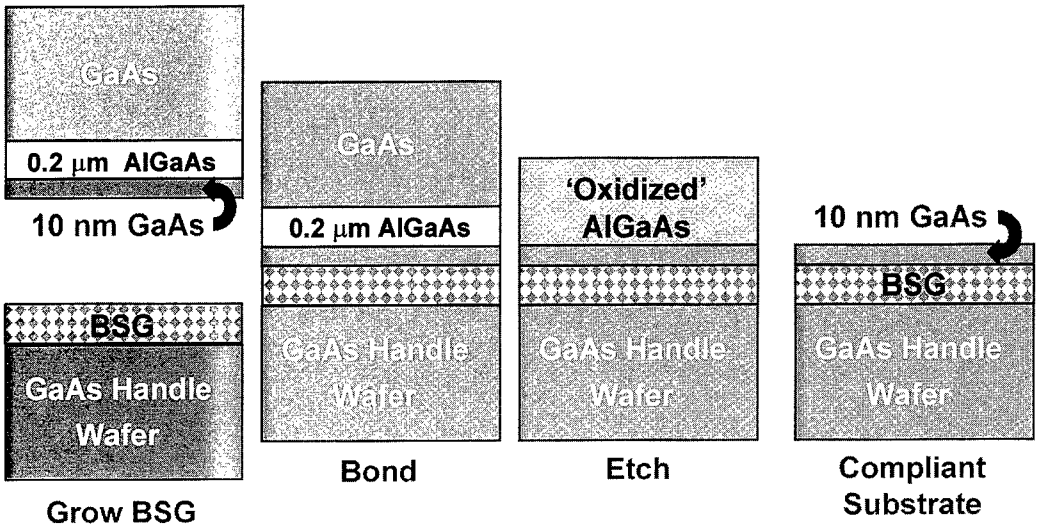

Figure 1: Layer structure and fabrication scheme for the compliant substrate.

EXPERIMENTAL

The layer structure and fabrication route of the BSG-bonded compliant substrate are illustrated in Fig. 1. A 10 nm thick GaAs layer is grown on top of an etch stop layer (250 nm $Al_{0.8}Ga_{0.2}As$) on a sacrificial GaAs handle wafer. This template layer is transferred, by wafer bonding, to the top surface of a 0.5 μm thick layer of borosilicate glass (BSG) on a GaAs handle wafer. The BSG layers were deposited in a conventional low-pressure chemical vapor deposition reactor operated at ~1 Torr pressure using tetraethylorthosilicate (TEOS) and trimethylborate (TMB) as the SiO_2 and B_2O_3 sources, respectively. Two different glass compositions, 30 and 50 mol % B_2O_3, were tested. O_2 was introduced into the reactor system in order to facilitate the incorporation of B_2O_3 [5]. After bonding, the sacrificial GaAs handle and the (AlGa)As etch stop layer were removed using a H_2O_2/NH_4OH solution with pH ≈ 8.4 and 10% HF, respectively. (InGa)As of nominal composition $In_{0.45}Ga_{0.55}As$ and 3.1% lattice mismatch to GaAs was grown on the resulting compliant substrate in a horizontal MOVPE reactor at 78 Torr and 650°C using trimethylgallium (TMGa), trimethylindium (TMIn) and AsH_3 as the precursors and purified hydrogen as the carrier gas. For comparison, (InGa)As was deposited simultaneously on (1) an epi-ready bulk GaAs substrate and (2) the etched surface of the "sacrificial" GaAs handle wafer (retained in this case) after the template and (AlGa)As layers had been removed with the same etching process as that used for the bonded structure. Cross-sectional scanning electron microscopy (SEM) and transmission electron microscopy (TEM) specimens were prepared using the tripod polishing method [6]. Plan view specimens were prepared by mechanical polishing and ion-milling from the handle wafer side.

RESULTS

Fig. 2 shows a secondary electron SEM image of the cross-section of the (InGa)As on compliant substrate for which the glass composition was 50 mol % B_2O_3. The thickness uniformity of the BSG layer and the quality of the bond are evident. The (InGa)As top surface is rough with a microstructure that is indicative of island growth. The template layer is not visible in this image. However, back-scattered electron Kikuchi patterns, from which the local (~ 0.1 μm) crystal orientation of the film and substrate can be determined, showed that the deposit has the same orientation everywhere along the ~ 2 mm long cross-sectional surface. The film also is

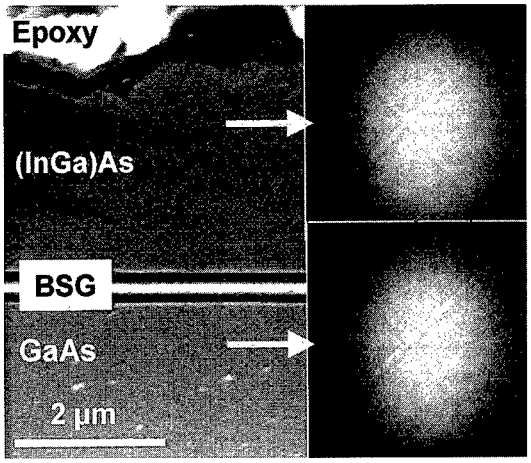

Fig. 2. High-resolution secondary electron SEM image of a polished cross-section of (InGa)As grown on the 50% BSG compliant substrate, showing both the surface and cross-sectional column topography.

crystallographically aligned with the GaAs handle wafer, as it should be for the bonding geometry used. These results show that the template layer is successfully transferred to the glass surface and that it is possible to achieve oriented grown on the chemically etched surface of the template layer.

Plan view secondary electron SEM images of the surface of this film and of the films grown on the epi-ready and etched bulk GaAs surface are shown in Fig. 3. The film grown on the epi-ready GaAs has a smoothness that is typical of this (InGa)As composition. The film grown on the compliant substrate is rough on a lateral scale of about 1 μm. The film grown on the etched GaAs surface is moderately smooth, but dotted with patches of rough material with a surface morphology that is similar to that of the film on the compliant substrate. These results suggest that the surface roughness may be caused by a residue, perhaps oxide, that is left on the GaAs surface after etching, or by some other surface defect that results from the etching process.

Fig. 4 shows plan view diffraction-contrast TEM images of the interface between the GaAs template and the (InGa)As deposit in the film grown on the 30% B_2O_3. Mismatch dislocations are observed in the interface. Patches of mismatch dislocations were observed throughout the electron transparent part of the TEM sample. As shown in Fig. 4., the average mismatch dislocation spacing varied from place to place by as much as a factor of 2. Furthermore, and perhaps more importantly, the measured mismatch dislocation spacing of 50 – 100 nm was considerably larger than the 8 nm spacing predicted for 60° ½<110>-type edge mismatch dislocations in a $(In_{0.45}Ga_{0.55})As/GaAs$ (001) interphase boundary. The increased dislocation spacing observed suggests that some of the mismatch strain might be accommodated by a mechanism other than dislocation formation. Thus, this result is consistent with partial compliance of the substrate.

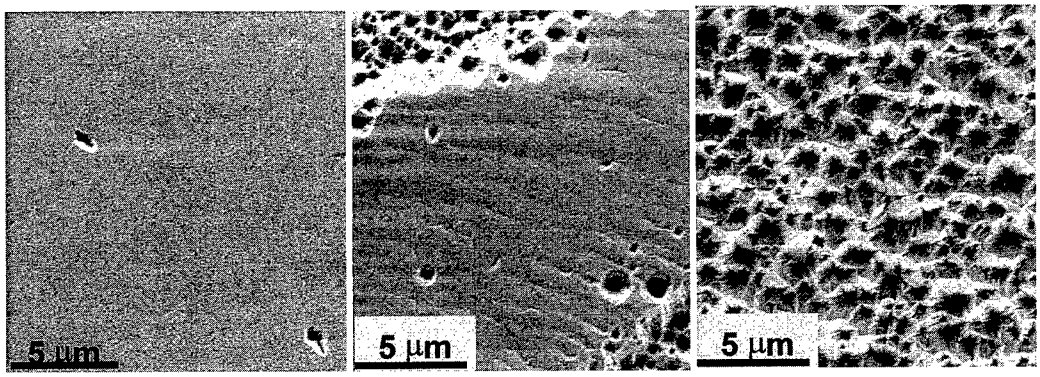

Fig 3: Secondary electron images of the surface of the (InGa)As grown on the epi-ready GaAs (left), etched surface of the "sacrificial" substrate (center), and the 50 mol% BSG (right).

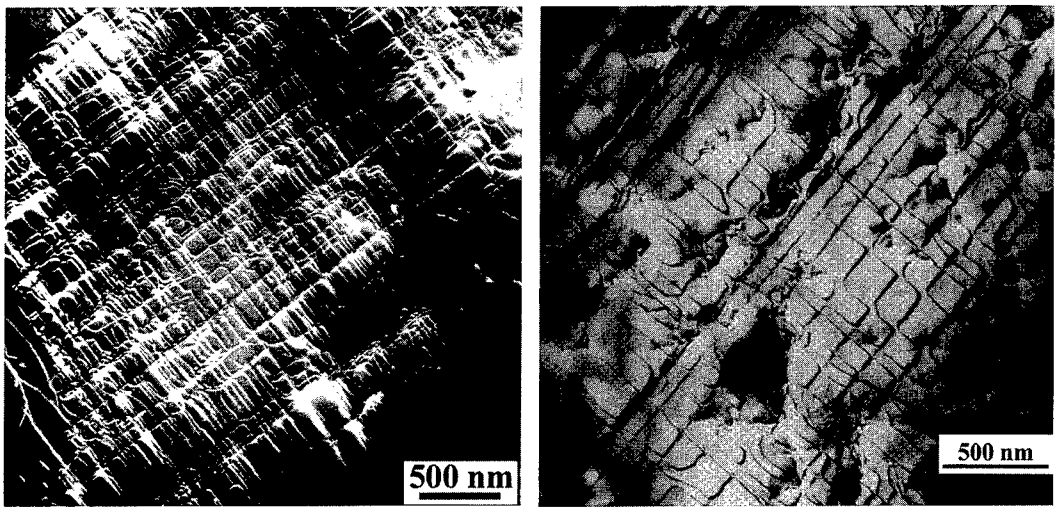

Figure 4: Diffraction contrast TEM images of the mismatch dislocation array at two different locations of the 30 mol % BSG compliant substrate.

CONCLUSIONS

Preliminary examination of a borosilicate glass bonded compliant substrate show that a thin template for epitaxial deposition can be bonded successfully to a BSG compliant layer and grown on. The microstructure of the deposit suggests that further development of the approach may lead to a fully compliant structure suitable for growth of compound semiconductors with large lattice mismatches to the template material.

ACKNOWLEDGEMENTS

This work is supported by the ONR MURI on Compliant Substrates at the University of Wisconsin-Madison. Partial support for electron microscopy facilities is provided by the NSF MRSEC on Nanostructured Materials at the University of Wisconsin-Madison.

REFERENCES

1. A.R. Powell, S.S. Iyer, and F.K. LeGoues, Appl. Phys. Lett. 64 (1994) p. 1865.
2. M.O. Tanner, M.A. Chu, K.L. Wang, M. Mushkinpour, and M.S. Goorsky, J. Cryst. Growth 157 (1995) p. 121.
3. F.J. Guaria, S.S. Iyer, Z. Yang, and W.I. Wang, Electrochem. Soc. Proc. 95-7 (1995) p. 561.
4. Z. Yang, F. Guarin, I.W. Tao, W.I. Wang, and S.S. Iyer, J. Vac. Sci. Technol. B 13 (1995) p.789.
5. D.S. Williams and E.A. Dein, J. Electrochem. Soc.: Solid-State Science and Technology 134 (1987) p.657.
6. J. Benedict, R. Anderson, and S.J. Klepeis, Specimen Preparation for Transmission Electron Microscopy of Materials III, Materials Research Society Symposium Proc. 254. (1992) p.121.

For correspondence (S.E. Babcock): babcock@engr.wisc.edu or Fax USA-608-263-1087

Materials Science Forum Vols. 294-296 (1999) pp. 787-790

The Grain Structure of Vacuum Arc Deposited Co Thin Films

B.B. Straumal[1,3], N.F. Vershinin[2], R. Dimitriou[3], W. Gust[1], T. Watanabe[4], Y. Igarashi[4] and X. Zhao[4,5]

[1] Institut für Metallkunde, Seestr. 75, D-70174 Stuttgart, Germany

[2] I.V.T. Ltd. (Institute for Vacuum Technology), P.O. Box 47, Moscow, RU-109180 Russia

[3] Institute of Solid State Physics, Chernogolovka, RU-142432 Russia

[4] Department of Machine Intelligence and Systems Engineering, Faculty of Engineering, Tohoku University, 980-77 Sendai, Japan

[5] School of Materials and Metallurgy, Northeastern University, Shenyang CN-110006, R. P. China

Keywords: Grain Structure, Vacuum Arc Deposition, Droplets, Co, Stable and Metastable Phases

ABSTRACT

Co layers on Si and NaCl substrates were produced with the aid of vacuum arc deposition and studied by transmission electron microscopy and electron back-scattering diffraction (EBSD). The vacuum arc deposited coatings are formed from a multiply charged ion flux and microparticles. The Co film formed from ions consists of a hexagonal close-packed phase and possesses a dense microstructure with uniform and extremely small grains (5 nm). The Co microparticles, which solidified after collision of liquid Co droplets with the substrate, have a metastable face-centred cubic structure. The EBSD method allowed one to resolve the thin semicircular grains having a size about 100 nm in the largest droplets.

INTRODUCTION

Vacuum arc deposition technology is important for the production of materials for construction and decoration. Vacuum arc deposited coatings possess high hardness and high wear and corrosion resistance. These properties depend critically on the phase and grain structure of the coating. In this process the vacuum arc discharges in the vapour of the cathode material [1]. A flux of the multiply charged ions and microdroplets form simultaneously. Both ions and microdroplets fly with a supersonic velocity towards the substrate forming the coating layer [2]. As a result, the conditions for the formation of the microstructure of vacuum arc deposited coatings are rather complicated. Even by magnetic filtering with the aid of a quarter-torus the microdroplets cannot be eliminated completely from the flux [3]. Usually, the presence of solidified microdroplets in the deposited film is not desired. However, for some applications the presence of microparticles can be useful, increasing the deposition rate and allowing one to produce the coatings of a controllable roughness [4]. One of the most important questions in the vacuum arc deposition technology is how the difference in the condensation conditions for individual ions and liquid droplets influences the phase and grain structure of the coating. In order to answer this question we investigated the microstructure of vacuum arc deposited Co layers. Co has two allotropic modifications. Above 422°C the face-centred cubic (fcc) structure is stable. Below 422°C Co has a hexagonal close-packed (hcp) structure [5]. During solidification from the melt it is easy to undercool bulk samples of Co and Co alloys such that the fcc phase is stable at room temperature.

Therefore, we can expect that the different condensation conditions for ions and liquid droplets can result in a mixed phase structure in the coating.

EXPERIMENTAL

The vacuum arc apparatus used in this work consists of a vacuum chamber having the form of a horizontal cylinder of 700 mm diameter and 700 mm length [6]. Its pumping system consists of a Balzers turbomolecular pump with a capacity of 1500 ℓ/s and two rotary pumps with a total capacity of 40 ℓ/s. A base pressure of $6 \cdot 10^{-5}$ Pa was achieved before deposition. The pressure during deposition was $8 \cdot 10^{-4}$ Pa. The vacuum arc apparatus with the system for spot stabilization and the Co cathode are placed on the end of the cylinder, . The cathode of diameter D = 60 mm was made from Co of 99.95% purity. The facilities for magnetic filtering of the microparticles were not used in this work. The material of the anode was not consumed in the arc process. The substrates (freshly cleaved NaCl and single crystalline Si) were placed at distances of L = 175, 300 and 425 mm from the surface of the cathode. The surface of the substrates was perpendicular to the surface of the cathode. The vacuum arc source voltage was maintained constant at U = 19 V, with a discharge current I = 120 A. No bias was applied to the substrates. The coating time t was the same for all samples t = 200 s. For the transmission electron microscopy (TEM), the cobalt films were stripped from their NaCl substrates and supported on a copper grid. TEM was performed using a cold field emission instrument (HF-2000, Hitachi Ltd.) equipped with an energy dispersion X-ray analysis system (Noran Instrument Inc.). The interplanar spacings were calculated from the measured diameter of the diffraction rings, using gold thin films as a reference substance to determine the camera constant. The electron back-scattering diffraction (EBSD) method has been used by us in order to determine the orientation of individual grains in the large microparticles formed in the Co coating. The EBSD method permits one to see the microstructure of the sample and to determine the orientation of the individual grains in the same experiment. Therefore, many grains can be analysed and an overall picture of the misorientation distribution can be obtained. The EBSD patterns were measured with the aid of Hitachi S-4200 instrument. The same instrument was used for the scanning electron microscopy (SEM) of the films. The spatial resolution of this instrument in the EBSD regime is about 100 nm. We have determined the orientation of the individual grains using the integrated software package for the semi-automated fit procedure for the indexing of the EBSD patterns.

RESULTS AND DISCUSSION

Figure 1 displays the microstructure of the Co coatings for L = 175, 300 and 425 mm deposited onto Si substrate. Both droplets and the homogeneous film formed by deposition of individual ions are clearly

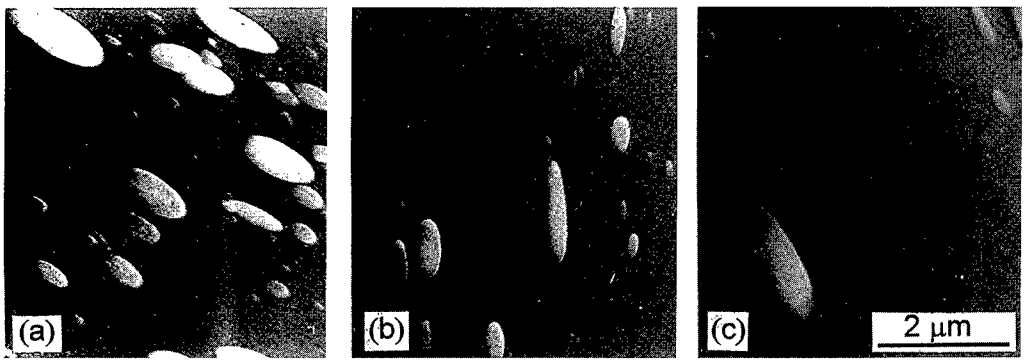

Fig. 1. SEM micrographs of the vacuum arc deposited Co layers on Si substrate at various distances L between the cathode and the substrate. I = 120 A, t = 200 s. L = 175 (**a**), 300 (**b**) and 425 mm (**c**).

seen in the micrographs. The electron diffraction patterns (EDP) from the film between particles reveal that the film is crystalline [7]. The comparison of the data for the interplanar spacings d measured from the EDPs with the tabular data for the fcc and hcp phases of Co shows that all diffraction rings present in a pattern can be identified as resulting from diffraction from the hcp phase. Some of the rings can result both from fcc and hcp phase, but no rings coming only from fcc phase are present [7]. Therefore, the deposition of individual Co ions on the substrate kept at room temperature leads to the formation of a film having a hcp structure which is thermodynamically stable below 422°C. A high magnification bright field TEM micrograph (not shown) reveals that the film between the particles is dense and uniformly thick [7]. The grain structure is uniform and the mean grain size is very small, about 5 nm.

The substrates were positioned perpendicular to the cathode surface. Therefore, the particles are elongated in the direction parallel to the axis of the vacuum chamber. The length-to-width ratio (aspect ratio) increases with increasing L from 2.2 (L = 175 mm) to 3.2 (L = 425 mm). The mean length a increases from 0.88 μm (L = 175 mm) to 0.99 μm (L = 425 mm). The mean width b decreases from 0.38 μm (L = 175 mm) to 0.29 μm (L = 425 mm). The fraction of substrate area covered by particles $\Sigma S_p/S_t$ decreases with increasing L (Fig. 2). Therefore, the particles gradually disappear from the flux by flying from the cathode. By collision with the substrate, the liquid microdroplets spread over the surface and solidify in a process analogous to the "splat cooling". As a result, the solidified microparticles are rather flat. Their height can be estimated from the SEM picture (Fig. 4) made for the EBSD measurements under a low incidence angle (about 20°). The EBSD pattern for the individual grain in a flat solidified Co droplet is shown in Fig. 3 together with the results of the identification of the crystallographic orientation. It was possible to resolve the individual grains with the aid of EBSD only for the biggest droplets, having a length and width about 10 to 20 times larger than the coresponding mean values a and b . Figure 4 represents such a droplet. The cross marks the position for the pattern represented in Fig. 3. Figure 5 displays the grain chart constructed with the aid of the EBSD data. The area represented in Fig. 5 is marked with a rectangle on the micrograph (Fig. 4). The patterns analogous to Fig. 3 were measured with a step of 100 nm. Each point in Fig. 5 represents one measurement. For each pair of neighbouring points the mutual misorientation was calculated. Two points were identified as belonging to different grains if their misorientation was above 3°. The smaller misorientation differences are represented in Fig. 5 as variations of the grey scale. The grains in the droplet have a semicircular form reproducing the outer form of the droplet. They can represent the solidification steps after the collision of the droplet with the substrate.

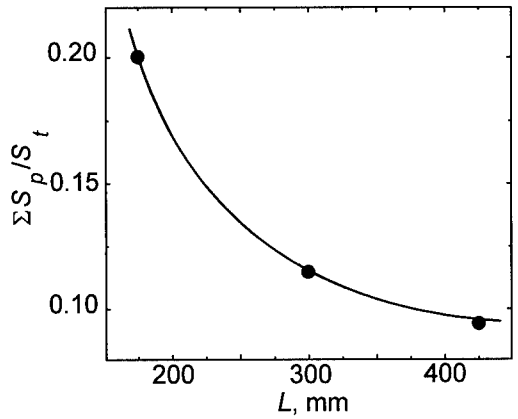

Fig. 2. The dependence of the fraction of the substrate area covered by particles $\Sigma S_p/S_t$ on L

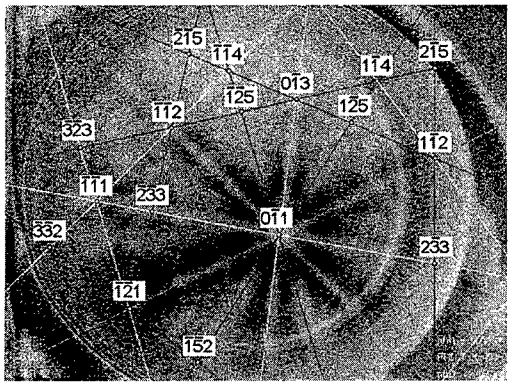

Fig. 3. EBSD pattern for the individual Co grain marked by a cross in the Fig. 4

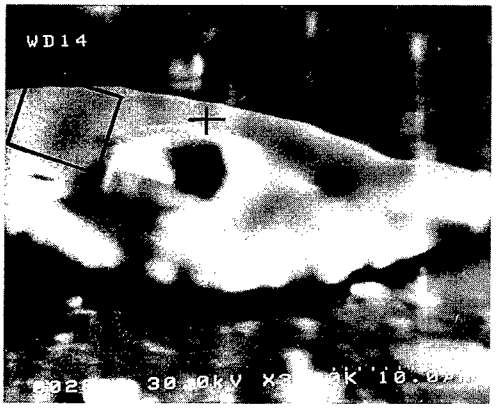

Fig. 4. SEM micrograph under a low incidence angle showing the analyzed Co microparticle

Fig. 5. Grain structure of the rectangle marked in Fig. 4 revealed with the aid of EBSD

Recently, it was shown that the smallest droplets are an integral part of a vacuum arc deposited coating having the same grain structure as the surrounding film [8]. Here another extreme case was analysed. The biggest droplets in a Co coating, possessing rather large fcc grains, are surrounded by nanosized grains of the film having a hcp structure. These data show that the question of the integrity of the grain structure of the medium-sized droplets in vacuum arc deposited coatings should be carefully studied.

ACKNOWLEDGEMENTS

This work has been partially supported by the INTAS programme (under contract 93-1451), NATO linkage grant HTECH.LG.970342, INCO-COPERNICUS Network PL978089, PECHINEY Corporation and Heiwa Nakajima Foundation. We thank Dr. V. Sursaeva, Dr. M. Benmalek and Dr. J. Bouvaist for helpful discussions.

REFERENCES

[1] R. L. Boxman, P. J. Martin and D. M. Sanders (eds.), Handbook of Vacuum Arc Science and Technology, Noyes Publications, Park Ridge, NJ (1995) p. 367.
[2] J. E. Daadler, J. Phys. D 9 (1976) p. 2379.
[3] M. Keidar, I. I. Beilis, R. Aharonov, D. Arbilly, R. L. Boxman, and S. Glodsmith, J. Phys. D, 30 (1997) p. 2972.
[4] B. Straumal, N. Vershinin, V. Semenov, V. Sursaeva, and W. Gust, Defect Diff. Forum 143–147 (1997) p. 1637.
[5] CRC Handbook of Chemistry and Physics, D. R. Lide (ed.), CRC Press, Boca Raton, FL (1995) p. 12.
[6] B. B. Straumal, W. Gust, N. F. Vershinin, V. G. Glebovsky, H. Brongersma, and R. Faulkner. Nuclear Instr. & Methods in Physics Res. B. 122 (1997) p. 594.
[7] B. B. Straumal, W. Gust, N. F. Vershinin, T. Watanabe, Y. Igarashi, and X. Zhao, Thin Solid Films 319 (1998) p. 127.
[8] B.Straumal, N.Vershinin, V.Semenov, V.Sursaeva, W.Gust, Defect Diff. Forum 143–147 (1997) p. 1637.

Corresponding author: D. Sc. Boris Straumal, e-mail straumal@issp.ac.ru and straumal@song.ru
web site http://www.issp.ac.ru/libm/straumal, fax +7 095 238 23 26 or +7 095 111 70 67

Materials Science Forum Vols. 294-296 (1999) pp. 791-794

Impurity Segregation and Intergranular Fractures in Continuously Cast Steel Products

M. Longauerová

Department of Materials Science, Metallurgical Faculty, Technical University of Košice, Park Komenského 11, SK-04200 Košice, Slovakia

Keywords: Low Carbon Steel, Impurity, Tin, Continuously Cast Slab, Nonequilibrium Microsegregation, Macrosegregation, Microstructure, Fractures, Intergranular Fracture

Abstract

The effect of impurity segregation, mostly Sn on the structure and the fracture surface morphology is investigated for surface zone samples of continuously cast steel slab after impact bending test. Low carbon steel with initial low level of impurities and same steel enriched by 0,134%Sn continuously casted on curve type plant were analysed. The results show, in the slab enriched by Sn, there was high enrichment by Sn of the subsurface region measured up to 0,42% Sn. Therefore, Sn affected failure of slab surface zone by formation of the intergranular fracture due to segregation of Sn and other present impurities on austenite grain boundaries. The mechanisms that might determine concentration profiles of Sn and other impurities are discussed.

Introduction

The segregation processes in steels are occuring during all steps of processing from crystallisation to final product. During the continuous casting of steel products, impurity segregation can occur during solidification or in solid state, too. For the quality control of continuous cast steel slabs, it is very important to understand the microsegregation and macrosegregation processes of impurities during solidification, due to the detrimental effect of impurities causing hot shortness. According to the latest reports the hot shortness is influenced not only by usual impurities, as Cu, S, P[1-2], but also by surface active elements, as Sb, Sn, As, Bi [3-7]. The effect of the last mentioned on the fractures of the continuous cast steel products and the knowledge of their distribution along the slab is not well known yet.

The aim of the present paper is to investigate the impurity distribution profiles across the slab thickness of low carbon steel enriched by Sn and effect of Sn segregation on the microstructure and the fractures for samples of the surface zone of continuously cast slab after impact bending test.

Experimental materials and methods

Two types of low carbon steels were analyzed continuously casted on the curved type plant. The initial steel No.1 contained low level of the impurities. The steel labeled No.2 was enriched by the addition of metallic Sn at the end of melting in the intermediate ladle. The chemical composition of the samples is given in Table 1.

Table 1

Steel No.	C (%)	Mn (%)	Si (%)	P (%)	S (%)	Al (%)	N (%)	Cu (%)	Sn (%)	Sb (%)	As (%)
1	0,06	0,32	0,06	0,017	0,01	0,07	0,0080	0,033	0,0065	0.0022	0,0117
2	0,09	0,31	0,05	0,009	0,016	0,071	0,0083	0,078	0,1340	0,0058	0,0038

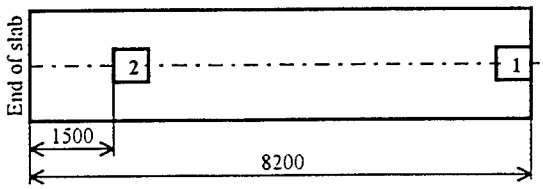

Fig.1 The sampling position on the slab (in mm)

The steels were bubled through in intermediate ladle by nitrogen gas. The cooling in the secondary cooling zone of continuous casting plant was simple (water). The casting temperature was 1575°C and the rate of slab pulling out was 0,8 m/min. The dimensions of the analysed slab were: width 1040 mm, thickness 200 mm. We investigated samples from the slab width in the center, Fig.1.

The impurity concentration was determined across the slab thickness in distance 1, 2, 4, 6, 7, 10, 20, 40, 70, 100 mm from its upper surface. Specimens for chemical analysis were taken from samples by stepwise machining the surface, or by drilling 5 mm diameter holes 20mm deep. The content of basic elements was determined by usual chemical analyses, the content of nitrogen using LECO. The concentration of surface active elements and Cu was analysed by atomic absorption spectrometry. The dendritic and the secondary structures were observed in longitudinal sections, in the direction of pulling out, from the upper surface zone of the slab using the light microscopy. From surface layers of slabs the flat samples 5x10x55mm were cut out parallel with drawing direction, which were then fractured by Charpy impact bending test at +20°C. The fractures were observed by a scanning electron microscopy (SEM) and for the local microanalysis on the fractures the energy-dispersive X-ray spectroscopy (EDX) as well as AES analysis were used.

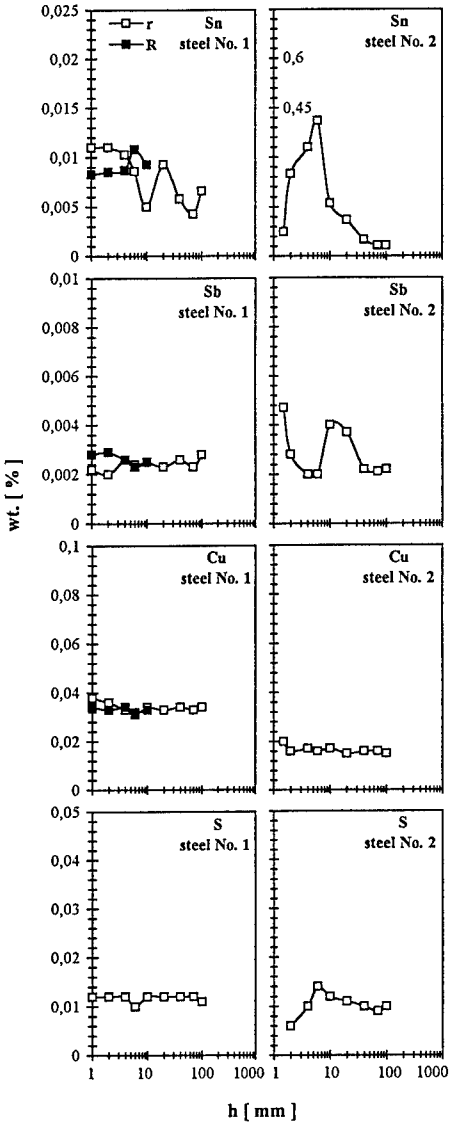

Fig.2 The change of concentration of Sn,Sb, Cu and S across the slab thickness

Results and discussion

The change of surface active elements concentration Sn, Sb and also usual impurities, such as Cu, S is shown in Fig.2 for all analysed samples. The concentration profile starts from the upper slab surface in the direction to the central zone. The most significant Sn enrichment of the surface zone was shown for sample No.2 with the highest mean content, i.e. 0,134%Sn. A concentration maximum was observed at a subsurface region in depth approximately of 6 mm with 0,45% Sn. The slight surface enrichment by Sn was shown at the material No.1 with low initial mean concentration

of Sn and other residual impurities. As can be seen in Fig.2 for steels No.1,2 the segregation of the other impurities is influenced by the addition of Sn. In the initial material No.1 with only trace content of Sn, there is a very small change of concentration of the other elements through the slab thickness (there is a mild surface enrichment by Cu and S). The high Sn content (steel No.2) drives the segregation activity of the other impurities, even at their very low or trace mean content. The surface active element Sb and also Cu at low content segregate first to the the slab surface. S has a tendency to segregate both into the body of the slab and also to the surface.

The observed macroscopic changes in the impurity content in the direction from the surface to the center of the slab are the result of microsegregation. They work as dendritic segregation and the solid state segregation. The crystallisation at the continuous casting is much faster than it was with the old casting methods. Due to this a larger portion of impurities is trapped in the solid solution during dendritic solidification. First the surface active elements with a higher coefficient of equilibrium will be in the solid solution, such as the analysed Sn with k_o=0,23 [8,9] and Sb with k_o=0,31 [8,9]. The surface active elements can then segregate to the austenite grain boundaries or to the free surfaces of the slab, or to the interface of very different structure zones as are interfaces between fine grained surface skin and the zone of columnar dendrites. We suppose this segregation in solid solution starts at the change of cooling rate, as the slab enters into the secondary cooling segment.Therefore, such impurity microsegregation in solid solution is nonequilibrium and is based on segregation induced by both faster cooling and stress. The stress-induced segregation is caused by some deformation of solid.

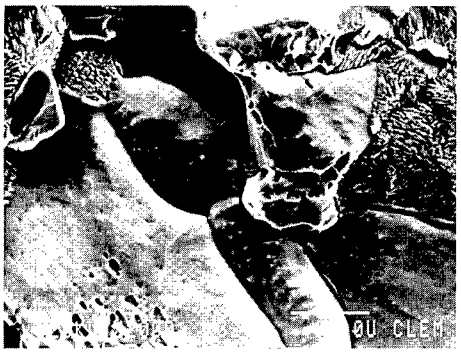

Fig.3 The intergranular fractures with smooth facets

Fig.4 The intergranular smooth fracture, additionally deformed

The results obtained for the concentration profiles support the assumption. Moreover, the diffusion coefficient for Sn is large; D_{Sn} in γFe, for example, at 1100°C is $1{,}9\times10^{-14}$ m^2/s [10] and D_{Sn} for αFe is still larger, that is $7{,}9\times10^{-13}$ m^2/s [10]. In addition, for Fe-Sn binary system, the solubility limit of Sn in αFe is about 16% at 1100°C, as reported in [11]. Therefore, even if Sn is enriched under the steel surface and the Sn enriched regions transform into α phase, liquid Sn-Fe alloys will not form.

The finest feritic microstructure occurs in the surface skin of steel No.2 with the high mean content of Sn. This is considered to be associated with the influence of large number of Sn atoms on grain nucleation. The distance (6mm), where the Sn concentration peak at the slab surface zone occurs, approximately corresponds to the onset of columnar zone, firstly in steel No.2. The skin structure of steel No.1 with a low initial concentration of Sn and other impurities, is heterogeneous. There is ferrite, not only in the form of equiaxed grains, but also acicular.

The fractures of the samples No.1 with the low mean Sn content from the slab surface zone showed transcrystalline cleavage facets, small fraction of transgranular fractures with dimples and a few intergranular facets. With the increase of the mean Sn concentration (sample No.2) there was a slight increase of intergranular facets. The cleavage facets revealed river structure and had different sizes. Although surface skin was extremely enriched by Sn, fracture surfaces contained only small total volume of intergranular facets probably thanks to low C content. The intergranular fractures were smooth with different defects, such as pores, dimples, particles, Fig.3. Also some intergranular smooth fractures were seen, additionally deformed, Fig.4. The other types of fracture morphology seen, were the conchoidal type intergranular facets with a dimpled morphology, Fig.5. The dimples were very shallow, in them, particles seen sometimes. The large intergranular dimpled fractures are initiated first on interfaces of fine grained skin and the zone of columnar dendrites where the concentration maximum of tin and other impurities exist. The presence of the Sn in intergranular fractures was confirmed by EDX as well as by Auger electron spectroscopy [12]. This suggests the weakening of the austenite grain boundary cohesion at high temperatures caused by the microsegregation of detrimental impurities, mainly by Sn.

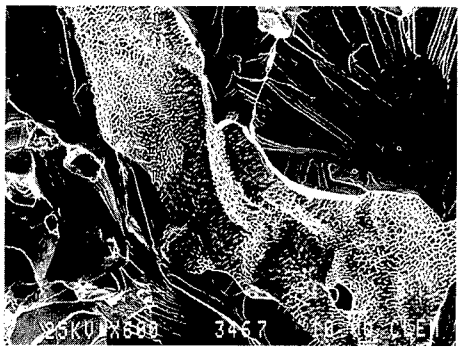

Fig.5 The conchoidal type intergranular facets with dimples

Conclusion

The impurity concentration profiles in the direction from the surface to the center of the low carbon steel slab and effect of tin segregation on the structure and the fracture morphology for the slab surface zone were investigated. Mechanisms of impurity microsegregation as well as macrosegregation during solidification of continuously cast steel slab have been discussed.
It was shown that Sn affected failure in the surface zone of slab by formation of the intergranular fracture due to segregation of Sn and other present impurities on austenite grain boundaries.

Acknowledgement

The presented work has been supported by the Scientific Grant Agency of the Slovak Republic as Grant Project No.10203/95.

References

[1] Brimacombe,J.K.-Sorimachi,K.: Met. Trans.B, 8B, 1977, 489
[2] Wolf,M.: Trans. ISIJ, 24, 1984, 351
[3] Pavlovič,P.-Mamuzič,I.: Freiberger Forsh. H. B193, VEB Grundstoffind, Leipzig, 1977, 25
[4] Nachtrab,W.T.-Chou,Y.T.: Met. Trans. A, 19A, 5, 1988, 1305
[5] Wolf,M.M.: Ironmaking and Steelmaking, 12, 1982, 299
[6] Suzuki,G. et al.: Trans. ISIJ, 22, 1982, 48
[7] Longauerová,M.-Sladík,Š.-Longauer,S.: Trans. of the Techn. Univer. of Košice, 3(4), 1993,341
[8] Barthel,J.-Buhrig,E.-Hein,K.-Kuchař,L.: Kristallisation aus Schmelzen. Leipzig, VEB Deutscher Verlag für Grundstoffindustrie 1983, 344
[9] Kuchař,L.-Repiská,L.-Komorová,Ľ.-Baffyová,Z.: Sbor. věd. prací VŠB Ostrava, 26, 1980, 119,
[10] Oikawa,H: Tetsu-to-Hagané, 68, 1982, 1489
[11] Imai,N.-Komatsubara,N.-Kunishige,K.: ISIJ International, Vol.37, 3, 1997, 217
[12] Longauerová,M.: Kovové materiály, 36,2, 1998,70

AUTHOR INDEX

KEYWORD INDEX

Still available

Intergranular and Interphase Boundaries in Materials: iib92

Eds. Ph. Komninou and A. Rocher

Proceedings of the 6th International Conference on Intergranular and Interphase Boundaries in Materials (iib 92) held in Thessaloniki, Greece, 1992

Materials Science Forum Vols. 126-128

ISBN 0-87849-660-2
1993, 878 pp, CHF 325.00 / US$ 270.00

The review and research papers presented in this volume may be subdivided into three aims:

(i) the investigation and modelling of interfacial structure (ii) efforts to correlate structure/property relationships and (iii) phenomenological descriptions of particular interfacial properties The conference focussed on four objectives: 1.Grain Boundaries Structure and Properties 2.Dynamical and Mechanical Properties 3.Heterophase Interfaces 4.Electrical Properties and Superconductors.

Contents Sections:

Trans Tech Publications Ltd

Brandrain 6
CH-8707 Uetikon-Zuerich
Switzerland

Fax: +41 (1) 922 10 33
e-mail: ttp@ttp.net
Web: http://www.ttp.net

Still available

Intergranular and Interphase Boundaries in Materials: iib95

Eds. A.C. Ferro, J.P. Conde and M.A. Fortes

Proc. 7th Intl. Conf. on Intergranular and Interphase Boundaries in Materials held in Lisboa, Portugal, June 1995

Materials Science Forum Vols. 207-209

ISBN 0-87849-722-6
1996, 920 pp, 2-Vol. Set, CHF 340.00 / US$ 283.00

The current publication focuses on the structural and chemical characterization of interfaces and their kinetic, mechanical and electrical properties. The size of the volume, consisting of almost 200 papers, with more than 900 pages, reflects the present interest in the field.

The papers presented cover wide variety of interfacial systems. The structural and chemical characterization of interfaces concentrated on combined experimental and theoretical studies of the local atomic structure, and local densities of electronic states. Techniques with very high spatial resolution were used in these studies. In general, it is found that a certain maturity of the subject is being attained in that theories are presented to pull the many strands of experimental observations together, to bring coherence and depth of understanding to the subject. Other papers are concerned with the vexing question of relating the properties of individual grain boundaries to the properties of polycrystals as a whole. With these advances the engineering of interfaces to design materials with required properties is becoming an increasingly attainable goal.

Intergranular and Interphase Boundaries in Materials is intended to promote both a better scientific understanding of interfaces and grain boundaries in materials and improvements in the technologies which utilize materials where properties are controlled by interfaces.

Trans Tech Publications Ltd

Brandrain 6
CH-8707 Uetikon-Zuerich
Switzerland

Fax: +41 (1) 922 10 33
e-mail: ttp@ttp.net
Web: http://www.ttp.net

Materials Science Forum

ISSN 0255-5476

As of January 1992 combined with Crystal Properties and Preparation

Editors, Editorial and Advisory Board

see front inside cover

Publication Manager

Hans Neber-Aeschbacher
Trans Tech Publications Ltd, Anton Graff-Str. 6, CH-8400 Winterthur, Switzerland
Fax +41 (52) 204 07 11, e-mail: h.neber-aeschbacher@ttp.net

Scope

Materials Science Forum specializes in the rapid publication of international conference proceedings in every area of Materials Science, Solid State Physics and Chemistry. This permits such proceedings to be conveniently referenced, abstracted and read. It also guarantees that the proceedings are available in major libraries within two to three months of the close of the conference.

Materials Science Forum also publishes, on a regular basis, collections of research and review papers on topics of current interest. Abstracted in all of the major abstract media, and available in practically all of the major libraries which service materials research communities, *Materials Science Forum* offers both very rapid publication (within two months of acceptance of the manuscript) and high visibility.

Internet

The table of contents of each volume is available on the World Wide Web at http://www.ttp.net.

Preview Service

Trans Tech Publications' Preview Service offers automatic delivery of tables of contents via e-mail - several weeks before the actual release of the respective publication. This service is free of charge. For more information, please visit our home page or send an e-mail to preview@ttp.ch containing simply the word *help* as the message body.

Subscription Information

Materials Science Forum is published in 30 volumes per year. In 1999, volumes 293-322 are scheduled to be published. The subscription rate is CHF 99.50 per volume (CHF 2985.00 per year).

Standing orders

Standing Orders are available for the following topical areas of interest: Pt. A: Electronic and Electro-optic Materials; Pt. B: Metal Physics; Pt. C: Ceramic Materials and Glasses; Pt. D: Ionic Materials, Oxides; Pt. E: Corrosion and Oxidation; Pt. F: Surfaces, Interfaces and Thin Films; Pt. G: Crystal Growth and Crystal Structures.

Standing orders for one or more of these sections may be placed: the topics are not meant to be exclusive, i.e. a given volume can be assigned to two or more of these sections. Should a title be assigned to more than one section, the subscriber will receive the respective title only once. The price per volume is CHF 99.50.

Trans Tech Publications Ltd
Brandrain 6 • CH-8707 Uetikon-Zuerich • Switzerland
Fax +41 (1) 922 10 33 • e-mail: ttp@ttp.net
http://www.ttp.net